

3

NASA Conference Publication 2210
AVRADCOM Technical Report 82-C-16

ADA 126186

Advanced Power Transmission Technology

DTIC FILE COPY

DTIC
ELECTE
S MAR 29 1983
D

*Proceedings of a symposium held at
NASA Lewis Research Center
Cleveland, Ohio
June 9-11, 1981*



NASA

88 03 28 067

COMPONENT PART NOTICE

THIS PAPER IS A COMPONENT PART OF THE FOLLOWING COMPILATION REPORT:

(TITLE): Advanced Power Transmission Technology, Proceedings of a Symposium Held at
NASA Lewis Research Center, Cleveland, Ohio on June 9-11, 1981.

(SOURCE): National Aeronautics and Space Administration, Cleveland, OH.
Lewis Research Center

TO ORDER THE COMPLETE COMPILATION REPORT USE AD-A126 186.

THE COMPONENT PART IS PROVIDED HERE TO ALLOW USERS ACCESS TO INDIVIDUALLY
AUTHORED SECTIONS OF PROCEEDINGS, ANNALS, SYMPOSIA, ETC. HOWEVER, THE
COMPONENT SHOULD BE CONSIDERED WITHIN THE CONTEXT OF THE OVERALL COMPILATION
REPORT AND NOT AS A STAND-ALONE TECHNICAL REPORT.

THE FOLLOWING COMPONENT PART NUMBERS COMPRISE THE COMPILATION REPORT:

AD#:	P000 697	TITLE: NASA Technology Transfer.
	P000 698	Army Readiness and the Production Base.
	P000 699	NASA Helicopter Transmission System Technology Program.
	P000 700	Present Technology of Rolling-Element Bearings.
	P000 701	Geared Power Transmission Technology.
	P000 702	A Historical Perspective of Traction Drives and Related Technology.
	P000 703	An Overview of Advancements in Helicopter Transmission Design.
	P000 704	Design of an Advanced 500-hp Helicopter Transmission.
	P000 705	Helicopter Transmission Arrangements with Split-Torque Gear Trains.
	P000 706	Design Study of Self-Alining Bearingless Planetary Gear (SABP).
	P000 707	Hybrid Gear Traction Transmissions.
	P000 708	Impact of NASA-Sponsored Research on Aircraft Turbine Engine Bearing Specifications.
	P000 709	Prediction of Ball and Roller Bearing Thermal Kinematic Performance by Computer Analysis.
	P000 710	Predicted and Experimental Performance of Large-Bore High-Speed Ball and Roller Bearings.
	P000 711	Lubrication of 35-Millimeter-Bore Ball Bearings of Several Designs to 2.5 Million DN.
	P000 712	High-Speed Spherical Roller Bearing Analysis and Comparison with Experimental Performance.
	P000 713	Large-Bore Tapered-Roller Bearing Performance and Endurance to 2.4 Million DN.
	P000 714	Evaluation of High Performance, Fixed-Ratio, Traction Drive.
	P000 715	Traction Calculations and Design Data for Two Traction Fluids.
	P000 716	Sizing Criteria for Traction Drives.
	P000 717	A Basis for the Analysis of Surface Geometry of Spiral Bevel Gears.

This document has been approved
for public release and sale; its
distribution is unlimited.

COMPONENT PART NOTICE (CON'T)

AD#:	P000 718	TITLE: Spiral-Bevel Geometry and Gear Train Precision. A Computer Solution for the Dynamic Load, Lubricant Film Thickness, and Surface Temperatures in Spiral-Bevel Gears. Comparison of Spur Gear Efficiency Prediction Methods. Compliance and Stress Sensitivity of Spur Gear Teeth. A Method for Static and Dynamic Load Analysis of Standard and Modified Spur Gears. An Update on the Life Analysis of Spur Gears. The Optimal Design of Standard Gearsets. Study of Lubricant Jet Flow Phenomena in Spur Gears-Out of Mesh Condition. Gear Lubrication and Cooling Experiment and Analysis. Dynamic Tooth Loads and Stressing for High Contact Ratio Spur Gears. A Computer Code for Performance of Spur Gears. Evaluation of High-Contact-Ratio Spur Gears with Profile Modification.
	P000 719	
	P000 720	
	P000 721	
	P000 722	
	P000 723	
	P000 724	
	P000 725	
	P000 726	
	P000 727	
	P000 728	
	P000 729	

Accession For	
NTIS GRA&I	<input checked="checked" type="checkbox"/>
DOC TAB	<input type="checkbox"/>
Unannounced	<input type="checkbox"/>
Justification	
Distribution/	
Availability Codes	
Dist	Avail and/or Special
A	

- conf - pub -
NASA Conference Publication 2210
AVRADCOM Technical Report 82-C-16

Advanced Power Transmission Technology

George K. Fischer, *Editor*
Lewis Research Center

Proceedings of a symposium sponsored by
Propulsion Laboratory, AVRADCOM Research and
Technology Laboratories and
NASA Lewis Research Center
and held at Lewis Research Center
Cleveland, Ohio
June 9-11, 1981

Accession For	
NTIS GRA&I	<input checked="checked" type="checkbox"/>
DTIC TAB	<input type="checkbox"/>
Unannounced	<input type="checkbox"/>
Justification	
By	
Distribution/	
Availability Codes	
Dist	Avail and/or Special
A	



DTIC
ELECTE
S MAR 29 1983 D
D

NASA
National Aeronautics
and Space Administration
Scientific and Technical
Information Branch

1983

Preface

It is my intention to introduce the Lewis Research Center and to give you an idea of the scope of our activities so that you will better understand the origins of the contents of this meeting.

We are called an energy conversion center in the broadest sense. We convert energy from one form to another: fuel to horsepower for aeronautics, ions to thrust for space, and wind to electricity for terrestrial energy. We consider ourselves the finest research and technology center in the free world to pursue these activities.

For those of you who are not acquainted with the National Aeronautics and Space Administration (NASA), it is an independent agency of the Federal government. The Administrator and the staff headquartered in Washington interface with the Office of Management and Budget and with the Congress. They advocate programs, present them to the Congress, and manage the broad programs of the agency.

The programs are implemented by eight NASA field centers and the Jet Propulsion Laboratory at the California Institute of Technology. Three of the field centers were formerly part of the National Advisory Committee for Aeronautics (NACA): Lewis Research Center (Ohio), Langley Research Center (Virginia), and Ames Research Center (California) are the research and technology centers of the agency. NASA's mission-oriented centers were acquired or created when NASA was organized. They are Goddard Space Flight Center (Maryland) mostly for space science, Lyndon B. Johnson Space Center (Texas) for manned spacecraft, John F. Kennedy Space Center (Florida) for space launches, George C. Marshall Space Flight Center (Alabama) for large launch vehicles, and the smaller National Space Technology Laboratories (Mississippi) for testing rocket engines and the Jet Propulsion Laboratory (California) for planetary missions. Among the centers, there is, of course, some interlocking of roles and missions.

Our job at Lewis is to work with industry and universities as a team, develop the research and technology base, transfer the technology to industry for commercialization or to a mission-oriented center, and then back away gracefully to seek bigger dragons to conquer. We have been doing that for many years in the aeronautics business.

The NASA Lewis Research Center occupies approximately 350 acres beside the Cleveland-Hopkins Airport and 6000 acres at Sandusky (about 60 miles west) where we have some larger facilities, including an experimental wind turbine, and storage facilities.

Lewis, then called the Aircraft Engine Research Laboratory (AERL), was formed in 1941 as an expansion of the powerplant work of the NACA Langley Laboratory. AERL contributed to our military air superiority during World War II. In the 1940's and 1950's researchers here developed many of the features still seen on today's gas turbine engines. As the joint sponsorship of this conference attests, we still have close relations with the Department of Defense, even though most of our activities are commercially oriented. The efforts to meet the requirements of military engines, although quite different from those of commercial engines, have often resulted in benefits to both technologies.

Also in the 1940's and 1950's, we built major propulsion test facilities, which are still active. We are very proud of our plant.

In 1948 the Center was renamed the NACA Lewis Flight Propulsion Laboratory. In 1958 it was again renamed the NASA Lewis Research Center, after which the Center role expanded, mainly to exploit for the space program the technologies that we had developed over the years. But aeronautical propulsion research and technology is still one of our bread-and-butter items, and we continue to be very active in that area.

To support NASA's space activities, we have greatly expanded chemical rocket and electric-propulsion technology. We developed space-power technology, and, in part because of that expertise, we are now developing technology for terrestrial-power systems for the Department of Energy.

Basic and applied mechanical components and lubrication research, especially in the high-temperature, high-speed bearing area, has become a center of excellence here at Lewis. The study of high-energy rocket propellants, including hydrogen, was pioneered here at Lewis. Of course, that activity opened new vistas.

We have had development and management responsibility for medium-class launch vehicles, specifically, Atlas, Agena, Atlas-Centaur, and Titan-Centaur. The Atlas-Centaur will continue to be the workhorse for medium-size payloads until the space shuttle becomes operational, at which time Atlas-Centaur will be phased out.

Recently we were designated as NASA's center for space-communications research and technology. That assignment came because of our electronics expertise with instrumentation and data gathering on various engines and our experience with the Communications Technology Satellite in the 12- to 14-gigahertz band. That assignment is new, and eventually you will see some big antennas here at Lewis Research Center for use in high-frequency research in the 20- to 30-gigahertz band.

The Congress amended the National Aeronautics and Space Act of 1958 to authorize NASA to work in terrestrial energy, where national needs are so acute. Some of our studies have dealt with the Stirling and gas-turbine automobile engines. Here again, we are teamed with industry—Ford Motor, General Motors, and American Motors General, who work with engine companies. Our objective is to develop the technology base and then back away. Those companies are accustomed to looking at the Government as a regulator. They are very pleased that NASA is not such an organization, and we are developing a very fine rapport, although it has taken a little doing.

We manage the Department of Energy's program for large wind turbines. That program started in 1975 with an experimental wind turbine at Plum Brook—a 100-kilowatt machine, which we still use for testing new techniques. We develop and install stand-alone photovoltaic systems, including energy generation, storage, and distribution. For example, the Papago Indian Village of Schuchuli, Arizona, now has lighting, refrigeration, sewing machines, and pumped water—all made possible by a Lewis-supplied solar cell system. So too, a village in Upper Volta, Africa, at the request of the State Department.

Among other topics of research and development are hydrodynamics, and coal cogeneration—a process intended to convert dirty, high-sulfur, Ohio coal to electricity without pollution.

In aeronautics, Lewis' work ranges from studies on basic processes like fluid flow and combustion, to components like compressors and turbines, to full-scale systems. Although we do not develop engines at Lewis, we do use engines as a research tool. For example, the F100 engine is used in one of our test cells to study control techniques, where inlet area, compressor blade angle, fuel flow, rotor speed, and exhaust nozzle area all vary as functions of altitude and flight speed.

We conduct propeller research for general-aviation and commercial transport aircraft. Recently we developed an energy efficient propeller that is 80 percent efficient at Mach 0.8 for a potential 33-percent improvement in fuel consumption. Because of the emphasis on energy conservation, the concept of a high-speed, advanced turboprop is of interest to the airlines and the aircraft industry in general; we are pursuing that concept.

In space propulsion, we are working on advanced engines that will take spacecraft from near-Earth orbit to geosynchronous orbit. Electric thruster technology is at the point where we are transferring it to the Marshall Space Flight Center so that they can develop a space electric propulsion system (SEPS), using ten of these thrusters in a stage for planetary missions. Also, we are actively pursuing low-thrust chemical rockets. Such rockets may be used to help construct large, space-based antennas for communications and air traffic control.

In space power research and technology (R&T), we are the Center for solar cell development for NASA. We are looking at gallium arsenide cells as well as at advanced techniques for silicon cells. We do all of NASA's R&T for batteries for space applications. Although we have concentrated on the silver-zinc system, some of our techniques have been transferred to both industry and the Department of Energy for the development of nickel-zinc batteries for terrestrial use. We do all the fuel-cell R&T work for space. That technology, too, has been transferred to systems for terrestrial applications.

From our studies of the communications market, we have concluded that the present frequencies, which include 14 to 16 gigahertz and lower, will be saturated in the mid-1980's. To create a new capability, we are looking at the 20- to 30-gigahertz range, which involves a new body of technology.

We are now in the process of defining what communications demonstration experiments are needed and what key technology developments are required. The intent is to put all the complicated equipment in the satellites and use very low-cost ground terminals. Eventually we will have antennas that can be fitted into a small suitcase. Such a multibeam satellite will service all the United States,

including Alaska, Hawaii, and Puerto Rico.

In the terrestrial energy business, we are very careful to pick technologies that are synergistic to our mainstream aeronautics and space efforts. We have two big gas-turbine development projects for automotive propulsion: one with AiResearch and Ford and one with Detroit Diesel Allison and Pontiac. The government puts up the high-risk front-end money and eventually the automotive industry will cost-share as we go downstream. We think we can obtain a 20 to 30 percent improvement in fuel consumption with virtually no pollution. The question is whether this can be done economically and with all the "ilities": reliability, maintainability, producibility, and so forth.

I keep emphasizing that we work with industry as a team to develop the concepts and then back away gracefully. We work very closely with the universities as well. We make research grants to universities; we have a cooperative program where faculty members are in residence here, especially during the summer; we have co-op students; and we have joint research programs. These joint programs generally involve basic and applied research. The results of several such working agreements are presented at this conference.

And, of course, we work with other government agencies, the previously mentioned Departments of Energy and Defense as well as the Department of Transportation. For example, we have developed a radar device that measures the extent and thickness of the ice on large bodies of water, in this application the Great Lakes. We have transferred the completed device to the Coast Guard. With the ice information the device provides, the Coast Guard produces, in season, daily ice charts. Being able to avoid iced areas has greatly extended the navigation season on the Great Lakes.

NASA expenditures are modest; in fact, we get less than nine-tenths of 1 percent of the U.S. Federal budget dollar. The largest outlays in the Federal budget are for direct benefit payments to individuals. Incidentally, in the last two decades, this item has gone up from 24 to 43 percent; national defense is now about 27 percent. NASA's budget is about 1/15 of what you pay as interest on the Federal debt.

The Lewis budget for Fiscal Year '81 is about \$500 million. Three-fourths of this money goes directly to research and development, about 80 percent of which is performed through contracts and grants; almost one-fourth is civil service salaries, utilities, guards, cutting the grass—keeping the plant going. About 2 percent is for new facilities and the major rehabilitation of old facilities.

The research and development dollar split is about one-third each: aeronautics, space, and energy. Our manpower split is quite different; about two-thirds of our staff is devoted to aeronautics. We consciously limit the staff associated with energy programs so that we can keep our aeronautics and space role consistent with the personnel ceiling of 2679 persons imposed by the Office of Management and Budget through NASA Headquarters.

At Lewis over half of the staff are scientists and engineers. Thus we are a very high-technology center. They are supported by over 1000 skilled craftsmen, technicians, and operators of big facilities, and by some 300 very fine administrative professionals.

We operate in a matrix fashion. Project offices in the Aeronautics, Space, and Energy Directorates receive support from the other parts of the organization. For example, the Automotive Gas Turbine Project Office is located in the Energy Directorate. It receives technical skills from the Science and Technology Directorate, for example, materials, bearings, seals, transmissions, compressors, turbines, and combustion. It receives computer services from the Engineering Services Directorate. From the Technical Service Directorate, it receives test-installation services, technicians, and related services. And from the Administrative Directorate, procurement services, photographic services, and so forth. The Aeronautics, Space, and Energy Directorates are responsible for advocacy, planning, work breakdown structure, and definition of the tasks associated with projects.

The science and technology people not only support the projects, but they are also responsible for maintaining expertise in their own disciplines. It is their work in basic and applied research that is the backbone of our superior technology.

The three support organizations are Administration, Engineering Services, which includes computing, engineering drafting, facility support, and design services, and Technical Services, which provides technicians and craftsmen.

Our investment cost in building and facilities is over \$300 million in 1950-1960 dollars; thus the estimated replacement cost is well over one and a half billion dollars.

This has been a very brief introduction to the Lewis Research Center. This Center, in partnership with American industry, has helped create the nation's prominence in aeronautics that contributes to

our national defense, assures a safe, reliable commercial transportation system, and greatly aids our position in international trade. The proceedings of the Advanced Power Transmission Technology Symposium reports on the results of cooperative efforts of NASA Lewis and the U.S. Army Propulsion Laboratory, Army Aviation Research and Development Command in bearing, gearing, lubrication, and transmission technologies. The cooperation has been productive. Our objective is to make the results of this effort available to the U.S. industrial community on a timely basis. We believe that you will find the technical content of these proceedings interesting and useful and we expect that you may be surprised at the breadth of our activities.

John F. McCarthy, Jr.
Director
NASA Lewis Research Center

Foreword

A nation's greatness in the course of history can be measured in part by its scientific and technological contributions and advances. These contributions and advances are reflected in the nation's standard of living and its stature in the international community. A function of the National Aeronautics and Space Administration (NASA) has always been to contribute scientific and technological advances in the aeronautical and space sciences. These contributions have also had significant technical impact in the nonaerospace industrial community. As a result, a very productive partnership has been formed between NASA and industry and university organizations. The NASA Helicopter Transmission System Technology Program is one such partnership.

The Helicopter Transmission System Technology Program is a cooperative effort between NASA and the U.S. Army Aviation Research and Development Command. The program, which has been funded for 5 years, began in October 1977. It comprises both fundamental and applied research on the bearing, gearing, lubrication, and mechanical power transmission technologies, with focus on helicopter power transfer systems. The program elements are being performed at the Lewis Research Center and on contract and grant with U.S. industry and universities. During the course of the program, more than 20 organizations have contributed to it. Within the first 3 years, these contributions have yielded advanced technology, which is believed to be broadly applicable to a variety of industries. This symposium was scheduled at the midpoint of the program to review the advances made to date.

The Advanced Power Transmission Technology Symposium, cosponsored by the NASA Lewis Research Center and the Army Aviation Research and Development Command, was held June 9 to 11, 1981, at the Lewis Research Center, Cleveland, Ohio, in conjunction with the NASA Lewis Research Center's Technology Utilization Office. Attendance at the symposium was approximately 350, representing the aerospace, mechanical power transmission, bearing, gearing, and lubrication industries, as well as the academic community.

The most important ingredient of any technical conference is the participants, whose interest and support are absolutely crucial. Of the technical presentations, 12 were by NASA and Army staff members, and 19 were by NASA contractors. Those who served as chairmen of the various technical sessions were: Bruce H. Pauley, Vice President, Engineering and Research, Eaton Corp.; Henry E. Sawicki, Manager, Drive System Design, Hughes Helicopter; Charles A. Moyer, Chief Engineer, Applications Development Laboratory, The Timken Co.; Walter G. O. Sonneborn, Director, Advanced Composite Airframe Program, Bell Helicopter Co.; Carl O. Albrecht, Manager, Power Train Technology, Boeing-Vertol Co.; Kenneth Rosen, Manager, Systems Design and Development Engineering, Sikorsky Aircraft Co.; and James B. Anderson, Mechanical Power Transmission Design Specialist, Bendix Corp. Harrison Allen, Chief, Technology Utilization Office, Lewis Research Center, and his staff coordinated all symposium arrangements. George K. Fischer and Herbert W. Scibbe coordinated the staff members of the NASA Lewis Bearing Gearing and Transmission Section in making arrangements for the technical presentations and symposium papers.

Numerous other people at the Lewis Research Center contributed to the success of the symposium. Among these are the staff of the Technical Services Directorate who provided outstanding technical support to the transmission program and the Management Services Division. We would therefore like to thank these people for their generous gifts of time and energy. These proceedings constitute a tribute to their dedication and contributions.

James E. Burnett	Erwin V. Zaretsky
Director, Technology	Head, Bearing, Gearing,
Utilization and Public Affairs	and Transmission Section

Symposium Cochairmen

Contents

Preface	iii
Foreword	vii
U.S. Army Aviation - NASA Interface <i>Richard Carlson</i>	1
NASA Technology Transfer <i>Harrison Allen, Jr.</i>	3
Army Readiness and the Production Base <i>James M. Hesson</i>	11

SESSION 1 - Technology Overviews

NASA Helicopter Transmission System Technology Program <i>Erwin V. Zaretsky</i>	15
Present Technology of Rolling-Element Bearings <i>Richard J. Parker</i>	35
Geared Power Transmission Technology <i>John J. Coy</i>	45
A Historical Perspective of Traction Drives and Related Technology <i>Stuart H. Loewenthal</i>	79

SESSION 2 - Advanced Transmission Concepts

An Overview of Advancements in Helicopter Transmission Design <i>Joseph H. Mancini</i>	109
Design of an Advanced 500-hp Helicopter Transmission <i>Charles E. Braddock and Roy A. Battles</i>	123
Helicopter Transmission Arrangements with Split-Torque Gear Trains <i>G. White</i>	141
Design Study of Self-Alining Bearingless Planetary Gear (SABP) <i>D. J. Folenta</i>	151
Hybrid Gear Traction Transmissions <i>A. L. Nasvytis and G. White</i>	161

SESSION 3 - Rolling-Element Bearing Technology

Impact of NASA-Sponsored Research on Aircraft Turbine Engine Bearing Specifications <i>A. H. Nahm</i>	173
Prediction of Ball and Roller Bearing Thermal Kinematic Performance by Computer Analysis <i>Juris Pirvics and Robert J. Kleckner</i>	185
Predicted and Experimental Performance of Large-Bore High-Speed Ball and Roller Bearings <i>Harold H. Coe</i>	203
Lubrication of 35-Millimeter-Bore Ball Bearings of Several Designs to 2.5 Million DN <i>Fredrick T. Schuller</i>	221
High-Speed Spherical Roller Bearing Analysis and Comparison with Experimental Performance <i>Robert J. Kleckner and George Dyba</i>	239
Large-Bore Tapered-Roller Bearing Performance and Endurance to 2.4 Million DN <i>Richard J. Parker</i>	253

SESSION 4 - Traction Drive Technology

Evaluation of High Performance, Fixed-Ratio, Traction Drive <i>Stuart H. Loewenthal, Neil E. Anderson, and Douglas A. Rohn</i>	271
Traction Calculations and Design Data for Two Traction Fluids <i>Joseph Leo Tevaarwerk</i>	285
Sizing Criteria for Traction Drives <i>Douglas A. Rohn, Stuart H. Loewenthal, and John J. Coy</i>	299

SESSION 5 – Spiral Bevel Gear Technology

A Basis for the Analysis of Surface Geometry of Spiral Bevel Gears <i>Ronald L. Huston and John J. Coy</i>	317
Spiral-Bevel Geometry and Gear Train Precision <i>Faydor L. Litvin and John J. Coy</i>	335
A Computer Solution for the Dynamic Load, Lubricant Film Thickness, and Surface Temperatures in Spiral Bevel Gears <i>H. C. Chao, M. Baxter, and H. S. Cheng</i>	345

SESSION 6 – Spur Gear Technology I

Comparison of Spur Gear Efficiency Prediction Methods <i>Neil E. Anderson and Stuart H. Loewenthal</i>	365
Compliance and Stress Sensitivity of Spur Gear Teeth <i>R. W. Cornell</i>	383
A Method for Static and Dynamic Load Analysis of Standard and Modified Spur Gears <i>Romualdas Kasuba</i>	403
An Update on the Life Analysis of Spur Gears <i>John J. Coy, Dennis P. Townsend, and Erwin V. Zaretsky</i>	421
The Optimal Design of Standard Gearsets <i>Michael Savage, John J. Coy, and Dennis P. Townsend</i>	435

SESSION 7 – Spur Gear Technology II

Study of Lubricant Jet Flow Phenomena in Spur Gears – Out of Mesh Condition <i>Dennis P. Townsend and Lee S. Akin</i>	461
Gear Lubrication and Cooling Experiment and Analysis <i>Dennis P. Townsend and Lee S. Akin</i>	477
Dynamic Tooth Loads and Stressing for High Contact Ratio Spur Gears <i>R. W. Cornell and W. W. Westervelt</i>	491
A Computer Code for Performance of Spur Gears <i>K. L. Wang and H. S. Cheng</i>	503
Evaluation of High-Contact-Ratio Spur Gears with Profile Modification <i>Dennis P. Townsend, Berl B. Baber, and Andrew Nagy</i>	519

U.S. Army Aviation—NASA Interface

Richard Carlson

Shortly after World War II, the Army Air Corps was combined with the newly organized U.S. Air Force. As a result, very little interest in aviation remained in the U.S. Army. The small amount of aeronautical research and development that was contemplated was conducted by the Ordnance Corps from 1945 to 1952. Engineering Development and Procurement was handled by the Air Force at Wright Field. In 1952 the Transportation Research Command (TRECOM) was formed at Fort Eustis, Virginia, and the elements of Army aviation R/D conducted by the Ordnance Corps were transferred to TRECOM. TRECOM existed until 1964, when the Aviation Systems Command (AVSCOM) was formed in St. Louis, Mo. The Aviation R/D portion of TRECOM was reorganized as the Army Aviation Material Laboratories, known as "AVLABS." About a year later General Chesarek and General Bill Bunker concluded, after numerous studies, that the Army needed to develop inhouse expertise in addition to that which was already available at AVLABS. At that time the AVLABS organization was conducting aviation R/D primarily by means of industry contracts. What was needed were additional personnel and facilities. Costing studies were conducted and revealed that the Army did not have available the resources necessary to expand its in-house R/D capability. However, it was the facilities requirements that resulted in prohibitive expansion costs, not the personnel or project costs. This prompted the Army to propose the NASA Ames, a joint Army-NASA agreement to occupy and operate one of the 7- by 10-foot subsonic wind tunnels at Ames Research Center to pursue low-speed Aeromechanics Research Projects of mutual interest. The initial Army organization was named the Army Aeronautical Research Laboratory (AARL). Fifty Army personnel spaces were involved, some of which were added to NASA Administrative and Technical Staff as the "Quid Pro Quo" for facilities and support required by the Army.

The AARL experiment prospered and in 1968, Phil Carlson of the Lockheed-California Company, was asked by General Chesarek to examine the entire requirement for Army Aviation Research. The industry-wide committee formed by Phil Carlson recommended that the Army form a new organization that contained AVLABS, AARL, and two new activities, similar to AARL, to be formed at NASA Lewis and NASA Langley. This new organization, the U.S. Army Air Mobility Research and Development Laboratory (USAAMRDL), is essentially the organization that exists today. Four years ago the old Aviation Systems Command (AVSCOM) was divided into the Aviation R/D Command (AVRADCOM) and the Troop Support and Readiness Command (TSARCOM). The current organization, now called the Army Aviation Research and Technology Laboratories, is composed of the Aeromechanics Laboratory at Ames, the Propulsion Laboratory at Lewis, the Structures Laboratory at Langley, and the Applied Technology Laboratory at Fort Eustis, Virginia.

As was the case with the original AARL operation, NASA and the Army share resources in a very unique fashion. The Army and NASA have a "quid pro quo" since the Army lacks Aeronautical Research Facilities and NASA lacks needed personnel spaces. Therefore, the Army provides personnel spaces to NASA in exchange for support and facilities provided by NASA. The result is one of those rare situations in which both parties are happy with the arrangement.

The Army and NASA have pursued four large programs in the last 10 years which required long-term resource commitment. These programs were the XV-15 tilt rotor, the rotor systems research aircraft (RSRA), the rotor systems integration simulator (BSIS), and the more recent integrated technology rotor/flight research rotor program (ITR/FRR). These types of programs are formulated at the bench level, are developed and go forward to NASA Headquarters and to the Department of the Army. If approved, a Memorandum of Understanding is prepared and signed by the Assistant Secretary of the Army for Research and Development, and the NASA Associate Administrator for Aeronautics and Space Technology.

Less visible, but by no means less important, are the various programs such as the NASA Helicopter Transmission System Technology Program. Although this program is not necessarily the type of effort that requires a long-range commitment of resources, it takes the same kind of planning and dedication to execute successfully. In fact, we have a problem in the Department of the Army (and Defense) with this type of joint Army/NASA program. New action officers read descriptions of such Army/NASA programs in the modern Army Research and Development Information System

(MARDIS) and then review the NASA RTOP's, and invariably call us to say that the Army/NASA programs sound identical. And, in many instances they are because they are, in fact, joint programs, with common goals.

Another type of NASA support is even less heralded than the programs that you will hear about for the next three days: The NASA involvement in the support of developing new systems and fielded equipment, which originates from all three NASA Aeronautical Research Centers. This support takes the form of wind tunnel tests, flight and ground simulation tests, and the very highest types of technical and professional support available in the country. John Acurio, who is the Director of the Army Aviation Propulsion Laboratory at the NASA Lewis Research Center prepared a list of this type of support that NASA Lewis has provided for the U.S. Army. It ranges across all systems, including the OH-58, UH-1's, CH-47's, and Army Helicopter Improvement Program (AHIP), as well as across all types of components including engines, shafting, transmissions, gears, bearings, seals, and clutches. This continued support, to every conceivable mechanical component in the helicopter, was one of the basic ingredients in Generals Chesarek's and Bunker's decision to seek out and nurture the NASA/Army relationship. We believe, some 16 years later, that the relationship is a two-way proposition since it provides the U.S. Army with much needed support. It provides NASA with the opportunity to get much closer to systems requirements issues and problems that develop downstream in fielded systems. The U.S. Army believes that NASA relationship is a positive element in Army Aviation R/D.

I would like to turn from history and the types of Army-NASA projects and show you what we think the new systems in the 1990's and early 2000's will look like. The Army has two new systems, the advanced attack helicopter (the Apache) and the utility tactical transport (the Blackhawk) that are currently being developed and introduced in the field. For these two systems we envision a number of product improvements and block improvements during the next 20 to 25 years. The Rotor Systems Research Aircraft (RSRA), the advancing blade concept (ABC), and the XV-15 Tilt Rotor Aircraft projects are all approaching completion and form the technological base for new systems being contemplated. These configurations expand the operational capabilities of Low Disk Loading Vertical Takeoff and Landing Vehicles—capabilities with regard to agility, speed and range that can be applied to the AHIP, the new Light Helicopter Experimental (LHX), and a new special Electronics Mission Aircraft (SEMA-X).

I would like to present what I consider to be a very special challenge to the U.S. Helicopter Industry in general and to the mechanical power transmission community, in particular. About seven years ago, a Soviet engineer produced a textbook, or a methodology outline dealing with Soviet helicopter design techniques that engineer, Tishenko, was a protege of M. L. Mil, for the most successful producer of Soviet helicopters. The first thing that fascinated us was that, the approach to system design was from purely economic, as is the case in the western world. More of a surprise was that they were using some of the Air Transport Association direct operating cost techniques developed in this country in the 1940's. The book was translated and analyzed by Professor W. Z. Stepniewski who pointed out that all of Tishenko's hypothetical helicopters seemed to include new technology trends, such as weight fractions, rotor performance, and Powerplant Specifics, that were consistent with the new technology being developed in this country and western Europe. This was in contrast to all of Mil's previous production helicopters, which were 15 to 20 years behind the times. Obviously, the Soviets are prodigious readers, and they have done an excellent job of assessing western technology. That these technology trends were so consistent with western practice was not coincidental; Tishenko had, in fact, set them as goals for new Soviet helicopters.

The reaction to the book was varied. Some of us said, "It's one thing to predict, but quite another to produce." Others said, "The Russians are coming." And indeed they are. One of the hypothetical configurations in Tishenko's book was a 52-metric-ton single-rotor heavy-lift helicopter. This helicopter was exhibited at the 1981 Paris air show. Designated the Mil-26, it weighs 110,000 pounds fully loaded. Many of the old design guidelines have modified: They have raised rotor disk loadings, recognized the design requirements for "hot-high" performance in Southern Asia, and increased rotor tip speeds. The relationship between system weight and output torque for previous Mil helicopters was higher than that for Western world single-rotor helicopters and tandem-rotor helicopters. The Mil-26 drive system weight falls on the Western world single-rotor trend line. So, the Russians have arrived; they have predicted and produced; and there is our challenge.

NASA Technology Transfer

Harrison Allen, Jr.*

NASA's aerospace programs provide research and development in a broad range of scientific and technical disciplines including the fields of bearings, gearing, lubrication, and transmissions. Such aerospace-related technology can often contribute significantly to nonaerospace applications in U.S. companies and industries. Consequently, the rapid dissemination of aerospace-related information to private industry is highly desirable. The NASA Technology Utilization Program is concerned with the transfer of new aerospace technology to nonaerospace use, including its application to new and improved industrial processes and to the development of new and improved commercial products.

The NASA Technology Utilization Program is a continuing effort to make aerospace innovations, new scientific knowledge, and new technical skills broadly available to industry and to the public. Technology transfer can occur in a variety of ways. Traditional modes of data transfer involve NASA's technological data bank, which consists of NASA reports and other documents. There are some 2 million documents (fig. 1) in this data bank, and about 10,000 additions are made each month. Some of these documents are from NASA and its contractors; the rest are from a worldwide information network. Just like private industry, NASA needs access to a world data bank to supplement its information sources.

The 10,000 new documents each month are abstracted in two journals (fig. 2): STAR, the Scientific and Technical Aerospace Reports, and IAA, the International Aerospace Abstracts. Together these journals provide comprehensive, current coverage of the world output of aerospace-related scientific and technical publications.

The STAR journal, published by NASA, is issued twice monthly and covers government and private industry reports (fig. 3). About 22 percent of these reports are published by NASA and NASA contractors, 22 percent by the Department of Defense and its contractors, 17 percent by the Department of Energy and its contractors, and 10 percent by other government agencies. The balance comes from foreign countries and miscellaneous sources. STAR is available on subscription at \$60.00 per year.

The companion journal, International Aerospace Abstracts, is published by the American Institute of Aeronautics and Astronautics under agreement with NASA. It, also, is issued twice monthly, covers documents reported in technical society meetings and in professional journals. STAR and IAA have identical formats and indexing systems. The technical documents abstracted in IAA (fig. 4) are 45 percent domestic and 55 percent foreign. Russia and Great Britain are the largest individual foreign sources. IAA is available on subscription at \$400 a year.

Of course, subscribing to these journals is easy, but a person normally does not have enough time to read these journals, consisting of 200 or more pages, every 2 weeks. Therefore, all documents in the data bank are under full bibliographic control; that is, they are categorized by subject, indexed, multiple cross-indexed based on selected key words, and microfilmed, and filed on magnetic tape for computer search and retrieval. Although this data bank and the computer search capability for the bank were set up to meet NASA's needs, the NASA Technology Utilization Program has taken steps to make this information available to American industry through the NASA application centers (fig. 5).

To promote technology transfer, the job of the NASA network of application centers is to provide information retrieval services and technical assistance to industrial and government clients. The network consists of eight Industrial Application Centers (IAC) and two State Technology Application Centers. Each center is located on a university campus and serves a geographical area. One of these centers, the Computer Software Management and Information Center (COSMIC), is responsible only for distributing NASA computer programs. The two IAC's closest to Lewis are at

*NASA Lewis Research Center.

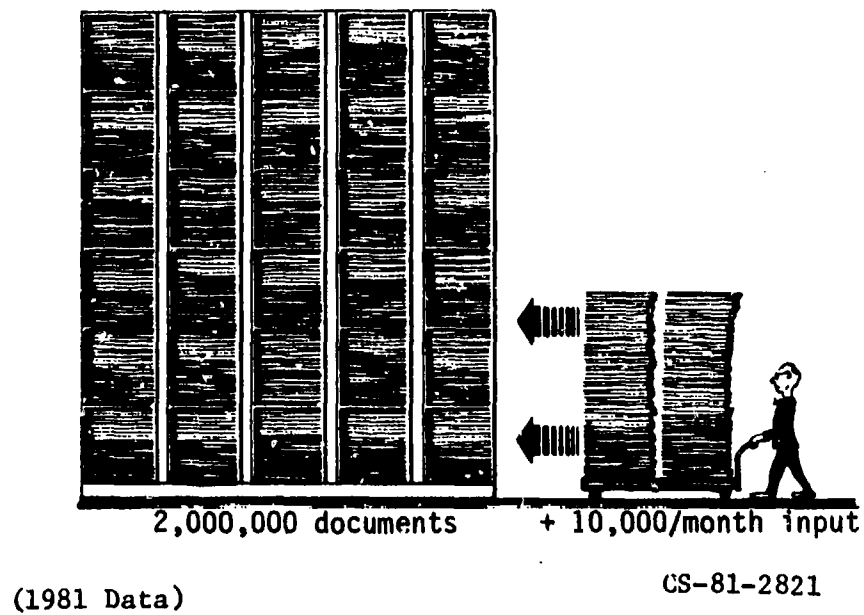


Figure 1. - Current NASA data bank.

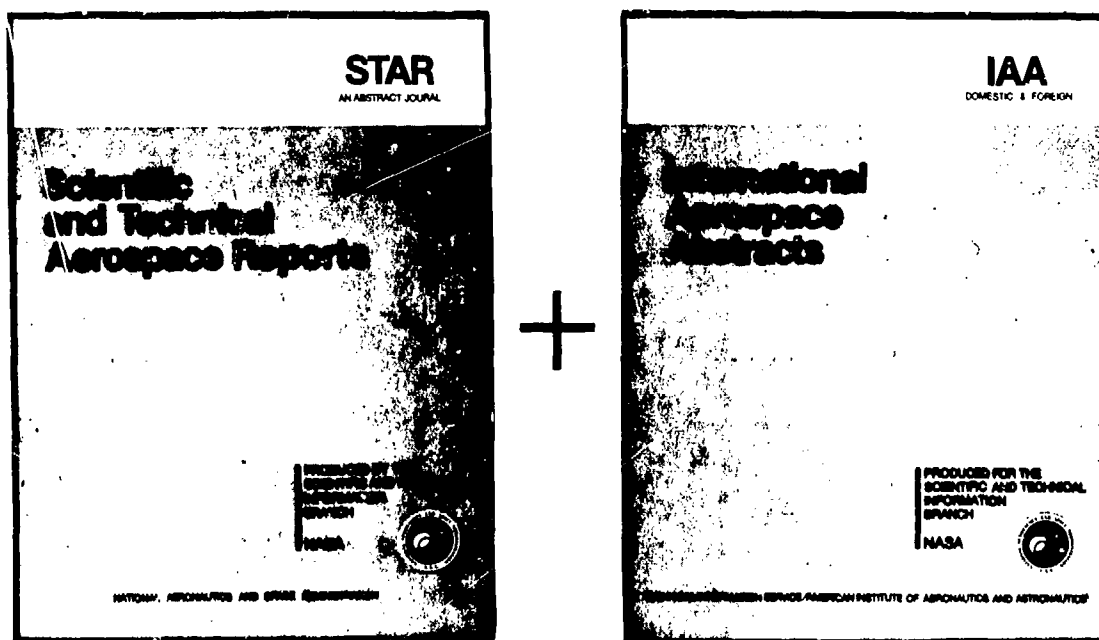


Figure 2. - Abstract journals.

the University of Pittsburgh and the University of Indiana. The IAC can search the NASA data bank using standard or specific profiles. The fee for the IAC service covers only the cost of the search, not NASA's cost to supply the data bank. The IAC's have a membership of over 10,000 companies with a yearly renewal rate of over 50 percent. The IAC service fee varies with the level of use. For more information about the services and fees, contact the Industrial Application Center in your region.

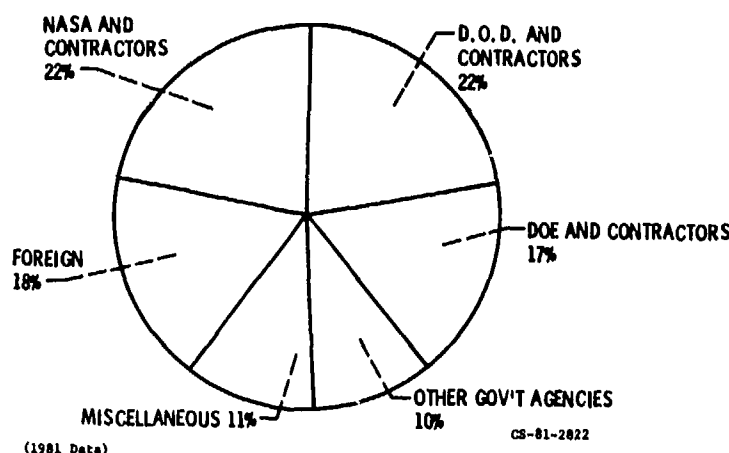


Figure 3. - STAR abstract of report literature.

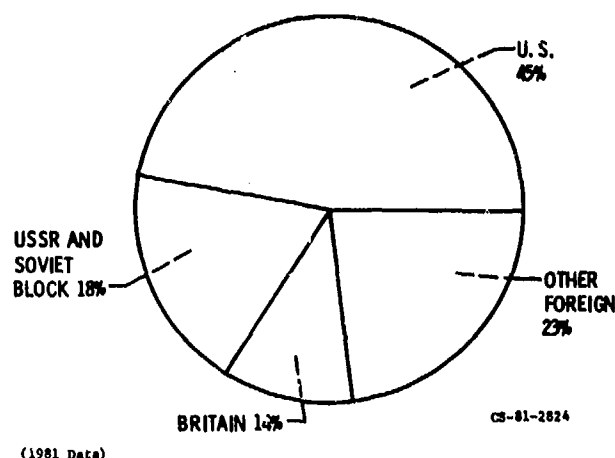


Figure 4. - IAA abstract of journal literature.

The NASA system of technology transfer personnel and facilities extends from coast to coast and provides geographical coverage of the nation's primary industrial concentrations, together with regional coverage of state and local governments engaged in technology transfer activities.

- ★ *NASA Field Center Technology Utilization Officers:* manage center participation in regional technology utilization activities.
- ★ *Regional Remote Sensing Applications Centers:* provide training, conduct demonstrations and offer technical assistance to users of remote sensing data.
- *Industrial Applications Centers:* provide information retrieval services and assistance in applying relevant technical information to users needs.
- *State Technology Applications Centers:* provide technology transfer services similar to those of the Industrial Applications Centers, but only to state governments and small businesses within the state.
- *The Computer Software Management and Information Center (COSMIC):* offers government-developed computer programs adaptable to secondary use.
- ▲ *Application Teams:* work with public agencies in applying aerospace technology to solution of public sector problems.

For specific information concerning the activities described above, contact the appropriate technology transfer personnel at the addresses listed on the following pages. For information of a general nature about the Technology Transfer Program, address inquiries to the Director, Technology Transfer Division, NASA Scientific and Technical Information Facility, Post Office Box 8757, Baltimore/Washington International Airport, Maryland 21240.

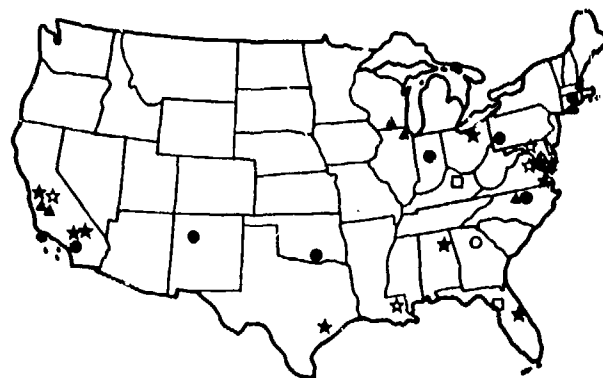
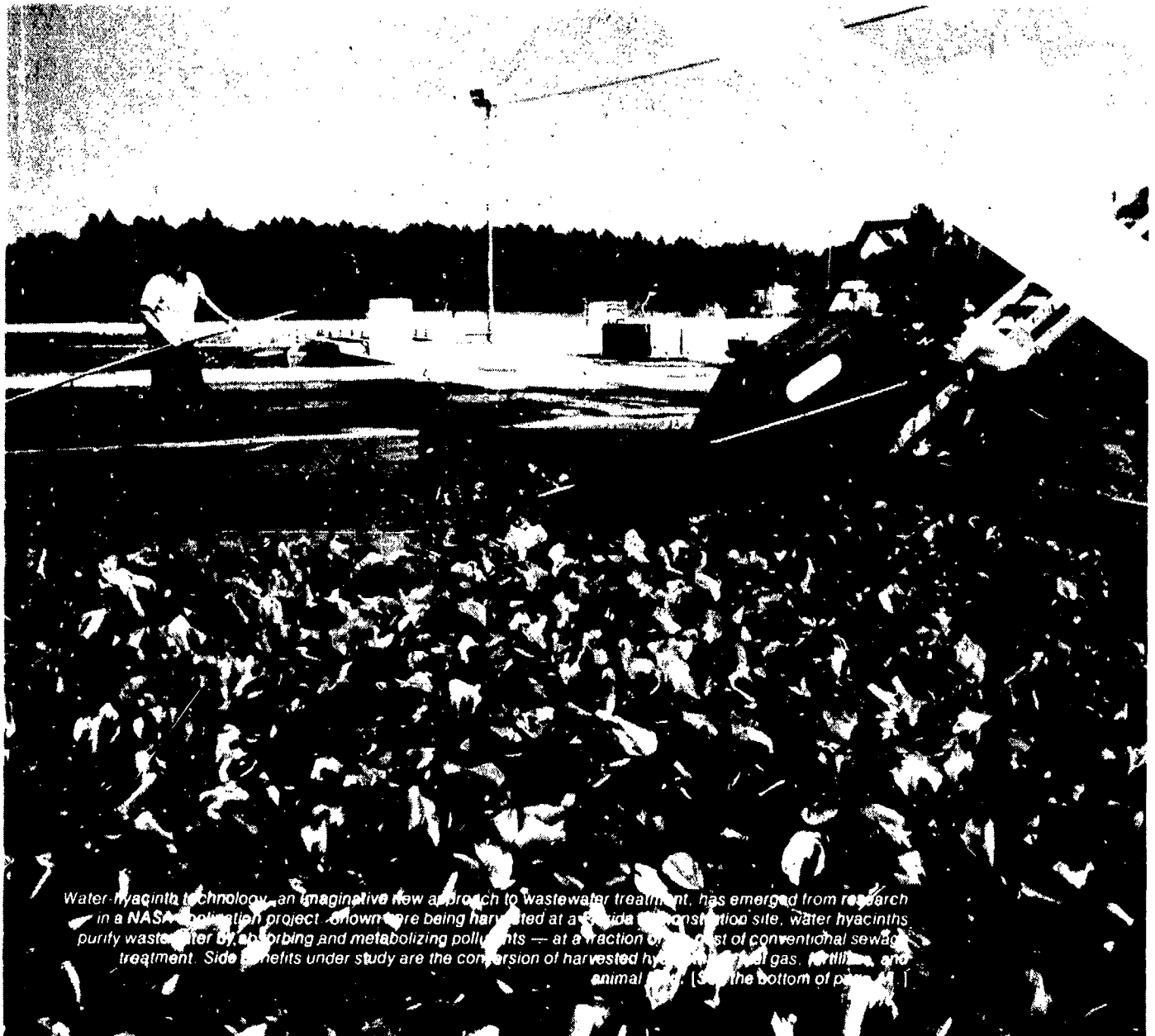


Figure 5. - NASA's technology transfer network. (Taken from a current Tech Briefs Journal. See the appendix of this report for the addresses of technology transfer personnel.)

NASA Tech Briefs

National
Aeronautics and
Space
Administration



Water hyacinth technology, an imaginative new approach to wastewater treatment, has emerged from research in a NASA pollution project. Known here being harvested at a Florida construction site, water hyacinths purify wastewater by absorbing and metabolizing pollutants — at a fraction of the cost of conventional sewage treatment. Side benefits under study are the conversion of harvested hyacinths into fuel gas, fertilizer, and animal feed. (See the bottom of page 4.)

Figure 6. - Cover page from Fall 1980 Tech Briefs Journal.

Originally, the IAC's started with the NASA data bank. However, their customers have encouraged them to expand their data banks so that they currently include such typical data banks as Chemical Abstracts, Engineering Index, and American Society of Metals. Presently, the IAC's provide information from over 240 data banks containing over 10 million documents.

A less traditional mode of transferring new technology, or more correctly, of transferring an awareness of new technology, is NASA's Technology Utilization (TU) conferences. At such conferences, NASA encourages the conference attendees to inquire about areas of interest to them. We then can arrange for telephone discussions with NASA field center technical staff or for private meetings with the engineers and scientists at a center.

At every NASA field center there is a TU Officer, whose mission is to transfer technology. (See fig. 5, and the appendix.) He is there to answer questions or find the people who can.

The NASA TU Program uses several other means to transfer technology. We publish Tech Brief Journal (fig. 6), which is a collection of one-page descriptions of innovations in a variety of fields. The journal is free and available to industry on request. An interested person or company can request to be put on our mailing list by completing a subscription card. Unfortunately, because of the large demand and the limited number of journals that we can publish at no charge, we have a waiting list.

The TU Program also produces a series of documents called "Special Publications," which cover technology of interest to a particular industry, such as

- SP-5053, Conference on Selected Technology for the Petroleum Industry
- SP-5057, Selected Technology for the Electric Power Industry
- SP-5103, Selected Technology for the Gas Industry
- SP-5111, Sputtered and Ion Plating
- SP-5112, NASA Contributions to Fluidic Systems
- SP-5059, (01), Solid Lubricants

The TU Program has a variety of applications projects whose aims are to transfer aerospace technology to recognized needs. An application project is undertaken by NASA in partnership with a user public-sector agency or American industry, with all partners providing funding. These projects are usually in the fields of health care, public safety, transportation, or industrial productivity.

For example, NASA approached the Parker Hannifin Corp. here in Cleveland in 1979 with the idea of developing, in conjunction with Johns Hopkins University researchers, a tiny pump that, once implanted in a patient, would deliver precise amounts of medication. Parker had developed for the Viking Mars Lander mission, a miniature valve they called a "peanut valve" that regulated the injection of precise amounts of nutrient solution into the Martian soil samples as part of an experiment to look for micro-organisms on Mars. Parker has successfully adopted the valve for the biomedical application, and clinical testing of the new device is scheduled to begin later this year (1981). A companion product, developed concurrently, is an external medication pump called "Micromed," that is much smaller than the smallest pump currently available to insulin-dependent diabetics.

NASA encourages private industry to contact the TU Officers at its field centers, who would be delighted to discuss aerospace technology that might be applicable to industrial needs.

Appendix—NASA TU Network

Technology Utilization Officers

Ben D. Padrick
Ames Research Center
Code AU: 240-2
Moffett Field, CA 94035
(415) 965-6471

John Samos
Langley Research Center
Mail Stop 139A
Hampton, VA 23665
(804) 827-3281

Gussie Anderson
Hugh L. Dryden Flight Research Center
Code OD/TU Office—Room 2015
P. O. Box 273
Edwards, CA 93523
(805) 258-3311, Ext. 787

Donald S. Friedman
Goddard Space Flight Center
Code 702.1
Greenbelt, MD 20771
(301) 344-6242

John T. Wheeler
Lyndon B. Johnson Space Center
Code AT 3
Houston, TX 77058
(713) 483-3809

U. Reed Barnett
John F. Kennedy Space Center
Code PT-SPD
Kennedy Space Center, FL 32899
(305) 867-3017

Industrial Applications Centers

Aerospace Research Applications Center
1201 East 38th Street
Indianapolis, IN 46205
John M. Ulrich, director
(317) 264-4644

Computer Software Management
and Information Center (COSMIC)
Suite 112, Barrow Hall
University of Georgia
Athens, GA 30602
John Gibson, director
(404) 542-3265

Kerr Industrial Applications Center
Southeastern Oklahoma State University
Durant, OK 74701
Robert Oliver, director
(405) 224-0121

NASA Industrial Applications Center
701 LIS Building
University of Pittsburgh
Pittsburgh, PA 15260
Paul A. McWilliamis, executive director
(412) 624-5211

Harrison Allen, Jr.
Lewis Research Center
Mail Stop 7-3
21000 Brookpark Road
Cleveland, OH 44135
(216) 433-4000, Ext. 422

Ismail Akbay
George C. Marshall Space Flight Center
Code AT01
Marshall Space Flight Center, AL 35812
(205) 453-2223

Aubrey D. Smith
NASA Resident Office—JPL
4800 Oak Grove Drive
Pasadena, CA 91109
(213) 354-4849

Gilmore H. Trafford
Wallops Flight Center
Code OD
Wallops Island, VA 23337
(804) 824-3411, EXt. 201

New England Research Applications Center
Mansfield Professional Park
Storrs, CT 06268
Daniel Wilde, director
(203) 486-4533

North Carolina Science and Technology
Research Center
P. O. Box 12235
Research Triangle Park, NC 27709
Peter J. Chenery, director
(919) 549-0671

Technology Applications Center
University of New Mexico
Albuquerque, NM 87131
Stanley Morain, director
(505) 277-3622

NASA Industrial Applications Center
University of Southern California
Denny Research Building
University Park
Los Angeles, CA 90007
Robert Mixer, acting director
(213) 743-6132

State Technology Applications Centers

NASA/University of Florida
State Technology Applications Center
311 Weil Hall
University of Florida
Gainesville, FL 32611
J. Ronald Thornton, director
Gainesville: (904) 392-6626
Orlando: (305) 275-2706
Tampa: (813) 974-2499

NASA/University of Kentucky
State Technology Applications Program
109 Kinkead Hall
University of Kentucky
Lexington, KY 40506
William R. Strong, manager
(606) 258-4632

AD P000698

Army Readiness and the Production Base

James M. Hesson*

4

The relationship of our defense industrial base to national security is so well known that it is considered to be "conventional wisdom." The two are so interdependent as to be completely inseparable. This has not always been so.

Before World War I, war involved men more than machines. When we entered World War I, we had to depend on our allies for much of our military equipment. Long lead times associated with the domestic production of war materiel precluded establishing a viable production base within the required time frames.

American-built combat aircraft were not provided to France until long after the end of hostilities, and early elements of the American expeditionary force in France had to use British Enfield rifles instead of American Springfields. What materiel the U.S. did provide was mostly produced by the arsenals of the Army's production base. While this lesson was fresh on our minds, Congress enacted a number of programs designed to accelerate industrial production and provide the needed reserves of weapons, equipment, and materiel.

In spite of this emphasis, the defense industrial base had deteriorated by 1939, and the United States found itself unprepared for World War II. Demands for war materiel by our allies provided an early stimulus to our industries, and before the end of the war we had demonstrated a vast industrial capability. Our ability to surge the industrial base to meet the requirements of a protracted war could not be questioned. As proof of this capability, at the height of the production effort we were producing 50 000 aircraft, 20 000 tanks, 80 000 artillery pieces, and 500 000 trucks a year. In March 1944 we built 9117 military aircraft. At the end of World War II this industrial might was realigned to the civilian sector. The advent of the nuclear age created the feeling that the last great conventional war had been fought and that a large-scale surge capability for war materiel production was no longer needed.

The Korean war revealed few industrial base problems. A healthy industrial base existed as a result of the buildup during World War II, and few shortages were experienced.

Recognizing the potential conflict between consumer and national security requirements, Congress passed the Defense Production Act in 1950. Basically, this act gave the President authority to accelerate the production of critical defense items, to guarantee loans to expedite deliveries of critical materiel, and to direct government loans to industry to expand plants and facilities in order to develop or produce essential materiel.

During the Vietnam war the industrial base had little difficulty responding to requirements for military supplies. Since the United States, for the most part, controlled the rate of buildup in Southeast Asia, production rates presented few problems.

In recent months we have heard a great deal about the deterioration of the American industrial base. The economic position of the United States relative to other major industrial powers is the primary indicator. The problem is fourfold: Aging capital equipment, lower employee productivity, shortage of employees with critical skills, and availability of critical materials. The problem of lower employee productivity is many-faceted and can be attributed in part to older, less sophisticated plant equipment and in part to lack of worker skills. Since there are many undefined variables, I will avoid the problem of worker productivity and address the problems associated with the remaining three areas: aging plant equipment, lack of workers with critical skills, and availability of critical materials.

First, our plant equipment is old and is getting older. For example, 77 percent of the DOD inventory of machine tools is 20 or more years old. In private industry approximately 36 percent of the machine tools are in the over-20 category. Our problem here is compounded by a multibillion dollar backlog of orders in the machine tool industry. Whereas many of our machines are old outmoded types, most Japanese and West German industries have been built since World War II. Their equipment is new and is based on the support of today's technology. Further, our current

*U.S. Army Troop Support and Aviation, Materiel Readiness Command.

economic conditions inhibit modernization. Top government and industry officials continue to wrestle with this problem with little signs of success.

The United Kingdom has many of the same plant equipment problems as the United States, while Japan and West Germany are examples of what modernized industry can accomplish. The first major step toward resolution of any problem is recognizing that a problem does, indeed, exist. The problem of insufficient capital investment to modernize our industrial base is recognized at all levels in both the public sector and the private sector, and positive steps at macrolevels are being taken to effect a solution.

Several actions are available to encourage and help expand the defense-related industrial base. Multiyear contracting, repeal of the cancellation costs ceiling for multiyear contracting, relief from the full funding policy, and relaxed restrictions on advanced procurement are being considered.

For the purposes of this discussion on the availability of workers with critical skills, our production workers may be placed into two broad categories: the skilled tool and machine trades and the manufacturing trades. The manufacturing trades are those people who man our production assembly lines. For the most part the tasks that these workers perform are simple and can be easily learned. By applying wages as an incentive, workers in this category can be obtained in the type and quantity needed and at the geographic location desired. There is little concern about this area. I am concerned, however, about the skilled manpower shortage that exists in the tool and machine trades. Current studies show that the nation will be short 250 000 machinists in the next 5 years. Both Department of Labor and private sector initiatives to qualify skilled machinists through training programs have met with limited success. The shortage leads to competition for available labor and upward pressure on costs. The problem is further complicated by the many years of intensive training required before a person reaches the status of master craftsman. Traditional apprenticeship programs require 8000 hours of on-the-job training plus a minimum of 576 hours of classroom study. The problem is further compounded because the aptitudes required for development of machinist skills are the same as those required for engineering and other highly technical professions, resulting in a high level of competition for available talent.

Even if capital equipment and skilled workers were available qualitatively and quantitatively, we would still have the problem of the availability of critical materials. Such minerals and metals as cobalt, chromium, manganese, and mica simply are not available in the United States. Design and manufacture of many of our modern armament systems depend on minerals that the United States is forced to import. The availability of most of these critical raw materials is dependent on politically unstable, third world, undeveloped nations. The availability of these raw materials on an uninterrupted basis cannot be assumed under ideal peacetime conditions. During time of war, the availability of these raw materials would be highly questionable. One answer to this problem would be to stockpile huge supplies of these materials—enough to satisfy any contingency. We do, in fact, maintain stockpiles of strategically critical minerals and metals, but such stockpiling is extremely expensive, and there is always the question of how much is enough.

Because of the factors that I have discussed—lack of modern, capital equipment, lack of skilled workers, and shortages of critical industrial raw materials—we are having to rely more and more on foreign sources for critical components. We are becoming more and more dependent on the productivity of other industrialized nations of the world rather than improving our own productivity.

Now, how does the design engineer fit into the overall scheme of things? What part can the designer play to help ease the problems that I have just discussed? One of your primary concerns must be "producibility" or "reproducibility." Let us look for a few minutes at some of the aspects of producibility that should be foremost in the designer's mind.

First, the designer should be concerned about unit cost—"design to cost." The name of the game is more bang for the buck. How many guns can we afford? How many planes, ships, and missiles? With a 1000-dollar budget, you can have one 1000-dollar gun or ten 100-dollar guns. (The purist may argue that the 1000-dollar gun is 10 times as good as a 100-dollar gun.) Unit cost reductions with enhanced capability are not outside of our reach and should be a design goal. Small, hand-held calculators that cost considerably less than 100 dollars now perform functions previously performed only by machines that cost many thousands of dollars. This, of course, can be called technology growth. The fact remains that cost defines quantity. Our adversaries deal in mass, and, while we generally are technologically superior, the lower the unit cost the more we are able to build up our readiness posture.

This brings me to the second "producibility" consideration. It is "designed to produce." As I mentioned previously, skilled tool and die makers represent critical skills, while production-line workers are in greater supply and can react more quickly to surge demands. Avoid high technology production methods that require higher-order workers whenever possible.

The designer should also avoid "sole source" situations whenever possible. I call this "designing for multiple producers." Hardware designs that can be produced by only one contractor and subsystems that are supplied by only one vendor drive cost up, affect production lead time, and severely reduce surge capability. Such situations are also highly sensitive to perturbations, such as labor problems, and natural disasters, such as storms, floods, fires, etc. Further, subcontractors and vendors may be reluctant to increase their production base because of the uncertain nature of military procurement. Sole-source production places heavy demands on the industrial base in terms of capital equipment, skilled workers, and critical materials required. Every effort should be taken to maximize the sources of supply.

The designer must also be sensitive to the availability and cost of materials required. This design parameter is difficult, for as we demand greater strength, longer life, and less weight, the materials' content tends to increase in composition complexity. However, as pointed out earlier, many minerals and metals used in the manufacture of modern technology materials are expensive, are in short supply, and are supplied by politically unstable nations. Copper is an expensive metal in fluctuating supply. At one time enormous amounts of copper tubing were used by the building industry. PVC (polyvinylchloride) is cheaper, easier, and quicker to install, the materials are readily available, and virtually untrained labor can be used. To top it all off, the PVC tubing has a longer life expectancy than its metal counterpart.

Reliability must also be high on the designer's list of concerns. Each of us has had, at one time or other, an unpleasant experience with an unreliable item—be it an automobile, lawn mower, or washing machine. (Sometimes we use less socially acceptable adjectives to describe these products.) These are the items that stay in the repair shop or are out of operation more than in. You soon develop strong feelings about both the item and its manufacturer. A field soldier is no different. An airplane or helicopter that is not reliable results in high maintenance cost, low mission capability, supply surges, and a lack of confidence by the pilot and maintenance technicians. An unreliable aircraft in a combat situation is intolerable, and combat is what defense preparedness is all about.

Simplicity of operation and maintenance is also a primary design thrust. True frustration is trying to change the spark plugs on an automobile only to find that you practically have to disassemble the automobile to get to them. Proper design of the automobile is when all of the spark plugs can be easily removed with a standard plug socket and when maintenance requirements are reduced through reliability design of the ignition system to maximize intervals between replacement.

Our interface with Army readiness begins before the production process. We must collectively optimize the design of our hardware around the considerations just outlined. The task is not easy but one we must all strive for.

How does the future look? I remain optimistic because we are becoming aware of the state of our industrial base. We recognize that the defense industrial base is dependent on private industry. However, as we review the past we must learn for the future.

As a result of mobilization of U.S. industry during World War II, a private sector defense industry did appear, and it was sustained by postwar production requirements. It was this segment of the industrial base that supplied most of the materiel needed during the Korean war. Additionally, a trend was established which deemphasized the use of costly government-owned facilities in favor of privately owned industrial resources that could produce war materiel faster and cheaper. As the military procurement budget has declined, defense contractors have continued to migrate from the military market to the more lucrative and stable commercial segment of the economy. The very low profit margin for government contracts and the increasing administrative complexity of our procurement process cause many contractors to shy away from defense production. These factors, coupled with industry's decline in productive capability, unless corrected, put our readiness posture at question. According to General Slay, as commander of the Air Force Systems Command speaking to the House Armed Services Committee's Industrial Preparedness Panel, "It is a gross contradiction to think that we can maintain our position as a first-rate military power with a second-rate industrial base." I have confidence that the Army industrial preparedness can improve significantly in the next few years. All budgetary, political, and economic factors point in that direction. However, we must

do our part through emphasis on producibility of design.

This production base has eroded over the past few years, and it will take time and tough political and economic decisions to rectify the problems. We must collectively work to ameliorate the situation to assure an improved military preparedness.

The readiness of the Army begins with all of you here, the people who are driving tomorrow's technology. But your technology must transit through an affordable and viable manufacturing process to be usable for the soldier in the field. I encourage all of you to make that transition process possible.

NASA Helicopter Transmission System Technology Program

Erwin V. Zaretsky*

Man's goal to achieve flight is recorded in the legends and mythology of the human race. By emulating the flapping of bird's wings, we made our first attempts at flying. The ancient Chinese developed a flying toy which by rotary motion produced lift. This rotary-winged toy eventually found its way to medieval Europe. In the later part of the 15th century, Leonardo de Vinci sketched his concept of a vertical flying machine (fig. 1), probably based on the Chinese rotary-winged toy. De Vinci's proposed powerplant for his rotorcraft was a spring. In 1843, over 300 years after de Vinci, Sir George Cayley sketched his concept of an "Aerial Carriage" (fig. 2), which showed some insight into rotary wing flight, including a mechanical power transmission system (refs. 1 and 2).

On November 13, 1907, nearly 4 years after the Wright brothers achieved man's first powered flight, Paul Cornu achieved the first free flight of a rotary-winged aircraft. The aircraft had twin rotors powered by a 24-horsepower engine. In 1910 Igor Sikorsky attempted, for the second time, vertical flight on his S-2 rotorcraft (fig. 3). He subsequently abandoned efforts on rotorcraft until the 1930's (refs. 1 and 3). In 1925 the first real breakthrough in rotary-wing design was achieved with the invention, by Juan de la Cierva (fig. 4), of the autogyro. Although his aircraft was not a true vertical-lift machine, his contribution to rotor design established the Design theory and data which the helicopter industry subsequently adopted (ref. 1).

Because of the success of Cierva, Sikorsky was motivated once again to look at the possibilities of helicopter design. On September 14, 1939, Sikorsky achieved his first successful flight in his VS-300 helicopter powered by a piston engine (fig. 5). The VS-300 became the prototype of all subsequent helicopter designs (ref. 3).

The next dramatic breakthrough was the advent of the turbojet aircraft engine and its application to the helicopter in the mid-1950's. With the higher propulsion power available, much bigger helicopters were practical. The mechanical power transmission system, which interfaces the engine and the rotor, was now subjected to higher loads and speeds. As turbine engine technology improved in the 1960's, the bearing and gearing technology required in the helicopter transmission did not keep pace with the engine technology improvements. As a result, the transmission became a key factor in limiting the life and reliability of the helicopter in the 1970's. It is also important to operating costs. For example, the mechanical drive system can account for as much as half the maintenance cost of the helicopter.

It has been estimated that the free world demand for helicopters in the 1980's will be in excess of 29 000 aircraft worth an estimated 30 billion dollars. Of this amount, the civil market will require approximately 21 000 aircraft worth approximately 14 billion dollars, and the military market will require approximately 8000 aircraft worth approximately 16 billion dollars. United States manufacturers are expected to capture 8 billion dollars of the civilian market and 6 billion dollars of the military market. Hence, the United States should remain the primary marketplace for new helicopters, providing we maintain a technology lead. With the increase in the civil helicopter market, the financial stakes justify a greater effort on part of the United States to capture a greater percentage of the world market.

It has long been a requirement to provide technology to obtain long-life, efficient, light weight, and compact mechanical power transmissions that are also low-cost and quiet for both commercial and military helicopter applications. In general, current state-of-the-art transmission systems are disturbingly noisy to the pilot and passengers. The maintenance rate on these transmission systems is unacceptably high and, as a result, their reliability for long-life application is relatively low. The time between overhaul (TBO) and mean time between failures (MTBF) on present-day helicopters is much

*NASA Lewis Research Center.

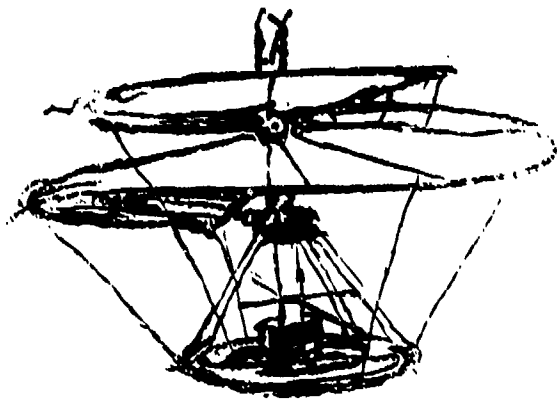


Figure 1. - Leonardo de Vinci's helicopter.

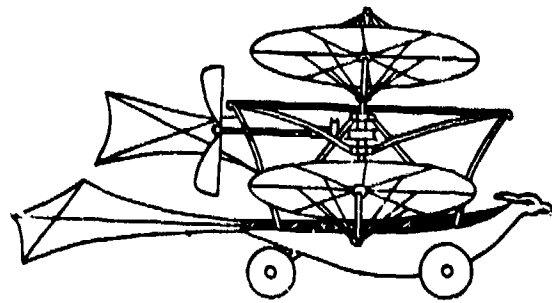


Figure 2. - Sir George Cayley's Aerial Carriage.



Figure 3. - Igor Sikorsky's S-2 helicopter.



Figure 4. - Juan de la Cierva's autogyro.



Figure 5. - Sikorsky's VS-300 helicopter.

lower than that required for economical commercial operation. The helicopter drive system is generally heavier than desired.

The realization of technological improvements for future helicopter drive systems can only be obtained through advanced research and development. The purpose of the NASA Helicopter Transmission System Technology Program is to improve specific mechanical components and the technology for combining these into advanced drive systems to make helicopters more viable and cost competitive for commercial applications.

Program History

The Bearing, Gearing, and Transmission Section of the NASA Lewis Research Center has had a long history of research in mechanical components technology. The section's genesis dates back to the early 1940's and the National Advisory Committee for Aeronautics (NACA), the predecessor to NASA. In 1970 the section began to act in a consulting capacity to U.S. Army Aviation in the area of mechanical components and transmission systems. Several joint programs were initiated between the U.S. Army Research and Development Command Propulsion Laboratory of the U.S. Army Research and Technology Laboratories, and the Section (refs. 4 to 8). In February 1973 NASA Headquarters suggested that the various research programs that the Section was performing be integrated into a transmission system technology program. By June 1973 the first draft of the proposed program was completed. The program was divided into four basic elements: (1) defining the operating characteristics of current state-of-the-art helicopter transmissions; (2) advancing the state-of-the-art for mechanical components such as rolling-element bearings, gears, and lubrication systems and integrating these components into advanced technology transmissions; (3) investigating the concept of traction and hybrid (combined traction and gear) transmissions for helicopter application, and (4) investigating advanced transmission concepts for helicopter applications. The proposed program was coordinated with the various elements of the Army Aviation Research and Development Command. Based on input from the Army and NASA Office of Aeronautics and Space Technology, the transmissions program focused on two classes of helicopter transmissions. The first was in the 300- to 500-hp range with a single engine input. The second was in the 3000-hp range with two engine inputs.

It was decided that baseline data were to be obtained with the 317-hp Bell OH-58 helicopter transmissions which has had a long service life. The transmission was derived from the OH-4 helicopter transmission. This helicopter was itself the forerunner of the five-seat civil Bell Jet Ranger, the civilian version of the OH-58. The Army has approximately 2000 OH-58 helicopters in its inventory. This well-proven transmission is representative of a line of helicopter transmissions which are continually being improved. Three OH-58 transmissions were furnished to the Lewis Research Center by the Army Research and Development Command, Director of Product Assurance.

At the time of program planning, the Army was making its decision to procure a 3000-hp Utility Tactical Transport Aircraft System (UTTAS) helicopter which would incorporate the most current state-of-the-art technology. There were two prototype versions of the UTTAS Helicopter under consideration. One was designed and manufactured by the Vertol Division of the Boeing Co., and the other by Sikorsky Aircraft Division of United Technologies. Baseline research would be performed under the NASA program on the transmission from the aircraft chosen by the Army. This ultimately turned out to be the Sikorsky UTTAS designated the UH-60 Blackhawk.

Funding was approved for the program beginning in October 1977 (fiscal year 1978). The resulting program was a 5-year funded, seven-million-dollar program with 6 years for performance.

A 500-hp transmission test stand, the design and fabrication stage of which began in October 1977, became operational in October 1979 (fig. 6). This test stand is capable of testing both conventional gear and hybrid (traction/gear) transmissions at input speeds of 6000 or 36 000 rpm.

A 3000-hp transmission test stand belonging to the Army Aviation Research and Development Command, on which tests were performed on the Boeing Vertol version of the UTTAS transmission, was transferred to NASA Lewis. The transmission test stand was refurbished by NASA and was put on line at the Lewis Research Center in March 1981 (fig. 7). It is being modified to be a universal test stand capable of accepting two input shaft arrangements of up to 3000 hp with both conventional

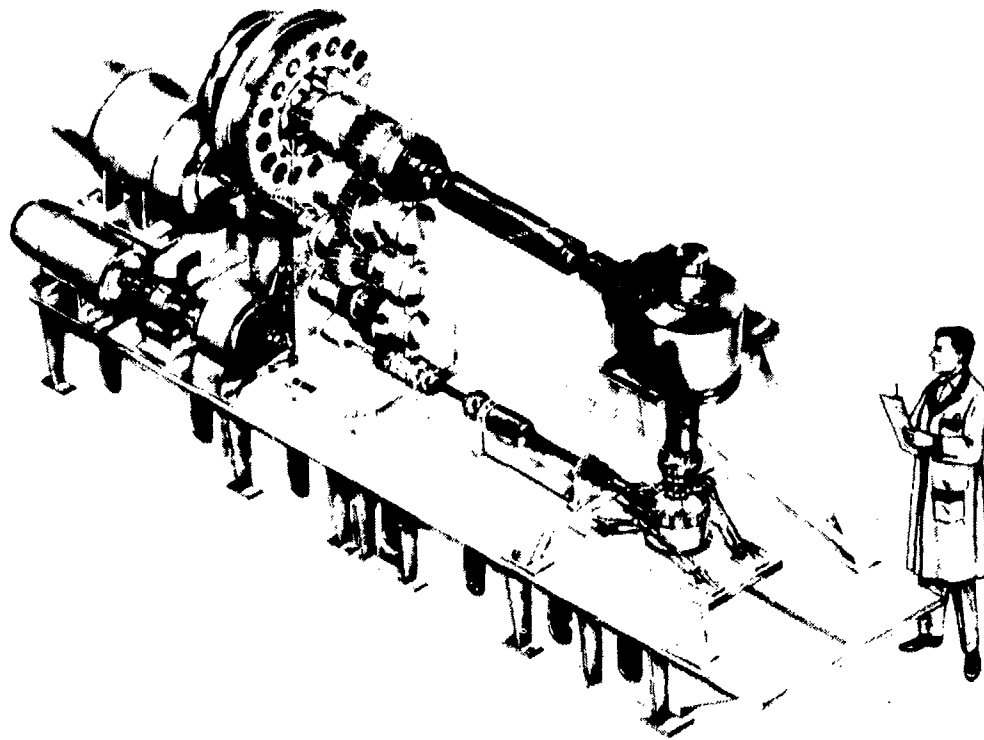


Figure 6. - NASA 500-hp helicopter transmission test stand.

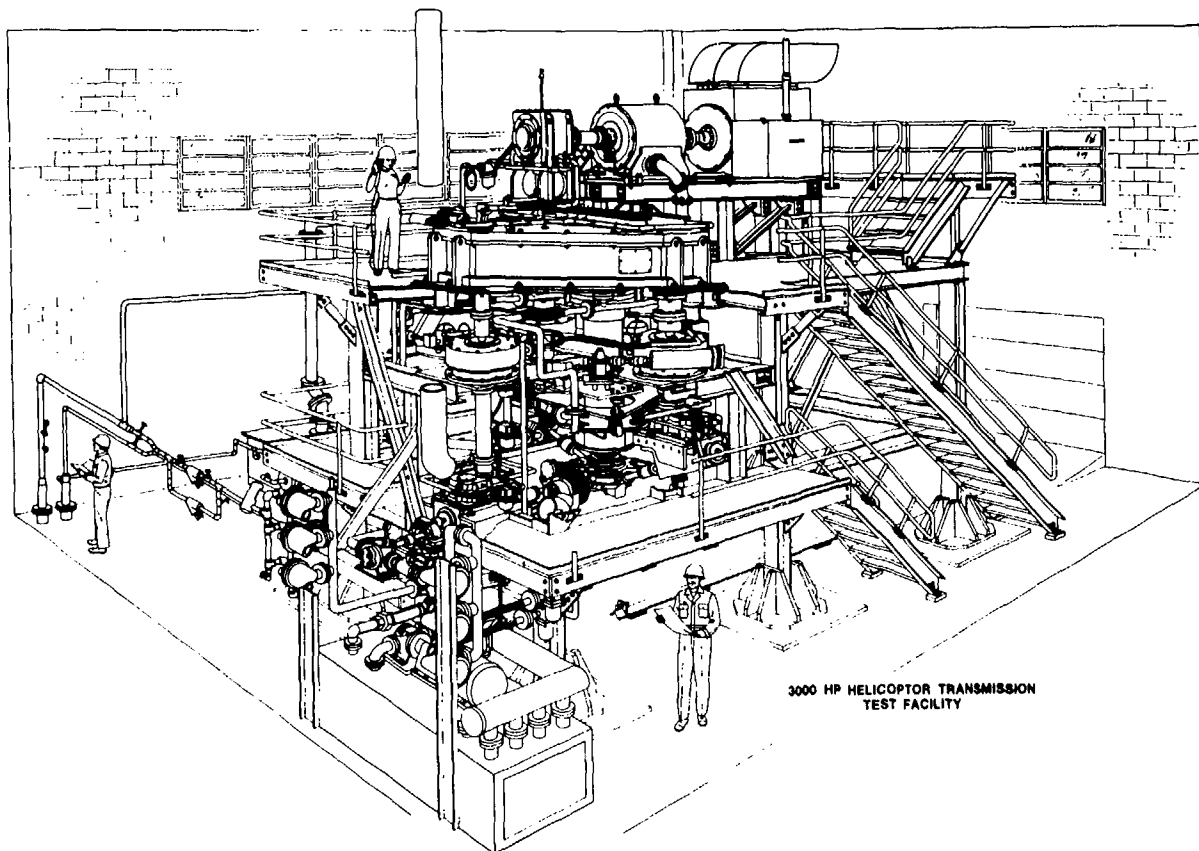


Figure 7. - NASA 3000-hp helicopter transmission test facility.

gear and hybrid traction/gear transmission systems. In addition to the transmission test stands, the other test rigs used for the program are listed in table I.

During the first 3 years of the program, 43 NASA technical papers and technical society journal articles were published reporting the results of the work under this program. A bibliography of these publications is in the appendix.

TABLE I.—FACILITIES AND TEST RIGS AT
LEWIS RESEARCH CENTER

Event	Dedication date
3000-hp Helicopter transmission test stand, dual input	1981
500-hp Helicopter transmission test stand, single input	1978
Bevel-gear endurance test rigs	1978
200-hp variable speed transmission test stand	1977
EHD lubrication test rig	1977
Ultrahigh-speed ball and roller bearing test rig	1977
300-hp transmission technology test stand	1975
Spur gear endurance test rigs	1972
Flywheel energy storage test rig	1978
High-speed flywheel bearing test rig	1978
Ball and roller bearing torque test rig	1965
Rolling element fatigue testers	1959

Program Goals

If the early pioneers in helicopter design and development were asked to state their goals for their aircraft, no doubt their answers would be

- (1) Improve maintainability
- (2) Improve reliability
- (3) Increase life
- (4) Reduce weight
- (5) Reduce noise
- (6) Reduce vibration
- (7) Improve efficiency.

The first three goals basically result in longer mean time between removal (MTBR) of the transmission. Available statistics for military aircraft in the 1970's indicated that transmission removals for repair or overhaul were occurring at a MTBR of between 500 and 1000 hr of operation. A goal of 2500 to 3000 hr was desired. A statistical analysis of both field experience and the stated goal of 2500 hr results in some rather interesting findings. If it is assumed that the transmission is properly designed, lubricated, and maintained, the failure mode of the transmission would be by surface pitting fatigue of the bearing or gear surfaces. Under most conditions, this failure mode should be benign and can be detected by increased transmission vibration, metal partical chip detectors, or spectrographic oil analysis. With this failure mode, it can be expected that from 51 to 63 percent of an original group of transmissions will be removed from service before the MTBR. The probability of the transmission surviving a given time will always be less than the probability of the shortest lived component in the transmission surviving to that given time. Hence, the transmission life or reliability is a function of the individual lives of the components and of the number of components. As a simplified example, if a transmission having 20 components of equal life must have an MTBR of 2500, then each component must have a mean life of approximately 50 000 hr (20×2500). Individual attention must then be given to the bearing and gearing technology to insure individual long lives.

Transmission weight as a function of power is shown in figure 8. Reduced weight can be achieved by a variety of means. These are improved structure and composite materials for the transmission case, longer life bearing and gear materials, reduced lubrication volume, and improved mechanical component design including reduced structure. However, the reduction of weight does not come without its penalties. These may include increased bending deflections of the gears and support structures, higher bending stresses, shorter component lives, increased noise levels, and higher operating temperatures. As a result, design trade-offs must be made to assure minimum weight at maximum life and reliability. Analytical tools must be developed to achieve this optimization as well as higher temperature gear materials.

Lower weight may also mean higher input speed. Hence, high-speed, rolling-element-bearing technology can become essential. Alternatively, transmission concepts that minimize the need for high-speed bearings, such as the bearingless planetary concept, become of interest. Also, traction transmission concepts that eliminate or minimize the need for gears and bearings become attractive. Split torque transmissions can also reduce weight.

Reduced noise and vibration are related. Representative noise levels in state-of-the-art transmissions are shown in figure 9. The primary noise generators within the transmission are the gears. While the use of high-contact-ratio gearing and gear profile modifications may reduce noise, the amount of noise reduction is not expected to be more than 10 dB from current noise levels. Hence, the elimination of the gears with traction rollers becomes attractive. Work performed by General Motors (ref. 9) with a single row planetary-roller traction drive and an equivalent geared planetary drive resulted in a reduction in noise level with the traction drive of approximately 30 dB. Whether the traction technology applied to helicopter transmissions systems will result in this magnitude of noise reduction is a question which remains to be answered.

Improving the efficiency of helicopter transmissions beyond their nominal 97.0 to 98.5 percent, at first blush, appears to be a more difficult task. It is doubtful that much can be done to the design of the bearings or gears that will decrease their power loss. However, it is well known that lubricant type, rheology, chemical and physical properties, as well as the amount and method of insertion into the transmission components affect efficiency. As a result, a key element to improve efficiency is to define the behavior of the lubricant both within the bearing and gear as well as in the transmission system. The effects of lubricant on transmission efficiency and on bearing and gear life must be defined. A lubricant that can provide for good efficiency can result in low component life. Hence, it becomes vital to select those lubricants that provide for both high efficiency and long life.

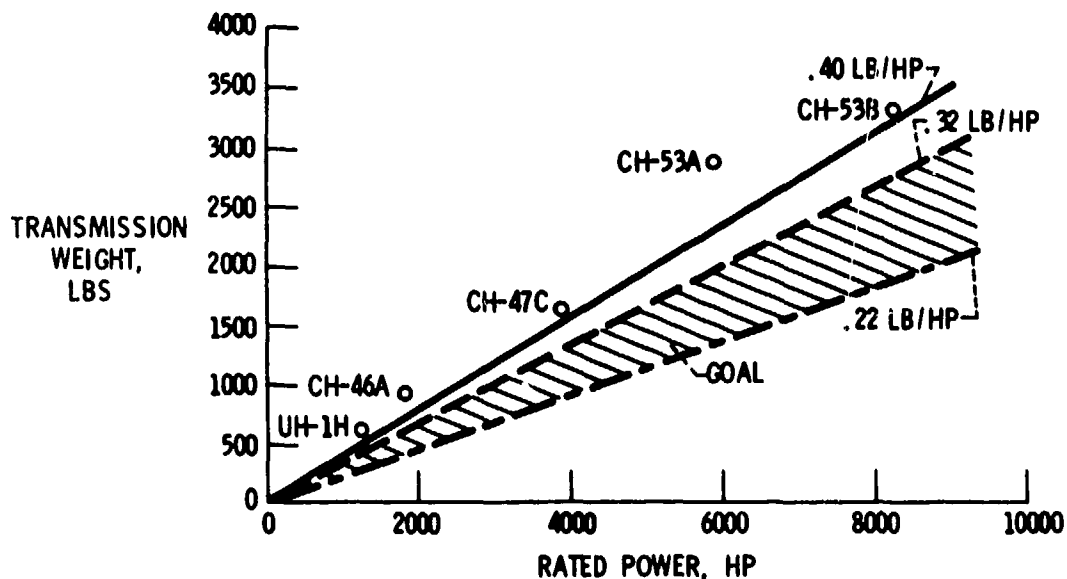


Figure 8. - Transmission weight as function of rated power.

In view of the aforementioned, it has become the purpose of the NASA Helicopter Transmission System Technology Program to make helicopters more cost competitive for commercial applications through improved transmission and mechanical component technologies. The program objectives are to (1) develop technology for the design of advanced transmission systems for helicopter applications; (2) extend bearing, gearing, and lubrication concepts to achieve lightweight, compact, low noise, long-life, low-cost, mechanical power transmission systems for advanced commercial helicopters; and (3) evaluate new concepts in component and transmission tests.

Program Elements

The NASA Helicopter Transmission System Technology Program is divided into four basic areas of research. These are

- (1) Components technology
- (2) State-of-the-art transmissions
- (3) Advanced transmission concepts
- (4) Hybrid and traction transmissions

Components Technology

Components technology research is concentrated in the field of rolling-element bearings, gearing, lubricants, and lubrication systems. Because of the requirement for higher temperature transmission applications, new materials are being used for gears with a minimal data base and limited experience. In addition, heat-treat specification and control can significantly affect the life and reliability of a gear system. Experimental definition of the relative life of gear materials and their heat treatment can aide in the selection of potential gear materials and in determining life-adjustment factors for life-prediction methods. Materials can rationally be selected for longer life application.

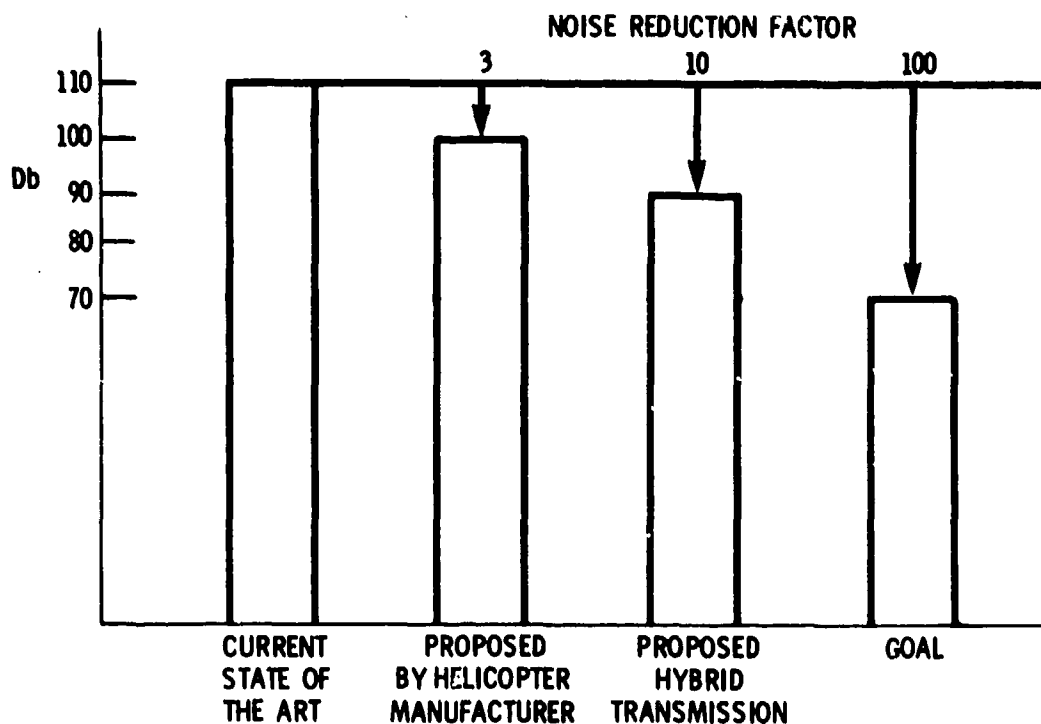


Figure 9. - Representative noise levels in state-of-the-art transmissions.

Proper gear lubrication and cooling has been basically an art. In general, the choice of lubricant flow, pressure, nozzle position, and type has been based on experience and trial-and-error methodology. Equations are being developed whereby the optimum position of the oil jets and lubricant flow rate can be predicted with reasonable certainty to obtain efficient lubrication. Oil volume and gear operating temperatures can be optimized for a given transmission design.

The application of elastohydrodynamic (EHD) lubrication analysis to gear design and operation will enhance gear life and operation. The effect of EHD film thickness in determining transmission life and reliability has, for the most part, been ignored by the transmission designer. Furthermore, lubricant temperature affects film thickness and gear tooth temperature. Hence, cooling analysis of the gear must be integrated with the EHD analysis. Selection of a lubricant affects both parameters and can affect the efficiency of a gearbox as well as its life.

Accurate dynamic stress predictions for tooth bending in the contact zone of gear teeth are very important factors in transmission design. Finite-element techniques for both spur and bevel gears will greatly improve stress predictions. This would allow the designer to more fully utilize the greater load capacity of advanced transmission systems and at the same time minimize transmission weight.

Tooth profile modifications and high-contact-ratio gearing offer the potential of higher transmission loads for a given transmission weight. Similarly, for a given transmission load, reliability and life should improve.

Rolling-element bearings operating under conditions that fall within the state-of-the-art will generally meet or exceed the predicted life, provided the bearing is properly handled and lubricated and providing load conditions have been correctly analyzed. For helicopter transmission applications, four types of rolling-element bearings are generally used:

- (1) Cylindrical roller bearings
- (2) Angular-contact ball bearings
- (3) Tapered roller bearings
- (4) Spherical roller bearings

Before the initiation of the transmission program, analytical methods that could reasonably predict the performance of cylindrical roller bearings and angular-contact ball bearings were fairly well established and had been experimentally verified. However, both tapered roller bearing and spherical-roller bearing analyses were limited. Tapered-roller bearings are being used in some helicopter transmissions to carry combined radial, thrust, and moment loads and, in particular, those loads from bevel gears such as high-speed input pinions. For this application tapered-roller bearings have a greater load capacity for a given envelope or for a given weight than the more commonly used ball and cylindrical roller bearings. The speed of tapered-roller bearings is limited to approximately 0.5 million DN (a cone-rib tangential velocity of approximately 36 m/sec (7000 ft/min) unless special attention is given to lubricating and designing this rib/roller-end contact. At higher speeds centrifugal effects starve this critical contact of lubricant. Moreover, the tapered bearing is sensitive to lubricant interruption at the rib/roller-end contact, making the bearing susceptible to early failure. Developing the design methodology to solve these problems could contribute to improved transmission life and load capacity.

Spherical roller bearings are advantageous for applications where misalignment can be expected such as in the planet gears of a helicopter transmission (fig. 10). Contemporary design of spherical roller bearings relies on "rules," hand calculations, and some modest computerized simulations. Operating speed has been restricted to maximum DN values of approximately 4.5×10^5 . Higher speed transmission systems may require a bearing speed of approximately 1×10^6 DN. Both analytical and experimental verification are required to advance the technology of these bearings.

Improved analytical methods to predict bearing power loss and operating temperature would greatly aid in optimizing transmission efficiency. Unfortunately, the bearing is not an isolated component functioning independent of the other bearings and gears within the transmission system. Proper modeling of the bearing within its operational environment is a condition precedent to the proper prediction of the bearing's operational characteristics.

State-of-the-Art Transmissions

Current design methodology for transmission systems uses relatively standard stress calculations and methods dictated by AGMA standards. These methods for the most part have proven

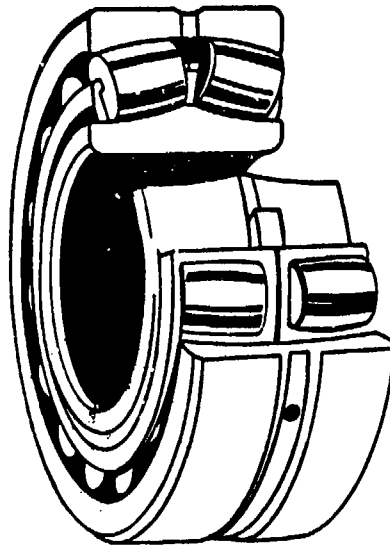


Figure 10. - Spherical roller bearing.

satisfactory for current applications. However, transmission life prediction methods are inadequate and, for the most part, inconsistent from one design group to another. Transmissions can be sized not only for stress, speed, and speed ratio but also for life. The traditional assumption of an infinite gear pitting life is not technically acceptable.

Analytical methods to accurately predict transmission noise is another potential design tool. While life and reliability as well as efficiency are prime design considerations, alternative designs of equal merit may result in significantly different noise amplitudes. Proven analytical methods for predicting noise would aide in the proper design, selection, or modification of gear systems whereby noise can be minimized while mechanical performance can be optimized.

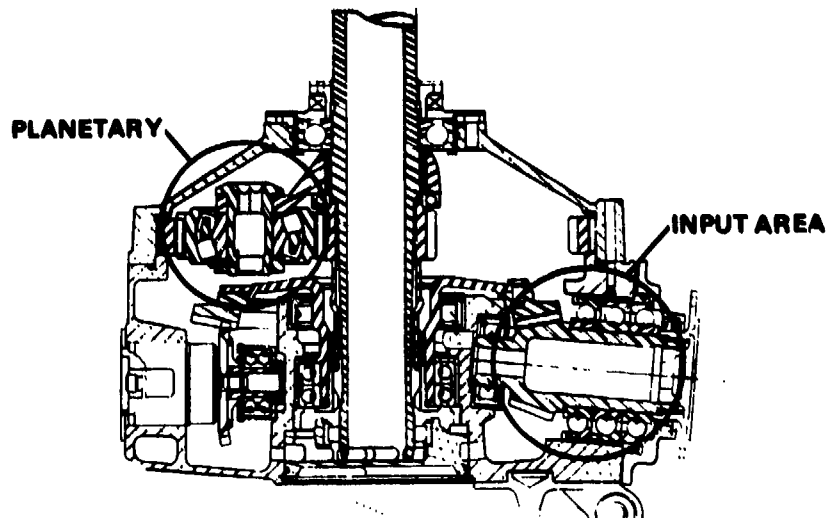
The data in the open literature defining current state-of-the-art transmission technology, supported by tests under carefully controlled conditions, are virtually nonexistent. If changes are to be made in gear and bearing technology as applied to transmission systems, the effect of this technology must be assessed. Hence, the operating parameters of current state-of-the-art transmissions must be evaluated. This knowledge would allow improvements in components and new transmission concepts to be quantified with respect to noise, vibration, efficiency, stresses, and thermal gradients.

Four state-of-the-art transmissions will be evaluated under this program: (1) the 317-hp OH-58 three-gear planetary transmission (fig. 11(a)), (2) the 317-hp OH-58 four-gear planetary transmission (fig. 11(b)), (3) the 3000-hp Sikorsky UH-60A transmission (fig. 12), and (4) the 3000-hp Boeing UTTAS transmission (fig. 13).

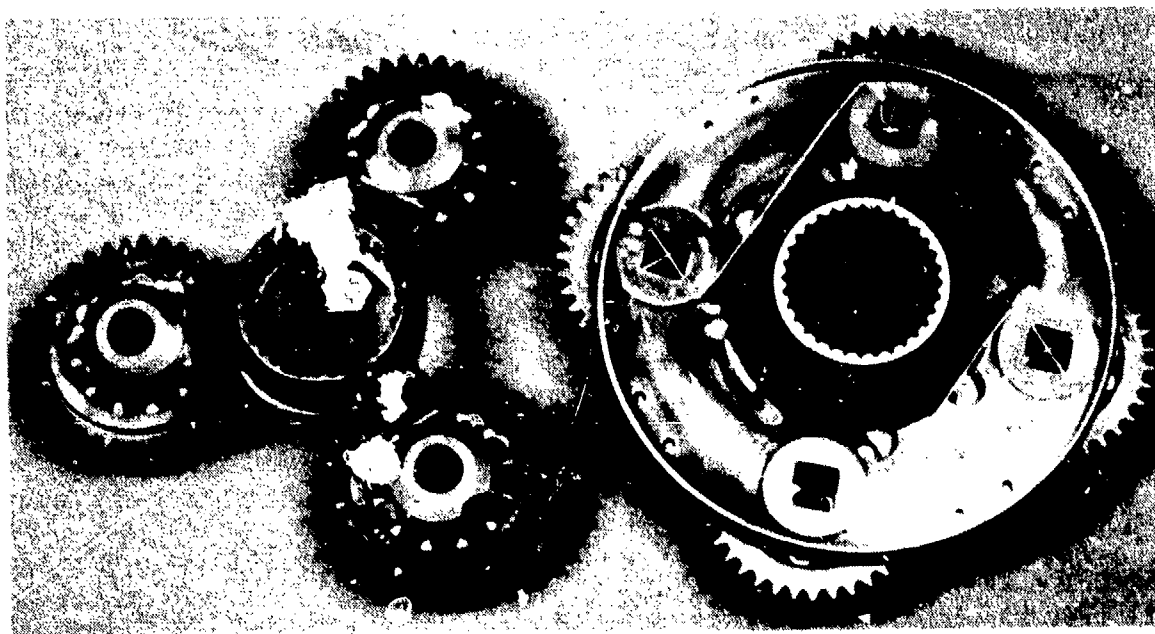
Advanced Transmission Concepts

Three advanced geared transmission concepts are being investigated under this program: (1) advanced components transmission (fig. 14), (2) bearingless planetary transmission (fig. 15), and (3) split-torque transmission (fig. 16). Of the three, the advanced components transmission and the bearingless planetary transmission will be fabricated under the current NASA Lewis program.

Advanced components transmission. - Based on fundamental research performed in mechanical components, an advanced 500-hp transmission has been designed (fig. 14(a)). The concept is a high-contact-ratio four-gear planetary transmission for improved load capacity and life. The high-contact-ratio gears are expected to result in lower noise and reduced dynamic loads. The main bevel gear has been straddle mounted to improve deflection of the gear mounting, thereby improving load sharing in the gear mesh. This, too, is expected to result in lower noise and improved life. The planetary ring gear has been cantilever-mounted to relieve problems inherent in the ring-gear-to-case-spline interface. Rolling-element bearings will be manufactured from vacuum-induction-melted, vacuum-



(a) Three-planet configuration.



(b) Planetary arrangements.

Figure 11. - 317-hp OH-58A transmission.

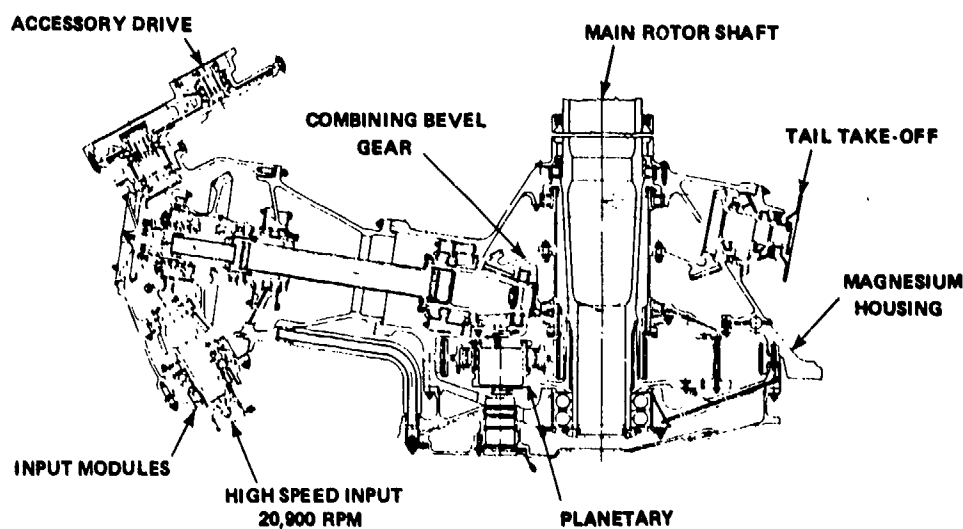
arc-remelted (VIM-VAR) AISI M-50 material. The VIM-VAR AISI M-50 will result in longer bearing life. The bevel gearset will be manufactured from VIM-VAR AISI 9310. The lubrication system will use the latest technology of positive radial-jet lubrication to the sun gear and spline. This will reduce wear and increase the load-carrying capacity of the gearset.

This advanced transmission will have a weight-to-power ratio of 0.24 lb of transmission weight per horsepower, as compared with the standard 317-hp OH-58 transmission of 0.34 lb/hp. A life analysis of the transmission will be conducted to assess its theoretical life. The transmission, which is being fabricated under the current NASA Helicopter Transmission Program, will be tested on the NASA 500-hp test stand.

The transmission design has been modified to allow for the replacement of the ball bearings with tapered-roller bearings (fig. 14(b)). Tapered-roller bearings on the output and input transmission shafts offer greater load capacity and longer life than the ball bearings. The modification also required some change to the existing housing and a new output shaft.



(a) Main gearbox.



(b) Main transmission.

Figure 12. - Black Hawk main transmission.

Bearingless planetary transmission. — The self-aligning bearingless planetary transmission (fig. 15) covers a variety of planetary-gear configurations, which share the common characteristic that the planet carrier, or spider, is eliminated, as are conventional planet-mounted bearings. The bearings are eliminated by load balancing the gears, which are separated in the axial direction. All forces and reactions are transmitted through the gear meshes and contained by simple rolling rings. The concept was first demonstrated by Curtis Wright Corp. under sponsorship of the U.S. Army Aviation Research and Development Command (ref. 10). The 500-hp bearingless planetary transmission for the NASA program is being designed to be comparable with the OH-58 baseline transmission. The transmission weight-to-power ratio is approximately 0.27 lb/hp. A transmission life analysis will also be performed. The transmission will be tested on the NASA 500-hp transmission test stand.

Split-torque transmission. — A means to decrease the weight-to-power ratio of a transmission or to decrease the unit stress of gear teeth is by load sharing through multiple power paths. This concept is referred to as the split-torque transmission (refs. 11 and 12). As part of the NASA Helicopter Transmission System Technology Program, feasibility studies are being conducted on two variants of

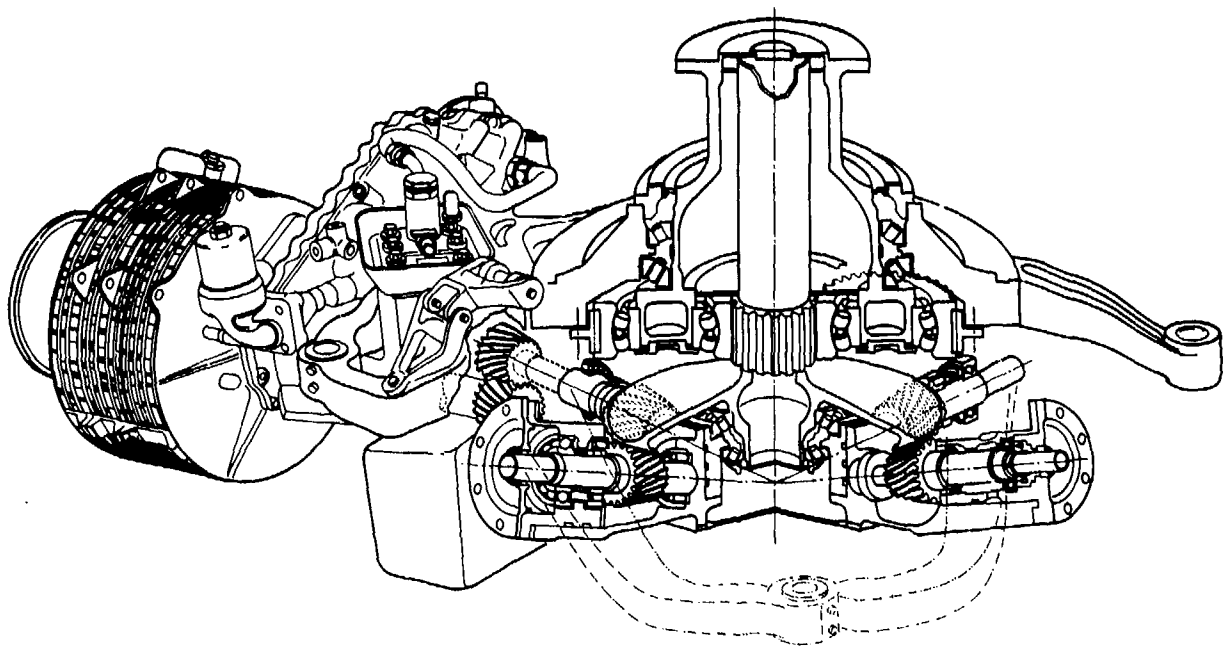
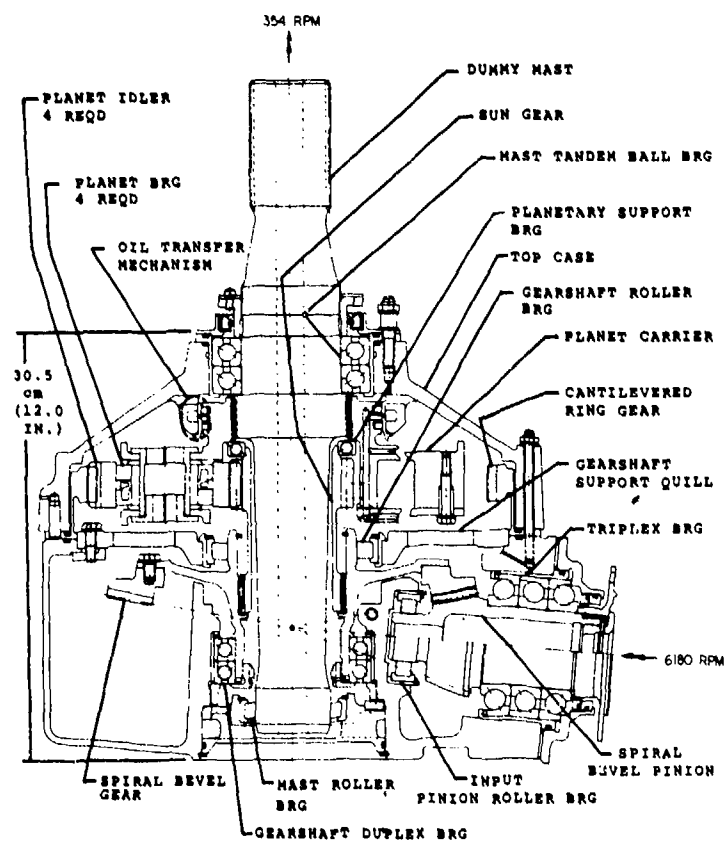
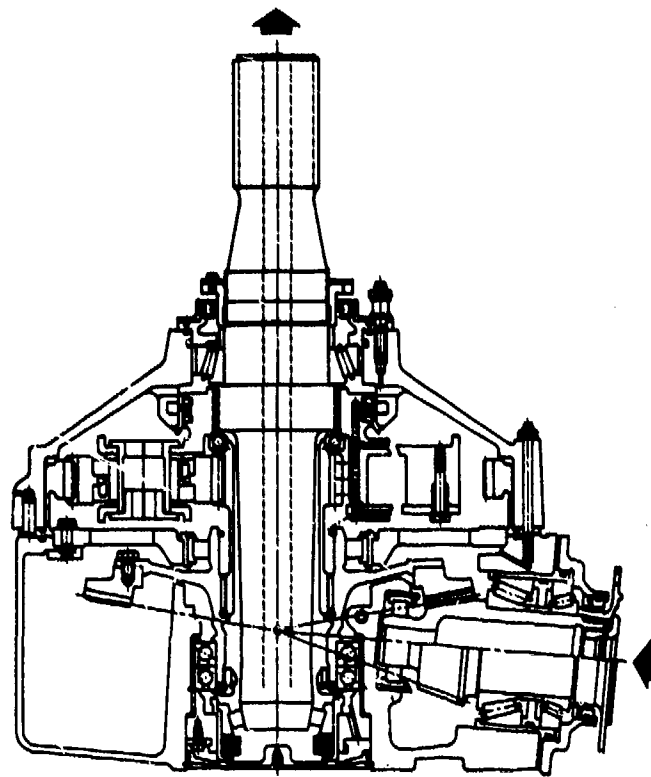


Figure 13. - Boeing 3000-hp UTTAS transmission.



(a) With ball bearings.

Figure 14. - 500-hp Advanced components transmission.



(b) With tapered roller bearings.
Figure 14. - Concluded.

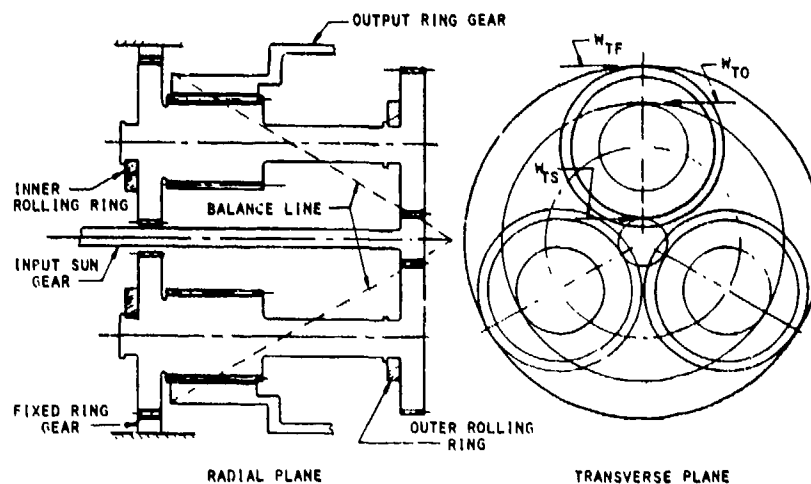


Figure 15 - 500-hp Bearingless planetary transmission.

this concept (fig. 16). The first variant is in the 500-hp range with a single-engine input (fig. 16(a)); the second is in the 3000-hp range with a two-engine input (fig. 16(b)). Instead of a planetary-gear arrangement, the input power is split into two or more power paths and recombined in a bull gear to the output power (rotor) shaft.

There has been no commitment to fabricate a drive of this type under the current program. Preliminary weight estimates indicate that the weight-to-power ratio is approximately 0.24 lb/hp. Life estimates of this concept have not been made. This concept appears to offer weight advantages over conventional planetary concepts without high-contact-ratio gearing. The effect of incorporating

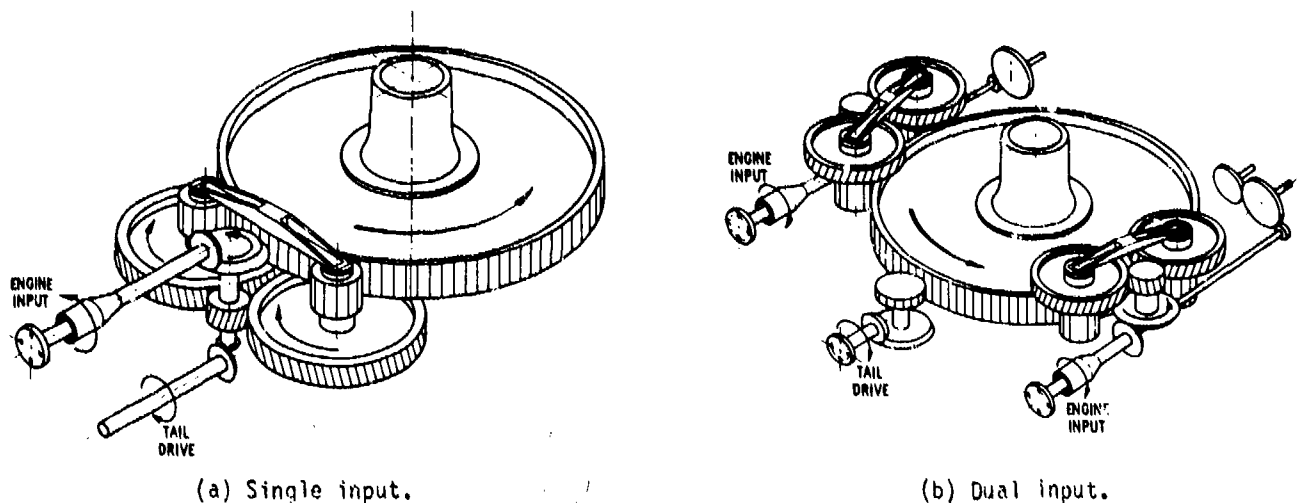


Figure 16. - Conceptual sketch split torque transmission.

high-contact-ratio gearing into the split torque concept is expected to further reduce transmission weight.

Hybrid and Traction Transmissions

Early traction drives were not competitive in size and weight with gear systems. There are several reasons for this. First, unlike a simple gear mesh, in order to prevent slip, the normal load imposed on a traction contact must be at least an order of magnitude larger than the transmitted traction force. Second, the steels used in early traction drives had a significantly lower fatigue life than today's metallurgically cleaner bearing steels. Third, the earlier traction drives did not benefit from the use of modern traction fluids which can produce up to 50 percent more traction than conventional mineral oils for the same normal load. In addition, recent advancements in the prediction of traction-drive performance and fatigue life have added a greater degree of reliability to the design of these drives.

To achieve high power density, the traction drive must be constructed with multiple, load sharing roller elements that can reduce the contact unit loading. For traction drives with a simple, single-row planet-roller format, the number of load sharing planets is inversely related to the speed ratio. For example, a four-planet drive would have a maximum speed ratio of 6.8 before the planets interfered with each other. A five-planet drive would be limited to a ratio of 4.8, and so on.

A remedy to the speed-ratio and planet number limitations of simple, single-row planetary systems was devised by A.L. Nasvytis (ref. 13). His drive system used the sun and ring-roller of the simple planetary traction drive, but replaced the single row of equal diameter planet-rollers with two or more rows of stepped, or dual diameter, planets (fig. 17). With this new, multiroller arrangement, practical speed ratios of 250 to 1 could be obtained in a single stage with three planet rows. Furthermore, the number of planets carrying the load in parallel could be greatly increased for a given ratio. This resulted in a significant reduction in individual roller contact loading with a corresponding improvement in torque capacity and fatigue life.

To further reduce the size and the weight of the drive for helicopter transmission applications, NASA incorporated with the second row of rollers, pinion gears in contact with a ring gear (fig. 18). The ring gear is connected through a spider to the output rotor shaft. The number of planet-roller rows and the relative diameter ratios at each contact are variables to be optimized according to the overall speed ratio and the uniformity of contact forces. The traction-gear combination is referred to as the hybrid transmission.

Three variants of the hybrid transmission have been studied and will be fabricated in the current NASA program. A 500-hp low-ratio variant has been fabricated (fig. 18) and will be tested. The transmission, which has a weight-to-power ratio of 0.27 and a speed reduction ratio of 17:1, could

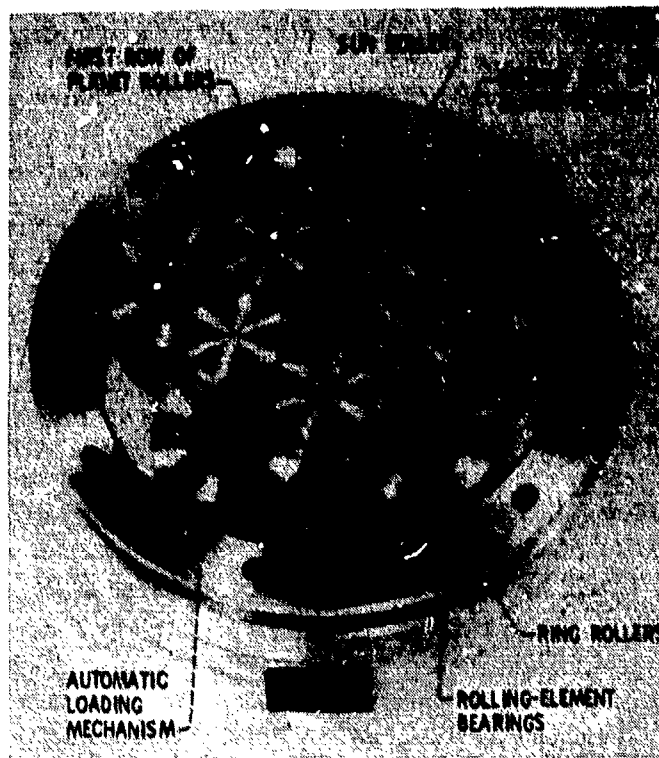


Figure 17. - Multiroller planetary traction drive.

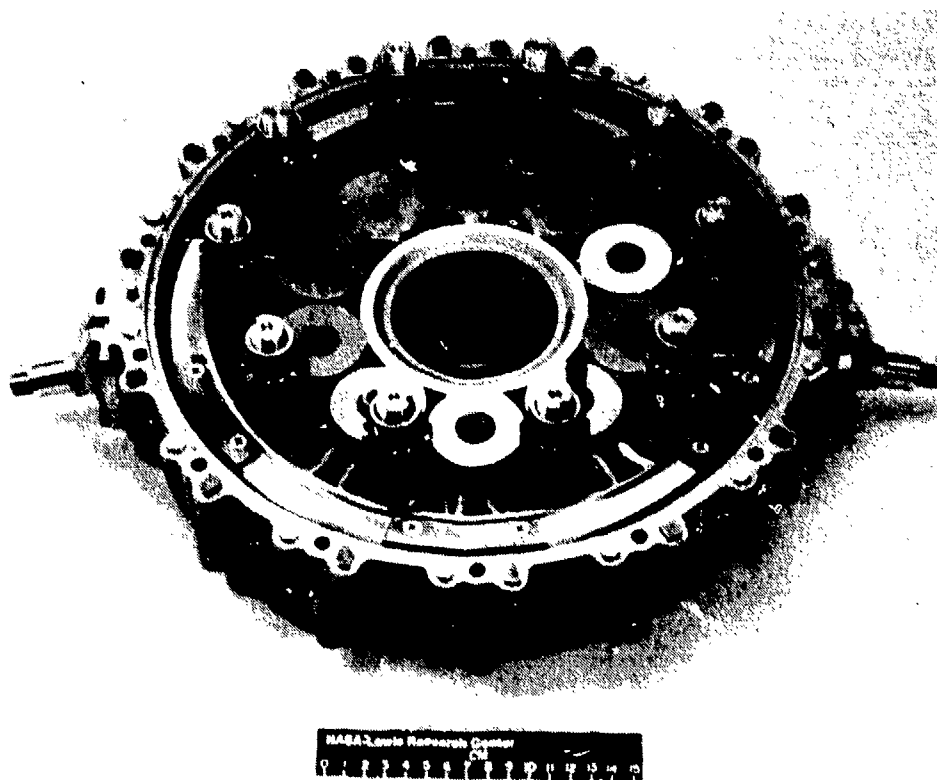


Figure 18. - Hybrid stage of 500-hp hybrid helicopter transmission.

retrofit the OH-58 helicopter. The second variant of the hybrid transmission is referred to as the 500-hp high-ratio variant. This transmission has a speed reduction of 101:1. The low-ratio hybrid is designed for a speed input of approximately 6020 rpm, and the high-ratio variant is designed for an input speed of approximately 36 000 rpm. Because the transmission can accommodate the higher input speed, the 40-lb, 6:1 reduction gearbox on the engine can be eliminated. Hence, the power train weight-to-power ratio is approximately 0.20 lb/hp.

Life estimates of both the low- and high-ratio variants were made. For the low-ratio variant the mean fatigue life is estimated to be approximately 3000 hr at a 70-percent prorated load. Under similar conditions the high-ratio variant has a mean fatigue life of approximately 50 000 hr.

The third variant of the hybrid transmission is a 3000-hp, two-engine input variant having a reduction ratio of 81:1 with an input speed of 20 000 rpm. The transmission, which is under design and which will be fabricated under the NASA program, could be compatible with the Army's UH-60 helicopter. It is expected to have a weight-to-power ratio of 0.25 lb/hp. Preliminary life calculations indicate that this transmission will have a mean fatigue life of approximately 47 000 hr at 70 percent prorated load and 16 000 hr at a continuous 100-percent load. Testing of this transmission will be on the NASA 3000-hp helicopter transmission test stand.

Summary of Results

The NASA Helicopter Transmission System Technology Program began October 1977. The purpose of the program is to make helicopters more feasible and cost competitive for commercial application. The program objectives are (1) to develop technology for the design of advanced transmission systems for helicopters; (2) to extend bearing, gearing, and lubrication concepts to achieve lightweight, compact, low-noise, long-life, low-cost, mechanical power transmission systems for advanced commercial helicopters; and (3) to evaluate new concepts in component and transmission tests.

The program is divided into four basic areas of research. These are (1) components technology, (2) state-of-the-art transmission, (3) advanced transmission concepts, and (4) hybrid and traction transmissions. The area of component technology is concentrated in the fields of rolling-element bearings, gearing, lubricants, and lubrication systems. The state-of-the-art transmissions to be evaluated are the (1) 317-hp OH-58 three-gear planetary transmission, (2) 317-hp OH-58 four-gear planetary transmission, (3) 3000-hp Sikorsky UH-60 transmission, and (4) 3000-hp Boeing UTTAS transmission. Three advanced gear transmission concepts are being investigated. These are the (1) advanced components transmission, (2) bearingless planetary transmission and (3) split-torque transmission. The advanced components transmission and bearingless planetary transmission are being fabricated in a 500-hp single-engine input version. The split-torque is being studied for a single-engine-input 500-hp and a 3000-hp two-engine-input version. However, the split-torque transmission will not be fabricated under the current program. Three variations of the hybrid transmission will be fabricated and tested: (1) 500-hp single-engine-input low-ratio hybrid transmission, (2) 500-hp single-engine-input high-ratio hybrid transmission, and (3) 3000-hp dual-engine-input hybrid transmission. These transmissions are expected to have longer lives and significantly lower noise than state-of-the-art transmissions and the other advanced-concept transmissions being evaluated.

The NASA Program will contribute technology towards quieter and more efficient transmission systems having higher power-to-weight ratios at lives and reliabilities greater than state-of-the-art systems. Further, the use of improved mechanical components, such as gears and bearings, advanced materials and lubricants and design methodology should improve transmission maintainability and mean time between removal.

Appendix

Bibliography of Publications Reporting Results of NASA Helicopter Transmission System Technology Program

1978

- Bamberger, E. N.; and Parker, R. J.: Effect of Wall Thickness and Material on Flexural Fatigue on Hollow Rolling Elements. *J. Lubr. Technol.*, vol. 100, no. 1, Jan. 1978, pp. 39-46.
- Coe, H. H.; and Zaretsky, E. V.: Predicted and Experimental Performance of Jet-Lubricated 120-Millimeter-Bore Ball Bearings Operating to 2.5 Million DN. NASA TP-1196, 1978.
- Jones, W. R., Jr.; and Parker, R. J.: Characterization of Wear Debris Generated in Accelerated Rolling-Element Fatigue Tests. NASA TP-1203, 1978.
- Loewenthal, S. H.: Proposed Design Procedure for Transmission Shafting Under Fatigue Loading. NASA TM-78927, 1978.
- Loewenthal, S. H.; Anderson, N. E.; and Nasvytis, A. L.: Performance of a Nasvytis Multiroller Traction Drive. AVRADCOM-TR-78-36, NASA TP-1378, 1978.
- Loewenthal, S. H.; and Moyer, D. W.: Filtration Effects on Ball Bearing Life and Condition in a Contaminated Lubricant. NASA TM-78907, 1978.
- Loewenthal, S. H.; Moyer, D. W.; and Sherlock, J. J.: Effect of Filtration on Rolling-Element-Bearing Life in a Contaminated Lubricant Environment. NASA TP-1272, 1978.
- Parker, R. J.; and Hodder, R. S.: Rolling-Element Fatigue Life of AMS 5749 Corrosion Resistant, High Temperature Bearing Steel. *J. Lubr. Technol.*, vol. 100, no. 2, Apr. 1978, pp. 226-232; discussion pp. 232-235.
- Parker, R. J.; and Signer, H. R.: Lubrication of High-Speed, Large-Bore Tapered Roller Bearings. *J. Lubr. Technol.*, vol. 100, No. 1, 1978, pp. 31-38.
- Parker, R. J.; and Zaretsky, E. V.: Rolling-Element Fatigue Life of AISI M-50 and 18-4-1 Balls. NASA TP-1202, 1978.
- Sidik, S. M.; and Coy, J. J.: Statistical Model for Asperity-Contact Time Fraction in Elastohydrodynamic Lubrication. NASA TP-1130, 1978.
- Townsend, D. P.; and Akin, L. S.: Study of Lubricant Jet Flow Phenomena in Spur Gears—Out of Mesh Condition. *J. Mech. Des.*, vol. 100, no. 1, Jan. 1978, pp. 61-68.
- Townsend, D. P.; Coy, J. J.; and Zaretsky, E. V.: Experimental and Analytical Load-Life Relation for AISI 9310 Steel Spur Gears. *J. Mech. Des.*, vol. 100, no. 1, Jan. 1978, pp. 54-60.

1979

- Anderson, W. J.; et al.: Mechanical Components. Aeropropulsion 1979. NASA CP-2092, 1979, pp. 273-308.
- Coy, J. J.: Correlation of Asperity Contact-Time Fraction with Elastohydrodynamic Film Thickness in a 20-Millimeter-Bore Ball Bearing. AVRADCOM TR-79-26, NASA TP-1547, 1979.
- Coy, J. J.; Gorla, R. S. R.; and Townsend, D. P.: Comparison of Predicted and Measured Elastohydrodynamic Film Thickness in a 20-Millimeter-Bore Ball Bearing. AVRADCOM TR-79-20, NASA TP-1542, 1979.
- Coy, J. J.; and Sidik, S. M.: Two-Dimensional Random Surface Model for Asperity Contact in Elastohydrodynamic Lubrication. *Wear*, vol. 57, no. 2, Dec. 1979, pp. 293-311.
- Jones, W. R., Jr.; and Loewenthal, S. H.: Ferrographic Analysis of Wear Debris from Full-Scale Bearing Fatigue Tests. NASA TP-1511, 1979.
- Jones, W. R.; and Parker, R. J.: Ferrographic Analysis of Wear Debris Generated in Accelerated Rolling-Element Fatigue Tests. *ASLE Trans.*, vol. 22, no. 1, Jan. 1979, pp. 37-44; discussion pp. 44-45.
- Schuller, F. T.: Operating Characteristics of a Large-Bore Roller Bearing to Speeds of 3×10^6 DN. NASA TP-1413, 1979.
- Townsend, D. P.; Baber, B. B.; and Nagy, A.: Evaluation of High-Contact-Ratio Spur Gears with Profile Modification. NASA TP-1458, 1979.
- Townsend, D. P.; Parker, R. J.; and Zaretsky, E. V.: Evaluation of CBS 600 Carburized Steel as a Gear Material. NASA TP-1390, 1979.
- Zaretsky, E. V.; Townsend, D. P.; and Coy, J. J.: NASA Gear Research and Its Probable Effect on Rotorcraft Transmission Design. NASA TM-79292, 1979.

1980

- Anderson, N. E.; and Loewenthal, S. H.: Spur Gear System Efficiency at Part and Full Load. NASA TP-1622, 1980.
- Coe, H. H.; and Schuller, F. T.: Comparison of Predicted and Experimental Performance of Large-Bore Roller Bearing Operating to 3.0 Million DN. NASA TP-1599, 1980.
- Parker, R. J.: Lubrication of Rolling Element Bearings. Bearing Design—Historical Aspects, Present Technology, and Future Problems. W.J. Anderson, ed., ASME, 1980, pp. 87-110.
- Parker, R. J.; Pinel, S. I.; and Signer, H. R.: Lubrication of Optimized-Design Tapered-Roller Bearings to 2.4 million DN. NASA TP-1714, 1980.
- Rohn, D. A.; Loewenthal, S. H.; and Anderson, N. E.: Parametric Tests of a Traction Drive Retrofitted to an Automotive Gas Turbine. DOE/NASA/1011-80/4, NASA TM-81457 AVRADCOM TR 80-8, 1980.
- Savage, M.; and Loewenthal, S. H.: Kinematic Correction for Roller Skewing. ASME Paper 80-DET-76, 1980.

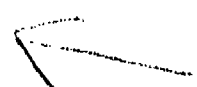
- Schuller, F. T.; Pinel, S. I.; and Signer, H. R.: Operating Characteristics of a High-Speed, Jet-Lubricated 35-Millimeter-Bore Ball Bearing with a Single-Outer-Land-Guided-Cage. NASA TP-1657, 1980.
- Townsend, D. P.; and Akin, L. S.: Analytical and Experimental Spur Gear Tooth Temperature as Affected by Operating Variables. *J. Mech. Des.*, vol. 103, no. 1, Jan. 1981, pp. 219-226.
- Townsend, D. P.; and Zaretsky, E. V.: Endurance and Failure Characteristics of Modified VASCO X-2, CBS 600 and AISI 9310 Spur Gears. *J. Mech. Des.*, vol. 103, no. 2, Apr. 1981, pp. 506-513, discussion pp. 514-515, NASA TM-81421.
- Townsend, D. P.; and Zaretsky, E. V.: Comparisons of Modified Vasco X-2 and AISI 9310 Gear Steels, NASA TP-1731, Nov. 1980.

1981

- Anderson, N. E.; and Loewenthal, S. H.: Effect of Geometry and Operating Conditions on Spur Gear System Power Loss. *J. Mech. Des.*, vol. 103, no. 1, Jan. 1981, pp. 151-159.
- Coe, H. H.; and Schuller, F. T.: Calculated and Experimental Data for a 118-mm-Bore Roller Bearing to 3 Million DN. *J. Lubr. Technol.*, vol. 103, no. 2, Apr. 1981, pp. 274-283.
- Coy, J. J.; Rohn, D. A.; and Loewenthal, S. H.: Constrained Fatigue Life Optimization of a Nasvytis Multiroller Traction Drive. *J. Mech. Des.*, vol. 103, no. 2, Apr. 1981, pp. 423-428; discussion pp. 428-429.
- Coy, J. J.; Rohn, D. A.; and Loewenthal, S. H.: Life Analysis of Multiroller Planetary Traction Drive. AVRADCOM-TR-80-C-16, NASA TP-1710, 1981.
- Coy, J. J.; and Zaretsky, E. V.: Some Limitations in Applying Classical EHD Film Thickness Formulas to a High Speed Bearing. *J. Lubr. Technol.*, vol. 103, no. 2, Apr. 1981, pp. 295-304.
- Huston, R. L.; and Coy, J. J.: Ideal Spiral Bevel Gears—A New Approach to Surface Geometry. *J. Mech. Des.*, vol. 103, no. 1, Jan. 1981, pp. 127-132; discussion pp. 132-133.
- Jones, W. R., Jr.; and Loewenthal, S. H.: Analysis of Wear Debris from Full-Scale Bearing Fatigue Tests Using the Ferrograph. *ASLE Trans.*, vol. 24, no. 3, July 1981, pp. 323-329; discussion, pp. 330.
- Loewenthal, S. H.; Anderson, N. E.; and Rohn, D. A.: Evaluation of a High Performance Fixed-Ratio Traction Drive. *J. Mech. Des.*, vol. 103, no. 2, Apr. 1981, pp. 410-417; discussion pp. 417-422.
- Parker, R. J.; Pinel, S. I.; and Signer, H. R.: Performance of Computer-Optimized Tapered-Roller Bearings to 2.4 Million DN. *J. Lubr. Technol.*, vol. 103, no. 1, Jan. 1981, pp. 13-20.
- Rohn, D. A.; Loewenthal, S. H.; and Coy, J. J.: Simplified Fatigue Life Analysis for Traction Drive Contacts. *J. Mech. Des.*, vol. 103, no. 2, Apr. 1981, pp. 430-438; discussion pp. 438-439.

References

1. Mondey, David, ed.: The International Encyclopedia of Aviation. Crown Publishers, 1977, pp. 342-346.
2. De Bono, Edward, ed.: Eureka! An Illustrated History of Inventions from the Wheel to the Computer. Holt, Rinehart and Winston, 1974, pp. 38-39.
3. Sikorsky, Igor I.: The Story of the Winged-S. Dodd, Mead & Co., 1952.
4. Dietrich, Marshall W.; Parker, Richard J.; and Zaretsky, Erwin V.: Comparative Lubrication Studies of OH-58A Tail Rotor Drive Shaft Bearings. NASA TM X-68118, 1972.
5. Townsend, D. P.; Coy, J. J.; and Hatvani, B. R.: OH-58 Helicopter Transmission Failure Analysis. NASA TM X-71867, 1976.
6. Hanau, Heinz; et al.: Bearing Restoration by Grinding. USAAVSCOM-TR-76-27, Army Aviation Systems Command, 1976. (AD-A025420.)
7. Loewenthal, Stuart H.; Moyer, Donald W.; and Sherlock, John J.: Effect of Filtration on Rolling-Element-Bearing Life in a Contaminated Lubricant Environment. NASA TP-1272, 1978.
8. Dow, T. A.; Kannel, J. W.; and Stockwell, R. D.: Determination of Lubricant Selection Based on Elastohydrodynamic Film Thickness and Traction Measurement. NASA CR-159428, 1979.
9. Hewko, Lubomyr O.: Roller Traction Drive Unit for Extremely Quiet Power Transmission. J. Hydronaut., vol. 2, no. 3, July 1968, pp. 160-167.
10. De Bruyne, Neil A.: Design and Development Testing of Free Planet Transmission Concept. USAAMRDL-TR-74-27, Army Air Mobility Research and Development Laboratory, 1974. (AD-782857.)
11. White, G.: New Family of High-Ratio Reduction Gears with Multiple Drive Paths. Proc. Inst. Mech. Eng. (London), vol. 188, no. 23/74, 1974, pp. 281-288.
12. Lastine, J. L.; and White, G.: Advanced Technology VTOL Drive Train Configuration Study. USAAVLABS-TR-69-69, Army Aviation Material Laboratories, 1970. (AD-867905.)
13. Nasvytis, A. L.: Multiroller Planetary Friction Drives. SAE Paper 660763, Oct. 1966.



Present Technology of Rolling-Element Bearings

Richard J. Parker*

The specification of rolling-element bearings has progressed significantly beyond the selection of ball or roller bearings from a manufacturer's catalog. Applications are becoming more commonplace where novel materials, unique lubrication techniques, and sophisticated computer analysis are required to satisfy difficult environmental and operating conditions. Primary motivation for advancements in the state of technology of rolling-element bearings has come from aerospace requirements. In particular, the aircraft gas-turbine engine has provided the impetus and driving force for quantum leaps in ball and roller bearing technology.

Dramatic improvements in high-speed capabilities of ball and roller bearings can be directly attributed to the under-race lubrication technique first described by Brown (ref. 1) in 1970. Its use for mainshaft bearing lubrication of present turbojet engines is commonplace. The successful application of this technique to tapered-roller bearings will encourage their use in higher speed applications.

Improvements in rolling-element fatigue life have been particularly dramatic with AISI M-50, which has evolved to a premium quality steel, incorporating improved processing, melting, and heat-treating techniques (ref. 2). This premium quality steel is now specified by major turbojet engine manufacturers for critical main shaft bearing applications.

The evolution of computerized rolling-element bearing analysis has significantly improved the reliability of design calculations, particularly for high-speed applications. The predictions of rolling-element bearing performance now can include thermal effects, ball or roller dynamics, time transient effects, and variations in lubricant modelling (ref. 3). *Technology advances*

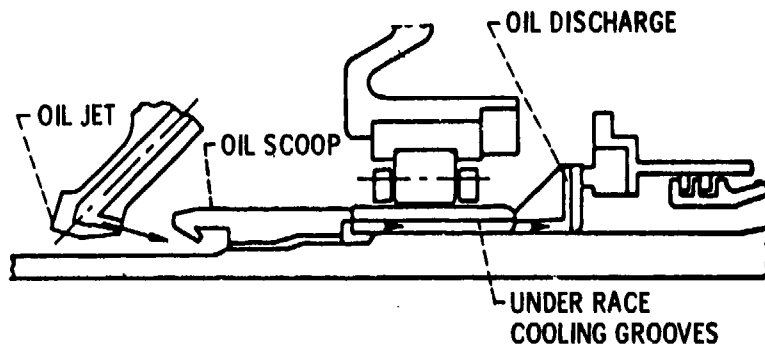
These advancements, among others, signify the progress in rolling-element-bearing technology resulting from efforts to meet advancing aerospace requirements. It is the purpose of this review paper to identify the present technology of rolling-element bearings, the barriers and limits which currently exist, and some of the future requirements that will demand further advancements.

High-Speed Bearing Lubrication

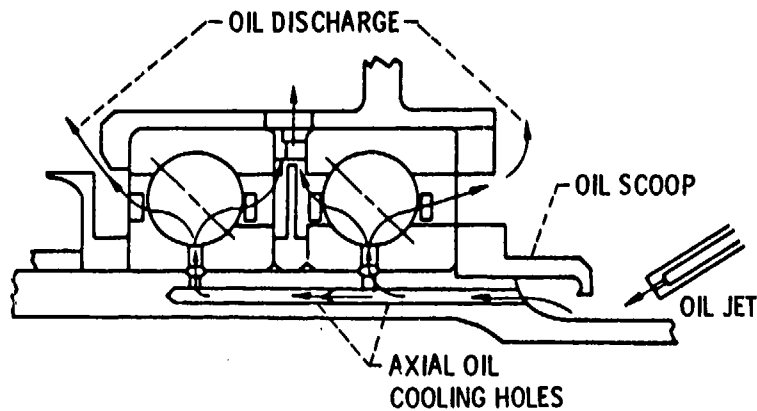
During the mid-1960's, as speeds of the main shaft of turbojet engines were pushed upwards, a more effective and efficient means of lubricating rolling-element bearings was developed. Conventional jet lubrication failed to adequately cool and lubricate the inner-race contact as the lubricant was thrown centrifugally outward. Increased flow rates only added to heat generation from churning the oil. Brown (ref. 1) described an "under-race oiling system" used in a turbofan engine for both ball and cylindrical roller bearings. Figure 1 (from ref. 1) shows the technique used to direct the lubricant under and centrifugally out through holes in the inner race to cool and lubricate the bearing. Some lubricant may pass completely through under the bearing for cooling only (fig. 1(a)). Although not shown in figure 1, some radial holes may be used to supply lubricant to the cage riding lands.

This lubricating technique has been thoroughly tested for large-bore ball and roller bearings up to 3 million DN. (DN is a speed parameter equal to the bore of the bearing in millimeters multiplied by the speed in rpm.) Results of these tests have been published by Holmes (ref. 4) with 125-mm (4.9212-in.) bore ball bearings, Signer, et al. (ref. 5), with 120-mm (4.7244-in.) bore ball bearings, Brown, et al. (ref. 6), with 124-mm (4.8819-in.) bore cylindrical roller bearings, and Schuller (ref. 7) with 118-mm (4.6457-in.) bore cylindrical roller bearings. An example of the effectiveness of under-race lubrication and cooling is shown in figure 2 from reference 8. Under-race lubricated ball bearings ran significantly cooler than identical bearings run with jet lubrication. Beyond 16 700 rpm

*NASA Lewis Research Center.



(a) CYLINDRICAL ROLLER BEARING.



(b) BALL THRUST BEARING.

Figure 1. - Under-race oiling system for main shaft bearings on turbofan engine. (From ref. 1.)

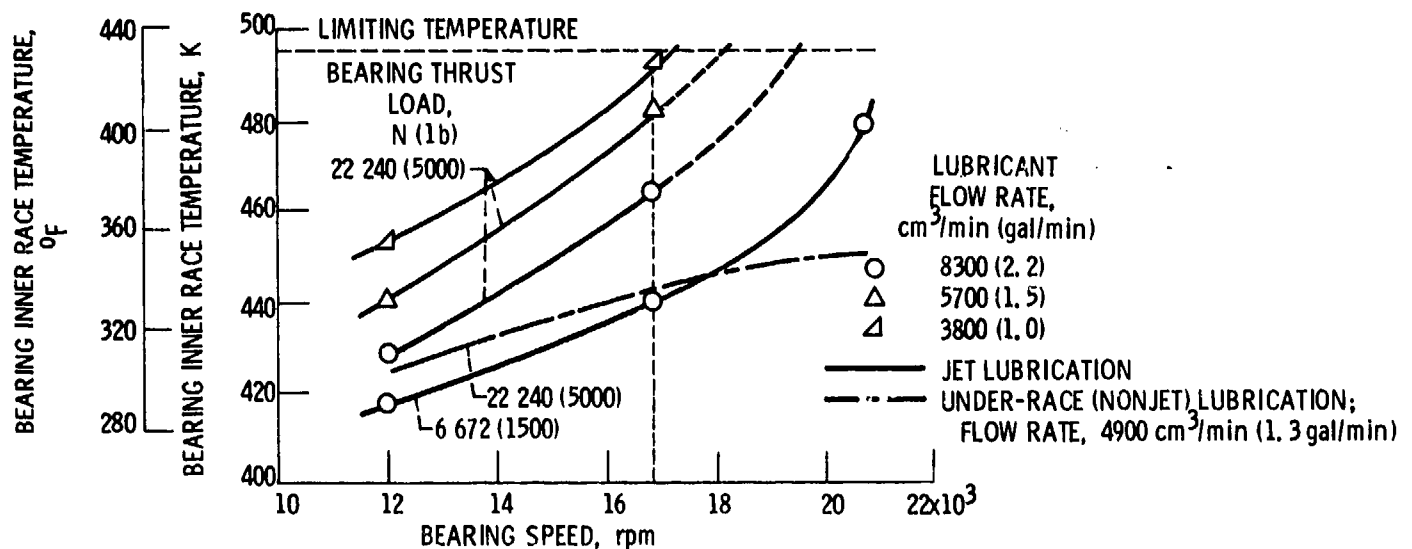


Figure 2. - Effectiveness of under-race lubrication with 120-mm-bore angular-contact ball bearings. Oil-in temperature, 394 K (250° F). (From ref. 8.)

(2 million DN) the bearing temperature with under-race lubrication increased only nominally, while that with jet lubrication increased at an accelerated rate. Only at reduced load could the jet lubricated bearings be run at 2.5 million DN. Under-race lubrication was successfully used under a variety of load conditions up to 3 million DN (refs. 5 and 8).

Applying under-race lubrication to small (<40 mm) bore-bearings is more difficult because of limited space available for grooves and radial holes and for the means to get the lubricant under the race. For a given DN value centrifugal effects are more severe with small bearings since centrifugal forces vary with DN^2 . Heat generated per unit of surface area is also much higher, and heat removal is more difficult in smaller bearings.

Although operation up to 3 million DN can be successfully achieved with small-bore bearings with jet lubrication, some advantages may be attained if under-race lubrication can be used. Schuller (ref. 9) has shown significantly cooler inner-race temperatures with 35-mm (1.3780-in.) bore ball bearings with under-race lubrication. As shown in figure 3 (taken from ref. 9) the effect is greater at higher speeds up to 72 000 rpm (2.5 million DN).

Tapered roller bearings have been restricted to lower speed applications than ball and cylindrical roller bearings. The speed of tapered-roller bearings is limited to that which results in a DN value of approximately 0.5 million DN (a cone-rib tangential velocity of approximately 36 m/sec (7000 ft/min)), unless special attention is given to lubricating and designing this cone-rib/roller-end contact. At higher speeds centrifugal effects starve this critical contact of lubricant.

In the late 1960's the technique of under-race lubrication, that is, lubrication and cooling of the critical cone-rib/roller-end contact, was applied to tapered-roller bearings. As described in reference 10, 88.9-mm (3.5-in.) bore tapered-roller bearings were run under combined radial and thrust loads to 1.42 million DN with cone-rib lubrication (the term used to denote under-race lubrication in tapered-roller bearings).

A comparison of cone-rib lubrication and jet lubrication was reported in reference 11 for 120.65-mm (4.75-in.) bore tapered-roller bearings under combined radial and thrust loads. These bearings were of standard catalog design except for the large end of the roller, which was made spherical for a more favorable contact with the cone-rib. Those bearings that used cone-rib

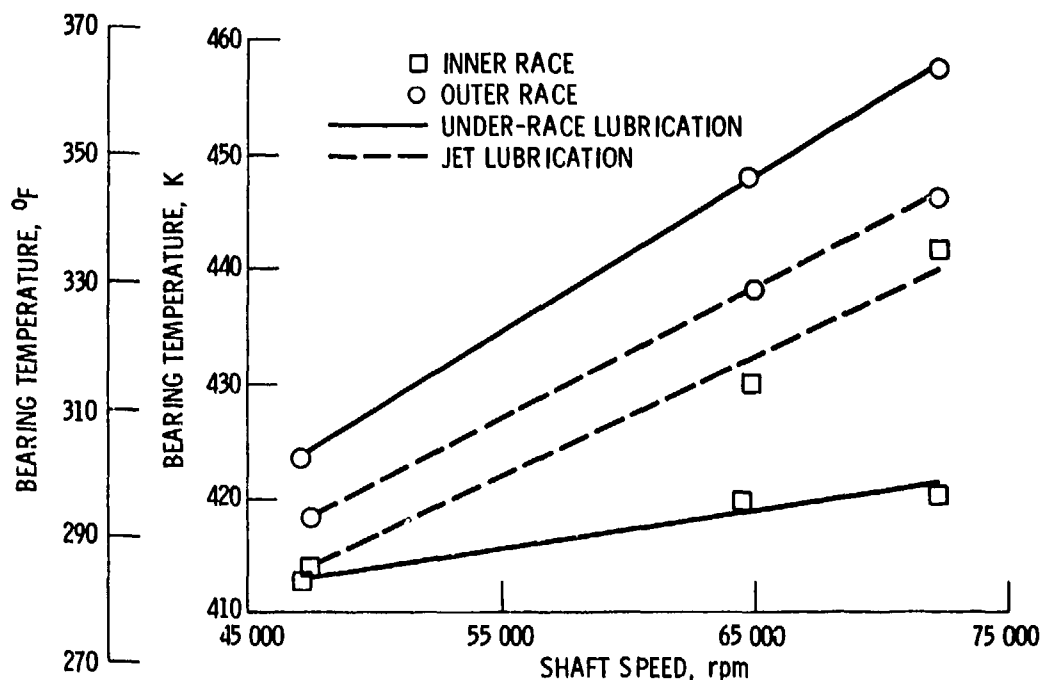


Figure 3. - Effect of under-race lubrication with 35-mm-bore angular-contact ball bearings. Total oil flow rate, 1318 cm³/min (0.348 gal/min); oil-in temperature, 394 K (250° F). (From ref. 9.)

lubrication also had holes drilled through from a manifold in the cone bore to the undercut at the large end of the cone (fig. 4). The results of reference 11 show very significant advantage of cone-rib lubrication as seen in figure 5. At 15 000 rpm (1.8 million DN) the bearing with cone-rib lubrication

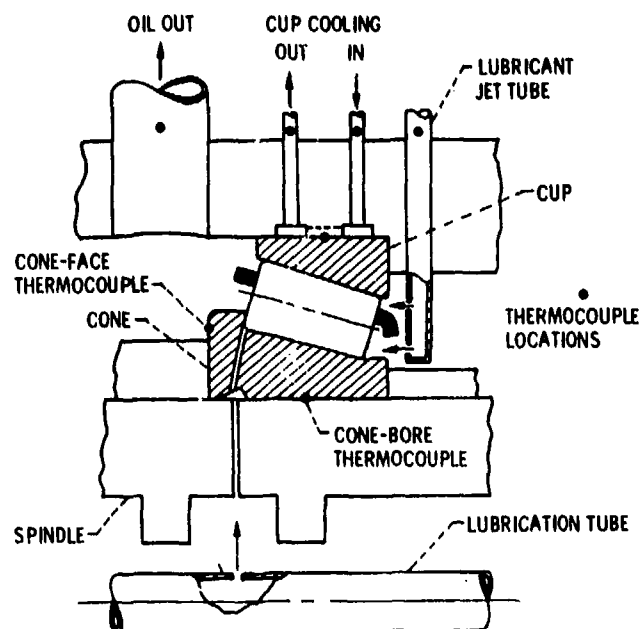


Figure 4. - Tapered-roller bearing with cone-rib and jet lubrication. (From ref. 11.)

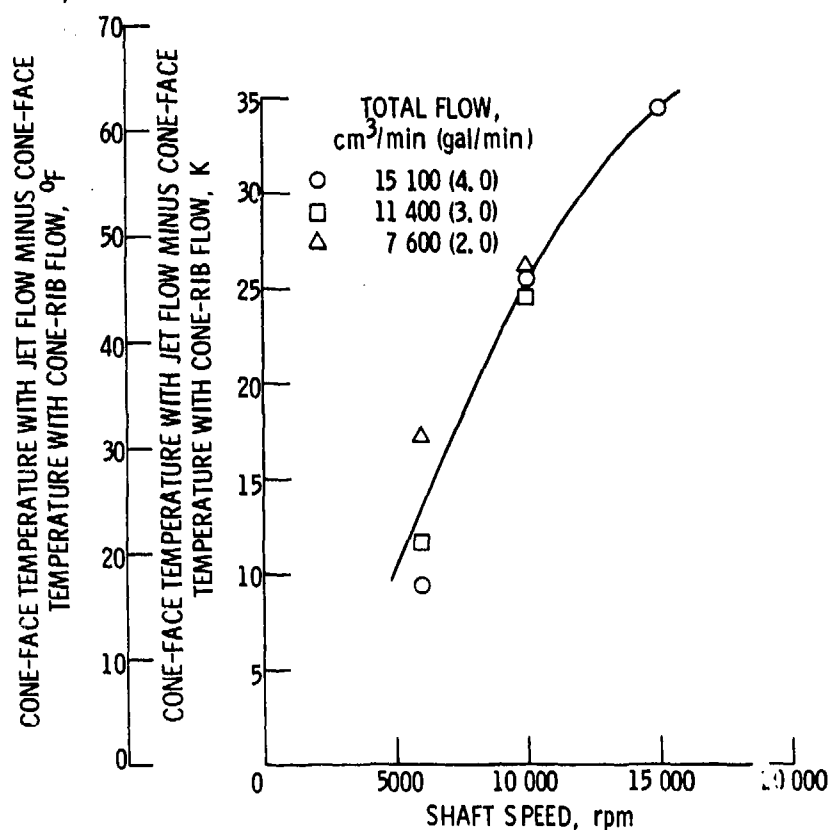


Figure 5. - Advantage of cone-rib lubrication over jet lubrication with tapered-roller bearings. Oil-in temperature, 350 K (170° F). (From ref. 11.)

had a cone-face temperature 34 K (62° F) lower than one with jet lubrication. Furthermore, reference 11 shows that the tapered-roller bearing would operate with cone-rib lubrication at 15 000 rpm with less than half the flow rate required for jet lubrication at that speed.

Further work has shown successful operation with large-bore tapered-roller bearings at even higher speeds. Orvos (ref. 12) reported on long-term operation of 107.95-mm (4.25-in.) bore tapered-roller bearings under pure thrust load to 3 million DN with a combination of cone-rib lubrication and jet lubrication. Optimized design 120.65-mm (4.75-in.) bore tapered-roller bearings were run under combined radial and thrust load with under-race lubrication to both large end (cone-rib) and small end to speeds up to 2.4 million DN (ref. 13).

Under-race lubrication has been shown to very successfully reduce inner-race temperatures. However, at the same time, outer-race temperatures either remain high (ref. 11) or are higher than those with jet lubrication (fig. 3 (from ref. 9)). Outer-race cooling can be used to reduce the outer-race temperature to levels at or near the inner-race temperature. This would further add to the speed capability of under-race lubricated bearings and avoid large differentials in bearing temperature that could cause excessive internal clearance.

The effect of outer-race cooling (or cup cooling in the case of tapered-roller bearings (fig. 4)) is shown in table I (from ref. 13). The cup outer-surface temperature is decreased to the cone bore temperature with cup cooling. With the 35-mm (1.3780-in.) bore ball bearings of reference 9, outer-race cooling significantly decreased outer-race temperatures as shown in figure 6.

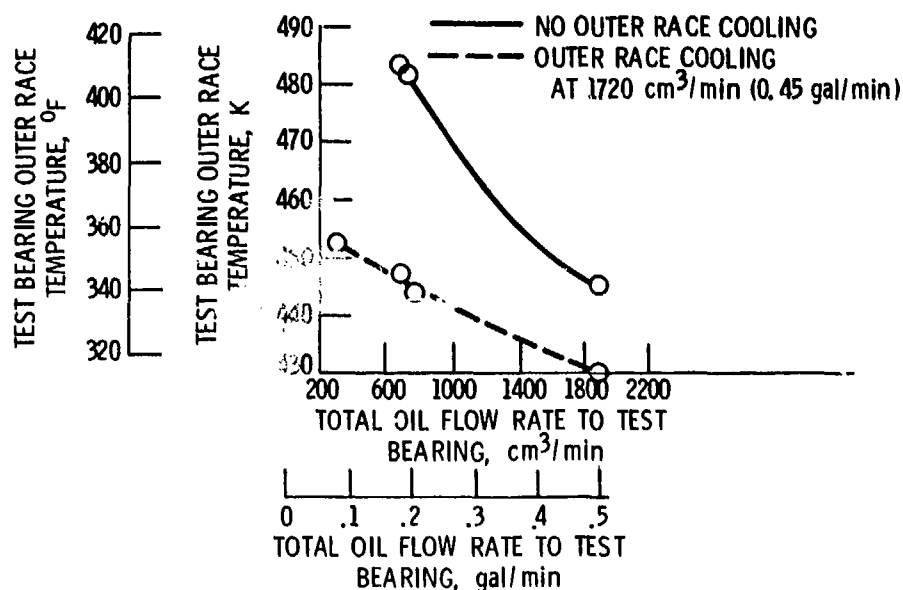


Figure 6. - Effect of outer-race cooling on outer-race temperature of 35-mm-bore ball bearings at 72 300 rpm. Oil-in temperature, 394 K (250° F). (From ref. 9.)

TABLE I. - EFFECT OF CUP COOLING ON TAPERED-ROLLER BEARING TEMPERATURES

[Shaft speed, 18 500 rpm; oil-in temperature, 314 K (195° F); total flow rate without cup cooling, 0.0114 m³/min (3.0 gal/min); from ref. 13.]

Cup cooling flow rate, m³/min (gal/min)	Temperature, K (°F)				
	Cone face	Cone bore	Cup outer surface	Oil-out	Cup cooling oil-out
0	389 (240)	423 (302)	438 (329)	426 (307)	---
0.0038 (1.0)	391 (245)	424 (303)	424 (304)	426 (308)	386 (235)

Under-race lubrication has been well developed for larger bore bearings and is currently being used with many aircraft turbine-engine mainshaft bearings. Because of the added difficulty of applying it, the use of under-race lubrication with small-bore bearings has been minimal, but the benefits have been demonstrated. It appears that the application of tapered roller bearings at higher speeds using cone-rib lubrication is imminent, but the experience to date has been primarily in laboratory test rigs.

The use of under-race lubrication in all the previous work referenced includes the use of holes through the rotating inner race. It must be recognized that these holes weaken the inner-race structure and could contribute to the possibility of inner-race fracture at extremely high speeds. This subject of fracture of inner races is discussed in a later section of this paper. It is apparent, however, that the fracture problem in the inner races exists even without the lubrication holes.

Rolling-Element Fatigue Life

The life of a rolling-element bearing is, for design purposes, generally considered the life to fatigue spalling of the raceways or rolling elements. The assumption is made that the bearing is properly maintained, not abused, and properly lubricated with oil or grease. The life, in stress cycles, to fatigue spalling is heavily dependent on the load on the bearing, the quality of the material, the size of the bearing, and, to a lesser extent, the lubricant.

Major advances have been made in the past two decades in the quality of bearing materials. Improved quality includes improved processing and cleanliness and greater control on material chemistry and heat treatment. In particular, AISI M-50, the bearing material used almost exclusively by aircraft gas-turbine-engine manufacturers in the United States, has seen development that has resulted in significant life improvements (ref. 2). The largest improvements are related to improved vacuum melting techniques. Specifically, the vacuum arc remelting (VAR) processing technique (ref. 2) produces a very homogeneous material with reduced nonmetallic inclusions, entrapped gases, and trace elements.

This process, when used in combination with the vacuum induction melting process (VIM), produces an outstandingly clean material (VIM-VAR). VIM-VAR AISI M-50 is currently being specified for virtually all main shaft bearings by major U.S. aircraft turbine engine manufacturers.

An example of the exceptionally long fatigue life that can be attained with VIM-VAR AISI M-50 is presented in reference 14. A group of 120-mm-bore, angular-contact ball bearings was endurance tested at 3 million DN and a thrust load of 22 200-N (5000 lb). The 10-percent fatigue life obtained was over 100 times the predicted AFBMA life. This long life includes lubrication effects, which are beneficial to life at these high speeds, so that the improvement attributed to VIM-VAR AISI M-50 was a factor of 44 (ref. 14).

AISI M-50 is a through-hardened material, heat treated such that the hardness is uniform throughout the section of a bearing component. Surface-hardened materials are frequently used for rolling-element bearings, primarily in the railroad and automotive industries. Most common are the carburized materials such as AISI 9310, 8620, and 4320 which are typically heat treated with hard cases of Rockwell C 58 to 62 and soft, tough cores of Rockwell C 20 to 48, depending on section size.

These common carburized materials have not seen widespread use in bearings in the aerospace industry, primarily because of their relatively low operating temperature capability of about 422 K (300° F) (ref. 15). Several carburized steels have been developed for higher temperature use, primarily through the addition of alloying elements such as Cr and Mo. CBS-600, CBS-1000M, and Vasco X-2 are carburized steels with continuous service capabilities of 505 K (450° F), 589 K (600° F), and 644 K (700° F), respectively. The hardness retention of these steels compared with the common carburized steels and through hardened materials is shown in figure 7 (ref. 16).

While some prototype bearings have been made with these materials, in particular, tapered-roller bearings of VAR CBS-1000M (refs. 12, 13, and 17), bearing fatigue life data are scarce. Accelerated rolling-element fatigue data and gear fatigue data (refs. 18 to 20) indicate that the rolling-element fatigue lives of these advanced carburized steels are comparable with the standard lower temperature carburized steels and with VAR AISI M-50 through-hardened steel. Life data from accelerated tests in the rolling-contact fatigue tester (ref. 18) are shown in figure 8. These advanced carburized steels show good life potential in these accelerated tests, but full-scale bearing life test data are scarce. It is apparent that more development is needed before they see widespread use in critical aircraft bearing applications.

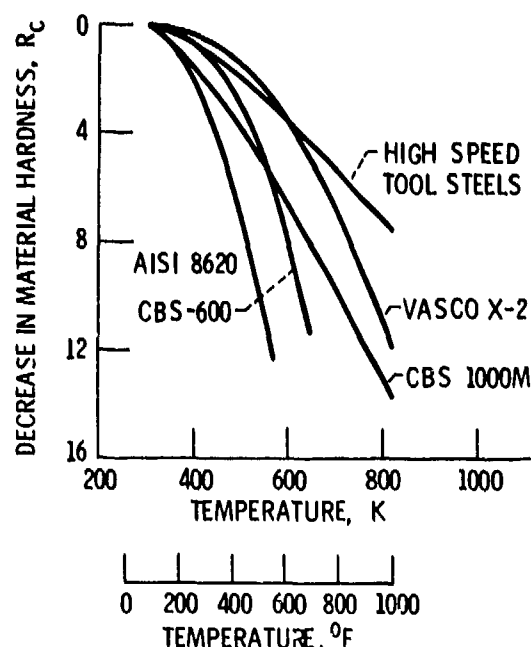


Figure 7. - Hardness retention of advanced carburizing grade steels compared with AISI 8620 steel and through-hardened, high-speed tool steels. (From ref. 16.)

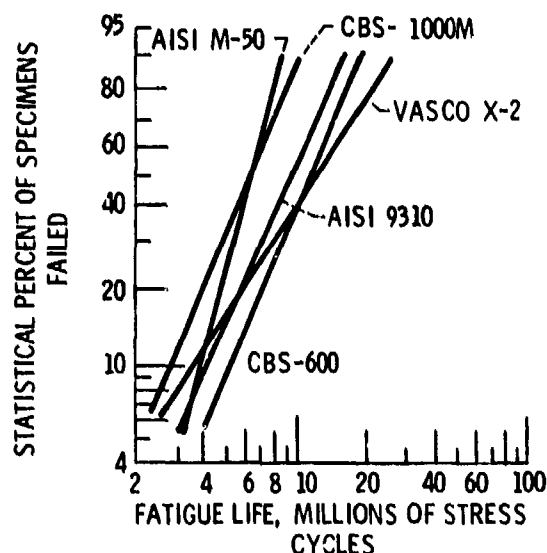


Figure 8. - Rolling-element fatigue life of carburizing grade steels and VAR AISI M-50 steel. (From ref. 18.)

Computerized Analysis

Rolling-element bearing life and performance predictions have been greatly enhanced by the use of some of the newer computer codes now available to design engineers. The ability to closely simulate the performance of a rolling-element bearing also aids in failure analysis of systems where the bearing or external conditions imposed on the bearing are suspect.

Computer analysis has progressed from the early elastic solutions of ball-bearing load distributions considering inertial and centrifugal effects (ref. 21) to a more generalized theory including lubrication and traction effects (ref. 22) and to current programs such as Shaberth (ref. 23) and Cybean (ref. 24), which include thermal analysis and calculation of temperature distributions in the bearing. These latter programs give essentially steady-state solutions (considered quasidynamic) and are useful for the majority of high-speed rolling-element bearing applications.

Computer programs of a fully dynamic nature have also been developed (refs. 25 to 29) in which time transient motions and forces of the rollers or balls and the cage are determined. Computing time with a dynamic program such as that described in reference 27 can become excessive (ref. 30). A direct comparison of a quasidynamic program (ref. 23) and a fully dynamic program (ref. 26) was described in reference 30. The "quasi-dynamic" program is more practical as a bearing design tool where fatigue life, torque, and heat generation are of primary interest. The dynamic program, although consuming large amounts of computer time, appears to be valuable as a diagnostic tool, especially where cage motions are of interest. Shaberth and Cybean, both quasidynamic computer programs, are discussed in more detail in references 3, 31, and 32.

The new computer codes can generate a great amount of output data describing bearing performance at given input conditions. Output data such as load distributions, Hertzian stresses, operating contact angle or skew angle, component speeds, heat generation, local component temperatures, bearing fatigue life, and power loss are typical. But, how well does this output predict actual conditions within an operating bearing? Only a few attempts have been made to compare predicted performance with experimental data. A major problem has been that of obtaining appropriate experimental data with enough detail and accuracy to make a correlation meaningful. Currently, the analyses compute operational characteristics such as component temperatures and roller skew angles which have not yet been experimentally verified.

A comparison of calculated and experimental performance of high-speed ball bearings is presented in reference 33. The analysis provided a good prediction of temperatures and power losses in jet-lubricated 120-mm-bore angular-contact ball bearings (fig. 9). In this work the critical assumptions were the form of the lubricant traction model and the lubricant volume percent (the assumed volume percent of the bearing cavity occupied by the lubricant).

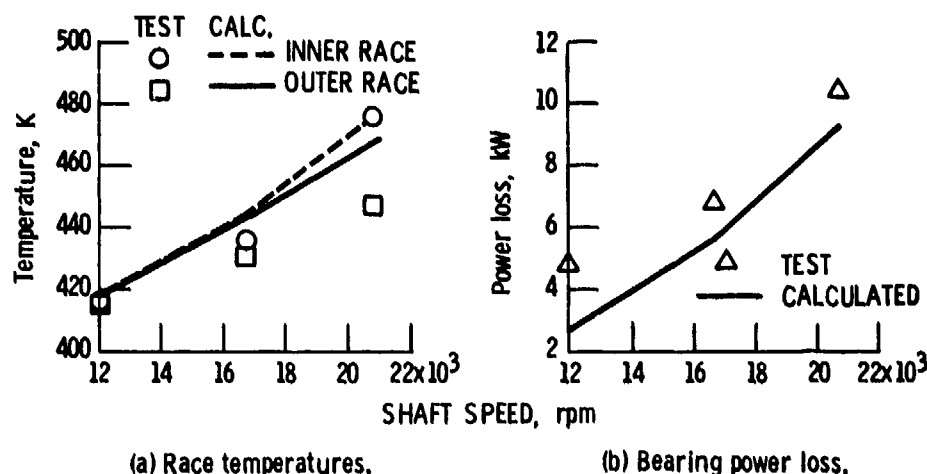


Figure 9. - Comparison of calculated and experimental ball-bearing temperatures and power loss as functions of shaft speed using Shaberth computer program. Thrust load, 6672 N (1500 lb); lubricant flow rate, 8300 cm³/min (2.2 gal/min); lubricant volume, 2 percent. (From ref. 33.)

Reference 34 presents a good correlation of predicted and experimental data for 118-mm-bore cylindrical roller bearings at speeds up to 3.0 million DN. Figure 10 shows the good correlation for race temperatures and heat transferred to oil at various flow rates. This work also shows the importance of knowing the operating diametral clearance that exists when mounting fits, temperatures, and rotational speed are considered.

Another correlation of predicted and experimental data for cylindrical roller bearings is shown in reference 35. Experiments were performed with 124.3-mm-bore bearings at speeds up to 3 million DN, and the results were compared with analysis using the computer program described in reference 6. Predictions of both heat rejection to the oil and outer-race temperature were within 10 percent of the experimental values.

The work reported in references 33 and 34 emphasizes the importance of selecting an appropriate volume percent of lubricant in the bearing cavity, since heat generation and bearing temperatures are dependent on this factor. Further work needs to be done to show how lubricant volume percent varies with bearing type and design, lubrication method, lubricant flow rate, and shaft speed. Despite the limitations, these computer programs have proven to be valuable tools in the development of rolling-element bearings for specific difficult applications.

Required Technology Advancements

One of the major forces pushing the technology of rolling-element bearings is higher shaft speeds and higher DN. This stems mainly from the aircraft turbine engine manufacturers who desire higher performance and efficiency from their engines with shaft speeds approaching 3 million DN (fig. 11 (ref. 2)). As previously discussed, operation of ball and cylindrical roller bearings up to this speed has been successfully accomplished in laboratory tests with proper regard for lubrication and cooling techniques. However, the high speeds bring on other problems for which solutions are not yet in hand but which, in most cases, are currently being studied. Several of the problem areas are discussed in the following paragraphs.

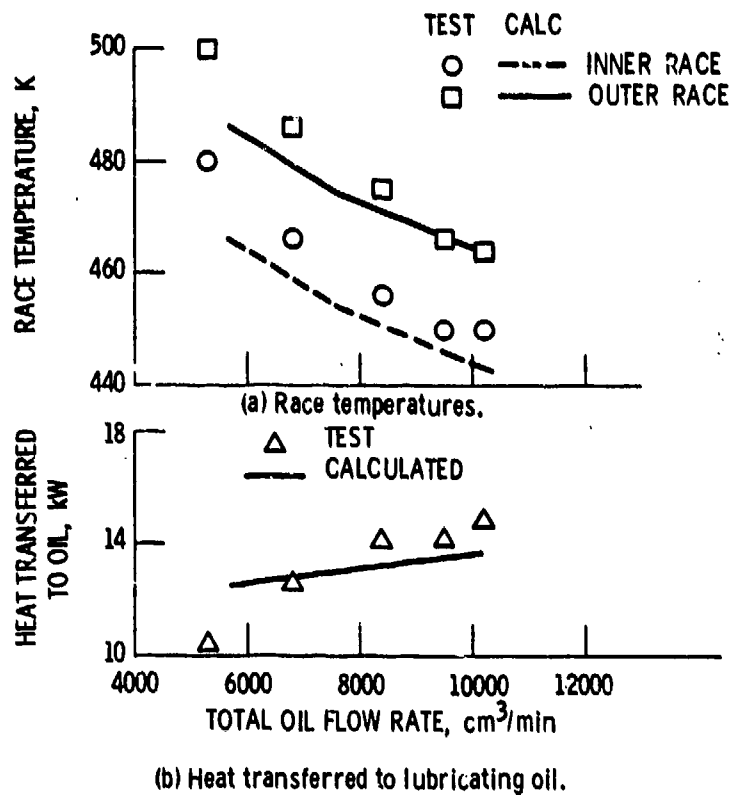


Figure 10. - Comparison of calculated and experimental cylindrical roller bearing data using a diametral clearance of -0.02 mm in the computer program. Shaft speed, 25 500 rpm; radial load, 8900 N (2000 lb); lubricant volume, 2 percent. (From ref. 34.)

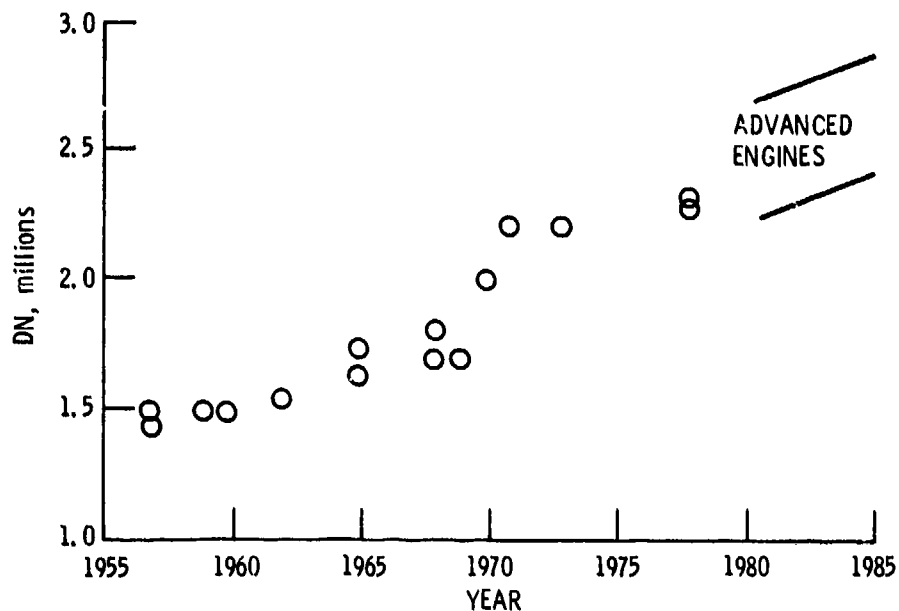


Figure 11. - Trend in aircraft engine main bearing DN. (From ref. 2.)

Rolling-Element Fatigue Life

As bearing speeds increase, bearing fatigue life decreases as shown in figure 12. This decrease is due to the increased rate of stress-cycle accumulation and centrifugal effects on the rolling elements. Therefore, to maintain an acceptable removal and/or overhaul time, increased rolling-element fatigue life in stress cycles or revolutions must be attained. This primarily applies to the thrust ball bearing on the high-speed shaft of a multishaft turbine engine where loads cannot be easily reduced and, in fact, may even be increased in the newer engines with higher thrust-to-weight ratios. Even though premium quality AISI M-50 material has shown great increases in rolling-element fatigue life, further life increases are needed. Modifications of the current alloys or the development of new materials along with improved processing and heat treatment is required to provide the desired fatigue life improvements.

Improved Fracture Toughness

It has been shown in references 14, 17, and 36, and discussed in some detail in reference 2, that bearing races made of through-hardened materials are susceptible to catastrophic fracture when exposed to the high tensile hoop stress often present in high-speed ball and rolling bearing inner races. To prevent this mode of failure, materials with improved fracture toughness must be used when bearing speeds exceed about 2.4 million DN (ref. 2). Case-hardened materials have fracture toughness values (ref. 15) high enough that they should prevent the fracture mode of failure. Further work is needed to assure that a case-hardened material can be developed that will also provide the required case hardness (Rockwell C 60 to 64), high-temperature hardness (up to 589 K (600° F) for main shaft engine application), and rolling-element fatigue life. Currently, programs sponsored by the DOD and the NASA are pursuing improved fracture toughness materials.

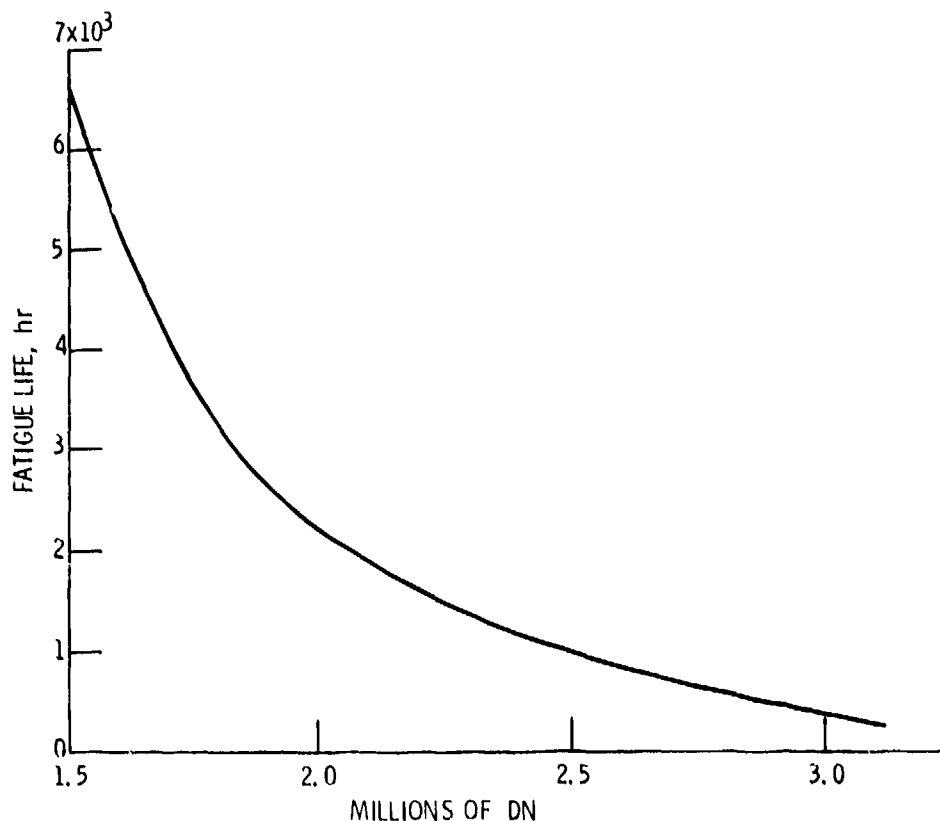


Figure 12. - Typical effect of DN on bearing fatigue life for a given bearing size.

Survivability

Of major concern in aircraft engine and transmission systems is the prevention of catastrophic failure in the unfortunate event of loss of lubricating oil. A typical requirement is 30 minutes of continued normal operation of a helicopter engine and transmission after loss of lubricating oil supply (ref. 37). This requirement was set primarily for military operations, but it is also applicable to civilian use, such as for off-shore drilling operations. Another military requirement for turbine engines is a capability of continued operation after a 1-minute interruption in the lubricant supply to the bearings.

These requirements are increasingly more difficult to meet as bearing speeds increase above 2 million DN for ball and cylindrical roller bearings. For tapered-roller bearings at speeds where lubrication through the cone to the cone-rib-roller-end contact is required (above about 1 million DN), lubricant interruption causes almost immediate bearing failure. Before tapered-roller bearings can be safely used in high-speed positions in engines or transmissions, a solution to this limitation must be found. Similar limits are applicable to a thrust-carrying cylindrical roller bearing (ref. 38), which also has critical roller-end-rib contacts. Solutions to the survivability problem may take the form of design modifications, supplementary lubrication systems, reduced-friction coatings or materials, or a combination of these.

Corrosion Resistance

The problem of corrosion is, of course, not unique to high-speed bearings as are the previous areas. The problem is most severe in systems with long periods of nonuse. A summary of causes for bearing rejection at a U.S. Navy facility (ref. 39) shows that corrosion accounts for nearly one-third of the bearing rejections from their aircraft systems, including drivelines, wheels, and accessories. Air Force experience (ref. 40) confirms that corrosion is a major cause of rejection at overhaul of aircraft turbine engine bearings.

The corrosion problem is being attacked on three major fronts: corrosion-resistant materials, corrosion-resistant coatings or surface modifications, and corrosion-inhibited lubricants. Materials such as AISI 440C and AMS 5749 are called corrosion resistant or stainless steels, but under some severe conditions in aircraft bearings, they will corrode. They are, however, more corrosion resistant than the common aircraft bearing materials such as AISI M-50, AISI 52100, and the commonly used case-carburized materials. Ceramics such as silicon nitride are truly corrosion resistant in the aircraft environment. Although this material is not yet well developed for widespread aircraft application, it could be applied in some specific cases.

Chromium-ion implantation has shown significant improvement in the corrosion resistance of AISI M-50 (ref. 41). Other surface modifications or coatings may also provide similar benefits but more work is needed in this area. It is probable that a combination of approaches, such as the use of silicon nitride balls or rollers and coated raceways may be a viable solution for some applications that require long periods of nonuse.

Currently, the lubricant provides some measure of corrosion protection in aircraft bearings simply by keeping the components coated and moisture free. Corrosion inhibiting additives for the commonly used MIL-L-23699 lubricant have shown promise in laboratory tests (ref. 42), and confirmation of the degree of improved corrosion resistance in actual aircraft systems is under way.

Concluding Remarks

This paper has reviewed the present state of technology of rolling-element bearings. The most recent advancements related to aircraft engine and transmission systems were emphasized, since it is within this area that major improvements have been realized. Improvements in the speed capabilities of large-bore ball and cylindrical and tapered-roller bearings have been realized with through-the-race lubrication. Spherical-roller bearings and small-bore (<40-mm) ball and cylindrical roller bearings have seen much less development for higher speeds, but efforts are currently under way.

Premium quality AISI M-50 steel has shown greatly improved rolling-element fatigue life over the previously used materials. However, further improvements as well as in fracture toughness and corrosion resistance are needed.

Life and performance predictions of rolling-element bearings are now much better because of the use of recently developed computer programs. The programs are valuable in designing for new, difficult applications and in diagnosing operating systems in which problems or failures have occurred. Further improvements in the analysis are needed, particularly in the definition of the lubricant-air mixture in an operating bearing and in the efficiency of fully dynamic programs which now consume large amounts of computer time.

References

1. Brown, P. F.: Bearings and Dampers for Advanced Jet Engines. SAE Paper 700318, Apr. 1970.
2. Bamberger, E. N.: Materials for Rolling-Element Bearings. Bearing Design—Historical Aspects, Present Technology and Future Problems, W. J. Anderson, ed., The American Society of Mechanical Engineers, 1980, pp. 1-46.
3. Pirvics, J.: Computerized Analysis and Design Methodology for Rolling Element Bearing Load Support Systems. Bearing Design—Historical Aspects, Present Technology, and Future Problems, W. J. Anderson, ed., The American Society of Mechanical Engineers, 1980, pp. 47-85.
4. Holmes, P. W.: Evaluation of Drilled Ball Bearings at DN Values to Three Million. NASA CR-2004 and NASA CR-2005, 1972.
5. Signer, H.; Bamberger, E. N.; and Zaretsky, E. V.: Parametric Study of the Lubrication of Thrust Loaded 120-mm Bore Ball Bearings to 3 Million DN. J. Lubr. Technol., vol. 96, no. 3, July 1974, pp. 515-524.
6. Brown, P. F.; et al.: Mainshaft High Speed Cylindrical Roller Bearings for Gas Turbine Engines. PWA-FR-8615, Pratt / Whitney Aircraft Group, 1977.
7. Schuller, F. T.: Operating Characteristics of a Large-Bore Roller Bearing to Speeds of 3×10^6 DN. NASA TP-1413, 1979.
8. Zaretsky, E. V.; Signer, H.; and Bamberger, E. N.: Operating Limitations of High-Speed Jet-Lubricated Ball Bearings. J. Lubr. Technol., vol. 98, no. 1, Jan. 1976, pp. 32-39.
9. Schuller, F. T.; and Signer, H. R.: Performance of Jet- and Inner-Ring-Lubricated 35-Millimeter-Bore Ball Bearings Operating to 2.5 Million DN. NASA TP-1808, 1981.
10. Lemanski, A. J.; Lenski, J. W., Jr.; and Drago, R. J.: Design Fabrication, Test, and Evaluation of Spiral Bevel Support Bearings (Tapered Roller). Boeing Vertol Co., 1973. (USAAMRDL-TR-73-16, AD-769064.)
11. Parker, R. J.; and Signer, H. R.: Lubrication of High-Speed, Large Bore Tapered-Roller Bearings. J. Lubr. Technol., vol. 100, no. 1, Jan. 1976, pp. 31-38.
12. Orvos, P. S.; and Dressler, G. J.: Tapered Roller Bearing Development for Aircraft Turbine Engines. Timken Co., 1979. (AFAPL-TR-79-2007, AD-A069440.)
13. Parker, R. J.; Pinel, S. I.; and Signer, H. R.: Performance of Computer Optimized Tapered-Roller Bearings to 2.4 Million DN. J. Lubr. Technol., vol. 103, no. 1, Jan. 1981, pp. 13-20.
14. Bamberger, E. N.; Zaretsky, E. V., and Signer, H.: Endurance and Failure Characteristics of Main-Shaft Jet Engine Bearing at 3×10^6 DN. J. Lubr. Technol., vol. 98, no. 4, Oct. 1976, pp. 580-585.
15. Jatzak, C. F.: Specialty Carburizing Steels for Elevated Temperature Service. Met. Prog., vol. 113, no. 4, Apr. 1978, pp. 70-78.
16. Anderson, N. E.; and Zaretsky, E. V.: Short-Term Hot-Hardness Characteristics of Five Case Hardened Steels. NASA TN D-8031, 1975.
17. Parker, R. J.; Signer, H. R.; and Pinel, S. I.: Endurance Tests with Large-Bore Tapered-Roller Bearings to 2.2 Million DN. ASME Paper 81-Lub-56, Oct. 1981.
18. Nehm, A. H.: Rolling-Element Fatigue of Gear Materials. (R78AEG476, General Electric Co.; NASA Contract NAS3-14302.) NASA CR-135450, 1978.
19. Townsend, D. P.; Parker, R. J.; and Zaretsky, E. V.: Evaluation of CBS 600 Carburized Steel as a Gear Material. NASA TP-1390, 1979.
20. Townsend, D. P.; and Zaretsky, E. V.: Endurance and Failure Characteristics of Modified Vasco X-2, CBS 600, and AISI 9310 Spur Gears. ASME Paper 80-C2/DET-58, Aug. 1980.
21. Jones, A. B.: A General Theory for Elastically Constrained Ball and Radial Roller Bearings Under Arbitrary Load and Speed Conditions. J. Basic Eng., vol. 82, no. 2, June 1960, pp. 309-320.
22. Harris, T. A.: Ball Motion in Thrust-Loaded, Angular Contact Bearings with Coulomb Friction. J. Lubr. Technol., vol. 93, no. 1, Jan. 1971, pp. 32-38.
23. Crecelius, W. J.: Users Manual for Steady State and Transient Thermal Analysis of a Shaft-Bearing System (SHABERTH). SKF-AL77P015, SKF Industries, Inc., 1978. (ARBRL-CR-00386, AD-A064150.)
24. Kleckner, R. J.; Pirvics, J.; and Castelli, V.: High-Speed Cylindrical Rolling Element Bearing Analysis "CYBEAN"—Analytic Formulation. J. Lubr. Technol., vol. 102, no. 3, July 1980, pp. 380-390.
25. Walters, C. T.: The Dynamics of Ball Bearings. J. Lubr. Technol., vol. 93, no. 1, Jan. 1971, pp. 1-10.
26. Gupta, P. K.: Dynamics of Rolling-Element Bearings—Part III, Ball Bearing Analysis. J. Lubr. Technol., vol. 101, no. 3, July 1979, pp. 312-318.
27. Gupta, P. K.: Dynamics of Rolling-Element Bearings—Part I, Cylindrical Roller Bearing Analysis. J. Lubr. Technol., vol. 101, no. 3, July 1979, pp. 293-304.
28. Conry, T. F.: Transient Dynamic Analysis of High-Speed Lightly Loaded Cylindrical Roller Bearings, I—Analysis. NASA CR-3334, 1981.

29. Conry, T. F.; and Goglia, P. R.: Transient Dynamic Analysis of High-Speed Lightly Loaded Cylindrical Roller Bearings, II—Computer Program and Results. NASA CR-3335, 1981.
30. Schulze, D. R.: An Evaluation of the Usefulness of Two Math Models for Predicting Performance of a 100-mm Bore, Angular Contact, High-Speed, Thrust Bearing. AFWAL-TR-80-2007, Air Force Wright Aeronautical Laboratories., Apr. 1980. (AD-A089161.)
31. Gupta, P. K.: A Review of Computerized Simulations of Roller Bearing Performance. Computer-Aided Design of Bearings and Seals, F. E. Kennedy and H. S. Cheng, eds., The American Society of Mechanical Engineers, 1976, pp. 19-29.
32. Sibley, L. B.; and Pirvics, J.: Computer Analysis of Rolling Bearings. Computer-Aided Design of Bearings and Seals, F. E. Kennedy and H. S. Cheng, eds., The American Society of Mechanical Engineers, 1976, pp. 95-115.
33. Coe, H. H.; and Zaretsky, E. V.: Predicted and Experimental Performance of Jet-Lubricated 120-Millimeter-Bore Ball Bearings Operating at 2.5 Million DN. NASA TP-1196, 1978.
34. Coe, H. H.; and Schuller, F. T.: Comparison of Predicted and Experimental Performance of Large-Bore Roller Bearing Operating at 3.0 Million DN. NASA TP-1599, 1980.
35. Brown, P. F.; Dobek, L. J.; and Tobiasz, E. J.: High-Speed Cylindrical Roller Bearing Development. PWA-FR-12598, Pratt & Whitney Aircraft Group, Aug. 1980. (AFWAL-TR-80-2072, AD-A095357.)
36. Clark, J. C.: Fracture Failure Modes in Lightweight Bearings. J. Aircr., vol. 12, no. 4, Apr. 1974, pp. 383-387.
37. Lenski, J. W.: Test Results Report and Design Technology Development Report—HLH/ATC High-Speed Tapered-Roller Bearing Development Program. T301-10248-1, Boeing Vertol Co., 1974. (USAAMRDL-TR-74-33, AD-786561.)
38. Morrison, F. R.; Pirvics, J.; and Crecelius, W. J.: A Functional Evaluation of a Thrust Carrying Cylindrical Roller Bearing Design. J. Lubr. Tech., vol. 101, no. 2, Apr. 1979, pp. 164-170.
39. Cunningham, J. S., Jr.; and Morgan, M. A.: Review of Aircraft Bearing Rejection Criteria and Causes. Lubr. Eng., vol. 35, no. 8, Aug. 1979, pp. 435-440.
40. Jones, H. F.: Discussion to Review of Aircraft Bearing Rejection Criteria and Causes. Lubr. Eng., vol. 35, no. 8, Aug. 1979, p. 441.
41. Hubler, G. K.; et al.: Application of Ion Implantation for the Improvement of Localized Corrosion Resistance of M-50 Steel Bearings. NRL-MR-4481, Naval Research Laboratory, March 1981. (AD-A097230.)
42. Brown, C.; and Feinberg, F.: Development of Corrosion-Inhibited Lubricants for Gas Turbine Engines and Helicopter Transmissions. Lubr. Eng., vol. 37, no. 3, Mar. 1981, pp. 138-144.

Geared Power Transmission Technology

John J. Coy*

Gears are the means by which power is transferred from source to application. Gearing and geared transmissions drive the many machines of modern industry. Gears move the wheels and propellers to move us through the sea, land, and air. A very sizeable section of industry and commerce in today's world depends on gearing for its economy, production, and, indeed, livelihood.

The art and science of gearing has roots in pre-Christian times, and yet many scientists and researchers continue to delve into the regions where improvement is necessary, seeking to quantify, establish, and codify the methods to make gears meet the ever widening needs of mankind.

The art and science of geared power transmission has changed over the years from the simplest of beginnings in wooden toothed gears for pumping water and turning grist mills to advanced applications in helicopters and automobiles and ocean-going vessels. Gears, which were originally conceived by men of genius and invention, now command the attention of men of no less skill. The gearing art has become interdisciplinary, spanning areas of endeavor which are too varied for any one man to master, no matter how talented he may be. Gearing art, science, and applications span the fields of kinematics, chemistry, metallurgy, heat transfer, fluid dynamics, stress analysis, vibration, and acoustics. The gear practitioner draws on a staggering array of scientific disciplines to assemble a good gear design.

→ It is the purpose of this paper to briefly review the historical path of the science and art of gearing. The present state of gearing technology is discussed along with examples of some of the NASA-sponsored contributions to gearing technology. Future requirements in gearing are summarized. ←

History of Gearing

The earliest written descriptions of gears are said to be made by Aristotle in the fourth century B.C. (ref. 1), but the oldest surviving relic containing gears is the Antikythera mechanism (fig. 1), so named because of the Greek island of that name near which the mechanism was discovered in a sunken ship in 1900. Professor Price (ref. 2) of Yale University has written an authoritative account of this mechanism. The mechanism is not only the earliest relic of gearing, but also it is an extremely complex arrangement of epicyclic differential gearing. The mechanism is identified as a calendrical sun and moon computing mechanism and dated to about 87 B.C. Because of the many difficulties surrounding attempts to authoritatively document the earliest forms of gearing, there is sometimes disagreement among authorities. It has been pointed out that (refs. 2 and 3) the passage attributed to Aristotle by some (ref. 1) was actually from the writings of his school, in *Mechanical Problems* of Aristotle (ca. 280 B.C.). In the passage in question there was no mention of gear teeth on the parallel wheels, and they may just as well have been smooth wheels in frictional contact. Therefore, the attribution of gearing to Aristotle is, most likely, false. There is more agreement that the real beginning of gearing was with Archimedes who in about 250 B.C. invented the endless screw turning a toothed wheel, which was used in engines of war. Archimedes also used gears to simulate astronomical ratios. The Archimedian spiral was continued in the odometer and dioptra, which were early forms of wagon mileage indicators (odometer) and surveying instruments. These devices were probably "thought" experiments of Heron of Alexandria (ca. 60 A.D.), who wrote on the subjects of theoretical mechanics and the basic elements of mechanism.

For such a complex device as the Antikythera mechanism to suddenly appear gives rise to speculation regarding the origins of the gearing art. Perhaps some unknown genius invented this complex mechanism in one shot, and spin-offs from the major invention gave manifold applications in the more mundane areas such as for grist mills and raising water. Or perhaps the art of gearing as

*Propulsion Laboratory, U.S. Army Research and Technology Laboratories (AVRADCOM), NASA Lewis Research Center.

seen in the astronomical device and clockworks are the culmination of much evolutionary trial and error and represent the paragon of synthesis in design.

Notwithstanding, the art of gearing was carried through the European Dark Ages after the fall of Rome, appearing in Islamic instruments such as the geared astrolabes (fig. 2), which were used to calculate the positions of the celestial bodies. Perhaps the art was relearned by the clock and instrument making artisans of 14th century Europe, or perhaps some crystallizing ideas and mechanisms were imported from the East after the crusades of the 11th, 12th, and 13th centuries.

It appears that the English Abbot of St. Alban's monastery, born Richard of Wallingford, in A.D. 1330, reinvented the epicyclic gearing concept. He applied it to an astronomical clock, which he began to build at that time and which was completed after his death. Translated manuscripts clearly tell of the problems of finance, management, and skeptic's ridicule that Richard suffered as his clock was being built. Indeed, this 14th century technological project was not so different from the research and technical projects of today!

A mechanical clock of a slightly later period was conceived by Giovanni de Dondi (1348-1364), a model of which is in the Smithsonian Institution (fig. 3). Diagrams of this clock, which did not use differential gearing (ref. 2), appear in the sketchbooks of Leonardo da Vinci, who designed geared mechanisms himself (refs. 2 and 5). In 1967 two of Leonardo da Vinci's manuscripts, lost in the National Library in Madrid since 1830 (ref. 6), were rediscovered. One of the manuscripts, written between 1493 and 1497 and known as "Codex Madrid I" (ref. 7), contains 382 pages with some 1600 sketches. Included among this display of Leonardo's artistic skill and engineering ability are his studies of gearing. Among these are tooth profile designs and gearing arrangements that were centuries ahead of their "invention."

A common interest of the period was perpetual motion machines (fig. 4), many of which used gearing arrangements. Leonardo, who studied friction and understood the implications this had for negating perpetual motion, categorized the seekers of such with the alchemists who vainly sought to synthesize gold from the more basic elements. The first page of Leonardo's "Codex Madrid I" contains these observations: "Among the superfluous and impossible delusions of man there is the search for continuous motion . . . always the same thing happened to them as to the alchemists . . . because of the impossible things they promised to sovereigns and heads of state. I remember that many people, from different countries, went to Venice with great expectation of gain to make mills in dead (still) water, and after much expense and effort, unable to set the machine in motion, they were obliged to escape."

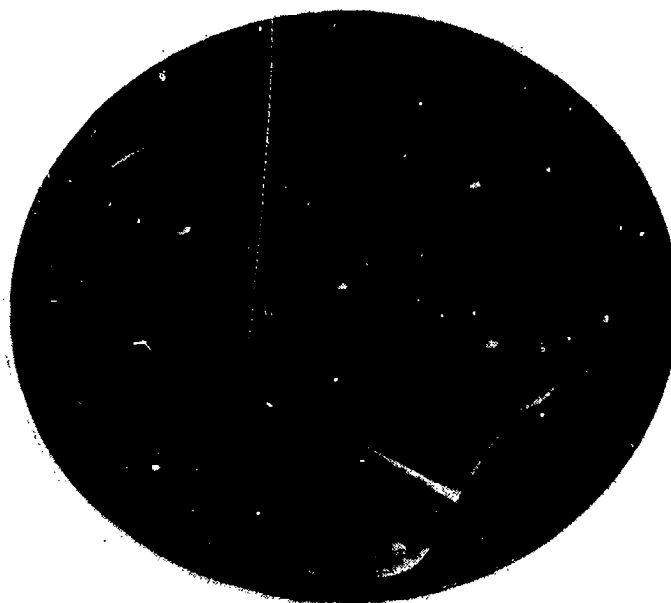


Figure 2. - Geared astrolabe of A.D. 1221-22 by Muhammed B. Abi Bakr of Isfahan. Interior mechanism is pictured. (Courtesy of The Smithsonian Institution.)



Figure 3. - Clock of Giovanni de Dondi (ca. 1364). Drive gears with triangular teeth are pictured. A modern reconstruction. (Courtesy of The Smithsonian Institution.)

In short, the gearing art and practice was certainly begun at least 2000 years ago and was preserved in the practical machines for doing work, measuring distance, and keeping time. Clearly, from the Antikythera machine onwards there was a high technology line of sophisticated gear work preserved in the craft of clockmakers all the way through history to the Industrial Revolution. Following another line from antiquity onwards in the tradition of the wheelwright and millwright, there were low technology gear pairs used in power transmission. These were mostly wooden gears with lantern pinions. There were therefore two traditions which only came together in the late 18th and early 19th centuries: clockwork gearing used for its ratio properties and rudimentary wooden gears used to transmit power.

Progress in Gearing

In the period 1450 to 1750, the mathematics of gear-tooth profiles and theories of geared mechanisms became established. Albrecht Dürer is credited with discovering the epicycloidal shape (ca. 1525). Philip de la Hire is said to have worked out the analysis of epicycloids and recommended the involute curve for gear teeth (ca. 1694). Leonard Euler worked out the law of conjugate action (ca. 1754; ref. 5). Gears, designed according to this law, have a steady speed ratio.

Gears were used in the early machines that powered the industrial revolution. Later, they were used in machines to make even more gears. Figure 5 shows a hand-powered production machine used to make clockwork gearing. This machine from the early 18th century is attributed to Christopher Polhem of Sweden.

Since the Industrial Revolution in the mid-19th century, the art of gearing blossomed, and gear designs steadily became based on more scientific principles. In 1893 (ref. 8) Wilfred Lewis published

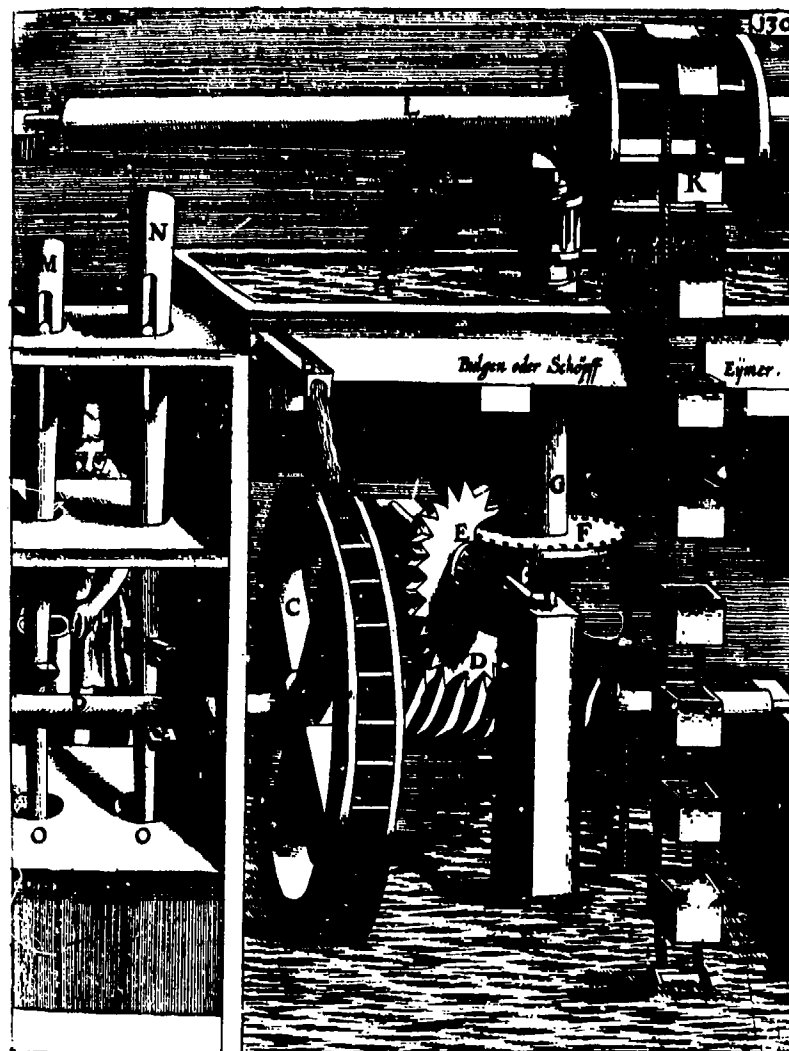


Figure 4. - Medieval perpetual motion machine driven by water wheel. Lantern pinions drove peg-toothed wheels (E, F, H, I). The Spiral of Archimedes (ca. 280 B.C.) was implemented as a worm drive (D, E). Cams (Q) on the shaft lifted and dropped pounding posts (M, N) which pulverized material in the container. Figure extracted from a book on machinery by George Andrean Bocklern published in Nuremberg in 1661. (Courtesy of The Smithsonian Institution.)

a formula for computing stress in gear teeth. This formula is in wide use today in gear design. In 1899 George B. Grant, the founder of five gear manufacturing companies, published "A Treatise on Gear Wheels" (ref. 9).

New inventions lead to new applications for gearing. For example, in the early part of this century (1910), parallel shaft gears were introduced to reduce the speed of the newly developed reaction steam turbine enough to turn the driving screws of oceangoing vessels. This application achieved an overall increase in efficiency of 25 percent in sea travel (ref. 1).

By 1916 the age of specialized machine tools for producing gears had definitely arrived. It was in 1916 that the American Gear Manufacturers Association was founded. Figure 6 shows the staff of one of today's leading gear companies as it was in 1902, 10 years after its founding by George Grant. Figure 7 shows one of the machine tools that may have been inside this gear workshop. In today's gear shops it is common to find gears cut with machinery kept in temperature-controlled environments. Figure 8 shows a gear grinder finishing a pinion shaft such as would be found in a turbine-driven oceangoing vessel or in large rolling mill gearing.

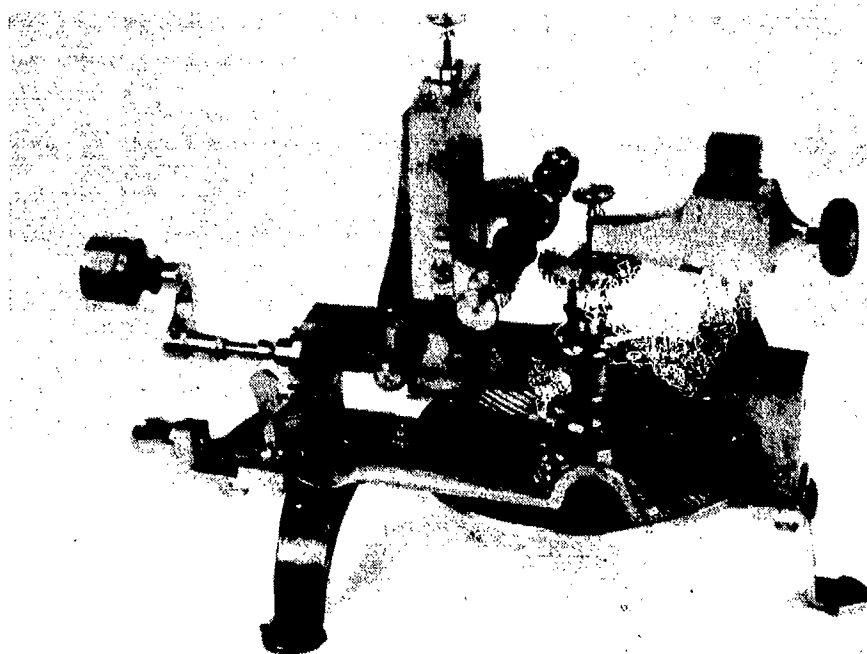


Figure 5. - Early hand-powered production machine for making clockwork gears by Christopher Polhem of Sweden (ca. 1729). Index plate for spacing teeth. (Courtesy of The Smithsonian Institution.)

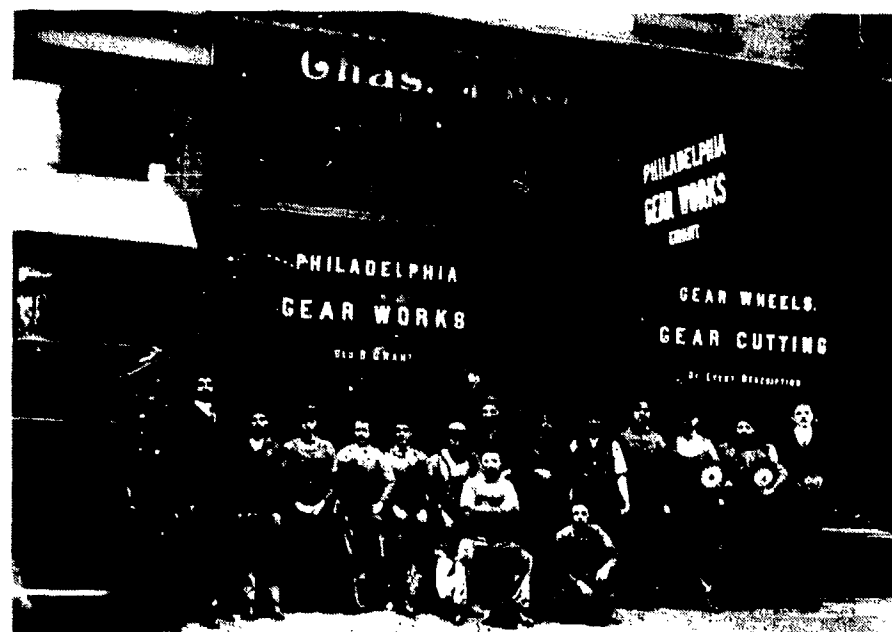


Figure 6. - Philadelphia Gear Works in 1902, 10 years after its founding by George B. Grant. Today Philadelphia Gear Corp. is one of the leading gear producers, employing over 2000 persons. (Courtesy of the Philadelphia Gear Corp.)

The need for more accurate and quiet-running gears became obvious with the advent of the automobile. Although the hypoid gear was within our manufacturing capabilities by 1916, it was not used practically until 1926 when it was used in the Packard automobile. The hypoid gear made it possible to lower the drive shaft and gain more usable floor space. By 1937 almost all cars used hypoid geared rear axles. Special lubricant antiwear additives were formulated in the 1920's which

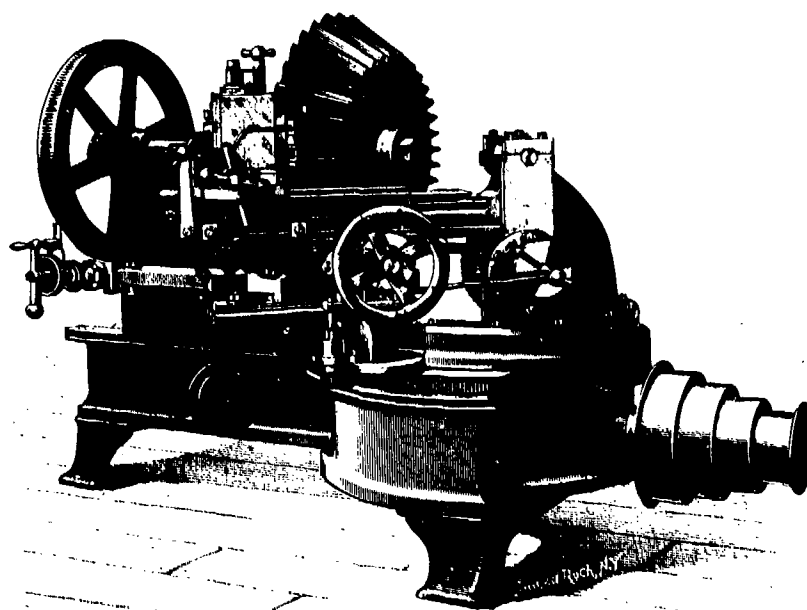


Figure 7. - Gleason bevel gear planing machine. This first commercially practical bevel gear planer was designed and built by William Gleason in 1874. (Courtesy of The Smithsonian Institution.)



Figure 8. - Maag precision gear grinding machine, custom built to Philadelphia Gear Corp. specifications. Such machines are located in temperature and humidity controlled environments to maintain precision control of manufacture. (Courtesy of Philadelphia Gear Corp.)

made it practical to use hypoid gearing. In 1931 Earle Buckingham, a professor at the Massachusetts Institute of Technology and chairman of an ASME research committee on gearing, published a milestone report on gear-tooth dynamic loading (ref. 10). This led to a better understanding of why faster running gears sometimes could not carry as much load as slower running gears.

In the early 1900's wear was the major problem in gearing, but, with the more severe service seen in aircraft applications in the 1930's, scoring problems began to occur. Scoring is caused by a combination of high sliding speed and high contact stress. These factors cause the lubricating oil film to break down in a sudden and unstable manner. This mode of failure emphasized that, in addition to cutting down friction, a prime contribution of a lubricating fluid is to provide cooling to the gears. In 1949 (ref. 11) the first real breakthrough in the theory of lubrication of concentrated contacts, such as in gearing, occurred with Grubin's theory of elastohydrodynamic lubrication. Although lubrication of gears had been investigated since the early 1900's, Grubin connected the interaction of elastic deformations in the gears with the increase in lubricant viscosity with pressure.

High-strength alloy steels for gearing were developed during the 1920's and 1930's. Nitriding and case-hardening techniques to increase the surface strength of gearing were introduced in the 1930's. Induction hardening was introduced in 1950. With new capability to predict strength and lubricating conditions for gears, wear and scoring became somewhat less difficult to deal with. This left surface pitting as the life limiting failure mode for gears. In this mode of failure small cracks develop on and under the surface as a result of metal fatigue. Eventually, pieces of the surface are lost, and the gears become rough and noisy in their operation and may even fail by secondary tooth breakage. Extremely clean steels produced by vacuum melting processes introduced in 1960 have proven effective in prolonging gear life.

Current State of the Gearing Art and Science

Gearing problems continue to occur as the ever increasing demands of power transmission and transportation systems require. One of the major ways of identifying and solving these problems is through the free exchange of ideas at national and international forums.

The American Gear Manufacturers Association (AGMA) membership represents approximately 80 percent of the gearmaking capacity in the United States and Canada, or approximately two-billion dollars worth of business annually. The AGMA holds two technical meetings each year, publishes the proceedings of these meetings, and maintains the standards used by the American gear industry.

In 1977 at the American Society of Mechanical Engineers (ASME) International Power Transmission and Gearing Conference held in Chicago, 82 technical papers were presented (fig. 9). At the 1980 conference in San Francisco 112 technical papers were given, and a 4-hour panel session on the gear standards of AGMA and the International Standards Organization (ISO) was presented. At both of these conferences there was worldwide contribution and attendance. The Fifth World Congress of the International Federation for the Theory of Machines and Mechanisms (IFTOMM) held in Montreal in 1979, drew 350 contributing technical papers. Approximately 35 of those papers were devoted to subjects in power transmission and gearing (ref. 12). These conferences present a very good collection of the problems, solutions, and achievements of today's gearing community. State of the art reviews on various aspects of gearing are periodically published in the ASME Transactions, Journal of Mechanical Design.

A few of the developments, originally reported in the previously mentioned forums and regarded as advances in the state of the gear art, are described next.

Applications and Capabilities

In the past 20 years there has been increased use of industrial gas turbines for electric power generation. In the range of 1000 to 14 000 hp epicyclic gear systems have been used successfully (fig. 10). Pitch-line velocities are from 50 to 100 m/sec (10 000 to 20 000 ft/min). These gear sets must work reliably for 10 000 to 30 000 hr between overhauls.

Bevel gears produced to drive a compressor test stand ran successfully for 235 hr at 2984 kW (4000 hp) and 200 m/sec (40 000 ft/min) (ref. 13). From all indications these gears could be used in an industrial application if needed. A reasonable maximum pitch-line velocity for commercial spiral-bevel gears with curved teeth is 60 m/sec (12 000 ft/min)(ref. 14).

Gear system development methods have been advanced in which lightweight, high-speed, highly loaded gears are used in aircraft applications. The problems of strength and dynamic loads, as well as resonant frequencies for such gearing, are now treatable with techniques such as finite-element analysis, siren and impulse testing for mode shapes, and application of damping treatments where required (ref. 15).

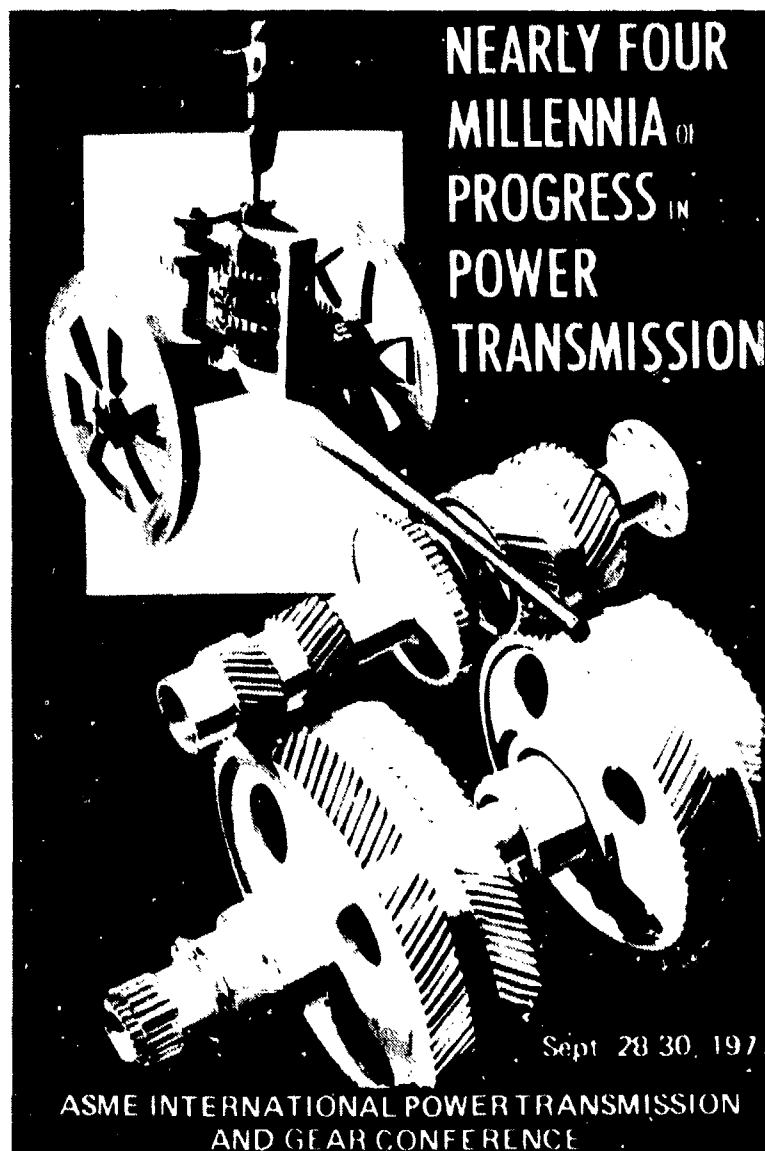


Figure 9. - Publicity poster used for 1977 ASME International Gear Conference portraying conference theme. Encyclopedia Britannica (ref. 1) dates the Chinese South Pointing Chariot to the 27th century B.C. The figure on the chariot points south and is driven by differential gearing as elaborated by George Lanchester in a lecture before the China Society. (Dates and gearing pertaining to the legendary South Pointing Chariot are conjectural.) Reference 4 contains a balanced summary of scholarly evidence connected with this interesting chariot.

Gear Materials

Gear materials and treatments are continuing to advance the capabilities of gears in hardness retention at elevated temperatures, in higher strength, in scoring resistance, and in durability (refs. 16 to 19).

Plastic gearing and other alternative materials are being studied, and their performances quantified to establish the boundaries on their usefulness. This endeavor is mandated by reasons of economy and the shortage of critical raw materials. Molybdenum disulphide-filled cast nylon gears are finding use today in a wide range of industries. If allowances for the special problems of thermal



Figure 10. - Gearbox with epicyclic gearing capable of handling 3700 hp used in a huge, 2500-kW wind turbine. Gear drive is a three-stage epicyclic speed increaser utilizing the Stoekicht principle of flexible annulus coupling rings for even load sharing. Design is smaller and lighter than parallel shaft configuration. (Courtesy of Philadelphia Gear Corp.)

expansion and creep are made, these gears were found to fail eventually by a fatigue fracture after many millions of stress cycles (ref. 20). Studies on the temperature rise in plastic gears during operation have also been conducted (ref. 21).

Gear Manufacture

Demands for high-power, high-strength bevel gears are made for steel rolling mills, bow thrusters for off-shore drilling rigs, and high-performance marine craft such as surface-effect ships. Spiral bevel gears for these applications have resulted in the development of production machinery for generating 203-cm (80-in.) diameter, 30-cm (12-in.) face-width gears (fig. 11) (ref. 14). The carbide toothed skiving hob for finishing hardened gear teeth was developed in Japan in 1963 and continues to be the object of research (ref. 22). Honing the skived surface can produce a finish of 0.5 to 0.8 μm rms roughness using a newly developed screw-shaped hone made of an elastic polymer embedded with abrasives. There is also a new shaped shaving hob for finishing gears of large pitch. While shaving to improve surface finish is not new, conventional gear-shaped shavers are expensive to maintain. The new screw-shaped shaver is economical to make and resharpen in a lathe (ref. 23).

Spiral bevel gears may now be finish-machined in the hardened condition on the same machine as was used to rough-cut the gear (fig. 12). The gears are brought to a surface hardness of 60 Rockwell C by carburizing and quenching, while holding the gear in a press to minimize distortions. The gears are then finished in the hard condition using carbide cutters to obtain surface finishes in the range of 0.5 to 0.8 μm (20 to 30 $\mu\text{in.}$) and precision comparable to AGMA quality 12.

Numerically controlled, three-axis dressing of finish grinding wheels has been developed. The system is capable of dressing complex shapes in the grinding wheel used to finish grind complicated worm-gear profiles (ref. 24).

In addition to this use of computers to control the gear manufacturing process, a more comprehensive application of computerized methods has been applied in Switzerland. The CAD/CAM manufacture of spiral-bevel gears is used to do design layout, calculate machine settings for manufacture, analyze the meshing conditions, and do the stress analysis (ref. 25).

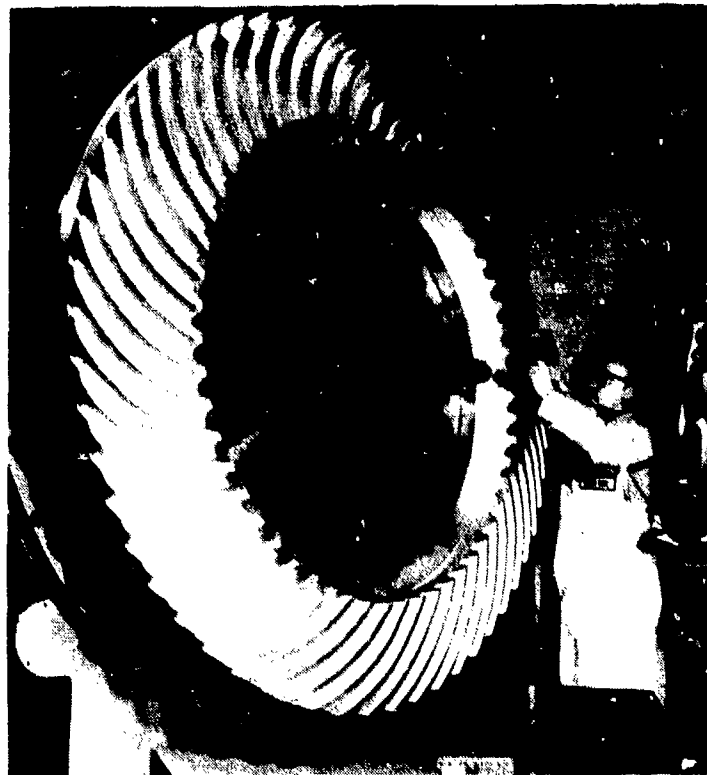


Figure 11. - Large spiral-bevel gear is manufactured using rotary cutter method. Gears can be cut in the 50- to 80-in.-diam range with up to 12-in. face and 0.75-in.-diam pitch. Such gears can transmit 5000 to 6000 hp. (Courtesy of Philadelphia Gear Corp.)

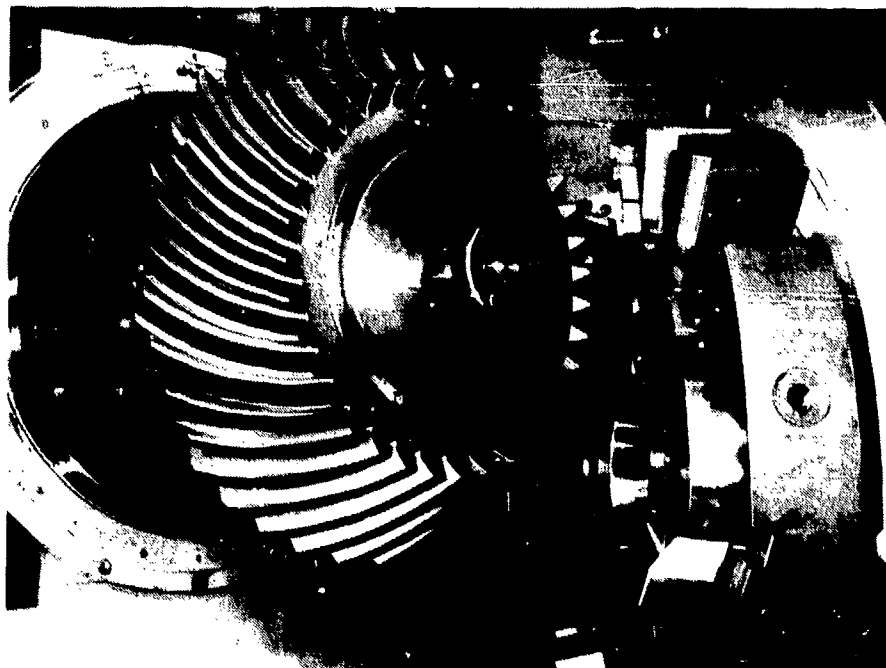


Figure 12. - Precision hard-cut process for generated spiral-bevel gears. Gears are cut in soft condition, deep carburized to Rockwell C 60, press quenched to minimize distortion, then precision finished in hard condition by special carbide cutters on the same machine as the original cut. (Courtesy of Philadelphia Gear Corp.)

NASA Contributions to Gearing

Beginning in 1969 the NASA Lewis Research Center embarked on a comprehensive gear technology research program. This work is being continued under the NASA Helicopter Transmission System Technology Program. Some of the important results and continuing programs are presented in this section.

Metallurgical Effects

The metallurgical processing imposed on a gear steel from its elemental plate to the finished component can significantly affect its ultimate performance. Even the type of ore from which the various elements are extracted can exercise some influence over later component life. Theoretically then, a large number of variables could be considered in determining the rolling-element (surface pitting) life of a potential gear material. This becomes a nearly impossible task.

There is only a small body of published data on material effects on gear pitting life. Many of the gear alloy improvement programs have been evaluated by mechanical tests rather than by rolling-element component or full-scale gear surface pitting fatigue tests. Since rolling-element fatigue is a unique property, it is not, as such, necessarily possible to correlate it with more standard mechanical tests (refs. 26 and 27).

An extensive program is being conducted by NASA to evaluate potential gear materials. Tests have been conducted on NASA Lewis' gear fatigue apparatus (fig. 13; see refs. 17 and 28 to 33) and General Electric's rolling-contact (RC) tester (fig. 14; see refs. 34 and 35). Figure 15 shows the spur test gears used at Lewis in the gear fatigue test rig. These gears are 8.9 cm (3.5 in.) in pitch diameter and have 28 teeth. Four such rigs (fig. 13) are used to perform long-term endurance tests. The effects of materials, lubrication, and design on gear life are being studied.

Several different types of gear failure occur, as shown in figure 15. Scoring is caused by poor lubrication and high-temperature operation. Tooth fracture is caused by high tooth bending stresses and is aggravated by poor heat treatment. Fracture usually begins at the root of the tooth, but may also originate at a surface fatigue pit. Surface fatigue pitting is caused by repeated application of contact stress. The higher the contact stress, the more rapidly failure occurs.

Gear Materials

Scoring and fracture failures may be controlled by proper design, but fatigue pitting is an intrinsic problem in gear applications. Pitting is an unavoidable event that eventually ends the useful life of a gear. Figure 16 shows data for test gear failures due to pitting fatigue. The failure points are plotted on Weibull coordinates, which give the cumulative percentage of failed specimens as a function of running time. The notable feature of presenting the data this way is that it emphasizes the relation between life and reliability. For instance, the life at which 10 percent of the gear specimens have failed is denoted the L_{10} life. This is conceptually identical to the B_{10} life for bearings. The L_{10} life corresponds to 90-percent reliability; the L_{50} life corresponds to 50-percent reliability. Other life numbers may be defined as the degree of reliability required changes.

Figure 17 shows the results of surface fatigue tests of six gear steels. AISI 9310, the baseline for comparison, is assigned a relative life of 100 percent. In the tests only pitting fatigue failures occurred in this material. The CBS 600 gears had an L_{10} life 7.5 times that of the AISI 9310 gears. The failure mechanism was primarily pitting. In some cases the cracks near the pitting failure propagated through the tooth to cause fracture. The forged AISI M-50 material behaved similarly, with a life six times that of the baseline AISI 9310. The AISI M-50 and CBS 1000 gear steels have good high-temperature hardness retention, which results in longer life at elevated operating temperatures.

Gear Forging

Gears made from through-hardened materials or case-carburized materials (having a high percentage of alloying elements) have a tendency for gear tooth fracture due to bending fatigue as a result of extended running after a surface fatigue spall. Figure 15 shows a typical tooth fracture emanating from a surface fatigue spall. One fabrication method that has the potential to improve the strength and life of gear teeth is ausforging. Ausforging is a thermomechanical metalworking process

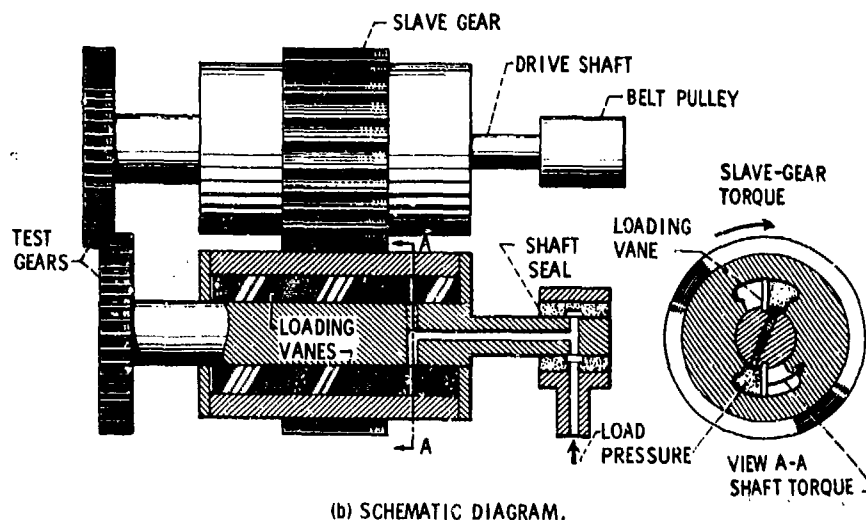
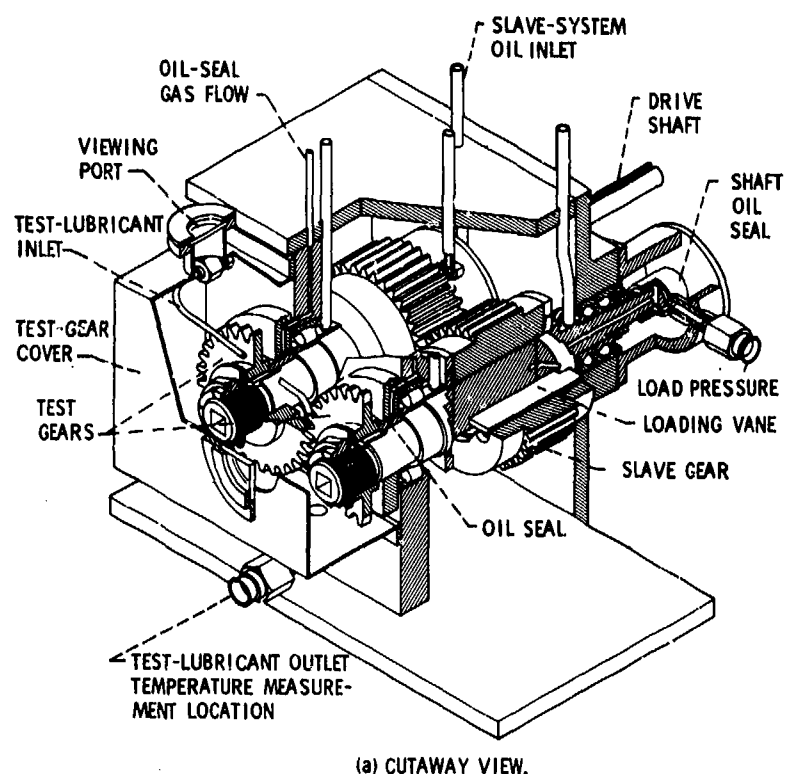


Figure 13. - NASA Lewis Research Center's gear fatigue test apparatus.

whereby a steel is forged or otherwise worked while it is in the metastable austenitic condition (ref. 36). The application of ausforming to machine elements such as rolling-element bearing was first reported (ref. 37).

Tests were conducted (refs. 31 and 32) at 350 K (170° F) with three groups of 8.9-cm (3.5-in.) pitch diameter spur gears made of double-vacuum melted (VIM-VAR) AISI M-50 steel and one group of CVM AISI 9310 steel. The pitting fatigue life of the standard forged and ausformed gears was approximately 5 times that of the CVM AISI 9310 gears and 10 times that of the bending fatigue life of the standard machined VIM-VAR AISI M-50 gears run under identical conditions. There was a slight decrease in the 10-percent life of the ausformed gears from that for the standard forged gears. However, the difference is not statistically significant.

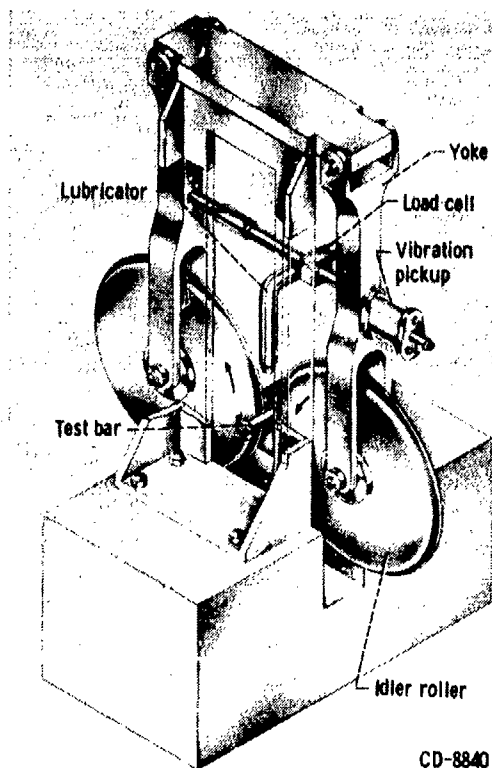


Figure 14. - Rolling-contact fatigue apparatus.

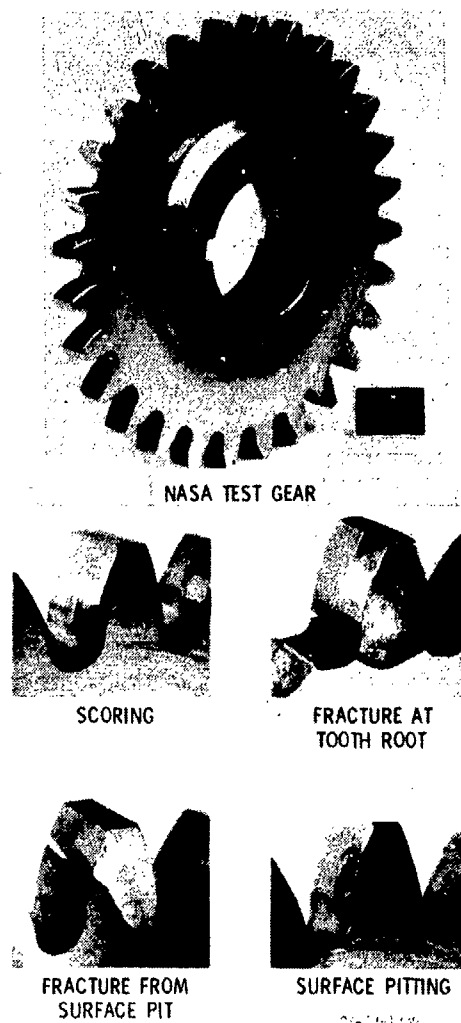


Figure 15. - Typical gear-tooth failure modes.

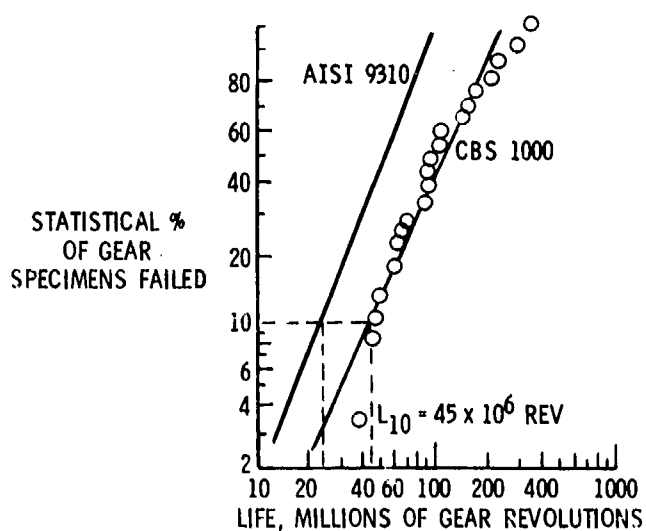


Figure 16. - Weibull plot for pitting fatigue failure of CBS 1000 specimen gears compared with baseline dispersion in life for AISI 9310 gears. Tests conducted on the NASA gear-fatigue test apparatus.

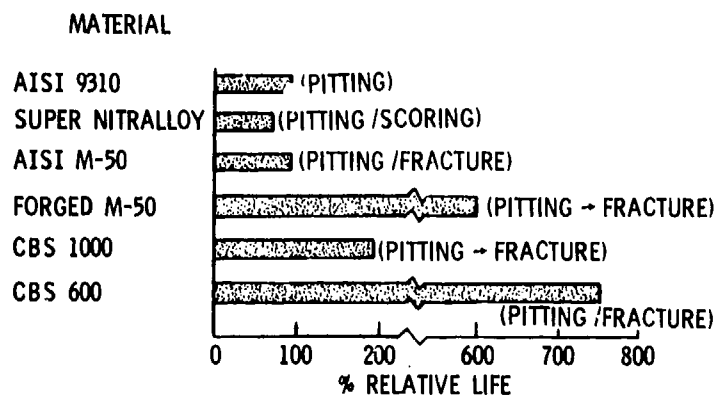


Figure 17. - Summary of gear-fatigue test results for six gear steels.

The standard machined gears failed primarily by gear-tooth fracture, while the forged and ausforged VIM-VAR M-50 and CVM AISI 9310 gears failed primarily by surface pitting fatigue. The ausforged gears had a slightly greater tendency to fail by tooth fracture than the standard forged gears.

While gear forging offers the potential for long-lived, reliable gearing, especially for the high alloy steels, both the cost and the availability of forging facilities may outweigh its advantages at the present time.

Gear Life Predictions

The fatigue-life model proposed in 1947 by Lundberg and Palmgren (ref. 38) is the commonly accepted theory to determine the fatigue life of rolling-element bearings. The probability of survival is expressed as follows:

$$\log \frac{1}{s} \propto \frac{\tau^c \eta^e v}{z^h} \quad (1)$$

where

e Weibull slope

h, c material dependent exponents

s probability of survival

v volume representative of the stress concentration or "stressed volume"

z depth of the critical stress

η millions of stress cycles

τ critical stress

Much of the work by Lundberg and Palmgren was concerned with connecting the basic equation to common bearing geometry and operating parameters (ref. 39). In order for the theory to be directly useful for gears, the NASA research used the same approach (refs. 40 and 41.)

The Weibull slope, e , and the load-life exponent, p , were directly determined by conducting life tests under several load conditions for a group of gears. The results of these tests conducted for three gear loads with three groups of AISI 9310 gears (ref. 42) are shown in figures 18 and 19. Life was found to vary inversely with load to the 4.3 and 5.1 power at the 10-percent and 50-percent life levels, respectively. The average Weibull slope was 2.5.

Using the exponent values determined experimentally from the gear tests, the life distributions for the three groups of AISI 9310 gears were calculated. These distributions are plotted for comparison with the experimental data in figure 18.

The AGMA has published two standards for tooth surface fatigue (refs. 43 and 44). These standards are AGMA 210.02 and 411.02. AGMA 210.02 provides for an endurance limit for surface fatigue below which it is implied that no failure should occur. In practice, there is a finite surface fatigue life at all loads. AGMA 411.02 recognizes this finite life condition. Therefore, it does not contain an endurance limit in the load-life curve but does show a continuous decrease in life with increasing load. Both standards are illustrated in figure 20. The AGMA load-life curves shown are for a 99-percent probability of survival or the L_1 life (ref. 45). The experimental L_1 , L_{10} , and L_{50} lives are plotted for comparison.

It is evident that the load-life relation used by AGMA is different from the experimental results reported herein. The difference between the AGMA life prediction and the experimental lives could be the result of differences in stressed volume. The AGMA standard does not consider the effects of stressed volume, which for many gears would be considerably different from that of the test gears used herein. The larger the volume of material stressed, the greater the probability of failure or the lower the life of a particular gearset. Therefore, changing the size or contact radius of a gearset, even though the same contact stress is maintained, would have an effect on gear life.

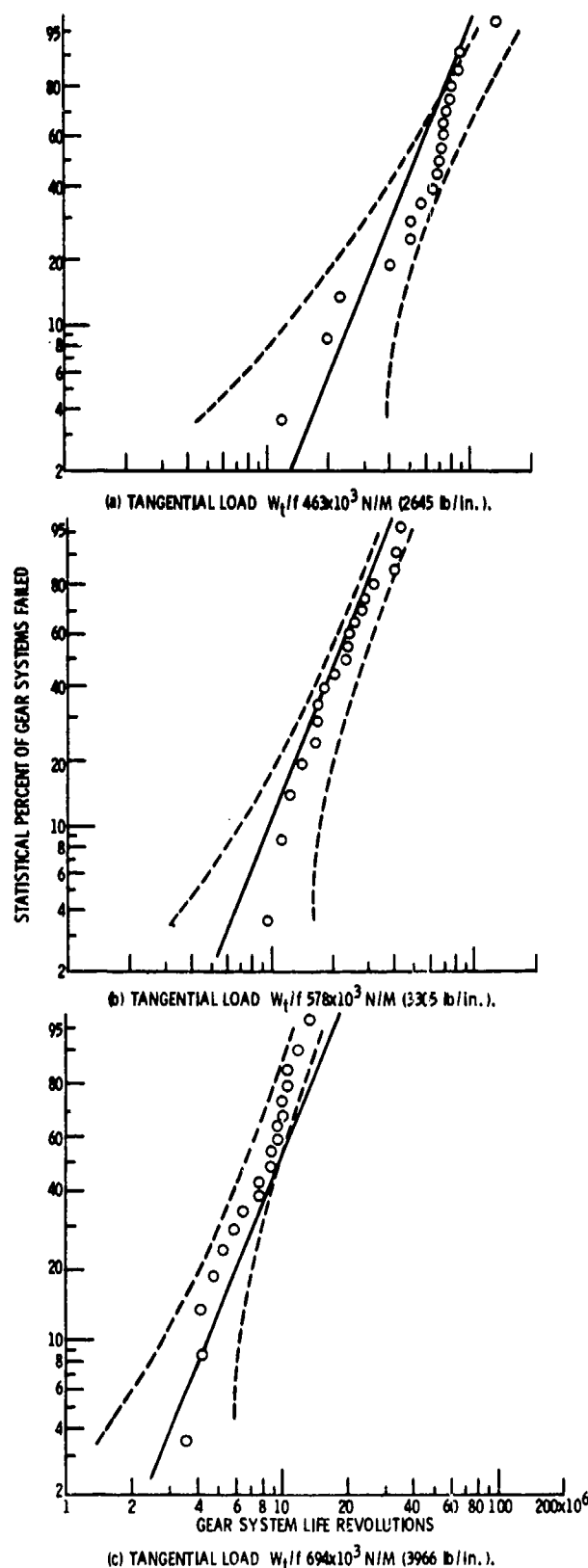


Figure 18. - Comparison of life prediction theory with experimental results for VAR AISI 9310 steel spur gears. Speed, 10 000 rpm; lubricant, superrefined naphthenic mineral oil with additive package.

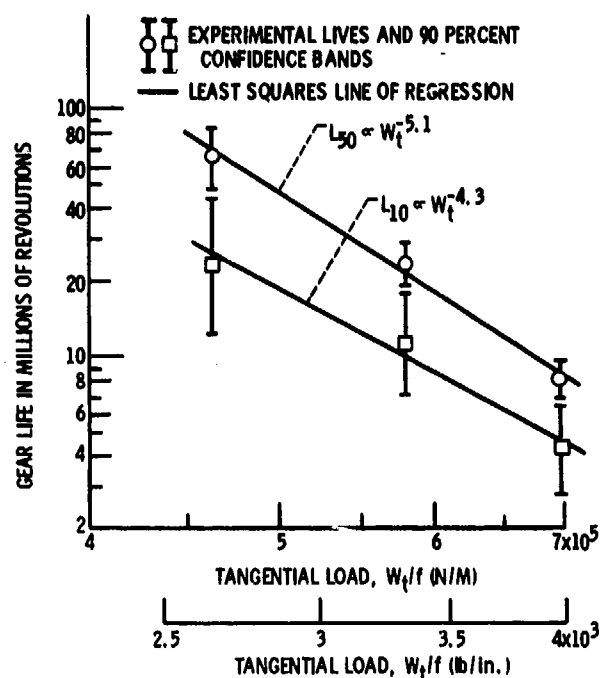


Figure 19. - Load life relationship for VAR AISI 9310 steel spur gears. Speed, 10 000 rpm; lubricant, superrefined naphthenic mineral oil with additive package.

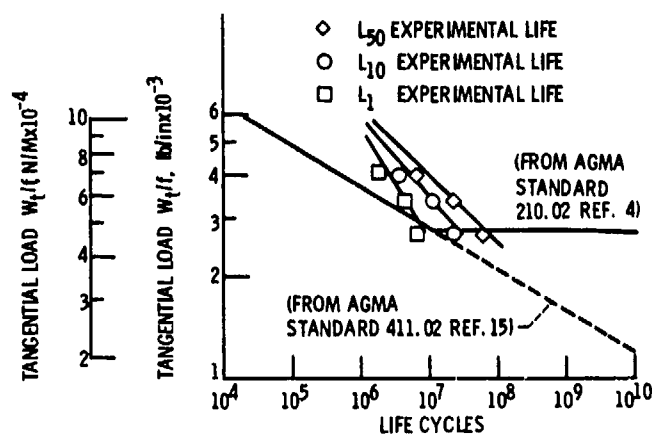


Figure 20. - Comparison of experimental life for (CVM) AISI 9310 spur gears with AGMA life prediction. Speed, 10 000 rpm; lubricant, superrefined naphthenic mineral oil with additive package.

Tooth Profile and Pressure Angle

A majority of current aircraft and helicopter transmissions have spur-gear contact ratios (average number of teeth in contact) of less than 2. The contact ratios are usually from 1.3 to 1.8, so the number of teeth in engagement is either one or two. Many gear designs use a pressure angle of 25° for improved tooth strength, giving a contact ratio of approximately 1.3. This low contact ratio increases dynamic loading of the gear teeth, increases noise, and may sometimes cause lower pitting fatigue life.

High-contact-ratio gears (contact ratio greater than 2) have been in existence for many years but have not been widely used. These gears have load sharing between two or three teeth during engagement; there is, therefore, usually less load per tooth, and the gears should operate with lower dynamic loads and thus less noise.

High contact ratios can be obtained in several ways: (a) by smaller teeth (large pitch), (b) by smaller pressure angle, and (c) by increased addendum. Any of these methods produce gears that tend to have lower bending strength and increased tooth sliding. Increased sliding may cause the gears to run hotter and have a greater tendency for surface-distress-related failures such as micropitting and scoring.

Profile modification (changing the involute profile at the addendum or dedendum or both) is normally done on all gears to reduce tip loading and scoring (ref. 46). However, if done improperly, the dynamic load could be increased (ref. 30). Several profile modifications have been produced that would reduce scoring and improve the performance of high-contact-ratio gears. One such proposal is the so-called new-tooth-form (NTF) gear, which has a large profile modification at both the addendum and dedendum. The profile radius of curvature of this proposal is also reduced at the addendum and increased at the dedendum in an attempt to lessen sliding and thereby reduce scoring of high-contact-ratio gears. However, a gear geometry analysis (ref. 47) indicates that sliding is independent of the profile radius of curvature.

Under NASA contract, the Boeing Vertol Co. designed and manufactured two sets of NTF gears and two sets of standard gears for the purpose of evaluating and comparing them. Scoring, surface-fatigue, and single-tooth-bending-fatigue tests were conducted using four sets of spur gears of standard design and three sets of spur gears of NTF design (ref. 48; fig. 21). The scoring tests were conducted on a Wright Air Development Division (WADD) gear test rig at a speed of 10 000 rpm at the Southwest Research Institute. The surface fatigue tests were conducted on the same test rig at a speed of 10 000 rpm and at maximum Hertz stresses of 173×10^7 and 148×10^7 Pa (250 000 and 214 000 psi). The single-tooth bending fatigue tests were conducted on both the standard and NTF gears starting at a bending stress of 104×10^7 Pa (150 000 psi). The stress was increased until failure occurred at 3×10^6 cycles or less.

The results of the surface fatigue tests are shown in figure 22. The pitting fatigue lives of the standard and NTF gears were statistically equal for the same maximum Hertz stress. The pitting fatigue life of the NTF gears was approximately 300 percent better than that of the standard gears at equal torque or load.

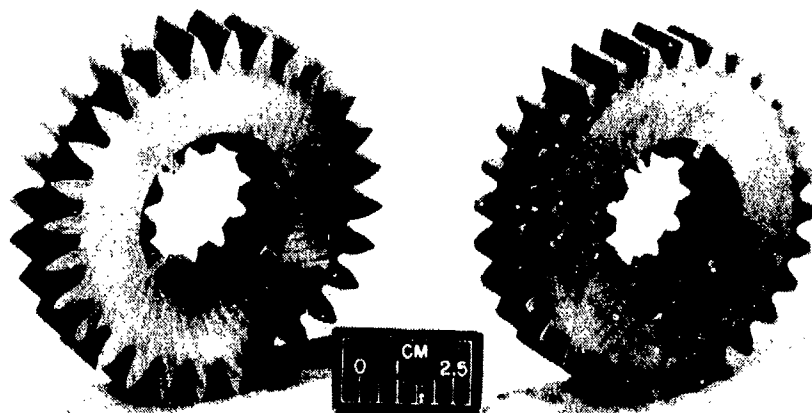


Figure 21. - New-tooth-form (high contact ratio) and standard low-contact-ratio gears. Test specimens for Wright Air Development Division gear test rig.

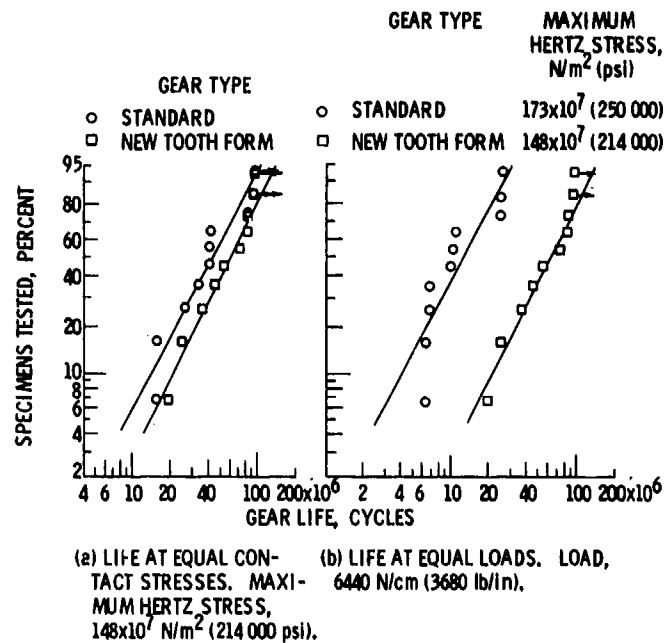


Figure 22. - Pitting fatigue lives of standard and new-tooth-form spur gears. Speed, 10 000 rpm; temperature, 370 K (207° F); lubricant, synthetic polyol ester.

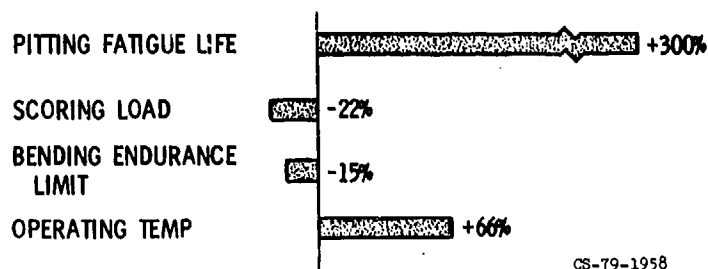


Figure 23. - Performance of new-tooth-form gears referenced to performance of standard low-contact-ratio gears. Testing conducted in Wright Air Development Division test rig.

The improvement in fatigue life, however, is not without a price (fig. 23). Additional tests showed that high-contact-ratio gears are more susceptible to scoring.

Both the standard and NTF gears scored at a gear bulk temperature of approximately 409 K (277° F). At this temperature the load on the NTF gears was 22 percent less than the load on the standard gears. The scoring failure was a function of gear bulk temperature, where for a given lubricant the temperature is a function of gear design, operating load, and speed.

The bending endurance fracture limit is 15 percent lower because the teeth of the high-contact-ratio gear are more slender. Also, these gears run hotter because of increased sliding of the longer teeth. With proper lubrication and design, though, the high-contact-ratio gear can be used to achieve longer life and more reliability.

Spiral Bevel Gears

NASA is conducting a fundamental study of spiral-bevel gear technology. From a study of the current state-of-the-art, significant advances can be achieved in reducing gear noise and vibration, better estimates of gear strength and life, as well as better lubrication techniques which will reduce wear and minimize temperature rise. Figure 24 shows a set of test specimen gears that are used on a spiral bevel gear fatigue tester.



Figure 24. - Spiral bevel test specimen gears for NASA spiral bevel gear-fatigue test rig. Spiral angle, 35° ; face width, 1 in.; shaft angle, 90° ; pressure angle, $22\frac{1}{2}^\circ$; 12T pinion, 36T gear.

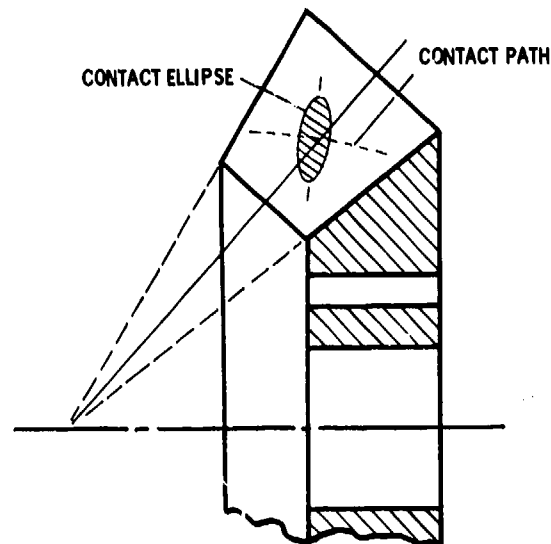


Figure 25. - Spiral bevel gear tooth showing features of tooth contact geometry.

Spiral-bevel gear noise is significantly higher than spur-gear noise. If gear noise in helicopter drives is to be significantly reduced, then this largest source of noise must be reduced. Also, stresses in the root of the spiral-bevel gears are significantly higher than handbook formulas would indicate.

To adequately understand the effects of spiral-bevel gear design parameters on noise, vibration, stress, temperatures, and lubrication, the gear-tooth surface geometry must be defined. Analysis is being performed to define the tooth surface geometry using differential geometry theory. Methods of optimizing the tooth surface contact are being studied (fig. 25).

A spiral-bevel gearset computer program has been developed that makes use of mesh stiffness calculations based on finite-element methods, gear shaft and bearing stiffnesses, current theories of tooth contact analysis (TCA), and elastohydrodynamic lubrication theory. The program will enable the calculation of such things as dynamic loads, bulk and flash temperatures, contact patterns, and lubricant film thickness. The NASA method of gear life prediction will be used as a subroutine of the gear program.

A method for calculating spur-gear efficiency has also been developed at NASA Lewis (ref. 49). This method algebraically accounts for gear sliding, rolling, and windage loss components and incorporates an approximate ball-bearing power-loss expression to estimate the loss of a ball-bearing support system. A theoretical breakdown of the total spur system loss into individual components was performed to show their respective contributions to the total system loss (fig. 26).

Full-Scale Transmission Experiments

When analysis and bench testing are successful in identifying those components that hold promise for improving helicopter transmission performance, they are designed into full-scale

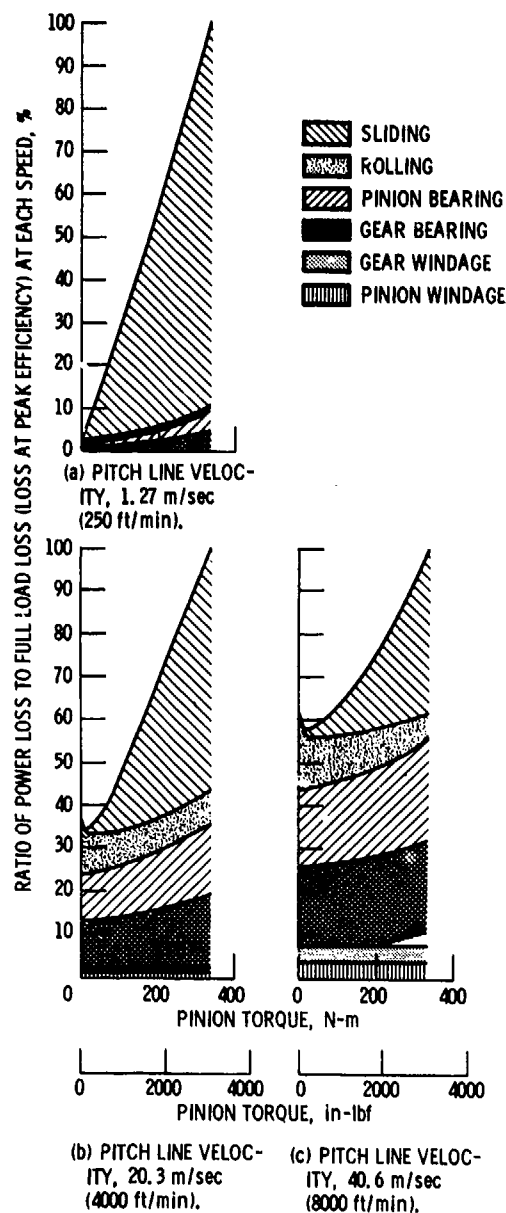


Figure 26. - Percentage breakdown of the sources of gearbox power loss as function of input torque for three speeds. Pitch diameter, 10 cm (4.0 in.); diametral pitch, 8; ratio, 1.0; pinion width to diameter ratio, 0.5; lubricant viscosity, 30 cP.

transmissions. The Lewis Research Center has two helicopter transmission test stands, the 500-hp test stand (figs. 27 and 28) and the 3000-hp test stand (figs. 29 and 30). Both stands operate on the torque regenerative principle, where power is recirculated through the closed loops of shafting. The 500-hp test stand has one loop of shafting, and the 3000-hp test stand has three. The 3000-hp test stand is capable of testing twin-engine input transmissions having a power takeoff to drive a tail rotor. Rotor loads are input by means of hydraulic actuators.

These test stands with their accompanying data acquisition equipment are capable of gathering all bearing and gear temperatures, measuring the noise and vibration signatures, recording mechanical strain on the gears and housing components, and measuring the operating efficiency. Figure 31 shows an installation of 20 strain gages on a spiral-bevel gear which is on the input shaft of one of the experimental transmission models.

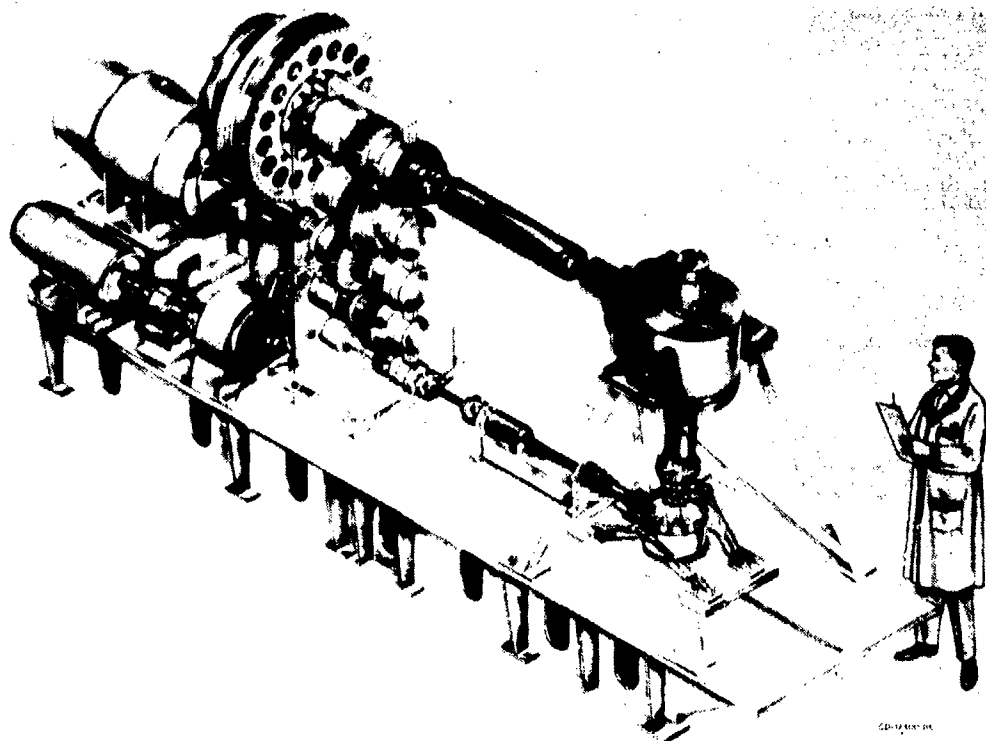


Figure 27. - NASA Lewis Research Center's 500-hp helicopter transmission test stand chain drive applies torque using the torque regenerative principle. Chain drive may turn continuously. Helicopter transmission mounted in pylon supports at lower right. A 200-hp motor provides driving power.

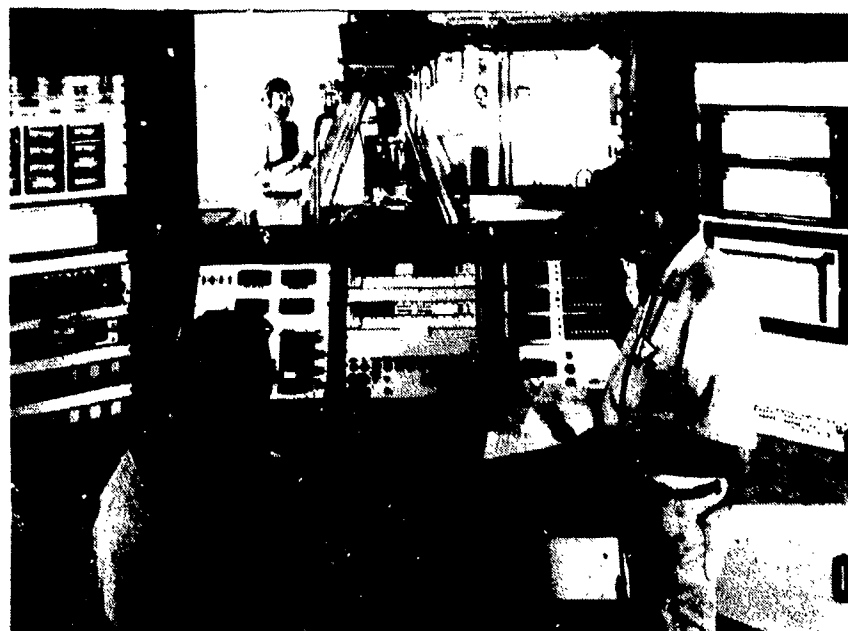


Figure 28. - View of NASA 500-hp test stand from the control room. Approximately 100 channels of static and dynamic data are recorded during experimental testing.

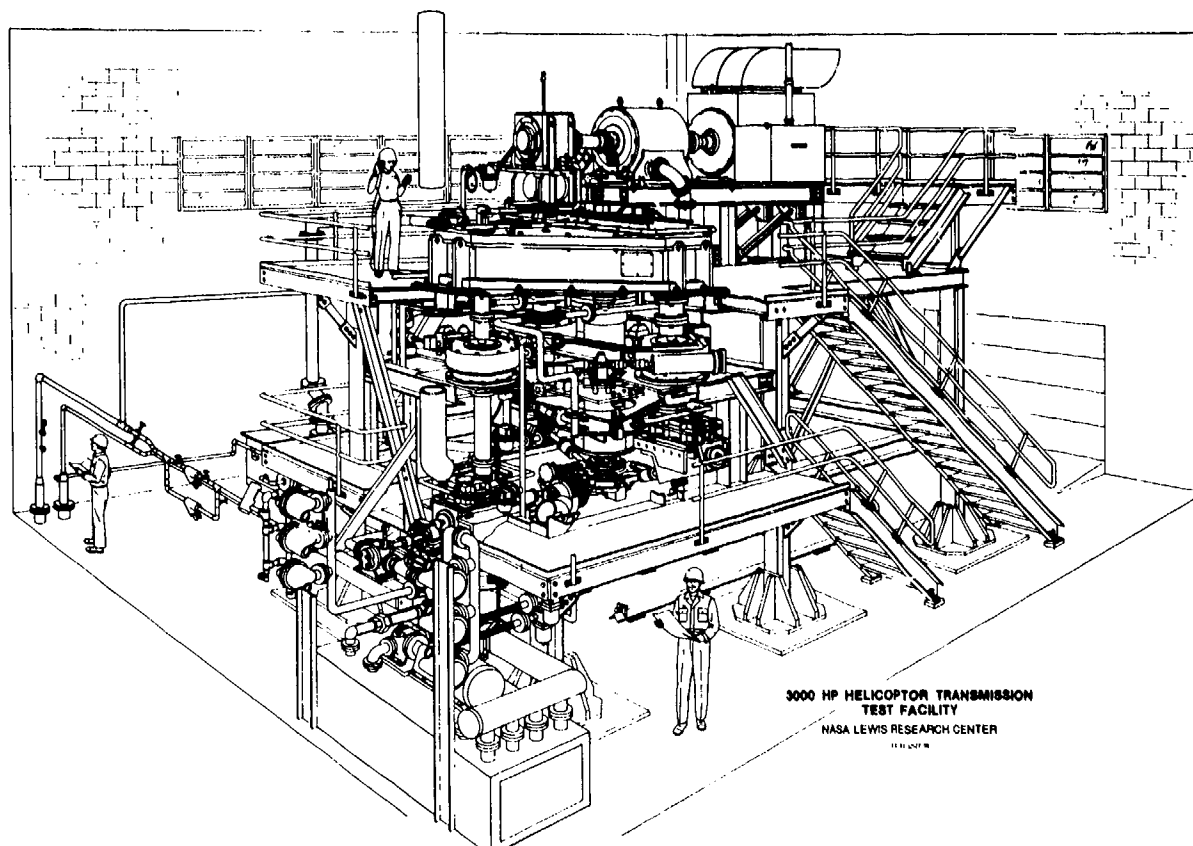
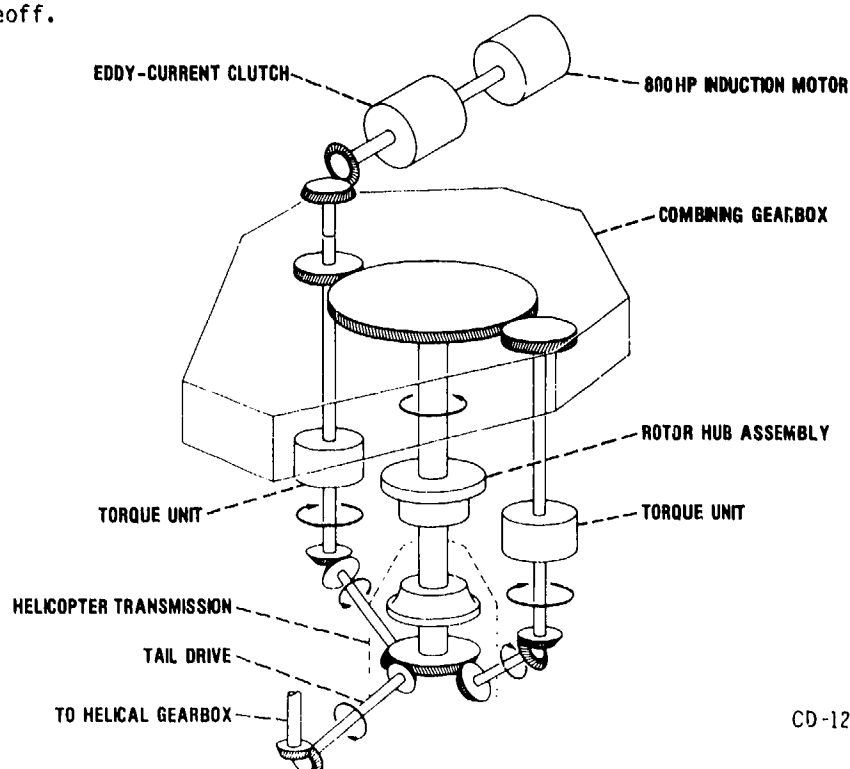


Figure 29. - NASA Lewis Research Center's 3000-hp helicopter transmission test stand. Stand has been operated since March 1981. Consists of three loops of torque regenerative shafting. Capable of providing rotor lift and shear loads for transmissions with twin engine drive and a tail rotor shaft power takeoff.



CD-12550-09

Figure 30. - 3000-hp helicopter transmission test stand schematic arrangement.

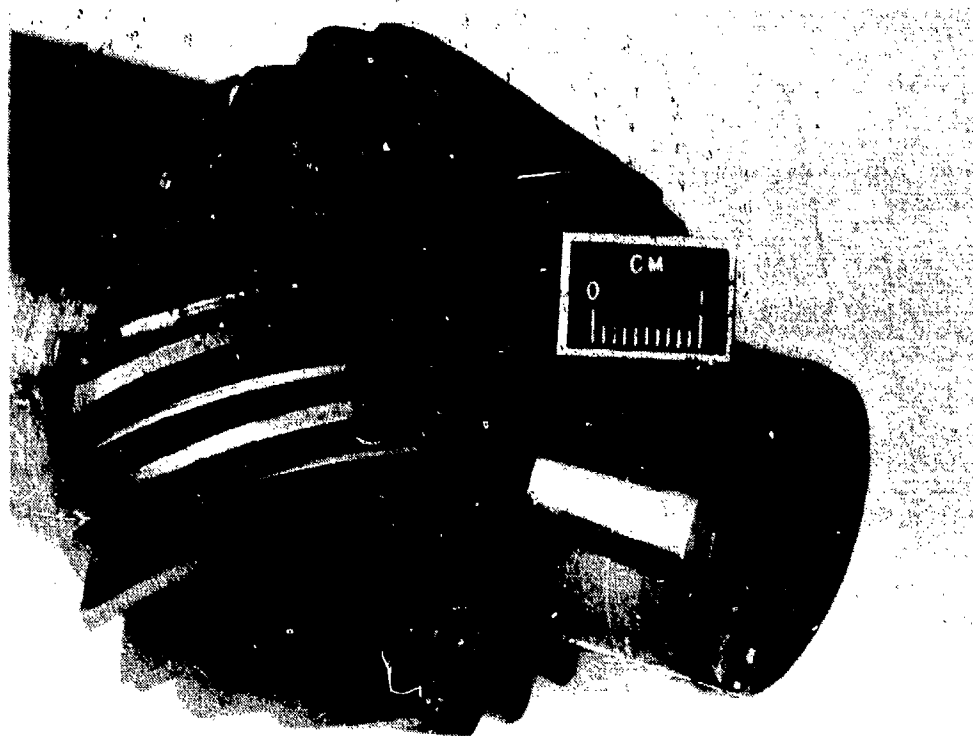


Figure 31. - Spiral bevel gear input shaft for OH-58 helicopter transmission. Twenty strain gages and nine thermocouples installed for research measurements.

Spur-Gear Dynamic Analysis

A gear dynamic analysis has been developed for standard and high-contact-ratio gears by Hamilton Standard Division of United Technologies under contract to NASA. The program will predict the gear dynamic loads for standard and high-contact-ratio gears with variations in gear-tooth profile modifications, in addition to variations in system mass and damping. The program is currently being extended to include rim effects, internal gears, and multiple gear meshes.

NASA is also conducting a spur-gear dynamic analysis program with Cleveland State University. This program is using a different approach for the dynamic analysis and has a finite-element program for gear-tooth deflections. Using this computer program for gear design will give a much better determination of the effects of various gear and system operating parameters on gear dynamic loads and life, and make it possible to improve the load-carrying capacity and life of gear systems.

Performance Prediction

A computer program was developed for calculating spur-gear performance characteristics (ref. 50). The computer program consists of an iterative solution of the bulk temperature, flash temperature, local traction, and the lubricant film thickness along the path of contact. The dynamic load is calculated from a torsional vibration analysis of the gear train. The bulk temperature is calculated from heat-transfer influence coefficients obtained from a finite-element analysis. This is solved iteratively with the elastohydrodynamic lubrication problem for the gears. It is assumed that the vibration problem is uncoupled from the thermal and EHD problems.

Typical results for dynamic load, bulk temperature, flash temperature, and EHD film thickness are shown in figure 32. The calculations were done for the case of two 20° pressure angle, 36-tooth, gears running at 7800 rpm and transmitting 750 hp. Figure 32 is a computer-generated plot, giving the results as a function of distance along the path of contact. The origin is taken at the pitch point.

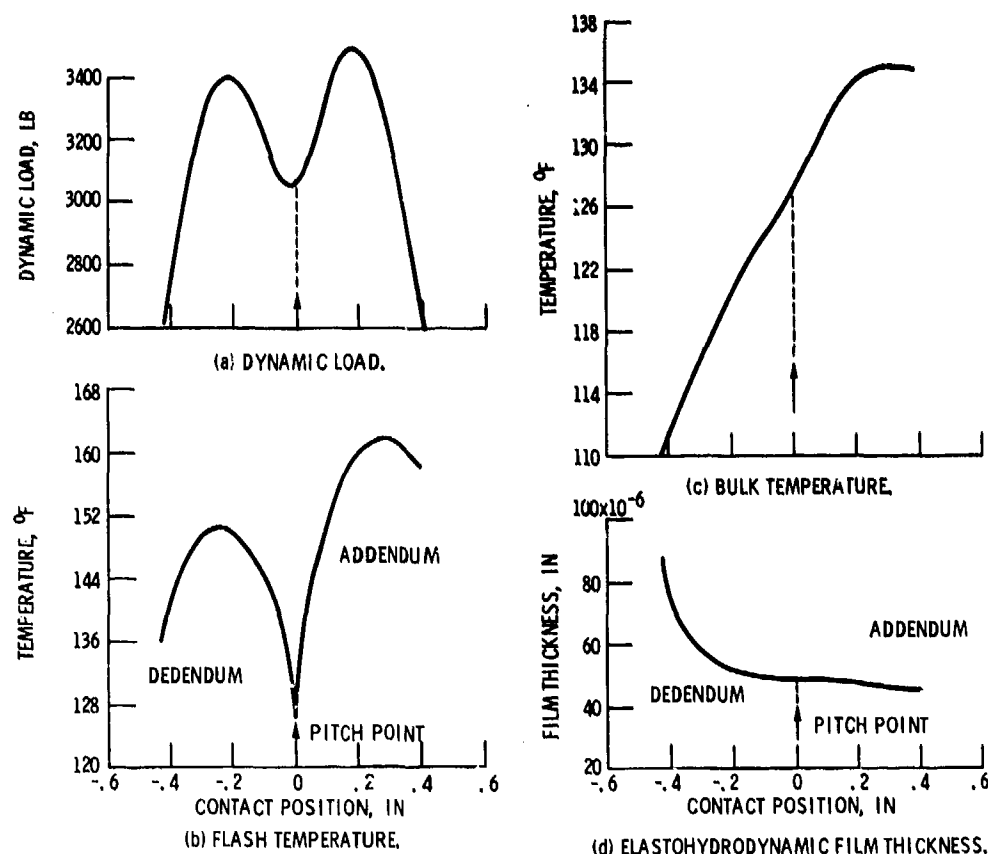


Figure 32. - Computer program results for a spur gear mesh. Ratio 1.1; pressure angle, 20°; 36 teeth; load, 2000 lb; speed, 7800 rpm.

Gear Lubrication and Cooling

The type of lubrication that prevents or minimizes surface asperity interaction is referred to as elastohydrodynamic lubrication. This lubrication mode is differentiated from boundary lubrication in which a chemical, usually oxide, film prevents gross wear or welding of asperities during metal-to-metal contact. In most gear applications a combination of elastohydrodynamic and boundary lubrication exists. Definition of those parameters that affect the lubrication of gears must be obtained and applied to gear design and operation. These parameters include surface finish, tooth design, lubricant type, and elastohydrodynamic lubrication principles (ref. 51).

As a first step in understanding the cooling phenomena in gears, it is important to understand how oil penetrates into the gear tooth spaces under dynamic conditions. Lubricant jet flow impingement and penetration depth into a gear tooth space were measured at 4920 and 2560 rpm using a 8.89-cm (3.5-in.) pitch diameter, 8-pitch spur gear at oil pressures from 7×10^4 to 41×10^4 Pa (10 to 60 psi) (ref. 52). A high-speed motion picture camera with xenon and high-speed stroboscopic lights was used to slow down or "stop" the motion of the oil jet so that the impingement depth could be determined (fig. 33). An analytical model was developed for the vectorial impingement depth and for the impingement depth with tooth space windage effects included. A comparison of the calculated and experimental impingement depth versus oil-jet pressure is shown in figure 34. The windage effects on the oil jet were small for oil drop sizes greater than 0.0076 cm (0.003 in.). The analytical impingement depth compared favorably with experimental results for an oil-jet pressure greater than 7×10^4 Pa (10 psi). Some of the oil penetrates farther into the tooth space after impingement. Much of this postimpingement oil is thrown out of the tooth space without further contacting the gear teeth.

A computer analysis was conducted for oil-jet lubrication on the disengaging side of a gear mesh (ref. 53; fig. 35). The analysis was used to determine the oil-jet impingement depth for several gear

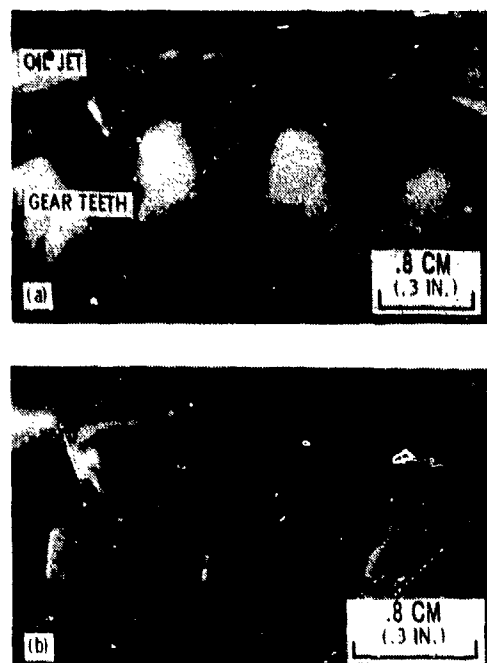


Figure 33. - Oil-jet penetrating tooth space and impinging gear tooth. Speed, 4920 rpm; oil pressure, 10.5×10^4 Pa (15 psi); xenon and stroboscopic light.

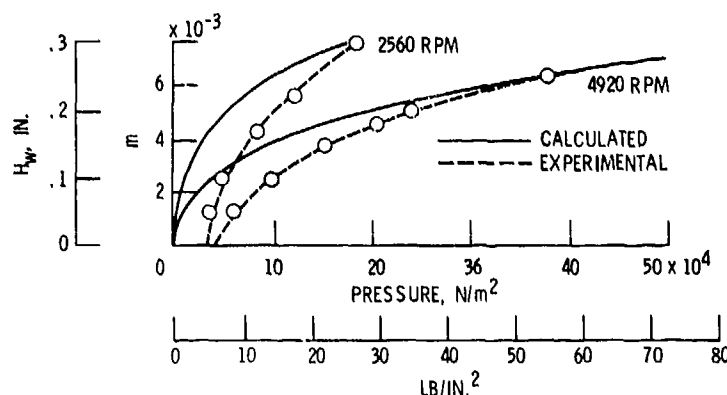


Figure 34. - Calculated and experimental impingement depth versus oil-jet pressure at 4920 and 2560 rpm.

ratios and oil-jet to pitch-line-velocity ratios. An experimental program was conducted on the Lewis gear test rig using high-speed photography to determine the oil-jet impingement depth on the disengaging side of mesh. Impingement depth reaches a maximum at gear ratios near 1.5 where chopping by the leading gear tooth limits the impingement depth. The pinion impingement depth is zero above a gear ratio of 1.172 for a jet velocity to pitch-line velocity ratio of 1.0 and is similar for other velocity ratios. The impingement depth for gear and pinion are equal and approximately one-half the maximum at a gear ratio of 1.0. Impingement depth on either the gear or pinion may be improved by relocating the jet away from the pitch line or by changing the jet angle. Results of the analysis were verified by experimental results using the high-speed camera and a well-lighted oil jet.

Gear Noise

Gear noise is being studied analytically by Lewis contractor Bolt, Beranek, and Newman, Inc. Since noise absorption material in helicopters adversely affects payload capacity, a method of

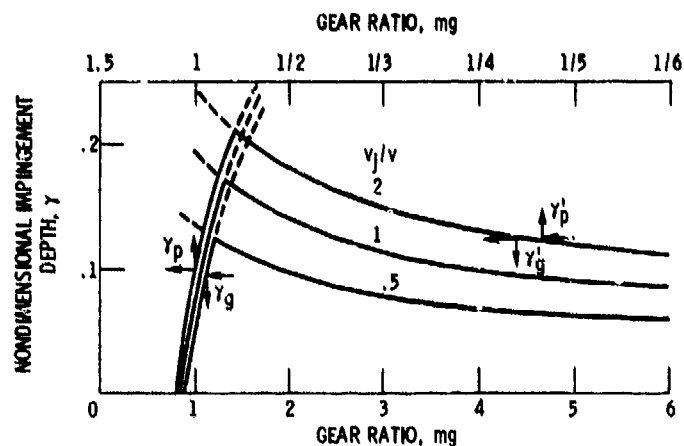


Figure 35. - Gear ratio versus nondimensional impingement depth. Speed, 3600 rpm; jet pressure, 17×10^4 Pa (25 psi); $N_p = 28$.

minimizing noise through better gear design is needed. This way gear noise can be minimized at the source, which is at the gear mesh. The approach is to develop a method for synthesizing optimum modifications of tooth surfaces that will minimize the dynamic loading and noise generated by gear teeth. The work includes developing computer programs for the tooth modification synthesis procedure and for predicting the Fourier series coefficients of vibratory excitation caused by elastic tooth deformations and deviations of tooth faces from perfect involute surfaces. A gear dynamic analysis program also will be written. These programs will be used to design an optimum gear pair to be tested at Lewis and to compute the expected dynamic improvement of the new design in comparison with conventional profile modifications for helicopter transmissions.

Effect of NASA Gear Research Programs

Current design methodology for transmission systems uses relatively standard stress calculations and methods derived from AGMA standards. These methods have proven satisfactory for current state-of-the-art applications. However, transmissions can be sized not only for stress, speed, and ratio, but also for life. Methods for transmission life predictions are inadequate and, for the most part, inconsistent from one design group to another. Assuming an infinite gear pitting life is not technically acceptable. The life-prediction analysis being developed at Lewis will allow for consistent and more accurate life-prediction methods.

Because of the requirement for higher temperature transmission applications, new gear materials, for which we have limited experience, are being used. In addition, heat treat specification and control can significantly affect the life and reliability of a gear system. Experimental definition of the relative life of gear materials and their heat treatment can aid in the selection of gear materials and in determining life-adjustment factors for life-prediction methods. Materials can be rationally selected for longer life application.

Proper gear lubrication and cooling has basically been an art. In general, choice of lubricant flow and pressure and nozzle position and type has been based on previous experience and trial and error methodology. Equations have been developed whereby the position of the oil jets and lubricant flow rate can be determined with reasonable certainty to obtain optimized oil volume and gear operating temperatures for a given transmission design.

The application of elastohydrodynamic (EHD) lubrication analysis to gear design and operation will enhance gear life and operation. The effect of EHD film thickness in determining transmission life and reliability has, for the most part, been ignored by the transmission designer. Furthermore, lubricant temperature affects film thickness and gear-tooth temperature. Hence, cooling analysis of the gear must be integrated with the EHD analysis. Selection of a lubricant affects both parameters and can affect the efficiency of a gearbox as well as its life.

Analytical methods to accurately predict transmission noise is another requirement which becomes a potential design tool. While life and reliability as well as efficiency are prime design considerations, alternative designs of equal merit may result in significant reduction of noise amplitudes. Proven analytical methods for predicting noise would aid in the proper design, selection, or modification of gear systems that minimize noise and optimize mechanical performance.

Accurate predictions for bending stress and dynamic Hertz stress in the contact zone of gear teeth are very important factors in transmission design. Finite-element techniques for both spur and bevel gears will greatly improve current predictions. This would allow the design to more fully utilize the potential load capacity of advanced transmission systems and at the same time minimize transmission weight.

Tooth profile modifications and high-contact-ratio gearing offer the potential to increase the power-to-weight ratio for a given transmission application. Conversely, for a given transmission load, reliability and life should improve.

In essence, the effect of the NASA gear program will be to contribute technology towards more efficient transmission systems having higher power-to-weight ratios, longer lives, and higher reliabilities than current state-of-the-art systems. Furthermore, the use of improved gear materials and design methodology should improve transmission maintainability and mean time between removal (MTBR).

Future Requirements

Gearing requirements will continue to evolve. The condition of society and its needs as well as new discoveries, inventions, and new goals will keep the pressure on gear practitioners to meet the challenges. For example, 40 years ago, not many suspected that gears may be required to operate in the extreme environment of outer space, in cryogenic temperatures, in a vacuum, and without conventional lubrication. Now we can only imagine what may be required of the gearing technologists in the next 20 or 30 years.

From the standpoint of aircraft applications for gearing, continuing improvements are needed. There are several important topics that need further research for applications both now and in the next decade.

The requirements for advanced helicopter transmission and aircraft engine gearboxes include weight reduction and higher temperature operations than present-day aircraft, as well as increased reliability and service life. The gearing systems in these aircraft are expected to carry greater loads, operate at higher temperatures because of increased engine speeds, and provide improved system life, in addition to providing low maintenance rates and higher reliability. Very-high-temperature operation of gears is also required where the transmission must operate for short periods without lubrication and cooling.

References

1. The New Encyclopedia Britannica. Fifteenth ed., Encyclopedia Britannica, Inc., 1974.
2. de Solla Price, Derek: Gears from the Greeks. Science History Publications, 1975.
3. Drachmann, A. G.: The Mechanical Technology of Greek and Roman Antiquity. Lubrecht and Cramer, 1963.
4. White, G.: Evolution of the Epicyclic Gear, Part 2. Chart. Mech. Eng., vol. 25, no. 4, Apr. 1978, pp. 85-90.
5. Dudley, D. W.: The Evolution of the Gear Art. American Gear Manufacturers Association, 1969.
6. Reti, Ladislao: Leonardo on Bearings and Gears. Sci. Am., vol. 224, no. 2, Feb. 1971, pp. 100-110.
7. da Vinci, Leonardo (L. Reti, transl.): The Madrid Codices of Leonardo da Vinci. McGraw-Hill Book Co., Inc., 1974.
8. Lewis, Wilfred: Investigations of the Strength of Gear Teeth. Proc. of the Engineers Club of Philadelphia, 1893, pp. 16-23.
9. Grant, George B.: A Treatise on Gear Wheels. Twenty-first ed., Philadelphia Gear Works, Inc., 1980.
10. Buckingham, Earle: Dynamic Loads on Gear Teeth. Am. Soc. Mech. Eng., 1931.
11. Grubin, A. N.: Fundamentals of the Hydrodynamic Theory of Lubrication of Heavily Loaded Cylindrical Surfaces. Investigation of the Contact of Machine Components, Kh. F. Ketova, ed., Translation of Russian Book No. 30, Central Scientific Institute for Technology and Mechanical Engineering, Moscow, 1949, Chapter 2. (Available from Department of Scientific and Industrial Research, Great Britain, Transl. CTS-235 and Special Libraries Association, Transl. R-3554.)

12. Proceedings of the Fifth World Congress on the Theory of Machines and Mechanisms, Vols. 1 and 2. Am. Soc. Mech. Eng., 1979.
13. Tucker, A. I.: Bevel Gears at 203 Meters per Second (40,000 FPM). ASME paper 77-DET-178, 1977.
14. Haas, L. L.: Latest Developments in the Manufacture of Large Spiral Bevel and Hypoid Gears. ASME paper 80C2/DET-119, Aug. 1980.
15. Drago, R. J.; and Brown, F. W.: The Analytical and Experimental Evolution of Resonant Response in High-Speed, Light-Weight, Highly Loaded Gearing. *J. Mech. Des.*, vol. 103, no. 2, Apr. 1981, pp. 346-356.
16. Fujita, K.; and Yoshida, A.: Effects of Case Depth and Relative Radius of Curvature on Surface Durability of Case Hardened Chromium Molybdenum Steel Roller. *J. Mech. Des.*, vol. 103, no. 2, Apr. 1981, pp. 474-481.
17. Townsend, D. P.; and Zaretsky, E. V.: Endurance and Failure Characteristics of Modified Vasco X-2, CBS 600, and AISI 9310 Spur Gears. *J. Mech. Des.*, vol. 103, no. 2, Apr. 1981, pp. 506-515.
18. Binder, S.; and Mack, J. C.: Experience with Advanced High Performance Gear Steel. ASME paper 80 C2/DET-77, Aug. 1980.
19. Winter, H.; and Weiss, T.: Some Factors Influencing the Pitting, Micro-Pitting (Frosted Areas) and Slow Speed Wear of Surface Hardened Gears. *J. Mech. Des.*, vol. 103, no. 2, Apr. 1981, pp. 499-505.
20. Chen, J. H.; Jaurbe, F. M.; and Hanley, M. A.: Factors Affecting Fatigue Strength of Nylon Gears. *J. Mech. Des.*, vol. 103, no. 2, Apr. 1981, pp. 542-548.
21. Gauvin, R.; Girard, P.; and Yelle, H.: Investigation of the Running Temperature of Plastic/Steel Gear Pairs. ASME paper 80-C2/DET-108, Aug. 1980.
22. Yonekura, M.; and Ainoura, M.: A Research on Finishing Hardened Gears of Large Modules. ASME paper 80-C2/DET-62, Aug. 1980.
23. Ainoura, M.; and Yonekura, M.: A Research for Developing a New Type Shaving Hob for Cutting Gears of Large Modules. ASME paper 80-C2/DET-65, Aug. 1980.
24. Weck, M.; Gogrewe, H.-U.; and Ernst, D.: Numerical Controlled Dressing of Profile Grinding Wheels. ASME paper 80-C2/DET-74, Aug. 1980.
25. Fort, P.: Computer Aided Design, Manufacturing and Inspection System for Spiral Bevel Gears. ASME paper 80-C2/DET-127, Aug. 1980.
26. Carter, T. L.; Zaretsky, E. V.; and Anderson, W. J.: Effect of hardness and Other Mechanical Properties on Rolling-Contact Fatigue of Four High-Temperature Bearing Steels. NASA TN D-270, 1960.
27. Zaretsky, E. V.; and Anderson, W. J.: Rolling-Contact Fatigue Studies with Four Tool Steels and a Crystallized Glass Ceramic. *J. Basic Eng.*, vol. 83, no. 4, Dec. 1961, pp. 603-612.
28. Townsend, D. P.; Chevalier, J. L.; and Zaretsky, E. V.: Pitting Fatigue Characteristics of AISI M-50 and Super Nitralloy Spur Gears. NASA TN D-7261, 1973.
29. Townsend, D. P.; and Zaretsky, E. V.: Effect of Tip Relief on Endurance Characteristics of Super Nitralloy and AISI M-50 Spur Gears. NASA TN D-7535, 1974.
30. Townsend, D. P.; and Zaretsky, E. V.: A Life Study of AISI M-50 and Super Nitralloy Spur Gears With and Without Tip Relief. *J. Lubr. Technol.*, vol. 96, no. 4, Oct. 1974, pp. 583-590.
31. Townsend, D. P.; Bamberger, E. N.; and Zaretsky, E. V.: Comparison of Pitting Fatigue Life of Ausforged and Standard Forged AISI M-59 and AISI 9310 Spur Gears. NASA TN D-8030, 1975.
32. Townsend, D. P.; Bamberger, E. N.; and Zaretsky, E. V.: A Life Study of Ausforged, Standard Forged, and Standard Machined AISI M-50 Spur Gears. *J. Lubr. Technol.*, vol. 98, no. 3, July 1976, pp. 418-425.
33. Townsend, D. P.; and Zaretsky, E. V.: Comparison of Modified Vasco X-2 and AISI 9310 Gear Steels. NASA TP-1731, 1980.
34. Nahm, A. H.: Rolling-Element Fatigue Testing of Gear Materials. (R-78AEG289, General Electric Co.; NASA Contract NAS3-14302.) NASA CR-135411, 1978.
35. Nahm, A. H.: Rolling-Element Fatigue Testing of Gear Materials. (R-78AEG476, General Electric Co.; NASA Contract NAS3-14302.) NASA CR-135450, 1978.
36. Zaretsky, E. V.; and Anderson, W. J.: Effect of Materials: General Background. Interdisciplinary Approach to the Lubrication of Concentrated Contacts, P. M. Ku, ed. NASA SP-237, 1970, pp. 379-408.
37. Bamberger, E. N.: The Effect of Ausforming on the Rolling-Contact Fatigue life of a Typical Bearing Steel. *J. Lubr. Technol.*, vol. 89, no. 1, Jan. 1967, pp. 63-75.
38. Lundberg, G.; and Palmgren, A.: Dynamic Capacity of Rolling Bearings. *Ing. Vetensk. Akad., Handl.*, no. 196, 1947.
39. Lundberg, G.; and Palmgren, A.: Dynamic Capacity of Roller Bearings. *Ing. Vetensk. Akad., Handl.*, no. 210, 1952.
40. Coy, J. J.; Townsend, D. P.; and Zaretsky, E. V.: Analysis of Dynamic Capacity of Low-Contact-Ratio Spur Gears Using Lundberg-Palmgren Theory. NASA TN D-8029, 1975.
41. Coy, J. J.; and Zaretsky, E. V.: Life Analysis of Helical Gear Sets Using Lundberg-Palmgren Theory. NASA TN D-8045, 1975.
42. Townsend, D. P.; Coy, J. J.; and Zaretsky, E. V.: Experimental and Analytical Load-Life Relation for AISI 9310 Spur Gears. *J. Mech. Des.*, vol. 100, no. 1, Jan. 1978, pp. 54-60.
43. Surface Durability (Pitting) of Spur Gear Teeth. AGMA 210.02, American Gear Manufacturers Assoc., Jan. 1965.
44. Standard Design Procedure for Aircraft Engine and Power Take-off Spur and Helical Gears. AGMA 411.02, American Gear Manufacturers Assoc., Sep. 1966.
45. Coy, J. J.; Townsend, D. P.; and Zaretsky, E. V.: Dynamic Capacity and Surface Fatigue life of Spur and Helical Gears. *J. Lubr. Technol.*, vol. 98, no. 2, Apr. 1976, pp. 267-276.
46. Bursoff, V. N.: On the Mechanisms of Gear Lubrication. *J. Basic Eng.*, vol. 81, no. 1, Jan. 1959, pp. 79-93.
47. Khiralla, T. W.: On the Geometry of External Involute Spur Gears. G/I Leaming, North Hollywood, Calif., 1976.

48. Townsend, D. P.; Baber, B. B.; and Nagy, A.: Evaluation of High-Contact-Ratio Gears with Profile Modification. NASA TP-1458, 1979.
49. Anderson, N. E.; and Loewenthal, S. H.: Effect of Geometry and Operating Conditions on Spur Gear System Power Loss. J. Mech. Des., vol. 103, no. 1, Jan. 1981, pp. 151-159.
50. Wang, K. L.; and Cheng, H. S.: A Numerical Solution to the Dynamic Load, Film Thickness, and Surface Temperatures in Spur Gears, Part 1: Analysis; and Part 2: Results. J. Mech. Des., vol. 103, no. 1, Jan. 1981, pp. 177-194.
51. Townsend, D. P.: The Application of Elastohydrodynamic Lubrication in Gear Tooth Contacts. NASA TM X-68142, 1972.
52. Akin, L. S.; Mross, J. J.; and Townsend, D. P.: Study of Lubricant Jet Flow Phenomena in Spur Gears. J. Lubr. Technol., vol. 97, no. 2, Apr. 1975, pp. 283-288, and p. 295.
53. Townsend, D. P.; and Akin, L. S.: Study of Lubricant Jet Flow Phenomena in Spur Gears—Out of Mesh Condition. J. Mech. Des., vol. 100, no. 1, Jan. 1978, pp. 61-68.



A Historical Perspective of Traction Drives and Related Technology

Stuart H. Loewenthal*

Traction or friction drives are perhaps the simplest of all rotary mechanisms and yet relatively little is known and even less has been written about them. In its simplest form a traction drive is just two smooth, unequal sized wheels in driving contact. Their simplicity suggests that their existence predates that of the gear drive. As speed regulators, oil-lubricated traction drives have been in industrial service for more than 50 years; yet the concept of transmitting power via traction remains unfamiliar and even alien to many. Indeed, traction drives are commonplace in our daily existence. Our car tires engaged against the road surface or a locomotive's driving wheels against the rail are but two common examples.

Many applications may be found in equipment where simple and economical solutions to speed regulations are required, such as phonograph drives, self-propelled lawnmowers, and even the amusement park ride driven by a rubber tire. Of course, in these examples, simple dry contact is involved. However, this same principle can be harnessed in the construction of an oil-lubricated transmission containing all steel components.

Traction drives can be constructed to give a single, fixed-speed ratio, like a gearbox or, unlike a gearbox, a speed ratio that can be continuously varied. This latter arrangement is of extreme interest to drive-train configurators since it provides them with an essentially "infinite" number of shift points to optimize the performance of their drive system.

Because power transfer occurs between smooth rolling-bodies, generally across a thin, tenacious lubricant film, traction drives possess certain performance characteristics not found in other power transmissions. Traction drives can be designed to smoothly and continuously vary the speed ratio with efficiencies approaching those of the best gear drives. Unlike transmissions with gear teeth, which, even when perfectly machined, generate torsional oscillations as the load transfers between teeth, power transfer through traction is inherently smooth and quiet without any "backlash." Film trapped between the rollers tends to protect against wear and to dampen torsional vibrations. The operating speed of some traction drives is limited only by the burst strength of the roller material and the available traction in the contact. In many cases traction drives can be designed to be as small as or smaller than their nontraction-drive counterparts. When manufactured in sufficient quantity, costs can also be quite competitive because of the similarities in manufacturing traction-drive components and ordinary mass-produced ball and roller bearings.

Although traction drives have been available for some time (refs. 1 to 7), it is perhaps within the past 15 years or so that they have been considered serious competitors of conventional mechanical power transmissions in some of the more demanding applications. The earlier drives, particularly those targeted for automotive applications, had their share of durability problems above nominal power levels and, as a consequence, relatively few succeeded in the market place. The underlying reason for this was that certain critical pieces of technology were generally lacking. Designs were based on mostly trial and error. No uniform failure theories were available to establish service life or reliability ratings. The drive materials of the day were crude by today's standards. In short, traction drives were in their technical infancy.

Prompted by the search for more efficient automotive transmissions and bolstered by advancements made in rolling-element bearing technology, interest in traction drives has been renewed. Today's analytical tools, materials, and traction fluids are far superior to those available only 10 years ago. This has led to the re-emergence of traction drives and the technology related to their design.

It is the intent of this review to trace the evolution of traction-drive technology, in a limited sense, from its early development to the efforts underway today. The reader will appreciate that no attempt has been made to comprehensively document the history of traction drives but rather to

*NASA Lewis Research Center.

AD P000702

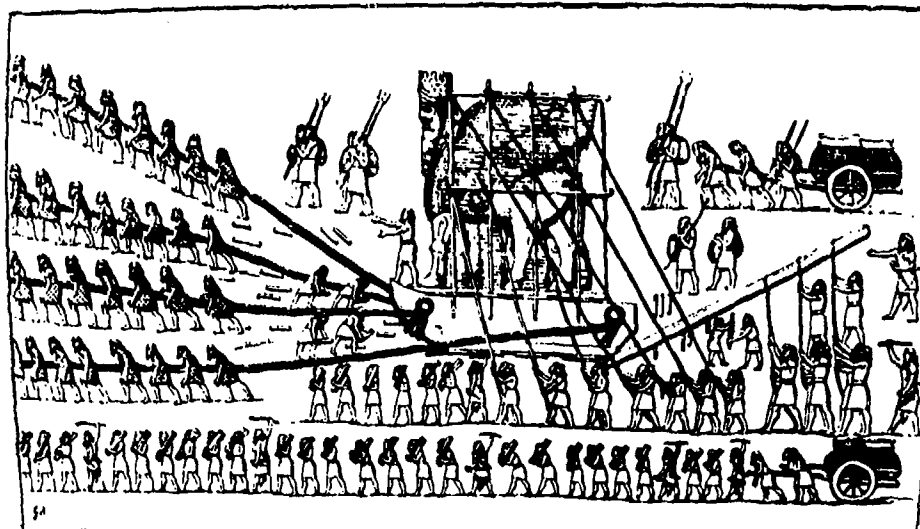


Figure 1. - Assyrians positioning stone figure using log rollers and "human traction," circa 700 B.C. (ref. 8).

assemble, in a single place, a collection of source material on this broad subject for the benefit of those unfamiliar with these interesting devices.

Early History

Since the development of machines there has been a need for transmissions to effectively match the speed of the power source to that of the driven device. In early human history, the power sources were either human or animal and in "direct" drive with the load. This is vividly illustrated in figure 1 (ref. 8). This scene (ca. 700 B.C.) depicts Assyrians positioning a stone figure with the aid of log rollers and "human traction." Traction as an assistance to motion is a natural part of the human experience. Also depicted are humans pulling wheeled-carts. It is clear that the ancients had knowledge of both the roller and the wheel. Thus, the ingredients to develop simple traction wheel mechanisms were available to them.

The existence of mechanical drive systems may even predate this by hundreds of years, according to Dudley (ref. 9). He speculates that gear devices might have been used in clocks, temple devices, and water-lifting machines as far back as 1000 B.C. by the ancient Greek, Egyptian, and Babylonian civilizations. Unfortunately, there is no tangible evidence to support this view. Drachmann (ref. 10) maintains that the origins of the toothed gear wheel are often erroneously associated with a passage in a book by Aristotle. The passage was, in fact, not due to Aristotle but to his school (ca. 280 B.C.), and there is no explicit mention of teeth on the wheels. These wheels may just as well have been smooth disks in *frictional contact* according to Drachmann. Although there seems to be no evidence in the literature or artifacts to establish when friction wheels were first used, it is reasonable to assume that before man went to the trouble of cutting notches in smooth wheels, he probably used them as they were to transmit rotary motion. Pins or cogs might have been added to the wheel to overcome dimensional variations due to the crude, out-of-round wheels of the day or when the driving load simply became too large to be sustained by frictional contact. It is ironic that these very cogs, though now more sophisticated than in earlier times, are often the source of many power transmission problems. Although the writer's limited efforts failed to uncover tangible examples of friction drives before the modern era, the likelihood of their use in primitive rotary machinery is too great to dismiss.

One of the earliest known examples of a friction drive¹ is that patented by C. W. Hunt in 1877 (fig. 2; ref. 11). This drive had a single, spoked transfer wheel, which was probably covered with

¹The term "friction drive" is normally used to refer to a drive that is nonlubricated, while "traction drive" refers to one with oil-wetted components. The friction terminology may have evolved from the fact that these drives intentionally used at least

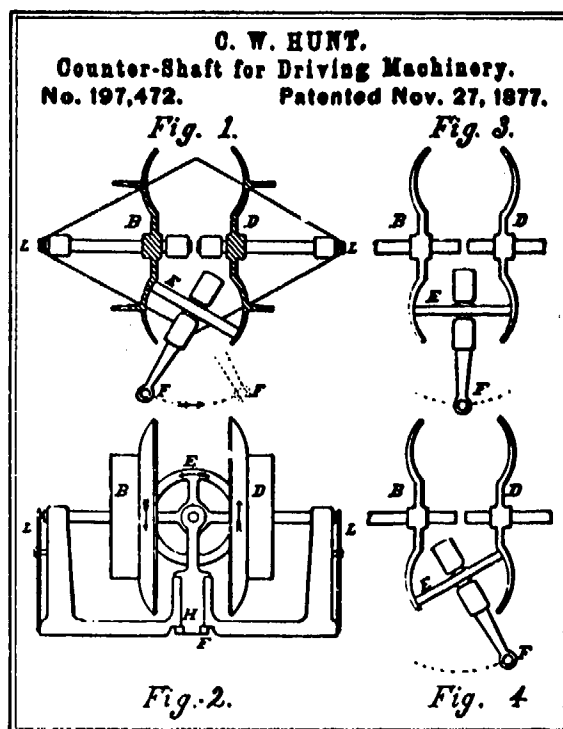


Figure 2. - Hunt's 1877 toroidal friction drive (ref. 11).

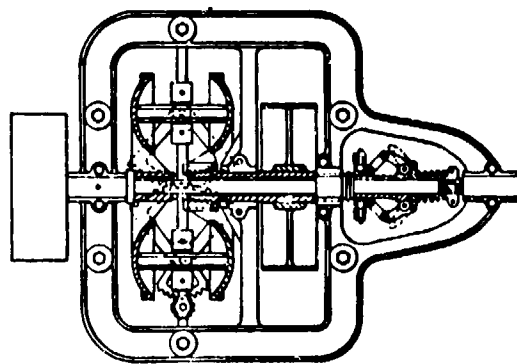


Figure 3. - 1899 Hoffman toroidal friction drive for belt-driven machinery (ref. 12).

leather, running against a pair of toroidally shaped metal disks. Judging by the pulley flanges attached to the toroidal disks, the drive was intended to regulate the speed of belt-driven machinery such as that commonly found in factories at the turn of the century. By tilting transfer wheel E, the effective rolling radii of toroids B and D could be altered and, hence, their relative speeds.

A similar drive was devised by W. D. Hoffman as shown in an 1899 British patent application (fig. 3 from ref. 12). The toroidal drive arrangement apparently has found great favor with traction-drive designers through the years. Work continues on this configuration even today, more than 100 years later!

one roller that was covered with a high friction material such as leather, rubber, fiber or even wood. This notwithstanding, the term "friction" is somewhat of a misnomer since it is still the traction force responsible for positive motion of the driven element.

"The Only Direct Drive Friction Transmission"

THE Gearless Transmission

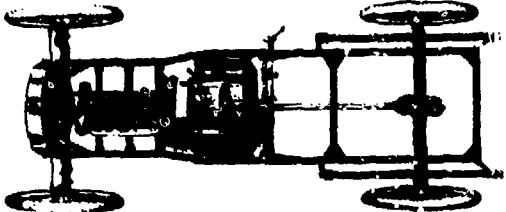
The Ideal Transmission for Both Pleasure and Commercial Vehicles.

Does Away Entirely With the Use of Gears Gives an Unlimited Number of Speeds

Giving a BROAD RANGE OF SPEEDS FORWARD OR REVERSE. DIRECT DRIVE ON HIGH SPEED. Single Lever Control, ELIMINATING ENTIRELY All of the Difficulties Encountered in the Present Forms of Transmissions Employing Gears with their Attendant Troubles.

Built in TWO Sizes For Light and Heavy Cars.

Can Be Used With Either Shaft or Chain Drive.

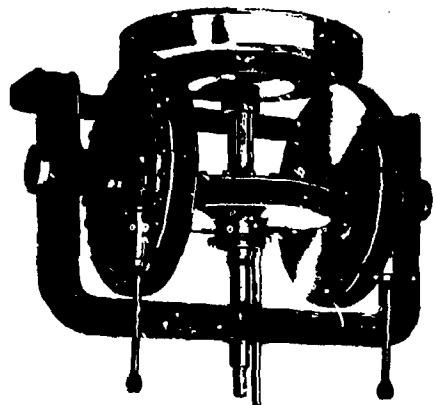


Showing Transmission Installed in Car

Write For Catalogue and Prices To-day.

Thoroughly Tested During the Past Two Years.

We Furnish the Transmission As Shown Here-with to Include Fly-wheel and Direct Clutch. The Frame is of Steel. Bearings, Balls and Rollers. Material and Workmanship of Highest Grade.



Showing Transmission in Reverse Speed

Side Friction Wheels Do Not Rotate on Direct Drive. Central Friction Wheel is Driven on Intermediate Speeds by Both Side Wheels From Flywheel. Note The Direct Clutch in Hub of the Flywheel.

Friction Surfaces only in use on Intermediate Speeds Forward and Reverse.

Write for Catalogue

Puts Less Strain on the Running Gear of a Car Than Any Other Transmission.

GEARLESS TRANSMISSION CO., Rochester, N. Y.

Figure 4. - An early automotive friction drive, circa 1906, (ref. 17).

Friction drives also found use on several types of wood-working machinery dating back before the 1870's. The 1876 edition of Knight's American Mechanical Dictionary (ref. 1) describes a deal-frame machine for slitting pine-timber which employed a friction disk drive for regulating the feed motion. In another source (ref. 2), a wood panel-planer is described whose feed rolls are driven by friction wheels. Appleton's Cyclopaedia of Applied Mechanics, published in 1880 (ref. 3), reports of frictional gearing being used on wood-working machinery in which one wheel was made of iron and the other, typically the driver, of wood or iron covered with wood. For driving light machinery, wooden wheels of basswood, cottonwood, or even white pine reportedly gave good results. For heavy work, where from 30 to 45 kW was transmitted by simple contact, soft maple was preferred. Appleton's Cyclopaedia also discusses bevel frictional gearing in which the bevel-gear is a smooth-faced iron cone being driven by a bevel pinion, with a wooden rim. This rim comprises several layers of hardwood followed by soft maple bolted on to a flanged-hub made of iron.

Automotive Transmissions

It was not until the introduction of the horseless carriage at the end of the 19th century that the goal of developing a continuously variable transmission (CVT) for the automobile sparked considerable friction drive activity. Although the potential performance benefits associated with a CVT for other types of machinery had been recognized before, the safety, simplicity, and reliability

of the gearset offered greater appeal. It was good enough to select roughly the right speed ratio and to up-size the powerplant slightly, if needed, to drive the load. It quickly became apparent to the designers of early automobiles that a highly flexible transmission was badly needed to compensate for the lack of flexibility of the early gasoline engines. These engines had a tendency to run well only at one speed. As noted by P. M. Heldt in an unusually comprehensive review of the development of the automatic transmission (ref. 13), the chief objection to early sliding-gear transmission, apart from their lack of flexibility, was the difficulty in gear shifting. The gearboxes used on many of the early vintage cars, such as 1890 Panhard, were adopted from the clash gears used in factory equipment (ref. 14). Gear changing was not merely difficult but potentially damaging to the gear teeth. According to Hodges and Wise (ref. 15), "the best technique with those early cars was to slip the clutch gently and bang the gears home as quickly as possible, in the hope that you might catch the cogs unawares." (Although Prentice and Shiels patented the synchromesh principle back in 1904, it wasn't until the late 1920's that General Motors developed the synchromesh gearshift for production. Synchromesh allowed almost any driver to shift from one speed to the next without clashing the gears (ref. 16).) In view of the limitations and inconveniences associated with gear changing, it is not surprising that the inventors of the day looked for a simple means of continuously and, hopefully, automatically varying the speed ratio between the engine and the wheels.

Mechanical ratchet, hydraulic, and electro-mechanical drives were all tried, but friction drives, because of their simplicity, were the first automobile transmissions to provide infinite ratio selection. The earliest of these was the rubber V-belt drives that appeared on the 1886 Benz and Daimler cars, the first massproduced gasoline-engine-powered vehicles. Friction disk drives, similar in construction to the gearless transmission illustrated in a 1906 advertisement (fig. 4 from ref. 17), were used as regular equipment on a number of early motor cars. These included the 1906 Cartercar, 1907 Lambert, 1909 Sears Motor Buggy, and 1914 Metz Speedster. An early advertisement for the Lambert appears in figure 5.

The Cartercar (fig. 6) had an extremely simple friction drive consisting of a metal disk, driven by the engine crankshaft, in traction contact with a large, fiber-covered spoked wheel mounted on a transverse countershaft. The countershaft, in turn, was connected to the rear axle by an ordinary chain drive. To vary speed ratio, a driver operated lever (fig. 6) was used to radially position the

MOTOR AGE

MARCH 7, 1907

"IT'S A STRONGER PROPOSITION THAN YOU HAVE IMAGINED"

DEALERS

EXAMINE

THE LAMBERT

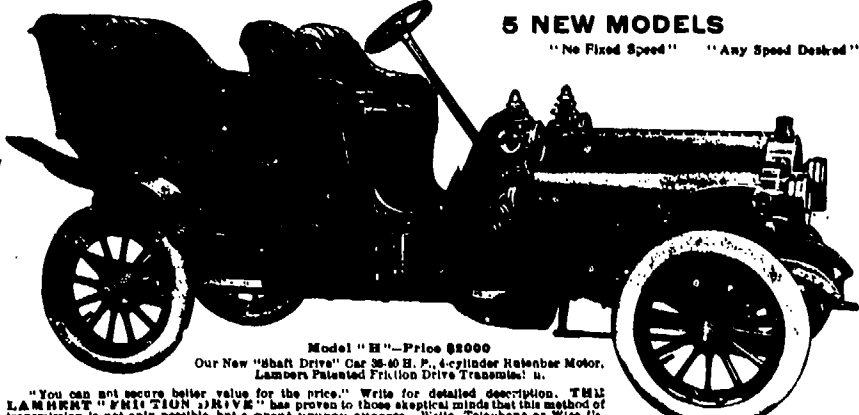
USERS

INVESTIGATE

THE FRICTION DRIVE CAR

5 NEW MODELS

"No Fixed Speed" "Any Speed Desired"



These Cars Are Mechanically Right. Lambert Cars Have Features Not Found on Other Cars

Lambert Cars Have Been A Proven Success for Years

Model "B" - Price \$3000
Our New "Shaft Drive" Car 25-40 H. P., 4-cylinder Retenbae Motor, Lambert Patented Friction Drive Transmission.

"You can not secure better value for the price." Write for detailed description. **THE LAMBERT "FRICTION DRIVE"** has proved to those skeptical minds that this method of transmission is not only possible, but a great proven success. Write, Telephone or Wire Us.

THE BUCKEYE MANUFACTURING CO., - ANDERSON, IND., U. S. A.

Good Dealer Agents Wanted in a Few Localities Members American Motor Car Manufacturers' Association, New York. Write for Special Art Catalogue

Figure 5. - An early advertisement for a friction-drive car (ref. 17).

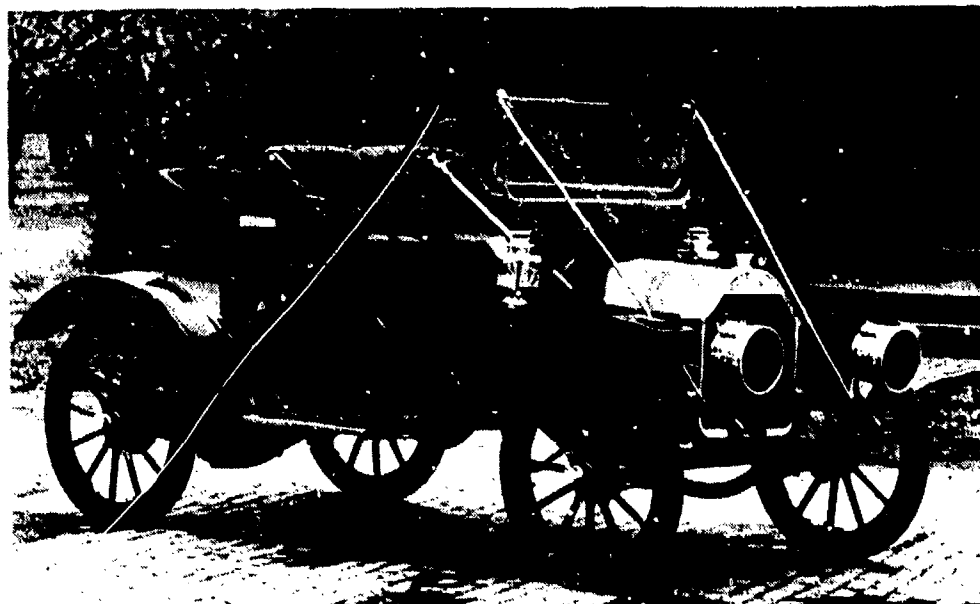


Figure 6. - 1909 Cartercar equipped with a friction, continuously variable transmission (CVT). (Courtesy of the Henry Ford Museum, Dearborn, Michigan.)

output follower wheel across the face of the metal disk—turntable fashion. Neutral was achieved when the follower wheel was centered. By moving the follower wheel past center, reverse rotation would occur to allow the vehicle to back up. The smoothness and ease of operation of the Cartercar transmission made it quite popular. It is not well-known that Mr. W. C. Durant, founder and first president of General Motors Company, acquired the Cartercar Company in 1908 because of his expectation that friction drives would soon be universally used in automobiles (refs. 16 and 18). In 1910 the Cartercar Company even produced a Model "T" truck, equipped with their friction drive. Despite its catchy slogan, "No clutch to slip—no gears to strip . . . a thousand silent speeds and only one control lever, that's a Cartercar," the Cartercar Company's commercial success was shortlived.

From 1909 until 1912, Sears marketed a two-cylinder, 14-horsepower "Motor Buggy," also equipped with a friction drive (ref. 19). "Absolute simplicity, its positiveness under the most severe conditions and its unequalled flexibility," boasted one of the Sear's ads. However, by about 1915, cars equipped with friction drives had virtually disappeared (ref. 19), presumably due, in part, to the need for frequent renewal of the friction material.

Despite the limited success of these earlier attempts, the goal of designing an automotive transmission that smoothly and automatically shifted was not lost. In the late 1920's the Buick Division of General Motors was given the task of developing a continuously variable, oil-lubricated, steel-on-steel traction drive. This transmission was similar in design to the Hayes double toroidal traction drive, patented in 1929. The Hayes Self-Selector Transmission (ref. 20), although originally developed here, was later offered as an option on the 1935 British Austin Sixteen (ref. 21).

The General Motors toroidal drive, later called the toric transmission, is illustrated in figure 7. The geometry of the drive is remarkably similar to the 1877 Hunt drive, with the addition of a second toroidal cavity and a ball differential to balance loading between the two cavities. An extensive test program was conducted on this drive. Seventeen road-test vehicles equipped with the toric drive accumulated over 300 000 miles of road testing (ref. 18). A 20-percent improvement in highway fuel mileage was reported. In 1932 General Motors decided to produce this type of transmission (ref. 16); however, no cars equipped with the toric drive were ever sold to the public. The reasons for halting production were never really made clear. Some say that there were unresolved discrepancies in service-life data obtained during road tests and that obtained from laboratory bench testers. Others believe that the availability of premium quality bearing steel, needed in large amounts to make each drive, was simply not great enough at the time to meet expected production requirements. Whatever the reasons, Alfred P. Sloan, Jr., then president of General Motors, turned the transmission down for production in the belief that it would simply be too expensive to make (ref. 16).

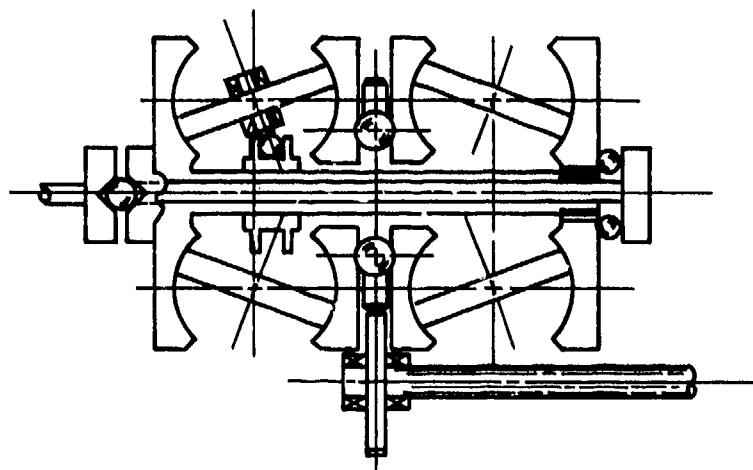


Figure 7. - General Motor's Toric transmission (ca. 1928).

Work on various types of automatic transmissions, beginning in the early 1920's finally led to the production of the 1937 Oldsmobile semiautomatic, self-shifting transmission. This transmission still required the use of a clutch pedal for stopping and starting. The hydramatic soon followed. It was the first mass-produced, fully automatic transmission—first appearing on the 1940 Oldsmobile (ref. 16). However, the old toric drive was not completely forgotten, it reappeared briefly in the 1960's on General Motor's experimental gas turbine RTX bus.

General Motor's New Departure Bearing Division produced an industrial counterpart to the toric drive. By 1935 when production was halted, over 1600 units of the "Transitorque" traction CVT had been marketed (ref. 20). The drive's design is credited to Richard T. Erban, an early traction-drive pioneer, who briefly worked for General Motors during this period (ref. 4).

In England, after several years of analyzing the Hayes Self-Selector drive, Perbury Engineering, Ltd., retrofitted a modified, scrapped Hayes transmission into Hillman Minx sedan in 1958 (ref. 21). Fuel savings were reported to be 20 to 25 percent but the concept really never caught on with any of the several dozen companies or so that had previously expressed interest in the drive (ref. 21).

In the United States in 1959, Charles Kraus installed a modified version of a toroidal CVT into an American Motors Nash Rambler (ref. 4). This unit had a semitoroidal roller geometry similar to that patented in 1932 by Jacob Arter for industrial service. The Arter drive is still commercially produced in Switzerland. In 1962 Mr. Kraus joined Curtis-Wright Corporation and headed up a program supported by the Army Tank-Automotive Center to retrofit this semitoroidal traction drive to an Army Jeep. A drive malfunction was encountered after approximately 17 000 miles of road testing (ref. 22). Design improvements were made on a second test drive but this unit also experienced operational problems that caused a halt to the program. In 1973 Tracor, Inc., demonstrated a Ford Pinto equipped with an improved version of the Kraus drive lubricated with Monsanto's new traction fluid. Although operational characteristics were established, expected fuel economy improvements were largely negated by the hydraulic losses in the thrust bearings used to clamp the toroids together (ref. 23). More recent toroidal drive designs partially overcame this problem by mounting two toroidal drive cavities back-to-back along a common shaft, thereby eliminating these troublesome thrust bearings.

Industrial Traction Drives

Starting with the 1877 Hunt drive, adjustable-speed traction drives have been in industrial service for more than 100 years. The bulk of these drives has been performing a speed matching function for light-duty equipment, such as drill presses. Typical uses are listed in table I.

A sample of representative traction-drive configurations appears in figure 8 (ref. 4). According to Carson (ref. 24), more than 100 United States patents on adjustable-speed traction drives are on file. Out of these, perhaps a dozen or so basic geometries are in production. Some of these drives are shown in figure 8. Of those commercially available, few are rated greater than 10-kW power capacity.

TABLE I. - TYPICAL APPLICATIONS FOR TRACTION DRIVES

Marine propulsion drives
Earthmoving equipment
Textile machinery
Farm equipment, agarmachinery
Rubber machinery
Propeller drives
Forest products and paper machinery
Crane drives
Construction equipment
Pump drives
Locomotive and railroad machinery
Machine tools
Outdoor tools and recreation vehicles
Oil field drives and offshore rigs
Household appliances
Auto transmissions
Air conditioning systems
Steel mill drives
Mining and ore processing machinery

The "ball and cone" geometry was commercially introduced in the 1940's by Jean Kopp in Switzerland. The Kopp Variator is said to be the most widely used traction drive, with more than 250 000 units sold around the world through 1975 (ref. 24). A more recent cone-roller variator developed by Kopp extends the variator's power rating to 75 kW in a 582-kg package.

The wheel and single-disk drive typify the Cartercar and Sears Motor Buggy transmission. Because heavy contact loads must be directly reacted by the support bearings, the torque capacity of this geometry is greatly restricted. The cone and ring with reducer drive, produced by Graham in 1935, is one of the earliest traction drives developed in the United States; Graham drives are available for ratio ranges to 10:1 and power levels to about 4 kW. The disk-to-disk drive, also known as the Beier disk drive, was one of the earliest (1949) industrial traction drives capable of handling high powers, with current power ratings to 164 kW. The drive components are imported from Japan, assembled, and marketed in the United States by Sumitomo Machinery Company. With the possible exception of the toroidal geometry, the commercial CVT's of figure 8 are generally too large and complex or have insufficient power capacity to be suitable for advanced automotive applications without substantial modifications. An early review of the basic types of adjustable-speed traction drives can be found in reference 25. Reference 26 gives descriptive information on 24 types of variable speed traction drives that were commercially available in 1963.

Early Drive Limitations

As we have seen, the earliest traction drives generally used leather, wood, rubber, or fiber covered friction wheels running against metal disks. As these soft friction materials aged, they lost flexibility and wore rapidly. The driving surfaces generally had to be renewed or replaced at frequent intervals, depending on the rate of usage. Despite this, friction drives found use in early steam tractors, factory machinery, wood-working tools, and in several vintage cars (ref. 20). These simple, smooth, low-cost speed changers are still in use today for light-duty applications ranging from hand tools, washing machines, and record players to amusement park rides and cement mixers. In these modern drives more durable rubber and reinforced plastic materials have been substituted for the leather and fiber wheels of yesteryear. However, the thermal capacity and wear characteristics of these softer materials still basically set the useful power capacity of this class of transmission. For applications needing a low-cost speed changer, adjustable-speed friction drives are good choices. Sizing criteria and typical design information for friction drives can be found in reference 27.

Oil-lubricated traction drives having hardened steel roller contacts appeared in the early 1920's. Caron (ref. 11) credits Erban in Austria with the development of the first metal-to-metal, oil-lubricated drive in 1922. The 1923, Arter drive is another example. The presence of hardened steel

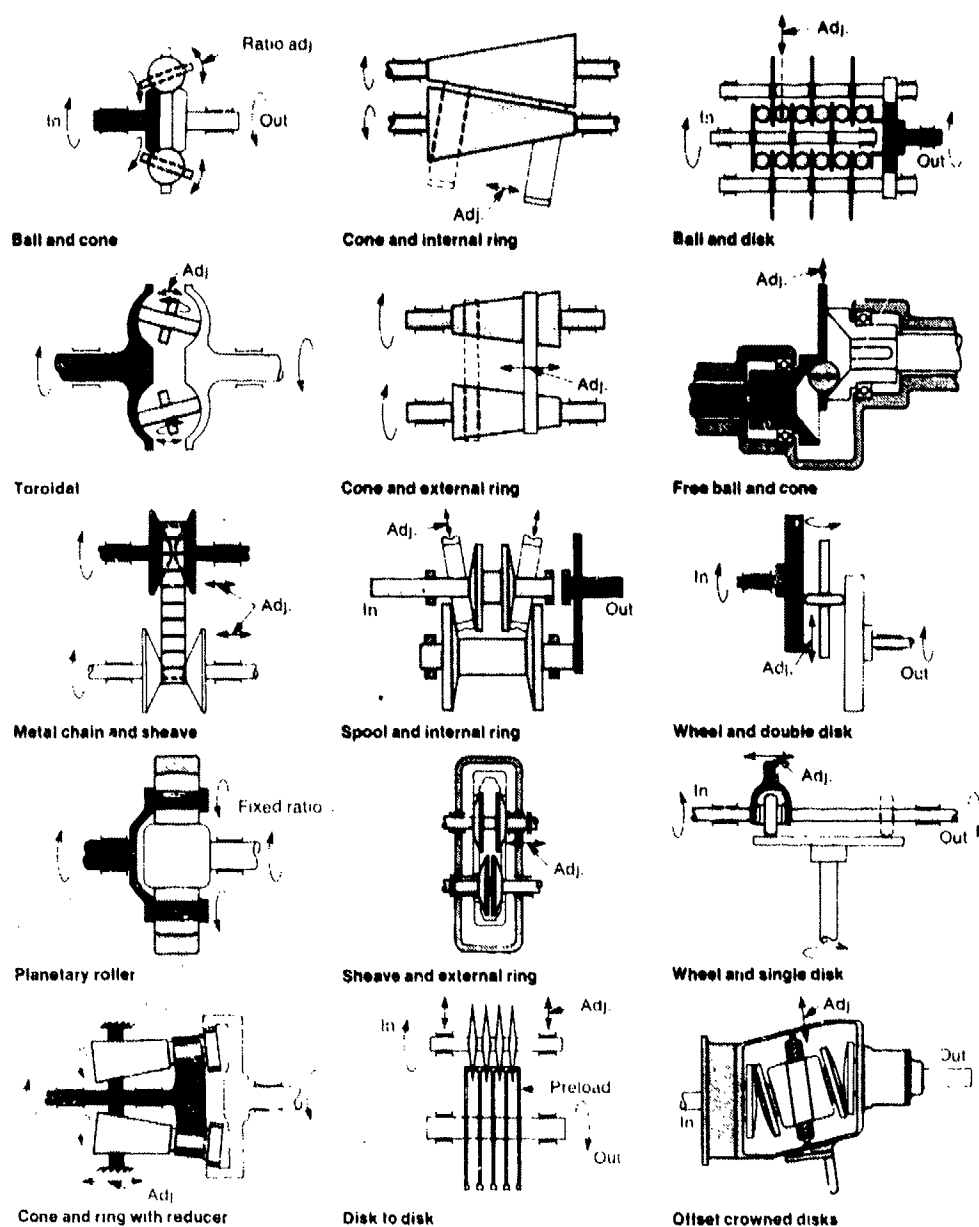


Figure 8 - Typical industrial traction-drive geometries. (Courtesy of Design Engineering (ref. 4).)

rollers in these drives significantly increased the allowable operating contact stresses. The purpose of the oil was to protect the contact surfaces from wear while providing cooling. However, the relatively low coefficient of traction of the oil meant that these drives had to carry unusually high contact loads to inhibit slip. High loading generally leads to early pitting, unless the torque rating of the drive was appropriately restricted. Even though the early traction drives tended to be bulky, their relatively high efficiency and smoothness of operation still made them attractive for many applications.

The very early friction drives were also vulnerable to slip damage in the event of an overtorque, since the normal load to prevent slip was set during assembly and did not change. To overcome this problem and to prevent the drive contact from being overloaded during periods of low power, Erban, while in Germany, patented in 1921 a mechanism to automatically regulate the contact normal load in proportion to the transmitted torque (ref. 20). Keeping the contact pressures low at light torques not only extended fatigue life but helped to reduce unnecessary power loss. Automatic loading mechanisms of this type have become regular features of almost all successful traction drives.

Advancements in Technology

Traction drive technology made relatively little progress for the first half of this century except for the occasional introduction of a new geometric variation. Designs were largely predicated on laboratory or field experience and very little of this information was reported in the open technical literature.

Because of the great similarity in the contact operating condition, traction-drive technology benefited greatly from the wave of technical advancements made for rolling-element bearings. Major advancements in bearing design occurred in the late 1940's with Grubin's work in elastohydrodynamic lubrication (ref. 28) and Lundberg-Palmgren's analysis of rolling-element fatigue life (ref. 29). In fact, the lubrication principles, operating conditions, and failure mechanisms of traction-drive contacts and bearing contacts are so similar that the design fundamentals are virtually interchangeable. The same may be said for gear contact design criteria as well.

In view of the durability shortcomings of earlier traction drives, much of the recent research has centered on improving the power capacity and reliability of these devices without sacrificing their inherent simplicity or high mechanical efficiency. Although work has been performed on many fronts, research efforts to date can be loosely categorized under one of several areas: (1) modeling the tractive behavior of the lubricant within the contact and its attendant power losses; (2) predicting the useful torque that can be passed between rollers without surface distress or that amount corresponding to a given fatigue life; (3) determining and improving the durability characteristics of traction-drive materials, primarily bearing-grade steels; (4) developing lubricants that produce higher traction forces in the contact without sacrificing conventional lubricant qualities; and (5) developing drive arrangements that maximize durability, torque capacity, and ratio capability and minimize size, weight, power loss, and complexity.

Traction Phenomena

A basic understanding of how power is transferred between traction-drive rollers is helpful in reviewing the contribution made in this area. Figure 9 shows a simple, lubricated, roller pair in traction contact. A sufficiently large normal load N is imposed on the rollers to transmit the tangential traction force T . The amount of normal load required to transmit a given traction force without destructive gross slip is dictated by the available traction coefficient, μ , which is the ratio of T to N . Since contact fatigue life is inversely related to the third power of normal load, it is extremely desirable to make use of lubricants that produce high values of μ . The search for lubricants having high traction capabilities will be discussed later.

The rollers, as illustrated in the enlarged view of the contact appearing in figure 9, are not in direct contact but are, in fact, separated by a highly compressed, extremely thin lubricant film. Because of the presence of high pressures in the contact, the lubrication process is accompanied by some elastic deformation of the contact surface. Accordingly, this process is referred to as elastohydrodynamic (EHD) lubrication. Ertel (ref. 30) and later Grubin (ref. 28) were among the first to identify this phenomenon, which also occurs for other oil-lubricated, rolling-element machine elements such as bearings and gears. The importance of the EHD film in traction contacts lies in its ability to reduce and/or eliminate wear while acting as the principal torque transferring medium. An excellent accounting of the role of EHD lubrication traction is given by Martin (ref. 31).

Traction Curve

The technological properties of the lubricant in the contact, particularly its traction characteristics, are fundamental to the design of traction drives. Figure 10 shows a typical traction-versus-slip curve for a traction fluid. This type of curve is typically generated with a twin-disk traction tester (refs. 32 to 35). Imposing a traction force across a lubricated disk contact which is rotating at an average surface velocity U gives rise to a differential surface velocity ΔU . Three distinct regions can generally be identified on a traction curve. In the linear region the traction coefficient increases linearly with slip. In the non-Newtonian regions it increases in a nonlinear fashion, reaches a maximum, and then begins to decrease. Finally, the curve shows a gradual decay with slip in the thermal region due to internal heating within the oil film. It is the linear region of the traction curve that is of the greatest interest to traction-drive designers. The design traction coefficient, which

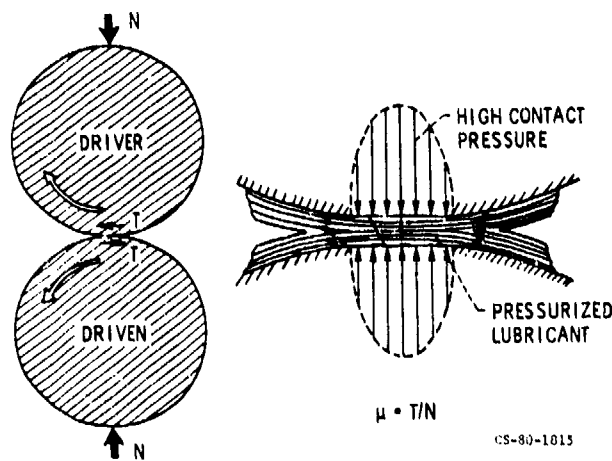


Figure 9. - Power transfer through traction.

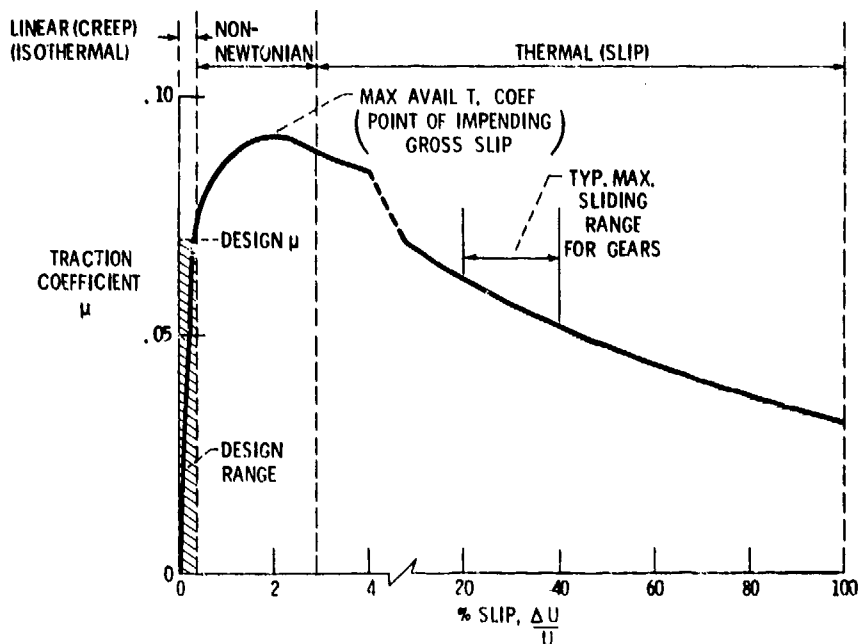


Figure 10. - Typical traction curve showing design range for traction drives.

dictates how much normal load is needed to transmit a given traction force, is always chosen to be less than (by, generally, 20 to 30 percent) the peak available traction coefficient to provide a safety margin against slip. Traction drives are generally equipped with a torque-sensitive loading mechanism that adjusts the normal contact load in proportion to the transmitted torque. Such mechanisms insure that the contact will always have sufficient load to prevent slip without needlessly overloading the contact under light loads.

Traction Coefficient

Perhaps the single most important factor affecting the torque capacity, life, and size of a traction drive is the maximum value of the available traction coefficient. It is this parameter that determines the necessary contact load. Since the fatigue life of a contact is inversely proportional to the cube of contact load, a 50-percent improvement in the traction coefficient would, for example, mean a 240-percent life increase for a given drive under a given set of operating conditions.

Solidification Behavior

In a typical traction-drive contact, severe transient operating conditions are imposed on the lubricant. The lubricant is swept into the contact, exposed to contact pressures, which are 10 000 times atmospheric or greater, and returned to ambient conditions, all in a few milliseconds. Clark, et al. (ref. 32), in 1951 were the first to experimentally observe that, under these high pressures and shear rates, the lubricant exhibits shearing properties of a plastic solid and will, in fact, yield at some critical shear stress. Although it had been known from static high-pressure viscometry experiments that an oil's viscosity would increase dramatically with increasing pressure and eventually solidify under high enough pressure, this was really the first time that this effect was observed to occur under the highly transient conditions of a traction contact. This solidification phenomenon was later also observed by experimentors Smith (ref. 33), Plint (ref. 34), and Johnson and Cameron (ref. 35), among others. Indeed, one can see a striking similarity in the shear-stress-shear-strain rate curves of a traction fluid and the tensile-stress-strain curves of a typical thermoplastic (fig. 11). It is also clear from figure 11 that temperature has a similar adverse effect on the limiting shear strength (maximum traction coefficient) of the traction fluid and the yield strength of the thermoplastic. Furthermore, both materials exhibit either viscous or elastic behavior depending on the rate of straining. Plastics will flow like a liquid if stretched slowly enough but will show elastic resiliency if pulled suddenly. An EHD film in the traction contact shows similar visco-elastic behavior.

Effects of Operating Conditions

Whether the lubricant exhibits viscous behavior or acts as an elastic solid depends on a number of factors. Contact pressure, temperature, shear rates, and lubricant composition all play important roles. Knowledge of the rheological characteristics of the lubricant as it passes through the contact is essential to predicting the performance of the contact, particularly in the absence of specific experimental data.

Visco-elastic lubricant behavior has been a subject pursued by a large number of investigators. Among them were Crook (ref. 36) and Dyson (ref. 37), who were among the first to call attention to such behavior, Johnson and Roberts (ref. 38), who experimentally demonstrated the transition from predominantly viscous to predominantly elastic response, and Trachman and Cheng (ref. 39), who used a compressional visco-elasticity model to numerically solve for the traction curve.

Based on the work of these investigators and on the comprehensive traction model advanced by Johnson and Tevaarwerk (ref. 40), one can assume that for most traction-drive contacts the maximum available traction coefficient is directly related to the shear yield strength of the solidified lubricant film.

From a large body of traction data generated on a twin-disk tester (refs. 41 to 44), it was found that an increase in contact pressure is beneficial to the available traction coefficient but that an increase in surface velocity, temperature, contact ellipticity ratio, misalignment, or spin (circumferential slip) has a negative effect. Figure 12 shows the typical effects that pressure and speed have on the traction coefficient of a traction fluid from test data generated in reference 45.

Creep

In the linear region of the traction curve, the transfer of torque will cause a small difference in velocity to be developed between the surfaces of the driver and driven rollers. This small velocity difference, generally less than 1 percent of the rolling velocity, is often referred to as creep rather than slip. This is because in creep only part of the contact is experiencing sliding while in slip there is total relative motion.

Creep is always present to some extent between rolling bodies that are transmitting torque, whether lubricated or not. Carter in 1926 was one of the first to identify the creep occurring between a locomotive's driving wheel and the rail (ref. 46). Typically, a region of microslip will occur between the surfaces in the trailing region of the contact while the surfaces in the leading region will be locked together without relative motion (ref. 47). As the tangential traction force is increased, the microslip region will encompass more and more of the contact until, at some point, the whole contact is in total slip. This is the point of impending gross slip. It occurs when the ratio of traction force to normal load is equal to the maximum available traction coefficient. When a mechanism to increase the

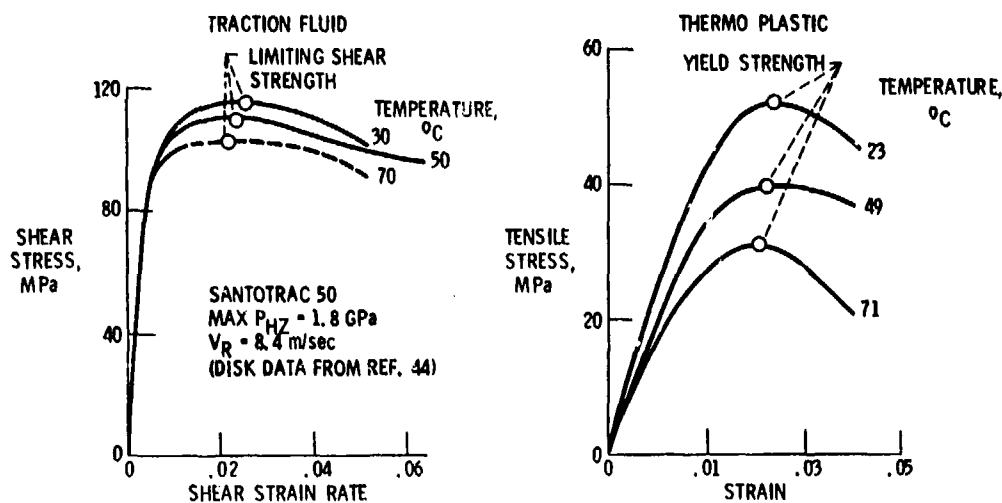


Figure 11. - Plastic behavior of a traction fluid.

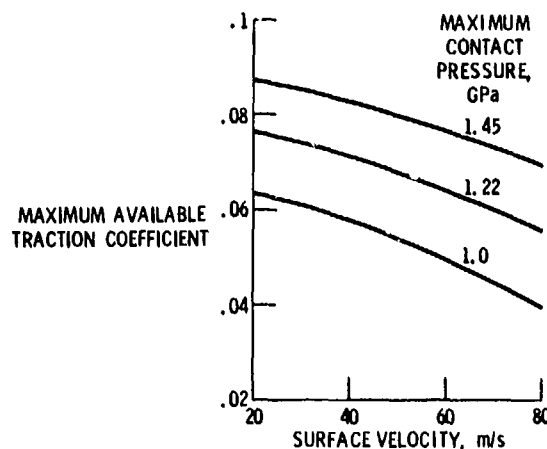


Figure 12. - Typical maximum available traction coefficient as function of surface velocity and maximum contact pressure. Synthetic hydrocarbon traction fluid; $a/b = 5$; zero spin; temperature, 343 K. Data obtained on a twin-disk machine (ref. 45).

normal load with increasing traction is present, the point of impending gross slip is not reached.

Creep is typically the result of the elastic stretching of the solidified lubricant film and that of the roller material. The lubricant film gets stiffer with increasing pressure and because it is so thin relatively little strain occurs. In fact, as pointed out by Tevaarwerk (ref. 48), for many traction drives that regularly operate at contact pressures above 1.2 GPa, most of the creep actually takes place in the steel rollers and not in the EHD film. Johnson, et al. (ref. 49), have developed relatively simple methods to determine how much of the elastic effects are due to the roller material and how much are due to the film.

The amount of creep in a lubricated traction-drive contact can vary from as little as 0.1 percent of the rolling velocity at high pressures and low speeds to 3 or 4 percent or more when the pressures are low, speeds are high, and sideslip (misalignment) or spin (circumferential contact slip) is appreciable. Although these creep values are quite small relative to gears, where sliding velocities can be 30 or 40 percent of the pitch-line velocity at the tooth engagement and disengagement points, it is nevertheless important to minimize the creep value through the proper selection of operating conditions, geometry, and lubricant. Every percentage point loss in creep represents a percentage point loss in speed and a corresponding percentage point loss in mechanical efficiency.

Traction Fluids

Because of the importance that the coefficient of traction has on the life, size, and performance of a traction drive, considerable attention has been given to identifying fluids with high traction properties, starting in the late 50's with Lane's experiments (ref. 50). Using a modified two-ball tester, Lane found an apparent inverse relationship between the traction coefficient and temperature-viscosity index for naphthenic and paraffinic mineral oils.

In a comprehensive investigation into traction phenomena, Hewko (ref. 42) obtained traction performance data for both compounded and uncompounded mineral oils as well as for a group of synthetic fluids. He also investigated the effect of oil additives on traction as well as the effects of operating conditions, roller geometry, and surface topography. His results indicated that the lubricant composition and surface topography had the greatest overall effects on traction and that naphthenic-based mineral oils gave better performance than paraffinic oils. He also observed that many common types of additives can markedly reduce traction (ref. 42).

The research of reference 51 describes the development of a formulated traction fluid, designated as Sunoco Traction Drive Fluid-86. This fluid was subsequently field tested in the General Motors turbine bus toric drive and in an automatic transmission for the Oldsmobile Toronado with reportedly good results.

Hammann, et al. (ref. 52), examined some 26 test fluids and, unlike Lane (ref. 50), could not find any obvious relationship between the coefficient of traction and the viscosity index. However, his tests did identify several synthetic fluids that had up to 50 percent higher coefficients of traction, depending on test conditions, than those reported for the best naphthenic base oils (ref. 52). This research laid the groundwork for the development of Monsanto's family of commercial traction fluids, Santotrac 30, 40, 50, and 70. These fluids are the most widely used traction oils today. The results of accelerated five-ball fatigue tests (ref. 53) indicated that these synthetic cycloaliphatic traction fluids have good fatigue-life performance, comparable with the reference tetraester oil used in this experiment.

In an unusually complete doctoral investigation into the nature of traction power transfer, Gaggermeier (ref. 44), in one part of his work, measured the coefficient of traction of 17 lubricants on a twin-disk traction tester at both high and low contact pressures and surface speeds. The traction fluids in his tests showed substantially higher coefficients of traction than all of the commercial naphthenic mineral oils tested. The greatest differences occur at relatively low pressures and high surface speeds (fig. 13). At relatively high pressures and low speeds the traction fluids show less of an advantage. Under such conditions a good quality naphthenic mineral oil would serve almost as well. However, for most traction-drive applications there is considerable incentive to using a traction fluid, with expected traction improvements falling somewhere between the two examples of figure 13.

What is noteworthy about the traction curves in figure 13 is the way they illustrate the common and important tendency of traction fluids to solidify into a plastic material at far lower pressures and high speeds than conventional oils (e.g., see the work of Blair and Winer, ref. 54). This is the basic reason why the traction coefficient for the two traction fluids is already at high levels in figure 13(a), while that for the mineral oils needs substantially higher pressure to attain high levels as indicated in figure 13(b). The tendency for early solidification has a lot to do with what makes a traction fluid a traction fluid.

Capacity and Durability

Failure Criteria

Traction drives, like rolling-element bearings are generally sized on the basis of rolling-element fatigue life. This is because, for most applications, other than those that are particularly short-lived, the stress levels required for acceptable fatigue life are generally well below those for static yield failure. Because of these relatively low maximum operating stress levels, traction drives can generally tolerate shock loads several times the maximum design value without plastic deformation or other ill effects. This is contrary to the misbelief that traction drives are particularly vulnerable to sudden overloads. Furthermore, if these transient overloads are brief and do not occur too frequently, only a relatively small penalty to the drive's total fatigue life will result.

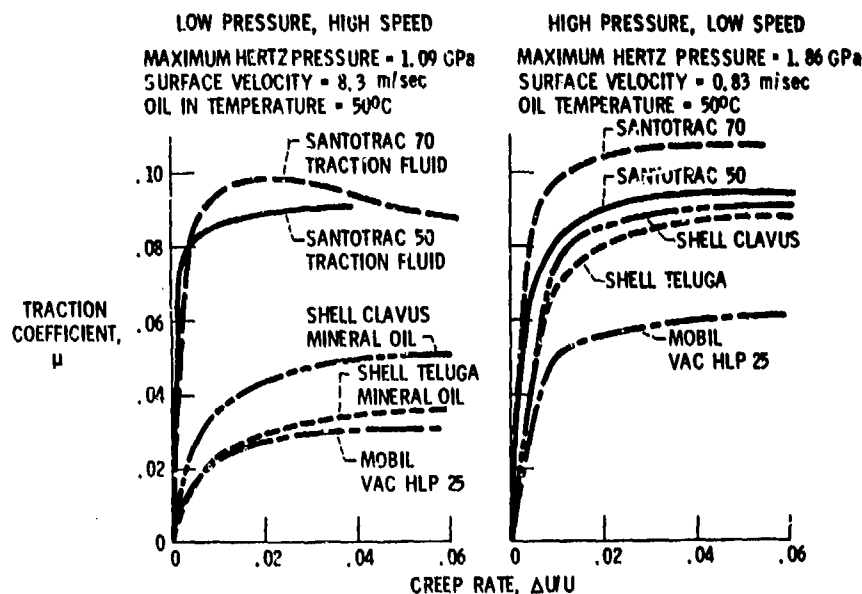


Figure 13. - Traction characteristics of a traction fluid compared with mineral oils (ref. 44).

A traction drive's sensitivity to shock loads is also dependent on the ability of the contact surface to avoid skidding or heating damage. If the drive is equipped with a fast-acting loading mechanism, skidding is unlikely. Also the transient nature of shock loads is such that there is usually insufficient time to overheat the contact, thus avoiding surface damage. However, sustained overloads can cause a thermal breakdown of the EHD film leading to failure.

Fatigue Life

The normally expected failure mode of a properly designed traction drive will be rolling-element fatigue. This failure criterion is exactly analogous to pitting failure in gears and spalling failure in rolling-element bearings. The risk of wear or scuffing failures of traction drive contacts can be eliminated or greatly minimized through the use of proper materials and also proper lubricating and cooling design practices such as those that have been successfully applied in bearing and gear design. In view of this similarity in the failure mechanism, rolling-element bearing fatigue-life theory can be used to determine the expected service life of a traction drive.

In 1947 Lundberg and Palmgren (ref. 29) published a statistical theory for the failure distribution of ball and roller bearings. They theorized that subsurface-originated fatigue pitting was due to high stresses developed at a subsurface defect in the bearing material. The probability of failure was related to the value of the maximum orthogonal reversing shear stress, the depth below the surface where this stress occurs and the volume of material that is being stressed. This is the theory on which bearing manufacturers, still today, base ball and roller bearing service-life ratings.

In 1971 an ASME life adjustment factors guide (ref. 55) was published to adjust the life ratings predicted by Lundberg and Palmgren analysis for recent advancements in bearing design, materials, processing, and manufacturing techniques.

In 1976 Coy, et al. (ref. 56), published a contact fatigue-life analysis for traction drives based on Lundberg-Palmgren theory. This analysis was used to predict the service life of a toroidal traction drive. In a 1980 publication, Rohn, et al. (ref. 57), presented a simplified version of this fatigue-life analysis and used it to show the effects of torque, size, speed, contact shape, traction coefficient, and number of multiple contacts on the predicted drive life. Their results show that multiple, load-sharing arrangements significantly benefit torque capacity and drive life, and that fatigue life is proportional to the 8.4 power of size for constant torque and traction coefficient.

The aforementioned Lundberg-Palmgren fatigue life analyses can be used with reasonable certainty to determine the durability characteristics of most traction drives. However, not presently considered in the analyses is a means to account for the potentially adverse effects of traction. Some

investigators (ref. 58) have found up to a several-fold decrease in rolling-element fatigue life when relative sliding and traction have been introduced; while others (ref. 59) have observed no change or even an improvement in fatigue life, depending on the direction of the applied traction force. A new analytical fatigue-life model, proposed by Tallian, et al. (ref. 60), considers the effects of surface traction on surface- and subsurface-originated spalling. This work is significant because it addresses surface spalling, the more likely fatigue failure mode of gear and traction drive contacts. However, in its present form, the model requires many metallurgical and surface microgeometry parameters, which are not readily available. Thus, the utility of the analysis is, at present, limited. Also, there are currently insufficient test data to properly substantiate this model or to develop universal fatigue-life adjustment factors for the possible negative effects of surface traction. An element of conservatism is in order when establishing service life ratings based on current prediction methods.

Materials

Earlier traction drives were not exploited to their full potential because of uncertainties regarding their longterm reliability. The limited durability characteristics of the materials used in these drives were a major contributing factor. The substitution of oil-lubricated, hardened steel roller components in place of rubber or reinforced plastic running dry against cast-iron parts raises their load capacity by at least an order of magnitude (ref. 27).

Because of the similarity in operating conditions, hardened bearing steels are logical choices for traction-drive rollers. Today's bearing steels are of significantly higher quality than the traditional air-melted, AISI 52100 steels used in rolling-element bearings since the 1920's. The introduction of vacuum remelting processes in the late 1950's has resulted in more homogeneous steels with fewer impurities and has extended rolling-element bearing life several-fold (ref. 61). Life improvements of eight times or more are not uncommon according to reference 55. This reference recommends that a life-improvement factor of six be applied to Lundberg-Palmgren bearing life calculations when using modern vacuum-melted AISI 52100 steel. A similar life-improvement factor is applicable to traction-drive life calculations. This improvement in steel quality in combination with improvements in lubricant traction performance has increased the torque capacity of traction drives several-fold.

Performance Predictions

Contact Traction

The distribution of local traction forces in the contact of an actual traction drive can be rather complicated as illustrated in figure 14. This figure shows the distribution of local traction vectors in the contact when longitudinal traction, misalignment, and spin are present. These traction forces will align themselves with the local slip velocities. In traction-drive contacts some combination of traction, misalignment, and spin is always present. To determine the performance of a traction-drive contact, the elemental traction forces must be integrated over the contact area.

Because of the parabolic pressure distribution, the elemental traction forces are largest near the center of the contact and diminish in magnitude near the contact perimeter. As expected, in the case of longitudinal traction (fig. 14(a)), the forces align themselves in the rolling direction. With the addition of misalignment (fig. 14(b)), a sideslip velocity is introduced causing the vectors to cock in line with the sideslip angle. Using conical rollers generally results in a circumferential slip pattern referred to as spin (fig. 14(c)). This rotary motion is due to the fact that the contact is in pure rolling only at its center. At the right hand edge of the contact the upper roller is sliding over the lower roller because of the mismatch in contact radii. At the left-hand edge the situation is reversed and so is the direction of slip. Because of solid-body rotation, a complete pattern of spin exists over all of the contact.

The power throughout the contact is determined from a summation of the traction force components aligned in the rolling direction times their respective rolling velocities. It is clear that in misalignment only a portion of the traction force is generating useful traction and that the remainder is generating useless side force. For pure spin no useful traction is developed, since the elemental traction forces cancel one another. Since the contact power loss is proportional to the product of the elemental traction forces and slip velocities, the presence of spin and misalignment can significantly

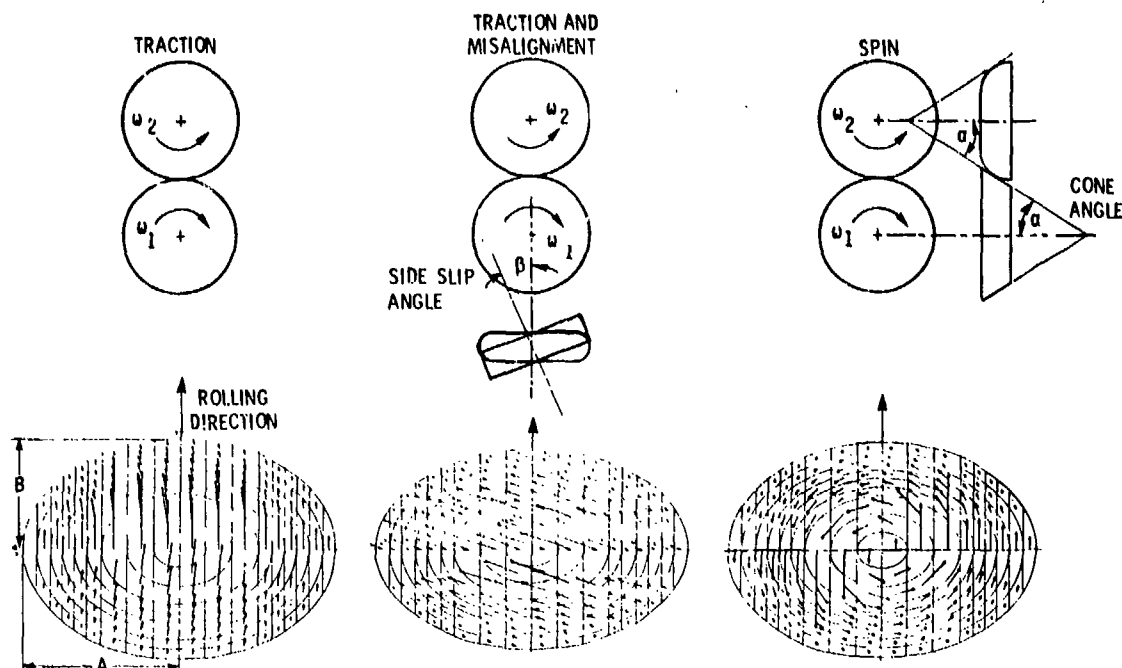


Figure 14. - Effect of misalignment and spin on contact traction force vectors.

decrease the efficiency of the contact. Furthermore, both conditions lower the available traction coefficient and reduce the amount of torque that can be transmitted safely. Designs that minimize spin and side slip can be quite efficient. Contact efficiency of 99 percent or higher is possible.

Traction Experiments

Although there have been previous attempts to analyze the losses associated with ball bearings (ref. 62), the first systematic attempt to research the losses of traction-drive contacts occurred at the "Institut Fur Maschinenelemente und Forder Technik" located at the Technical University of Braunschweig in Germany between 1955 and 1960 (refs. 63 to 67). These investigations, which are summarized in an excellent manner by Wernitz (ref. 68), include analysis and test work on both simple traction contact test machines and on a commercially available Kopp ball variator. Tables and plots were developed which permit the calculation of friction losses due to creep (microslip) and spin (circumferential slip). This analysis treats the EHD film in the contact as behaving as perfectly plastic, that is, the material yields at some critical shear stress, exhibiting no elastic behavior. This model gives satisfactory results for contacts experiencing relatively high local strain rates such as those drives that have moderately high spin. In reference 69 Magi takes a similar, but more general approach and gives examples with experimental justification.

In the United States some of the earliest investigations into traction contact phenomena as they relate to traction drives were conducted by Hewko (refs. 42, 43, and 70). As mentioned earlier, Hewko (ref. 42) obtained basic traction performance data for various roller geometries, operating conditions and lubricants. He later extended much of these data to roller contacts that operate at very high surface speeds (up to 127 m/sec) (ref. 23). Much of this test information served as a data base for the construction of several fixed-ratio, simple planetary traction drives, of the type used in English life boats back in the 1930's (ref. 71). One of these units, a 6.25 to 1 speed reducer attached to a 4.5-kW electric motor, was used as the main drive for General Motors oceanographic submarine. A second, 6 to 1 reduction ratio drive delivering 373 kW at 8000 rpm was built for a turbine-powered torpedo system. In reference 70 Hewko compared the efficiency and noise characteristics of a 75-kW, 3.5 to 1 ratio, planetary traction drive with that of a class 8, planetary gear drive of similar size, ratio, and power capacity. His test results showed that the traction drive had not only better part-load efficiency but provided substantial noise reductions as well. An overall sound pressure level of just 70 dB, about conversation noise level, was recorded for the traction drive at a particular operating condition. By contrast, at this same condition the gear drive registered 94 dB, or 16 times the noise of

the traction drive. The set of noise signature traces from this experiment with the integrated overall sound pressure levels appears in figure 15 (ref. 70). The quiet running characteristics of traction drives are undoubtedly appreciated by those who design drive systems for passenger carrying vehicles or for factory equipment under current OSHA noise standards.

Theory

In the 1960's numerous papers were presented on the prediction of traction in EHD contacts. Some of these included Cheng and Sternlicht (ref. 72), Bell, Kannel, and Allen (ref. 73), and Dowson and Whitaker (ref. 74). In the early 1970's simplifications and refinements in the traction models took place as exemplified by Dyson (ref. 37), Kannel and Walowit (ref. 75), and Trachman and Cheng (ref. 39).

About this time, Poon (ref. 76) and Lingard (ref. 77) developed grid methods to predict the available traction forces of a contact experiencing spin. Poon's method utilized the basic traction data from a twin-disk machine together with contact kinematics to predict the available traction. Lingard used a theoretical approach in which the EHD film exhibited a Newtonian viscous behavior at low shear rates until a critical limiting shear stress was reached. At this point the film yielded plastically with increasing shear rate. This model showed good correlation with experimental traction data from a toroidal, variable-ratio drive of the Perbury type. This same model was also used successfully by Gaggermeier (ref. 44) in a comprehensive investigation of the losses and characteristics of traction-drive contacts. In addition to copious amounts of twin-disk traction data for numerous lubricants under various combinations of slip, sideslip, and spin, Gaggermeier (ref. 44) also investigated the sources of power losses of an Arter type toroidal drive. His findings were that, of the total power losses, the load-dependent bearing and drive idling (no-load) losses were always greater than the losses due to traction power transfer. This underscores the need to pay close attention to these tare losses in order to end up with a highly efficient traction drive.

The most recent and perhaps most comprehensive traction contact model is that proposed by Johnson and Tevaarwerk (ref. 40). Their model covers the full range of viscous, elastic, and plastic behavior of the EHD film. The type of behavior depends on the Deborah number, a relative measure of elastic to inelastic response of the lubricant film, and the strain rate. At low pressures and speeds (low Deborah number), the film exhibits linear viscous behavior at low strain rates, becoming increasingly more nonlinear with increasing strain rate. At higher pressures and speeds, more typical of traction-drive contacts, the response is linear and elastic at low rates of strain. At sufficiently high strain rates, the shear stress reaches some limiting value and the film shears plastically as in the case of some of the earlier traction analytical models.

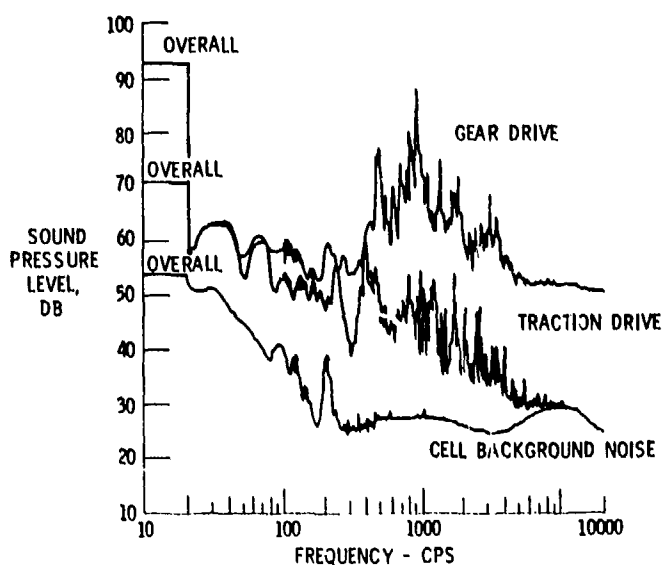


Figure 15. - External noise spectra for traction drive compared with planetary gear reducer at 2000 rpm input speed and 136 N-m input torque (ref. 70).

In reference 48 Tevaarwerk presents graphical solutions developed from the Johnson and Tevaarwerk elastic-plastic traction model. These solutions are of practical value in the design and optimization of traction-drive contacts. By knowing the initial slope (shear modulus) and the maximum traction coefficient (limiting shear stress) from a zero-spin/zero-sideslip traction curve, the traction, creep, spin torque, and contact power loss can be found over a wide range of spin values and contact geometries.

Figure 16 shows that this analysis compares favorably with test data, taken from experiments of Gaggermeier (ref. 44). The observed, pronounced reduction in the available traction coefficient with just a few degrees of misalignment, underscores the need to maintain accurate alignment of roller components in traction drives.

The Johnson and Tevaarwerk model, like many of the previous theories, provides an isothermal solution to the ascending portion of the traction curve. Under most circumstances the results from this isothermal analysis are quite satisfactory from a design standpoint. However, at higher surface speeds and for substantial spin, thermal effects start to become important. In reference 78 Daniels introduces a temperature-dependent elastic shear modulus term into the model, but this seems to have a rather weak effect on the results. Using an elaborate heat balance computer analysis, Tevaarwerk (ref. 79) in 1979 was able to correctly predict the heating effects occurring in a traction contact; but his solution is a bit too formidable for general design purposes. In reference 80 Tevaarwerk presents a simple, empirical technique to predict the thermally influenced, large-spin, traction curve from the large slip portion of a no-spin traction curve, but this requires knowledge of the full curve, which is not always available. Simpler analytical techniques are now being investigated (refs. 81 and 82) to better predict how heat generation within the contact affects the available traction coefficient.

Fluid Traction Data

To be able to apply the aforementioned traction drive, certain fundamental fluid properties, namely, the lubricant's shear modulus and limiting yield shear stress, must first be known under the required operating speeds, pressures, and temperatures. Because of the difficulty of simulating the highly transient nature of an actual traction contact, the most reliable basic fluid property data are deduced, using methods described in reference 44, from the initial slope and maximum traction coefficient of an experimental traction curve. Unfortunately, there has been a general scarcity of these types of data over sufficiently broad enough operating conditions for design purposes. Recently, experimental traction data were obtained under a NASA program for both the Monsanto and Sun Oil traction fluids over a range of speeds, pressures, temperatures, spin, and sideslip values that might be encountered in traction drives (ref. 45). A regression analysis applied to the data resulted in a correlation equation that can be used to predict the initial slope and maximum traction coefficient at any intermediate operating condition (ref. 45).

Recent Developments

During the past 5 years, several traction drives, which incorporate much of the latest technology, have reached the prototype stage. Laboratory tests and design analysis of these drives show them to have relatively high-power densities and, in some cases, to be ready for commercialization.

Nasvytrac Drive

Although light-duty variable-ratio traction drives have been reasonably successful from a commercial standpoint, very few, if any, fixed-ratio types have progressed past the prototype stage. This is somewhat surprising in view of the outstanding ability of traction drives to provide smooth, quiet power transfer at extremely high or low speeds with good efficiency. They seem particularly well suited for high-speed machine tools, pump drives, and other turbomachinery. In other industrial applications they offer potential cost advantages because traction rollers should not be much more expensive to manufacture in quantity than ordinary rollers in roller bearings.

In terms of earlier work on fixed-ratio traction drives, the developmental effort at General Motors Research Laboratories on their planetary traction drive (as described by Hewko (ref. 70)),

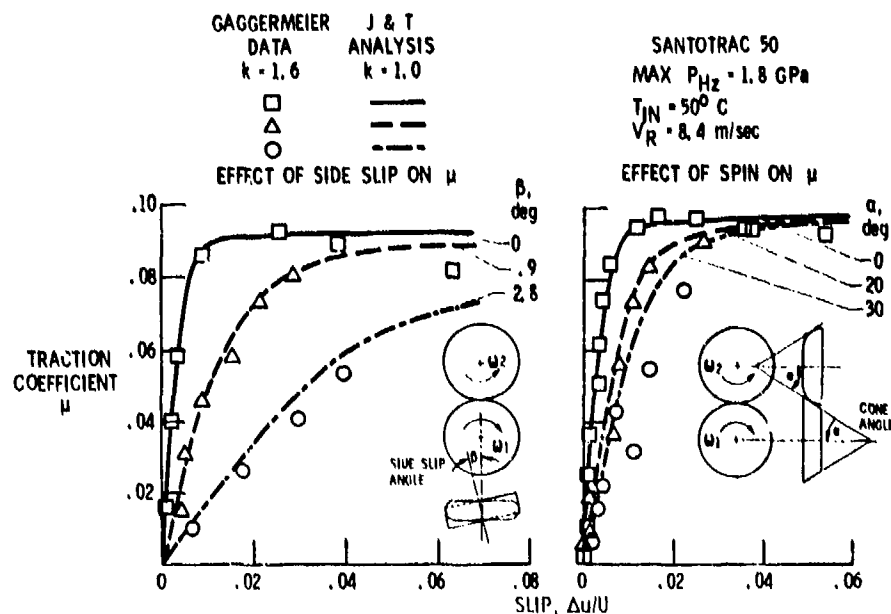


Figure 16. - Comparison of Johnson and Tavaarwerk analysis (ref. 48) with Gaggermeier test data (ref. 44).

was perhaps the most complete. As mentioned earlier, several of these drives were built and tested, including a 6-to-1 ratio, 373-kW unit for a torpedo and a 3.5-to-1 ratio, 75-kW test drive. This last drive exhibited better efficiency and lower noise than a comparable planetary gear set.

Interest in fixed-ratio traction drives is also high outside of the United States. Tests were recently conducted in Japan on a planetary traction drive of a construction similar to the General Motors unit for use with a gas-turbine auxiliary propulsion unit (APU) system (ref. 83). Planetary traction drives have also been studied in Finland.

The traction drives described thus far have a simple, single-row planet-roller format. For drives like these the number of load sharing planets is inversely related to the speed ratio. For example, a four-planet drive would have a maximum speed ratio of 6.8 before the planets interfered. A five-planet drive would be limited to a ratio of 4.8 and so on.

A remedy to the speed ratio and planet number limitations of simple, single-row planetary systems was devised by Nasvytis (ref. 84). His drive system used the sun and ring-roller of the simple planetary traction drive, but replaced the single row of equal diameter planet-rollers with two or more rows of "stepped" or dual-diameter planets. With this new "multiroller" arrangement, practical speed ratios of 250 to 1 could be obtained in a single stage with three planet rows. Furthermore, the number of planets carrying the load in parallel could be greatly increased for a given ratio. This resulted in a significant reduction in individual roller contact loading with a corresponding improvement in torque capacity and fatigue life.

In reference 84 Nasvytis reports the test results for several versions of his multiroller drive. The first drive tested was a 373-kW (500-hp) torpedo drive of three planet row construction with a reduction ratio of 48.2 and an input speed of 53 000 rpm. The outside diameter of the drive itself was 43 cm (17 in.), and it weighed just 930 N (210 lb) including its lightweight magnesium housing. It demonstrated a mechanical efficiency above 95 percent. To investigate ultrahigh-speed operation, Nasvytis tested a 3.7-kW (5-hp), three-row, 120-to-1 ratio speed increaser. The drive was preloaded and operated without torque at 480 000 rpm for 15 min and ran for 43 consecutive hr at 360 000 rpm without lubrication but with air cooling. Two back-to-back drives were operated for 180 hr at speeds varying from 1000 to 120 000 rpm and back to 1000 rpm. They transmitted between 1.5 and 2.2 kW (2 and 3 hp). Another 3.7-kW (5-hp), three-row speed increaser, with a speed ratio of 50, was tested for more than 5 hr at the full rated speed of 150 000 rpm with oil-mist lubrication and air cooling. It successfully transmitted 3.7 kW (5 hp) at 86 percent efficiency (ref. 84).

The basic geometry of the Nasvytis traction (Nasvytrac) drive is shown in figure 17. Two rows of stepped planet-rollers are contained between the concentric, high-speed sun roller and low-speed ring rollers. In the drive shown the planet rollers do not orbit but are grounded to the case through relatively low-speed and lightly loaded reaction bearings that are contained in the outer planet row only. The high-speed sun-roller and other planet bearings have been eliminated. The sun-roller and first row rollers float freely in three-point contact with adjacent rollers for location. Because of this floating roller construction, an excellent force balance situation exists even with thermal or mechanical housing distortion or with slight misalignments in roller dimensions.

Based on the inherent qualities of the Nasvytrac drive, a NASA program was initiated (refs. 85 and 86) to parametrically test two versions of the drive. These drives of nominally 14-to-1 ratio were tested at speeds to 73 000 rpm and power levels to 180 kW. Parametric tests were also conducted with the Nasvytis drive retrofitted to an automotive gas-turbine engine. The drives exhibited good performance, with a nominal peak efficiency of 94 to 96 percent and a maximum speed loss due to creep of approximately 3.5 percent. The drive package size of approximately 25 cm diameter by 11 cm wide (excluding shafting) and total weight of about 26 kg (58 lb) makes the Nasvytrac drive, with a rated mean life of about 12 000 hr at 75 kW and 75 000 rpm, size competitive with the best commercial gear drive systems.

A 70 000 rpm, 10.8-to-1-reduction-ratio Nasvytrac drive weighing just 4 kg was designed and built for a long-life, rocket-engine pump drive system to drive the low-speed liquid-oxygen and liquid-hydrogen boost pumps (ref. 87). Either an auxiliary turbine or a gear drive off the main pump can be used. Use of an auxiliary turbine complicates the design, while gear drives were not well suited for this application because they wore badly in a matter of 20 min or so in this hostile cryogenic environment. This fell far short of the 10-hr life requirement envisioned for future, reusable rocket engines. The relatively low sliding characteristics of the Nasvytrac drive, coupled with its demonstrated ability to run for long periods of time unlubricated, make it an excellent candidate for this application. Preliminary tests on this drive in liquid oxygen, including tests in which the drive was repeatedly accelerated under full power (15 kW) to 70 000 rpm in 5-sec intervals, showed it to perform satisfactorily (ref. 87). Cumulative operating times up to an hour have been recorded. Future work is needed to realize the 10-hr life goal, but the potential of this transmission for this application has been clearly demonstrated.

Current work with variations of the Nasvytis traction-drive concept are underway at NASA. A recently fabricated, 370-kW (500-hp) helicopter main rotor transmission combines the best features of gears with traction rollers. This experimental hybrid transmission, which offers potential cost, noise, and reliability benefits, will be tested shortly. Test of a 2240-kW (3000-hp) hybrid, twin-engine helicopter transmission is also planned. This 81-to-1-reduction-ratio, traction transmission will be the most powerful ever tested, carrying an output torque in excess of 73 000 N·m (650 000 in·lb) in an estimated 515-kg package. Hybrid and pure-traction Nasvytis drives are also being considered for wind-turbine applications where a low-cost but highly reliable speed increaser is needed to drive the high-speed alternator. Also, tests are being conducted on an infinitely variable-ratio Nasvytis drive, but the performance data are still too preliminary to be reported here.

Promising Variable Speed Drives

Taking advantage of the latest technology, several designers have attempted to develop traction CVT's for automotive use. The potential of improving the city fuel mileage 20 to 25 percent, or more, of cars normally equipped with three- or four-speed automatic transmissions (ref. 88) or of doubling the fuel mileage in the case of flywheel equipped cars (ref. 89) has been the major incentive for the resurgence in automotive CVT research and development. These applications represent a significant challenge, since compactness, efficiency, cost, and reliability are all at a premium.

Perbury CVT. — One such automotive effort is that being conducted by BL Technology, Ltd., formerly British Leyland, on a Perbury, double-cavity toroidal drive. This concept is rather old (first patented in the U.S. by C. W. Hunt in 1877). It is also rather well-explored, as mentioned earlier, having been investigated by the General Motors Research Laboratory in the early 1930's and late 1950's, demonstrated in a 1934 Austin-Hayes, later in a 1957 Hillman-Minx, and also in a 1973 Ford Pinto, but with offset rollers.

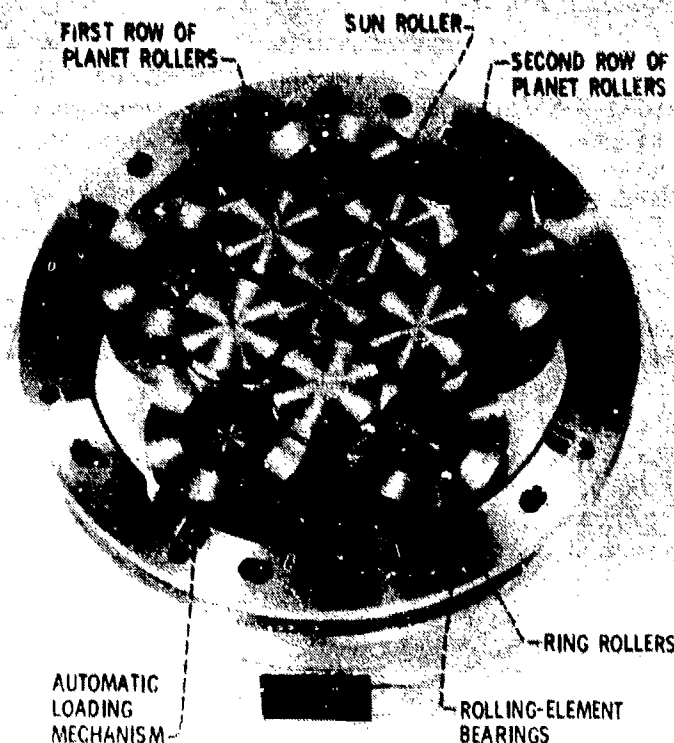


Figure 17. - Geometry of the Nasvytis traction (Nasvytrac) test drive (ref. 85).

In 1977 Lucas Aerospace in England adapted the Perbury drive for maintaining constant frequency of the AC generators on the Sidley Hawker Harrier, a VSTOL jet fighter. This single cavity, toroidal drive is suitable for driving aircraft generators having output ratings up to 30 kV A. More than 20 years before this, Avco Lycoming, in the U.S., also offered a line of mechanical constant-speed drives based on the toroidal traction-drive principle. They were used on several aircraft in the 50's, including the Douglas A-4E fighter, but have long since been discontinued.

In the case of the Leyland-Perbury automotive CVT (fig. 18; ref. 90), the double-toroidal drive cavities have six tiltable transfer rollers between input and output toroids. A hydraulically controlled linkage system can tilt these rollers from one extreme position to another. By combining this toroidal drive with a two-range, output planetary gear system, the overall transmission ratio range is greatly expanded.

The BL/Perbury transmission was installed in a medium size test car having a four-cylinder, 60-kW engine. The test car showed fuel mileage improvement of 15 to 20 percent for an average mix of European driving (ref. 90). Also, acceleration times were comparable with a manual transmission car having 10 percent higher power to weight ratio and driven by a skilled driver. However, the future production picture for this transmission is not clear.

Vadotec CVT. - A promising traction CVT that is of a rather new vintage is the nutating drive being developed by Vadotec Corp. As shown in figure 19 (refs. 91 and 92) a double-conical-roller assembly, complete with an automatic loading mechanism, is mounted at an angle in a drive cylinder that is driven by the input shaft. As the input shaft rotates, the double-cones perform a nutating motion and at the same time are forced to rotate about their own axis as they make drive contact with a pair of moveable control rings. These rings are grounded to the housing but can be axially moved together or apart. A gear pinion attached to the end of the cone shaft orbits the output shaft axis at input shaft speed, while spinning about its own axis, due to cone rotation, in the opposite direction. By varying the axial position of the control rings, the rolling radius of the cones can be synchronously changed. This, in turn, causes a change in rotational speed of the cone shaft pinion but does not affect the pinion's rotating speed, which occurs at input shaft frequency.

Since the cone shaft pinion is in driving engagement with the output shaft through one of several possible interchangeable gear arrangements, the variation in pinion rotational speed causes a

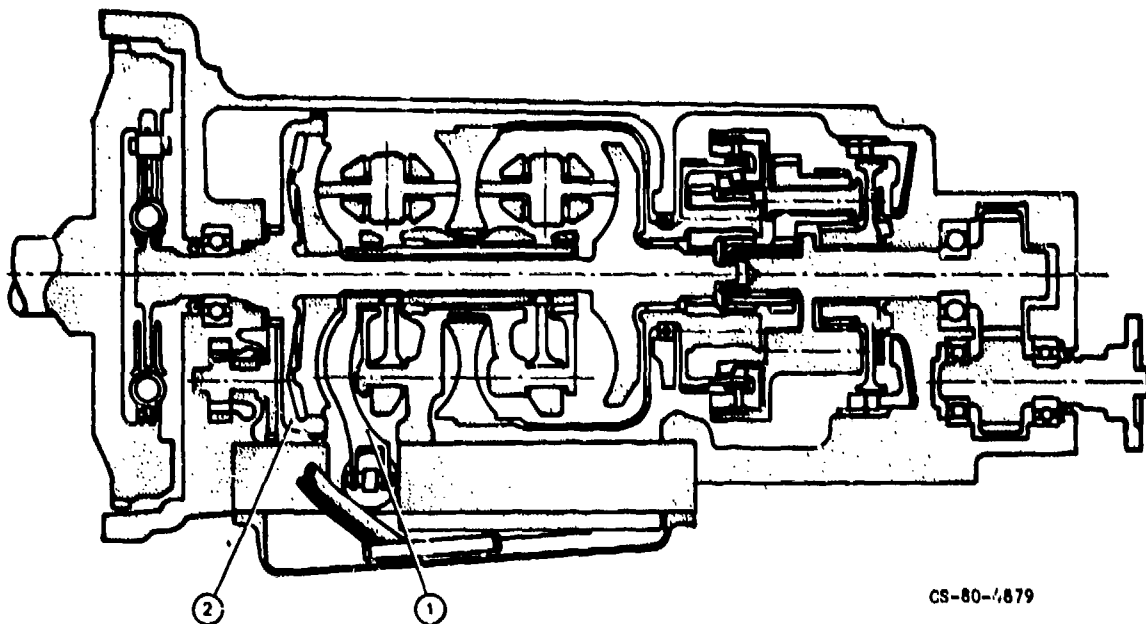


Figure 18. - BL Technology/Perbury traction CVT, 60-kW passenger car test installation (ref. 90).

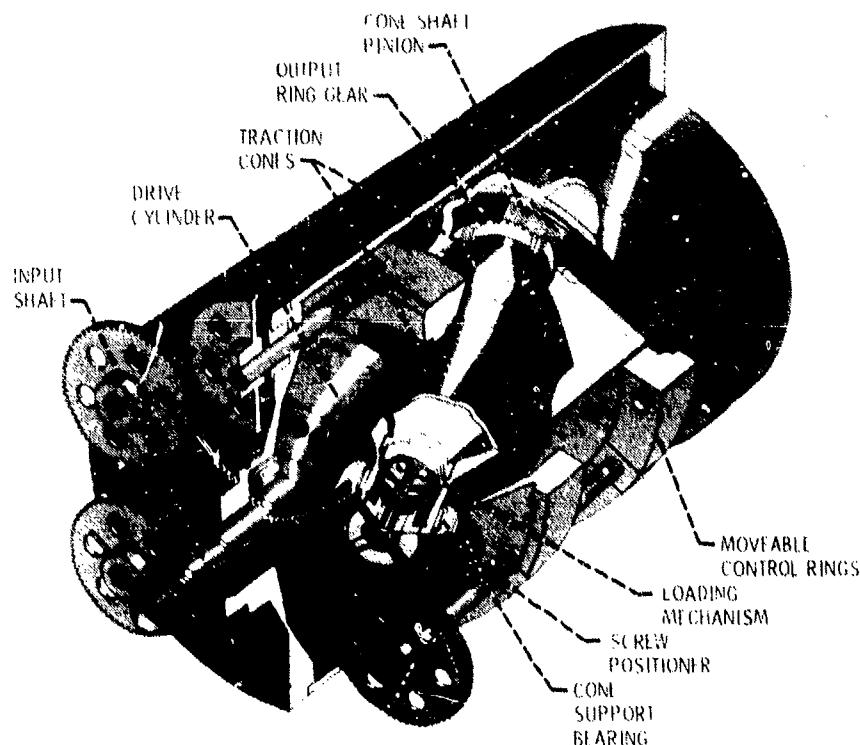


Figure 19. - Vadetec nutating traction CVT. (Courtesy of Vadetec Corp., Troy, Michigan.)

corresponding variation in output shaft speed. By changing the output gearing, the pinion speed can either vectorially subtract from pinion/input shaft orbital speed, allowing the output shaft speed to reach zero, if desired, or vectorially add to input orbital speed. The latter arrangement results in a transmission with only overdrive capability.

A couple of Vadetec CVT's have already been built and tested. One of these prototypes has shown successful operation as part of a tractor drive train. Although this transmission is still in the development and acceptance stage, it is a good example of the new breed of traction drive.

Fafnir CVT. - A planetary, cone roller type CVT under development by the Fafnir Bearing Division of Textron appears in figure 20 (ref. 93). This transmission is directed toward the mobile equipment market, particularly as a replacement to hydrostatic transmission in garden and light-duty tractors up to about 37 kW (50 hp). A set of double-sided, conical traction rollers is trapped between a pair of inner races and a pair of outer races. The conical rollers are mounted in a carrier that drives the planet gears in the output gear differential. The gear differential serves the purpose of expanding the limited ratio range of the traction drive to cover output speeds from forward to reverse, if desired. This is an example of power-recirculating transmission. The traction inner races are splined to the sun gear shaft of the planetary which is, in turn, keyed to the input shaft. To change the ratio, the outer traction race halves, which are grounded to the housing, can be either manually or hydraulically, in a later version, pushed together or spread apart. This causes the cone rollers' rolling radii at the outer-race contact to increase or decrease while simultaneously causing the opposite to occur at the inner-race contact. The change in rolling radii causes a corresponding change in the orbital speed of the cones and, thus, output-shaft speed. Because the inner-race load-springs, the transmission automatically "down shifts" with increased load. The current design was specifically intended to be one of low cost with maximum flexibility, so a single range output planetary was selected. Consequently, a high degree of power recirculation exists, limiting efficiency to about 85 percent maximum for the current design (ref. 6). A more efficient version would be needed for automotive applications.

Other traction CVT's. - The traction developments previously cited are by no means the only efforts underway. Many of the industrial manufacturers are no doubt upgrading the ratings of their systems by taking advantage of the latest technology. Furthermore, variations of older concepts are being re-evaluated and upgraded with design improvements. Two notable examples are the AiResearch toroidal drive and the Bales-McCoin cone-roller CVT. Both of these systems were carried to the preliminary design stage under a NASA contract for DOE to develop CVT's for use in advanced electric vehicles.

The AiResearch design (ref. 94) is a double-cavity toroidal CVT, containing two power rollers per cavity. The double toroidal drive elements, similar in many respects to the toroidal drive units mentioned earlier, are permanently connected to differential gearing.

The Bales-McCoin unit (ref. 95) consists of a central input traction roller surrounded by four cone-rollers which in turn are connected to the output planetary differential via idler gears. The cones are hydraulically loaded against the central roller using a novel microprocessor control system. Based on current slip rate signals, the control system adjusts the normal load between rollers to the minimum required to prevent significant roller slip at any given operating condition.

Both of the above CVT's are in early stages of development. Estimated weights and sizes of these transmissions are comparable with equivalent conventional automatic transmissions, and calculated efficiencies are generally in the low 90's. General information on these CVT's can be found in reference 96.

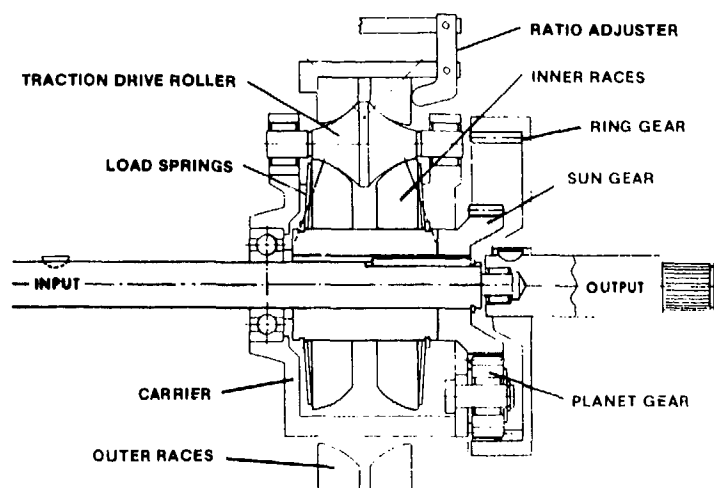


Figure 20. - Fafnir Bearing Division's planetary cone roller traction drive (ref. 93).

Future Technology Requirements

Although there has been significant progress within the last decade in the development of technology for traction drives, future refinements in certain areas are still needed.

Traction Fluids

Today's traction fluids are far superior to the earlier lubricants used in traction drives. However, modern traction fluids generally have poor viscosity index characteristics. At temperatures well below freezing, traction fluids can be too viscous to pour properly. Pour-point suppressants such as those incorporated in conventional oils for Arctic service might help.

Traction fluids and the additives that they contain have a tendency to capture and retain air at temperatures below about 70° C. Aeration of the oil is undesirable from both a cooling and hydraulic control system standpoint. This problem is minimized when the oil is subjected to some nominal pressure which tends to significantly condense trapped air bubbles, as occurs in the contact between rollers.

The key to faster and more powerful traction drives is the development of traction fluids whose coefficient of traction shows less degradation with higher surface speeds, operating temperatures, and contact spin. Higher traction at lower contact pressures is also desirable for drives that have extra long life requirements. Today's synthetic traction fluids appear to be reasonably stable but further work may be needed for "sealed-for-life" drive systems.

Materials

Although today's bearing steels are well suited for traction drives, durability improvements and lower material costs are always welcome. Studies are required to determine if special coatings or nonmetallic materials might be useful in certain applications.

Sizing and Design Criteria

Fatigue-life prediction methods based on Lundberg-Palmgren theory are available to size traction drives. These methods are well established for determining life ratings of rolling-element bearings. However, they tend to underestimate the fatigue life obtained with today's bearings. As a result, life-adjustment factors have been identified (ref. 55) to more accurately reflect the longer lives attendant with improved bearing materials, design, and manufacturing techniques. It is anticipated that many of these same life factors are also applicable to traction drives, but endurance test data are needed to corroborate this and to identify what life adjustment factors, if any, are needed.

The upper limit of power transfer for traction drives is relatively unexplored. Drives having power capacities of thousands of kilowatts can theoretically be constructed. Not enough is known about the practical thermal limits of traction contacts or their ability to tolerate transient slips under unusual circumstances. The fact that gear teeth regularly experience momentary slips of 30 or 40 percent on entering or leaving mesh suggest that transient slip values can be remarkably high.

Another important task is the establishment of a consistent, universally accepted design standard for traction drives, similar to those that currently exist for gear drives, bearings, and other mechanical components. The design guides of Wernitz (ref. 27) and Kraus (ref. 97), published about 20 years ago, were most welcome contributions to the field, but our basic understanding of traction phenomena has greatly improved during the interim. A clear, practical, and comprehensive guide for the design and assessment of traction transmissions would benefit the designer and user alike. The bulk of such a guide can probably be assembled from the wide spectrum of information that currently exists.

Manufacturing

In principle, traction drives should be relatively inexpensive to make in large quantities. Manufacturing techniques are essentially the same as those used in the production of rolling-element bearings. To date, traction drives have been produced in relatively limited quantities or on special order and as a result have not yet realized their low cost potential.

Summary

The evolution of traction-drive technology has been traced over the past 100 years. Some of the more prominent events in the development of traction drives appear in table II. This list is by no means intended to be comprehensive but, rather, to give the reader some appreciation of the scope of activities leading to traction drives of today.

The earliest of traction drives, constructed of wood-, leather-, or fiber-covered disks running in dry contact, found first use in factory equipment before the turn of the century. The ability of traction drives to smoothly and efficiently vary speed made them natural choices as main transmissions for several early vintage cars, such as those produced by Cartercar, Sears, Lambert, and Metz. Apparently, durability problems with the soft-material-covered disks used in these drives foreshortened their commercial success. In the 1920's traction drives equipped with oil-lubricated, hardened, steel rollers started to appear. These drives had much greater power capacity, and by the 1930's several industrial adjustable speed traction drives were being marketed both here and in Europe. About this time, there were several projects to develop toroidal traction car transmissions, notably the Hayes and later, the Perbury efforts in England and the General Motors' work in the United States. In the 1940's modern lubrication and fatigue theories for rolling-contact elements were developed, and these were later adapted to the design of traction drives. In the 1950's work began on identifying fluids with high traction properties and experiments on how these fluids actually behaved within the traction contact. A basic understanding was also obtained on how the fluid film within the contact was compressed into a thin, stiff, tenacious solid-like film across which considerable torque transfer could safely occur. By the end of the 1960's high-quality bearing steels and traction fluids were commercially available. The power capacity of traction drives using the new steels and fluids virtually tripled. In the 1970's improved traction models and fatigue-life prediction methods were developed. This all led to the development of a new generation of traction drives—drives with a bright potential role to play in the power transmission industry.

In 1980 the Power Transmission and Gearing Committee of ASME took a major step in recognizing the potential viability of traction drives by establishing a subcommittee to follow the developments in the technology for these transmissions. A primary function of this subcommittee is to assist in the dissemination of technology related to traction drives and to foster their potential use in industry.

TABLE II. - LIMITED CHRONOLOGY OF TRACTION DRIVE DEVELOPMENTS

<u>Date</u>	<u>Event</u>
1870	Wooden friction drives used on wood-working machinery
1877	Hunt toroidal friction drive patented
1906	Friction drive equipped Cartercar introduced
1921	Automatic contact loading mechanism patented by Erban in Germany
1923	Oil lubricated, Arter industrial drive marketed in Switzerland
1926	Carter analyses creep between locomotive wheel and rail
1928 - 1933	General Motors Research Labs. road tests toric traction transmission
1935	Austin Motor Company offers Hayes Self-Selector toroidal transmission on Austin Sixteen
1939	EHD lubrication theory advanced by Ertel and, later, Grubin
1947	Lundberg and Palmgren develop fatigue theory for rolling elements
1949	Kopp Ball Variator commercially introduced in Switzerland
1951	Clark, et al., theorize oil solidifies in EHD contact
1955 - 1962	Braunschweig University experiments on traction contact phenomena in Germany
1955	Vacuum-melted bearing steels introduced
1957	Lane's experiments to identify high traction oils in England
1962 - 1968	Hewko's investigations into traction contact performance
1965	Nasvytis devises fixed-ratio, multiroller planetary drive
1968	Monsanto and Sun Oil introduce commercial traction fluids
1976	Coy, et al., apply Lundberg-Palmgren fatigue life theory to traction drive contacts
1978	Johnson and Tevaarwerk traction model applied to the design of traction drives
1980	ASME establishes traction drive committee

Field experience has been gathered by industrial traction-drive manufacturers, some of whom have been making traction drives for more than 40 years. However, traction-drive technology is relatively young. The latest generation of traction drives has reached a high level of technical readiness. As these drives find their way into industrial service and as work continues in the laboratories, further improvements and increased usage of these drives can be expected.

Concluding Remarks

In reviewing traction-drive developments through the years, it becomes evident that relatively few developments resulted from basic research. Technical advancements were largely due to individual organizations striving to perfect their own specific systems. As a consequence, meager fundamental information was left behind for those who followed. Of course, as this review has attempted to point out, there have been notable exceptions to this, but, by and large, relatively little is known about the reasons for the many commercial disappointments that occurred along the way.

It is encouraging, at least to this writer, that there currently seems to be greater communication among people working in the field. Admittedly, their numbers are miniscule compared with those working in the bearing and gear disciplines. Nonetheless, traction-drive technology of late seems to be making good progress. This is due, in no small measure, to much of the fine work that has been performed on tribological fundamentals, common to all rolling-element components. It is likely, in the years to come, that traction drives will find an increasingly larger role to play in the power transmission industry.

References

1. Knights, Edward H.: Knight's American Mechanical Dictionary. Vol. I. Hurd and Houghton, 1876, p. 680.
2. Trobridge: Census Office Report on Power and Machinery used by Manufacturer. Washington, 1888, p. 220.
3. Appleton's Cyclopedia of Applied Mechanics. Vol. II. D. Appleton and Co., 1830, pp. 36-37.
4. Yeaple, F.: Metal-To-Metal Traction Drives now have a New Lease on Life. *Product Eng.*, vol. 42, no. 15, Oct. 1971, pp. 33-37.
5. Carson, R. W.: New and Better Traction Drives are Here. *Mach. Des.*, vol. 46, no. 10, Apr. 18, 1974, pp. 148-155.
6. McCormick, D.: Traction Drives Move to Higher Powers. *Des. Eng.*, Dec. 1980, pp. 35-39.
7. Hewko, L. O.: Traction Drives and Their Potential Role in Energy Conservation. Presented at the Joint ASLE Energy-Sources Technology Conference, New Orleans, LA, Feb. 1980.
8. Hamrock, B.; and Dowson, D.: *Ball Bearing Lubrication*. John Wiley & Sons, 1981.
9. Dudley, D. W.: *The Evolution of the Gear Art*. American Gear Manufacturers Association, 1969.
10. Drachmann, A. G.: *The Mechanical Technology of Greek and Roman Antiquity*. Lubrecht and Cramer, 1963, pp. 200-203.
11. Carson, R. W.: 100 Years in Review: Industrial Traction Drives. *Power Transm. Des.*, vol. 19, no. 10, Oct. 1977, pp. 99-100.
12. Fellows, T. G.; et al.: Perbury Continuously Variable Ratio Transmission. *Advances in Automobile Engineering*, Pt. II, Pergamon Press (Oxford), 1964, pp. 123-142.
13. Heldt, P. M.: Automatic Transmissions. *SAE J.*, vol. 40, no. 5, May 1937, pp. 206-220.
14. DeBono, E.: *Eureka: An Illustrated History of Inventions from the Wheel to the Computer*. Holt, Rinehart, and Winston, 1974, p. 33.
15. Hodges, D.; and Wise, D. B.: *The Story of the Car*. Hamlyn Publication Group, Ltd. (London), 1974, p. 18.
16. Sloan, Alfred P.: *My Years with General Motors*. Doubleday and Co., Inc., 1964.
17. Clymer, F.: *Historical Motor Scrapbook*. Vols. 1 and 2. Clymer Motor Publications, 1944.
18. Caris, D. F.; and Richardson, R. A.: Engine-Transmission Relationships for High Efficiency. *SAE Trans.*, vol. 61, 1953, pp. 81-96.
19. Improved Technology is Giving an Old Principle a New Drive. *Monsanto Magazine*, Summer 1974, pp. 14-16.
20. Carson, R. W.: Focus on Traction Drives: 100 Years of Traction Drives. *Power Transm. Des.*, vol. 17, no. 5, May 1975, pp. 84 and 88.
21. Perry, F. G.: The Perbury Transmission. ASME Paper No. 80-GT-22, Mar. 1980.
22. Final Report on the Follow-On Phase of the Evaluation of the Wright Aeronautical Division Toroidal Drive Using a 1/4 Ton Military Truck as a Test Bed Vehicle. WAD R273-F, Curtis-Wright Corporation, Feb. 1966.
23. Carson, R. W.: Focus on Traction Drives. *Power Transm. Des.*, vol. 17, no. 3, Mar. 1975, pp. 48-49.
24. Carson, R. W.: Today's Traction Drives. *Power Transm. Des.*, vol. 17, no. 11, Nov. 1975, pp. 41-49.
25. Cahn-Speyer, P.: Mechanical Infinitely Variable Speed Drives. *Eng. Dig. (London)*, vol. 18, no. 2, Feb. 1957, pp. 41-43.
26. Dvorak, D. Z.: Your Guide to Variable-Speed Mechanical Drives. *Prod. Eng.*, vol. 34, Dec. 1963, pp. 63-74.

27. Wernitz, W.: Friction Drives. *Mechanical Design and Systems Handbook*, H. A. Rothbart, ed., McGraw Hill Book Co., Inc., 1964, pp. 14-1 to 14-22.
28. Grubin, A. N.: Fundamentals of the Hydrodynamic Theory of Lubrication of Heavily Loaded Cylindrical Surfaces. Investigation of the Contact of Machine Components, Kh. F. Ketova, ed., Translation of Russian Book No. 30, Central Scientific Institute for Technology and Mechanical Engineering, Moscow, 1949, Chapter 2. (Available from Department of Scientific and Industrial Research, Great Britain, Transl. CTS-235 and Special Libraries Association, Transl. R-3554.)
29. Lundberg, G. and Palmgren, A., "Dynamic Capacity of Rolling Bearings," *Ingenioersvetenskapsakademian, Handlinger*, No. 196, 1947.
30. Ertel, A. M.: Hydrodynamic Lubrications Based on new Principles. *Prikl. Mat. Mekh.*, vol. 3, no. 2, 1939 (in Russian).
31. Martin, K. F.: A Review of Frictional Predictions in Gear Teeth. *Wear*, vol. 49, 1978, pp. 201-238.
32. Clark, O. H.; Woods, W. W.; and White, J. R.: Lubrication at Extreme Pressure with Mineral Oil Films. *J. of Appl. Phys.*, vol. 22, no. 4, Apr. 1951, pp. 474-483.
33. Smith, F. W.: The Effect of Temperature in Concentrated Contact Lubrication. *ASLE Trans.*, vol. 5, no. 1, Apr. 1962, pp. 142-148.
34. Plint, M. A.: Traction in Elastohydrodynamic Contacts. *Proc. Inst. Mech. Eng. (London)*, vol. 182, no. 1, 1967, pp. 300-306.
35. Johnson, K. L.; and Cameron, R.: Shear Behavior of Elastohydrodynamic Oil Films at High Rolling Contact Pressures. *Proc. Inst. Mech. Eng. (London)*, vol. 182, no. 1, 1967, pp. 307-318.
36. Crook, A. W.: Lubrication of Rollers. Pt. IV. Measurements of Friction and Effective Viscosity. *Phil. Trans. Roy. Soc., London, Ser. A.*, vol. 255, no. 1056, Jan. 1963, pp. 281-312.
37. Dyson, A.: Frictional Traction and Lubricant Rheology in Elastohydrodynamic Lubrication, *Phil. Trans. Roy. Soc., London, Ser. A.*, vol. 266, no. 1170, Feb. 1970, pp. 1-33.
38. Johnson, K. L.; and Roberts, A. D.: Observation of Visco Elastic Behavior of an Elastohydrodynamic Lubricant Film. *Proc. R. Soc. (London), Ser. A.*, vol. 337, 1974, pp. 217-242.
39. Trachman, E. G.; and Cheng, H. S.: Thermal and Non-Newtonian Effects on Traction in Elastohydrodynamic Contacts. Symposium on Elastohydrodynamic Lubrication, *Inst. of Mech. Eng. (London)*, 1972, pp. 142-148.
40. Johnson, K. L.; and Tevaarwerk, J. L.: Shear Behavior of Elastohydrodynamic Oil Films. *Proc. R. Soc. (London), Ser. A.*, vol. 356, no. 1685, Aug. 1977, pp. 215-236.
41. Walowit, J. A.; and Smith, R. O.: Traction Characteristics of a MIL-L-7808 Oil. *ASME Paper No. 76-Lubs-19*, 1976.
42. Hewko, L. O.; Rounds, F. G., Jr.; and Scott, R. L.: Tractive Capacity and Efficiency of Rolling Contacts. *Rolling Contact Phenomena*, J. B. Bidwell, ed., Elsevier Publishing Co. (Amsterdam), 1962, pp. 157-185.
43. Hewko, L. O.: Contact Traction and Creep of Lubricated Cylindrical Rolling Elements at Very High Surface Speeds. *ASLE Trans.*, vol. 12, no. 2, Apr. 1969, pp. 151-161.
44. Gaggermeier, Helmut: Investigations of Tractive Force Transmission in Variable Traction Drives in the area of Elastohydrodynamic Lubrication. Ph.D. Dissertation, Technical University of Munich, July 1977.
45. Tevaarwerk, J. L.: Traction Contact Performance Evaluation at High Speeds. *NASA CR-165226*, 1981.
46. Carter, F. W.: On the Action of a Locomotive Driving Wheel. *Proc. R. Soc. (London), Ser. A.*, vol. 112, 1926, pp. 151-157.
47. Johnson, K. L.: Tangential Traction and Micro-Slip in Rolling Contact. *Rolling Contact Phenomena*, J. B. Bidwell, ed., Elsevier Publishing Co. (Amsterdam), 1962, pp. 6-28.
48. Tevaarwerk, J. L.: Traction Drive Performance Prediction for the Johnson and Tevaarwerk Traction Model. *NASA TP-1530*, 1979.
49. Johnson, K. L.; Nayak, L.; and Moore, A. J.: Determination of Elastic Shear Modulus of Lubricants from Disc Machine Tests. *Elastohydrodynamics and Related Topics: Proc. 5th Leeds-Lyon Symposium on Tribology*, Mech. Eng. Publ. Ltd., 1979, pp. 204-213.
50. Lane, T. B.: The Lubrication of Friction Drives. *Lubr. Eng.*, vol. 13, Feb. 1957, pp. 85-88.
51. Haseltine, M. W.; et al.: Design and Development of Fluids for Traction and Friction Type Transmissions. *SAE Paper 710837*, Oct. 1971.
52. Hamman, W. C.; et al.: Synthetic Fluids for High Capacity Traction Drives. *ASLE Trans.*, vol. 13, 1970, pp. 105-116.
53. Loewenthal, S. H.; and Parker, R. J.: Rolling-Element Fatigue Life with Two Synthetic Cycloaliphatic Traction Fluids. *NASA TN D-8124*, 1976.
54. Blair, Scott; and Winer, W. O.: Shear Strength Measurements of Lubricants at High Pressures. *J. Lubr. Tech.*, vol. 101, no. 3, July 1979, pp. 251-257.
55. Bamberger, E. N., et al.: Life Adjustment Factors for Ball and Roller Bearings—An Engineering Guide. *Am. Soc. of Mech. Eng.*, 1971.
56. Coy, J. J.; Loewenthal, S. H.; and Zaretsky, E. V.: Fatigue Life Analysis for Traction Drives with Application to a Toroidal Type Geometry. *NASA TN D-8362*, 1976.
57. Rohn, D. A.; Loewenthal, S. H.; and Coy, J. J.: Simplified Fatigue Life Analysis for Traction Drive Contacts. *J. Mech. Des.*, vol. 103, no. 2, Apr. 1981, pp. 430-439.
58. MacPherson, P. B.: The Pitting Performance of Hardened Steels. *ASME Paper No. 77-DET-39*, Sept. 1977.
59. Soda, N.; and Yamamoto, T.: Effect of Tangential Traction and Roughness on Crack Initiation/Propagation During Rolling Contact. *NASA TM-81608*, 1981.
60. Tallian, T. E.; Chiu, Y. P.; and Van Amerongen, F.: Predictions of Traction and Microgeometry Effects on Rolling Contact Fatigue Life. *J. Lubr. Tech.*, vol. 100, no. 2, Apr. 1978, pp. 156-166.
61. Bamberger, E. N.: Materials for Rolling Element Bearings. *Bearing Design—Historical Aspects, Present Technology, and Future Problems*, *Am. Soc. Mech. Eng.*, 1980, pp. 1-46.

62. Poritsky, H.; Hewlett, C. W., Jr.; and Coleman, R. E., Jr.: Sliding Friction of Ball Bearings of the Pivot Type. *J. Appl. Mech.*, vol. 24, no. 4, Dec. 1947, pp. A-251 to A-268.
63. Lutz, O.: Grundsatzliches über stufenlos verstellbare Walzgetriebe. *Z. Konstruktion*, vol. 7, 1955, p. 330; vol. 9, 1957, p. 169; vol. 10, 1958, p. 425.
64. Wernitz, W.: Walz-Bohrreibung-Bestimmung der Bohrmomente und Umfangskräfte bei Hertzscher Pressung mit Punktberührung. Vol. 19 of *Schriftenreihe Antriebstechnik*, Fr. Vieweg und Sohn, Braunschweig, 1958.
65. Maass, H.: Untersuchung über die in elliptischen Hertzscher Flächen übertragbaren Umfangskräfte, Dissertation, Technical University of Braunschweig, 1959.
66. Kutter, F.: Theoretische Untersuchung eines Reibgetriebes, Thesis, Technical University of Dresden, 1944.
67. Thomas, W.: Reibscheiben-Regelgetriebe (Linienberührung), Vol. 4 of the *Schriftenreihe Antriebstechnik*, Fr. Vieweg und Sohn, Braunschweig, 1954.
68. Wernitz, W.: Friction at Hertzian Contact with Combined Roll and Twist. *Rolling Contact Phenomena*, J. B. Biddwell, ed., Elsevier Publishing Co. (Amsterdam), 1962, pp. 132-156.
69. Magi, M.: On Efficiencies of Mechanical Coplanar Shaft Power Transmissions. Chalmers University, Gothenburg, Sweden, 1974.
70. Hewko, L. O.: Roller Traction Drive Unit for Extremely Quiet Power Transmission. *J. Hydronautics*, vol. 2, no. 3, July 1968, pp. 160-167.
71. New Departures in Automotive Ideas. New Departure Press, 1937, pp. 5-6.
72. Cheng, H. S.; and Sternlicht, B.: A Numerical Solution for the Pressure, Temperature, and Film Thickness Between Two Infinitely Long Lubricated Rolling and Sliding Cylinders under Heavy Loads. *J. Basic Eng.*, vol. 87, no. 3, Sept. 1965, pp. 695-707.
73. Bell, J. C.; Kannel, J. W.; and Allen, C. M.: The Rheological Behavior of the Lubricant in the Contact Zone of a Rolling Contact System. *J. Basic Eng.*, vol. 83, no. 3, Sept. 1964, pp. 423-425.
74. Dowson, D.; and Whitaker, B. A.: A Numerical Procedure for the Solution of the Elastohydrodynamic Problem of Rolling and Sliding Contacts Lubricated by a Newtonian Fluid. *Proc. Inst. of Mech. Eng. (London)*, vol. 180, pt. 3B, 1965, pp. 57-71.
75. Kannel, J. W.; and Walowit, J. A.: Simplified Analysis for Traction Between Rolling-Sliding Elastohydrodynamic Contacts. *J. Lubr. Tech.*, vol. 93, Jan. 1971, pp. 39-46.
76. Poon, S. Y.: Some Calculations to Assess the Effect of Spin on the Tractive Capacity of Rolling Contact Drives. *Proc. Inst. Mech. Eng. (London)*, vol. 185, no. 76/71, 1970, pp. 1015-1022.
77. Lingard, S.: Traction at the Spinning Point Contacts of a Variable Ratio Friction Drive. *Tribol. Int.*, vol. 7, Oct. 1974, pp. 228-234.
78. Daniels, B. K.: Traction Contact Optimization. ASLE Preprint No. 79-LC-1A-1, 1979.
79. Tevaarwerk, J. L.: Traction Calculations Using the Shear Plane Hypothesis. Thermal Effects in Tribology: Proc. 6th (1979) Leeds/Lyon Conf. on Tribology, Mech. Eng. Publ., Ltd., 1980, pp. 201-213.
80. Tevaarwerk, J. L.: A Simple Thermal Correction for Large Spin Traction Curves. *J. Mech. Des.*, vol. 103, no. 2, Apr. 1981, pp. 440-446.
81. Johnson, K. L.; and Greenwood, J. A.: Thermal Analysis of an Eyring Fluid in Elastohydrodynamic Traction. *Wear*, vol. 61, 1980 pp. 353-374.
82. Tevaarwerk, J. L.: Thermal Influence on the Traction Behavior of an Elastic/Plastic Model. Presented at the Leeds/Lyon Conference on Tribology, (Leeds, England), Aug. 1981.
83. Nakamura, L.; et al.: A development of a Traction Roller System for a Gas Turbine Driven APU. SAE Paper No. 790106, Feb. 1979.
84. Nasvytis, A. L.: Multiroller Planetary Friction Drives. SAE Paper No. 660763, Oct. 1966.
85. Loewenthal, S. H.; Anderson, N. E.; and Nasvytis, A. L.: Performance of a Nasvytis Multiroller Traction Drive. NASA TP-1378, 1978.
86. Loewenthal, S. H.; Anderson, N. E.; and Rohn, D. A.: Evaluation of a High Performance Fixed-Ratio Traction Drive. *J. Mech. Des.*, vol. 103, no. 2, Apr. 1981, pp. 410-422.
87. Meyer, S.; and Connelly, R. E.: Traction Drive for Cryogenic Boost Pump. NASA TM-81704, 1981.
88. Radtke, R. R.; Unnewehr, L. E.; and Freedman, R. J.: Optimization of a Continuously Variable Transmission with Emission Constraints. SAE Paper No. 810107, Feb. 1981.
89. Strauch, S.: Flywheel Systems for Vehicles. Proc. Electric and Hybrid Vehicle Advanced Technology Seminar, Dec. 8-9, 1980, California Institute of Technology, Pasadena, pp. 219-236.
90. Stubbs, P. W. R.: The Development of a Perbury Traction Transmission for Motor Car Applications. *J. Mech. Des.*, vol. 103, no. 4, Jan. 1981, pp. 29-40.
91. Kemper, Y.: A High Power Density Traction Drive. SAE Paper No. 790849, 1979.
92. Elu, P.; and Kemper, Y.: Performance of a Nutating Traction Drive. ASME Paper No. 80-C2/DET-63, Aug. 1980.
93. Dickinson, T. W.: Development of a Variable Speed Transmission for Light Ractors. SAE Paper No. 770749, Sept. 1977.
94. Raynard, A. E.; Kraus, J. H.; and Bell, D. D.: Design Study of Toroidal Traction CVT for Electric Vehicles. (Rept-80-16762, AiResearch Manufacturing Company; NASA Contract DEN3-117.) DOE/NASA/0117-80/1, NASA CR-159803, 1980.
95. Walker, R. D.; and McCain, D. K.: Design Study of a Continuously Variable Cone/Roller Traction Transmission for Electric Vehicles. DOE/NASA/0115-80/1, NASA CR-159841, Sept. 1980.
96. Parker, R. J.; Loewenthal, S. H.; and Fischer, G. K.: Design Studies of Continuously Variable Transmissions for Electric Vehicles. DOE/NASA/10444-12, NASA TM-81642, 1981.
97. Kraus, C. E.: An Up-To-Date Guide for Designing Traction Drives. Pt. I. *Mach. Des.*, July 2, 1964, pp. 106-112; and Pt. II. *Mach. Des.*, July 16, 1964, pp. 147-152.

An Overview of Advancements in Helicopter Transmission Design*

Joseph H. Mancini†

The AVRADCOM/NASA sponsored Advanced Transmission Development Investigation directed its attention towards the attainment of a high temperature operating helicopter gearbox. This capability will either eliminate the gearbox oil cooler or permit the use of a reduced-size oil cooler, will provide payoffs in system weight and cost, and decrease the vulnerable area. The advanced components selected for this program were designed and fabricated for and tested in the Black Hawk transmission system.

The Black Hawk helicopter (fig. 1) is the Army's advanced twin-engine tactical transport helicopter manufactured by Sikorsky Aircraft to perform the missions of assault, resupply, medical evacuation, command and control, and tactical positioning of reserves. The GE-T700 turboshaft engines deliver 1560 hp each, to power the Black Hawk drive system. The drive system (fig. 2) consists of three major components: the main gearbox, which combines engine power, drives the main and tail rotors, and provides secondary subsystem power; drive shafts, which deliver power to the tail rotor; and intermediate and tail gearboxes, which provide the proper speed and angle changes for the tail rotor drive system.

The main transmission (fig. 3) consists of a main module, two input modules, and two accessory modules. The production Black Hawk main transmission weighs 1245 pounds, which includes the five modules, oil, oil cooler and blower, oil lines, and related hardware. The left and right hand input modules are interchangeable—as are the accessory modules. The main transmission transmits 2828 maximum continuous horsepower with an input speed of 20 900 rpm, a reduction ratio of 81 to 1 through three stages of reduction (two spiral bevel gear stages and one planetary stage), a dry weight of 1081 pounds, and demonstrated survivability that exceeds the 30-minute requirement. Some of the design features include modular design; no external lubrication lines; standard tools used to replace modules; redundant gearbox mounting and accessory drive; oil lubricated accessory drive splines; and fuzz suppression chip detectors.

Under the sponsorship of AVRADCOM and NASA Lewis, Sikorsky Aircraft conducted an Advanced Transmission Components Investigation that evaluated three component programs that could enter engineering development in this decade: a stainless-steel-fabricated main transmission housing; an advanced thrust-carrying cylindrical roller bearing; and advanced high-contact-ratio (HCR) buttress-tooth-form gears manufactured from CBS-600 steel. The goal of the program was to develop high-temperature helicopter transmission operation capability.

Figure 4 shows a cross section of the main transmission and defines the input, main, and accessory modules. The advanced, thrust-carrying cylindrical roller bearing was designed to carry the loads of the ball-roller-bearing combination on the input bevel pinion shaft. The fabricated housing, designed, manufactured, and tested as part of this program, encloses the main module. The HCR buttress-tooth-form planetary gears are interchangeable with the standard spur tooth form planetary gears in the main module.

The program also included the design and fabrication of full-size hardware that will be integrated into a Black Hawk gearbox for conduct of a system integration test.

Fabricated Transmission Housing

Design and Fabrication

Goals for the fabricated housing concept were to obtain 20 percent lighter weight and a high-temperature capability in the 450° to 550° F range, to reduce vulnerability, and to virtually eliminate corrosion problems associated with service operation.

*Work done under NASA contract NAS3-17859 and under AVRADCOM contract DAAJ02-76-C-0044.

†Sikorsky Aircraft Division, United Technologies Corporation.



Figure 1. - Black Hawk utility helicopter.

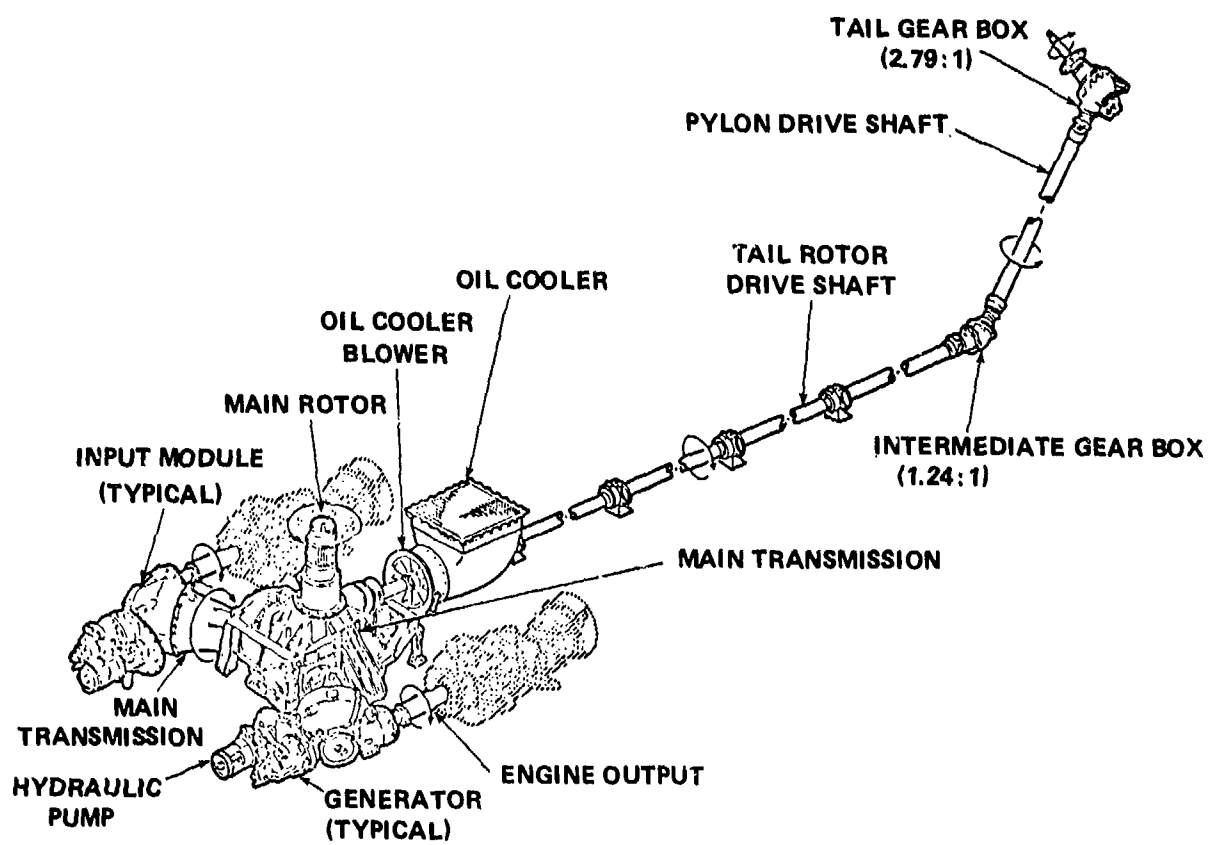


Figure 2. - Black Hawk drive train schematic.

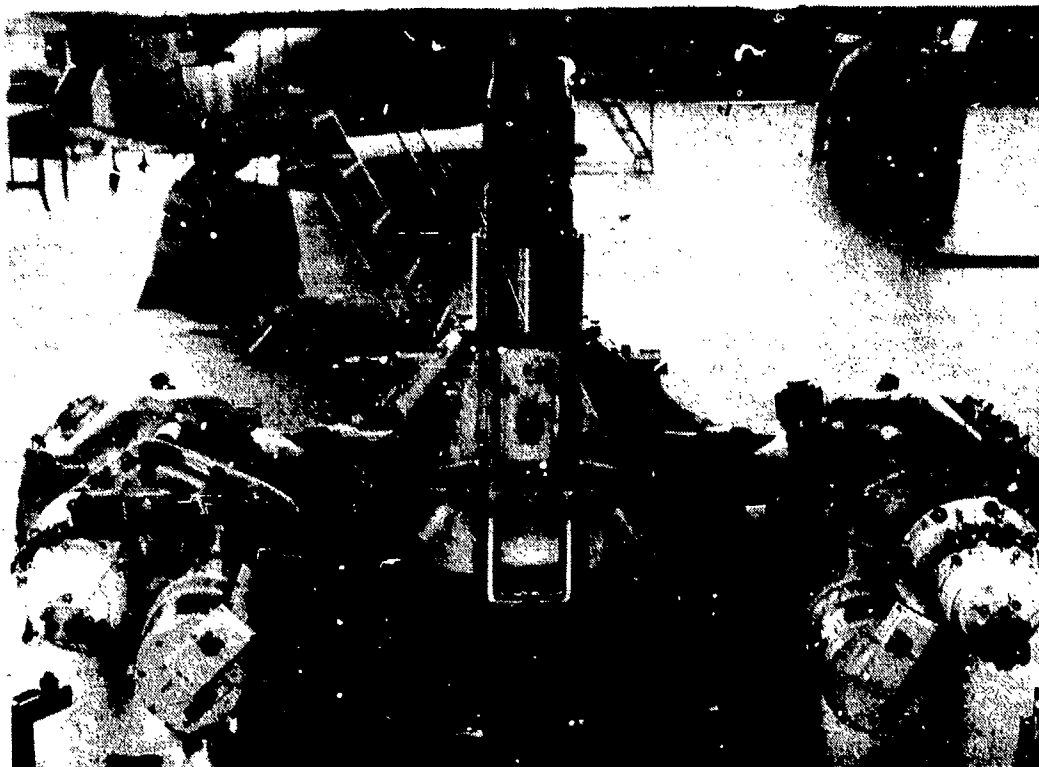


Figure 3. - Black Hawk main gearbox.

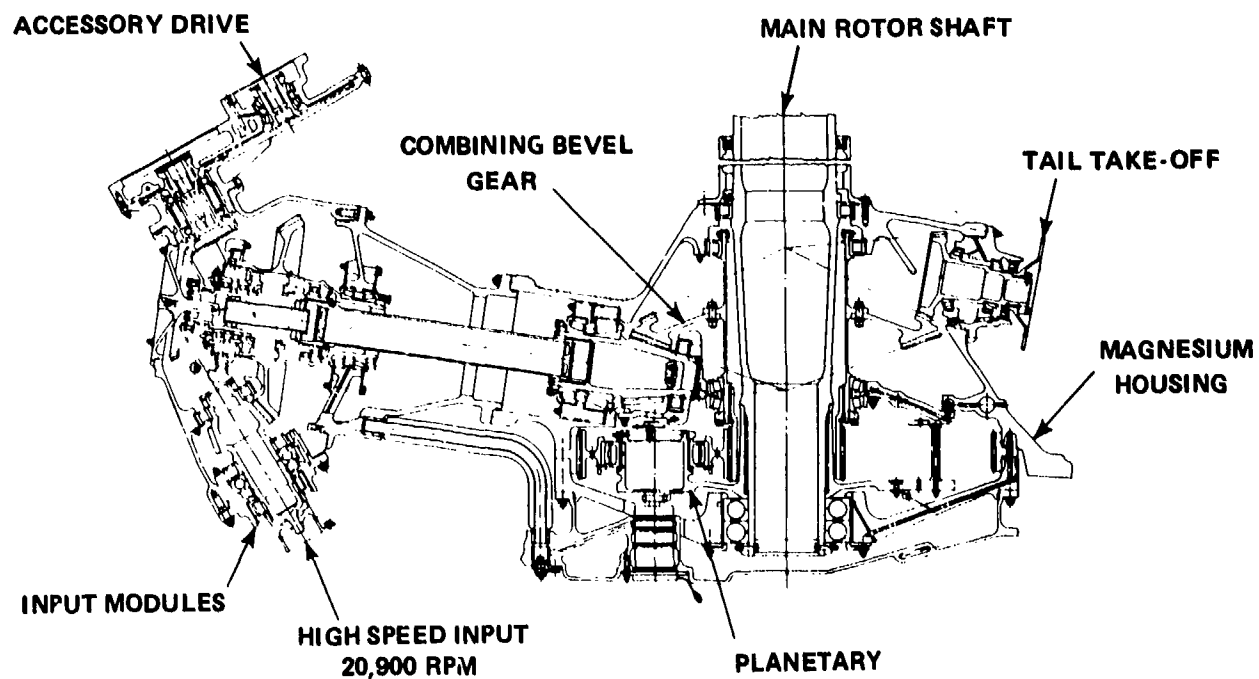


Figure 4. - Black Hawk main transmission.

Carpenter Custom 450 was selected for its combination of strength, fracture toughness, ease of fabrication and welding characteristics. The chemical composition of Carpenter Custom 450 in table 1 was balanced to achieve a martensitic structure in all conditions of heat treatment. The low carbon content in the alloy results in a tough, ductile martensite that resists cracking in the weld metal and in the heat-affected zone of the parent metal and does not require preheating before welding. The production Black Hawk main housing is made from a ZE41 magnesium alloy casting, shown in figure 5 for comparison with the fabricated housing shown in figure 6. The fabricated housing consists of a stainless-steel sheet metal shell to which the input and tail takeoff pods were welded. Flanges made from steel plate were welded to the top and bottom of the shell and to the input and tail takeoff pods. Channel-shaped ribs, welded to the shell, transfer main rotor shaft bearing loads into the airframe, and stiffening ribs provide additional support for the inputs and tail takeoff pods. The shell reacts shear loads and retains the lubricating oil. Figure 7 depicts the finite-element model used to design the fabricated housing. The primary design objective for the housing was to withstand a simulated forward crash load of 20 g's without catastrophic failure and to provide the same stiffness as the production housing.

TABLE 1 CARPENTER CUSTOM 450 COMPOSITION

CARBON	0.05% MAX	CHROMIUM	14.00/16.00%
MANGANESE	1.00% MAX	NICKEL	5.00/7.00%
SILICON	1.00% MAX	MOLYBDENUM	0.50/1.00%
PHOSPHORUS	0.03% MAX	COPPER	1.25/1.76%
SULFUR	0.03% MAX	COLUMBIUM	8 x C MIN

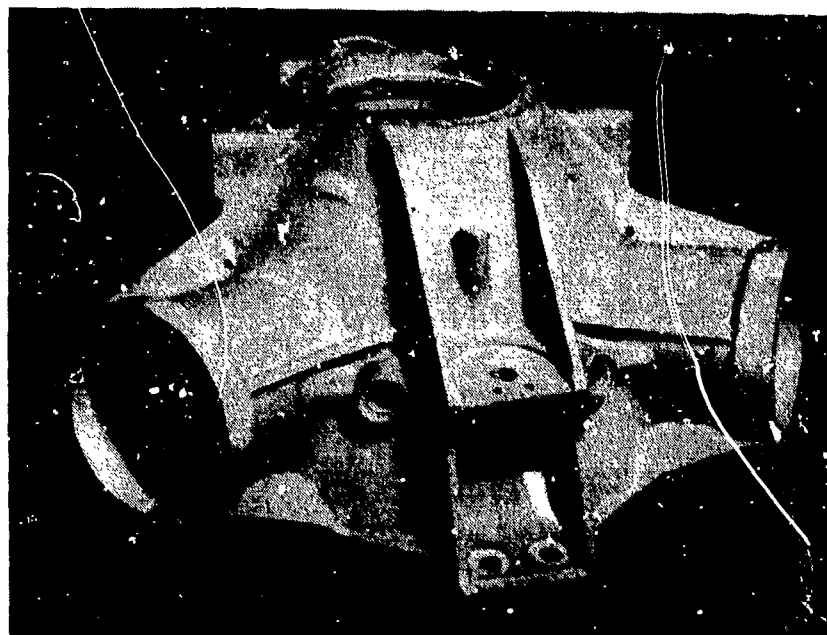


Figure 5. - Black Hawk cast magnesium housing.

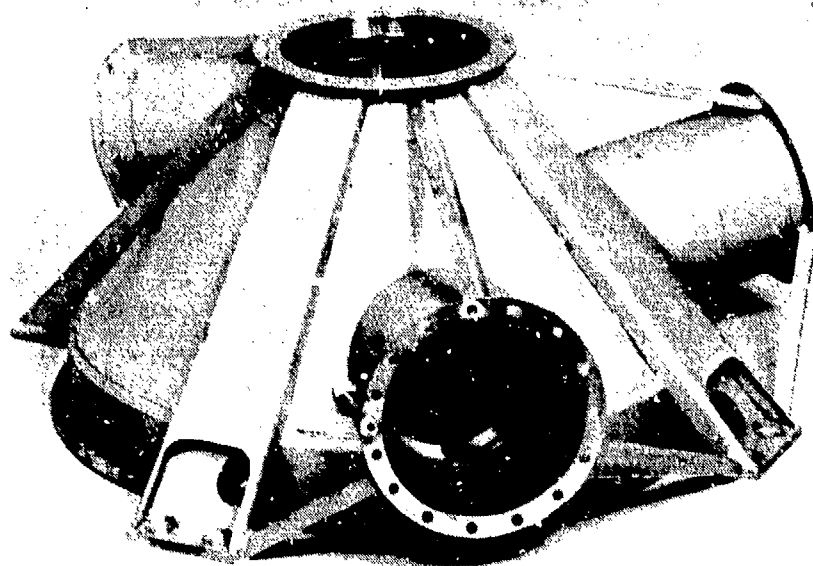


Figure 6. - Fabricated main transmission housing.

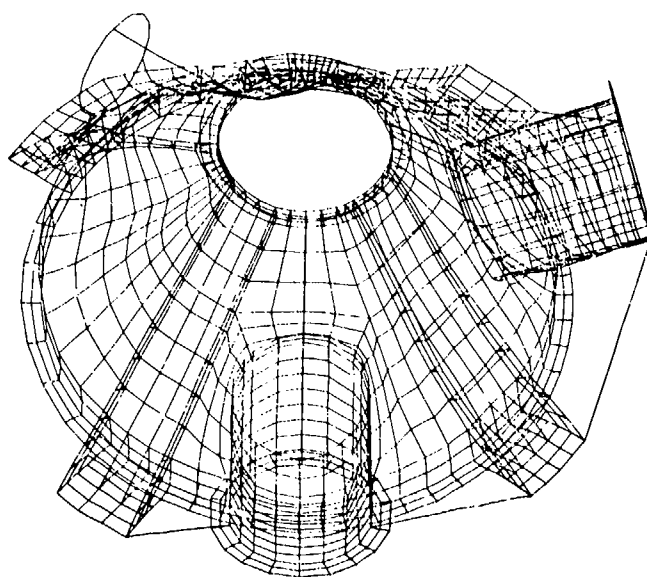


Figure 7. - NASTRAN model fabricated housing.

Fabricated Housing Tests

Sikorsky assembled the fabricated housing with a main-rotor shaft, shaft bearing supports, ring gear, input modules, and lower housing into a static-test configuration for conduct of a crash load test. Figure 8 illustrates the crash load test setup. Hydraulic cylinders applied the loads that were monitored by calibrated load cells.

A second fabricated housing was assembled with dynamic components and also installed in the Sikorsky Aircraft universal static-test facility to conduct a torque test (fig. 9). Indications of localized buckling, excessive deflection, or stresses were used as criteria for termination of the tests. The purpose of the crash load test was to demonstrate the failure modes of the stainless-steel-fabricated



Figure 8. - Main transmission crash load test setup.

housing. This test indicated a relatively benign buckling of the forward compression strut on the input module and a crack in the weld on the rear tension strut weld at the junction to the rear mounting pad. These areas will be easily strengthened during any forthcoming production effort. The purpose of the torque test was to evaluate the stress and deflection characteristics of the fabricated housing under torque conditions ranging to 120 percent of operating torque. The torque test demonstrated stress and deflection characteristics comparable with those of the production magnesium housing. These tests verified the feasibility of the stainless-steel-fabricated housing concept.

Plans for the fabricated housing include: participation in a system integration test that will include the advanced bearing and the HGR buttress-tooth-form gears, made from CBS-600 steel, assembled in a Black Hawk main transmission system; a program to productionize design and fabrication techniques to reduce manufacturing costs; and, finally, fabrication and testing of production versions before production incorporation.

Advanced, Thrust-Carrying, Cylindrical Roller Bearing

Design and Fabrication

The standard cylindrical roller bearing has flat ended rollers retained in the bearing by straight flanges that form a 90° angle to the race. In high-speed applications roller skewing can result in edge contact between the roller and the flange and produce high localized stresses that can destroy the lubricant film, resulting in premature failures. To provide a solution to this problem as part of the component development program, Sikorsky Aircraft issued a subcontract to SKF to develop a thrust-carrying, cylindrical roller bearing for helicopter gearbox operation. This advanced bearing (fig. 10) incorporates sphere-ended rollers with an angled flange. The flange-roller-end contact area remains

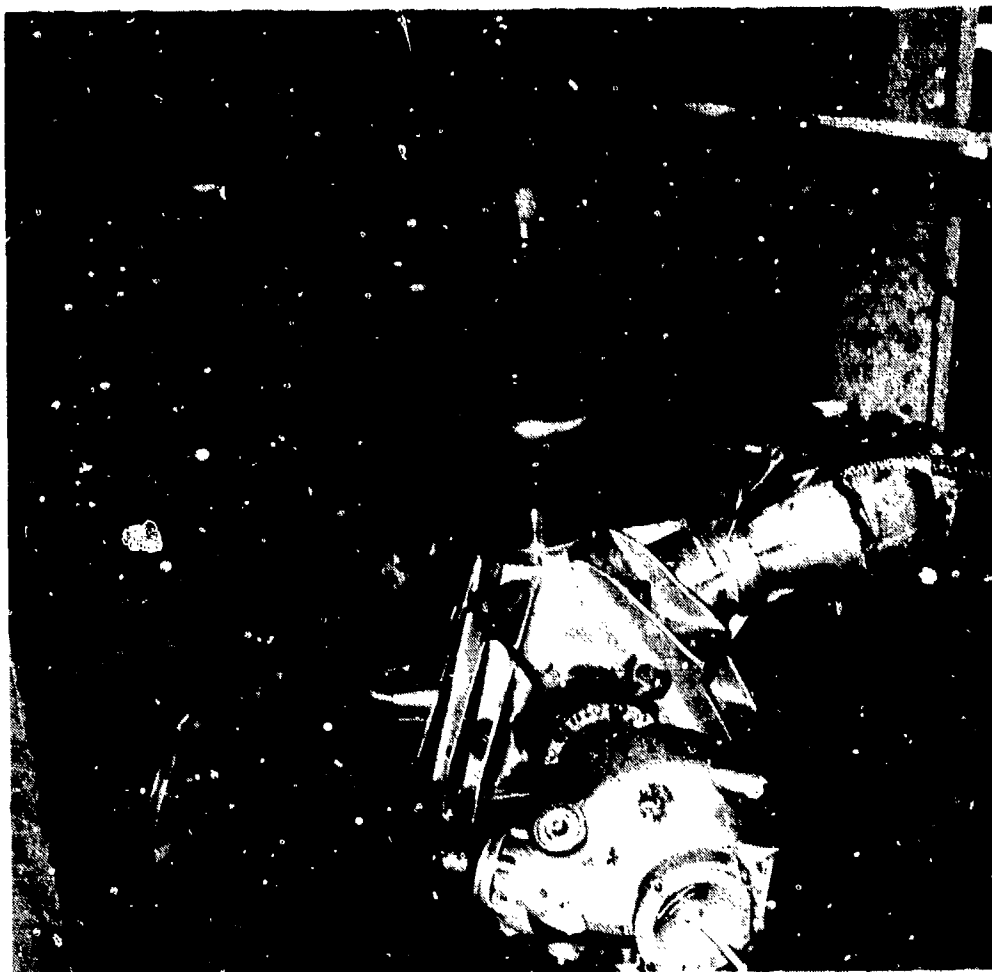


Figure 9. - Main transmission torque test setup.

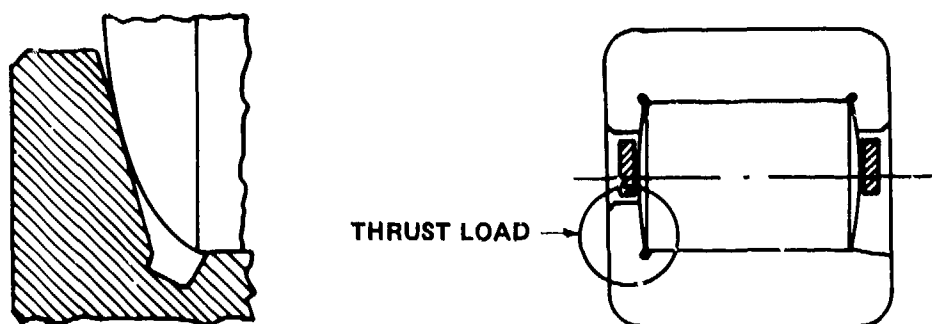


Figure 10. - Thrust - roller bearing concept.

nearly circular under skewing, and thrust loads can be applied without excessive stress or breakdown in the lubricant film. Both bearing races were made from vacuum-induction-melted-vacuum-arc-remelted (VIM-VAR) AISI M-50 steel and heat treated to Rockwell C 60 (minimum); the cage was made from AMS 6414 steel and silver plated. VAR AISI M-50 steel rollers were used. The goals of this component development were to reduce weight, to improve reliability, to reduce cost, and to determine the validity of this bearing concept.

Bearing Test

SKF conducted a series of three tests to evaluate the advanced bearing configuration. The first bearing evaluation test determined the capability of the bearing to carry combinations of radial and thrust loads throughout the operating speed range. This included radial loads to 1600 pounds and thrust loads to 1520 pounds with speeds to 21 500 rpm. The test was completely satisfactory. The second bearing performance test, at 21 500 rpm, was conducted to optimize lubrication flow rates and mode of distribution through the jets. Oil was centrifuged through radial holes in the inner race to the critical sliding contact areas. Drain holes in the outer race prevented flooding of the outer race and prevented churning. Figure 11 illustrates the decrease in bearing heat generation as the thrust load was held constant at 1520 pounds and the radial load was incrementally reduced. This test demonstrated the bearing's capability to carry thrust load with reduced radial load. Loads during this test ranged from 1600 pounds radial with 1520 pounds thrust to 160 pounds radial with 1520 pounds thrust. The endurance test consisted of 140 hours of satisfactory operation at maximum load and speed conditions: 1600 pounds radial load, 1520 pounds thrust load, and 21 500 rpm. This bearing development program clearly established the functional validity of the thrust-carrying cylindrical roller bearing design concept.

Bearing Future Plans/Recommendations

The thrust-carrying cylindrical roller bearing will operate in the Black Hawk input module during the planned 10-hour system integration test to demonstrate its operational compatibility.

After loss of lubrication, the thrust-carrying roller bearing would be expected to have a high heat-generation rate at the inner-ring flange contact area. Consequently, additional work is planned to improve this advanced bearing's lost-lubrication survivability capability. Also, analytical techniques are not currently available to directly calculate the 10-percent life of a thrust-carrying cylindrical roller bearing, or the life at which 90 percent of the bearings survive. This life analysis should be developed before this bearing is used in a production design.

Advanced Gear-Tooth-Form and Materials Development

Two programs were conducted simultaneously during the gear development program: The first consisted of the development of an advanced geometry tooth form, and the second investigated the suitability of CBS-600, a carburizing bearing steel developed by the Timken Company, as a material for helicopter gears. The advantage of HCR gears (fig. 12) depends on the fact that two or more teeth

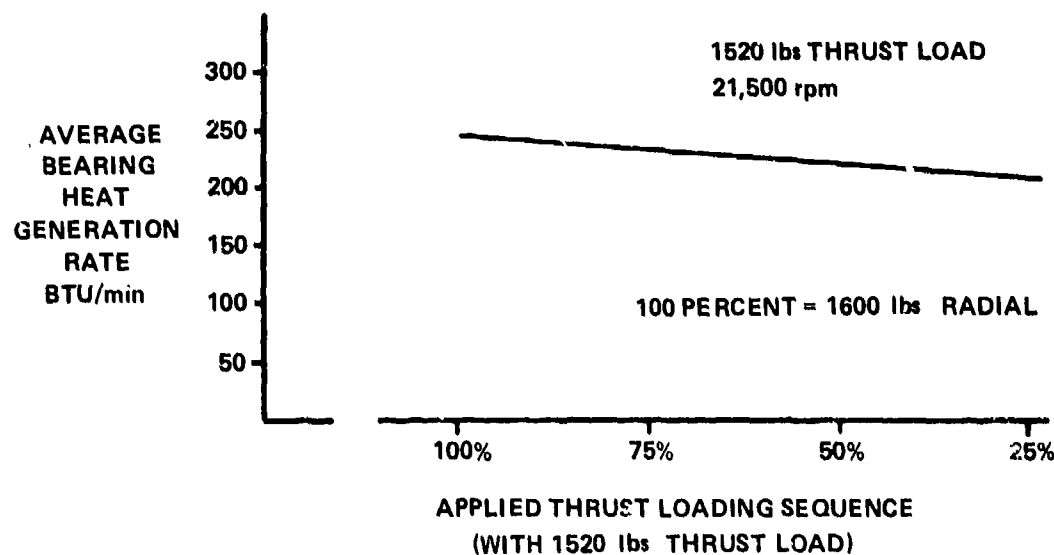


Figure 11. - Thrust - radial load versus heat generation.

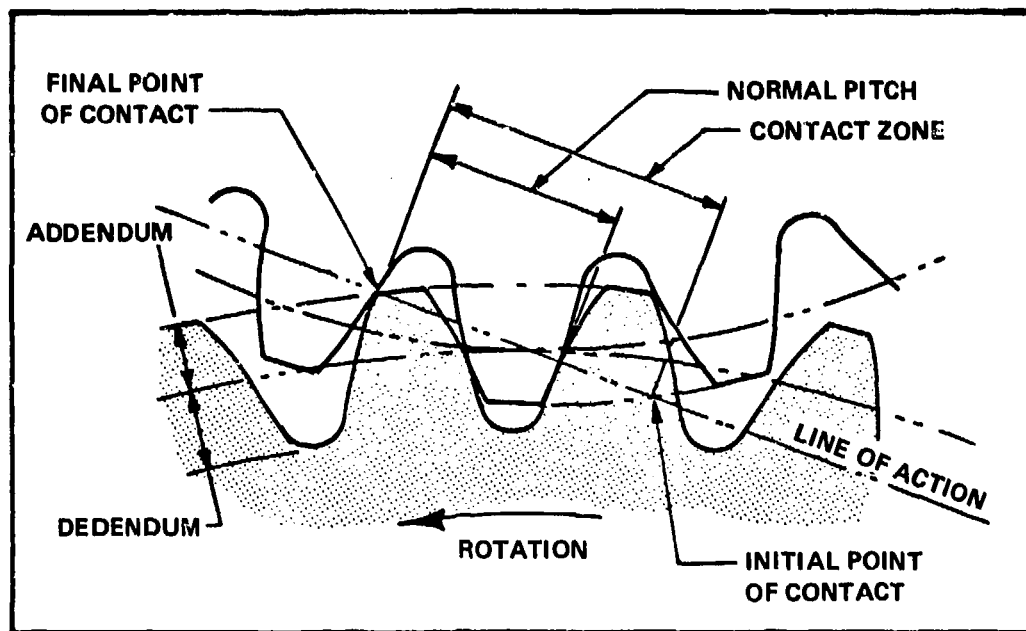
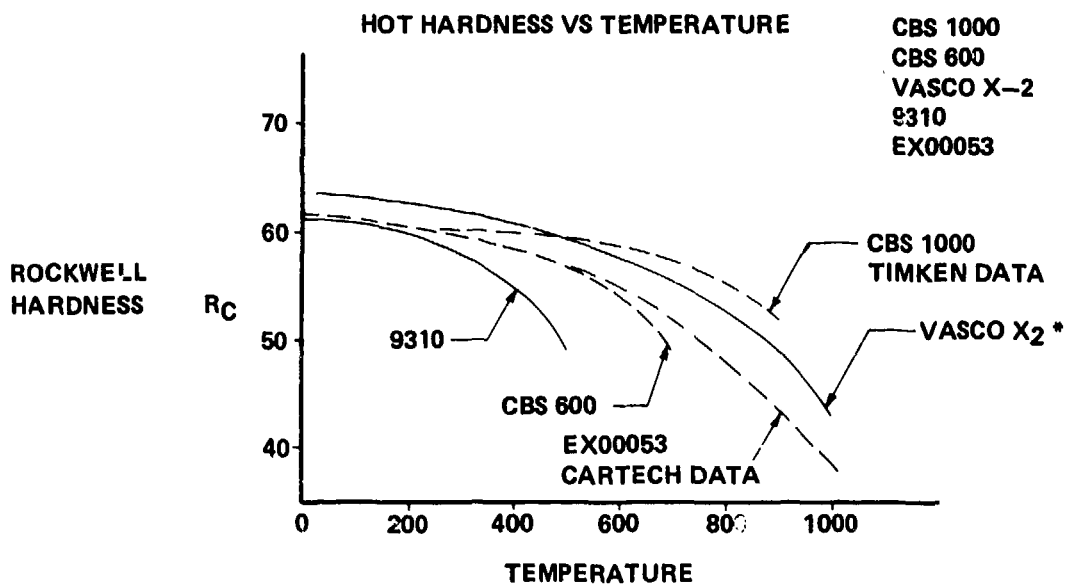


Figure 12. - High-contact-ratio gearing.



*BOEING VERTOL DATA

Figure 13. - Hardness versus temperature comparison.

teeth always share the transmitted load. Consequently, they decrease the individual tooth load and the associated tooth bending and contact stresses. However, the means taken to increase the contact ratio (i.e., lower pressure angle, finer pitch, etc.) tend to reduce the tooth section. To offset this reduction in tooth section, Sikorsky Aircraft strengthened the tooth by increasing the pressure angle on the coast side, forming an asymmetrical, buttress-shaped tooth. High-contact-ratio buttressed gears offer the potential payoffs of increased strength and decreased noise level.

The advantage of CBS-600 as a potential gear material is its high temperature capability compared with 9310 steel (fig. 13). Although CBS-600 sacrifices some hot hardness when compared with other steels, its relatively low alloy compositions and high fracture toughness properties (fig. 14), warranted its evaluation for helicopter transmission gearing.

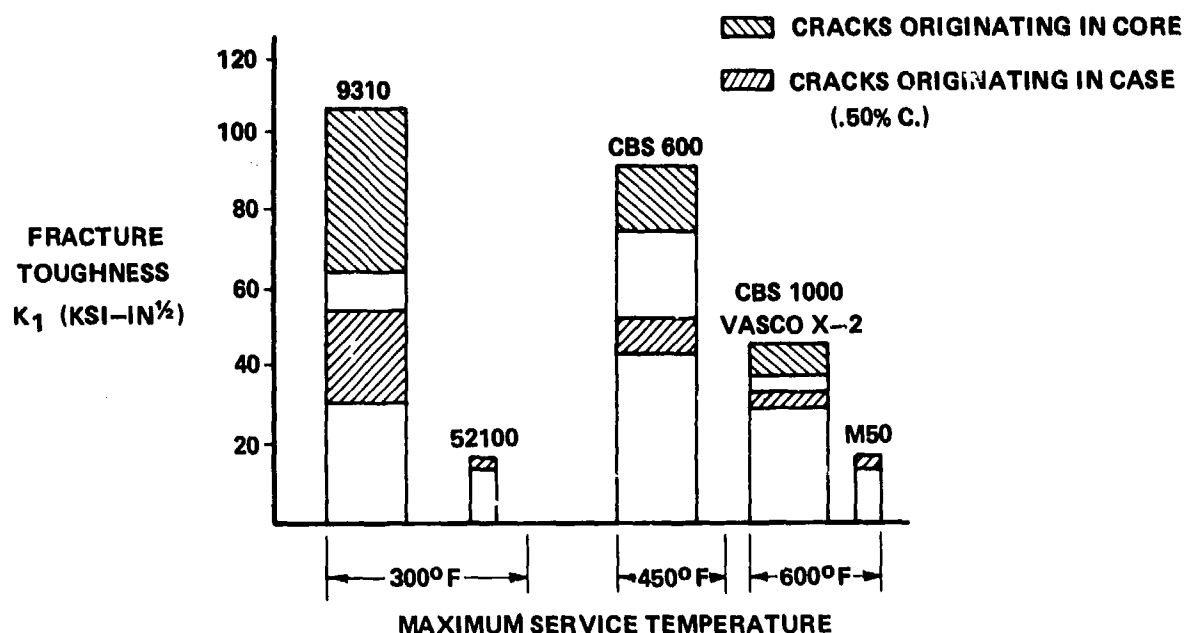


Figure 14. - Material fracture toughness comparison.

TABLE 2 MATERIAL AND TOOTH FORM COMBINATIONS

MATERIAL	TOOTH FORM
9310	HCR BUTTRESS
9310	STANDARD
CBS 600	HCR BUTTRESS
CBS 600	STANDARD

Gear-Tooth-Form and Material Evaluation Testing

The test program evaluated the improved gear tooth form and also determined the suitability of the hot-hardness steel as an aircraft-quality gear material. The evaluation test program consisted of two types of fatigue tests. The first was a series of constant-load dynamic tests on four gear configurations (table II) to determine their relative lives at a particular load level. The second fatigue test evaluated the CBS-600 material at variable load levels with a sufficient number of test points to generate a load-cycle curve for this material.

The 6.0-inch-diameter standard spur gear specimen (the baseline gear) had an 8-pitch symmetrical gear tooth with a $22\frac{1}{2}^\circ$ pressure angle and a tooth contact ratio of 1.628. The advanced gear tooth was also 8-pitch with an asymmetric (buttress) shape, drive side pressure angle of 20° , coast side pressure angle of 25° , and with a contact ratio of 2.322. The CBS-600 is a case-hardening, carburizing bearing steel with superior hot-hardness characteristics compared with the standard 9310 (AMS 6265) steel.

Sikorsky tested the gears in its regenerative 6-inch gear test facility and tested two pairs of test gears simultaneously. The test stand is illustrated pictorially and schematically in figures 15 and 16. Torque loading of the enclosed gear train loop was achieved during operation by applying an axial load, through a calibrated hydraulic cylinder, to a pair of sliding helical gears in the main gearbox. A constant-speed motor and an electric clutch provided the rotational speed and torque required to overcome bearing and gear frictional losses. The output of the clutch was controllable and allowed operation of the test gears at speeds to 8000 rpm. A separate lubrication/cooling system, consisting of reservoir, oil pump, filter, and heat exchanger was used for each set of test gears. A 40-micrometer filter in each supply maintained oil cleanliness and prevented oil jet blockage. The test gears were lubricated and cooled by both in-to-mesh and out-of-mesh jets.

This facility was equipped with automatic shutdown and data recording features which allowed unattended operation for extended periods. A low-oil-pressure switch protected the facility from failure due to malfunctioning oil pumps, ruptured oil lines, or low oil level. Excessive oil temperature would also activate the shutdown sequence. Magnetic chip detectors were incorporated in the sump to stop the test should magnetic particles enter the lubrication system. A unique feature of this shutdown system was a missing tooth detector. This device compared an input signal from a magnetic tooth counter to an internal signal generated by an oscillator. If a tooth fractured, the comparison on the cycle would trigger a flip-flop that would trip the motor relay to shut off the machine. The time from detection to relay shutoff was approximately equal to the relay closing time, thus limiting possible second debris damage. Accelerometers were also installed to detect vibrations occurring as a result of fatigue spalling. Vibration levels exceeding preset limits would also activate the shutdown system.

Test Procedures and Results

Dynamic gear testing was continued until either failure occurred or 10^7 cycles were completed. In the event that only one gear of a pair failed, both gears were replaced. Gear pairs and the position on the gear tester were randomly selected. The first series of tests on the four gear configurations were

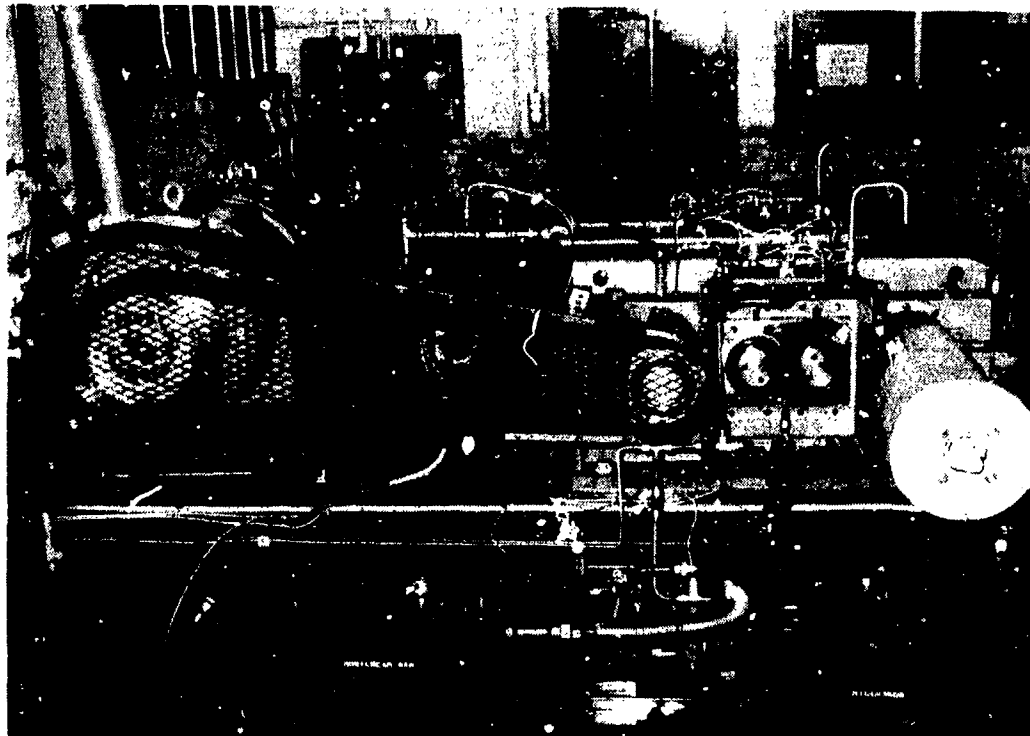


Figure 15. - Sikorsky 6-inch dynamic test facility.

conducted at a 2500 pound tangential tooth load. The results of these screening tests are shown in figure 17. These are Weibull plots of the test data derived using linear regression analysis to determine the best fit line. Based on the life comparison at a 50 percent failure rate, the relative life ranking of the four configurations are 9310 HCR buttress, 62; CBS-600 HCR, 10; CBS-600 standard, 4; and 9310 standard, 1. These plots show the considerable life advantage attributable to the HCR buttress tooth form. All of the gears tested, whose failure times are summarized in figure 17, exhibited the same failure mode—root bending fatigue. No surface pitting was evident in any of the test gears at the 2500-pound load level. The projected strength advantage of the 9310 HCR buttress gears, compared with the baseline, calculated by drawing standard S-N curve shapes through the test data, and for endurance limits at 10 cycles, was approximately 19 percent, a substantial improvement. The benefits shown, however, for CBS-600 material indicate a Weibull slope of less than 1.0, which is uncharacteristic of material fatigue tests of this kind. This may indicate the presence of another failure mechanism which is different from the classical fatigue failure mode. Additional testing is planned to thoroughly evaluate this material and to determine the significance of the low Weibull slopes.

The second dynamic fatigue tests were designed to determine the load/life characteristics of the CBS-600 materials. A sample of 42 gears was tested at various load levels to failure or run out at 10^7 cycles, whichever occurred first. The results of these tests are shown in figure 18. Similar test data for the 9310 HCR buttress configuration are not yet available to compare endurance limit loads or allowable operating stresses.

During the initial testing of the CBS-600 steel gears, capping of the gear teeth occurred. Capping is the separation of a tooth corner at the intersection of the tip and tooth end face. Subsequent CBS-600 gears were machined with a full 0.03-inch edge break on the gear teeth. It was reasoned that by increasing the edge break, the load at the edge of the tooth would be relieved and redistributed over a larger area, thus reducing the possibility of tooth tip fractures. Similar capping did not occur for the 9310 material.

During the initial dynamic fatigue tests, some slight scuffing was noted on the tooth tips of the HCR buttress gears. Because of this tendency to scuff, the tip profile modification on the CBS-600 HCR buttress gears was increased before running the load/cycle fatigue tests. This modification

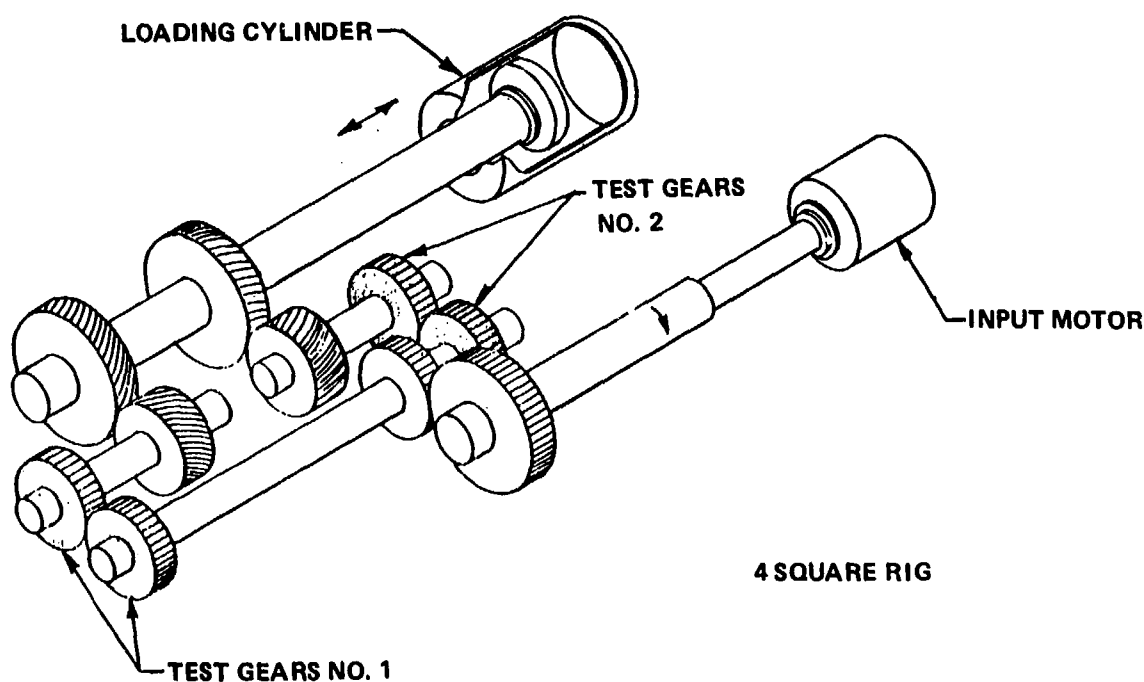


Figure 16. - Test facility schematic.

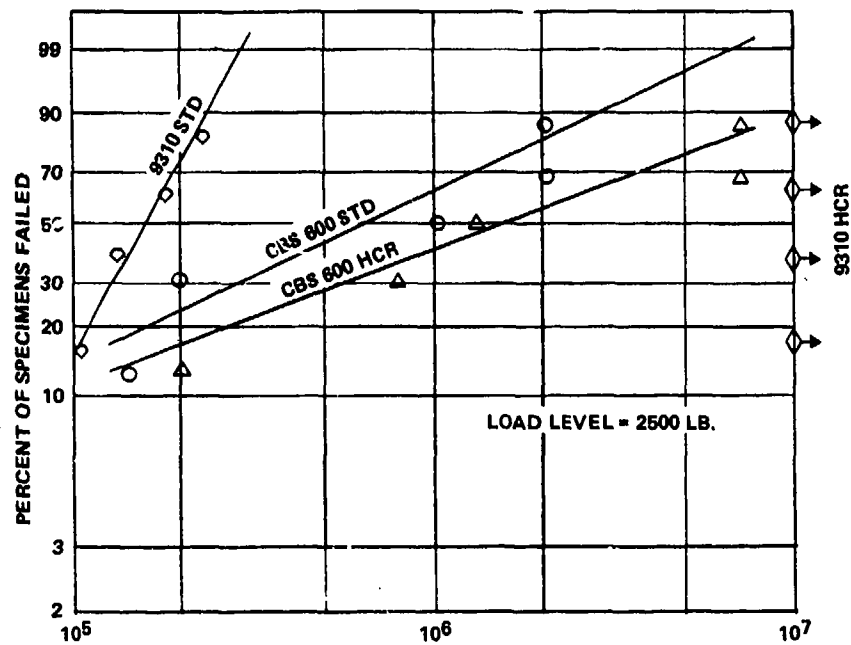


Figure 17. - Results - constant load fatigue tests.

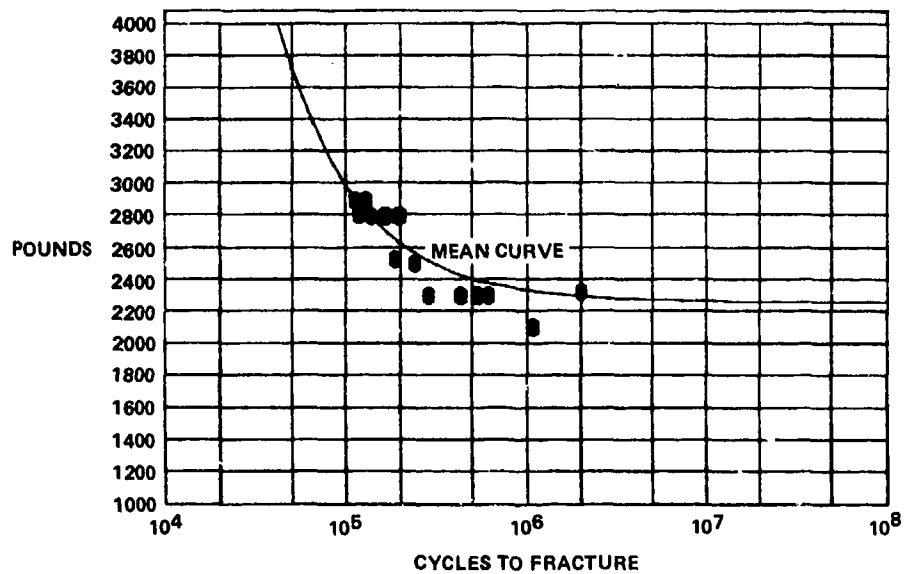


Figure 18. - Results - Load/cycle fatigue tests for CBS-600.

allowed for the greater-than-anticipated deflection of the HCR gears at the high loads and prevented load concentration in the upper portion of the tooth profile. Unfortunately, gears relieved to run well at the high load level suffer somewhat at the lower loads and can result in a lower endurance limit. This is particularly true of HCR gears which are more sensitive to tooth errors and profile modification than standard tooth form gears.

System Integration Tests

Sikorsky Aircraft will conduct the system integration tests using a Black Hawk main transmission that includes the fabricated stainless-steel housing, the advanced, thrust-carrying, cylindrical roller bearing, and the HCR buttress-tooth-form planetary made from CBS-600 steel. The purpose of these tests is to determine the capability of these advanced components to operate compatibly with the other Black Hawk main transmission dynamic components.

This series of tests will be conducted in the Black Hawk main transmission regenerative test facility. The test transmission will be connected through interconnecting shafts to a dummy aircraft main transmission and commercial gearboxes that subject the test gearbox to torque loads simulating and exceeding flight loads. Sliding helical gears in the commercial gearboxes control the input and tail rotor torque loads. Direct current electric motors provide rotational speeds up to 110 percent times normal aircraft rated speed. Thirty-eight thermocouples will monitor oil, bearing, gear, and housing temperatures. Sikorsky will also monitor oil pressure and flow, torque, and vibration.

A lubrication test will verify proper operation of the gearbox lubrication system and will include measurements of temperature, flow rates, and pressures that will be compared with baseline test data. A preliminary load test will verify acceptable transmission performance and will consist of loading the system incrementally up to full load at operating speed and then comparing test data with baseline test data. Disassembly of the transmission after completion of this test will permit a visual examination of gear patterns, then we will conduct a 10-hour evaluation test at Black Hawk qualification loads. At the completion of this evaluation test, we will conduct a split inspection of the gearbox to determine the condition of the test components. An oil cooler bypass test will evaluate the high-temperature operating capabilities of the advanced bearing design, fabricated housing and HCR buttress-tooth-form planetary gears for 10 hours or until the oil temperature reaches 400° F, whichever occurs first.

The results of these tests will be published in a forthcoming report.

Conclusions

The fabricated stainless-steel housing provides a lightweight, high-temperature capability, improved life cycle cost, corrosion resistant approach to helicopter gearbox housing application. The thrust-carrying cylindrical roller bearing offers a viable solution for high-speed operation under load conditions that include both thrust and radial loads. The HCR buttress-tooth-form gearing demonstrated superior strength over the baseline standard spur tooth form regardless of material selection; also, CBS-600 is suitable gear material for high-temperature operation. This investigation presents the helicopter transmission designer with three advanced components to use as design options and an advanced hot-hardness gear material to use after its design allowables are established.

Design of an Advanced 500-hp Helicopter Transmission*

Charles E. Braddock† and Roy A. Battles†

The emphasis on the design of the NASA/Bell Helicopter Textron (BHT) 500-hp advanced technology demonstrator transmission, which subsequently will be referred to as the 500-hp transmission, was placed on designing a 500-hp version of the OH-58C 317-hp transmission that would have the capabilities for a long, quiet life at a minimum increase in the cost, weight, and space that usually increases along with power increases. This was accomplished by implementing advanced technology that has been developed during the last decade and making improvements dictated by field experience.

These advanced technology components, concepts, and improvements and their anticipated effect on the 500-hp transmission are:

- High contact ratio spur gear teeth in the planetary will tend to reduce the noise level and increase gear life.
- Spiral bevel gears made of cleaner gear steels, stronger gear steels, vacuum carburized, shot peened for increased gear tooth pitting fatigue life, as well as gear tooth bending fatigue strength, and lubricated with Aerosheli 555 oil will save weight and space and increase gear life.
- Bearings made of cleaner steels in conjunction with improved analytical tools required to predict the effect of these cleaner steels and other variables on the fatigue life of a bearing will save weight and space and increase the reliability.
- The investment cast planet carrier, hot isostatic pressed, as a replacement for the planet carrier made of two-piece construction of forging and plate stock will reduce cost.
- *Improvements in* The investment cast stainless-steel top case, also hot isostatic pressed and shot peened, will provide maximum corrosion resistance, excellent fatigue strength, no significant creeping, and good strength-to-weight ratio, all at a reasonable cost.
- The cantilever-mounted planetary ring gear has no working spline to generate wear debris; it isolates the meshing teeth from the housing for noise reduction; and it provides a soft mount for a more uniform load distribution among the planets.
- The sun gear still has its working spline; however, it is crown hobbled and hardened and will be submerged in a bath of flow-through oil, which should prevent the spline from wearing.
- The straddle-mounted bevel gear will enable higher torques to be transmitted without destroying the tooth contact patterns.

Figure 1 shows the 500-hp transmission, and figure 2 shows the 317-hp transmission; the latter is shown without the dummy mast and the mast ball bearing. Not shown on the 500-hp transmission, but a part of it, is the oil pump and hydraulic pump drive quill identical to that shown on the 317-hp transmission.

The system of units used for the principal measurements and calculations for the data in this paper are the customary units and these are shown in parentheses.

High Contact Ratio Spur Gear Planetary

High contact ratio (HCR) spur gearing is not new; however, the first application of this concept by BHT was the transmission for the Model 222, designed in 1974. There are approximately 50 Model 222 helicopters in service at this writing, with the HCR spur gears in the planetary. The Model 222

*Work performed under NASA contract NAS3-21595.

†Bell Helicopter Textron.

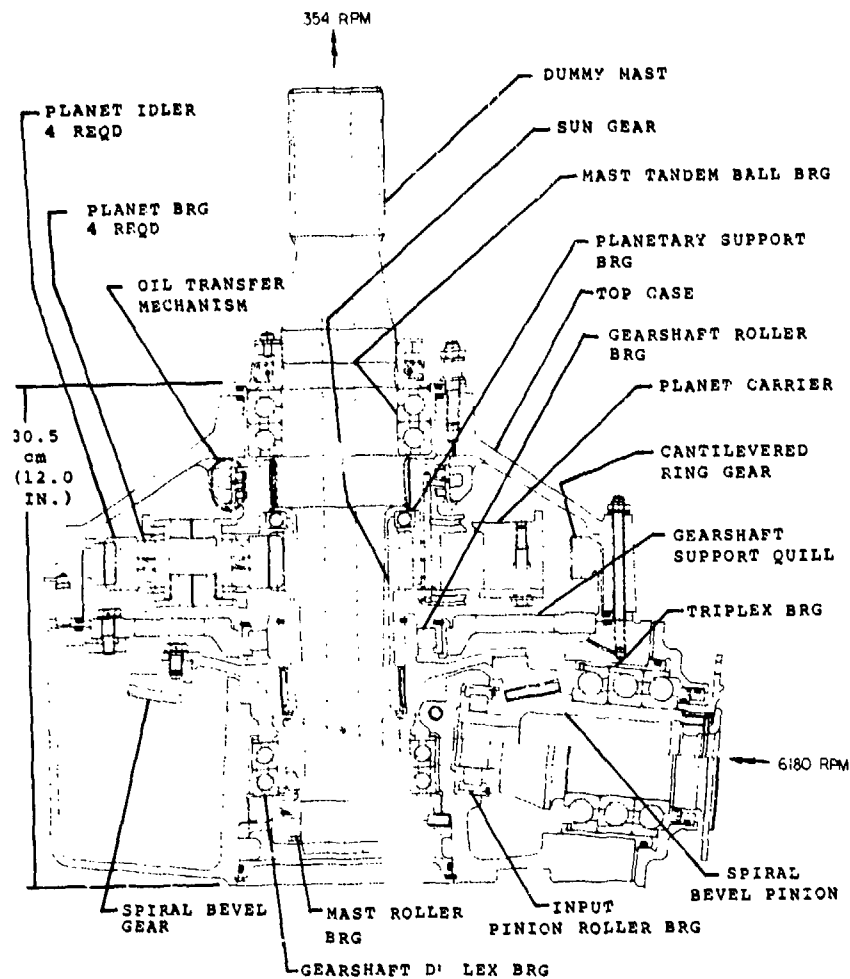


Figure 1. - NASA/BHT 500-hp transmission.

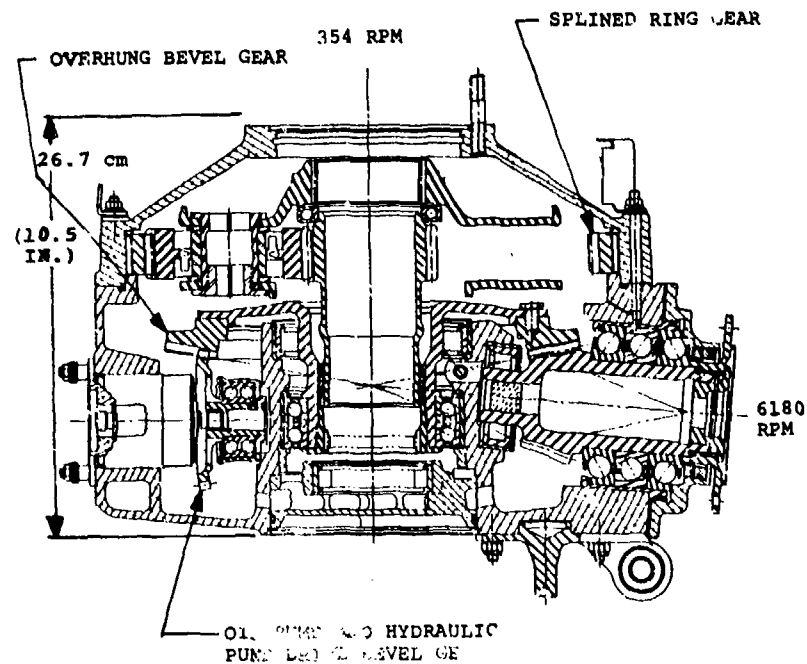


Figure 2. - OH-58C 317-hp transmission.

planetary is the same size and ratio as the final stage standard (STD) spur gear planetary in BHT's XV-15 tilt rotor aircraft transmission designed in 1969. The reason for selecting the HCR design over the STD design for the Model 222 is summarized in table 1. A study performed by BHT showed that when both planetaries are sized to transmit the same torque with identical gear tooth root bending fatigue stresses (per AGMA with all K-factors equal to 1), the HCR spur gear planetary is lighter, generates less noise, and has a longer life. The tooth numbers and the ratio of the Model 222 planetary made it easy to transform an STD design into an HCR design.

To advance the technology of planetary gearing, NASA Lewis contract NAS3-21595 specified that the planetary for the NASA/BHT 500-hp transmission be of an HCR design. NASA Lewis was aware that BHT had the HCR planetary designed, developed, and in production for the Model 222, and they were equally aware that it would not be feasible to transform all STD planetary designs into HCR designs because of the effects that the numbers of teeth and the ratio have on the transformation. Table 2 shows some basic data for the STD planetaries in the XV-15 transmission and the 317-hp transmission. Notice that the sum of the numbers of teeth of the sun gear and planet idler is 91 for the XV-15 transmission and 62 for the 317-hp transmission. Referring to figure 3, one can readily see the effects of the sum of the numbers of teeth on the profile contact ratio. The profile contact ratio of a gearset is defined as the number of times the base pitch is contained in the active length of line of action. Therefore, the maximum profile contact ratio on a particular gearset exists when the active length of line of contact is equal to the total length of line of contact, that is, when the active length of contact extends from the tangency point on the base circle of one gear to the tangency point on the base circle of the mating gear. Figure 3 shows that the maximum profile contact ratio on the 48×43 gearset (48-tooth sun gear driving a 43-tooth planet) is 5.27 as compared with only 3.59 for the 27×35 gearset.

Figure 3 also shows the active line of action for a contact ratio of 2.000 on each gearset. Even though both active lines of contact are centered about the pitch point (that is, the approach action zone and the recess action zone are equal), it can be seen that more flexibility exists for the 48×43 gearset should it be desirable to shift the active portion of the line of action more into the recess action zone. Any significant amount of shifting of the active line of contact on the 27×35 gearset will result in large increases in sliding velocities since the ends of the active line of contact (the first and last points of contact) are relatively close to the base circles of the two gears.

It can be shown that the maximum profile contact ratio for different gearsets varies directly as the sum of their numbers of teeth. It can also be shown that there are only two variables that affect the maximum profile contact ratio: the sum of the numbers of teeth of the gearsets and their pressure angle. The increase in either variable causes an increase in the maximum profile contact ratio.

The discussion to this point has made no mention of the physical limitations that usually prevent a gearset from having the maximum profile contact ratio. These limitations are pointed teeth (zero top land width), teeth too thin on one member or the other, and root clearance. At the higher

TABLE 1. COMPARISON OF A STANDARD AND A HIGH CONTACT RATIO SPUR GEAR PLANETARY

	WT, Kg(lb)	EFF, %	NOISE, db	LIFE
Standard (XV-15 Final Stage)	18 (40)	99.7	X	X
High Contact Ratio (Model 222)	17 (38)	99.4	X-9.5	2X

Both planetaries are sized to transmit the same torque with the same gear tooth bending stresses.

TABLE 2. BASIC DESIGN DATA FOR THE STANDARD PLANETARIES IN
THE XV-15 TRANSMISSION AND THE 317-HP TRANSMISSION

XV-15 TRANSMISSION

	Sun	Planet	Planet	Ring
Number of teeth	48	43	43	138
Diametral pitch	11.375	11.575	11.875	11.875
Pressure angle, deg	24.95	24.95	18.82	18.82
Pitch diameter, cm(in.)	10.7183 (4.2198)	9.6017 (3.7802)	9.1976 (3.6211)	29.5176 (11.6211)

317 HP TRANSMISSION

	Sun	Planet	Planet	Ring
Number of teeth	27	35	35	99
Diametral pitch	8.8571	8.8571	9.1429	9.1429
Pressure angle, deg	24.60	24.60	20.19	20.19
Pitch diameter, cm(in.)	7.7424 (3.0484)	10.0371 (3.9516)	9.7234 (3.8281)	27.5034 (10.8281)

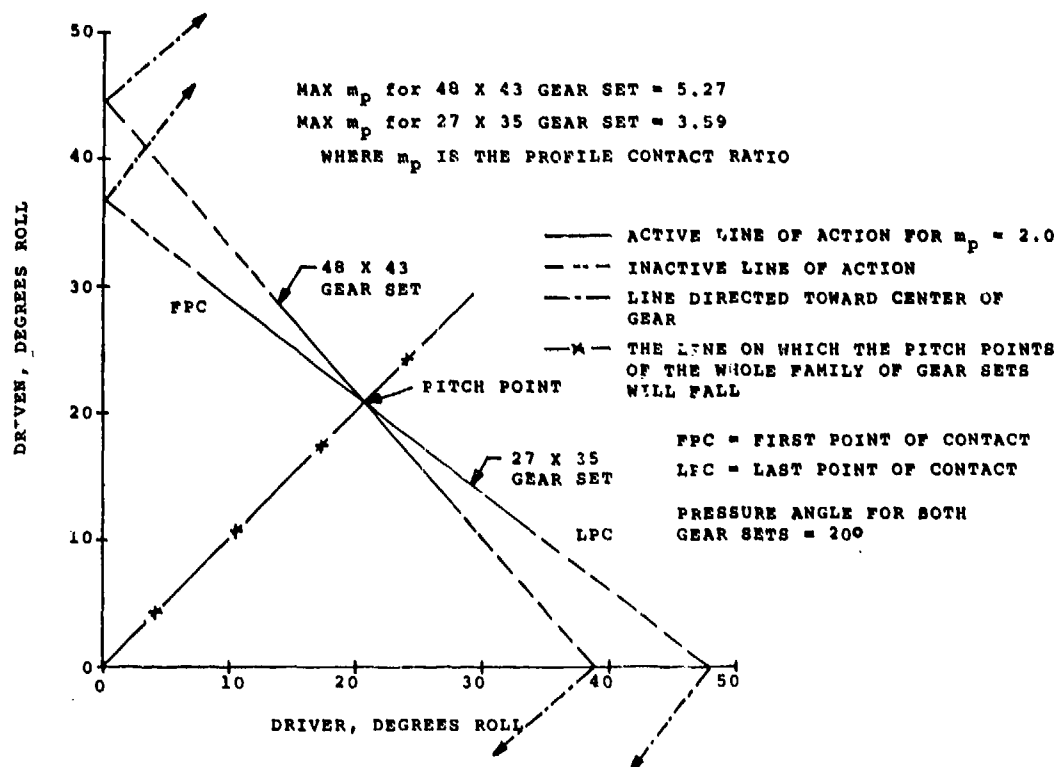


Figure 3. - Relationship of tooth contact ratios on gearsets of different numbers of teeth but with equal pressure angles.

pressure angles, the teeth become pointed. When the teeth on one member are increased in thickness to prevent them from becoming pointed, the root clearance is reduced, and the teeth on the mating gear become thinner and weaker.

Table 3 shows the design data for the selected planetary gears for the 500-hp transmission. The gears are shown in figure 1. Several iterations were made in the selection process: two at a pressure angle of 18° and one each at pressure angles of 20°, 22°, and 24.95°. The 20° pressure angle resulted in the best compromise between top land width, tooth thickness, and root clearance.

Table 4 shows the stress analysis (per AGMA) of the selected planetary gears, and for comparison the stress analysis of the planetary gears in the 317-hp transmission is also shown. The significance of this comparison is that for the same weight (the corresponding gears have equal face widths) both the planetaries appear to be capable of meeting their performance requirements. Even though the 500-hp planetary is more highly stressed, it does not exceed the allowables used at BHT. But the comparison between an HCR and STD gear planetary can be made only if they are sized to some common baseline such as the same torque with equal tooth bending stresses or the same torque with equal weights. The latter method will be used in this case as the 500-hp planetary of HCR design is compared with the 317-hp planetary of STD design. Their weights are equal, and, to make their torques equal, the 317-hp planetary will be stressed at the 500-hp level. The results can be seen in table 4. The tooth bending stress of 367 MPa (53 200 psi) on the planet of the 500-hp transmission is the most severe of the bending stresses because of the reversed bending that is inherent in a planet idler. This value is 1 percent higher than the bending stress of 363 MPa (52 600 psi) on the 317-hp planet operating at 500 hp; however, it is still below the allowable used at BHT.

The Hertz stress of 1420 MPa (205 900 psi) on the sun-planet mesh of the 317-hp transmission operating at 500 hp is the most severe of the compressive stresses. This value is 10 percent higher than the Hertz stress of 1286 MPa (186 500 psi) on the 500-hp planet. Transforming these compressive stress values into gear tooth pitting lives, using the relationship that the life is inversely proportional to the Hertz stress raised to the 5.22 power, shows that the L_{10} life of the 317-hp planetary sun-planet mesh operating at 500 hp is only 60 percent of the L_{10} life of the same mesh in the 500-hp planetary.

TABLE 3. BASIC DESIGN DATA FOR THE HCR PLANETARY IN THE 500-HP TRANSMISSION

	Sun	Planet	Planet	Ring
Number of teeth	27	35	35	99
Diametral pitch	8.8571	8.8571	9.1429	9.1429
Pressure angle, deg	20	20	14.0682	14.0682
Pitch diameter, cm (in.)	7.7429 (3.0484)	10.0371 (3.9516)	9.7234 (3.8281)	27.5034 (10.8281)
OD/ID, cm (in.)	8.623 (3.395)	10.668 (4.200)	10.668 (4.200)	27.292 (10.745)
Root diameter, cm (in.)	7.036 (2.770)	9.080 (3.575)	9.080 (3.575)	28.537 (11.235)
Face width, cm (in.)	3.492 (1.375)	3.178 (1.251)	3.178 (1.251)	2.540 (1.000)
Top land width, cm (in.)	.114 (.045)	.076 (.030)	.076 (.030)	.372 (.147)
Contact ratio	2.086		2.086	
Number of planets	4			

TABLE 4. STRESS ANALYSIS OF THE PLANETARY GEARS IN
THE 317 HP AND 500 HP TRANSMISSIONS AND IN
THE 317 HP TRANSMISSION OPERATING AT 500 HP

	Tangential load, N (lb)	Bending stress, MPa (psi)	Hertz stress, MPa (psi)
<u>500 hp Trans.</u>			
Sun	14,176 (3,187)	253 (36,700)	1,286 (186,500)
Planet/Sun	14,176 (3,187)	325 (47,200)	1,286 (186,500)
Planet/Ring	14,629 (3,289)	367 (53,200)	859 (124,600)
Ring	14,629 (3,289)	381 (55,200)	859 (124,600)
<u>317 hp Trans.</u>			
Sun	8,989 (2,021)	201 (29,100)	1,131 (164,000)
Planet/Sun	8,989 (2,021)	230 (33,400)	1,131 (164,000)
Planet/Ring	9,274 (2,085)	214 (31,000)	698 (101,300)
Ring	9,274 (2,085)	285 (41,300)	698 (101,300)
<u>317 hp Trans. Oper. @ 500hp</u>			
Sun	14,176 (3,187)	316 (45,800)	1,420 (205,900)
Planet/Sun	14,176 (3,187)	363 (52,600)	1,420 (205,900)
Planet/Ring	14,629 (3,289)	336 (48,800)	878 (127,000)
Ring	14,629 (3,289)	449 (65,100)	878 (127,300)

(This comparison in life is no doubt dependent on the sliding velocity; however, since the effect of sliding velocity on pitting life is unknown at this time, no attempt will be made to adjust the pitting life ratio. The maximum sliding velocity at the sun-planet mesh is 234 cm/s (92 in/s) on the 500-hp HCR design and 163 cm/s (64 in/s) on the 317-hp STD design.)

Thus, it appears that an HCR spur gear planetary in the 500-hp transmission will have 1.68 times the gear tooth pitting life of a STD spur gear planetary in the 317-hp transmission operating at 500 hp. But the anticipated weight saving did not materialize. In fact, if the two planetaries had been sized for the same torque and the same tooth bending stress, the 500-hp HCR planetary would have been heavier than the 317-hp STD planetary operating at 500-hp. As shown in table 1, there was a weight saving in transforming the XV-15 STD planetary into the model 222 HCR planetary. This is attributed to the large numbers of teeth in the sun and planet gears and to the favorable ratio of the same gearset.

Spiral Bevel Gears

When a new spiral bevel gearset is required, the normal routine is to design it, test it, and put it into service. Any design or manufacturing deficiencies uncovered during the testing phase are corrected and the testing phase repeated. Little has been done in the last decade to change this routine except in the area of developing finite-element analysis and stress measurement techniques to aid in designing large spiral bevel gears where the tendency is to minimize gear tooth backup material and the web thickness in order to save weight. Thus, except for specialized applications, the real technological advancements in recent years that have affected, or that have the potential to affect, spiral bevel gears have to be the use of cleaner gear steels, stronger gear steels, vacuum carburization, and shot peening for increased gear tooth pitting fatigue life as well as gear tooth bending fatigue strength, and the use of Aeroshell 555 oil for increased gear tooth pitting fatigue life.

The bevel gears in the 500-hp transmission take advantage of all five of these technological advancements as the gears increase in power capabilities with no change in size. The bevel gears will be made from two different types of steels: VIM VAR 9310 and VIM VAR EX-00053. Both steels will be produced by the vacuum induction melt (VIM) process followed by the vacuum arc remelt (VAR) process. The gears will be shot peened after finish grind, and the gears will be lubricated with Aeroshell 555 oil.

The bevel gears in the 500-hp transmission are identical in size to those in the 317-hp transmission. Figure 1 shows the bevel gears and table 5 shows the stress analysis data on the same bevel gears operating in both transmissions. Shown also are the allowables that are generally used as guidelines at BHT. As can be seen, the bending stress on the pinion at 500 hp is 327 MPa (47 408 psi), 13 percent above the allowable of 290 MPa (42 000 psi) for spiral bevel gears made of VAR 9310 and conventionally (atmospheric) carburized, ground, and shot peened. There are two methods by which the 13 percent increase is planned to be overcome. One is using VIM VAR 9310, vacuum carburized, ground, and shot peened. The other is using VIM VAR EX-00053, vacuum carburized, ground, and shot peened. BHT is actively engaged in an internal R&D program to determine the magnitude of these benefits by performing single-tooth bending fatigue tests on 10-pitch spur gear teeth on a Sonntag machine. Table 6 shows how this will be accomplished. All tests are scheduled to be completed by the end of 1982.

In the process of designing the bevels for the 500-hp transmission, it was assumed that the combination of VIM VAR 9310 steel and vacuum carburizing would account for the tooth bending stress being 13 percent above the allowable for VAR 9310 and conventional carburizing. Data exist that allow substantial increases in gear tooth bending fatigue strength design limits for gears made of VAR 9310 versus air melt steels. Coleman (ref. 1) states that testing performed by Gleason Works justifies an increase of 78 percent in the allowable tooth bending stress for carburized VAR 9310 gears over carburized air melt steel gears. The degree of cleanliness going from air melt to VAR is no doubt much larger than going from VAR to VIM VAR; however, only 13 percent increase in strength is required.

Relative to vacuum carburizing, BHT had some fine pitch helical gears vacuum carburized and metallurgically evaluated. A higher carbon gradient was easily obtained with vacuum carburizing. This provides for more R_c 60 depth in the root fillet area of the teeth where the maximum bending stresses are present. Thus, it is anticipated that there will be some gain in tooth bending fatigue strength by vacuum carburizing. This gain would be in addition to the primary reason that vacuum carburizing is becoming so popular: cost and energy savings, which is clearly a technological advancement.

Should the combination of VIM VAR 9310 and vacuum carburizing not produce the 13 percent more bending fatigue strength required, backup bevel gears made of the new stronger VIM VAR EX-00053 gear steel are being provided. Although not thoroughly tested yet, indications are that conventional carburized VIM VAR EX-00053 is stronger than conventional carburized VAR 9310 (ref. 2). Whether the indicated increase in strength is due to material difference or steel processing difference (VAR versus VIM VAR) is not yet known; however, it is assumed at this time that the VIM VAR EX-00053 is stronger than the VIM VAR 9310. In addition to its strength, EX-00053 is a moderately high hot hardness material (tempered at 533 K (500° F)) and exhibits excellent fracture toughness properties (especially at normal transmission operating temperatures of 366 K (200° F)): 262 MPa \sqrt{m} (238 ksi \sqrt{in}) for EX-00053 as compared with 85 MPa \sqrt{m} (77 ksi \sqrt{in}) for CBS 600; 125

MPa \sqrt{m} (114 ksi \sqrt{in}) for CBS 1000; 60 MPa \sqrt{m} (55 ksi \sqrt{in}) for Vasco X-2M and 110 MPa \sqrt{m} (100 ksi \sqrt{in}) for 9315. These data were taken from figure 25 in reference 3. The 9310 steel was not included in the Terratek work; however, the 9315 is probably close enough for a good comparison.

TABLE 5. STRESS ANALYSIS DATA ON THE SAME SPIRAL BEVEL GEARS AT TWO POWER LEVELS: 317 HP AND 500 HP

	Bending stress, MPa (psi)	Hertz stress, MPa (psi)	Calculated temp. rise, K (°F)
317 hp: Pinion	207 (30,057)	1,474 (213,728)	410 (277)
Gear	171 (24,868)		
500 hp: Pinion	327 (47,408)	1,851 (268,421)	449 (348)
Gear	270 (39,223)		
Allowables:			
VAR 9310	241 (35,000)	1,551 (225,000)	443 (338)
VAR 9310, Shot peened	290 (42,000)	1,668 (242,000)	443 (338)
VAR 9310, Shot peened, Aeroshell 555 oil	290 (42,000)	2,275 (330,000)	?

The allowable hertz stress values shown are the values for L_{10} life of 10^9 cycles.

For other L_{10} lives, use the following relationship:

$$L_{10} \propto \left(\frac{1}{\text{Hertz stress}} \right)^{5.22}$$

TABLE 6. BHT IR&D PROGRAM FOR SINGLE TOOTH BENDING FATIGUE TESTS ON VARIOUS MATERIALS AND PROCESSES (ALL SPECIMENS ARE SHOT PEENED)

Gear specimen material	Carburizing method	Carburizing temp., K (°F)	Quenching medium	Shot peen intensity, cm (in.)
VAR 9310	Conventional	1200 (1700)	Oil	.029A (.008A)
VAR 9310	Vacuum	1200 (1700)	Oil	.020A (.008A)
VIM VAR 9310	Conventional	1200 (1700)	Oil	.020A (.008A)
VIM VAR 9310	Vacuum	1200 (1700)	Oil	.020A (.008A)
VIM VAR 9310	Vacuum	1311 (1900)	Oil	.020A (.008A)
VIM VAR EX-00053	Conventional	1144 (1600)	Air	.020A (.008A)
VIM VAR EX-00053	Conventional	1144 (1600)	Oil	.020A (.008A)
VIM VAR EX-00053	Conventional	1144 (1600)	Oil	.033A (.013A)
VIM VAR EX-00053	Vacuum	1144 (1600)	Oil	.020A (.008A)

Referring again to table 5, one can see that the Hertz stress of 1851 MPa (268 421 psi) on the 500-hp gearset is significantly above the allowable normally used at BHT. There are two areas of advanced technology achievements that are being used to overcome the detrimental effects of the high compressive stresses: shot peening and Aeroshell 555 oil. Neither of these technological achievements are new; however, the effect of each on the gear tooth pitting fatigue life in helicopter transmissions has been only recently determined. This was done by a joint effort of NASA Lewis and BHT. With regard to shot peening, it has been known for many years that shot peening the root fillet areas of carburized gear teeth increases the tooth bending fatigue endurance limit by about 20 to 50 percent, but the effect of shot peening on tooth pitting fatigue life were not known. Thus, in 1980, NASA Lewis provided the ground-carburized spur gear specimens made of VAR 9310 steel. BHT did the shot peening on the roots and the working surfaces of the gear teeth, and NASA Lewis performed the tooth pitting tests on their gear test rigs. The results showed a 50 percent increase in the L_{10} life over unpeened gears of the same lot.

With regard to Aeroshell 555 oil, it has also been known for many years that the relatively low pitting life on helicopter transmission gears was primarily the result of being forced, for logistical reasons, to use either the MIL-L-7808 or MIL-L-23699 synthetic lubricants developed specifically for turbine engine use. These engine oils caused the gear designer to demand smoother and smoother ground tooth surfaces over the years, and finally, honed teeth in attempting to maintain separation of gear tooth contacts in low-speed final drive applications. In recent years in the commercial market where the customer is more concerned about transmission overhaul intervals (TBO) than whether the transmission and the engine use the same oil, the trend is shifting to oils of the same viscosity but containing friction modifiers in special additive packages. Aeroshell 555, a 5×10^{-6} m²/s (5 cS) synthetic oil, falls into this category. In 1980 NASA Lewis again provided the carburized and ground spur gear specimens made of VAR 9310 steel, BHT furnished four different types of oil, and NASA Lewis again performed the gear tooth pitting tests. One of the oils was Aeroshell 500, which is qualified to the MIL-L-23699 specification. This oil was used as the reference oil. The results of the tests showed Aeroshell 555 oil the best with a 500 percent increase in the L_{10} life over the Aeroshell 500 reference oil. Transforming this 500-percent increase in life into a higher allowable Hertz stress (as shown in table 5) was done using the relationship that the life is inversely proportional to the Hertz stress raised to the 5.22 power. Thus, the allowable Hertz stress of 2275 MPa (330 000 psi) is significantly higher than the 1851-MPa (268 421-psi) operating stress shown for the 500-hp condition. Treating this 500-percent increase in life as a life adjustment factor of 5 at the L_{10} level also shows that the use of Aeroshell 555 oil is sufficient to overcome the increase in Hertz stress:

$$\frac{L_{10} \text{ 317 hp}}{L_{10} \text{ 500 hp}} \propto \left(\frac{500 \text{ hp}}{317 \text{ hp}} \right)^{5.22/2} = 3.29$$

which is less than 5.

The last column in table 5 (the calculated temperature rise of the tooth contacts of the bevel gearset, an indication of the gear tooth scoring tendency) shows that the value of 449 K (348° F) for the 500-hp gearset is 6 K (10° F) higher than the allowable of 443 K (338° F), which is the highest ever used at BHT. The allowable was established on a bevel gearset operating in MIL-L-23699 oil. Since Aeroshell 555 oil contains friction modifiers in its additive package that should reduce the amount of heat generated at the tooth contacts, thereby reducing the temperature rise, no problem is anticipated in exceeding the allowable shown by only 1.3 percent K (3.0 percent °F).

Thus, it appears that the advancements in technology of cleaner steels, stronger steels, vacuum carburizing, shot peening, and better oils can combine to allow a spiral bevel gearset, originally designed for 317 hp, to operate safely at 500 hp. The Hertz stress allowable increased in greater proportion than the Hertz stress such that the 500-hp bevel gearset has a 2.25 longer L_{10} life than the 317-hp bevel gearset. However, in the tooth bending category, the story is different. Battles (ref. 2) shows the rotating beam mean strength of oil-quenched EX-00053 to be 21 percent higher than that of AMS 6265 (VAR 9310). If this turns out to be true on gear teeth, then the allowable tooth bending stress for shot peened EX-00053 spiral bevel gears will be 350 MPa (50 800 psi) (which is larger than the 327-MPa (47 408-psi) bending stress on the 500-hp bevel pinion), but the tooth bending margin of safety on the 317-hp bevel pinion has dropped down to 0.07 on the 500-hp bevel pinion. If vacuum carburizing EX-00053 could raise its tooth bending strength 9 percent, then the allowable

would be 381 MPa (55 300 psi), and the margin of safety would go back up to 0.17. Thus, whether or not the above advancements in technology will cover the 58 percent increase in tooth bending stress from the 317-hp transmission to the 500-hp transmission, without reducing the margin of safety will depend largely on the effects of vacuum carburizing.

Bearings

Probably the two most important recent technological advancements in the area of rolling element bearings are cleaner steels and improved analytical tools to predict the effect of these cleaner steels and other variables on the fatigue life of a bearing. An example of a cleaner bearing steel for the aircraft industry is the contemporary M-50 tool steel produced by the vacuum induction melt (VIM) process followed by the vacuum arc remelt (VAR) process. This bearing steel is usually referred to as VIM VAR M-50 steel. Some tests on high-speed ball bearings made of VIM VAR M-50 and operating in a 5×10^{-6} m²/s (5 cS) type II oil qualified to the MIL-L-23699 specification have shown a 7.33 increase in the L_{10} life over similar bearings made of VAR M-50 (ref. 4).

An example of an improved analytical tool considered by BHT to be a significant technological advancement in the discipline of predicting bearing lives is the engineering design guide titled "Life Adjustment Factors for Ball and Roller Bearings" (ref. 5). This design guide was sponsored by the Rolling-Elements Committee of the Lubrication Division of the ASME and offers a unified approach to considering the many variables that affect the lives of bearings. The use of this guide enables the relationship between the designer and the user to be one of complete understanding. This is not to say that all bearings will operate as predicted, but it does mean that variables such as the kind of material, material processing, lubrication, speed, and shaft misalignment can be addressed in a meaningful and consistent manner.

Both of these technological advances have been used in the design of the 500-hp transmission. (See fig. 1 for the identification and location of the bearings.) Most of the bearings in this transmission are the same as used in the 317-hp transmission (fig. 2) except for a material change from a VAR steel to VIM VAR M-50 tool steel. The planetary support bearing and the mast roller bearing were not changed. Since there is very little difference between the weights of the OH-58C planetary and the 500-hp planetary, there was no need to change the planetary support bearing. The mast roller bearing was not changed because it has adequate life in its present condition. Table 7 shows the bearing lives for the 317-hp transmission and table 8 shows the bearing lives for the 500-hp transmission. All the bearing lives are calculated using a computer program from A. B. Jones, shown unadjusted and then adjusted in accordance with the aforementioned engineering design guide.

As previously mentioned, some tests indicate that a factor of 7.33 may be used when going from VAR M-50 to VIM VAR M-50. The design guide allows the use of a factor of 3 for VAR M-50. This would indicate that a factor of $7.33 \times 3 = 22$ may be used for VIM VAR M-50. However, in performing the life calculations shown in table 8, a conservative approach was taken: the 22 factor was divided by 2. This gives a life adjustment factor for processing of 11 for VIM VAR M-50.

Since all the torque-dependent bearings are not in the same physical position relative to each other in the two transmissions and thus the loads are not proportional to the power transmitted, the most meaningful method of comparing the lives of the two transmissions in terms of bearing lives only is to compare the mean lives of the two transmissions. This is best accomplished by summing the individual bearing lives and determining the mean life of the sum.

The individual lives of the bearing in each transmission may be summed as follows:

$$\frac{1}{\bar{L}} = \left[\sum_{i=1}^k N_i \left(\frac{1}{L_i} \right)^e \right]^{1/e}$$

where

- k total number of different bearings
- N total number of like bearings of kind i
- e dispersion exponent (Weibull slope)

TABLE 7. SUMMARY OF BEARING LIVES FOR 317-HP
TRANSMISSION AT 270 HP AND 6180 RPM INPUT

Bearing	Unadjusted L ₁₀ life, hr	Life adjustment factors						Adjusted L ₁₀ life, hr
		D	E	F	G	H	Total	
Triplex	1,238	2	3	2.00	1	1	12.00	14,856
Input pinion roller	3,343	2	3	.74	1	1	4.44	14,843
Gearshaft duplex	659	2	3	.3	1	1	1.80	1,186
Gearshaft roller	1,961	2	3	.34	1	1	2.04	4,000
Planet roller	3,723	2	3	.30	1	1	1.80	6,701
Planetary support	26,602,000	2	3	.30	1	1	1.80	47,883,600
Mast tandem	1,849	2	3	.30	1	1	1.80	3,328
Mast roller	22,429	2	3	.30	1	1	1.80	40,372

TABLE 8. SUMMARY OF BEARING LIVES FOR 500-HP
TRANSMISSION AT 427 HP AND 6180 RPM INPUT

Bearing	Unadjusted L ₁₀ life, hr	Life adjustment factors						Adjusted L ₁₀ life, hr
		D	E	F	G	H	Total	
Triplex	362	2	11	1.90	1	1	41.80	15,132
Input pinion roller	630	2	11	.66	1	1	14.52	9,148
Gearshaft duplex	477	2	11	.30	1	1	6.60	3,148
Gearshaft roller	935	2	11	.33	1	1	7.26	6,788
Planet roller	654	2	11	.30	1	1	6.60	4,316
Planetary support	26,602,000	2	3	.30	1	1	1.80	47,883,600
Mast tandem	1,399	2	11	.30	1	1	6.60	9,233
Mast roller	6,695	2	3	.30	1	1	1.80	12,051

D = Material factor
E = Processing factor
F = Lubrication factor
G = Speed factor
H = Misalignment factor

$$\text{Total} = D \times E \times F \times G \times H$$

The dispersion exponent e is given the value 4, based on test experience at BHT using MIL-L-7808 and MIL-L-23699 oils and VAR steels. Because of the VAR bearing steels and MIL-L-23699 oil in the 317-hp transmission and the VIM VAR bearing steels and Acroshell 555 oil in the 500-hp transmission, it may be logical to use different values of e ; however, BHT has few test data on this subject, and the results are inconclusive. Thus, the dispersion exponent of 4 is used for both transmissions in this analysis.

After the lives have been summed as shown above, the L_{10} life will be transformed into the characteristic life, $L_{63.2}$, from a Weibull plot by extending the L_{10} life up slope e to the $L_{63.2}$ position as follows:

$$\log L_{63.2} = \frac{\log \log \frac{1}{1-0.632} - \log \log \frac{1}{1-F(t)}}{e} + \log t$$

where

t percent failed life L

$F(t)$ probability of failure prior to time t

If $t = L_{10}$ life, then $F(t) = F(L_{10}) = 0.10$. The mean life is now calculated (ref. 6) as

$$\bar{x} = L_{63.2} \Gamma\left(1 + \frac{1}{e}\right)$$

where

\bar{x} mean life

Γ gamma function

If $e = 4$, then

$$\Gamma\left(1 + \frac{1}{4}\right) = 0.9064$$

If $e = 1$, then

$$\Gamma\left(1 + \frac{1}{1}\right) = 1.000$$

The mean life is the mean time between failures (MTBF) or the time to one failure.

Table 9 shows the results of these calculations and how they compare for the two transmissions. As expected, the mean life of 3703 hr for the 500-hp transmission is greater than the 1872 hr for the 317-hp transmission.

This large increase in the mean life is primarily caused by two factors: the processing factor of 11 for VIM VAR M-50, and the reduced load (reduced in proportion of the 58 percent increase in torque) on the gear shaft duplex bearing as the result of straddle mounting the spiral bevel gear mesh that lets the gearshaft roller bearing carry more of the load. By virtue of the method used to sum the lives of all the bearings, the mean life of the system of bearings can never be greater than that of the bearing with the shortest adjusted life. In both transmissions the shortest adjusted life bearing is the gearshaft duplex bearing. Thus, the change from the overhung mounting on the 317-hp transmission to the straddle mounting on the 500-hp transmission not only stiffened the bevel gear mesh but also increased the mean life of the bearings.

Since the data substantiating the large life adjustment factor of 11 are limited, shown also in table 9 are the bearing life data for the 500-hp transmission using a life adjustment factor for processing of 3.91 instead of 11. This 3.91 factor was obtained recently in some limited tests performed by BHT on some low-speed, highly loaded roller bearings made of VIM VAR M-50. (This work was performed under contract DAAJ02-76-C-0046, Advanced Transmission Components

TABLE 9. COMPARATIVE LIFE DATA OF THE 317-HP AND 500-HP TRANSMISSIONS IN TERMS OF BEARING LIVES ONLY

Hour	317-hp Trans.	500-hp Trans.	
	E = 3	E = 11	E = 3.91
Sum of L_{10} lives	1177	2328	828
Characteristic life, $L_{63.2}$	2065	4086	1453
Mean life (MTBF)	1872	3703	1317

E = Life adjustment factor for steel processing

Investigation, with the Applied Technology Laboratory of the U.S. Army Research and Technology Laboratories (AVRADCOM), Fort Eustis, Virginia.) Thus, in the event that the 3.91 factor is correct, the system of bearings in the 500-hp transmission has a mean life of 1317 hr which is significantly less than the 1872 hr shown for the 317-hp transmission, but only 12 percent less than the 1500 hr existing on the contemporary transmissions in service today.

Investment-Cast Planet Carrier

Advanced technology items are seldom accompanied with cost reductions; however, the investment-cast planet carrier is a distinct exception. The current method of making planet carriers at BHT is of a two-piece construction of forging and plate stock, bolted together as shown in figure 1. The investment cast planet carrier concept is currently being developed for the new Jet Ranger IV helicopter. Using the investment-cast one-piece construction concept to replace the two-piece planet carrier on the Jet Ranger IV, the recurring cost savings are estimated to be 50 percent. The carrier represents 14 percent of the cost of the transmission. Thus, for the Jet Ranger IV helicopter, the cost of the transmission would be reduced by a one-piece investment-cast carrier. For a \$30 000 transmission, this represents a cost savings of \$2100.

The investment-cast planet carrier for the 500-hp transmission will be similar to the carrier shown in figure 1, except that it will be of a one-piece construction. It is the same size as the carrier in the Jet Ranger IV transmission. The primary difference between the two carriers is that the 500-hp carrier also serves as the oil distributor to the sun-planet gear meshes, the planet bearings, and the sun gear spline. The many oil passages required in the distribution of the oil make the casting concept superior to the forging-plate concept.

The investment-cast carrier concept was selected for the 500-hp transmission as a means of expanding the concept to include the oil distribution tasks. The two-piece planet carrier on the Model 222 has practically the same oil distribution task as required on the 500-hp transmission, and, because it is machined from a forging, the oil distribution feature becomes expensive. The casting concept should lessen this expense significantly.

The anticipated payoff is high; however, the risk is not without significance. There are some differences between the forging-plate and the casting concept that must be investigated thoroughly before putting the cast carrier into service. These differences are related to material and material processing differences: VAR 4340 forging and air melt 4140 plate for the two-piece carrier, and investment-cast 15-5 PH stainless steel for the one-piece carrier. The following potential problem areas exist and are being investigated during the development of the investment-cast carrier for the Jet Ranger IV transmission:

- Impact resistance
- Fracture toughness
- Notched and smooth fatigue strength
- Stress corrosion cracking
- Fretting and wear
- Assembly abuse (pressing planet shafts in and out)
- Torsional spring rate of the carrier

The first three parameters are being checked on cast specimens configured for the particular test involved. The last four parameters will be checked on an actual investment-cast carrier on bench test. The last four parameters will also be evaluated on the investment-cast carrier for the 500-hp transmission as it is being tested.

To get the cast carrier to perform more like the original two-piece wrought carrier, the cast carrier will be subjected to the hot isostatic pressing (HIP) process before final heat treatment. The HIP process should increase the castings' impact resistance and fracture toughness, but this has not been verified yet. It does have an effect on the smooth rotating beam (R. R. Moore) fatigue strength of cast 15-5 PH specimens. (See fig. 4.) It increases the mean reversed bending endurance limit on smooth specimens, where no stress raisers exist, by 23 percent. It has little or no effect on the unidirectional endurance limit of "as-cast" rectangular flexures. This was expected because of the inherent stress raisers at the corners of the flexures. The HIP process appears to be ineffective on stress raisers but in combination with shot peening, the "as-cast" rectangular flexures show an endurance limit approximately equal to that for smooth round specimens when the difference in reversed bending and unidirectional bending is resolved with the aid of a Goodman diagram. Thus, the investment-cast 15-5 PH planet carrier for the 500-hp transmission will be subjected to the HIP process and shot peened for maximum strength and reliability. All these benefits can be had for 50 percent of the cost of the two-piece machined construction.

Investment-Cast Stainless-Steel Housings

The top case of the 500-hp transmission will be made of investment-cast 15-5 HP stainless steel. The non-load-carrying walls will be cast as thin as practical (about 0.254 cm (0.100 in.)) and then chemically milled to a thickness of 0.152 cm (0.060 in.). The top case will then be treated in the same manner as the investment-cast planet carrier: it will be subjected to the HIP process and shot peened. The result will be an advanced technology transmission housing with maximum corrosion resistance, excellent fatigue strength, no significant creeping, and good strength-to-weight ratio, all at a reasonable cost and a low risk in demonstrating each of the attributes.

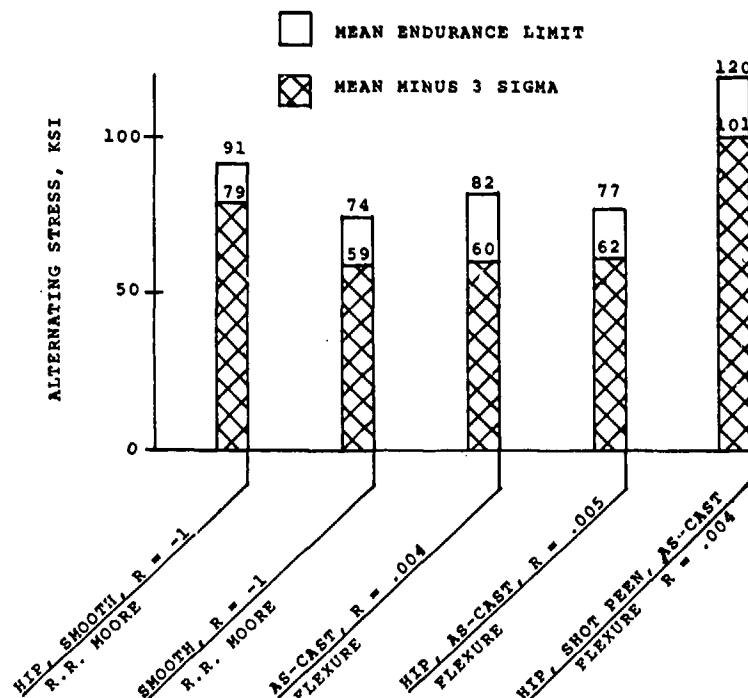


Figure 4. - Investment cast 15-5PH stainless steel fatigue test results, reversed and unidirectional bending, for various conditions. To transform these values to MPa multiply the value in ksi by 6.895.

Most contemporary transmission housings are made of either magnesium or aluminum alloy castings. Both of these materials creep rather rapidly at operating temperatures. This is especially detrimental to spiral bevel gear housings where the gears must be located accurately relative to each other to maintain proper tooth contact patterns. Both of these materials also have low fatigue strengths, and magnesium alloy castings are very susceptible to corrosion.

Other types of housings that some helicopter manufacturers are proposing and developing for the 1980's are the metal matrix composite, the graphite filament polyimide resin system, and the stainless-steel weldment. The composite and resin housings are costly and appear to be many years away from a usable product that can be as highly reliable as existing cast housings. The welded stainless-steel housing appears to be a viable concept except for the many welds required to connect the stiffening ribs and cylinders to each other and to the thin sheet metal shell. The approach being taken by BHT for advanced technology transmission housings, the investment-cast stainless-steel housing, selectively chemically milled for weight reduction, hot isostatic pressed, and shot peened, should be equivalent to or exceed all the capabilities of the welded stainless-steel housing and be more favorable in cost but void of welds. Recent developments in the ability to investment cast large housings combined with chemical milling permits this direction to be taken in providing advanced technology transmission housings for the 1980's. Heretofore, nothing has been able to out-perform magnesium castings as a transmission housing in the area of weight savings. But for a certain size of housing, Fitzgerald (ref. 7) has reported as much as a 23 percent weight saving in going from a cast magnesium housing to the stainless-steel weldment. Obviously, the size of the weight saving will depend on the size and complexity of the housings; however, the fact that the potential is there adds impetus to the other benefits predicted for a stainless-steel housing, especially one that is investment cast, hot isostatic pressed, chemically milled, and shot peened, instead of welded.

Miscellaneous Improvements

Three other distinct improvements were made in upgrading the 317-hp transmission to the 500-hp transmission: the straddle-mounted spiral bevel gear, the positive flow-through oiling to the sun gear spline, and the cantilever-mounted ring gear. These items/concepts are shown in figure 1. They represent improvements dictated by field experience and logic. The wear of the sun gear spline and the ring gear spline has been shown to be sporadic and not conducive to long transmission operating lives. The overhung spiral bevel gear performed satisfactorily for the 317-hp transmission; however, the additional rigidity inherent in the straddle-mounted design will no doubt be required to maintain proper tooth contact patterns for the 500-hp transmission during normal operation and especially during overtorque testing.

The straddle-mounted bevel gear concept is already in use on the 206L-1 435-hp transmission. At first glance this 435-hp rating is only 13 percent less than 500 hp; however, because the difference in reduction ratio in the spiral bevel gearset between the 317-hp transmission and the 206L-1 transmission, the 500-hp rating represents a 32 percent increase in torque on the gear member of the set. The penalty for straddle mounting adds to the increased height and weight of the transmission.

The sun gear spline is a working spline in that it must accommodate the off-axis operation of the bevel gear shaft and the planetary. In a perfect nonloaded position, the bevel gear shaft and the sun gear have a common axis of rotation, but, due to tolerances and deflections, a condition of misalignment exists that causes the spline connection to work. In the 317-hp transmission, both the external spline on the sun gear and the mating internal spline in the bevel gear shaft, are of core hardness, noncrowned (straight), heavily shot peened, and oil-mist lubricated. The wear problem exists primarily because the wear particles are not washed out of the contact area.

Based on experience on the XV-15 tilt rotor aircraft, the splined connection on the 500-hp transmission will have the sun gear spline crown hobbled, nitrided, and the white layer blasted off with garnet, and the bevel gear shaft internal spline will be of core hardness and noncrowned. The oil for the positive oiling feature is being supplied from an orifice in the investment-cast planet carrier as shown in figure 1. Note that there is a dam at both ends of the splined area of such height that the working surfaces of the spline teeth are always submerged in oil. In addition to this, since the spline area is being constantly fed with oil, the oil flows through, flushing out any wear particles that have been generated. This prevents the accumulation of wear particles that tend to act as a lapping

compound and cause excessive wear. Thus, it is anticipated that the crowned and hardened male spline working inside a core hardness straight female spline submerged in a bath of flow-through oil will prevent the spline from wearing.

The cantilever-mounted ring gear is used in the 500-hp transmission primarily to eliminate the spline wear that is inherent in the ring gear-to-case spline connection on the 317-hp transmission. The spline wear is not excessive for the life requirements of the 317-hp transmission; however, it would be for an advanced technology long-life transmission. The cantilevered mounted ring gear is also used in the 500-hp transmission for two other reasons: noise reduction and more uniform load distribution. The cantilevered mounting tends to isolate the ring gear from the housing and thus reduces any structure-borne noise emanating from the meshing gear teeth, and the cantilevered mounting provides a soft mounting to equalize load sharing among the four planets. The soft mounting minimizes the effect of the positional and runout inaccuracies associated with the location of the mast, mast spline, planet carrier spline, planet pinions, ring gear teeth, and ring gear mounting flange.

Size and Weight Comparison

The size and weight of the 500-hp transmission has been alluded to in nondiscrete terms throughout this paper. This section will address the subject in detail by comparing the weights and heights of the 500- and 317-hp transmissions. Figure 1 shows that the 500-hp transmission is 30.50 cm (12.00 in.) high. This is 3.81 cm (1.50 in.) higher than the 317-hp transmission. The increase in height is primarily due to the addition of the bevel gear shaft support quill to straddle mount the bevel gear, the oil transfer mechanism for transferring oil from the top case to the rotating planet carrier, and the

TABLE 10. WEIGHT COMPARISON OF 317-HP AND 500-HP TRANSMISSIONS, KG (LB)

	317-HP Trans.	500-HP Trans.
Gearshaft	2.6 (5.7)	3.4 (7.6)
Gearshaft support	0 (0)	1.3 (2.9)
Planet carrier	4.6 (10.2)	6.0 (13.2)
Ring gear	2.7 (5.9)	3.5 (7.7)
Mast ball brg.	.9 (1.9)	1.3 (2.8)
Top Case	3.8 (8.4)	4.6 (10.2)
Remaining parts less mast	39.5 (87.2)	39.5 (87.2)
TOTAL	53.7 (118.4)	59.6 (131.6)
Weight increase	-	5.9 (13.2)
Percent weight increase	-	11%
Weight includes lubricating oil		
Lb/hp	.37	.26

mast tandem ball bearing. The 317-hp transmission does not have the support quill and the oil transfer mechanism, and it has a single, instead of a tandem, ball bearing on the mast (not shown in fig. 2).

The diameter of the 500-hp transmission is the same as that for the 317-hp transmission. Thus, the 3.81-cm (1.50-in.) growth in height is the only external size change for the 58-percent increase in power capability. Table 10 shows the weights of the two transmissions. The weight of the 500-hp transmission is only 11 percent greater than that of the 317-hp transmission; 11 percent greater for a 58-percent increase in power capability. In pounds per horsepower this represents a 29-percent reduction. The weights for the 317-hp transmission are actual; whereas, those for the 500-hp transmission are calculated. The only assumption made is that the investment-cast stainless-steel top case can be designed to weigh no more than a comparable magnesium top case. In the section "Investment Cast Stainless-Steel Housings," reference was made to a 23-percent weight saving in changing from a cast magnesium housing to a stainless-steel weldment. This was accomplished on a 34-kg (75-lb) magnesium housing. The 500-hp transmission top case is much smaller (4.6 kg (10.2 lb), as originally designed in magnesium), which makes it more difficult to exact a weight saving; however, it is anticipated that by careful design, the top case can be made of investment-cast stainless steel for the same weight required for the cast magnesium top case.

Thus, this size and weight comparison shows just how close the objective came to being met, the objective being that by using existing advanced technology components, the 317-hp transmission could be made into a 500-hp transmission with no change in size or weight. Except for the 3.81-cm (1.50-in.) increase in height and the 5.9-kg (13.2-lb) increase in weight, the objective was met.

References

1. Coleman, Wells: A New Perspective on the Strength of Bevel Gear Teeth. AGMA 229.13, Oct. 1969.
2. Battles, R. A.: Development of Helicopter Transmission Components for the 1980's. American Helicopter Society HPS-10, Nov. 1979.
3. Cutler, R. A.; et al.: Elevated Temperature Fracture Toughness and Fatigue Testing of Steels for Geothermal Applications. TR80-87 under DOE Contract No. EY-76-C-02-0016, Terratek, University Research Park, 420 Wakara Way, Salt Lake City, Utah, Nov. 1980.
4. Bamberger, E. N.; Zaretsky, E. V.; and Signer, H.: Endurance and Failure Characteristic of Main Shaft Jet Engine Bearing at 3 Million DN. ASME 76-Lubs-16, May, 1976.
5. Bamberger, E. N.; et al.: Life Adjustment Factors for Ball and Roller Bearings. ASME Engineering Design Guide, Sept., 1971.
6. Johnson, L. J.: The Statistical Treatment of Fatigue Experiments. Elsevier Publishing Company, New York, New York, 1964.
7. Fitzgerald, P. C.; and Gardner, G. F.: Advanced Transmission Component Development and Test Program. American Helicopter Society HPS-8, Nov. 1979.

AD P000705

Helicopter Transmission Arrangements with Split-Torque Gear Trains*

G. White†

A need for progressive improvement in the performance of helicopter propulsion systems leads the transmission designer to examine alternative methods for transferring power from the engines to the rotors. Predominant in this effort is the problem of designing main rotor gearboxes having higher power to weight ratios with increased life and reliability.

Development and uprating of components used in production gearboxes has, in the past, enabled transmission designers to match improvements elsewhere in the propulsion system. This short-term form of development is attractive since the design loads and problem areas are known in advance and the improved design can be incorporated into an existing transmission with minimum changes. But the uprating of conventional components results in progressively smaller gains and, as is historically demonstrable, contributes little to the problem of weight reduction for there is a natural tendency to trade-off any potential weight benefit with component life and reliability.

As an alternative to component development, this work argues the case for improved drive-train configurations. In particular, the use of torque-splitting gear trains is proposed as a practicable means of improving the effectiveness of helicopter main gearboxes; the work thus makes use of and extends concepts presented earlier in references 1 and 2. The potential for major weight reduction exists, but since significant changes to the propulsion configuration may be required, the development of such gear trains is necessarily longterm. Of equal importance, however, is that no advance in technology level is required, for split-torque gear trains merely involve novel arrangements of well developed components such as gears, shafts and bearings.

Areas of Application

Traditional gear train arrangements for main rotor gearboxes comprise spur, bevel, and planetary gear units. These units must be sized for main rotor power if located between the main rotor and the point of engine power combination; otherwise the drive units must be sized for single-engine power.

Now split-torque gear trains provide parallel drive paths for the transmission of power, and, as shown later, the torque split can be achieved through spur, bevel, or planetary gear trains. In consequence the transmission designer has more options to call on than if the choice were limited to conventional gear arrangements which transmit all power through a single path. The challenge to the designer then lies in exploiting the advantages of torque-splitting devices at an appropriate point in the drive train.

While weight reduction remains the principal aim, split-torque drive trains provide a means of forestalling technology limitations set at one extreme by advanced, high-speed engines and, at the other extreme, by the high torques required by the main rotors of heavy lift helicopters (HLH). Further, the ability in some arrangements to maintain separation of individual engine drive trains until the final speed-reduction stage provides redundancy between drive paths from each engine.

Consideration of such properties in relation to transmission designs spanning the light observation helicopter (LOH) to HLH aircraft allows identification of the following areas of application for split-torque gear trains:

- (1) Offset, final-stage reduction gears based on a combining gear driven by multiple pinions
- (2) Intermediate speed-reduction stages which torque-balance drive trains upstream and downstream through balanced reaction members

*Previously presented at the First European Rotorcraft and Powered Lift Aircraft Forum, Southampton University, Sept. 1975.

†Transmission Research, Inc.

- (3) With high-speed engines of low torque capacity, an engine reduction stage based on a high-ratio, counter-rotating epicyclic unit
- (4) With engines of high torque capacity, an engine reduction stage based on dual bevel pinions driven through a torque dividing mechanism
- (5) Coaxial, final-stage reduction gears for transmission of very large torques to the main rotor. These gear trains are appropriate to HLH transmissions with output torques greater than so far encountered on a production aircraft. Owing to the shift in emphasis from items (1) to (3), however, these coaxial drive trains are eliminated from discussion in the present work.

Methods of Torque Splitting

Mechanisms for achieving torque division can be subdivided into

(1) Static-load torque dividers characterized by having no internal relative motion of the loaded elements other than the small adjustments necessary to accommodate manufacturing tolerances and structural deflections. In consequence, this type of torque-divider provides no change in speed ratio across its input and output members. Typical examples of static-load torque dividers, discussed later, include torque tubes, pivot beams, flexible beams and a number of three-shaft geared mechanisms.

(2) Rotary torque-dividers having continual relative motion within the mechanism. In this way a speed-reduction ratio can be generated between the input and output members concurrently with the division of torque. This group of mechanisms includes epicyclic torque dividers, double-helical gears with axial freedom, and floating idler pinions.

(3) Reaction-balance torque dividers which combine the properties of static-load and rotary-torque dividers to achieve a speed reduction while retaining the advantage of torque equalization through a static reaction member.

Static-Load Torque Dividers

Elastic deformation

Elastic deformation of structural members provides a simple means of dividing torque between a pair of gears while avoiding the introduction of wearing elements such as bearings: examples include flexible cantilever-beams and torsionally flexible drive shafts. The equality of torque division provided by elastic members depends on

- (1) Indexing accuracy on assembly
- (2) Attainment of equal and low stiffness of each drive path
- (3) Over a range of torques, equal deflection of the housings and bearings supporting the gears.

Low stiffness in the drive paths allows the gears and their support bearings to experience sensibly equal loads despite the runout errors arising from machining tolerances. But to achieve confidence in load sharing between the gears over a period of operation necessitates continual monitoring or periodic checking of the torque levels in each drive path. High-performance marine reduction gears provide an example of load sharing through torsionally flexible drive shafts. In this application a combining gear is driven by pairs of pinions, near equality of tooth loads being assisted by the low torsional stiffness of the drive shafts to the pinion.

Figure 2 illustrates a flexible-beam mechanism for dividing an input torque between two coaxial members. Variants of the mechanism have been developed commercially since the device offers simplicity and the ability to attain high torque capacity by duplication of the beam elements.

Zero-Stiffness Mechanisms: Limited Motion

Ideal torque distribution between a pair of gears is attained with a torque-dividing mechanism having zero stiffness. This characteristic contrasts with the finite stiffness of elastic torque dividers. Examples of a zero-stiffness device include the axial pivot-beam arrangement of figure 1 as used in Mil helicopter transmissions to divide the torque from each engine between a pair of bevel pinions.

The ratio of the torque division varies with the length of the pivot arms and the radius of the pivot points as noted in table I; but equal-length arms at a common radius clearly result in each output torque being one-half of the input torque.

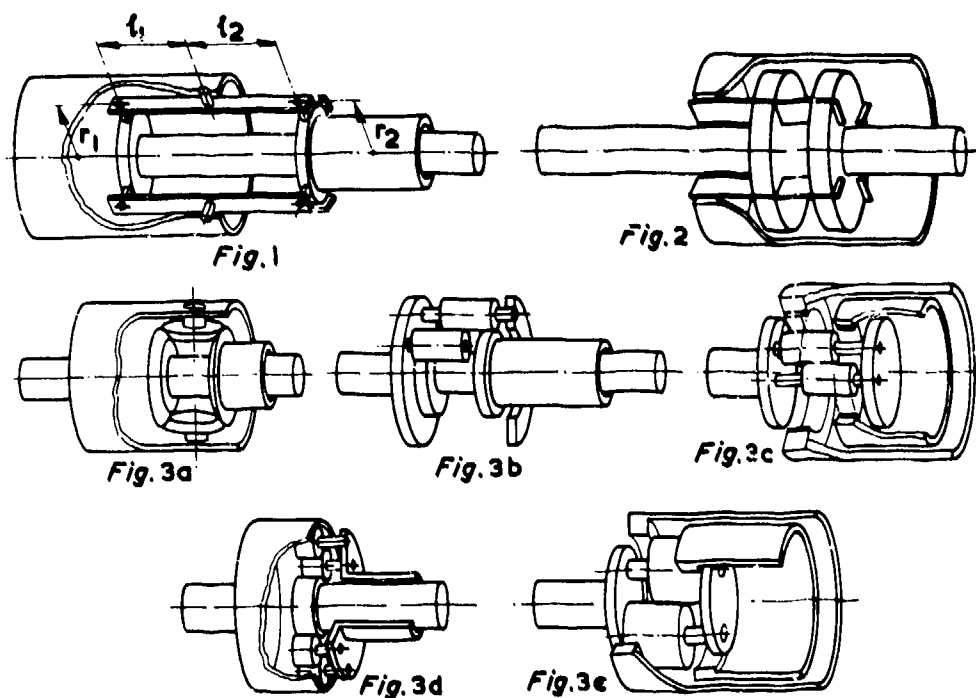
Radial equivalents to figure 1 can be devised, but each pivot beam still requires three bearings. These bearings, of course, are the critical elements of a torque divider for they are loaded and have no relative motion across the races other than small-amplitude oscillation, a condition which favors the selection of rod-end bearings. A future possibility with figure 1, however, involves the use of elastomeric bearings on the pivot beams to eliminate possible wear and life problems. In this case the torque-divider would become a member of the elastic group.

In normal operation, with drive paths of equal stiffness, each end of a pivot-beam in the torque divider experiences a motion amplitude not exceeding about 1 mm. Then, if motion limit stops are included allowing only 2-mm amplitude, a complete failure in one of the gear drive paths leads to the total input torque being carried by the remaining drive path. In this way the motion limit stops, possibly in the form of a large-clearance spline, provide redundancy such that failure in either drive path transfers the total torque to the remaining drive path.

Zero Stiffness Mechanisms: Unlimited Motion

Alternatives to the pivot-beam mechanism of figure 1 include a family of geared torque dividers. These mechanisms comprise three-shaft differentials capable of providing two torque outputs, each equal to half the torque applied to the input member. The commonest example is, of course, the bevel differential as used in vehicle rear axles (fig. 3(a)). General terms for the output torques are summarized in table I from which it is clear that these torques are equal when the side bevels B_1 and B_2 are the same diameter.

Figure 3(b) illustrates the spur-gear equivalent of figure 3(a). In this case the pairs of pinions mesh with each other, but only one sun gear meshes with each pinion. The torques delivered by each of the output sun gears are given in table I; when $S_1 = S_2$ the output torques are each equal to one-half of the input torque. A similar result obtains (table I) if the two sun gears are removed and replaced by two annulus gears as in figure 3(c). The double-annulus design is somewhat shorter than the double sun design on account of the reduced face width (conformal contact) required at the annulus-pinion mesh.



Figures 1 - 3. - Static-load torque dividers.

TABLE I. - TORQUES DELIVERED BY ZERO-STIFFNESS MECHANISMS

Figure	Member carrying input torque	Output torques obtained	Condition for equal output torques
1	Beam carrier	$T_1 = T_c/[1 + (L_1/L_2)(r_2/r_1)]$ $T_2 = T_c/[1 + (L_2/L_1)(r_1/r_2)]$	$(L_2/L_1) = (r_2/r_1)$
3a	Planet carrier	$T_{B1} = T_c R_1/(B_2 + B_1)$ $T_{B2} = T_c B_2/(B_2 + B_1)$	$R_1 = B_2$
3b	Planet carrier	$T_{S1} = S_1 T_c/(S_1 + S_2)$ $T_{S2} = S_2 T_c/(S_1 + S_2)$	$S_1 = S_2$
3c	Planet carrier	$T_{A1} = A_1 T_c/(A_1 + A_2)$ $T_{A2} = A_2 T_c/(A_1 + A_2)$	$A_1 = A_2$
3d	Annulus	$T_c = T_A[1 - (S/A)]$ $T_S = T_A(S/A)$	$A = 2S$
3e	Planet carrier	$T_{A1} = T_c P_1/(P_2 + P_1)$ $T_{A2} = T_c P_2/(P_2 + P_1)$	$P_1 = P_2$
4a	Sun gear	$T_A = T_S(A/S)$ $T_c = T_S[(A/S) + 1]$	Not possible

Notation:

A annulus diameter	T_A annulus torque
B bevel gear diameter	T_B bevel gear torque
P planet pinion diameter	T_c carrier torque
S sun gear diameter	T_S sun gear torque

Lesser-known torque dividers include the idler-pinion differential shown in figure 3(d). The inclusion of idler pinions allows the sun gear and the planet carrier to deliver equal output torques, each one-half of the input torque, when the annulus diameter is twice that of the sun gear; then $(A/S) = 2$ as shown in table I.

The two-pinion differential of figure 3(e) is developed from figure 3(c) by omitting all but one set of pinions. It can also be recognized as a rotary equivalent of the pivot-beam arrangement shown in figure 1. But while figure 3(e) brings the economy of a minimum total of gears and bearings, the use of a single gear mesh for reacting the transmitted torque leads to a larger size in comparison with the other geared torque splitters.

General Property of Torque Dividers.

A general property of all the static-load torque dividers outlined (figs. 1 to 3) is that, if the member used for torque input is held stationary, a motion of one output member produces a reverse motion of the remaining output member. Further, if equal output torques are required, the forward and reverse motions noted must have the same amplitude. It follows that, for equal output torques, the mechanisms of figures 1 to 3 must provide a speed ratio of 1:-1 across the output members when the input member is held stationary.

The above property also holds true for the rotary torque dividers of figure 4, discussed in section 5. But in the case of figure 4(a), any gear trains downstream of the epicyclic unit must be considered as part of the torque dividing mechanism, for these gear trains rectify the torque imbalance between the planet carrier and annulus members.

Combined Torque-Divider and Speed-Reduction Gear

The development of static-load torque-dividing mechanisms leads to the examination of gear trains that perform the dual function of speed reduction and torque division. An attraction of such gear trains is the need for fewer components than with a separate torque-dividing mechanism and gear train. Three distinct types of torque-dividing gear trains are summarized below; these types are incorporated in main rotor transmission arrangements described later.

Epicyclic Torque Divider

Epicyclic speed-reduction gears in helicopter transmissions normally have the annulus grounded to the transmission housing. But by accepting two counterrotating outputs, with a single-input drive, the torque normally reacted to the transmission housing can be utilized as a secondary drive path as shown in figure 4(a).

Recombination of the separate drive paths prior to driving the main rotor can be achieved in a number of ways, some of which are outlined in references 1 and 2. The gear trains driven through the planet carrier and the annulus are always torque-balanced by the epicyclic unit so that the gear tooth loads in each drive path are predictable. The division of torque in the epicyclic torque divider of figure 4(a) is not equal but corresponds to the ratios given in table I. It follows that the output torques differ in the ratio $T_C/T_A = (S/A) + 1$.

A further property of the epicyclic torque divider, and the principal attraction of the device, is the large speed-reduction ratio generated by counterrotation of the planet carrier and the annulus. In this way high input-speeds can be accepted by the sun gear while keeping the speed of the planet carrier sufficiently low to avoid bearing life being absorbed by centrifugal load from the planet pinions.

Helical Gear Torque Divider

The ability of double-helical gears to divide load between a pair of gears by balancing the axial thrusts is well known. Figure 4(b) illustrates this technique as a means of obtaining two output drive paths transmitting equal torques. But free axial motion of the double helical gear is difficult to realize for, if driven by a spline, friction in the spline prevents axial float for all but large differences in end thrust on the helical gears. Thus, the input gear of figure 4(b) must be driven by a diaphragm coupling with low stiffness in the axial direction. But a preferable solution, if circumstances allow, is to employ the additional spur-gear train of figure 4(c) as a means of obtaining axial float and equality of torque division between the helical gears.

Dual Idler Pinions

An effective method of torque dividing to increase the torque capacity of a final-stage combining gear consists of introducing dual idler-pinions as shown in figure 4(d). This approach doubles the torque capacity at the critical output stage without increasing the diameter of the combining gear. Floating the primary pinion between a pair of idler pinions has obvious advantages when the three centers lie on a straight line, for then perfect load sharing between the idler pinions is

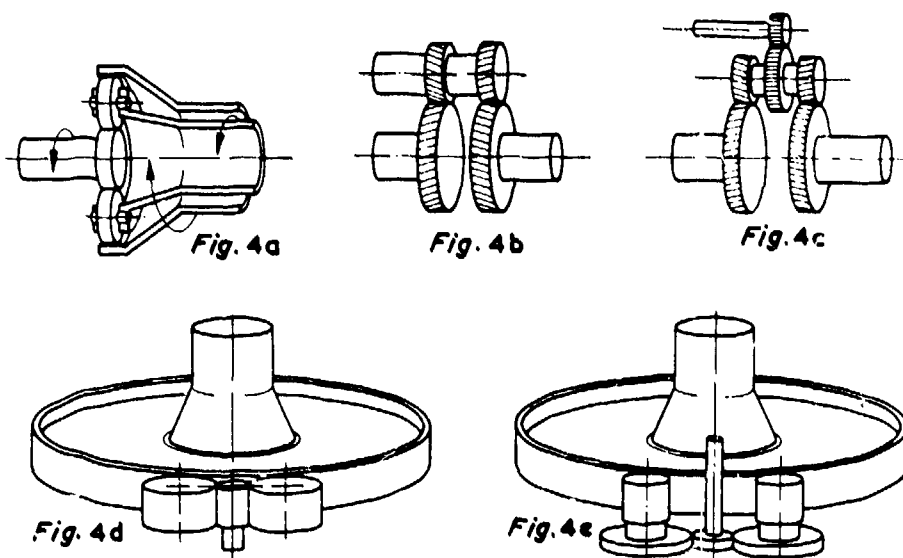


Figure 4. - Rotary torque dividers.

ensured by allowing the primary pinion to float with the tooth forces. Location of the pinion by a light bearing mounted in a low-stiffness (rubber) support ring gives heavy damping to the primary pinion with negligible resistance to the small motions required for load-sharing between the primary pinion, the idler pinions and the combining gear.

With the three gear centers in line (as in fig. 4(d)) the idler pinions need to be larger than the primary pinion in order that teeth on the primary pinion clear teeth on the combining gear. Now the compressive stress at the tooth contacts decreases with an increase in the diameter ratio of idler pinion-primary pinion; hence, it is preferable from a tooth stress standpoint that the idler pinions be at least twice the diameter of the primary pinion. But idler pinions of such a diameter bring a significant weight addition; hence, the justification of figure 4(e), still with ideal torque division, in which the use of compound pinions allows a speed ratio to be taken at the primary-idler pinions. The weight of the compound pinions is then partly offset by the transmission of reduced torques upstream.

Transmission Arrangements Based on Final-Stage Combining Gear

The different methods of torque splitting available at the output, input, and intermediate reduction stages of a transmission can be permuted to give a large number of drive-train configurations. A number of configurations can be eliminated on the basis of weight and complexity; hence, only the more practicable arrangements are discussed below. For uniformity the arrangements are assumed to be for a single-rotor aircraft having horizontal engines. These arrangements aim to reduce the weight of the main gearbox by combinations of the factors:

- (1) Achieving a high reduction ratio at the final stage by driving a combining gear through multiple, torque balanced pinions. In this way the transition to low torque levels is made through a minimum number of simple components.
- (2) Reducing component sizes and internal loads by dividing torque between parallel drive paths.
- (3) Obtaining increased reduction ratios in a single stage by the use of either a counterrotating epicyclic unit or a floating idler pinion having two mesh points.
- (4) Where possible, achieving torque division from the gear trains themselves in preference to adding a separate torque dividing unit.
- (5) Maximizing the number of final-stage pinions by the use of up to four pinions per engine in conjunction with multiple engines.
- (6) Minimizing the height of the transmission by radial stacking of the reduction stages.

Two Final-Stage Pinions Per Engine

Final-Stage Torque Split

The arrangement of figure 5(a), based on torque division through a floating idler pinion, is appropriate to light helicopters in which the engine reduction planetary provides a bevel pinion speed of about 6600 rpm. The scheme has obvious attractions from a reliability standpoint since only eight gears are required after the engine reduction unit.

Preliminary designs for single-engine LOH transmissions demonstrate the ability to obtain a 6.4:1 reduction ratio at the final stage preceded by about 3:1 speed reduction at the idler-pinion mesh. This ability to obtain a 19:1 speed reduction from six gears of the last two reduction stages highlights the advantage of torque dividing as a means of moving to low torque levels through a minimum number of components.

Figures 5(b) and (c) replace the planetary gear at the engine by a bevel and spur reduction unit, respectively, so reducing to 10 the total number of gears required. Figure 5(c) avoids a high-speed bevel pinion and therefore presents a minimum-risk arrangement.

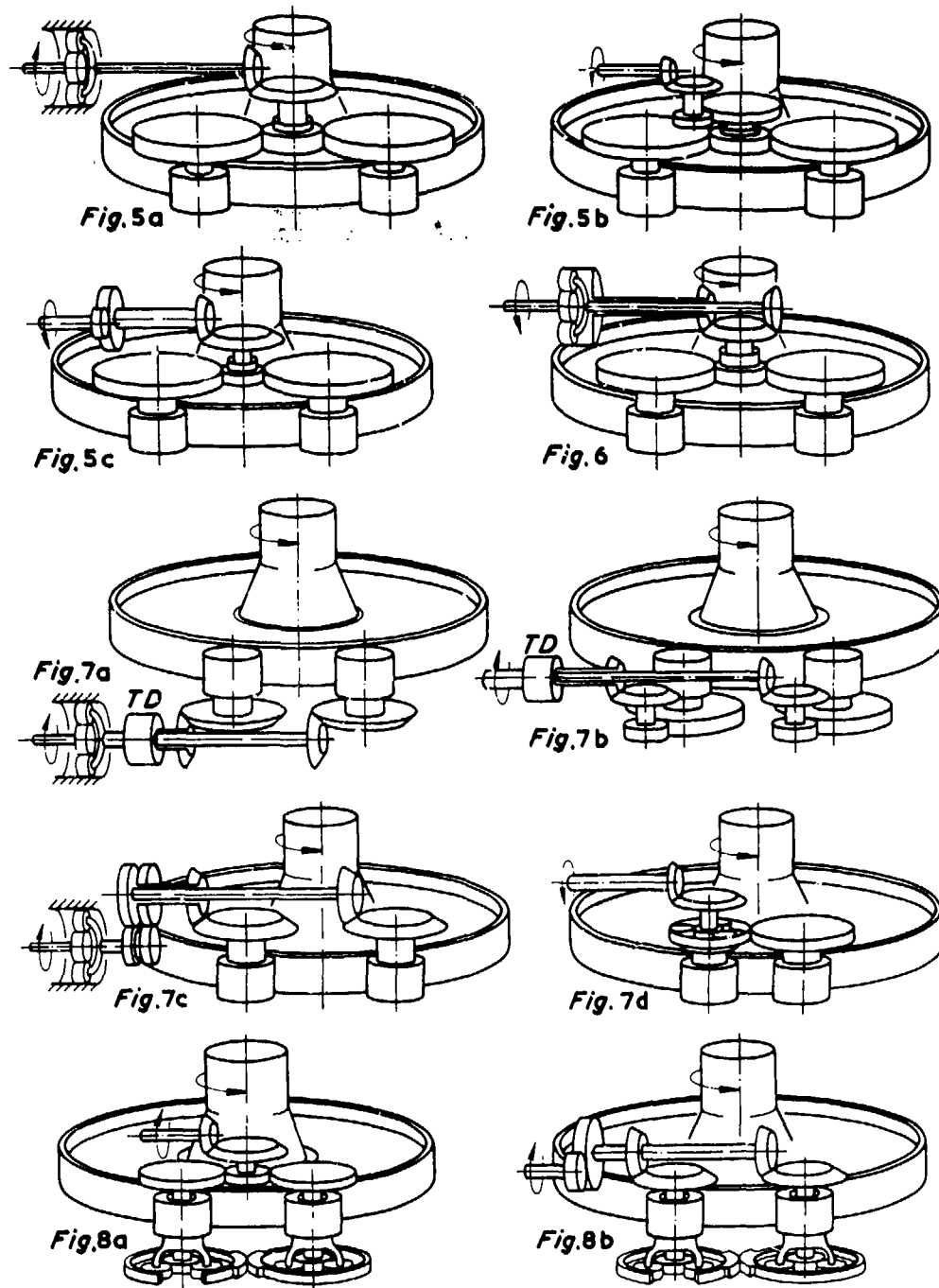
Input-Stage Torque Split

Torque dividing at the engine reduction stage can be achieved as shown in figure 6; in this case the counterrotating outputs from the epicyclic unit are combined on a single bevel gear. This input section is followed by the idler pinion stages of figure 4(e). Thus, while figure 6 requires only one

additional bevel gear in comparison with figure 5(a), increased engine speed can be accepted on account of the doubled reduction ratio made possible by counter rotation of the epicyclic members. A useful long-term development is clearly that of accepting the fixed-annulus planetary unit from an engine manufacturer and adapting it to form a counterrotating, high-ratio reduction gear.

Alternative Arrangements

Further arrangements for obtaining two final-stage pinions per engine are shown in figure 7. Figure 7(a) employs a static-load torque divider (TD) after the engine reduction gear; in consequence, the transmitted torque is split equally between the dual-bevel pinions. In figure 7(b) the engine



Figures 5 - 8. - Gear-train configurations with two final-stage pinions per engine.

reduction gear of figure 7(a) has been eliminated, so that the dual bevel-pinions are driven at engine speed. The engine of figure 7(c) employs floating helical gears to divide torque. But the counter-rotating epicyclic unit in figure 7(d) provides the basis for a higher overall reduction ratio than figure 7(c), eliminates the torque-balance units, and employs the same number of gears as figure 7(a).

Balanced Annulus Gears

Reacting torque between identical annulus gears provides a further method of torque dividing. Figure 8(a) shows such a gear train in which the annulus gears are not clamped to the transmission housing but are geared together and allowed to rotate a few degrees until the tooth forces, and, hence, the annulus torques, self-balance. This self-balancing action then imposes equal torque division between the spur gears driving the sun gears.

Figure 8(b), developed from figure 8(a), depicts a gear train which offers the ability to split the torque from a high-power engine between a pair of torque-balanced bevel pinions. As in the case of figure 8(a), structural deflection of the gear trains, and backlash, are accommodated by small rotations of the annulus gears until the bevel pinions are equally loaded. Figures 8(a) and (b) show the annulus torques reacted through gear teeth; but an alternative design (fig. 10(e)) involves linking the annulus gears with a tie bar, the connections being such that any motion of the tie bar causes the annulus gears to rotate in opposite directions.

Three Final-Stage Pinions Per Engine

Efforts to increase the torque capacity of the combining gear lead to drive-train arrangements which torque-balance between more than two final-stage pinions per engine. For example, figure 9(a) is developed from figure 8 by allowing the annulus gears to react onto a floating double-helical gear. In this way the annulus gears become power flow paths such that, by appropriate choice of gear ratios, each annulus transmits one-sixth of the engine power and each final-stage pinion transmits one-third of the engine power.

The combination of linked epicyclic torque dividers and helical gears of figure 9(a) has sufficient degrees of freedom to provide ideal torque division between the three final-stage pinions and the two input bevel pinions. Reduction ratios across the epicyclic are found to be $(s/c) = 1.5 [(A/S) + 1]$ and $(s/a) = -2A/S$, these ratios corresponding to $\alpha = 2$ in equations (16) and (17) of reference 1, where α is defined as the ratio of power through the planet carrier to power through the annulus.

Figure 9(b) (extracted from ref. 1) also places three torque-balanced pinions per engine on the combining gear. But in this case the single input bevel changes the split ratio and effectively doubles the speed reduction across the epicyclic in comparison with figure 9(a). Thus, with figure 9(b), $\alpha = 1/2$ and $(s/c) = 3[(A/S) + 1]$ (ref. 1).

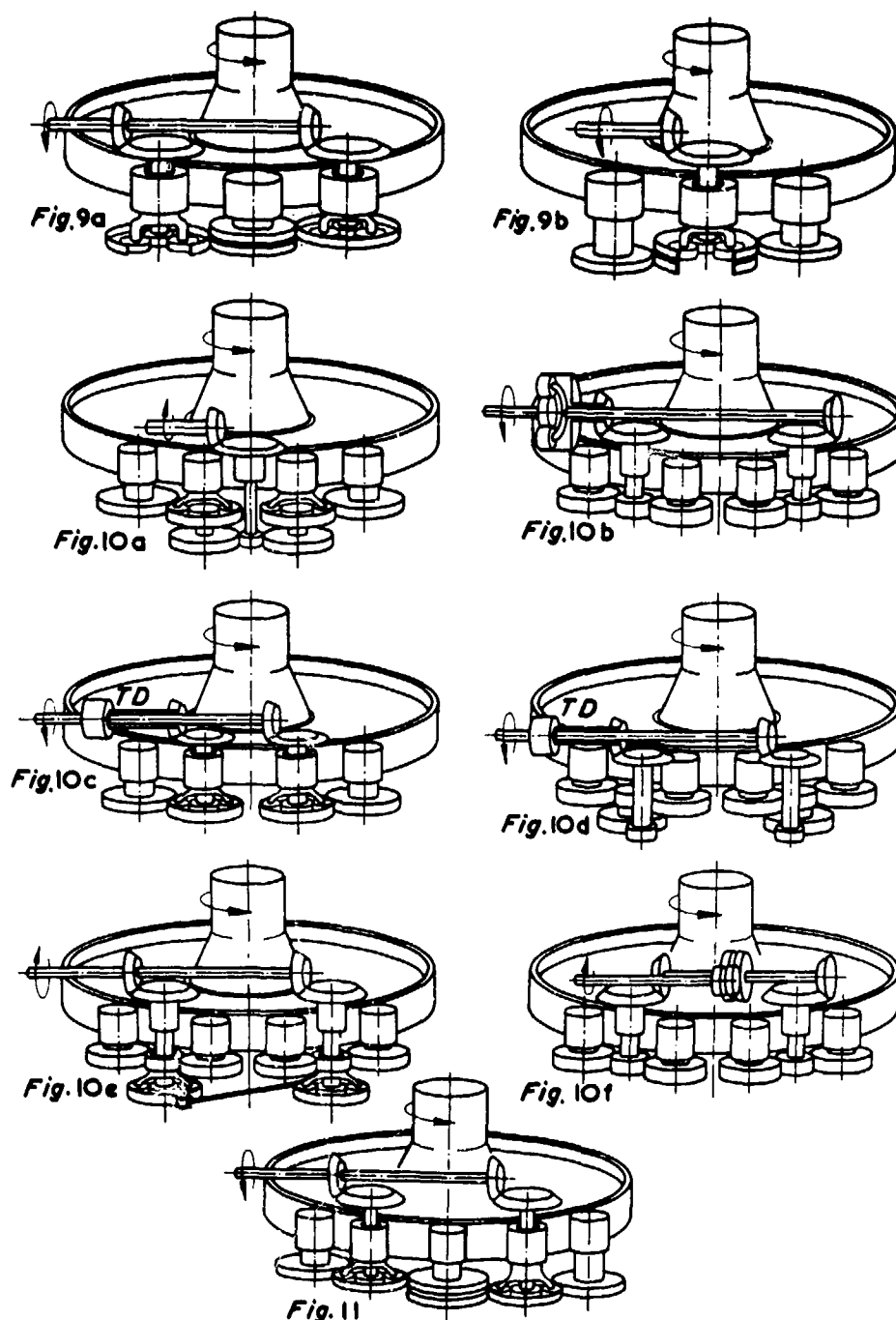
Four Final-Stage Pinions Per Engine

Figure 10 illustrates drive-train arrangements which allow the power from each engine to be divided equally between four final-stage pinions. These arrangements are seen to be extensions of the torque-dividing schemes previously described; the options available include input sections based on torque-balance units, single- and dual-bevel pinions, and epicyclic torque dividers. With four pinions per engine, the torque capability of the combining gear can be raised sufficiently to accommodate the main rotor torques appropriate to HLH aircraft, that is, for torques up to $1.1 \text{ MN}\cdot\text{m}$ ($107 \text{ in}\cdot\text{lb}$). The potential for transmitting torques of this magnitude is best illustrated by considering a 1.37-m-diameter combining gear driven at 125 rpm by four pinions per engine.

With each engine rated at 3.73 MW (5000 hp) the main rotor receives $282 \text{ kN}\cdot\text{m}$ of torque per engine. Gear loading to the accepted levels of $1100 \text{ MN}/\text{m}^2$ compressive stress and $360 \text{ MN}/\text{m}^2$ bending stress leads to pinions of only 140-mm diameter and 127-mm face width. In consequence the final reduction ratio is raised to no less than 9.8:1, the equivalent of two planetary stages, and the main rotor can be rated at 11.2 and 14.9 MW with aircraft having three and four engines, respectively.

More Than Four Final-Stage Pinions Per Engine

Gear trains can be devised which divide the transmitted torque equally between more than four final-stage pinions. Figure 11 shows an example of a five-pinion arrangement in which dual epicyclic torque dividers and a double-helical gear pair ensure that each final drive pinion carries one-fifth of the input power. Concurrently, the torque balance reacts back to the input bevels such that each bevel mesh carries only one-half of the input power. In this case the planet carrier to annulus power split ratio is $\alpha = 2/3$, with the result (ref. 1) that the reduction ratio from the sun gear to planet carrier is raised to $2.5[(A/S) + 1]$. But it is evident that the complexity associated with torque balancing five pinions nullifies the advantage of a high reduction ratio.



Figures 9 - 11. - Gear-train configurations with three or more final-stage pinions per engine.

Recent Design Work

Recent efforts in conjunction with NASA Lewis have resulted in the selection of two split-torque drive-train configurations for further detailed analysis and design.

A lower powered single-engine design rated at 500 hp is based on figure 5(b) with the offset spur-gear train omitted. Thus the 103:1 reduction ratio from an engine speed of 35 560 rpm to a main shaft speed of 347.5 rpm is achieved in only three stages from a total of eight gears. Two additional gears are required to form a tail rotor drive. The last reduction stages are of split-torque form; these gear trains provide a speed reduction ratio of almost 25:1, leaving a ratio of 4.1:1 at the engine reduction bevel.

In comparison with uprated OH 58 designs, preliminary results show reductions in total weight, gear and bearing numbers, drive-train losses and noise. These advances are achieved at the expense of an increased diameter on the main housing.

A twin-engine 3000-hp transmission design is based on the OH 60A speeds of 258 and 21000 rpm at the main shaft and engine input respectively. Four pinions driving a final-stage combining gear result in this gear being only 12 percent larger than the ring gear of an equivalent planetary unit. Yet the speed ratio achieved at the final reduction stage is over 7:1, which should be compared with the 4.7:1 available from a five-pinion planetary unit.

This high ratio at the final stage allows the overall ratio of 81:1 to be generated in only three reduction stages of fixed-axis gears. Consequently the drive-train losses and numbers of gears and bearings are as low as with any comparable design, and yet, in comparison with a planetary unit, the combining gear and its four pinions show a major weight benefit.

Different drive-train options are available according to the engine input positions required. Accordingly, the configuration and method of torque division selected changes as a result of engine separation being less than or greater than about 100 cm. Detail design work on the 3000-hp transmission is not yet sufficiently advanced to allow weight predictions of any accuracy, but in comparison with conventional designs, benefits of at least 15 percent appear realistic.

Conclusion

Split-torque drive trains allow the grouping of multiple pinions around a combining gear. Such a combining gear always provides a higher speed-reduction ratio than a final-stage planetary unit and achieves this advantage at reduced weight with fewer gears and bearings.

Torque dividing at intermediate reduction stages also generates higher speed-reduction ratios per stage than do conventional fixed-axis and planetary gear trains. A consequence is reduced torque levels through the transmission and, in favorable circumstances, the ability to eliminate one speed-reduction stage. The principal devices proposed for boosting the reduction ratio per stage are

- (1) A counterrotating epicyclic unit
- (2) A floating pinion driving through two diametrically opposed mesh points
- (3) Multiple pinions driving a combining gear.

Given these mechanism elements, the designer's problem is to devise drive-train configurations that harness the high reduction ratios while ensuring equality of tooth loading at the multiple-gear meshes. Figures 5 to 10 illustrate a number of configurations worthy of investigation. Current technology components are assumed in the configurations described, but conformal gear forms can be accommodated at the final reduction stage.

The above factors, in combination with the potential for weight reduction, drive-train redundancy, and a transmission of low overall height, provide a case for further evaluation of split-torque gear trains as a means of improving the effectiveness of helicopter transmissions.

References

1. White, G.: New Family of High-Ratio Reduction Gears with Multiple Drive Paths. Proc. Instn. Mech. Eng., vol. 188, pp. 281-288, 1974.
2. Lastine, J. L.; and White, G.: Advanced Technology VTOL Drive Train Configuration Study. USAAVLABS Report No. 69-69, 1970.

AD P000706

Design Study of Self-Alining Bearingless Planetary Gear (SABP)*

D. J. Folenta†

The ever-present pressure on the aircraft and helicopter power transmission designers to reduce weight, size, and cost of power transmissions has given impetus to many innovations and technological improvements. This pressure is further compounded by the user demand for higher horsepower, improved reliability, improved maintainability, and improved survivability of both military and commercial crafts.

One recent promising development in the area of high performance power transmissions has been the self-alining, bearingless planetary (SABP). This transmission arrangement can be generically classified as a quasi-compound planetary which utilizes a sun gear, planet spindle assemblies, ring gears, and rolling rings.

The SABP transmission concept was first introduced in the mid-1960's. Following the introduction of this new design, numerous studies were undertaken to evaluate the viability of this new arrangement as an advanced helicopter and VTOL aircraft transmission system. The results of reference 1 concluded that this new gear concept offered potential advantages over conventional helicopter planetary gears in the following areas:

1. Eliminating planet bearing power losses and failures
2. Having low planetary weight
3. Permitting high reduction in two compound stages of high efficiency
4. Providing sufficient flexibility and self-centering to give good load distribution between planet pinions
5. Effectively isolating planetary elements from housing deflections
6. Increasing operating time after loss of lubricant, since there were no planet bearings.

In early 1970 this transmission design concept was reduced to practice by manufacturing and testing two 373-kW (500-hp) prototype transmissions (ref. 2). This program demonstrated the technical feasibility of this new transmission. Following the successful completion of the prototype testing, further transmission studies were undertaken (refs. 3 and 4).

These studies concluded that the new transmission concept was in fact superior to the contemporary helicopter epicyclic gears. Both studies recommended that this new transmission be subjected to further work and development testing. The results summarized in this paper are the next step in this evolutionary process and present several preliminary designs of a SABP as applicable to a specific helicopter.

The objective of the study was to evaluate the feasibility of using the SABP transmission in an uprated version of the OH-58 helicopter and to make specific performance comparisons of this new transmission with contemporary helicopter transmission systems and with the uprated version of the OH-58 power transmission.

Prudence dictates that the introduction of new ideas, materials, designs, etc., into aircraft usage must be preceded by various studies, developments, and testing phases. During this evolutionary process, good ideas advance, and ultimately the advantages and the benefits these new designs offer can be and are incorporated into their respective product lines. To date, the SABP transmission concept has been subjected to several engineering studies, to hardware prototype demonstration programs, and to the study reported herein.

*Work done under NASA contract NAS3-21604.

†Transmission Technology Co., Inc.

Symbols

F	fixed ring gear
f	gear clash frequency, cps
Mg	gear ratio
N	number of gear teeth
n	rotational speed of gear, rpm
O	output ring gear
PF	planet/fixed ring gear
PO	planet/output ring gear
PS	planet/sun gear
R	pitch radius (R_1, R_2, \dots, R_N)
RRI	rolling ring internal
RRO	rolling ring external
R_T	total reduction ratio
S	sun gear
V_O	output velocity
V_I	initial velocity
W_O	output angular rate, rad
W_I	input angular rate, rad
WPF	tangential load fixed ring gear
WPO	tangential load output ring gear
W_{RF}	radial fixed force
W_{RO}	radial output force
W_{RS}	radial sun force
WS	tangential load sun mesh
W_{TF}	tangential fixed force
W_{TO}	tangential output force
W_{TS}	tangential sun force

Technical Discussion

Principle of Operation of the SABP

The self-aligning, bearingless planetary (SABP) transmission concept covers a variety of planetary gear configurations which share the common characteristic that planet carriers or spiders are eliminated, as are conventional planet mounting bearings. All forces and reactions are transmitted through the gear meshes and through simple rolling rings. In its simplest form this transmission concept is illustrated schematically in figures 1 and 2. These figures show the major components of a SABP type transmission and illustrate the gear tooth balancing principle of this new power transmission arrangement. As can be observed from figure 2, the planet gear faces are so spaced that the tangential gear tooth forces leave the planet spindles in equilibrium. Tooth separating and centrifugal forces are reacted via ID or OD cylindrical rings which are concentric with the sun gear axis. The planet spindles have diameters which freely roll in or on the cylindrical support rings.

The concept can be further illustrated by first studying a simple conventional compound planetary drive (fig. 3). This design requires bearings to react loads in the tangential and radial planes. The forces in the transverse plane are already in equilibrium as a result of the reduction ratio. The bearing load in the tangential plane is approximately 5 to 6 times that in the radial plane.

The SABP design evolved from recognition of the advantages afforded through the elimination of the bearings which react loads in the tangential plane. The bearings could be eliminated by separating the gears in an axial direction. One can verify that all forces and moments add up to zero about any point in or parallel to the three planes.

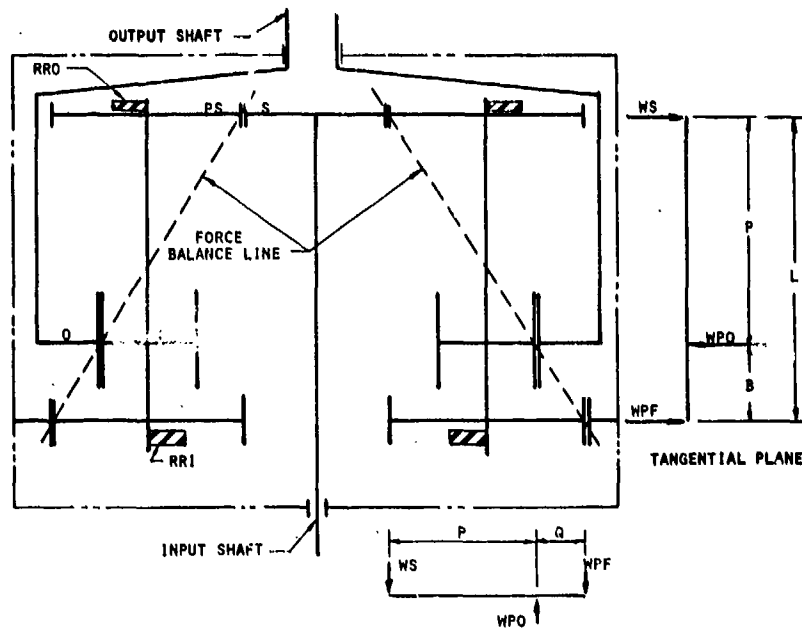


Figure 1. - Schematic arrangement of self-aligning, bearingless, planetary gear - tangential plane.

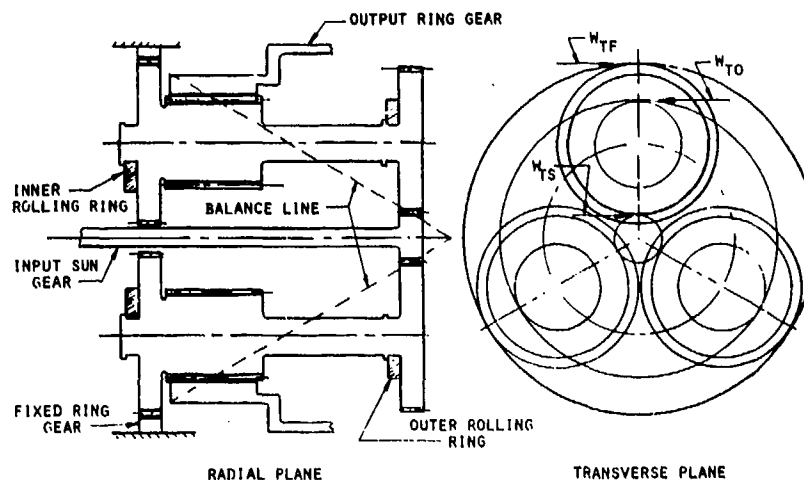


Figure 2. - Schematic arrangement of self-aligning, bearingless, planetary gear - radial and transverse planes.

The SABP drive concept, as it has evolved, can be summarized as follows:

- (a) The reduction ratio requirement and maximum diameter define the forces and the geometry in the transverse plane.
- (b) Free-floating rings react the loads in the radial plane.
- (c) Skewing moments in the tangential plane are eliminated by spacing the gears axially.

Prototype Demonstration and Test Experience

The demonstration of the prototype SABP units was conducted by the Curtiss-Wright Corporation under U.S. Army Air Mobility Research and Development Laboratory sponsorship (refs. 2 and 5).

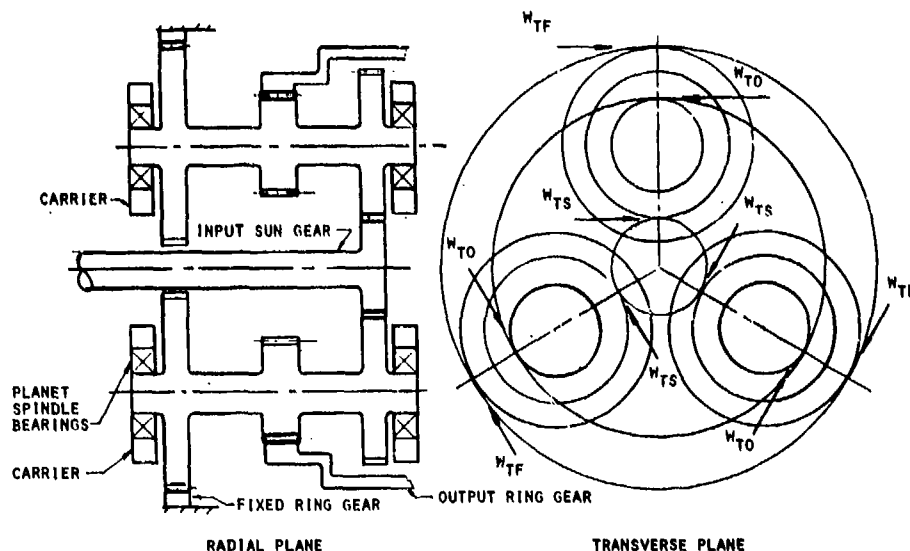


Figure 3. - Conventional compound planetary schematic.

Static Test Results

The prototype units were strain gaged to determine the load distribution among the spindles. Static torque tests indicated good load distribution among the five planet spindles, including good full face gear tooth patterns.

Dynamic Test Results

A 50-hr endurance test was conducted in a back-to-back test arrangement at an input speed of 8000 rpm and at a torque value equivalent to 373 kW (500 hp). The dynamic testing showed that the unrestrained spindles were stable and that, on completion of the endurance test, all hardware was in excellent condition.

Design Study

The objective of the design study was to evaluate the feasibility of using a SABP transmission in an uprated version of the OH-58 helicopter and to make specific comparisons with contemporary OH-58 power transmissions. The table below presents a summary of gearbox specifications used in this study.

Power rating (at 100 %), kW (hp)	335 (450)
Maximum power (at 110 %), kW (hp)	369 (495)
Maximum main rotor speed, rpm	347
Maximum gearbox input speed, rpm	6060
Maximum tail rotor power, kW (hp)	61.8 (83)
Maximum tail rotor output speed, rpm	4130
Angle between rotor and input shaft, deg	95
Power turbine speed	35 000 rpm

Using the above design specifications, three preliminary design layouts were prepared. The first variant, low ratio, has a reduction ratio of 17.46 to 1 and is retrofitable to an OH-58 airframe. The second and third variants, High Ratio and Hybrid, can be coupled directly to the engine's power turbine. All major components have been sized to transmit the rated power at stress levels comparable with those in use in contemporary helicopter transmissions.

For the low ratio variant the gearbox envelope constraints were dictated by the design specification and envelope constraints. Preliminary layouts have shown that, in order to tuck the input stage of the planetary gear down and inside the bevel pinion, the bevel gear must be as large as possible. A bevel gear on the order of 0.3048 m (12 in.) in diameter and a bevel ratio of about 3 to 1 were ultimately selected. Since the design specification calls for an overall reduction ratio of 17.45 to 1, the SABP must have a reduction ratio of about 5.8 to 1. Previous parametric studies have shown that a 5.8 to 1 ratio across the SABP, although technically feasible, is low and not in an optimum range. However, since this configuration met the design requirements and envelope constraints, it was selected as a candidate for the preliminary layout.

Since the high ratio variant and the hybrid design did not have the envelope constraints cited above, it was possible to optimize the gear arrangement to favor higher ratios and to take advantage of the high ratio capability of the SABP. In the high ratio variant a reduction ratio of 26.3 to 1 was selected. This selection resulted in a gear unit approximately 0.4572 m (18 in.) high and 0.4826 m (19 in.) in diameter.

An alternative configuration to the high ratio was also evolved (herein called hybrid). In this arrangement a 15.9 to 1 ratio was taken across the SABP, and the remainder was taken across the spiral bevel mesh and a parallel offset mesh. Here, the height of the unit was reduced to 0.3683 m (14.5 in.) from 0.4572 m (18 in.), and the diameter remained unchanged at 0.4826 m (19 in.).

Figures 4 and 5 depict typical results of parametric studies and illustrate the flexibility of this design concept to vary the height or the diameter of the transmission. Figure 6 illustrates a typical velocity diagram for the SABP using the instantaneous center method.

Efficiency

Power losses were calculated using AGMA gear efficiency formulas. The losses ranged from 8.8 to 11.3 kW (11.85 to 15.2 hp) at the 373-kW (500-hp) rated condition. Comparing these losses with those of a single-stage planetary shows the latter to be more efficient. Comparing these losses with those of a two-stage planetary shows the SABP to be more efficient. These results are consistent with other analysis and indicate that at low gear reduction ratios the SABP does not compare favorably with single-stage reduction gears and that at higher ratios the SABP compares favorably with two-stage planetary gear systems.

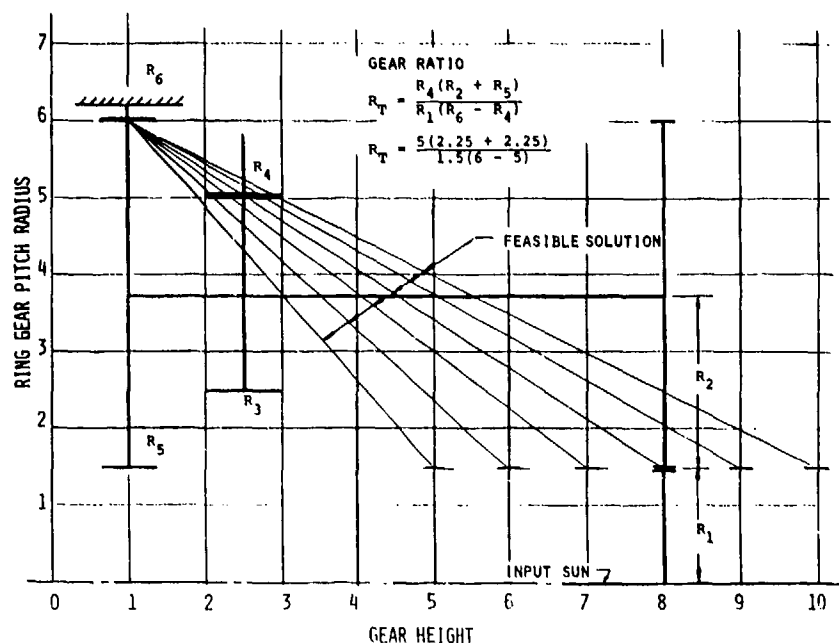


Figure 4. - Parametric study of ring gear pitch radius versus gear height.

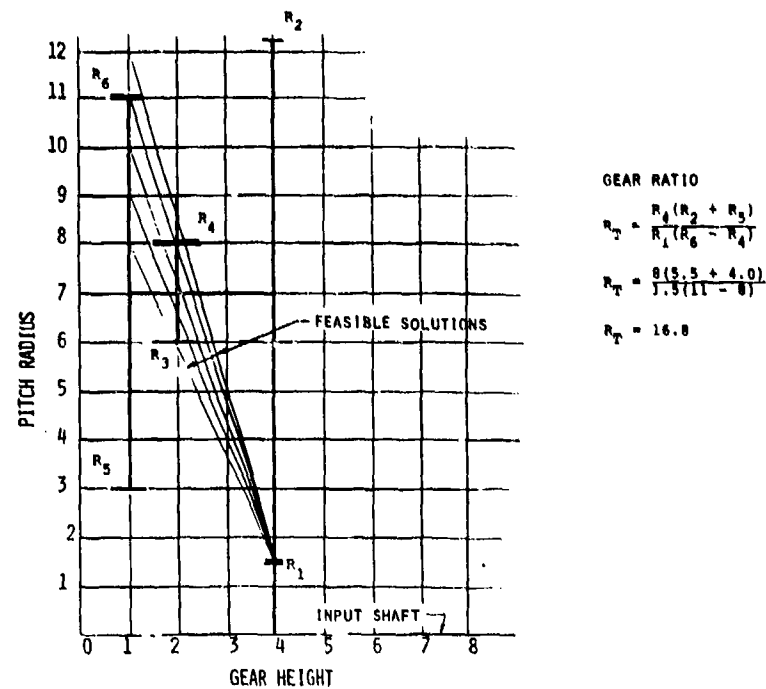


Figure 5. - Parametric study of fixed gear height versus ring gear pitch radius.

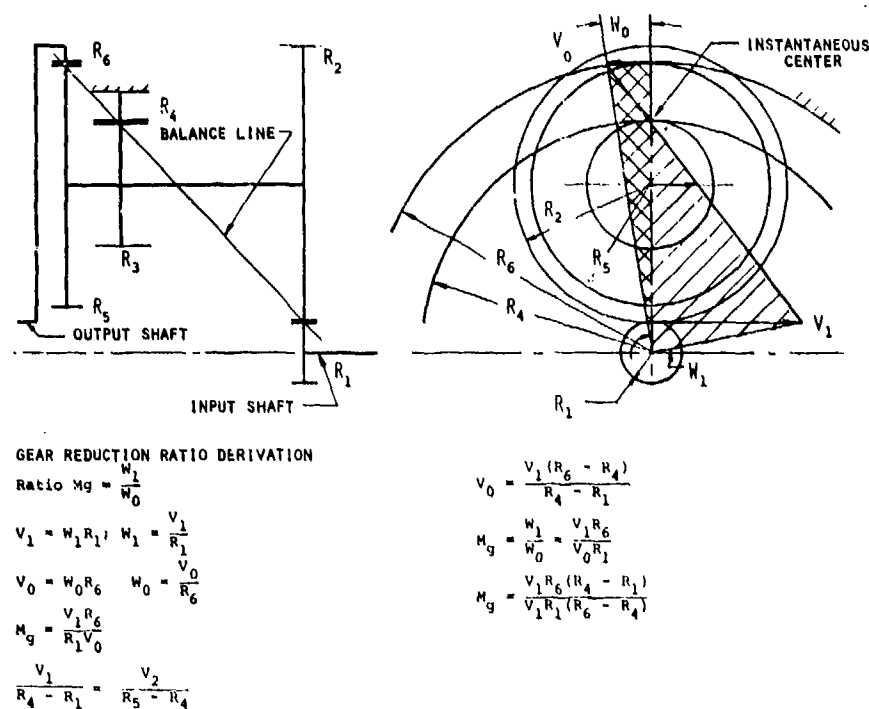


Figure 6. - Velocity diagram.

Weight Analysis

Numerous studies have been undertaken to quantify helicopter transmission weights and to plot the weights of specific helicopter transmissions against various design parameters. References 6 and 7 present the results of two such studies. In these reports the respective authors have compiled actual

helicopter transmission weights and have plotted these weights against such parameters as helicopter gross weight, rotor output torque, the time period in which the transmission was designed, etc.

One of the plots in each report is a curve depicting the weight of the main power transmission as a function of rotor shaft output torque. It is interesting to note that a logarithmic plot of these data produces a straight-line relationship between the weight of a helicopter transmission system and rotor torque. Figure 7 was replotted from reference 5 and depicts this relationship. This plot is very useful in estimating transmission weights of new helicopters and in studying the desirability of new or proposed transmission concepts.

Using the average line drawn through the points plotted in figure 7 and assuming the original power rating of the OH-58 helicopter to be 201 kW (270 hp), the estimated weight of the main power transmission is 56.8 kg (125 lb). This estimate compares favorably with the actual transmission weight of 50.8 kg (112 lb).

Using the average line from figure 7 and uprating the OH-58 gearbox to 335 kW (450 hp), the projected transmission weight is 81.6 kg (180 lb). Using the same slopes established by the average lines in these figures and correcting for the actual transmission weight of 50.8 kg (112 lb), the projected weight of a 335 kW (450 hp) transmission is approximately 74.8 to 77.1 kg (165 to 170 lb). These projected weight values now can be compared with the 62.1 kg (137 lb) calculated weight of the SABP.

These results were also compared with the results and conclusions presented in references 3 and 4. The conclusions of references 3 and 4 are in agreement with the results obtained during this study.

Cost Considerations

In considering producibility of the SABP, the question was analyzed from two points of view: (a) ability to manufacture the required components using current gear manufacturing processes, and (b) cost comparison of the major components of the SABP with the major components of conventional helicopter transmissions.

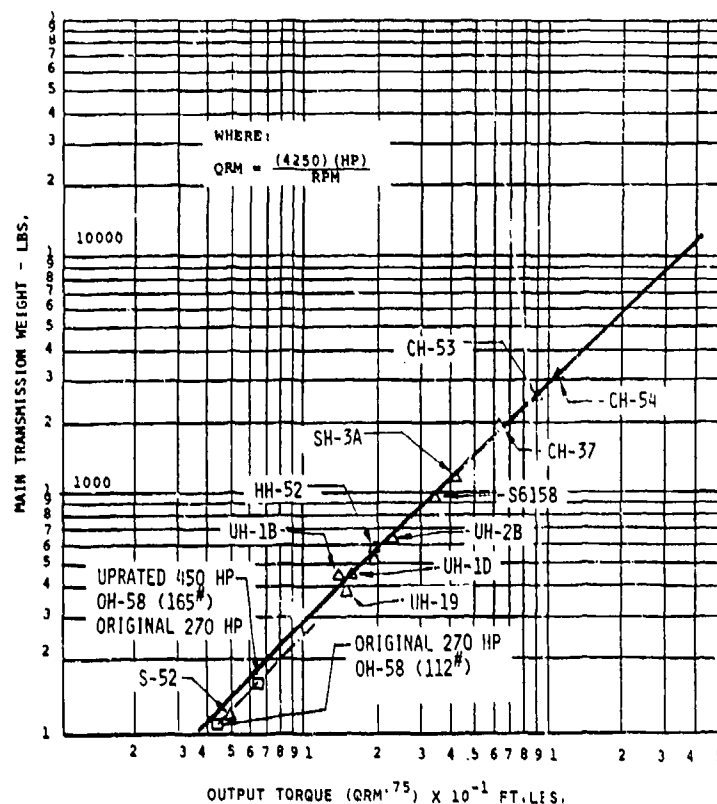


Figure 7. - Main transmission weight versus output torque.

Using the preliminary layouts evolved during this study, a detailed review of all major components was made from manufacturing and processing points of view. This study showed that the processes required to produce the SABP gear units were similar to those required to produce conventional helicopter transmission systems. The SABP design does require that the three gears which form a spindle subassembly be indexed to each other. The tolerance for indexing is on the order of 0.0254 to 0.0762 mm (0.001 to 0.003 in.). This level of accuracy is considered to be readily achievable and is not expected to have an adverse influence on the cost of the spindles. Elimination of the planet carrier and close tolerances associated with the manufacturing of this component on the order of 0.00508 to 0.0127 mm (0.0002 to 0.0005 in.), however, does have a favorable implication on the cost of manufacturing the SABP. Combining the elimination of the planet carriers (one of the most expensive components in the helicopter transmission system) with the reduced number of components in the SABP results in a projected reduction in the overall manufacturing cost of 16.5 to 28 percent when compared with the manufacturing cost of a conventional two-stage helicopter transmission system. There is good agreement between the results of this study and the results of cost studies reported in references 1 and 3.

Survivability and Vulnerability

Assessment of survivability characteristics indicates that the SABP offers improved operation after loss of lubricant when compared with conventional helicopter transmissions. One of the most important of these improvements is the elimination of planet gear bearings which have been found to be the major source of failure after loss of lubricant (ref. 8). The second improvement worth noting is that the gears themselves appear to be more tolerant of loss of oil. The fewer number of parts within the transmission itself means fewer sources of heat—another potential improvement. The mechanical efficiency of the SABP transmission is higher than that of a comparable two-stage planetary; thus, less heat is generated. The SABP transmission density is lower than that of a functionally comparable two-stage helicopter transmission; thus, more cooling air is available.

Reliability

Past experience with helicopter power transmission systems dealing with the subject of reliability and maintainability (R&M) indicates that rolling contact bearings represent one of the major R&M problem areas. If these elements could be eliminated from the helicopter power transmission or if their use could be minimized, the R&M of these units could be improved significantly. It should be noted that one of the inherent characteristics of the SABP is the elimination of planet bearings and carriers (spiders). This characteristic is ranked as one of the most striking features of the SABP and has favorable implication on the projected reliability.

Reliability of the SABP was addressed during the studies reported in references 2 to 4 (as well as during the current effort). These studies considered this question from three points of view:

- (a) Quantitative comparison of the number of major components in the SABP versus contemporary helicopter transmissions (ref. 2)
- (b) Previously established reliability index for critical transmission components (ref. 4)
- (c) Reliability analysis based on over 300 000 flight hr at operating stress levels (ref. 3).

In reference 3 the reliability of the SABP was compared with that of a conventional two-stage planetary transmission. The analysis indicated a 2 to 1 improvement in reliability of the SABP.

Gear Noise

The subject of gear noise has been addressed by numerous investigators, researchers, and practitioners of the art. There is good agreement among the various gear experts that noise is a product of many factors and many design parameters. One of the primary causes of gear noise is the clashing of loaded gear teeth caused by various tolerances, tooth deflections, and vibrations. Gear

noise can be correlated with gear clash frequencies and component resonances. Ordinarily, gear clash noise dominates and can be heard as a combination of distinct tones. Gear clash frequency can be calculated from

$$f = \frac{nN}{60}$$

where f is the gear clash frequency in Hz, N is the number of teeth on a gear, and n is the rotational speed of a gear in rpm.

Gear clash noise is caused by the vibration resulting from two types of impulses which stem from tooth engagement forces. The two types of impulses are pitch circle impulse and engagement impulse.

The magnitude of these factors is controlled by a number of design parameters; the more important of which are diametral pitch, contact ratio, pressure angle, backlash, face width, type of gear, tooth profile, finish, web thickness, material, and natural frequencies.

Pitch Circle Impulse

While undergoing an engagement cycle, gear teeth do not have perfect rolling contact. In the transmission of circumferential force between gears, the point of pressure application travels from the root of the driving gear to its tip and from the tip of the driven gear to its root. As a result of this load variation through an engagement cycle, deflection of the teeth contributes to sliding between them. At the beginning and end of engagement, sliding velocity is maximum, and at the pitch cycle, it is zero. At the pitch circle the direction of sliding reverses, thus reversing the direction of sliding force between the mating teeth and thereby causing the pitch circle impulse. The direction of this impulse is perpendicular to the line of action, and its sense depends on which side of the pitch point the action is taking place.

Engagement Impulse

Whenever a tooth engages, it picks up part of the load carried by the previously engaged tooth. The reduction in loading on the original driving teeth causes them to deflect toward their unloaded positions; thus, imparting tangential acceleration to the gear body. Since the previously engaged teeth are deflected slightly due to loading, the incoming engaging tooth cannot make the smooth contact that it should. Instead, it impacts its mate on the meshing gear and sends an impulse through the bodies of both gears.

Noise Transmission

Gear noise is transferred from its source at the tooth in action to the atmosphere in a number of ways. The direct sound wave radiation from the gear teeth accounts for only a small percentage of the gear noise emitted. The largest amount of transmitted noise is that caused by ringing of the gear bodies and by radiation from other components, including bearings and gear casings.

Gear Noise Design Trends

Over the years, the gear industry has identified parameters which lead to the reduction of gear noise. The voluminous amount of literature available on the subject of gear noise suggests that a gear designer now has sufficient data to design quiet gear trains.

Upon detailed examination of the characteristics required for quiet gears, it can be readily seen that there is a conflict between these design parameters and such considerations as cost of the gear train, envelope constraints, weight constraints, etc. Accordingly, a properly designed gear train must achieve a balance which will satisfy both the design requirements as well as the constraints of cost, performance, weight, size, etc.

Analysis of the SABP shows that many design parameters such as gear size, accuracy, pitch line velocity, gear materials, etc., are comparable to contemporary helicopter transmissions. Therefore, it can be anticipated that the noise intensity of the SABP would be comparable to contemporary helicopter transmissions. Results of hardware testing of prototype SABP type gear units support the above observation. Since comparable quantitative data are not available at this time for the SABP, specific noise levels cannot be cited nor can comparisons be made.

Conclusion

The subject study concluded that the SABP offers significant potential weight and reliability advantages over the contemporary two-stage helicopter power transmissions. Weight savings of 17 to 30 percent have been projected during this study, and a reliability improvement by a factor of 2 to 1 has been calculated. Considering other design parameters such as efficiency, vulnerability, maintainability, and cost, the SABP achieved in all areas a higher rating than conventional two-stage helicopter transmissions. For lower gear reduction ratios, the SABP does not compare favorably with a single-stage planetary.

The potential for weight and size reduction of this new transmission concept appears to lie in its ability to transmit higher torques in a given size due to improved load distribution among the planets and due to the elimination of the planet carriers and planet bearings. These improvements can have significant implications when space and weight limitations are imposed on the transmission designer.

Considering the failure modes and vulnerability of contemporary helicopter transmissions and of the SABP, the new concept should be more tolerant to the loss of lubricant and loss of bearings. The study concluded that for the same output torque and approximately the same gear sizes, the SABP has lower operating gear tooth stress levels, higher mechanical efficiency, and lower heat rejection rate.

The most promising arrangements of the SABP studied are where the reduction ratios ranged from approximately 16:1 to 26:1.

References

1. Lestine, James: Advanced Technology VTOL Drive Train Configuration Study. Sikorsky Aircraft, USAAVLABS Technical Report 69-69, U.S. Army Aviation Material Laboratories, Fort Eustis, Va., AD867905.
2. De Bruyne, Neil: Design and Development Testing of Free Planet Transmission Concept. Curtiss Wright Corporation, N.J., USAAMRDL TR-74-27, Eustis Directorate, Fort Eustis, Va., April 1974.
3. Korzum, A.: Investigation of Advanced Helicopter Structural Designs. Sikorsky Aircraft Division, Conn., USAAMRDL TP-75-59B, Eustis Directorate, Fort Eustis, Va., May 1976.
4. Mack, John and Rumberger, William: Advanced Helicopter Structural Design Investigation. Boeing Vertol, P.A., USAAMRDL TR-75-56-B, Eustis Directorate, Fort Eustis, Va., March 1976.
5. Givens, E. R.; De Bruyne, Neil; and Folenta, D. J.: Design and Development of a Free Planet Transmission. Technical Paper No. 973, presented to the American Helicopter Society, May 1975.
6. Bossler, R. B.: Power Transfer Systems for Future Navy Helicopters. Kaman Aircraft, Conn., Report No. R-1032, Naval Air Systems Command, Department of the Navy.
7. Conboy, J. D.: State-of-the-Art Review on Helicopter Transmissions, Turboprop Gearboxes, and Lubrication Thereof. Naval Air Propulsion Test Center, Report No. NAEC-AEL-1849, Feb. 1967.
8. Bowen, C. W.; Dyson, L. I.; and Walker, R. D.: Mode of Failure Investigation of Helicopter Transmissions. Bell Helicopter Co., Bell Report No. 299-099-479, Jan. 1971.

AD P000707

Hybrid Geared Traction Transmissions*

A. L. Nasvytis† and G. White†

Roller traction drives and geared planetary drives have the common characteristic of multiple drive elements clustered symmetrically around a central member. This form of construction, adopted in order to maximize torque capacity, results in the drive input and output members being coaxial.

Geared planetary drives are associated with high torque delivered from a unit of low frontal area, whereas fixed ratio and variable ratio types of traction drives are renowned for their ability to accept high input speeds at moderate torque levels with least noise.

A combination of the two drive systems retains the feature of coaxial construction and results in a geared section which is capable of providing high torque and a traction section which transfers torque from the toothed pinions to the high-speed input member. Direct coupling of the traction planet rollers with the pinions of the geared unit allows generation of a speed ratio much higher than possible from a planetary unit.

This present work explores the basic configuration of geared traction drives, outlines geometric and structural factors to be considered in their construction, and describes current work on hybrid helicopter transmissions rated at 500 and 3000 hp.

Reduction Ratios from Coaxial Drives

A drawback of conventional planetary gears is that, as more planet pinions are fitted to increase torque capacity, the reduction ratio available decreases. Accordingly, highest torque from a planetary unit of given diameter is associated with many planet pinions and a low speed ratio. But a high speed ratio is possible when many pinions are present, if these pinions are driven directly rather than through the sun gear of a planetary unit. This effect is illustrated in figure 1 where a set of toothed pinions is shown between a sun gear and a ring gear. The lower central section is a conventional planetary drive with a stationary ring gear and input to the sun gear. The top left of the figure shows a ring gear driven by pinions, while the top right shows similar pinions driving an externally toothed gear, termed a sun gear for convenience.

In all cases the gear proportions are the same, with $S = 4P$ and $A = 6P$ where A , P , S denote the pitch diameter of the ring gear, pinion, and sun gear, respectively. Speed ratios obtained from the three arrangements are

Arrangement	Speed ratio	Numerical value
Planetary, fixed ring gear	$(A/S) + 1$	2.50
Sun output, input to pinions	$-S/P$	-4.0
Ring output, input to pinions	A/P	6.0

These trends, true for $P < 0.6 S$, illustrate that, with a coaxial gear arrangement formed from a sun gear, ring gear, and intermediate pinions, the larger reduction ratios are obtained by supplying input torque to the intermediate pinions and taking the high output torque from either of the two gears on the central axis. It follows that the one central gear not used to supply output torque is redundant.

Symbols

a radius of sun roller
 A, P, S pitch diameter of ring gear, planet pinion, and sun roller, respectively

*Work done under NASA Lewis contracts NAS3-20812, -22108, and -22120.

†Transmission Research, Inc.

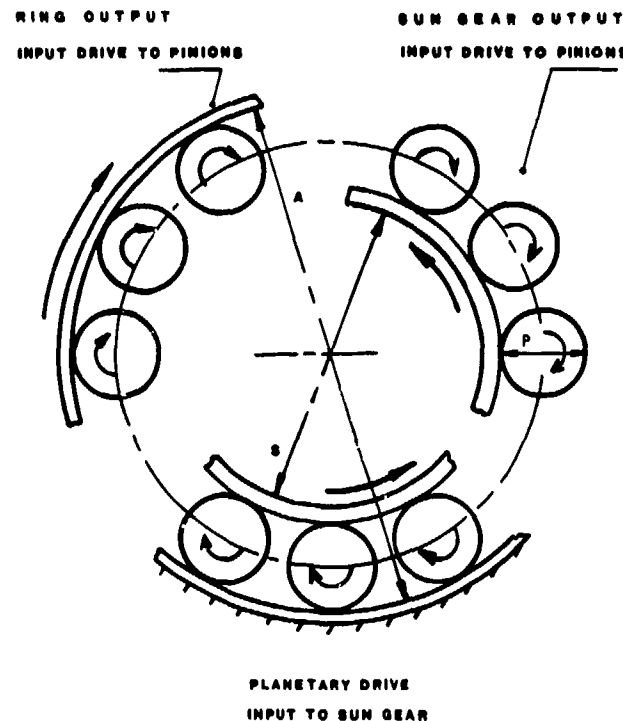


Figure 1. - Comparison of pinion drive arrangements with planetary drive.

B_1, B_2	cone semiangle at first row and second row rollers, respectively
b, c, d	axial spacing of retaining rings
E	Young's modulus
F_1, F_2	radial forces on roller retaining rings
g	radius from central axis of drive to center of ramp contact
k_1, k_2	radial stiffness of retainer rings
n	number of tractive contacts on sun rollers
$P_a, P_{x,1}, P_{y,1}$	normal force at each sun roller contact, x_1 roller contact, and y_1 roller contact, respectively
r	ramp angle of torque loading mechanism, measured from roller axis
S_c	maximum contact stress at roller contacts
T	torque transmitted
t	traction coefficient, defined as ratio of tractive force to normal load
w	roller contact width
x_1, y_1	first-row roller radii (see fig. 2)
x_2, y_2	second-row roller radii (see fig. 2)
α	angular location of second-row rollers (see fig. 2)
φ	pressure angle of gear teeth

Traction Drive to Toothed Planet Pinions

The foregoing section demonstrates that one way of overcoming the ratio limitation of a fixed-ring planetary unit, while still retaining torque capacity, is to drive the planet pinions individually instead of collectively through the sun gear. This procedure is clearly most effective when many pinions can be fitted, a condition at which a planetary unit offers high torque capacity but low ratio.

Given that a high ratio unit can be formed by driving a central output gear through many pinions, there remains the problem of transmitting torque to these pinions and ensuring that each pinion contributes only its designed share of total torque.

In this respect the introduction of a traction unit shows to advantage. The creep phenomenon associated with a traction drive determines that each traction roller receives a torque which is dependent on the creep rate between the sun roller and the planet roller interface. Essentially, the traction unit divides torque between its rollers by fluid film traction. This torque distribution then passes to any geared elements connected to the traction rollers. In the case of these geared pinions driving a collector gear, all the pinions and attached traction rollers are locked at a common speed, and so the only factor affecting creep rate and hence torque distribution is that of film thickness between the sun roller and the nominally identical pinions.

At the interface pressure used in traction drives the incremental stiffness of the fluid film is higher than the radial stiffness of the drive support structure. Moreover, traction roller surfaces can be held to tolerances approaching those associated with rolling contact bearings. These conditions, in combination with the load-balancing properties of a three-point support, lead to equality of film thickness at each roller contact, and, in consequence, ideal matching of torques between as many pinions as drive the gear.

Type of Traction Unit

The traction section of a hybrid drive consists of a central roller surrounded by one or more rows of planet rollers. With the simplest and traditional method of construction only one row or ring of planet rollers is present. The number of torque points then is limited to the number of planet rollers that can be fitted, and there is no benefit in respect of speed ratio.

In addition to distributing torque to geared pinions, however, the traction unit must span the radial distance between the drive central axis and the geared pinions. High ratios at the geared stage are associated with a large diameter output gear, and consequently a greater radial distance to the pinion axes than can be conveniently bridged by a simple sun, planet, and ring roller type of traction unit.

With a double row of planetary traction rollers the complexity of the design increases, but several benefits are realized:

- (1) The number of traction contact surfaces is twice that of the number of rollers fitted.
- (2) An increased number of rollers can be fitted.
- (3) Stepped rollers pack compactly and also provide a gain in speed ratio.
- (4) Dual rows of stepped rollers provide axial stability and assist in the fitting of a torque loading mechanism.
- (5) An increased radial distance to the outer-row rollers makes it convenient for these rollers to drive geared pinions.

These factors can be seen in figure 2, which shows the structural arrangement of a two-row traction drive.

Speed Ratios

When stepped rollers are used, a speed ratio in the region of 3.5:1 at the traction section can be combined with a ratio between 8:1 and 10:1 at the geared stage. In this way the combined geared-traction assembly can provide overall ratios of about 30:1. This ratio is larger than feasible from two planetary units in series. Accordingly, geared traction assemblies show to best advantage at higher speed ratios than those which are naturally suited to geared planetary units.

For very high speed ratios (over 40:1 in total) three-row traction assemblies are appropriate, especially in the case of speed-increasing applications where the sun rollers of the traction unit have to rotate at speeds above 30 000 rpm.

Similarity with Pure Traction Drive

Previous work on pure traction drives (refs. 1 and 2) has demonstrated successful operation of the two-row roller configuration at high speeds and moderate torques. Experimental results from

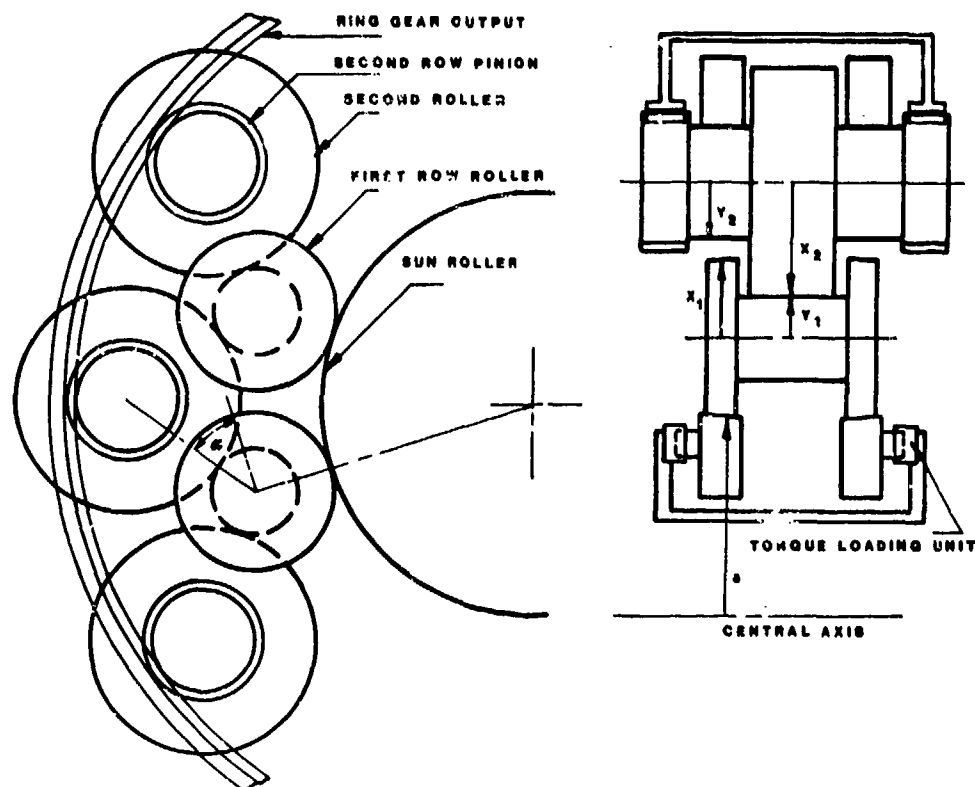


Figure 2. - Structural arrangement of two-row geared traction drive.

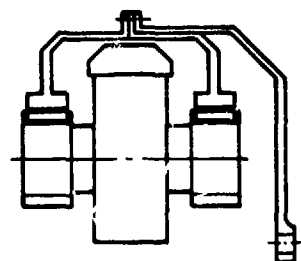


FIG.3A DUAL PINIONS AND SINGLE RETAINING RING

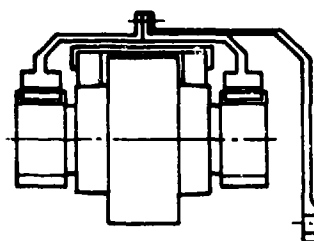


FIG.3B DUAL PINIONS AND LINKED RETAINER RINGS

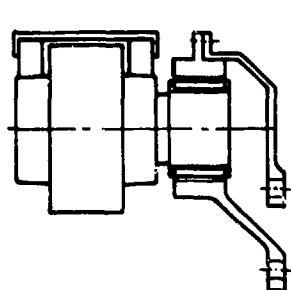


FIG.3C ASYMMETRIC ARRANGEMENT WITH SINGLE PINION AND EITHER INTERNAL OR EXTERNAL OUTPUT GEAR

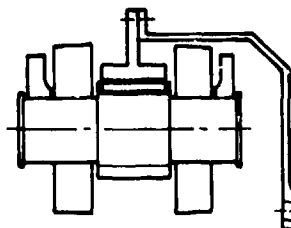


FIG.3D SINGLE PINION WITH DUAL RETAINER RINGS AND INTERNAL GEAR OUTPUT

Figure 3. - Arrangements of second-row roller toothed pinion.

these designs, obtained in back-to-back tests, provide a background from which to select roller geometry, operating stresses, fluid temperatures, and design traction coefficient. Attempts to provide increased torque capacity from these pure traction drives led to the present work in which the torque capability and overall ratio are extended by combining toothed pinions with the outer-row rollers.

Arrangements of Second-Row Rollers and Geared Stage

Coupling of the outer-row traction rollers to the toothed pinions can take a number of forms (fig. 3). Symmetric arrangements with no resultant skewing motion on a planet shaft involve the use of a ring gear. Figures 3(a) and (b), for instance, make use of dual ring gears and either a single retaining ring or dual retaining rings.

Figure 3(d) is also symmetrical, with a single ring gear, whereas the asymmetric arrangement of figure 3(c) can involve either an internal gear or an external gear to combine the pinion torques. Design work demonstrates that for high torque applications the asymmetric arrangement of figure 3(c) offers the least weight as a result of keeping to a minimum the number of large-diameter torque transfer rings. It is for this reason that the helicopter transmission designs discussed are based on figure 3(c).

Traction Unit Components

Torque Loading Mechanism

Roller contact loads are made proportional to transmitted torque by means of a torque loading mechanism. The reason for introducing such a device is to avoid rollers carrying high contact loads when low torques are being transmitted; a result is a marked increase in fatigue life according to the difference between mean torque transmitted and maximum design torque.

Torque loading mechanisms invariably act on conical members in order that an axial motion of a cone takes up the radial elasticity of the drive. Thus the greater the radial stiffness of the traction section, the less the cone angle of the torque sensing rollers can be, and the lower is the ratio of spin/roll motion at the contacts. Low spin, of course, is associated with low losses and high efficiency.

For any applied torque there is a unique relation linking the ramp angle r of a torque loading mechanism with the radius g at which it acts and the contact radius a of the traction roller or cone. With a traction cone of semiangle B designed to work at a traction coefficient t defined as the ratio of tangential to radial force at each contact,

$$g \sin B = at \tan r$$

This nondimensional expression is independent of torque, as it ought to be. Typically, designing for a traction coefficient t of 0.06 and for $B = 3^\circ$ results in the geometry, $\tan r = 0.872 g/a$. If g/a is in the region of unity, the ramp angle r is 41° , which is higher than would be initially anticipated.

A further aim is that the torque loading mechanism operate progressively with no frictional loss; that is, a pure rolling motion in the loading mechanism is preferred.

First-Row Rollers

Each roller in the first row is in equilibrium under the contact forces set up at one sun/roller contact and two second-row roller contacts. The number of these contacts is of course doubled if a two-sided configuration is adopted. Early designs of traction units tended to the use of true roller surfaces on all diameters, with shoulders to restrict axial motion. More recently, however, it has been demonstrated that axial positioning and stability of the first-row rollers can be maintained by certain convex/concave roller surfaces (ref. 1). This technique brings two major advantages. First, there is no possibility of flange scuffing, and, second, any flange power loss, as experienced in alternative designs, is eliminated.

First-Row Contact Conditions

The necessary normal load P_a at each contact point of the sun roller with a first-row roller is set by the torque transmitted T and the operating traction coefficient t . Thus, with n contacts on a sun roller of radius a ,

$$T = tnaP_a$$

and the axial force necessary to set up the required normal load on each half of a split sun roller is

$$\text{Sun roller axial force} = T \sin B / (2at)$$

This axial force is imposed by the torque loading mechanism.

A first approximation to surface contact stress is given by assuming that the contacting surfaces are cylinders. Then with roller width w_1 roller radii a and x_1 semicone angle B_1 modulus E and contact stress S_c conventional contact stress analysis gives, with Poisson's ratio = 0.3,

$$w_1 a x_1 S_c^2 = 0.175 E P_a (a + x_1) \cos B_1$$

from which the torque capacity can be expressed as

$$T = 0.57 S_c^2 w a^2 x_1 n t / [E(a + x_1) \cos B_1]$$

Second-Row Rollers

Second-row traction rollers transmit torque to the pinions of the geared section. It is through these rollers that torque reaction passes to the transmission housing; in consequence, only these rollers need support by bearings. Radial components of the two contact loads on each second row roller are reacted by the free-floating retaining rings. In this way the second row bearings do not carry radial forces, provided freedom is given to accommodate any radial growth of the retaining rings.

Second-Row Contact Loads

A normal force P_a acting at each sun roller/first-row contact results in a corresponding radial force $P_a \cos B_1$. This force is supported on two second-row rollers, each inclined at $90^\circ - \alpha$ from the line of action of the radial force. The interface load $P_{y,1}$ between the first- and second-row rollers of radius y_1 and x_2 , respectively, and semicone angle B_2 then is, ignoring the traction force difference,

$$P_{y,1} = P_a \cos B_1 / (2 \sin \alpha \cos B_2)$$

Eliminating force P_a results in a general relation linking contact stress S_c torque T transmitted by the sun cones, and the roller contact width w_2 such that

$$S_c^2 w_2 t n a \sin \alpha \cos B_2 = 0.88 E T \cos B_1 (y_1 + x_2) / (y_1 x_2)$$

Retaining Ring Conditions

Internal radial forces acting on the traction rollers are contained by floating retaining rings. To avoid the retaining rings carrying edge loads the contact surfaces are made slightly convex, or the two rings are coupled so that any endwise creep and consequent edge loading is avoided. A form of retaining shoulder is included, however, which is normally inactive, but serves to keep the rings normal to the central axis when the unit is unloaded.

The radial load F set up by each second-row roller and reacted by the retaining ring, or rings, is derived from the vector sum of $P_{y,1}$ loads:

$$F = 2P_{y,1} \cos y = T \cos B_1 / (t n a \sin \alpha \cos B_2)$$

Different positions for the rings can be chosen (fig. 3), depending on any restriction in either the radial or axial direction. If a single retaining ring is chosen, this fits symmetrically around the outer-row rollers. Variable-ratio traction drives based on a spherical outer member adopt this type of construction. But separate retaining rings on each side of the outer roller are effective when axial length is not restricted. Further, this design is essential if each outer roller drives a single pinion; for a single pinion makes the radial forces asymmetric.

Forces Acting on Rings

A general arrangement from which any special case can be derived consists of two retaining rings, distances b and c , respectively, from the centers of the outer-row roller. The midpoint of a toothed pinion is distance d from the centers of the adjacent ring. Forces acting on each outer row roller must be in equilibrium and comprise the reaction forces F_1 and F_2 from the retaining rings, $P_{x,2}$ from the first-row rollers, and the tangential tooth load W_t from the pinion. The radial load from the pinion is accordingly $\pm W_t \tan \theta$, the plus and minus signs being appropriate to a collector gear with external teeth and internal teeth, respectively. Conditions to be satisfied are

$$\text{Radial equilibrium, } F_1 + F_2 + W_t \tan \varphi = P_{x,2}$$

$$\text{Radial stiffness, } k, \quad F_1/k_1 = F_2/k_2$$

$$\text{Moment balance, } bF_1 = cF_2 + (c+d)W_t \tan \varphi$$

Forces on each retaining ring are found to be

$$F_2 = P_{x,2}b/(b+c) - W_t \tan \varphi(b+c+d)/(b+c)$$

$$F_1 = P_{x,2}c/(b+c) + W_t \tan \varphi(d)/(b+c)$$

and the ring stiffness are related by

$$k_1 = k_2(c/b) + k_d(c+d)/b$$

where k_d is the total drive stiffness as measured, for instance, by the ratio of ring radial deflection to applied load.

Equivalent expressions for ring loads in terms of a known torque T applied to the sun rollers are

$$F_2 = \frac{bT \cos B_1}{2(b+c) \tan \alpha \sin \alpha \cos B_2} - \frac{(b+c+d)W_t \tan \varphi}{b+c}$$

$$F_1 = \frac{cT \cos B_1}{2(b+c) \tan \alpha \sin \alpha \cos B_2} + \frac{dW_t \tan \varphi}{b+c}$$

Conditions for Equal Ring Forces

Ring forces F_2 and F_1 can be equal at the conditions set by

$$(b-c)P_{x,2} = (b+c+2d)W_t \tan \varphi$$

when b , c , and d must be adjusted appropriately. For the symmetrical condition of $b=c$, the only solution for equal loads is with $d=-c$; that is, with the pinion equally spaced between the two retaining rings.

Helicopter Transmission Design

Present work on geared traction-drives centers on their application to helicopter main gearboxes. These designs are based on the torque rating and overall speed ratio of existing commercial transmissions, principally those of the OH 58 and the UH 60A aircraft. Benefits attempted in these applications can be summarized as

- (1) High speed-ratio from coaxial geared/traction section
- (2) Elimination of a speed reduction stage
- (3) Weight benefit at speed ratios higher than naturally suited to geared planetary units
- (4) Equal loading of toothed pinions by tractive creep mechanism
- (5) Noise reduction in roller drive section.

Low Ratio 500-hp Transmission

This transmission follows the speeds and torques appropriate to an OH 58 unit uprated to 500 hp. The input speed to the transmission is only 6060 rpm as a result of a double reduction stage being present in the engine reduction gearbox. The overall speed ratio required in the transmission is 17.4:1 for a main shaft speed of 347.5 rpm.

Since a bevel gear train is necessary in the transmission and a speed reduction is taken at this point, there remains only a modest ratio to be generated by the geared traction unit. Speed ratios selected for each section of the drive are

Geared traction section	8.5:1
Input bevel train	2.05:1

While a ratio greater than 8.5:1 would be preferable at the traction section, this is not feasible, given the input speed of 6060 rpm. This ratio, however, contrasts with the 4.7:1 ratio taken in the planetary unit of the OH 58 design.

Figure 4 shows a schematic arrangement of the drive elements. The combined geared-traction section fits around the transmission main shaft exactly like a planetary unit. But the carrier frame for the final row rollers and pinions is held stationary by the housing, against which torque is reacted, while output torque to the main shaft is taken from the ring gear. Input torque to the bevel pinion is carried by the bevel gear to a ramp and roller type of torque loading unit. This unit drives the dual-sun rollers. Compression springs also are included in the torque loading unit so that, at zero and low torques, the traction rollers experience a contact force.

Ten sets of traction rollers in each row results in there being 20 torque transmitting contacts at the sun rollers. Similarly, there are 10 pinions meshing with the output ring gear. This arrangement gives the benefit of conformal tooth contacts at the high-torque section of the transmission. The toothed output pinions are located in hollow, splined outer-row rollers. Earlier designs included pinions which were electron-beam welded to the rollers; but the splined design was adopted to avoid a weld in an area of high cyclic stress and, also, to permit regrinding of the pinion teeth.

Bearings locating the outer-row rollers are mounted in sleeves that can roll slightly in the housing surrounding the bearing. In this way radial growth of the outer roller axis, allowed by expansion of the retaining rings, does not result in a radial load on the bearings. Accordingly, bearings on the outer-row rollers react only tangential loads into the carrier frame.

To minimize height, the shaft carrying the bevel gear is supported at each side of the traction unit. The top bearings on this shaft react bevel gear thrust into the carrier frame and to tie bolts which connect the middle and lower housings of the transmission. Three main housing sections are present, although a two-section design is possible. The top section contains the main lift bearings, and the transmission torque-reaction spigots; the middle section contains the traction unit and allows this unit to be assembled entirely on the bench; the lower housing carries the input bevel pinion, the lubrication pump, and associated items.

Design weight for the low ratio design is 146 lb with an all-steel carrier frame. This weight is competitive with the 141 lb of an uprated OH 58 design, detailed in reference 3, as a result of incorporating lower gear and bearing stresses.

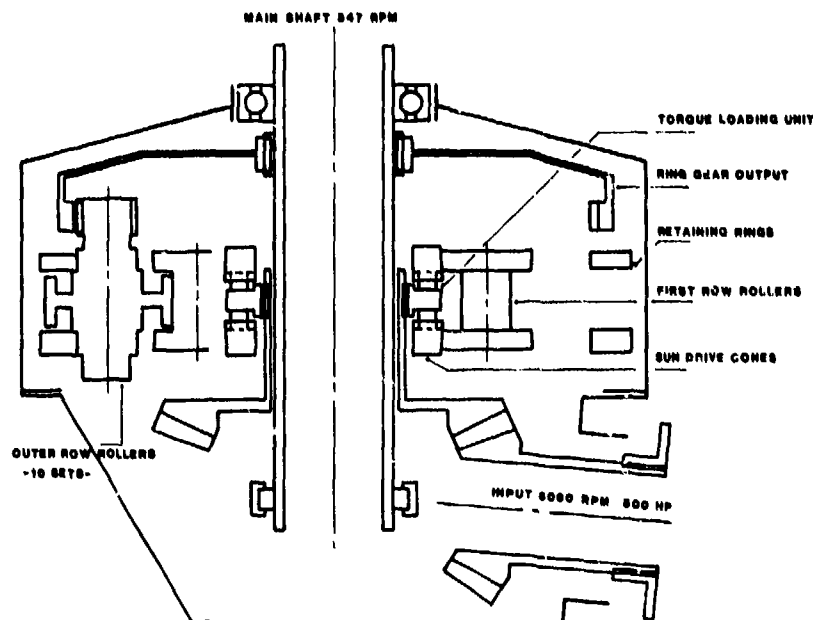


Figure 4. - Schematic of 500-hp helicopter transmission with 6060 rpm input speed.

High Ratio 500-hp Transmission

Parametric studies on designs with different speed ratios but the same output torque capacity have demonstrated that hybrid geared traction drives can provide gains in overall ratio with only minor weight increments. Thus, from a weight standpoint, a geared traction drive shows to best advantage at high speed ratios. On this basis a 500-hp helicopter transmission was investigated based on a main shaft speed of 347.5 rpm and an input speed of nominally 36 000 rpm. These speeds, with an overall speed ratio of 103:1, correspond to those of the OH 58 transmission from the main shaft to engine.

Three reduction stages are present and consist of

- (a) A final gear-reduction stage based on seven pinions driving a rotating ring gear
- (b) An intermediate stage traction drive in which the outer-row rollers drive the toothed pinions
- (c) A bevel reduction stage which accepts an engine speed of about 36 000 rpm.

A schematic arrangement of the transmission is shown in figure 5. Engine input power passes through an overrunning clutch to a bevel train of 3.75:1 ratio. The remaining 27.5:1 reduction ratio is taken in the geared traction section. This high ratio contrasts with the lower ratio of 8.5:1 necessary when the transmission input speed is 6060 rpm as a result of retaining the engine reduction gearbox. With the high ratio design, however, the transmission housing diameter increases in consequence of the larger second-row rollers. Seven sets of rollers and toothed pinions are present in the traction section.

A later design of the high ratio transmission involves inversion of the bevel gear and the traction drive section in order that the transmission can fit conveniently on the same test stand as the low ratio design. An overrunning clutch unit is omitted from the design, and the input shaft is connected directly to the bevel pinion. Bearings for this high-speed pinion consist of a front roller bearing, a tandem pair of angular-contact bearings to react thrust, and a forward-mounted bearing to preload the tandem bearing pair.

Otherwise the design follows closely that of the low ratio unit. The bevel gear is straddle-mounted across the traction section, oil transfer tubes and retaining bolts pass through hollow first-row rollers, toothed pinions are splined to the second-row rollers, and the main housing separates into three sections.

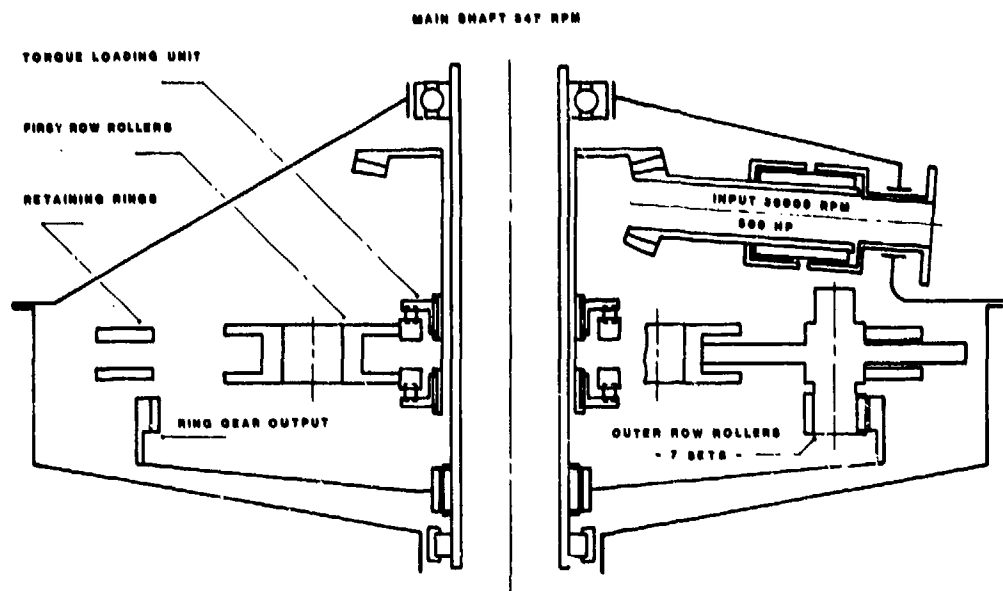


Figure 5. - Schematic of 500-hp helicopter transmission with 36 000 rpm input speed.

Weight estimates for this design give a dry weight of 158 lb for a main rotor torque of 90 680 in-lb. The incremental weight gain from the low ratio design is only 12 lb, a feature that emphasizes the benefit of including all the reduction trains from the engine to the main shaft in one transmission. This trend to eliminate gear trains in an engine reduction gearbox also results in reduced drive train losses.

3000-hp Transmission

Attempts to design traction drives of high power capacity coincided with the development of several twin-engine helicopter transmissions rated at 3000 hp. Accordingly, it proved convenient to adopt the torques and speeds of the UH 60A geared transmission as a design specification for a hybrid traction drive.

The overall speed ratio required is 81:1 between the main shaft at 258 rpm and the engine at 20 900 rpm. This ratio is spanned in three stages consisting of

- (1) A final, geared stage with six pinions, 10:1
- (2) Intermediate traction unit, six roller sets, 3.39:1
- (3) Engine reduction and combining bevel, 2.4:1

The ratio of 34:1 taken in the geared traction section is sufficiently high that only one bevel gear stage is necessary to match the engine speed of 20 900 rpm. In consequence, to avoid a second bevel train, the engine axes intersect the transmission main shaft and are inclined outward at 30° from the centerline of the fuselage. In this way the number of speed reduction stages is kept to the minimum of three, and the engines are widely separated.

Figure 6 shows a schematic layout of a 3000-hp transmission, being a section through the main shaft, one engine input, the traction section, and the tail drive gears. Each engine drives through an overrunning spring clutch to a bevel pinion and a combining bevel gear. The bevel gear thus carries the sum of engine powers.

Tail drive power is extracted from the bevel gear shaft by a train of spur gears. This arrangement ensures that the traction drive carries engine power less tail drive power. With a free choice of tail drive position, one stage of spur gears could be eliminated. The arrangement adopted, however, allows the exact speed ratios and drive shaft positions of the UH 60A transmission to be duplicated.

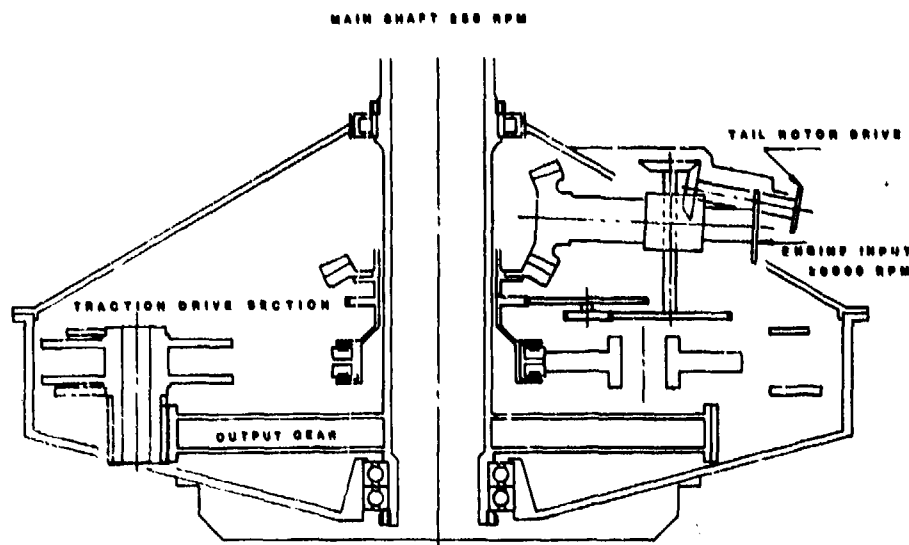


Figure 6. - Schematic of 3000-hp twin-engine helicopter transmission.

Input bevel pinions are larger in diameter than would normally be the case because the bevel gear is limited in minimum diameter by having to pass around the main shaft; the low ratio in the bevel train then sets the bevel pinion at a larger diameter than necessary from a tooth load standpoint. The torque loading unit is driven from the main bevel gear and serves to load equally each side of the split sun rollers. Outer-row rollers are located by bearings which fit directly in the main housing at the lower end and in a subsidiary cover at the top end. In this way the geared traction section is held independently of the top section of the transmission housing. Similarly, the engine input sections and the combining bevel gear and bearings are contained in the upper housing.

The traction unit serves to divide transmitted torque equally between six final-stage pinions which drive the output gear. This output gear is of the external tooth type. The alternative design with internal teeth does not show to advantage from a weight standpoint, since the benefit of a slightly narrower face width on the combining gear is negated by a gain in support structure weight for the ring gear. The combining gear is mounted directly on the main shaft, thus avoiding the need for separate support bearings.

Weight estimates for the 3000-hp design yield a total of 1020 lb for a dry unit without accessory drives. Some 4-percent reduction from this figure appears possible by design refinements in the areas of the housing and the combining gear webs.

Discussion and Summary

Completion of design work on the 500- and 3000-hp transmissions enables general trends to be established for hybrid geared traction drives.

1. A weight advantage can be demonstrated at speed ratios in the geared traction unit, which are higher than those naturally suited to a geared planetary unit. Thus, if the ratio in the coaxial section of the drive is in the region of 3:1 for a single planetary unit, 9:1 for a double planetary unit, and 30:1 for a three-stage unit, the advantage from a weight standpoint lies with planetary units. In these cases, however, the large number of planet pinions present require a corresponding number of support bearings.

If the ratio per planetary stage is greater than about 3.8:1, then the geared traction drive shows a weight advantage.

2. The housing diameter for the geared traction drives is larger than that of a wholly geared unit, especially when high ratios are needed.

3. Noise levels for the geared traction transmission are anticipated to be lower than for an equivalent geared system. Numerical data on this effect are available from pure traction units, but confirmation in the case of high power awaits test results from a 500-hp unit now at the assembly stage.

4. The coaxial arrangement of a geared traction unit enables its installation in a helicopter transmission to follow procedures established by the use of geared planetary units. The trend to high ratios in the geared traction unit means that there is little advantage in employing an epicyclic arrangement in place of the fixed-axis design. Restrictions on the diameter of the main shaft are not present as a result of the sun traction rollers being larger than the sun gear of an equivalent geared drive.

5. Benefits in respect of traction drive sizing and life result from extracting tail drive power prior to the geared traction unit.

6. Torque capacity and overall weight are dependent on the allowable contact stress at the traction surfaces. Test data from smaller traction drives indicate that surface stressing to levels between those experienced in gear teeth and rolling-contact bearings is appropriate. This is a result of the elliptical contacts at roller surfaces, with a minor axis in the direction of rolling, being able to accommodate structural misalignment more easily than gear teeth of wide facewidth.

7. The tendency for geared traction units to show advantage at high speed ratios means that the total drive train from engine to main shaft must be included in a design. The least advantage is present, as with the low ratio 500-hp design, when an existing engine reduction gearbox has to be accommodated.

References

1. Loewenthal, S. H.; Anderson, N. E.; and Nasvytis A. L.: Performance of a Nasvytis Multiroller Traction Drive. NASA TP-1378, Nov. 1978.
2. Loewenthal, S. H.; Anderson, N. E.; and Rohn, D. A.: Evaluation of a High Performance Fixed-Ratio Traction Drive. ASME Trans., vol. 103, April 1981.
3. Braddock, C. E.: Design of an Advanced 500 HP Helicopter Transmission. Advanced Power Transmission Technology. NASA CP-2210, 1982.

Impact of NASA-Sponsored Research on Aircraft Turbine Engine Bearing Specifications

A. H. Nahm

The current General Electric Premium Quality Bearing Materials Specifications and Design Practices for aircraft gas turbine engine bearings is the culmination of many years of R&D work and engine operational experience. The R&D investigations have been carried out as in-house work or as a cooperative approach among government agencies, academic and research communities, and bearing and steel manufacturers. The GE bearing material specification (C50TF56), for example, requires double vacuum melting (VIM-VAR), certain hardness range, restricted grain size, forging flow conformity, precise control of chemical composition, etc.

For familiarization, a cutaway view of a typical high bypass turbofan engine is shown in figure 1. It has eight main engine bearings: two ball and six roller. The main thrust bearing runs at about 1.7×10^6 DN (168-mm bore \times 10 000 rpm) with a cubic mean load of 2500 lb. (DN is a measure of bearing speed: the bore diameter, D , in millimeters, multiplied by the rotational speed in rpm.) Most main engine bearings manufactured in the U.S.A. are made with AISI M-50 material.

To present a historical background, figure 2 shows the evolutionary development of AISI M-50 as a major bearing material in aircraft gas-turbine engines. A significant improvement in bearing life has been achieved during the last two decades. The improvement may be a conservative estimate. Full-scale bearing tests indicated greater than 40 in the material life factor (ref. 1). Before the mid-1950's, AISI 52100 steel was a major bearing material in aircraft engines and is still in use today in some restricted engine applications.

The purpose of the present paper is to briefly review the advancement of the state-of-the-art in aircraft bearing materials technology. For more details on the subject, other reviews (e.g., refs. 2 and 3) are available. In the present paper, particular reference will be made to current specifications and design practices resulting from NASA-sponsored programs.

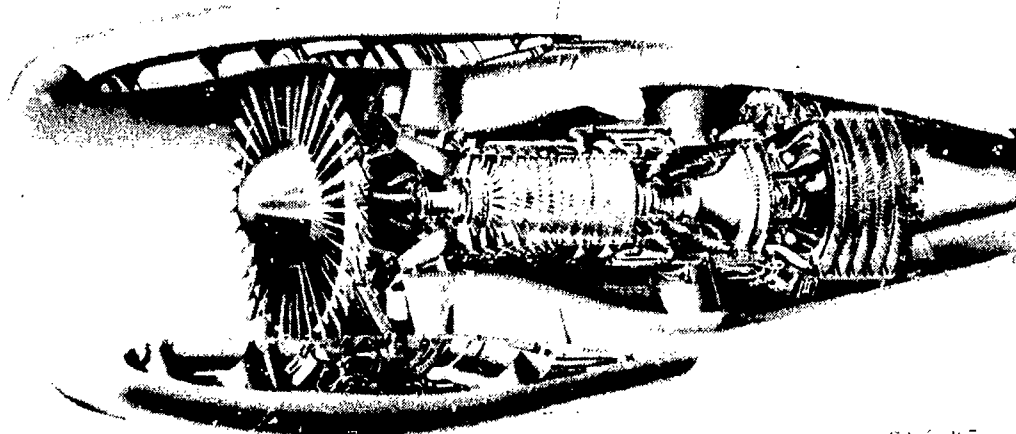
Melting Practice

One of the technical breakthroughs in materials engineering is the advent of the vacuum melting process in steel industries in the late 1950's to early 1960's. With the development of larger scale production melting furnaces, drastic improvement in micro- and macroscopic homogeneity and cleanliness was realized. This, consequently, resulted in a significant improvement in materials properties including rolling contact fatigue life. Macroscopic inhomogeneity is, for example, characterized by freckles, segregation, and casting structure. Microscopic cleanliness can be described in terms of the amount of inclusions and gas content. Carbide distribution and chemical composition can be favorably controlled by employing the vacuum melting process. Earlier studies, including those performed by NASA (refs. 4 to 7), showed that certain types and locations of inclusions strongly influence the rolling contact fatigue-life performance of bearing steels. In general, cleaner steels with less inclusions, gas elements, and trace elements will improve the fatigue life.

In fatigue life testing of 6309-size bearings, AISI 52100 bearing (ref. 8) inner races made from air melt and five successive vacuum consumable remelts of the same heat showed four times the fatigue life of those of air melted heats (fig. 3).

Currently, the bearing material for aircraft engines, AISI M-50 is being processed via a double vacuum melting process—vacuum induction melting (VIM) followed by vacuum arc remelting (VAR). Each process has its own advantages and disadvantages. It was recognized in the mid 1960's

*General Electric Company.



CS-0287

Figure 1. - Cutaway view of a typical high-bypass turbofan engine.

Life Improvement
(Baseline
AISI-52100
Air Melt = 1.0)

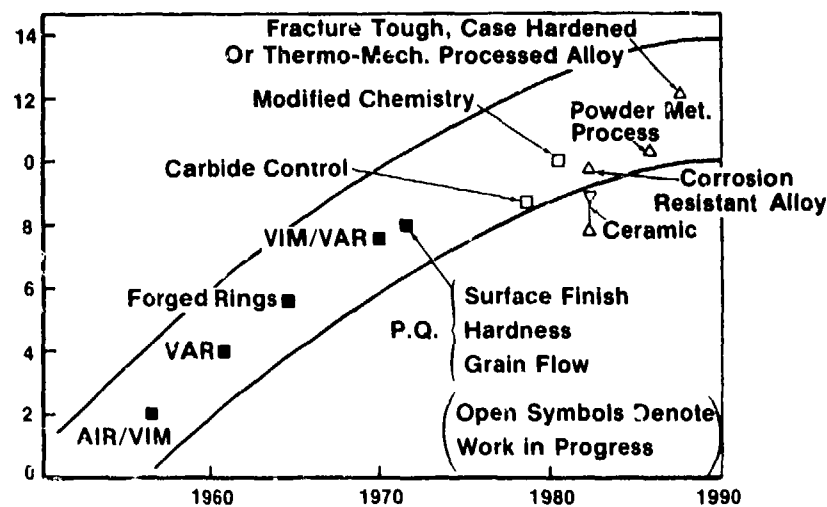


Figure 2. - Evolution of AISI 52100 bearing steel.

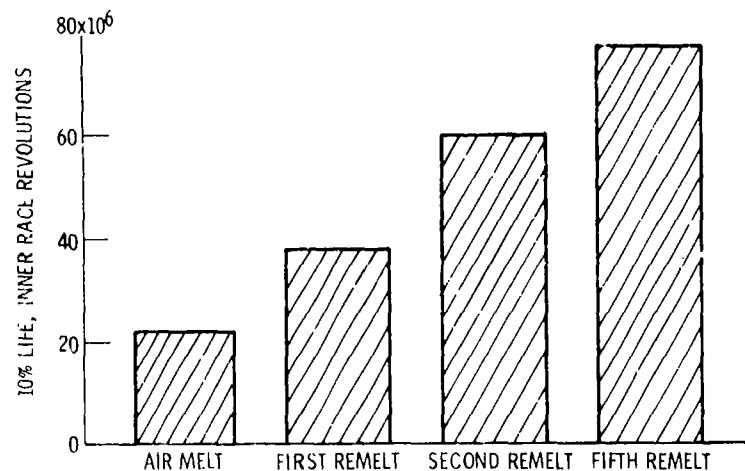


Figure 3. - Life of 52100 inner races made from air melt and suc-

that the combination of these two processes produced an even better product by obtaining the advantages of both as well as eliminating the disadvantages of the first process (VIM). The two principal disadvantages of the VIM process are the reaction with crucibles and the solidification pattern developed in cast ingots. These limitations are largely eliminated in a subsequent vacuum arc remelting furnace (ref. 9). Figure 4 shows these processes.

In concurrence with the development of the large scale, commercial double vacuum melting facilities in the steel industry, General Electric, initiated an extensive evaluation of the melting processes using rolling contact (RC) fatigue rigs. Figure 5 shows a summary of the RC rig evaluation of air melted and vacuum arc remelted (AM-VAR), double vacuum arc remelted (VAR-VAR), and vacuum induction melted and vacuum arc remelted (VIM-VAR) heats. More than 20 heats of AISI M-50 were evaluated. The advantage of the VIM-VAR process in AISI M-50 is apparent in figure 5. Based on this, it was decided to standardize the VIM-VAR AISI M-50 material as the aircraft engine

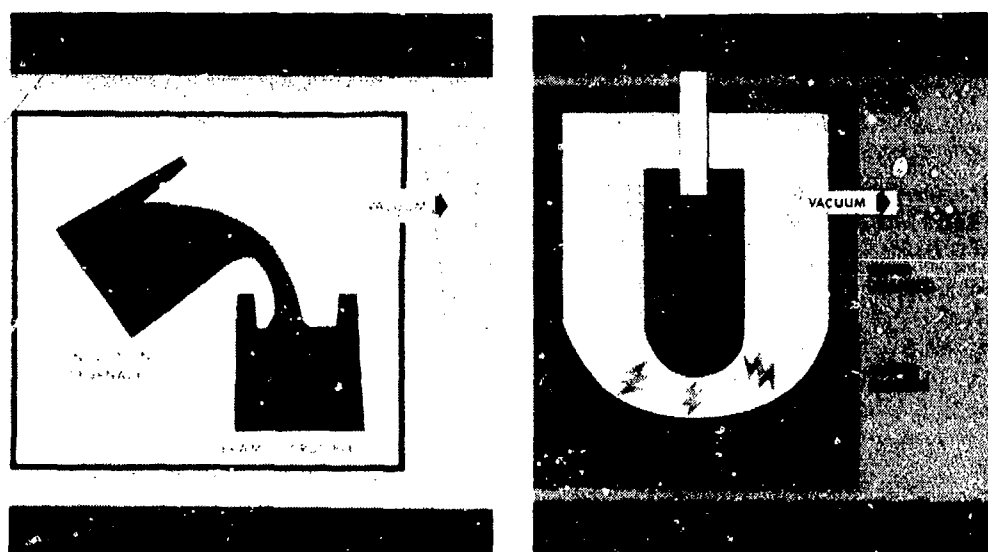
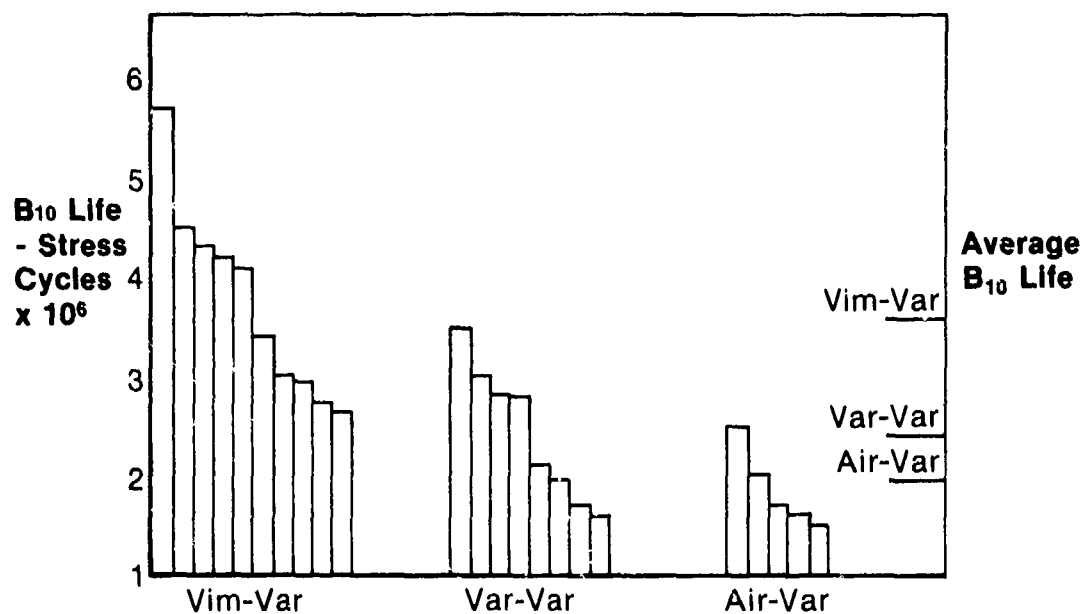


Figure 4. - Schematics of VIM (left) and VAR processes.



bearing material. However, full-scale bearing test data were not available to validate the advantages from the double vacuum melting process. To accomplish this, 120-mm-bore angular contact engine bearings were life tested as part of a series of NASA-GE-Industrial Tectonics, Inc., programs. The results showed that VIM-VAR AISI M-50 had at least five times the life of VAR AISI M-50 (ref. 10).

Forging Flow

One of the important variables affecting bearing life is the forging flow orientation with respect to rolling contact fatigue surfaces. Most bearing races and balls are manufactured by forging, which is known to influence the rolling contact fatigue life of bearings and gears. Figure 6 shows a view of macroetched cross sections of forged bearing races showing conforming and nonconforming grain flow.

An early experimental work by NASA performed on AISI 52100 balls using test rigs showed a significant improvement when rolling contact surfaces ran over areas other than the polar areas of forged balls (ref. 11). Another NASA work (ref. 12) was performed on AISI T-1 cylinders in test rigs to study the effect of forging flow on the rolling contact fatigue life. The cylinders, simulating bearing races, were machined from an AISI T-1 billet with the controlled forging flow orientation, 0° , 45° , and 90° to billet forging axis (see fig. 7). A trend toward increasing fatigue life was observed with transition from perpendicular to parallel forging flow.

Full scale bearing tests confirmed the above results (ref. 13). Bearings were manufactured with AISI 52100 steels having two different orientations. The bearings with side grains (parallel flow) showed at least 10 times the B-10 life when compared with the bearings with end grains (perpendicular flow). This is shown in figure 8.

Based on the findings from these investigations as well as other corroborating data from the author's in-house effort, the present GE bearing specifications require conforming forging (grain flow) for main shaft and other critical engine bearings.

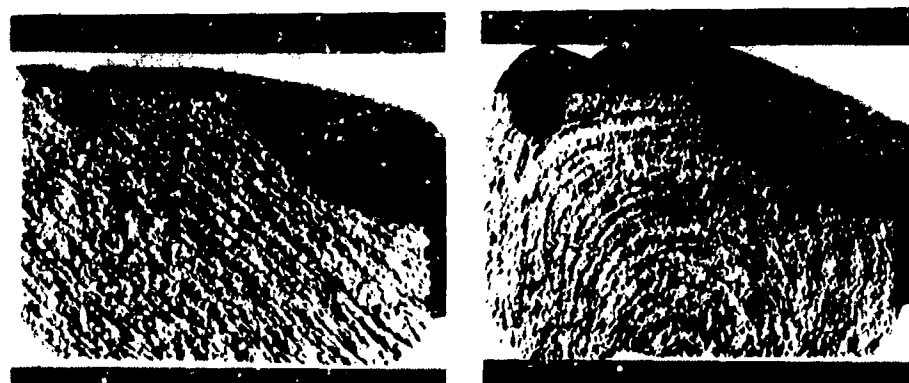
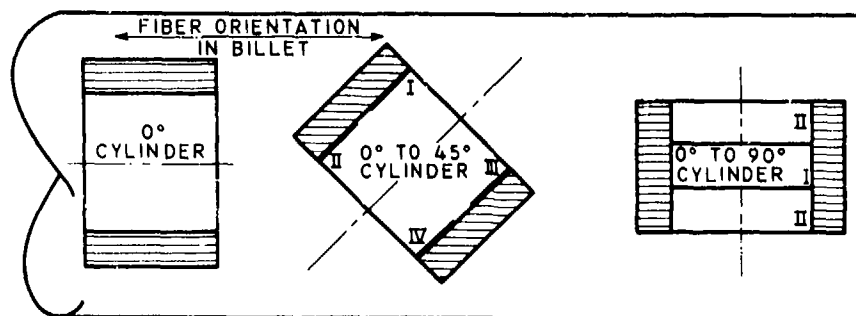


Figure 6. - Forged bearings showing (left) conforming fiber flow and (right) nonconforming fiber flow with respect to the raceway.



Heat Treating Practice

Heat treating may be the most important process influencing the rolling contact fatigue life of bearing materials. Hardness, grain size, carbide morphology, retained austenite, and other microstructural features are determined mainly by heat treating.

Early studies including NASA's (refs. 4, 14 and 15) showed that hardness was the most critical variable in achieving the optimum life of bearing materials. The differential hardness concept for optimum life was also proposed in the 1960's (refs. 16 to 18). Figure 9 shows the results from 52100

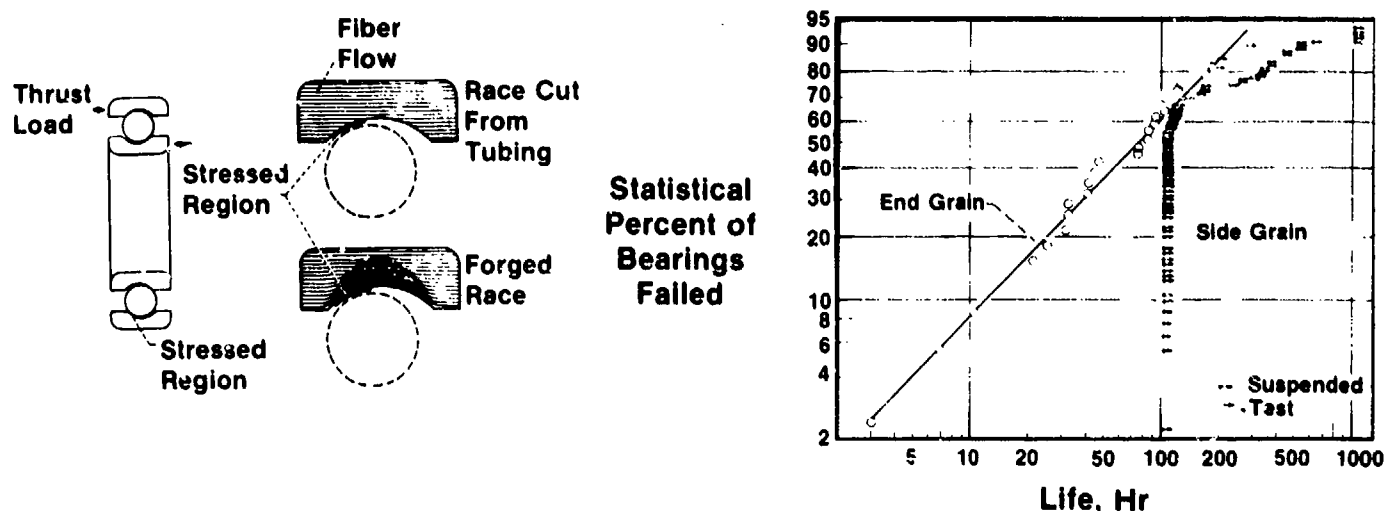


Figure 8. - Effect of end grain and side grain on bearing fatigue life for 140-mm-bore, angular-contact, ball bearing. MIL-L-7808 lubricant; thrust load 9500 lb; speed, 10 000 rpm; temperature, 250° F.

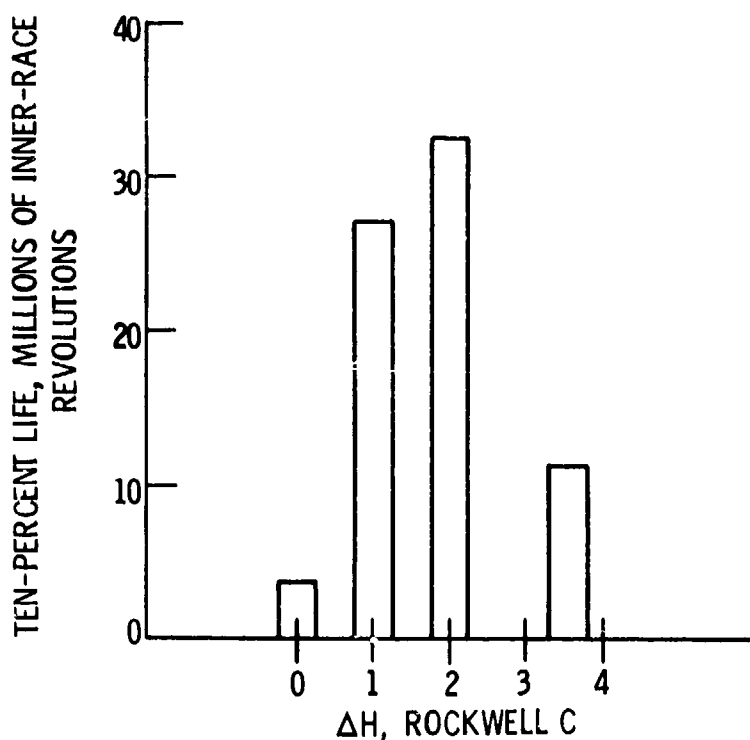


Figure 9. - 10-Percent life as function of difference in Rockwell C hardness of balls and races for AISI 52100 207-S size deep-groove ball bearings.

bearing tests (ref. 19), indicating a maximum life with a differential hardness of 1 to 2 in Rockwell C hardness (HRC) between race and rolling element. However, the beneficial effect of the differential hardness was not found in M-50.

In general, most aircraft engine manufacturers specify metallurgical characteristics resulting from the heat treating process rather than requiring specific heat treat cycles. This is because the required characteristics can be obtained only by an optimized heat treating process and can vary somewhat because of heat-to-heat variation or even a specific vendor's capabilities and facilities. Table 1 provides a typical heat treating cycle applied to VIM-VAR M-50. For example, the current General Electric Specification on bearing material M-50 specifies the following items:

- Rollers, balls, and races shall have an average hardness of HRC 62 to 64.
- All hardness values must be in the range of HRC 61 to 65.
- Retained austenite shall not exceed 3 percent as measured by X-ray diffraction analysis.
- Prior austenite grain size shall be ASTM #8 or finer. Individual grains shall not exceed ASTM #5.

High *DN* Bearing

Main shaft bearings in a typical high-technology engine operate at *DN* values to about 2.2 million; this is expected to approach 3 million in the coming decade. Figure 10 shows the evolutionary trend of increasing toward high *DN*, starting from the late fifties. The higher *DN* values are associated with improved performance and better fuel economy as well as lighter engine weight.

In anticipation and support of this trend, NASA launched an extensive R&D program in the area of high speed bearings with General Electric Company and Industrial Tectonics, Inc. The program

TABLE 1.—HEAT TREATMENT OF AISI M-50

Preheat:	816° C (1500° F) 15 min in salt
Austenitize:	1107° C (2025° F) 5 min in salt
Quench into:	566° C (1050° F) 10 min in salt
Temper:	524° C (975° F) 2 hr
Deep freeze:	-73° C (-100° F) 2 hr

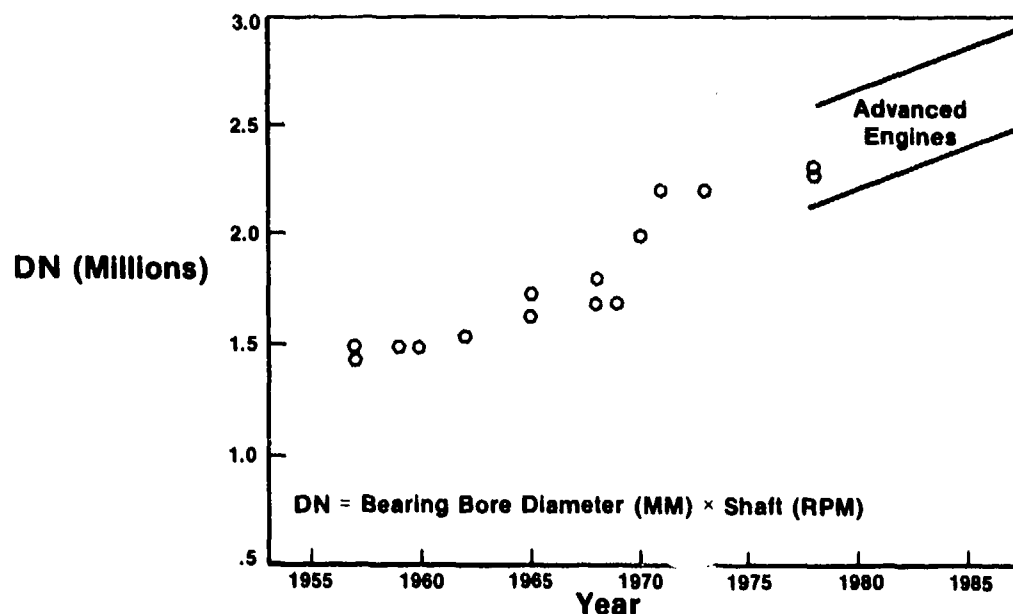


Figure 10. - Trend in aircraft engine main bearing DN.

title was "High DN Bearing Fatigue Investigation." Several modifications were made to maximize the program payoffs during the program period starting from May 1971 to February 1981. The objective was to obtain design information relating the effects of high rotational speeds (up to 25 000 rpm and 3×10^6 DN) on the fatigue life, thermal behavior, lubrication characteristics, and operational conditions of rolling element bearings. The bearings investigated were typical main shaft thrust bearings: thrust loaded, 120-mm-bore angular contact ball bearings.

Parametric information, which is a requisite for bearing design, was generated under varying thrust loads and speeds, bearing and lubricant temperatures, and lubricant flow rates (ref. 10). Endurance life tests were also performed at 3×10^6 DN. Main shaft bearings were successfully run at 3×10^6 DN. A B-10 life of more than 1000 hours was obtained, exceeding both the AFMBA catalog life of 16 hours and the ASME design guide prediction of 175 hours (ref. 1). This is shown in figure 11. During these endurance tests, it was found that two inner race failures exhibited cracking associated with fatigue spalling. When these cracks were opened up for inspection, it was observed that radial, inward propagation of the crack had occurred. This indicated a new mode of failure, race fracture at high rotational speeds. This was expected because of the significant tensile hoop stress, which develops in rotating races at high speed. Figure 12 shows the estimated tangential hoop stress as a function of bearing DN in a 120-mm bearing inner race (ref. 20). Figure 13 also schematically shows that bearing life will be decreased because of this new failure mode at high speed.

Consequently, it was decided in the NASA-GE-ITI program that the raceway fracture mode be verified in testing using 120-mm M-50 bearings at 3×10^6 DN. A bearing with an artificially induced defect in its raceway was installed in the high speed, high temperature fatigue tester. The bearing was run at 25 000 rpm (3×10^6 DN) with a thrust load of 5000 lb. The expected inner race spalling at the induced defect occurred after 6 hours and 17 minutes. Testing was continued until an obvious severe

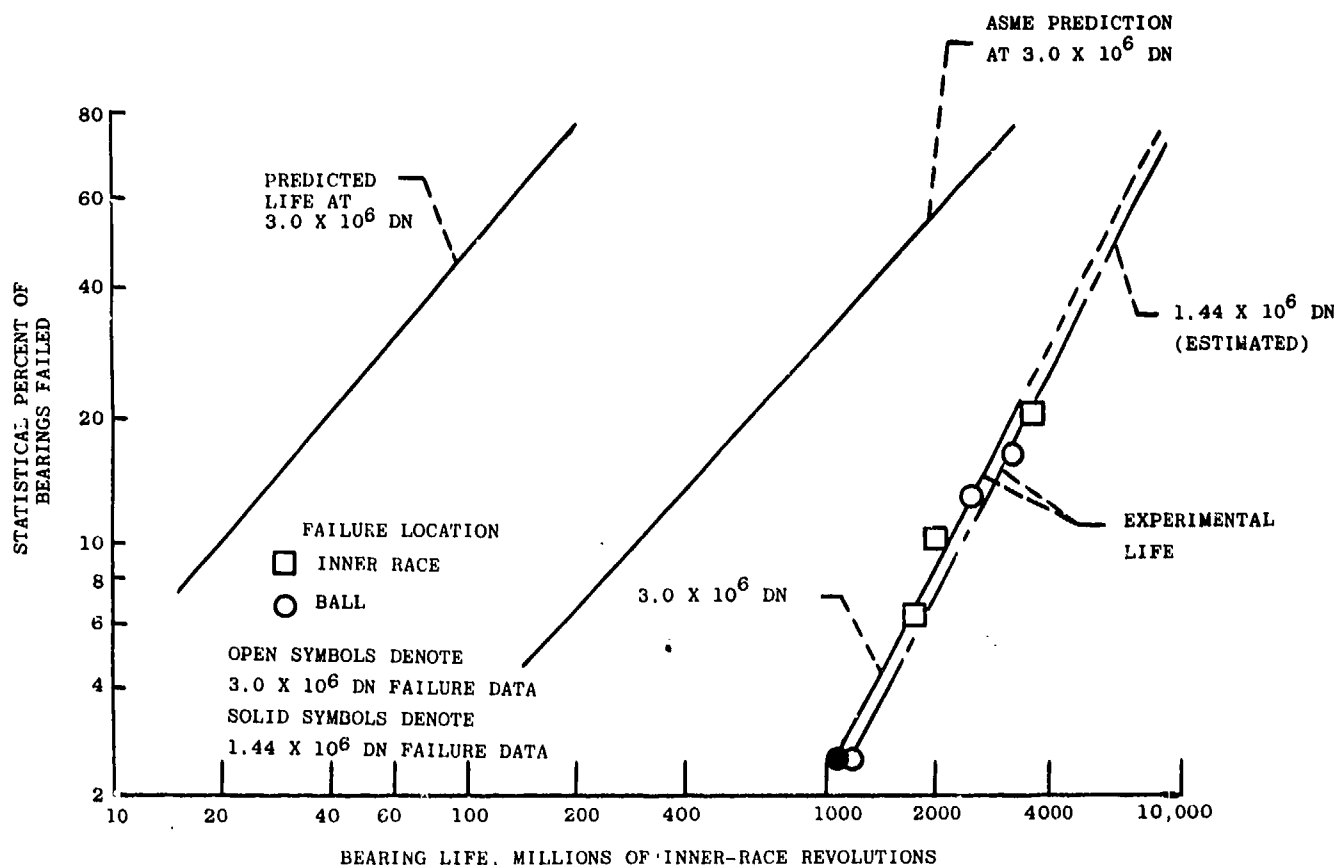


Figure 11. - Endurance characteristics of 120-mm-bore, angular-contact, ball bearings. Thrust load, 22 241 N (5000 lb); temperature, 492 K (420 F); material, AISI M-50 steel; lubricant, tetraester.

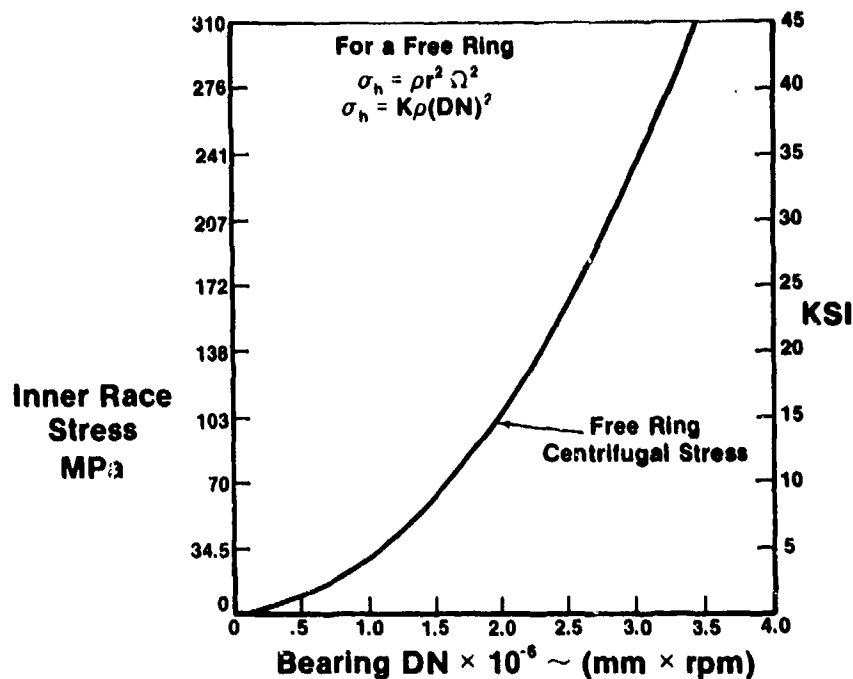


Figure 12. - Estimated inner race tangential stress versus bearing DN.

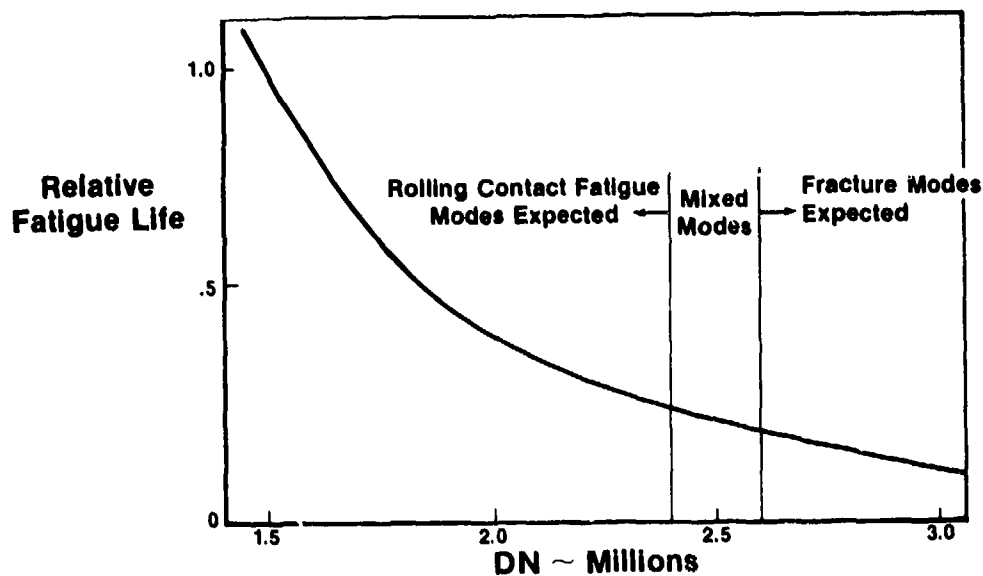


Figure 13. - Mainshaft bearing lives and expected failure mode as function of speed for a constant bore.

fragmentation fracture occurred to the inner race, terminating the test, 7.5 minutes after detection of the spalling. Post test examination showed that the inner race had fractured into eight discrete segments (fig. 14). The results of this are described in detail in reference 1. Because of this potential failure mode, GE (ref. 20) is currently limiting engine design up to the bearing speed of 2.4×10^6 DN. This remains in effect until a new material/process/design bearing becomes available. One way of mitigating this technical barrier is to utilize a bi-hardness (carburized) raceway in which the case structure will provide rolling contact fatigue life while the core will provide toughness. Work is continuing in this area.

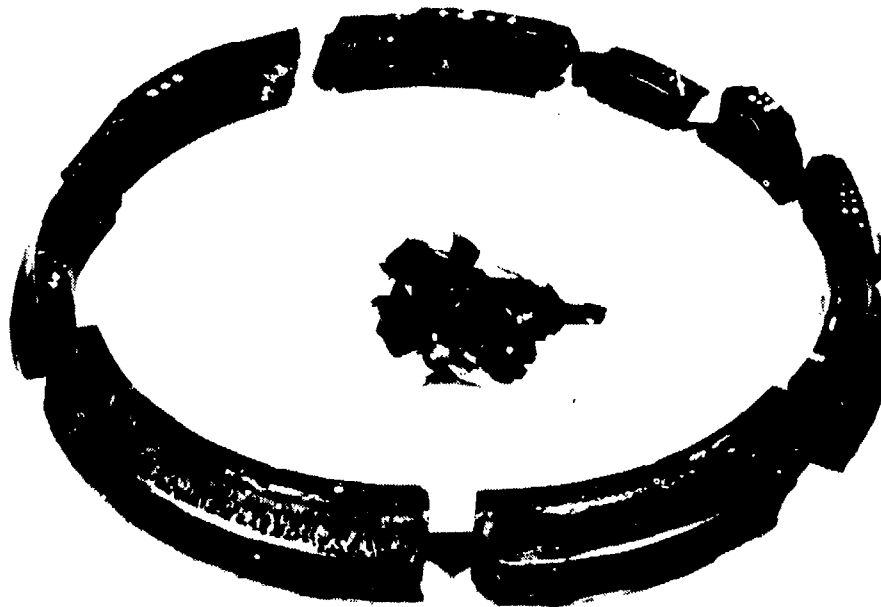


Figure 14. - Fractured bearing inner race initiated by a rolling-element fatigue spall.

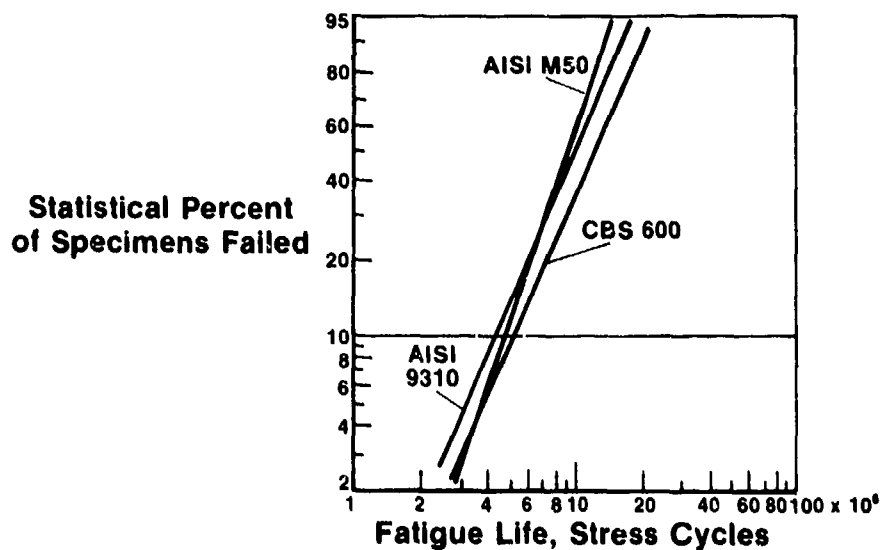


Figure 15. - Summary of rolling-element fatigue life data of CBS 600, AISI M-50, and CVM AISI 9310.

Alternate Materials

To overcome the technical challenges mentioned previously, fracture toughness and longer life in aircraft engine bearings, new processes, and materials other than M-50 may have to be utilized. Advanced engines may require more sophistication of the bearing, its support, and its mounting system.

General Electric has been working on a NASA sponsored program to evaluate the rolling contact fatigue life performance of various materials and processes (ref. 21). It was found that alloys, such as CBS600, AISI 9310, CBS1000, etc., had the equivalent rolling contact fatigue capability of M-50 (fig. 15). Based on this information, aircraft engine bearings using other materials can be considered;

for example, mounting or supporting brackets could be made integral with bearings made from case carburized material. This would be extremely difficult to achieve with through-hardened M-50 because of the difficulty involved in the final machining operation of the geometrically complex shape of a bearing system.

Typical chemical compositions of candidate bearing and gear steels are given in table 2. It is interesting that T-1 (18-4-1) is equivalent to M-50 in the rolling contact fatigue life comparison (ref. 22), as shown in figure 16. The T-1 material is widely used for bearings by British and European aircraft engine manufacturers.

**TABLE 2.—TYPICAL CHEMICAL COMPOSITIONS OF
SELECTED BEARING STEELS**

Alloying Elements (% By Weight)

Designation	C	P (max)	S (max)	Mn	Si	Cr	V	W	Mo	Co	Cb	Ni
SAE 52100	1.00	0.025	0.025	0.35	0.30	1.45	—	—	—	—	—	—
MHT*	1.03	0.025	0.025	0.35	0.35	1.50	—	—	—	—	—	—
AISI M-1	0.80	0.030	0.030	0.30	0.30	4.00	1.00	1.50	8.00	—	—	—
AISI M-2	0.83	0.030	0.030	0.30	0.30	3.85	1.90	6.15	5.00	—	—	—
AISI M-10	0.85	0.030	0.030	0.25	0.30	4.00	2.00	—	8.00	—	—	—
AISI M-50	0.80	0.030	0.030	0.30	0.25	4.00	1.00	—	4.25	—	—	—
T-1 (18-4-1)	0.70	0.030	0.030	0.30	0.25	4.00	1.00	18.0	—	—	—	—
T15	1.52	0.010	0.004	0.26	0.25	4.70	4.90	12.5	0.20	5.10	—	—
440C	1.03	0.018	0.014	0.48	0.41	17.30	0.14	—	0.50	—	—	—
AMS 5749	1.15	0.012	0.004	0.50	0.30	14.50	1.20	—	4.00	—	—	—
Vasco Matrix II	0.53	0.014	0.013	0.12	0.21	4.13	1.08	1.40	4.80	7.81	—	0.10
CRB-7	1.10	0.016	0.003	0.43	0.31	14.00	1.03	—	2.02	—	0.32	—
AISI 9310(C)	0.10	0.006	0.001	0.54	0.28	1.18	—	—	0.11	—	—	3.15
CBS 600(C)	0.19	0.007	0.014	0.61	1.05	1.50	—	—	0.94	—	—	0.18
CBS 1000M(C)	0.14	0.018	0.019	0.48	0.43	1.12	—	—	4.77	—	—	2.94
Vasco X-2(C)	0.14	0.011	0.011	0.24	0.94	4.76	0.45	1.40	1.40	0.03	—	0.10

* Also Contains 1.38% Al
C - Carburizing Grades

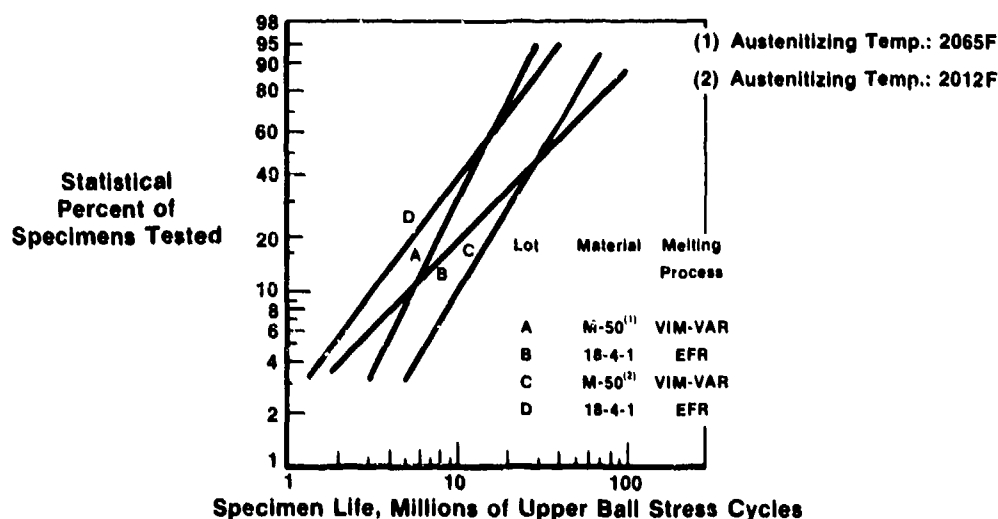


Figure 16. - Rolling-element fatigue life of VIM-VAR AISI M-50 and EFR 18-4-1 steel balls in five-ball fatigue tester. Maximum Hertz stress, 5520×10^5 Pa (800 000 psi); shaft speed, 10 700 rpm; contact angle, 30°; temperature, 65° C (150° F).

The ASME Design Guide (ref. 23) has become an underlying universal practice in aircraft engine bearing design. References cited in this document show that NASA has had a significant role in the contribution in this area of technology.

Summary

An attempt is made to briefly review the aircraft engine bearing materials and to discuss some of the impact made from a cooperative and collaborative effort among parties involved, such as government agencies, academic communities, steel companies, research institutes, and users (aircraft engine manufacturers). NASA's impact on the GE bearing design and specifications has been mentioned as an example. Without this concentrated and coordinated effort, the success we are enjoying in current gas-turbine-engine technology would be impossible. This team approach is important and must be continued to advance technology, to achieve improved performance, and to achieve better efficiency and reliability.

References

1. Bamberger, E. N.; Zaretsky, E. V.; and Signer, H.: Endurance and Failure Characteristic of Main-Shaft Jet Engine Bearing at 3×10^6 DN. J. Lubr. Technol., vol. 98, Series F, No. 4, Oct. 1976.
2. Bamberger, E. N.: Materials for Rolling Element Bearings. Bearing Design—Historical Aspects, Present Technology and Future Problems. ASME Century 2 Publication #H00160.
3. Anderson, W. J.; Zaretsky, E. V.: Rolling Element Bearing—A Review of the State-of-the-Art. NASA TM X-71441, 1973.
4. Jackson, E. R.: Rolling Contact Fatigue Evaluations of Bearing Materials and Lubricants. ASLE Trans., vol. 2, no. 1, 1959, pp. 121-128.
5. Carter, T. L.: A Study of Some Factors Affecting Rolling Contact Fatigue Life. NASA TR R-60, 1960.
6. Carter, T. L.; Butler, R. H.; Bear, H. R.; and Anderson, W. S.: Investigation of Factors Governing Fatigue Life with the Rolling Contact Fatigue Spin Rig. ASLE Trans., vol. 1, no. 1, Apr. 1958, pp. 23-32.
7. Johnson, R. F.; and Sewell, J. F.: The Bearing Properties of 1 Percent C-Cr Steel as Influenced by Steelmaking Practice. J. Iron and Steel Inst., vol. 196, pt. 4, Dec. 1960, pp. 414-444.
8. Morrison, T. W.; Tallian, T.; Walp, H. O.; and Baile, G. H.: The Effect of Material Variables on the Fatigue Life of AISI 52100 Steel Ball Bearings. ASLE Trans., vol. 5, no. 2, Nov. 1962, pp. 347-364.
9. Schlatter, R.: Vacuum Melting of Specialty Steels. J. Metals, April 1970.
10. Signer, H.; Bamberger, E. N.; and Zaretsky, E. V.: Parametric Study of the Lubrication of Thrust Loaded 120 mm Bore Bearings to 3 Million DN. J. Lubr. Technol. July 1974, pp. 515-526.
11. Butler, R. H.; Bear, H. R.; and Carter, T. L.: Effect of Fiber Orientation on Ball Failures Under Rolling Contact Conditions. NASA TN 3933, 1957.
12. Carter, T. L.: Effect of Fiber Orientation in Races and Balls Under Rolling Contact Fatigue Conditions. NASA TN 4216, 1958.
13. Zaretsky, E. V.: The Changing Technology of Rolling Element Bearings. Machine Des., vol. 38, no. 24, Oct. 13, 1966, pp. 206-223.
14. Baughman, R. A.: Effect of Hardness, Surface Finish and Grain Size on Rolling Contact Fatigue Life of M-50 Bearing Steel. J. Basic Eng., vol. 82, no. 2, June 1960, pp. 287-294.
15. Carter, T. L.; Zaretsky, E. V.; and Anderson, W. J.: Effect of Hardness and Other Mechanical Properties on Rolling Contact Fatigue Life of Four High-Temperature Bearing Steels. NASA TN D-270, 1960.
16. Scott, D.; and Blackwell, J.: Study of the Effect of Material and Hardness Combinations in Rolling Contact. Proc. Inst. Mech. Eng., vol. 180, 1965-66, pp. 32-36.
17. Zaretsky, E. V.; Parker, R. J.; Anderson, W. J.; and Reichard, D. W.: Bearing Life and Failure Distribution as Affected by Actual Component Differential Hardness. NASA TN D-3101, 1965.
18. Zaretsky, E. V.; Parker, R. J.; and Anderson, W. J.: Component Hardness Differences and Their Effect on Bearing Fatigue. J. Lubr. Technol., vol. 89, no. 1, Jan. 1967, pp. 47-62.
19. Irwin, A. S.: Effect of Bearing Temperatures on Capacities of Bearing of Various Materials. Paper Presented at ASME Third Spring Lubrication Symposium, New York, N.Y., March 14-15, 1960.
20. Clark, J. C.: Fracture Failure Modes in Lightweight Bearings. J. Aircr., vol. 12, no. 4, Apr. 1975.
21. Nahm, A. H.: Rolling Element Fatigue Testing of Gear Materials. NASA CR-135411 and CR-135450, 1978.
22. Parker, R. J.; and Zaretsky, E. V.: Rolling Element Fatigue Life of AISI M-50 and 18-4-1 Balls. NASA TP-1202, 1978.
23. Bamberger, E. N.; et al.: Life Adjustment Factors for Ball and Roller Bearings—An Engineering Design Guide, ASME, New York 1971.

Prediction of Ball and Roller Bearing Thermal and Kinematic Performance by Computer Analysis*

Juris Pirvics† and Robert J. Kleckner†

Bearings act within a load support system in mutual support of a load vector and share in the control of shaft motion. The load system contains (as a minimum) a shaft, housing, and more than one bearing. The system is part of machinery which experiences a thermomechanical dialogue within and across the boundaries of its physical volume. Analysis examines this dialogue and constructs mathematical models. Their complexity requires computerization. This results in software which then enables a design methodology emphasizing numerical exploration of a competitive variety of load support system concepts, prior to hardware commitment.

Rotating load support has received parallel attention with the evolution in the sophistication of machinery. Prior to constraints on mass content and in the presence of loads, speeds, and temperatures which were moderate for rolling element bearing materials, little need was seen for detailed analysis of the component. There was even less motivation to understand the surrounding interactions. Large margins available in the reserves of bearing material properties allowed escape from the penalties for the severe approximations in computation techniques. This design efficiency can no longer be afforded as the luxury which it now is recognized to be. Applications, for example, have materialized in which highly loaded precision supports have to survive for short periods, minutes instead of years. Thermomechanical environments have been specified in which only solid-solid lubrication is present. These and other needs have provided motivation for the creation and use of novel materials. Their property definitions and performance in bearings demand new and accurate representation.

The explicit need for design calculation reliability requires a detailed assessment of the role of primary and secondary effects within local control volumes of individual bearing contacts. The cross-coupling interactions of the global thermomechanical environment with its local counterpart require similar detailed understanding. This is fortunately made possible by the evolving body of knowledge concerning concentrated contact micromechanics and by the availability of contemporary high speed digital computers.

The material which follows suggests characteristics of good computerized analysis software. These general remarks and an overview of representative software precede a more detailed discussion of load support system analysis program structure. Particular attention is directed at a recent cylindrical roller bearing analysis as an example of the available design tools. Selected software modules are then examined to reveal the detail inherent in contemporary analysis. This leads to a brief section on current design computation which seeks to suggest when and why computerized analysis is warranted. An example concludes the argument offered for such design methodology. Finally, remarks are made concerning needs for model development to address effects which are now considered to be secondary but are anticipated to emerge to primary status in the near future.

Software Design and Evolution

Preferred Software Design

The past 20 years have witnessed a remarkable increase in the computation power and flexibility available for practical analysis and design. Cumbersome multiple-pass executions with extended user

*This report was summarized from the material presented in reference 1.

†SKF Industries, Inc.

participation in the processing steps have given way to interactive communication. Contemporary software for the analysis of load support systems can be constructed as an accurate detailed simulation whose execution teaches a novice, serves a practitioner, and improves by "instruction" from the expert. Good software is made so that it and the user are an evolving symbiotic entity whose ability to assess and create grows with experience. It should be designed so that novice users default into *standard* conditions and obtain knowledge for that realm of operation. For example, all materials have the same standard steel properties. Housings do not deflect; temperatures are standard ambient; full symmetry prevails; a standard lubricant is selected; and so on. Deactivation of any of these defaults by the user parallels the user's developing experience and enables the investigation of the influence of these specific parameters on performance. As examples, rings are allowed to misalign and influence L_{10} life, or oil supply rate is varied to remove heat generated at higher operating speeds.

Finally, experienced users can incorporate their own subroutines or variants. At this stage of participation, the user is an active partner in computerized analysis and design.

Evolution of Contemporary Software

The first use of digital computers for the analysis of bearings can be credited to Jones. He examined a single ball bearing under thrust load (ref. 2). By postulating a hypothesis concerning the kinematic behavior of balls, he formulated a definition of ball motion. The first load support system analysis paper followed shortly thereafter in 1960, again by Jones (ref. 3). Here an elastic shaft was considered mechanically together with ball and/or roller bearings in mutual support of a general load vector. The formulation was reported to be implemented on an IBM 704 computer. Both papers presented the details of mathematical formulation. Software architecture description, discussions of success with the convergence of iterative procedures or computation time experiences, were noticeably absent. Eleven years later, Harris (refs. 4 and 5) extended Jones' single ball bearing analysis by relaxing the restriction of single raceway response to gyroscopic moments. Using digital computers, he then incorporated a description of a Newtonian separating lubricant, which was characterized by a pressure and temperature dependent viscosity (ref. 6). In 1966 Harris (ref. 7) introduced an analysis which considered skidding at high speeds in the presence of a fluid whose viscosity was assumed to be an exponential function of pressure and temperature. But a severe restriction was imposed which insured that all rollers experience the conditions identical to those present at the most heavily loaded one. Each contact was specified to have the same film thickness, rolling speed, etc. Boness (ref. 8) revealed experimental data which contradicted this assumption on roller speeds, and set Poplawski (ref. 9) on an alternative extended formulation of the field equation set. Poplawski included the roller speed about its own center as an independent variable. This kinematic condition allowed for the computation of a speed distribution among rollers and a load distribution of the retainer. Fluid churning and cage pilot surface friction effects were also included. Rumbarger (ref. 10) continued the evolution of high speed roller bearing analysis by relaxing the isothermal elastohydrodynamic (EHD) film requirement and by adding a comprehensive fluid drag formulation. The major contribution of this work was to display the interdisciplinary computerized systems analysis approach necessary to obtain meaningful results.

Major advances in further software generation have taken place within the past few years. Systems analysis has been written which considers the whole spectrum of partial to full EHD formulations for a variety of shaft-mounted bearing types in mutual support of a load vector. Ball, cylindrical, and tapered roller bearings are considered in load-support system software by Crecelius (ref. 11), as well as mechanical assembly programs by Ragen (ref. 12), and Crecelius and Kleckner (ref. 13). These specific formulations consider the systems to reside in, and interact with, a time transient thermal environment. Other programs have been written to treat a single cylindrical (ref. 14) or spherical (ref. 15) rolling-element bearings in a transient thermal environment. Cylindrical bearing isothermal dynamic analysis has been written by Conry (ref. 16), Brown (ref. 17), and Gupta (ref. 18). Ball-bearing dynamics, originally formulated by Walters (ref. 19), were expanded in generality and implemented by Gupta (ref. 20).

Various aspects of the substantial efforts to develop tribological understanding by analysis and experimentation, which led to the development of models and then individual software modules are

summarized in discussions by Dowson (ref. 21), McGrew (ref. 22), Cheng (ref. 23), Anderson (ref. 24), Tallian (ref. 25) and Pirvics (ref. 26). Additional commentary of software characteristics as well as selected descriptions have been noted by Gupta (ref. 27) and Sibley (ref. 28).

Software Architecture

Introduction and General Definition

Software is built to automate the sequence of numerical computation steps taken to solve for the unknown values of variables in an equation set. The correctness of the calculated values depends on the validity of the mathematical models and on the processing of the information between steps in the computation sequence. Each module representing the models within the software must present a parallel level of simulation sophistication detail. The least sensitive module contributing to the governing field equation set determines the performance level of the complete program.

Software architecture presents a plan which is sensitive to these elementary but essential concepts. It does so in the form of a master flowchart which itemizes computation needs, displays the logic flow, and defines the solution strategy.

Example

A flowchart which describes the control of 131 modules, represented by approximately 12 000 card images, is shown in figure 1. It represents the architecture for Cybean (cylindrical bearing analysis) (ref. 14). Exchanges of data with the user world, logic flow, and computation sequence are readily seen. For example, the computations performed by modules within box 1 in figure 1 provide roller and ring loads. Figure 2 details a module that computes the force which arises in a rolling element to flange interaction.

Once the field equations are assembled, a "solver" module (box 2 in fig. 1) is activated. Derived quantities are then computed (box 3). After output is prepared for the user (box 4) a table of options is checked and program control is appropriately transferred.

Cybean examines a single cylindrical bearing's performance. The architecture for more complex systems software, like Shaberth (ref. 11) and Transim (ref. 12), bears the skyscraper to single family residence analogy. However, the elements of successful software design, with emphasis on balanced sophistication and modularity, are common.

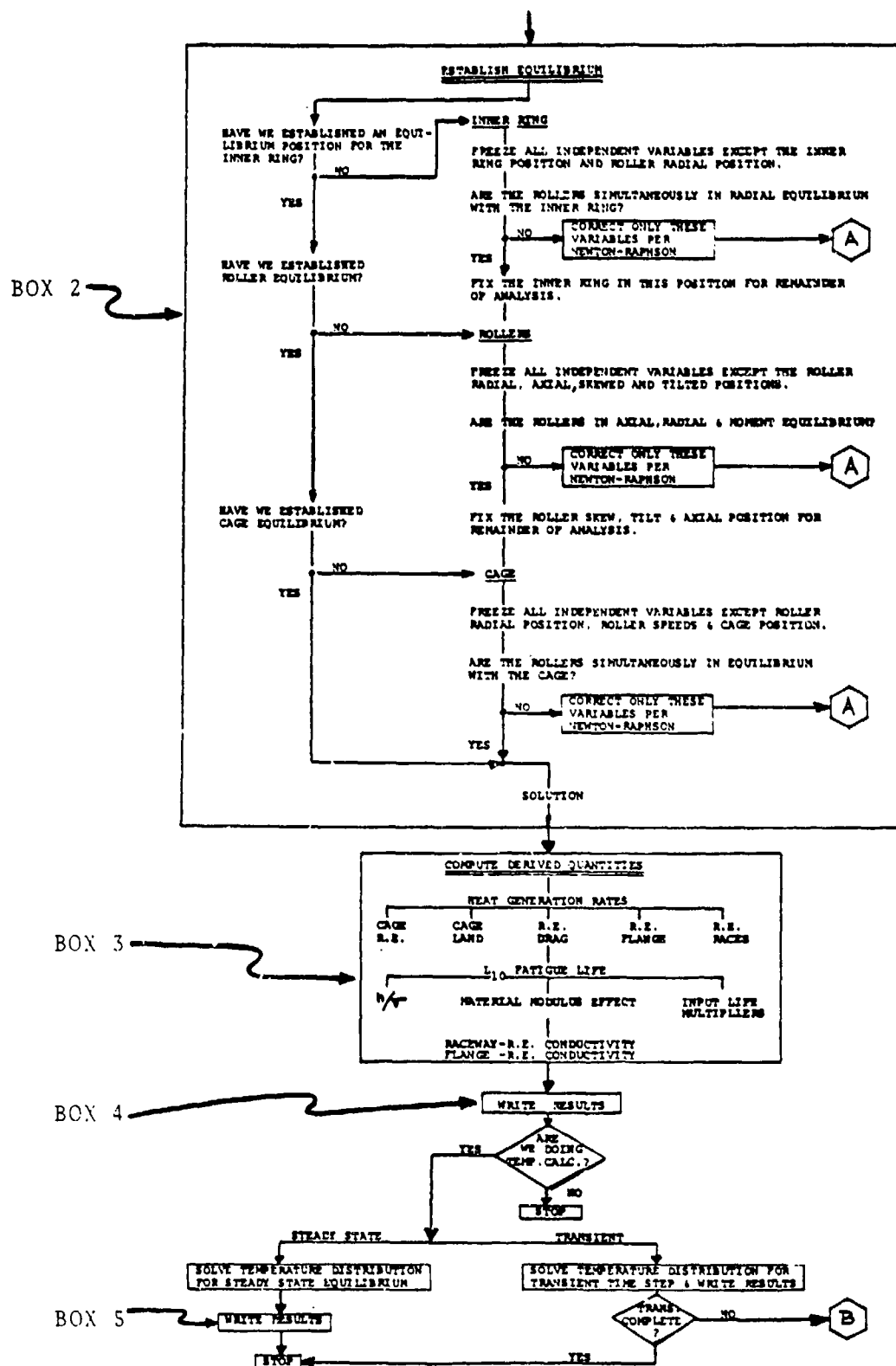
Classification

General software for bearing analysis examines forces and moments in a three dimensional space which are time transient and temperature dependent. A complete mechanical assembly, containing one or more load support systems, is considered. This general software contains, as subsets within its architecture, levels which consider systems of decreasing complexity:

Level	What is simulated	Kinematic representation	Thermal representation
1	Assembly	Dynamic	Time transient thermal
2	Assembly	Quasidynamic	Time transient thermal
3	Component	Dynamic	Time transient thermal
4a	↓	Dynamic	Steady state thermal
4b		Quasidynamic	Time transient thermal
5		Quasidynamic	Steady state thermal
6		Quasidynamic	No thermal analysis
7		Quasistatic	No thermal analysis
8		Static	No thermal analysis

Classification Nomenclature

An *assembly* contains one or more load support systems within the nomenclature used above. A *component* is a single load support unit which may be a ball, cylindrical, tapered, or spherical rolling element bearing. The assembly can be represented by a lumped mass nodal network. The nodes



Key:

F_{XO} - Outer Raceway Induced
X-directed Force

F_{XI} - Inner Raceway Induced
X-directed Force

T - Tolerance

δ - Geometric Interpenetration

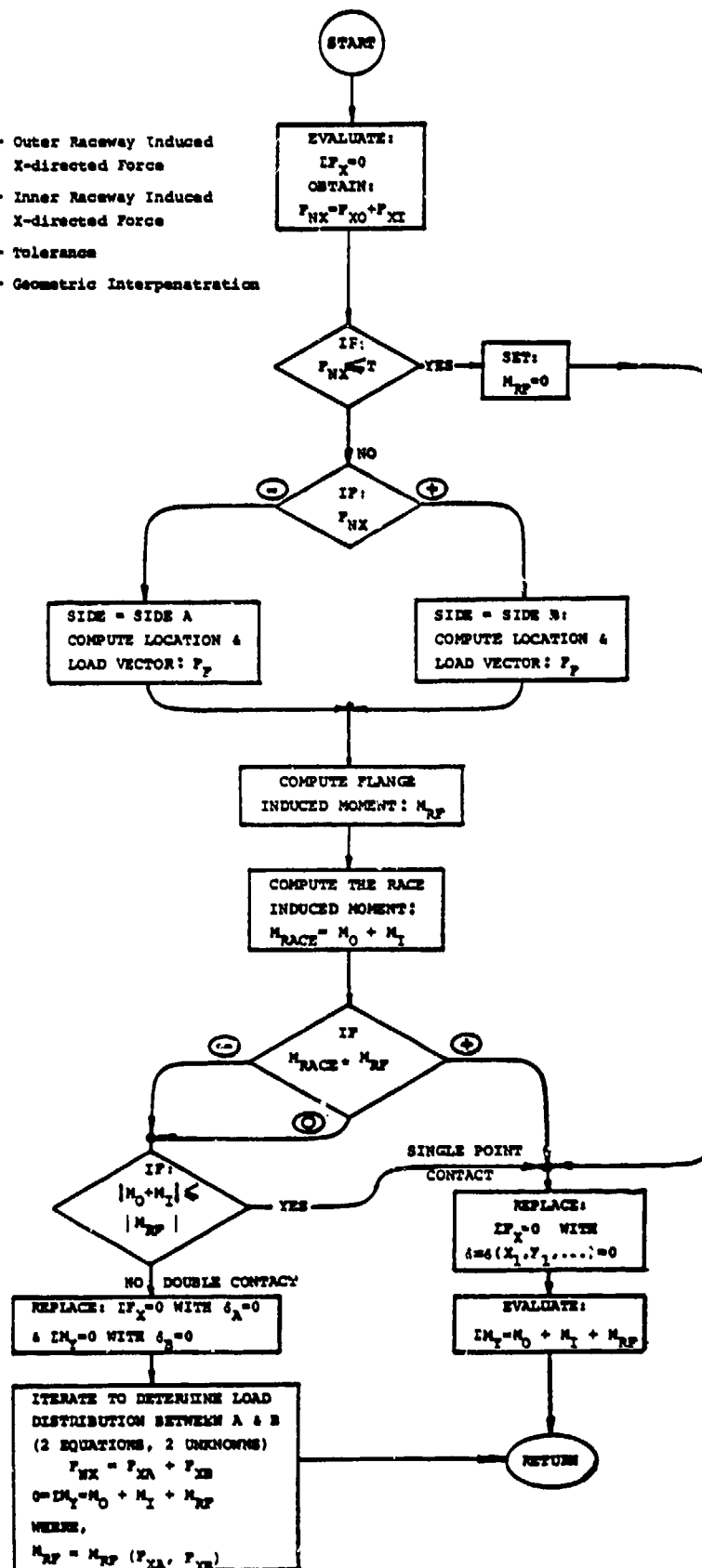


Figure 2. - Solution algorithm for multiple flange contacts.

transfer energy by conduction, convection, and radiation. They represent the mass, surface area, and physical properties of the space they replace. They may be heat sources or sinks. Thus, thermal refers to the software's ability to account for temperature distribution effects on a scale defined by the nodal volumes within the assembly. Time transient thermal capability refers to the updating of the system temperature map to reflect the cross-coupled influence of heat exchange mechanisms and temperature dependent material properties as time progresses. Isothermal refers to the assumption that all locations within the control volume considered are at the same temperature.

Static, quasistatic, quasidynamic and dynamic program designations refer to the degree with which time transient motions of individual elements of a component are detailed.

A fully "dynamic" code defines a field equation set within which force, F_j , and moment, G_j , Newtonian equilibrium is written for each i^{th} element, retainer, raceway and shaft of mass, M_i , and moment of inertia, I_i , in the j^{th} direction:

$$M_i \ddot{\xi}_{ij} = F_j$$

$$I_i \ddot{\omega}_{ij} = G_j$$

Three independent variables, ξ , and their derivatives in time, describe the motion of a given i^{th} mass center in an inertial reference frame. Three more variables define rotations about that mass center. Numerical formulation for N rolling elements, two raceways and a retainer require a field equation set of magnitude $[6(N+1)+1]$. A typical 30-element cylindrical roller bearing dynamic description requires the integration of 187 simultaneous nonlinear equations for each time step.

The opposite extreme for the characterization of time transient motion is to specify its absence, and equate F_j and G_j to zero. This gives rise to level 8, "static" formulations. Here, Hertzian pressure distributions in contacts are assumed to govern the interactions between elements and rings due to an applied force vector. No account is taken of traction or those forces created by centrifugal and gyroscopic effects. The individual motion of elements within the component is not recognized.

The departure from this elementary viewpoint begins with the recognition that load distribution, at higher speeds, is altered by centrifugal loads. Recognition of speed begins with examination of spin as well as roll components in element motion. Initially, Coulomb friction was assumed to govern the creation of traction forces, and angular velocities were determined by "raceway control" (ref. 2). The latter specified that a ball would experience pure rolling on the controlling raceway and spin with respect to the other. This restriction was progressively relaxed (ref. 4) as Coulomb friction gave way to the traction simulation generality afforded by the consideration of fluid film separation in the contact conjunctions. The implementation of these considerations of motion in ball and roller bearing programs, the departure from epicyclic constraints, the formulation to account for velocity vector variation in the rolling element set classifies level 7, "quasistatic" software.

The admission of circumferential inertial terms into that equilibrium set leads to the definition of "quasidynamic" software resident in level 2 as well as levels 4b to 6. Specifically, individual element angular velocities $\omega_{\theta i}$ are computed together with element positions in the retainer. With $\omega_{\theta i}$ and its position known for each i^{th} element, the circumferential inertial term is accounted for in a particular equilibrium state in time (ref. 11) by evaluating $F_{\theta i}$ as

$$F_{\theta i} = M_i \dot{\omega}_{\theta i} = M_i \frac{\partial \omega_{\theta i}}{\partial t} = M_i \omega_{\theta i} \frac{\partial \omega_{\theta i}}{\partial \theta}$$

The partial derivative $\partial \omega_{\theta i} / \partial \theta$ is evaluated from numerical differences of $\omega_{\theta i}$ in the θ direction.

Discussion

The transition from static to dynamic programs recognizes the significance of individual component velocity and acceleration vectors. It also notes that increasingly detailed individual stress distributions are needed within the multiple contact conjunctions for any given element in the formulation of accurate force and moment equilibrium. The sensitivity of the element kinematics to traction coefficient values and, in turn, the sensitivity of the latter to sliding speed, temperature, and EHD film thickness creates mathematical convergence difficulties for solution procedures. It also

highlights the requirement for comprehensive level 1 software for a truly detailed representation.

The eight program categories classified in the preceding paragraphs require additional comments concerning availability. Level 1 does not exist, but its assembly is possible. Level 2 is represented by Shaberth (ref. 11) and Transim (ref. 12). Level 3 does not exist but can be conceived as the sequential execution of programs in level 4. Level 4a contains DREB (refs. 18 and 20) and software by Brown (ref. 17) and Conry (ref. 16). Level 4b has Cybean (ref. 14) and Spherbean (ref. 51). The remaining levels contain subsets of the noted programs, specialty software for rougher approximation, and historical programs. The programs noted do not exhaust those available, but are representative of the current state-of-the-art.

Software Modules

Background

Load support assembly analysis starts with the definition of work and heat flux across the global boundaries of the control volume drawn to contain it. The boundaries displace as load vectors are applied, and heat is driven by temperature differences between contents of the volume and the surrounding environment. The understanding of assembly behavior comes from the description of local thermomechanics and their equilibrium cross-coupling with the global system.

The concept of "local" is understood if the global control volume is examined under ever increased magnification. The assembly enlarges out of the viewing window and a particular load support system appears. The system in figure 3 gives way to an element of a rolling bearing complement, as it in turn recedes as focus is achieved for one of several surface contacts seen in figure 4. Examination of this "local" view reveals a volume in space within which reside as many as three deformable materials with temperature dependent properties and irregular topography. The materials interact with each other in a time dependent search for thermodynamic equilibrium with the surrounding space. Evaluation of the energy exchange, within, as well as across, the boundaries of this small volume scales the thermomechanical effects considered to be "local." The evaluation is provided by local software modules which are assembled and coordinated by the plan resident in the program architecture to simulate the global system.

Modules Found Within LS System Analysis Software

Most basic modules begin with the description of the geometries considered to occupy the control volume. An absolute reference frame is established and moving coordinate frames associated with each moving component of the assembly. Figure 5 gives an example of the geometric relationships involved. A transformation module is constructed to map vectors between any two frames. These modules are standard but particular note has to be made concerning accuracy. Typically, linear distances for geometric description are several orders of magnitude larger than interpenetration magnitudes descriptive of contact deformities. Therefore, differences in distances used to describe material interpenetration and partial derivative numerics have to be treated with respect for the single word precision length of the digital computer used. Modules which are developed on extended single precision hardware take considerably longer to execute and may not be transportable to other main frame environments.

Once initial condition geometries are described, their material characteristics have to be identified. This calls for modules which store data, and which represent the constitutive equations for materials. The viscosity and density of a lubricant, for example, are functions of pressure and temperature. Solid materials are characterized by thermal expansion coefficients as well as elastic constants. Heat transfer coefficients may vary with temperature. Modules of this nature describe the assembly and distinguish it as an identifiable geometric and physical entity.

Further identification is provided by modules defining response to excitation. Shafts deflect, rings misalign, and housings distort within a thermal environment as the applied load is processed through load support components.

The execution of geometry and material characterization modules together with the information from the response modules enables the construction of a series of equalities. These consider the balance of surface and body forces to define Newtonian equilibrium for each element.

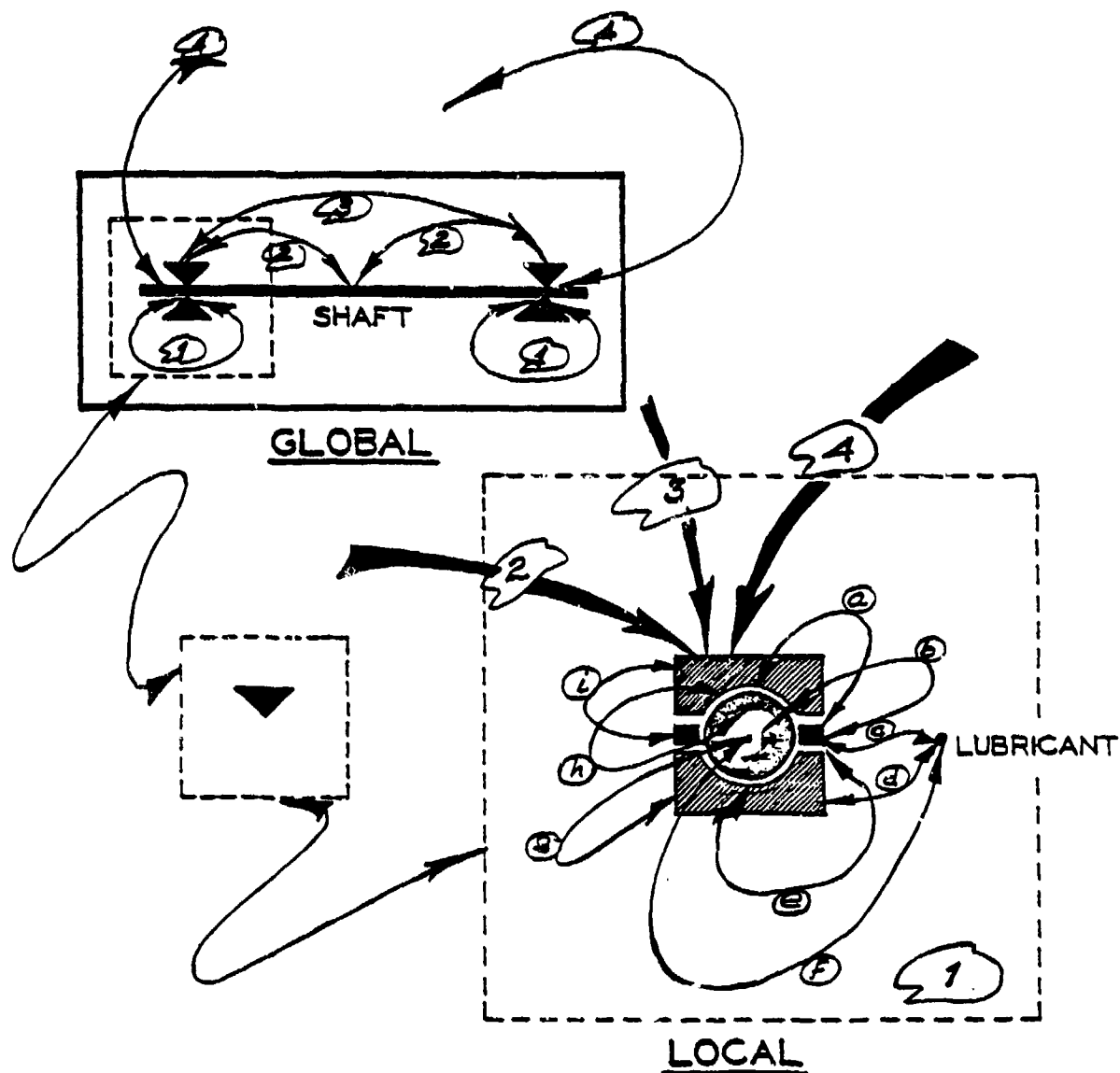


Figure 3. - Load support system thermomechanical dialogue.

Forces can be characterized as those originating from solid-solid and those from solid-fluid interactions. The solid-solid interaction modules start with the definition of a given set of values for the independent position variables which are found for all the load support system components in space. With these positions fixed, the relative positions of the bearing components are examined to determine if their geometries interact or if a free space exists between them. Locations and magnitude of interpenetration are recorded. These values are then used to determine contact stress, contact size, and the integrated force.

The solid-fluid interaction occurs in four ways: raceway/rolling-element traction, flange/rolling element traction, rolling element drag, and cage pocket and land friction. These effects can be computed for the raceway using established contact models (refs. 31 to 35). Flange/rolling element and raceway/rolling element interactions are treated similarly. Rolling element drag is approximated as a function of lubricant properties, speed, and geometry using established equations for external flow. Typical interactions are detailed in work by Kleckner (ref. 14), Ragen (ref. 12), and Gupta (refs. 18 and 20).

The completion of the force equilibrium equations leads to modules whose function is to solve nonlinear field equation sets. Classical Newton-Raphson iterative procedures are conventionally used

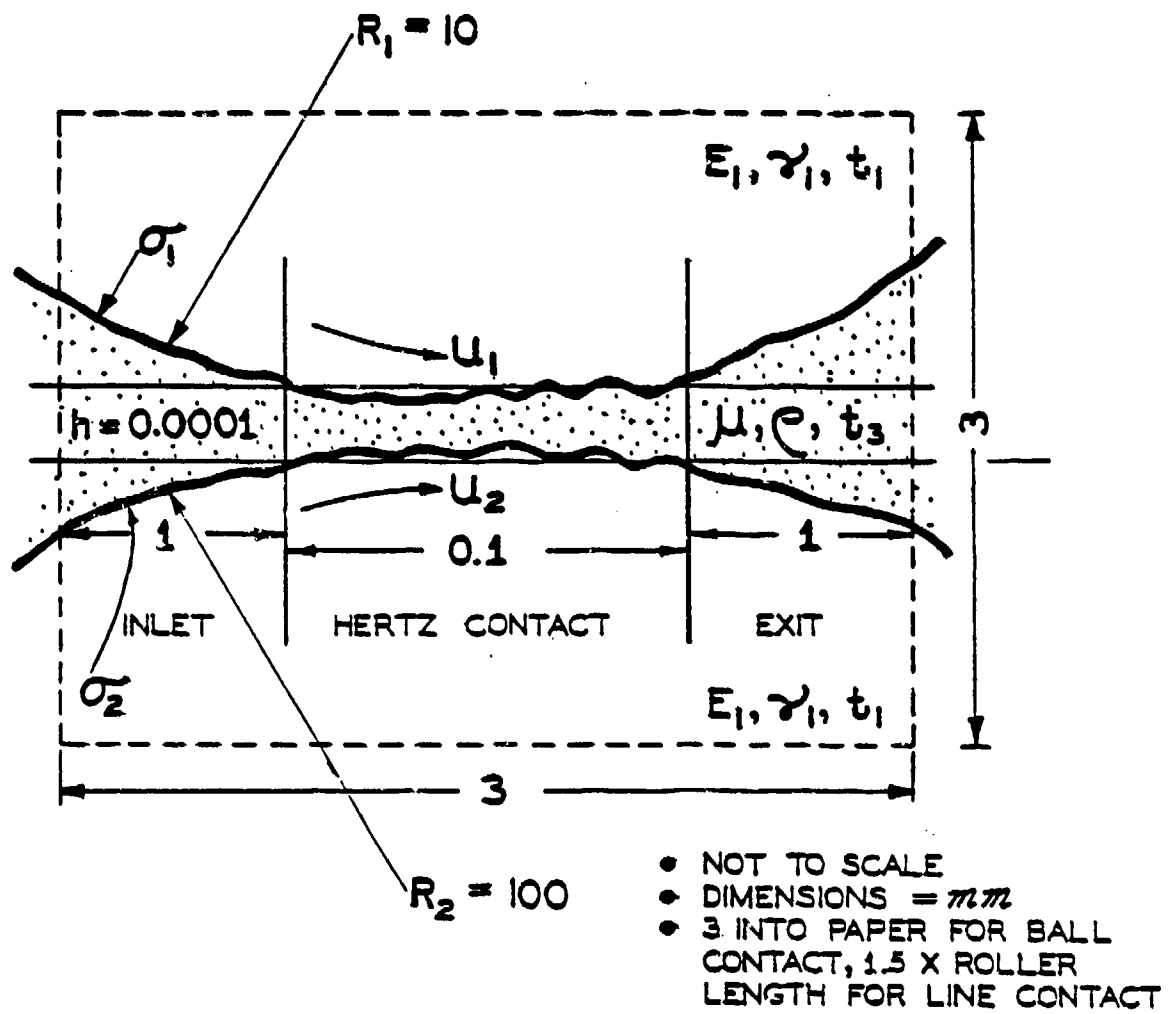
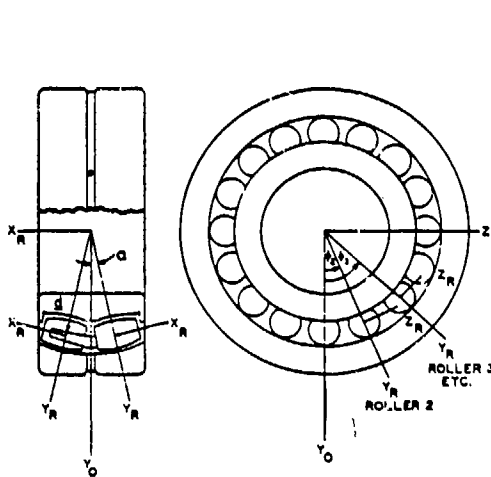
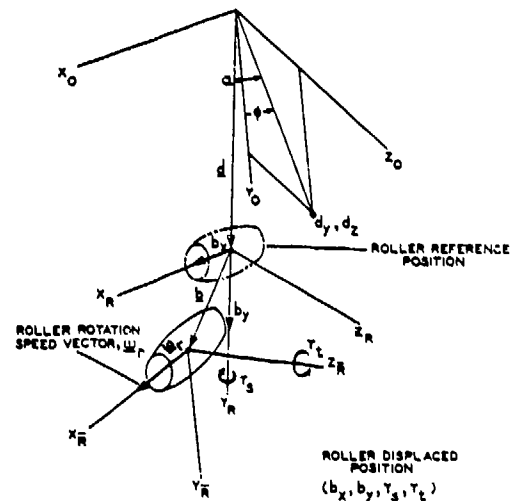


Figure 4. - Local contact control volume.



5A) OUTER RING AND ROLLER INERTIAL REFERENCE FRAMES



5B) ROLLER MOVING COORDINATE FRAMES

Figure 5. - Spherical roller bearing coordinate frames.

in all but the dynamic formulations. In the latter, Gear's predictor-corrector algorithms (ref. 16), as well as fourth order Runge-Kutta techniques, are used (ref. 18).

Contact Analysis Modules

The "local" nature of contact behavior and its simulation by software modules is at the heart of accurate system representation and deserves additional discussion.

Contact characterization begins by examining the micromechanics of its local control volume (refs. 43 to 47). Relative dimensions of two bodies approaching each other are shown in figure 4. They are characterized by material properties E and ν , and by temperature, t . They are separated from each other by a distance, h , due to the presence of a third medium. The latter has individual temperature and pressure dependent physical properties μ and ρ . The parameter $\Lambda = h/\sigma$, with σ defining surface roughness height, is used to describe the nature of the contact. If $h=0$, we have dry lubrication in which friction can be represented, to the first order, by a Coulomb relationship. With $\Lambda > 4$, a full separating film exists, preventing the direct solid-solid interaction of asperities. The $0 > \Lambda > 4$ middle ground identifies partial elastohydrodynamic behavior, the practical regime where load is shared by solid-solid as well as solid-fluid interactions. On the local detail level of contact characterization there are no absolute but rather statistical, expectation values for the boundary location of a body. The likelihood that some asperities will interact becomes significant for $\Lambda > 4$.

Software modules which describe the full Λ regime now exist. Most use starvation and thermal adjustment factors to account for inlet heating and quantity of lubrication supply. Cheng (ref. 23), in a recent review paper, summarizes the state-of-the-art in EHD and partial EHD contact formulation. The latter is still under intense investigation.

Contributions to the quantification of surface topography, and micromechanics in the mixed regime, were made by McCool and Gassel (refs. 29 and 30) who recently advanced the ability to simulate the contact of statistically anisotropic rough surfaces.

Methodology for Design with Rolling Element Bearings

Customarily, bearings are incorporated in rotating machinery by selection and not design. Usually a bearing is selected according to load ratings presented in a manufacturer's catalog and sized so that the space left over, after the satisfaction of other requirements, can accommodate it. The manufacturer's load rating is based on work originally performed by Lundberg and Palmgren (refs. 36 and 37). Bearing L_{10} life refers to that load C for which 90% of a group of bearings under identical operating conditions will exhibit one million inner ring revolutions without failure. The formulation of C assumes that failure originates within a subsurface volume which is repeatedly exposed to the stress distributions created by rolling contact. Experimental data were accumulated for bearing steels and led to the standard expression for life L under load P as

$$L_{10} = \left(\frac{C}{P} \right)^K$$

with $K=3$ or $10/3$, depending on the type of bearing. Multiplicative factors can be applied to L to increase the reliability beyond 90%, account for improved quality of modern steel manufacture and the manner in which a separating lubricant film is generated between rolling surfaces (refs. 40 to 42). For example, a 100% reliability can cut 50 000 hours at L_{10} to 2500 at L_0 ; M-50 steels can raise L_{10} by a factor of 5; and full film separation of rolling surfaces can at least double L_{10} values. The ranges of factor values, the load rating C , and particular geometry for which they hold, appear in manufacturer's catalogs. However, the C values result from simplifications of the basic Lundberg-Palmgren equations and are not directly applicable when bearings experience high speed variations in geometric fit, misalignment, large temperature excursion, inadequate lubrication, flexible supports and multiplane load vectors. Within the AFBMA (Anti Friction Bearing Manufacturers Association) standards leading to catalog ratings, bearing steels are assumed to be clean and to exhibit a minimum of Rockwell C58 hardness. The ratings are based on the additional assumption that radial bearings are loaded so that half of the ball or roller complement carries load, at zero clearance, with rigid

rings. Thrust bearings are assumed to distribute load evenly to each element and the axes of inner and outer rings are presumed to be aligned.

Contemporary rotating equipment has little respect for these simplifying assumptions. Misalignment of rings by less than 10 minutes in some cylindrical rolling bearings can lead to more than 80 percent decrease in L_{10} life (ref. 38). Changes in shaft mounting fits for tapered roller bearings result in complicated redistribution of radial and axial load (ref. 39).

Typically, a load support assembly is required to restrict shaft deflections to values smaller than a specified maximum over a specified speed and applied load vector range. The required bearing stiffness must be accurately determined by including terms which describe the housing, and shall be such as not to decrease L_{10} life below a specified maximum. The assembly shall fit within a defined space envelope which contains no more than an upper mass limit. The same envelope shall be subject to a temperature gradient which distorts the manufactured geometry. Further requirements may be placed on efficiency and noise generation.

The information needed to calculate these performance variable values is not provided in manufacturer's catalogs. Efforts to bypass the requirement for computerized analysis, by rules of thumb which restrict C/P values to those above 3, 4, or 5, are satisfactory only under conditions where enough equipment has functioned successfully so that the "safety margin" has proven to be adequate. Design by safety margins is a technical and economic luxury which is found to be increasingly unavailable as developing technology makes demands on materials which exhaust their performance capabilities.

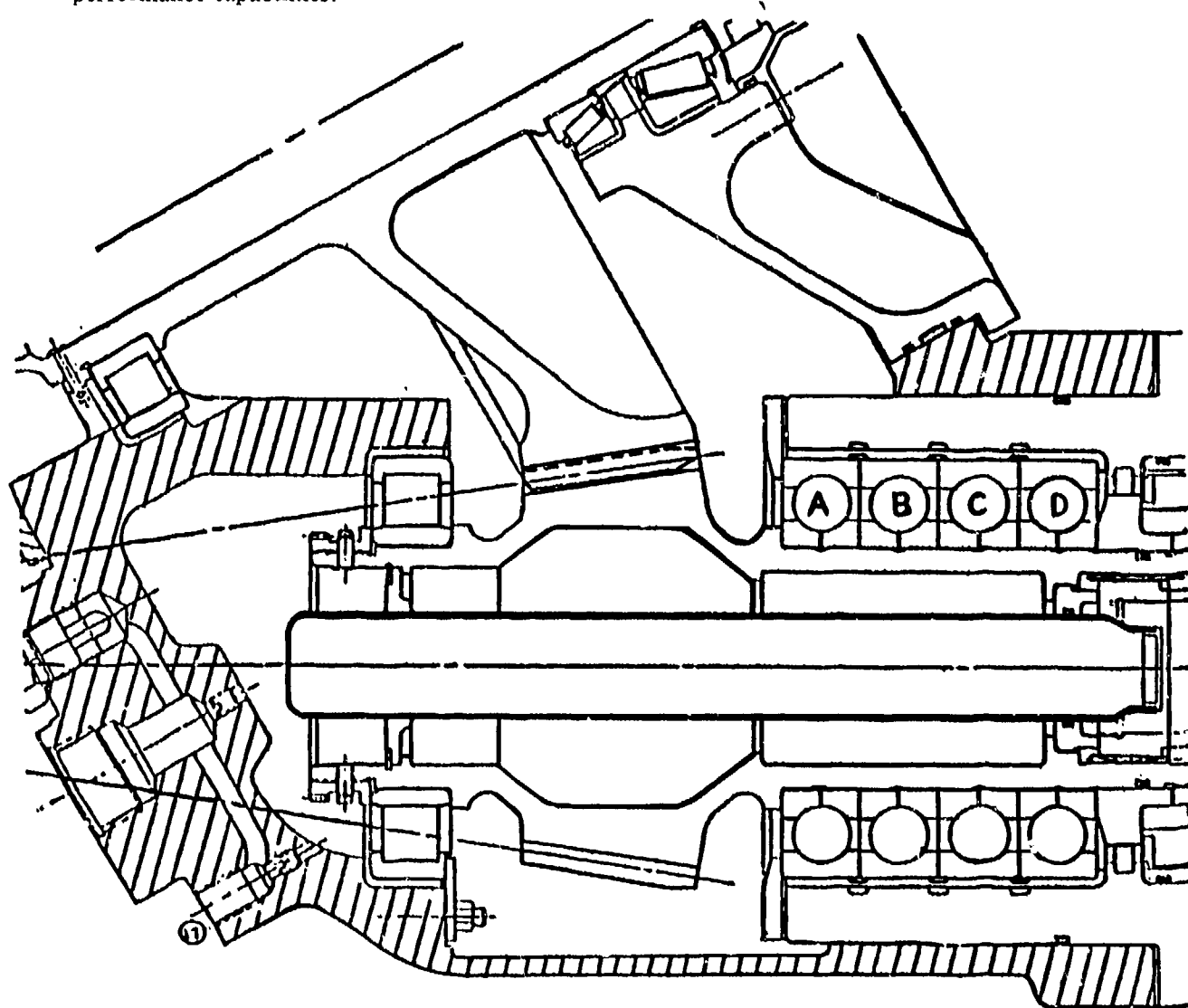


Figure 6. - High speed input pinion (from ref. 25).

The need for computerization of systems analysis results from the complex and interdisciplinary nature of modeling formulations. The nonlinear field equation sets simulating the thermomechanical dialogue are large. If we consider one 30-element cylindrical roller bearing under quasidynamic conditions, 185 variables are needed to describe element and ring positions. The full dynamic representation requires approximately the same. A typical input pinion load support system may contain a cylindrical and two angular contact bearings, a flexible shaft and a temperature field. Very quickly 600 simultaneous equation sets appear for the quasidynamic formulation. Their solution is clearly not possible without the use of numerical methods and high speed digital computers. It also indicates that the expertise required to do so is of a specialized nature.

A specific example of a fully activated level 2 program execution has been reported in detail by Pirvics (ref. 26) for the physical configuration in figure 6. The application is a 13 000-rpm helicopter gearbox input pinion, delivering 1089 kW of power. The system consists of an 80-mm shaft with an integral pinion gear supported between a 16-element cylindrical roller bearing and a stack of four, 15-element ball bearings. Three of the latter are in tandem, one is opposed. The lumped mass equivalent network is seen in figure 7; the lubricant model network in figure 8. A table of computed

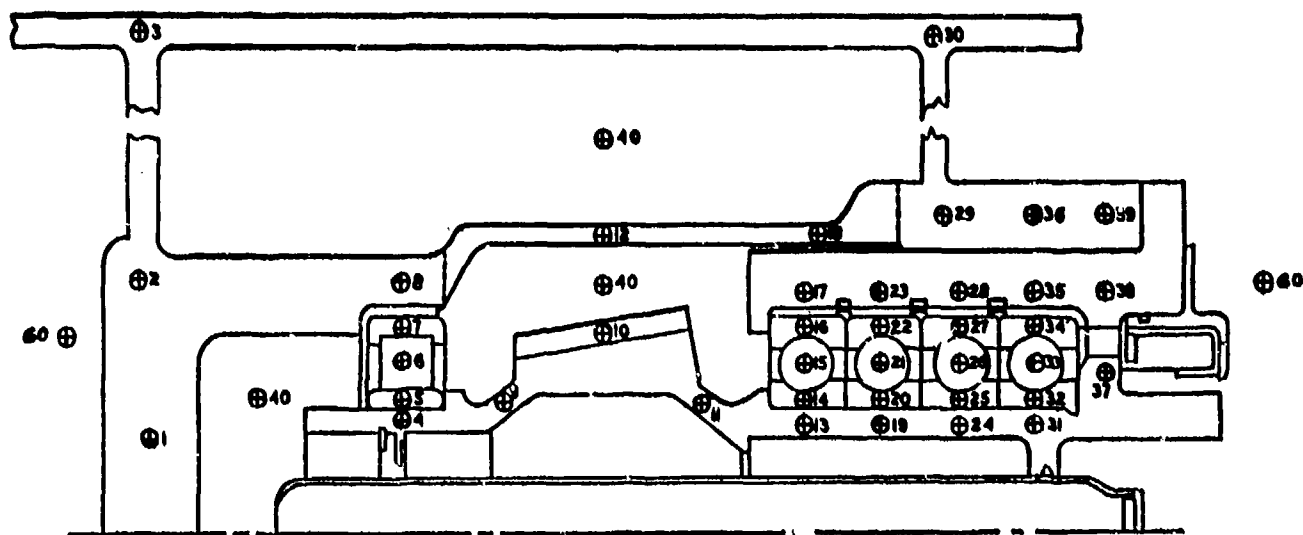


Figure 7. - Lumped mass nodal network (from ref. 25).

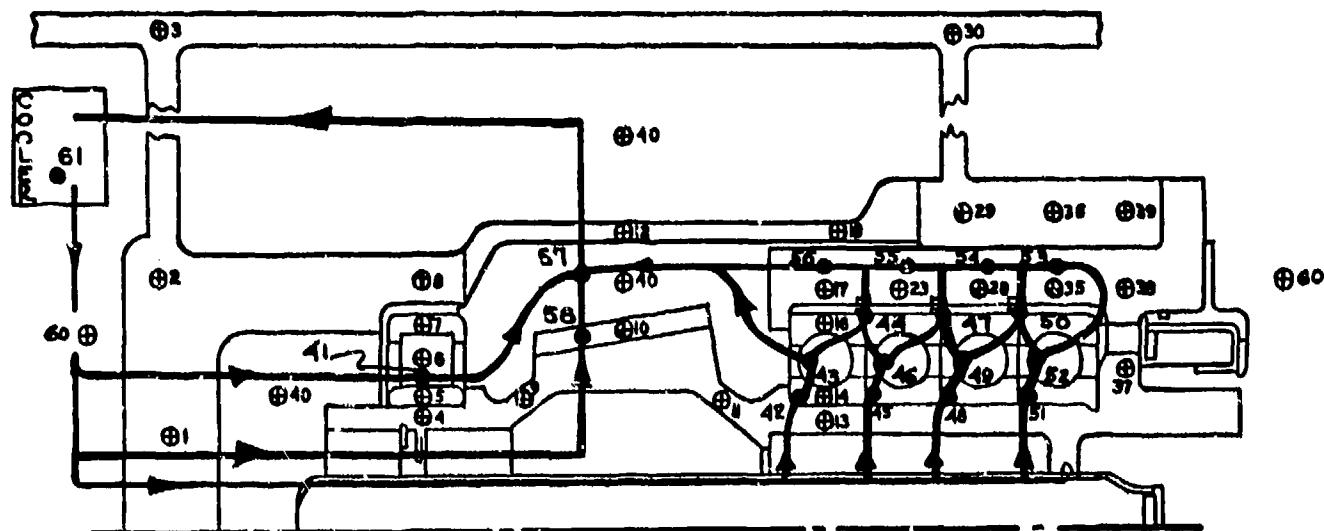


Figure 8. - Lubricant nodal network.

NODE	TEMPERATURE	NODE	TEMPERATURE	NODE	TEMPERATURE	NODE	TEMPERATURE	NODE	TEMPERATURE
1	95	2	97	3	81	4	104	5	104(122)
6	111	7	110(106)	8	105	9	103(89)	10	106
11	95(65)	12	101	13	79	14	83	15	91
16	89(92)	17	99	18	90	19	79	20	84(96)
21	97	22	91(93)	23	90	24	79	25	84(62)
26	97	27	91(90)	28	90	29	88	30	80
31	81	32	86	33	97	34	91(87)	35	89
36	87	37	102	38	86	39	86	40	92
43	100	42	72	43	83	44	94	45	72
46	86	47	97	48	72	49	86	50	97
51	73	52	87	53	97	54	97	55	97
56	96	57	102	58	88				

KNOWN BOUNDARY TEMPERATURES

NODE	TEMPERATURE	NODE	TEMPERATURE	NODE	TEMPERATURE
59	75	60	24	61	70

Figure 9. - Global temperature map calculated temperatures (measured temperatures).

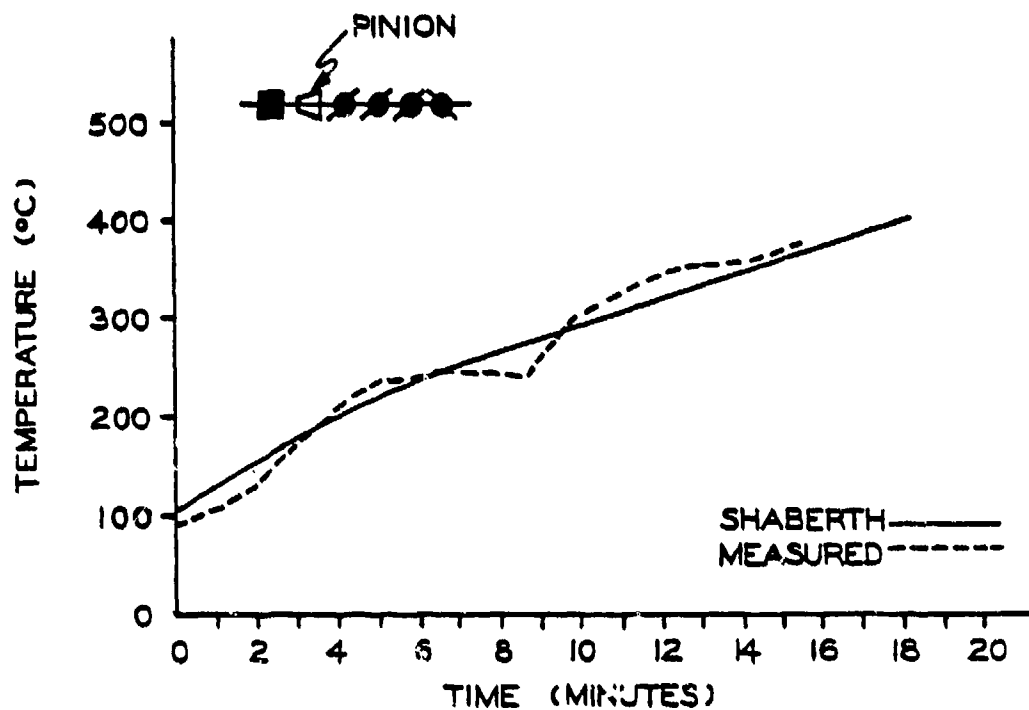


Figure 10. - Pinion shank temperature versus time (from ref. 25).

and measured temperatures and a graph of a time transient computation are in figures 9 and 10. The objective for the analysis was to produce the location and time required to reach an operating temperature of 500° C following lubricant shutoff. The 16-minute computerized projection correlates well with the experimentally observed 16.5 minutes.

Individual ball and cylindrical rolling element bearing dynamic performance simulation results appear in work by Gupta (refs. 48 and 49). Quasidynamic results for a single spherical bearing analysis can be found in reference 15. A system analysis approach for the design of a high speed input pinion is reported by Gassel (ref. 39). The significance of systems analysis may also be seen in the assessment of thermal effects in the early work by Rumbarger (ref. 10). More current discussions are presented by Thompson (ref. 50).

The methodology advocated for load support design is as simple as the message contained in the following statements. Contemporary design is based on interdisciplinary analysis of system performance. System performance is characterized by complex cross-coupling of many variables. Their evaluation requires computerized system simulation of hardware. Simple computer programs give simplistic answers. Sophisticated software is useful only when credibility is established by corroboration with experiment. Such programs exist and should be used before any material is cut.

Summary Remarks

This report attempts

The preceding material represents an effort to review the existing need and tools present for analytic computerized design of load support systems. It advocates system as opposed to component design. In doing so, it illustrates the peculiar nature of design where concentrated contacts are involved. The point is made, that the concentrated contact *local* thermomechanical event cannot be ignored in the *global* system assessment. This is so because *local* performance failure very quickly cascades to *global* system destruction. The cross-coupled sensitivity of local and global events demands understanding prior to hardware commitment. Such understanding is noted to be available in a variety of programs. The use of software, however, requires an intelligent selection and assurance that results computed are meaningful. Therefore, notes are made concerning good software design, its architecture, and particular modular content.

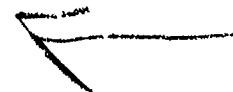
The basic message is simple. Responsible state-of-the-art design of new, high technology, prototypes which employ rotating supports proceeds at risk without computerized systems analysis. Tools are there to be used. More are evolving with ever increased sophistication and corroboration with actual hardware performance.

References

1. Pirvics, J.: Computerized Analysis and Design Methodology for Rolling Element Bearing Load Support Systems. ASME International Conference on Bearing Design: Historical Aspects, Present Technology, and Future Problems, Century 2—Emerging Technology Conference, August 1980.
2. Jones, A. B.: Ball Motion and Sliding Friction in Ball Bearings. J. Basic Eng., vol. 81, 1959, pp. 1-12.
3. Jones, A. B.: A General Theory for Elastically Constrained Ball and Radial Roller Bearings Under Arbitrary Load and Speed Conditions. J. Basic Eng., vol. 82, 1960, pp. 309-320.
4. Harris, T. A.: Ball Motion in Thrust-Loaded, Angular Contact Bearings with Coulomb Friction. J. Lubr. Technol., vol. 93, 1971, pp. 32-38.
5. Harris, T. A.: An Analytic Method to Predict Skidding in Thrust-Loaded, Angular-Contact Ball Bearings. J. Lubr. Technol., vol. 93, 1971, pp. 17-24.
6. Archard, J. F.; and Cowking, E. W.: Elastohydrodynamic Lubrication at Point Contacts. Proc. Inst. Mech. Eng., vol. 180, pt. 3B, 1965-66, pp. 47-56.
7. Harris, T. A.: An Analytical Method to Predict Skidding in High Speed Roller Bearings. Trans. ASLE, vol. 9, 1966, pp. 229-241.
8. Boness, R. J.: The Effects of Oil Supply on Cage and Roller Motion of Lubricated Roller Bearings. J. Lubr. Technol., vol. 92, 1970, pp. 39-53.
9. Poplawski, J. V.: Slip and Cage Forces in a High Speed Roller Bearing. J. Lubr. Technol., vol. 94, 1972, pp. 143-152.
10. Rumbarger, J. H.; Filetti, E. G.; and Gubernick, D.: Gas Turbine Engine Mainshaft Roller Bearing-System Analysis. J. Lubr. Technol., vol. 95, 1973, pp. 401-416.
11. Crecelius, W. J.: User's Manual for Steady State and Transient Thermal Analysis of a Shaft-Bearing System (SHABERTH). Contract Report ARBRL-CR-00386 to U. S. Army Ballistic Research Laboratory, 1978, SKF Industries, Inc.

12. Ragen, M. A.: Steady State and Transient Thermal Analysis of a Transmission System—SKF Computer Program "TRANSIM" SKF Report No. AT79Y001, May 1979, Prepared for U. S. Army Ballistic Research Laboratory under Contract No. DAAK11-77-C-0102.
13. Crecellus, W. J.; and Kleckner, R. J.: PLANETSYS, A Computer Program for the Steady State and Transient Thermal Analysis of a Planetary Power Transmission System. SKF Report No. AL77P011, 1977, SKF Industries, Inc.
14. Kleckner, R. J.; Pirvics, J.; and Castelli, V.: High Speed Cylindrical Rolling Element Bearing Analysis "CYBEAN" Analytic Formulation. ASME Paper No. 79-LUB-35, 1979.
15. Kleckner, R. J.; and Pirvics, J.: High Speed Spherical Rolling Element Bearing Analysis "SPHERBEAN," accepted for publication at the 1981 Joint ASME/ASLE Lubrication Conference.
16. Conry, T.: Transient Dynamic Analysis of High Speed Lightly Loaded Cylindrical Rolling Element Bearings. Part I—Analysis, NASA CR-3334.
17. Brown, P. F.; et al.: Mainshaft High Speed Cylindrical Roller Bearings for Gas Turbine Engines. P&W Aircraft Group, Contract Report FR8615, April 1977.
18. Gupta, P. K.: Dynamics of Rolling-Element Bearings—Part I, Cylindrical Roller Bearing Analysis. J. Lubr. Technol., vol. 101, July 1979, p. 293.
19. Walters, C. T.: The Dynamics of Ball Bearings. J. Lubr. Technol., vol. 93, 1971, pp. 1-10.
20. Gupta, P. K.: Dynamics of Rolling-Element Bearings. Part III—Ball Bearing Analysis. J. Lubr. Technol., vol. 101, July 1979, p. 312.
21. Dowson, D.: Elastohydrodynamics, in Lubrication and Wear: Fundamentals and Application to Design. Inst. Mech. Eng., vol. 182, pt. 3a, 1968, pp. 151-167.
22. McGrew, J. M.; et al.: Elastohydrodynamic Lubrication, Phase I. AD-877768, 1970, Prepared for Wright-Patterson AFB under Contract No. AFAPL-TR-70-27.
23. Cheng, H. S.: Fundamentals of Elastohydrodynamic Contact Phenomena. Presented at International Conference on Fundamentals of Tribology, Massachusetts Institute of Technology, Cambridge, Massachusetts, June 19-22, 1978.
24. Anderson, W. J.: The Practical Impact of Elastohydrodynamic Lubrication. Proc. 5th Leeds/Lyon Symposium on Tribology at Leeds, Sept. 1978.
25. Tallian, T. E.: Elastohydrodynamic Effects in Rolling Contact Fatigue. Proc. 5th Leeds/Lyon Symposium on Tribology at Leeds, Sept. 1978.
26. Pirvics, J.: The Analysis of Thermal Effects in Rolling Element Bearing Load Support Systems. Proc. 6th Leeds/Lyon Symposium on Tribology at Lyon, Sept. 1979.
27. Gupta, P. K.: A Review of Computerized Simulations of Roller Bearing Performance. ASME-WAMI, New York, Dec. 1976.
28. Sibley, L. B.; and Pirvics, J.: Computerized Analysis of Rolling Bearings. ASME-WAM, New York, Dec. 1976.
29. McCool, J. I.; and Gassel, S. S.: The Contact of Two Surfaces Having Anisotropic Roughness Geometry. Energy Sources Technology Conference and Exhibition, New Orleans, La, Feb. 1980.
30. McCool, J. I.; et al.: Lubrication of Engineering Surfaces. Prepared Under DOE Contract No. ER-78-C-01-6637, Final Report, AT80D017, SKF Industries, Inc.
31. Hamrock, B. J.; and Dowson, D.: Isothermal Elastohydrodynamic Lubrication of Point Contacts. Part I—Theoretical Formulation. J. Lubr. Technol., vol. 98, no. 2, April 1976, pp. 223-229.
32. Chiu, Y. P.: An Analysis and Prediction of Lubricant Film Starvation in Rolling Contact Systems. Trans. ASLE, vol. 17, no. 1, 1974, pp. 22-35.
33. Murch, L. E.; and Wilson, W. R. D.: A Thermal Elastohydrodynamics Inlet Zone Analysis. Trans. ASME, J. Lubr. Technol., vol. 97, 1975, p. 212.
34. Johnson, K. L.; Greenwood, J. A.; and Poon, J. Y.: A Single Theory of Asperity Contact in Elastohydrodynamic Lubrication. Wear, vol. 92, 1972, pp. 91-108.
35. Tevaarwerk, J. L.; and Johnson, K. L.: The Influence of Fluid Rheology on the Performance of Traction Drives. ASME Paper No. 78-LUB-10, Oct. 1978.
36. Lundberg, G.; and Palmgren, A.: Dynamic Capacity of Rolling Bearings. Acta Polytechnica, Mechanical Engineering Series 1, Proc. Royal Swedish Academy of Engineering Sciences, no. 3 and 7, 1947.
37. Lundberg, G.; and Palmgren, A.: Dynamic Capacity of Roller Bearings. Acta Polytechnica, Mechanical Engineering Series 2, Proc. Royal Swedish Academy of Engineering Sciences, no. 4 and 96, 1952.
38. Liu, J. Y.: The Effect of Misalignment on Life of High Speed Cylindrical Roller Bearings. Trans. ASME, J. Lubr. Technol., Jan. 1971, pp. 60-68.
39. Gassel, S. S.; and Pirvics, J.: Load Support System Analysis—High Speed Input Pinion Configuration. Trans. ASME, J. Lubr. Technol., vol. 102, Jan. 1980, pp. 97-106.
40. Liu, J. Y.; et al.: Dependence of Bearing Fatigue Life on Film Thickness to Surface Roughness Ratio. Trans. ASLE, vol. 18, no. 2, 1975, pp. 144-152.
41. Harris, T.: Rolling Bearing Analysis. Wiley, New York, 1966.
42. McCool, J. I.; et al.: Effects of Stylus Dynamics and Tip Size in Profilometry. SKF Industries, Inc. (report in preparation).
43. Gassel, S. S.; et al.: Three Dimensional Microscale Topography Characterization System. SKF Industries, Inc. (report in preparation).
44. Tallian, T. E.; Chiu, Y. P.; and Van Amerongen, E.: Prediction of Traction and Microgeometry Effects on Rolling Contact Fatigue Life. Trans. ASME, J. Lubr. Technol., vol. 100, no. 2, 1978, pp. 156-166.
45. Chiu, Y. P.: On the Stress Field Due to Initial Strains in a Cuboid Surrounded by an Infinite Elastic Space. J. Appl. Mech., vol. 49, 1977, pp. 587-591.

46. Chiu, Y. P.: On the Stress Field and Surface Deformation in a Half Space With a Cuboidal Zone in Which Initial Strains Are Uniform. J. Appl. Mech., vol. 45, 1978.
47. Chiu, Y. P.: Analysis of Residual Stresses in Elasto-Plastic Contact of Half Planes. Proc. S.E. Conf. Theoretical and Applied Mechanics, May 1978.
48. Gupta, P. K.: Dynamics of Rolling-Element Bearings—Part IV, Ball Bearing Results. J. Lubr. Technol., vol. 101, July 1979, p. 319.
49. Gupta, P. K.: Dynamics of Rolling-Element Bearings—Part III, Cylindrical Roller Bearing Results. J. Lubr. Technol., vol. 101, July 1979, p. 305.
50. Thompson, W. S.; and Pirvics, J.: Methodology for Performance Prediction of a Helicopter Transmission Under Oil Starvation. Proc. JTCGS/AS, Third Biennial Aircraft Survivability Symposium, 1978.
51. Kleckner, R. J.; et al.: SKF Computer Program SPHERBEAN. Vol. I—Analysis; II—User's Manual; and III—Correlation with tests. Submitted to the NASA Lewis Research Center under NASA Contract No. NAS3-20824; NASA CR-165203 through CR-165205, 1980.





AD P000710

Predicted and Experimental Performance of Large-Bore High-Speed Ball and Roller Bearings

Harold H. Coe*

Trends in gas-turbine design have indicated that future aircraft engines may require bearings that can operate reliably at DN values of 3 million or higher (refs. 1 to 3) (the speed parameter DN is the bearing bore in millimeters multiplied by the shaft speed in rpm). Consequently, there has been a large amount of work done in the area of high-speed bearings over the last several years. Successful operation of ball bearings at 3 million DN was reported in references 4 and 5. Roller bearing operation to 3 million DN was reported in references 3 and 6.

The question of how to design bearings for high-speed applications is increasingly being answered by computer studies (refs. 3 and 7). Several comprehensive computer programs currently in use are capable of predicting rolling-bearing operating and performance characteristics (e.g., refs. 8 to 14). These programs generally accept input data of bearing internal geometry (such as sizes, clearance, and contact angles), bearing material and lubricant properties, and bearing operating conditions (load, speed, and ambient temperature). The programs then solve several sets of equations that characterize rolling-element bearings. The output produced typically consists of rolling-element loads and Hertz stresses, operating contact angles, component speed, heat generation, local temperatures, bearing fatigue life, and power loss. Two of these programs, Shaberth (ref. 9) and Cybean (refs. 10 and 11) developed under government sponsorship, have been used extensively at the Lewis Research Center.

After a computer program is developed, it is important that values calculated using such program be compared with actual bearing performance data to assess the programs predictive capability. Therefore, the objective of the work reported herein was to compare the values of inner- and outer-race temperatures, cage speed, and heat transferred to the lubricant or bearing power loss, calculated using the computer programs Shaberth and Cybean, with the corresponding experimental data for the large-bore ball and roller bearings described in references 6 and 15. Most of this work has been previously reported in references 16 to 18.

Test Data

Ball Bearing

The experimental work used for comparison, originally reported in reference 15, was performed on the high-speed bearing tester described in reference 19. Lubrication was provided to the test bearings through a jet feed system with two lubricant jets positioned 180° apart. The jets had a double orifice (fig. 1). The lubricant used was a tetraester, type II oil qualified to the MIL-L-23699 specification. The major properties of the oil are listed in table I.

The test bearing specifications are listed in table II. The bearings were 120-mm-bore, split inner race with fifteen 20.6-mm (0.8125-in.) diameter balls and a contact angle of 20°. The races and balls were made of double-vacuum-melied (VIM-VAR) AISI M-50 material. The bearings had one-piece machined cages which were inner-race riding. These cages were made of silver-plated AMS 6415 steel.

Power loss per bearing was determined by measuring line-to-line voltage and line current to the test-rig drive motor. Motor-drive power was then calculated as a function of line current, reflecting bearing power usage at the various operating speeds.

Data were recorded at bearing thrust loads of 6672, 13 350, and 22 240 N (1500, 3000, and 5000 lb) and at three shaft speeds, 12 000, 16 700, and 20 800 rpm. The lubricant flow rates were 0.0038 and 0.0083 m³/min (1.0 and 2.2 gal/min). The oil inlet temperature was held constant at 394 K (250° F).

*NASA Lewis Research Center.

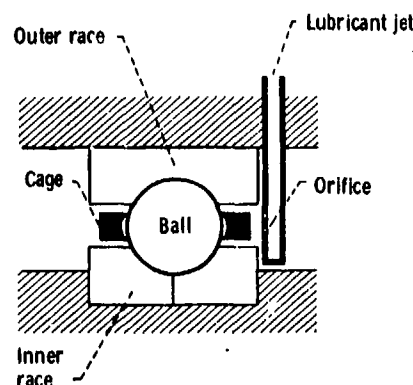


Figure 1. - Bearing lubrication schematic. Number of jets, two per bearing; dual orifice; inner-land riding cage.

TABLE I. - PROPERTIES OF TETRAESTER LUBRICANT^a

Additives	Antiwear, oxidation inhibitor, antifoam
Kinematic viscosity, cS, at -	
311 K (100° F)	28.5
372 K (210° F)	5.22
477 K (400° F)	1.31
Specific heat at 477 K (400° F)	2340 (0.54)
J/(kg)(K), (Btu/(lb)(°F))	
Thermal conductivity at 477 K (400° F), J/(m)(sec)(K), (Btu/(hr)(ft)(°R))	0.13 (0.075)
Specific gravity at 477 K (400° F)	0.850

^aFrom ref. 15.

TABLE II. - BALL BEARING^a SPECIFICATIONS

Bearing outside diameter, mm	190
Bearing inside diameter, mm	120
Bearing width, mm	35
Bearing contact angle, deg	20
Outer-race curvature	0.52
Inner-race curvature	0.54
Number of balls.	15
Ball diameter, mm (in.)	20.6 (0.8125)
Retainer design	One-piece machined
Retainer material	AMS 6415 ^b
Race and ball material	AISI M-50 ^c
Ball surface finish, μm ($\mu\text{in.}$)	0.025 (1)
Raceway surface finish, μm ($\mu\text{in.}$)	0.05 (2)

^aTolerance grade ABEC-5.

^bSilver plated per AMS-2410.

^cVacuum-induction melted, vacuum-arc remelted.

Roller Bearing

The experimental roller bearing data used for comparison were initially reported in reference 6. In this reference a large-bore roller bearing was tested at speeds up to 3 million DN. Lubrication was provided to the test bearing through axial grooves under the inner race with small radial holes through to the rolling elements. The inner ring was also cooled by oil flowing through axial grooves that had no radial holes. About one-half of the total oil introduced to the inner ring was used for cooling only.

The lubricant used was also a tetraester, type II oil qualified to the MIL-L-23699 specification (table I). The bearing tester is described in detail in reference 6.

The test roller bearing had a 118-mm bore, a flanged inner ring, and 28 rollers, each 12.65 mm (0.4979 in.) in diameter by 14.56 mm (0.573 in.) long. More complete specifications are shown in table III.

Oil inlet temperature was held constant at 366 K (200° F). Accurate measurement of bearing oil inlet and outlet temperatures allowed determination of the amount of heat transferred to the lubricant at any operating condition. Data were recorded at bearing loads of 2220, 4450, 6670, and 8900 N (500, 1000, 1500, and 2000 lb), and at shaft speeds of 10 000, 15 000, 20 000, and 25 500 rpm. The total oil flow rates to the inner ring varied from 0.0019 to 0.0102 m³/min (0.5 to 2.7 gal/min).

Computer Programs

Two computer programs were used. The program called Shaberth (ref. 8) was used to calculate the ball bearing data, and Cybean (refs. 10 to 12) was used for the cylindrical roller bearing calculations. Shaberth can analyze up to five bearings on a single shaft and includes shaft deflection. Cybean analyzes a single cylindrical roller bearing. Both programs are capable of calculating the thermal and kinematic performance of high-speed bearings, and Cybean includes a roller skew prediction for misaligned conditions. The calculations include determination of inner- and outer-ring temperatures, oil outlet temperatures, cage speed, and bearing power loss.

Use of either Shaberth or Cybean to predict bearing performance requires as input an estimate of the volume percent of the bearing cavity that is occupied by the lubricant. The bearing cavity is defined as the space between the inner- and outer-races that is not occupied by the cage or the rolling elements. The authors of references 8 and 11 recommended that the values used be less than 5 percent. When these programs are used for a thermal analysis, additional input is required, since all the thermal nodes must be defined. The maximum number of nodes permitted is 100. With Shaberth, a relatively simple thermal grid system was chosen, using only 17 nodes for the ball bearing. With Cybean, 41 nodes were used, including 19 in the lubricant system (fig. 2). It should be noted here that, because of the simple nodal system, the lubricant flow rate was not included directly in the thermal calculations with Shaberth. However, the flow rate was used directly with the Cybean program.

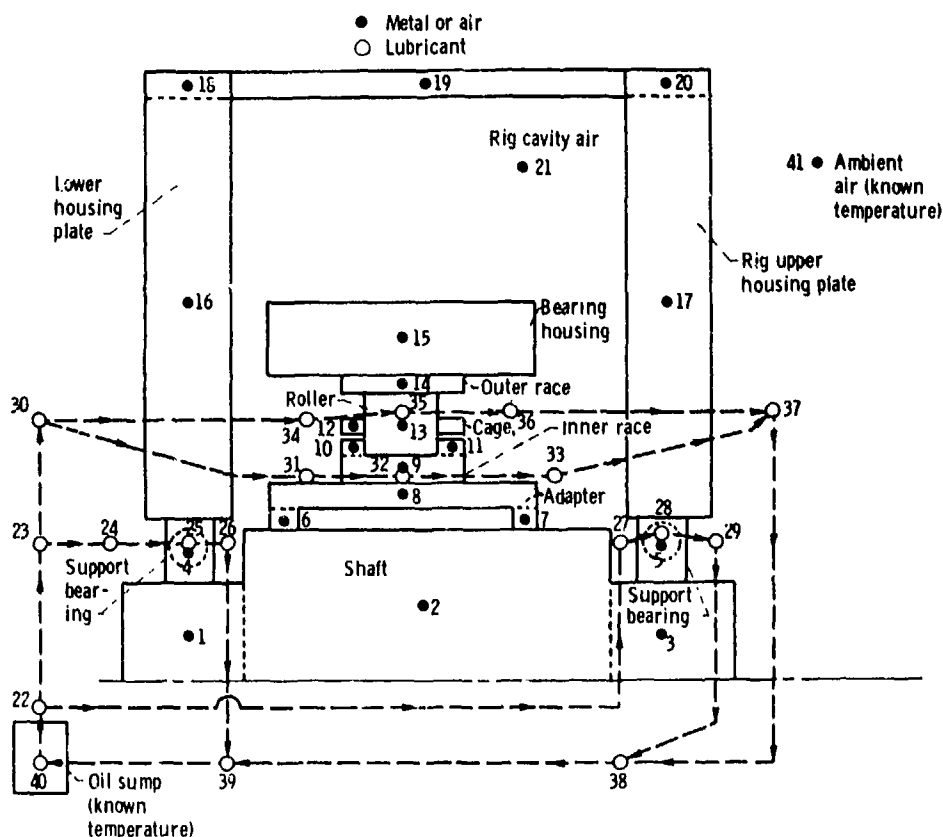


Figure 2. - Nodal system used for thermal routines in Cybean.

TABLE III. - ROLLER-BEARING SPECIFICATIONS

Inner race	
Bore diameter, mm (in.)	118 (4.6457)
Raceway diameter, mm (in.)	131.6 (5.1834)
Flange diameter, mm (in.)	137.47 (5.4122)
Total width, mm (in.)	26.92 (1.060)
Groove width, mm (in.)	14.59 (0.5746)
Flange angle, deg	0.6
Outer race	
Outer diameter, mm (in.)	164.49 (6.4760)
Raceway diameter, mm (in.)	157.08 (6.1842)
Total width, mm (in.)	23.9 (0.942)
Rollers	
Diameter, mm (in.)	12.55 (0.4979)
Length, mm (in.):	
Overall	14.56 (0.5733)
Effective	13.04 (0.5133)
Flat	8.40 (0.3307)
Crown radius, mm (in.)	622.3 (24.5)
End radius, mm (in.)	381.0 (15)
Number	28
Cage	
Land diameter, mm (in.)	137.95 (5.4312)
Axial pocket clearance, mm (in.)	0.020 (0.0008)
Tangential pocket clearance, mm (in.)	0.221 (0.0087)
Single rail width, mm (in.)	4.6 (0.18)
Bearing	
Cold diametral clearance, mm (in.)	0.12 (0.0047)

Results and Discussion

To effect a direct comparison of predicted and experimental bearing performance, the computer programs were generally run at the stated operating conditions of the bearings tested (refs. 6 and 15). All combinations of load, speed, and flow rate were not computed, because they are not all necessary for the comparisons and would require unnecessary computer time. Note that in all the figures in this report, the calculated values are always just connected with straight line segments.

Shaft Bearing Program (Shaberth)

Calculations were made for the 6672-N (1500-lb) thrust load case at 12 000, 16 700, and 20 000 rpm. The lubricant volume was set at 1.0 percent. The calculated results are shown in figure 3 compared with the experimental data for an oil flow rate of 3.8×10^{-3} m³/min (1 gal/min). The calculated values of inner- and outer-race temperatures are lower than the experimental data, and the calculated bearing power loss (fig. 3(b)) is close to the measured value.

To compare with the experimental data taken at the oil flow rate of 8.3×10^{-3} m³/min (2.2 gal/min), the Shaberth program was run for the same conditions given previously except that the lubricant volume in the cavity was set at 2 percent. This value was chosen assuming that the percentage of lubricant should increase with increased flow rate. The results are shown in figure 4. The calculated race temperatures are reasonably close to the experimental data. The calculated bearing power losses resulted in fairly good agreement with the experimental data.

A comparison of figures 3 and 4 shows that the experimental temperature data decreased with the increased flow rate; whereas the calculated temperature increased with the increased percent lubricant. The predicted values would have undoubtedly been even better if flow rate were included

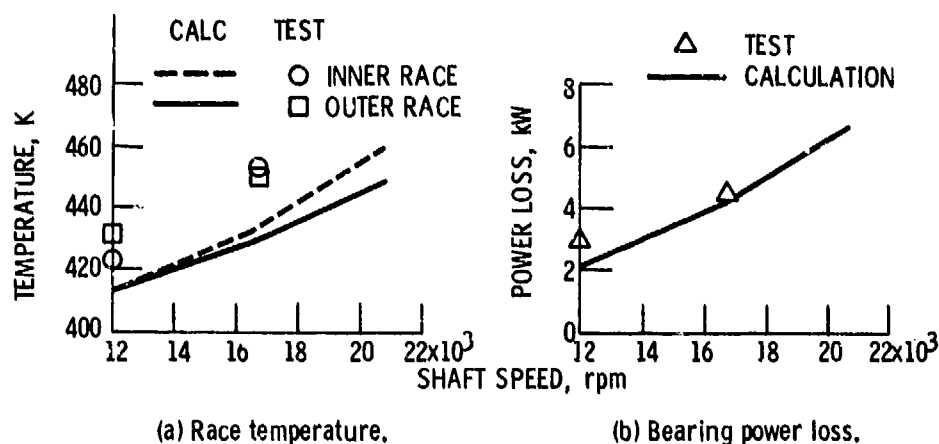


Figure 3. - Comparison of calculated and experimental (ref.15) bearing operating characteristics as functions of shaft speed using Shaberth computer program. Lubricant flow rate, 0.0038 m³/min (1 gal/min); volume of lubricant, 1.0 percent; thrust load, 6672 N (1500 lb).

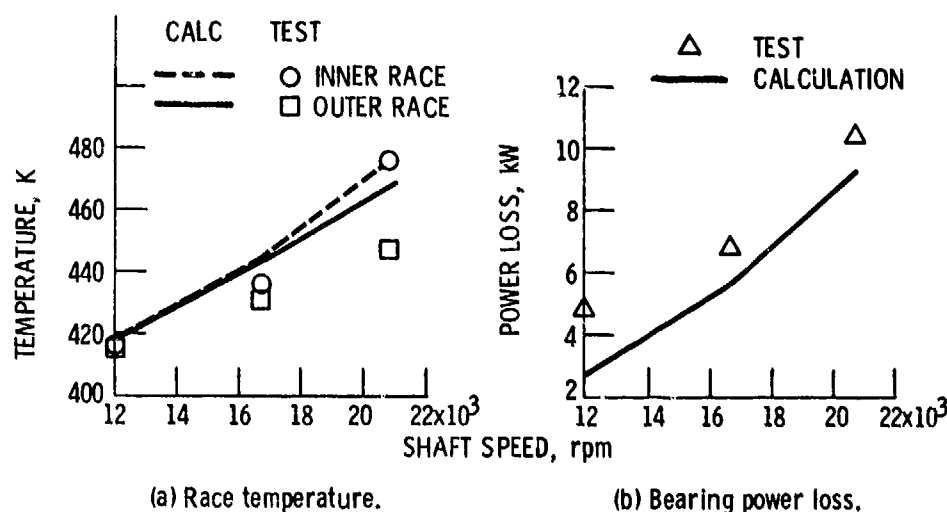
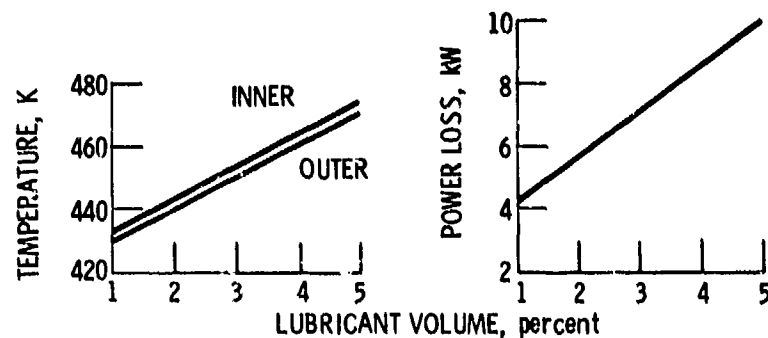


Figure 4. - Comparison of calculated and experimental (ref.15) bearing temperatures and power loss as function of shaft speed using Shaberth computer program. Lubricant flow rate, 0.0083 m³/min (2.2 gal/min); volume of lubricant, 2.0 percent; thrust load, 6672 N (1500 lb).

the thermal calculations. The experimental bearing power loss increased with flow rate, and the calculated values increased with percent lubricant. To observe how the race temperatures and power loss might vary, the program was run at one condition for several other values of percent lubricant. The results with 6672-N (1500-lb) thrust load and 16 700-rpm shaft speed are shown in figure 5. Both the inner- and outer-race temperatures, as well as the bearing power loss, increased linearly with the volume percent over the range calculated. The change in temperature is about 10 percent over the volume range, while the change in power loss is a very significant 150 percent.

The relatively good agreement between calculated and measured values shown in figures 3 and 4 indicates that for these operating conditions the values of percent lubricant in the bearing cavity assumed for the comparison calculations were reasonably correct.

The Shaberth program (as noted in ref. 8) uses a modification to the film thickness calculation as proposed by Loewenthal, Parker, and Zaretsky (ref. 20). Therefore, the lubricant film thicknesses, as calculated by the program for the same 6672-N (1500-lbf) load and 8.3×10^{-3} m³/min (2.2-gal/min) oil flow case as before, were plotted as shown in figure 6. The values show little change with shaft speed, and the outer-race contact film is slightly thicker than that at the inner race. Apparently the effects of speed on film thickness are offset by the effects of temperature and load.



(a) Race temperature.

(b) Power loss.

Figure 5. - Calculated bearing operating characteristics as functions of volume percent lubricant in bearing cavity using Shaberth program. Thrust load, 6672 N (1500 lb); shaft speed, 16 700 rpm.

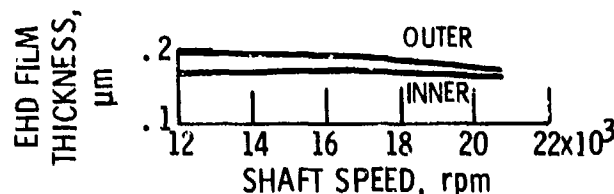
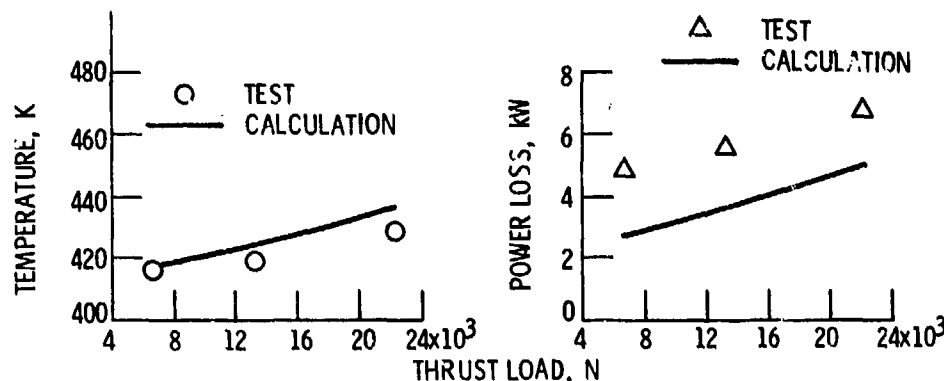


Figure 6. - Values of elastohydrodynamic (EHD) film thickness at inner- and outer- race-ball contacts as functions of speed as calculated by Shaberth computer program. Thrust load, 6672 N (1500 lb); lubricant volume, 2 percent.



(a) Inner race temperature.

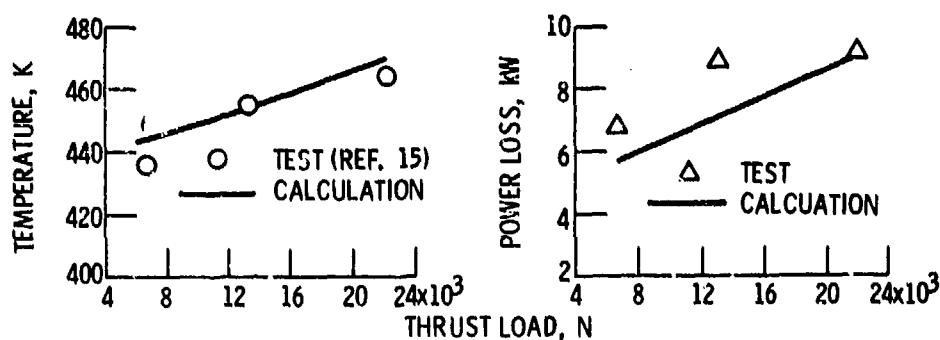
(b) Power loss.

Figure 7. - Comparison of calculated and experimental (ref.15) values of race temperatures and bearing power loss as functions of thrust load using Shaberth. Shaft speed, 12 000 rpm; lubricant flow rate, $8.3 \times 10^{-3} \text{ m}^3/\text{min}$ (2.2 gal/min); lubricant volume, 2.0 percent.

To determine the effect of load on bearing operation, Shaberth was run at the 13 350- and 22 240-N (3000- and 5000-lbf) load conditions. The results are shown in figures 7 and 8, where the inner-race temperatures and bearing power loss are plotted as functions of bearing thrust load for shaft speeds of 12 000 and 16 700 rpm. The calculated values increase with thrust load and give a reasonably close prediction of the experimental data.

Cylindrical Roller Bearing Program (Cybean)

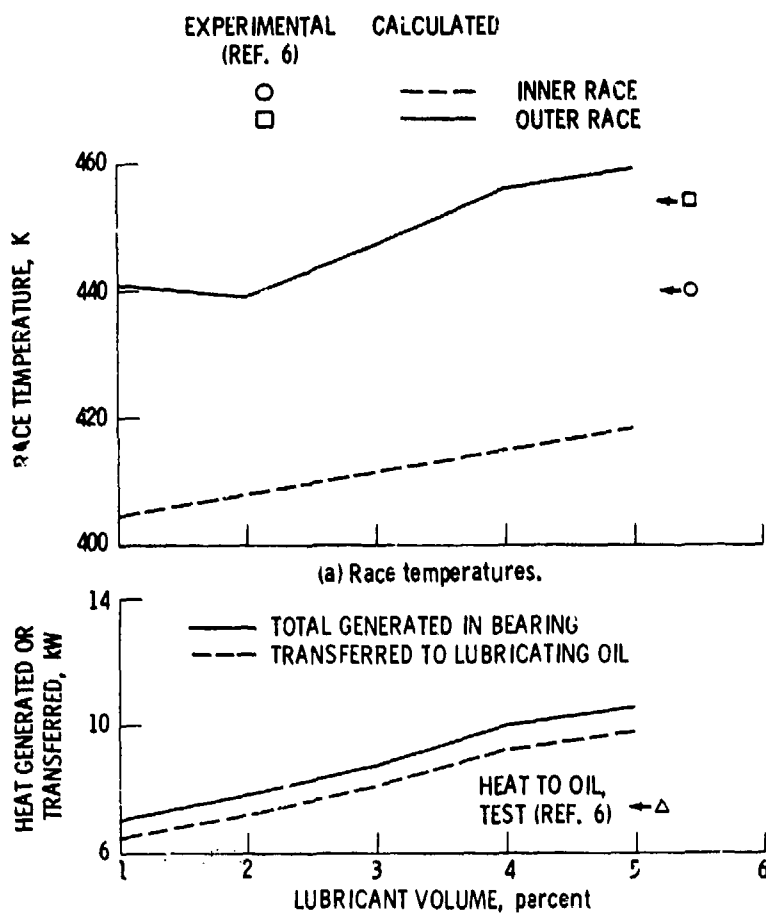
Using the computer program Cybean, the effect of load was calculated using one speed (20 000 rpm), the effect of speed was determined using one load (8900 N (2000 lb)), and the effect of flow rate was observed using one load and one speed (8900 N (2000 lb) and 25 500 rpm).



(a) Inner race temperature.

(b) Power loss.

Figure 8. - Comparison of calculated and experimental values of bearing characteristics as functions of thrust load using Shaberth. Shaft speed, 16 700 rpm; lubricant flow rate, $0.0083 \text{ m}^3/\text{min}$ (2.2 gal/min); lubricant volume, 2.0 percent.



(b) Heat generated in bearing, or transferred to lubricant.

Figure 9. - Calculated bearing operating characteristics as functions of volume percent lubricant. (Test data shown for comparison.) Thrust load, 4450 N (1000 lb); shaft speed, 20 000 rpm; lubricant flow rate, $0.0057 \text{ m}^3/\text{min}$ (1.5 gal/min).

Effect of lubricant volume. - To determine how the race temperatures and bearing heat generation vary with the value assumed for percent lubricant in the bearing cavity, the program was run for several values of this volume percent at the 4450-N (1000-lb), 20 000-rpm condition. The total oil flow rate chosen was $0.0057 \text{ m}^3/\text{min}$ (1.5 gal/min). The results are shown in figure 9. Also shown are the corresponding experimental data points.

The race temperatures (fig. 9(a)) increased with increasing lubricant volume. This would be expected since the fluid drag on the rollers and the cage would increase with the amount of liquid available. Over the full range from 1 to 5 percent oil volume, the temperature changes seem to be nearly linear and not too large, about 5 percent at these conditions.

The total heat generated in the bearing (fig. 9(b)) increased with increasing lubricant volume. These changes were also linear but the total change in heat generation over the volume range was a more significant 50 percent. Since reference 6 includes data on heat transferred to the lubricant (as an indication of the power loss within a bearing), this type of data was calculated from the computer-predicted oil-outlet temperature and is also shown in figure 9(b). The amount of heat transferred to the oil closely follows the amount of heat generated in the bearing. Over this range of volume percent, the amount of heat transferred to the lubricant is about 90 percent of the heat generated in the bearing. Based on the experimental data for this test condition, the range of volume percent from 1 to 5 percent is adequate for the outer-race temperature and the heat transferred to the oil. The calculated inner-race temperature remained below the experimental value for the whole volume range.

Effect of bearing load and speed. — The computer program Cybean was run to determine the effect of bearing load on race temperature and heat generation. Calculations were made with a lubricant flow rate of $0.0057 \text{ m}^3/\text{min}$ (1.5 gal/min) for two lubricant volumes (2 and 3 percent), and a shaft speed of 20 000 rpm. The results, compared with experimental data, are shown in figure 10 for radial loads from 2220 to 8900 N (500 to 2000 lb). The predicted race temperatures (fig. 10(a)) increase very slightly over the load range, and the experimental values are practically constant. While the outer-race temperatures compare favorably, the predicted inner-race temperatures remain about

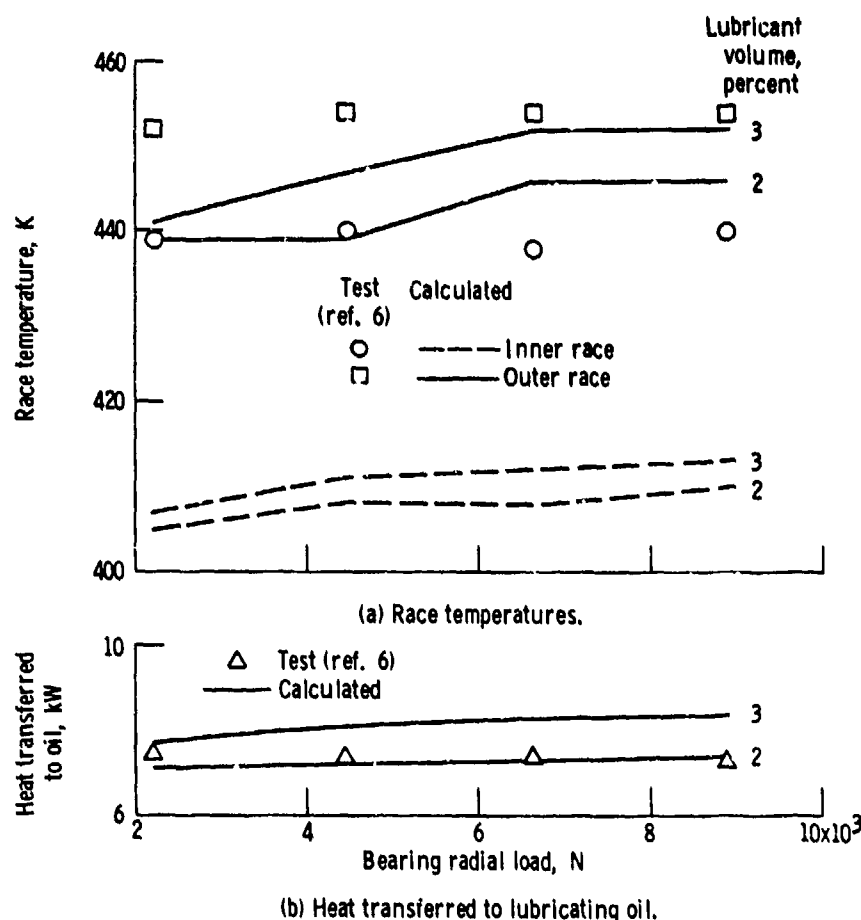
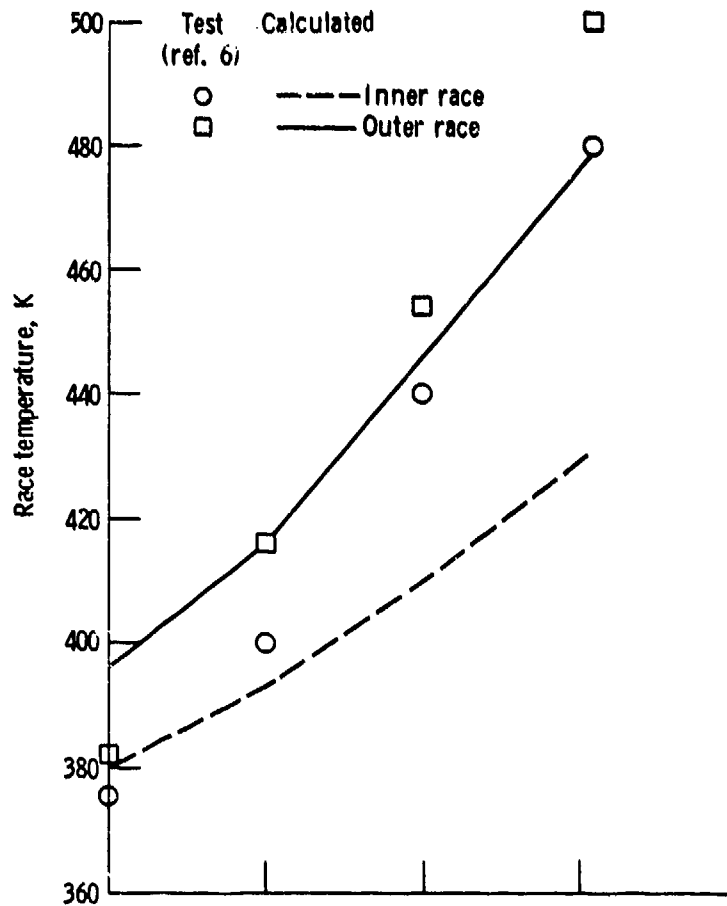


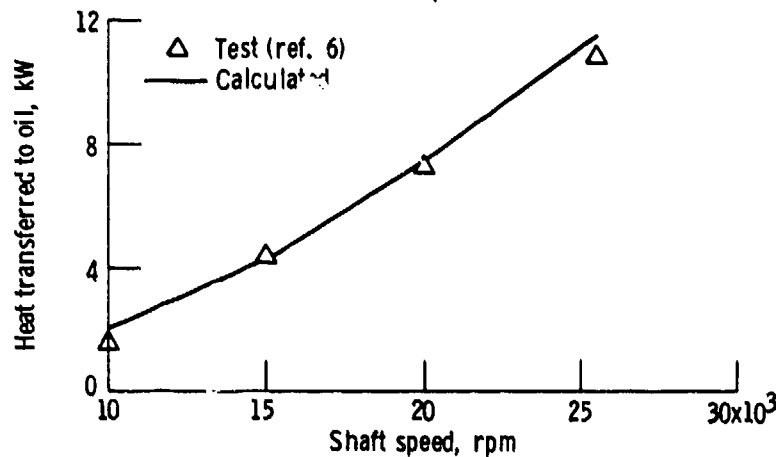
Figure 10. - Calculated and experimental bearing operating characteristics as functions of radial load. Shaft speed, 20 000 rpm; lubricant flow rate, $0.0057 \text{ m}^3/\text{min}$ (1.5 gal/min).

10 percent lower than the test values. The amount of heat transferred to the oil, predicted using the lubricant volume of 2 percent, compares very well with the test data (fig. 10(b)).

The effect of shaft speed was observed by using the program with an 8900-N (2000-lb) load for several values of shaft speed. The flow rate was set at 0.0057 m³/min (1.5 gal/min), and the lubricant volume at 2 percent. The results are shown in figure 11 for shaft speeds from 10 000 to 25 500 rpm (1.2 to 3.0 million DN). The predicted values of outer-race temperature (fig. 11(a)) compared with



(a) Race temperatures.



(b) Heat transferred to lubricating oil.

Figure 11. - Calculated and experimental bearing operating characteristics as functions of shaft speed. Load, 8900 N (2000 lb); lubricant flow rate, 0.0057 m³/min (1.5 gal/min); lubricant volume, 2 percent.

the experimental data are slightly high at the lower speeds and slightly low at the higher speeds. The predicted inner-race temperature, fairly close to the experimental data at the lower speeds, becomes very low at the higher speeds. The heat transferred to the oil, however, as predicted by the program compared very well with the experimental values over the whole speed range (fig. 11(b)). It appears that the calculations for the total bearing heat generation are correct but that insufficient heat transfer is predicted to the inner race at the higher speeds. At this point it is not clear whether the discrepancy with the inner-race temperature is a problem of using a proper thermal model or of using proper input data.

Effect of lubricant flow rate. — Since the oil flow rate can have a significant effect on bearing temperature and power loss, Cybean was run over a range of oil flow rates from 0.0038 to 0.0102 m³/min (1.0 to 2.7 gal/min) for several values of lubricant volume percent. Calculations were made at 8900-N (2000-lb) load for 25 500 rpm. The results are shown in figure 12. The calculated trends are in the right direction; that is, the race temperatures are reduced by increasing the oil flow rate for the values of lubricant volume shown. The calculated outer-race temperatures (fig. 12(a)) are reasonable for volumes of 2 or 3 percent, while the calculated inner-race temperatures remain low over the entire

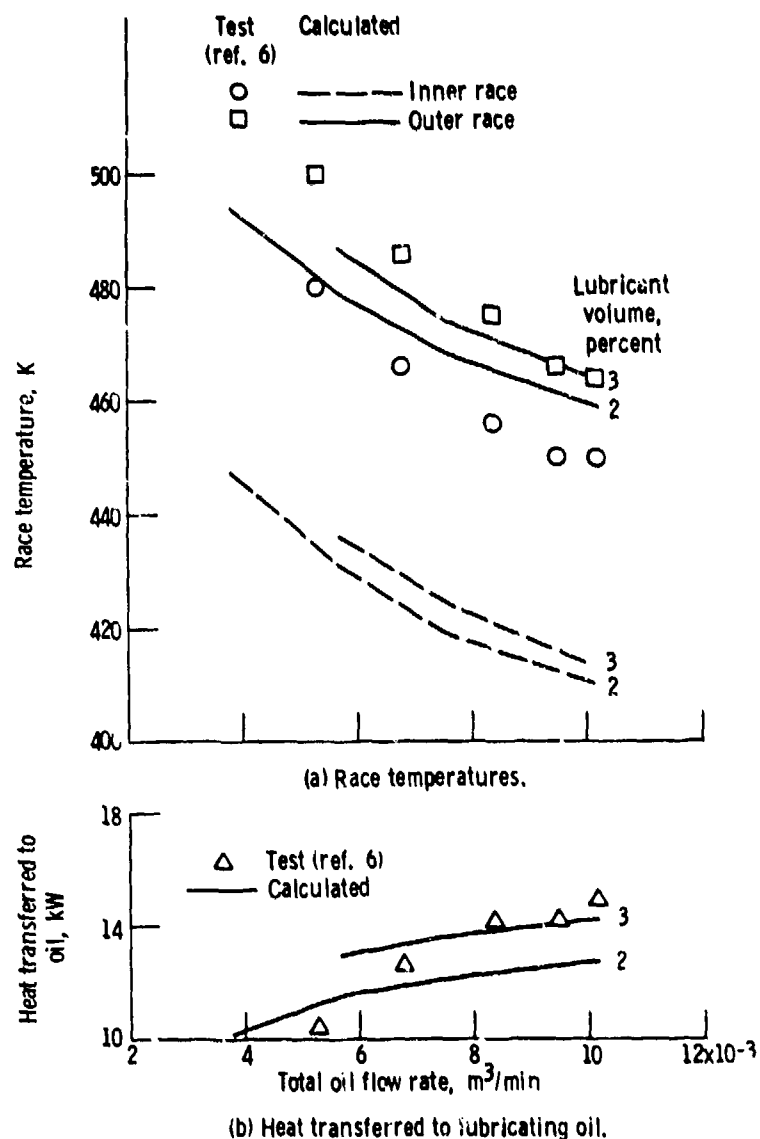


Figure 12. - Calculated and experimental bearing operating characteristics as functions of lubricant flow rate. Shaft speed, 25 500 rpm; radial load, 8900 N (2000 lb).

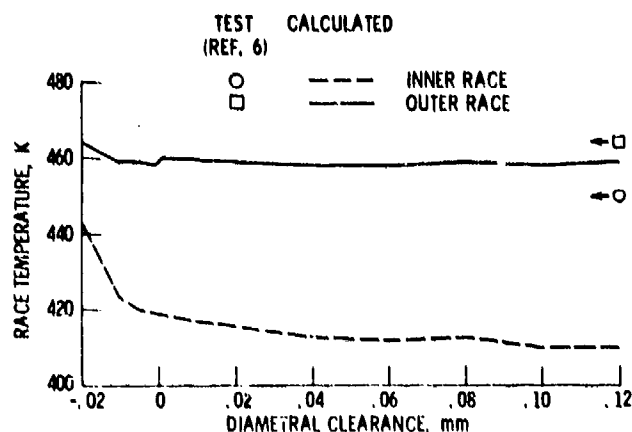


Figure 13. - Calculated race temperature as function of diametral clearance. Shaft speed, 25 500 rpm; radial load, 8900 N (2000 lb); lubricant flow rate, 0.0102 m³/min (2.7 gal/min); lubricant volume, 2 percent. Test values are shown for comparison, plotted at maximum possible clearance.

flow rate range. The computed heat transferred to the oil (fig. 12(b)) compares fairly well with the test data over the flow range for these two set values of lubricant volume.

From these results it is not clear how the lubricant volume should vary with flow rate. The outer-race temperature comparison would indicate that the volume percent should decrease with flow rate. A comparison of the heat transferred to the lubricant suggests that the lubricant volume should increase with flow rate. More work needs to be done in this area.

Effects of miscellaneous input data. - Several calculations were made in an effort to detect any errors in data input or thermal modeling that would explain why inner-race temperature predictions were low. The program was run at the 8900 N (2000 lb), 25 500-rpm condition with a flow rate of 0.0102 m³/min (2.7 gal/min). The convergence criterion (used with an iterative procedure to determine when a solution has been reached; explained in detail in ref. 11) was changed from 0.1 to 0.05 and 0.01, and the calculated temperatures remained the same. A bearing misalignment of 5 minutes was assumed, and the race temperatures changed only 1 K. An additional 300-W heat generation was arbitrarily added to nodes 1 and 3 (shaft ends, see fig. 2) (in case proper accounting was not made for the support-bearing heat generation). While this managed to raise the inner-race temperatures 3 K, the temperature of nodes 1 and 3 became unacceptably high, 610 K (638° F). The nodal structure was changed slightly by adding four nodes, two on the shaft and two on the inner-ring adapter. The resulting calculated temperatures did not change. The value of the heat-transfer coefficient relating the rotating shaft and inner-ring adapter to the air in the rig cavity (e.g., from node 2 to node 21, fig. 2) was changed from 981 to 170 W/m² °C. The inner-race temperature changed 1 K. It was concluded that, since none of the above items had any significant effect on the bearing race temperatures, the inner-race temperatures were mostly affected by the bearing's internally generated heat.

Effect of diametral clearance. - One item that could have a large effect on the bearing heat generation is the diametral clearance, that is, the total free movement of the bearing components in a radial direction. Initial calculations using the original thermal nodes (fig. 2) showed only a small change in inner-race temperature from a clearance of 0.12 mm (maximum unmounted value) down to 0.001 mm. However, reference 6 suggests that a negative clearance exists at 25 500 rpm, so additional calculations were made using the revised nodal structure for several values of negative clearance. The results are shown in figure 13. The increase in inner-race temperature as the clearance is lowered below zero is dramatic and approaches the experimental value closely when the clearance is a minus 0.02 mm. At this point, and for the first time, all 28 rollers are loaded at the inner ring. At minus 0.01-mm clearance, 13 of the rollers were loaded at the inner race. This is possible because the actual operating clearance is slightly larger due to the contact deformations. These calculations indicate that it is very likely the bearing (ref. 6) was indeed operating with a negative clearance at 25 500 rpm.

For comparison purposes, the data of figure 12 were recalculated using a diametral clearance of minus 0.02 mm. These results are shown in figure 14. Both race temperatures (fig. 14(a)) and heat

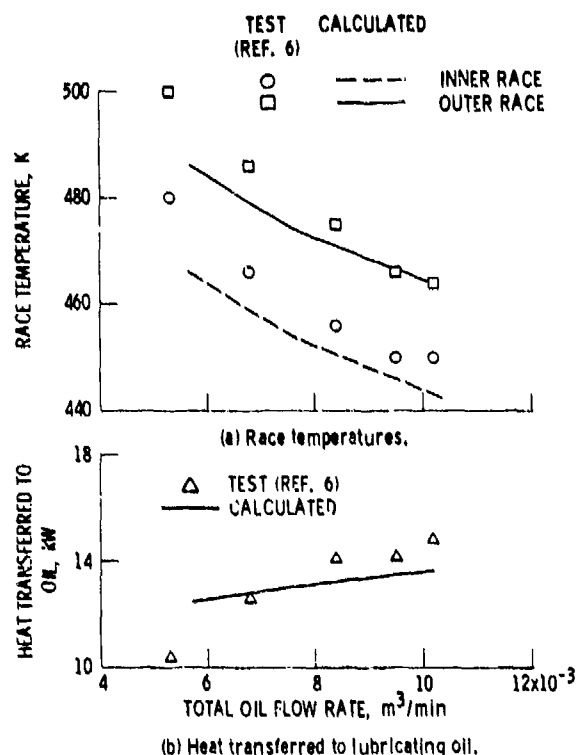


Figure 14. - Comparison of calculated and experimental bearing data using a diametral clearance of -0.02 mm in the computer program. Shaft speed, 25 500 rpm; lubricant volume, 2 percent.

transferred to the lubricant (fig. 14(b)) compare very well with the experimental data.

Although the computer program Cybean has the capability of evaluating bearings with out-of-round outer raceways, the program at this point did not predict the effective bearing operating clearance (i.e., the diametral clearance that would exist at operating speed and temperature). Since it became very evident that this was an important parameter for high-speed bearings, subroutines were added to Cybean to calculate changes in diametral clearance due to initial fits and due to temperature and high-speed effects. Further calculations were then made utilizing this capability.

The program Cybean was run for several values of bearing unmounted diametral clearance to determine the values of diametral clearance of the mounted bearing at operating speeds and temperatures calculated by the program. This clearance, which does not yet contain the effects of bearing load, will be called the effective hot, mounted diametral clearance. The bearing conditions used were 8900-N (2000-lb) load, 25 500-rpm shaft speed, 0.0102 - m^3/min (2.7-gal/min) lubricant flow rate, and a lubricant volume of 2 percent. The initial shaft, inner-ring interference was set at the measured value of 0.0712 mm on the diameter. The results are shown in figure 15. With the actual measured value of 0.12 mm for cold, unmounted diametral clearance, the program predicted about 0.03 mm remaining as the effective hot, mounted clearance at operating conditions. To obtain a negative effective clearance, closer to the value of minus 0.02 mm noted previously, an input of only 0.09 mm initial unmounted clearance had to be used. Again, at this point, all 28 rollers are in contact with the inner race. It is interesting to note the large change in fatigue life of this bearing as the clearance gets smaller and the number of rollers in contact with the inner race gets larger. At first, the fatigue life increases and probably becomes a maximum at just that point where all 28 rollers are first in contact. The fatigue life then decreases rapidly as the tighter clearance causes increased stress.

To check program operation with the new clearance change subroutines, Cybean was run again for several flow rates, with an input of 0.09 mm cold, unmounted diametral clearance. The results at 25 500-rpm shaft speed were virtually the same as shown in figure 14 (i.e., the predicted temperatures were very close to the experimental values); however, the results with 20 000-rpm shaft speed again showed the calculated inner-race temperature almost 30 K low (i.e., similar to the results in fig. 12).

Case slip and misalignment. - Two final checks were made by Cybean, using the original,

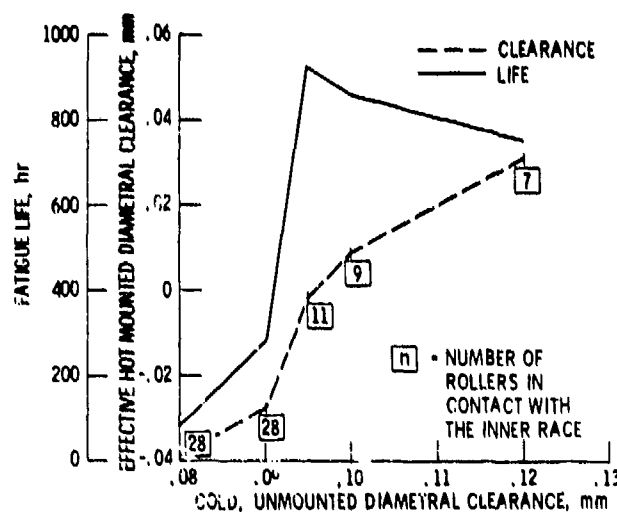


Figure 15. - Calculated values of effective hot, mounted clearance and fatigue life as functions of cold, unmounted clearance. Shaft speed, 25 500 rpm; radial load, 8900 N (2000 lb); oil flow rate, 0.0102 m³/min (2.7 gal/min); lubricant volume, 2 percent.

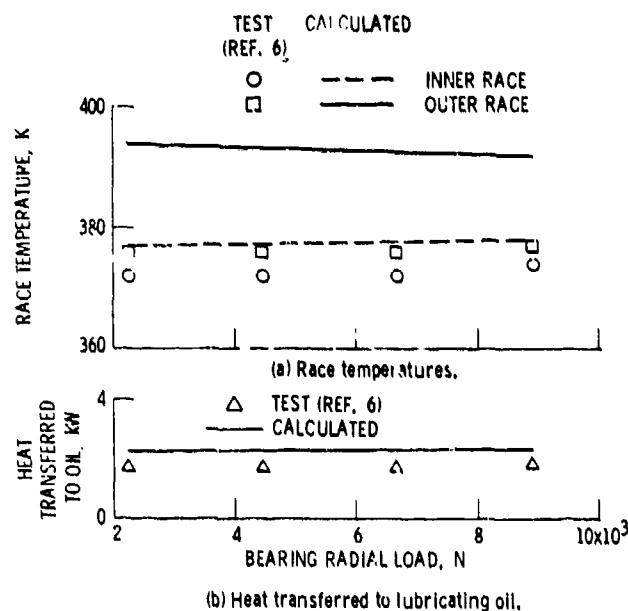


Figure 16. - Comparison of test data with values calculated using a cold diametral clearance of 0.12 mm in the computer program. Shaft speed 10 000 rpm; lubricant flow rate, 0.0102 m³/min (2.7 gal/min); lubricant volume, 2 percent.

measured, cold, unmounted diametral clearance of 0.12 mm. The first check was with several loads at the low-speed (10 000 rpm) condition. This low-speed condition was chosen because of the large values of cage slip indicated in reference 6. All previous calculated values of cage slip were less than 1 percent at 8900 N (2000 lb) and less than 3 percent at 2220 N (500 lb). The experimental values at the higher speeds (20 000 and 25 500 rpm) were all less than 2 percent. The flow rate was set at 0.0102 m³/min (2.7 gal/min), and the lubricant volume at 2 percent. The results are shown in figure 16. Here, the inner-race temperature predictions are close to the experimental values, and the outer-race temperature predictions are about 20 K higher than the corresponding data. The heat transferred to the oil compares well (fig. 16(b)). The calculated values were only slightly higher than the test values.

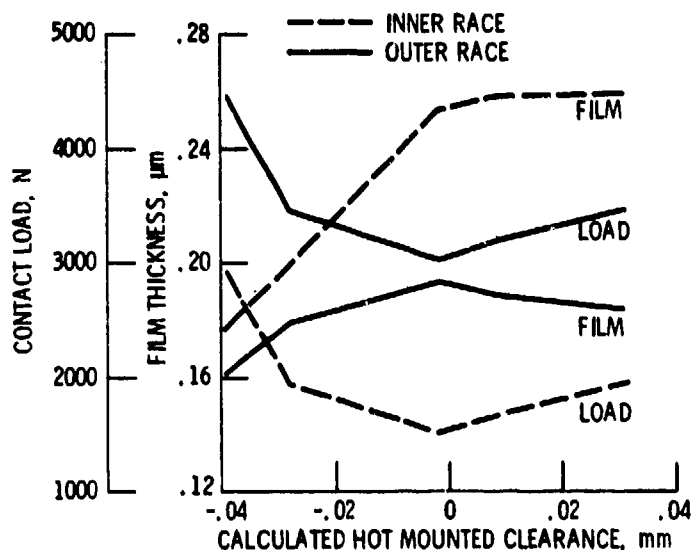


Figure 17. - Film thickness and contact load at most heavily loaded roller as function of calculated hot, mounted clearance. Shaft speed, 25 500 rpm; radial load, 8900 N (2000 lb); lubricant flow rate, 0.0102 m³/min (2.7 gal/min); lubricant volume, 2 percent.

However, while the tests indicated cage slips of over 46 percent, for the entire load range from 2220 to 8900 N (500 to 2000 lb), the corresponding predicted values were all less than 3 percent. Without this slip, the experimental temperatures would have been somewhat higher (see ref. 6, where the bearing temperatures varied inversely with cage slip). The calculated effective hot, mounted diametral clearance was about 0.08 mm.

The second check was to run the program at the high-speed condition (25 500 rpm) with 8900 N (2000 lb) load, set the misalignment angle to 5 minutes, and see if the resulting skew would be sufficient to change the predicted race temperatures significantly. This calculation showed the inner-race temperature to be only 8 K higher with skewing and the outer-race temperature to be 3 K higher. The heat transferred to the lubricant was the same. The calculated effective hot, mounted clearance was about 0.03 mm. Since the 5-minute misalignment angle is large for this test rig, it may be concluded that the presence of misalignment alone would not have been sufficient to cause the experimental inner-race temperatures to be so much higher than calculated values. Since the effect of misalignment on bearing temperatures was small, and the amount of computer time increased by a factor of 10, no further calculations were made with misalignment.

Roller loads, film thickness, and skew angle. - While the main focus of the work reported herein was to calculate bearing characteristics that were measured experimentally, the program Cybean does provide calculated values of other items of interest. Some of these are the EHD film thickness at the roller-raceway contact, the individual roller-race contact loads and stresses, the roller-cage forces, and, with misalignment, the roller-flange forces and the roller skew and tilt angles. Several of these items are shown in figures 17 to 21. The calculations were performed for a shaft speed of 25 500 rpm, a radial load of 8900 N (2000 lb), a flow rate of 0.0102 m³/min (2.7 gal/min), and a lubricant volume of 2 percent.

The values of the EHD film thickness for the most heavily loaded roller contact, calculated for those conditions of figure 15, are shown in figure 17. The film thickness is plotted as a function of the calculated effective hot, mounted clearance. Also shown is the corresponding roller contact load. In general, the film thickness diminishes, and the contact loads increase rapidly once the bearing clearance becomes negative, and all the rollers are in contact with the inner ring (see fig. 15). Other calculations with a fixed diametral clearance as input for those same bearing operating conditions (see fig. 13) indicate that the film thickness changes very little as the clearance increases from 0 to 0.12 mm. The corresponding outer-ring contact load continues to increase slightly and reaches 4000 N at 0.12-mm clearance. Likewise, the inner-ring load increases to 2600 N at 0.12-mm clearance.

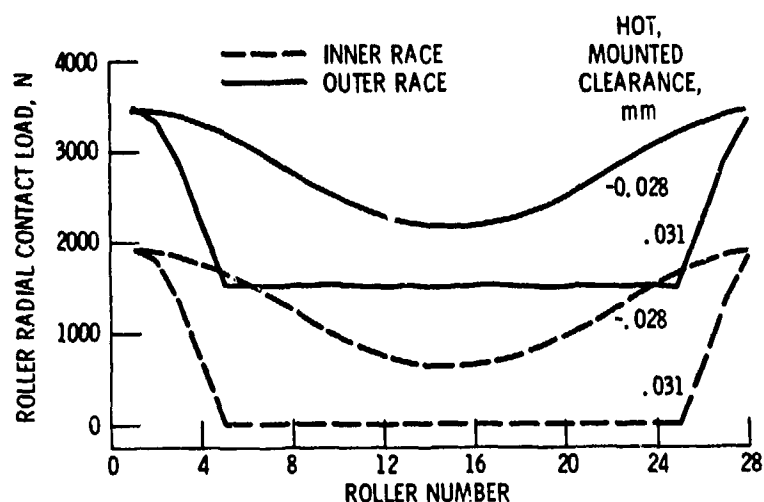


Figure 18 - Roller-race contact load variation with roller position for two values of clearance. Applied load at number 1 roller position. Shaft speed, 25 500 rpm; radial load, 8900 N (2000 lb); lubricant flow rate, 0.0102 m³/min (2.7 gal/min); lubricant volume, 2 percent.

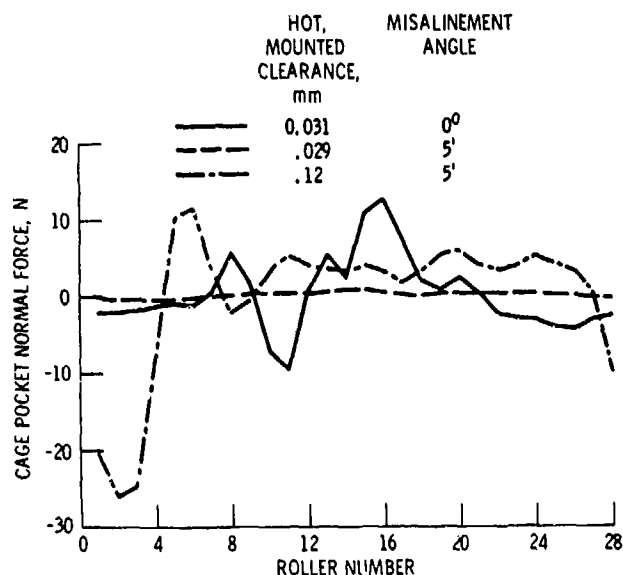


Figure 19. - Cage pocket forces as function of roller number. Positive force is the cage pushing the roller. Bearing load at roller 1 position. Shaft speed, 25 500 rpm; radial load, 8900 N (2000 lb); lubricant flow rate, 0.0102 m³/min (2.7 gal/min); lubricant volume, 2 percent.

The inner- and outer-ring contact loads for each roller, calculated for these same conditions, are shown in figure 18 for two values of hot, mounted clearance. For the 0.031-mm clearance bearing, there are seven rollers in contact with the inner ring, and the remaining rollers have only the centrifugal loading at the outer ring. When all 28 rollers are in contact at the clearance of -0.028 mm, the maximum load is about the same. However, all the other rollers are carrying heavier loads at both the inner and outer rings than with the positive clearance. When the clearance was at -0.039 mm, the contact loads for each of the 28 rollers increased by 1000 N at both the inner and outer rings. The calculation for these same operating conditions with a 5-minute mislinement, where the hot mounted clearance was 0.029 mm, showed little change from the contact loads of the 0.031-mm clearance curve.

The program estimates of the roller-cage forces are shown in figure 19 for three combinations of

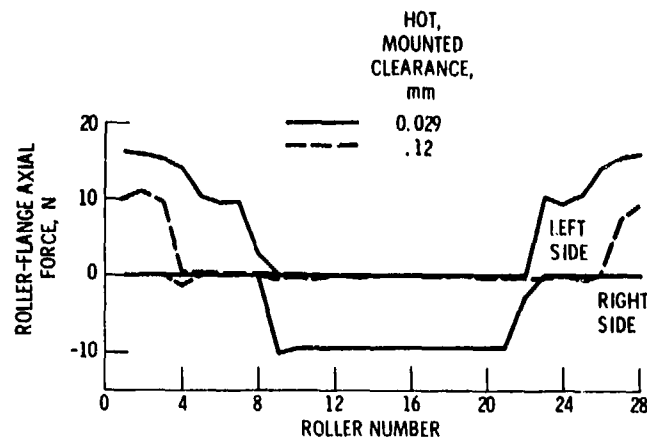


Figure 20. - Roller-flange forces as function of roller number. Bearing load at roller 1 position. Misalignment angle, 5 minutes; shaft speed, 25 500 rpm; radial load, 8900 N (2000 lb); lubricant flow rate, $0.0102 \text{ m}^3/\text{min}$ (2.7 gal/min); lubricant volume, 2 percent.

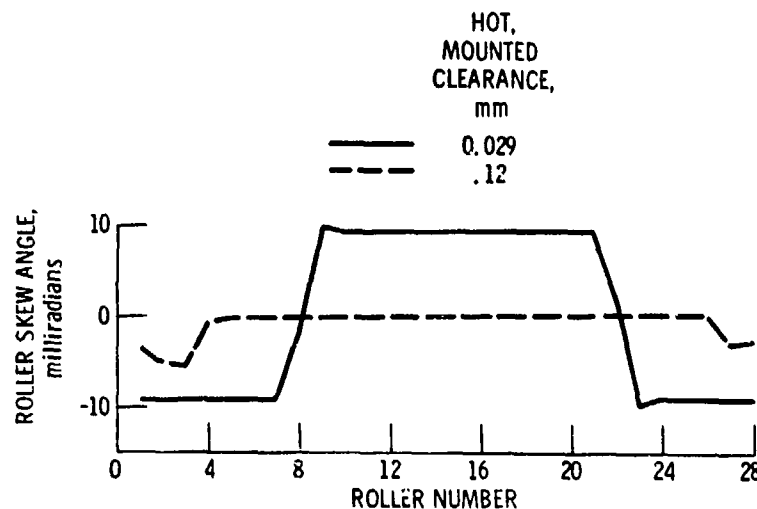


Figure 21. - Roller relative skew angle as function of roller position.

Bearing load at roller 1 position. Misalignment angle, 5 minutes; shaft speed, 25 500 rpm; radial load, 8900 N (2000 lb); lubricant flow rate, $0.0102 \text{ m}^3/\text{min}$ (2.7 gal/min); lubricant volume, 2 percent.

hot, mounted clearance and misalignment angle. A positive force means the cage is pushing the roller. With no misalignment the maximum cage forces were about 10 N. For the same clearance, with a 5-minute misalignment, the cage forces seemed to be all very small. With a large clearance of 0.12 mm, however, and a 5-minute misalignment, the maximum cage force reached 25 N. These forces are of the same order of magnitude as those measured experimentally for the same size bearing. (See refs. 21 and 22. The sign convention in refs. 21 and 22 is of the opposite sense to that used here.)

The flange axial forces calculated for the same two cases with the 5-minute misalignment are shown in figure 20. These forces are small, about the same order of magnitude as the cage-roller forces. The larger clearance bearing shows less roller-flange contact.

The predicted roller skew angle for these same two cases is shown in figure 21. In both cases there is a negative skew angle at the load zone. For the 0.029-mm clearance case, the remainder of the rollers exhibits a positive skew angle of about the same size. With the large 0.12-mm clearance, however, the remaining rollers show essentially zero skew. The skew angle shown is the angle of the roller relative to the inner ring and is called the relative skew angle. The angle of the roller relative to the outer ring, called the absolute skew angle, would be the relative angle plus (or minus) the amount

of the misalignment present at that particular roller position. These skew angles are also of the same order of magnitude as those measured experimentally for the same size bearing and reported in reference 23.

Concluding Remarks

The Shaberth thermal predictions were fairly close even though the program capabilities were not fully utilized. For example, since the calculated bearing-race temperatures were fairly close to the experimental data using the small thermal grid, we speculate that the temperatures could be predicted more accurately if a larger or more complex thermal grid system were used. Also, in the present calculations a constant coefficient of convective heat transfer, calculated as suggested in reference 8, was used. This coefficient could be calculated in the program as a function of the lubricant viscosity for a closer approximation. Furthermore, the lubricant flow rate was not used directly in the thermal calculations. There were no temperature nodes in the fluid, other than oil inlet to the bearing and oil outlet from the bearing. This would have some influence on the temperature calculations, as noted previously. Introduction of lubricant flow rate could permit the race temperatures to decrease with flow rate and still have increasing power loss.

In general, the Cybean computer program as used predicted values of outer-race temperature and heat transferred to the oil that compared reasonably well with the corresponding experimental data. However, the calculated values of inner-race temperature were usually somewhat low, especially at the higher shaft speeds. The program did not predict the high cage slip experienced (ref. 6) at the lower shaft speeds. This is probably the reason the experimental temperatures were lower than the calculated values for those low-speed conditions. Nevertheless, it should be noted that on the basis of absolute temperatures, all calculated values were within 10 percent of the corresponding experimental data and most were within 5 percent. Considering the nature of heat-transfer calculations, this is reasonably close correlation. In all cases outer-race temperature was predicted to be greater than inner-race temperature, which agreed with all experimental data. The predicted trends of changing bearing temperature and power loss with shaft speed, load, and lubricant flow rate compared well with experimental data.

The calculations performed also show the importance of the effective hot, mounted diametral clearance for useful bearing operation. Care should be taken that the bearing effective diametral clearance remains positive at all operating conditions to assure a reasonable rolling-element fatigue life for the bearing.

The largest unknown quantity of the input data required for both Shaberth and Cybean is the volume percent of lubricant in the bearing cavity. The values chosen for these calculations were in the range recommended by the authors of references 8 and 11. From the comparisons presented in this paper, it can be concluded that the values of percent lubricant used are reasonably correct for these programs. However, since it is still not clear how these values should vary with oil flow rate and/or shaft speed, work needs to be done in this area.

Summary of Results

Computer programs (Shaberth for ball bearings, Cybean for roller bearings) were used to predict bearing inner- and outer-race temperatures, cage speed, and friction power loss or heat transferred to the lubricant over a range of operating conditions. The results were compared with experimental data obtained previously. The 120-mm-bore ball bearings were operated at thrust loads of 6672, 13 350, and 22 240 N (1500, 3000, and 5000 lb) and at shaft speeds of 12 000, 16 700, and 20 800 rpm with jet-lubrication flow rates of 0.0038 and 0.0083 m³/min (1.0 and 2.2 gal/min). The oil inlet temperature was maintained constant at 394 K (250° F).

The 118-mm-bore, cylindrical roller bearings were operated at radial loads of 2220, 4450, 6670, and 8900 N (500, 1000, 1500, and 2000 lb) and at shaft speeds of 10 000, 15 000, 20 000, and 25 500 rpm. The bearings were lubricated and cooled by flowing oil through and under the inner race at total rates of 0.0038 to 0.0102 m³/min (1.0 to 2.7 gal/min). The inlet temperature was maintained constant at 366 K (200° F). The following results were obtained:

1. The bearing-shaft program (Shaberth) can predict race temperatures and bearing power loss reasonably well.

2. The cylindrical roller bearing analysis computer program (Cybean) can predict outer-race temperature and the amount of heat transferred to the lubricant reasonably well; however, at the higher shaft speeds, the calculated inner-race temperatures were much lower than the corresponding experimental data, unless the effective hot, diametral clearances were set negative, about 0.02 mm.

3. Cybean did not predict the high cage slip experimentally obtained with the roller bearing at low shaft speeds; however, the computer-estimated values of roller-cage forces were of the same order of magnitude as that obtained experimentally for the same size bearing.

4. The bearing power losses predicted by the computer programs were a strong function of the value assumed for the volume percent of the bearing cavity occupied by the lubricant.

References

1. Brown, P. F.; Dobek, L. J.; and Tobiasz, E. J.: High Speed Cylindrical Roller Bearing Development. PWA-FR-12598, Pratt & Whitney Aircraft Group, 1980. (AFWAL-TR-80-2072, AD-A095357.)
2. Povinelli, V. P., Jr.: Current Seal Designs and Future Requirements for Turbine Engine Seals and Bearings. *J. Aircr.*, vol. 12, no. 4, Apr. 1975, pp. 266-273.
3. Brown, P. F.; et al.: Mainshaft High Speed Cylindrical Roller Bearings for Gas Turbine Engines. PWA-FR-8615, Pratt & Whitney Aircraft Group, 1977. (AD-A052351.)
4. Holmes, P. W.: Evaluation of Drilled-Ball Bearings at DN Values to Three Million. I—Variable Oil Flow Tests. NASA CR-2004, 1972.
5. Signer, H.; Bamberger, E. N.; and Zaretsky, E. V.: Parametric Study of the Lubrication of Thrust Loaded 120-mm Bore Ball Bearings to 3 Million DN. *J. Lubr. Technol.*, vol. 96, no. 3, July 1974, pp. 515-524.
6. Schuller, F. T.: Operating Characteristics of a Large Bore Roller Bearing to Speeds of 3×10^6 DN. NASA TP-1413, 1979.
7. Kennedy, F. E.; and Cheng, H. S., eds.: Computer-Aided Design of Bearings and Seals. American Society of Mechanical Engineers, 1976.
8. Crecelius, W. J.; Heller, S.; and Chiu, Y. P.: Improved Flexible Shaft-Bearing Thermal Analysis with NASA Friction Models and Cage Effects. SKF-AL76P003, SKF Industries, Inc., 1976.
9. Crecelius, W. J.; and Pirvics, J.: Computer Program Operation Manual on SHABERTH: A Computer Program for the Analysis of the Steady State and Transient Thermal Performance of Shaft-Bearing Systems. SKF-AL76P030, SKF Industries, Inc., 1976. (AFAPL-TR-76-90, AD-A042981.)
10. Kleckner, R. J.; and Pirvics, J.: High Speed Cylindrical Roller Bearing Analysis. SKF Computer Program CYBEAN. Volume I: Analysis. (AL78P022-VOL-1, SKF Industries, Inc.; NASA Contract NAS3-20068.) NASA CR-159460, 1978.
11. Kleckner, R. J.; and Pirvics, J.: High Speed Cylinder Roller Bearing Analysis. SKF Computer Program CYBEAN: Volume II: User's Manual. (AL78P023-VOL-2, SKF Industries, Inc.; NASA Contract NAS3-20068.) NASA CR-159461, 1978.
12. Kleckner, R. J.; Pirvics, J.; and Castelli, V.: High Speed Cylindrical Rolling Element Bearing Analysis "CYBEAN"—Analytic Formulation. ASME Paper 70-LUB-35, Oct. 1979.
13. Gupta, P. K.: Dynamics of Rolling Element Bearings, Parts I, II, III, and IV. *J. Lubr. Technol.*, vol. 101, no. 3, July 1979, pp. 293-326.
14. Conry, T. F.; and Goglia, P. R.: Transient Dynamic Analysis of High-Speed Lightly Loaded Cylindrical Roller Bearings. Part II, Computer Program and Results. NASA CR-3335, 1981.
15. Zaretsky, E. V.; Signer, H.; and Bamberger, E. N.: Operating Limitations of High-Speed Jet-Lubricated Ball Bearings. *J. Lubr. Technol.*, vol. 98, no. 1, Jan. 1976, pp. 32-39.
16. Coe, H. H.; and Zaretsky, E. V.: Predicted and Experimental Performance of Jet-Lubricated 120-Millimeter-Bore Ball Bearings Operating to 2.5 Million DN. NASA TP-1196, 1978.
17. Coe, H. H.; and Schuller, F. T.: Comparison of predicted and Experimental Performance of Large-Bore Roller Bearing Operating to 3.0 Million DN. NASA TP-1599, 1980.
18. Coe, H. H.; and Schuller, F. T.: Calculated and Experimental Data for a 118-mm-Bore Roller Bearing to 3 Million DN. ASME Paper 80-C2/Lub-14, Aug. 1980.
19. Bamberger, E. N.; Zaretsky, E. V.; and Anderson, W. J.: Effect of Three Advanced Lubricants on High Temperature Bearing Life. *J. Lubr. Technol.*, vol. 92, no. 1, Jan. 1970, pp. 23-33.
20. Loewenthal, Stuart H.; Parker, Richard J.; and Zaretsky, Erwin V.: Correlation of Elastohydrodynamic Film Thickness Measurements for Fluorocarbon, Type II Ester, and Polyphenyl Ether Lubricants. NASA TN D-7825, 1974.
21. Nypan, L. J.: Roller to Separator Contact Forces and Cage to Shaft Speed Ratios in Roller Bearings. NASA CR-3048, 1978.
22. Nypan, L. J.: Separator Contact Forces and Speed Ratios in Roller Bearings. ASLE Preprint 79-LC-4D-1, Oct. 1979.
23. Nypan, L. J.: Roller Skewing Measurements in Cylindrical Roller Bearings. NASA CR-3381, 1981.

Lubrication of 35-Millimeter-Bore Ball Bearings of Several Designs to 2.5 Million DN

Fredrick T. Schuller*

Parametric tests were conducted in a high-speed, high-temperature bearing tester with a 35-mm-bore, angular-contact ball bearing with either a single- or a double-outer-land-guided cage. The bearings were either lubricated by jets (using a jet velocity of 20 m/sec (66 ft/sec)) or lubrication was achieved by flowing oil through axial grooves and radial holes machined in the inner ring of the bearing.

An outer-ring cooling-oil flow rate maintained at 1700 cm³/min (0.45 gal/min) at 394 K (250° F) oil-inlet temperature was used in some tests. For some tests the distribution of the total oil supplied to the inner ring was 50 percent for bearing lubrication and 50 percent for inner-ring cooling. In other tests the distribution was 25 percent lubrication and 75 percent cooling.

All tests were conducted at a radial load of 222 N (50 lb) and/or a thrust load of 667 N (150 lb), shaft speeds from 48 000 to 72 000 rpm, and an oil-inlet temperature of 394 K (250° F). Lubricant flow rates to the bearing ranged from 300 to 1900 cm³/min (0.08 to 0.50 gal/min). The lubricant was neopentylpolyol (tetra)ester meeting the MIL-L-23699 specifications.

Successful operation of the bearings with jet lubrication was accomplished up to 2.5 million DN. The jet-lubricated bearing with a double-outer-land-guided cage always had a higher power loss and generated higher temperatures than the bearing with a single-outer-land-guided cage over the range of shaft speeds and lubricant flow rates used.

Percent cage slip for a double-outer-land-guided-cage-bearing ranged from 1.5 to 2.7 times that for a single-outer-land-guided-cage bearing.

Successful operation of the bearing with through-the-inner-ring lubrication was also accomplished to 2.5 million DN for both oil distribution patterns. Cooler bearing operation was experienced with a total oil distribution of 50-50 percent than with 25-75 percent.

Outer-ring cooling for both oil-flow distribution and for the jet-lubricated bearing resulted in a substantial decrease in outer-ring temperature but had a minimal effect on inner-ring temperature. A maximum power loss of 2.8 kW (3.7 hp) occurred at 72 300 rpm with an inner-ring oil-flow distribution of 25-75 percent at a total oil-flow rate of 1900 cm³/min (0.50 gal/min).

For the inner-ring-lubricated bearings, a maximum cage slip of 7.0 percent occurred at 72 300 rpm at a total oil flow rate of 1900 cm³/min (0.50 gal/min) with a total oil-flow distribution of 50-50 percent. The increase in percent cage slip with lubricant flow rate was minimal for each lubrication method used; however, cage slip increased significantly with speed.

Introduction

Small, advanced turbine engines with total airflows of 0.5 to 4.6 kg/sec (1 to 10 lb/sec) require bearings that can operate in the speed range 2.5 million DN (product of the bearing bore in mm and the shaft speed in rpm) at high temperatures to achieve the performance objectives set by the U.S. Army for programs such as STAGG (Small Turbine Advanced Gas Generator) and UTTAS (Utility Tactical Transport Aircraft System). The bearing designs and lubrication techniques used must be refined and optimized for reliable engine performance and long bearing life.

Large-bore ball and roller bearings have been successfully tested at speeds to 3.0 million DN (refs. 1 to 4). In these tests, however, the lubricant was fed to the bearings through radial holes in the inner ring. Because of the dimensional limitations of the inner ring in smaller bore bearings, the

*NASA Lewis Research Center.

fabrication of radial holes and axial grooves for lubricant passages through the inner ring can become complex and cost restrictive. In these circumstances jet lubrication is the more practical method of bearing lubrication.

However, there is a limiting DN value above which jet lubrication is no longer adequate for reliable bearing operation. Centrifugal forces prevent the oil jet from properly lubricating and cooling the rolling elements and cage. This results in bearing thermal instability and/or cage wear. This limiting DN value is about 2.5 million for small-bore bearings. With sufficient oil flow and proper cage design, this limit can be increased slightly to 2.8 million, as was achieved in reference 5 for a 30-mm-bore, deep-groove ball bearing with an outer-land-guided cage.

One of the principal bearing elements that affects satisfactory high-speed operation is the bearing cage. As indicated in reference 5, bearing wear and ultimate failure at a high DN value has occurred on the land surface of the cage, and cage lubrication was the principal factor that brought about the failure. Consequently, the cage design is expected to greatly affect the limiting speed. For example, in reference 5, with a jet-lubricated bearing, an outer-ring-land-guided cage limited the DN value to 2.85×10^6 , where failure occurred; whereas an inner-ring-land-guided cage limited the DN value to 1.65×10^6 . For satisfactory high-speed operation of a small-bore, jet-lubricated bearing, therefore, an outer-ring-land-guided cage is usually recommended. The outer-ring-land surfaces are more efficiently lubricated by means of centrifugal oil flow effect, and they are generally cooler than the corresponding surfaces of an inner-ring controlled cage (ref. 6). Several cage designs for a 75-mm jet-lubricated roller bearing have been tested, and the best overall performance was reported in reference 7 for bearings with outer-ring-land-guided cages.

In an effort to overcome the detrimental centrifugal effects in high-speed applications, which cause some of the lubricant supplied by jets to be slung off the inner ring, oil was supplied to the bearing through grooves in the bore and then through radial holes from the grooves to the rolling elements of the bearing. Effective lubrication and cooling in a very severe centrifugal force field are the principal problems in achieving successful operation of small-bore bearings at ultrahigh speeds. Inner-ring lubrication might be a solution, although the limited space available for machining grooves and radial holes can be a problem.

The objectives of this study were to determine the parametric effects of cage design, shaft speed, lubricant flow rate, and method of lubrication on the operation of a 35-mm-bore angular contact bearing. Test conditions included a radial load of 222 N (50 lb) and/or a thrust load of 667 N (150 lb). Nominal shaft speeds were from 48 000 to 72 000 rpm. Jet lubrication was accomplished by dual jets at flow rates from 303 to 1894 cm³/min (0.08 to 0.50 gal/min) at a calculated jet velocity of 20 m/sec (66 ft/sec) with an oil-in temperature of 394 K (250° F). Inner-ring lubrication was accomplished by a modification of the inner ring, where radial holes are machined in the axial grooves of the bearing bore.

In some tests the distribution of the total oil supplied to the inner ring was 50 percent for bearing lubrication and 50 percent for inner-ring cooling. In other tests 25 percent of the oil was used for lubrication and 75 percent for cooling.

The bearing had a nominal unmounted contact angle of 24° and either a single- or double-outer-land-guided cage. Provisions were also made for outer-ring cooling. The oil was injected to the inner ring at flow rates from 300 to 1900 cm³/min (0.08 to 0.50 gal/min). Outer-ring cooling oil flow rate was maintained at 1700 cm³/min (0.45 gal/min) at 394 K (250° F) oil-inlet temperature. The lubricant in all tests reported herein was a neopentylpolyol (tetra)ester that meets the MIL-L-23699 specifications.

Apparatus

High-Speed Bearing Tester

A general view of the air-turbine-driven test machine is shown in figure 1. A sectional drawing is shown in figure 2. The shaft is mounted horizontally and is supported by two, preloaded, angular-contact ball bearings. The test bearing is assembled into a separate housing that incorporates the hardware for lubrication, oil removal, thrust and radial load application, and instrumentation for cage speed measurement. Test bearing torque is measured with strain gages located near the end of an

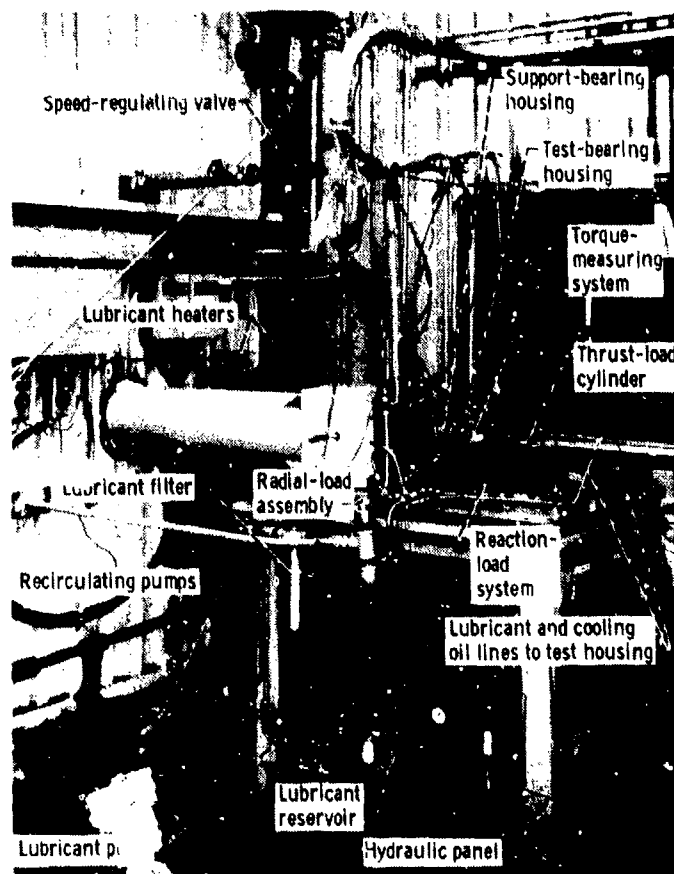


Figure 1. - High-speed, small-bore-bearing test machine.

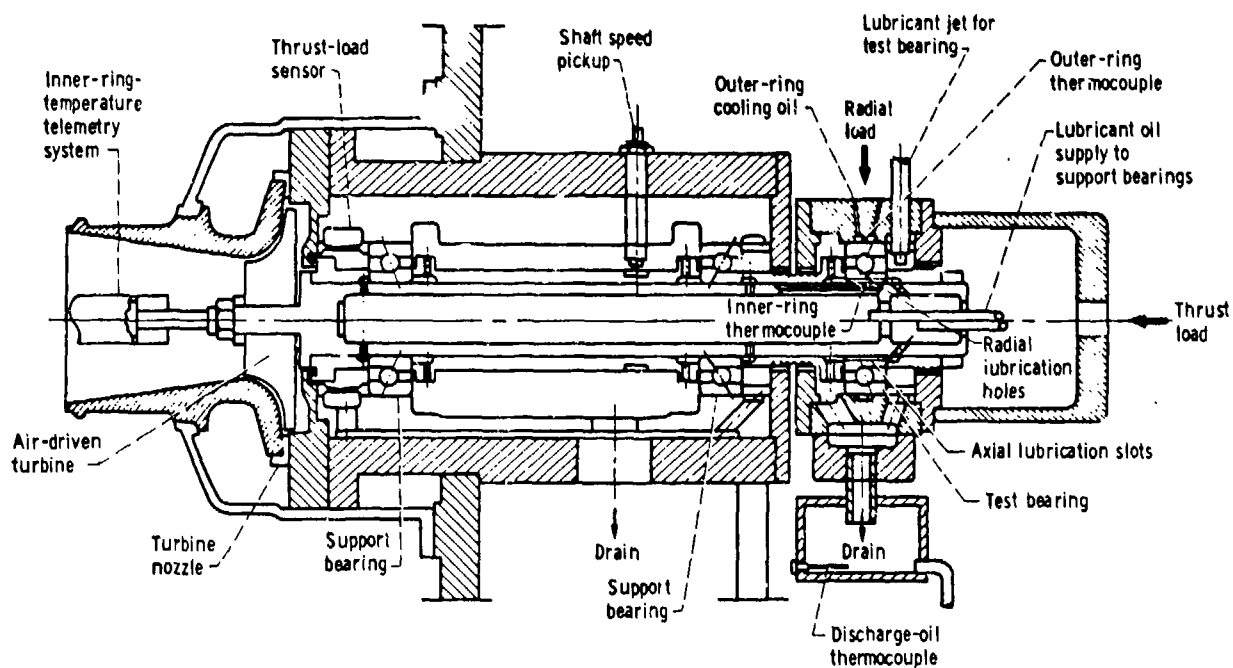


Figure 2. - Schematic of high-speed, small-bore-bearing test machine.

arm that prevents the housing from rotating. Thrust force is applied through a combination of a thrust needle bearing and a small roller support bearing to minimize test-housing restraint during torque measurements. The test bearing was lubricated either by jets or through the inner ring. The jet

outlets on the nonloaded side of the inner ring were located approximately 3.0 mm (0.12 in.) from the face of the bearing and were aimed at the inner raceway. In separate tests, not reported herein, it was determined that a 20-m/sec (66-ft/sec) jet velocity provided the most efficient lubrication of the test bearing; that velocity was used in all the tests reported. (Ref. 5 reports a similar result with a 20-m/sec (66-ft/sec) jet velocity compared with other velocities investigated.) When inner-ring-injected lubrication was used, oil was pumped by centrifugal force from the center of the hollow shaft through axial grooves in the test-bearing bore and through a series of small radial holes, 0.762 mm (0.030 in.) in diameter, to the bearing inner race. Those axial grooves in the bearing bore that did not have radial holes allowed oil to flow under the ring for inner-ring cooling. To vary the distribution of the total oil flow for lubrication and for inner-ring cooling, certain radial holes were plugged before the test bearing was installed. Cooling oil was supplied to the outer ring by means of holes and grooves in the bearing housing as shown in figure 2.

Shaft speed (inner-ring speed) was measured with a magnetic probe. Ball-pass frequency (cage speed) was determined by analyzing signals from a semiconductor strain gage mounted on the inside diameter of the test-bearing housing. Two thermocouples were assembled in the shaft to measure inner-ring temperatures through a rotating telemetry system. Outer-ring temperatures were obtained by two thermocouples installed in the test bearing housing. The high-speed bearing tester is described in detail in references 8 and 9.

Test Bearings

The test bearings were ABEC7 grade, 35-mm-bore, angular-contact ball bearings with a double- or single-outer-land-guided cage (fig. 3). The outside diameter of both cages was a nominal 52.68 mm (2.074 in.). The effective land area of the double-outer-land-guided cage bearing was approximately three times that of the single-outer-land-guided cage bearing. The double-outer-land-guided cage weighed 16 percent more than the single-outer-land-guided cage. The inner rings of both bearings were geometrically and dimensionally the same. The land diameter on the oil-inlet side of the outer ring of the single-land-guided-cage bearing was 13.21 mm (0.52 in.) smaller than that on the outlet side. The land diameters of both sides of the double land-guided-cage bearing outer ring were of equal dimension.

The bearings contained 16 balls, each with a nominal diameter of 7.14 mm (0.281 in.). One bearing design (fig. 3(c)) permitted lubrication through the inner ring by means of axial grooves machined in the bore. There were 16 axial grooves in the bearing bore. Eight 0.762-mm (0.030-in.) diameter holes (one in every other axial groove), radiating from the bearing bore, formed a flow path for bearing lubrication. Therefore, it was assumed that 50 percent of the oil supplied to the inner ring lubricated the bearing and 50 percent flowed axially through those grooves that contained no radial holes and cooled the inner ring. In some tests four of the eight radial holes were plugged to allow 25 percent of the total flow to be used for bearing lubrication and 75 percent for inner-ring cooling.

The inner and outer rings and the balls were manufactured from consumable-electrode-vacuum-melted AISI M-50 steel. Nominal hardness of the balls and rings was Rockwell C 62 at room temperature. The cage was made from AISI 4340 steel (AMS 6415) heat treated to a hardness of Rockwell C 28 to 36 and completely plated with 0.0203- to 0.0381-mm (0.0008 to 0.0015-in.) thick silver (AMS 2412). The cage balance was within 0.05 g-cm (7×10^{-4} oz-in). More complete specifications are shown in table I.

Lubricant

The oil used for the parametric studies was a neopentylpolyol (tetra)ester. This type II oil is qualified to the MIL-L-23699 specifications. The major properties of the oil are presented in table II.

Test Procedure

After warming the test machine by recirculating heated oil and calibrating the torque-measuring system, a test load of 222 N (50 lb) radial and/or a test load of 667 N (150 lb) thrust load was applied and the lubricant flow rate was set at 1900 cm³/min (0.50 gal/min). Outer-ring cooling was not employed at this time. The shaft speed was then slowly brought up to a nominal 28 000 rpm. When

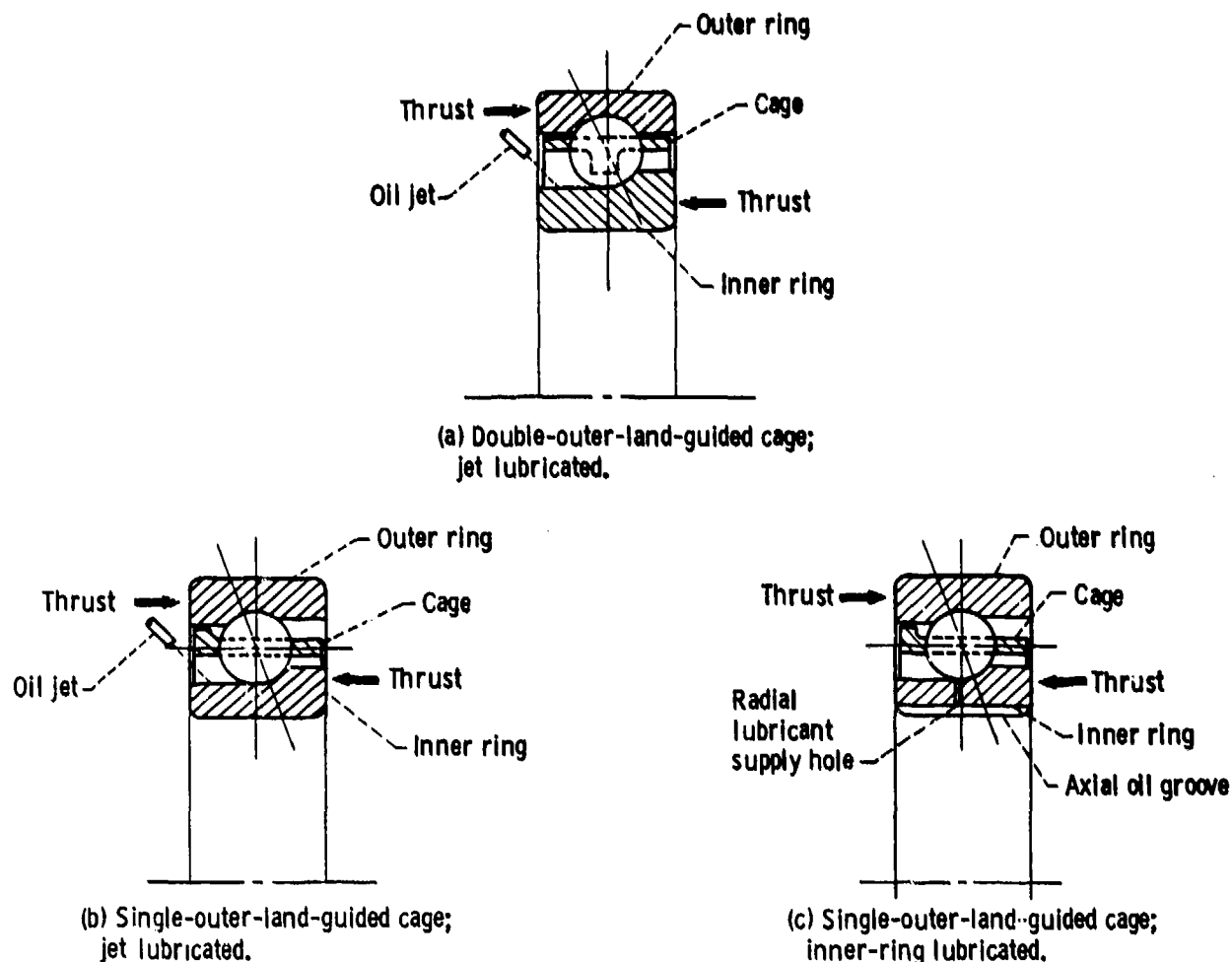


Figure 3. - Angular-contact ball bearing.

bearing and test-machine temperatures stabilized (after 20 to 25 min), the oil-inlet temperature, lubricant flow rate, and speed were set to the desired values. A test series was run by starting at the lowest speed, a nominal 48 000 rpm, and progressing through 65 000 and 72 000 rpm before changing the lubricant flow rate. Four lubricant flow rates to the bearing inner ring of 300 to 1900 cm³/min (0.08 to 0.50 gal/min) were used. In some tests a separate run was made, during which outer-ring cooling oil flow was employed.

If it became apparent during the course of testing that a test condition would result in distress of the test bearing or test rig or generate a bearing temperature above 491 K (425° F), that test was terminated.

Results and Discussion

Comparison of Single- and Double-Outer-Land Riding Cage Bearings

In the cage design portion of this study parametric tests were conducted in the high-speed bearing tester with jet-lubricated 35-mm-bore ball bearings having either a single- or a double-outer-land-guided cage. Other than cage design and the inside diameter of the outer ring (figs. 3(a) and (b)), the two bearings were identical.

Effect of cage design on bearing temperature. - The effect of lubricant flow rate on bearing temperature at three different speeds is shown in figure 4. Bearing temperatures for both the single-

TABLE I. - TEST BEARING SPECIFICATIONS

Bearing dimensions, mm (in.):	
Bore	35 (1.3780)
Outside diameter	62 (2.4409)
Width	14 (0.5512)
Cage specifications:	
Diametral land clearance, mm (in.)	0.406 (0.016)
Diametral ball-pocket clearance, mm (in.)	0.660 (0.026)
Material	^a AISI 4340, silver plated
Rockwell C hardness	28-36
Bearing ball specifications:	
Number	16
Diameter, mm (in.)	7.14 (0.28)
Grade	10
Material	^b CEVM M-50
Rockwell C hardness (minimum)	60
Race conformity, percent:	
Inner	54
Outer	52
Assembly:	
Internal radial clearance, mm (in.)	0.074 (0.0029)
Contact angle, deg.	24

^aAMS 6415.^bAMS 5490.

TABLE II. - PROPERTIES OF TETRAESTER LUBRICANTS

Additives	Antiwear, corrosion and oxidation inhibitors, and antifoam
Kinematic viscosity, cS, at—	
311 K (100° F)	28.5
372 K (210° F)	5.22
477 K (400° F)	1.31
Flashpoint, K (°F)	533 (500)
Autogenous ignition temperature, K (°F)	694 (800)
Pourpoint, K (°F)	214 (-75)
Volatility (6.5 hr at 477 K (400° F), wt %	3.2
Specific heat at 372 K (210° F), J/kg K (Btu/hr ft °F)	2140 (0.493)
Thermal conductivity at 372 K (210° F), J/m sec K (Btu/hr ft °F)	0.15 (0.088)
Specific gravity at 372 K (210° F)	0.931

and the double-outer-land-guided cage decrease with an increase in lubricant flow rate for each test speed.

The double-outer-land-guided cage bearing generated the higher bearing temperature at each speed tested. Figure 4 shows that the temperature differential between the two bearings of different cage design increases with speed and reaches 25 K (45° F) at 72 250 rpm at a flow rate of 1804 cm³/min (0.50 gal/min). This indicates that the double-outer-land-guided cage bearing becomes less desirable at high speeds.

The elevated temperatures of the bearing with the double-outer-land-guided cage are partially due to the heat generated by the shearing of oil over an area about three times that of the single-outer-land-guided cage bearing. Another disadvantage of the double-outer-land-guided cage is that the oil entering and lubricating the rotating members of the bearing has a tendency to become trapped by the extra land, adding heat due to excessive churning within the bearing. The single land, in contrast,

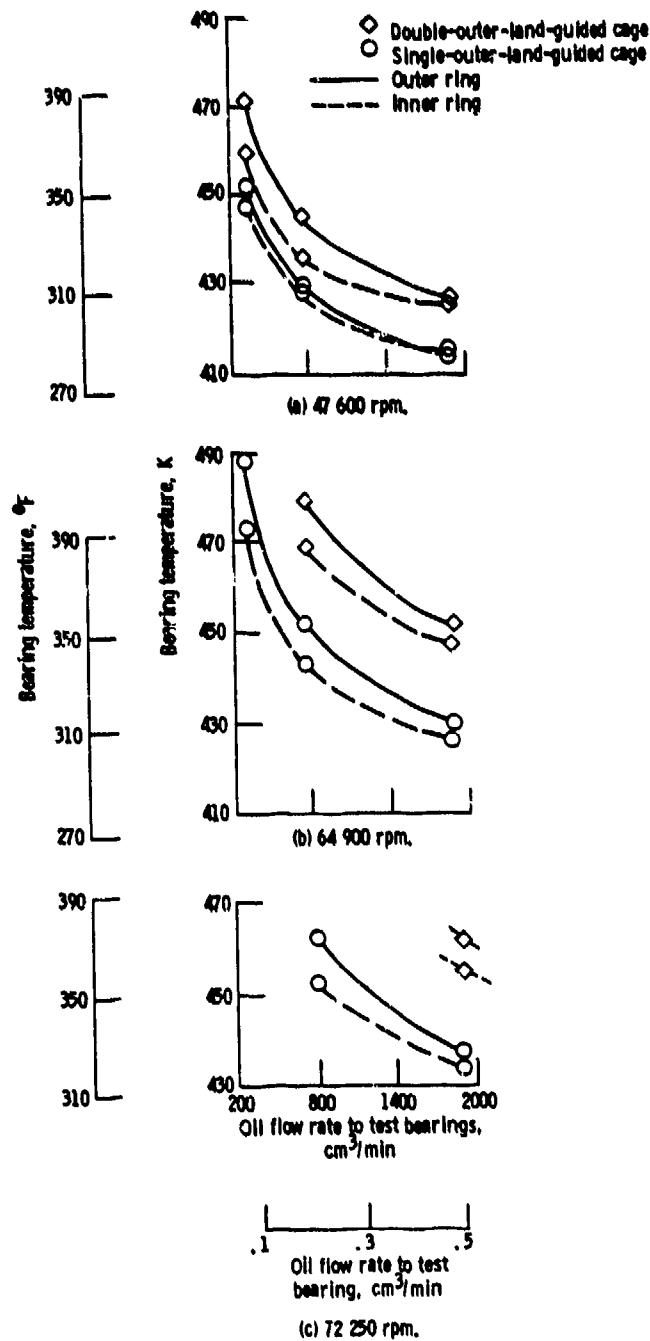


Figure 4. - Effect of oil flow on test bearing temperature for two jet-lubricated bearing configurations; no outer-ring cooling. Combined load: thrust, 667 N (150 lb); radial, 222 N (50 lb).

allows the free flow of lubricant into the bearing and a less restrictive exit of oil, reducing churning and subsequent internal heat generation in the bearing.

Effect of cage design on bearing power loss. - Two approaches were used to determine bearing power loss. In the first outer-ring torque was measured. In the second the heat rejected to the lubricant was determined.

Bearing power loss is dissipated in the form of heat rejected to the lubricant and transferred by conduction, convection, and radiation to the surrounding environment. To obtain a measure of this heat rejection and, thus, power loss within the bearing, oil inlet and outlet temperatures were

obtained for all conditions of lubricant flow. Total heat absorbed by the lubricant was obtained from the standard heat-transfer equation.

$$Q_T = MC_p(t_{out} - t_{in})$$

where

Q_T total heat-transfer rate to the lubricant, J/min (Btu/min)

M mass flow rate, kg/min (lb/min)

C_p specific heat, J/kg K, (Btu/lb °F)

t_{out} oil outlet temperature, K (°F)

t_{in} oil inlet temperature, K (°F)

The power loss of the double- and single-outer-land-guided cage jet-lubricated bearings is shown in figure 5. Power loss obtained from torque readings and power loss determined from heat rejected to the oil are plotted.

Figure 5 shows that power loss increases with speed and lubricant flow rate for both the single- and double-outer-land-guided cage bearing configurations. However, comparison of power losses shows that the double-outer-land-guided cage bearing has a decided disadvantage compared with the single-outer-land-guided-cage design. The higher power loss of the double-outer-land-guided cage bearing is due, in part, to the excessive oil churning in this design bearing and, in part, to the drag resulting from a total land area three times that of the single-land design. Figure 5 shows that a very high lubricant flow rate (1894 cm³/min (0.50 gal/min)) can be undesirable because it increases the power loss in the bearing (see fig. 5(a)).

Figure 5 also compares power losses obtained from torque readings with those from heat rejected to the lubricant. No outer-ring cooling was used in these particular tests. Power losses determined from heat rejection to the lubricant were lower than those obtained from torque readings over the speed range tested. Two reasons for this are (1) that the heat dissipated by conduction, convection, and radiation to the surrounding environment is not accounted for and (2) that locating thermocouples in ideal positions for a most accurate reading of oil-in and oil-out temperatures is difficult.

The results from both methods of obtaining bearing power loss (fig. 5) are in agreement except for magnitude.

Effect of lubricant flow rate on cage slip. — To determine percent cage slip, the epicyclic cage speed C_{epi} at the various test shaft speeds was obtained from a computer program called Shaberth (ref. 10), which considers centrifugal force effects on contact angle. Elastic-contact forces are considered in a race-control type of solution. Thermal and lubricant effects were not considered in this computer solution of epicyclic cage speed. Also, a fit analysis was not included in the Shaberth computations for this report.

However, a subsequent calculation at the highest speed (72 300 rpm), at a thrust load of 667 N (150 lb), and for all the centrifugal growth effects on the inner ring showed the epicyclic speed to change only from 33 000 to 32 720 rpm. This resulted in the calculated slip changing from 7.0 to 6.2 percent for that point. Therefore, all the values of C_{epi} were not recalculated. The calculated epicyclic cage speeds were combined with the measured experimental cage speed C_{exp} to obtain percent cage slip as follows:

$$\text{Percent cage slip} = (1 - C_{exp}/C_{epi}) 100$$

Figure 6 shows that percent cage slip increases with speed at about the same rate for each of the three lubricant flow rates tested. The double-outer-land-guided cage bearing showed a higher percent cage slip than the single-outer-land-guided cage at all speeds and lubricant flow rates. It also showed a higher change of cage slip with increased flow.

For all speeds and flow rates tested, the percent cage slip ranged from 1.0 to 10.2 percent for both jet-lubricated bearing configurations. The small increase in slip with flow rate is primarily due to additional drag on the balls and cage. Percent cage slip for a double-outer-land-guided cage bearing ranged from 1.5 to 2.7 times that for a single-outer-land-guided cage bearing over the range

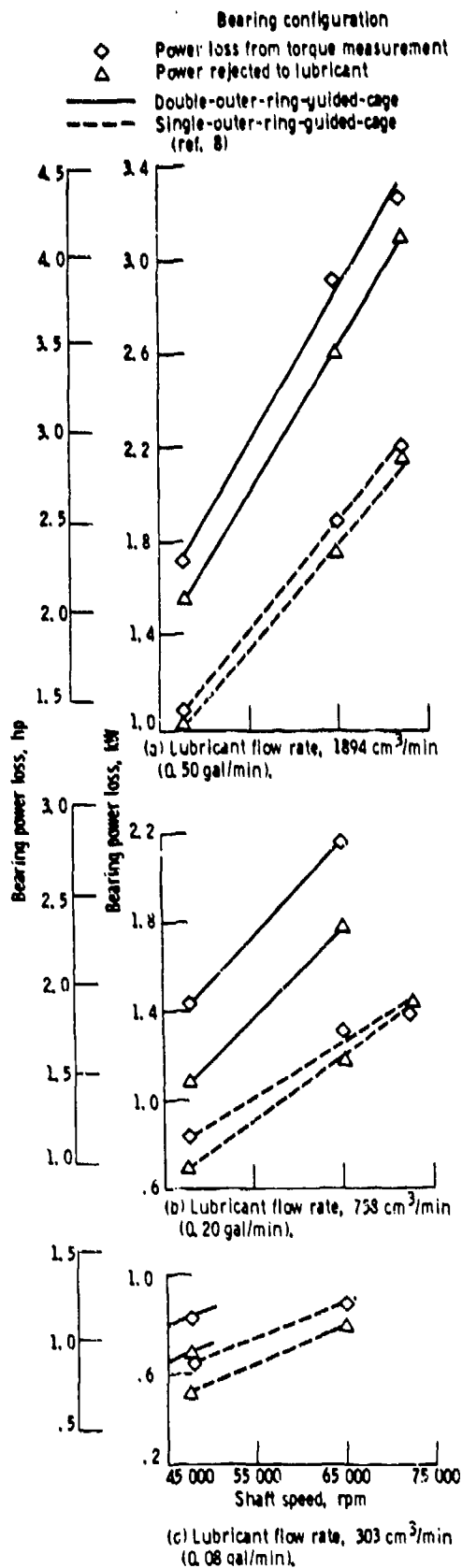


Figure 5. - Power loss as function of shaft speed for two jet lubricated bearing configurations; no outer-ring cooling. Combined load: thrust, 667 N (150 lb); radial, 222 N (50 lb).

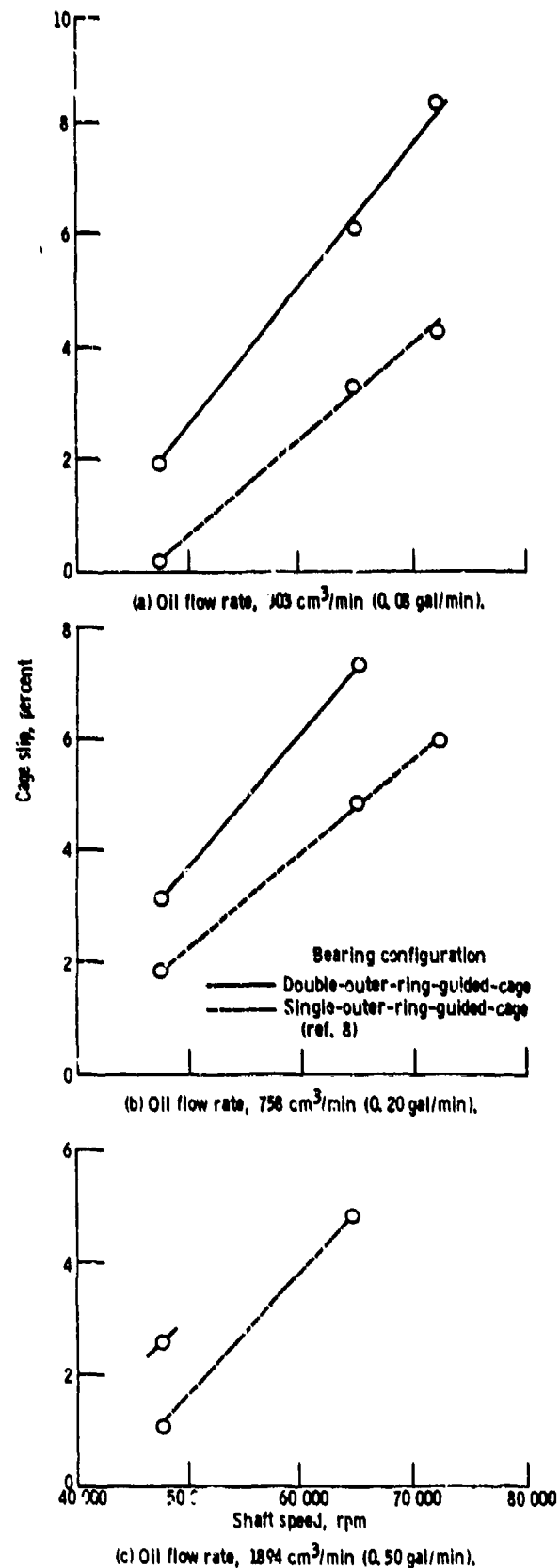


Figure 6. - Effect of shaft speed on cage slip for two jet lubricated bearing configurations; no outer-ring cooling. Combined load: thrust, 667 N (150 lb); radial, 222 N (50 lb).

of lubricant flow rates and speeds shown. The double-outer-land-guided cage, because of its greater surface area, has more drag as it rotates against the outer ring. This increased drag, and the oil churning, reduces cage speed (increases slip) to a greater extent than with the (less surface area) single-outer-land-guided cage. The observed increase in percent cage slip with increased shaft speed for both configurations could be expected because of centrifugal forces decreasing the ball load, and thus traction, at the inner raceway contact. Increased shaft speed also increases the drag at the land area, especially with the double-land design, increasing cage slip.

Through-the-Inner-Ring Lubricated Bearing

Parametric tests were also conducted in the high-speed bearing tester with bearings having a single-outer-land-guided cage with lubricant supplied through the inner ring (fig. 3(c)).

Effect of oil-flow distribution through inner ring on bearing temperature. — The effect that the distribution of lubricant through the inner ring has on bearing inner- and outer-ring temperature is shown in figures 7 and 8. The total flow was apportioned in two ways. In one way 50 percent of the oil flowed through the bearing inner ring to lubricate the bearing and 50 percent flowed axially only, for inner-ring cooling. In the other way the distribution of oil flow was 25 percent for lubrication and 75 percent for cooling. Figures 7 and 8 also show the effect of outer-ring cooling on bearing temperature (to be discussed later). Bearing temperature decreased with increased lubricant flow rate to the bearing for all conditions investigated. The flow distribution allowing the majority of the oil to cool the inner ring, namely, the 25–75 percent, resulted in a higher outer-ring temperature than the 50–50 percent distribution. This was true for all three shaft speeds. This higher outer-ring temperature was the result of the decreased amount of oil flowing radially through the bearing. The added cooling flow through the axial grooves in the inner ring afforded by a flow distribution of 25–75 percent did not aid in cooling the inner ring. This is shown in figure 8, where the inner-ring temperature is actually higher for a flow distribution of 25–75 percent than for a 50–50 percent distribution at speeds from 47 200 to 72 300 rpm. The cooling effect of the oil is less when it is channeled through axial grooves at the inner ring than when it is permitted to radially enter the bearing. The amount of cooling that can be accomplished with the axial oil flow path in the inner-ring grooves is greatly limited by the small surface area in contact with the oil.

The results shown in figures 7 and 8 indicate that an oil flow distribution of 50–50 for lubrication and inner-ring cooling is the more desirable of the two methods used here. Both inner- and outer-ring temperatures were lower at all speeds and lubricant flow rates when the bearing was tested under the conditions of 50–50 percent flow distribution.

Effect of outer-ring cooling. — Outer-ring cooling in which the oil was maintained at a flow rate of 1700 cm³/min (0.45 gal/min) at 394 K (250° F) oil-inlet temperature was employed in some tests. These results are also shown in figures 7 and 8. At the lowest shaft speed of 47 200 rpm (fig. 7(a)) outer-ring cooling reduced the outer-ring temperature by about 36 to 8 K (65° to 14° F) as the total oil flow to the inner ring was increased from 300 to 1900 cm³/min (0.08 to 0.50 gal/min). At the higher speeds, 64 700 and 72 300 rpm (figs. 7(b) and (c)), the outer-ring temperature reduction was about 42 to 16 K (75° to 28° F) as the total oil flow was increased from 580 to 1900 cm³/min (0.15 to 0.50 gal/min). The magnitude of the reduction in outer-ring temperature with outer-ring cooling was approximately equal for the 50–50 percent and 25–75 percent total oil flow distributions.

Outer-ring cooling had very little effect on the inner-ring temperature (fig. 8) for either oil-flow distribution. The reduction of inner-ring temperature varied from 0 to 6 K (0° to 11° F) over the entire range of total oil flows, shaft speeds, and oil-flow distributions used in these tests.

Comparison of Inner-Ring and Jet Lubricated Bearings

Temperatures. — The effect of speed on test bearing temperature for 50–50 and 25–75 percent total oil-flow distributions through the inner ring is shown in figure 9 and is compared with that of the jet-lubricated bearing (fig. 3(b)). Both bearings were dimensionally identical and had a single-outer-land-guided cage. Bearing temperature varied directly with speed and inversely with total oil flow. Outer-ring temperatures were higher than inner-ring temperatures for both lubrication methods used. Outer-ring temperatures were lower and inner-ring temperatures higher for the jet-lubricated bearing over the range of speeds and total oil-flow rates investigated. The oil impinging on the inner

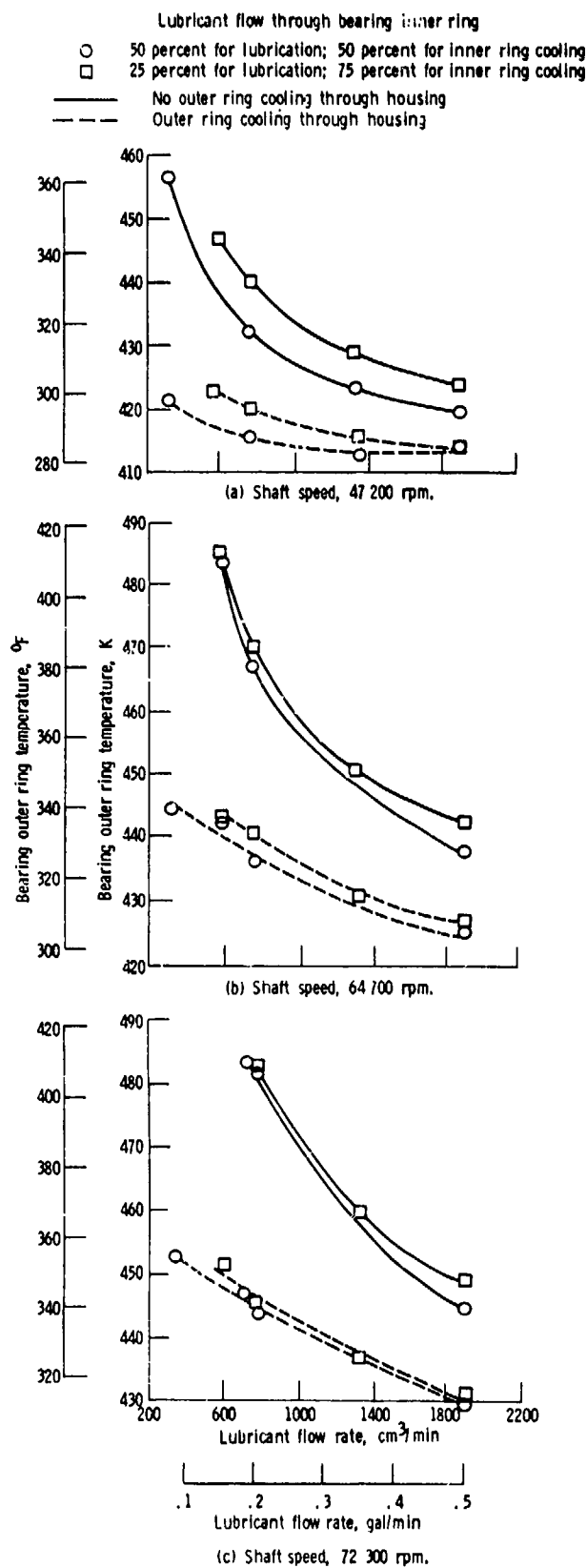


Figure 7. - Effect of lubricant flow rate on bearing outer-ring temperature for two oil distribution paths with and without outer-ring cooling.

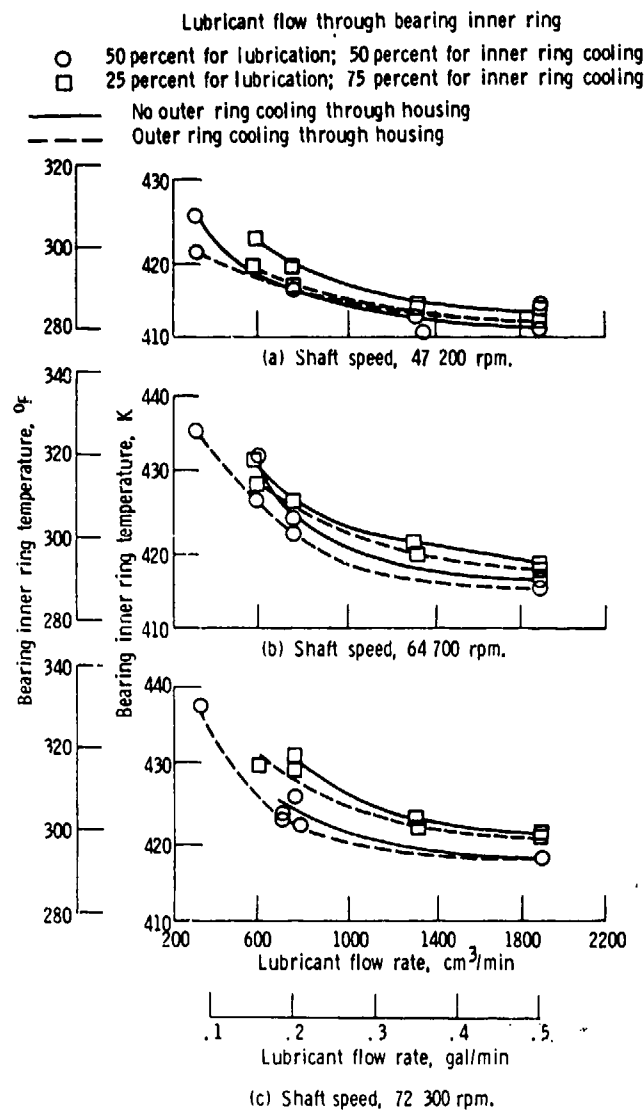


Figure 8. - Effect of lubricant flow rate on bearing inner-ring temperature for two oil distribution paths with and without outer-ring cooling.

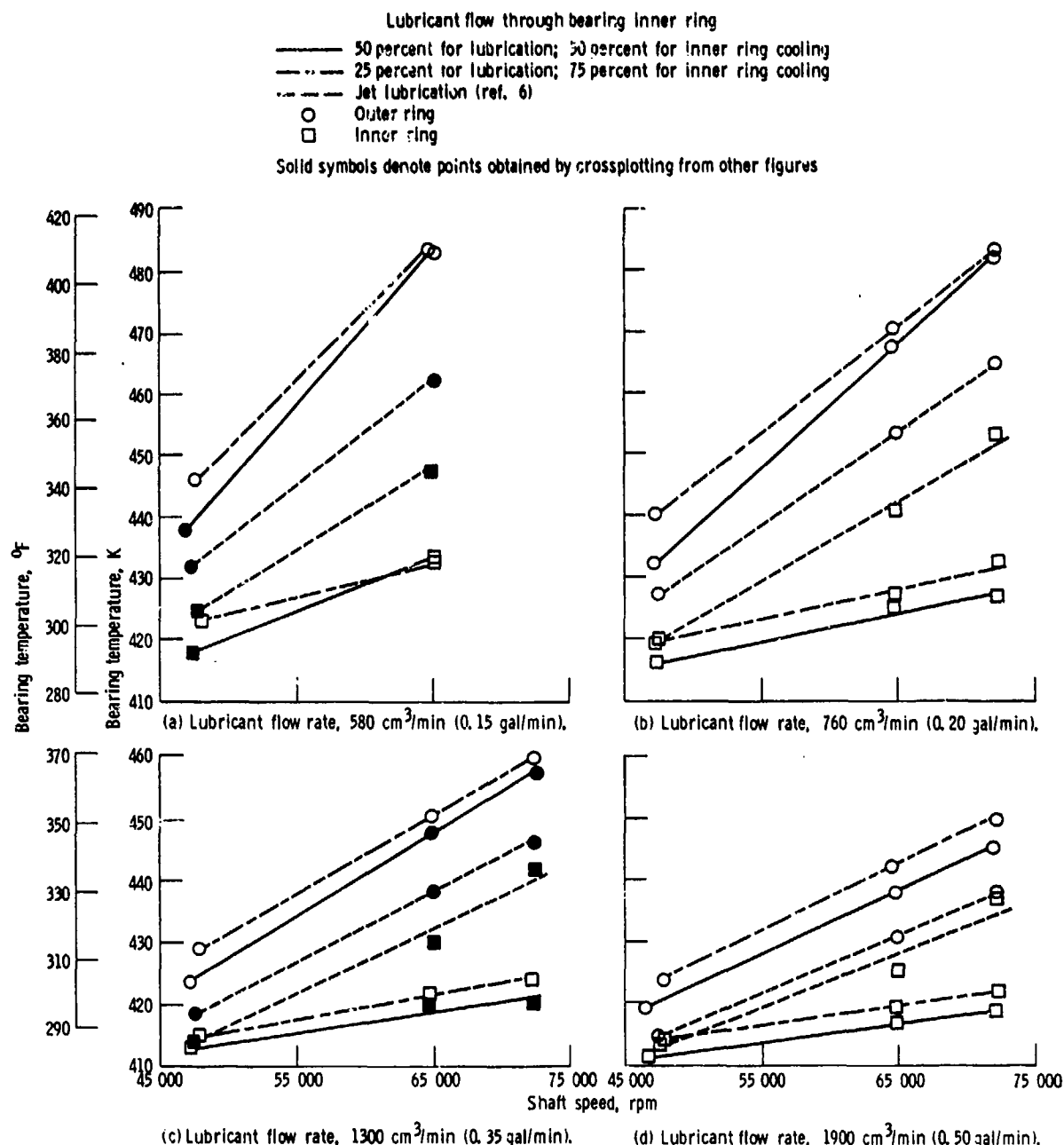


Figure 9. - Comparison of test bearing temperatures as function of shaft speed for two lubricant supply systems. No outer-ring cooling.

ring from the jets was apparently slung off the ring so rapidly that only a minimal amount of inner-ring cooling occurred, and thus inner-ring temperatures were high. However, since this oil had not gained much heat from the inner ring, it impinged on the outer ring at a cooler temperature than did the oil in the inner-ring lubricated bearings. Also, most of the total oil flow through the jets contacted the outer race to provide cooling, whereas a maximum of 50 or 25 percent of the total oil flowing through the inner-ring grooves contacted the outer race when inner-ring lubrication was used. For these reasons the outer ring of the jet-lubricated bearing was at a lower temperature than the outer ring of the inner-ring-lubricated bearing.

Power loss. - The power loss in the bearing, obtained from torque measurements taken with a strain gage attached to the bearing housing, is shown in figure 10. The measured torque for the jet-lubricated and inner-ring-lubricated bearings was 0.011 to 0.033 N·m (1.00 to 2.90 lb·in.) over the

range of lubricant flow rates and speeds tested. Power loss increased with speed at each flow rate investigated. The greatest increase in power loss was about 1.27 kW (1.7 hp) at a total oil flow rate of 1900 cm³/min (0.50 gal/min) over a speed range of about 47 000 to 72 000 rpm (fig. 10(d)). There was very little difference in power loss for the two methods of lubrication except at the two highest flow rates (figs. 10(c) and (d)). The jet-lubricated bearing at oil-flow rates of 1300 and 1900 cm³/min (0.35 and 0.50 gal/min) showed slightly less power loss than the inner-ring-lubricated bearing.

The results of power loss as determined from heat-transfer calculations for a single-outer-land-guided-cage bearing using two different methods of lubrication are compared in figure 11. These data are almost identical to those in figure 10 for power loss from torque measurements. The values of power rejected to the lubricant for both methods of lubrication are similar except at the two higher lubricant flow rates (figs. 11(c) and (d)). At these flow rates the jet-lubricated bearing had the lowest value of heat rejected to the lubricant. Maximum power loss was 2.8 kW (3.7 hp) at 72 300 rpm (fig. 11(d)) with a total oil-flow distribution pattern of 25-75 percent through the bearing.

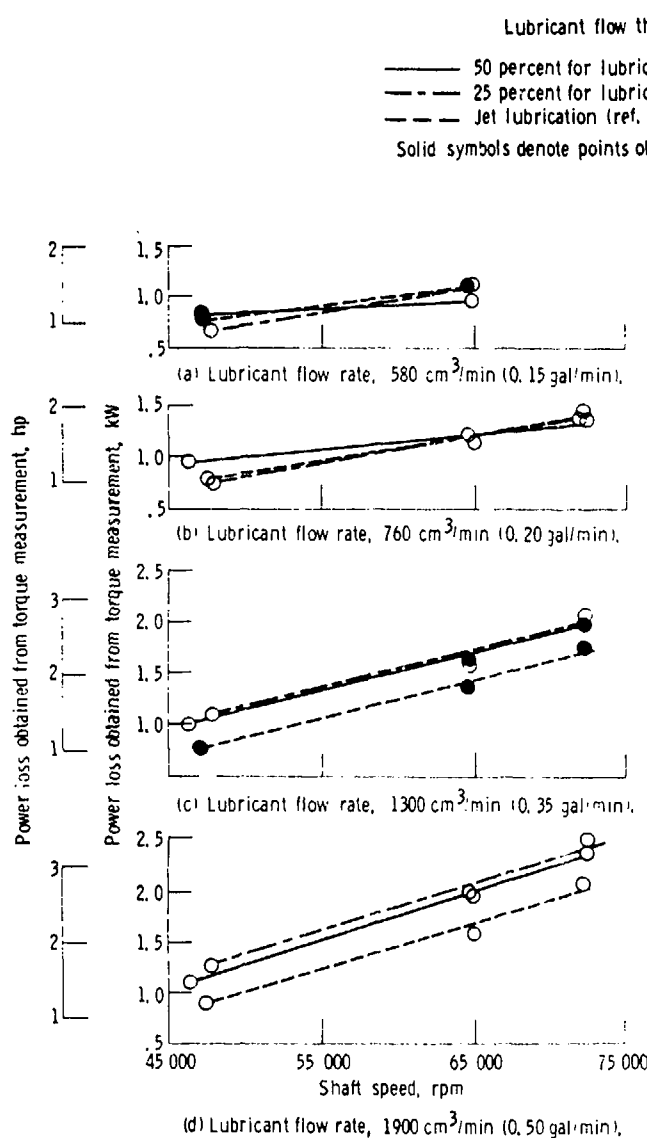


Figure 10. - Power loss obtained from torque measurement as function of shaft speed for inner-ring and jet lubrication. No outer-ring cooling.

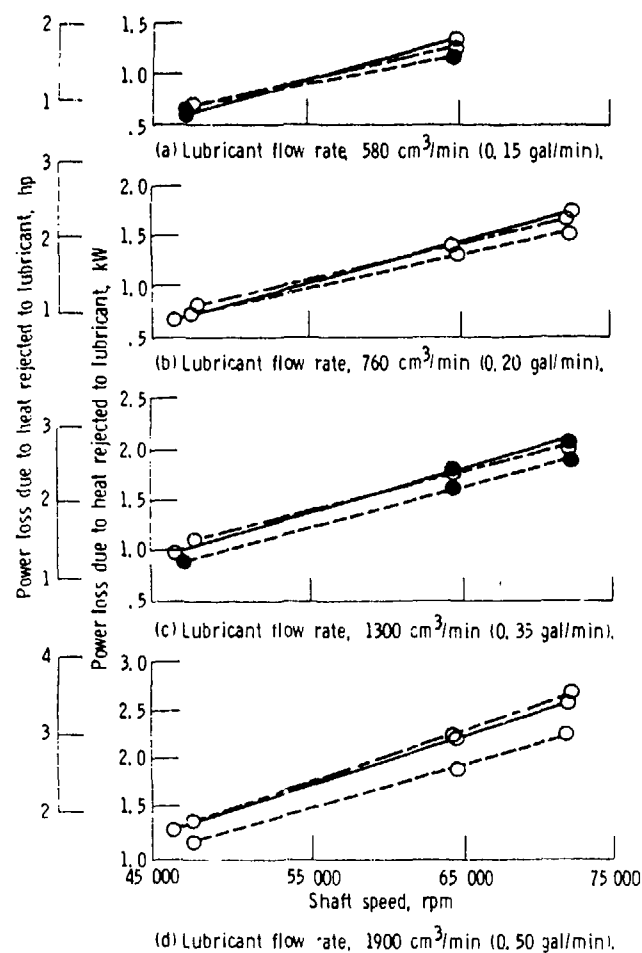


Figure 11. - Power loss due to heat rejected to lubricant as function of shaft speed for inner-ring and jet lubrication. No outer-ring cooling.

Cage slip. -- The effect of lubricant flow rate on percent cage slip for a single-outer-land-guided-cage bearing is shown in figure 12. For the three speeds (47 200, 64 800, and 72 300 rpm) and the flow rates tested, the percent cage slip was minimal for each method of lubrication. The small increase in slip with increasing flow rate is primarily due to additional drag on the balls. The jet-lubricated bearing showed a higher percent slip than the two inner-ring-lubricated bearings at speeds of 47 200 and 64 800 rpm (figs. 12(a) and (b)). However, at the maximum speed of 72 300 rpm (fig. 12(c)), the percent cage slip for all three bearings was essentially equal, with the jet-lubricated bearing showing a slightly lower percent cage slip at lubricant flow rates above approximately 1100 cm³/min (0.30 gal/min). As the speed was increased, the centrifugal force generated caused more oil from the jets to be slung off the bearing, thus allowing less to enter as a lubricant for the rolling elements. With less oil present, less plowing of the balls and cage occurred, and this resulted in a lower rate of increase in cage slip than for the inner-ring-lubricated bearings. The maximum percent cage slip of 7.0 occurred at 72 300 rpm, at a total oil-flow rate of 1900 cm³/min (0.50 gal/min) (fig. 12(c)) with a total oil-flow distribution pattern of 50-50 percent through the inner ring.

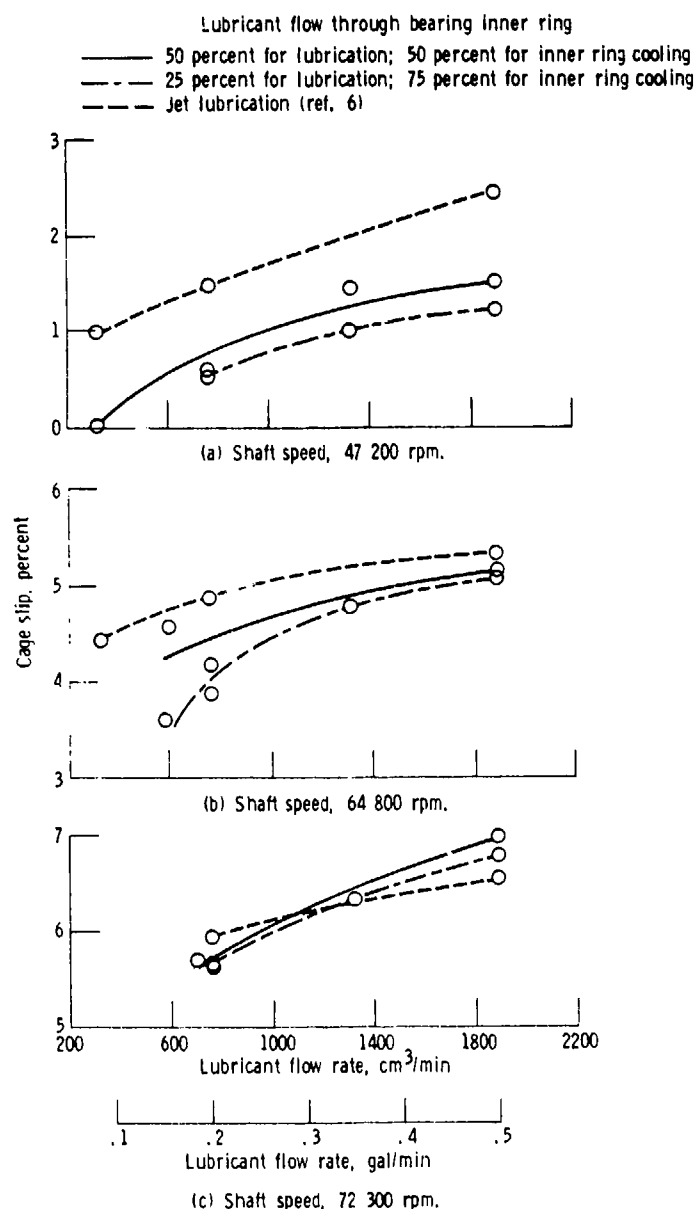


Figure 12. - Effect of lubricant flow rate on cage slip for inner-ring and jet lubrication. No outer-ring cooling.

Figure 13 shows that percent cage slip increases with speed at about the same rate for each method of lubrication and independently of the lubricant flow rate, especially for the inner-ring-lubricated bearings. Increased percent cage slip with increased shaft speed may be partially due to centrifugal forces decreasing the ball load and thus the traction at the inner-ace contact. The jet-lubricated bearing showed a higher percent cage slip than the inner-ring-lubricated bearings at the lower flow rates of 580 and 760 cm^3/min (0.15 and 0.20 gal/min) over the entire speed range tested (figs. 13(a) and (b)). However, as the flow rate was increased to 1300 and 1900 cm^3/min (0.35 and 0.50 gal/min), the rate of increase in cage slip of the jet-lubricated bearing was less than that of the inner-ring-lubricated bearings (figs. 13(c) and (d)). This resulted in a cage slip value equal to or less than the percent cage slip of the inner-ring-lubricated bearing at the higher speeds. Although the flow

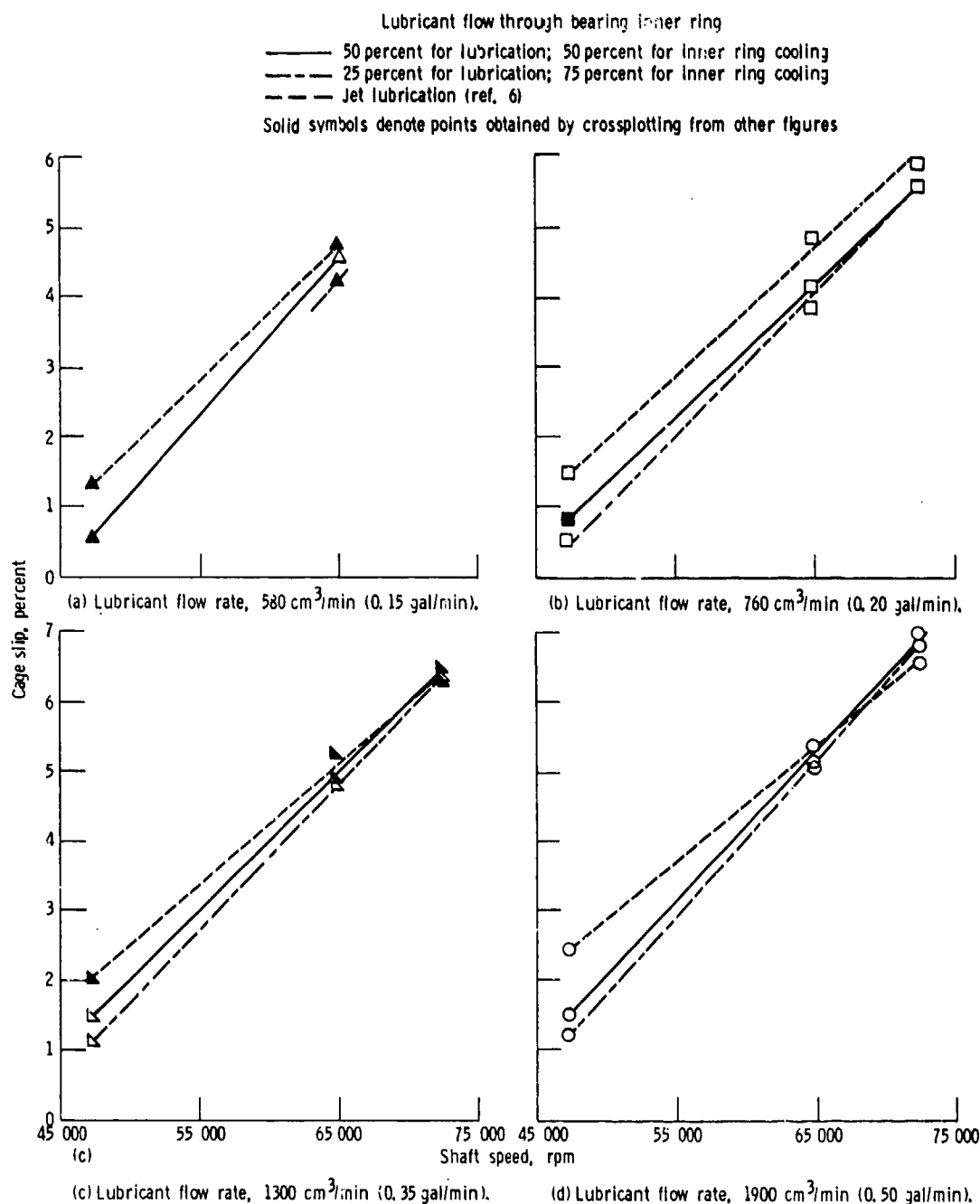


Figure 13. - Effect of shaft speed on cage slip for inner-ring and jet lubrication. No outer-ring cooling.

rate was high, the jet-lubricated bearing had a large percentage of its oil slung off the bearing at the higher speeds, and the remaining amount of oil flowing through the bearing approximated the oil flowing through the inner-ring-lubricated bearings at these test conditions. Thus the percent cage slips became about equal, as shown in figures 13(c) and (d).

Visual examination of the bearing after running showed no damage to the raceways or the balls, indicating that the cage slip was not of sufficient magnitude to affect the satisfactory operation of the bearing. There was no sign of significant wear on the cage surfaces, and the silver plate had not worn through.

Summary of Results

Parametric tests were conducted in a high-speed, high-temperature bearing tester using 35-mm-bore, angular-contact ball bearings with either a single- or double-outer-land-guided cage. The bearing had a nominal contact angle of 24° . The bearing was jet-lubricated (with a 20 m/sec (66 ft/sec) jet velocity) or had axial grooves and radial holes which permitted lubrication through the bearing inner ring. An outer-ring cooling oil flow rate maintained at 1700 cm³/min (0.45 gal/min) at 394 K (250° F) oil-inlet temperature was used in some tests. The distribution of the total oil supplied to the inner ring was 50 percent for lubrication of the rolling elements and 50 percent for inner-ring cooling in some tests. In other tests the distribution was 25 percent lubrication and 75 percent cooling. Test results for a bearing with oil supplied through the inner ring were compared with those for a jet-lubricated bearing with identical dimensions and cage design.

Test conditions for all tests included a radial load 222 N (50 lb) and/or a thrust load of 667 N (150 lb), shaft speeds of a nominal 48 000 to 72 000 rpm, and an oil-inlet temperature of 394 K (250° F). Total oil flow to the bearing was 300 to 1900 cm³/min (0.08 to 0.50 gal/min).

The oil used for the parametric studies was a neopentylpolyol (tetra)ester. This type II oil is qualified to the MIL-L-23699 specifications. The following major results were obtained:

1. Successful operation of a 35-mm-bore ball bearing, employing a double-outer-land-guided cage and jet lubrication, was accomplished up to 72 600 rpm (2.5 million DN) at a combined load of 667 N (150 lb) thrust and 222 N (50 lb) radial.

2. The double-outer-land-guided cage bearing generated substantially higher temperatures than the single-outer-land-guided cage bearing over the entire range of shaft speeds and lubricant flow rates tested.

3. The power loss for the double-outer-land-guided cage bearing was always higher than that for the single at similar test conditions.

4. Percent cage slip for a double-outer-land-guided cage bearing ranged from 1.5 to 2.7 times that for a single-outer-land-guided cage bearing of similar dimensions over the entire range of speed and lubricant flow rates tested.

5. A 35-mm-bore, angular-contact ball bearing with inner-ring lubrication was successfully operated to 2.5 million DN for both the 50-50 percent and 25-75 percent oil-flow distributions.

6. Cooler bearing operation was experienced with a total oil-flow distribution of 50 percent lubrication and 50 percent inner-ring cooling than with a 25-75 percent distribution for the inner-ring-lubricated bearings.

7. Jet-lubrication data showed lower outer-ring temperatures and higher inner-ring temperatures than the results for inner-ring-lubricated bearings.

8. Outer-ring cooling of both jet-lubricated and inner-ring-lubricated bearings resulted in a substantial decrease in outer-ring temperature but had a minimal effect on inner-ring temperature.

9. Maximum power loss of 2.8 kW (3.7 hp) occurred at 72 300 rpm with a total oil-flow distribution pattern of 25-75 percent at a total oil flow rate of 1900 cm³/min (0.50 gal/min).

10. For inner-ring-lubricated bearings a maximum percent cage slip of 7.0 occurred at 72 300 rpm at a total oil-flow rate of 1900 cm³/min (0.50 gal/min) with a total oil flow distribution pattern of 50-50 percent. The increase in percent cage slip with lubricant flow rate was minimal for each flow distribution pattern used.

References

1. Signer H.; Bamberger, E. N.; and Zaretsky, E. V.: Parametric Study of the Lubrication of Thrust Loaded 120-Millimeter Bore Ball Bearings to 3 Million DN. J. Lubr. Technol., vol. 96, no. 3, July 1974, pp. 515-524.
2. Zaretsky, E. V.; Bamberger, E. N.; and Signer, Hans: Operating Characteristics of 120-Millimeter-Bore Ball Bearings at 3×10^6 DN. NASA TN D-7837, 1974.
3. Bamberger, E. N.; Zaretsky, E. V.; and Signer, Hans: Effect of Speed and Load on Ultra-High-Speed Ball Bearings. NASA TN D-7870, 1975.
4. Schuller, F. T.: Operating Characteristics of a Large-Bore Roller Bearing to Speeds of 3×10^6 DN. NASA TP-1413, 1979.
5. Miyakawa, Y.; Seki, K.; and Yokoyama, M.: Study on the Performance of Ball Bearings at High DN Values. NASA TTF-15017, 1973. Transl. of "Koh dn Chi Ni Okeru Gyokujikuu No Seino Ni Kansuru Kenkyu." National Aerospace Laboratory, Tokyo (Japan), Report NAL-TR-284, May 1972.
6. Matt, R. J.; and Giannotti, R. J.: Performance of High Speed Ball Bearings with Jet Oil Lubrication. ASLE Paper 66AM-1B4, Aug. 1966.
7. Anderson, W. J.; Macks, E. F.; and Nemeth, Z. N.: Comparison of Performance of Experimental and Conventional Cage Designs and Materials for 75-Millimeter-Bore Cylindrical Roller Bearings at High Speeds. NACA Report 1177, 1954.
8. Schuller, F. T.; Pinel S. I.; and Signer, H. R.: Operating Characteristics of a High-Speed-Jet-Lubricated 35-Millimeter-Bore Ball Bearing with a Single Outer Land Guided Cage. NASA TP-1657, 1980.
9. Pinel, S. I.; and Signer, H. R.: Development of a High-Speed Small Bore Bearing Test Machine. (ITI P-1249, Industrial Tectonics, Inc.; NASA Contract NAS3-17358.) NASA CR-135083, 1976.
10. Crecelius, W. J.; Heller, S.; and Chiu, Y. P.: Improved Flexible Shaft-Bearing Thermal Analysis with NASA Friction Models and Cage Effects. SKF-AL-76P003, SKF Industries, Inc., Feb. 1976.
11. Schuller, F. T.; Pinel, S. I.; and Signer, H. R.: Effect of Cage Design on Characteristics of High-Speed-Jet-Lubricated 35-Millimeter-Bore Ball Bearing. NASA TP-1732, 1980.



High Speed Spherical Roller Bearing Analysis and Comparison with Experimental Performance*

Robert J. Kleckner[†] and George Dyba[†]

The general class of load support systems consists of mechanical assemblies which transfer force and moment vectors. The transfer is constrained to maintain component displacements within prescribed, and frequently severe, limits.

Rolling-element bearings are a subset of this general load support system class, characterized by high load carrying capacity, low power loss, stability during load fluctuations and rotation reversal, and tolerance of start-stop operation. Various rolling-element-bearing configurations are contained within this subset to service specific application requirements. The ball bearing, for example, supports combined direction loading and tolerates some misalignment. They do so at a penalty because elements with "line" in comparison with "point" contact conjunctions offer superior capacity for a given design volume (fig. 1). However, bearings having tapered and cylindrical roller geometries with "line" contact are less tolerant of misalignment.

The relative displacement of components is an inescapable physical reality when mechanical assemblies transfer force. Typically, structural elements distort within the generally asymmetric assembly, causing a misalignment of bearing raceways. This departure from the idealized "rigid" assembly can be compensated for but not eliminated by manufacture, assembly, and operation. In the presence of such deflections, and resulting misalignment, line-contact geometries can be optimized only for a specific single-load condition (ref. 1). Severe penalties, including loss of bearing life and operating performance, result for off-optimum load support.

The self-aligning spherical roller bearing (fig. 2) answers some shortcomings of the configurations noted above. The geometry is unique. At low loads, the load vector is transferred by point contacts. At higher loads, modified line contacts perform this function. The bearing also supports combined radial and axial loading. This versatility has led to successful implementation in the large load support systems required by the steel, paper, and marine industries. Successful application has also been achieved in high-reliability mechanical assemblies, such as airborne planetary gear reduction sets.

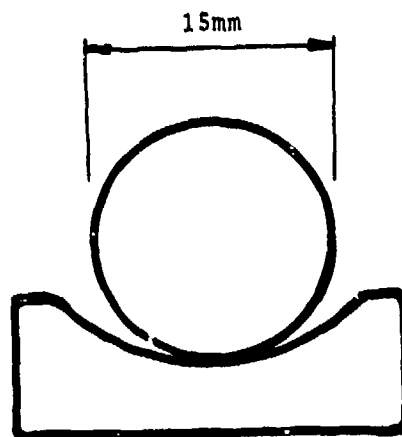
The rolling-element bearing subset of the load support system class, in today's technology, is being required to operate at ever increasing DN values. Ball and cylindrical bearings, for example, have seen numerous applications at the 3.0 MDN¹ level. Tapered bearings are being asked to follow in this regime. These new demands result from the requirements posed by advanced hardware missions and the increased emphasis on extracting maximum energy from a given process cycle. Basic thermodynamics, particularly in mobile powerplant design, dictates higher temperatures, stresses, and speeds. Simultaneously, the assembly is required to occupy a smaller volume and weigh less. The combination of these parameters defines a lighter assembly, under increased stress, in a high-temperature environment. The bearings which reside in assemblies of decreased structural rigidity, must sustain high combined loads under conditions of misalignment and, furthermore, do so at higher speeds.

The conventional spherical rolling-element bearing design meets all but one of the challenges posed by these emerging requirements. Operating speed has been restricted to maximum DN values of about 0.4 MDN. Efforts are now under way to reach higher speeds. Particular emphasis is placed on reaching a 1.0 MDN value.

*This work done under NASA contract NAS3-20824.

[†]SKF Industries, Inc.

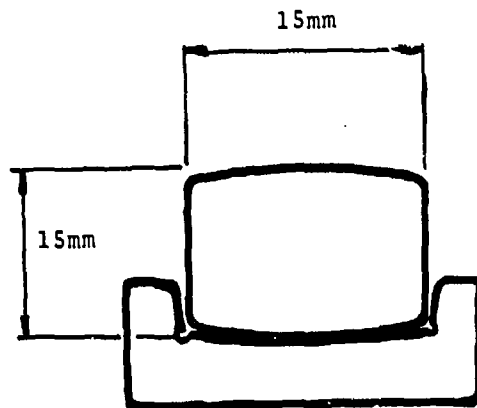
¹The term MDN refers to million DN, where DN is the bearing bore in mm times the speed in rpm. For the 40-mm-bore bearing test case, 0.8 MDN is approximately 4 times the catalog maximum speed limit.



BALL

POINT CONTACT CAPACITY

= 22,240 N (5000 lbs)



SPHERICAL

MODIFIED LINE CONTACT
CAPACITY

= 36,200 N (8,140 lbs)

Figure 1. - Example of capacities of line and point contacts.

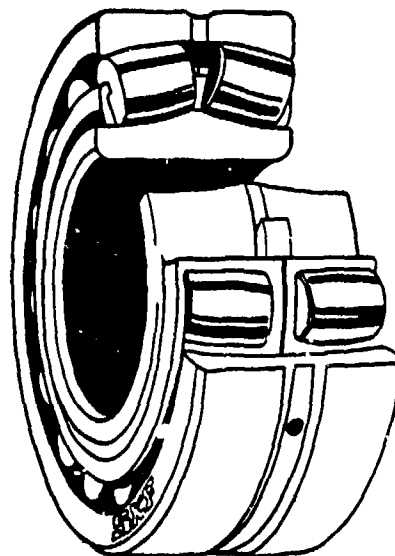


Figure 2. - Typical spherical rolling-element bearing geometry.

The need to extend the operating DN regime for spherical roller bearings requires a realistic assessment of current methods for their design. Examination reveals that the contemporary design relies on "rules," hand calculations, and some modest computerized simulations. The presence of mandated safety factors in these rules for successful application reveals the measure of design performance buffers. At the same time, it reveals an opportunity for increasing performance and thus DN values to satisfy emerging load support needs.

Practical use of design reserves requires a more detailed understanding of and the ability to predict bearing performance within a load support system. The complexity of the interactions between the bearing and its environment requires an analytic/design tool to describe the thermomechanical dialogue present (ref. 2). Such a simulation tool can be created using high-speed digital computers.

Several investigators have addressed the analysis of spherical roller bearings, setting the stage for the required computerized simulation. Recently, Kellstrom (ref. 3) explored the fundamental mechanics that control symmetric roller behavior. He specifically addressed roller "self-guidance" and explored the optimization of their skewing angles to minimize heat generation. Wieland and Poesl (ref. 4) have presented an interpretation of the empirical state of the art in spherical roller bearing design and application. Harris and Broschard (ref. 5) as well as Liu and Chiu (ref. 6) have examined these bearings in planetary-gear applications in earlier investigations. Palmgren (ref. 7) and Harris (ref. 8) touch on computational procedures. Manufacturers' catalog data and popularized applications articles further serve to highlight the need for a thorough analytic examination of the coupled phenomena which occur during spherical roller bearing operation.

This paper describes the capabilities of a spherical roller bearing analysis/design tool, Spherbean (spherical bearing analysis). Capabilities of the analysis are demonstrated then verified by comparison with experimental data. A practical design problem is presented where the computer program is used to improve a particular bearing's performance (refs. 9 to 11).

Program Description

Spherbean (refs. 9 to 11) has been created to simulate the performance of double-row spherical roller bearings under a variety of operating conditions (fig. 3). Emphasis has been placed on detailing the effects of roller skew, roller-end-to-flange contact, and change in clearance as a function of speed, interference fit, and temperature.

The complete range of EHD contact considerations has been treated in the computation of raceway and flange contact detail. A flexible outer-ring analysis is among the several options made available to address special applications (fig. 3). For simulation of planet bearing performance, where the bearing's outer ring is integral with the planet gear (fig. 4), the carrier speed is considered in the computation of bearing kinematics. The user can choose the capabilities to be activated in a given simulation, or let the program default to a "standard" configuration. Spherbean also checks user-supplied data for magnitude and consistency. A failed check results in a diagnostic abort message.

Program capabilities also include both time transient and steady-state temperature mapping of a spherical bearing system. This option permits exploration of the bearing's temperature as a function of speed. When coupled with the option to compute the bearing's operating clearance, thermally induced bearing seizure can be examined. Activating the time transient thermal analysis allows the user to follow the system temperature rise and bracket the time-to-failure after loss of lubricant, for example.

Demonstration of Capabilities

The program's thermal option is illustrated in the following steady-state analysis of a 40-mm-bore bearing to 20 000 rpm. Program results are then compared with instrumented test results.

USER MUST PROVIDE

LOAD VECTOR FX, FY, FZ

OPERATING SPEED

GEOMETRY {
 ROLLER
 RACEWAYS
 FLANGE
 CAGE

USER OPTIONALLY PROVIDES

INTERFERENCE FIT DATA

PLANET GEAR BEARING DATA

SYSTEM DESCRIPTION FOR TEMPERATURE CALCULATIONS

SPLIT CAGE DATA

LUBRICANT PROPERTIES

MATERIAL PROPERTIES

Figure 3. - User supplied data requirements.

Test Rig and Subsystems

The experimental data used for comparison were generated on the spherical bearing test rig² (fig. 5). The rig has the capability to load the specimen both axially and radially at inner ring speeds to 20 000 rpm. Instrumentation is provided to measure the bearing oil-in and oil-out temperatures, inner- and outer-ring temperatures, inner-ring and cage speeds, operating torque, oil flow rates, and the operating parameters of secondary equipment.

Lubrication is provided to the test bearing at 93° C by way of a circumferential groove in the outer ring where it enters the bearing cavity through three radial holes. The lubricant used in all tests was a type II ester, conforming to the MIL-L-23699 specification.

The test rig consists of a hollow rectangular housing, which accommodates a solid shaft, support bearings, and lubrication rings, which direct recirculating oil into one side of each support bearing at three equally spaced locations.

The shaft extends from both ends of the housing through labyrinth seals. The test bearing is mounted on one end of the shaft extension. The other end is attached to a flexible quill. The quill is attached to either a jack shaft (for low-speed operation) or a gear box (for high-speed operation). The jack shaft or gear box is driven through a belt and pulley arrangement by a variable-speed motor.

The test bearing inner ring is mounted to the shaft with an interference fit and clamped between a shoulder and an end cap. The shaft section located under the test bearing is hollow to accommodate the circuitry for the resistance temperature detectors (RTD's) mounted in slots machined into the shaft surface.

The outer ring of the test bearing is mounted in a housing which doubles as the inner ring of a radial hydrostatic bearing. The outer ring of the radial hydrostatic bearing contains the oil supply holes, restrictors, and bearing pads. The hydrostatic bearing outer ring is attached to a hydraulic ram that applies the radial load through the center of the test bearing.

The test bearing is enclosed on the inboard side by a faceplate mounted to the housing, which forms a labyrinth seal around the shaft. The outboard enclosure is formed by a spherical segment

²Details of the test facility were documented by Rosenlieb (ref. 12).

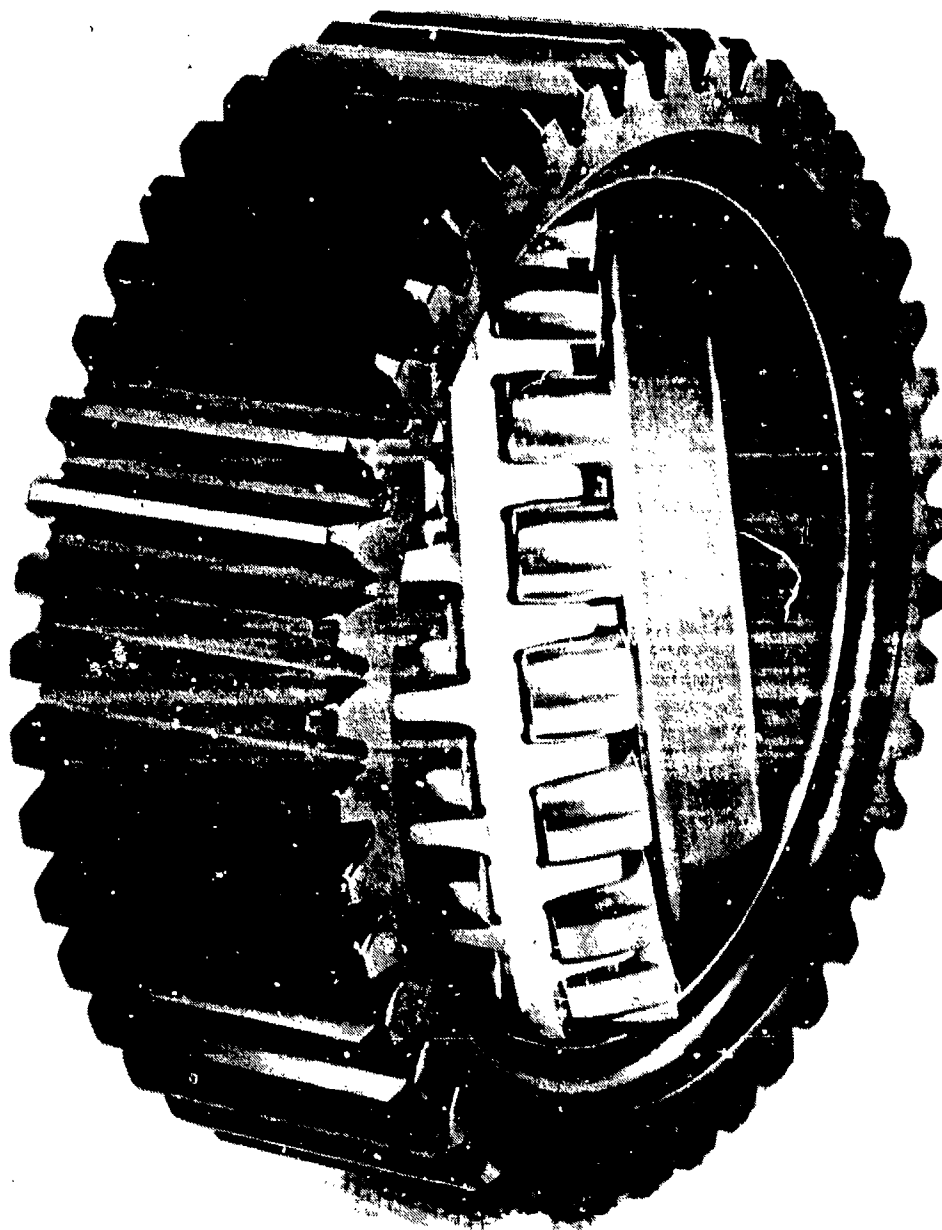


Figure 4. - Spherical roller planet bearing.

which doubles as the face plate of an axial hydrostatic bearing. The axial hydrostatic block, containing the oil supply holes, restrictors, and pads, has a matching contour. Axial load is applied to the bearing by a hydraulic ram located on an angle bracket bolted to the rig's foundation.

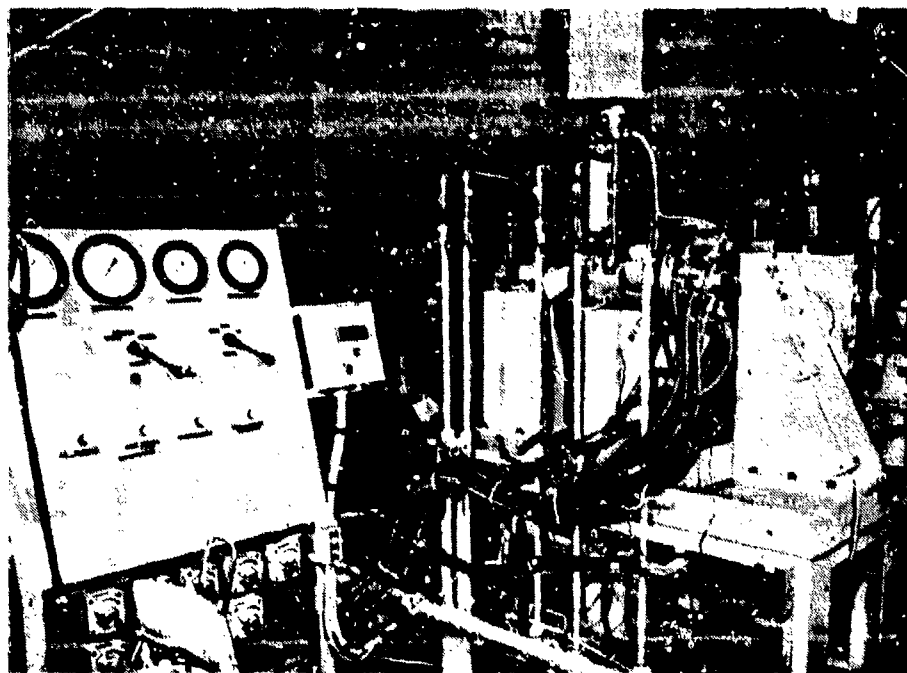
Test Rig System Model

Test rig geometry and material properties were used to reduce the configuration to an equivalent, cross-coupled, lumped-mass nodal network containing 50 temperature nodes. Of these, the temperatures of 44 nodes are determined by Spherbean, and the remaining six are specified as system boundary conditions.

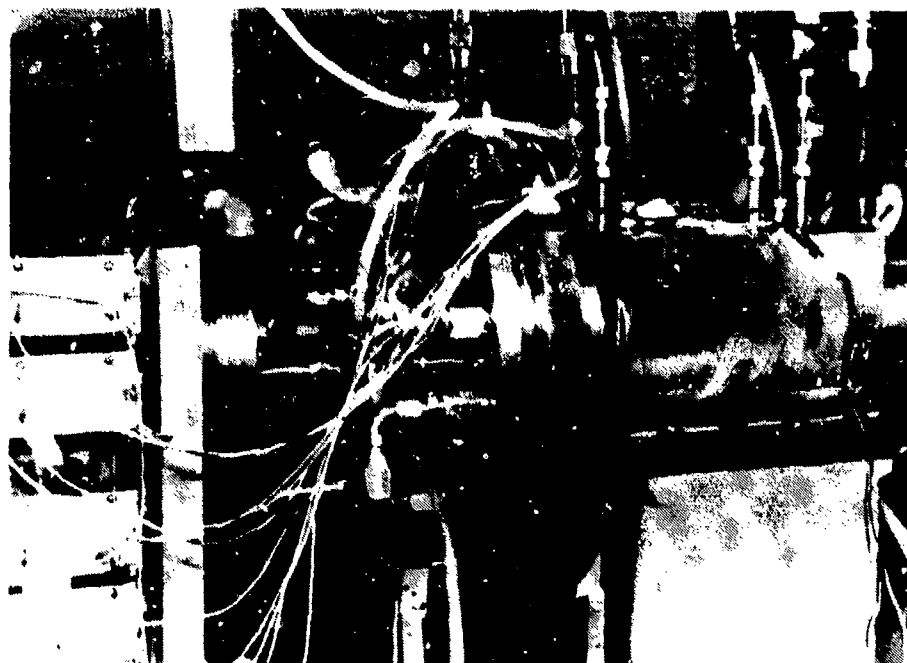
Figures 6 and 7 show the extent of the test rig that was thermally simulated. The model is bounded on the left (nodes 1, 21, and 47 in fig. 5) by the axial hydrostatic bearing and ambient air.

The actual test rig continues past this point in the form of (thermally) minor support hardware for the thrust bearing and a rotary transformer drive quill. Approximately 50 percent of the quill was modeled, since its diameter (7 mm) is small in comparison with the test bearing bore (40 mm), and, therefore, contributes very little to the overall heat balance within the rig.

The thermal model is bounded on the right side by a support cylindrical roller bearing. The support bearing model was included to increase the accuracy of the predicted test bearing inner-ring temperatures, since the test bearing thermally communicates with the support bearing by transferring heat through the drive shaft.



(a) Rig controls.



(b) Test bearing housing.

Figure 5. - High-speed test rig.

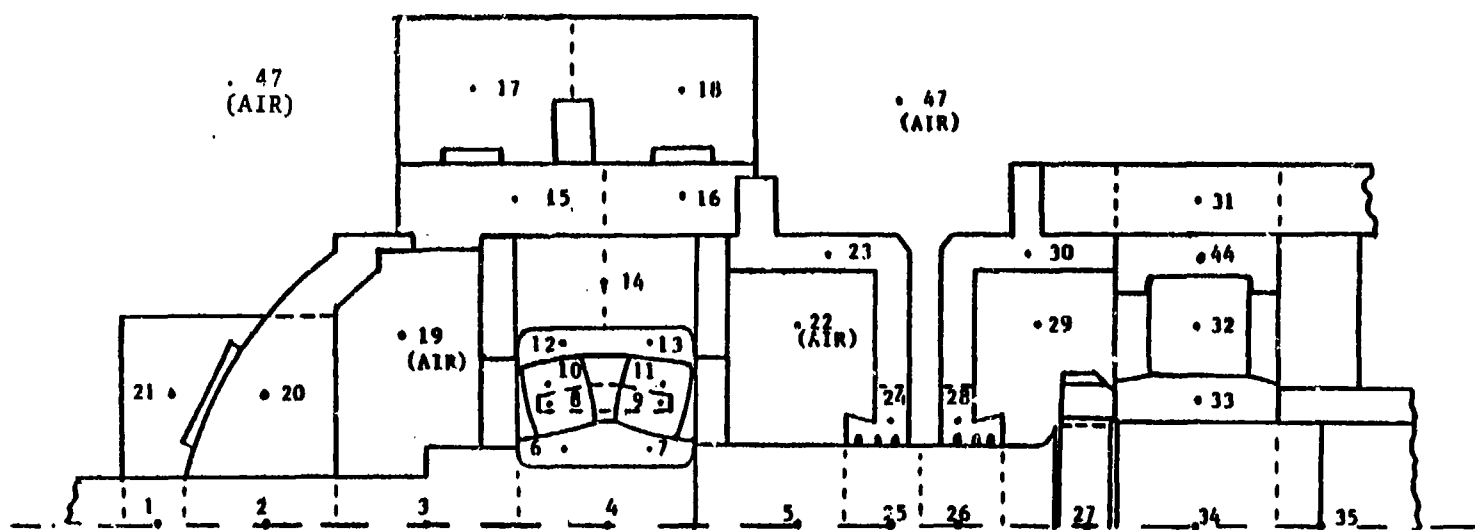


Figure 6. - System model; metal and air nodes.

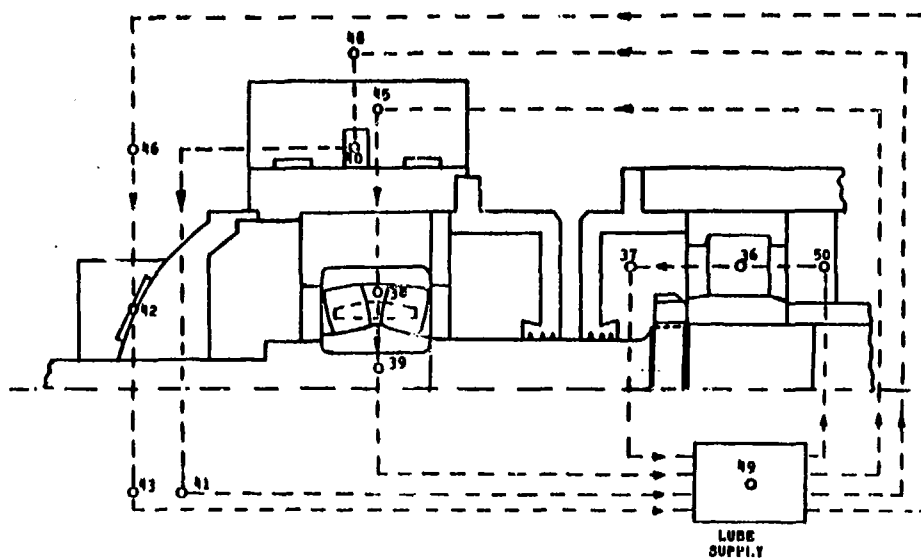


Figure 7. - System model; lubricant system nodes

Three sources of heat generation, other than the test bearing, were considered. These are two labyrinth seals, located at nodes 24 and 28, and the roller bearing, defined by nodes 32, 33, and 44. The small quantity of heat created at the labyrinth seals was assumed to vary linearly with speed from 2.2 to 11 W, each, for inner-ring speeds from 1000 to 5000 rpm. Heat generated by the cylindrical bearing was assumed to vary with speed and load and was computed using a handbook equation (ref. 13).

Four independent lubrication systems were considered in the rig model (fig. 7). The two outermost loops (nodes 46, 42, 43 and 48, 40, 41) represent lubricant delivered to the axial and radial hydrostatic thrust bearings, respectively. The two innermost loops (nodes 45, 38, 39 and 50, 36, 37) simulate the lubricant delivered to the test and support bearings. Flow rates, delivery temperature, and heat-transfer properties were individually specified for each loop.

Comparison of Experimental Measurements with Performance Predicted by Spherbean

The test rig model was used to generate system performance data at the operating conditions listed in table I. Every combination of load and speed documented in reference 12 was not simulated. Steady-state thermomechanical performance was examined, with the operating bearing clearance computed as a function of speed, interference fit, pressure, and operating temperature. Measured dimensions of the four bearings used for tests and simulation are given in table II. The five operating parameters used for comparison of measured and calculated performance are defined in table III.

The computed operating parameters are generated as single-valued functions. Physical reality imposes a diffusion of that uniqueness. This could be simulated, for example, by exploring the effect of dimension tolerance extremes, material property variations, and heat-transfer coefficient differences. Computer predicted bearing performance would then be represented by a "bandwidth," not a line. However, the extent and the crosscoupling of these variations within the load support system precludes full exploration within the scope of this effort. Therefore, a minimum ± 5 percent bandwidth should be assumed to surround the computerized results presented.

No repeat-run experimental data were available and, thus, the absolute bandwidth spread, which represents experiment-to-experiment parameter variations, is unknown. Based on the measured results, it is prudent to assume that, for a particular test bearing, the experimental temperature bandwidth will be at least ± 5 percent of the minimum temperature value.

Calculated predictions and experimental values obtained under pure radial load of 6672 N (1500 lb) are presented for comparison in figure 8. Computed cage-to-shaft speed ratios were all within 2 percent of the measured values investigated and are, therefore, not graphically displayed. This close correlation occurs because of the limited roller slip.

Figure 8 shows that the computed system temperatures are within 3 percent of measured values for shaft speeds to 5000 rpm. The largest difference between measured and calculated temperatures (3.5°C) is found at the inner ring (fig. 8(a)), at 1000 rpm. Lubricant outlet temperature predictions are within 4 percent of measured values for speeds to 5000 rpm.

The comparison of experimental and calculated temperature data in figure 8 was made over an operating speed range having an upper bound near the bearing manufacturer's recommended

TABLE I. - TEST CONDITIONS SIMULATED IN REFERENCE 11 FOR COMPARISON OF CALCULATED AND MEASURED DATA

Test	Description	Identification number of bearing ^a	Speed, rpm	Applied loads, N (lb)	
				Radial	Axial
A	Pure radial load ^b	02	1000 - 5000	6 672 (1500)	0 (0)
				13 345 (3000)	0 (0)
B	Combined load	02	1000 - 5000	6 672 (1500)	3114 (700)
				13 345 (3000)	4448 (1000)
C	Effect of clearance	01	1000 - 5000	6 672 (1500)	0 (0)
				13 345 (3000)	0 (0)
				6 672 (1500)	3114 (700)
				13 345 (3000)	4448 (1000)
D	Effect of Osculation ^b	03	1000 - 5000	6 672 (1500)	0 (0)
				13 345 (3000)	0 (0)
E	High speed	06	5000 - 20 000	311 (70)	4448 (1000)

^aTable II lists specific test bearing dimensions.

^bResults are presented in figs. 8 to 11.

TABLE II. - TEST BEARING (MEASURED) DIMENSIONS USED
AS INPUT TO SPHERBEAN

	Bearing identification number			
	01	02	03	04
Inner-ring groove radius ^a , mm (in.)	39.774 (1.5659)	39.901 (1.5709)	40.749 (1.6043)	41.300 (1.6250)
Outer-ring groove radius ^a , mm (in.)	40.371 (1.5894)	40.350 (1.5886)	40.345 (1.5884)	40.381 (1.5898)
Roller diameter ^b , mm (in.)	13.00 (0.5117)	13.00 (0.5118)	13.00 (0.5117)	13.01 (0.5122)
Roller crown radius ^b , mm (in.)	39.421 (1.5520)	38.915 (1.5321)	38.918 (1.5322)	38.583 (1.5584)
Roller total length ^b , mm (in.)	12.05 (0.4745)	11.97 (0.4713)	11.97 (0.4713)	12.02 (0.4732)
Surface roughness, μ m (μ in.):				
Inner raceway ^c	0.071 (2.8)	0.066 (2.6)	0.069 (2.7)	0.13 (5.1)
Outer raceway ^d	0.277 (10.9)	0.269 (10.6)	0.282 (11.1)	0.14 (5.5)
Roller ^e	0.076 (3.0)	0.076 (3.0)	0.066 (2.6)	0.11 (4.3)
Diametral clearance ^f , mm (in.)	0.0991 (0.0039)	0.0749 (0.0029)	0.0762 (0.0030)	0.0749 (0.0029)

^aAverage of two rows.

^bAverage value for three rollers.

^cAverage of three equally spaced readings per row.

^dAverage of three equally spaced readings.

^eAverage of three rollers, three readings each.

^fAverage of three readings.

TABLE III. - PREDICTED AND MEASURED OPERATING PARAMETERS

Parameter	Instrumentation	Program analog
Cage speed	Proximity probe and counter	Direct program output
Inner-ring temperature	Average of simultaneous reading of 4 RTD's	Average temperature of nodes 6 and 7
Outer-ring temperature	Average of simultaneous reading of 4 J-type thermocouples	Average temperature of nodes 12 and 13
Oil outlet temperature	J-type thermocouple	Temperature of node 39
Drag torque	Strain gaged beam on inner ring of radial hydrostatic bearing	Torque computed from program predicted steady-state heat generation rate

"limiting speed." Conventional bearing operation above the limiting speed can result in overheating and thermal seizure. To avoid a possible catastrophic test bearing failure at elevated speeds, Spherbean was used to explore high-speed rig performance before execution of the full-scale tests.

The performance of bearing 06 (table I) was examined over a speed range of 5000 to 20 000 rpm. The peak speed is approximately four times greater than the manufacturer's recommended limiting speed. Two load conditions were simulated: pure radial and pure axial. An average hydrostatic bearing inlet oil temperature of 90° C, a value at least 10° C higher than later used in the actual test series, was chosen to simulate a conservative upper temperature limit of bearing performance.

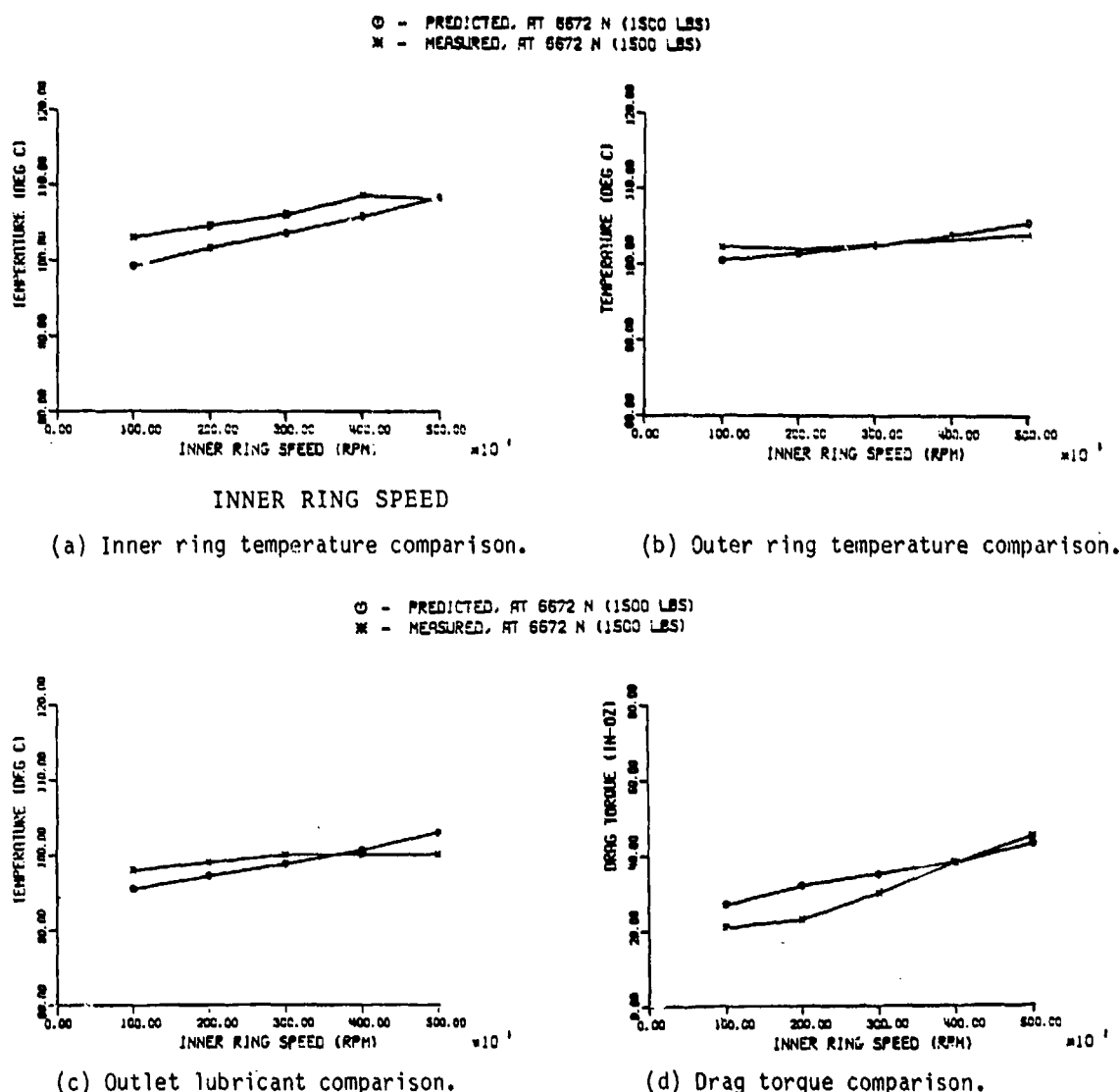


Figure 8. - Comparison of predicted and measured data for bearing no. 02 to 5000 rpm. Pure radial load, 6672 N (1500 lb).

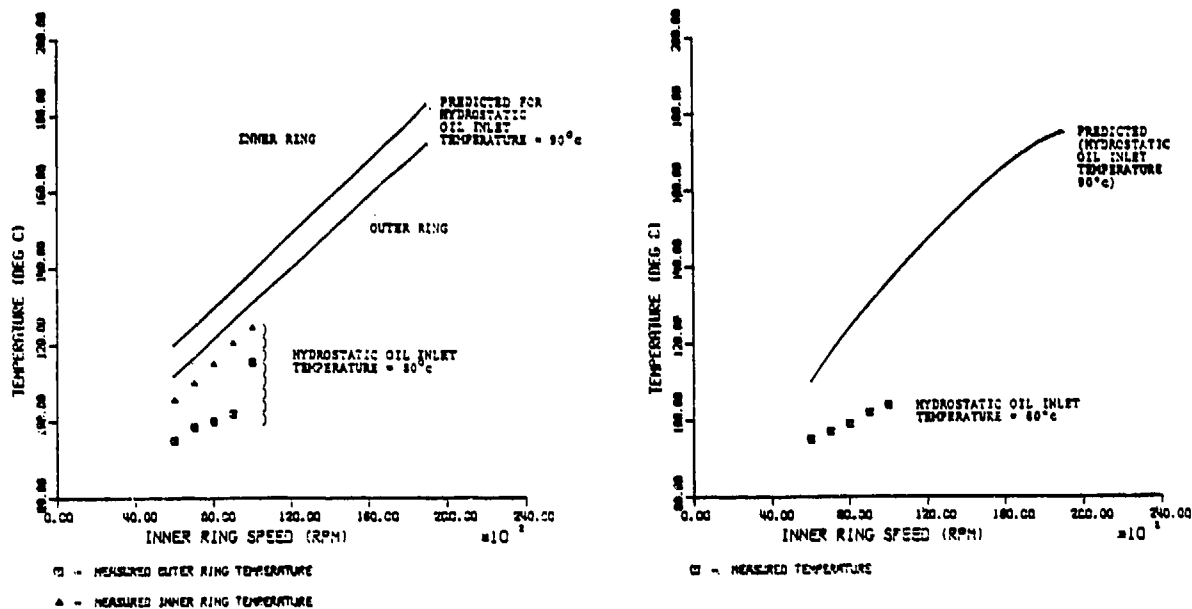
Figure 9(a) shows ring temperatures to speeds of 20 000 rpm (0.8 MDN) under a pure axial load of 4448 N (1000 lb). A peak temperature of 195° C is predicted for the inner ring, and 182° C for the outer ring. Both temperatures are well within the material and lubricant oxidation limits.

The bearing diametral clearance remains positive over the speed range investigated (fig. 10(a)). The predicted 0.01-mm loss is attributed to the rise in rolling-element temperature and rotation-induced radial growth of the inner ring. By comparison the 13° C temperature difference between inner and outer rings has a negligible effect (-0.005 mm) on operating clearance.³

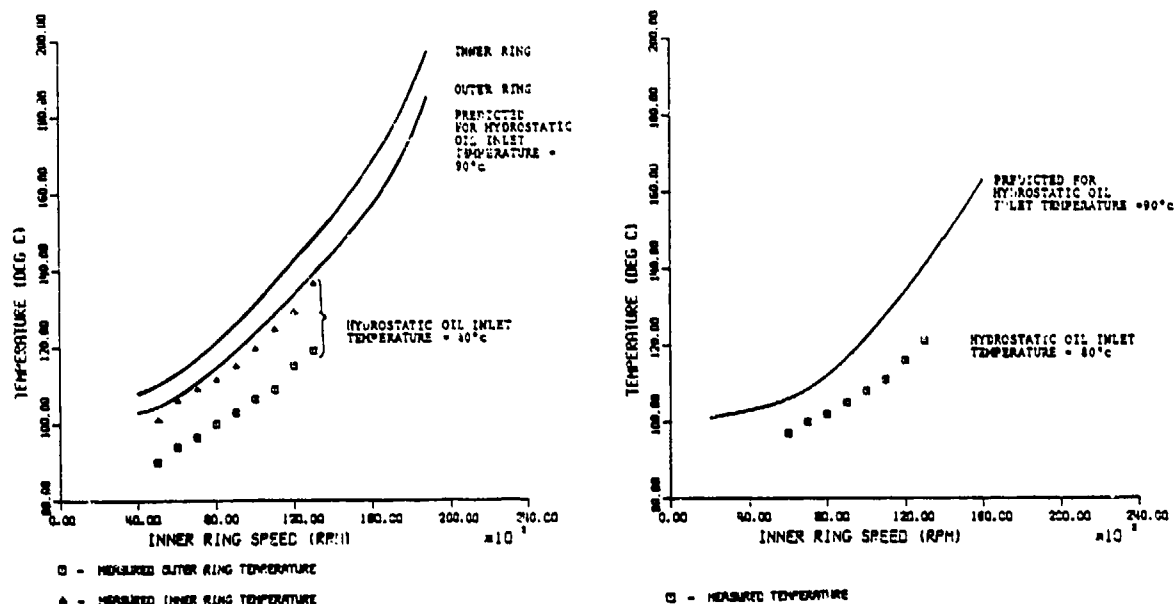
Film thickness increases 50 percent with speed at the inner ring and 30 percent at the outer ring (fig. 10(a)). The improvement is due to increased rolling velocity, since lubricant viscosity decreases with the higher temperatures encountered at higher shaft speeds.

Predicted ring temperatures under a pure radial load of 13 345 N (3000 lb) are shown in figure 9(b). Peak temperatures of 187° C at the inner ring and 176° C at the outer are achieved at 20 000 rpm. A stable temperature difference of 6° to 11° C is maintained over the entire speed range, and no indications of thermal seizure are seen.

³Inner- to outer-ring temperature difference is strongly dependent on the load-support system geometry and lubrication method. It is not likely to be a secondary effect in designs such as pillow blocks or grease lubricated spherical bearings.



(a) Results under 13 345-N (3000-lb) radial load.



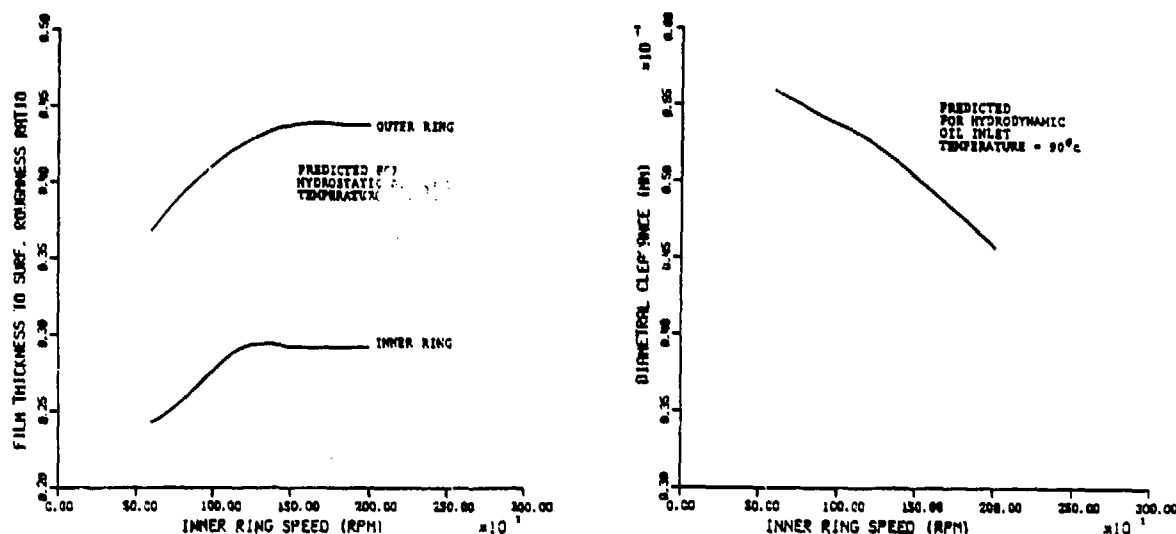
(b) Results under 4448-N (1000-lb) axial load.

Figure 9. - Component temperatures as function of speed to 20 000 rpm (0.8 MDN) under pure axial and pure radial loads.

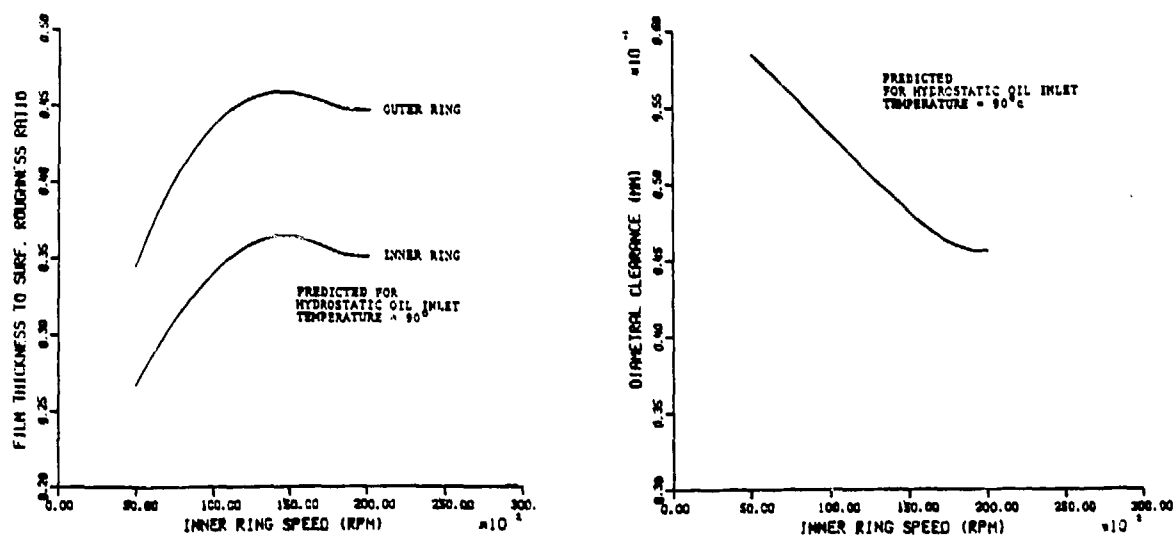
Bearing diametral clearance remains positive (fig. 10(b)), changing by 18 percent from its initial operating value of 0.056 mm at 6000 rpm. The clearance trend with speed is similar to the trend seen under pure axial load. Clearance change is primarily due to rotation-induced ring growth and heating of the rolling elements.

Film thickness to surface roughness ratio at each raceway increases by 20 percent with speeds to 10 000 rpm, then maintains a nearly constant value to 20 000 rpm (fig. 10(b)).

None of the predicted temperature data to 20 000 rpm were found to indicate a thermal or thermodimensional problem, which may limit the test bearing speed. Also, the predicted cage speed was found to be near epicyclic, indicating that skid would not be a problem.



(a) Results under 13 345-N (3000-lb) radial load.



(b) Results under 4448-N (1000-lb) axial load.

Figure 10. Effect of speed on film thickness and diametral clearance.

During the rig checkout, which followed later, output from the test bearing torque transducer would quit at elevated speeds under each load condition. Therefore, torque data are not available for comparison. The cause for instrument failure was found to be thermal seizure of the radial hydrostatic bearing. Figure 11 shows the program-predicted difference in the radial hydrostatic bearing inner- and outer-ring temperatures (nodes 15 and 17 in fig. 6). The hydrostatic bearing geometry can tolerate an approximately 50°C temperature difference between inner and outer rings before losing all clearance. Referring to figure 11, clearance will be lost, and, therefore, torque transducer output, within the anticipated test speed range.

Design Problem

The example which follows was chosen to demonstrate Spherbean's capability to model roller skew⁴ and its effect on bearing performance. Skew was first explored by Kellstrom (ref. 3), who addressed its mechanics and showed how it can effectively provide roller guidance.

⁴Skew refers to rotation of the roller about an axis extending radially outward from the bearing center.

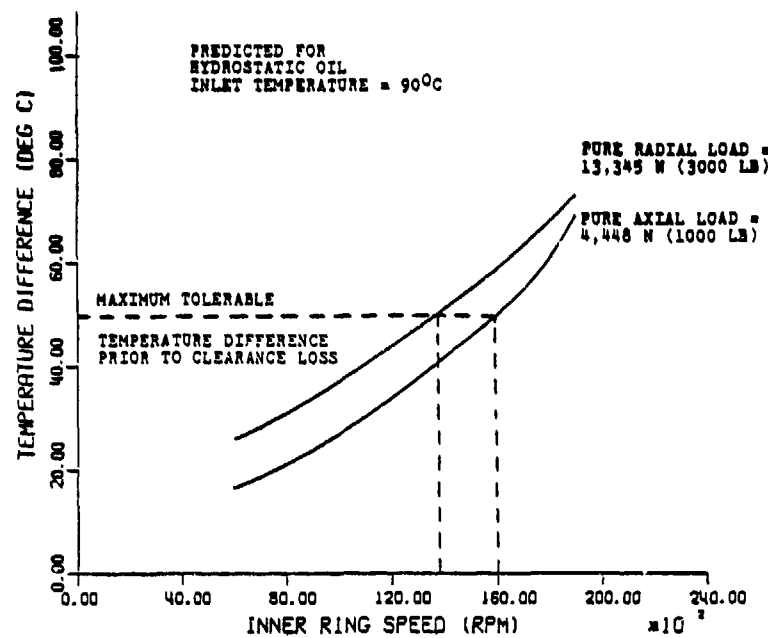


Figure 11. - Calculated temperature difference between inner and outer rings of radial hydrostatic bearings as function of speed.

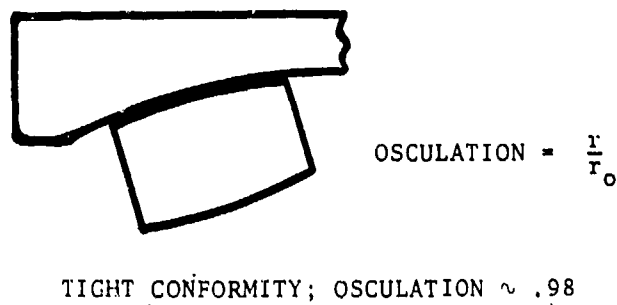
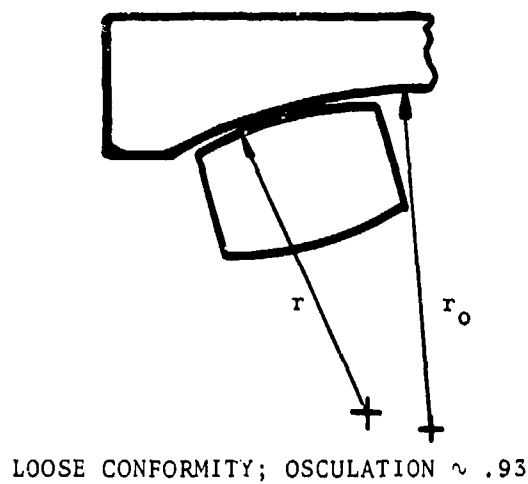


Figure 12. - Examples of loose and tight osculations (osculation = r/r_o).

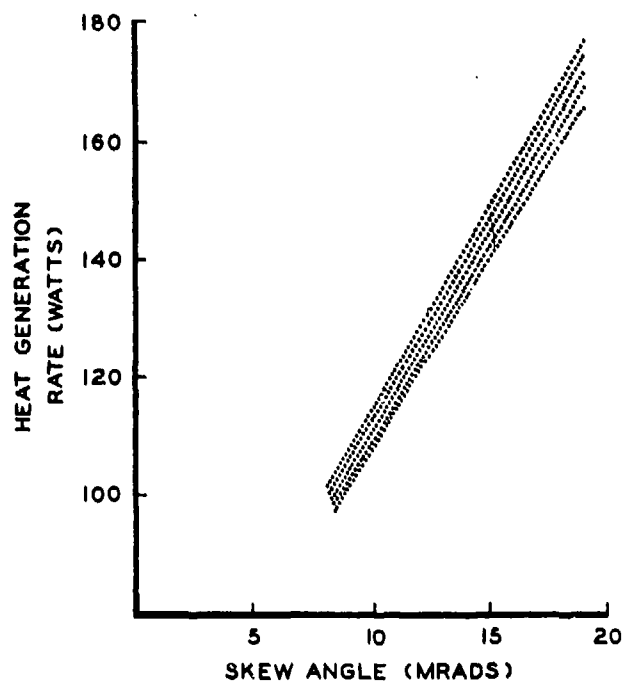


Figure 13. - Relationship between skew angle and power loss.

Skew is affected by several design parameters, including roller and raceway geometry. This is perhaps the simplest practical way to manipulate skew because roller and raceway geometries already receive particular attention during the design process. Currently, a designer may select the geometry only on the basis of contact stress. Geometry resulting in a "loose" conformity (fig. 12) results in a stress peak at the roller center; that resulting "tight" conformity distributes stress, but at the risk of high edge stresses. The designer selects a geometry, lying somewhere between these two extremes, that produces an optimum contact stress field. Thus, a design is achieved by assuming that contact performance is only a function of stress.

Spherbean gives the option of tapping into existing design reserves by exploring performance as a function of several variables. For example, roller-to-raceway sliding at points within the concentrated contact is responsible for 70 percent of the total heat generated by the bearing in the previous example. Power loss heats the bearing components, reduces lubricant effectiveness, and causes a loss of clearance. At very low speed power loss can have minimal effect on performance, but its effect is accentuated with increased speed, and ultimately limits the capability of the bearing.

The effect of roller skew on heat-generation rate was explored at 3000 rpm (0.12 MDN) by simulating bearing performance over a range of outer- and inner-raceway osculations⁵ from 0.94 to 0.97. Heat generation was found to increase 60 percent as skew angle increased from 7 to 19 mrad. (fig. 13). The lowest heat-generation rate was found for a combination of high osculation at the outer raceway (0.96) with low osculation at the inner raceway (0.94). The highest heat-generation rate was predicted for low outer- high inner-raceway osculations.

The practical significance of these results, assuming a design goal of a high-speed spherical roller bearing, can be seen in figure 13. A design reserve is tapped by lowering the heat-generation rate from 160 to 100 W. The computer designed bearing can operate at a 33 percent higher speed before generating the same 160 W as a bearing having off-optimum design.

⁵Osculation is the ratio of roller crown radius to raceway groove radius (fig. 12). Typical values lie between 0.93 and 0.98.

References

1. Harris, T. A.: The Effect of Misalignment on the Fatigue Life of Cylindrical Roller Bearings Having Crowned Roller Members, ASME J. Lubr. Techn., vol. 91, no. 2, April 1969, pp. 294-300.
2. Pirvics, J.: The Analysis of Thermal Effects in Rolling Element Bearing Load Support Systems. Proc. 6th Leeds/Lyon Symposium on Tribology at Lyon, Sept. 1979.
3. Kellstrom, E. M.: Rolling Contact Guidance of Roller in Spherical Roller Bearings. ASME Paper No. 79-LUB-23, 1979.
4. Weiland, W. P.; and Poesl, W.: State of the art in Spherical Roller Bearings. SAE Paper No. 790850, 1979.
5. Harris, T. A.; and Broschard, J. L.: Analysis of an Improved Planetary Gear—Transmission Bearing. ASME J. Bas. Eng., Sept. 1964, pp. 457-462.
6. Liu, J. Y.; and Chiu, Y. P.: Analysis of a Planet Bearing in a Gear Transmission System. ASME Paper No. 75-LUB-23.
7. Palmgren, A.: Ball and Roller Bearing Engineering. 3rd Ed., Burbank, 1959.
8. Harris, T. A.: Roller Bearing Analysis, Wiley Inc., 1966.
9. Kleckner, R. J.; and Pirvics, J.: SKF Computer Program SPHERBEAN—Volume I: Analysis. SKF Report No. AT81-D006 (NASA Contract No. NAS3-20824, NASA CR-165203), Jan. 1981.
10. Kleckner, R. J.; and Dyba, G.: SKF Computer Program SPHERBEAN—Volume II: User's Manual. SKF Report No. AT81-D007 (NASA Contract No. NAS3-20824, NASA CR-165204), Jan. 1981.
11. Kleckner, R. J.; Rosenlieb, J. W.; and Dyba, G.: SKF Computer Program SPHERBEAN—Volume III: Program Correlation with Full Scale Hardware Tests. SKF Report No. AT81-D008 (NASA Contract No. NAS3-20824, NASA CR-165205), Jan. 1981.
12. Rosenlieb, J. W.: Appendix A of reference 11, Full Scale Bearing Tests.
13. SKF Industries, Inc., Engineering Data Book, 1973.

Large-Bore Tapered-Roller Bearing Performance and Endurance to 2.4 Million DN

Richard J. Parker*

Tapered-roller bearings are being used in some helicopter transmissions to carry combined radial, thrust, and moment loads and, in particular, those loads from bevel gears such as high-speed input pinions. Tapered-roller bearings have greater load capacity for a given envelope or for a given bearing weight than the combinations of ball and cylindrical roller bearings commonly used in this application. Speed limitations have restricted the use of tapered-roller bearings to lower speed applications than ball and cylindrical roller bearings. The speed of tapered-roller bearings is limited to approximately 0.5 million DN (a cone-rib tangential velocity of approximately 36 m/sec (7000 ft/min) unless special attention is given to lubricating and designing the cone-rib/roller-large-end contact. At higher speeds, centrifugal effects starve this critical contact of lubricant.

Several means of supplying lubricant directly to this cone-rib contact were investigated at higher speeds (ref. 1). Results of that work indicate that the most successful means was to supply lubricant to the cone-rib contact through holes from the bore of the cone. Additionally, the radius of the spherical, large end of the roller was optimized at 75 to 80 percent of the apex length. Development of a large, high-speed tapered-roller bearing for a heavy-lift helicopter transmission was reported in reference 2.

The feasibility of tapered-roller bearings for the high-speed and nearly pure thrust-load conditions of turbine engine main-shaft bearings has been reported for large and small bores in references 3 and 4. Under these thrust-load-only conditions, speeds as high as 3.5 million DN have been attained (ref. 5). Life tests with these specially designed bearings at 3 million DN yielded an estimated experimental life of approximately three times the adjusted manufacturer's catalog life.

The use of computer programs can increase the capability of designing and analyzing tapered-roller bearings for such high-speed applications. These programs (described in refs. 6 and 7) take into account the difficulty of lubricating the contacts in high-speed tapered-roller bearings, and consider the effects of the elastohydrodynamic (EHD) films in these contacts. The effects of the EHD films in tapered-roller bearing contacts are discussed in reference 8. Experimental data at higher speeds are needed to verify the predictions of these computer programs.

Advanced helicopter transmissions which require the higher-speed capability of tapered-roller bearings also require higher temperature capability (ref. 2). Thus, materials with temperature capabilities higher than the conventional carburizing steels are required.

The objective of the research reported herein was to determine the operating characteristics and experimental life estimates for 120.65-mm (4.750-in.) bore tapered roller bearings of two designs under combined radial and thrust loads. A modified standard bearing design was tested at speeds up to 15 000 rpm. A computer-optimized, high-speed design was tested at speeds up to 20 000 rpm. Both designs were tested at a combined load of 26 700 N (6000 lb) radial load and 53 400 N (12 000 lb) thrust load.

Apparatus and Procedure

High-Speed Tapered-Roller Bearing Test Rig

The mechanical arrangement of the test rig is shown in figure 1 where one of the two test bearings is shown in a cutaway view. Thrust and radial loads are applied with hydraulic actuators. A

*NASA Lewis Research Center.

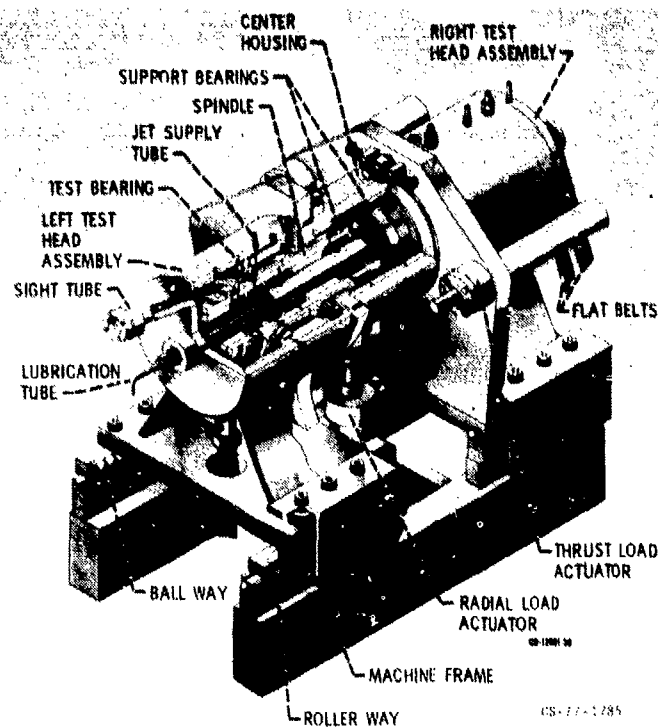


Figure 1. - Pictorial view of high-speed tapered roller bearing test rig.

flat-belt pulley system is used to drive the test spindle from a 93-kW (125-hp), 3600-rpm, 460-V, three-phase electric motor. Test spindle speeds are chosen by exchanging drive pulleys on the motor. The pair of flat belts is guided by an idler pulley arrangement which maintains controlled preload on the slack side of the belts.

The hollow spindle contains annular grooves on the inside diameter to distribute lubricant to radial holes for lubrication of the test bearings and the load bearings. A stationary lubrication tube delivers the desired lubricant flow to the annular grooves. For jet lubrication of the test bearings, two supply tubes are located 180° apart at the roller small end of each test bearing. The lubrication system, including pumps, filters, flowmeters, and load actuators, is described in detail in reference 9.

Thermocouples are installed for temperature measurements of each test bearing cup outer surface, each cylindrical load bearing outer ring, and oil inlet and outlet of both test and load bearings. Temperatures of the cone bore and cone face (fig. 2) on the drive end of the test spindle were measured with thermocouples and transmitted with an FM telemetry system. For the endurance tests, the cone-face temperature was measured with an infrared pyrometer aimed through an air-purged sight tube assembly.

The test rig vibration level is measured with piezoelectric accelerometers which automatically shut down the rig when vibration due to bearing failure exceeds a predetermined level. Chip detectors were located in the oil drain line from each test bearing for additional failure detection. Proximity probes measure shaft excursion in two planes as well as shaft speed and test bearing separator speed. A power meter was incorporated to monitor test rig power requirements. Preset safety flow switches and oil level switches were used to shut down the test machine in the event of lubrication system malfunction.

Test Bearings

Both designs of the tapered-roller test bearings had bores of 120.65 mm (4.750 in.). Other significant geometry and dimensions are given in table I.

The standard bearings were of catalog design with modified roller ends, which were ground to a spherical radius equal to 80 percent of the apex length. The cone was also modified with 40 oil holes, 1.02 mm (0.040 in.) in diameter, drilled through from a manifold on the cone bore to the undercut at

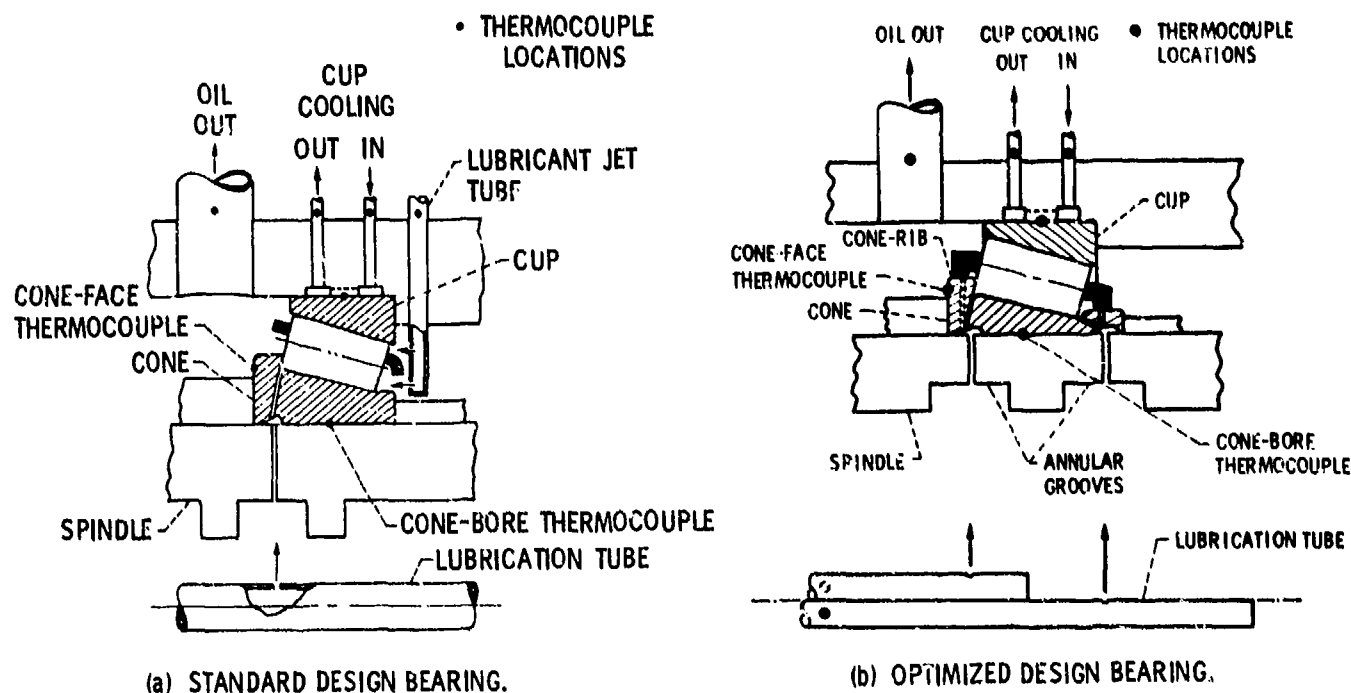


Figure 2. - Test bearing lubrication, cooling, and thermocouple locations.

TABLE 1. - TEST BEARING GEOMETRY

	Standard design	Computer-optimized design
Cup half angle	17°	15°53'
Roller half angle	1°35'	1°35'
Roller large end diameter, mm (in.)	18.29 (0.720)	18.29 (0.720)
Number of rollers	25	23
Total roller length, mm (in.)	34.17 (1.3452)	34.18 (1.3456)
Pitch diameter, mm (in.)	166.8 (6.569)	155.1 (6.105)
Bearing outside diameter, mm (in.)	206.4 (8.125)	190.5 (7.500)
Roller crown radius, mm (in.)	25.4x10 ³ (1000)	25.4x10 ³ (1000)
Roller spherical end radius, percent of apex length	80	80

the large end of the cone. The cage was silver-plated AISI 1010 steel, also of the standard roller riding design. Two groups of bearings of this design were used: one group was made from consumable-electrode, vacuum-melted (CVM) AISI 4320 steel, and the other from CVM CBS 1000M. Both were case carburized and finished to the specification shown in table II. The AISI 4320 material is representative of the conventional carburizing steels with high industrial usage. CBS 1000M is a material alloyed for hardness retention at temperatures to 589 K (600° F) for continuous service. Chemical compositions of the materials used for cups, cones, and rollers are shown in table III.

The selection of the computer optimized high-speed bearing design was based on bearing fatigue life, total heat generation, and cone-rib contact stress and heat generation at speeds to 20 000 rpm (ref. 10). Major differences from the standard bearing design were smaller cup angle, smaller pitch and outside diameters, and fewer rollers. The cage of the high-speed design bearing was made of silver-plated AISI 4340 and was designed to be guided by lands on the cone. The cone contained 48 oil holes, 1.02 mm (0.040 in.) in diameter at each end, drilled through from manifolds on the cone bore to the undercuts at each raceway end. In addition, six oil holes of the same size were drilled at each end to lubricate the cage-land riding surfaces.

Two material groups of high-speed design bearings were used. One group was made of case-carburized CVM CBS 1000M, and the other from through-hardened, double vacuum melted AISI

TABLE II. - TEST BEARING SPECIFICATION

	Standard design ^a	Computer optimized design (CBS 1000M) ^b
Case hardness, Rockwell C	58 to 64	58 to 64
Core hardness, Rockwell C	25 to 48	25 to 48
Case depth (to 0.5 percent carbon level after final grind), cm (in.):		
Cup and cone	0.086 to 0.185 (0.034 to 0.073)	0.061 to 0.185 (0.024 to 0.073)
Roller	0.091 to 0.201 (0.036 to 0.079)	0.091 to 0.201 (0.036 to 0.079)
Surface finish ^c , μm ($\mu\text{in.}$), rms:		
Cone raceway	0.15 (6)	0.10 (4)
Cup raceway	0.20 (8)	0.10 (4)
Cone rib	0.18 (7)	0.15 (6)
Roller taper	0.13 (5)	0.05 (2)
Roller spherical	0.15 (6)	0.08 (3)

^aIdentical specifications for both AISI 4320 and CBS 1000M bearings.

^bAISI M-50 bearings through-hardened to Rockwell C 61 to 63 and finished to the same specifications as the CBS 1000M bearings.

^cMeasured values.

TABLE III. - CHEMICAL COMPOSITION OF THE TEST BEARING MATERIALS

Alloying element, wt. %, (balance Fe)							
	C	Mn	Si	Cr	Ni	Mo	V
AISI 4320	0.17/0.23	0.45/0.65	0.20/0.35	0.40/0.60	1.65/2.00	0.20/0.30	-----
CBS 1000M	.12/0.16	.40/0.60	.40/0.60	.90/1.20	2.75/3.25	4.75/5.25	0.25/0.50
AISI M-50	.80/0.85	.15/0.35	.10/0.25	4.00/4.25	.10 max.	4.00/4.50	.90/1.10

M-50. (Double vacuum melting refers to vacuum induction melting followed by vacuum arc remelting or VIM-VAR). The specifications on hardness, case depth, and surface finishes for the CBS 1000M bearings are shown in table II. The AISI M-50 bearings were through-hardened to Rockwell C 61 to 63 and were ground and lapped to the same finishes as the CBS 1000M bearings.

Procedure

Performance tests. - The test procedure was adjusted according to the test conditions to be evaluated. Generally, a program cycle was defined that would allow the evaluation of a number of conditions without a major interruption. Test parameters such as load, speed, and oil inlet temperature were held constant while the tester was in operation. Lubricant flow rates were adjusted during operation. The test bearings were allowed to reach an equilibrium condition before data were recorded and the next test condition was sought.

Lubrication of the standard bearing was accomplished with a combination of cone-rib flow, through holes in the cone directly to the cone-rib roller-end contact, and jet flow at the roller small end (fig. 2(a)). For the high-speed design, all lubricant was supplied through holes in the cone at both ends of the roller and through the cage-riding lands (fig. 2(b)).

Life testing. - During life testing, the following data were recorded twice per day: test bearing cup and cone temperatures, support-bearing outer-ring temperature, lubricant in and out temperatures, lubricant flow rates to test bearings and support bearings, spindle rotational speed, spindle excursion, test rig vibration level, and load system pressures. Tests were run continuously until a failure was indicated or until a predetermined cutoff time of 1100 hr was reached. When one of the two bearings on test failed, the other was later mated with another suspended bearing and continued on test until failure or the 1100-hr cutoff.

The test conditions for these life tests are given in table IV. During initial testing with the standard bearings, superficial surface peeling failures occurred rather than spalling fatigue failures. Several changes in lubricant temperatures and flow rates were made, as will be discussed in a later section. The conditions listed in table IV are those used in subsequent tests, where the peeling failures no longer occurred.

TABLE IV. - LIFE TEST CONDITIONS

	Standard design	Computer-optimized design
Spindle speed, rpm	12 500	18 500
Thrust load, N (lb)	53 400 (12 000)	53 400 (12 000)
Radial load, N (lb)	26 700 (6000)	26 700 (6000)
Lubricant flow rate, m ³ /min (gal/min):		
Jet at small end	0.0076 (2.0)	0
Through cone, small end	0	0.0055 (1.45)
Through cone, large end	0.0038 (1.0)	0.0055 (1.45)
Cup cooling flow rate, m ³ /min (gal/min)	0.0019 (0.5)	0.0023 (0.6)
Lubricant-in temperature, K (°F)	350 (170)	355 (180)
Average cup temperature, K (°F)	391 (245)	419 (295)
Average cone face temperature, K (°F)	391 (245)	425 (305)

Results and Discussion

Performance Tests with Standard Design Bearing

The modified standard design bearing was tested over a range of speeds, loads, lubricant flow rates, and temperatures. Lubricant was delivered to the bearing either by jets (jet lubrication) or through holes in the cone (cone-rib lubrication).

Test spindle speeds were 6000, 10 000, 12 500, and 15 000 rpm. Thrust load was varied from 26 700 to 53 400 N (6000 to 12 000 lb); radial load was varied from 13 300 to 26 700 N (3000 to 6000 lb). Lubricant flow rate was varied from 1.9×10^{-3} to 15.1×10^{-3} m³/min (0.5 to 4.0 gal/min). When cone-rib lubrication was used a constant 3.8×10^{-3} m³/min (1.0 gal/min) of jet flow was also used to assure some lubrication of the roller small end. The lubricant was a 5-cS neopentylpolyol tetraester (MIL-L-23699).

The results of these tests are discussed in detail in reference 9. Briefly, it was shown that increasing speed resulted in increased bearing temperatures and power loss. Increased lubricant flow rate decreased bearing temperature, but increased heat generation. The effect of load on bearing temperatures was very small relative to speed and flow rate effects. Increasing oil-in temperature from 350 to 364 K (170° to 195° F) increased bearing temperature approximately 7 to 10 K (12° to 18° F).

Of greatest significance in these tests was the improvement in bearing performance with cone-rib lubrication compared with jet lubrication. The effect of shaft speed on cone-face temperature is shown in figure 3 for an oil-in temperature of 350 K (170° F). Increasing the shaft speed from 6000 to 15 000 rpm increases cone-face temperature by as much as 49 K (89° F). Shaft speed has a lesser effect on cone-face temperature where cone-rib lubrication is used rather than jet lubrication. It is apparent that extrapolation of the data in figure 3(a) to 15 000 rpm for jet flow rates less than 7.6×10^{-3} m³/min (2.0 gal/min) at 350 K (170° F) oil-in temperature would give cone-face temperatures in excess of 430 K (320° F)—where previous tests had indicated that failure of the cone-

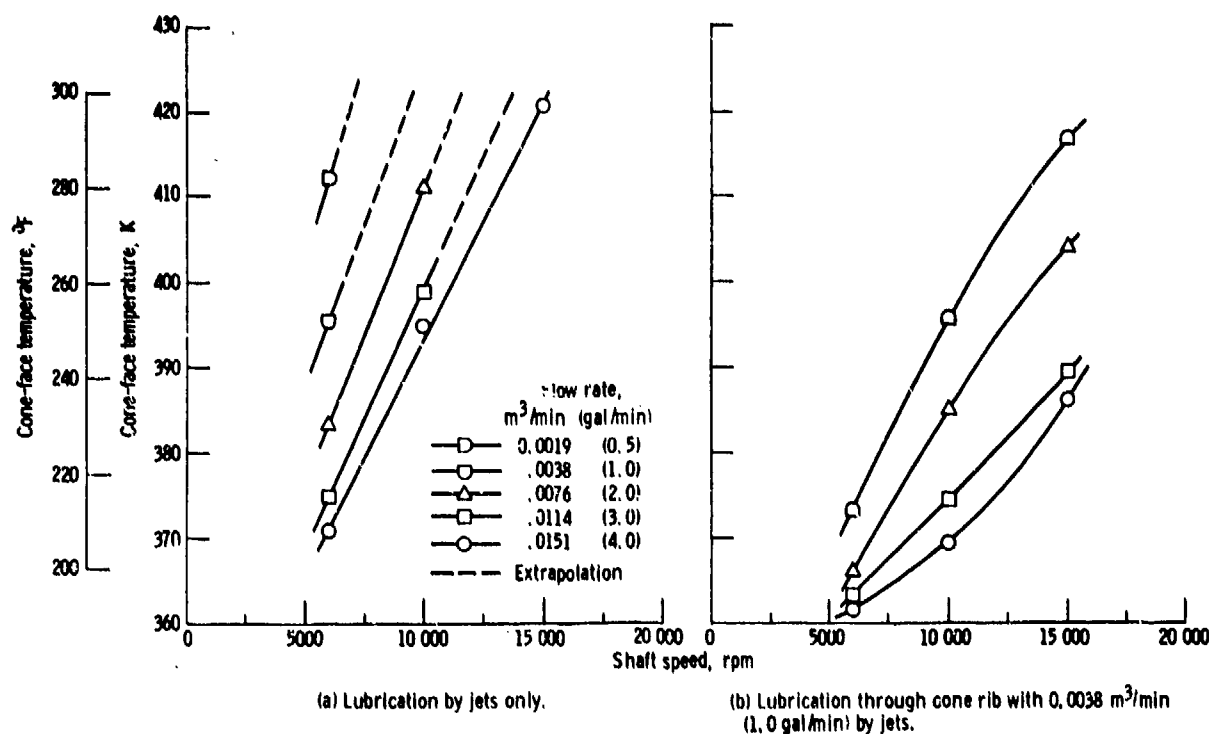


Figure 3. - Effect of shaft speed and flow rate on cone-face temperature.
Oil-in temperature, 350 K (170° F); thrust load, 53 400 N (12 000 lb);
radial load, 26 700 N (6000 lb).

rib would occur. For lubrication through the cone-rib (with $3.8 \times 10^{-3} m^3/min$ (1.0 gal/min) jet flow), satisfactory cone-face temperatures were obtained at 15 000 rpm with total flow rates as low as $5.7 \times 10^{-3} m^3/min$ (1.5 gal/min) (fig. 3(b)).

The advantage of cone-rib lubrication is further illustrated in figure 4. The difference in the temperature of the cone-face with jet lubrication and that with cone-rib lubrication increases with shaft speed. At 15 000 rpm the difference is 34 K (62° F). Even at the lower speed of 6000 rpm, the temperature improvement is an average 13 K (23° F).

It was observed that when cone-rib lubrication is used, the highest bearing temperature measured at each condition is at the cup outer surface. When jet lubrication alone is used, the highest measured temperatures were on the cone face. This effect is illustrated in figure 5 where the temperatures are plotted against shaft speed for an oil-in temperature of 364 K (195° F) and a total oil flow of $11.4 \times 10^{-3} m^3/min$ (3.0 gal/min). Cone-bore and oil-out temperatures for jet lubrication and for cone-rib lubrication are not significantly different.

It is believed that, when cone-rib lubrication is used, less oil is thrown centrifugally outward to cool the cup before it leaves the bearing. Also, the oil that is directed through the cone-rib and does contact the cup has been heated somewhat in cooling the cone rib. Thus, a somewhat greater cup temperature has accompanied a cooler cone rib, but because of the critical nature of the cone-rib contact in high-speed tapered roller bearings, this small sacrifice appears justified.

The higher cup temperatures may be decreased with the use of cup cooling oil flowing in the cup housing in contact with the outer surface of the cup. Figure 6 includes some additional temperature data obtained at a shaft speed of 12 500 rpm and $5.7 \times 10^{-3} m^3/min$ (1.5 gal/min) total oil flow (cone-rib flow of $1.9 \times 10^{-3} m^3/min$ (0.5 gal/min) plus jet flow of $3.8 \times 10^{-3} m^3/min$ (1.0 gal/min). With the addition of $2.6 \times 10^{-3} m^3/min$ (0.7 gal/min) cup cooling flow (solid symbols in fig. 6), the cup outer surface temperature is decreased 14 K (25° F) without significant change in cone-face and cone-bore temperatures. Oil-out temperature was 6 K (11° F) lower because of the quantity of heat removed by the 364 K (195° F) cup cooling oil, which was measured at 380 K (225° F) upon exit from the cooling passages.

The heat generated in the bearing is dissipated in the form of heat by conduction to the lubricant and by conduction, convection, and radiation to the surrounding environment. Lubricant outlet

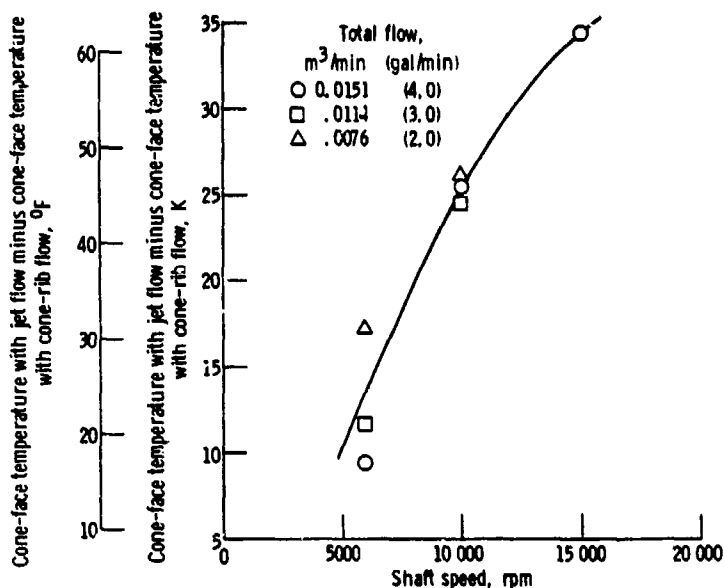


Figure 4. - Effect of shaft speed on cone-face temperature with jet lubrication minus that with cone-rib lubrication. Oil-in temperature, 350 K (170° F); thrust load, 53 400 N (12 000 lb); radial load, 26 700 N (6000 lb).

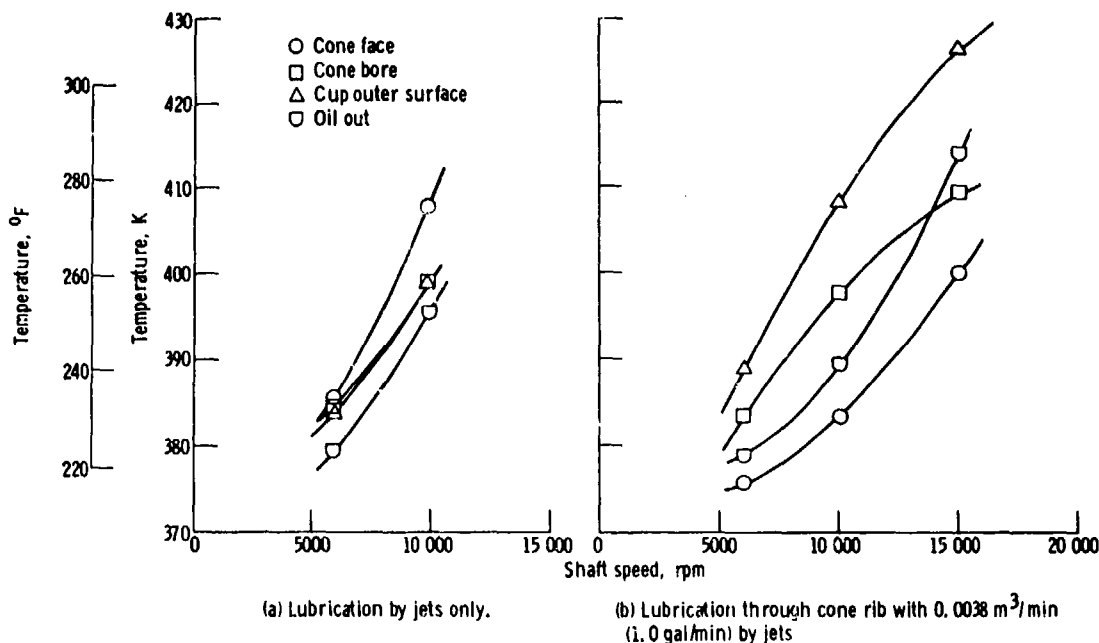


Figure 5. - Effect of jet lubrication and cone-rib lubrication on bearing and oil-out temperatures. Oil-in temperature, 364 K (195° F); total oil flow rate, 0.0114 m³/min (3.0 gal/min); thrust load, 53 400 N (12 000 lb); radial load, 26 700 N (6000 lb).

temperature from the bearing was measured for all conditions of flow. Heat transferred to the lubricant was calculated using the standard heat-transfer equation:

$$Q_T = MC_P(t_{out} - t_{in}) \quad (1)$$

where

Q_T total heat transfer to lubricant, J/min (Btu/min)

M lubricant mass flow, kg/min (lb/min)

c_p specific heat, J/kg K (Btu/lb °F)
 t_{out} oil outlet temperature, K (°F)
 t_{in} oil inlet temperature, K (°F)

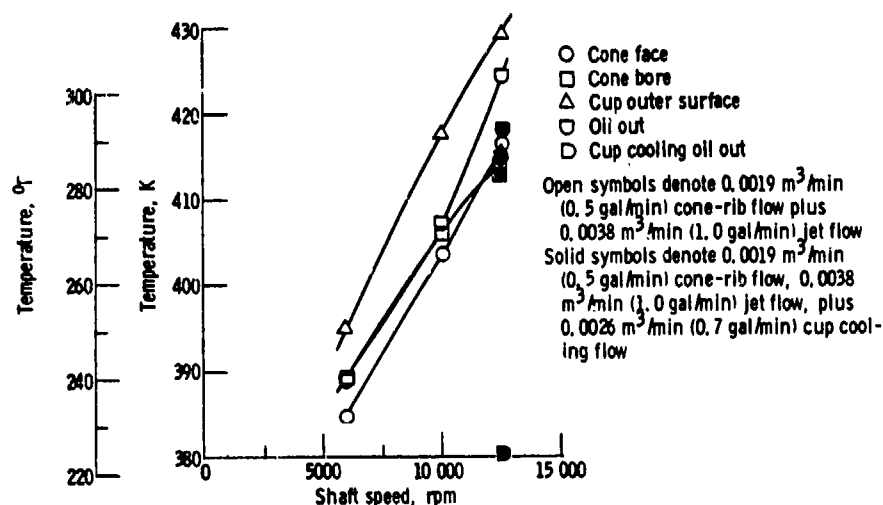


Figure 6. - Effect of cup cooling on bearing and oil-out temperatures. Oil-in temperature, 364 K (195° F); thrust load, 53 400 N (12 000 lb); radial load, 26 700 N (6000 lb).

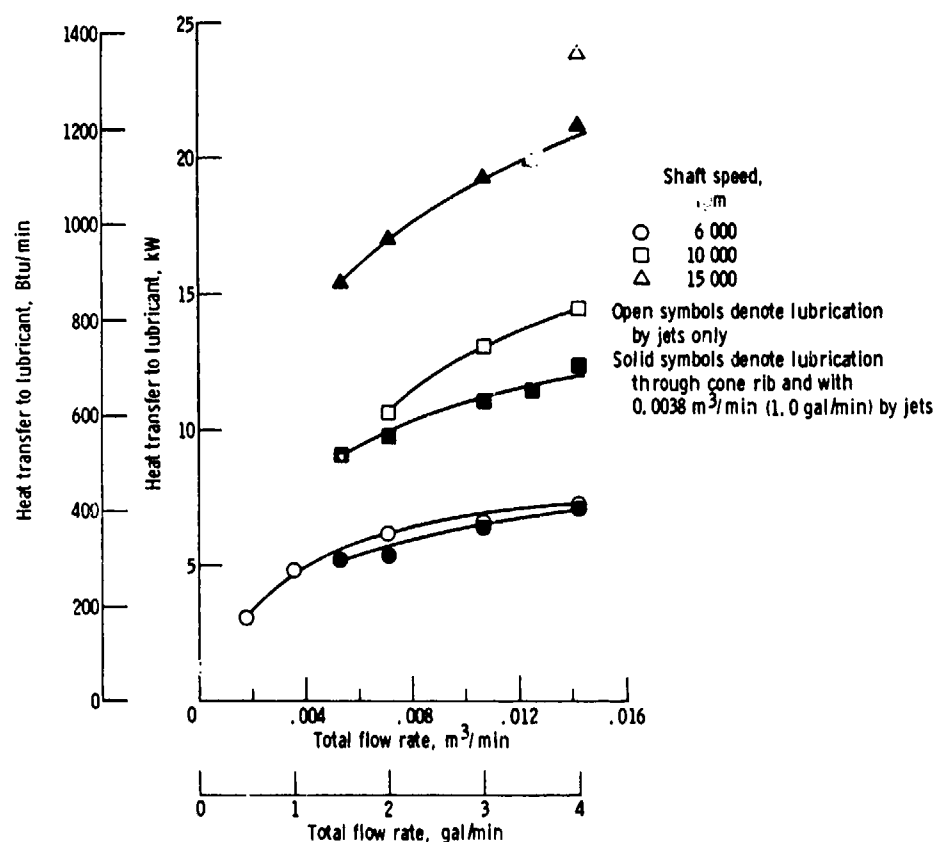


Figure 7. - Heat transferred to lubricant as function of total flow rate. Oil-in temperature, 350 K (170° F); thrust load, 53 400 N (12 000 lb); radial load, 26 700 N (6000 lb).

The result of these heat-transfer calculations are shown in figure 7 as a function of shaft speed and total flow rate. (For convenience, heat values were converted from J/m² to kW.) The heat transferred to the lubricant increases with both increased shaft speed and increased lubricant flow rate. These increases are expected because of increased lubricant drag or churning. These heat quantities are a portion of the heat generated in the test bearings and do not include heat transferred from the bearing by conduction, convection, and radiation. At higher bearing temperatures, the heat transferred by these latter forms should become a greater portion of the total.

Lower heat generation is observed with cone-rib lubrication than with jet lubrication at the same flow rates. The effect is greater at higher total flow rates and higher speeds.

Performance Tests with Computer Optimized Design Bearing

The computer optimized design bearing was tested over the same load and lubricant flow rate conditions as the standard bearing. The optimized design bearing was run at speeds to 20 000 rpm, whereas the standard bearing was limited to 15 000 rpm.

Similar trends were observed with the optimized design bearing and the standard design bearing; that is, bearing temperature and heat generation increased with increased shaft speed. Also, with increased lubricant flow rates, bearing temperatures decreased and heat generation increased. More detailed discussion of these results can be found in reference 10.

The improvement in performance of the computer-optimized design bearing was assessed by comparing temperature and heat generation with the two designs at identical conditions. Although lubricant to the standard bearing was directed through holes in the large end of the cone to the cone-rib surface, lubricant at the small end was through a pair of jets directed at the small end of the rollers. Comparisons herein were made with equal flow rates for both bearings at both the large end and the small end. At the small end, a constant rate of 3.8×10^{-3} m³/min (1.0 gal/min) was used, and oil was fed through jets for the standard design and through the cone small end for the high-speed design.

Materials with higher temperature capabilities were used for the computer-optimized design bearings. Cups, cones, and rollers were made of CBS-1000M, and the cage was of AISI 4340. The standard design bearing had AISI 4320 cups, cones, and rollers and AISI 1010 cages.

In figure 8 cone-face temperatures of the two bearing designs are compared. The data symbols are used to identify the curves at each flow rate. At 15 000 rpm the optimized design bearing operates 8 to 11 K (15° to 20° F) cooler than the standard design. The improvement at 6000 rpm is much less.

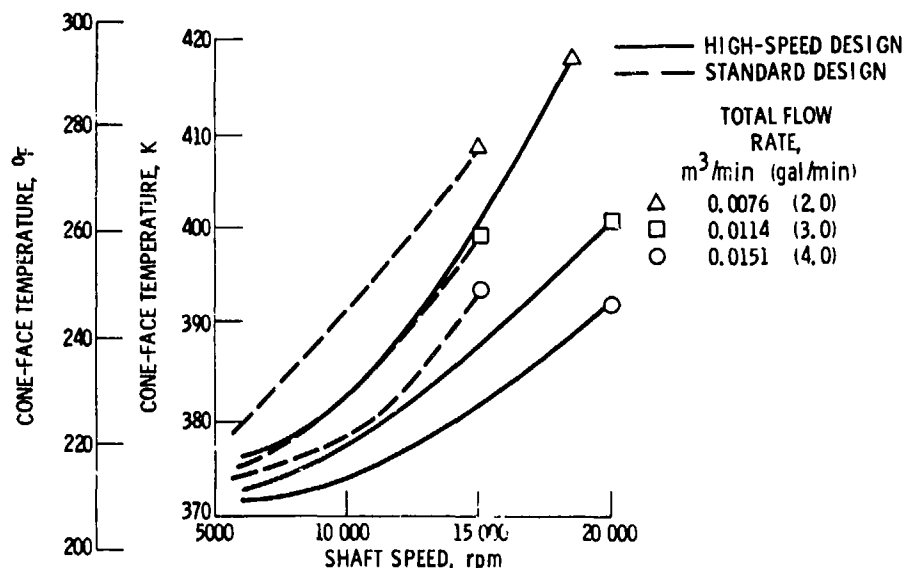


Figure 8. - Cone face temperature with optimized design compared with that with standard design. Oil-in temperature, 364 K (195° F); small end flow rate, 0.0038 m³/min (1.0 gal/min); thrust load, 53 400 N (12 000 lb); radial load, 26 700 N (6000 lb).

The cup outer-surface temperature is also lower for the optimized design bearing as shown in figure 9. Here, the improvement is slightly less than that at the cone face.

Figure 10 compares data for the standard and optimized design bearings showing heat transferred to the lubricant at 6000 and 15 000 rpm. The optimized design bearing has lower heat generation, as represented by heat transferred to the lubricant, than the standard design bearing at both speeds. As shown in figure 11, the improvement with the optimized design is approximately 16 percent throughout the range of 6000 to 15 000 rpm.

Life Tests with Standard Design Bearings

Life testing was initiated with standard design bearings of AISI 4320 material at 12 500 rpm, a thrust load of 53 400 N (12 000 lb) and a radial load of 26 700 N (6000 lb). Lubricant flow rates were a cone-rib flow rate of $1.9 \times 10^{-3} \text{ m}^3/\text{min}$ (0.5 gal/min), a jet flow rate of $3.8 \times 10^{-3} \text{ m}^3/\text{min}$ (1.0 gal/min), and a cup cooling flow rate of $2.6 \times 10^{-3} \text{ m}^3/\text{min}$ (0.7 gal/min). The lubricant-in temperature was 366 K (200° F). These conditions were selected to maintain cup and cone temperatures less than 422 K (300° F), based on results of the performance tests with identical bearings previously discussed. Measured cup and cone temperatures ranged from 416 to 422 K (290° to 300° F) in these initial tests.

Peeling surface distress.— Inspection of the test bearings from the first two tests, which were stopped due to test facility malfunction and support bearing failure after 330 and 569 hr, revealed that a shallow surface distress was occurring on the raceway and roller taper surfaces. This type of distress is called peeling (ref. 11) and appears as a very shallow area of uniform depth. Typical peeled areas in these bearings, approximately 0.008 mm (0.0003 in.) deep, are shown in figure 12. The peeling tended to initiate at minor surface defects such as the deeper surface scratches or indentations.

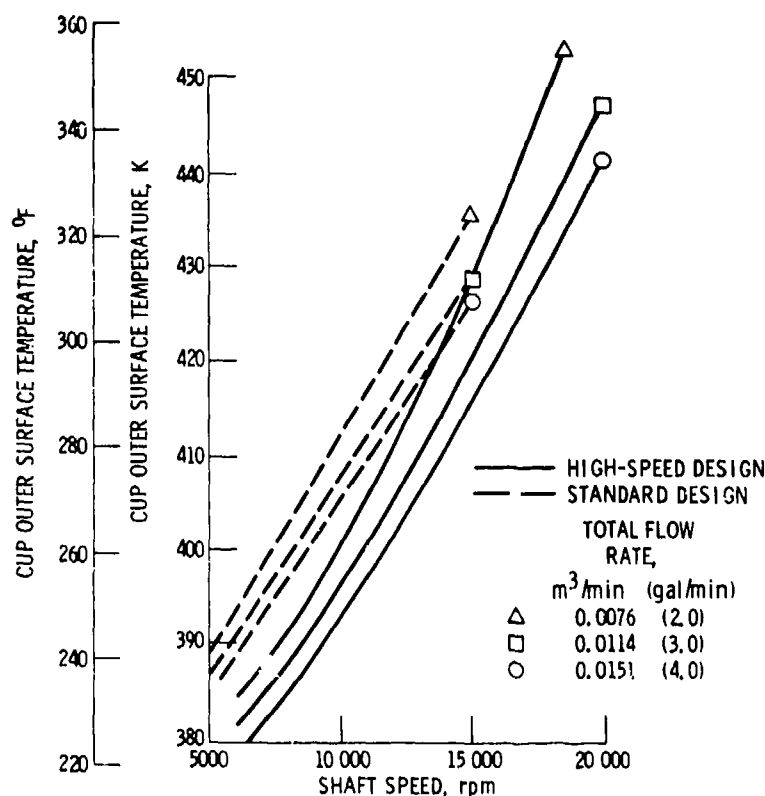


Figure 9. - Cup outer surface temperature with optimized design compared with that with standard design. Oil-in temperature, 364 K (195° F); small end flow rate, $0.0038 \text{ m}^3/\text{min}$ (1.0 gal/min); thrust load, 53 400 N (12 000 lb); radial load, 26 700 N (6000 lb).

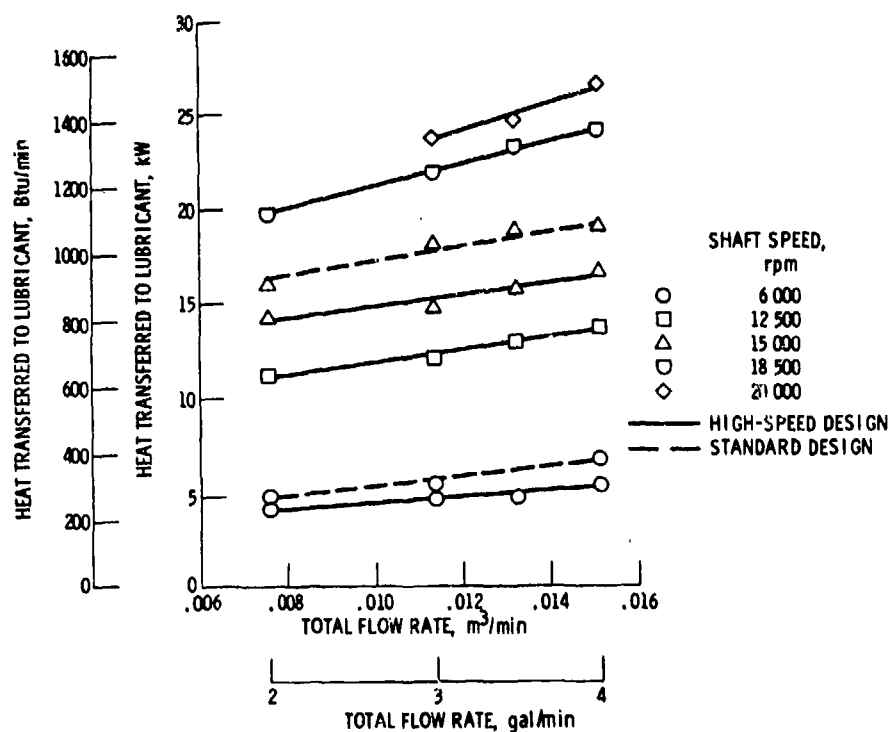


Figure 10. - Heat transferred to lubricant as function of total flow rate with optimized design. Oil-in temperature, 364 K (195° F); small end flow rate, 0.0038 m³/min (1.0 gal/min); thrust load, 53 400 N (12 000 lb); radial load, 26 700 N (6000 lb).

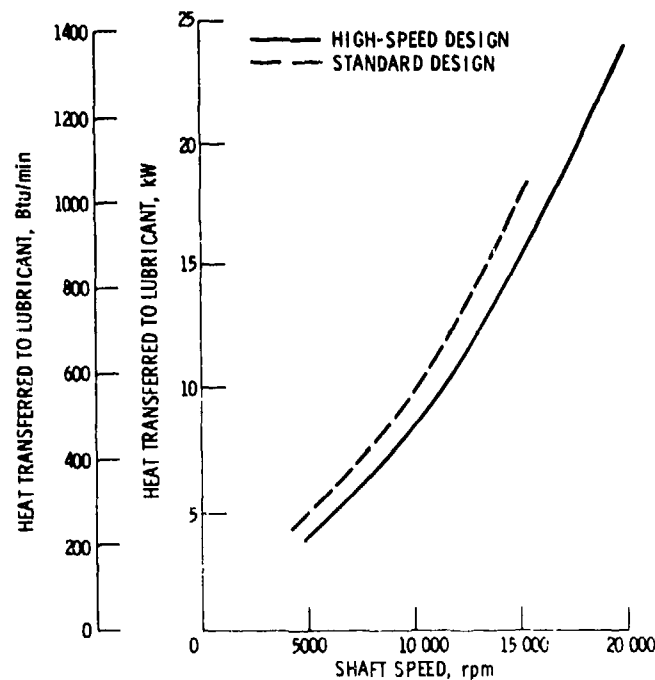


Figure 11. - Heat transferred to lubricant as function of shaft speed. Oil-in temperature, 364 K (195° F); small end flow rate, 0.0038 m³/min (1.0 gal/min); large end flow rate, 0.0076 m³/min (2.0 gal/min); thrust load, 53 400 N (12 000 lb); radial load, 26 700 N (6000 lb).

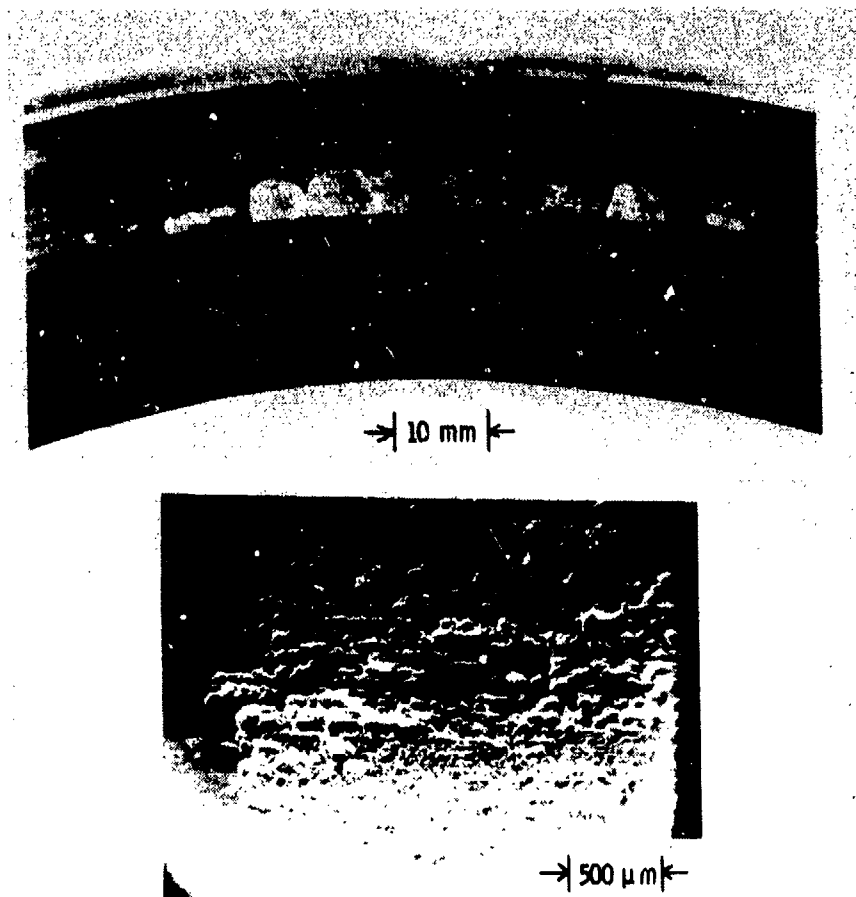


Figure 12. - Peeling failure on cup raceway surface after 569 hr with standard design bearing run at 12 500 rpm.

The peeling also tended to be concentrated near the axial center of the raceways and roller with a slight bias toward the roller large end. This effect may be expected since the rollers are slightly crowned and the contact stress is somewhat higher in the center of the raceway. Profile traces across the raceways and along the roller tapers of the initial test bearings revealed that the roller crown radius had been decreased to approximately one-third of its original value. Further stress concentration occurred at the center of the roller and aggravated the peeling. This exaggerated crown is attributed to material growth caused by an uneven transformation of retained austenite to martensite (refs. 2 and 12).

The major cause of peeling type surface distress is believed to be due to an inadequate lubricant film parameter, Λ , which is the ratio of the elastohydrodynamic (EHD) film thickness in the roller-raceway contact to the composite surface roughness. The composite surface roughness is the square root of the sum of the squares of the rms roughnesses of the two surfaces.

Lubricant flow rates and lubricant-in temperature were varied to improve the EHD film thickness conditions. Cup and cone temperatures were reduced to less than 394 K (250° F), but the peeling failures continued to occur. Identical tests were also run with CBS 1000M bearings, and the results were similar.

Improved surface finish. - Further reduction of bearing temperatures to improve the lubricant film parameter was considered to be impractical since lower lubricant-in temperatures would not be representative of helicopter transmissions and a further increase in flow rate would not result in significantly lower bearing temperatures (ref. 9). The alternative means of increasing the film parameter is improving the surface roughness of the raceways and/or rollers. The remaining untested bearings were returned to the manufacturer where the raceways and roller tapers were honed to improve the surfaces from the values given in table II to $0.10 \mu\text{m}$ ($4 \mu\text{in.}$) or better. After honing, the measured roughness of the raceways and roller tapers was typically 0.09 and $0.06 \mu\text{m}$ (3.5 and $2.5 \mu\text{in.}$), respectively. Also, the number of deeper surface scratches appeared to be minimized.

After honing, the bearings were reassembled, and testing was resumed at previous conditions selected to maintain bearing temperatures at 394 K (250° F) or less. A shutdown for test bearing inspection after 640 hr revealed no peeling or distress on any surface of the bearings. The life test conditions were thus established for the remaining tests with the standard bearings of both materials. A summary of the effect of the lubricant film parameter on peeling surface distress is shown in table V.

Life tests at 12 500 rpm. — The remaining test bearings of both materials, after rehoning, were run at the test conditions shown in table IV. Twelve bearings of the AISI 4320 material ran to the 1100-hr cutoff without failure of any type. At these conditions the rated catalog life of this bearing design is 102 hr, so that the experimental 10-percent life is greater than 10 times the catalog life. (The 10-percent life is the life within which 10 percent of the bearings can be expected to fail by rolling-element fatigue spalling; this 10-percent life is equivalent to a 90-percent probability of survival.)

Sixteen rehoned bearings of the CBS 1000M material were run to spalling fatigue failure or to the 1100-hr cutoff. Twelve of the bearings ran to 1100-hr without failure. Three bearings experienced spalls on the cup or cone raceways. One bearing was suspended at 820 hr without spalling failure, because it had received surface damage on the cone-rib due to an obstruction in a lubricant orifice. These data are plotted on Weibull coordinates according to the procedures of reference 13 in figure 13. A least-squares line drawn through the three failure points shows an estimated 10-percent life of approximately 600 hr, or about six times the rated catalog life.

A comparison of the results with the two materials shows that the CBS 1000M bearing life is less than the AISI 4320 bearing life. However, a quantitative estimate of the difference is not possible

TABLE V. — EFFECT OF LUBRICANT FILM PARAMETER ON PEELING OF
TAPERED-ROLLER BEARING RACEWAY

Bearing temperatures, K (°F)	Surface roughness, μm ($\mu\text{in.}$)			Calculated film thickness μm ($\mu\text{in.}$)	Film param- eter	Result
	Raceway	Roller	Composite			
416 (290)	0.15 (6)	0.13 (5)	0.20 (7.8)	0.28 (11)	1.4	Peeling
391 (245)	.15 (6)	.13 (5)	.20 (7.8)	.38 (15)	1.9	Peeling
391 (245)	.09 (3.5)	.06 (2.5)	.11 (4.3)	.38 (15)	3.5	No Peeling

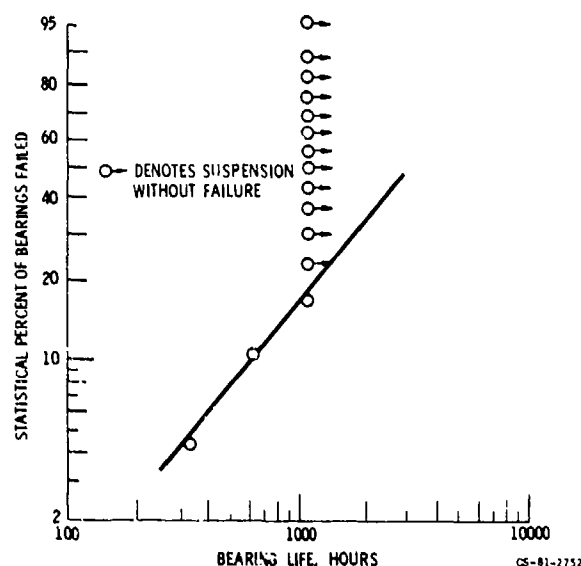


Figure 13. — Rolling-element fatigue life of standard design CBS1000M tapered-roller bearings at 12 500 rpm. Thrust load, 53 400 N (12 000 lb); radial load, 26 700 N (6000 lb); bearing temperature, 394 K (250° F).

from these results since no fatigue failures occurred with the AISI 4320 bearings. Metallurgical analysis of the CBS 1000M bearings revealed that the cup and cone materials had coarser than desired grain structure. These bearings were made from the first large heat of the material and were exposed to forging temperatures later found to be excessive. Recent knowledge in forging and heat treating this material should provide a more desirable structure for better rolling-element fatigue life.

Life Tests with High-Speed Design Bearings

AISI M-50 bearing tests.—Life testing with the computer-optimized, high-speed-design, tapered-roller bearings was initiated with the AISI M-50 bearings at 18 500 rpm. The externally applied load was identical to that for the standard design bearings. Under these load and speed conditions, the rated catalog life of this bearing design is 46 hr. Lubricant flow rates and temperatures are shown in table IV.

Five pairs of the AISI M-50 bearings were run at these conditions. Two tests (four bearings) were stopped after 36 and 283 hr because of failures in the lubrication system. Another pair of bearings ran to the 1100-hr cutoff without failure. Another test was stopped after 106 hr because of a test rig malfunction, and upon inspection of the test bearings, a very small spall was found on one of the rollers.

After 188 hr, the other test was stopped because of severe rig vibrations. Disassembly revealed that both test bearings had cracked cones. One cone had cracked entirely through the cone section. The crack in the other cone was entirely contained in the load zone of the raceway.

The cone of bearing serial number 78-9 was subsequently cut partially through and fractured at that location to reveal the crack. The extent of the crack is shown in figure 14. The dimensions are approximately 9.5 mm (0.37 in.) long and 1 mm (0.04 in.) deep.

The cone of bearing serial number 78-10, with the complete fracture is shown in figure 15. Initial crack dimensions were observed to be approximately 22 mm (0.87 in.) long and 6 mm (0.24 in.) deep.

Fatigue spalling was noted on both cone raceways adjacent to the cracks. It is believed that the fatigue cracks, related initially to the spalling process, propagated at an accelerated rate because of the presence of the superimposed high-hoop tensile stress field in the cones. In the case of bearing serial number 78-10, the crack propagated to its critical value and destructive fracture occurred. Fortunately, the test rig was shut down before complete fragmentation of the cone occurred. The crack in bearing serial number 78-9, although at an advanced stage, had not yet reached the critical fracture stage.

The average tangential tensile hoop stress, based on the assumption of thin rings, was estimated for the 18 500-rpm condition to be approximately 0.145 GPa (21 000 psi). This calculated stress also includes effects of the cone-shaft interference fit. This stress is at the lower end of the range where in references 14 and 15 it was shown that the critical crack size can readily be reached in through-hardened AISI M-50 and that fracture of inner races (or cones in the case of tapered roller bearings) is probable.



Figure 14. - Photomicrograph of cone raceway crack on AISI M-50 bearing serial number 78-9 after 188 hr of operation at 18 500 rpm.



Figure 15. - Fractured cone of AISI M-50 bearing serial number 78-10 after 188 hr of operation at 18 500 rpm.

These results indicate that the use of a through-hardened material such as AISI M-50, to accommodate high temperatures in high-speed tapered-roller bearing applications involves risk of catastrophic fracture of the cone similar to that for ball bearing inner rings at high speeds (ref. 16). It is apparent that materials for high-speed tapered-roller bearings must have higher fracture toughness such as that associated with case-hardened materials.

CBS 1000M bearing tests. - Five computer optimized, high-speed-design tapered-roller bearings made of case-carburized CBS 1000M material were also life tested at conditions identical to those of the AISI M-50 bearings. Four of these bearings ran to the 1100-hr cutoff time without failure. One bearing suffered a severe failure after 135 hr as a result of failure detection and shutdown-system malfunction. The extent of damage was too great to determine the cause of the failure. However, close observation revealed two spalls in the cone raceway. The largest spall is shown in figure 16. No cracks or fracture of the cone was observed, although considerable damage to the raceway, cone rib, and cage occurred. This result offers some evidence that a high-temperature, case-carburized material such as CBS 1000M can resist fracture or cracking at conditions of high tensile hoop stress after spalling and significant cone raceway damage occurs.

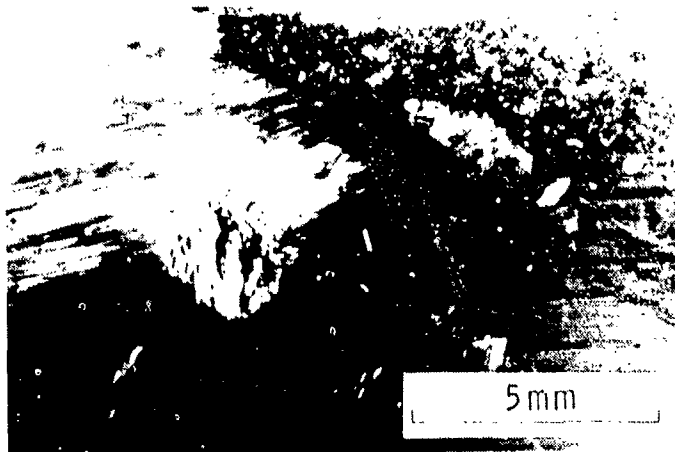


Figure 16. - Fatigue spall on cone raceway of CBS-1000M bearing serial number 76-17 after 135 hr of operation at 18 500 rpm.

Too few bearings were run at these conditions, because of their availability, to obtain a reasonable statistical estimate of the rolling-element fatigue life. However, because four of the five bearings survived the 1100-hr cutoff (24 times rated catalog life) this bearing design/material combination does show promise for future high-speed tapered-roller bearing applications.

Summary of Results

The performance and endurance life of 120.65-mm (4.75-in.) bore tapered-roller bearings of two designs were investigated under heavy combined radial and thrust loads. Performance tests were run to 15 000 rpm with the modified standard design bearing and to 20 000 rpm with the computer-optimized design bearing. Temperature distribution and bearing heat generation were determined as functions of shaft speed, radial and thrust loads, lubricant flow rate, and lubricant inlet temperature. Lubricant was supplied to the test bearings either by jets or through holes in the cone to the undercuts at the edges of the raceway.

Endurance tests were run with the modified standard design bearings of two materials at 12 500 rpm. With the computer-optimized design bearings, endurance tests were run with two materials at 18 500 rpm. Bearing temperatures were maintained in the range from 394 to 422 K (250° to 300° F). The following results were obtained:

1. Direct cone-rib lubrication significantly improved the performance of the modified standard design tapered-roller bearings at high speeds. With cone-rib lubrication, total flow rates as low as 5.7×10^{-3} m³/min (1.5 gal/min) provided stable bearing operation at 15 000 rpm, whereas with jet lubrication alone, a flow rate of 15.1×10^{-3} m³/min (4.0 gal/min) was required. Bearing heat generation was less with cone-rib lubrication than with jet lubrication at the same lubricant flow rates.
2. The computer-optimized, high-speed-design, tapered-roller bearing operated successfully at shaft speeds up to 20 000 rpm under heavy thrust and radial loads. Stable temperatures were reached, and no surface distress was observed.
3. Bearing temperatures and heat generation with the high-speed-design bearing were significantly less than those of a modified standard bearing.
4. Bearing temperatures and heat generation increased as expected with increased shaft speed. The highest temperatures measured were at the cup outer surface.
5. With increased lubricant flow rate, bearing temperatures decreased, and bearing heat generation increased.
6. Standard design bearings of CBS 1000M material gave an estimated 10-percent life about six times the rated catalog life. Twelve identical bearings of AISI 4320 material ran to a cutoff time of 10 times the rated catalog life without failure.
7. Under conditions of marginal lubricant-film-thickness-to composite-surface-roughness ratio, peeling surface distress was a dominant mode of failure. However, by reducing bearing temperatures to increase lubricant film thickness and re honing the raceways and rollers to improve surface finish, the peeling mode of failure was effectively eliminated.
8. Cracking and fracture of the cones of AISI M-50 bearings occurred as a result of the high tensile hoop stresses at 18 500 rpm with the optimized high-speed design bearings.
9. CBS 1000M bearings of the optimized high-speed design did not crack or fracture. Four of these bearings ran to 24 times the rated catalog life without failure.

References

1. Lemanski, A. J.; Lenski, J. W., Jr.; and Drago, R. J.: Design, Fabrication, Test, Evaluation of Spiral Bevel Support Bearings (Tapered Roller). Final Report, Boeing Vertol Co., 1973. (USAAMRDL-TR-73-16, AD-769064.)
2. Lenski, J. W., Jr.: Test Results Report and Design Technology Development Report. HLH/ATC High Speed Tapered Roller Bearing Development Program. T301-0248-1, Boeing Vertol Co., 1974. (USAAMRDL-TR-74-33, AD-786561.)
3. Cornish, R. F.; Orvos, P. S.; and Dressler, G. J.: Design, Development, and Testing of High Speed Tapered Roller Bearings for Turbine Engines. Final Report, Timken Co., 1975. (AFAPL-TR-75-26, AD-A012300.)
4. Conners, T. F.; and Morrison, F. R.: Feasibility of Tapered Roller Bearings for Main-Shaft Engine Applications. SKF-AL73T009, SKF Industries, Inc., 1973. (USAAMRDL-TR-73-46, AD-771984.)

5. Orvos, P. S.; and Dressler, G. J.: Tapered-Roller Bearing Development for Aircraft Turbine Engines. Final Report, Timken Co., 1979. (AFAPL-TR-79-2007, AD-A069440.)
6. Crecelius, W. J.; and Milke, D. R.: Dynamic and Thermal Analysis of High Speed Tapered Roller Bearings under Combined Loading. (SKF-AL73P010, SKF Industries, Inc.; NASA Contract NAS3-15700.) NASA CR-121207, 1973.
7. Cornish, R. F.; Orvos, P. S.; and Gupta, S. R.: Development of High Speed Tapered Roller Bearing. IR-1, Timken Roller Bearing Co., 1973. (AFAPL-TR-73-85, AD-771547.)
8. Wren, F. J.; and Moyer, C. A.: Understanding Friction and EHL Films in Concentrated Contacts of a Tapered Roller Bearing. Elastohydrodynamic Lubrication: 1972 Symposium, Institution of Mechanical Engineers (London), 1972, Paper No. C10/72, pp. 55-60.
9. Parker, R. J.; and Signer, H. R.: Lubrication of High-Speed, Large Bore Tapered-Roller Bearings. J. Lubri. Technol., vol. 100, no. 1, Jan. 1978, pp. 31-38.
10. Parker, R. J.; Pinel, S. I.; and Signer, H. R.: Performance of Computer-Optimized Tapered-Roller Bearings to 2.4 Million DN. J. Lubri. Technol., vol. 103, no. 1, Jan. 1981, pp. 13-20.
11. Littmann, W. E.; and Moyer, C. A.: Competitive Modes of Failure in Rolling Contact Fatigue. SAE Paper 620 A, Jan. 1963.
12. Parker, R. J.; Signer, H. R.; and Pinel, S. I.: Endurance Tests with Large-Bore Tapered-Roller Bearings to 2.2 Million DN. ASME Paper 81-Lub-56, Oct. 1981.
13. Johnson, L. G.: Statistical Treatment of Fatigue Experiments. GMR-202, General Motors Corp., 1959.
14. Clark, J. C.: Fracture Failure Modes in Lightweight Bearings. J. Aircr., vol. 12, no. 4, Apr. 1975, pp. 383-387.
15. Bamberger, E. N.: Materials for Rolling Element Bearings. Bearing Design—Historical Aspects, Present Technology and Future Problems, Anderson, W. J., ed, American Society of Mechanical Engineers, 1980, pp. 1-46.
16. Bamberger, E. N.; Zaretsky, E. V.; and Signer, H.: Endurance and Failure Characteristic of Main-Shaft Jet Engine Bearing at 3×10^6 DN. J. Lubr. Technol., vol. 98, no. 4, Oct. 1976, pp. 580-585.

Evaluation of a High Performance, Fixed-Ratio, Traction Drive*

Stuart H. Loewenthal,[†] Neil E. Anderson,[‡] and Douglas A. Rohn[†]

Although light-duty, variable-ratio traction drives have been reasonably successful from a commercial standpoint (ref. 1), very few, if any, fixed-ratio types have progressed past the prototype stage. This is somewhat surprising in view of the outstanding ability of traction drives to provide smooth, quiet power transfer at extremely high speeds with good efficiency. They seem particularly well suited for high speed machine tools, pump drives, and other turbomachinery. However, the fixed-ratio traction drives of the past have generally not been weight or size competitive with their gear drive counterparts. There are several reasons for this. First, the steels used in earlier traction drives had significantly less fatigue life than today's metallurgically cleaner bearing steels. Second, the earlier traction drives did not benefit from the use of modern traction fluids, which can produce up to 50 percent more traction than conventional mineral oils for the same normal load (ref. 2). In addition, recent advancements in the prediction of traction-drive performance (refs. 3 to 6) and fatigue life (refs. 7 and 8), have added a greater degree of reliability to the design of these devices.

Perhaps the most significant reason why traction drives have not been competitive in size with gear systems is fundamental to the way they transmit torque. Unlike a simple gear mesh, the normal load imposed on a traction contact must be at least an order of magnitude larger than the transmitted traction force to prevent slip. Thus, to achieve high power density, the traction drive must be constructed with multiple, load-sharing roller elements to reduce the contact unit loading. This was recognized by Lubomyr Hewko who performed some of the earliest traction contact experiments (refs. 9 and 10). His data provided design information for a high performance, multicontact, simple planetary roller drive (ref. 11). The planetary arrangement ensured that the relatively large normal contact loads on the rollers were internally balanced and reacted by the ring-roller rather than by bearings. Tests with a 3.5 to 1 ratio, six planet, 75-kW unit (ref. 11) showed it to have better efficiency and substantially lower noise than a comparable planetary gearset. Recently, tests of a planetary type traction drive of similar construction for use with a gas-turbine APU system were reported in (ref. 12).

For traction drives with a simple, single-row planet-roller format, the number of load sharing planets is inversely related to the speed ratio. For example, a four-planet drive would have a maximum speed ratio of 6.8 before the planets interfered. A five-planet drive would be limited to a ratio of 4.8, and so on.

A remedy to the speed ratio and planet number limitations of simple, single-row planetary systems was devised by A.L. Nasvytis (ref. 13). His drive system used the sun and ring roller of the simple planetary traction drive, but replaced the single row of equal diameter planet rollers with two or more rows of stepped or dual-diameter planets. With this new multiroller arrangement, practical speed ratios of 150 to 1 could be obtained in a single stage with three planet rows. Furthermore, the number of planets carrying the load in parallel could be greatly increased for a given ratio. This resulted in a significant reduction in individual roller contact loading with a corresponding improvement in torque capacity and fatigue life.

Based on the inherent qualities of the Nasvytis configuration and the results from earlier prototype tests (ref. 13), a test program was initiated to evaluate the key operational and performance factors associated with the Nasvytis multiroller traction-drive concept. To accomplish this objective, two sets of Nasvytis drives, each of slightly different geometry, were parametrically tested on a back-to-back test stand. Initial results from these tests are reported in (ref. 14). One of these units was later retrofitted to the power turbine of an automotive gas-turbine engine and dynamometer tested.

*Previously published as NASA TM 81425; AVRADCOM 80-C-1.

[†]NASA Lewis Research Center.

[‡]Propulsion Laboratory, U.S. Army Research and Technology Laboratories (AVRADCOM), NASA Lewis Research Center.

Nasvytis Traction Drive Concept

The basic geometry of the Nasvytis traction drive is shown in figure 1. Two rows of five stepped planet rollers are contained between the concentric, high-speed sun and low-speed ring rollers. The planet rollers do not orbit but are grounded to the base through reaction bearings contained only in the second or outer row of planets. This is a favorable position for the reaction bearings since the reaction forces and operating speeds are relatively low.

The sun roller and the first row of planets float freely, relying on contact with adjacent rollers for location. Because of this self-supporting roller approach, the number of total drive bearings is greatly reduced, and the need for the often troublesome, high-speed shaft-support bearings has been eliminated. In addition, both rows of planets are in three-point contact with adjacent rollers, promoting a nearly ideal internal force balance. In the event of an unbalance in roller loading, the first and second row of planets (supported by large clearance bearings) will shift under load until the force balance is reestablished. Consequently, slight mismatches in roller dimensions, housing distortions under load, or thermal distortions merely cause a slight change in roller orientation without affecting performance. Because of this roller-cluster flexibility, the manufacturing tolerances set for dimensions can be rather generous relative to the standard set for mass-produced bearing rollers.

The number of planet-roller rows, the number of planet rollers in each row, and the relative diameter ratios at each contact are variables to be optimized according to the overall speed ratio and the uniformity of contact forces. In general, drives with two-planet rows are suitable for speed ratios to about 45, and drives with three-planet rows are suitable for ratios to about 250.

Geometry of Test Drives

Two sets of Nasvytis drives of nominally 14.7 to 1 and 14 to 1 ratios were tested. Both drive designs had two rows of five-planet rollers, each, but were equipped with different roller-cluster loading mechanisms. Figure 2 shows a cross section cut through the roller contact points of the drive

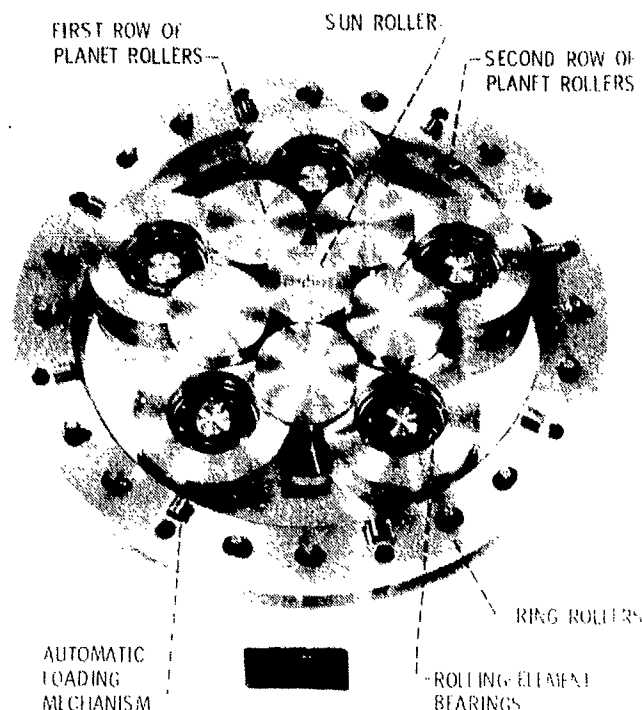


Figure 1. - Basic geometry of a Nasvytis multiroller traction drive.

with the loading mechanism contained in the ring assembly. This ring-loader drive had speed ratios between the sun and the first planet, first and second planet, and between the second planet and ring roller of 1.28, 3.87, and 2.97, respectively, for a nominal drive ratio of 14.7. The second test drive had the loading mechanism incorporated into the sun roller. The sun-loader drive had speed ratios of 1.21, 3.94, and 2.93 across these respective contacts, for a nominal drive ratio of 14.0.

Both test drives were equipped with a loading mechanism that automatically adjusted the normal contact load between the rollers in proportion to the transmitted torque. These mechanisms operated above some preselected, minimum preload setting. The automatic loading mechanism insured that there was always sufficient normal load to prevent slip under the most adverse operating conditions without needlessly overloading the contact under light loads. Thus, the load mechanism improved part load efficiency and extended drive service life.

In the case of the ring-loader drive, the loading mechanism consisted of eight small rollers contained in wedge-shaped pockets, equally spaced circumferentially between the ring rollers and the backing rings as illustrated in figures 1 and 2. The inside diameters of the ring rollers and outside diameter of the second row planets had slightly tapered (5.7°) contact surfaces. When torque was applied, the ring rollers would either circumferentially advance or retreat relative to the backing rings. This would cause the loading rollers to move up the ramped pocket, squeezing the ring rollers together axially and, in turn, radially loading the roller cluster through the tapered contact. The amount of normal force imposed on the traction-drive contacts for a given torque, or, in other words, the applied traction coefficient, could be varied by simply changing the slope of the wedge-shaped pockets. In this investigation the loading mechanism was designed to produce a constant applied traction coefficient of 0.05 for torques in excess of the initial preload values of about 25 to 40 percent of the maximum value.

The drive equipped with the sun-roller loading mechanism used the same principle, but loaded the drive radially outward through a two-piece, sun roller. Packaging the loading mechanism into the sun roller simplified the drive design and reduced the cluster weight from 9.0 kg for the ring drive down to 7.6 kg for the sun-loader design. Both test drive roller clusters were roughly of the same size, being approximately 21 cm in overall diameter and 6 cm wide.

The ring and planet rollers of both drives and the two-piece, sun roller of the sun drive were fabricated from consumable vacuum-melted (CVM) SAE-9310 (AMS-6265) steel, case carburized to a Rockwell C hardness of 60 to 62. The sun roller on the ring drive was made of through-hardened CVM, AISI 52100 steel of similar hardness. All roller running surfaces were ground to $0.2 \mu\text{m}$ rms or better.

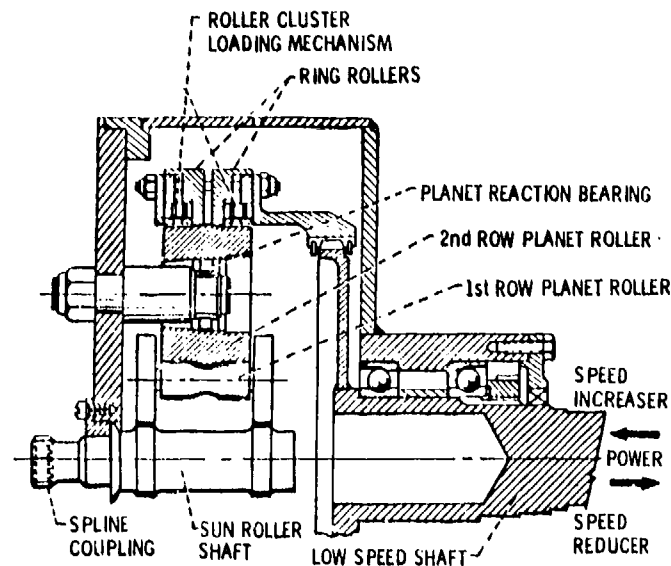


Figure 2. - Cross section of ring-loader Nasvytis traction drive.

Traction Power Transfer

In a traction drive torque is mainly transmitted by shear forces acting through a thin, elastohydrodynamic (EHD) lubricant film which separates the driving and driven rollers. Under the high pressures and severe shear rates present within a typical traction contact, the lubricant is thought to be transformed into an amorphous solid-like material (ref. 15). Because of this lubricant transformation within the EHD film, appreciable torque transfer can occur without appreciable metal-to-metal contact or wear.

The torque capacity of a given traction contact is strongly dependent on the maximum available traction coefficient, that is, the peak value of the ratio of tangential-to-normal force before gross slip. Figure 3 shows a typical traction coefficient versus creep curve for Santotrac 50, one of the two synthetic cycloaliphatic hydrocarbon traction fluids used in this investigation. The other test fluid used was Santotrac 40. These traction lubricants offer about a 50-percent improvement in traction coefficient over mineral oils and exhibit good fatigue-life performance (ref. 2). Santotrac 50 and Santotrac 40 have comparable traction coefficients, but the 50 grade is slightly more viscous and has a complete additive package. Their physical properties are reported in (ref. 2).

The curve in figure 3 was generated under the operating conditions noted with the twin-disk machine described in (ref. 16). Imposing a traction force across a lubricated disk contact, rotating at an average surface velocity U , gives rise to a differential surface velocity ΔU . The ratio of ΔU to U is generally referred to as creep in traction-drive terminology. Traction drives with a torque sensitive roller-loading mechanism generally operate at a nearly fixed value of μ . This value is selected to be sufficiently below the peak value of μ to assure safe operation. In this region creep arises from the viscoelastic and plastic straining of the plastic-like lubricant material together with the plastic, tangential deformation or compliance of the disk material. In fact for a typical steel traction-drive contact operating at high pressures (greater than 1.2 GPa) and lubricated with a traction fluid, most of the creep is observed to take place in the disks and not in the fluid film (ref. 17).

Since the creep rate represents a loss in speed, each percentage point loss due to creep represents a percentage-point loss in efficiency. Design operating conditions should be selected to maximize the available traction coefficient and minimize the creep rate. As shown in figure 3, an increase in surface speed tends to decrease μ and increase creep. An increase in contact temperature or spin as well as a decrease in contact pressure tends to do the same.

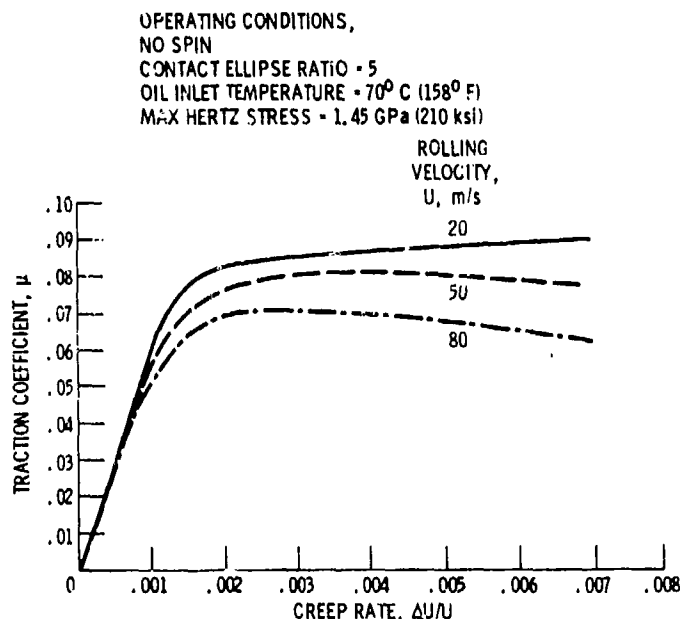


Figure 3 - Typical traction data for a traction fluid (Santotrac 50) from a

Parametric Performance Tests

Apparatus

Both Nasvytis drive variants were parametrically tested on a specially constructed back-to-back test stand, described in detail in (ref. 14). In this stand, two identical drives were tested concurrently with their sun-roller shafts coupled via a flexible spline coupling. One drive functioned as the speed increaser; the other unit as the speed reducer.

Efficiency was determined by comparing, at the same operating conditions, the total test-stand power losses with the test drives in place to the test-stand tare power losses with the test drives removed. The test-stand tare power losses were measured under load by replacing the test drives with a dummy shaft. With this technique, peak efficiency can be determined accurately to within ± 0.3 percent. By measuring the flow rate, the temperature rise across the cooling oil, and the temperature of each drive housing, a heat balance method was developed, as reported in reference 14, to proportion the total power loss between each test model according to its heat dissipation. In this way differences in efficiency between the speed increaser and speed reducer test units could be estimated.

Procedure

Typically, the back-to-back increaser and reducer test drives were tested at constant input speed while the output torque on the reducer unit was increased in uniform increments until the maximum required torque level was attained. At this point the torque was dropped to the initial level, the next level of speed was set, and the process was repeated. To insure steady-state readings, typically 45 to 60 minutes of running was required between speed changes and 5 to 15 minutes between torque changes.

During these tests a nominal oil inlet temperature of 65°C was maintained at a total flow rate of 8.3 l/min. Approximately 60 percent of this oil was used to cool the sun roller with the rest going to the drive bearings and remaining drive rollers. Santotrac 40 was used as the test lubricant.

Results and Discussion

The effect of sun-roller speeds to 46 000 rpm and torques to 42 N·m on the power loss of the sun-loader variant, Nasvytis traction drive is presented in figure 4. The results from five independent test runs show that the test data are reasonably consistent. The heat balance technique mentioned previously was used to proportion the total power loss between the speed reducer and increaser. With this technique the reducer exhibited slightly higher losses than the increaser, particularly at the lower torque levels. The variation in power loss with torque is nearly linear above torque levels of about 40 percent in the region where the roller cluster loading mechanism is operating. This trend is generally in accordance with the traction-performance prediction techniques of reference 17. This analysis indicates that the contact power loss is composed of two major components, a traction creep loss term and a spin torque term, both of which are directly proportional to transmitted torque at constant creep rate.

Also apparent in figure 4 is the zero torque or tare power loss value for the test drives. The principal constituents of this tare loss are the nonslip or rolling traction contact losses of the rollers under the initial preload and miscellaneous bearing and drive-element churning and windage losses. As in the case of gears (ref. 18), these tare losses can represent a significant portion of the total drive loss, particularly at the lower torque levels and higher speeds. It is expected that lowering the initial preload levels to 5 or 10 percent of the maximum rated torque could reduce these tare power losses by up to a third, based on the data of figure 4.

The variation in increaser and reducer efficiency as a function of input torque for the sun- and ring-loader test drives is presented in figure 5. The ring-loader drives were tested to a maximum sun-roller speed and torque of 73 000 rpm and 20 N·m. The cross-hatched region represents the relatively small influence that operating speeds from 25 to 100 percent of maximum have a overall efficiency. As would be expected, the lowest speeds which produce the lowest relative tare losses and lowest creep rate resulted in the highest efficiency at a given torque level.

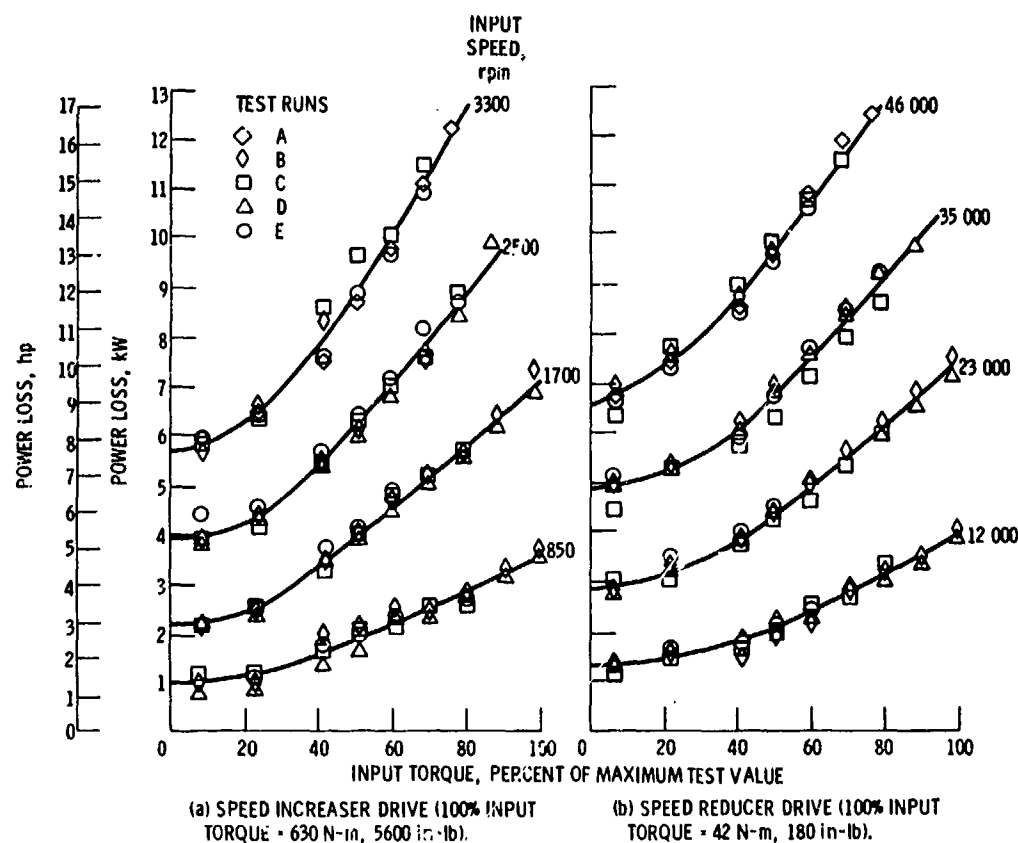


Figure 4. - Power loss of sun-loader test drive as function of input torque and speed.

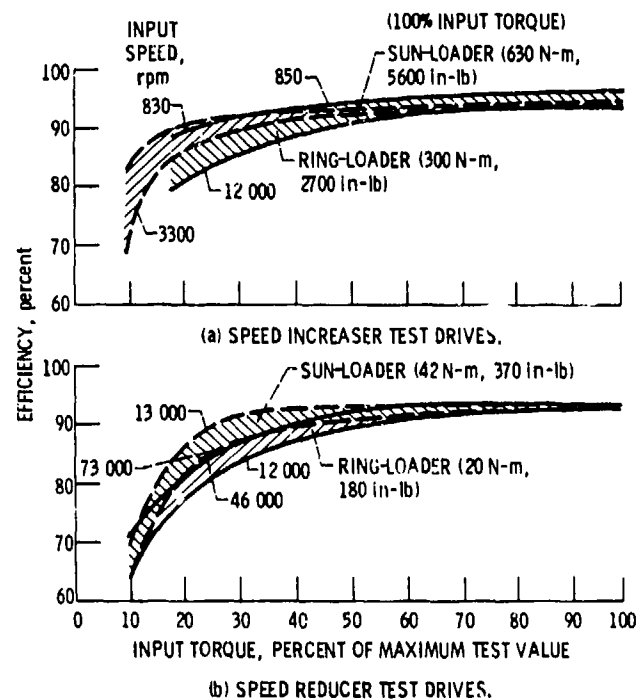


Figure 5. - Comparison of sun and ring-loader Nasvytis drive efficiencies as function of input torque and speed.

In general, the ring-loader drive had slightly higher peak efficiency values than the sun-loader unit (96 versus 94 percent for the speed increaser and 94 versus 93 percent for the speed reducer, respectively). Part of this difference is attributed to the somewhat tighter conformity of the planet and ring-roller contact surfaces in the sun-loader drive. Tighter contact conformity causes some reduction in contact stress (see fig. 6) but at the expense of slightly higher spin losses and higher creep. Although the tapered sun-roller contact in the sun-loader drive has less conformity than the sun contact in the ring unit, its tapered geometry and high roller speed contribute to higher spin losses and creep rate.

The effect of operating torque and speed on test drive creep rate is shown in figure 7. The total loss in efficiency due to creep across the drive's three contacts is generally less than about 3.5 percent for the sun-loader drives and less than 2 percent for the ring-loader units. At comparable torque levels, their creep rates were similar. Creep curves generally rise in a linear fashion with an increase in torque during the initial fixed-preload region of operation and level out as the roller-loading mechanism begins to function (see fig. 7). This behavior can be understood by examining the traction-versus-creep curves of figure 3. As the traction force is increased on a roller with a given initial normal load, the traction coefficient increases from zero, causing a corresponding linear increase in creep. At the design value of traction coefficient, the loading mechanism is activated. At this point the creep rate is held essentially constant except for small variations due to changes in the slope of the traction curve. Some degradation in creep rate performance with torque was observed for the sun-loader, reducer test model.

To determine the effectiveness of the roller-loading mechanism, a proximity probe was installed in the sun-loader drive. The probe monitored the axial position of one side of the two-piece sun-roller assembly. In this drive, as the tapered sun-roller halves moved together, the normal load on the roller-cluster was correspondingly increased. During the initial preload region of operation (fig. 8),

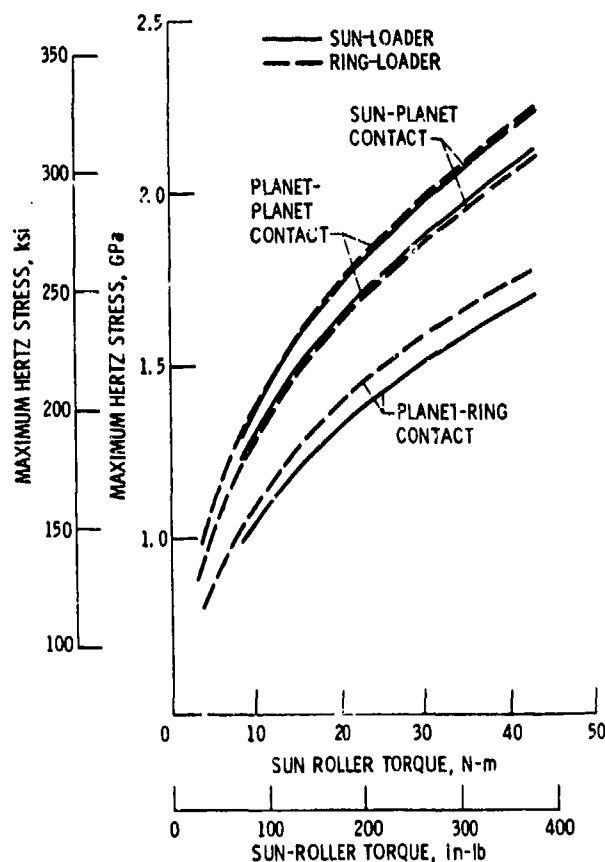


Figure 6. - Comparison of maximum Hertz stress for sun- and ring-loader drive contacts.

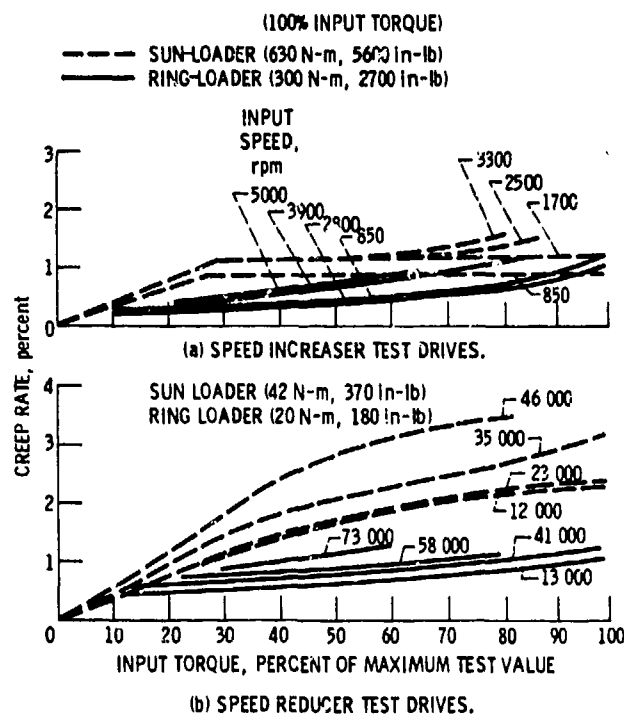


Figure 7. - Comparison of sun- and ring-loader Nasvytis drive creep rates as a function of input torque and speed.

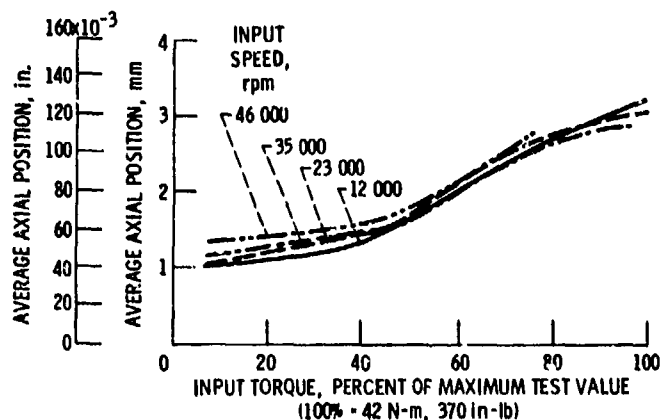


Figure 8. - Average axial position of loading mechanism in sun-loader Nasvytis drive.

the sun-roller position was reasonably constant up to a torque level of approximately 40 percent. Above 40 percent, the sun-roller halves move inward together in a nearly linear fashion with increasing torque, indicating satisfactory roller-loading action. Because of a centrifugal force effect on the loading balls, an increase in speed causes a slight increase in initial preload. The loading mechanisms on both the speed increaser and reducer test units showed similar behavior.

Temperatures of the rollers in the test drives increased steadily with an increase in operating speed. The sun-roller temperature, as measured by a thermocouple near the surface, was higher than any other component in the drive. Sun-roller temperatures never exceeded approximately 110° and 150° C for the sun- and ring-loader drives, respectively.

Gas Turbine Engine Tests

Parametric dynamometer tests were conducted with a Nasvytis traction drive that had been incorporated into 112 kW (150 hp) automotive gas-turbine engine. For this installation, the 14-to-1 ratio roller cluster from the sun-loader test drive was retrofitted into the engine's power turbine assembly in place of the original 9.7 to 1 helical gear mesh. A cross section of the Nasvytis drive installation within the power-turbine housing is shown in figure 9. The sun roller was coupled to the end of the power turbine rotor through a semiflex spline coupling. The ring roller was spline coupled to the output shaft, which, in turn, would normally drive the vehicle's automatic transmission. However, for this test, the output shaft of the drive was directly coupled to a power absorbing dynamometer via a prop shaft.

Modifications to the original power-turbine assembly included the replacement of the rotor's rear fluid-film journal bearing and hydrostatic thrust bearing with a thrust carrying, split-inner-race, angular-contact ball bearing. Changes were made to the power-turbine housing to incorporate the concentric Nasvytis drive. The self-supported sun roller eliminated the need for the high-speed, fluid-film bearings, which normally straddle the pinion and react gear-tooth separating loads.

Two series of parametric tests were conducted on the traction-drive-equipped turbine engine under nominally the same test conditions as described earlier for the back-to-back stand tests. However, power-turbine speeds were limited to 45 000 rpm and power levels to 112 kW. Santotrac 50 was used as the test oil. In the first series of tests the sun-roller loading mechanism was locked out, and a fixed preload was set at the value required to prevent gross slip under full load. The second series of tests made use of the variable, sun-roller loading mechanism.

Figure 10 shows the comparative efficiency results from these two test series. The efficiency values shown in this figure were estimated from the increase in heat content of the cooling oil as it passed through the drive cavity. Using a similar heat balance estimate, an efficiency value was assigned to the rotor's front fluid-film journal bearing and rear ball bearing based on the heat power dissipated to the bearings' cooling oil. Although this heat balance method is rather imprecise, due to the uncertainties in the amount of heat either dissipated by the cooling oil to the power-turbine housing or vice versa, the efficiencies from the back-to-back stand measurements and those estimated by this method (fig. 10) are similar.

The data in figure 10 show that the equivalent efficiency of the power-turbine rotor bearings as well as the efficiency of the Nasvytis drive are relatively speed insensitive. It is also apparent from figure 10 that the fixed-preload operation causes an appreciable decrease in part-load efficiency. At the high torque levels, the variable loading mechanism imposes a normal load approaching that of the fixed-preload system, and their respective efficiencies merge as would be expected.

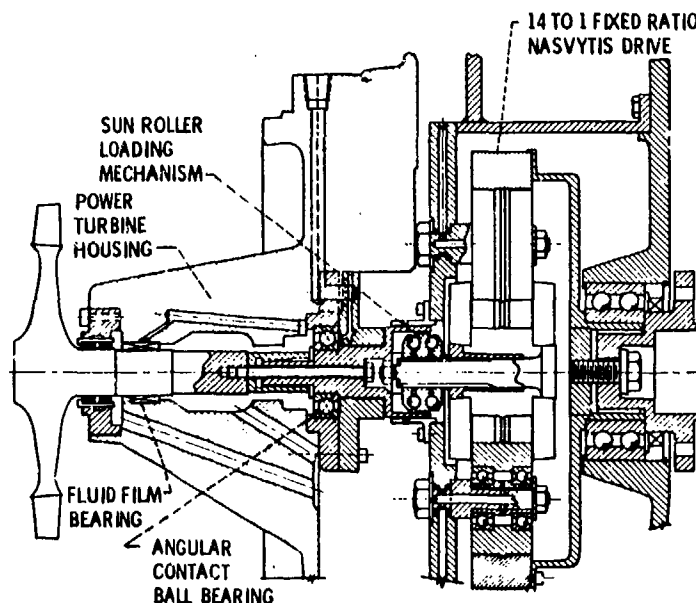


Figure 9. - Installation of Nasvytis traction drive with power turbine assembly.

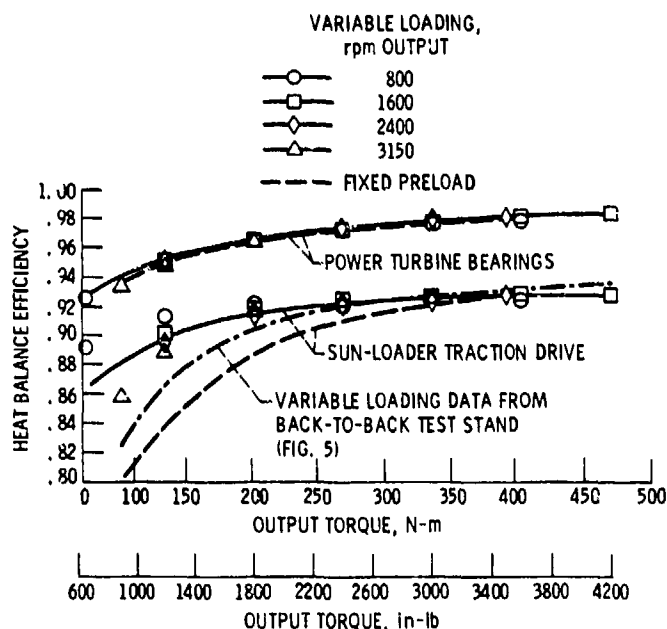


Figure 10. - Heat balance efficiency of sun-loader Nasvytis drive from gas-turbine-engine tests as compared with back-to-back test stand measurements.

Creep rate data for the engine tests are presented in figure 11. Also included for comparison are the back-to-back stand data from figure 7 for the sun-loader reducer drive at 35 000 rpm. The agreement between both sets of creep data is within 0.2 percentage point at all corresponding test speeds (not shown in fig. 7) except at 44 000 rpm. At this speed the stand measurements indicate about 0.5 percentage point greater creep rate than the engine test data at the higher torque levels.

Although the creep rate associated with fixed-preload operation is about 0.6 percentage point less than that with variable preloading (fig. 11), the overall efficiency is decidedly inferior (fig. 10) because of contact overloading. The lower creep rate is due to the high initial normal load associated with fixed preload operation. This lowers the applied traction coefficient so that the resulting creep rate from the traction curve (see fig. 3) will also be relatively small. Also the upward trend of the fixed-preload creep data suggests that a slip condition is being approached.

In general, the Nasvytis drive demonstrated good operational compatibility and performance with the gas-turbine engine throughout the engine's torque and speed range. Orthogonal, radial proximity probes mounted at two axial positions along the power-turbine shaft, showed that the coupled rotor-traction-drive system was reasonably stable from engine idle to maximum speed. No synchronous whirl instabilities were encountered. Temperature distributions of rollers and bearings were quite satisfactory, similar to those obtained in the back-to-back stand tests.

Capacity and Durability

Traction drives, like rolling-element bearings, are generally sized on the basis of rolling-element fatigue life. This is because, for most applications other than those that are particularly short lived, the stress levels required for acceptable fatigue life are generally well below those for static yield failure. For example, maximum bending stresses in the Nasvytis test drives at a peak sun-roller torque of 42 N·m is less than 350 MPa, and maximum contact stresses are less than 2.2 GPa. For the case-hardened steel rollers in the Nasvytis drive, the expected yield stress in bending would be approximately 1400 MPa and the Brinelling stress limit would be on the order of 4 GPa.

Because of these relatively low maximum operating stress levels, occasional momentary overloads, several times the maximum design value can generally be tolerated. Furthermore, if these transient overloads are of a brief duration and do not occur too frequently, then only a relatively small penalty to the drives' total fatigue life will result.

A traction drive's sensitivity to shock loads is also dependent on the ability of the contact surface to avoid skidding or heating damage. If the drive is equipped with a fast acting loading mechanism,

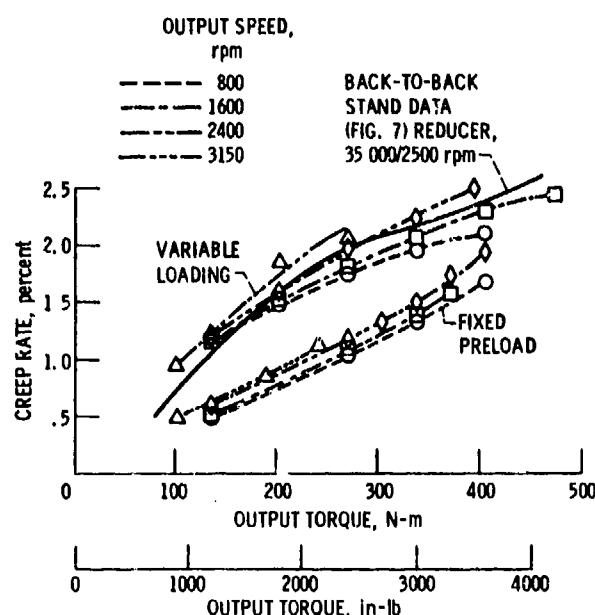


Figure 11. - Comparison of fixed preload and variable loading creep rate for sun-loader reducer from gas-turbine-engine tests. Drive ratio, 14.

such as the mechanical type used in the Nasvytis test units, and if the overload is of sufficiently short duration to avoid overheating the contact, then no surface damage would be expected.

The normally expected failure mode of a properly-designed traction drive will be rolling-element fatigue. This failure criterion is exactly analogous to pitting failure in gears and spalling failure in rolling-element bearings. The risk of wear or scuffing failures of traction-drive contacts can be eliminated or greatly minimized through the use of proper materials and also proper lubricating and cooling design practices such as those that have been successfully applied in bearing and gear design. In view of this similarity in the failure mechanism, it is anticipated that the fatigue-life theory of Lundberg and Palmgren (ref. 19), the accepted method of establishing load capacity ratings for rolling-element bearings by bearing manufacturers, can be adapted to predict traction-drive service life. In reference 7 the basic life equations for traction drives were developed from Lundberg-Palmgren theory and applied to a toroidal traction drive. Life adjustment factors due to advances in materials, lubricants, and design technology were also considered. In reference 20 this life analysis was applied to the Nasvytis traction-drive geometry. Theoretical B_{10} (90-percent survival) life ratings for the Nasvytis test drives based on the work of reference 20 appear in figure 12. These data were generated at a constant sun-roller speed of 50 000 rpm. It includes a life-adjustment factor of 6 for through-hardened CVM AISI-52100 or case-hardened CVM AMS-9310 steels, a life factor of approximately 2.5 for a favorable film thickness-to-surface roughness ratio, and an estimated life penalty of 0.5 for the potentially adverse effects of traction on fatigue life.

At a given required life level (fig. 12), the sun-loader test unit shows slightly higher power capacity than the ring-loader traction drive. Continuous power capacity ranged from 42 kW for 10 000 hours of system life to 185 kW for a minimum of 100 hours at sun-roller speeds of 50 000 rpm (or about 3500 rpm on the low-speed shaft). Increasing the size of the drive has a significant increase in power capacity. Reference 7 reports that traction drive fatigue life, L , is related to size factor and to torque T as follows:

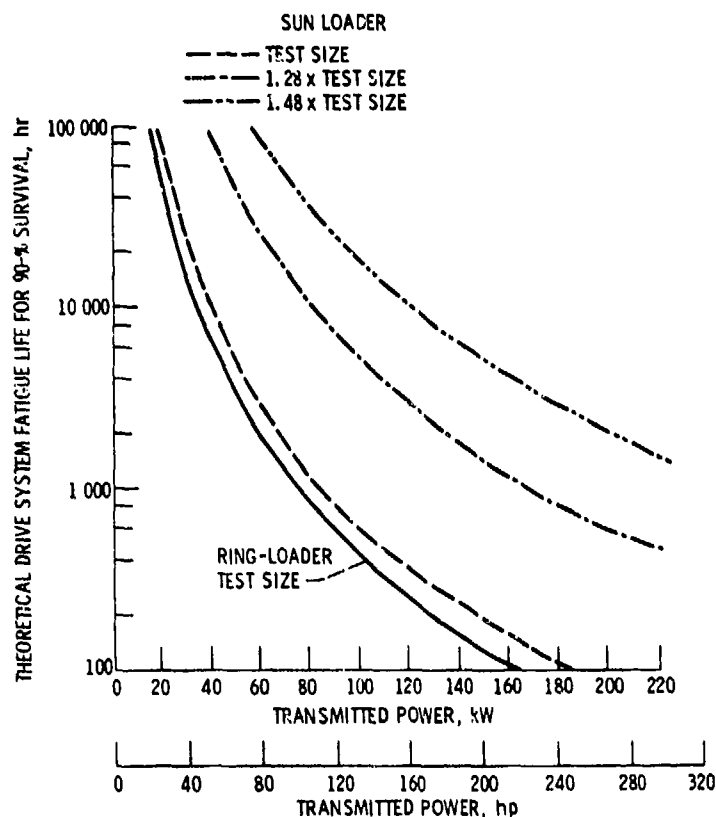


Figure 12. - Effect of size and power on theoretical Nasvytis drive fatigue life at a sun-roller speed of 50 000 rpm.

$$L \propto (\text{size factor})^{8.4}$$

and

$$L \propto T^{-3}$$

It, therefore, follows that the torque capacity of the drive for a given required fatigue life is related to size by

$$T \propto (\text{size factor})^{2.8}$$

Thus, increasing the test drive size by 28 percent, that is, increasing the roller-cluster's overall diameter to 27 cm and width to 8 cm, will double torque capacity at a given life level. Similarly a 48-percent size increase will more than triple the load capacity, as illustrated in figure 12. This scaling assumes that the design or applied traction coefficient remains constant with size. However, with an increase in size, the rolling surface speed of the contact increases and the contact stress decreases, causing some loss in the available peak traction coefficient. If additional roller-loading is needed to compensate for this loss in traction coefficient, then a small life derating will be needed.

The capacity ratings shown in figure 12 are for the test drive geometry under the specified operating conditions. These ratings can change significantly with changes in drive geometry. The most durable traction-drive geometry (the number of planet rows, the number of planet rollers in each row, and the relative diameter ratios at each contact) can be determined for a given application from a computerized optimization technique such as that described in (ref. 21).

Summary and Conclusions

Parametric back-to-back stand tests and gas-turbine engine dynamometer tests were conducted on two fixed-ratio Nasvytis multiroller traction drives. The effects of speed and torque on drive efficiency, creep rates, temperature distribution, roller stability, and loading mechanism action were investigated. Two traction fluids were used. The 14.7 to 1 ratio ring-loader drive in which the loading mechanism was incorporated into the ring assembly, was tested to sun speeds of 73 000 rpm and power levels to 130 kW. The sun-loader drive of 14.0 to 1 ratio was tested to 46 000 rpm and 180 kW. The cluster from this drive was retrofitted to the power turbine of an automotive gas turbine in place of the original helical gear reducer. Tests were conducted to full-engine speed (45 000 rpm) and power (110 kW). The effects on drive performance of fixed-preload (constant normal load) operation were compared with those obtained with variable-roller-cluster loading (proportional to the transmitted torque). Comparisons were also made of the data from engine dynamometer tests and those obtained from the back-to-back stand tests. The sun- and ring-loader roller-clusters measured approximately 21 cm in diameter and weighed 7.6 and 9.0 kg, respectively. Predictions of test drive system fatigue life as function of size and transmitted power were made using Lundberg-Palmgren fatigue theory. Based on the above, the following results were obtained:

1. The ring- and sun-loader test drives exhibited peak efficiency levels of 96 to 94 percent, respectively, for the speed increaser units and 94 and 93 percent, respectively, for the speed reducer units.
2. The Nasvytis drive showed good operational compatibility with the gas-turbine engine. Test data from these engine tests showed reasonable agreement with the back-to-back stand tests.
3. Efficiency loss due to creep was generally less than 3.5 percent for the three drive contacts under the worst-test conditions.
4. Theoretical fatigue lives of the sun- and ring-loader drives were comparable. The 90-percent survival life rating ranged from 10 000 hours at 42 kW to 100 hours at 185 kW for a sun-roller speed of 50 000 rpm. A 28-percent increase in size would theoretically double these power ratings.

References

1. Carson, R. W.: Traction Drives Update, *Power Transmis. Des.*, vol. 19, no. 11, Nov. 1977, pp. 37-42.
2. Loewenthal, S. H.; and Parker, R. J.: Rolling-Element Fatigue Life with Two Synthetic Cycloaliphatic Traction Fluids. NASA TN D-8124, 1976.
3. Magi, M.: On Efficiencies of Mechanical Coplanar Shaft Power Transmissions. Chalmers University, Gothenburg, Sweden, 1974.
4. Gaggermeier, H.: Investigations of Tractive Force Transmission in Variable Traction Drives in the Area of Elastohydrodynamic Lubrication. Ph. D. Dissertation, Technical University of Munich, July 1977.
5. Tevaarwerk, J. L.; and Johnson, K. L.: The Influence of Fluid Rheology in the Performance of Traction Drives. *J. Lubr. Technol.*, vol. 101, no. 3, July 1979, pp. 266-274.
6. Daniels, B. K.: Non-Newtonian Thermo-Viscoelastic EHD Traction from Combined Slip and Spin. ASLE Preprint 78-LC-2A-2, Oct. 78.
7. Coy, J. J.; Loewenthal, S. H.; and Zaretsky, E. V.: Fatigue Life Analysis for Traction Drives with Application to a Torodial Type Geometry. NASA TN D-8362, 1976.
8. Rohn, D. A.; Loewenthal, S. H.; and Coy, J. J.: Simplified Fatigue Life Analysis for Traction Drive Contacts. *J. Mech. Des.*, vol. 103, no. 2, Apr. 1981, pp. 430-438, discussion, pp. 438-439.
9. Hewko, L. O.; Rounds, F. G., Jr.; and Scott, R. L.: Tractive Capacity and Efficiency of Rolling Contacts. *Rolling Contact Phenomena*, J.B. Bidwell, ed., Elsevier Publ. Co., Amsterdam, 1962, pp. 157-185.
10. Hewko, L. O.: Contact Traction and Creep of Lubricated Cylindrical Rolling Elements at Very High Surface Speeds. *ASLE Trans.*, vol. 12, no. 2, Apr. 1969, pp. 151-161.
11. Hewko, L. O.: Roller Traction Drive Unit for Extremely Quiet Power Transmission. *J. Hydronaut.*, vol. 2, no. 3, July 1968, pp. 160-167.
12. Nakamura, L.; et al.: A Development of a Traction Roller System for a Gas Turbine Driven APU. SAE Paper No. 790106, Feb. 1979.
13. Nasvytis, A. L.: Multiroller Planetary Friction Drives. SAE Paper No. 660763, Oct. 1966.
14. Loewenthal, S. H.; Anderson, N. E.; and Nasvytis, A. L.: Performance of a Nasvytis Multiroller Traction Drive. NASA TP-1378, 1978.
15. Smith, F. W.: The Effect of Temperature in Concentrated Contact Lubrication. *ASLE Trans.*, vol. 5, no. 1, Apr., 1962, pp. 142-148.
16. Johnson, K. L.; and Tevaarwerk, J. L.: The Shear Behaviour of Elastohydrodynamic Oil Films. *Proc. Roy. Soc. (London)*, ser. A, vol 356, no. 1685, Aug., 1977, pp. 215-236.
17. Tevaarwerk J. L.: Traction Drive Performance Prediction for the Johnson and Tevaarwerk Traction Model. NASA TP-1530, 1979.
18. Anderson, N. E.; and Loewenthal, S. H.: Part and Full Load Spur Gear Efficiency. NASA TP-1979.
19. Lundberg, G.; and Palmgren, A.: Dynamic Capacity of Rolling Bearings. *Ingeniorsvetenskapsakademiens, Handlingar*, No. 196, 1947.
20. Coy, J. J.; Rohn, D. A.; and Loewenthal, S. J.: Life Analysis of a Nasvytis Multiroller Traction Drive. NASA TP-1980.
21. Coy, J. J.; Rohn, D. H.; and Loewenthal, S. H.: Constrained Fatigue Life Optimization of a Nasvytis Multiroller Traction Drive. *J. Mech. Des.*, vol. 103, no. 2, Apr. 1981, pp. 423-428, discussion pp. 428-429.

Traction Calculations and Design Data for Two Traction Fluids*

Joseph Leo Tevaarwerk†

Traction drives for automotive applications have a rather checkered history. After a brief period of acceptance during the first quarter of this century they disappeared in rapid fashion. The main reason for their initial acceptance was the simplicity with which a variable speed output can be obtained from a nearly constant input speed. Their rapid demise was due to the fact that, while simple in concept, the average life expectancy was very low indeed. With the advent of a more demanding motoring public, this short life expectancy became unacceptable, and other solutions were found to the speed match problem. In recent years traction drives have had a resurgence because of the energy crisis and the fact that a lot of the initial problems have now been, partially, at least, solved.

In simple terms the basic elements in a traction drive are two rollers, pressed into nominal contact and rolled about their respective axes. Power is transmitted in the form of a shear stress across the contact area. A fluid is present to prevent initial surface scuffing damage and to provide for some form of cooling. The rolling motion of the disks draws this fluid into the contact zone, and a thin layer of this fluid will separate the actual contact area. It is also in this region where the torque is transmitted from one roller to the next, and it should not surprise one that the performance of a traction drive depends to a large extent upon the rheological properties of the fluid. Close examination of the fluid as it passes through the contact gap reveals that it experiences a sudden pressure pulse from atmospheric to possibly several gigapascals in a period of 1 to 0.1 msec. The shear stress that is transmitted from one disk to the other (about 10 percent of the normal stress) passes through this layer of fluid "trapped" in the contact and causes a shear. This, in turn, will lead to heat generation, and from simple calculations, temperatures in the center of the film can easily reach several hundred degrees centigrade.

To study the rheological properties of the fluid under these conditions precludes the use of most of the conventional instruments used for steady-state measurement. In fact the only suitable type of instrument is a disk machine where most of the conditions are the same or similar to those in traction drives. From the resulting traction tests, certain models are inferred, and it is in this area where there has been a lot of activity recently.

To the designer of traction drives, the traction behavior of the fluid under the severe conditions is of utmost importance because of the direct influence that it has on the efficiency, size, and life of a given drive.

Previous Traction Investigations

As mentioned in the introduction, there has been a lot of activity in the area of traction research, both in the past and recently. Notable contributions have come from Clark, et al., Hewko, Smith, Smith, et al., Johnson and Cameron, Niemann, and more recently Johnson and Roberts and Johnson and Tevaarwerk (refs. 1 to 8). Some of these investigations were strictly experimental, and aimed at obtaining traction-drive design data, while others were aimed at understanding the traction phenomena so that rheological models could be formulated. This latter research is, of course, ultimately aimed at relating fluid molecular properties to traction properties. Research by Johnson and Tevaarwerk (ref. 8), Daniels (ref. 9), Hirst and Moore (ref. 10), and Alsaad, et al. (ref. 11) is directed specifically towards this purpose. The reader is referred to an excellent review by Johnson (ref. 12) for further aspects of this topic.

*Work done under contract DEN 3-35.

†Applied Tribology, Ltd.

Many of the rheological models derived so far have been isothermal because of the degree of complexity that thermal analysis introduces. Thermal effects are important. However, a simple method is sought to include them in the analysis.

Current understanding of traction has led to traction models that describe the fluid shear behavior in terms of an elastic and a dissipative element. An analysis of traction-drive performance using such a model was done by Tevaarwerk (ref. 13). It showed that under certain conditions the prediction technique by Magi (ref. 14) can be used. The work of reference 13 has recently been further expanded by developing a simple method to correct for thermal effects due to spin (ref. 15) and by performing an overall thermal traction study (ref. 16).

As with all models, however, their usefulness is severely restricted if inadequate input traction data are available to the designer. This is especially so if high-traction fluids are used that have not been tested extensively for use under the wide range of conditions that exist in modern, highly advanced traction drives.

Nomenclature

		First used
A_i	regression constants	eq. (11)
a, b	semi-Hertz contact size for x, y direction, m	eq. (1)
C_i	regression constants for traction variables	eq. (14)
F_x	contact force in the x -direction, N	eq. (5)
F_z	normal force on the contact, N	eq. (5)
\bar{G}	average fluid shear modulus for contact, Pa	eq. (1)
h	EHL film thickness of the fluid in contact, m	eq. (1)
J_1	dimensionless longitudinal slip variable	eq. (4)
J_2	dimensionless side slip variable	eq. (9)
J_3	dimensionless spin variable	eq. (6)
J_4	dimensionless traction variable	eq. (5)
k	contact aspect ratio, $= b/a$	eq. (4)
$k_{1,2}$	coefficients for rigid/plastic model	eq. (8)
m	initial slope for zero spin traction curve	eq. (1)
p	Hertzian contact pressure, GPa	eq. (11)
S	dimensionless slip grouping	eq. (9)
U	rolling speed of the disks, m/sec	eq. (4)
ΔU	longitudinal slip velocity of the disks, m/sec	eq. (4)
ΔV	side slip velocity of the disks, m/sec	eq. (9)
Z	dimensionless spin grouping	eq. (15)
ϵ	speed pole parameter	eq. (7)
θ	temperature of the inlet fluid, °C	eq. (11)
μ	peak traction coefficient for a given test	eq. (2)
$\bar{\tau}_c$	critical shear strength of fluid, Pa	eq. (2)
ω	spin velocity on the contact, rad/sec	eq. (6)
Superscripts		
'	nondimensional regression variable	
—	denotes averaged variables	

Traction Predictions

The principal traction information for the designer comes from the so-called traction curve. This curve is obtained by sliding and rolling two disks relative to each other and measuring the resulting

traction force. The data are normally plotted in dimensionless form as traction coefficient versus slide to roll ratio. Figure 1 shows such a typical curve. The exact shape and features of this curve depend on several external variables such as type of fluid, contact pressure, rolling speed, inlet temperature, and the kinematic conditions that exist in the contact. These kinematic conditions may consist of spin, side slip, and longitudinal slip, or a combination of these. It is, of course, not practical to experimentally measure the traction under every single variation of these conditions, so traction models are resorted to. With a suitable traction model and the knowledge of a few of the fluid rheological parameters, traction under varying kinematic conditions can then be predicted. Present-day traction models take into account the fluid and disk elasticity effect as well as the dissipative behavior of the fluid film. This model can be simplified for purposes of traction-drive analysis to a simple linear elastic spring in series with a Coulomb friction model (fig. 2).

The method of operation of this model is as follows: Upon the application of a shear force, τ , the linear spring element will extend. This extension is directly proportional to the stress at all levels of stress until a certain critical stress τ_c is reached. At this point the Coulomb friction is insufficient, and the extension in the spring element ceases. Sliding will now take place provided that the stress is maintained at τ_c . Upon a reduction or reversal of stress, the elastic element will retract and recover the energy stored in it. The frictional work is, however, lost. (This frictional work will result in heat generation which, in turn, results in a local temperature rise. This temperature rise influences the level of stress, τ_c , in a complicated manner but always reduces it.) The modulus, G , of the elastic element is related to the initial traction slope through contact geometry and the kinematic conditions.

For simple slip traction curves, m and G are related as follows:

$$\bar{G} = \frac{3}{8} m F_z \frac{\bar{h}}{a^2 b} \quad (1)$$

where \bar{h} is the average film thickness, a and b are the semicontact dimension, and F_z is the contact normal load. The quantity \bar{G} is indicated here rather than G . This is to signify that we only deduce an average shear modulus. The reason for this is that we do not know exactly how the fluid shear modulus is influenced by the local pressure in the contact. (The extraction of G for the fluid is further

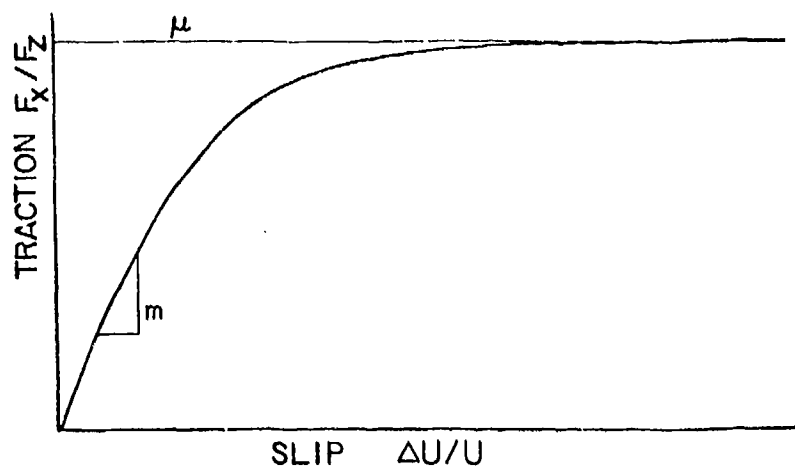


Figure 1. - General features of a traction curve showing the initial traction slope m and the peak traction coefficient μ .



Figure 2. - Schematic of the elastic/plastic traction model.

complicated by the fact that in the traction slope a certain amount of elastic creep of the disk material is invariably present.)

The frictional stress, τ_c , is directly related to the peak traction coefficient, μ , through the following equation:

$$\tau_c = \mu \frac{F_z}{\pi ab} \quad (2)$$

Again, we are only extracting the average quantity τ_c because of the lack of knowledge about the variation of τ_c with pressure. (This limiting stress is temperature dependent. The temperature of the fluid is not constant but rises as more and more slip occurs on the contact. For simplicity, however, we often use the peak traction coefficient, if such a peak exists.) A detailed description of how this model can be used to predict traction under conditions of spin, side slip, and the usual longitudinal slip is given by Tevaarwerk and Johnson (ref. 17) and Tevaarwerk (ref. 13). The analysis described in these references is entirely isothermal in nature.

To show how powerful this model is, consider the traction curves shown in figure 3 and reported by Tevaarwerk (ref. 18). These are curves obtained under a variety of conditions on two different traction testers and with two different fluids. Yet, by using an elastic/plastic traction model, all these curves can be reduced to fall on a single master traction curve (fig. 4). Each individual traction curve requires now only two parameters to describe it completely: the initial slope, m , and the peak traction coefficient, μ . This applies only to the simple slip traction curves, but the important parameters, m and μ , can be used to predict traction under any combination of spin and slip.

Theoretical Traction Results

The theoretical traction results, as calculated by Tevaarwerk and Johnson (ref. 17) and Tevaarwerk (ref. 13), for the elastic/plastic model are now presented. The reader is referred to the above two papers for further details. Although for a number of special cases analytical solutions exist, the general situation of combined slip, side slip, and spin was solved using digital techniques.

Traction Due to Slip

For simple dimensionless slip, J_1 , on the contact aspect ratio, k , the resulting traction, J_4 , is as follows:

$$J_4 = \frac{1}{\pi} \left[2 \tan^{-1} S + \frac{2S}{1+S^2} \right] \quad (3)$$

$$\text{where } S = \frac{2}{3} \frac{J_1}{\sqrt{k}}$$

and the dimensionless slip is

$$J_1 = \frac{3\pi}{8} \frac{m}{\mu} \frac{\Delta U}{U} \sqrt{k} \quad (4)$$

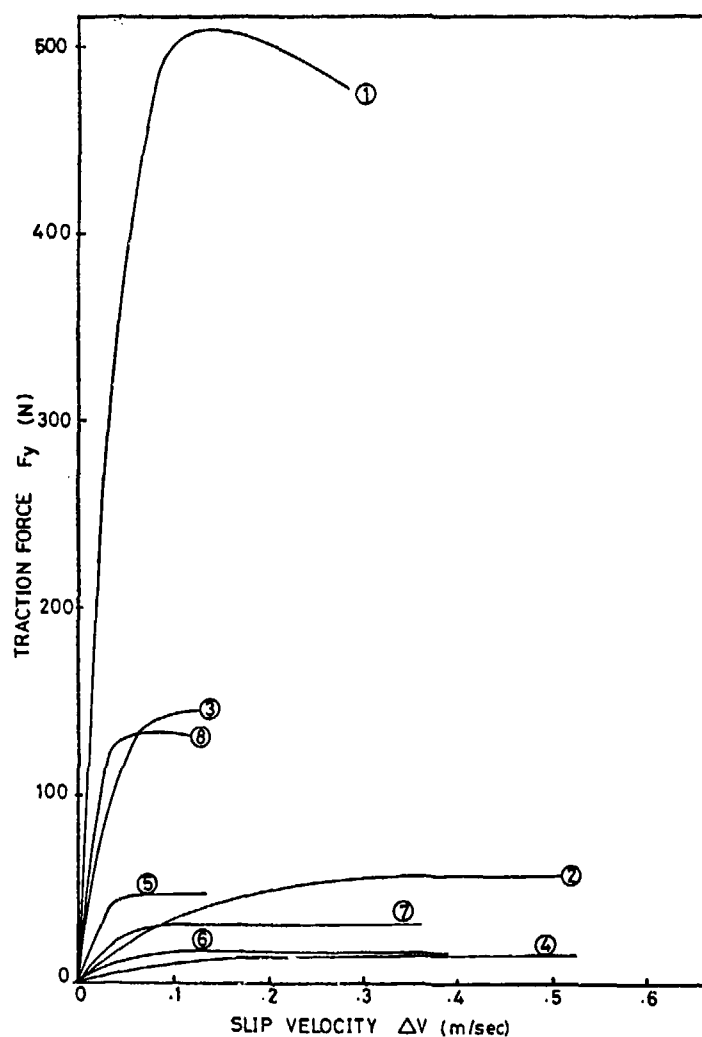
and the dimensionless traction is

$$J_4 = \frac{F_x}{\mu F_z} \quad (5)$$

This traction J_4 is a function of J_1 and k , as shown in figure 5. It may be observed from figure 5 that contacts of low aspect ratio have a superior performance in terms of traction at a given slip value.

Influence of Spin on Traction

For the combined action of slip and spin the resulting traction is given in figure 6. Dimensionless spin is defined as



Fluid type	curve number	inlet temp	Hertz press.	speed U	aspect ratio	normal load
(-)	(-)	(°C)	(GPa)	(m/sec)	(-)	(N)
SANTO 50	1	32	1.45	20	5	5000
"	2	69	1.0	80	5	1500
"	3	29	1.9	20	1	1400
"	4	69	1.0	80	1	200
TDF-88	5	30	1.9	10	1	416
"	6	70	1.45	30	1	185
"	7	70	1.0	30	5	460
"	8	33	1.45	10	5	1400

Figure 3. - Typical traction curves obtained on two fluids at a range of speeds, aspect ratios, inlet temperatures, and contact pressures.

$$J_3 = \frac{3\pi}{8} \frac{m}{\mu} \frac{\omega \sqrt{ab}}{U} \sqrt{k} \quad (6)$$

No known analytical solution exists, and the results were obtained by digital integration. The influence of spin is to increase the slip, though this appears to be so only above a certain threshold value of spin. When the spin is sufficiently high, it is expected that elastic strain may be neglected and the rigid/plastic model may be used.

The resulting traction due to the shear of a rigid/plastic-like material in the contact is shown in figure 7. The independent parameters are the aspect ratio k and the speed pole location ϵ . The speed pole location parameter is identical to that used by Magi (ref. 14). It is related to the dimensionless parameters used in this analysis as follows:

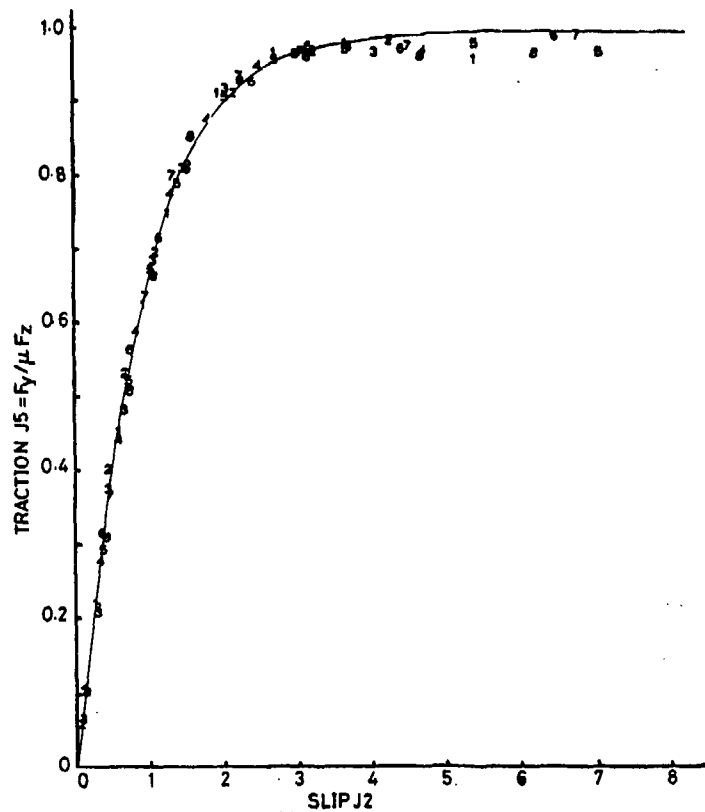


Figure 4. - Traction curves of figure 3 reduced to standard form of elastic/plastic curve.

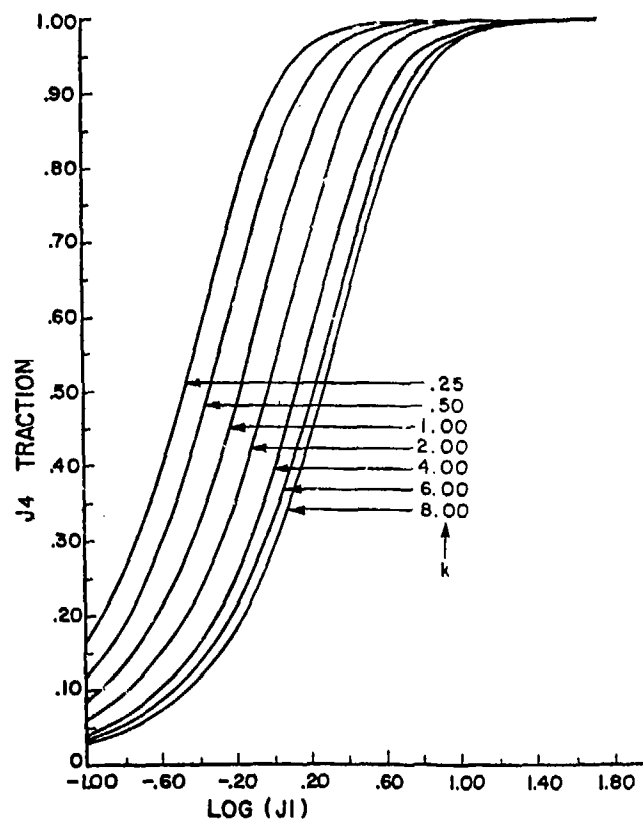


Figure 5. - Dimensionless traction curves for the elastic/plastic traction model at various ratios. These may be collapsed into one by dividing J_1 by \sqrt{k} .

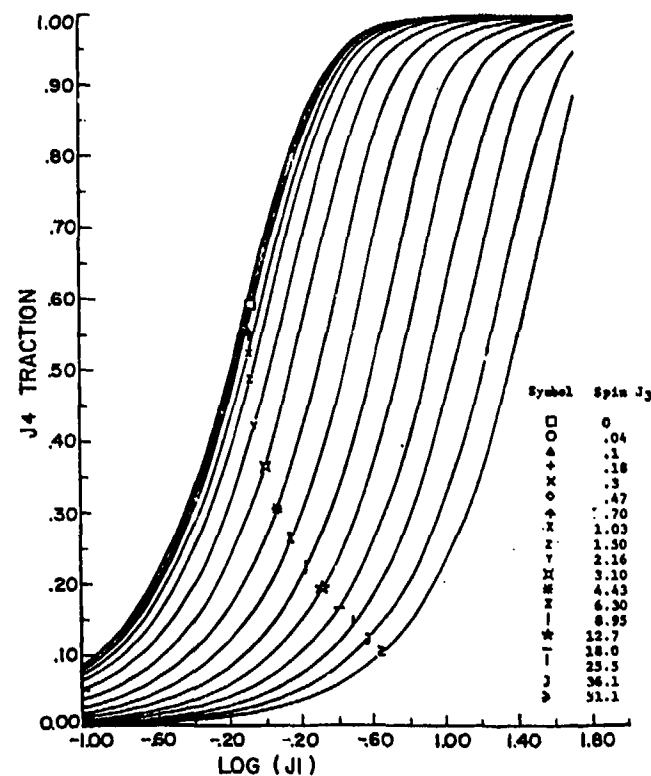


Figure 6. - Dimensionless traction curves for the elastic/plastic traction model under combinations of spin, J_3 , and slip, J_1 , for an aspect ratio of $\sqrt{k} = 1$.

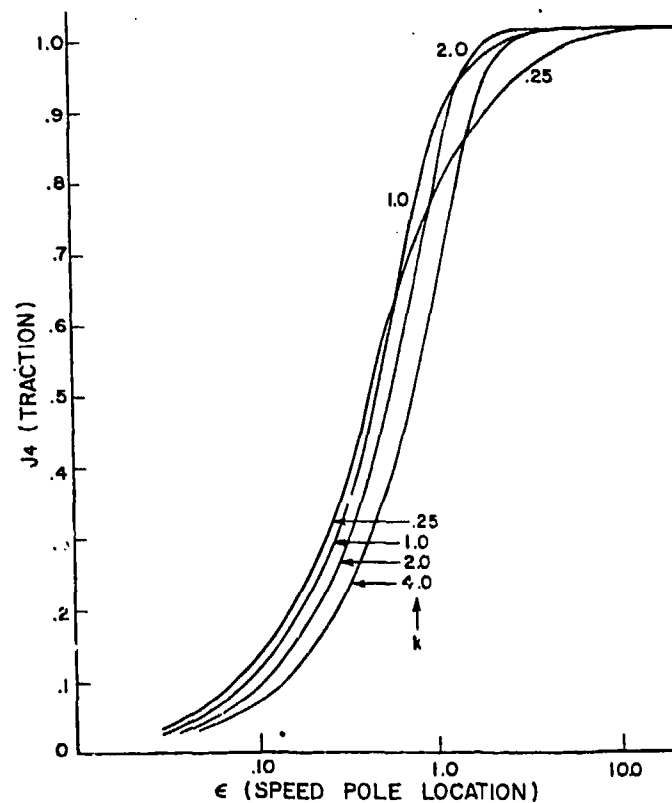


Figure 7. - Dimensionless traction curves for the rigid/plastic traction model at different speed pole locations. The speed pole location is given by $\epsilon = J_3/J_1$.

$$\epsilon = \frac{J_1}{J_3} = \frac{\Delta U}{\omega \sqrt{ab}} \quad (7)$$

Comparison with results obtained by Magi showed complete agreement. The results were obtained by numerical integration, and no known analytic expression exists for the traction in terms of the speed pole parameters. However, the curves shown in figure 7 do lend themselves to a simple empirical expression of the form:

$$J_4 = 1 - \exp[-(\epsilon k_1)^{k_2}] \quad (8)$$

This expression can also be written explicitly for ϵ . Coefficients k_1 and k_2 are given in table I for various aspect ratios. The largest error between the theoretical and predicted traction, according to equation (8), occurs in the low traction region and is less than 7 percent of the peak traction coefficient.

The traction curves and the influences of spin, as shown in figure 6, can be divided into three regions of influence. These regions are shown in figure 8 as a function of aspect ratio and dimensionless spin. The three regions represent:

- (1) Traction predicted by neglecting spin and by using the elastic/plastic model
- (2) Traction predicted by using the elastic/plastic model and by including spin
- (3) Traction predicted by using the rigid/plastic model and by including spin.

It is in this latter region, where thermal effects become important, the methods outlined by Tevaarwerk (ref. 15) may have to be used to obtain more accurate traction predictions.

Influence of Side Slip on Traction

For the combined action of slip and side slip, the resulting traction J_4 for an elastic/plastic model are given by

$$J_4 = \frac{2}{3} \frac{J_1 \psi}{S \sqrt{k}} \quad (9)$$

where

$$S = \frac{2}{3\sqrt{k}} \sqrt{(J_1^2 + J_2^2)}$$

$$J_2 = \frac{3\pi}{8} \frac{m}{\mu} \frac{\Delta V}{U} \sqrt{k}$$

and

$$\psi = \frac{1}{\pi} \left[2 \tan^{-1} S + \frac{2S}{1+S^2} \right]$$

Figure 9 shows traction J_4 as a function of slip J_1 at various levels of J_2 for an aspect ratio of $k=1$. The effect of side slip J_2 is to reduce the obtained traction in the working range.

When the imposed side slip becomes sufficiently large, the elastic effects may be neglected, and the traction can then be obtained by the rigid/plastic model:

$$J_4 = \frac{J_1}{\sqrt{J_1^2 + J_2^2}} \quad (10)$$

The reader might inquire as to the importance of being able to calculate the effect of side slip on traction. Side slip in traction drives results from misalignment of the axes of rotation of the principal shafts. Only very little misalignment is needed before 0.1 to 0.2 percent side slip is introduced. This can influence the longitudinal traction significantly, especially when little spin is present on the contact.

TABLE 1. - COEFFICIENTS
FOR THE RIGID/PLASTIC
TRACTION CURVE
EXPRESSION

Aspect ratio, k	k_1	k_2
0.5	1.8	0.9
1.0	1.9	1.1
2.0	1.4	1.5
4.0	1.1	1.5
8.0	.8	1.5

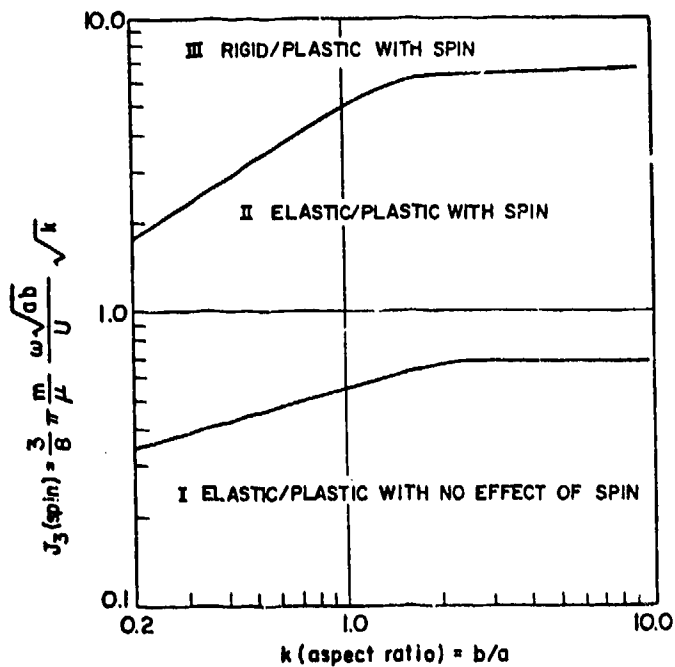


Figure 8. - Regions of influence of spin on the traction prediction of an elastic/plastic model. Dimensionless traction, J_4 , is maintained at 0.75.

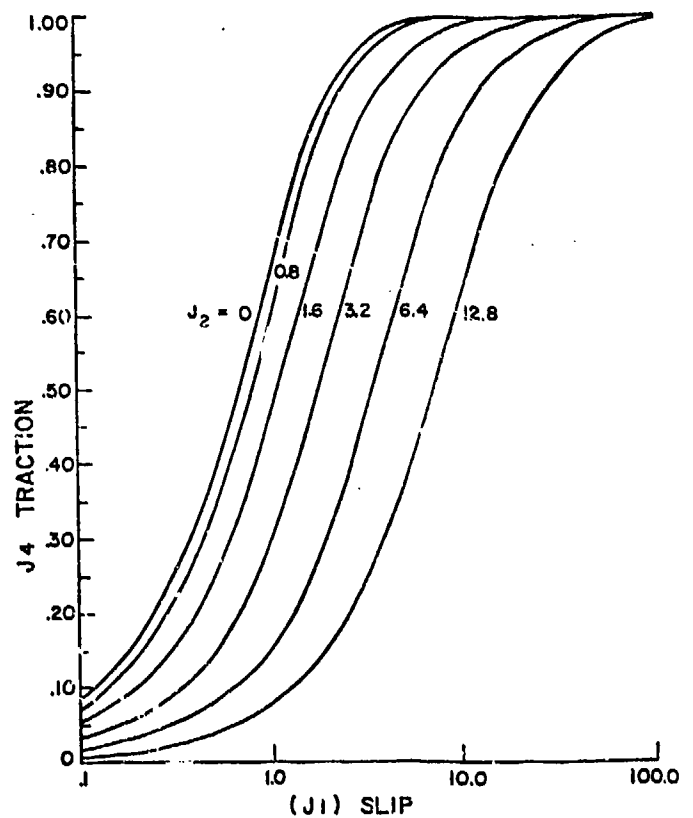


Figure 9. - Dimensionless traction curves predicted for combinations of slip, J_1 , and side slip, J_2 , using the elastic/plastic model.

Fluid Traction Data

Without the knowledge of the two fluid traction parameters, m and μ , the above models are not much use to the traction-drive designer. They do indicate traction trends when one or two parameters are varied, but no quantitative data can be obtained from them. To use the theory effectively one does need m and μ . These are related to fundamental fluid properties as we have seen before, but how these fundamental properties tie in with molecular structure of the fluid is not yet fully understood and often one resorts to experimentally available data for the particular fluid of interest.

To generate the experimental traction data for two fluids the Bearing, Gearing, and Transmission Section of NASA Lewis managed an extensive traction research under a Department of Energy program. This research was undertaken by Transmission Research, Inc. The main purpose of this research was to establish the traction parameters for two high-traction fluids at high speeds (10- to 80-m/sec surface velocity), at various contact aspect ratios ($k=0.5$ to 5), at inlet temperatures of 30° to 70° C, and at contact pressures as encountered in traction drives. Also, the traction was measured under a variety of spin, side slip, and longitudinal slip combinations.

The traction data obtained from this investigation is reported by Tevaarwerk (ref. 18). The two important parameters for the traction curves were extracted and correlated with the various independent parameters that were imposed.

Traction Data Correlation

Examination of the traction parameters obtained by the above investigation revealed that there are certain trends when one of the external parameters, such as pressure, speed, inlet temperature or aspect ratio, is varied. The trends are

- Traction coefficient decreases with decreasing pressure.
- Traction coefficient decreases with increasing speed.
- Traction coefficient decreases with increasing temperature.
- Traction coefficient decreases with increasing aspect ratio.

Similar observations were found on the initial traction slope. By linearization of these trends the following equations may be written:

$$\mu \propto A_1 + A_2 P \quad \mu \propto A_3 + A_4 U \quad \mu \propto A_5 + \frac{A_6}{\theta} \quad \mu \propto A_7 + A_8 k \quad (11)$$

These equations can be used directly for correlation purposes; however, to reduce the influence of weighting, because of the physical magnitude of certain of the variables, nondimensional variables should be used. These can be obtained quite easily by using transformations of the type

$$U' = \frac{U - \bar{U}}{\bar{U}} \quad P' = \frac{P - \bar{P}}{\bar{P}} \quad \theta' = \frac{\theta - \bar{\theta}}{\bar{\theta}} \quad k' = \frac{k - \bar{k}}{\bar{k}} \quad (12)$$

where the prime indicates the transformed variable and the barred variable is the average magnitude. Because the trends are all equally likely for a given condition of speed, temperature, pressure, and aspect ratio, the following general equation may be expected:

$$\mu = (A_1 + A_2 P')(A_3 + A_4 U') \left(A_5 + \frac{A_6}{\theta'} \right) (A_7 + A_8 k') \quad (13)$$

Multiplication yields the following expression:

$$\begin{aligned} \mu = & C_1 + C_2 k' + C_3 P' + C_4 P' k' + \frac{C_5}{\theta'} + C_6 \frac{k'}{\theta'} + C_7 \frac{P'}{\theta'} + C_8 k' \frac{P'}{\theta'} + C_9 U' + C_{10} U' k' \\ & + C_{11} U' P' + C_{12} U' P' k' + C_{13} \frac{U'}{\theta'} + C_{14} k' \frac{U'}{\theta'} + C_{15} P' \frac{U'}{\theta'} + C_{16} k' P' \frac{U'}{\theta'} \end{aligned} \quad (14)$$

where the coefficient C_1 to C_{16} are directly related to the coefficients A_1 to A_8 .

Initial Traction Slope

Equation (14) was also used on the initial traction slope data to obtain the coefficients C_1 to C_{16} by a least squares regression. The resulting regression coefficients are shown in appendix A for the two fluids tested. For these regression coefficients all the traction slopes for a given fluid were nondimensionalized by using equation (12). Before one can use the regression results to predict the initial traction slope, the variables need to be transformed according to this equation. This requires the knowledge of the average quantities of the variables and these are given in appendix A. Thus equation (14) can also be used to predict initial slope in using the appropriate coefficients C_1 to C_{16} given in appendix A.

Traction Coefficients

A similar analysis to the above could be done for the peak traction coefficient; however, it is also influenced by thermal effects due to spin. When spin is present, therefore, a further variation in the traction coefficient is possible. A similar treatment to the initial traction slope results gives the following expression for the traction coefficient:

$$\begin{aligned} \mu = & C_1 + C_2 Z' + C_3 k' + C_4 k' Z' + C_5 P' + C_6 P' Z' + C_7 P' k' + C_8 P' k' Z' + \frac{C_9}{\theta'} + C_{10} \frac{Z'}{\theta'} + C_{11} \frac{k'}{\theta'} \\ & + C_{12} k' \frac{Z'}{\theta'} + C_{13} \frac{P'}{\theta'} + C_{14} P' \frac{Z'}{\theta'} + C_{15} k' \frac{P'}{\theta'} + C_{16} k' P' \frac{Z'}{\theta'} + C_{17} U' + C_{18} U' Z' \\ & + C_{19} U' k' + C_{20} U' k' Z' + C_{21} U' P' + C_{22} U' P' Z' + C_{23} U' P' k' + C_{24} U' P' k' Z' \\ & + C_{25} \frac{U'}{\theta'} + C_{26} U' \frac{Z'}{\theta'} + C_{27} k' \frac{U'}{\theta'} + C_{28} U' k' \frac{Z'}{\theta'} + C_{29} P' \frac{U'}{\theta'} + C_{30} U' P' \frac{Z'}{\theta'} \\ & + C_{31} k' P' \frac{U'}{\theta'} + C_{32} U' k' P' \frac{Z'}{\theta'} \end{aligned} \quad (15)$$

where

$$Z = \frac{\omega \sqrt{ab}}{U}$$

and

$$Z' = \frac{Z - \bar{Z}}{\bar{Z}}$$

The regression coefficients for the traction coefficient of the two fluids are given in appendix A. They can be used to predict the traction coefficient whether spin is present or not.

It could be argued that a regression of the above type is not desirable because of the large number of coefficients involved. This is certainly true, and it is hoped that at some future time all the data can be reduced to two or three fundamental fluid parameters. However, such a model has not been sufficiently developed for inclusion here.

Example Traction Predictions

As an example of how the foregoing material may be used, let us take a look at some existing traction information and see how well the current methods will predict this traction. We will take some traction results as reported by Gaggermeier (ref. 19) and shown in figure 10. These data were

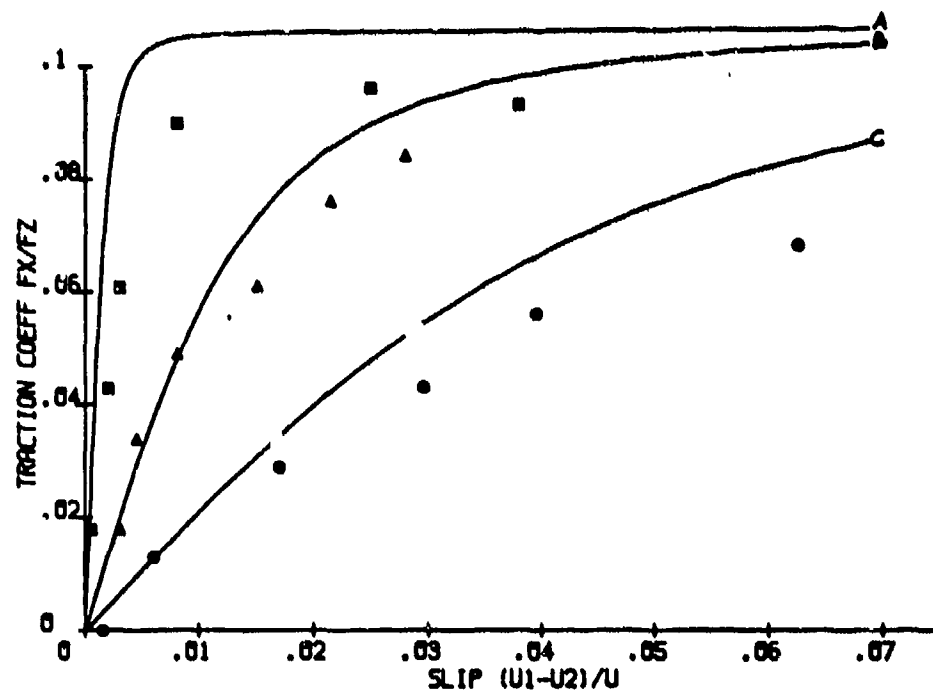


Figure 10. - Comparisons of measured and predicted traction under slip and side slip combinations. The following side slip was applied: ■ and curve A, 0 percent; ▲ and curve B, 1.57 percent; ● and curve C, 4.93 percent.

obtained on Santotrac 50 at a peak pressure of 1.854 GPa, an inlet temperature of 50° C, and a rolling speed of 8.4 m/sec. The aspect ratio for the contact was 1.5. The three sets of data points shown are for different degrees of side slip. These data, then, are a combination of side slip and longitudinal slip. The traction prediction based upon the elastic/plastic model as presented here is given by equation (9). To predict the actual traction, we need to know the initial traction slope and the peak traction coefficient for the particular fluid under the experimental conditions. These two parameters may be predicted by using the correlated data as reported here. We need to use equations (14) or (15) together with the coefficients as listed in appendix A. For Santotrac 50 at the particular conditions, as applicable to the experimental data, we get

$$m = 55.3 \quad (16)$$

$$\mu = 0.106$$

These two values can then be used in predicting the traction from equation (9). The predicted traction is shown in figure 10 as solid curves. It may be observed that the predicted values are somewhat higher than the experimental data. The most probable reason for this difference is the influence of thermal effects, which tend to reduce the traction at higher slip values. To get an improved prediction, methods as outlined in references 15 and 16 should be used.

Conclusion

In this paper it has been demonstrated how the traction performance of a typical drive can be

predicted from the basic knowledge of two fluid parameters, the initial traction slope, and the peak traction coefficient. These two parameters are given for two high-traction fluids as a function of inlet temperature, contact pressure, surface velocity, aspect ratio, and, in the case of the peak traction coefficient, the amount of spin on the contact. The traction behavior of the two fluids is very similar, with only minor differences. Thermal effects are not treated in this paper but can play a major part in the traction behavior of a contact. Current research indicates that a fairly simple thermal correction gives very good results. Also, very recent research by the author has indicated that the fundamental fluid properties of shear modulus and fluid shear strength can be represented by as few as three terms involving pressure and temperature only.

References

1. Clark, O. H.; Woods, W. W.; and White, J. R.: Lubrication at Extreme Pressure with Mineral Oil Films. *J. Appl. Phys.*, vol. 22, no. 4, Apr. 1951, pp. 474-483.
2. Hewko, L. O.: Contact Traction and Creep of Lubricated Cylindrical Rolling Elements at Very High Surface Speeds. *ASLE Trans.*, vol. 12, 1969, pp. 151-161.
3. Smith, F. W.: The Effect of Temperature in Concentrated Contact Lubrication. *ASLE Trans.*, vol. 5, no. 1, Apr. 1962, pp. 142-148.
4. Smith, R. L.; Walowit, J. A.; and McGrew, J. M.: Elastohydrodynamic Traction Characteristics of 5P4E Polyphenyl Ether. *J. Lubr. Technol.*, July 1973, pp. 353-362.
5. Johnson, K. L.; and Cameron, R.: Shear Behaviour of Elastohydrodynamic Oil Films at High Rolling Contact Pressures. *Proc. Inst. Mech. Eng. (London)*, vol. 182, pt. 1, no. 14, 1967, pp. 307-319.
6. Niemann, G.; and Stoessel, K.: Reibungszahlen bei elasto-hydrodynamischer Schmierung in Reibrad- und Zahnradgetrieben. *Konstruktion*, vol. 23, no. 7, 1971, pp. 245-260.
7. Johnson, K. L.; and Roberts, A. D.: Observations of Viscoelastic Behaviour of an Elastohydrodynamic Oil Film. *Proc. Roy. Soc. (London)*, Ser. A, vol. 337, no. 1609, Mar. 19, 1974, pp. 217-242.
8. Johnson, K. L.; and Tevaarwerk, J. L.: Shear Behaviour of Elastohydrodynamic Oil Films. *Proc. Roy. Soc. (London)*, Ser. A, vol. 356, no. 1685, Aug. 24, 1977, pp. 215-236.
9. Daniels, B. K.: Non-Newtonian Thermo-viscoelastic EHD Traction from Combined Slip and Spin. *ASME Preprint* 78-1.C-2A-2, Oct. 1978.
10. Hirst, W.; and Moore, A. J.: The Effect of Temperature on Traction in Elastohydrodynamic Lubrication. *Phil. Trans. Roy. Soc. (London)*, Sept. 1980, vol. 298, no. 1438, pp. 183-208.
11. Alsaad, M.; Pair, S.; Sandorn, D. M.; and Winer, W. O.: Glass Transition in Lubricants: Its Relation to Elastohydrodynamic Lubrication. *J. Lubr. Technol.*, vol. 100, July 1978, pp. 404-417.
12. Johnson, K. L.: Introductory Review of Lubricant Rheology and Traction. *Proc. Leeds-Lyon Conf.*, Leeds, England, 1978, pp. 155-161.
13. Tevaarwerk, J. L.: Traction Drive Performance Prediction for the Johnson and Tevaarwerk Traction Model. *NASA TP-1530*, 1979.
14. Magi, Mart: On Efficiencies of Mechanical Coplanar Shaft Power Transmissions. Chalmers University of Technology, Gothenburg, Sweden, 1974.
15. Tevaarwerk, J. L.: A Simple Thermal Correction for Large Spin Traction Curves. *J. Mech. Des.*, vol. 103, no. 2, April 1981, pp. 440-446.
16. Tevaarwerk, J. L.: Thermal Influence on the Traction Behaviour of an Elastic/Plastic Model. *Proc. Leeds/Lyon Conf.*, Leeds, England, 1980.
17. Tevaarwerk, J. L.; and Johnson, K. L.: The Influence of Fluid Rheology on the Performance of Traction Drives. *ASME J. Lubr. Technol.*, vol. 101, p. 266, 1979.
18. Tevaarwerk, J. L.: Traction Contact Performance Evaluation at High Speeds. *NASA CR-165226*, 1980.
19. Gaggermeier, H.: Untersuchungen zur Reibkraftuebertragung in Regel-Reibradgetrieben im Bereich elasto-hydrodynamischer Schmierung. Ph.D. Dissertation, University of Munich, 1977.

Appendix A

This appendix contains the regression coefficients for the traction data from the two fluids. The coefficients for slope are listed under column " m ," and the coefficients for the traction coefficient are listed under " μ ."

Coefficient	Santotrac 50			Sunoco TDF-88		
	μ eq. (14)	μ eq. (15)	m eq. (14)	μ eq. (14)	μ eq. (15)	m eq. (14)
U	44.906	45.933	45.890	22.340	23.076	22.476
P	1.356	1.331	1.369	1.449	1.408	1.424
Q	53.491	53.420	54.890	49.489	50.296	49.076
R	3.340	3.321	2.753	2.239	2.441	2.262
Z		5.786E-03			.639E-03	
C1	0.843E-01	0.745E-01	0.450E-02	0.877E-01	0.859E-01	0.452E-02
C2	-.685E-02	-.536E-02	-.719E-01	-.515E-02	-.582E-03	-.492E-01
C3	.434E-01	-.175E-02	.114E-02	.154E-01	-.480E-02	.649E-01
C4	.421E-01	-.219E-02	.109E-01	-.379E-02	.581E-03	-.102E-02
C5	-.960E-03	.204E-01	-.701E-01	-.676E-03	.162E-01	.202E-01
C6	.114E-02	-.208E-01	-.817E-01	-.428E-03	.211E-03	-.154E-01
C7	-.419E-03	.109E-01	.444E-00	.444E-03	-.601E-02	-.559E-00
C8	-.120E-02	-.258E-02	.805E-00	-.346E-02	-.542E-04	.609E-00
C9	-.197E-01	-.592E-03	-.755E-01	-.126E-01	-.102E-02	-.124E-02
C10	.299E-02	-.415E-03	-.577E-00	.356E-02	-.353E-03	.101E-02
C11	.350E-01	.705E-03	.124E-02	.141E-01	-.136E-03	.157E-02
C12	.664E-02	.957E-03	.115E-02	.764E-02	.401E-03	.270E-01
C13	.172E-02	.176E-02	-.921E-02	.167E-02	-.132E-02	-.639E-00
C14	-.317E-02	.305E-02	-.759E-01	.317E-03	-.848E-03	.558E-00
C15	-.285E-02	-.588E-02	.173E-00	-.851E-04	-.255E-02	.245E-01
C16	.956E-02	-.427E-02	.250E-01	.532E-02	.103E-02	-.196E-01
C17		-.162E-01			-.137E-01	
C18		-.273E-02			-.585E-03	
C19		-.534E-02			.344E-02	
C20		-.907E-03			.143E-02	
C21		.490E-01			.277E-02	
C22		.282E-01			-.382E-02	
C23		-.406E-01			.141E-01	
C24		-.588E-01			.701E-02	
C25		.324E-03			.177E-02	
C26		.790E-04			.104E-03	
C27		-.138E-04			-.162E-02	
C28		-.302E-03			-.723E-03	
C29		-.993E-02			-.850E-04	
C30		-.112E-01			.791E-03	
C31		.212E-01			.389E-03	
C32		.202E-01			-.291E-02	

→ Sizing Criteria for Traction Drives

Douglas A. Rohn,* Stuart H. Loewenthal,* and John J. Coy†

17

The development of reliable, lightweight, high-power traction drives for aerospace and terrestrial applications is rapidly expanding. Adjustable-speed drives have been used in a variety of commercial applications for over 50 years. Recent improvements, in terms of fluids with higher traction, materials with greater fatigue resistance, and design techniques with greater accuracy, have helped to increase their performance and reliability.

When designing or selecting a traction drive, one must be concerned with the service life of the unit. Presently, very little fatigue life data are available from well-controlled traction contact fatigue tests. However, many investigations have been conducted on rolling-element fatigue for rolling-element bearings (ref. 1). Because of the similarity in the expected failure mode, namely, rolling-element fatigue, the life analysis methods used to establish rolling-element bearing capacity ratings should be applicable to determining the service life and capacity of traction drive contacts (ref. 2).

The purpose of this paper is to present a simplified traction drive fatigue analysis (ref. 3), which was derived from the Lundberg-Palmgren theory (ref. 4). A second objective is to use this analysis to investigate the effects of rotational speed, multiplicity of contacts, and variation in the available traction coefficient on traction-drive system life, size, and power capacity. Some of these effects were studied in reference 3. Simplified equations are provided for determining the 90 percent survival life rating of steel traction-drive contacts of arbitrary geometry. References to life-modifying factors for material, lubrication, and traction will be made.

Symbols

a	contact ellipse semimajor axis, m (in.)
a^*	dimensionless contact ellipse semimajor axis
b	contact ellipse semiminor axis, m (in.)
b^*	dimensionless contact ellipse semiminor axis
c	orthogonal shear stress exponent
E	modulus of elasticity parameter, Pa (psi)
E'	material elasticity parameter, Pa (psi)
e	Weibull exponent
F	relative curvature difference
g	auxiliary elliptical contact size parameter, m (in.)
H	drive system life, hr
h	depth to critical stress exponent
K_1	material constant
K_2	geometric life variable
L	life, millions of stress cycles
N	number of planet rollers
n	speed of rotation, rpm
Q	rolling body normal load, N (lbf)
R	rolling radius, m (in.)
r	radius, m (in.)
u	number of stress cycles per revolution

*NASA Lewis Research Center.

†Propulsion Laboratory, U.S. Army Research and Technology Laboratories (AVRADCOM), NASA Lewis Research Center.

V stress volume, m^3 (in.³)
 W roller width, m (in.)
 z_0 depth to critical stress, m (in.)
 μ traction coefficient
 μ^* applied traction coefficient
 ξ Poisson's ratio
 ρ inverse curvature sum, m^{-1} (in.⁻¹)
 σ_0 maximum surface contact pressure, Pa (psi)
 τ_0 maximum reversing orthogonal shear stress, Pa (psi)

Subscripts:

A, B elastic bodies
 i system element
 s system
 x, y reference planes

Analysis

Fatigue Life Model

In 1947 Lundberg and Palmgren (ref. 4) published a statistical theory for the failure distribution of ball and roller bearings. The mode of failure was assumed to be subsurface-originated (SSO) fatigue pitting. Lundberg and Palmgren theorized that SSO fatigue pitting was due to high stresses in the neighborhood of a stress raising incongruity in the bearing material. Their theory is used by bearing manufacturers to establish rolling-element-bearing fatigue-life ratings. In references 5 and 6 the theory was applied to predicting the fatigue lives of spur and helical gears. The predicted life of a steel gearset was confirmed with life data from full-scale spur-gear tests (ref. 6). The theory has also been adapted to analyzing the fatigue lives of traction drives (refs. 2 and 7). The theory that follows is an extension of that presented in reference 3.

For a steel rolling-element the number of stress cycles endured before failure occurs is given by the following equation (ref. 2):

$$L = \left(\frac{K_1 z_0^h}{\tau_0^c V} \right)^{1/e} \quad (1)$$

This modified form of the Lundberg-Palmgren theory for contact-fatigue-life prediction is applicable to gears, bearings, and other rolling-contact elements. The critical shear stress τ_0 is considered to be the maximum orthogonal reversing shear stress, which occurs below the surface of the contacting elements. This stress is not the largest of the subsurface stresses, but it has the largest fluctuating component, which is critical to the fatigue process. The stress volume term V is important since Lundberg-Palmgren theory is based on the probability of encountering a fatigue-initiating flaw in the volume of the material that is being stressed. The depth to the critical stress z_0 is a relative measure of the distance the fatigue crack must travel in order to emerge at the surface and thus cause a failure. For rolling-element bearings (and bodies in rolling contact in general) made of AISI 52100 steel (Rockwell-C 62 hardness), with a fatigue life at a 90-percent probability of survival, the following values are appropriate for use in equation (1) to determine life (in millions of stress cycles):

$$K_1 = 1.430 \times 10^{95} \text{ (N and m units)} \quad = 3.583 \times 10^{56} \text{ (lbf and in. units)}$$

Based on life tests of ball and roller bearings, the accepted exponent values are $h = 7/3$, $c = 31/3$, and $e = 10/9$ for an elliptical point contact or $e = 3/2$ for a line contact (ref. 4).

Contact Stress Analysis

The stress analysis of elastic bodies in contact was developed by Hertz (ref. 8). Hertz assumed homogeneous, solid, elastic bodies made of isotropic material, which are characterized by Young's

modulus E and Poisson's ratio ξ . Bodies A and B in contact are assumed to have quadratic surfaces in the neighborhood of the contact point. The theory of Hertz is summarized by Harris (ref. 9).

Figure 1 shows two bodies in contact. Planes x and y are the respective planes of maximum and minimum relative curvature for the bodies. These planes are mutually perpendicular. They are also perpendicular to the plane that is tangent to the contacting bodies' surfaces at the point of contact. Planes x and y must be chosen so that the relative curvature in plane x is greater than in plane y , thus:

$$\frac{1}{r_{Ax}} + \frac{1}{r_{Bx}} > \frac{1}{r_{Ay}} + \frac{1}{r_{By}} \quad (2)$$

The radii of curvature may be positive or negative depending on whether the surfaces are convex or concave, respectively.

When the bodies are pressed together, the point of contact is assumed to flatten into a small area of contact which is bounded by an ellipse with major axis $2a$ and minor axis $2b$ as shown in figure 1. Plane y contains the major axis of the contact ellipse, and plane x contains the minor axis. The ratio a/b is called the ellipticity ratio of the contact. The values of a/b range from 1 to ∞ for various curvature combinations of contacting surfaces. For cylinders in contact the ellipticity ratio approaches ∞ , and the flattened area of contact is a rectangular strip. For spheres in contact the ellipticity ratio is 1. The first type is called line contact and all other types are called point contacts.

When performing contact analysis, one must be aware of the geometrical orientation of the rolling radii and of principal planes. The principal radii r_{Ax} and r_{Bx} are not, in general, equal to the rolling radii. A typical pair of traction rollers in contact is shown in figure 2. Bodies A and B are generalized traction rollers which rotate, in this case, about coplanar axes. The distance from the axis of rotation of a body to the point of contact is the rolling radius of the body. This is the radius which determines rotational speed and drive ratios. The plane of contact is the plane which is tangent to both bodies at the point of contact. The principal radii r_{Ax} and r_{Bx} lie in the principal plane, which is perpendicular to the plane of contact. Thus, the value of r_{Ax} or r_{Bx} is defined by a line segment that is normal to the contact plane between the point of the contact and some point on the axis of rotation (fig. 2). A trigonometric relationship exists between the principal radii, r_{Ax} and r_{Bx} and the rolling radii, R_A and R_B as a function of the angles between the rotational axes and the contact plane. As shown in the figure, the principal transverse radii r_{Ay} and r_{By} lie in the plane of the cross section which is also perpendicular to the contact plane.

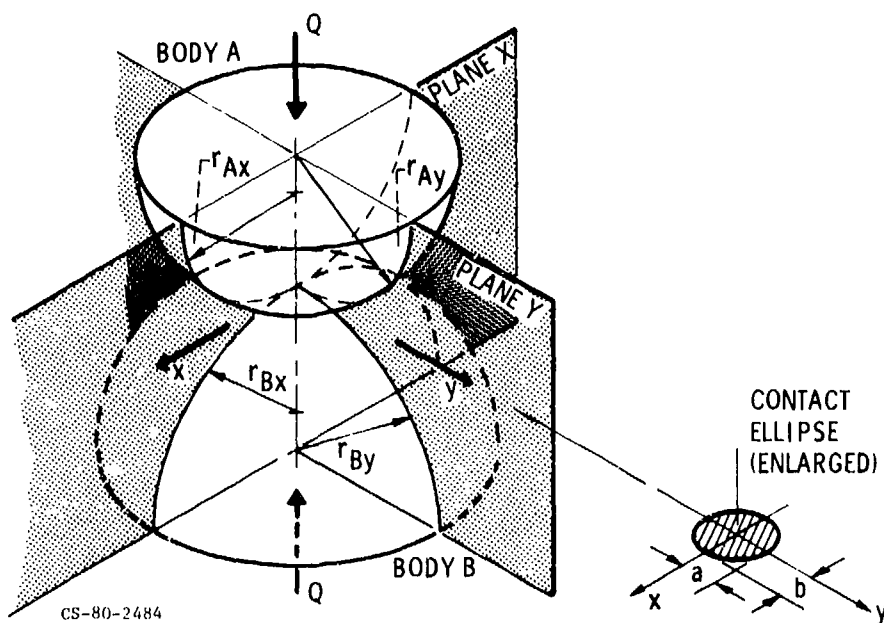


Figure 1. - Geometry of contacting solid elastic bodies.

It is instructive to note that when performing elastohydrodynamic (EHD) film thickness calculations or those having to do with traction, the orientation of the contact ellipse relative to the direction of rolling becomes important. While in most applications the semimajor ellipse axis a is oriented perpendicular to the rolling direction, this is not always the case. In many EHD film thickness equations, dimension a is taken to be perpendicular to the rolling direction, irrespective of whether it is the semimajor or semiminor ellipse axis. Since, in this analysis, dimension a is always taken to be the semimajor axis, it may not always correspond to dimension a for purposes of calculating EHD film thickness.

In figure 2 the axes of rotation are in the same plane. This is the case for nearly all traction drives. If the rollers rotate about axes that are significantly skewed in relation to one another or if extreme misalignment exists, then the principal radii must be redetermined on the basis of three mutually perpendicular planes which satisfy equation (2). For slight misalignments the difference in the radii will be very small.

The maximum surface contact pressure at the center of the elliptical pressure distribution is

$$\sigma_0 = \frac{3Q}{2\pi ab} \quad (3)$$

where the semimajor and semiminor contact ellipse axes are

$$a = a^*g \quad (4)$$

$$b = b^*g \quad (5)$$

and the auxiliary contact size parameter is

$$g = \sqrt[3]{\frac{3Q}{2\rho} \left(\frac{1 - \xi_A^2}{E_A} + \frac{1 - \xi_B^2}{E_B} \right)} \quad (6)$$

and where the inverse curvature sum is

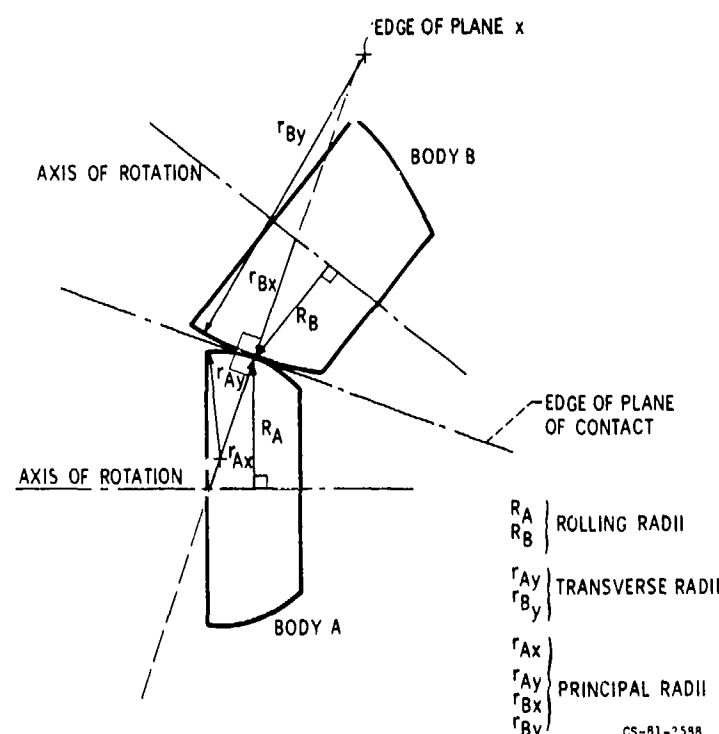


Figure 2. - Geometry of typical traction rollers.

$$\rho = \frac{1}{r_{Ax}} + \frac{1}{r_{Bx}} + \frac{1}{r_{Ay}} + \frac{1}{r_{By}} \quad (7)$$

For steel contacting bodies, with $E_A = E_B = 207$ GPa (3.0×10^7 psi) and $\xi_A = \xi_B = 0.3$, the auxiliary contact size parameter can be expressed as

$$g = 2.36 \times 10^{-4} \sqrt[3]{\frac{Q}{\rho}} \quad (\text{N and m units})$$

or

$$g = 4.50 \times 10^{-3} \sqrt[3]{\frac{Q}{\rho}} \quad (\text{lbf and in. units})$$

The dimensionless contact ellipse semimajor and semiminor axes, a^* and b^* , can be determined from the elliptical integrals used in Hertzian theory (ref. 9). The values of a^* and b^* are plotted in reference 9. Curve-fitted equations for the elliptical integrals can be found in references 7 and 10. The magnitude of the critical stress, that is, the subsurface maximum orthogonal reversing stress τ_0 and its depth z_0 in equation (1), are also given in references 7, 9, and 10. The stressed volume V for a rolling-element contact is given by

$$V = az_0 2\pi |R| \quad (8)$$

where R is the element's rolling radius. This assumes that the semimajor axis a is perpendicular to the rolling direction. Thus, the term $2\pi R$ is equal to the length of the rolling track which is traversed during one revolution.

Fatigue Life Equation

Elliptical contacts. – Estimation of the theoretical fatigue life of a rolling-element contact based on the aforementioned equation is fairly straightforward. By substituting the previously discussed terms into equation (1), a simpler formula can be developed, which expresses the life in terms of material constants, applied load, and contacting body geometry.

Assuming both contacting bodies are made of steel (i.e., $E_A = E_B = 208$ GPa (3.0×10^7 psi) and $\xi_A = \xi_B = 0.3$) and using the exponents and material factor already presented, equations (1) to (8) can be combined to obtain

$$L = K_4 (K_2)^{0.9} Q^{-3\rho - 6.3} |R|^{-0.9} \quad (9)$$

where L = 90 percent survival life of a single contacting element in millions of stress cycles, and

$$K_2 = \left(\frac{z_0}{b}\right)^{4/3} \left(\frac{\tau_0}{\sigma_0}\right)^{-31/3} (a^*)^{28/3} (b^*)^{35/3} \quad (10)$$

$$K_4 = 2.32 \times 10^{19} \quad (\text{N and m units})$$

$$= 6.43 \times 10^8 \quad (\text{lbf and in. units})$$

where R is the rolling radius of the body whose life is L . The geometry variable K_2 contains four factors, each of which depend only on the relative curvature difference, F , where

$$F = \frac{\left(\frac{1}{r_{Ax}} + \frac{1}{r_{Bx}}\right) - \left(\frac{1}{r_{Ay}} + \frac{1}{r_{By}}\right)}{\rho} \quad (11)$$

From the values of a and b given in reference 9, it can be determined that the contact ellipticity ratio a/b is also a function of F . Thus, given either F or a/b , the variable K_2 can be determined as shown in figure 3.

For convenience an approximation for K_2 can be developed from an expression appearing in Lundberg and Palmgren's (ref. 4) rolling-element bearing capacity equation. After suitable rearrangement of terms, K_2 can be directly calculated from F , by the approximation

$$K_2 = 4.80 \times 10^6 (1 - F)^{-1.367} (1 + F)^{-5.633} \quad (12)$$

As can be seen from the plot of this equation (fig. 4), it is accurate to within 10 percent for $F > 0.8$ or $a/b > \text{about } 4$. For more accurate K_2 values or when $a/b < 4$, figure 4 can be used directly, or equation (10) can be used together with the curve-fitted parameters appearing in references 7 and 10.

In many traction drives the contact ellipse is oriented such that semimajor axis is perpendicular

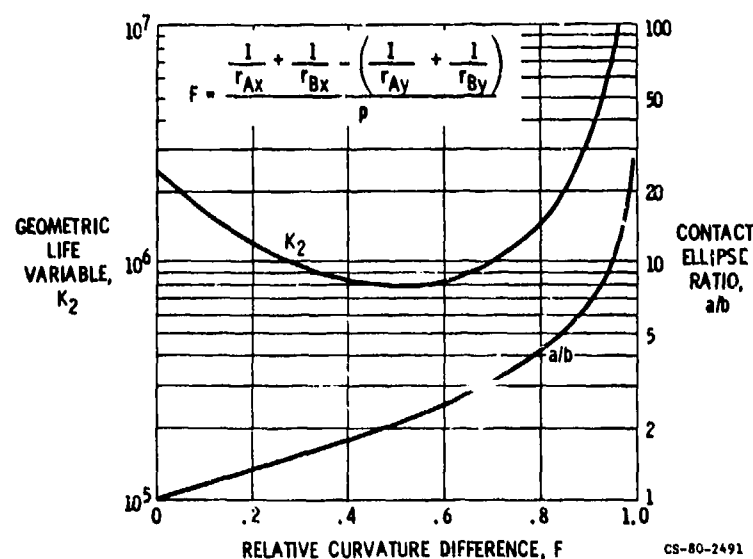


Figure 3. - Geometric life variable K_2 and contact ellipticity ratio a/b versus relative curvature difference F .

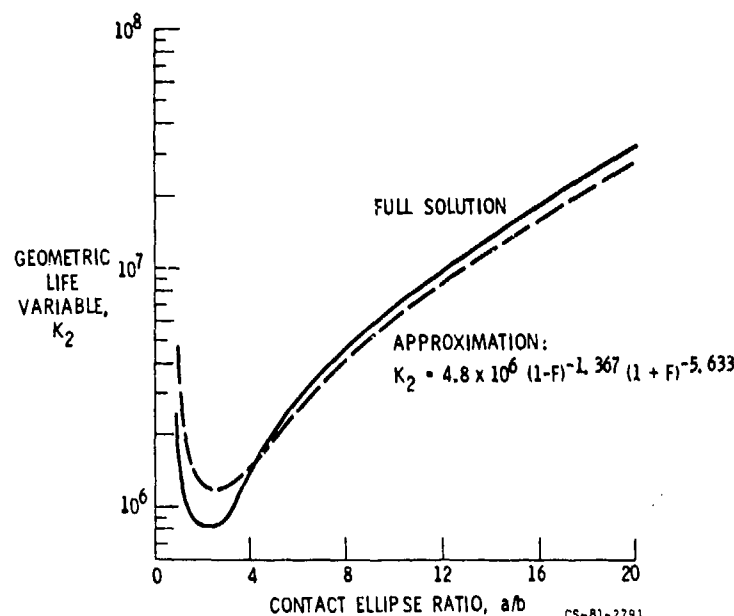


Figure 4. - Approximation for geometric life variable.

to the direction of rolling. If this is the case and if the rolling radii are also equal to the principal radii, that is, $R_A = r_{Ax}$ and $R_B = r_{Bx}$, then

$$\rho = \frac{2}{R_A} \left(\frac{1 + \frac{R_A}{R_B}}{1 + F} \right) \quad (13)$$

and from equation (9)

$$L = K_5 (K_2)^{0.9} Q^{-3} \left(\frac{\left| 1 + \frac{R_A}{R_B} \right|}{1 + F} \right)^{-6.3} |R_A|^{5.4} \quad (14)$$

where

$$K_5 = 2.95 \times 10^{17} \text{ (N and m units)}$$

$$= 8.16 \times 10^6 \text{ (lbf and in. units)}$$

and where R_A is the rolling radius of the body whose life in millions of stress cycles is L and R_B is the rolling radius of the mating body.

In the calculation of the stressed volume term V in equation (8), the contact ellipse semimajor axis has been assumed to be oriented perpendicular to the direction of rolling. However, if the semiminor axis is perpendicular to the rolling direction, the stressed volume expression (eq. (8)) must contain the semiminor axis, b , instead of semimajor axis, a . Equations (9) and (10) are still valid with the exception that in equation (10) the exponent of a^* becomes $31/3$ and the exponent on b^* becomes $32/3$. Also figure 4 and the approximation (eq. 12) are no longer valid. Then K_2 can be found from the modified equation (10) together with the curve-fitted parameters of references 7 and 10.

An expression for the maximum surface contact pressure can also be developed for steel bodies from equations (5) to (8) where

$$\sigma_0 = \frac{8.55 \times 10^6}{a^* b^*} Q^{1/3} \rho^{2/3} \text{ (N and m units)} \quad (15)$$

or

$$\sigma_0 = \frac{2.36 \times 10^4}{a^* b^*} Q^{1/3} \rho^{2/3} \text{ (lbf and in. units)}$$

Line contacts. — The analysis presented thus far has been confined to point contact. In the case of the line contact, it can be shown that

$$L = K_6 Q^{-3} |R_A|^{3.22} W^{2.33} \left(\left| 1 + \frac{R_A}{R_B} \right| \right)^{-3.89} \quad (16)$$

where

$$K_6 = 4.21 \times 10^{25} \text{ (N and m units)}$$

$$= 6.71 \times 10^{14} \text{ (lbf and in. units)}$$

and where R_A is the rolling radius of the body whose life, in millions of stress cycles, is L , and R_B is the rolling radius of the mating body.

The expression for maximum surface contact pressure in line contact is

$$\sigma_0 \propto Q^{1/2} \quad (17)$$

and, therefore, from equation (17)

$$L \propto \sigma_0^{-6} \quad (18)$$

However, the sixth power relationship between fatigue life and contact pressure is unlike that of any rolling-contact fatigue data known to the authors. Most data show at least a ninth-power relationship (ref. 11). In reference 6 fatigue tests on spur gears whose contact geometry approximate that of a line contact, life was inversely related to the 8.6 power of stress. Additionally, the Lundberg-Palmgren data, which were used to establish the line-contact exponents, were generated for a roller bearing that assumed a "modified" line contact. This contact was analytically developed from an elliptical contact stress distribution that had been mathematically corrected (ref. 4). Furthermore, it is not desirable to design traction contacts without some transverse curvature. Transverse curvature is required to avoid the adverse effects of excessive edge loading as a result of possible axis skew, misalignment, or overhang. In view of the above the life equation for line contact should be used with discretion.

System life. — Heretofore, the equations express rolling-element fatigue life for a single rolling element in terms of millions of stress cycles. However, in the case of a traction drive, it is system life that is important. All bodies in a system accumulate stress cycles at different rates because their speeds of rotation and number of stress cycles per revolution may not all be the same. To compare lives of the various bodies, clock time should be used. Assume that the speed in revolutions per minute of the i^{th} body is n_i and that there are u_i stress cycles per revolution, then the life of body, i , in hours is given by

$$H_i = \frac{L_i}{u_i n_i} \frac{10^6}{60} \quad (19)$$

The life of the system is then found by applying Weibull's rule (ref. 9). If the system consists of i roller bodies and the life of each is designated H_i ($i = 1$ to j), then the system life in hours is given by

$$H_S = \left[\frac{1}{(H_1)^e} + \frac{1}{(H_2)^e} + \dots + \frac{1}{(H_j)^e} \right]^{-1/e} \quad (20)$$

Thus, for the simplest arrangement, a single pair of rollers, the contact life in hours for an elliptical contact would be

$$H_S = \left[\frac{1}{(H_1)^{10/9}} + \frac{1}{(H_2)^{10/9}} \right]^{-9/10} \quad (21)$$

where H_1 and H_2 are equal to the individual lives of each roller.

Reliability. — The material constant K_1 required in equation (1) was deduced from fatigue-test data at a 90-percent probability of survival. Such a fatigue life is the life which 90 percent of a large number of identical traction drive systems will equal or exceed under a given operative condition. Rolling-element bearing capacities, given in manufacturer's catalogs, are generally defined at this 90-percent life. However, the service life of many gearboxes and other mechanical components is based on some mean or average time before failure. The effect of different reliability levels on rolling-element and traction contact fatigue life is shown in figure 5. Note that at the median life level (50-percent survival) the life is over five times the life at 90-percent survival. Because of the statistical distribution of rolling-element fatigue life, the median fatigue life is not equal to the mean or average life. For the accepted values of the exponent e in equation (1) of 10/9 and 3/2 for ball and roller

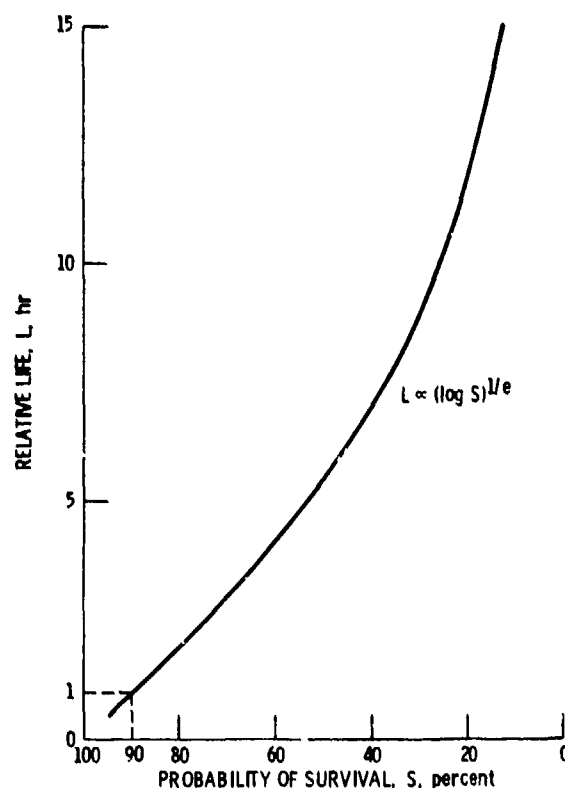


Figure 5. - Relative probability of survival.

bearings, the mean life corresponds to 61.7-percent and 57.6-percent failed, respectively (ref. 12). One should thus be aware of the difference between designing for 90-percent reliability and designing on the basis of mean life, as is the case for many machine elements.

Life Adjustment Factors

Advancements in rolling-element bearing technology since the publication of the Lundberg-Palmgren theory have generally increased bearing fatigue lives. These improvements resulted from the use of improved materials and manufacturing techniques along with a better understanding of the variables affecting fatigue life. In recognition of these advancements, life adjustment factors have been developed (ref. 1) for adjusting Lundberg-Palmgren fatigue-life ratings for ball and roller bearings. Several of these factors are considered to be equally applicable to traction-drive elements in view of the similarities in contact geometry, operating conditions, failure modes, materials, and lubrication (ref. 2). The factors that are appropriate are material, processing, and lubrication.

An additional factor, not considered for rolling-element bearings in reference 1, but important to traction-drive contacts is the potentially deleterious effect that traction may have on fatigue life. The addition of a tangential force component to the contact can alter the subsurface stress field which may, in turn, change the fatigue life. Some investigators (ref. 13) have found a decrease in life from rolling-element fatigue tests when relative sliding and traction are introduced. Rolling-element fatigue tests (ref. 14) with increased spin (i.e., rotational sliding within the contact area) also showed a reduction in fatigue life. However, insufficient data currently exist to properly quantify the effects of traction on rolling-element fatigue life. It is prudent to include in life calculations the possibility of a reduction in fatigue life due to traction. A life factor arbitrarily set to 1/2 would not be unreasonable until better test data are available. In this paper the effects of the operating variables on fatigue life have not been adjusted by the life modifying factors cited. Such factors are much more important on an absolute basis than on a relative basis as used here.

Results and Discussion

Effects of Size, Speed, and Traction Coefficient

The relative effects of roller size and speed on drive system life and torque capacity are of immense interest to the designer of traction drive systems. Generally, for a given power level and life, the size of a power transmitting element, such as a gear or a traction drive roller, can be reduced as speed is increased, since torque decreases. This effect and several others can easily be studied for general and specific cases through the use of equation (9).

Size effects. — It is evident from equation (9) that for a given rolling contact, increasing the load will decrease life by a power of 3. In other words, for a constant available traction coefficient and body size,

$$L \propto T^{-3} \quad (22)$$

In addition, a direct relationship exists between life and element size (radius and contact width). For constant torque and traction coefficient, $Q \propto 1/R$. For constant relative radii difference F , the transverse radius or contact width is proportional to the rolling radius. Therefore, $\text{size} \propto R$. Also, $K_2 = \text{constant}$ and $\rho \propto 1/R$. Substituting these proportionalities into equation (9) and noting that size and rolling radius can be interchanged yield

$$L \propto \left(\frac{1}{\text{size}}\right)^{-3} \left(\frac{1}{\text{size}}\right)^{-6.3} (\text{size})^{-0.9} \quad (23)$$

or

$$L \propto (\text{size})^{8.4}$$

for constant torque and traction coefficient. Similarly, since load Q is directly related to torque and inversely related to radius, we may write: $Q \propto (\text{torque}/\text{size})$. Substituting this into equation (9) and holding life constant produces

$$\text{Torque} \propto (\text{size})^{2.8} \quad (24)$$

The above two relationships are shown graphically in figure 6. It should be emphasized that, while they are very useful for preliminary sizing, they hold only for a constant available traction coefficient. In detailed drive design, the effect of changes in operating conditions on the traction performance of the lubricant must also be considered.

Size, speed, and traction coefficient effects. — Traction data (refs. 15 and 16) for various lubricants show that the maximum available traction coefficient μ decreases with an increase in surface speed and with a decrease in contact pressure. Typical traction data from a twin-disk machine (described in ref. 16) are given in figure 7 where the maximum available traction coefficient μ is plotted versus surface speed for various maximum contact pressures and a contact ellipse ratio of 5. To provide a safe margin against gross slippage, 75 percent of this maximum coefficient is often used as the operating coefficient in a traction drive.

An arbitrary roller pair of constant ratio and $a/b = 5$, operating at a given power level, was analyzed for fatigue life. The contacting rollers were assumed to operate, first, under a fixed applied traction coefficient μ^* and, second, with the highest possible traction coefficient based on the data of figure 7. The appropriate value of μ for this comparison was found from an iterative process, since μ is dependent on the contact pressure and speed and vice versa.

Figure 8 shows the effect of size on contact fatigue life. Figure 9 includes the effect of both size and speed. In figure 8 an increase in size increases life as would be expected. Increasing the operating speed in figure 9 accumulates more stress cycles per hour, but since the speed and torque are inversely related for constant power, the decrease in torque and thus normal load is more significant. This results in longer life at higher speeds. Additionally, figure 9 shows that for a constant-life condition, the rolling-traction element size can be reduced with increased rotational speed.

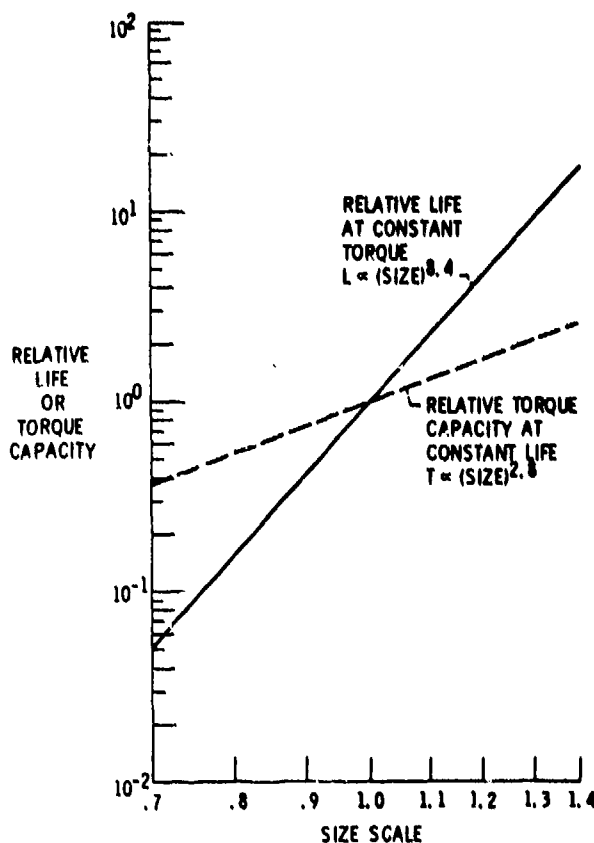


Figure 6. - Relative life at constant torque and relative torque capacity at constant life versus relative size

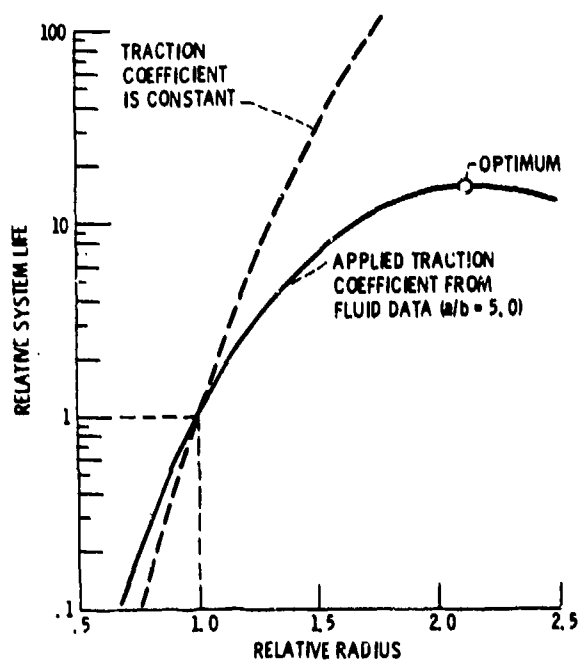


Figure 8. - Relative life versus relative radius for a roller pair in simple traction contact. Power, speed, and a/b are constant.

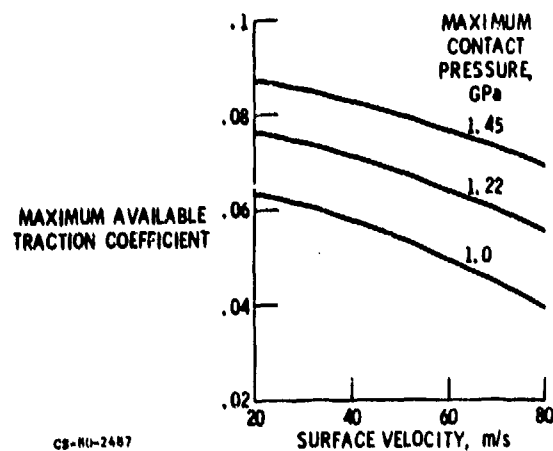


Figure 7. - Typical maximum available traction coefficient versus surface velocity and maximum contact pressure. Synthetic hydrocarbon traction fluid; $a/b = 5$; zero spin; temperature, 343 K. Data from a twin-disk machine described in reference 16.

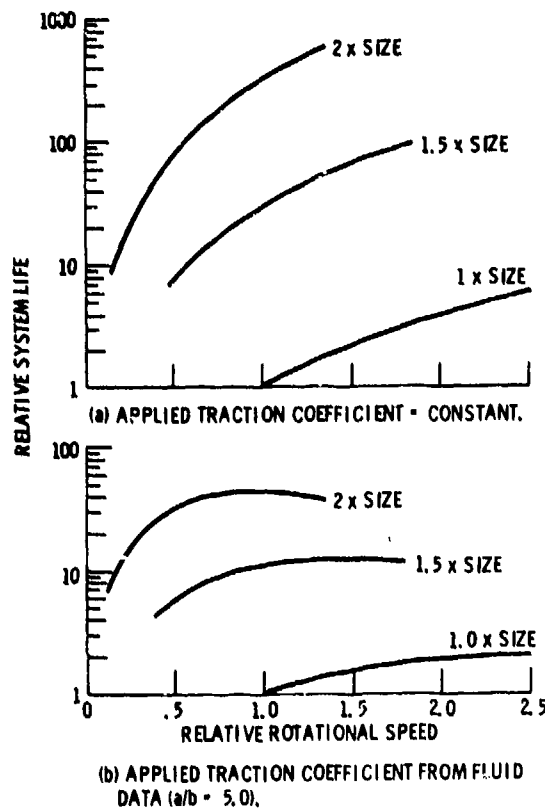


Figure 9. - Relative life versus relative speed for various size roller pairs in simple traction contact. Power, ratio, and a/b are constant.

The reason for higher life in either the constant μ or variable μ case is that increasing traction roller's size or rotational speed for constant power reduces the tangential force and thus the normal load and contact pressure. However, reducing the contact pressure or increasing the surface speed produces a loss of available traction coefficient and thus a need for a higher normal load to transmit the torque. This loss in μ causes a flattening of the life trend with increased size as shown in figure 8. In fact, for the range shown, the life curve reaches a maximum and then diminishes, indicating an optimum size for best life. Similarly, the life trends in figure 9(b) also flatten due to a loss in μ . The curves of the $1.5\times$ and $2\times$ size rollers show an optimum speed.

The importance of the available traction coefficient to the performance of a traction drive can be related to various design parameters. The drive's overall size (i.e., element diameters), system life, torque capacity, weight, and power-to-weight ratio are quite sensitive to the lubricant's traction coefficient. By substituting $Q = T/\mu$ (where T is the tractive force) into equation (9), the direct effect of traction coefficient on the above parameters can be determined in figure 10, where a/b is held constant. The curves are arbitrarily normalized relative to $\mu = 0.05$. The trend and proportionality between μ and each of the three parameters is valid where the other two parameters are held constant. Life shows the highest sensitivity to μ , but all three performance factors exhibit improvements with higher values of the traction coefficient.

By multiplying the diameter squared by the width of the Hertzian contact, a measure of the drive volume and thus weight can be obtained. The influence of the traction coefficient on relative weight is shown in figure 11. Also shown in figure 11 is the relative power-to-weight ratio, determined by dividing torque capacity at constant speed by weight. These relationships again demonstrate the benefits of using high-traction-coefficient lubricants.

Effect of multiple contacts on capacity and life. - Weight and size efficient traction drives (refs. 17 to 21) generally require multiple, load-sharing contacts. The extent that multiple, parallel contacts reduce unit loading, improve life, and increase power capacity can easily be explored with the analysis presented here. The configurations used to demonstrate this are a set of multiple, identical planetary rollers in external contact with a central sun roller and a set of multiple, identical planetary rollers in internal contact with a ring roller. These arrangements typify the multiple contacts that can

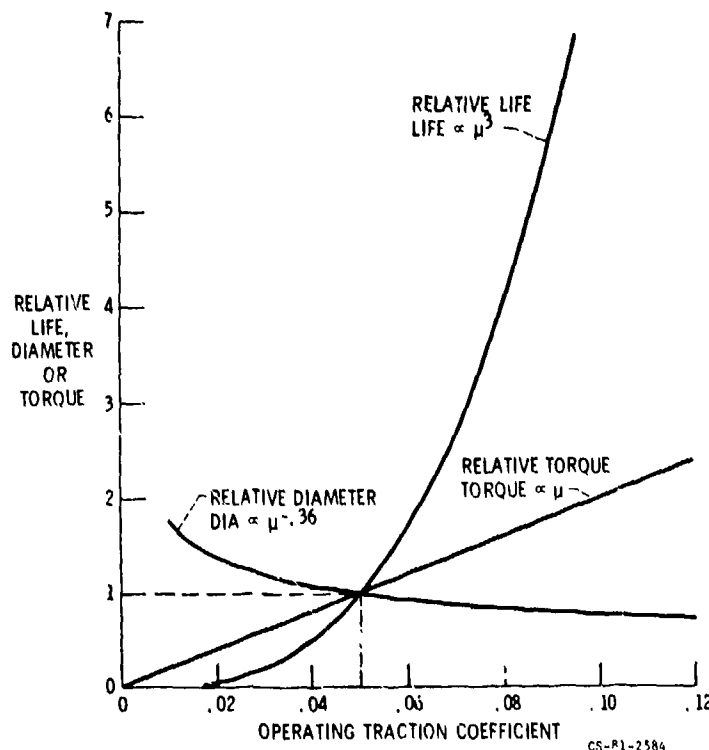


Figure 10. - Relative life, diameter, and torque capacity versus applied traction coefficient.

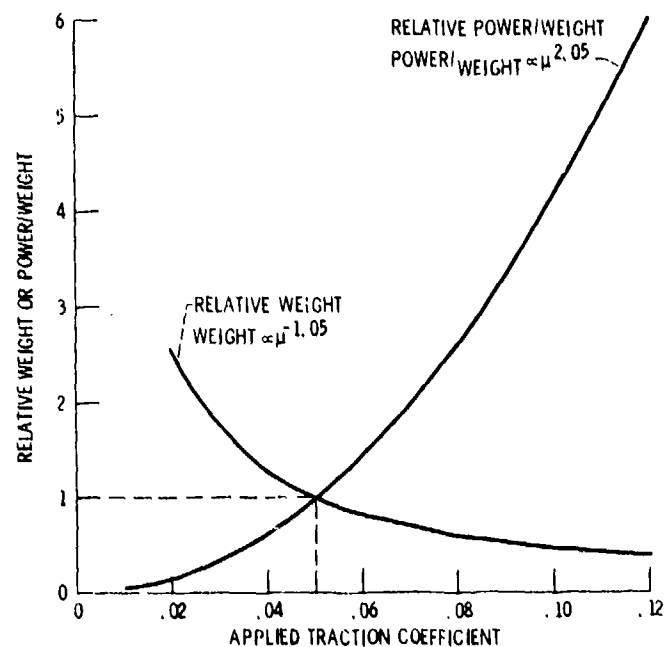


Figure 11. - Relative weight and power-to-weight ratio versus applied traction coefficient.

be found in many types of traction drives.

By beginning with a simple two-roller contact, carrying a certain torque, a multiple roller cluster is formed by adding additional rollers without changing speed, roller size, and sun or ring torque. The life increase and contact pressure decrease for multiple roller contacts are shown in figure 12. Because of the parallel paths, each element is loaded in proportion to the inverse of the number of planets in the cluster. However, life is not proportional to the cube of the number of planets, as equation (9) alone would indicate, because the system life decreases with an increase in the number of components according to equation (18) and because the sun or ring roller experiences more stress cycles per revolution with more planets. Figure 12 is valid for both external and internal contact configurations of any size, ratio, and allowable number of rollers for constant torque, traction coefficient, ellipticity ratio, and element size. An expression for the life as a function of the number of planets can be derived from equation (9) and is given in figure 12. A sample calculation for a three-planet external contact configuration using equation (9) is shown in table 1.

Another advantage of the multiple-contact geometry is the relative compactness of such a traction-drive assembly. Figure 13 shows the relative cluster diameter and contact pressure versus the number of multiple-planet rollers for both external and internal configurations of any ratio operating under constant sun or ring torque conditions at equal system fatigue life. The relative cluster diameter is defined as the ring roller bore diameter or as the pitch diameter of the planet rollers in the case of the sun arrangement. The effect of planet number on the relative sun or ring torque capacity of a certain cluster package size is illustrated in figure 14 for constant size, ratio, traction coefficient, and fatigue life in both external and internal contact arrangements. Figures 12 to 14 show that, for a given application, the maximum number of multiple, load-sharing rollers possible within geometrical ratio limits is advantageous to fatigue life, drive size, and torque capacity.

Application to Multiroller Drive

One high-performance traction drive that has benefitted from multiple, load-sharing elements is the Nasvytis multiroller traction drive (refs. 19 and 21). The drive configuration (fig. 15) consists of

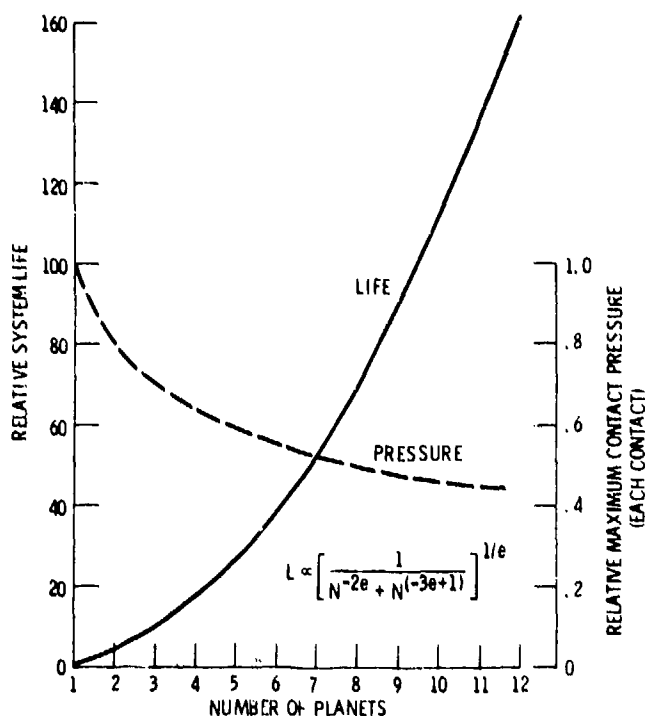


Figure 12. - Relative life and maximum contact pressure versus number of planets for external or internal contact. Torque, element radii, a/b , and traction coefficient are constant.

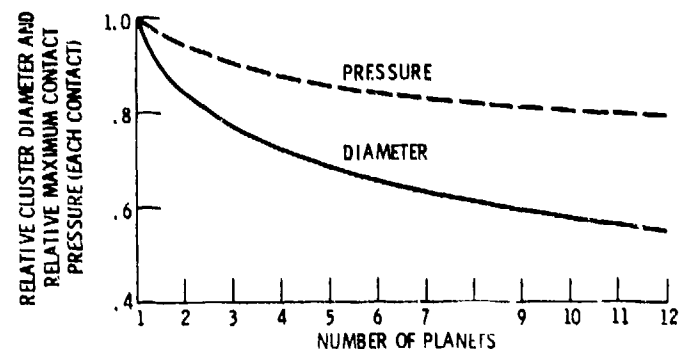
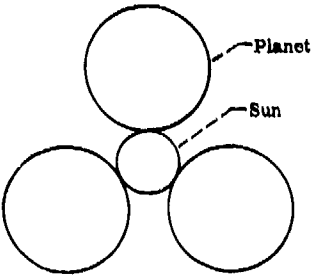


Figure 13. - Relative cluster and relative maximum contact pressure versus number of planets for external or internal contact. System life, a/b , and torque are constant.

TABLE I. - SAMPLE CALCULATIONS

<p>Arrangement: External, three load sharing rollers</p> <p>Sun diameter, mm: 25</p> <p>Planet diameter, mm: 50</p> <p>Load, each contact, N: 1000</p> <p>Sun speed, rpm: 10 000</p> <p>Transverse radii, sun, mm: 500</p> <p>Transverse radii, planets, mm: 100</p>			
			
Parameter	Symbol	Formula	Result
Normal load, each contact, N	Q	-----	1000
Orthogonal principal radii, m	r_{Ax}	$\left. \begin{array}{l} \text{Must satisfy:} \\ \frac{1}{r_{Ax}} + \frac{1}{r_{Bx}} > \frac{1}{r_{Ay}} + \frac{1}{r_{By}} \end{array} \right\}$	0.0125
	r_{Ay}		0.5
	r_{Bx}		0.025
	r_{By}		0.1
Inverse curvature sum, m^{-1}	ρ	$\frac{1}{r_{Ax}} + \frac{1}{r_{Ay}} + \frac{1}{r_{Bx}} + \frac{1}{r_{By}}$	132
Relative curvature difference	F	$\frac{\frac{1}{r_{Ax}} + \frac{1}{r_{Bx}} - \left(\frac{1}{r_{Ay}} + \frac{1}{r_{By}} \right)}{\rho}$	0.818
Geometric life variable	K_2	Fig. 4	1.65×10^6
Sun rolling radius, m	R_{sun}	-----	0.0125
Sun life, millions of cycles	L_{sun}	$K_4(K_2)^{0.9} Q^{-3} \rho^{-6.3} R_{sun}^{-0.9}$	2.07×10^4
Sun stress, cycles/rev	u_{sun}	-----	3
Sun speed, rpm	n_{sun}	-----	10 000
Sun life, hr	H_{sun}	$\left(\frac{L}{u_{sun}} \right)_{sun} \left(\frac{10^6}{60} \right)$	11 500
Planet rolling radius, m	R_{pl}	-----	0.025
Planet life, millions of cycles	L_{pl}	$K_4(K_2)^{0.9} Q^{-3} \rho^{-6.3} R_{pl}^{-0.9}$	1.11×10^4
Planet stress, cycles/rev	u_{pl}	-----	1
Planet speed, rpm	n_{pl}	-----	5000
Planet life, hr	H_{pl}	$\left(\frac{L}{u_{pl}} \right)_{pl} \left(\frac{10^6}{60} \right)$	37 000
System life, hr (without adjustment factors)	H_s	$\left[\left(\frac{1}{H_{sun}} \right)^{10/9} + 3 \left(\frac{1}{H_{pl}} \right)^{10/9} \right]^{-9/10}$	6700

concentric sun and ring elements with two rows of planet rollers. The planets do not orbit, but are located on bearings which take reaction torque to the case. Either the sun or ring can act as the input, depending on whether a speed reducer or increaser is desired. A complete life analysis was performed in reference 7, a portion of which is repeated here. The specific drive analyzed was approximately 21 cm in overall diameter and 6 cm wide with a nominal 14.7-to-1 ratio. Table 2 from reference 7 summarizes the calculation results and life-adjustment factors for three typical points, which cover a range of operating conditions up to the maximum rated condition of 194 kW (200 hp) at 75 000 rpm input speed. It is apparent from table 2 that these factors vary relatively little over the entire operating condition spectrum. Also listed is the Lundberg-Palmgren life at each contact, the contact life adjusted for life factors, and the adjusted drive system life. Figure 16 from reference 7 shows the

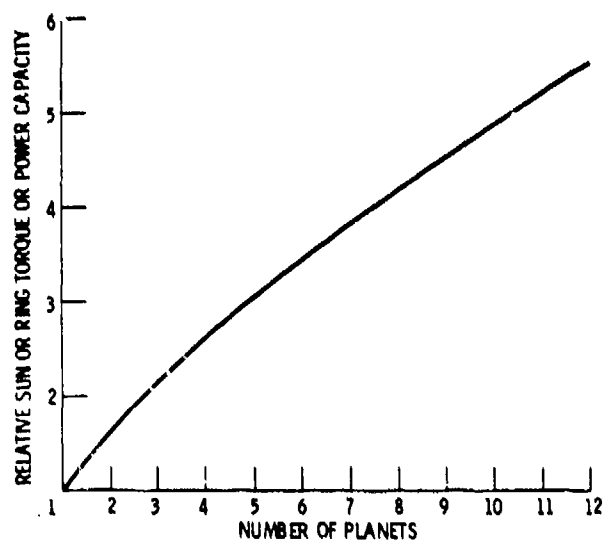


Figure 14. - Relative torque or power capacity versus number of planets for external or internal contact. System life, a/b , and rolling radii are constant.

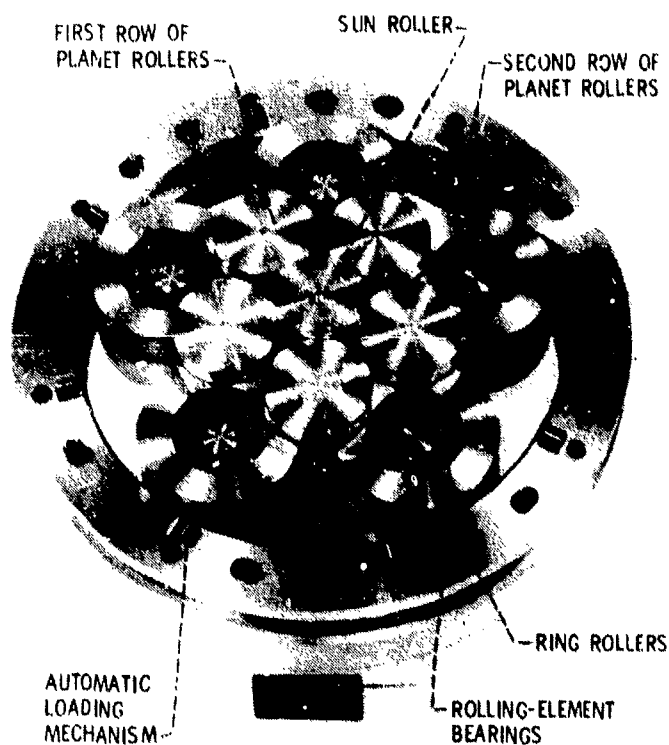


Figure 15. - Basic geometry of a Nasvytis multiroller traction drive.

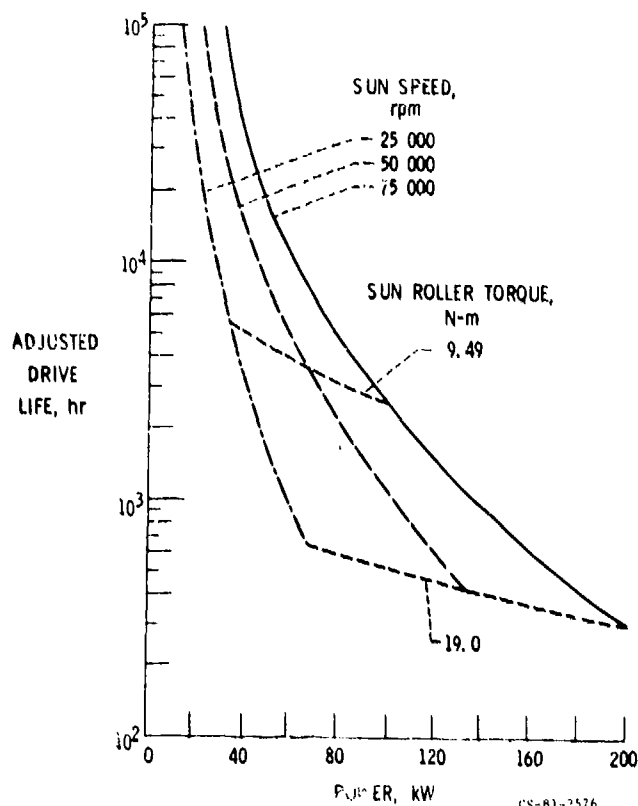


Figure 16. - Adjusted drive system life versus power and speed.

life over a range of input speeds and power levels based on the contact fatigue life theory and life adjustment factors.

**TABLE II. - SUMMARY OF CONTACT CONDITIONS, LIFE ADJUSTMENT FACTORS AND
DRIVE LIFE FOR THREE DRIVE OPERATING CONDITIONS**

	Sun- first planet	First- second planet	Second planet- ring	Sun- first planet	First- second planet	Second planet- ring	Sun- first planet	First- second planet	Second planet- ring
	16.6 kW (22.2 hp) 25 000-rpm sun speed			74.6 kW (100 hp) 75 000-rpm sun speed			149 kW (200 hp) 75 000-rpm sun speed		
Material and processing factor	6	6	6	6	6	6	6	6	6
Surface speed, m/sec	36.6	14.3	14.5	110	43.0	43.5	110	43.0	43.5
Normal load, N	978	1361	2296	1470	2040	3440	2940	4080	6890
Maximum contact pressure, GPa	1.11	1.18	0.950	1.27	1.35	1.09	1.60	1.70	1.37
Film thickness, μm	1.14	0.489	0.972	1.14	1.07	1.14	1.14	1.02	1.14
h/σ	4.0	1.70	3.39	4.0	3.72	4.0	4.0	3.54	4.0
Lubrication factor	2.65	1.85	2.55	2.65	2.6	2.65	2.65	2.6	2.65
Traction factor	0.5	0.5	0.5	0.5	0.5	0.5	0.5	0.5	0.5
Total life adjustment factor	7.95	5.55	7.65	7.95	7.80	7.95	7.95	7.80	7.95
Lundberg-Palmgren life, hr	11 400	4040	1.41×10^6	1130	399	139 000	141	49.9	17 400
Adjusted life, hr	90 600	22 400	1.08×10^7	8980	3110	1.11×10^6	1120	389	138 000
Adjusted drive life, hr	18 8			2440			305		

Summary

A simplified calculation method for predicting the rolling-element fatigue life of traction drive systems with elliptical contacts was presented. It is a useful design tool for properly establishing traction drive size and torque capacity based on fatigue life. A modified form of the Lundberg-Palmgren theory is used as the basis of this fatigue-life model. This life model considers stress, stressed volume, and depth to the critical shear stress as well as the effect of multiple contacting elements. The method was applied to a simple pair of rolling-element traction bodies transmitting a constant power level over a range of element sizes and rotational speeds. The effects of available traction coefficient as a function of contact pressure and surface speed were also investigated. The relationship between available traction coefficient and the design parameters of life, diameter, torque capacity, weight, and power-to-weight ratio were determined.

The method was also applied to systems of multiple, load-sharing rollers in external (sun) and internal (ring) contact arrangements. The system fatigue life for the Nasvytis multiroller traction drive, including life adjustment factors, was reviewed. The following results were obtained.

1. Traction drive size, life, and torque capacity per unit size improve with an increase in number of multiple load-sharing rollers.
2. For a given power and size, the fatigue life of a traction contact increases with an increase in speed. Similarly, for a given power and speed, the fatigue life increases with an increase in size. However, an optimum size or speed exists, beyond which the loss in traction coefficient causes a loss in life.
3. High-traction-coefficient lubricants are beneficial to traction drive life, diameter, torque capacity, weight, and power-to-weight ratio.

References

1. Bamberger, E. N.; et al.: Life Adjustment Factors for Ball and Roller Bearings: An Engineering Design Guide, American Society of Mechanical Engineers, 1971.
2. Coy, John J.; Loewenthal, Stuart H.; and Zaretsky, Erwin V.: Fatigue Life Analysis for Traction Drives with Application to a Toroidal Type Geometry. NASA TN D-8362, 1976.
3. Rohn, D. A.; Loewenthal, S. H.; and Coy, J. J.: Simplified Fatigue Life Analysis for Traction Drive Contacts. J. Mech. Des., vol. 103, no. 2, Apr. 1981, pp. 430-439.

4. Lundberg, G.; and Palmgren, A.: Dynamic Capacity of Rolling Bearings. Ingenioersvetenskapsakademien, Handlingar, no. 196, 1947.
5. Coy, J. J.; Townsend, D. P.; and Zaretsky, E. V.: Dynamic Capacity and Surface Fatigue Life for Spur and Helical Gears. J. Lubr. Technol., vol. 98, no. 2, Apr. 1976, pp. 267-274; discussion, pp. 275-276.
6. Townsend, D. P.; Coy, J. J.; and Zaretsky, E. V.: Experimental and Analytical Load-Life Relation for AISI 9310 Steel Spur Gears. J. Mech. Des., vol. 100, no. 1, Jan. 1978, pp. 54-60.
7. Coy, John J.; Rohn, Douglas A.; and Loewenthal, Stuart H.: Life Analysis of Multiroller Planetary Traction Drive. NASA TP-1710, 1981. (AVRADCOM TR-80-C-16.)
8. Hertz, H.: The Contact of Elastic Solids. Part V—Miscellaneous Papers. The MacMillan Company (London), 1896, pp. 146-162.
9. Harris, Tedric A.: Rolling Bearing Analysis. Wiley, 1966.
10. Brewe, David E.; and Hamrock, Bernard J.: Simplified Solution for Point Contact Deformation Between Two Elastic Solids. NASA TM X-3407, 1976.
11. Parker, R. J.; Zaretsky, E. V.; and Bamberger, E. N.: Evaluation of Load-Life Relation with Ball Bearings at 500 Deg F. J. Lubr. Technol., vol. 96, no. 3, July 1974, pp. 391-397; discussion, pp. 397-409.
12. Johnson, Leonard G.: The Statistical Treatment of Fatigue Experiments. Elsevier Publishing Co., 1964.
13. MacPherson, P. B.: The Pitting Performance of Hardened Steels. ASME Paper No. 77-DET39, Sept. 1977.
14. Zaretsky, Erwin V.; Anderson, William J.; and Parker, Richard J.: The Effect of Contact Angle on Rolling-Contact Fatigue and Bearing Load Capacity. ASLE Trans., vol. 5, no. 1, Apr. 1962, pp. 210-219.
15. Hewko, L. O.; Rounds, F. G., Jr.; and Scott, R. L.: Tractive Capacity and Efficiency of Rolling Contacts. Rolling Contact Phenomena, Joseph B. Bidwell, ed., Elsevier Publishing Co., 1962, pp. 157-182; discussion, pp. 182-185.
16. Johnson, K. L.; and Tevaarwerk, J. L.: Shear Behaviour of Elastohydrodynamic Oil Films. Proc. R. Soc., London, ser. A, vol. 356, no. 1685, Aug. 24, 1977, pp. 215-236.
17. Nasvytis, Algirdas L.: Multiroller Planetary Friction Drives. SAE Paper No. 660763, Oct. 1966.
18. Hewko, Luhomyr O.: Roller Traction Drive Unit for Extremely Quiet Power Transmission. J. Hydronaut., vol. 2, no. 3, July 1968, pp. 160-167.
19. Loewenthal, Stuart H.; Anderson, Neil E.; and Nasvytis, Algirdas L.: Performance of a Nasvytis Multiroller Traction Drive. NASA TP-1378. (AVRADCOM TR-78-36.)
20. Nakamura, Kenya; et al.: A Development of the Traction Roller System for a Gas Turbine Driven APU. SAE Paper No. 790106, Feb. 1979.
21. Loewenthal, S. H.; Anderson, N. E.; and Rohn, D. A.: Evaluation of a High Performance Fixed-Ratio Traction Drive. J. Mech. Des., vol. 103, no. 2, Apr. 1981, pp. 410-417; discussion, pp. 417-422.



A Basis for the Analysis of Surface Geometry of Spiral Bevel Gears*

Ronald L. Huston† and John J. Coy‡

This paper contains a summary of some geometrical procedures helpful in the fundamental studies of the surface geometry of spiral bevel gears. These procedures are based upon (1) fundamental gear geometry and kinematics as exposited by Buckingham, et al. (refs. 1 and 2), (2) formulas developed from differential geometry, and (3) geometrical concepts developed in recent papers and reports (refs. 3 to 5) on spiral bevel gear surface geometry.

Spiral bevel gears are found in virtually every transmission or gear box where power is transmitted through intersecting rotating shafts. In the majority of these transmissions, the tolerances are moderate, and thus relatively small deviations in geometrical design do not create major operating problems. However, in many cases—particularly in aircraft and helicopter transmissions—careful compliance with narrow tolerances is essential for safe and reliable performance of the gears. But, even with adherence to these narrow tolerances, the performance of the gears is, at times, unsatisfactory. This dissatisfaction has stimulated a desire for improvement in design, fabrication, and maintenance of the gears.

To attain these desired improvements, it is necessary to have a better understanding of the fundamental aspects of the kinematics, lubrication, stresses, and wear of the gears. Since gear surface geometry plays a critical role in each of these phenomena, there has recently been renewed interest by a number of investigators in studying the surface geometry. In this paper a review is presented of some recently proposed procedures for studying the surface geometry.

The emphasis of the paper is on those procedures which characterize the geometry so that the surface parametric equations, the principal radii of curvature, and the meshing kinematics are systematically determined. Initially, the focus is on theoretical, "logarithmic" spiral bevel gears as defined by Buckingham (ref. 1). These gears, however, are difficult to fabricate and are sometimes considered to be too "straight." Hence, as an alternative, most manufacturers and users have employed "circular-cut" spiral bevel gears. Therefore, the second focus of the paper is the analysis of surface characteristics of crown circular-cut gears.

Symbols

A, A'	points on a circular disk (figs. 2 to 4)
a	logarithmic spiral constant
B, B'	points on a circular disk (fig. 4)
C	involute generating circle (fig. 1); a curve defining a surface of revolution; cutter center (figs. 14 and 16)
e_i ($i = 1, 2$)	surface base vectors (eq. (8))
g	determinant of g_{ij}
g_{ij} ($i, j = 1, 2$)	metric tensor coefficients
H, V	coordinates of C (fig. 16)
h_i ($i = 1, 2$)	fundamental vector defined by eq. (12)
h_{ij} ($i, j = 1, 2$)	second fundamental tensor defined by eq. (13)
I	involute curve (figs. 1 and 8)
J	mean curvature

*Work partially supported under NASA Lewis Research Center Grant NSG 3188.

†University of Cincinnati.

‡Propulsion Laboratory, U.S. Army Research and Technology Laboratories (AVRADCOM), NASA Lewis Research Center.

K	gaussian curvature
m	logarithmic spiral constant
N	normal line to a surface of revolution
N_1, N_2, N_3	mutually perpendicular unit vectors (figs. 8, 9, and 11)
N'_1, N'_2, N'_3	mutually perpendicular unit vectors (figs. 9 to 11)
N_ϕ	unit vector parallel to OP (fig. 11)
n	a unit vector normal to a surface
n_c	defined in fig. 12
n_r	radial unit vector (fig. 12)
n_t	defined in fig. 12
n_x, n_y, n_z	unit vectors parallel to XYZ
O	origin of XYZ axis system (See also fig. 12.)
O'	center of involute generating circle (figs. 1 and 12); back cone apex (figs. 8 to 10)
\hat{O}	center of base-cone-back-cone intersection circle (figs. 2, 8, and 11)
P	typical point on a surface
P'	point of intersection of line segment $O'P$ and base-cone-back-cone intersection (figs. 1 and 11)
P	position vector to a typical point on surface
P_m	midpoint of crown gear tooth
Q	base point of involute curve (fig. 1) and typical point on base-cone-gear-tooth intersection (figs. 8 to 11, also fig. 12.)
R	involute circle radius (fig. 1) and back-cone element length (figs. 8 and 10); radial line (fig. 8)
R_c	distance CP_m (fig. 16); cutter radius (fig. 15)
R_1, R_2	principal surface radii of curvature
r	disk radius (fig. 2) and back-cone element distance (figs. 3, 6, and 8); radius of a surface of revolution; radial distance
r_0	radius of base-cone-back-cone intersection circle (fig. 2)
S	general surface
T	tangent line to C , tangent point
u^1, u^2	surface defining parameters
X, Y, Z	mutually perpendicular coordinate-axis system
$\hat{X}, \hat{Y}, \hat{Z}$	mutually perpendicular coordinate-axis system (fig. 16)
x	length of line segment $O'P$ (fig. 1)
x, y, z	coordinates of P relative to X, Y, Z
$\hat{x}, \hat{y}, \hat{z}$	coordinates relative to X, Y, Z
α	base-cone half central angle (figs. 2, 3, 8, and 10)
α_c	back-cone half central angle (figs. 6, 10, and 11)
β	involute generating angle (fig. 1)
γ	complement to the spiral angle (fig. 7)
δ	cutout sector angle (fig. 2)
θ	angle between R and X axis; pressure angle (figs. 15 and 16); polar angle
$\hat{\theta}$	projected polar angle (figs. 9 and 11)
ϕ	involute generating angle (fig. 1) and central disk angle (fig. 4); angle between N and the Z axis (fig. 5); angle between n_T and the Z axis (figs. 12 and 13)
$\hat{\phi}$	central angle in the base of a cone from a spindled disk (fig. 4) and involute angle in the base-cone-back-cone intersection (fig. 11)
ψ	inclination angle of T (fig. 5); spiral angle (figs. 9 and 16)

Preliminary Considerations

Geometrical characteristics of spiral bevel gears have been documented by the American Gear Manufacturer's Association and others (refs. 1, 2, and 6 to 12). From this documentation it is seen that spiral bevel gears (and, hence, also hypoid gears) could be considered to be at the top of a hierarchy of gears beginning with spur gears and then helical gears, straight bevel and skewed bevel gears, and finally to spiral bevel gears. In each of these gears a tooth geometry can be developed by generalizing the involute geometry commonly associated with spur gears. Therefore, for notational and other purposes, it will be helpful to briefly restate some of the fundamentals of involute curve geometry.

Involute Geometry

Consider the involute curve I (fig. 1), which for simplicity may be considered as the curve traced by the end of a cord being unwrapped around circle C . In the figure O' is the center of C , P is a typical point on I , and Q is at the base of I . The line segments QO' and PO' then form an angle φ as shown. The T is the tangent point of the tangential segment PT . The segments TO' and QO' then form the angle β . Finally, P' is the intersection point of $O'P$ and C .

If R is the circle radius, it is immediately seen that the radius of curvature ρ of I at P is

$$\rho = R\beta \quad (1)$$

Hence, in terms of β , it is easily seen that

$$x = R(1 + \beta^2)^{1/2} \quad (2)$$

and that

$$\varphi = \beta - \tan^{-1}\beta \quad (3)$$

where x is the length of the line segment $O'P$. (Eq. (2) follows immediately eq. (1), and the Pythagorean identity and eq. (3) are obtained by observing that $\tan(\beta - \varphi) = \rho/R$.)

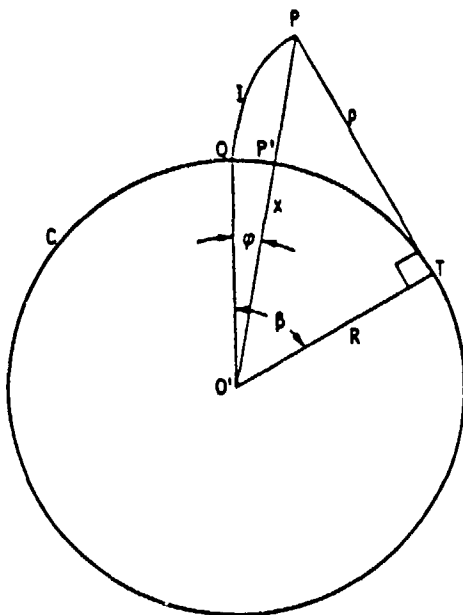


Figure 1. - Involute geometry.

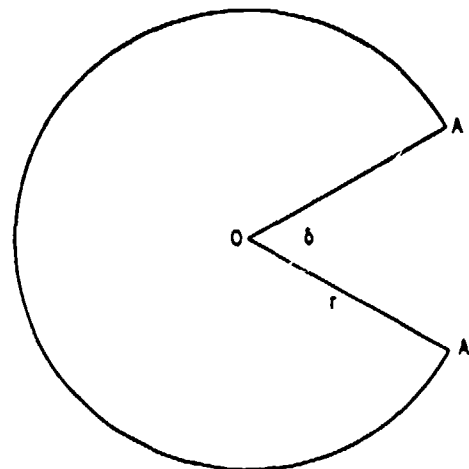


Figure 2. - Circular disk with cut out sector.

Spindling a Disk into a Cone

Just as a spur can be generated by "wrapping" a basic rack into a circle, so also a bevel gear can be generated by spindling a "crown gear" (a circular disk or face gear, sometimes called a "crown rack") into a cone. Therefore, it is useful to review the geometrical aspects of spindling a disk into a cone.

Consider the disk with radius r with a cutout sector with angle φ as shown in figure 2. If points A and A' are brought together, the disk forms a cone as shown in figure 3. When r_0 is the radius at the base of the cone, it is immediately seen that

$$2\pi r_0 = (2\pi - \delta)r \quad (4)$$

Therefore, if α is the half central angle of the cone, α and δ are related as

$$\sin \alpha = \frac{r_0}{r} = 1 - \frac{\delta}{2\pi} \quad (5)$$

Finally, consider the disk of figure 2 with two points B and B' on the circumference. Then B and B' with O form the angle φ as shown in figure 4(a). After spindling, the top view of the resulting cone is shown in figure 4(b), where O is on the cone axis at its base. Since the arcs BB' are of equal lengths in figure 4, the angle $\hat{\varphi}$ formed by B , \hat{O} , and B' is then related to φ through the equation

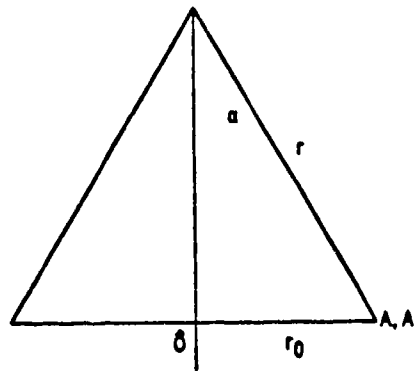


Figure 3. - Cone formed from disk of figure.

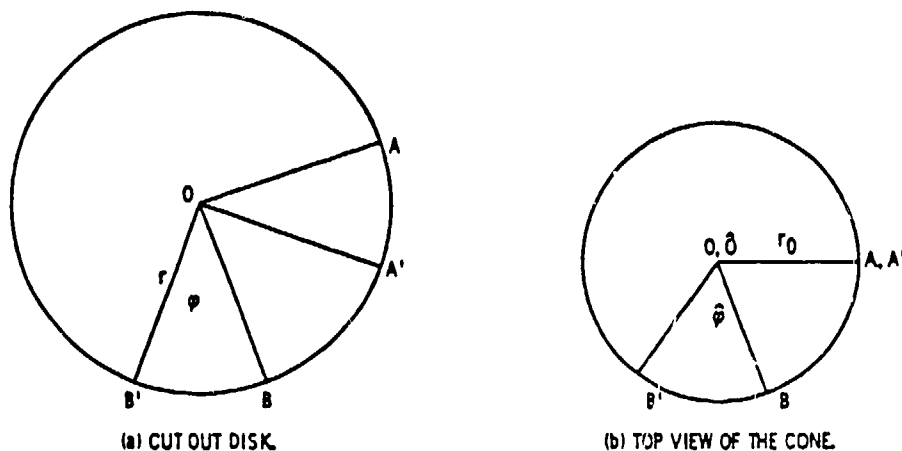


Figure 4. - Disk with cut out section and top view of resulting cone.

$$r\varphi = r_0\hat{\varphi} \quad (6)$$

or, by using equation (5) as

$$\hat{\varphi} = \frac{\varphi}{\sin \alpha} \quad (7)$$

Differential Geometry Formulation

Major factors affecting the lubrication, surface fatigue, contact stress, wear, and life of gear teeth are the maximum and minimum radii of curvature of the tooth surface at the point of contact with the meshing tooth. To obtain the radii of curvature, it is convenient to employ some relations developed in elementary differential geometry formulations. These relations are briefly summarized here.

Suppose a surface S is described by a pair of parameters u_1 and u_2 through the vector parametric equation $\mathbf{P} = \mathbf{P}(u_1, u_2)$, where \mathbf{P} is the position vector of a typical point P on S . Then base vectors $\mathbf{e}_i (i=1,2)$ tangent to S at P are given by

$$\mathbf{e}_i = \frac{\partial \mathbf{P}}{\partial u^i} \quad (i=1,2) \quad (8)$$

A surface metric tensor $g_{ij} (i,j=1,2)$ may then be defined as

$$g_{ij} = \mathbf{e}_i \cdot \mathbf{e}_j \quad (i,j=1,2) \quad (9)$$

Let g be $\det g_{ij}$. Then it is easily shown that

$$\sqrt{g} = |\mathbf{e}_1 \times \mathbf{e}_2| \quad (10)$$

Hence, a unit vector \mathbf{n} normal to S is given by

$$\mathbf{n} = \frac{\mathbf{e}_1 \times \mathbf{e}_2}{|\mathbf{e}_1 \times \mathbf{e}_2|} = \frac{\mathbf{e}_1 \times \mathbf{e}_2}{\sqrt{g}} \quad (11)$$

Next, let the fundamental vectors $\mathbf{h}_i (i=1,2)$ be defined as

$$\mathbf{h}_i = \frac{\partial \mathbf{n}}{\partial u^i} \quad (i=1,2) \quad (12)$$

Then the second fundamental tensor $h_{ij} (i,j=1,2)$ is defined as

$$h_{i,j} = -\mathbf{h}_i \cdot \mathbf{e}_j \quad (i,j=1,2) \quad (13)$$

Finally, the Gaussian curvature K and the mean curvature J are defined as

$$K = \frac{h}{g} \quad (14)$$

and

$$J = k_{ii} \quad (15)$$

where h is $\det h_{ij}$ and k_{ij} is defined as

$$k_{ij} = g_{il}^{-1} h_{lj} \quad (16)$$

where g^{-1} is the inverse tensor of g_{ij} . Regarding notation, repeated indices represent a sum (i.e., from 1 to 2) over that index.

The principal normal radii of curvature R_1 and R_2 are then easily calculated in terms of J and K as

$$R_1, R_2 = \frac{2}{[J \pm (J^2 - 4K)^{1/2}]} \quad (17)$$

Surfaces of Revolution

The tooth surface of a circular cut spiral bevel crown gear is a "surface of revolution;" that is, it can be developed by rotating a curve, in the shape of the cutter profile, about a fixed axis. Consider, for example, the curve C shown in figure 5. If C is rotated about the Z axis, it generates a surface of revolution S , a portion of which can be considered as the surface of a circular cut spiral bevel crown gear. Let C be defined by the expression

$$Z = f(r) \quad (18)$$

where r is the distance from the Z axis to a typical point P on C . Let φ be the angle between the Z axis and the normal line N of S at P . Then r and φ are dependent on each other; that is,

$$r = r(\varphi) \quad (19)$$

Let ψ be the inclination angle of the tangent line T to C at P as shown in figure 5. Then ψ , φ , and the slope of T are related as follows:

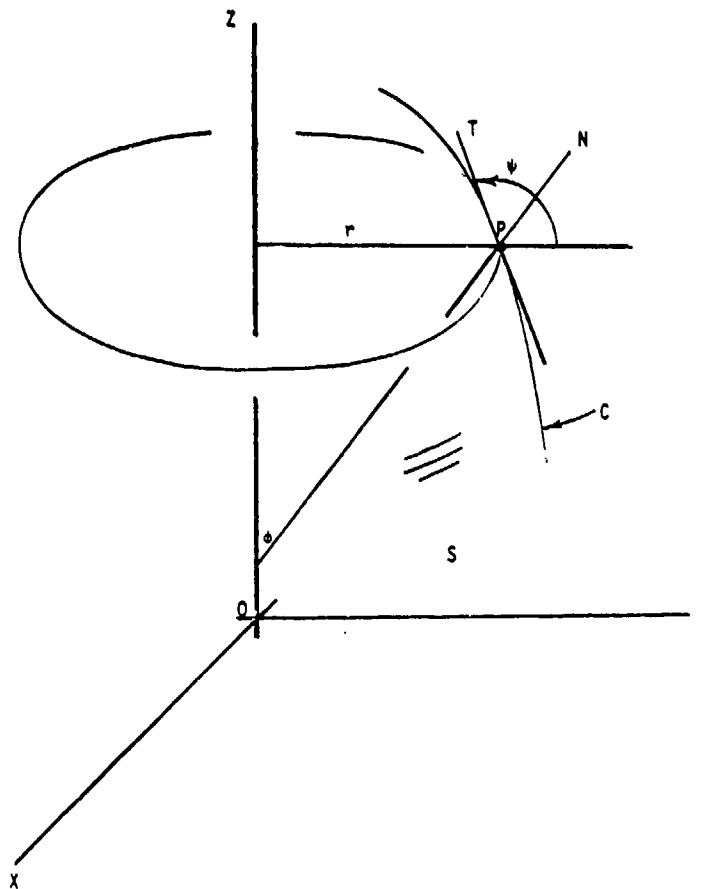


Figure 5. - A surface of revolution about the Z axis.

$$\frac{dz}{dr} = \frac{df}{dr} = -\tan \psi = +\tan(\pi - \psi) = -\tan \varphi \quad (20)$$

Consider a top view of S as shown in figure 6. In this view P is seen to lie on a circle of radius r , and on a radial line R , which makes an angle θ with the X axis. Then the position vector \mathbf{P} of P relative to O , a fixed point on the Z axis (fig. 5.), is

$$\mathbf{P} = z\mathbf{n}_z + r\mathbf{n}_r = r\mathbf{n}_r + f(r)\mathbf{n}_z \quad (21)$$

where \mathbf{n}_r and \mathbf{n}_z are unit vectors parallel to R and the Z axis. Hence, in terms of \mathbf{n}_x , \mathbf{n}_y , and \mathbf{n}_z , unit vectors parallel to the X , Y , and Z axes, \mathbf{P} become

$$\mathbf{P} = r \cos \theta \mathbf{n}_x + r \sin \theta \mathbf{n}_y + f(r)\mathbf{n}_z \quad (22)$$

Since $r = r(\varphi)$, P is a function of φ and θ . Therefore, it is convenient to let φ and θ be the parameters u^1 and u^2 defining S in the parametric representation $\mathbf{P} = \mathbf{P}(u^1, u^2)$ of the foregoing differential geometry formulas.

From equation (8), the surface base vectors \mathbf{e}_1 and \mathbf{e}_2 become

$$\mathbf{e}_1 = \mathbf{e}_\varphi = \left(\frac{dr}{d\varphi} \right) \cos \theta \mathbf{n}_x + \left(\frac{dr}{d\varphi} \right) \sin \theta \mathbf{n}_y + \left(\frac{df}{d\varphi} \right) \left(\frac{dr}{d\varphi} \right) \mathbf{n}_z \quad (23)$$

and

$$\mathbf{e}_2 = \mathbf{e}_\theta = -r \sin \theta \mathbf{n}_x + r \cos \theta \mathbf{n}_y \quad (24)$$

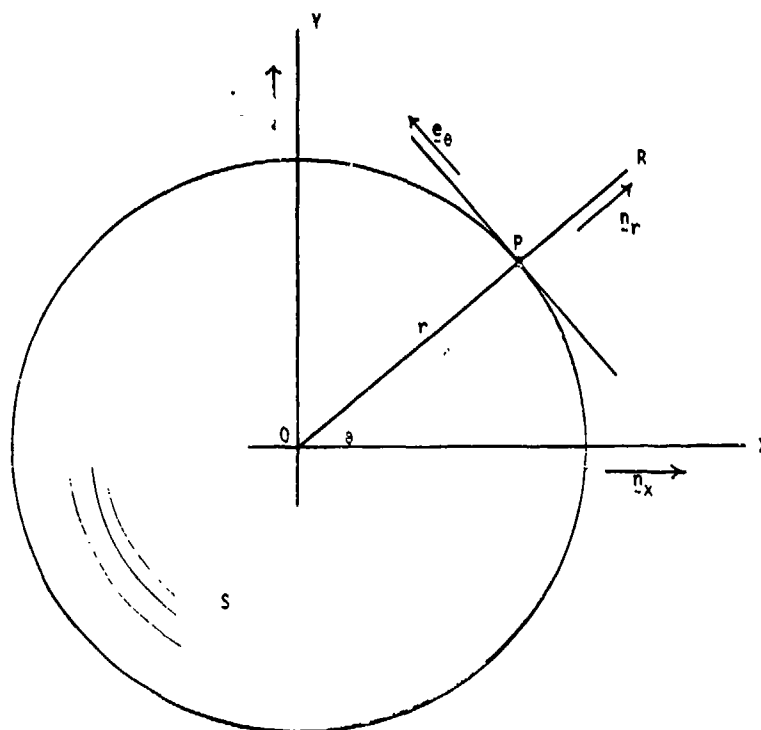


Figure 6. - Top view of surface of revolution.

Then, from equation (9) the metric tensor components become

$$g_{11} = g_{\varphi\varphi} = \left(\frac{dr}{d\varphi} \right)^2 \sec^2 \varphi \quad (25)$$

$$g_{12} = g_{21} = g_{\varphi\theta} = g_{\theta\varphi} = 0 \quad (26)$$

and

$$g_{22} = g_{\theta\theta} = r^2 \quad (27)$$

where equation (20) has been used to simplify the expressions. Hence, from equation (11) the unit vector \mathbf{n} normal to S becomes

$$\mathbf{n} = \sin \varphi \cos \theta \mathbf{n}_x + \sin \varphi \sin \theta \mathbf{n}_y + \cos \varphi \mathbf{n}_z \quad (28)$$

The fundamental vectors $\mathbf{h}_i (i = \varphi, \theta)$ and the second fundamental tensor $h_{ij} (i, j = \varphi, \theta)$ are then

$$\mathbf{h}_1 = \mathbf{h}_\varphi = \frac{\partial \mathbf{n}}{\partial \varphi} = \cos \varphi \cos \theta \mathbf{n}_x + \cos \varphi \sin \theta \mathbf{n}_y - \sin \varphi \mathbf{n}_z \quad (29)$$

$$\mathbf{h}_2 = \mathbf{h}_\theta = \frac{\partial \mathbf{n}}{\partial \theta} = -\sin \varphi \sin \theta \mathbf{n}_x + \sin \varphi \cos \theta \mathbf{n}_y \quad (30)$$

$$h_{11} = h_{\varphi\varphi} = - \left(\frac{dr}{d\varphi} \right) \sec \varphi \quad (31)$$

$$h_{12} = h_{21} = h_{\varphi\theta} = h_{\theta\varphi} = 0 \quad (32)$$

and

$$h_{22} = h_{\theta\theta} = -r \sin \varphi \quad (33)$$

From equations (14) and (15) the Gaussian curvature and the mean curvature become

$$K = \frac{\sin \varphi \cos \varphi}{r \, dr/d\varphi} \quad (34)$$

and

$$J = - \left(\frac{\cos \varphi}{dr/d\varphi} + \frac{\sin \varphi}{r} \right) \quad (35)$$

Finally, using equation (17), the principal surface radii of curvature become

$$R_1 = \left| \frac{dr/d\varphi}{\cos \varphi} \right| \quad (36)$$

and

$$R_2 = \left| \frac{r}{\sin \varphi} \right| \quad (37)$$

These expressions may be expressed in terms of f by using equation (20); that is, since

$$\varphi = -\tan^{-1} \left(\frac{df}{dr} \right) \quad (38)$$

then $(d\phi/dr)$ becomes

$$\frac{d\phi}{dr} = - \frac{(d^2f/dr^2)}{1 + (df/dr)^2} \quad (39)$$

and hence, R_1 and R_2 become

$$R_1 = \left| \frac{[1 + (df/dr)^2]}{(d^2f/dr^2) \cos[\tan^{-1}(df/dr)]} \right| \quad (40)$$

and

$$R_2 = \left| \frac{r}{\sin[\tan^{-1}(df/dr)]} \right| \quad (41)$$

Theoretical Spiral Bevel Gear Tooth Surface Geometry

A Logarithmic Spiral

The name "spiral bevel" stems from the fact that, if the centerline of a crown gear tooth follows a logarithmic spiral, the spiral angle will be constant along the tooth; that is, the tangent to the tooth centerline makes a constant angle with the radial lines. Figure 7 illustrates this where ψ_1 and ψ_2 are the angles between the tooth centerline and the radial lines at typical points P_1 and P_2 . It is easily shown (ref. 13) that if the polar form of the tooth centerline equation is $r = aem^\theta$, a logarithmic spiral, then $\psi_1 = \psi_2$; that is, the spiral angle is constant along the tooth. This is significant since then the complementary angles γ_1 and γ_2 are also equal and therefore constant along the tooth. This means that the tooth profile, which is normal to the radial direction, makes a constant angle with the tooth

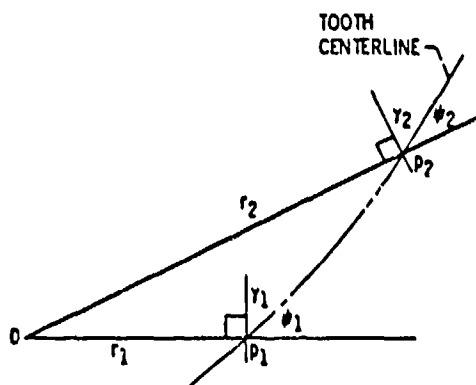


Figure 7. - Radial inclination of the tooth centerline.

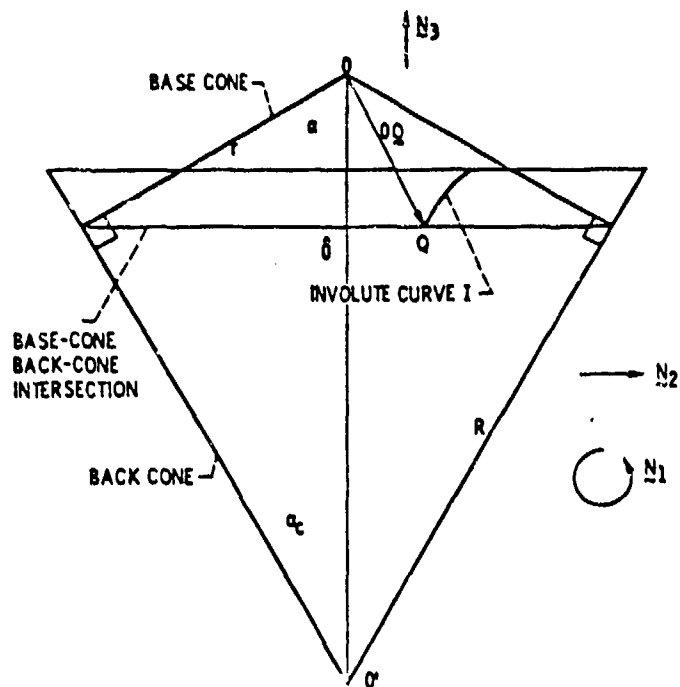


Figure 8. - Base cone involute spindling around a back cone.

centerline. This, in turn, is significant since it insures uniform meshing kinematics along the gear tooth with the mating gear.

The next section examines the spindling of a crown gear, with gear teeth in the shape of logarithmic spirals, into a cone.

Base Cone Geometry

To develop the geometrical basis of an ideal spiral bevel gear, imagine a crown gear with an involute tooth profile. (The tooth profile is normal to the radial direction.) Next, let this gear be spindled into a cone as described in the foregoing section. The details of this can be seen by considering figure 8 where the *base cone* and a corresponding orthogonal *back cone* of a typical gear are shown. In this figure, Q is a typical point on the base cone of a gear tooth; R is the elemental distance from the back cone apex O' to the base-cone-back-cone intersection; r is the elemental distance from the base-cone apex to the base-cone-back-cone intersection; α and α_c are the half central angles of the base and back cones, respectively (α_c is the complement of α); and N_1 , N_2 , and N_3 are mutually perpendicular unit vectors, with N_3 being parallel to the cone axis. Figure 8 also shows an exaggerated view of an involute curve I starting at Q and being wrapped around the base cone. Here, as in figure 1, R corresponds to the radius of the circle of the unwrapping cord which defines the involute; that is, the curve is formed by unwrapping a cord about a circle of radius R and then by spindling the resulting involute around the back cone. Finally, in figure 8 OQ is the position vector of Q relative to O and its magnitude is r .

Figure 9 shows a top view of the base-cone-back-cone intersection of figure 8. Therein, θ is the angle between N_1 and the projection of OQ onto the intersection plane, and N'_1 , N'_2 , and N'_3 are mutually perpendicular unit vectors, with N'_3 coinciding with N_3 . Figure 9 also shows the logarithmic spiral spindled about the base cone. If the logarithmic spiral is defined by $r = ae^{m\theta}$, as described in the preceding section, then $\hat{\theta}$ is related to θ by equation (7); that is,

$$\hat{\theta} = \frac{\theta}{\sin \alpha} \quad (42)$$

Position Vectors

The surface geometry of a spiral bevel gear tooth is determined once a position vector to a typical point P on the tooth surface is known. Relative to O , the base cone apex, such a position vector could take the form

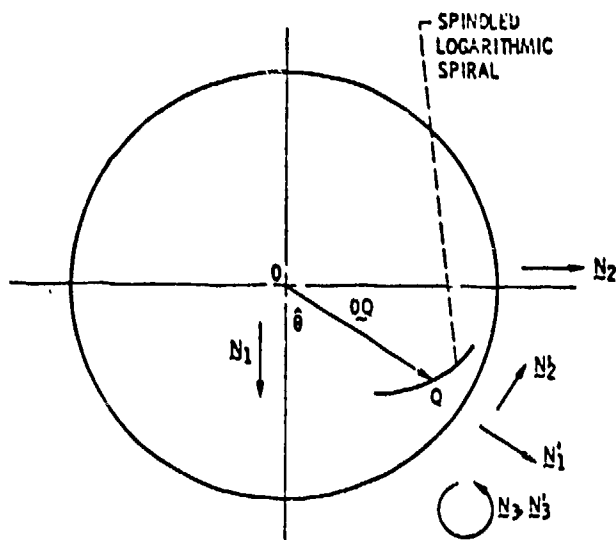


Figure 9. - Top view of base-cone - back-cone intersection and curve of a typical tooth.

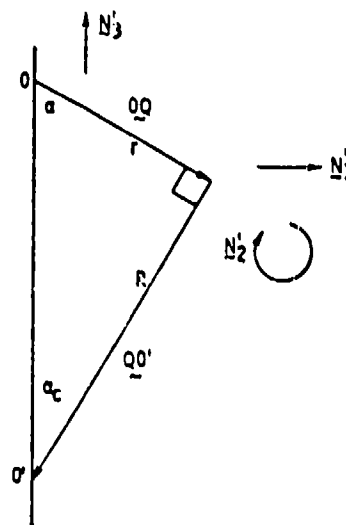


Figure 10. - True view of vectors OQ and QO' .

$$\mathbf{P} = \mathbf{OP} = \mathbf{OQ} + \mathbf{QO}' + \mathbf{O}'\mathbf{P} \quad (43)$$

where the notation is self-defining. By examining figures 8 and 9, it is readily seen that in terms of \mathbf{N}_1 , \mathbf{N}_2 , and \mathbf{N}_3 , \mathbf{OQ} is

$$\mathbf{OQ} = r \sin \alpha \cos \hat{\theta} \mathbf{N}_1 + r \sin \alpha \sin \hat{\theta} \mathbf{N}_2 - r \cos \alpha \mathbf{N}_3 \quad (44)$$

Next, consider figure 10 which shows a true view of the vectors \mathbf{OQ} and \mathbf{QO}' . From this figure, it is immediately seen that R is equal to $r \tan \alpha$ and that \mathbf{QO}' is then given by

$$\mathbf{QO}' = -r \tan \alpha \cos \alpha \mathbf{N}_1' - r \tan \alpha \sin \alpha \mathbf{N}_2' \quad (45)$$

Finally, to determine $\mathbf{O}'\mathbf{P}$, note that from figure 1, $\mathbf{O}'\mathbf{P}$ can be written in the simple form

$$\mathbf{O}'\mathbf{P} = x \mathbf{N}_\varphi \quad (46)$$

where x is given by equation (2) and where \mathbf{N}_φ is a unit vector parallel to $\mathbf{O}'\mathbf{P}$ as shown in figure 11. If \mathbf{N}_1'' is a unit vector parallel to \mathbf{OP}' as shown, \mathbf{N}_φ may be written as

$$\mathbf{N} = \sin \alpha_c \mathbf{N}_1'' + \cos \alpha_c \mathbf{N}_3 \quad (47)$$

However, \mathbf{N}_1'' may be expressed in terms of \mathbf{N}_1 and \mathbf{N}_2 as

$$\mathbf{N}_1'' = \cos(\hat{\theta} + \hat{\varphi}) \mathbf{N}_1 + \sin(\hat{\theta} + \hat{\varphi}) \mathbf{N}_2 \quad (48)$$

where φ is the projected involute generating angle and is related to φ of figure 1 by equation (7); that is,

$$\hat{\varphi} = \frac{\varphi}{\sin \alpha_c} \quad (49)$$

Hence, from equations (46) to (48), $\mathbf{O}'\mathbf{P}$ becomes

$$\mathbf{O}'\mathbf{P} = x \sin \alpha_c \cos(\hat{\theta} + \hat{\varphi}) \mathbf{N}_1 + x \sin \alpha_c \sin(\hat{\theta} + \hat{\varphi}) \mathbf{N}_2 + x \cos \alpha_c \mathbf{N}_3 \quad (50)$$

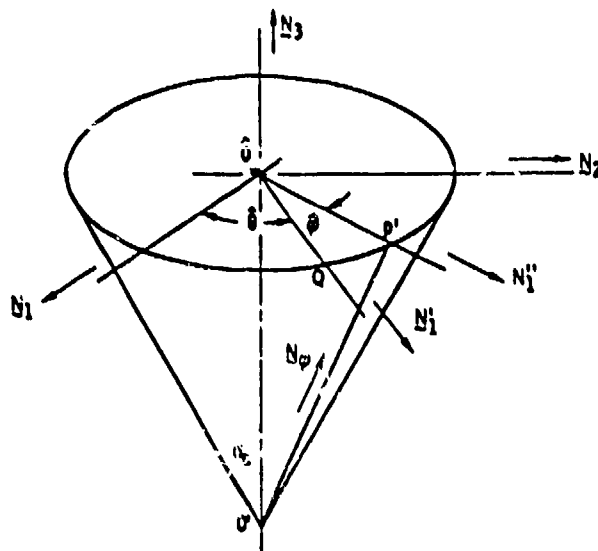


Figure 11. - Back cone unit vectors.

Finally, by using equations (43) to (45) and (50), \mathbf{P} becomes

$$\mathbf{P} = x \sin \alpha_c \cos(\theta + \hat{\varphi}) \mathbf{N}_1 + x \sin \alpha_c \sin(\theta + \hat{\varphi}) \mathbf{N}_2 + (x \cos \alpha_c - r \sec \alpha) \mathbf{N}_3 \quad (51)$$

By noting that α and α_c are complementary (hence, $\sin \alpha_c = \cos \alpha$ and $\cos \alpha_c = \sin \alpha$) and that by equation (2) $x = r(1 + \beta^2)^{1/2} \tan \alpha$, equation (51) may be rewritten as

$$\mathbf{P} = r \left\{ [(1 + \beta^2)^{1/2} \sin \alpha \cos(\theta + \hat{\varphi})] \mathbf{N}_1 + [(1 + \beta^2)^{1/2} \sin \alpha \sin(\theta + \hat{\varphi})] \mathbf{N}_2 + [(1 + \beta^2)^{1/2} \sin \alpha \tan \alpha - \sec \alpha] \mathbf{N}_3 \right\} \quad (52)$$

Equation (52) can be shown to be of the form $\mathbf{P} = \mathbf{P}(u^1, u^2)$ where $u^1 = \theta$ and $u^2 = \beta$. This is immediately seen by recalling from equations (3) and (7) that r and θ may be written as

$$r = a \exp(m\theta \sin \alpha) \quad (53)$$

and

$$\hat{\varphi} = \frac{\beta - \tan^{-1} \beta}{\cos \alpha} \quad (54)$$

If equation (28) is considered to be of the form $\mathbf{p} = \mathbf{p}(\theta, \beta) = \mathbf{p}(u^1, u^2)$, then the differential geometry formulas of equations (8) to (17) are directly applicable. However, a glance at equations (11), (12), (16), and (17) shows that, beyond the metric tensor components, the calculation of the unit normal vector \mathbf{n} , the second fundamental tensor h_{ij} , and the radii of curvature R_1 and R_2 , could be quite laborious and cumbersome. Hence, they are not presented here. But, the expressions of equations (11) to (17) are in a form suitable for calculation by one of the symbolic manipulative computer languages (e.g., Formac or Macsyma). As such, the foregoing analysis provides a basis for a computerized analysis of the surface geometry of the gears.

Circular-Cut Crown Gear Tooth Surface Geometry

An Involute Curve

Although it is not practical to generate a spiral-bevel gear-tooth surface with a rotating cutter in the shape of an involute curve, it is nevertheless informative, as a first illustration, to examine the surface of revolution formed by an involute curve.

Consider the involute curve C of figure 12. The radius of curvature ρ of C at a typical point P is simply the length TP . It is easily seen that ρ is one of the principal radii of curvature of the surface of revolution, which is obtained by revolving C about the Z -axis.

To see this, consider using equations (36) and (37) of the foregoing analysis. These equations require knowledge of the radial distance r as a function of the angle. To obtain $r(\varphi)$ let O be that point on the Z axis that is at the same elevation as O' , the center of the circle generating C . Then, r may be expressed as

$$r = \mathbf{n}_r \cdot \mathbf{OP} \quad (53)$$

The vector \mathbf{OP} may be written as

$$\mathbf{OP} = \mathbf{OO}' + \mathbf{O}'\mathbf{T} + \mathbf{TP} \quad (54)$$

or

$$\mathbf{OP} = b\mathbf{n}_r + a\mathbf{n}_c - a\varphi_c\mathbf{n}_t \quad (55)$$

where b is the distance OO' , a is the circle radius, and φ_c is the complement of φ . In terms of \mathbf{n}_r and \mathbf{n}_z , \mathbf{OP} may be written as

$$\mathbf{OP} = \left[b - a \cos \varphi + a \left(\frac{\pi}{2} - \varphi \right) \sin \varphi \right] \mathbf{n}_r + \left[a \sin \varphi + a \left(\frac{\pi}{2} - \varphi \right) \cos \varphi \right] \mathbf{n}_z \quad (56)$$

Hence, from equation (58), r and $dr/d\varphi$ become

$$r = b - a \cos \varphi + a \left(\frac{\pi}{2} - \varphi \right) \sin \varphi \quad (57)$$

and

$$\frac{dr}{d\varphi} = a \left(\frac{\pi}{2} - \varphi \right) \cos \varphi \quad (58)$$

Therefore, from equations (36) and (37) the principal radii of curvature of the generated surface of revolution are

$$R_1 = \left| a \left(\frac{\pi}{2} - \varphi \right) \right| \quad (59)$$

and

$$R_2 = \left| b \csc \varphi - a \cot \varphi + a \left(\frac{\pi}{2} - \varphi \right) \right| \quad (60)$$

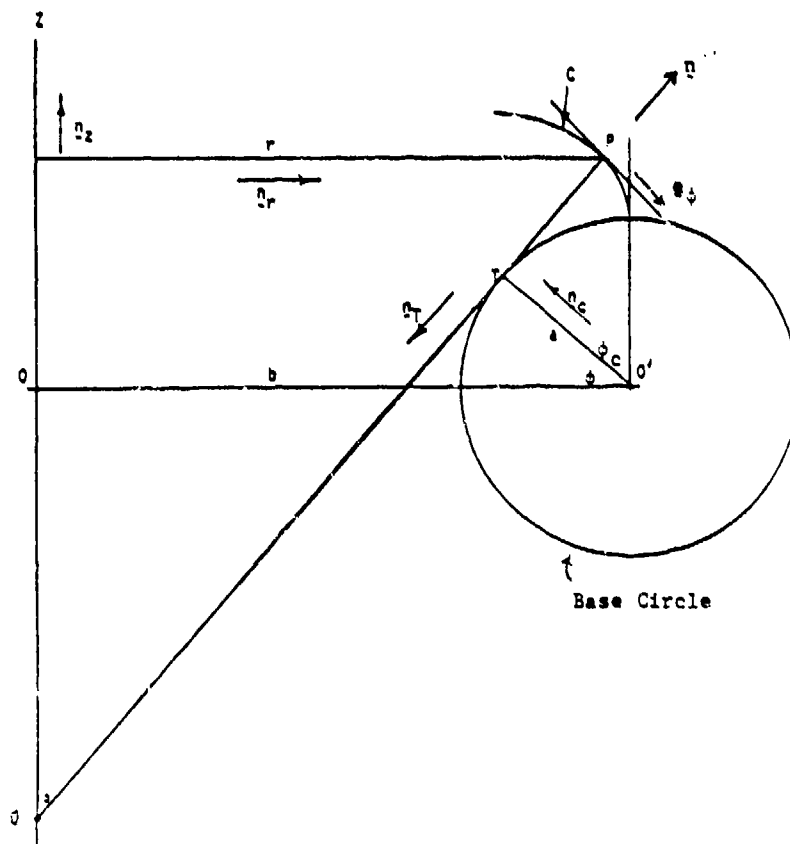


Figure 12. - Involute curve as generator for surface of revolution.

An examination of figure 12 shows that these expressions can be interpreted simply as

$$R_1 = |\overline{TP}| = R_{\min} \quad (61)$$

and

$$R_2 = |\overline{QP}| = R_{\max} \quad (62)$$

Finally, it is interesting to observe that, if the same analysis is carried out for an involute curve generated in the opposite direction (as shown in fig. 13) the corresponding surface of revolution has the principal radii of curvature:

$$R_1 = |\overline{TP}| = R_{\min} \quad (63)$$

and

$$R_2 = |\overline{QP}| = R_{\max} \quad (64)$$

These results are, of course, identical to equations (61) and (62). However, in this case, the centers of curvature are on opposite sides of the surface, since the Gaussian curvature is negative.

Straight Line Profile—Normal Plane

Consider next a rotating gear-tooth cutter with a straight-line profile that forms a gear-tooth surface with a straight-line profile in the normal plane as shown in figures 14 and 15. Viewed as a surface of revolution, this is a cone. Its defining equation may be expressed as

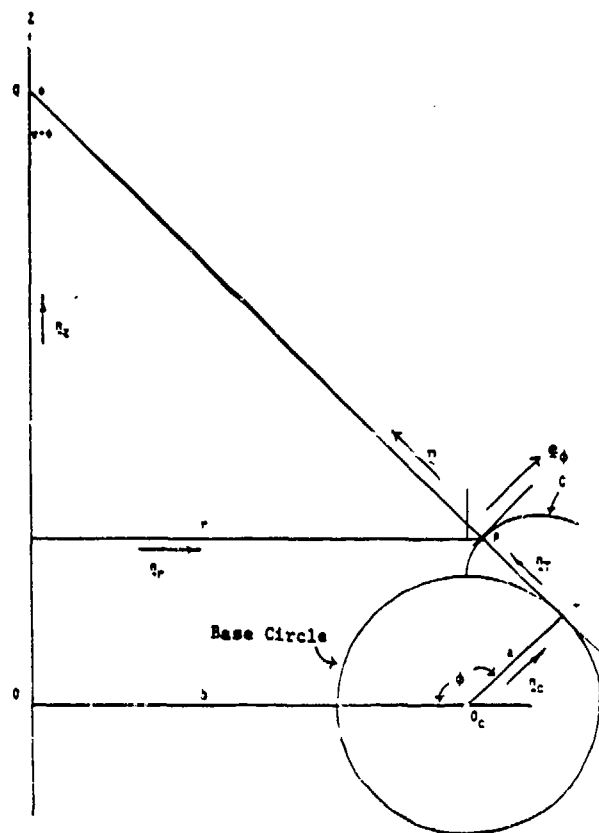


Figure 13. - Second involute curve as generator for surface of revolution.

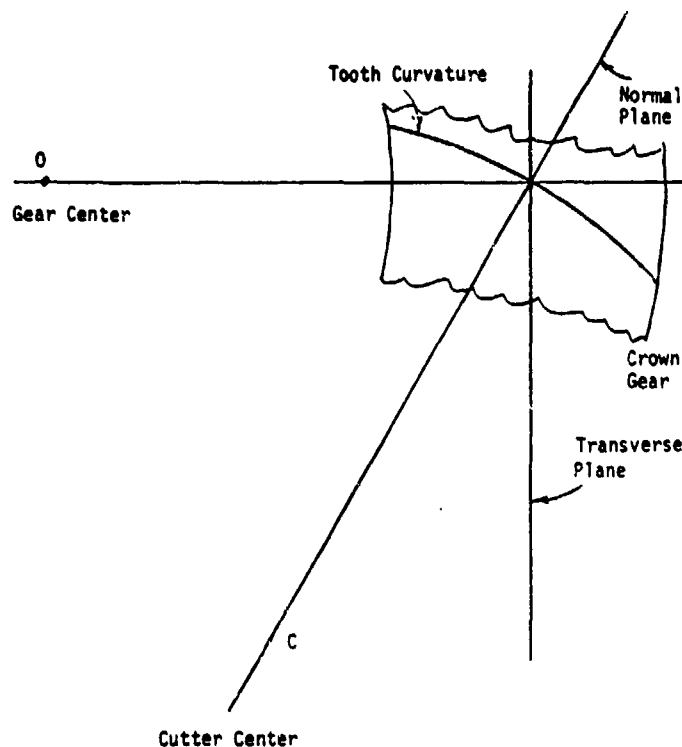


Figure 14. - Top view showing gear cutter centers and edge view of normal and transverse planes.

$$z = (r - R_c) \cot \theta \quad (65)$$

where θ is the pressure angle (fig. 15) and R_c is the cutter radius at the base of the tooth. From this expression dz/dr and d^2z/dr^2 are readily obtained as

$$\frac{dz}{dr} = \cot \theta = \tan \varphi \quad (66)$$

and

$$\frac{d^2z}{dr^2} = 0 \quad (67)$$

where φ is the complement of θ as shown in figure 15. Hence, equations (50) and (41) give the maximum and minimum surface radii of curvature as

$$R_{\max} = \infty \quad (68)$$

and

$$R_{\min} = \left| \frac{r}{\cos \theta} \right| \quad (69)$$

These results might also have been obtained by recalling that a cone is generated by straight-line elements (hence, infinite radius of curvature) and that the minimum radius of curvature is the distance QP as shown in figure 15.

Straight Line Profile—Transverse Plane

Finally, consider a rotating cutter which generates, for a crown gear, a straight-line meshing profile. Specifically, consider figure 16, that shows the pitch plane of a crown gear where O is the gear center and C (with X, Y coordinates H, V) is the center of the rotating cutter. Let P_m be the midpoint at the base of the gear tooth surface and let ψ be the spiral angle. The transverse plane is normal to the X axis at P_m . Since O is the gear center, the X axis is a radial line, and the intersection of the transverse plane and the gear tooth surface defines the transverse meshing profile shown in figure 17. If θ is the transverse pressure angle, the equation of the inclined tooth profile is simply

$$z = y \cot \theta = ky \quad (70)$$

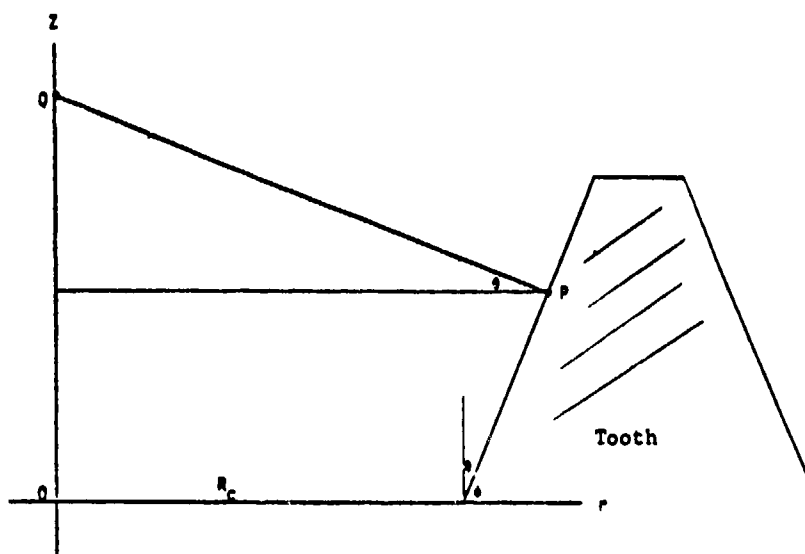


Figure 15. - True view of normal plane showing crown tooth profile.

where z and y refer to coordinates along the Z and Y axis and k is defined as $\cot \theta$. Relative to the \hat{X} , \hat{Y} , and \hat{Z} axes of figure 16, equation (70) becomes

$$z = \hat{z} = k(\hat{y} + V) \quad (71)$$

In terms of x , y , and z , the profile of the cutter radius can be expressed in general as

$$\hat{z} = f(r) = f[(\hat{x}^2 + \hat{y}^2)^{1/2}] \quad (72)$$

The form of f , which defines the tooth surface of revolution, may be determined by observing that the intersection of the revolution surface of the cutter with the transverse plane must coincide with the tooth profile of figure 17. If R_c is the distance between C and P_m , then the \hat{X} coordinate of P_m is simply $R_c \sin \psi$. Hence, by letting $\hat{x} = R_c \sin \psi$ and by matching equations (71) and (72), the following relation is obtained:

$$f[(R_c^2 \sin^2 \psi + \hat{y}^2)^{1/2}] = k(\hat{y} + V) \quad (73)$$

Let \bar{r} be defined as

$$\bar{r} = (R_c^2 \sin^2 \psi + \hat{y}^2)^{1/2} \quad (74)$$

Then, in terms of \bar{r} , \hat{y} becomes

$$\hat{y} = (\bar{r}^2 - R_c^2 \sin^2 \psi)^{1/2} \quad (75)$$

where the negative root is required to be consistent with the coordinate system of figure 16. Hence, by equation (73), f is determined as

$$f(\bar{r}) = k[V - (\bar{r}^2 - R_c^2 \sin^2 \psi)^{1/2}] \quad (76)$$

which is the equation of an hyperboloid.

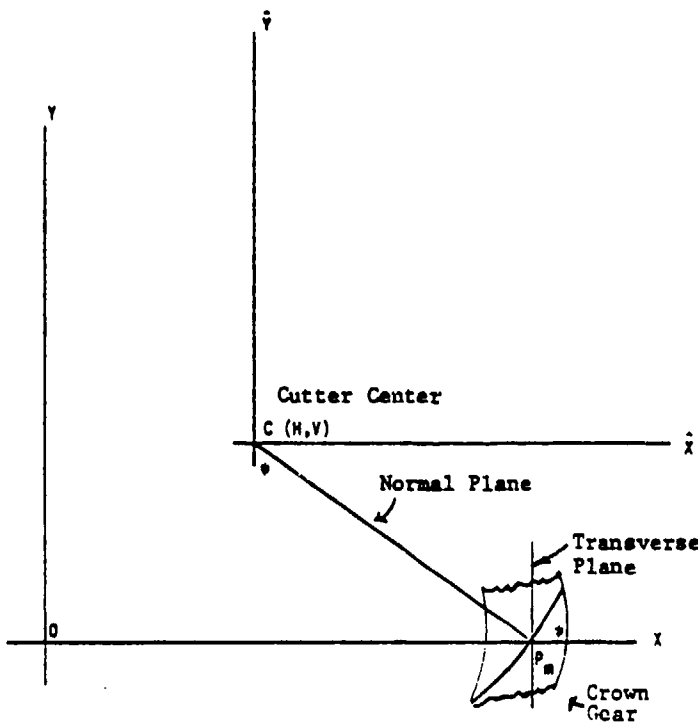


Figure 16. - View of crown gear pitch plane.

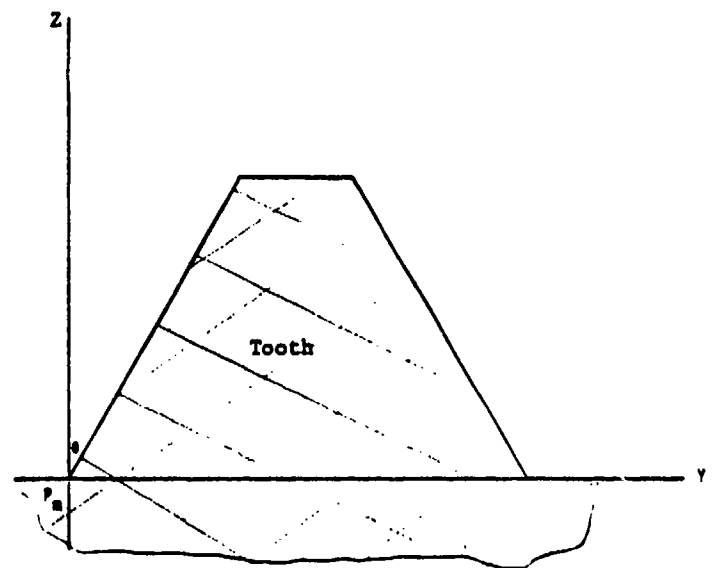


Figure 17. - True view of transverse plane showing crown tooth profile.

The maximum and minimum radii of curvature may now be determined directly by substitution into equations (40) and (41) or, alternatively, into equations (36) and (37). To do this, note that, based on equation (2), df/dr is

$$\frac{df}{dr} = -\tan \varphi = \frac{-kr}{(r^2 - R_c^2 \sin^2 \varphi)^{1/2}} \quad (77)$$

where φ is still defined as the angle between the tooth surface normal and the Z axis. Then r and $dr/d\varphi$ become

$$r = \frac{R_c \sin \psi \tan \varphi}{(\tan^2 \varphi - k^2)^{1/2}} \quad (78)$$

and

$$\frac{dr}{d\varphi} = \frac{-k^2 R_c \sin \psi \sec^2 \varphi}{(\tan^2 \varphi - k^2)^{3/2}} \quad (79)$$

Hence, on using equations (36) and (37), R_1 and R_2 become

$$R_1 = \left| \frac{k^2 R_c \sin \psi \sec^3 \varphi}{(\tan^2 \varphi - k^2)^{3/2}} \right| \quad (80)$$

and

$$R_2 = \left| \frac{R_c \sin \psi \sec \varphi}{(\tan^2 \varphi - k^2)^{1/2}} \right| \quad (81)$$

These expressions may be written in more convenient form by expressing φ in terms of z ; that is, by identifying z with f in equation (76), it is readily seen that

$$r^2 = R_c^2 \sin^2 \psi + \left(\frac{kV - z}{k} \right)^2 \quad (82)$$

Then, by equation (77), $\sec^2 \varphi$ becomes

$$\sec^2 \varphi = 1 + \tan^2 \varphi = 1 + k^2 + \left(\frac{k}{kV - z} \right)^2 k^2 R_c^2 \sin^2 \psi \quad (83)$$

Hence, R_1 and R_2 may be written as

$$R_1 = \frac{\{[(kV - z)/k]^2(1 + k^2) + k^2 R_c^2 \sin^2 \psi\}^{3/2}}{k R_c^2 \sin^2 \psi} \quad (84)$$

and

$$R_2 = \frac{\{(1 + k^2)[(kV - z)/k]^2 + k^2 R_c^2 \sin^2 \psi\}^{1/2}}{k} \quad (85)$$

Discussion

The basis of the foregoing exposition with theoretical spiral bevel gears is the assumption of a gear tooth having an involute profile in the transverse plane and a centerline as a logarithmic spiral. Although such gears are not convenient to manufacture, it is clear that unless the tooth centerline is a logarithmic spiral, the tooth profile, which engages the meshing gear, will not be uniform along the tooth. This could adversely modify the surface characteristics which, in turn, could affect the pressure angle, the bending stress, the contact stress, the lubrication, and the wear of the gear. Also, unless the gear tooth is spindled around the base cone, there could occur excessive sliding at the heel and toe of the tooth during meshing—particularly if the tooth is long.

The geometry of the circular-cut spiral bevel gears is somewhat simpler than that of the theoretical logarithmic spiral bevel gears. Admittedly, the restriction in the foregoing analysis to circular-cut *crown* gears contributes to the simplification. However, the modification of the foregoing expressions for conical gears can be obtained by following the procedures used for the logarithmic spiral gears.

The formulas for the radii of curvature of a surface of revolution (eqs. (36), (37), (40), and (41)) are applicable to circular-cut gear surfaces of any profile. The involute profile was used as an example because of its simplicity and because of the interesting results. It should be noted, however, that the involute profile as considered above is in the radial plane of the cutter (the normal plane of the gear) and *not* the transverse plane.

Finally, the straight-line crown profile in the transverse plane, when considered in the radial plane of the cutter, that is, the normal plane, generates a hyperboloid. Although this is a surface of revolution, it is also a "ruled surface" since it can be considered as generated by a one-parameter family of lines. Equations (84) and (71) show that the maximum radii of curvature occurs when $z = kv$ or when $y = 0$, that is, at the pitch surface. Similarly, equation (84) shows that the minimum radii of curvature occurs at the greatest elevation above the pitch surface.

Although the analysis and fabrication of circular-cut gears is considerably simpler than the theoretical logarithmic spiral gears, the apparent difference in their centerlines is relatively small. Indeed, Buckingham (ref. 1) has shown that within reasonable limits, the inclinations of the centerlines differ by less than $\pm 6^\circ$. However, the consequences of this difference in terms of its effects on the kinematics, the stresses, the lubrication, and the wear need further study. It is believed that the analytical procedures presented herein provide a basis for such studies.

References

1. Buckingham, E.: *Analytical Mechanics of Gears*. Dover, New York, 1963.
2. Dudley, D. W., ed.: *Gear Handbook*, 1962.
3. Huston, R. L.; and Coy, J. J.: *Ideal Spiral Bevel Gears—A New Approach to Surface Geometry*. NASA TM-82446 and AVRADCOM 80-C-5, 1980.
4. Huston, R. L.; and Coy, J. J.: *A New Approach to Surface Geometry of Spiral Bevel Gears. Part I—Ideal Gears*. J. Mech. Des., vol. 103, Jan. 1981, pp. 127-133.
5. Huston, R. L.; and Coy, J. J.: *Surface Geometry of Circular Cut Spiral Bevel Gear*. NASA TM-82622, 1981.
6. AGMA Standard Gear Nomenclature—Terms, Definitions, Symbols and Abbreviations. AGMA Publication 112.05, 1976.
7. AGMA Reference Information—Basic Gear Geometry. AGMA Publication 115.01, 1959.
8. AGMA Standard System for Spiral Bevel Gears. AGMA Publication 209.03, 1964.
9. Dyson, A.: *A General Theory of the Kinematics and Geometry of Gears in Three Dimensions*. Clarendon Press, Oxford, 1969.
10. Baxter, M. L., Jr.: *Exact Determination of Tooth Surfaces for Spiral-Bevel and Hypoid Gears*. American Gear Manufacturers Association Semiannual Meeting, 1966. AGMA paper No. 139.02.
11. Coleman, W.: *Guide to Bevel Gears*. Product Engineering, vol. 34, June 10, 1963, p. 87.
12. Litvin, F. L.: *Relationships Between the Curvatures of Tooth Surfaces in Three-Dimensional Gear Systems*. NASA TM X-75130, 1977.
13. Schwartz, A.: *Analytical Geometry and Calculus*. Holt, Rinehart, and Winston, New York, 1960, p. 528.

Spiral-Bevel Geometry and Gear Train Precision

Faydor L. Litvin* and John J. Coy†

Spiral-bevel gears have widespread applications in the transmission systems of helicopters, airplanes, trucks, automobiles and many other machines. Some of the major requirements in almost all the fields of application for transmissions are (1) improved life and reliability, (2) reduction in overall weight (i.e., a larger power-to-weight ratio) without compromising the strength and efficiency during the service life, and (3) reduction in the transmission noise.

Spiral-bevel gears used in practice are normally generated with approximately conjugate tooth surfaces by using special machine and tool settings. Therefore, designers and researchers cannot solve the Hertzian contact stress problem and define the dynamic capacity and contact fatigue life (ref. 1) until these settings are calculated. The geometry of gear tooth surfaces is very complicated and the determination of principal curvatures and principal directions of tooth surfaces necessary for calculating the Hertz stress is a very hard problem.

Baxter (refs. 2 and 3), Litvin (refs. 4 to 7), Litvin and Gutman (refs. 8 and 9) and Wildhaber (ref. 10) completed works dealing with the theory of gearings as well as with the theory of spiral bevel gears. Coy, Townsend, and Zaretsky (ref. 1), Coy, Rohn, and Loewenthal (ref. 11) completed work dealing with dynamic capacity and surface fatigue life of gears. Townsend, Coy, and Hatvani (ref. 12) analyzed failures of a helicopter transmission.

In this paper a novel approach to the study of the geometry of spiral bevel gears and to their rational design is proposed. The nonconjugate tooth surfaces of spiral-bevel gears are, in theory, replaced (or approximated) by conjugated tooth surfaces. These surfaces can be generated (1) by two conical surfaces rigidly connected with each other and in linear tangency along a common generatrix of tool cones, and (2) by a conical surface and a surface of revolution in linear tangency along a circle.

We can imagine that four surfaces are in mesh: two of them are tool surfaces Σ_F and Σ_K ; and two are gear tooth surfaces Σ_1 and Σ_2 . Surfaces Σ_F and Σ_1 are in linear contact, and contact lines of different form appear on the contacting surfaces in the process of meshing of the generating and the generated surfaces. The same can be said about the contact of surfaces Σ_K and Σ_2 . Surfaces Σ_F and Σ_K are rigidly connected and move in the process of meshing as one body. Surfaces Σ_1 and Σ_2 are in point contact and the point of their contact moves along these surfaces in the process of meshing. Surfaces Σ_1 and Σ_2 are hypothetical conjugate tooth surfaces which approximate the actual nonconjugate tooth surfaces.

The determination of surface principal curvatures and directions is a complicated problem. Therefore, a new approach to the solution of these is proposed in this presentation. In this approach direct relationships between the principal curvatures and directions of the tool surface and those of the generated gear surface are obtained. Therefore, the principal curvatures and directions of gear-tooth surface are obtained without using the complicated equations of these surfaces. This makes it easier to apply previously worked out methods for calculating life and reliability for spur and helical gears and traction-drive contacts to the spiral-bevel gear problem.

A general theory of the train kinematical errors exerted by manufacturing and assembly errors is discussed. Two methods for the determination of the train kinematical errors can be worked out: (1) with the aid of a computer, and (2) with an approximate method. Results from noise and vibration measurement conducted on a helicopter transmission are used to illustrate the principals contained in the theory of kinematical errors.

*University of Illinois at Chicago Circle.

†NASA Lewis Research Center.

Spiral-Bevel Geometry

Figure 1 shows the generating gear g and the member-spiral bevel gear 2 in mesh by cutting. The generating gear rotates about the axis x_f , and the member-gear rotates about the axis z_2 . Axes x_f and z_2 form an angle $90^\circ + (\gamma_2 - \Delta_2)$, where γ_2 is the pitch cone angle and Δ_2 is the addendum angle Δ_2 of the member gear 2.

Figure 2 shows the generating gear g and the pinion in mesh by cutting. The axes of rotation x_f and z_1 form an angle $90^\circ - (\gamma_1 - \Delta_1)$, where γ_1 is the pitch-cone angle and Δ_1 is the addendum angle of the pinion 1. It is assumed that gears 1 and 2 rotate in the train about perpendicular axes.

Surfaces of gears 1 and 2 can be generated as conjugated ones if axis z (fig. 3) is an instantaneous axis of rotation in relative motion for all four gear (for gears 1 and 2 and two generating gears). This requirement cannot be fulfilled for spiral bevel gears because the axes of rotation of the generating gears do not coincide with each other but form an angle $\Delta_1 + \Delta_2$ (fig. 3). Therefore, special machine settings by pinion 1 cutting are applied (fig. 2): axes of rotation x_f and z_1 do not intersect with each other and are dislocated by ΔL_1 and ΔE_1 in two perpendicular directions (ΔE_1 is not shown in fig. 2).

The novel approach to the study of the geometry of spiral-bevel gears is based on the substitution of nonconjugated tooth surfaces by conjugated ones, which can be realized in the following two ways or versions. It is well known that the generating surface for spiral-bevel gears is conical (fig. 4). The first version of spiral-bevel geometry is based on the following propositions: (a) two generating conical surfaces are in linear tangency along a common generatrix of both cones (fig. 5); (b) it can be imagined that two generating surfaces are rigidly connected with each other and rotate as one body by gear generation. The surfaces of the generated gears will therefore be in point tangency. The point of contact of the gear surfaces in mesh moves along the common generatrix of the tool cones. This imaginary way of gear meshing results in elliptical-shaped Hertzian contacts which move across the tooth surfaces in the profile direction.

The second version of the spiral-bevel geometry is based on these propositions: (1) One of the generating surfaces is conical, and the other is a surface of revolution (fig. 6); (2) both generating surfaces are in linear tangency along a circle of radius r_d ; (3) it is assumed that both generating surfaces are rigidly connected and rotate as one body by gear generation.

Surfaces of generated gears with geometry II will also be in point contact. The point of contact between the gear surfaces in mesh moves along the circle of radius r_d (fig. 6). This second version of gear generation provides that motion of the Hertzian ellipse contact will be along the gear tooth surface in the longitudinal direction. The advantages of spiral-bevel geometry II that are possible to achieve are improved conditions of lubrication and increased contact ratio.

Figure 7 shows a generating surface Σ_d which is covered with lines of contact. The generating and generated surfaces are in instantaneous contact at one of these lines. The point of instantaneous

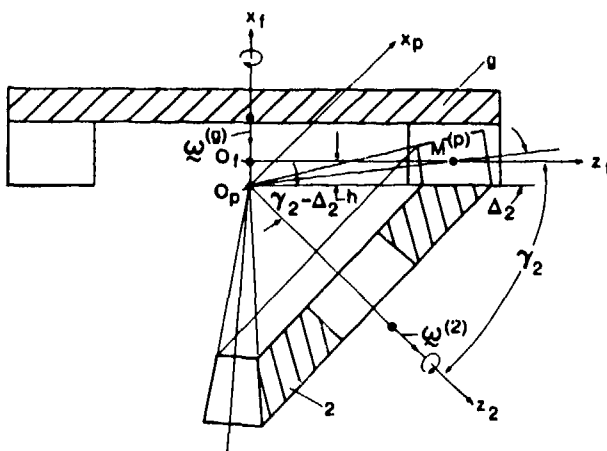


Figure 1. - Generating gear and member gear.

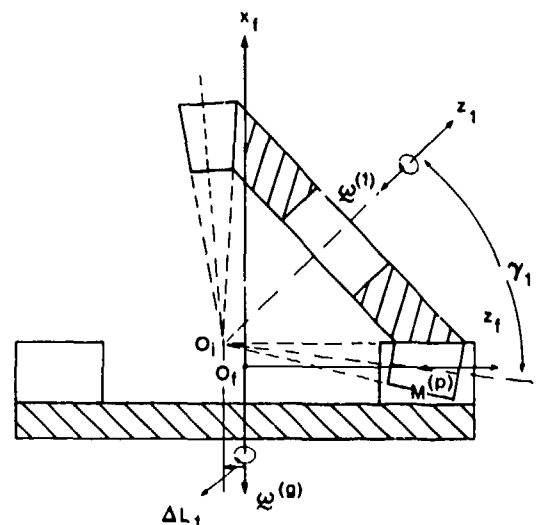


Figure 2. - Generating gear and pinion.

contact of gear surfaces is the point of intersection of the corresponding contact line with the tool cone generatrix (fig. 7). This generatrix is the line of contact of two tool cones for gears with the geometry I. An analogous picture pertains for gear geometry II, but the contact point between the gear surfaces is the point of intersection of the instantaneous contact line with the circle of radius r_d , which is the line of tangency of the two tool surfaces (fig. 6).

The analytical representation of the gear surface contact condition is based on the proposition that radii-vectors and unit normals of surfaces coincide at the contact point, M (fig. 8).

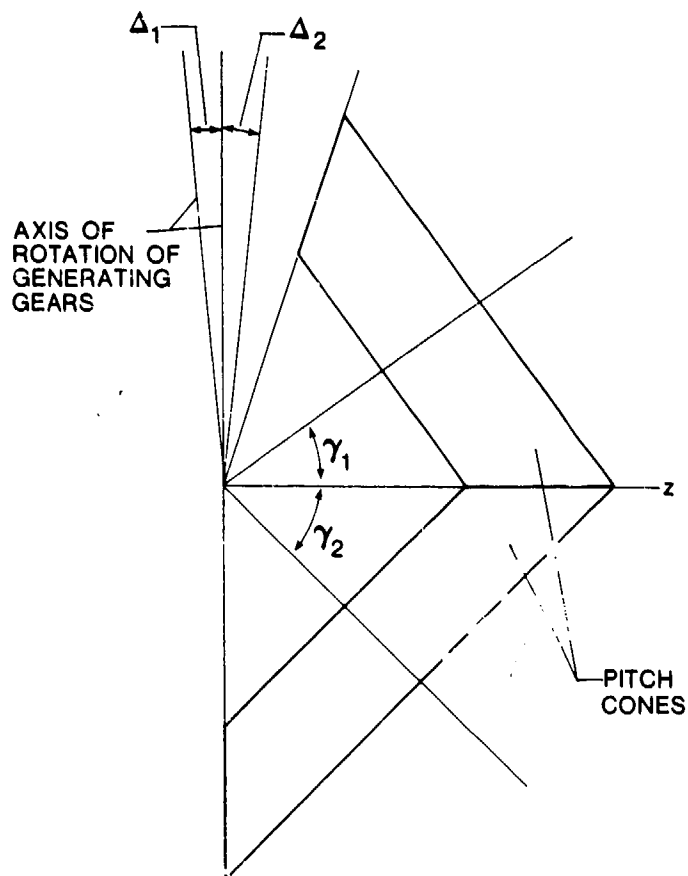


Figure 3. - Axes of rotation of generating gears and member gears.

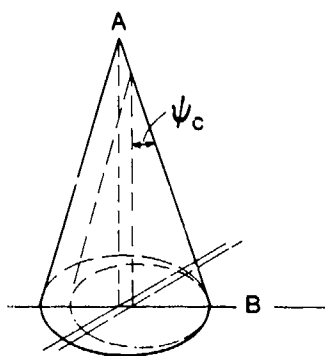


Figure 5. - Generating surfaces for geometry I.

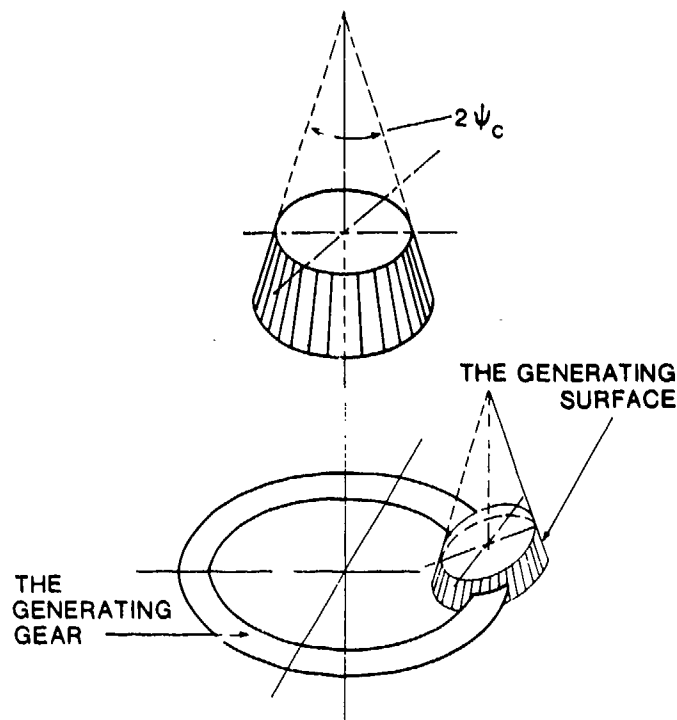


Figure 4. - Tool cone and generating gear.

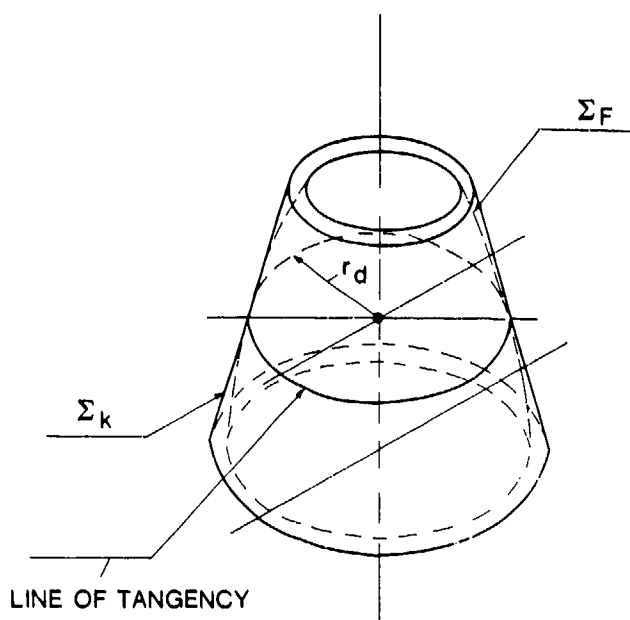


Figure 6. - Generating surfaces for geometry II.

Because of elasticity of gear surfaces, their contact under a load is spread over an area (fig. 9) which, when projected on the tangent plane, is an ellipse. Figure 10 shows how the bearing contact is formed for gears with geometry I (fig. 10(a)) and for gears with geometry II (fig. 10(b)). The location of the bearing contact on the tooth surface depends on the direction of motion of the elliptical spot over the tooth surface.

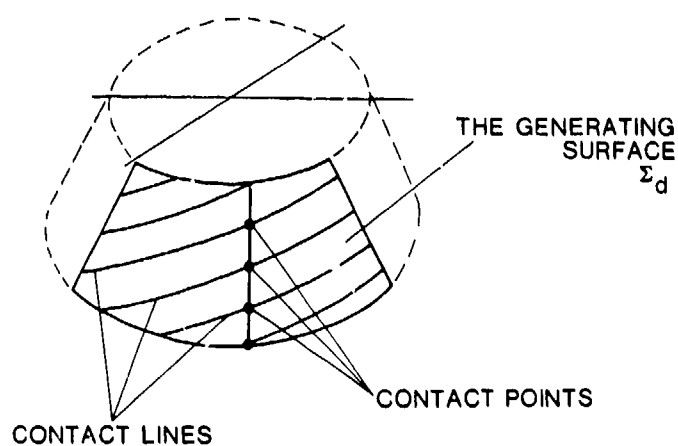


Figure 7. - Contact lines and contact points on generating surface Σ_d .

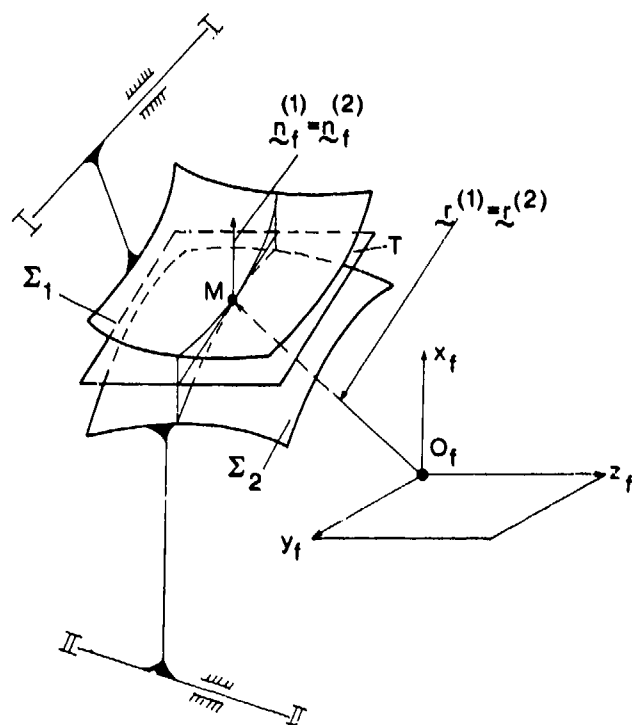


Figure 8. - Gear tooth surfaces at contact.

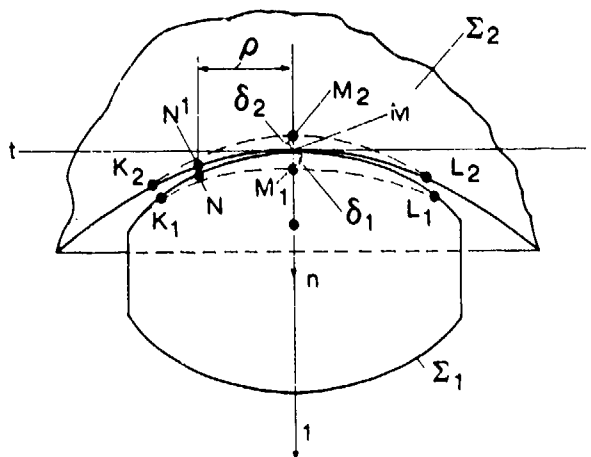


Figure 9. - Deformation of two contacting surfaces.

Method of Calculation of Dynamic Capacity and Surface Fatigue Life of Spiral Bevel Gears

In reference 1 a method of adapting the Lundberg-Palmgren method of life analysis for rolling-element bearings was applied to spur and helical gears. The method has also been applied to life analysis of traction drives (ref. 11). An update of the method applied to spur gears, with applications for various gearing arrangements, is presented in another paper in this symposium.

In the life analysis theory the important parameters are number of stress cycles, η , magnitude of critical stress, τ , amount of stressed volume, V , and depth below the surface at which the critical stress occurs, z . For spiral bevel gears, the stressed volume is taken as

$$V \propto wzl \quad (1)$$

where l is the length of the contact path which is traversed during one tooth mesh cycle and the semi-width of the contact path is designated w .

The probability of survival, S , for a tooth contact is given by the following expression:

$$\log \frac{1}{S} \propto \frac{\tau c \eta^e V}{z^h} \quad (2)$$

This relation is consistent with experimental observations in the case of fatigue. The formula reflects the known fact that the more localized the stress is in the material (less stressed volume), the greater is the endurance. This is because, on a statistical basis, there is less likelihood of a fatigue nucleation site being coincident with a condition of high stress. Conversely, there is a greater probability of a crack forming in the zone of maximum critical stress, because the material is more rapidly cycled toward failure in that region. Hence the depth to the critical stress, as well as the magnitude of the stress is important, and with each stress cycle the probability of failure increases.

The number of stress cycles endured with 90 percent reliability is given by the following equation (ref. 11):

$$\eta = \left(\frac{K z^h}{\tau c V} \right)^{1/e} \quad (3)$$

Based on life testing of air-melted steel rolling-element bearings, the following values are valid for equation (3): $K = 1.43 \times 10^{95}$ (SI units), 3.58×10^{56} (English units); $h = 7/3$; $c = 31/3$; and $e = 10/9$ (point contact), $3/2$ (line contact) (ref. 11).

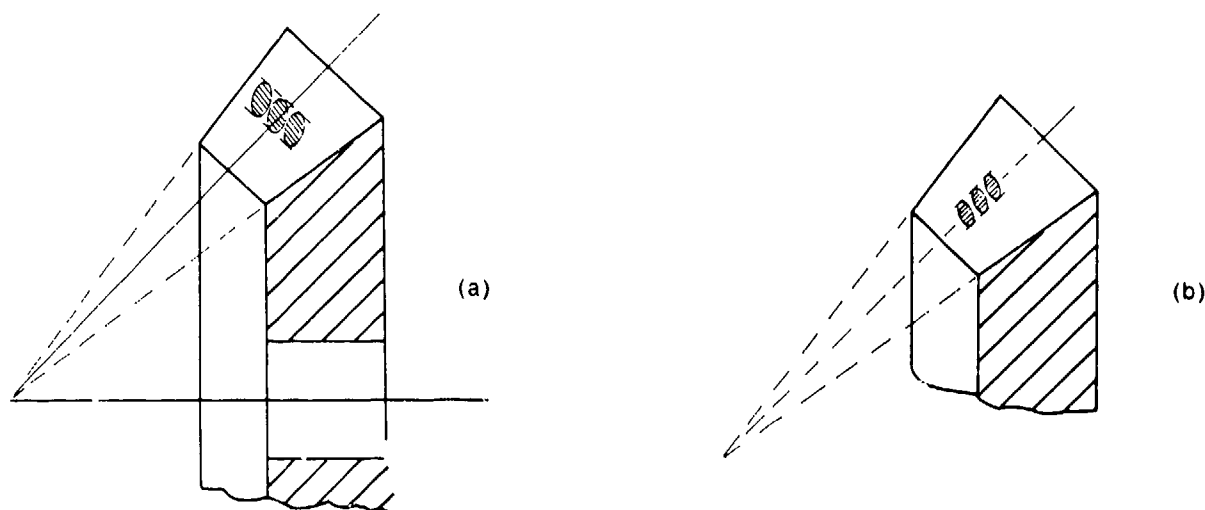


Figure 10. - Formation of bearing contact.

From the probability theory the life, L , of a gear with N teeth then is obtained by the equation

$$\left(\frac{1}{L}\right)^e = N \left(\frac{1}{\eta}\right)^e \quad (4)$$

The foregoing has been a brief summary of how the gear life analysis originally presented in reference 10 may be applied to spiral-bevel gears. All of the approximations, service life factors and lubricant-condition-related life-modifying factors that pertain to spur and helical gears will also have counterpart effects for spiral-bevel gears. These factors are discussed in reference 11.

Gear Train Precision

Angles of rotation φ_2 and φ_1 of a pair of gears are related by a linear function only for an ideal train. The difference

$$\varphi_2(\varphi_1) - \varphi_2^0(\varphi_1) = \Delta\varphi_2(\varphi_1) \quad (5)$$

represents a function of kinematical errors induced by errors of manufacturing and assembly. Here, $\varphi_2^0(\varphi_1)$ is the theoretical function, and $\varphi_2(\varphi_1)$ is the real function.

The function $\Delta\varphi_2(\varphi_1)$ of kinematical errors may be determined in the following two ways:

The first method is based on the investigation of the meshing of gear surfaces generated and assembled with some errors. The basic principle of such an investigation is the requirement of equality of radii vectors and unit normals of contacting surfaces (fig. 8). The determination of gear-train kinematical errors with such a method is a computer problem.

The second method is based on the following suggestions (fig. 11): Suppose that, because of errors of manufacturing and assembly, the expected contact points $M^{(1)}$ and $M^{(2)}$ do not coincide with each other and that between surfaces Σ_1 and Σ_2 there occurs clearance or interference. To bring both surfaces into contact, it is necessary and sufficient to rotate the driven gear 2 about the axis II-II by some small angle $\Delta\varphi_2$, the magnitude of which depends on the magnitude of clearance or

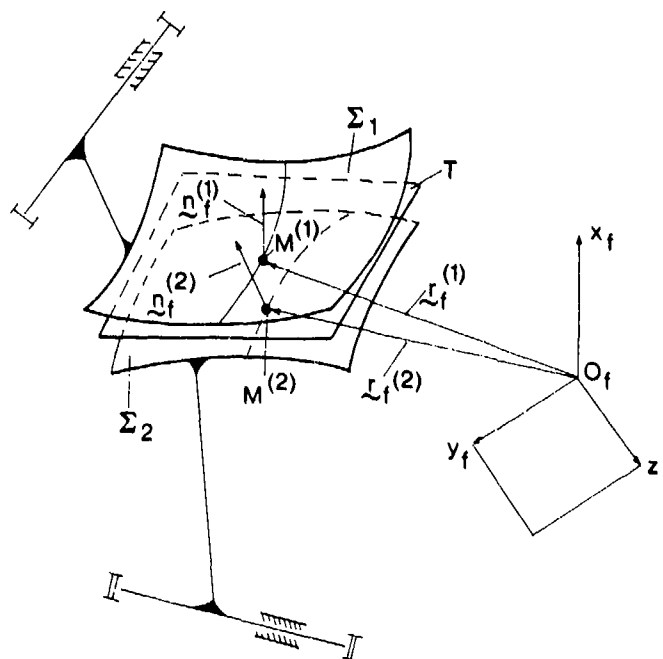


Figure 11. - Tooth surfaces with clearance induced by errors.

interference induced by errors of manufacturing and assembly. Equations relating kinematical errors with errors of manufacturing and assembly have been developed by Litvin (refs. 4 and 5).

Figure 12 shows kinematical errors $\Delta\phi_2(\phi_1)$ represented by equation (5). Figure 13 shows two types of the function $\Delta\phi_2(\phi_1)$. The first one (fig. 13(a)) corresponds to the case when the gear axis does not coincide with the axis of rotation and rotates about it in the process of meshing. The typical example of such errors is the gear eccentricity. The second type of kinematical errors of a train with spiral-bevel gears and hypoid gears is the result of the approximate way of gear generation (fig. 13(b)).

Figure 14 shows a case when a gear axis, z_1 , forms an angle $\Delta\delta$ with the axis of rotation, z , and the shortest distance between z_1 and z is the rotated vector Δe . With $\Delta\delta=0$ the vector Δe represents the vector of gear eccentricity.

Figure 15 shows two spur involute gears with vectors of eccentricity Δe_1 and Δe_2 . Gear axis of rotation are $O^{(1)}$ and $O^{(2)}$, geometric centers of gears are O_1 and O_2 . These centers rotate about $O^{(1)}$ and $O^{(2)}$ as shown in figure 16. The eccentricity of a spur gear exerts a harmonic function (fig. 17) of kinematical errors $\Delta\theta_1(\phi_1)$, the period of which coincides with the period of a complete revolution of the considered gear. The distribution of this function in positive and negative areas depends on the location of the vector eccentricity.

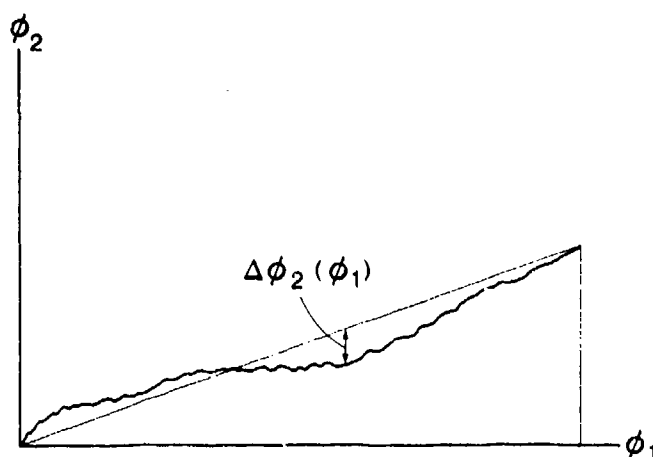


Figure 12. - Kinematic error functions.

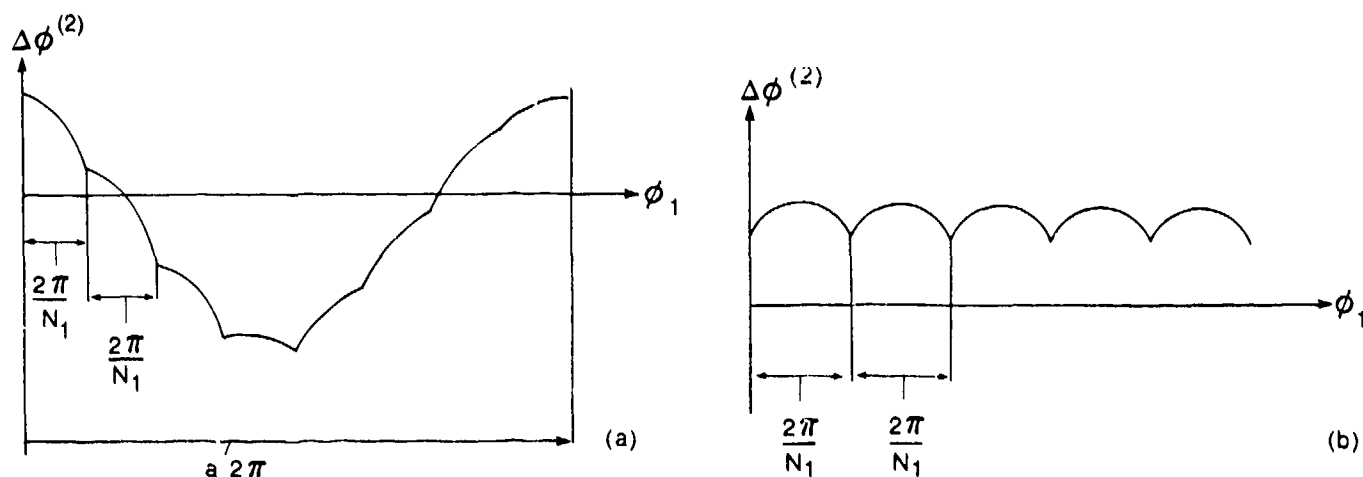


Figure 13. - Two types of kinematic functions.

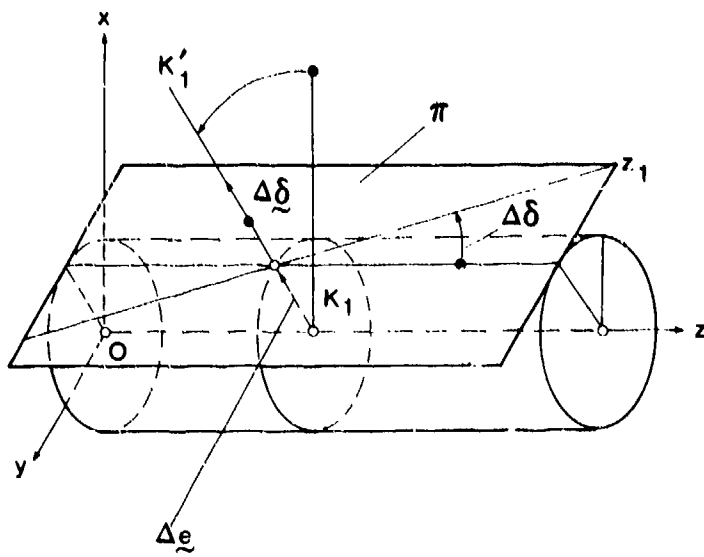


Figure 14. - Crossing of gear axis and rotation axis.

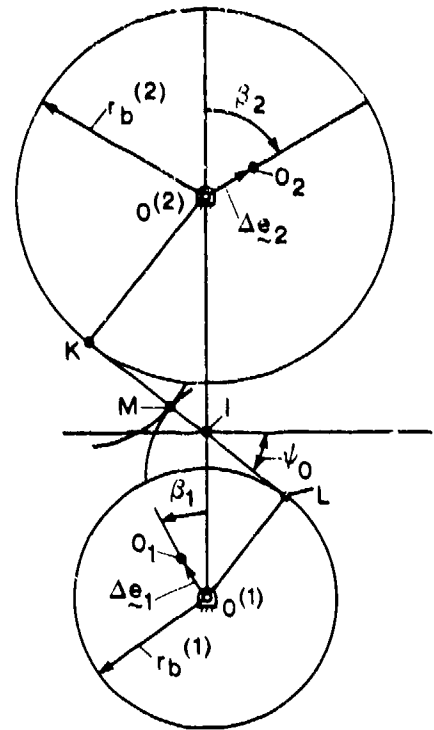


Figure 15. - Eccentricity of spur gears.

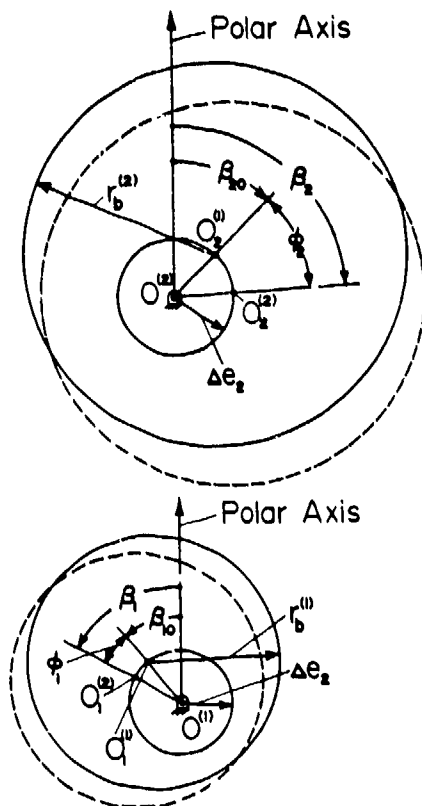


Figure 16. - Eccentric base circles.

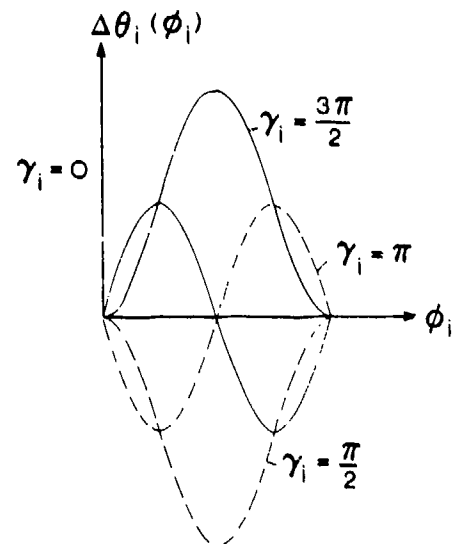


Figure 17. - Distribution of kinematic errors by eccentricity.

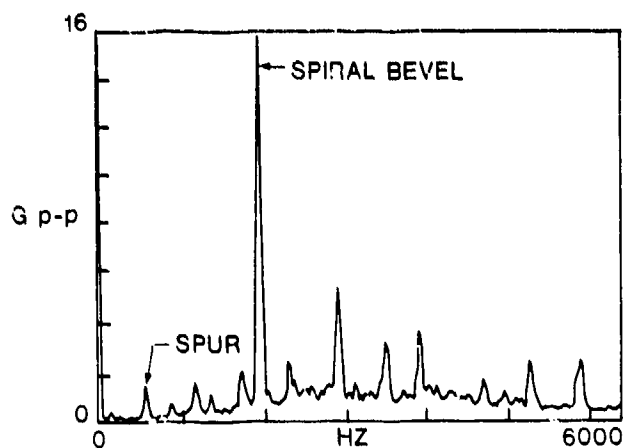


Figure 18. - Baseband frequency spectrum showing spiral bevel amplitude compared with spur.

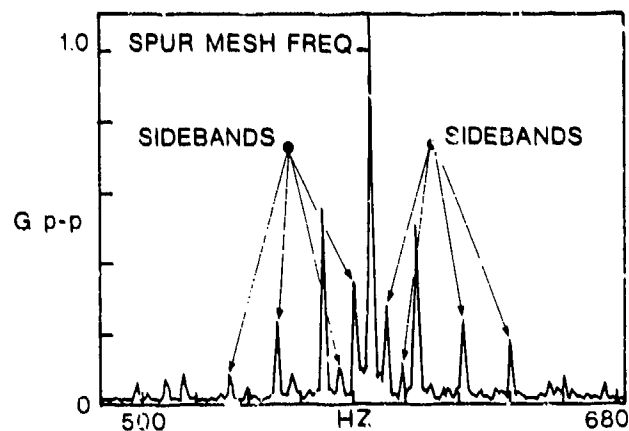


Figure 19. - Narrowband frequency spectrum showing sidebands around the spur mesh frequency.

Gear Train Vibration and Noise Measurement

To illustrate the principles discussed on the subject of gear-train precision, figures 18 and 19 are used. These figures show some frequency spectrum measurements made on a helicopter transmission running in a test stand (ref. 12). The transmission had a spiral-bevel input stage with 19 teeth on the pinion and 71 teeth on the gear. The pinion was turning at 6200 rpm and the output shaft at 355.5 rpm. The output stage was a spur planetary arrangement with a 27-tooth sun, 3 planet gears, each with 35 teeth, and a 99-tooth ring gear which was splined to the transmission housing. An accelerometer was mounted on the case immediately outside the spline.

Figure 18 shows a broadband frequency spectrum measurement of the vibration signal. The spur mesh frequency was 583 Hz, and the spiral bevel mesh frequency was 1963 Hz. The spiral bevel vibration signature was much stronger than the spur signature. This indicates that the meshing accuracy according to figure 13(b) was better for the spur mesh than for the spiral-bevel mesh. There are also other peaks in the spectrum at multiples of the fundamental frequencies of 1963 and 583 Hz. These other peaks are the higher harmonics due to the noise and vibration pulsations as the teeth mesh being different from the pure sinusoidal shape, as shown in figure 17.

Figure 19 shows an expanded region of the autospectrum plot given in figure 18. This figure shows many peaks which are symmetrically located about the spur gear mesh fundamental frequency peak at 583 Hz. These peaks locate the sideband frequencies which are due to sources of modulation in the time-dependent vibration waveform. Each source of modulation may produce one pair of sidebands if it is a harmonic modulator. If nonharmonic, the sidebands will repeat many times, as is the case in figure 19.

In this particular example, there are three major causes of modulation: (1) the planet gears passing the stationary accelerometer at approximately 18 Hz; (2) the planet gears rotational speed of 16 Hz; and (3) the planet carrier turning at the output shaft speed of 6 Hz. The misalignments and eccentricities associated with the rotational frequencies of the mentioned gear components cause these modulation sidebands to appear, as discussed in the previous section.

Conclusions

Two types of spiral-bevel geometry for a simplified study and investigation of such gears were described. The line of action and bearing contact for gears of both types of geometry were determined. A method for calculating the expected service life for pitting fatigue of the spiral-bevel gear teeth was given.

Two methods for the determination of kinematical errors induced by errors of manufacturing and assembly were proposed. The first is an exact computerized method, the second is an approximate one but one which allowed the analytical relations between source errors and resulting kinematical errors to be written. Results of noise and vibration measurements on a helicopter transmission were shown to illustrate the principles contained in the theory of kinematical errors.

References

1. Coy, J. J.; Townsend, D. P.; and Zaretsky, E. V.: Dynamic Capacity and Surface Fatigue Life for Spur and Helical Gears. *J. Lubr. Technol.*, vol. 98, no. 2, April 1976, pp. 267-276.
2. Baxter, M.: Second-Order Surface Generation. *Ind. Math.*, vol. 23, pt. 2, 1973, pp. 85-106.
3. Baxter, M.: Effect of Misalignment on Tooth Action of Bevel and Hypoid Gears. ASME Paper No. 61-MD-20.
4. Litvin, F.: Theory of Gearing, 2nd. Ed., Nauka, 1968 (in Russian).
5. Litvin, F.: Die Beziehungen zwischen den Krümmungen der Zahnoberflächen bei räumlichen Verzahnungen. *ZAMM*, 49 (1969), Heft 11, Seite 685-690.
6. Litvin, F.: The Synthesis of Approximate Meshing for Spatial Gears. *J. Mechanisms*, vol. 4, 1969, Pergamon Press, pp. 187-191.
7. Litvin, F.: An Analysis of Undercut Conditions and of Appearance of Contact Lines Envelope Conditions of Gears. *J. Mech. Des.*, July 1978, pp. 423-432.
8. Litvin, F.; and Gutman, Ye.: Methods of Synthesis and Analysis for Hypoid Gear Drives of "Formate" and "Helixform," Pts. 1-3, *J. Mech. Des.*, vol. 103, Jan. 1981, pp. 83-113.
9. Litvin, F.; and Gutman, Ye.: A Method of Local Synthesis of Gears Grounded on the Connections Between the Principal and Geodetic Curvatures of Surfaces. *J. Mech. Des.*, vol. 103, 1981, pp. 114-125.
10. Wildhaber, E.: Surface Curvature—A Tool for Engineers. *Ind. Math.*, vol. 5, 1954, pp. 31-116.
11. Coy, J. J.; Rohn, D. A.; and Loewenthal, S. H.: Life Analysis of Multiroller Planetary Traction Drive. NASA TP-1710, April 1981.
12. Townsend, D. P.; Coy, J. J.; and Hatvani, B. R.: OH-58 Helicopter Transmission Failure Analysis. NASA TM X-71867, Jan. 1976.



A Computer Solution for the Dynamic Load, Lubricant Film Thickness, and Surface Temperatures in Spiral-Bevel Gears*

H. C. Chao,[†] M. Baxter,[‡] and H. S. Cheng[§]

Spiral-bevel gears, found in many machine tools, automobile rear-axle drives, and helicopter transmissions, are important elements for transmitting power. However, the basic mechanisms which govern the major failure modes of spiral gears are still not fully understood. Because of the complicated geometry of spiral-bevel gears, the analyses are considerably more difficult than those conducted earlier for spur and helical gears. In military applications, such as the transmissions used in V/STOL aircraft, gears are often designed under conditions very close to the failure limits for maximum power density. A thorough understanding of spiral-bevel gears under critical operations is urgently needed to prevent premature failure.

Gear failures usually fall into two categories, structural failures, which include flexure fatigue, tooth breakage, case crushing, and lubrication-related failures, which include wear, surface pitting, and scuffing. Among these types of failure modes, lubrication-related failures are much more difficult to predict since the basic mechanisms are still not fully understood. Current methods used for predicting gear pitting and scuffing are mainly empirical and are not completely reliable. Recent failure tests of gears and rollers strongly suggest that surface pitting as well as scuffing are critically influenced by lubricant film thickness and surface temperature in the gear teeth contact. To develop improved methods for failure prediction, it is important to develop accurate tools to determine the film thickness and surface temperature.

In this paper a computer method is first described for determining the dynamic load between spiral-bevel pinion and gear teeth contact along the path of contact. The dynamic load analysis is necessary because it governs both the surface temperature and film thickness. Computer methods for determining the surface temperature and film thickness are then presented along with some results obtained for a pair of typical spiral-bevel gears.

Symbols

$\{D\}$	displacement column vector for pinion or gear in x, y, z coordinates, m or rad (ft or rad)
$\{D'\}$	displacement column vector for pinion or gear in x', y', z' coordinates, m or rad (ft or rad)
$[DC_{ji}]$	elastic compliance matrix, m/N (ft/lb)
$[DK_j]$	bearing stiffness matrix, N/m (lb/ft)
F_c	teeth contact force, N (lb)
F_r	bearing force, N (lb)
$I_{x'}, I_{y'}, I_{z'}$	polar moment of inertia about x', y', z' axes, $\text{kg}\cdot\text{m}^2$ (slug·ft ²)
i', j', k'	unit vectors along the x', y', z' axes

*Work done under NASA Lewis contract NSG-3143.

[†]Garrett Turbine and Engine Co.

[‡]Consultant, Gear Technology.

[§]Northwestern University.

m	mass of pinion or gear shaft, kg (slug)
r_c	position vector of the teeth contact point with respect to the mass center, m (ft)
r_r	position vector of the bearing supports with respect to the mass center, m (ft)
T_{in}, T_{out}	average input torque, average output torque, N·m (ft·lb)
X, Y, Z	fixed coordinates with origin at the intersection of two shafts
x, y, z	fixed coordinates with origin at the mass center of the pinion or gear
x', y', z'	moving coordinates along the principal axes of inertia of pinion or gear
x'_c, y'_c, z'_c	displacements of mass center of pinion or gear, m (ft)
$\theta_{x'}, \theta_{y'}, \theta_{z'}$	angular displacements of pinion or gear, rad
ω	angular velocity of pinion or gear shaft, rad/sec
Subscripts:	
g	gear shaft
p	pinion shaft

Dynamic Load

Equations of Motion

Figure 1 shows the model used for deriving the equations of motion to simulate the steady-state, periodic motion of both pinion and gear as well as the tooth load during a typical cycle during which a pair of teeth traverse through the zone of action from point A to point C. In developing the equations of motion, the pinion and gear are assumed to be rigid bodies each having 6 degrees of freedom. The supporting radial and thrust bearings are assumed to be flexible with known spring stiffnesses. At the contact of each mesh, the teeth are assumed to be connected by a linear spring, which is oriented normal to the contact point and has a stiffness to be determined separately by a finite-element model.

Based on Newtonian mechanics, it is shown (ref. 1) that the equations governing the pinion motion can be expressed in a moving coordinate axes x'_p, y'_p, z'_p , which are instantaneous principal axes of inertia of the pinion. However, the pinion is not fixed in the axes x'_p, y'_p, z'_p , but rotates about the y'_p axis with a nominal angular velocity ω_p . The two vectorial equations of motion for the pinion are

$$\sum_{i=1}^M \mathbf{F}_{rpi} + \sum_{i=1}^N \mathbf{F}_{cpi} = m_p(\ddot{x}'_p \mathbf{i}'_p + \ddot{y}'_p \mathbf{j}'_p + \ddot{z}'_p \mathbf{k}'_p) \quad (1)$$

$$\begin{aligned} \sum_{i=1}^M \mathbf{r}_{rpi} \times \mathbf{F}_{rpi} + \sum_{i=1}^N \mathbf{r}_{cpi} \times \mathbf{F}_{cpi} + \mathbf{T}_{in} = & (I_{x'p} \ddot{\theta}_{x'p} - I_{y'p} \omega_p \dot{\theta}_{z'p}) \mathbf{i}'_p \\ & + I_{y'p} \ddot{\theta}_{y'p} \mathbf{j}'_p + (I_{z'p} \ddot{\theta}_{z'p} + I_{y'p} \omega_p \dot{\theta}_{x'p}) \mathbf{k}'_p \end{aligned} \quad (2)$$

where M is the total number of bearing forces acting on the pinion shaft and N is the total number of contact forces.

Similarly, the equations of motion for the gear can be expressed in the coordinate axes x'_g, y'_g, z'_g , and the gear rotates about the x'_g axis with a nominal angular velocity, ω_g . The two vectorial equations for the gear appear as

$$\sum_{i=1}^M \mathbf{F}_{rgi} + \sum_{i=1}^N \mathbf{F}_{cgi} = m_g(\ddot{x}'_g \mathbf{i}'_g + \ddot{y}'_g \mathbf{j}'_g + \ddot{z}'_g \mathbf{k}'_g) \quad (3)$$

$$[m] \begin{Bmatrix} \{\ddot{D}'\}_g \\ \{\ddot{D}'\}_p \end{Bmatrix} + [C] \begin{Bmatrix} \{\dot{D}'\}_g \\ \{\dot{D}'\}_p \end{Bmatrix} + [K] \begin{Bmatrix} \{D'\}_g \\ \{D'\}_p \end{Bmatrix} = \{R\} \quad (7)$$

The details of matrix $[m]$, $[c]$, $[k]$, and $\{R\}$ can be found in reference 2.

It was also found that the rotational equations governing the perturbed gear rotation θ'_{x_g} and the perturbed pinion rotation θ'_{y_p} can be combined into one equation to solve for the relative angles θ'_{y_p} and θ'_{x_g} . Thus, the reduced system becomes a set of 11 equations which are solved by Runge-Kutta procedure for the displacements of pinion and gear mass center and their small angular rotations.

In implementing these equations, the information needed includes

- (1) The tooth contact position as a function of the relative rigid body displacements of the two shafts
- (2) The direction of normal vector at the contact point
- (3) The combined stiffness of the teeth at the contact point.

The teeth contact position and the direction of the contacting normal vector are obtained from a computer code (ref. 3). Because of the geometric complexity of spiral-bevel gears, calculations of combined teeth stiffness are not as simple as those shown in reference 4 for spur gears. For this study, a large-scale finite-element program is used to calculate the deformation due to a unit load at various contact points in the zone of action for a given set of spiral-bevel gears.

Tooth Deflection

For most gears the contact ratio is greater than one, and the load is, in general, not equally shared among the pairs of teeth in contact because the system is a statically indeterminate case. Therefore, one must consider the tooth deflection under the load for each pair in order to determine the load sharing characteristics among the pairs.

Because of the complexity of the spiral-bevel gear geometry, there is no simplified method currently available to calculate the tooth deflection. In order to investigate the system response, shaft deformation must also be included in the calculation of tooth deflection. Therefore, it is more difficult to calculate the tooth deflection by some simple equations. A numerical solution using finite-element method is used to overcome these difficulties.

Some of the recent work (refs. 5 and 6) has proven that the finite-element method yields better results in determining tooth deflection. However, most of this work dealt with two-dimensional problems and did not include the whole gear body. In the present work the spiral-bevel geometry necessitates the use of a three-dimensional, finite-element code. Figure 2 shows a typical eight-node, solid-element grid pattern for a typical spiral-bevel gear and pinion with three adjacent teeth attached to the gear wheel and shaft. Figure 3 shows a central tooth and its attached ring element of gear. Figure 4 shows parts of a gear shaft and gear wheel. Figure 5 shows whole ring elements with three adjacent teeth of pinion. Figure 6 shows the elements of pinion shaft. Only the central tooth is loaded to calculate the deflection. There are 941 nodes, 562 elements for the gear model and 1029 nodes, 584 elements for the pinion model. Using these grids, one can readily compute the deflection δ under a load P applied at any grid point on the tooth surface. For this analysis the MARC-CDC program was used; the boundaries are considered to be fixed for all the points connected to the thrust bearing to eliminate rigid body displacement; and the boundary nodes connected to the radial bearing were allowed to move in the direction of the rotational axis.

The stiffness at grid point i is defined as

$$KS_{gi} = \frac{P}{\delta_{gi}}$$

$$KS_{pi} = \frac{P}{\delta_{pi}}$$

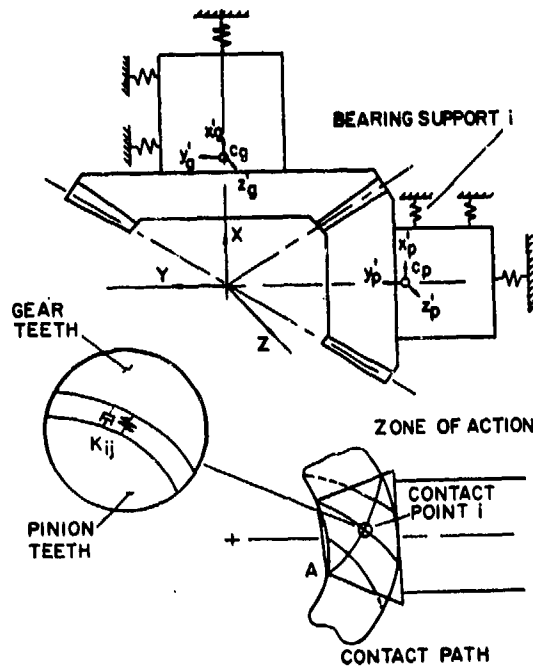


Figure 1. - Geometry and mathematical model of spiral-bevel gears.

$$\sum_{i=1}^M \mathbf{r}_{rgi} \times \mathbf{F}_{rgi} + \sum_{i=1}^N \mathbf{r}_{cgi} \times \mathbf{F}_{cgi} + \mathbf{T}_{out} = I_{x'g} \ddot{\theta}_{x'g} \mathbf{i}'_g + I_{y'g} \ddot{\theta}_{y'g} \mathbf{j}'_g + I_{z'g} \ddot{\theta}_{z'g} \mathbf{k}'_g + (I_{x'g} \omega_g \dot{\theta}_{z'g}) \mathbf{j}'_g + (I_{z'g} \omega_g \dot{\theta}_{x'g}) \mathbf{i}'_g \quad (4)$$

In these four equations of motion, \mathbf{F}_{rpi} and \mathbf{F}_{rqi} are the bearing reaction forces for the pinion and gear. These can be expressed directly as the product of the stiffness and the displacement vectors in matrix form as

$$\{\mathbf{F}_{rj}\}_g = -[DK_j]_g \{\mathbf{D}\}_g \quad (5)$$

$$\{\mathbf{F}_{rj}\}_p = -[DK_j]_p \{\mathbf{D}\}_p$$

The tooth contact forces \mathbf{F}_{cpi} and \mathbf{F}_{cqi} at the contact point are equal and opposite forces, and \mathbf{F}_{cqi} in matrix form can be expressed in terms of the combined teeth elastic compliance matrix $[DC_{ij}]$ and the displacement vectors $\{\mathbf{D}\}_p$ and $\{\mathbf{D}\}_g$ as

$$\{\mathbf{F}_{ci}\}_g = -([DC_{ji}]_g + [DC_{ji}]_p)^{-1} ([DG]_{ig} \{\mathbf{D}\}_g + [DG]_{ip} \{\mathbf{D}\}_p) \quad (6)$$

Substituting equations (5) and (6) into equations (1) to (4), one obtains a set of 12 equations, which can be put in the following matrix form:

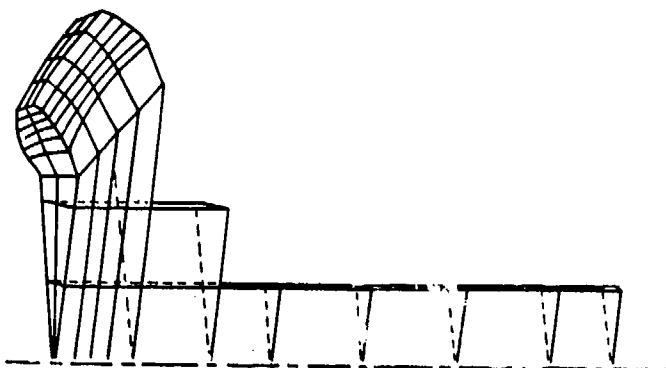


Figure 2. - Typical section of finite elements of gear segment.

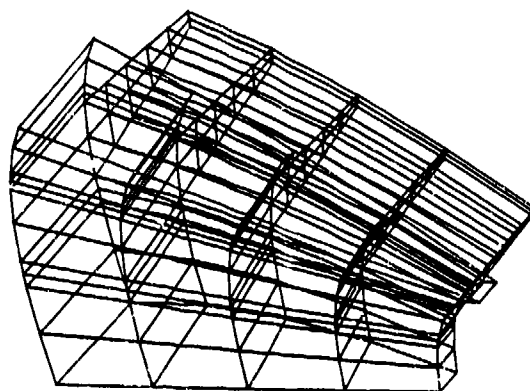


Figure 3. - Center tooth elements and attached ring elements of gear.

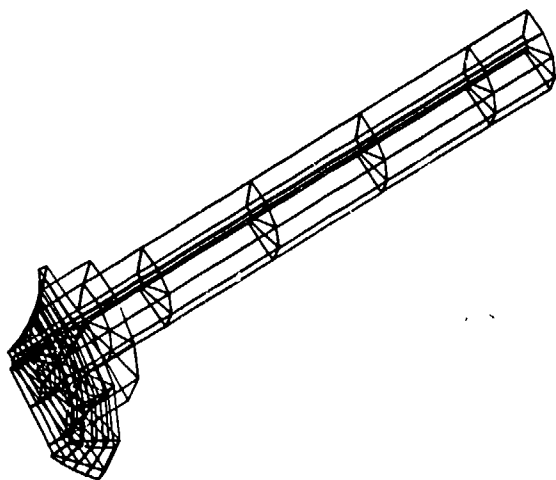


Figure 4. - Elements for segment of shaft and wheel.

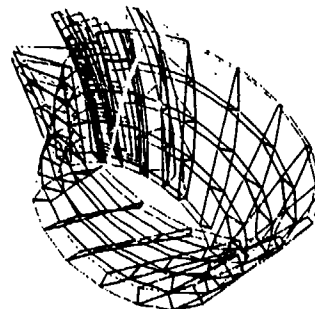


Figure 5. - Elements of three pinion teeth and rim.

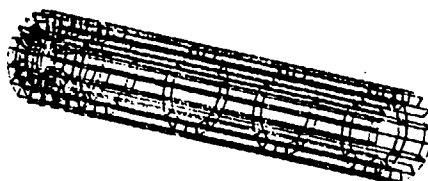


Figure 6. - Elements of pinion shaft.

The stiffness of a point other than a grid point on the tooth surface can be calculated by the interpolation method. The combined stiffness at the contact point is found to be

$$KS = \frac{KS_g \cdot KS_p}{KS_g + KS_p}$$

Results of Dynamic Load

A series of solutions were obtained to simulate the dynamic response of a set of spiral-bevel gears currently being tested at NASA Lewis. The data for this gearset and the lubricant data are listed in table I. Effects studied include the running speed, shaft misalignment, and system damping. These results are presented in this section. The dynamic response is expressed by a dynamic load factor defined as the ratio of the maximum dynamic load along the contact path to the average static load. This factor is plotted as a function of speed with different damping ratios and contact ratios.

TABLE I. - GEAR AND LUBRICANT DATA

Gear data:	
Number of teeth:	
Gear	36
Pinion	12
Pitch angle:	
Gear	71°34'
Pinion	18°26'
Shaft angle, deg	90
Spiral angle, deg	35
Diametral pitch	5.14
Standard operating conditions:	
Gear rpm	5000
Pinion rpm	15 000
Load at pitch point, N (lb)	11 800 (2660)
Ambient temperature, °C (°F)	37.8 (100)
Geometry dimensions (see fig. 25), m (in.):	
DGG	0.1658 (6.527)
ROG	0.07620 (3.0)
RIG	0.04336 (1.707)
RZG	0.1964 (7.733)
DGP	0.2515 (9.901)
ROP	0.07620 (3.0)
RIP	0.09311 (3.6656)
RZP	0.1987 (7.824)
Gear material data:	
Material	steel
Density, g/cm ³ (lb/in ³)	7.81 (0.282)
Thermal conductivity at 311 K (100° F), W/mK (Btu/sec·in·°F)	46.7 (0.000625)
Young's modulus, GPa (psi)	207 (30 000 000)
Poisson ratio	0.3
Surface convectivity, W/m ² K (Btu/sec·in ² ·°F):	
Oil jet	397 (0.000135)
Oil/air mist	19.8 (0.00000765)
Air	3.97 (0.00000135)
Lubricant data:	
Material	superrefined, naphthenic, mineral oil
Dynamic viscosity at 311 K (100° F), cp (lb·sec/in ²)	64.7 (0.00000938)
Density at 311 K (100° F), g/cm ³ (lb/in ³)	0.61 (0.022)
Thermal conductivity at 311 K (100° F), W/mK (Btu/sec·in·°F)	0.125 (0.00000168)
Pressure viscosity coefficient, α, m ² /MN (in ² lb)	0.023 (0.00016)
Temperature-viscosity coefficient, β, K (°R)	3890 (7000)
Viscosity-pressure temperature relation	$\mu = \mu_0 \exp[\alpha p + \beta[(1/T) - (1/T_0)]]$

Dynamic Load Variation

For constant input torque the load on the contact point of the two meshing teeth along the path of contact is not constant; this load variation is mainly caused by the following factors:

- (1) The variation of stiffness along the contact path
- (2) The transition from single pair of contacts to double and from double to single
- (3) The effective radius not constant along the contact path.

Figure 7 shows the variation of stiffness for the transition of contacts.

The main excitation to the gear system comes from the periodical change in teeth stiffness due to the alternating engagement of single and double pairs of teeth. The frequency of this excitation force expressed as a meshing frequency depends on the operating speed. Therefore, it dominates the resulting mode of vibration. Figures 8 to 11 show dynamic load variation at four different speeds in the case of central contact; that is, the contact path located centrally between the toe and heel of the tooth.

Since there are 11 degrees of freedom in the system, 11 resonating frequencies of the system should exist. In the low-speed region where the excitation frequency from the change of stiffness is much lower than all resonating frequencies, the dynamic load response along the path of contact is somewhat like static load superimposed by an oscillatory load due to the system's resonating frequency.

When the speeds are near the resonance region (fig. 8), the dynamic load response becomes very severe (figs. 9 and 10). The maximum dynamic load is much higher than the static load, which is the

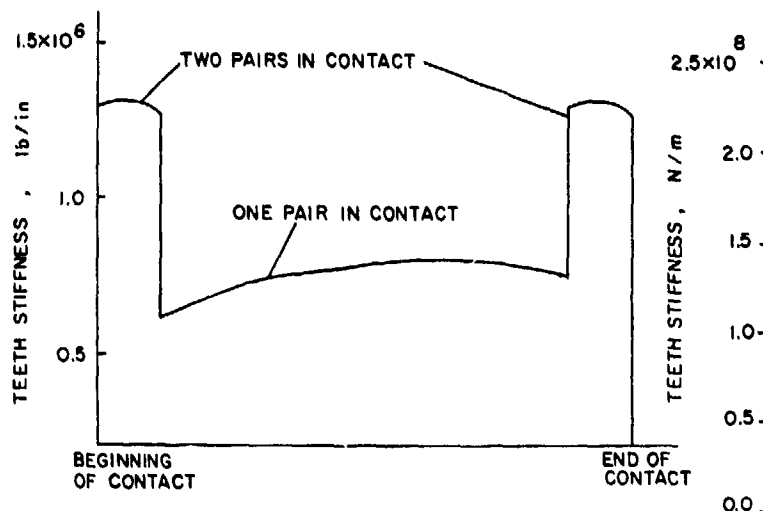


Figure 7. - Stiffness variation along contact path.

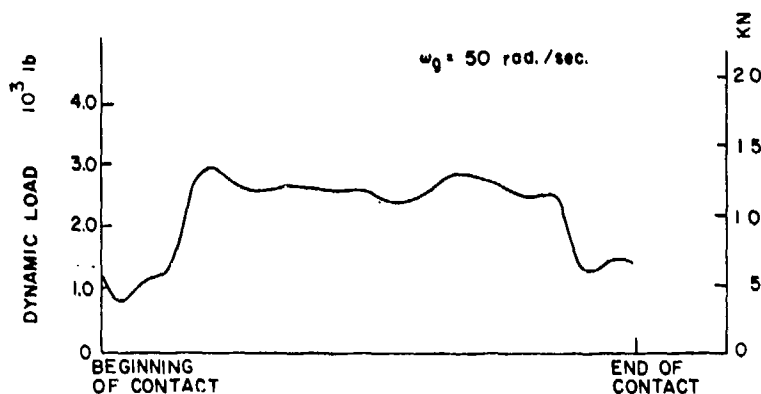


Figure 8. - Dynamic load variation along contact path. Central contact position, $\omega_g = 50$ rad/sec.

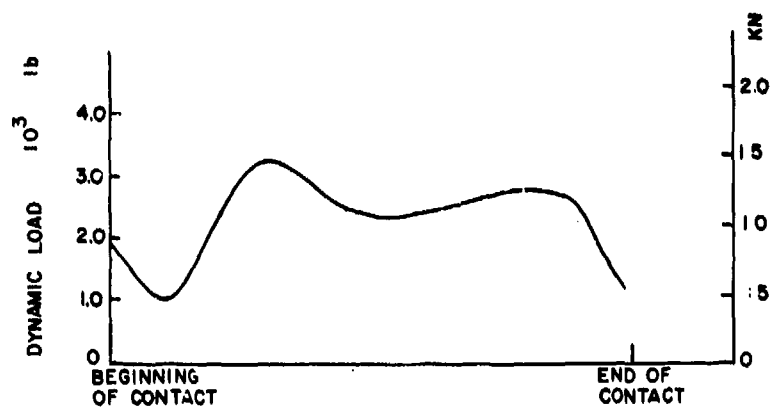


Figure 9. - Dynamic load variation along contact path. Central contact position, $\omega_g = 150$ rad/sec.

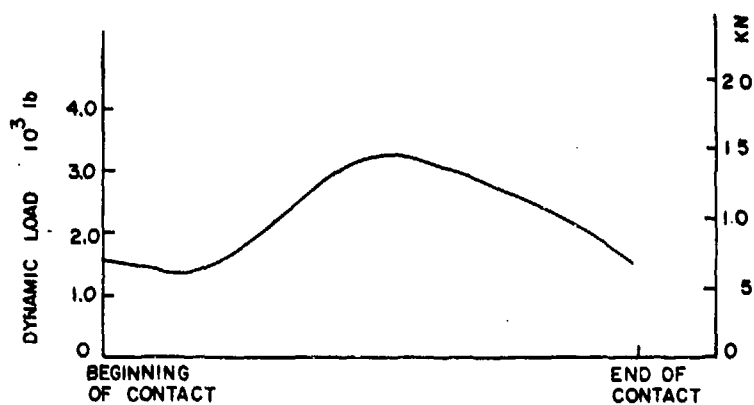


Figure 10. - Dynamic load variation along contact path. Central contact position, $\omega_g = 300$ rad/sec.

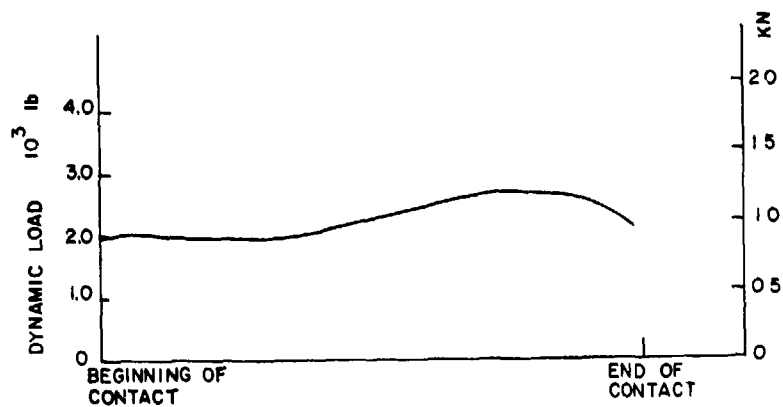


Figure 11. - Dynamic load variation along contact path. Central contact position, $\omega_g = 523$ rad/sec.

case when overloading occurs. Sometimes the oscillation of dynamic load will make meshing teeth separate when the load becomes negative and thus will generate noise and surface fatigue.

As the speed increases beyond the zone of resonating frequencies, the dynamic load becomes smoother along the contact path, and the value is less than the static load (if the contact ratio is greater than one). The variation of dynamic load at this region is out of phase with the change of the teeth stiffness (fig. 11).

Effect of Shaft Misalignment

When the assembly errors are introduced in the system, the contact bearing will shift to either end of the tooth surface (ref. 7). Figure 12 shows the typical paths of central contact, toe contact, and heel contact. Usually the central contact is desired because it can tolerate more possible running position errors and avoid edge contact. The dynamic load response of toe and heel contact is shown in figures 13 and 14. The change of the contact bearing from center to either edge will also change the contact ratio of the system because the tooth surface is not a perfect involute along the profile direction and is mismatched along the lengthwise direction. In the current example the contact ratio for the toe contact is 1.26, the central contact, 1.16, and the heel contact, 1.0. In this case, if the contact bearing is moved farther toward the heel region, there would be no tooth contacts between the time when the previous tooth finishes the contact and the current tooth goes into the contact zone (discontinuity in tooth mesh). This situation would cause very large impact force which would generate noise and severe damages to the tooth surface. The effect of the tooth contact ratio on dynamic response is shown later.

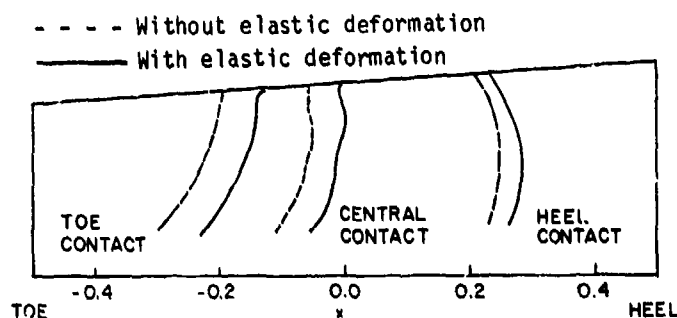


Figure 12. - Typical contact path for central, toe, and heel contact positions.

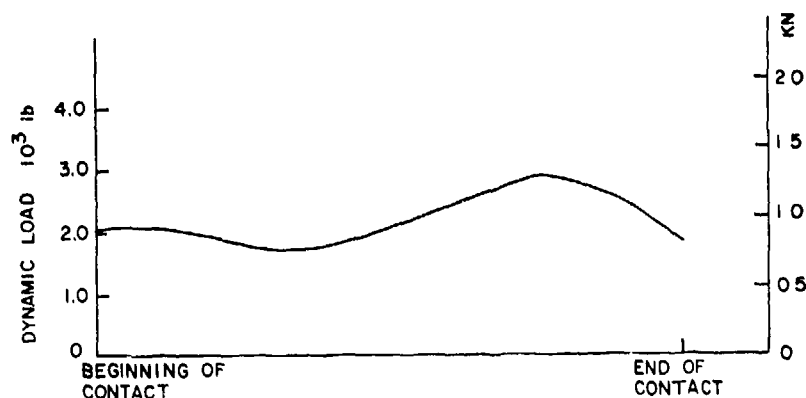


Figure 13. - Dynamic load variation along contact path. Toe contact position, $\omega_g = 523$ rad/sec.

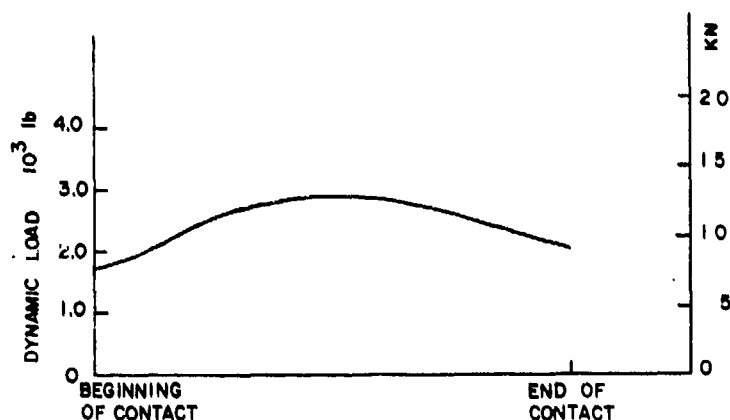


Figure 14. - Dynamic load variation along contact path. Heel contact position, $\omega_0 = 523$ rad/sec.

Contact Path Variation Due to Dynamic Response

In addition to showing the contact paths due to the assembly errors in the system in figure 12, the real contact path, not only due to the assembly errors but also to the running position errors induced by the dynamic responses, is plotted in the same figure. When this real contact path is compared with that caused by the assembly errors and running position errors induced by the average static elastic deformations, the deviation is found to be surprisingly small. One explanation of this small difference might be that the displacements changes due to the dynamic oscillation are small and that they do not produce a large change in contact path compared with those caused by the static displacements only. The closeness between these two contact paths suggests that one can use average static elastic deformation to calculate contact path, which can be used directly to solve for the dynamic load and lubrication problems without having to solve the dynamic load and contact path simultaneously using an iterative technique. The elimination of this iterative procedure greatly reduces the computation time.

Effect of Speed

Once the physical conditions of a gearset are determined, the dynamic response depends on the operating speed. For the system of 1 degree of freedom, such as spur gears, the maximum dynamic load occurs when the meshing frequency, which depends on the operating speed, is near the system natural frequency. Some peaks of dynamic load are caused by the varied meshing stiffness along the contact path, and they appear at meshing frequencies lower than the system natural frequency. The dynamic load factor, defined as the ratio of maximum dynamic load to the average static load, is plotted against the gear speed to illustrate the effect of speed in figure 15. Since there are 11 degrees of freedom in the spiral-bevel gear system, more peaks of dynamic load are expected.

The highest dynamic load appears to occur near the natural frequencies that correspond to the mode associated with a larger displacement in the motion along the line of action. The frequency marked \uparrow in figure 15 shows the system natural frequency causing a larger displacement in the motion along the line of action, and the one marked \downarrow shows the system natural frequency with a small displacement in that motion. It is clearly shown that the dynamic load factor at the frequency marked \uparrow has a peak response and that the response at the natural frequency marked \downarrow is not necessarily a peak.

Effect of Contact Ratio

The contact ratio is defined as the ratio of the duration for one tooth going through the whole contact zone to the duration of a periodic meshing cycle. It is believed that the load sharing characteristics caused by more than one tooth in contact will reduce the static load. The dynamic load factor due to the effect of contact ratio is shown in figure 16. It can be seen that the maximum

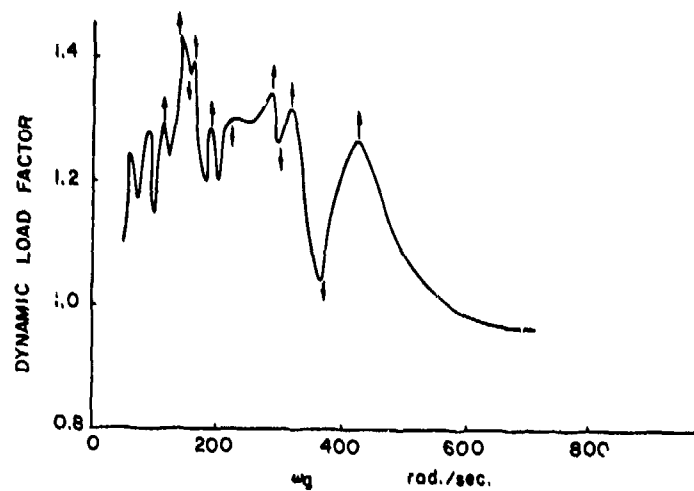


Figure 15. - Dynamic load factor versus gear speed. All damping coefficients, 2627 N*s/in (15 lb*s/in); contact ratio, 1.16.

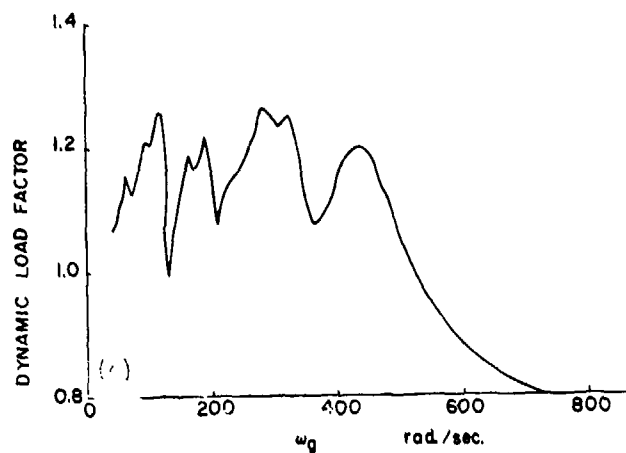
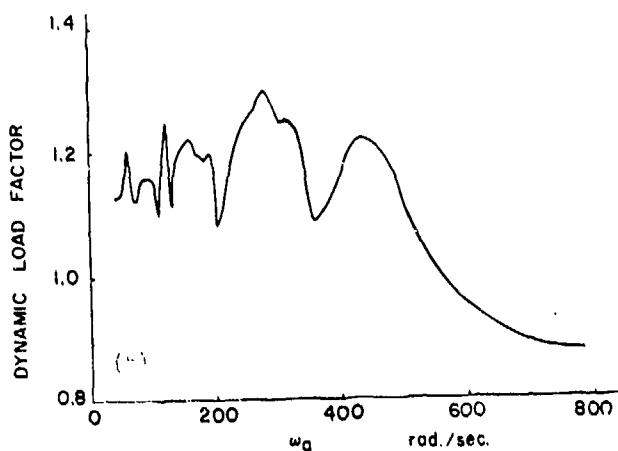
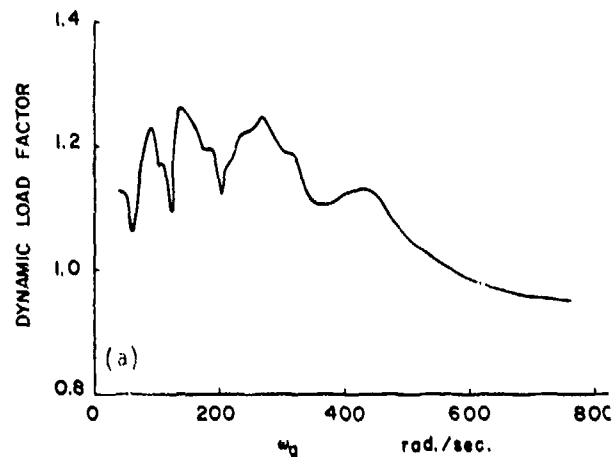


Figure 16. Dynamic load factor versus gear speed. All damping coefficients, 4378 N*s/in (25 lb*s/in). (a) Contact ratio, 1.16; (b) contact ratio, 1.35; (c) contact ratio, 1.72.

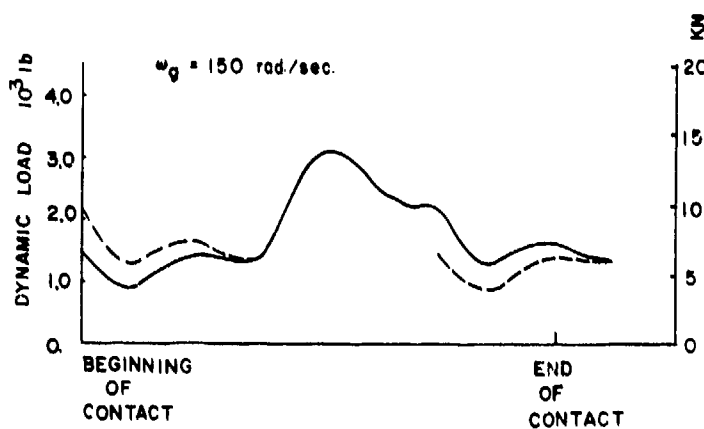


Figure 17. - Dynamic load variation along contact path. Damping coefficient, 4378 N·s/in (25 lb·s/in); contact ratio, 1.72.

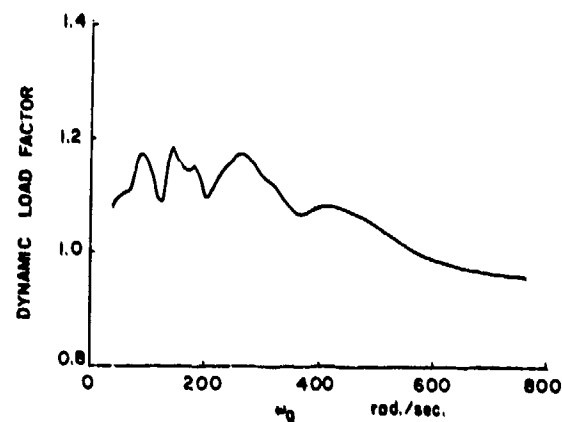


Figure 18. - Dynamic load factor versus gear speed. All damping coefficients, 6129 N·s/in (35 lb·s/in); contact ratio, 1.16.

dynamic load factor does not change much. However, the effect of contact ratio is significant in high-speed region, where the load is spread out averagely between meshing teeth path. A typical dynamic load variation with a high contact ratio along the contact path is shown in figure 17.

Effect of Damping

Since the damping forces are usually not known in the gear system, three arbitrary values are chosen for the damping coefficients: 2627, 4378, and 6129 N·sec/m (15, 25, and 35 lb·sec/m). These values are selected to give a range of nondimensional damping ratios corresponding to those commonly used in spur gears (0.1 to 0.2). The nondimensional damping ratios that correspond to the above three damping coefficients are 0.087, 0.14, and 0.203. The dynamic response for these damping cases can be observed from figures 15, 16(a), and 18. It is expected that the larger the damping force, the smaller the dynamic load factors will be in the resonance region. The large damping force will also level off the peak of dynamic load factor in the subresonance region, and there is no effect to the dynamic load factor due to damping force in the superresonance region.

Lubrication of Spiral-Bevel Gears

It is well accepted that the two major modes of gear failure, surface pitting and scuffing, are most strongly related to lubrication at the contact. Considerable gains in pitting life can be realized if the ratio of the lubricant film thickness to the surface roughness is increased. The knowledge of film thickness is believed to be essential for developing new analytical models for the prediction of surface durability for spur and helical, as well as spiral-bevel, gears. The variation of film thickness along the path of contact is mainly controlled by the local inlet lubricant viscosity, the local entrainment velocity, and the local contacting load. The local inlet lubricant viscosity, in turn, depends on the bulk surface temperature at the inlet of the contact. Since the bulk surface temperature is directly controlled by the sliding heat generated by the sliding tractive force which is, in turn, affected by the film thickness, the temperature and film thickness are mutually dependent and are solved simultaneously. The approach used in solving the simultaneous film thickness and bulk surface temperature is very similar to that used by Wang and Cheng (ref. 7) with the exception that the three-dimensional, spiral gear geometry necessitates the use of the point contact EHL theory for the film thickness and a three-dimensional, finite-element temperature code for the temperature influence coefficients, which are required for calculating the bulk surface temperature.

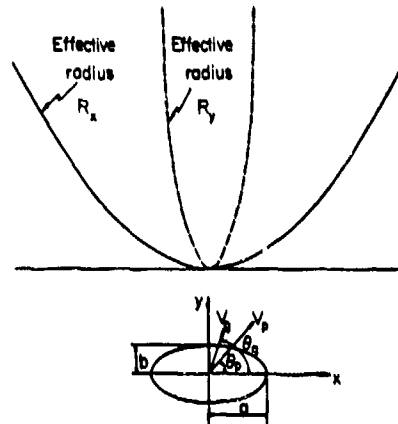


Figure 19. - Equivalent EHL point contact for spiral-bevel pinion and gear.

Lubricant Film Thickness

In determining the lubricant film thickness, the quasi-steady-state model is used, and the transient squeeze-film effect, which was included in a previous work for spur gears, is neglected in this film analysis for spiral-bevel gears. The neglecting of this squeeze-film effect is justified on the basis that it was shown by Wang and Cheng in spur gears to be a secondary effect.

The contact of a spiral-bevel gear and pinion set can be seen in figure 19, in which there is effectively a flat plane contact with a body, which is described by the difference of the neighboring surfaces between gear and pinion at contact point. This curved body has effective radii R_x and R_y along the principal axes, x and y , respectively. Under a load P , the surface near the flat plane will deform to an elliptical shape with semimajor axis a and semiminor axis b . The velocities of the pinion and gear at the contact point are V_p and V_g . The ellipticity parameter is defined as a/b . The minimum film thickness in the contact zone, following Hamrock and Dowson (ref. 8), can be related to Dowson-Higginson's line contact solution (ref. 9) by the equation

$$H_{\min} = H_{\min,l} (1.0 - 1.6 e^{-0.62 k}) \quad (10)$$

$$k = \frac{a}{b}$$

$$H_{\min} = \frac{h_{\min}}{R_x}$$

$$R_x = \frac{R_{x1} R_{x2}}{R_{x1} + R_{x2}}$$

$$u_{px} = V_p \cos \theta_p$$

$$u_{py} = V_p \sin \theta_p$$

$$u_{gx} = V_g \cos \theta_g$$

$$u_{gy} = V_g \sin \theta_g$$

$$u_x = \frac{U_{px} + U_{gx}}{2}$$

$$u_y = \frac{Y_{py} + U_{gy}}{2}$$

$$V = \sqrt{U_x^2 + U_y^2}$$

where

$H_{min,l}$ dimensionless film thickness of Dowson-Higginson solution

V_p, V_g velocity of pinion or gear tangent to contact plane

θ_p, θ_g angle between pinion or gear velocity and y axis

The dimensional $h_{min,l}$ can be expressed as

$$h_{min,l} = 1.6 \alpha^{0.6} (\eta_o V)^{0.7} E'^{0.03} \frac{R_x^{0.43}}{W^{0.13}} \quad (11)$$

where

α pressure viscosity coefficient

η_o viscosity taken at bulk surface temperature

W effective line contact load per unit length

$E' = [(1 - \nu_1^2)/2E_1 + (1 - \nu_2^2)/2E_2]^{-1}$

It is important to note that η_o , W , k , and V are variables along the contact path. The V depends on the gear kinematics; a and b depend on the gear geometry; and η_o depends strongly on the local bulk surface temperature which is, in turn, influenced by the local film thickness through the frictional heating. Thus, the film thickness and the bulk surface temperature are interdependent and are solved as a coupled system.

Bulk Temperature

Before the gear system starts to operate, all elements are in ambient temperature. Then the temperature builds up as gears are running, due to the frictional heat generation. After a sufficient period of running, the gears reach a steady-state temperature, that is, the heat flux flowing into the body equals that flowing out of the body. At each revolution the tooth is subject to the same heating condition. Since the time period of each contact point in the contact zone is only a very small fraction of the period of revolution, the local temperature jump (flash temperature) is completely damped out before it enters the contact zone at the next revolution. An average heat input over one revolution will be used to calculate the temperature rise of the body at the steady state.

The heat input is due to the heat generated at the instantaneous contact ellipse, and the amount depends on the load and the shear force of the lubricant. The heat flux flowing out of the body is due to the heat convection to surrounding air and lubricant. The relative importance of the heat-transfer coefficient at different surface areas was discussed by Patir and Cheng and Townsend and Akin (refs. 10 and 11) in spur gear systems. They also revealed the significant effect of lubrication method on temperature distribution. In this study, the oil-jet impingement depth is assumed to cover the whole area of contact side, which can be obtained by using a properly placed pressurized oil jet. The heat-transfer coefficients at other various areas are estimated to calculate the bulk temperature.

A three-dimensional, finite-element program is used to calculate the temperature coefficient. The mesh of the system includes gear shaft, gear body, and contact tooth with one adjacent tooth in both sides. The eight node element, which is used for the elastic deflection, is also used here for the bulk temperature. However, the boundary conditions are different. In the temperature analysis all surfaces are subject to heat convection with different heat-transfer coefficients.

The heat-transfer coefficient h_j is assigned to the contacting tooth face which is oil-jet cooled. The top land, bottom land, and another side of the tooth surface, which are not cooled by the oil jet,

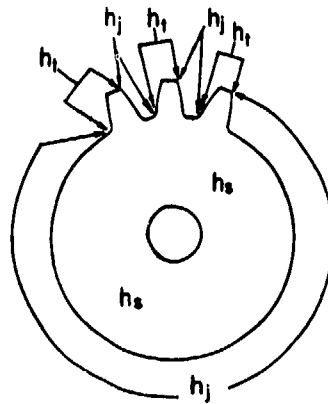


Figure 20. - Convective heat transfer coefficients for a three-tooth model for a spiral-bevel gear or pinion.

have a heat-transfer coefficient h_t for air or air/oil mist. Since only three teeth are made in the model, there is a surface region A (fig. 20) that covers the surfaces where the teeth are taken off and the bottom land which is in between these teeth. The heat-transfer coefficient at this region A is given a value h_j , which is the same as that of the coefficient for the surface cooled by the oil jet. The reason is that, because there is an oil-jet-cooled surface on each tooth, ~~and~~ most of the heat will flow out of the tooth from this surface ($h_j > h_t$). All the other convective surfaces of the gear system are given a coefficient h_s (fig. 20). The theoretically estimated values of h_s and h_j can be found in references 12 and 13. However, the estimated values of h_s , h_j , and h_t , based on the experimental results (ref. 11), are used in this study.

There are 30 nodes created in the contacting surface. A unit heat flux is applied to the grid node i . The temperature distribution in this surface due to the heat flux is T_{ji} , which is the temperature at the grid node j due to the heat flux at node i . By the interpolation method, the temperature at the contact point m , due to the unit heat flux at the contact point n (T_{mn}^c) can be obtained in terms of T_{ji} . Once the contact path is located and the heat flux flowing into each body at each contact point is calculated, the bulk temperature at the contact point m can be found as

$$T_{m,B} = \sum T_{mn}^c Q_n \quad n = 1, \dots, k_{\max}$$

where k_{\max} is the total number of contact points along the contact path.

The heat generation term Q_n is based on the recent traction models developed for EHL contacts by Johnson and Tevaarwerk (ref. 14), Bair and Winer (ref. 15), and Dyson (ref. 16). All three models are incorporated as subroutines in the bulk temperature calculation. Because there is a lack of the rheological constants for gear oils in the Johnson and Tevaarwerk's model and Bair and Winer's model, the limiting shear stress formula developed by Dyson for mineral oils in general is used first to obtain some preliminary results for the bulk temperature.

Flash Temperature

During meshing each tooth face experiences a sudden temperature increase (flash temperature) due to the frictional heat developed at the contact moving along the tooth face. This temperature rise is restricted in the instantaneous contact area and disappears very rapidly as soon as this instantaneous area of tooth face is out of contact. Usually, this temperature is very high and is a contributor to the gear scuffing failure.

The first successful prediction of flash temperature, introduced by Blok (ref. 17), is based on the heat-conduction analysis in a semi-infinite body with a uniformly distributed moving heat source. Jaeger (ref. 18) solved the problem of a moving source of heat with variable heat source and variable velocity. Archard introduced a simple harmonic mean to obtain the interface temperature. A refined

solution including a local heat partition coefficient between a pair of disks was derived by Cameron, et al. (ref. 19). More recently, Francis (ref. 20) made a further refinement in Blok's calculation by considering a variable heat flux in the contact.

Archard showed that when the Peclet number, vR/α , is greater than 10, the heat flow in the direction perpendicular to sliding may be neglected. The temperature distribution within a heat source of finite area can be determined by dividing the whole contact area into differential strips parallel to the sliding direction. And the temperature profile along each strip is the same as that of an infinitely long band source (in the perpendicular direction to sliding) of width equal to the strip length and has the same heat flux profile along the strip.

For the division of heat between the two contacting surfaces, an average heat partition factor is used throughout the entire contact region. The average heat partition factor is determined by a method suggested by Francis (ref. 20) for a thin film with heat generated at the midfilm. Once the average partition factor is known, the flash temperature within each strip is calculated by the method suggested by Cameron, et al., (ref. 19) assuming a uniform heat source within the strip. Details of this procedure are documented (ref. 2).

Results of Lubrication Performance

The same set of gears used for the dynamic load calculation are used here to demonstrate calculation of lubrication performance. Results were obtained for a range of operating conditions to determine the effect of speed, load, lubricant viscosity, and ambient temperature on the film thickness, bulk temperature, and flash temperature. A sample of results is presented here. More complete results can be found in reference 2.

The sliding velocity decreases from the beginning of the contact path where the gear tip contacts the pinion root, until the contact point is near the pitch point where the sliding velocity becomes zero. Then the sliding velocity increases all the way to the end of the contact path where the pinion tip contacts the gear root. The current set of gears has the feature that the sliding velocity at the end of the contact path is larger than that at the beginning of the contact path; this fact creates a situation that more heat is generated at the end of the contact path.

A typical distribution of bulk temperature along the contact position is shown in figure 21. The bulk temperature of the pinion is always larger than that of the gear because the pinion speed is three times faster than the gear speed and receives more heat per unit time than the gear does. Although the temperature coefficients are higher near the gear tip, the maximum bulk temperature of both gears occurs at the end of the single-tooth contact point where the maximum heat is generated. A distribution of the total flash temperature for the same case is plotted in figure 22. The minimum flash temperature occurs at the pitch point where the sliding velocity is zero. For this high-speed case the variation of dynamic load is less pronounced along the contact path. The rise of flash temperature on both sides of the pitch corresponds directly to the variation of sliding speed at the contact. The slight decrease at the end of the contact path is attributable to the decrease in dynamic load in this region.

Figure 23 shows the distributions of film thickness for four different gear speeds. No excessive variations are seen along the contacting path. A moderate peak is evident at the pitch point for the high-speed cases, and this is associated with the slight drop of bulk temperature at the pitch point. The steady rise of film thickness along the contact path is due to the increase in the entrainment velocity. The final uptrend of film thickness near the end of contact is again due to the decrease in bulk temperature.

Finally, the effect of increase in ambient viscosity on the minimum film thickness, h_{\min} , maximum bulk temperature as well as total flash temperature is demonstrated in figure 24. As expected, an increase in viscosity would improve lubrication performance with a much thicker film thickness and a slight drop in both bulk and flash temperature.

Concluding Remarks

↘ A computer solution to the dynamic load in a pair of spiral-bevel gearsets was developed by

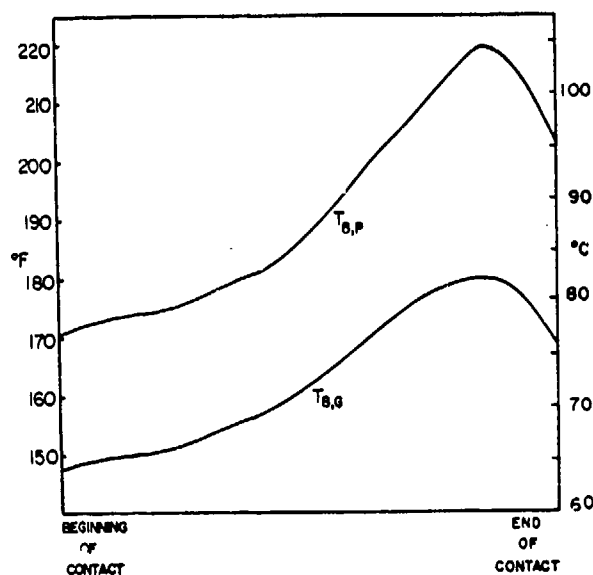


Figure 21. - Typical bulk temperature distribution for pinion and gear. Contact position, ω_g , 523 rad/sec.

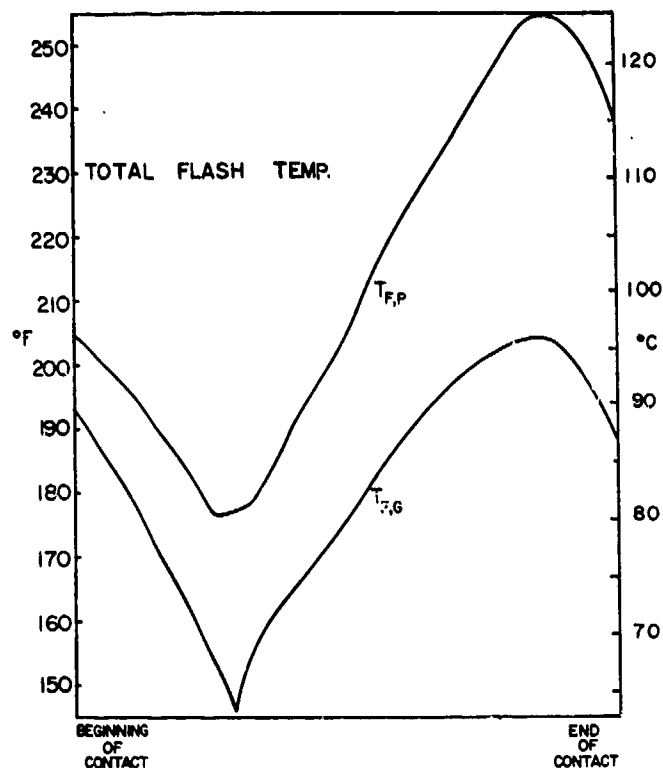


Figure 22. - Typical total flash temperature distribution for pinion and gear. Contact position, ω_g , 523 rad/sec.

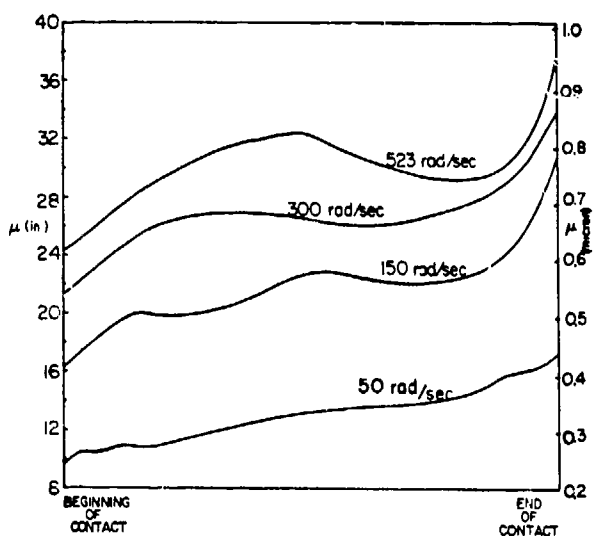


Figure 23. - Film thickness distributions.

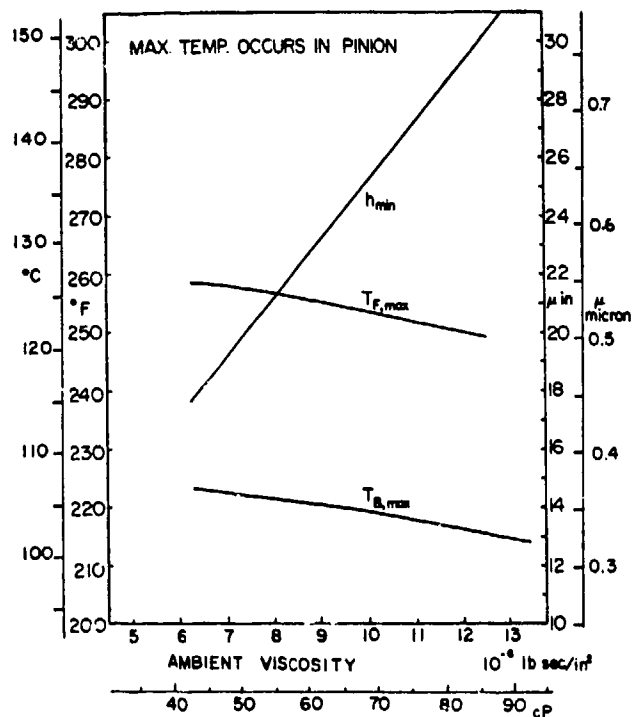


Figure 24. - Effect of lubricant viscosity on lubrication performance.

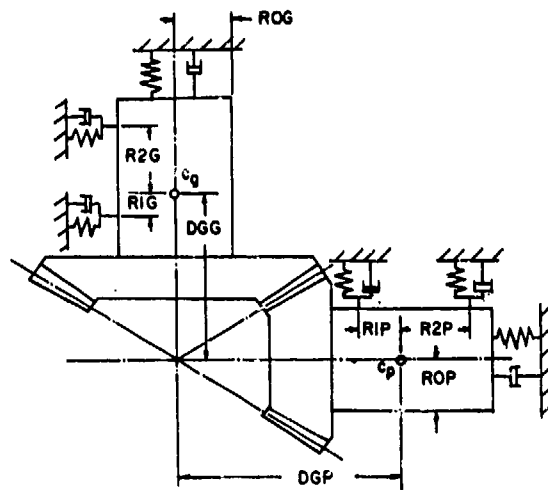


Figure 25. - Labels for distances between pinion and gear, mass centers to bearing supports.

solving the equations of motion for the pinion and gear shaft. An existing finite-element code was used to calculate the combined stiffness of the contacting pinion and gear teeth as a function of contacting position in the zone of action. In addition to the dynamic load analysis, a computer solution was also developed to predict the bulk surface temperature, the flash temperature, and the film thickness along the contact path. An existing finite-element heat code was also used to calculate the temperature influence coefficients from which the bulk surface temperature is calculated. Both the lubricant film thickness and the sliding traction are calculated from the recent findings in EHL theories.

Results were obtained for a set of experimental spiral-bevel gear currently being tested at the NASA Lewis Research Center. The results of dynamic load tests show that there exist numerous peaks in the variation of dynamic load against the gear shaft speed. These fluctuations correspond reasonably well with the critical frequencies of the system. The envelope of the peaks suggests that the highest dynamic load occurs somewhere near the critical frequency corresponding to the rotational mode oscillations of the two gears.

Results of the film thickness show that its variation along the contact path is not large and that it is caused mainly by the increase in the entrainment velocity and the change in bulk surface temperature. The total flash temperature variation is controlled by the sliding velocity and has its maximum near the end of the contact path where the transition from double to single mesh occurs. Effects of operating variables on the minimum film thickness and maximum surface temperatures along the contact path can also be obtained readily with this program. Results for the effect of ambient viscosity show trends consistent with those anticipated from existing EHL theories.

References

1. Goldstein, H.: Classical Mechanics. Addison-Wesley, 1960.
2. Chao, H. C.; and Cheng, H. S.: Dynamic Load, Lubricant Film Thickness, and Surface Temperatures in Spiral Bevel Gears. To appear as a NASA Contract Report.
3. Chao, H. C.: Tooth Profile and Contact Pattern of Spiral-Bevel Gears. M.S. Thesis, Northwestern University, Sept. 1979.
4. Wang, K. L.: Thermal Elastohydrodynamic Lubrication of Spur Gears. Ph.D. Dissertation, Northwestern University, Apr. 1976.
5. Wallace, D. W.; and Seireg, A.: Computer Solution of Dynamic Stress, Deformation and Fracture of Gear Teeth. J. Eng. Ind., Nov. 1973.
6. Wang, K. L.; and Cheng, H. S.: A Numerical Solution to the Dynamic Load, Film Thickness, and Surface Temperatures in Spur Gears. Part I—Analysis. J. Mech. Des., vol. 103, Jan. 1981, pp. 177-187.
7. Wang, K. L.; and Cheng, H. S.: A Numerical Solution to the Dynamic Load, Film Thickness, and Surface Temperatures in Spur Gears. Part II—Results. J. Mech. Des., vol. 103, Jan. 1981, pp. 188-194.

8. Hamrock, B. J.; and Dowson, D.: Isothermal Elastohydrodynamic Lubrication of Point Contact, Part II. J. Lubr. Technol., July, 1976.
9. Dowson, D.; and Higginson, G. R.: Elastohydrodynamic Lubrication. Pergamon Press, Ltd., 1966.
10. Patir, N.: Estimate of the Bulk Temperature in Spur Gears Based on Finite Element Temperature Analysis. M.S. Thesis, Northwestern University, Aug. 1976.
11. Townsend, D. P.; and Akin, L. S.: Analytical and Experimental Spur Gear Tooth Temperature as Affected by Operating Variables. J. Mech. Des., Jan. 1981, pp. 219-226.
12. DeWinter, A.; and Blok, H.: Fling-off Cooling of Gear Teeth, J Eng. Ind. vol. 96, no. 1, 1974.
13. Van Heijningen, G. J. J.; and Blok, H.: Continuous As Against Intermittent Fling-off Cooling of Gear Teeth. J. Lubr. Technol., vol. 96, no. 4, 1974.
14. Johnson, K. L.; and Tevaarwerk, J. L.: Shear Behavior of EHD Oil Film. Proc. Roy. Soc. (London), Ser. A, vol. 356, 1977.
15. Bair, S.; and Winer, W. O.: Shear Strength Measurements of Lubricant at High Pressure. J. Lubr. Technol., vol. 101, 1979.
16. Dyson, A.: Friction Traction and Lubrication Rheology in EHD Lubrication. Philos. Trans. Roy. Soc. (London), ser. A., vol. 266, 1970.
17. Blok, H.: Theoretical Study of Temperature Rise at Surfaces of Actual Contact Under Oiliness Lubricating Conditions. Proc. Inst. Mech. Engrs., Pt. 2, 1973.
18. Jaeger, J. C.: Moving Sources of Heat and Temperature at Sliding Contact. Proc. Roy. Soc. N.S.W. 76, 1942.
19. Cameron, A.; Gordon, A. N.; and Symm, G. T.: Contact Temperature in Rolling and Sliding Surfaces. Proc. Roy. Soc., A286, 1955.
20. Francis, H. A.: Interfacial Temperature Distribution Within a Sliding Hertzian Contact. Trans. ASLE, vol. 14, 1970.

Comparison of Spur Gear Efficiency Prediction Methods

Neil E. Anderson* and Stuart H. Loewenthal†

The prediction of spur-gear efficiency has been the subject of several investigations in the last 20 years (refs. 1 to 5). The methods proposed are necessarily approximate because of the difficulty in modelling the gear mesh and its associated losses. Efficiency prediction techniques to date have either utilized a friction coefficient deduced from gear power-loss measurements or adapted disk machine data to simulate the gear contact conditions. When using disk machine data, either an integration (averaging) technique or selection of a representative operating point along the path of contact must be accomplished to accurately model the actual gear mesh. The instantaneous values of power loss along the path of contact provided by the disk machine data must be converted into an average power loss for the entire mesh.

The five methods, Anderson and Loewenthal (ref. 1), Buckingham (ref. 2), Chiu (ref. 3), Merritt (ref. 4) and Shipley (ref. 5), use various approaches to spur gear efficiency. The major differences among these methods are the friction coefficient used for sliding power loss and the number of additional terms included to account for sources of power loss other than sliding. In reference 6 Martin provides a summary of the many friction coefficients available in the literature and the lubrication conditions under which they apply. Each of the five efficiency prediction methods (refs. 1 to 5) uses a different friction coefficient expression.

Of the five methods only Anderson and Loewenthal and Chiu include an additional expression for rolling or pumping power loss. This is the additional power required to form the elastohydrodynamic (EHD) oil film that separates the gear teeth during engagement. Rolling loss was shown to be significant, particularly at higher operating speeds, in reference 1. This loss combines with windage losses to form the tare, or no-load, loss of a gearset. Expressions for windage loss were given only by Anderson and Loewenthal and Shipley. Bearing losses were also found to be a significant portion of the total gearset loss in reference 1, where an approximate ball-bearing loss expression was used (ref. 11). Only gear losses will be considered in the present work, however.

Three sources of spur-gear power-loss data were located to allow comparison of the five theories with actual measurements (refs. 7 to 9). These data include pitch-line velocities from 1 to 20 m/sec (200 to 4000 ft/min) and K-factor (ref. 10) loading conditions from 17 to 1600. The data selected for comparison purposes were limited to jet-lubricated and ground gears.

It is the objective of this paper to compare the accuracy of the five gear efficiency methods in references 1 to 5 using three sources of test data (refs. 7 to 9) over a wide range of operating conditions.

Symbols

CR	contact ratio
C_1 to C_{14}	constants of proportionality; see table I
D	pitch circle diameter, m (in.)
E	modulus of elasticity, N/m ² (lbf/in ²)
E'	equivalent modulus of elasticity, $2/[(1 - \gamma_g^2/E_g) + (1 - \gamma_p^2/E_p)]$, Pa (lbf/in ²)
F	face width of tooth, m (in.)
f	coefficient of friction
H_S	specific sliding at start of approach action
H_T	specific sliding at end of recess action

*Propulsion Laboratory, U.S. Army Research and Technology Laboratories (AVRADCOM), NASA Lewis Research Center.

†NASA Lewis Research Center.

h	length of path of approach, m (in.)
\bar{h}	isothermal central film thickness, m (in.)
K	gear capacity factor (ref. 10)
l_T	length of path of contact, m (in.)
m_g	gear ratio, N_g/N_p
N	number of gear teeth
n	rotational speed, rpm
P	power loss
ϕ	diametral pitch
R	pitch circle radius or radius in general, m (in.)
R_{eq}	equivalent rolling radius, m (in.)
s	length of path of approach, m (in.)
T	pinion torque, N-m (in-lbf)
\bar{V}	velocity, m/sec (ft/min)
\bar{V}_S	average sliding velocity, $V_g - V_p$, m/sec (in/sec)
\bar{V}_T	average rolling velocity, $V_g + V_p$, m/sec (in/sec)
W	average gear contact, normal load, N (lbf)
W_n	gear contact, normal load, N (lbf)
x	coordinate along path of contact, m (in.)
β_a	arc of approach, rad
β_r	arc of recess, rad
θ	gear tooth pressure angle, deg
μ, η	lubricant absolute viscosity, 10^{-3} N sec/m ² (lbf sec/in ²)
ν	lubricant kinematic viscosity, 10 ² cm ² /sec (ft ² /sec)
ρ	equivalent rolling radius as defined in ref. 3, m (in.)
σ	surface roughness, μ m, (μ in)

Subscripts:

a	approach
B	Buckingham
b	base
e	entraining
g	gear
M	Merritt
P	pitch line
p	pinion
R	rolling
r	recess
S	sliding
t	tip
W	windage

Spur Gear Efficiency Theories

Five spur-gear efficiency prediction methods were used to predict the efficiency of three gear geometries from the three experimental studies (refs. 7 to 9). Selected for comparison were the methods of Anderson and Loewenthal (ref. 1), Buckingham (ref. 2), Chiu (ref. 3), Merritt (ref. 4), and Shipley (ref. 5).

All of the methods are similar in that each considers gear-tooth sliding losses through the use of a friction coefficient. The methods differ in the choice of the friction coefficient, the form of the

efficiency equation, and the number of additional terms included to account for gear pumping and windage power loss. Only the methods of Anderson and Loewenthal and Chiu include terms for rolling traction or pumping loss, while windage loss expressions are only given by Anderson and Loewenthal and Shipley.

Method of Anderson and Loewenthal

The method of Anderson and Loewenthal considers three components of gear power loss: sliding, rolling, and windage. In reference 1 the sliding and rolling losses were calculated by numerically integrating the instantaneous values of these losses over the path of contact. The friction coefficient used to calculate sliding loss was based on disk machine data generated by Benedict and Kelley (ref. 12). This friction coefficient expression is considered to be applicable to gear sliding loss calculations in the EHD lubrication regime where some asperity contact occurs, that is, for λ ratios less than 2 (λ = ratio of minimum EHD film thickness to composite surface roughness). In reference 1 rolling losses were based on disk machine data generated by Crook (ref. 13). Crook found that the rolling loss was simply a constant value multiplied by the EHD central film thickness. Gear tooth film thickness was calculated by the method of Hamrock (ref. 14) and adjusted for thermal effects using Cheng's thermal reduction factor (ref. 15). At high pitch-line velocities the isothermal equations, such as Hamrock's, will predict an abnormally high film thickness since inlet shear heating of the lubricant is not considered. Cheng's thermal reduction factor will account for the inlet shear heating and reduce the film thickness accordingly. Inlet starvation effects at high speeds were not considered, however.

In reference 16 a simplified version of this analysis was developed to study the sensitivity of gear power loss to changes in tooth geometry and operating variables. It was found to agree with the numerically integrated solution to within 0.1 percentage point of efficiency except at combinations of light load and high speed. Under these conditions the EHD thermal reduction factor, which was omitted for simplicity, is needed to properly predict the rolling losses. The simplified version will be used for comparison with the other theories herein.

In reference 16 the sliding and rolling loss equations were

Sliding loss,

$$\bar{P}_S = C_1 f \bar{W} \bar{V}_S \quad (1)$$

Rolling loss,

$$\bar{P}_R = C_2 \bar{h} \bar{V}_T F C R \quad (2)$$

where f , \bar{V}_S , \bar{h} , and \bar{V}_T are evaluated at a point halfway between the pitch point and the start of engagement along the path of contact. The constants C_1 to C_{14} can be found in table 1.

Pinion and gear windage expressions were given as

$$P_{W,p} = C_3 \left(1 + 2.3 \frac{F}{R_p} \right) n_p^{2.8} R_p^{4.6} (0.028 \mu + C_4)^{0.2} \quad (3)$$

$$P_{W,g} = C_3 \left(1 + 2.3 \frac{F}{R_g} \right) \left(\frac{n_p}{m_g} \right)^{2.8} R_g^{4.6} (0.028 \mu + C_4)^{0.2} \quad (4)$$

The required supporting equations are as follows:

Length of path of contact,

$$l_T = 0.5 \left\{ \left[\left(D_p + \frac{2}{C_5 \phi} \right)^2 - (D_p \cos \theta)^2 \right]^{1/2} + \left[\left(D_g + \frac{2}{C_5 \phi} \right)^2 - (D_g \cos \theta)^2 \right]^{1/2} - (D_p + D_g) \sin \theta \right\} \quad (5)$$

TABLE I. - CONSTANTS USED IN GEAR POWER LOSS EQUATIONS

Constant	Value for SI unit	Value for U.S. customary unit
C ₁	2x10 ⁻³	3.03x10 ⁻⁴
C ₂	9x10 ⁴	1.970
C ₃	2.82x10 ⁻⁷	4.05x10 ⁻¹³
C ₄	0.019	2.86x10 ⁻⁹
C ₅	39.37	1.0
C ₆	29.66	45.94
C ₇	2.05x10 ⁻⁷	4.34x10 ⁻³
C ₈	196.9	1.0
C ₉	1x10 ⁻³	1.515x10 ⁻⁴
C ₁₀	1.54x10 ⁻⁵	5.738x10 ⁻⁶
C ₁₁	1.0	0.0254
C ₁₂	1.43x10 ⁻³	1.383x10 ⁻⁵
C ₁₃	0.0114	0.180
C ₁₄	9.226x10 ⁸	1.0

Average sliding velocity,

$$\bar{V}_S = 0.262 n_p \frac{1 + m_g}{m_g} l_T \quad (6)$$

Average rolling velocity,

$$\bar{V}_T = 0.1047 n_p \left[D_p \sin \theta - \frac{l_T}{4} \left(\frac{m_g - 1}{m_g} \right) \right] \quad (7)$$

Average normal load,

$$\bar{W} = \frac{T_p}{D_p \cos \theta} \quad (8)$$

Friction coefficient from Benedict and Kelley (ref. 12),

$$f = 0.0127 \log \left(\frac{C_6 \bar{W}}{F \mu \bar{V}_S \bar{V}_T} \right) \quad (9)$$

(where f is limited to a minimum of 0.01 and a maximum of 0.2).

Equivalent contact radius,

$$R_{eq} = \frac{\left[D_p (\sin \theta) + \frac{l_T}{2} \right] \left[D_g (\sin \theta) - \frac{l_T}{2} \right]}{2(D_p + D_g) \sin \theta} \quad (10)$$

Central EHD film thickness,

$$h = C_7 (\bar{V}_T \mu)^{0.67} \bar{W}^{(-0.067)} R_{eq}^{0.464} \quad (11)$$

Contact ratio,

$$CR = \frac{C_5 I_T \phi}{\pi \cos \theta} \quad (12)$$

Method of Buckingham

In reference 2 Buckingham developed a gear efficiency expression based solely on sliding friction loss. Noting that the coefficient of friction changes along the path of contact, he set forth a final expression that was an average coefficient of friction during the arc of approach β_a and another average value during the arc of recess β_r :

$$\text{Efficiency} = 1 - \left[\frac{1 + (1/m_g)}{\beta_a + \beta_r} \right] \left(\frac{f_a}{2} \beta_a^2 + \frac{f_r}{2} \beta_r^2 \right) \quad (13)$$

where

$$\beta_a = \frac{(R_{tg}^2 - R_{bg}^2)^{1/2} - R_g \sin \theta}{R_{bp}} \quad (14)$$

and

$$\beta_r = \frac{(R_{tp}^2 - R_{bp}^2)^{1/2} - R_p \sin \theta}{R_{bp}} \quad (15)$$

Since the present comparison is considering only hardened steel gears, the average coefficients of friction during approach and recess were taken to be equal as described in reference 2.

$$f_a = f_r = \frac{2}{3} f \quad (16)$$

where

$$f = \frac{0.05}{e^{(C_8 0.125 V_{SB})}} + 0.002 (C_8 V_{SB})^{1/2} \quad (17)$$

and

$$V_{SB} = \frac{V_P}{2} \left(1 + \frac{N_p}{N_g} \right) \beta_r \cos \theta \quad (18)$$

This friction coefficient was derived from several sets of data, including reference 17 by Buckingham, by solving equation (13) for f and introducing measured data. Because neither equation (13) nor (17) is a function of load, the predicted efficiencies are independent of load.

Method of Chiu

The method of Chiu (ref. 3), like that of Anderson and Loewenthal, used a numerical integration of instantaneous values of sliding and rolling loss to obtain an average loss across the path of contact. However, windage losses were not included.

$$\text{Power loss} = P_S + P_R \quad (19)$$

where P_S and P_R are sliding and rolling losses:

$$P_S = C_9 \frac{W_n}{(h+s)} \int_{-s}^h V_S f dx \quad (20)$$

$$P_S = C_{10}(C_{11}\sigma + 0.55)W_n V^{1/2} \rho^{-1/2} \mu^{-1/8} I_1 \quad (21)$$

$$P_R = \frac{C_{12} \mu^{0.71} (E')^{0.29} F}{(h+s)} \int_{-s}^h V_e^{1.71} \rho^{0.29} dx \quad (22)$$

$$P_R = C_{12} \sin^2 \theta V_P \left(\frac{\mu V_P}{E' \rho} \right)^{0.71} E' \rho F I_2 \quad (23)$$

The constants I_1 and I_2 can be found in graphical form in reference 3 or they can be evaluated by integration. Values for I_1 and I_2 were taken from the graphical data for the present comparison.

The friction coefficient used by Chiu was that of O'Donoghue and Cameron (ref. 18). Friction coefficients predicted by this method are substantially greater than those predicted by Benedict and Kelley (ref. 12). The rolling loss expression used by Chiu was based on work done by Dowson and Higginson (ref. 19).

Method of Merritt

In reference 4 Merritt provides a simple expression for the calculation of spur gear efficiency:

$$\text{Percent loss} = \frac{f}{2} \pi \left(\frac{1}{N_p} + \frac{1}{N_g} \right) 100 \quad (24)$$

where

$$f = C_{13} \left(\frac{1.6}{\nu^{0.15} V_e^{0.15} V_{SM}^{0.35} R_M^{0.5}} \right) \quad (25)$$

and where

$$V_e = 2 V_P \sin \theta \quad (26)$$

$$V_{SM} = V_P \left[\frac{\pi}{2} \cos \theta \left(\frac{1}{N_p} + \frac{1}{N_g} \right) \right] \quad (27)$$

$$R_M = \frac{D_p D_g}{(D_p + D_g)} \frac{\sin \theta}{2} \quad (28)$$

This equation was derived from more complete equations for instantaneous loss similar to those used by Anderson and Loewenthal and Chiu. Merritt made several assumptions to reduce the general equations to the simplified form given above: (1) power loss is evaluated at a point whose distance from the pitch point is equal to 1/4th the base pitch along the path of contact, (2) the diametral pitch equals 1, (3) the contact ratio equals 1.5, and (4) the tooth loading diagram is trapezoidal. The friction coefficient is based on the Benedict and Kelley expression and others. Merritt realized that his gear loss expression was approximate and suggested that this analysis might serve as a starting point for further investigation.

Method of Shipley

Shipley's method appears in references 5 and 20. The method used here is that published in reference 5 since it is more recent and more complete. (It should be noted that there are several differences in these two works). This method considers both sliding and windage losses but not rolling loss:

$$\text{Percent sliding loss} = \frac{50 f}{\cos \theta} \frac{(H_S^2 + H_T^2)}{(H_S + H_T)} \quad (29)$$

where H_S is the specific sliding at the start of approach action, such that

$$H_S = (m_g + 1) \left\{ \left[\left(\frac{P_1}{K_g} \right)^2 - \cos^2 \theta \right]^{1/2} - \sin \theta \right\} \quad (30)$$

where H_T is the specific sliding at the end of recess action, such that

$$H_T = \frac{m_g + 1}{m_g} \left\{ \left[\left(\frac{R_{1p}}{R_p} \right)^2 - \cos^2 \theta \right]^{1/2} - \sin \theta \right\} \quad (31)$$

and where

$$\text{Windage loss} = \frac{C_{14} n_3 D^5 F^{0.7}}{100 \times 10^{15}} \quad (32)$$

In Shipley's method (ref. 5) the friction coefficient is given in graphical form as a function of "K-factor" (a nondimensional loading term, ref. 10), pitch-line velocity, and type of oil (light or medium weight). The K-factor gives an indication of gearset loading and thus adds the effect of load to the power-loss calculation. Limitations placed by Shipley on the windage equation are that gear diameters are to be less than 0.51 m (20 in.) and that gear width to diameter ratios are approximately equal to 0.5.

Gear Power-Loss Data

Although there is a scarcity of published gear power loss data, three sources were located for comparison with the predictions from the five methods described earlier. In reference 7 Fletcher and Bamborough used a power recirculating test rig (four-square rig) to determine the effects of oil-jet location, lubricant flow rate, lubricant viscosity, and gear face width on gear power loss. Care was taken to accurately calibrate the 28-kW (37.5-hp) dynamometer to ± 0.07 N-m (± 0.6 in-lbf) (ref. 21). The gear geometry and operating conditions used in these tests are shown in table II. The data presented here are for a lubricant flow rate of 1.9 to 11.4 l/min (0.5 to 3.0 gal/min) with the supply jet located at the into mesh locations.

Ohlendorf (ref. 9) also used a recirculating power test rig to generate spur gear power loss data. Ohlendorf conducted an extensive test program on the effects of type of lubricant, lubrication method, gear fabrication method, tooth shape, and operating conditions on the power loss of spur gears. The data presented here are only for one of Ohlendorf's many test conditions—a jet lubricated gearset with geometry and operating conditions as described in table II.

Yada, in references 8 and 22, took a different approach to the measurement of gear power loss. He submerged his test gears in oil. By comparing the time-temperature characteristics of the oil surrounding the loaded gearset with that of the same gearset rotating in an unloaded condition but with a known amount of electrical power heating the oil, the gear-mesh power losses were deduced with high accuracy, according to Yada (ref. 22). This method automatically calibrates out any windage loss since the temperature rise in the oil is due only to losses in the gear mesh. In addition to speed and torque, Yada also investigated the effects of various fabrication techniques. The data used for comparison here include gears that were ground by Niles, Reishauer, and Maag machines.

Discussion of Results

In figures 1 to 3 the power-loss predictions of Anderson and Loewenthal, Buckingham, Chiu, Merritt, and Shipley are compared with three sets of test data. Power loss is shown as a function of pinion torque at constant speed. It is apparent that, although these methods vary widely in the prediction of power loss, some give consistently good agreement with the three sets of data.

TABLE II. - TEST GEAR DATA AND OPERATING CONDITIONS

	Fletcher and Bamborough (ref. 7)	Yada (ref. 8)	Ohlendorf (ref. 9)
Pinion diameter, m (in.)	0.152 (6)	0.076 (3)	0.089 (3.5)
Ratio	1.67	1.07	1.0
Face width to diameter ratio	0.26	0.06	0.23
Diametral pitch	8	5	5.6
Pressure angle, deg	20	20	20
Oil viscosity, cP	54	32	39
K-factor range	17 - 137	400 - 1600	30 - 449
Pitch line velocity range, m/sec (ft/min)	2.0 - 15.2 (400 - 3000)	1.5 - 8.1 (300 - 1600)	1.0 - 20.3 (200 - 4000)

Fletcher and Bamborough Data

In figure 1 a comparison is made with the Fletcher and Bamborough data. The data shown are for into mesh lubrication at 1.9- to 11.4-l/min (0.5- to 3.0-gal/min) flow rate. At the lowest speed most methods tend to overestimate the power loss, but as speed increases most tend to underestimate the losses. The method of Chiu consistently overestimates the losses not only for the gearset of Fletcher and Bamborough but also for the gears of Yada and Ohlendorf as will be shown. This is due to the use of the O'Donoghue and Cameron friction coefficient which predicts abnormally high values.

In figures 1(b) and (c) a significant distinction can be made among these methods. Only the methods of Anderson and Loewenthal and Chiu predict a tare or no-load power loss as suggested by the data. The methods of Merritt, Buckingham, and Shipley cannot predict this tare loss since all three use only a friction coefficient term to predict the power loss (Shipley does not predict any windage loss at these speeds). Since the power loss is proportional to transmitted load, at zero load the power loss must also equal zero. Overall, the method of Anderson and Loewenthal provides the best estimates of power loss for this gearset.

Yada Data

In figure 2 the five methods are compared with the data of Yada. The three data points at each torque represent three manufacturing methods. None of the prediction methods are sufficiently refined to include surface finish effects. Both the Anderson and Loewenthal and Shipley methods provide good agreement with the data. Again Chiu's predictions are greater than the others. Although the methods of Merritt and Buckingham show good agreement, at times, these methods do not consistently follow the data.

In these data no tare loss was measured or predicted by the methods of Anderson and Loewenthal or Chiu. This is thought to be due to the narrowness of the gear, which reduces the rolling loss and also to the lower pitch-line velocities, which minimize the windage loss.

The torque range of these test data shows a span in K-factor of 400 to 1600. This variation in K-factor represents a moderate to a heavy load situation (ref. 10) and thus is a good test of the load dependence of these prediction methods.

Ohlendorf Data

The five methods are compared with the data of Ohlendorf in figure 3. The range in pitch-line velocity shown is from 1 to 20 m/sec (200 to 4000 ft/min). Again, the methods of Anderson and Loewenthal and Shipley show the best agreement with the data over the range shown. Buckingham's prediction is fair at the lower speeds but is very poor at 4211 rpm. Merritt's prediction is unsatisfactory at all speeds.

The Ohlendorf data show a rather small tare loss for the pitch-line velocity and gear width that was used. Both Anderson and Loewenthal and Chiu predict higher tare losses than that indicated by the data.

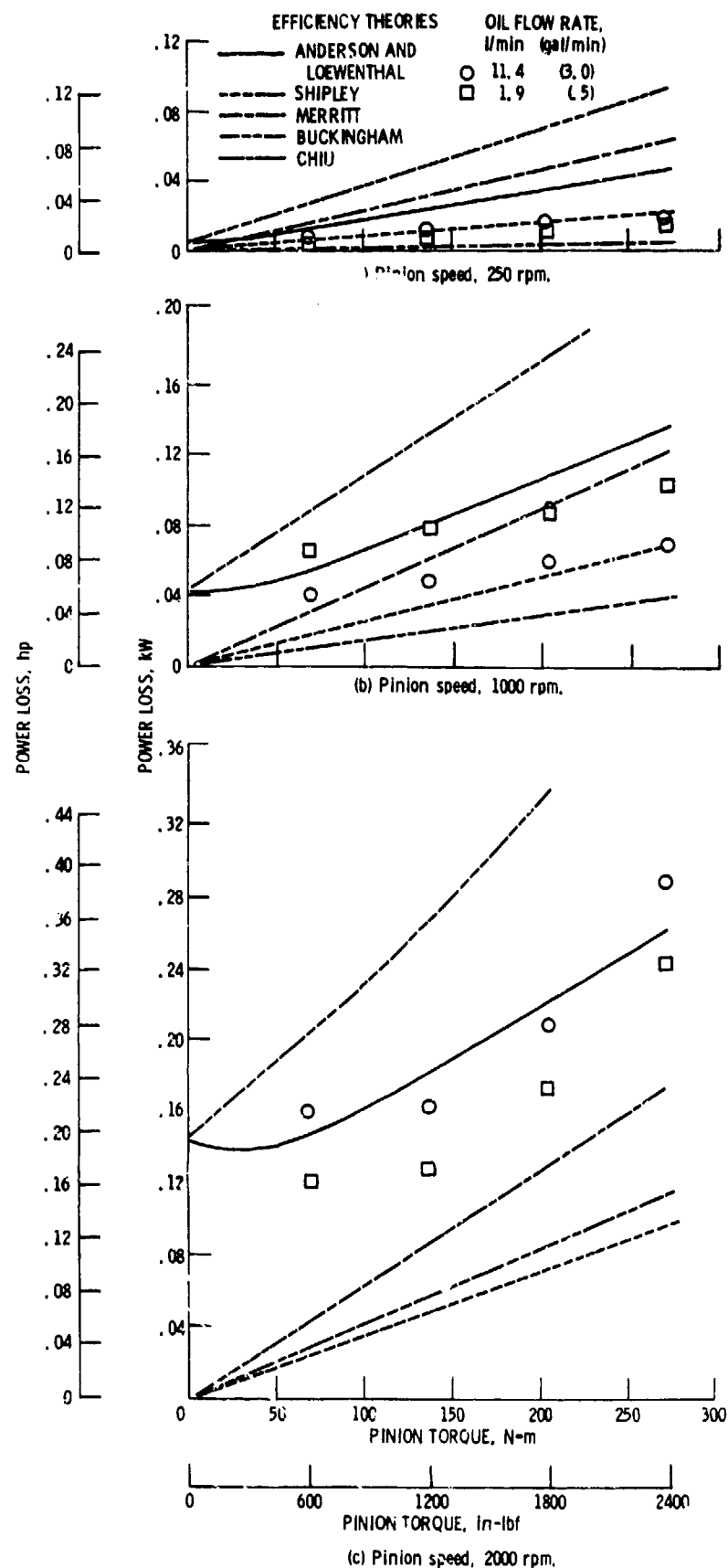


Figure 1. - Comparison of five power-loss prediction methods with the data of Fletcher and Bamborough.

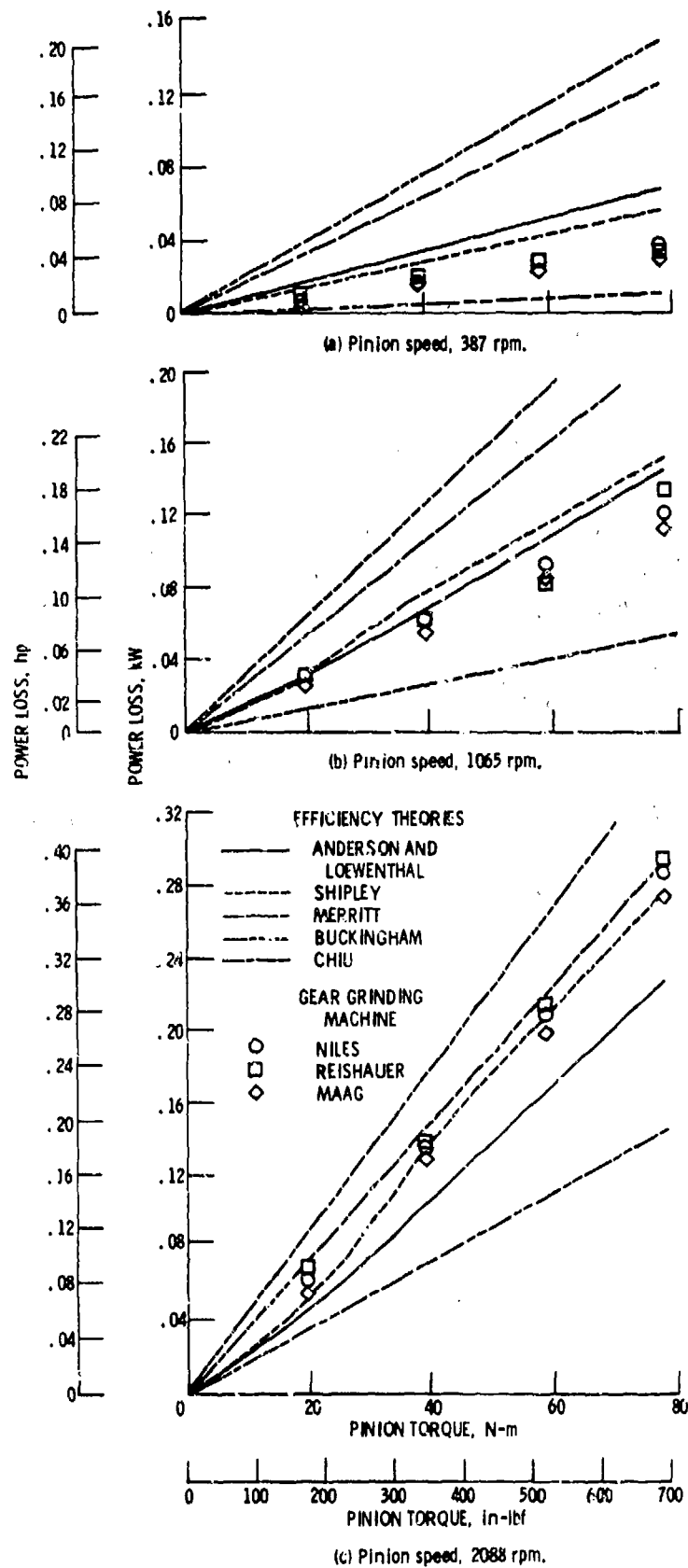


Figure 2. - Comparison of five power-loss prediction methods with the data of Yada.

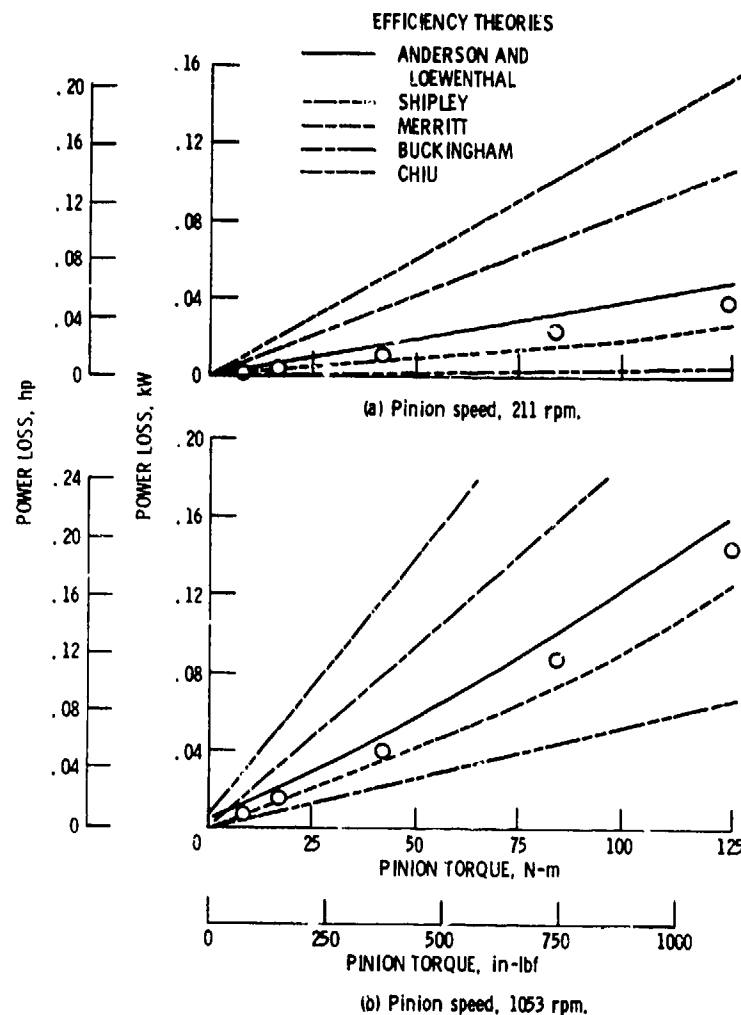


Figure 3. - Comparison of five power-loss prediction methods with the data of Ohlendorf.

Tare Losses

Figure 4 summarizes the tare loss measurements and predictions from all sources as shown in the previous figures. Tare losses are shown as a function of pitch-line velocity. Figure 4 shows that the methods of Anderson and Loewenthal and Chiu accurately predict the tare losses for the Fletcher and Bamborough data but tend to overestimate the tare losses for Ohlendorf's gearset. The other methods predict no tare losses at all. No comparisons were made with Yada's data since no tare loss was predicted by any method and none was measured by Yada.

Comparison of Sliding Loss Equations

As stated earlier, each of the five investigations arrived at a different expression for sliding power loss as well as a different friction coefficient. The question then arises as to whether the difference in power-loss prediction lies in the friction coefficient used or in the form of the equations relating the friction coefficient to the power loss. To make this determination, the Benedict and Kelley friction coefficient, as defined in the method of Anderson and Loewenthal, was used in place of the coefficient specified in each method. The results of this substitution (shown in fig. 5) are typical for all other gearsets and speeds examined.

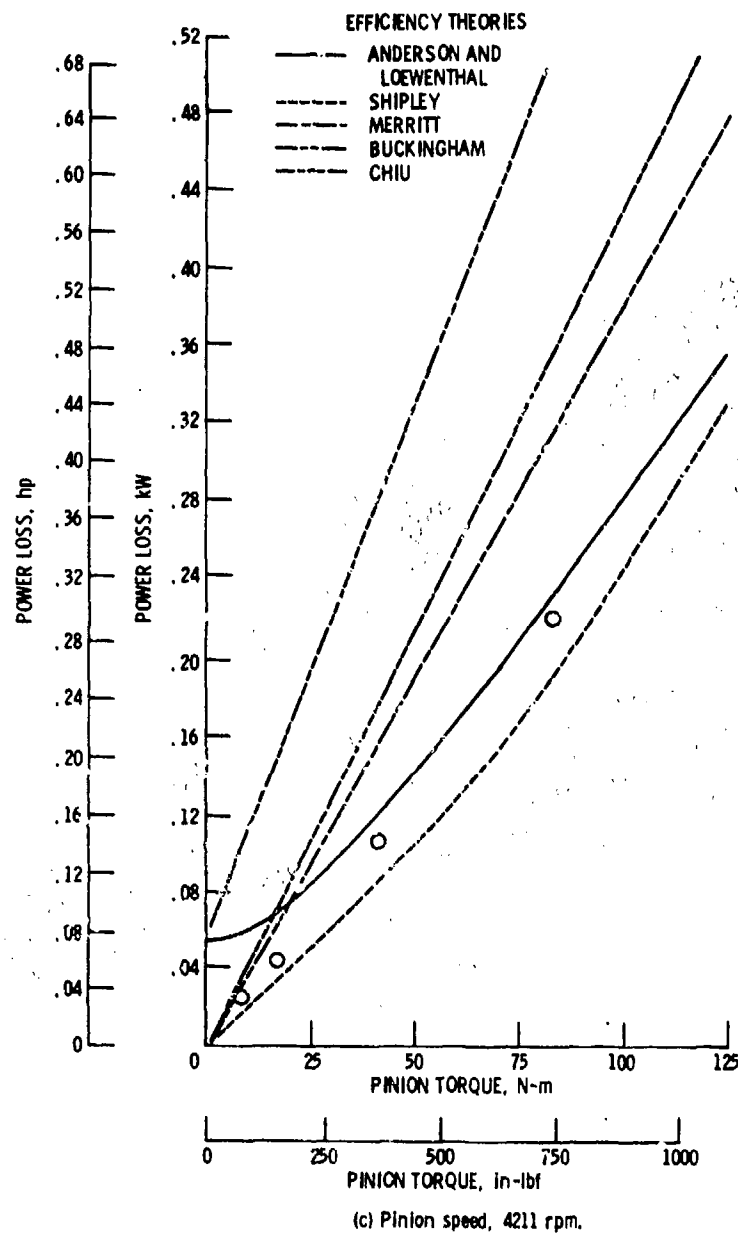


Figure 3. - Concluded.

All methods except Merritt's predict the same sliding power loss when the same friction coefficient is used. This result has several implications. First, all methods, except Merritt's, show basic agreement in calculating sliding power loss. Secondly, the choice of a friction coefficient is crucial. In the methods that use only a sliding loss term, the friction coefficient must account for rolling and windage losses as well as the sliding loss. Thus, the friction coefficient that is used in these methods will not agree with a true sliding loss coefficient such as that determined from disk machine data. This procedure is acceptable except at light loads where the friction coefficient method alone cannot predict tare losses.

The last observation that can be drawn from figure 5 is that the results of Merritt's sliding loss expression do not agree with the other methods. This is probably due to the assumptions Merritt made to simplify the loss equation. It is the simplest expression, but it lacks the flexibility to handle the various gear geometries accurately.

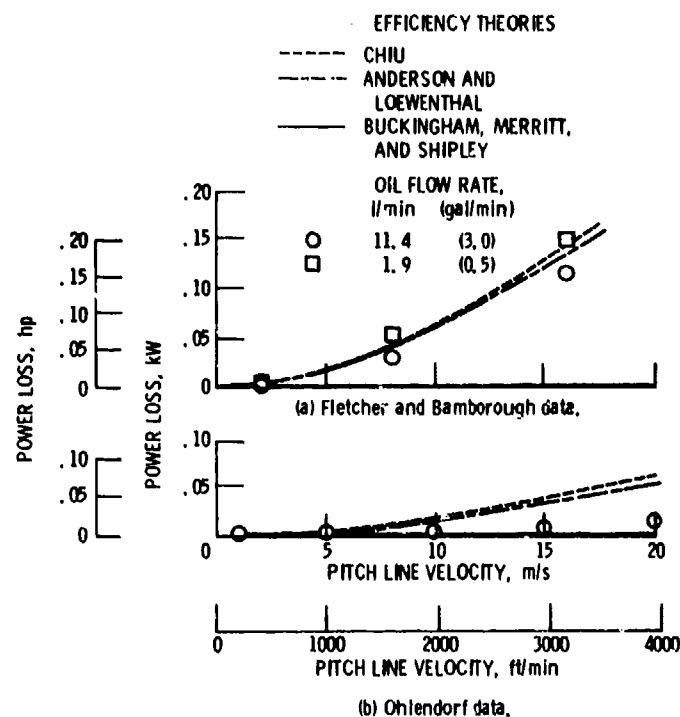


Figure 4. - Comparison of predicted tare (no-load) loss with data.

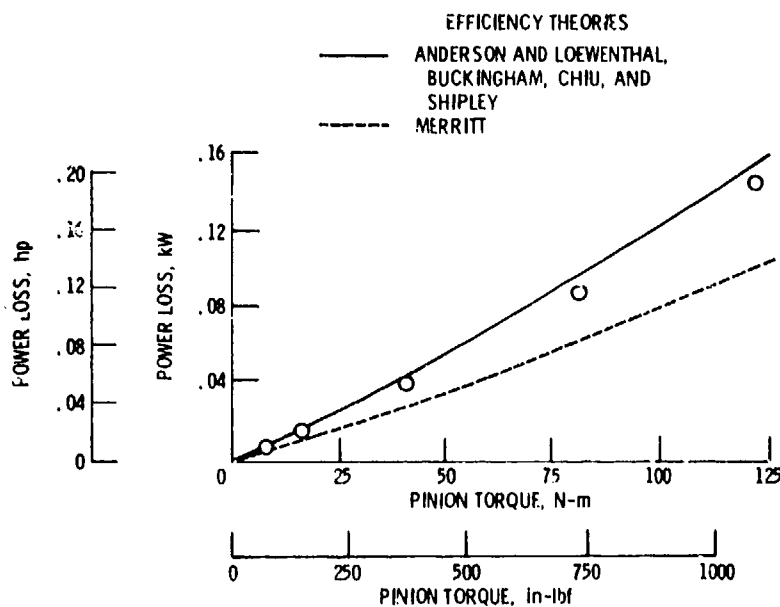


Figure 5. - Comparison of sliding power-loss equations from five power-loss prediction methods, all using the Benedict and Kelley friction coefficient (eq. (9)). Ohlendorf's gearset at a pinion speed of 1053 rpm was used for this comparison.

Efficiency Comparison

In figures 6 to 8 the power-loss data are shown as efficiency versus torque for constant values of speed. The data shown in this manner bring out several points that are not obvious from the power-loss curves. First, the methods of Buckingham and Merritt show no variation in efficiency with load. Their friction coefficients lack a load factor, thus the loss is a constant percentage of the transmitted load. This results in a constant efficiency at any torque.

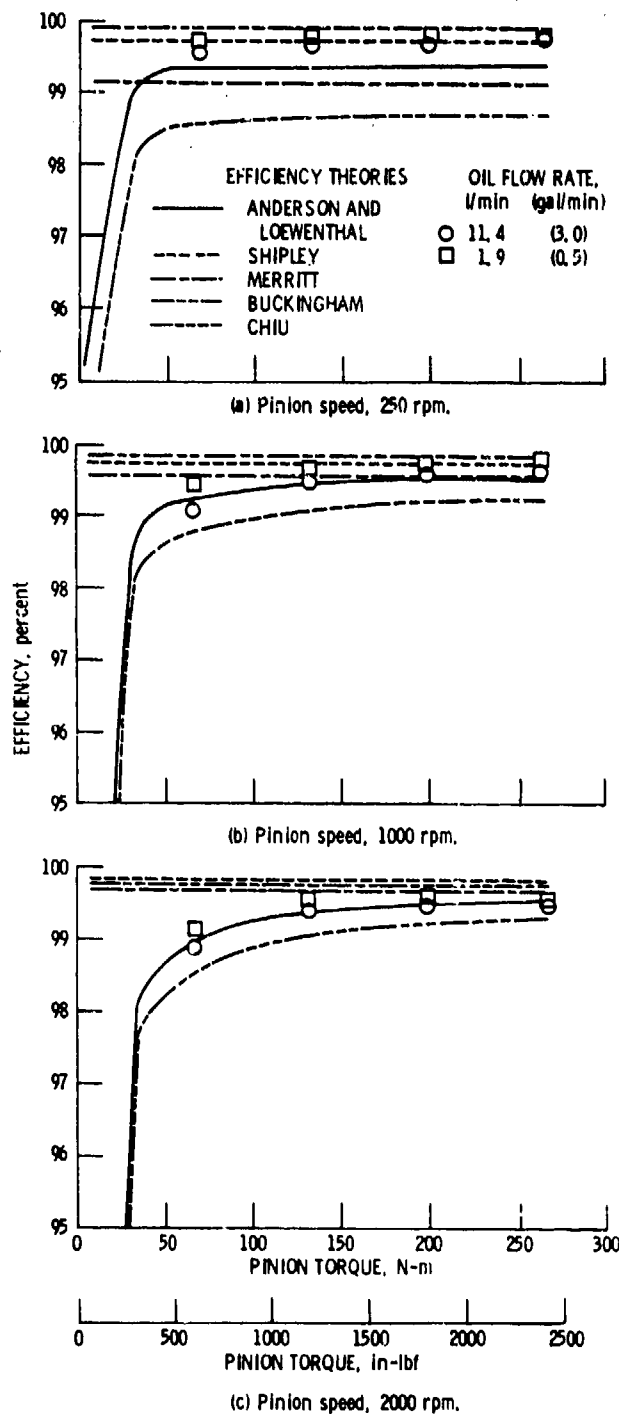


Figure 6. - Gearset efficiency predictions of five methods compared with data of Fletcher and Bamorough.

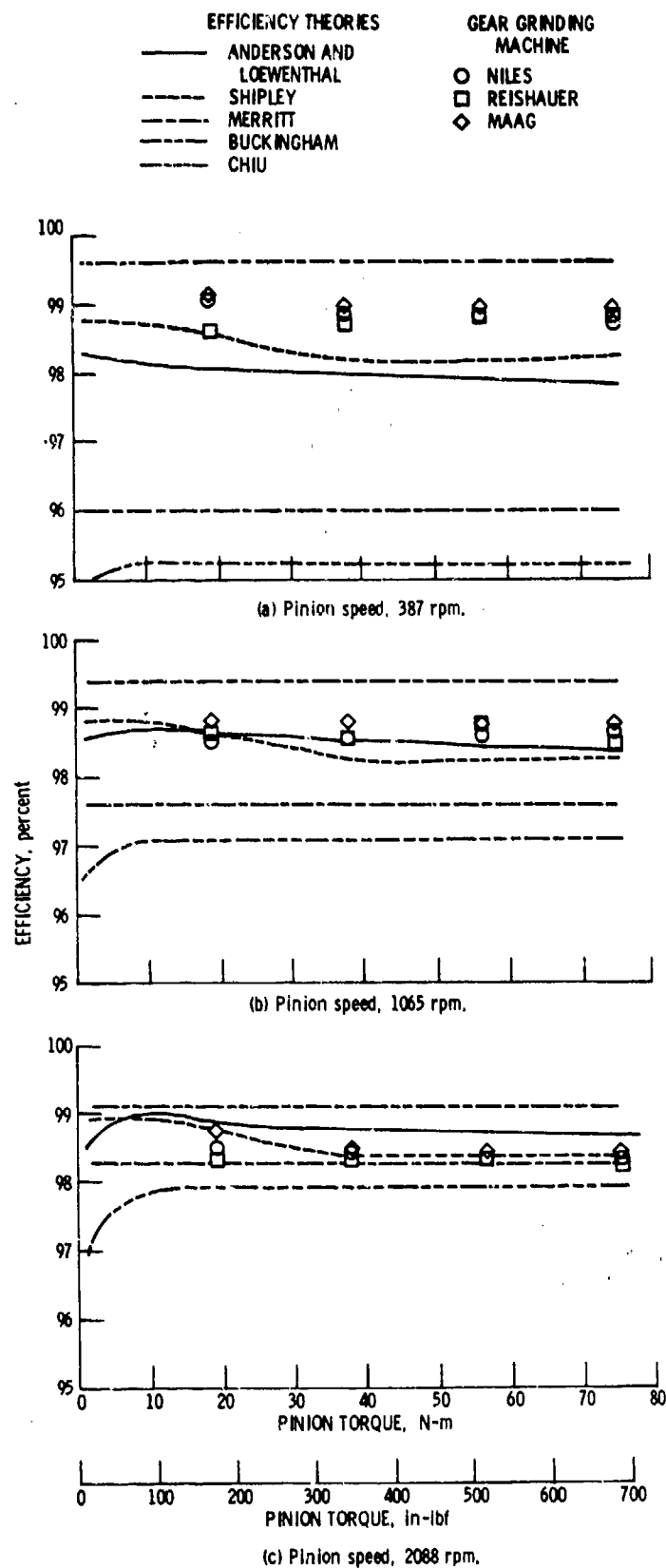


Figure 7. - Gearset efficiency predictions of five methods compared with data of Yada.

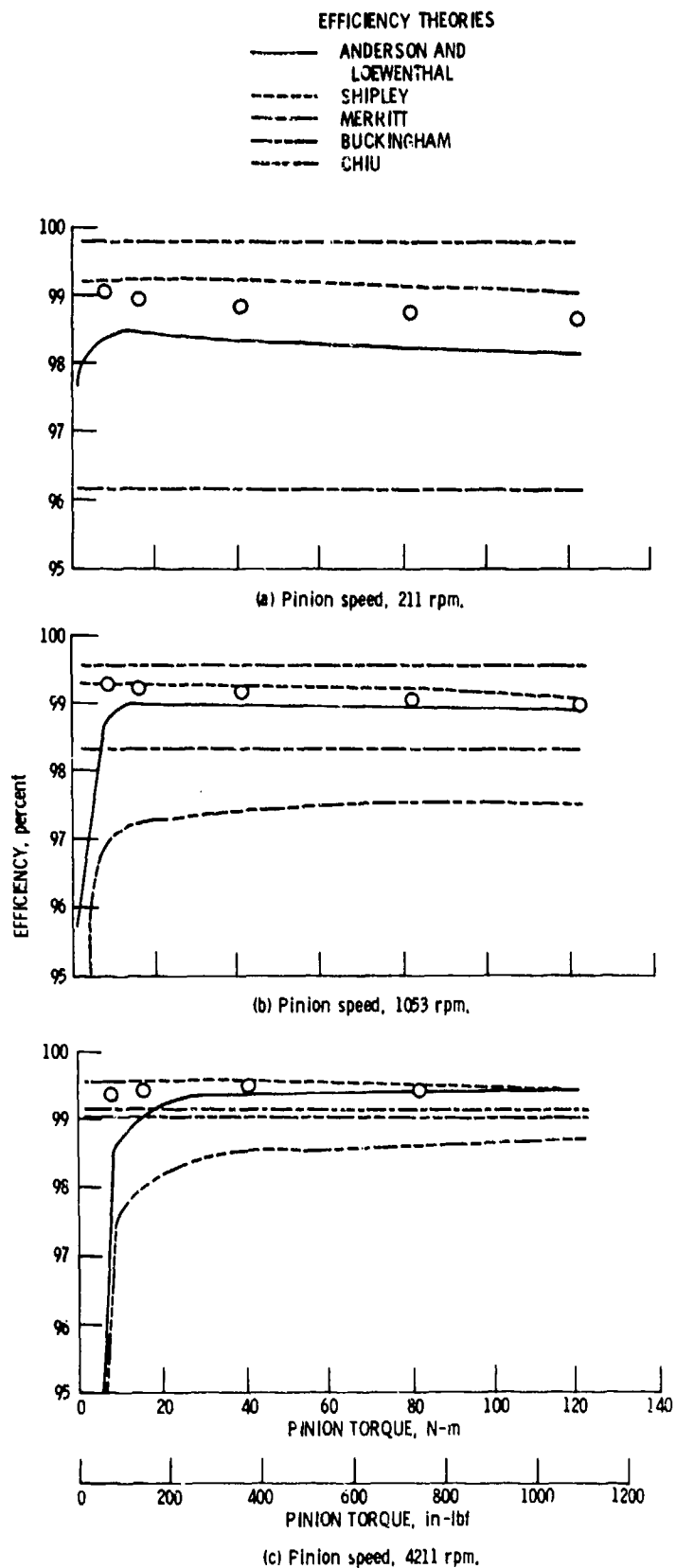


Figure 8. - Gearset efficiency predictions of five methods compared with data of Ohlendorf.

As noted earlier only the methods of Anderson and Loewenthal and Chiu predict no-load, or tare, losses. In figure 6 a decrease in efficiency at lower torques occurs because of the tare losses. The methods that do not predict tare losses show constant efficiency as torque levels are reduced to an unloaded condition. The data of Ohlendorf at 4211 rpm in figure 8(c) show the same effect but to a lesser degree.

In general, the largest variation in predicted efficiency occurs at low speeds. As speed is increased the variations are not as great. For example, at the maximum test speed and torque in each of the three sets of data, the variation in the five prediction techniques was less than 1 percentage point in efficiency. At this same set of conditions the Anderson and Loewenthal and Shipley predictions were within 0.3 percentage point of each other and within 0.5 percentage point of the test data.

It is instructive to note that the measured gear-mesh losses (excluding support bearings) at medium to heavy loads ranged from approximately 0.3 percentage point in the Fletcher and Bamborough test gears (at low speeds) to about 1.7 percentage points for Yada's test gears at high speeds. The Ohlendorf gears showed measured losses from about 0.6 to 1.4 percent. This wide variation in measured efficiency underscores the risk of the common practice of allowing 0.5 percent loss for each spur gear mesh. It should be kept in mind that these data do not include support bearing losses which can often be as great or greater than the mesh losses.

The five methods were rated for closeness of fit to each of the nine sets of experimental data (three gearsets at three speeds). The methods of Anderson and Loewenthal and Shipley gave the best overall correspondence with these data. Buckingham's method showed the next best correlation with data followed by Merritt and Chiu. The largest error at any data point was 1 percentage point for Anderson and Loewenthal, Shipley, and Buckingham, 3 percentage points for Merritt, and 5 percentage points for Chiu.

Summary of Results

The predictions of five spur-gear efficiency calculation methods were compared with three sets of test data generated by different investigators using different gear geometries. The prediction methods were those of Anderson and Loewenthal, Buckingham, Chiu, Merritt, and Shipley. The test data were those of Fletcher and Bamborough, Ohlendorf, and Yada. The data and the analysis methods were limited to jet lubricated, ground, spur gears. The data covered a range in pitch-line velocity of 1 to 20 m/sec (200 to 4000 ft/min) and K-load factor range of 17 to 1600. The following results were obtained:

1. Of the five calculation methods only the method of Anderson and Loewenthal was able to make consistently good prediction of full and part load losses for all sets of tests data.
2. The method of Shipley gave results comparable with those of Anderson and Loewenthal when tare (no-load) losses were not significant. Buckingham's method showed the next best agreement with the data followed by Merritt and Chiu.
3. Tare losses were predicted only by the methods of Anderson and Loewenthal and Chiu. The other methods which use a friction coefficient expression alone to predict mesh losses, cannot account for tare losses.
4. All expressions for sliding power loss gave the same result when the same friction coefficient was used. The only exception was Merritt's expression.
5. Measured mesh losses (without bearing losses) varied from approximately 0.3 to 1.7 percentage points for the loaded spur test gears.

References

1. Anderson, N. E.; and Loewenthal, S. H.: Part and Full Load Spur Gear Efficiency. NASA TP-1622, 1979; AVRADCOM TR 79-46, 1979.
2. Buckingham, E.: Efficiencies of Gears. Analytical Mechanics of Gears. Dover Publications, Inc., 1963, pp. 395-425.
3. Chiu, Y. P.: Approximate Calculation of Power Loss in Involute Gears. ASME Paper No. 75-PTG-2, Oct. 1975.
4. Merritt, H. E.: Efficiency and Testing. Gear Engineering, John Wiley & Sons, Inc., 1972, pp. 345-357.

5. Shipley, E. E.: Loaded Gears in Action. Gear Handbook, D. W. Dudley, ed., McGraw Hill Book Co., Inc., 1962, pp. 14-1 to 14-60.
6. Martin, K. F.: A Review of Friction Predictions in Gear Teeth. Wear, vol. 49, no. 2, Aug. 1978, pp. 201-238.
7. Fletcher, H. A. G.; and Bamborough, J.: Effect of Oil Viscosity and Supply Conditions on Efficiency of Spur Gearing. National Engineering Laboratory Report No. 138, East Kilbride Glasgow, Crown, 1964.
8. Yada, Tsuneji: Relation of Frictional Loss of Gear to Speed and Torque. Bull. JSME, vol. 16, no. 95, May, 1973, pp. 872-880.
9. Ohlendorf, H.; and Richter, W.: Stirnradgetriebe—Zahnreibung, Verlustleistung und Erwaermung. (Spur Gearings—Friction, Damage and Heating.) W. Richter, ed., Friedrick Vieweg and Sohn (Braunschweig), 1964, pp. 1-58.
10. Wellauer, E. J.: Load Rating of Gears. Gear Handbook, D. W. Dudley, ed., McGraw Hill Book Co., Inc., 1962, pp. 13-3 to 13-6.
11. Harris, T. A.: Rolling Bearing Analysis. John Wiley & Sons, Inc., 1966.
12. Benedict, G. H.; and Kelley, B. W.: Instantaneous Coefficients of Gear Tooth Friction. ASLE Trans., vol. 4, no. 1, Apr. 1961, pp. 59-70.
13. Crook, A. W.: The Lubrication of Rollers. IV. Measurements of Friction and Effective Viscosity. Philos. Trans. R. Soc. London, ser. A., vol. 255, no. 1056, Jan. 17, 1963, pp. 281-312.
14. Hamrock, B. J.; and Dowson, D.: Isothermal Elastohydrodynamic Lubrication of Point Contacts, Part III—Fully Flooded Results. J. Lubr. Technol., vol. 99, no. 2, Apr. 1977, pp. 264-276.
15. Cheng, H. S.: Prediction of Film Thickness and Traction in Elastohydrodynamic Contacts. Design Engineering Technology Conference, American Society of Mechanical Engineers, 1974, pp. 285-293.
16. Anderson, N. E.; and Loewenthal, S. H.: Design of Spur Gears for Improved Efficiency. NASA TM-81625, 1980; AVRADCOM TR 81-C-3.
17. Dynamic Loads on Gear Teeth, Report of the ASME Special Research Committee on the Strength of Gear Teeth. American Society of Mechanical Engineers, 1931.
18. O'Donoghue, J. P.; and Cameron, A.: Friction and Temperature in Rolling, Sliding Contact. ASLE Trans., vol. 9, no. 2, Apr. 1966, pp. 186-194.
19. Dowson, Duncan; and Higginson, Gordon R.: Elasto-Hydrodynamic Lubrication; The Fundamentals of Roller Gear Lubrication. Pergamon Press, 1966.
20. Shipley, E. E.: How to Predict Efficiency of Gear Trains. Product Eng., vol. 29, no. 31, Aug. 1958, pp. 44-45.
21. Fletcher, H. A. G.; and Collier, P.: A Precision Dynamometer of 37.5 hp, 3750 rev/min Rating. Report No. 111, National Engineering Laboratory, East Kilbride, Glasgow, Sept. 1963.
22. Yada, Tsuneji: Accuracy of Oil Immersion Gear Loss Measuring Formula. Bull. JSME, vol. 16, no. 95, May 1973, pp. 862-871.

Compliance and Stress Sensitivity of Spur Gear Teeth*†

R.W. Cornell‡

As the result of recent interest in the possible weight saving obtained by using high contact ratio gear (HCRG) meshes, a computer program was developed using a time history, interactive, closed form solution for the dynamic tooth loads for both low and high contact ratio spur gears (ref. 1). Because the magnitude and variation of the tooth pair compliance with load position can affect the dynamics and loading significantly, and because the tooth root stressing per load varies significantly with load position, it was desirable to include in the dynamic gear program preprocessors and postprocessors, respectively, for calculating these two important factors. Since the tooth forms for HCRG deviate appreciably from the tooth forms for conventional low contact ratio gears (LCRG), improved and simplified methods were developed for calculating the compliance and stress sensitivity for three involute tooth forms as a function of load position—a standard LCRG tooth with no undercut and two HCRG teeth with different forms of undercut (see fig. 1).

The method developed for calculating the compliance of spur gear teeth follows to a great extent that developed by Weber (ref. 2) and includes three factors: (1) the basic deflection of the tooth as a beam, (2) the deflection of the tooth caused by the fillet and foundation flexibility (ref. 3), and (3) the local deflection caused by the contact between the two teeth. The principal improvement in the compliance analysis was for the fillet/foundation deflection, which was found to be defined by different fillet angles for various load positions; whereas previous studies assume a given fillet angle of about 75°. The resulting compliance analysis was evaluated by applying it to available test, finite-element, and analytic-transformation results and was found to give compliance results which agreed well with measurement and "exact" analyses.

The method developed for calculating the stress sensitivity is an improved and simplified version of the Heywood analysis (ref. 4). Because the tooth forms for HCRG deviate appreciably from conventional LCRG tooth forms, the stress sensitivity analysis had to include most of the factors affecting the stressing. The improved analysis does not assume the peak stress occurs at 30° from the base of the fillet, as the Heywood analysis does, but allows it to be a function of load position. The sensitivity analysis was found to give results which agreed well with the Heywood (ref. 4) and Kelly and Pederson methods (ref. 13), which, in turn, have been found to correlate well with test results. Evaluation of the modified Heywood stress sensitivity analysis showed that its results compared very well with available test, finite element, and analytic transformation results. The differences between the improved Heywood type stress sensitivity analysis and the conventional Lewis and AGMA analyses were found to be significant for low and high contact ratio gears, being about 25 percent higher for the LCRG and about 15 percent higher for the HCRG.

Gear Tooth Compliance

Derivation of Compliance Formula.

The determination of the compliance of gear teeth is considerably more difficult than determining the stress sensitivity because it is an integral function of the entire loaded tooth, rather than just a function of the section properties at the peak stress point and the load location. In addition, because of the stubbiness of the teeth, the foundation and shear effects are important. The method developed herein parallels to a great extent Weber's work (ref. 2) but using O'Donnell's foundation factors (refs. 3 and 5). The total compliance or flexibility of a gear tooth at the point of

*Work done under NASA contract NAS3-22138.

†Previously published in J. Mech. Des., vol. 103, no. 2, Apr. 1981.

‡Hamilton Standard Division of United Technologies Corp.

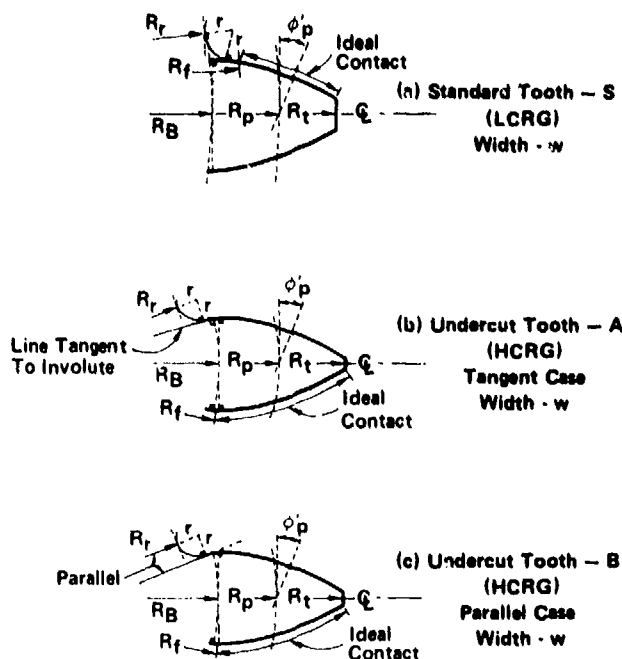


Figure 1. - Gear tooth geometries.

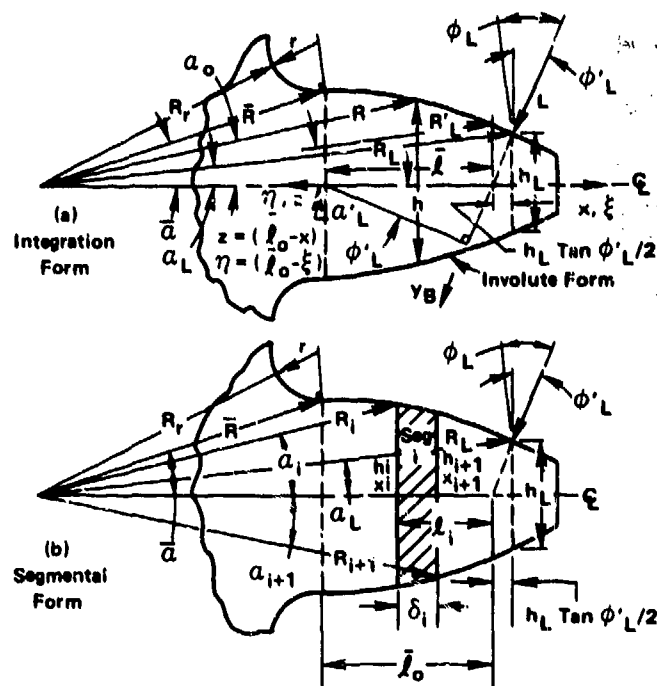


Figure 2. - Beam compliance of gear tooth.

load, y_T , is made up of three deflections: (1) the basic tooth as a cantilever beam, y_B ; (2) the fillet and foundation, y_F ; and (3) the local contact and compression, y_L . The compliance, C , of a gear tooth pair, 1 and 2, is their combined deflection per unit of load at the contact position or

$$C = (y_{T1} + y_{T2})/L = [(y_{B1} + y_{B2} + (y_{F1} + y_{F2}) + (y_L))]/L \quad (1)$$

where L is the applied load and the deflections y are in the direction of the load. The derivation of the three factors in equation (1) follows.

In order to determine the beam compliance of a gear tooth its geometry must be defined over its entire load length. Three different involute tooth forms are considered in this study, which depend on the contact ratio, number of teeth and pitch, and manufacturing process. The three involute tooth forms are depicted in figure 1, form S being for standard LCRG teeth with no necking and forms A and B being for HCRG and small radius LCRG teeth. For tooth form S the tangency of the fillet radius with the involute form occurs outboard of the base circle. For forms A and B the tangency with the tooth form occurs inboard of the base circle. The tooth form inboard of the base circle is machined along a line tangent to the involute surface at the base circle for form A, whereas it is plunged ground along a line parallel to the fillet radius centerline for form B. The appendix gives the expressions for defining the tooth geometry for three forms of teeth. The applicable tooth geometry, form S, A, or B in figure 1, is determined by the expressions

$$\begin{aligned} \text{Form S: } (R_f^2 + 2rR_r) &\geq R_B^2 \\ \text{Form A or B: } (R_f^2 + 2rR_r) &< R_B^2 \end{aligned} \quad (2)$$

Whether form A or B applies is defined by the manufacturing process used, that is, fillet region made tangent or plunge ground, respectively. Having analytically defined the geometry of the gear tooth, the compliance of the tooth can be determined.

The deflection and, therefore, compliance of a gear tooth over its beam portion is easily obtained using elementary strength of materials. Referring to figure 2(a), the total bending and shear

deflection in the direction of and at the applied tooth load, L , which is at radius R_L or position S along the line of action, can be expressed in integral form as

$$y_B = \frac{L \cos^2 \phi_L'}{E} \int_0^{l_0} \left\{ \frac{l_0 \eta}{I} d\eta + \frac{2.40(1+\mu) + \tan^2 \phi_L'}{A} \right\} dz \quad (3)$$

where I is the section modulus of the tooth as a function of $\xi = x$ or $n = z$; $n = (\bar{l} - \xi) = z = (\bar{l} - x)$ and is the distance along the centerline of the tooth from the load position; a value of 1.2 has been assumed for the shear factor based on a rectangular tooth; $G = E/2(1 + \mu)$; and A is the cross-sectional area as a function of x or z . The deflection of the basic tooth can also be defined in a summation expression rather than integral form (see fig. 2(b)), which would be more applicable for a hand calculation or a programmable calculator. In this case the tooth beam deflection at and in the direction of the load is

$$y_B = \frac{L \cos^2 \phi_L'}{E} \sum_{i=1}^n \delta_i \left\{ \frac{(l_i^2 - l_i \delta_i + \frac{1}{3} \delta_i^2)}{I_i} + \frac{(2.4(1+\mu) + \tan^2 \phi_L')}{A_i} \right\} \quad (4)$$

where $1/\bar{I}_i = (1/I_i + 1/I_{i+1})/2$ and $(1/A_i + 1/A_{i+1})/2$. Using these inverse forms for the values of \bar{I}_i and \bar{A}_i improves the accuracy for a small number of elements. In equation (4) $I_i = (\bar{i} - x_i)$ and $\delta_i = (x_{i+1} - x_i)$ (see the appendix). Both approaches for beam flexibility assume a narrow tooth width, W . For wide teeth where $W/h_p > 5$, the flexibility is decreased by the anticlastic effect, so that the values of I in equations (3) and (4) should be divided by $(1 - \mu^2)$.

Because of the fillet and the flexibility of the material to which the tooth is attached, additional deflection will occur at the load (refs. 2, 3, and 5). This fillet and foundation deflection in the direction of the load, y_F , is a function of the fillet geometry and the load position and direction and is determined by the effective fillet length or angle γ_F for which the maximum deflection or work occurs at the load. In other references this effective fillet angle has been assumed constant at about 70 (ref. 3) or neglected (ref. 2).

Based on figure 3, O'Donnell (refs. 3 and 5) shows that the deflection at and in the direction of the tooth load due to the foundation effects, y_{FF} , for plane stress is

$$y_{FF} = \frac{L \cos^2 \phi_L'}{WE} \left[\frac{16.67}{\pi} \left(\frac{l_F}{h_F} \right)^2 + 2(1 - \mu) \left(\frac{l_F}{h_F} \right) + 1.534 \left(1 + \frac{\tan^2 \phi_L'}{2.4(1 + \mu)} \right) \right] \quad (5)$$

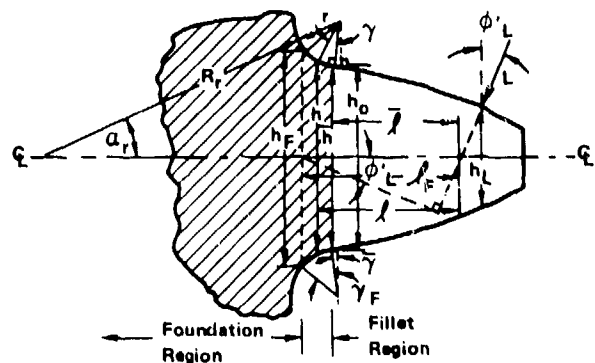


Figure 3. - Fillet and foundation compliance of a gear tooth.

For wide teeth the expression for plane strain is used or

$$y_{FF} = \frac{L \cos^2 \phi'_L}{WE} (1 - \mu^2) \left[\frac{16.67}{\pi} \left(\frac{l_F}{h_F} \right)^2 + 2 \left(\frac{1 - \mu - 2\mu^2}{1 - \mu^2} \right) \left(\frac{l_F}{h_F} \right) + 1.534 \left(1 + \frac{\tan^2 \phi'_L}{2.4(1 + \mu)} \right) \right] \quad (6)$$

The O'Donnell coefficients in equations (5) and (6) differ slightly from those given by Weber (ref. 2). The first term in the brackets is the deflection at L due to the rotation caused by the moment at h_F . The second term is the sum of the deflections at L due to the displacement at h_F caused by the moment at h_F and the rotation at h_F caused by the shear force at h_F . The first part of the third term is the displacement at L due to the shear force at h_F , based on the assumption that the effective depth for determining this deflection is $2\frac{1}{2}$ times the tooth thickness (ref. 2). The second part of the third term is the deflection at L due to the normal component of the load assuming the same relationship holds as indicated by the beam deflection equation (see eqs. (3) and (4)). The question now follows: What values of l_F and h_F should be used in equations (5) and (6), that is, what is the effective fillet length or angle γ_F ?

Referring to figure 3, the deflection at and in the direction of the load due to the flexibility of the fillet and foundation, y_F , the shaded region, is obtained from the summation of the fillet beam deflection, y_{FB} , using equations (3) and (4), and the foundation deflection y_{FF} , using equation (5) or (6), that is,

$$y_F = y_{FF} + y_{FB} \quad (7)$$

where $l_F = \bar{l} + r(\sin \gamma_F - \sin \bar{\gamma})$, $h_F = \bar{h} + 2r(\cos \bar{\gamma} - \cos \gamma_F)$, $l_i = \bar{l} + r(\sin \gamma_i - \sin \bar{\gamma})$, and $h_i = \bar{h} + 2r(\cos \bar{\gamma} - \cos \gamma_i)$. The value of γ_F is the one that maximizes the value of y_F or y_T , which can be easily done as one integrates or sums up the deflection of the tooth starting at the beginning of the fillet or at the load position.

The significance of maximizing the deflection due to fillet effects can best be realized by expressing in nondimensional form the deflection at the load due to the fillet and foundation flexibility. If this is done, it is found that the effective fillet angle, γ_F , is a function of four quantities $-\bar{l}/\bar{h}$, r/\bar{h} , $\bar{\gamma}$, and ϕ'_L . Figure 4 shows the effect of r/\bar{h} and \bar{l}/\bar{h} on γ_F for typical values of $\phi'_L = 20^\circ$ and $\bar{\gamma} = 0$. Apparent from these curves is that assuming a value of 75° for γ_F (ref. 3) applies only for small values of \bar{l}/\bar{h} and r/\bar{h} and that a more universal value would be 55° to 60° . The effects of $\bar{\gamma}$ and ϕ'_L on γ_F were studied and found to be small. Figure 5 presents the corresponding fillet and foundation flexibility results. Apparent from these curves is that assuming a value of 75° for γ_F results in progressively greater error as \bar{l}/\bar{h} and r/\bar{h} increase (HCRG). However, for typical values of \bar{l}/\bar{h} and r/\bar{h} , particularly for LCRG, the likely difference will be less than 10 percent from that given by solving for γ_F .

The local compliance, y_L , consists of the Hertz or line contact deflection plus the compression of each tooth between the point of contact and the tooth centerline. Figure 6 gives the nomenclature for the parameters that determine the local deformation. Three viable approaches were reviewed with regard to calculating the local compliance: (1) an approximate Hertzian and compression approach originally used at Hamilton Standard, (2) a semi-empirical approach developed by Palmgren (ref. 6), and (3) a closed form approach developed by Weber (ref. 2).

The approximate approach assumes that the true Hertz contact deformation, y_H , must be doubled to account for the cupping action discussed in reference 7, that is,

$$y_H \approx 2 \cdot \frac{b^2}{2} \left(\frac{1}{r_1} + \frac{1}{r_2} \right) \approx \frac{4I}{\pi W} \left(\frac{1 - \mu_1^2}{E_1} + \frac{1 - \mu_2^2}{E_2} \right) \quad (8)$$

The local compression of each tooth between the contact point and tooth centerline is approximated by assuming the load spreads at a 45° angle, that is from $2b$ on the top to $2(b + h)$ at the bottom over a length h . Assuming the compression deflection is given by the average width, we find

$$y_c = \frac{L}{W} \left[\left(\frac{1 - \mu_1^2}{E_1} \right) \left(\frac{h_1}{2b + h_1} \right) + \left(\frac{1 - \mu_2^2}{E_2} \right) \left(\frac{h_2}{2b + h_2} \right) \right] \quad (9)$$

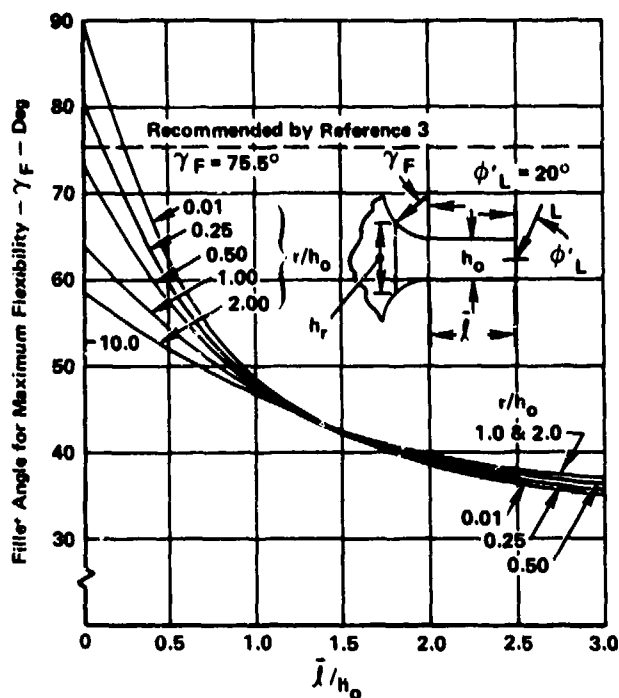


Figure 4. - Fillet angle for maximum flexibility versus load point from fillet.

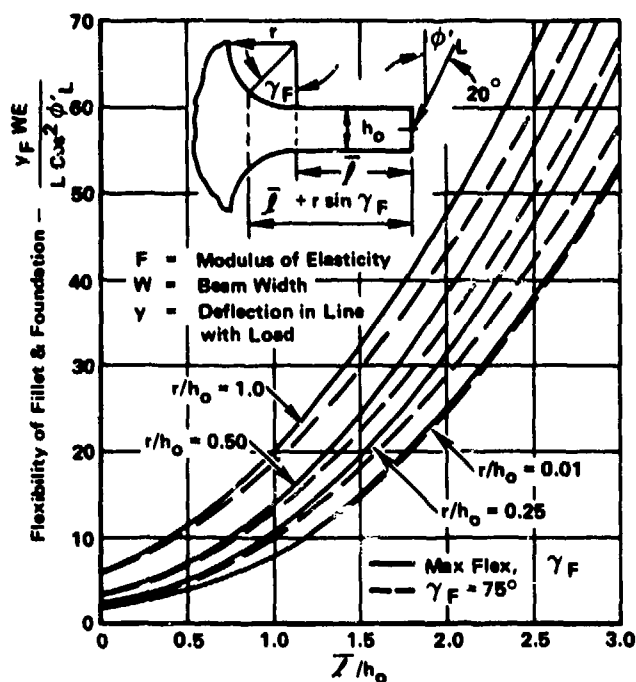


Figure 5. - Flexibility of fillet and foundation
versus load position from fillet.

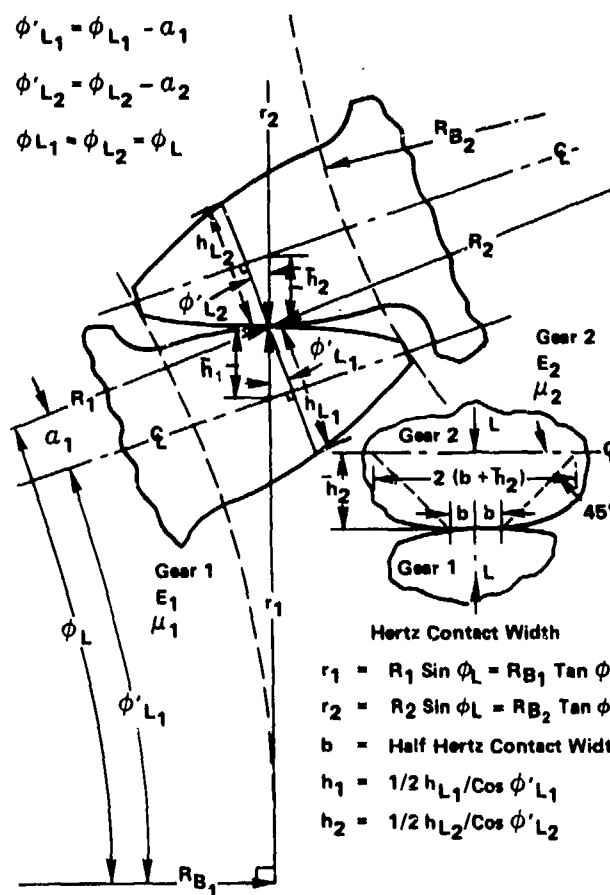


Figure 6. - Nomenclature for local compliance.

where

$$b = \left\{ \frac{4L}{\pi W} \left[\left(\frac{1-\mu_1^2}{E_1} \right) + \left(\frac{1-\mu_2^2}{E_2} \right) \right] / \left[1/r_1 + 1/r_2 \right] \right\}^{1/2} \quad (10)$$

Assuming \bar{h}_1/b and \bar{h}_2/b are both greater than 1, the local compression of the two teeth reduces to

$$y_c = \frac{L}{W} \left[\left(\frac{1-\mu_1^2}{E_1} \right) + \left(\frac{1-\mu_2^2}{E_2} \right) \right] \quad (11)$$

so that the overall local compression of the two teeth is

$$y_L = y_H + y_c = \frac{4L}{\pi W} \left[\left(\frac{1-\mu_1^2}{E_1} \right) + \left(\frac{1-\mu_2^2}{E_2} \right) \right] \left[1 + \frac{\pi}{4} \right] \quad (12)$$

which for $E_1 = E_2$ and $\mu_1 = \mu_2$ reduces to the simple expression

$$y_L = 3.57 \frac{4(1-\mu^2)}{\pi E} \frac{L}{W} = 4.55(1-\mu^2) \frac{L}{WE} \quad (13)$$

Although equations (12) and (13) show y_L increases linearly with L/W , in actuality it increases at a slightly lower rate because the effect of the contact width was neglected. This nonlinear effect can be included if desired.

Reference 6 presents an expression for the local deformation based on the semi-empirical equation developed by Palmgren for contacting cylinders in roller bearings. Because only half a tooth thickness is being compressed instead of the entire roller, the local tooth deflection was assumed to be half that for the roller bearing or

$$y_L = \frac{1.275 L^3}{E_{12}^3 W^3} = \frac{4(1-\mu^2)L}{\pi E_{12} W} \left\{ 1.10 \frac{W^2 E_{12}}{L} \right\}^{-1} \quad (14)$$

where $1/E_{12} = (1/E_1 + 1/E_2)/2$. Weber in reference 2 developed an expression specifically for the local deformation of two gear teeth. In order to obtain a closed form solution, he assumed small deformations so that just the first two terms of the binomial expansion of the deformation needed to be used, that is,

$$y_L = \frac{2L}{\pi W} \left[\left(\frac{1-\mu_1^2}{E_1} \right) \left\{ \ln \frac{2\bar{h}_1}{b} - \left(\frac{\mu_1}{2(1-\mu_1)} \right) \right\} + \left(\frac{1-\mu_2^2}{E_2} \right) \left\{ \ln \frac{2\bar{h}_2}{b} - \left(\frac{\mu_2}{2(1-\mu_2)} \right) \right\} \right] \quad (15)$$

where b is given by equation (10). If $E_1 = E_2$ and $\mu_1 = \mu_2$, equation (15) reduces to

$$y_L = \frac{4(1-\mu^2)}{\pi E} \frac{L}{W} \left[\ln \left(2 \frac{\sqrt{\bar{h}_1 \bar{h}_2}}{b} \right) - \left(\frac{\mu}{2(1-\mu)} \right) \right] \quad (16)$$

All of the expressions for the local deformation are nonlinear with load because of the Hertz half contact width b . For simplicity the nonlinearity can be circumvented by assuming a value of b based on the maximum nominal value of tooth load during the mesh, that is, $T/CR_{\min} \cos \phi_p R_p$, or assuming a maximum value of Hertz stress. This latter option should be used after the initial dynamic gear tooth analysis is run and a first approximation of the maximum Hertz stress is obtained including dynamic effects.

In order to decide which of the three local compliance methods should be adopted, they were evaluated for several cases. The first case was for a pair of steel, standard 2-in. pitch radius, 8 pitch, 0.375-in. wide, 20° pressure angle gears in contact at the pitch radius ($\bar{h} = 0.0998$ in.) under load levels of $L/W = 1279$ and 2875 lb/in ($q = 140\,000$ and 210 000 psi), respectively. The second case is from reference 2 and was for the meshing of an 18 tooth, steel gear with a rack under three loading conditions, where $\bar{h}_1 = 0.80$ m, $\bar{h}_2 = 0.84$ m, $r_1 = 3.1$ m, and $r_2 = \infty$. Here, m is the tooth module-pitch diameter in millimeters divided by the number of teeth. The local deflections predicted by the three methods for these two cases are summarized in table 1. For the first case, the empirical method gives

Table 1 Comparison of Methods for Calculating Local Tooth Compliance: Approximate; Empirical (Palmgren); Closed Form (Weber)

Factor	Equation	Gear Case 1		Gear Case 2		
		16 Teeth/16 Teeth R Pitch, W = 0.375 in., $R_p = 2.0''$ $E = 30 \times 10^6$ psi; $\phi_p = 20^\circ$; $\bar{r} = 0.0008''$		16 Teeth/ ∞ Teeth $R_1 = 0.80$ m, $R_2 = 0.84$ m; $r_1 = 3.1$ m; $r_2 = \infty$ $E = 2.15 \times 10^6$ Kg/cm ² , m = Module in mm		
Load/Width	L/W	1279 lb/in.	2875 lb/in.	16.16 Kg/cm ²	23.08 Kg/cm ²	32.33 Kg/cm ²
Hertz Stress	q	140 ksi	210 ksi	1400 Kg/cm ²	2000 Kg/cm ²	2800 Kg/cm ²
Half Contact Width	b	0.00561 in.	0.00671 in.	0.00735 m	0.01060 m	0.0147 m
Local Compliance $\frac{\gamma}{4L(1-\mu^2)}$	Approx-Linear	(13)	3.57	3.57	3.57	3.57
	Approx-Non Linear	(9)	3.41	3.34	3.52	3.44
	Empirical	(14)	2.50	2.31	3.88*	3.58*
	Closed Form	(15)	3.32	2.31	5.19	4.46

*W Assumed Equal to Sm

results about 80 percent of those by Weber's method, probably because it includes a width effect, whereas the approximate method gives 10 to 20 percent high values, particularly for the higher Hertz stressing. For the second case there is considerable difference in the local deflections predicted by the three methods for these relatively low Hertz stress cases. Weber's expression gives values about 20 to 25 percent greater than the other two. Because the empirical method is width dependent and appears to give values somewhat low and because the approximate method does not appear to include the nonlinear effects properly, it was decided to use the closed form expression of Weber's equation (15), for the local compliance.

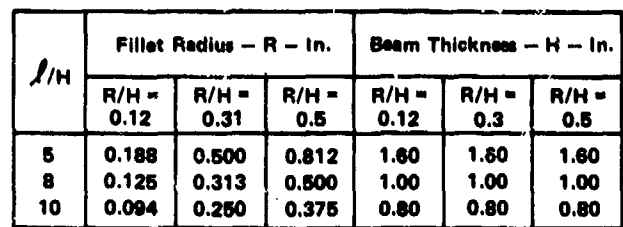
The overall compliance, C , of the tooth pair is obtained by adding the local gear tooth compliance defined by equation (15) with the gross tooth compliances for the two gear teeth ($\gamma_B + \gamma_F$)/ L given by equations (3) or (4) and (7). (See eq. (1).) In order to obtain the necessary compliance information for the dynamic gear analysis of reference 1, the tooth pair compliance must be determined for at least five different load contact positions, S , along the line of action, so that the compliance can be expressed in the required five term power series

$$C = C_o \left[1 + A(S/S_o) + B(S/S_o)^2 + C(S/S_o)^3 + D(S/S_o)^4 \right] \quad (17)$$

Here, S_o is the reference distance along the line of action corresponding to the tip radius of the gear, C_o is the tooth pair compliance for a load at the pitch radius, and A , B , C , and D are curve fitting coefficients.

Evaluation of Compliance Formula

The cantilever beam test and finite elements results of reference 8 provided a means for checking the basic fillet and foundation formulation, because of the three deflection measurements along the beam, the simplicity of the beam itself, and the three different fillet sizes and beam thicknesses. (See fig. 7.) A summary of the comparison of the finite element, O'Donnell, and formulas (4) and (7) theoretical results with test is given in table 2. Although the latter formulas are based on O'Donnell's foundation analysis, the effective fillet length is solved for based on maximum energy, resulting in a fillet length equivalent to an angle γ_F of about 32° to 34° , depending on the case. Table 2 shows that all three theoretical methods do quite well at predicting the load deflection; however, the O'Donnell approach appears to be inaccurate for small values of r/h_o and l_o/h_o and for load positions close to the support juncture or small x . The error for the formulas herein tends to be more uniform for the various tooth geometries as does the finite element results. Correcting the test results for the Poisson swelling (see ref. 8) makes the error variation with position x nearly uniform at about $+1 \pm 3$ percent for the results based on formulas (4) and (7). However, because of the large load moment arm, the concept of variable effective fillet length developed herein could not be fully confirmed.



respectively, of those predicted by the method herein. Also, the shapes of the compliance curves are more consistent with the other results, for the added correlation increases as S/P becomes more negative. Figure 9 gives the derived values of effective fillet angle, γ_F , for the various load positions and gear teeth which will result in the maximum deflection or work done by the applied load. For load positions inboard of the pitch circle, the assumed value of 75° by O'Donnell is a good approximation; however, for load positions towards the tooth tip, particularly for HCRG, the effective angle should be considerably less resulting in greater flexibility.

As a further check on the accuracy of the beam and fillet compliance formulas (4) and (7), they were used to predict some of the tooth pair beam stiffnesses presented in reference 10, which used the same analytic transformation method as reference 9. Because the results included the local effects based on Weber (ref. 2), they were corrected for this effect. Table 3 summarizes the results and the corresponding results from reference 9 and formulas (4) and (7). Apparent is the very good correlation of the results of this work and reference 10, whereas those of reference 9 (fig. 8) appear low. The differences between the results of references 9 and 10 are strange because they are based on the same transformation equations; however, the reference points for defining the tooth deformation might be different. In general, the results using the compliance beam formulas herein and those of reference 10 agree within 20 percent, and for the tooth pair they agree within 1 percent.

Reference 12 presents the measured stiffness of a pair of standard form, steel gear teeth with the load at the pitch radius. The 20° pressure angle gears were $3/4$ -in. wide and had a diametral pitch of 3, one with 27 teeth and the other with 18 teeth. The measured stiffnesses at 1275 and 1492 lb tooth loads were 1.28×10^6 and 1.49×10^6 lb/in, respectively. The theoretical method herein gives tooth stiffnesses of 1.37 and 1.38×10^6 lb/in, respectively. The local flexibility represented about 25 percent of the overall flexibility. These results compare very favorably with the measured values, being only about 1 percent greater than their average value. This, coupled with the good correlation with the tooth pair results of reference 10 (see table 3) indicates the compliance method presented herein is probably as accurate as any available.

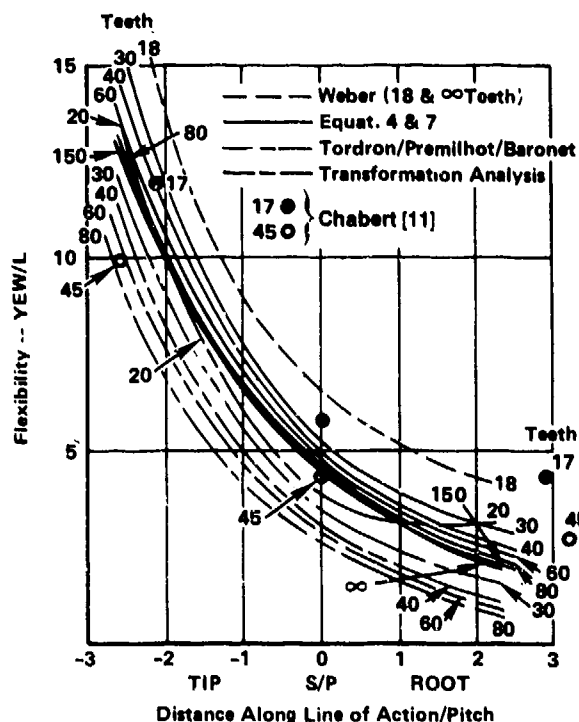


Figure 8. - Normalized beam displacement at load.
 $\phi_0 = 20^\circ$; $A = 1.0/P$; $D = 1.25/P$; $r = 0.38/p$;
 plane strain (refs. 9 and 10).

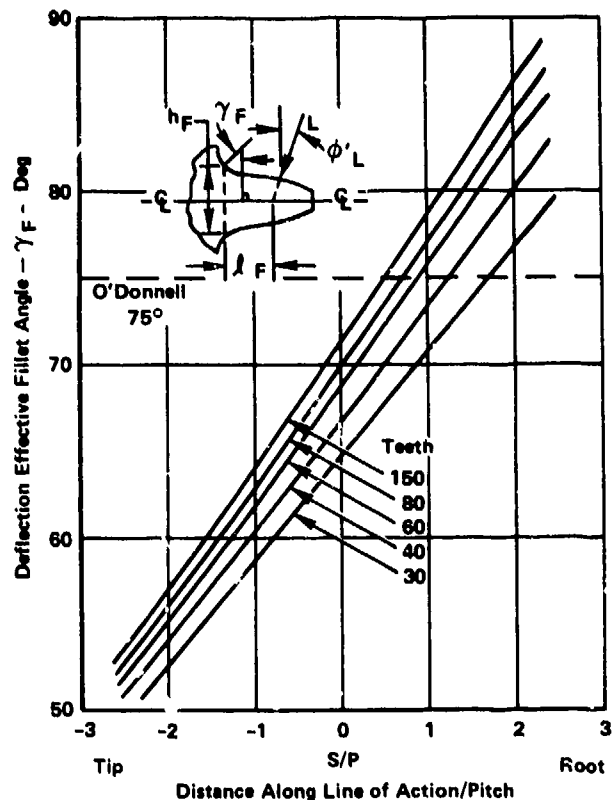


Figure 9. - Deflection effective fillet angle versus
 load position and gear teeth.

Table 3 Comparison of Tooth Beam Compliances: Full Depth, $P = 4$ Teeth; $\phi = 20^\circ$, $A = 1.0/P$, $D = 1.25/P$, $r = .38/P$; references [9 and 18]

Case		Deflection Under 1000 Lbs - 10^{-6} in.				Normalized Compliance - γ_T EW/L		
Tooth Combination Gear/Pinion	Load Position S/P	Chakraborty and Hunoshikatti (9)				Chakraborty & Hunoshikatti	Premilhet Tordion & Baronet	Equations 4&7
		$(\gamma_{T1} + \gamma_{T2})$	γ_{Local}	$(\gamma_{B1} + \gamma_{F1} + \gamma_{B2} + \gamma_{F2})$	$(\gamma'_{B1} + \gamma'_{F1})$			
30/30	0	431	139	292	146	4.37	3.40	5.25
50/50	0	380	102	278	139	4.16	2.90	4.85
70/70	0	405	96	309	154	4.61	2.70	4.50
30/30	2.5	741	135	606	—	(Pair) 18.2	(Pair) ~13.0	(Pair) 18.0

Gear Tooth Stress Sensitivity

Derivation of Stress Formula.

For incorporation in the High Contact Ratio Dynamic Gear Program (ref. 1) a gear tooth stress sensitivity or stress per load expression was needed that would be applicable for both LCRG and HCRG. After a review of various methods, it was decided that the Heywood formula (ref. 4) was the most viable; however, it was modified so that it could be more easily applied and yet give approximately the same stress sensitivities as the Kelley/Pederson and Heywood methods. References 13 and 4 had shown that these latter two methods correlate well with experimental and finite element analyses of standard gear teeth.

The modified Heywood formula for tooth stress sensitivity is

$$\frac{\sigma W}{L \cos \phi_L} = \left[1 + .26 \left(\frac{h_s}{2r} \right)^{.7} \right] \left[\frac{6l'_s}{h_s^2} \right. \\ \left. + \sqrt{\frac{.72}{h_s l_s}} \left(1 - \frac{h_t}{h_s} \nu \tan \phi'_L \right) - \frac{\tan \phi'_L}{h_s} \right] \quad (18)$$

①
②
③
④
⑤

where $\nu \approx 1/4$ per Heywood (ref. 4) and the rest of the nomenclature is defined in figure 10. The values of h_s , l'_s , and l_s are obtained from the gear tooth geometry, the load position, and the point of peak stress in the fillet defined by angle γ_s . This formula is based on simple stress analysis and uses parameters that are easier to define than those used in the Heywood (ref. 4) and Kelley/Pederson (ref. 13) formulas. Equation (18) consists of five factors, in order, ① stress concentration of the fillet, ② beam cantilever bending stress, ③ bending load proximity stress, ④ axial load proximity stress, and ⑤ axial stress. The formula logically makes the proximity effects die out as the bending and axial load get further from the fillet and closer to the neutral axis.

In contrast to the Heywood and Kelley/Pederson methods, for the modified Heywood method the position of the maximum stress in the fillet, which is defined by γ_s and determines the values of h_s , l'_s , and l_s , is determined by maximizing the stress neglecting the proximity terms in equation (18)—terms ③ and ④. This is done by taking the derivative of equation (18) without the proximity terms, setting it equal to zero, and solving for γ_s . The resulting transcendental equation is

$$\tan \gamma_{si+1} = (1 + .16A_i^{.7})A_i / \left[B_i (4 + .416A_i^{.7}) \right. \\ \left. - (1/3 + .016A_i^{.7})A_i \tan \phi'_L \right] \quad (19)$$

where $A_i = h_o/r + 2(1 - \cos \gamma_{si})$ and $B_i = l_o/r + \sin \gamma_{si}$. (See fig. 10.) Equation (19) can be easily solved by iteration in the given form by assuming a value for γ_{si} in the expressions for A_i and B_i and

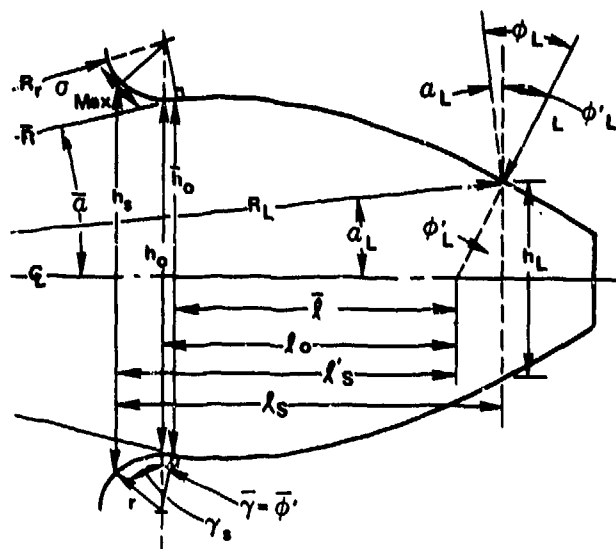


Figure 10. - Nomenclature for modified Heywood formula.

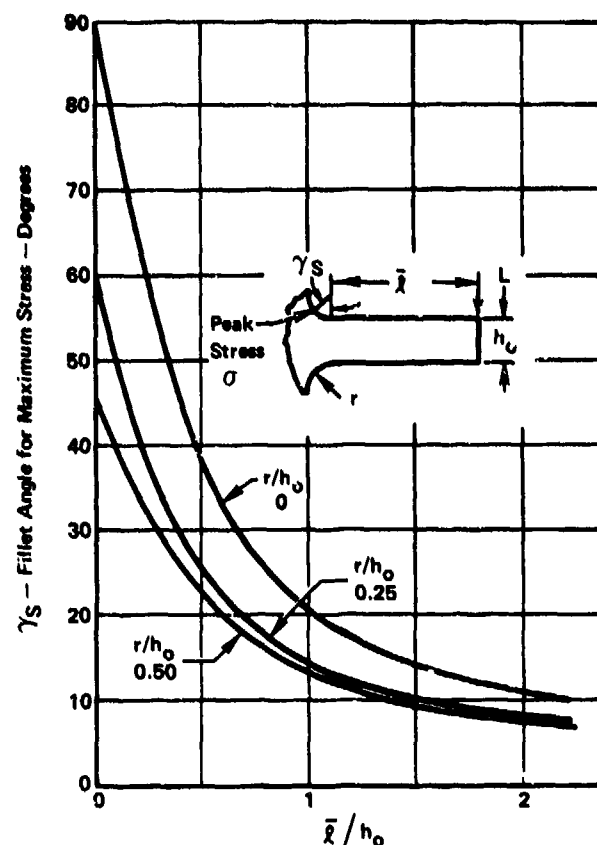


Figure 11. - Fillet angle for maximum stress versus geometry parameters \bar{l}/h_o and r/h_o .

solving for γ_{si+1} . Usually only two or three iterations are needed to obtain γ_s to within 0.1° . Some additional refinement of equation (19) should be done because it gives $\gamma_s \approx 0$ for very large values of l_o/r , whereas it should be about 20° . For short beams, such as gear teeth, this deficiency is probably minor.

Formula (19) was solved for the simple cantilever beam case with no axial load, that is, $\phi'_L = 0$. The position of the maximum stress as defined by angle γ_s is given in figure 11 as a function of fillet radius, r/h_o , and load position, \bar{l}/h_o . The results show that for typical LCRG values of r/h_o and \bar{l}/h_o , the angle of about 30° or so assumed by Heywood is a fairly reasonable average value. However, for HCRG with greater \bar{l}/h_o values, the magnitude of γ_s for maximum tooth stress should be considerably lower than that used by Heywood. Figure 11 shows that the smaller the fillet the higher up the fillet the peak stress occurs, which is consistent with Jacobson's test results given in reference 14 and Winter's test work in reference 18. In general, the point of peak stress varies significantly with load position and geometry and, therefore, should be included in the derivation of the stress sensitivity of gear teeth.

Evaluation of Stress Formula.

Various gear tooth designs were evaluated using the modified Heywood formulas (18) and (19) as well as those developed by Heywood (ref. 4) and Kelley/Pederson (ref. 13). Comparison of the results with photoelastic measurements is given in figure 12. This figure shows that all three methods do a good job in predicting the maximum tensile tooth stressing as a function of load position, geometry, and number of teeth. It appears that the modified Heywood method correlates slightly better than the other two in some instances. Because of this and its simplicity in defining the necessary parameters, its use is justified over the other methods. In general, the correlation with the photoelastic results are within about 5 percent, and slightly on the conservative side.

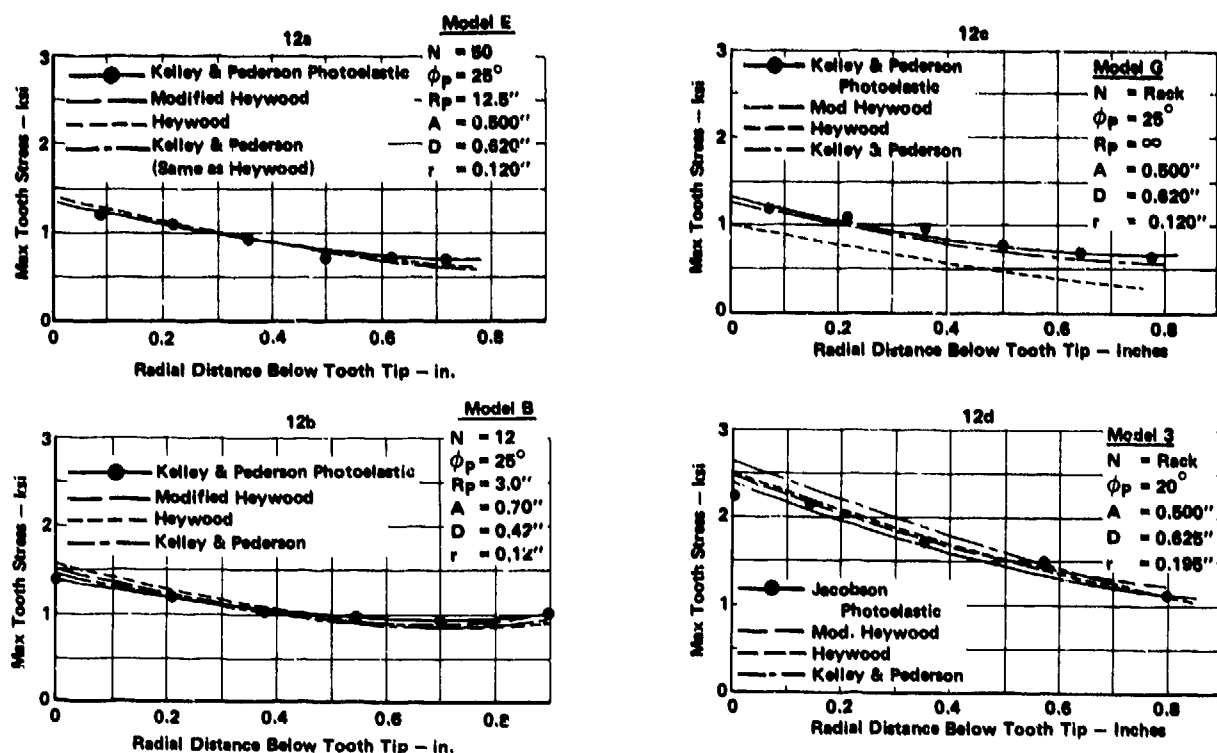


Figure 12. - Improved modified Heywood results versus photoelastic tests, Kelley/Pederson and Heywood.

Table 4 Comparison of Improved Modified Heywood and Exact Methods for Full Depth Involute Spur Gear Teeth: $A = 1/P$, $D = 1.25/P$, $r_{20} = .380/P$, $r_{25} = .433/P$; reference [15] +

Case		Pitch Line Loading $H_W = 0.0/P$				Tip Loading $H_W = 1.0/P$			
ϕ_p	Number of Teeth	Stress Factor J_t^+		Peak Stress $H_t \times P$		Stress Factor J_t^+		Peak Stress $H_t \times P$	
		"Exact" *	Modified Heywood	"Exact" *	Modified Heywood	"Exact" *	Modified Heywood	"Exact" *	Modified Heywood
20°	20	0.328	—	1.17	—	0.221	—	1.14	—
	30	—	0.378	—	1.11	—	0.223	—	1.01
	40	0.407	0.397	1.16	1.11	0.254	0.238	1.11	1.01
	60	0.462	0.443	1.15	1.12	0.289	0.249	1.11	1.01
	80	0.473	0.459	1.15	1.12	0.291	0.252	1.11	1.01
	150	0.483	0.480	1.14	1.13	0.286	0.260	1.09	1.00
25°	20	0.451	—	1.24	—	0.307	0.254	1.19	1.00
	30	—	0.498	—	1.13	—	0.280	—	1.00
	40	0.494	0.531	1.19	1.13	0.315	0.290	1.15	0.99
	60	0.517	0.565	1.17	1.13	0.317	0.298	1.14	0.99
	80	0.532	0.586	1.17	1.14	0.323	0.304	1.14	0.99
	150	0.569	0.608	1.17	1.14	0.336	0.307	1.14	0.99

+ $\sigma_t = L_t P/J_t W$; W = Width; P = Pitch; L_t = Tangent Load at Pitch Radius

Table 4 and figure 13 present the comparison of the stress sensitivities for a family of 20° and 25° pressure angle, full depth involute gear using the modified Heywood and an "exact" transformation analysis (ref. 15). In general, the trends with number of teeth, load position, and pressure angle are predicted by the modified Heywood formulas. For the 20° pressure angle gears, the pitch circle loading results correlate very well, but the tip loading results are about 10 percent

Table 5 Finite Element, Modified Lewis, and Modified Heywood Tooth Stressing: $R_p = 2.50"$, $\phi_p = 20^\circ$, $W = 1.0"$; $A = .25"$, $D = .289"$, $r = .060"$, $t_p = .390"$

Parameter See Figure 10	Finite Element & Impulse Test			Modified Lewis			Modified Heywood		
Load Position	1	2	3	1	2	3	1	2	3
R_L - in.	~ 2.70	~ 2.65	~ 2.40	~ 2.70	~ 2.65	~ 2.40	2.70	2.65	2.40
ϕ'_L - deg	27.10	18.83	6.62	27.10	18.83	6.62	27.15	18.86	6.68
h_g - in.	-	-	-	0.45	0.46	0.47	0.426	0.424	0.451
δ_g - in.	-	-	-	0.40	0.26	0.15	0.403	0.265	0.150
σ_t/L - psi/lb	16*	12.8*	10.6*	15.3	12.2	9.3	20.2	14.7	11.7
$(\gamma_g + \gamma')$ - deg	~ 10*	~ 30*	~ 45*	-	-	-	23.0	32.5	47.1

*Impulse Failure Test; *Below Surface 0.008"; Therefore Values Low

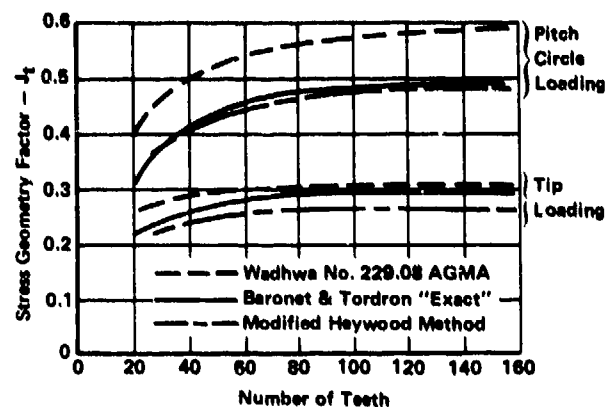


Figure 13. - Comparison of geometry factors from various formulas and "exact" analysis. $\phi_p = 20^\circ$; $P = 1$; $A = 1/P$; $D = 1.25/P$; $r = 0.38/P$; $\sigma = L_t P / J_t W$.

high, whereas the reverse is true for the 25° pressure angle gears. The "exact" analysis indicates the peak stress occurs further up the fillet than the modified Heywood analysis results. (See table 4.) The accuracy of the analytical function in defining the fillet region could influence its results and the correlation with the modified Heywood results.

Wallace and Seireg performed a finite element analysis of a gear tooth (ref. 16) and also conducted impulse strain gage tests of a standard, 4 pitch gear tooth. Comparison of their finite element results, those by the modified Lewis formula, and those by formulas (18) and (19) are summarized in table 5. This summary indicates that the modified Lewis results are a little low, particularly if the finite element results are corrected for the effect of element size. In contrast, the modified Heywood results are slightly higher, 10 to 20 percent, but this difference would be decreased if the effects of the coarse finite element mesh were taken into account. The locations of the peak stressing predicted by the modified Heywood method for the three tested tooth loading positions correlate well with those predicted by the modified Lewis method and the failure locations found during the impulse tests. Some of the discrepancy in the results between the two methods of analysis appears to be due to the definition of the tooth geometry. Although the distance from the load to peak stress, l_s , is about the same for the two methods, their respective tooth thicknesses, h_s , are about 5 percent different, which would account for about 10 percent of the differences in the stress sensitivities.

As a more fundamental check on the modified Heywood stress sensitivity analysis, it was used to calculate the maximum stress and its position for photoelastic models H and F tested by Dolan and Broghamer (ref. 17). The first model is a simple rectangular, cantilever beam loaded normally close to the fillet, $l/h_0 = 0.55$, whereas the second model is similar to the first but the beam is tapered 15° on each side with the load normal so as to introduce an axial compressive load. The photoelastic results for the first model gave a tensile stress sensitivity of $\sigma W/L = 6.20/\text{in.}$ and a maximum stress position at about 25° up the fillet. The modified Heywood method gives a stress sensitivity value of $6.06/\text{in.}$, 2 percent low, at an angle of 24° up the fillet. The photoelastic results for the second model gave a tensile stress sensitivity of $4.46/\text{in.}$ at about 35° up the fillet, whereas the modified Heywood method predicts values of $4.37/\text{in.}$ and 33° , respectively. The good correlation in magnitude and position of the maximum tensile stress shows that formulas (18) and (19) can handle accurately loads close to the fillet.

The importance of having an accurate method for calculating the maximum stress in various gear teeth was illustrated in reference 1. A comparison was made of the calculated tooth stress sensitivity versus load position for both HCRG and LCRG using various conventional and Heywood type analyses. The results, reproduced in figure 14, show that the three Heywood type analyses agree quite well with each other, whereas the usual Lewis and AGMA analyses give lower and significantly different results. The relative differences between the modified Heywood and the Lewis and AGMA results at the load position for maximum likely peak stress are quite different for LCRG and HCRG, being about 20 to 28 percent higher for the LCRG and only about 10 to 18 percent higher for the HCRG, respectively. Such differences would have significant effect on the tooth bending fatigue life.

Improvements in Dynamic Gear Program

The High Contact Ratio Dynamic Gear Program developed and discussed in reference 1 already incorporated the stress sensitivity formula developed herein. However, the program since has been improved by including a preprocessor which defines the gear tooth structural and manufacturing parameters from a few simple input parameters and calculates the gear tooth pair compliance based on the equations developed herein. A postprocessor has been added which calculates the design outputs of PV, Hertz stress, flash temperature, load, and stressing for the two gears. In addition, the formulation of the basic program was expanded to include centerline error, which affects the pressure angle and length of engagement, and a three term definition of tooth profile relief, Δ , rather than a two term expression (see ref. 1), for example, for engagement

$$\Delta_e = C_e (S_{oe} - S_e)^2 [1 + \bar{\gamma}_e (S_{oe} - S_e)] \quad (20)$$

in place of

$$\Delta_e = C_e (S_{oe} - S_e)^2$$

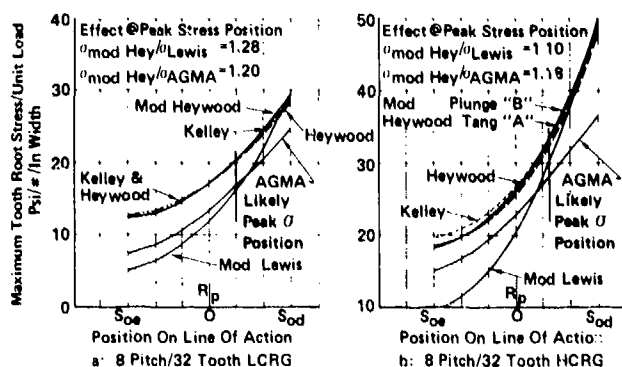


Figure 14. - Comparison of gear tooth stress sensitivities for different analysis methods.

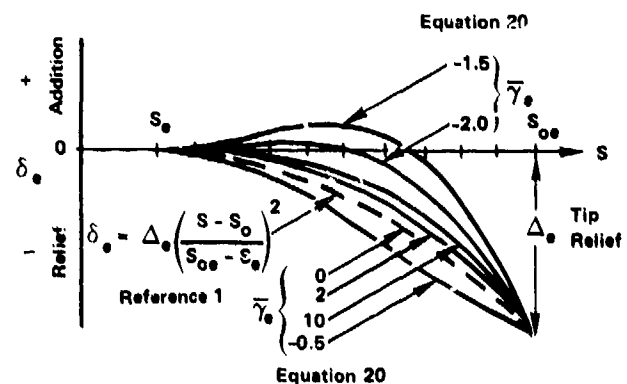


Figure 15. - Tooth profile modification shapes; engagement cam.

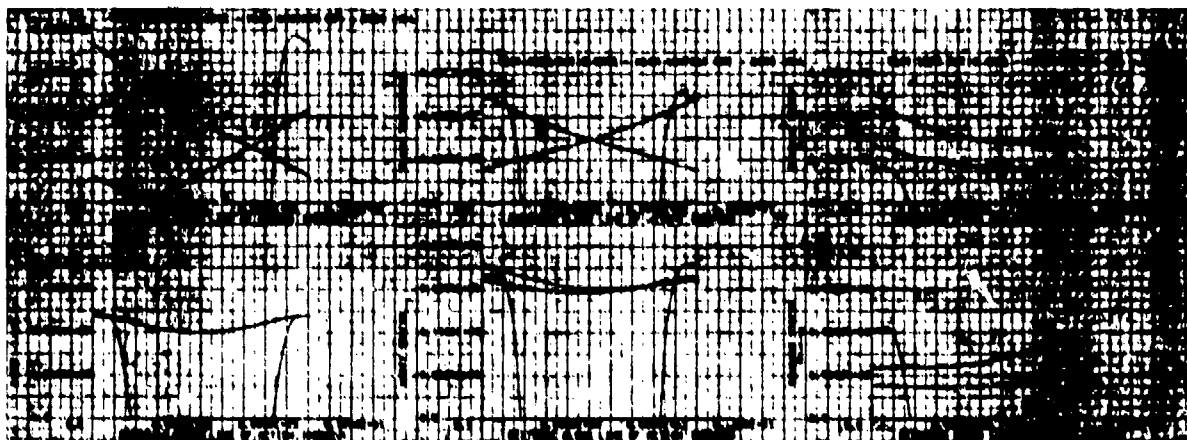


Figure 16. - Dynamic tooth loads and stressing for HCRG-no tooth error case: 2.2 contact ratio, 8 pitch, 20° pressure angle; 5000 in-lb torque; 44/52 gear ratio; 6-in. center distance; ref. 1 analysis.

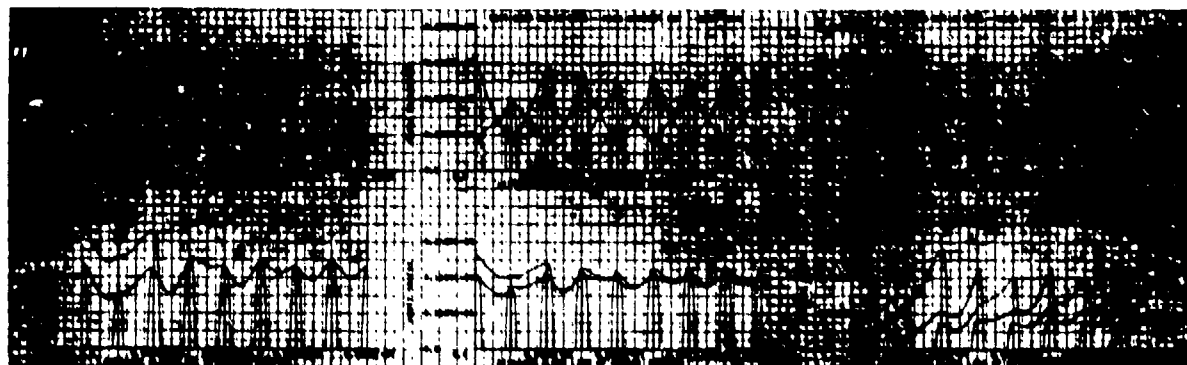


Figure 17. - Dynamic tooth loads and stressing for HCRG-tooth error case: 2.2 contact ratio, 8 pitch, 20° pressure angle; 5000 in-lb torque; 44/52 gear ratio; 6-in. center distance; ref. 1 analysis.

The effect of this additional parameter γ_e on the allowable profile or cam shapes is shown in figure 15. Figures 16 and 17 are examples of the plotted outputs for the improved program. The first figure depicts the results for an HCRG, 8 pitch, 44/52 tooth pair with a nominal 2.20 contact ratio, a 20° pressure angle, and no tooth error under 5000 in.-lb. of torque. The second figure is for the same gear pair but with tooth spacing error and is for eight mesh cycles.

Conclusions

Formulas have been developed based on work done by Heywood (ref. 4), Weber (ref. 2) and O'Donnell (ref. 3) for the stress sensitivity and compliance of low and high contact ratio, involute, spur gear teeth. The parameters used in these formulas require the derivation of the effective fillet length or angle rather than assuming particular values as done by Heywood (ref. 4) and O'Donnell (ref. 3). The stress sensitivity formula is a modified version of the Heywood formula, using simple beam parameters. The compliance formula uses O'Donnell's foundation flexibility factors and Weber's local contact compliance.

The modified Heywood gear tooth stress sensitivity formula was evaluated by comparing its predicted results with test, finite element, and analytic transformation results for gears with various

pressure angles, tooth proportions, number of teeth, and load contact position. In general, the formula predicts the maximum tensile fillet stress within about 5 percent and gives the proper trends with contact position, number of teeth, and tooth geometry. It also predicts fairly well the location of the peak stress in the fillet. Comparison with similar formulas by Kelley/Pederson and Heywood show good correlation, but with the proposed modified Heywood method giving slightly more consistent results as well as being easier to use.

The beam and foundation portion of the gear tooth compliance formula was evaluated using available test, finite element, and analytic transformation results and found to correlate quite well. The inclusion of a derived, variable effective fillet length or angle appears to improve upon the results which assumed a given effective fillet length. In general, the combined beam and foundation deflection as a function of gear teeth and load contact position agreed well with other methods. The Weber method of calculating the local contact deflection is universally used and was found to give more consistent results than two other methods. The gear tooth pair compliance formula was found to predict the overall compliance (beam + foundation + local) consistent with the test results of Howland.

In summary, although further evaluation of the gear tooth stress sensitivity and compliance formulas presented herein might be desirable, the evaluation results indicate that the formulas predict the spur gear tooth pair stress sensitivity and compliances quite well.

↑

References

1. Cornell, R. W.; and Westervelt, W. W.: Dynamic Tooth Loads and Stressing for High Contact Ratio Spur Gears. *J. Mech. Des.*, vol. 100, Jan. 1978.
2. Weber, C.: The Deformations of Loaded Gears and The Effect on Their Load-Carrying Capacity. Sponsored Research (Germany), British Dept. of Scientific and Industrial Research, Report No. 3, 1949.
3. O'Donnell, W. J.: Stress and Deflection of Built-in Beams. ASME Paper No. 62-WA-16, 1974.
4. Heywood, R. B.: Designing by Photoelasticity, Chapman and Hall, Ltd., 1952.
5. Metusz, J. M.; O'Donnell, W. J.; and Erdloc, R. J.: Local Flexibility Coefficients for the Built-in Ends of Beams and Plates. *J. Eng. Ind.*, Aug. 1969.
6. Laskin, I.; Orcut, F. K.; and Shipley, F. F.: Analyses of Noise Generated by UH-1 Helicopter Transmission. USAAVLABS Tech. Report 68-41, June 1968.
7. Cooper, D. H.: Hertzian Contact Stress Deformation Coefficients. ASME *J. Appl. Mech.*, June 1969.
8. Durocher, L. I.; Kosh, W. S.; and Wongphadung, S.: Design Considerations in Force-Deflection Retentions of Cantilever Beams. ASME Paper No. 77-DE-50, May 1977; and supporting information from L. I. Durocher, June 29, 1977.
9. Premilhot, A.; Tordion, G. V.; and Baronet, C. N.: An Improved Determination of the Elastic Compliance of a Spur Gear Tooth Acted on by a Concentrated Load. ASME Paper 72-PTG-9, Oct. 1972.
10. Chakraborty, J.; and Hanoshikatt., H. G.: Determination of the Combined Mesh Stiffness of a Spur Gear Pair Under Load. ASME Paper 74-DET-39, 1974.
11. Chabert, G.; Dang Tran, T.; and Mathis, R.: An Evaluation of Stresses and Deflection of Spur Gear Teeth Under Strain. ASME, *J. Eng. Ind.*, Feb. 1974.
12. Howland, J. S.: An Investigation of the Dynamic Loads in Spur Gear Teeth. Masters Thesis-MIT Report, Feb. 1962.
13. Kelley, B. W.; and Pederson: The Beam Strength of Modern Gear Tooth Design. SAE Trans., vol. 66, 1958.
14. Jacobson, M. A.: Bending Stresses in Spur Gear Teeth: Proposed New Design Factors Based on a Photo-Elastic Investigation. *Proc. Inst. Mech. Eng.*, vol. 169, no. 31, 1955, pp. 587-609.
15. Baronet, C. N.; and Tordion, G. V.: Exact Stress Distribution in Standard Gear Teeth and Geometry Factors. ASME, *J. Eng. Ind.*, Nov. 1973.
16. Wallace, D. B.; and Seireg, A.: Computer Simulation of Dynamic Stress, Deformation, and Fracture of Gear Teeth. *J. Eng. Ind.*, Feb. 1974.
17. Dolan, T. J.; and Broghamer, E. L.: A Photoelastic Study of Stresses in Gear Tooth Fillets. University of Illinois Engineering Experimental Station Bulletin No. 335, 1942.
18. Winter, H.; and Hirt, M.: The Measurement of Actual Strains at Gear Teeth, Influence of Fillet Radius on Stresses and Tooth Strength. *J. Eng. Ind.*, Feb. 1974.

Appendix—Definition of Different Gear Tooth Forms

General equations are given which define the involute tooth form based on pitch, P ; pitch pressure angle ϕ_p ; pitch radius, R_p ; circular pitch tooth thickness t_p ; root radius, R_r ; fillet radius, r ; and tooth width, W . The load position on the tooth can be defined in terms of the distance along the line of action from the pitch circle, S , or by the contact or load radius R_L (fig. 2). Knowing these eight quantities, the basic tooth parameters common to all three tooth forms (fig. 1), are

$$\text{number of teeth: } N = 2PR_p$$

$$\text{base radius: } R_B = R_p \cos \phi_p$$

$$\text{base radius included tooth angle: } \alpha_B = t_p/2R_p + \tan \phi_p - \phi_p$$

$$\text{contact radius: } R_L^2 = S^2 + 2R_p \sin \phi_p S + R_p^2$$

$$\text{contact pressure angle: } \cos \phi_L = R_B/R_L$$

$$\text{contact included tooth angle: } \alpha_L = \alpha_B - \tan \phi_L + \phi_L$$

$$\text{contact tooth thickness: } h_L = 2R_L \sin \alpha_L$$

$$\text{contact load angularity with } L: \phi'_L = (\phi_L - \alpha_L)$$

Gear Tooth Form S; standard case: $R_r^2 + 2rR_r \geq R_B^2$ (fig. 2)

$$\bar{R}^2 = (R_r + r)^2 - 2r\sqrt{(R_r + r)^2 - R_B^2} + r^2$$

$$\cos \bar{\phi} = R_B/\bar{R}$$

$$\bar{\alpha} = \alpha_B - \tan \bar{\phi} + \bar{\phi}$$

$$\bar{h} = 2\bar{R} \sin \bar{\alpha}$$

$$\bar{\gamma} = \phi' = (\bar{\phi} - \bar{\alpha})$$

$$l_o = [R_L \cos \alpha_L - (h_L \tan \phi'_L)/2 - (\bar{R} \cos \bar{\alpha} + r \sin \bar{\gamma})] \text{ (stress)}$$

$$h_o = 2\bar{R} \sin \bar{\alpha} - 2r(1 - \cos \bar{\gamma}) = \bar{h} - 2r(1 - \cos \bar{\gamma})$$

The term γ_s is iterated using equation (19).

$$h_s = h_o + 2r(1 - \cos \gamma_s)$$

$$l'_s = l_o + r \sin \gamma_s$$

$$l_s = l'_s + (h \tan \phi'_L)/2$$

The term γ_F is iterated using equation (7) as in.

$$X = R \cos \alpha - \bar{R} \cos \bar{\alpha}$$

$$\bar{l} = R_L \cos \alpha_L - (h_L \tan \phi'_L)/2 - R \cos \bar{\alpha} \text{ (compliance)}$$

The term R'_L is iterated until $(R_L \cos \alpha'_L - \bar{R} \cos \bar{\alpha}) = \bar{l}$.

$$h'_L = 2R'_L \sin \alpha'_L$$

Gear Tooth Form A; tangent Case: $R_r^2 + 2rR_r < R_B^2$ (fig. 18(a))

$$\bar{\gamma} = \alpha_B$$

$$\sin \alpha_r = r/(R_r + r)$$

$$h_o = 2(R_r + r) \sin (\alpha_B + \alpha_r) - 2r$$

$$l_o = R_L \cos \alpha_L - (h_L \tan \phi'_L)/2 - (R_r + r) \cos (\alpha_B + \alpha_r)$$

$$h_B = 2R_B \sin (-\bar{\gamma}) = 2R_B \sin \alpha_B$$

Between the tangency point of the fillet and base circle, for example, $\bar{R} \leq R \leq R_B$,

$$h = \frac{h_B}{R_B} \left[(R_r + r) / \cos \alpha_r + X / \cos \bar{\gamma} \right]$$

$$= h_B \frac{R}{R_B}, \text{ where } X = (R - \bar{R}) \cos \alpha_B$$

α_s is iterated using equation (19), and h_s , l'_s , and l_s are the same as for form S

α_F is iterated using equation (7), but including additional beam section $(R_B - \bar{R}) \cos \alpha_B$

Gear Tooth form B, parallel case: $R_r^2 + 2rR_r < R_B^2$ (fig. 18(b))

$$\bar{\gamma} = -\bar{\theta}$$

$$\bar{\theta} = \pi/N \text{ or } 180^\circ/N$$

$$\delta = R_B \sin (\bar{\theta} - \alpha_B) - R$$

$$\Delta = R_B \cos (\bar{\theta} - \alpha_B) - (R_r + r)$$

$$l_o = R_L \cos \alpha_L - R_B \cos \alpha_B + \Delta \cos \bar{\theta} + r \sin \bar{\theta} - (h_L \tan \phi'_L)/2$$

$$h_o = h_B - 2 \Delta \sin \bar{\theta} - 2r(1 - \cos \bar{\theta})$$

$$h_B = 2R_B \sin \alpha_B$$

Between the tangency point of fillet and base circle, for example, $0 < X < \Delta \cos \bar{\theta}$,

γ_s is iterated using equation (19), and h_s , l'_s , and l_s are the same as for form S.

γ_F is iterated using equation (17) but including beam section $\Delta \cos \bar{\theta}$

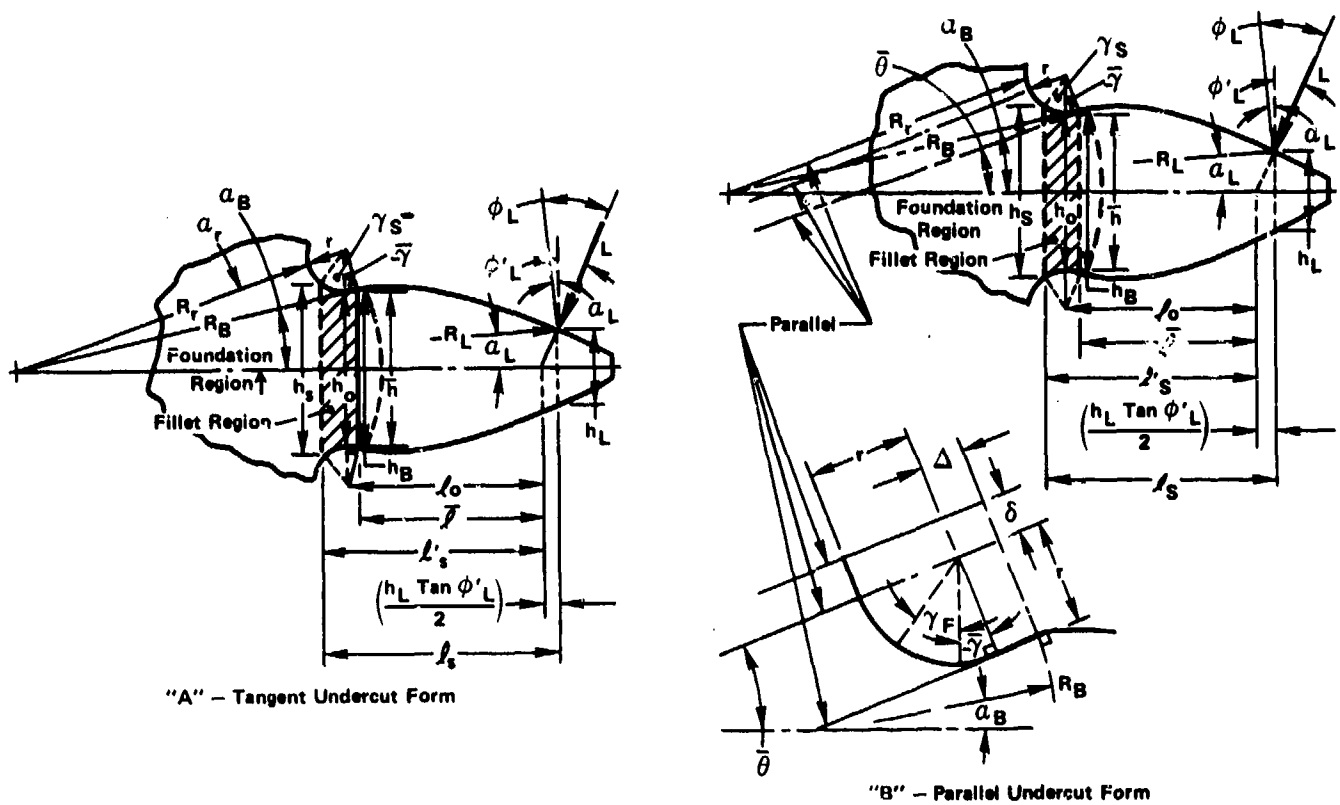


Figure 18. - Fillet regions for tooth forms A and B.

A Method for Static and Dynamic Load Analysis of Standard and Modified Spur Gears*

Romualdas Kasuba†

Many advanced technology applications have a general requirement that the power to transmission weight be increased. Engineers, as a result of those requirements, attempt to design gear systems to maximum load capacity. For this purpose the ability to accurately calculate the dynamic loads becomes essential for advanced transmission design. Most of the previously proposed methods (refs. 1 to 8) are limited to the normal contact ratio (NCR) gearing and are based on a number of simplifications, which can be generalized as follows:

(a) Gear-tooth errors have negligible or no effect on mesh stiffness. This implies that, for a given load, a gear with errors will have equal mesh stiffness as the same gear without errors.

(b) Contact is assumed to occur only on the line of action.

(c) The contact ratio (CR) and/or mesh stiffness are not affected by transmitted load or premature or delayed engagement.

(d) Dynamic simulations use uninterrupted periodic rectangular stiffness functions and error displacement strips.

The high-contact-ratio (HCR) gearing is also considered for many applications. However, the number of available methods for analyzing the HCR gearing is very limited. A parametric static analysis of HCR gearing was published by Staph (ref. 9) in 1975. A Richardson-type cam model was extended by Cornell and Westervelt in 1977 (ref. 10). In 1980 Kasuba and Evans presented an extended digitized model for determining the gear-mesh stiffness and dynamic loads for any operational contact ratio (ref. 11). This method removes the previously listed simplifications mentioned in the previous paragraph. In this case the variable gear-mesh stiffness is determined by solving the statically indeterminate problems of multipair contact gear-tooth error effects on contacting point locations and gear-tooth and gear-hub deflections. Importantly, this method does not rely on the commonly used assumption that a gear pair with errors has the same gear-mesh stiffness as an identical pair without errors. Such an assumption would be completely unacceptable in analysis of HCR gearing. Gear-tooth errors can cause interruptions of gear-mesh stiffness and, thus, affect the dynamic loads in gearing. Identical gear-tooth errors in the NCR and HCR spur gearing affect the mesh stiffness and dynamic loads to different degrees. This paper discusses the mesh stiffness and dynamic load characteristics for several cases of the NCR and HCR gearing. The considered contact ratios were grouped in the general range of 1.7, 2.0, and 2.3.

In this study the HCR gearing is defined by contact ratios equal to or greater than 2.0. The HCR gearing in this study is represented by a group of small pressure angle, fine pitch, and long addendum gearing.

Nomenclature

BGM	backlash
C	center distance
C_B	bearing damping
C_S	shaft damping
CR	loaded contact ratio
CR_T	theoretical contact ratio
DF	dynamic load factor

*This paper is based in part on work supported by NASA Lewis Research Center and the U.S. Army Aviation Research and Technology Laboratories under NASA contract NAS3-18547.

†Fenn College of Engineering, Cleveland State University.

E	Young's modulus
F	gear face width
F_H	hub face width
G	torsional modulus
GP	gear-tooth pair
HSF	hub torsional stiffness factor
J	mass moment of inertia
J_G	$\frac{1}{2} M_G / (RBC)^2$
K	shaft stiffness
KG	gear-mesh stiffness, N/m
KP	gear pair stiffness, N/m
M	mass
P_H	Hertz stress
PE	profile error
PM	profile modification
PSITP	static angular position
PV	$P_H \times C$, N/m sec
Q	static GP load, normal
Q_t	total mesh static load, normal
QD	dynamic GP load, normal
QD_t	total mesh dynamic load, normal
RA	roll angle
RABOT	RA at bottom of involute
RAPP	RA at pitch point
RATIP	RA at tip of involute
RBC	radius of base circle
RCCP	radius of curvature
RCP	radius to contacting point
RH_f	hub fixity radius
RRC	radius of root circle
TR	transmission ratio
V	sliding velocity
μ	Poisson's ratio
δ	deflection
ξ	critical damping ratio, gear mesh
ξ_s	critical damping ratio, shafts
ψ	dynamic displacement, rad
$\dot{\psi}$	dynamic velocity, rad/sec

Subscripts:

D	driving element
G	gear
HRC	high contact ratio gearing
i	mesh arc position
k	k^{th} gear-tooth pair
L	load element
NCR	normal contact ratio gearing

S shafting
 1 gear 1
 2 gear 2
 ' instantaneous

Definition of Spur Gear Tooth Profiles and Coordinates

The variable gear-mesh stiffness is a function of load, errors, position of contact, gear and hub geometry, and respective deflections. For this purpose the actual gear-tooth profiles must be used. By employing the involute chart approach (figs. 1 to 3), a number of gear-tooth profiles can be

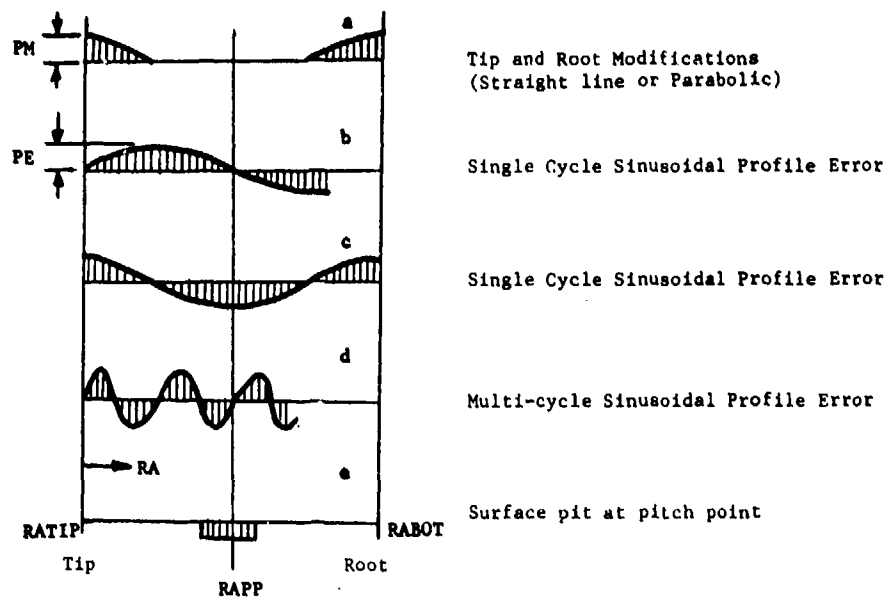


Figure 1. - Sample simulated gear tooth profile charts.

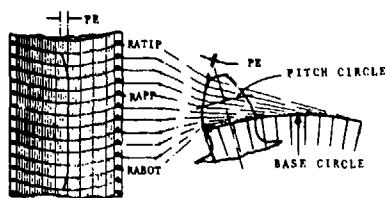


Figure 2. - Involute chart - profile relationship.

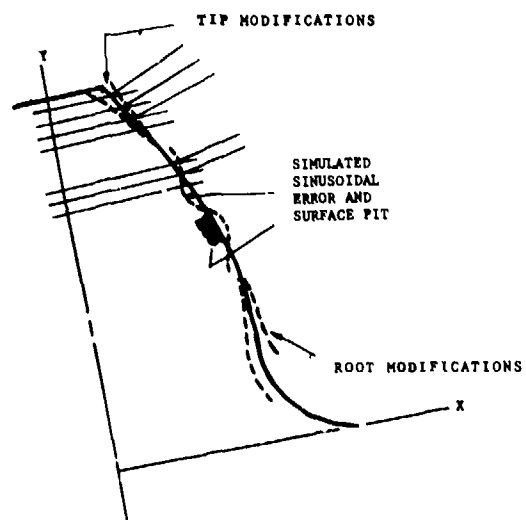


Figure 3. - Gear tooth profiles.

defined. The profile modifications (PM) and profile errors (PE) can be expressed as

$$\Delta M = \delta P(RA) \quad (1)$$

where

ΔM deviation from the line of action

RA roll angle limited to active profile

δP profile variation (error or amount of modification) as a function of RA

A true involute profile is defined by

$$\Delta M = \delta P(RA) = 0$$

(straight line in involute chart).

For example, the simulated profile chart can accommodate the parabolic and straight-line modifications of the tip and root zones (fig. 1(a)). The profile errors can be approximated by sinusoidal representation. By varying the number of cycles and phase angle, the sinusoidal profile errors (figs. 1(b) to (d)) could describe a large number of practical and theoretical cases. A simulated surface pitting damage is shown in figure 1(e). The defined surface faults and their respective involute charts are then numerically transferred to the previously digitized true involute profile. This is accomplished by subtracting or adding the specified amounts of material perpendicularly to the true involute profile, as shown in figures 2 and 3.

The digitized profile points and the subsequent deflections were analyzed in a rotating gear pair coordinate system. The position of contacting points, number of contacting tooth pairs, operational contact ratio, and variable gear-mesh stiffness were established by iterative procedures under fully loaded and deflected conditions. Five gear-tooth pairs are analyzed in search of potential contacting points. Figure 4 illustrates the general gear and gear-tooth coordinate system. For establishing the points of contact, load transfers, and deflections within the mesh arc, three coordinate systems are used:

(1) U, V —Fixed global coordinate system for the pinion and gear-tooth profiles, gears 1 and 2, respectively. The U, V coordinate system is used to determine the number of contacting pairs and position of contacting points.

(2) X, Y —Local coordinate system fixed at the root of individual teeth for the pinion and gear, respectively. The Y -axes coincide with the tooth centerlines. The X, Y coordinate system is used in digitizing the profiles and for determining the appropriate deflections of the teeth.

(3) W, Z —Intermediate coordinate system rotating with the pinion and gear, respectively. The origins of the W, Z coordinate systems for each gear are at the respective gear centers. The Z -axes coincide with the tooth centerlines.

The transformations between the coordinate systems for each considered gear pair ($k = 1, 2$) are

$$W1 = X1; W2 = X2(2)$$

$$Z1 = Y1 + RR01; Z2 = Y2 + RR02$$

$$U1 = W1 \sin \text{PSI1TP}(k) + Z1 \cos \text{PSI1TP}(k) \quad (2)$$

$$V1 = -W1 \cos \text{PSI1TP}(k) + Z1 \sin \text{PSI1TP}(k)$$

$$U2 = -W2 \cos (\text{PSI2TP}(k) - 1.5 \pi) + Z2 \sin \text{PSI2TP}(k) - 1.5 \pi$$

$$V2 = C - [W2 \sin (\text{PSI2TP}(k) - 1.5 \pi) + Z2 \cos (\text{PSI2TP}(k) - 1.5 \pi)]$$

Determination of Gear Tooth Deflections and Gear Mesh Stiffness

The digitized profile points describe each gear tooth in space and include the profile errors and modifications. In the iteration process the digitized points also incorporate the appropriate

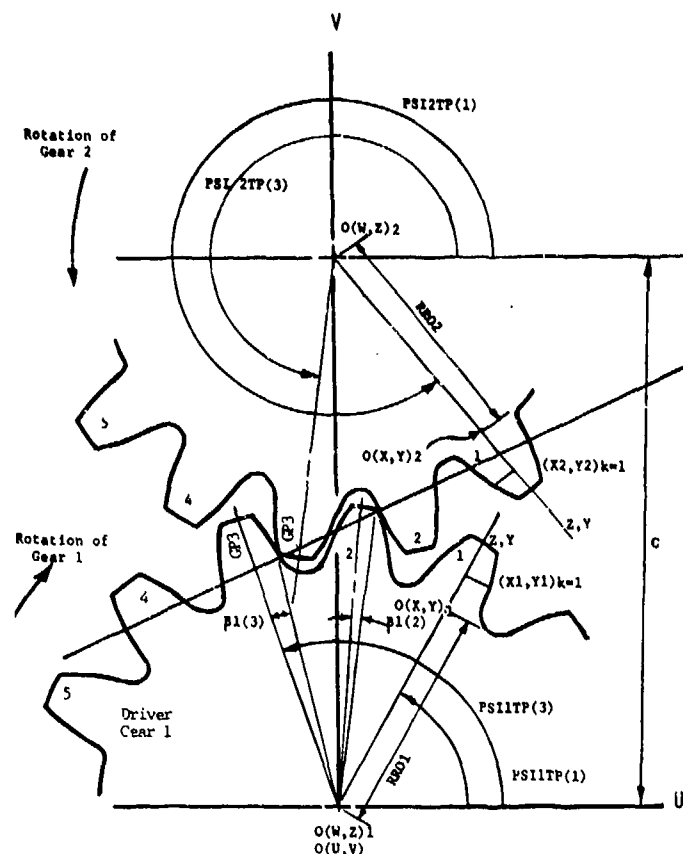


Figure 4. - Gear tooth coordinate system.

deformations to simulate the noninvolute action caused by gear-tooth deflections.

The contacting points on the gear teeth and the number of contacting gear-tooth pairs are determined by using a three-step process. First, the gears are preloaded by a unit load and rotated by incrementing the $PSI1TP(k)$ and $PSI2TP(k)$ angles and examining the potential contact between the calculated $(U1(k), V2(k))$ profile points for five gear-tooth pairs. The beginning and the end of the meshing arc are established by tracking gear pair 3 (GP3) through its complete meshing arc. After the limiting points of mesh arc are determined, the mesh arc is divided into 50 segments. Next, the gears are fully loaded for further analysis. The actual load sharing and deflections are calculated for 50 arc segments by tracking the movement of fully loaded gears through the established mesh arc.

The gear-tooth pair deflection $(k)_i$ can be expressed in the following form:

$$\delta(k)_i = \delta_1(k)_i + \delta_2(k)_i + \delta_H(k)_i \quad (3)$$

where

$\delta_1(k)_i$ deflection of the k th tooth of gear 1 at mesh arc position i

$\delta_2(k)_i$ deflection of the k th tooth of gear 2 at mesh arc position i

$\delta_H(k)_i$ localized Hertz deformation at the point of contact

For the contacting pairs the gear-tooth deflections $\delta_1(k)_i$ and $\delta_2(k)_i$ incorporate a number of constituent deflections:

$$\delta_1(k)_i = \delta_{M1}(k)_i + \delta_{N1}(k)_i + \delta_{S1}(k)_i + \delta_{B1}(k)_i + \delta_{R1}(k)_i \quad (4)$$

and similarly for gear 2. In equation (4)

- δ_M gear-tooth deflection due to bending
- δ_N gear-tooth deflection due to normal force
- δ_S gear-tooth deflection due to shear force
- δ_B gear-tooth deflection due to deformation of surrounding hub area (rocking action)
- δ_R gear-tooth deflection due to gross torsion of the rim or hub

The general gear-tooth deflection model is shown in figure 5. Numerical integration of digitized gear-tooth slices was used to obtain the δ_M , δ_N , and δ_S deflections. The circumferential deformation of the gear hub and deformation of the adjacent part of the gear body were reflected to the contacting point as (δ_R) and (δ_B) deflections, respectively.

The methods for calculating the δ_B and the localized Hertzian deflection δ_H are amply described in references 13 to 15. The δ_R deflections cannot be easily defined. Following the method of reference 14, these deflections can be approximated by employing equation (5). For gear 1

$$\delta_{R1}(k)_i = \frac{Q(k)_i (RCP1(k)_i)^2 \cos \alpha_{B1}}{4 \times G1(FH1)} \left[\left(\frac{1}{RH1_f} \right)^2 - \left(\frac{1}{RH1_o} \right)^2 \right] \quad (5)$$

where

- $Q(k)_i$ load along instantaneous line of action at contact point, k^{th} pair
- $RCP1(k)$ radius to the contacting point (gear 1) k^{th} pair (fig. 6)
- FH1 hub face (gear 1)
- $RH1_o$ outside hub/rim radius (gear 1)
- $RH1_f$ effective radius of circumferential hub fixity (gear 1)
- G1 torsional modulus of elasticity (gear 1)

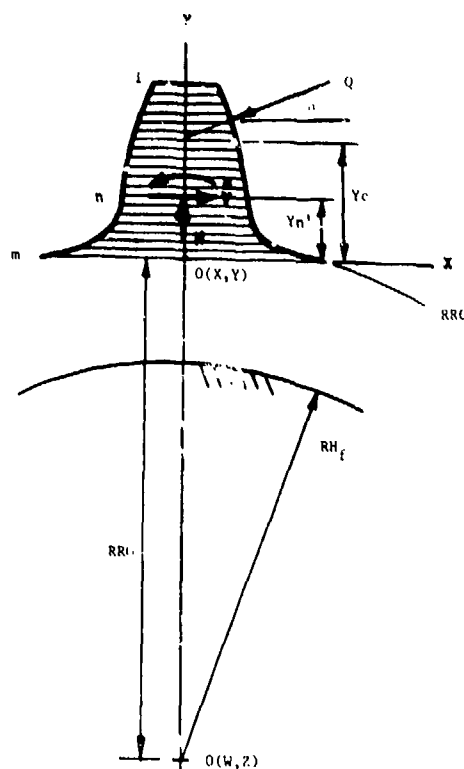


Figure 5. - Gear tooth deflection model.

angular position i , then the contact will be established for GP2. In this case the final load sharing and deflections will be recalculated on the basis of three contacting pairs (step 3). These calculation methods can handle both the involute and noninvolute gear actions, HCR gearing, etc.

The individual gear-tooth pair stiffness can be expressed as

$$KP(k)_i = \frac{Q(k)_i}{\delta(k)_i} \quad (7)$$

If the effective errors prevent contact, $KP(k)_i = 0$. The sum of gear-tooth pair stiffnesses for all pairs in contact at position i represents the variable mesh stiffness (KG),

$$KG_i = \sum_{k=1}^K KP(k)_i \quad (8)$$

The load carried by each of the pairs moving through the mesh arc in the static mode can be determined as

$$Q(k)_i = \frac{KP(k)_i}{KG_i} (Q_i) \quad (9)$$

where Q_i is the total normal static load carried by the gears at any mesh position i in the static mode. For any mesh arc position i , the calculated K^{th} gear-tooth pair stiffness $KP(k)_i$, mesh stiffness KG_i , and load sharing incorporate the effects due to manufactured profile errors, profile modifications, and deflections by means of the iterated numerical solutions of equations (3) to (9).

Deflections and profile faults will cause gears to contact away from the theoretical line of action.

For the instances when the contact points are not on the theoretical lines of action (nonconjugate action), we must refer to instantaneous pressure angles, instantaneous lines of action, and transmission ratios. The need for instantaneous lines of action was indicated in references 11 and 12. Figure 6 is used to define the instantaneous parameters (designated by ') for the contact point A' (defined by UCP(k), VCP(k) in the U, V coordinate system). For example, the distance to the instantaneous pitch point PP' is

$$PPD' = \frac{RBC1}{\cos \alpha'} \quad (10)$$

where α' is the instantaneous pressure angle

$$\alpha' = \alpha_{A1} + \alpha_{B1} \quad (11)$$

where

$$\alpha_{A1} = \arcsin (UCP(k)/RCP1)$$

$$\alpha_{B1} = \arctan (RCCP1/RBC1)$$

Again, using figure 6, the instantaneous transmission ratio is

$$TR' = \frac{C - PPD'}{PPD'} \quad (12)$$

The involute (theoretical) transmission ratio is

$$TR = \frac{RPC2}{RPC1} \quad (13)$$

The instantaneous base circle (gear 2) is

$$RBC2' = RBC1 \times TR' \quad (14)$$

The equivalent instantaneous radius of curvature (gear 1) is

$$RCCP1' = \sqrt{(RCP1)^2 - (RBC1)^2} \quad (15)$$

And the equivalent instantaneous radius of curvature (gear 2) is

$$RCCP2' = \sqrt{(RCP2)^2 - (RBC2')^2} \quad (16)$$

The same procedure is used for determining the instantaneous parameters as the above gear pair k traverses the mesh arc and, similarly, for other gear pairs. The instantaneous transmission ratio TR' is influenced by the deformations in the contact zone and tooth profile errors. It is important to note that for no-load and no-surface fault conditions $TR' = TR$, and similar analogy exists for other parameters.

Discussion of Gear Mesh Parameters

The performed analyses have indicated that the gear-hub flexibility can have a significant effect on the operational gear-mesh stiffness, KG . The hub stiffness factor (HSF) will be used to indicate a degree of influence of the hub flexibility on the overall gear-mesh stiffness.

$$HSF = \frac{KG_{\max}}{KG_{\max}^*} \quad (17)$$

where

KG_{\max} maximum attainable gear mesh stiffness with designated hubs

KG_{\max}^* maximum gear-mesh stiffness with torsionally rigid max hubs, circumferential fixity at the gear root circle

The torsionally rigid hubs can be theoretically obtained when the radius of circumferential or torsional fixity will coincide with the root circle. The opposite case can be visualized with the thin hubs being fixed to small shafts. A combination of rigid hubs for both gears is identified by $HSF = 1.0$.

Tables 1 and 2 indicate substantial changes in the contact ratio with increasing loads and/or gear-hub flexibilities. By increasing the hub torsional flexibility (lower HSF), the contact ratio increases, the variation of the instantaneous transmission ratio (TR') increases, and the sensitivity to gear-tooth errors decreases. The opposite occurs by decreasing the hub flexibility. The gear-tooth contacts due to deflections and errors may occur off the theoretical line of action, thus affecting the transmission ratio. The ΔTR can be viewed as a percent change in the output torque. The approximate variation (cycling) of TR' is illustrated in figure 7. The maximum variation in TR' is defined as $\Delta TR'$.

Various profile errors, pitting, and the previously discussed hub flexibility can affect the mesh stiffness characteristics to varying degrees. A case where only one of the meshing gears has surface

TABLE 1. - EFFECTS OF GEAR FLEXIBILITY ON MESH STIFFNESS, TRANSMISSION RATIO, AND CONTACT RATIO
[All gears without errors or modifications $RH1_f$, $RH2_f$ = torsional fixity radius; gears 1, 2.]

$RH1_f$, mm	$RH2_f$, mm	KG_{\max} , N/m	$KG_{f,2}$, N/mm ²	HSF	ΔTR , percent	CR
10.0	14.5	3.07×10^8	1.21×10^4	0.476	2.4	2.47
12.7	18.3	3.80	1.50	.591	1.9	2.42
12.7	38.1	5.08	2.00	.794	1.6	2.36
35.1	114.3	6.36	2.50	.992	1.0	2.32
47.2	148.8	6.45	2.54	1.0	1.0	2.32

TABLE 2. - LOAD EFFECTS ON TRANSMISSION RATIO
AND CONTACT RATIO GEARS
[32 and 96T; 8DP; 14.5° PA; $CR_T = 2.14$; $HSF = 0.992$.]

Load, N/mm	TR, percent	CR
88	0.8	2.29
175	1.0	2.32
350	1.0	2.38
525	1.8	2.43
700	2.2	2.45

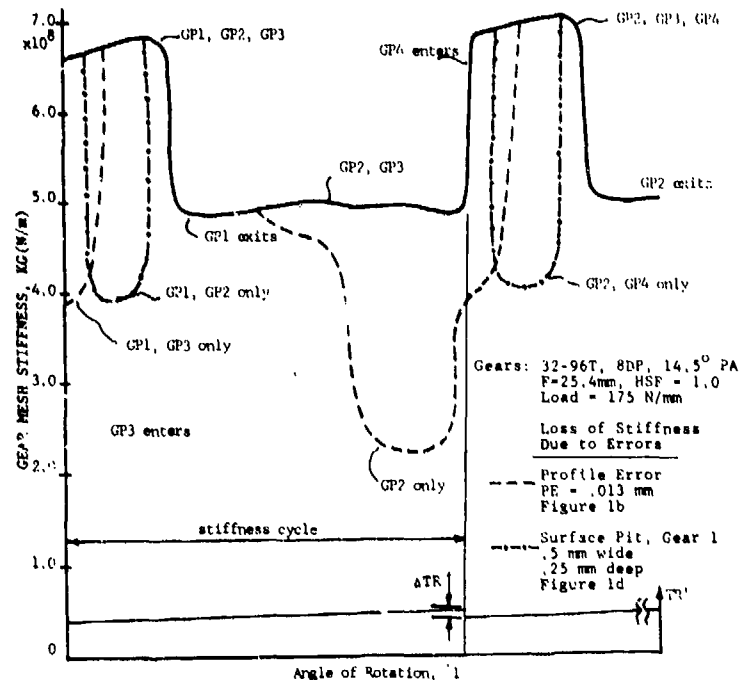


Figure 7. - Effects of profile faults on gear mesh stiffness.

imperfections will be considered first. For example, with torsionally flexible hubs ($HSF=0.5$), the sinusoidal errors of 0.013 mm (0.0005 in.) and narrow surface pits 0.5 mm wide (0.02 in.) were absorbed by the mesh flexibility consequently producing the errorless mesh stiffness characteristics. On the other hand, when the hubs were torsionally rigid ($HSF=1$) the mesh flexibility was not able to absorb the errors of above magnitudes. Unabsorbed errors can cause loss of stiffness thus causing significant changes in the gear-mesh stiffness characteristics (dashed lines in fig. 7). With increasing hub flexibility there was a gradual return to normal mesh stiffness characteristics, that is, the flexibilities in the mesh were able to narrow or bridge the noncontact zones. For example, a 32- and 96-tooth gear pair mesh with $HSF=0.6$ was able to absorb a portion of the sinusoidal error by eliminating about 50 percent of the mesh stiffness interruption shown in figure 7. Unabsorbed errors in the NCR gearing will cause a complete momentary loss of gear mesh stiffness.

The developed method can also be used to investigate other error combinations acting on both gears. For example, errors shown in figure 1(b) with PE_1 and PE_2 of 0.013 mm are nearly self-compensating in terms of developed stiffness characteristics. Other profile combinations, especially of large error magnitudes, could lead theoretically to nonoperational contact ratios or to unacceptable interruptions of the mesh stiffness function. The sinusoidal profile errors of approximately one cycle (fig. 1(b)) and 0.013 mm in magnitude are probably the maximum tolerable profile errors in accurate spur gearing applications.

It can be also noted that by selecting an appropriate combination of transmitted loads and gear-

hub flexibilities some of the NCR gear pairs can be theoretically made to operate in the HCR regime.

Dynamic Model

The gear train shown in figure 8 was used in dynamic simulations. This model is assumed to represent one of the practical cases in gearing. The dynamic model is based on the same coordinates as the static model. The developed gear-mesh stiffness characteristics and other parameters were then automatically transferred to the dynamic simulation of the system.

The equations of motion for this model along the instantaneous (noninvolute) line of action can be given in the following form:

$$J_D \ddot{\psi}_D + C_{B1} \dot{\psi}_D + C_{DS}(\dot{\psi}_D - \dot{\psi}_1) + K_{DS}(\psi_D - \psi_1) = T_{IN} \quad (18)$$

$$J_{G1} \ddot{\psi}_1 + C_{B2} \dot{\psi}_1 + C_{DS}(\dot{\psi}_1 - \dot{\psi}_D) + K_{DS}(\psi_1 - \psi_D) + CG_i(RBC1 \dot{\psi}_1 - RBC2' \dot{\psi}_2)RBC1 \\ + KG_i(RBC1 \psi_1 - RBC2' \psi_2)RBC1 = 0 \quad (19)$$

$$J_{G2} \ddot{\psi}_2 + C_{B3} \dot{\psi}_2 + C_{LS}(\dot{\psi}_2 - \dot{\psi}_L) + K_{LS}(\psi_2 - \psi_L) + CG_i(RBC2' \dot{\psi}_2 - RBC1 \dot{\psi}_1)RBC2' \\ + KG_i(RBC2' \psi_2 - RBC1 \psi_1)RBC2' = 0 \quad (20)$$

$$J_L \ddot{\psi}_L + C_{B4} \dot{\psi}_L + C_{LS}(\dot{\psi}_L - \dot{\psi}_2) + K_{LS}(\psi_L - \psi_2) = -T_{IN} \times TR' = -T_L(TR') \quad (21)$$

In equations (19) and (20) KG_i represents the variable gear pair mesh stiffness and is a function of gear-tooth profile errors and modifications, deflections of gear teeth, load sharing, and height of engagement for any angular position i of engagement. The mesh stiffness cycle is also illustrated in figure 7. The basic sources of excitation for a rotating pair of gears are the variation and interruptions of mesh stiffness and the changes in the transmission ratio caused by noninvolute action. The input torque T_{IN} is assumed to be constant while the output of load torque T_L is a function of the instantaneous transmission ratio shown as the $T_L(TR')$. In this study it is assumed that the instantaneous transmission ratio is dominated by the incoming tooth pair as it moves through one gear-mesh stiffness cycle.

Operational situations, which may involve momentary disengagement of gears in mesh, will impose the following conditions on the dynamic gear-mesh forces in equations (3) and (4); if $RBC2' \psi_2 < RBC1 \psi_1$, then

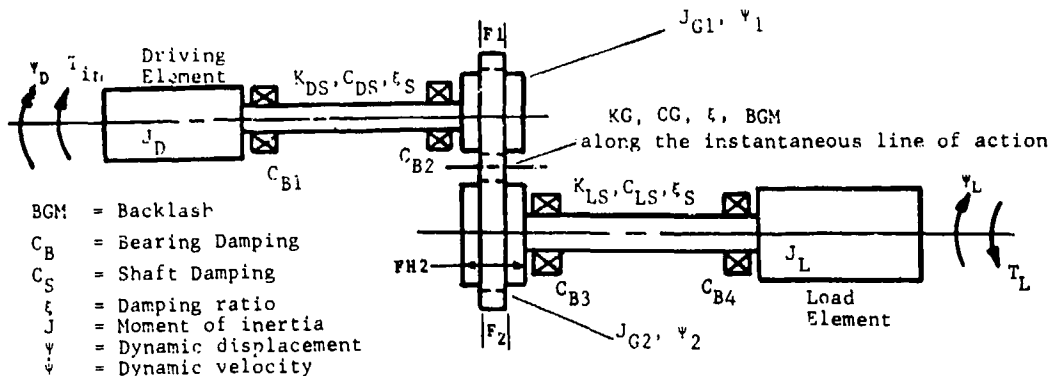


Figure 8. - Gear train dynamics model.

$$(QD)_i = CG_i(RBC1\psi_1 - RBC2'\psi_2) + KG_i(RBC1\psi_1 - RBC2'\psi_2) \quad (22)$$

if $RBC2'\psi_2 > RBC1\psi_1$ and $(RBC2'\psi_2 - RBC1\psi_1) < BGM$, then

$$(QD)_i = 0 \quad (23)$$

if $RBC2'\psi_2 > RBC1\psi_1$ and $(RBC2'\psi_2 - RBC1\psi_1) > BGM$, then

$$(QD)_i = CG_i(RBC1\psi_1 - RBC2'\psi_2) + KG_i(RBC1\psi_1 - RBC2'\psi_2) - BGM \quad (24)$$

Also, when $KG_i = 0$, $(QD)_i = 0$.

The equivalent damping in gear mesh CG_i was related to KG_i by means of a critical damping coefficient ξ .

A fourth-order Runge-Kutta integration scheme was used to integrate the indicated differential equations of motion. The initial displacements $\psi_1(0)$, $\psi_2(0)$, $\psi_D(0)$, and $\psi_L(0)$ were determined by statically twisting the entire system with the prescribed T_{IN} and T_L torques. For the initial velocities $\dot{\psi}_1(0)$, $\dot{\psi}_2(0)$, $\dot{\psi}_D(0)$, and $\dot{\psi}_L(0)$, the anticipated steady-state involute action velocities were selected.

The numerical integration of the equations of motion (eqs. (18) to (21)) is carried out for a length of time equivalent to the time required for the startup transient to decay. This time is assumed to be equal to five times the longest system natural period. The integration time step was taken either as one tenth of the shortest system natural period or 1 percent of the mesh stiffness period with $CR < 2$ (2 percent for $CR > 2$), whichever is smaller.

For illustration purposes two computer outputs for the static and dynamic loads are shown in figures 9 and 10. The static and dynamic load distributions are shown along the gear-tooth profiles as the gear tooth traverses the meshing arc. The dynamic load can be also plotted as a function of time.

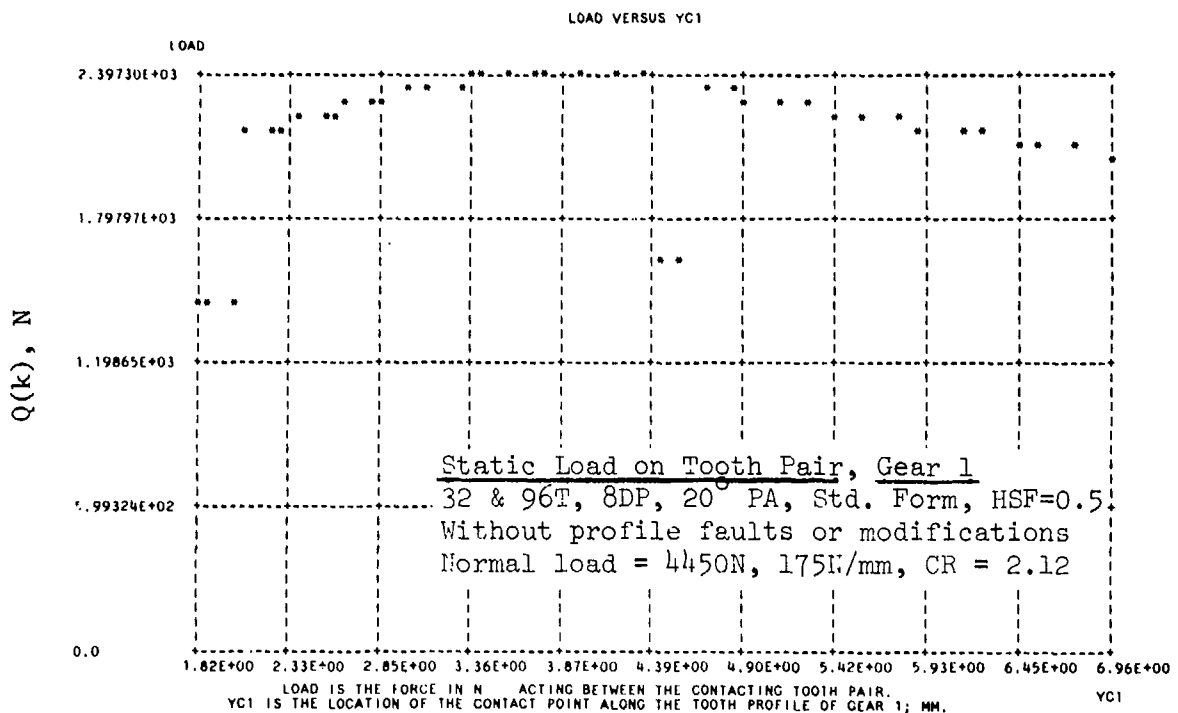


Figure 9. - Typical static load distribution.

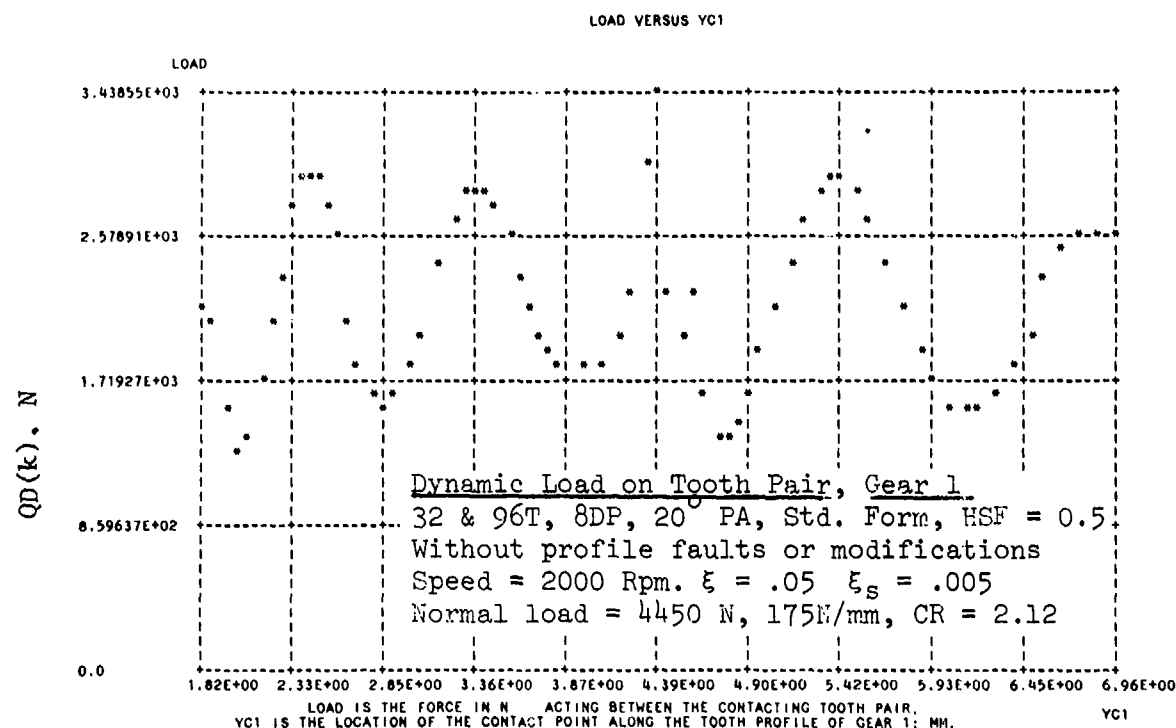


Figure 10. - Typical dynamic load distribution.

The dynamic load $QD(k)$ for a contacting gear-tooth pair k in the mesh position i was established as

$$QD(k)_i = \frac{KP(k)_i}{KG_i} (QD)_i \quad (25)$$

In this study the dynamic load factors were defined as

$$(DF_1)_i = \frac{(QD)_i}{Q_t} \quad (26)$$

and

$$(DF_2)_i = \frac{QD(k)_i}{Q(k)_i} \quad (27)$$

where DF_1 can be interpreted as the dynamic load factor for the mesh or as the dynamic load factor for the gear pair, adjacent shafts, and bearings and where DF_2 is the dynamic load factor for an individual gear-tooth pair traversing the mesh arc. The DF_2 is of main significance when the strength of the gear teeth is of primary importance. The larger of the two dynamic load factors will be defined as the dynamic load factor for design, DF .

Dynamic Analysis

The dynamic loads are influenced by a large number of variables such as the mass moments of inertia of all elements, shaft stiffnesses, transmitted loads, gear-mesh stiffness characteristics, damping in the system, amount of backlash and speed. The mesh stiffness characteristics are affected

by various error-caused interruptions. Figure 7 suggests considerable variations of the harmonic contents. Consequently, the harmonic contents of the mesh stiffness characteristics can excite a number of natural frequencies.

Because of the large number of variables, only four sets of HCR and NCR gearing (table 3) loaded with a normal load of 4450 N or 175 N/mm (1000 lb/in) will be discussed.

The developed method has the capability for analyzing the distribution of the dynamic loads, dynamic factors, load sharing, contact-Hertz stress (P_H), and the contact stress-sliding velocity product (PV) for the entire meshing zone.

Figure 11 illustrates the dynamic characteristics in terms of (DF) for a gear drive (fig. 8) with errorless HCR gearsets. The trends indicate that various gear drive systems could be designated for best performance in terms of acceptable dynamic loads by proper selection of masses, gears, gear-mesh and shafting flexibilities, and damping. The primary excitation for errorless gears with $CR \neq 2.0$ is the inherent variation in mesh stiffness. An interestingly new response characteristic is exhibited by several gearsets having $CR = 2.0$ (almost flat gear-mesh stiffness). The main excitation for $CR = 2.0$ is due to variation in the transmission ratio (ΔTR) caused by noninvolute action. However, $CR = 2.0$ could be obtained only for some specific load and geometrical conditions.

The HCR gearing with $CR = 2.0$ showed reasonably good tolerance to several types of surface faults. In general, the dynamic loads can be reduced by introducing higher damping, higher applied loads, and lower HSF's.

TABLE 3 NCR and HCR Gearing Grouping

1. Inherent HCR gearing with small pressure angle and fine pitch represented by 32 & 96T, 8DP, 14.5° PA, $CR_T = 2.14$.
2. Long addendum HCR gearing represented by:
32 and 96T, 8DP, 20° PA, 1.1 x std. addendum, $CR_T = 2.15$, $CR = 2.42$, $HSF = 0.5$, and $HSF = 1.0$
32 & 96T, 8DP, 25° PA, 1.1 x std. addendum, $CR_T = 1.89$, $CR = 2.16$, $HSF = .5$
3. HCR gearing with $CR = 2.0$ represented by a number of 20° PA gear sets, HSF , and loads. For example, 32 & 96T, 8DP, 20° PA, $CR_T = 1.76$, $CR = 2.0$, $HSF = .73$
4. NCR gearing represented by:
20 & 20T, 4DP, 20° PA, $CR_T = 1.56$; $CR = 1.67$, $HSF = .7$
32 & 96T, 8DP, 25° PA, $CR_T = 1.53$; $CR = 1.72$, $HSF = 1.0$
40 & 40T, 8DP, 20° PA, $CR_T = 1.51$, $CR = 1.68$, $HSF = 1.0$

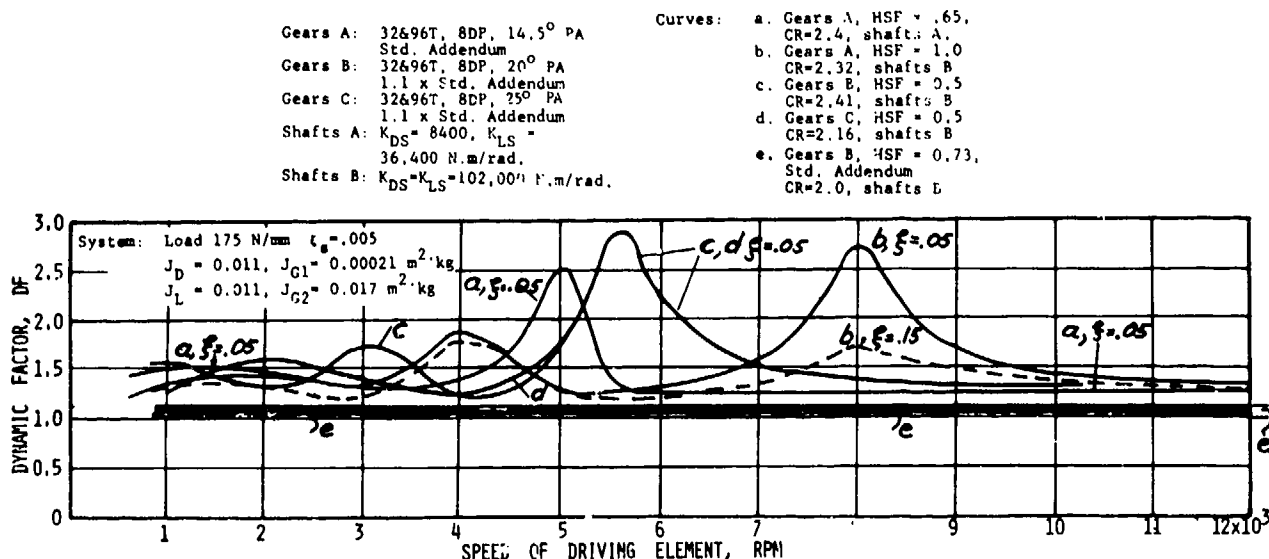


Figure 11. - Damping and system flexibility effects on dynamic factors for errorless HCR gear sets.

Reference 17 indicated a 300 percent increase in dynamic amplitudes caused by a zero stiffness zone due to a single tooth pit. In this study surface imperfections were assigned to all teeth for a given gear.

The analyses tend to suggest that the main sources of excitation are the variable mesh stiffness function and its interruptions.

The effects of unabsorbed profile surface imperfections (sinusoidal and pitting) are illustrated in figures 12 and 13 for the HCR and NCR gearing. In the presented cases momentary gear separation can occur when $DF > 2$. The resonant peaks are the average dynamic load factors based on the backlash between zero and 0.25 mm.

The unabsorbed errors in the NCR situations considered caused a momentary loss of mesh

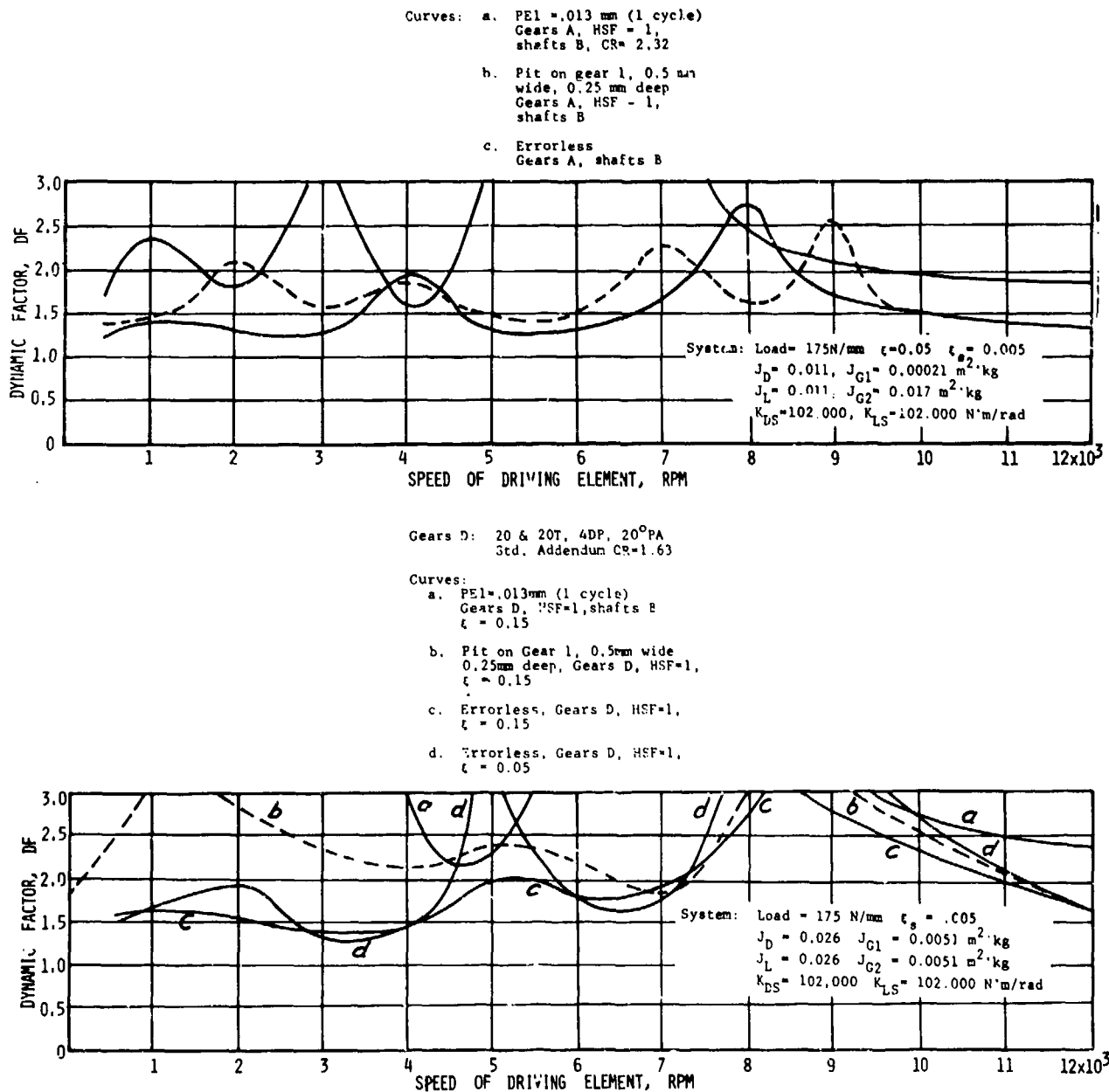


Figure 13. - Influence of profile faults on dynamic factors for a characteristic NCR gear pair.

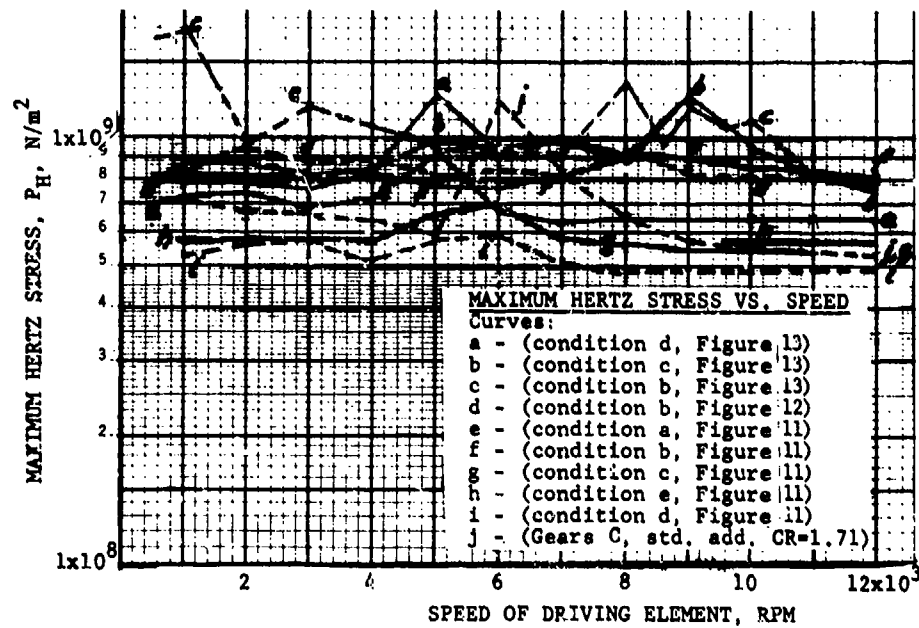


Figure 14. - Maximum Hertz stress.

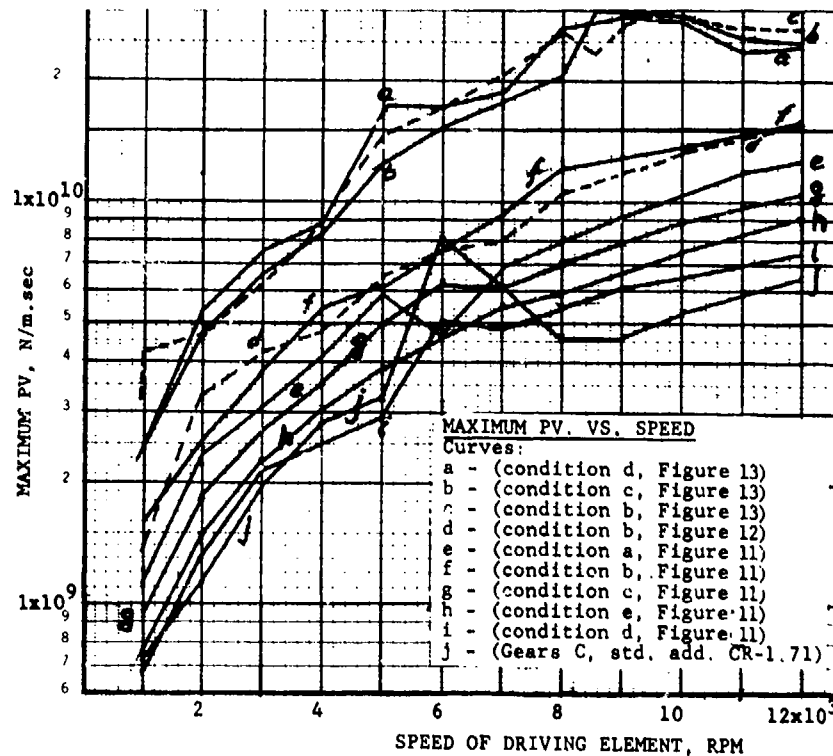


Figure 15. - Maximum product of Hertz stress and sliding velocity.

stiffness, resulting in high dynamic loads and gear separation over a wide region of considered speeds. In the slow speed range there is a large zone of high dynamic load factors affected by a number of the mesh stiffness function harmonics and separation of gears. The same unabsorbed errors in the HCR gearing cause only a partial loss of stiffness and, thus, indicate lower error-caused dynamic loads than in the NCR gearing. The ΔTR quantity which represents variation of load torque due to noninvolute action appears to be of secondary importance as a source of excitation.

References

1. Buckingham, E.: Dynamic Loads on Gear Teeth. Report of Special Research Committee on the Strength of Gear Teeth, ASME, New York, 1931.
2. Tuplin, W. A.: Dynamic Loads on Gear Teeth. Machine Design, vol. 25, Oct. 1953, pp. 203-211.
3. Reswick, J. B.: Dynamic Loads on Spur and Helical Gear Teeth. ASME, vol. 77, no. 5, July 1955, pp. 635-644.
4. Nakada, T., and Utagawa, M.: Dynamic Loads Caused by the Varying Elasticity of Mating Gear Teeth. Proc. 6th Japan National Congress on Applied Mechanics, 1956, pp. 493-497.
5. Zeman, J.: Dynamische Zusatzkrafte in Zahnradgetrieben. Z. Ver. Dtsch. Ing., vol. 99, 1957, pp. 244-254.
6. Harris, S. L.: Dynamic Loads on the Teeth of Spur Gears. Proc. Institute of Mechanical Engineers, vol. 172, 1958, pp. 87-112.
7. Richardson, H. H.: Static and Dynamic Load, Stress and Deflection Cycles in Spur Gearing. Sc.D. Thesis, Department of Mechanical Engineering, M.I.T., Cambridge, Mass., 1958.
8. Bolm, F.: Drehschwingungen von Zahnradgetrieben. Oesterr. Ing., vol. 13, no. 2, 1959, pp. 82-103.
9. Staph, H. E.: A Parametric Analysis of High-Contact-Ratio Spur Gears. ASLE Trans., vol. 19, no. 3, 1976, pp. 201-215.
10. Cornell, R. W.; and Westervelt, W. W.: Dynamic Tooth Loads and Stressing for High Contact Ratio Spur Gears, ASME Paper 77-DET-101.
11. Kasuba, R.; and Evans, J. W.: An Extended Model for Determining Dynamic Loads in Spur Gearing. J. Eng. Ind., vol. 103, no. 3, April 1981, pp. 398-409.
12. Niemann, G.; and Baethge, J.: Drehwegfehler. Zahnfederharte und Gerausch bei Stirnradern, Z. Ver. Dtsch. Ing., vol. 112, no. 4, 1970, pp. 205-214.
13. Weber, C.: The Deformation of Loaded Gears and the Effect on Their Load-Carrying Capacity. Part I, Department of Scientific and Industrial Research, Sponsored Research (Germany) no. 3, London, 1949.
14. Attia, A. Y.: Deflection of Spur Gear Teeth Cut in Thin Rims, J. Eng. Ind., vol. 86, no. 4, Nov. 1964, pp. 33-342.
15. Chakraborty, J.; and Hunashikati, H. G.: Determination of the Combined Mesh Stiffness of a Spur Gear Pair Under Load. ASME Paper 74-DET-39, 1974.
16. Utagawa, M.; and Harada, T.: Dynamic Loads on Spur Gear Teeth Having Pitch Errors at High Speed. Bull. JSME, vol. 5, no. 18, 1962, pp. 374-381.
17. Drosjack, M. J.; and Houser, D. R.: An Experimental and Theoretical Study of the Effects of Simulated Pitch Line Pitting on the Vibration of a Geared System. ASME Paper 77-DET-123.



An Update on the Life Analysis of Spur Gears

John J. Coy*, Dennis P. Townsend†, and Erwin V. Zaretsky†

Gears used in aircraft and other applications may fail from scoring, tooth fracture due to bending fatigue, or surface pitting fatigue. Figure 1 illustrates a few of the failure modes that have occurred during experimental gear testing at the Lewis Research Center. The scoring type of failure is usually lubrication related and can be corrected by proper lubricant selection and/or changes in gear operating conditions (ref. 1). Tooth breakage is caused by tooth loads that produce bending stresses above the endurance limit of the material (ref. 2). It is usually accepted that the endurance limit, if it does exist, can be predicted from available stress-life (S-N) curves for the material being used (ref. 3). Current methods (ref. 4) of predicting gear surface-pitting failures are similar to those used for predicting the bending fatigue limit. According to the method of reference 4, the maximum surface contact stress (Hertz stress) should be limited to a value less than the surface endurance limit of the gear material. It is commonly believed that the gears would then have an infinite surface-pitting life. But, based on gearing studies (refs. 5 and 6) and on rolling-element bearing-life studies (ref. 7), there is no real evidence to support the concept of a surface-fatigue limit under normal operating conditions of bearings and gears. Rather, it appears that all gears, even if designed properly to avoid failure by scoring and tooth-bending fatigue, will eventually succumb to surface pitting in much the same way as rolling-element bearings.

In references 8 to 10 a method of predicting the surface-fatigue lives of low-contact-ratio spur gears was presented. The method is based on the commonly accepted Lundberg-Palmgren theory that has been used for many years to predict the lives of rolling-element bearings. Fatigue testing of spur gears of various materials, using different methods of manufacture and lubricants, has been in progress for the past 10 years at Lewis.

The objective of the information presented in this paper is to summarize and update the spur-gear life analysis and to relate the analysis to some of the experimental results from NASA tests.

Symbols

- b half width of Hertzian contact, m (in.)
- C gear center distance, m (in.); constant of proportionality, see eq. (14)
- c orthogonal shear stress exponent
- D_a rolling-element diameter, m (in.)
- E Young's modulus, Pa (psi)
- e Weibull exponent
- f face width of tooth in contact, m (in.)
- G_{10} 10 percent life of a gear, millions of revolutions
- h depth to critical stress exponent
- K proportionality constant
- L_{10} 10 percent life, millions of revolutions (Mr), or, equivalently, hr
- L_i gear rotations in millions
- l involute profile arc length, m (in.)
- M contact ratio
- m_g gear ratio, N_1/N_2

*Propulsion Laboratory, U.S. Army Research and Technology Laboratories (AVRADCOM), NASA Lewis Research Center.

†NASA Lewis Research Center.

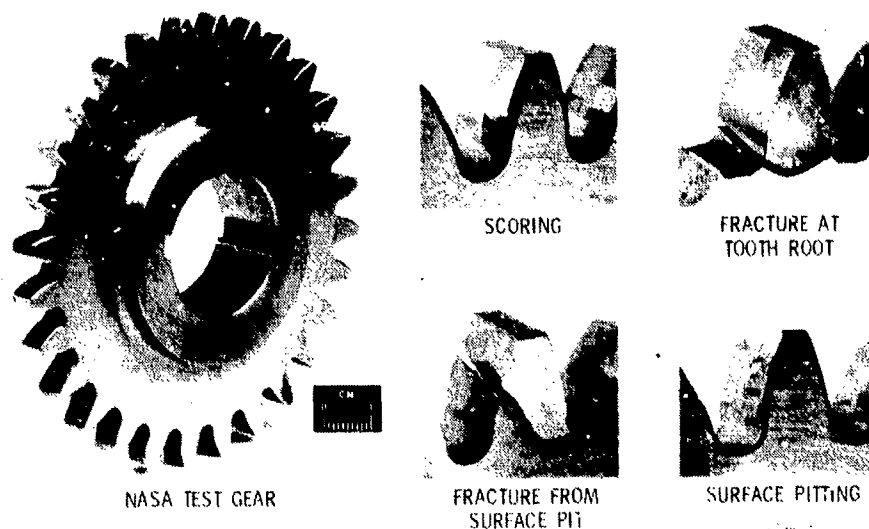


Figure 1. - Typical gear tooth failure modes. From tests run on NASA Lewis spur gear tester.

- N number of teeth
 p_b base pitch, m/tooth (in./tooth)
 Q load normal to involute profile, N (lb)
 Q_c dynamic capacity for bearing, N (lb)
 Q_m dynamic capacity of gear mesh, N (lb)
 q maximum Hertz stress, Pa (psi)
 r pitch circle radius, m (in.)
 r_a addendum circle radius, m (in.)
 r_b base circle radius, m (in.)
 S probability of survival
 T_{10} 10 percent life of a tooth, millions of cycles
 U number of contact cycles per bearing revolution
 u stress cycles per revolution
 V volume, m³ (in.³)
 x, y Cartesian coordinates, m (in.)
 Z contact path length, m (in.)
 z depth of occurrence of critical shearing stress, m (in.)
 β roll angle increment, rad
 δ precontact roll angle, rad
 η millions of stress cycles
 θ base circle roll angle, rad
 μ Poisson's ratio
 ρ curvature radius, m (in.)
 $\Sigma\rho$ curvature sum, m⁻¹ (in.⁻¹)
 τ maximum subsurface orthogonal reversing shear stress, Pa (psi)
 φ pressure angle, rad
 Subscripts:
 H high load
 i index representing 1 or 2

- L low load
- M mesh of pinion and gear
- 1 reference to high speed member, pinion
- 2 reference to low speed member, gear

Theory

Theory of Gear Tooth Life

The fatigue-life model proposed in 1947 by Lundberg (ref. 11) is the commonly accepted theory to determine the fatigue life of rolling-element bearings. The probability of survival as a function of stress cycles is expressed as

$$\log \frac{1}{S} \propto \frac{\tau^c \eta^e V}{z^h} \quad (1)$$

Hence, if the probability of survival is specified, the life η for the required reliability can be considered a function of the stressed volume V , the maximum critical stress τ and the depth to the critical shearing stress z . As a result, the proportionality can be written as

$$\eta \propto \frac{z^{h/e}}{\tau^{c/e} V^{1/e}} \quad (2)$$

The above formula reflects the idea that greater stress shortens life. The depth below the surface z at which the critical stress occurs is also a factor. A microcrack beginning at a point below the surface requires time to work its way to the surface. Therefore, we expect that life varies by an inverse power of depth to the critically stressed zone.

The stressed volume V is also an important factor. Pitting initiation occurs near any small stress-raising imperfection in the material. The larger the stressed volume, the greater the likelihood of fatigue failure. By the very nature of the fatigue-failure phenomenon, it is the repetitive application of stress that causes cumulative damage to the material. The greater the number of stress cycles, the greater the probability of failure. By experience it has been found that the failure distribution follows the Weibull model.

As an expression for the stressed volume let

$$V \propto fzI \quad (3)$$

where I is the involute length across the heavy load zone as defined in the appendix. The choice of this length is a simplification, in that a more complicated treatment would be to integrate across the entire involute length, which is composed of both heavy and light load zones. The simplification is justifiable, however, since operation under lighter loads greatly diminishes the probability of failure. Another reason for choosing the heavily loaded zone is that all observed failures on the NASA gear tests occurred in that zone, mostly where the Hertz load on the pinion is greatest (ref. 12). It is also assumed that the most severe Hertz stress generated in the contact of the teeth is acting over the entire load zone of single-tooth contact. The calculation of stresses is considered next. From Hertz theory (ref. 13) the maximum stress at the surface where line contact is assumed is given by

$$q = \frac{2Q}{\pi f b} \quad (4)$$

The semiwidth of the contact strip is

$$b = \sqrt{\frac{8Q(1-\mu^2)}{\pi f E \Sigma \rho}} \quad (5)$$

where $\Sigma \rho$ is the curvature sum, such that

$$\Sigma \rho = \frac{1}{\rho_1} + \frac{1}{\rho_2} \quad (6)$$

The expression for radius of curvature, ρ , is given in the appendix. According to reference 11, the cause of fatigue flaking of bearings is the maximum reversing orthogonal shear stress that occurs at a depth z below the surface and has an amplitude that varies between $\pm \tau$ where

$$z = \frac{b}{2} \quad (7)$$

and

$$\tau = \frac{q}{4} \quad (8)$$

Using the foregoing expressions for stress, stressed volume, and depth of stress allows equation (1) to be written as

$$\log \frac{1}{S} \propto Q^{(c-h+1)/2} f^{-(c-h-1)/2} \Sigma \rho^{(c+h-1)/2} l \eta^e \quad (9)$$

Assuming a probability of survival of 90 percent and making use of the foregoing expressions for z , τ , and V , we may express life as

$$\eta \propto Q^{-(c-h+1)/2} e^{f^{(c-h-1)/2} \Sigma \rho^{-(c+h-1)/2} l^{-1/e}} \quad (10)$$

Evaluation of Exponents

It has been shown in reference 14 that life is inversely proportional to the 4.3 power of load and that the dispersion in life (Weibull exponent), e , equals 2.5 for AISI 9310 steel gears. From reference 11 the dependence of dynamic capacity on bearing size leads to the following proportionality:

$$Q_c \propto D_a^{(c+h-3)/(c-h+1)} \quad (11)$$

where Q_c is the dynamic capacity and is defined as the load that gives a bearing life of 1 million stress cycles at a 90-percent reliability level and where D_a represents ball size and as such is a measure of the size effect. In reference 11 the exponent of D_a is 1.07. Using the foregoing values, c and h are calculated to be 23.2525 and 2.7525, respectively. The life equation then becomes

$$\eta = K Q^{-4.3} f^{3.9} \Sigma \rho^{-5} l^{-0.4} \quad (12)$$

where K is a constant of proportionality and η is tooth life in millions of stress cycles. Based on the data presented in reference 14, it has been calculated that $K = 3.72 \times 10^{18}$ when the units used in the equation are pounds and inches.

Gear Life

According to the relation for survival probability of a single gear tooth under constant service conditions,

$$\log \frac{1}{S} \propto \eta^e \quad (13)$$

For a 90-percent survival rate $S=0.90$ and for the corresponding life $\eta = T_{10}$, a constant of proportionality C is defined by

$$\log \frac{1}{0.9} = C T_{10}^e \quad (14)$$

The life T_{10} is conceptually identical to the B_{10} life for rolling-element bearings. For any general survival rate the following equation holds:

$$\log \frac{1}{S} = \left(\frac{\eta}{T_{10}} \right)^e \log \frac{1}{0.9} \quad (15)$$

From basic probability theory the probability of survival for N teeth is the product of survival probabilities for the individual teeth. Then, the probability of survival for the gear "i" with N_i teeth is

$$S_i = S^{N_i} \quad (16)$$

and

$$\log \frac{1}{S_i} = N_i \left(\frac{u L_i}{T_{10}} \right)^e \log \frac{1}{0.9} \quad (17)$$

where L_i is gear rotations and u is stress cycles per gear revolution. Normally $u = 1$, but in the case of a bull gear used to collect power from a number of inputs, u would be set equal to the number of inputs, assuming that equal power was applied through each input. For a 90-percent survival for the gear $S_i = 0.9$, $L_i = G_{10}$, and

$$\log \frac{1}{0.9} = N_i \left(\frac{u G_{10}}{T_{10}} \right)^e \log \frac{1}{0.9} \quad (18)$$

Then the 10-percent life for the gear is related to the 10 percent life of a single tooth by the following equation:

$$\left(\frac{1}{G_{10}} \right)^e = N_i \left(\frac{u}{T_{10}} \right)^e \quad (19)$$

For the case of an idler gear, where power is transferred without loss from an input gear to an output gear through the idler gear, both sides of the tooth are loaded once per revolution. The stressed volume is doubled in this case, which is the same as doubling the number of teeth.

$$\left(\frac{1}{G_{10}} \right)^e = 2N_i \left(\frac{u}{T_{10}} \right)^e \quad (20)$$

For most circumstances the basic tooth life, as calculated by equation (12), can be applied to teeth on both member gears in a mesh. However, for cases where the tooth proportions of one gear member are different from those of the mating member, a separate calculation for each gear tooth must be made.

Life and Dynamic Capacity of the Mesh

From probability theory the probability of survival of the two gears in mesh is given by

$$S = S_1 \cdot S_2 \quad (21)$$

and, therefore,

$$\left(\frac{1}{L} \right)^e = \left(\frac{1}{L_1} \right)^e + \left(\frac{1}{L_2} \right)^e \quad (22)$$

where the subscript 1 denotes the higher speed gear (pinion) and 2 denotes the other gear. This equation is valid for a 90-percent probability of survival for the mesh combination of gear 1 and gear 2. In this equation it should be noticed that all lives L should be expressed in the same time base, for example, in hours or in rotations of gear 1.

The dynamic capacity Q_m for the mesh is defined as the normal tooth load that may be carried with a 90-percent probability of survival for one million revolutions of the highest speed shaft. Then for any other pitch line load, the corresponding mesh life is calculated from the following equation:

$$L_{10} = \left(\frac{Q_m}{Q} \right)^{4.3} \quad (23)$$

For example, imagine that gear 1 is on the higher speed gear shaft. Also assume that the teeth on the gear members are of the same proportions and are running in a simple mesh. In this case, based on the foregoing analysis, the dynamic capacity of the gear mesh is given by

$$Q_m = \left[\frac{K 2.5 f^{0.75}}{\Sigma \rho^{12.5} N_1 (1 + m_g^{1.5})} \right]^{0.093} \quad (24)$$

Results and Discussion

Gear fatigue tests were conducted at the Lewis Research Center with gears made from AISI 9310 steel (ref. 14).

The test rig is shown in figure 2. The dimensions of the gears are given in table I.

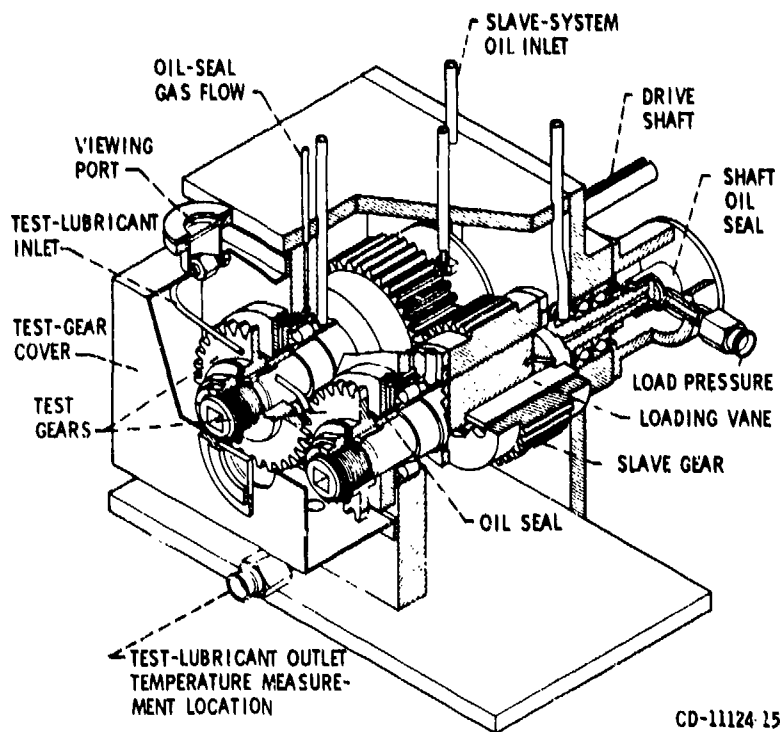
Three groups of vacuum arc remelted (VAR) AISI 9310 case carburized and hardened steel gears were fatigue tested under loads of 463×10^3 , 578×10^3 , and 694×10^3 N/m (2645, 3305, and 3966 lb/in.), which produced maximum Hertz stresses of 1.531, 1.710, and 1.875 GPa (222 000, 248 000, and 272 000 psi). The lubricant was a superrefined naphthenic mineral oil with a 5 percent extreme-pressure additive package. Failure of the gears was due to surface fatigue pitting. Test results were statistically evaluated using the methods of reference 15. The results of these tests are plotted on Weibull coordinates in figure 3. Weibull coordinates are the log-log of the reciprocal of the probability of survival graduated as the statistical percent of specimens failed (ordinate) against the log of stress cycles to failure or system life (abscissa). In each test group there were 19 failures out of 19 tests. All failures occurred in the zone of single tooth loading at or just below the pitch diameter.

The 90-percent confidence interval limits were determined for each group of test data (fig. 3). The interpretation of these limits is that the true life determined from an extremely large sample of gears running at each stress condition will fall between these confidence limits 90 percent of the time. Were these confidence limits to overlap, the life differences as determined from the test would not be considered statistically significant. The consistent trend of decreasing life with increasing stress indicates good statistical significance in the data that resulted from these three test series.

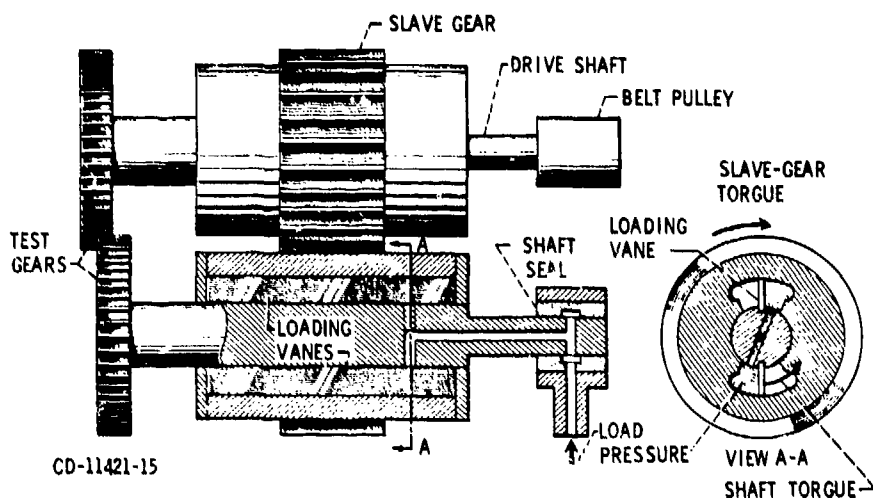
TABLE I. - SPUR GEAR DATA

[Gear tolerance per ASMA class 12.]

Tooth width in contact, cm (in.)	0.25 (0.10)
Tooth width, cm (in.)	0.64 (0.25)
Number of teeth	28
Diametral pitch	8
Circular pitch, cm (in.)	0.9975 (0.3927)
Whole depth, cm (in.)	0.762 (0.300)
Addendum, cm (in.)	0.318 (0.125)
Chordal tooth thickness reference, cm (in.)	0.485 (0.191)
Pressure angle, deg	20
Pitch diameter, cm (in.)	8.890 (3.500)
Outside diameter, cm (in.)	9.525 (3.750)
Root fillet, cm (in.)	0.102 to 0.152 (0.04 to 0.06)
Measurement over pins, cm (in.)	9.603 to 9.630 (3.7807 to 3.7915)
Pin diameter, cm (in.)	0.549 (0.216)
Backlash reference, cm (in.)	0.0254 (0.010)
Tip relief, cm (in.)	0.001 to 0.0015 (0.0004 to 0.0006)



(a) CUTAWAY VIEW.



(b) SCHEMATIC DIAGRAM.

Figure 2. - NASA Lewis Research Center's gear fatigue test apparatus.

The American Gear Manufacturers Association (AGMA) has published two standards for tooth surface fatigue, AGMA 210.02 and AGMA 411.02 (refs. 4 and 16). AGMA 210.02 provides for an endurance limit for surface fatigue below which it is implied that no failure should occur. In practice, there is a finite surface fatigue life at all loads. AGMA 411.02 recognizes this finite-life condition. Therefore, it does not contain an endurance limit in the load-life curve but does show a continuous decrease in life with increasing load. Both AGMA standards are illustrated in figure 4. The AGMA load-life curves shown are for a 99-percent probability of survival or the L_1 life. The experimental L_1 , L_{10} , and L_{50} lives from the data of figure 3 are plotted for comparison.

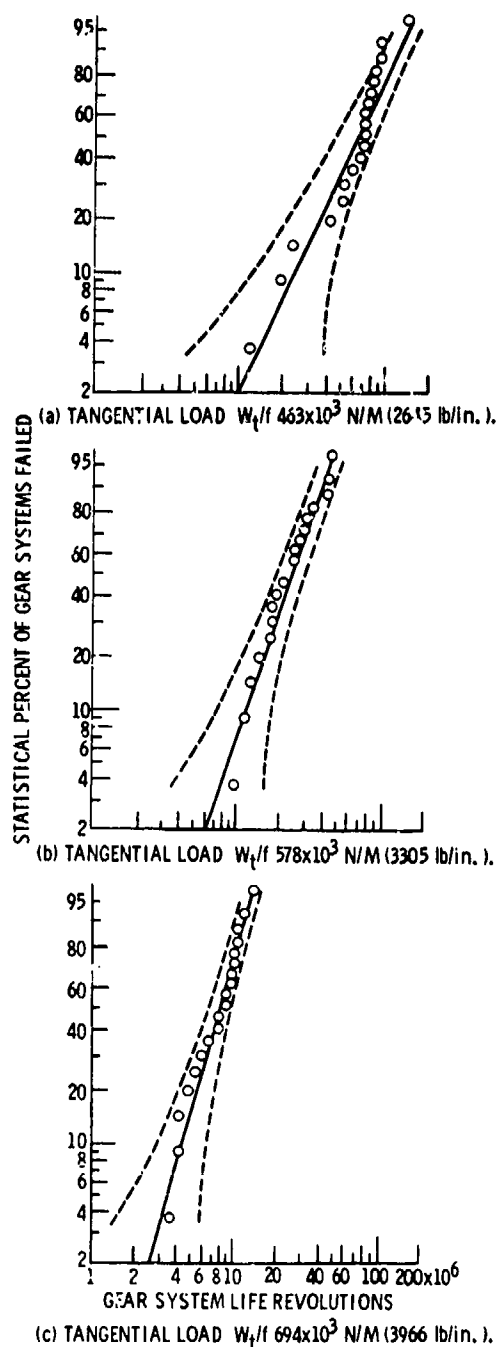


Figure 3. - Comparison of life-prediction theory with experimental results for VAR AISI 9310 steel spur gears. Speed, 10 000 rpm.

It is evident that the load-life relation used by AGMA is different from the experimental results reported herein. The difference between the AGMA life prediction and the experimental lives could be the result of differences in stressed volume. The AGMA standard does not consider the effects of stressed volume, which may be considerably different from that of the test gears used herein. The larger the volume of material stressed, the greater the probability of failure or the lower the life of a particular gearset. Therefore, changing the size or contact radius of a gearset, even though the same contact stress is maintained, would have an effect on gear life.

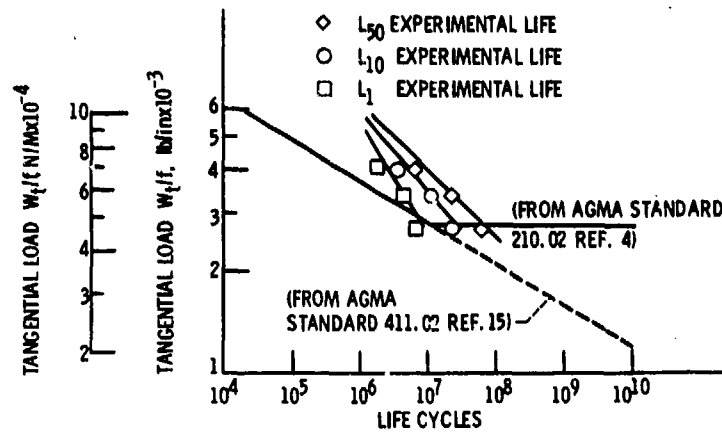


Figure 4. - Comparison of experimental life for VAR AISI 9310 spur gears with AGMA life prediction. Speed, 10 000 rpm; lubricant superrefined naphthenic mineral oil with additive package.

It should be mentioned here that the Weibull slope e was assumed to be independent of the stress level in the original work by Lundburg and Palmgren. There is some evidence to suggest that the Weibull slope is a function of the applied stress. This was noticed by Schilke (ref. 6); and the tests conducted at Lewis (ref. 14) at various stress levels gave Weibull slopes from 1.9 to 2.9. The Weibull slope $e=2.5$ that is suggested for use in this report is an average value that will serve in most applications where the stress is not unusually high or low. When life calculations are made using the method outlined in this paper, the predicted life can be considered a reasonably good engineering approximation to what may be expected in a practical gear application. However, the theoretical prediction does not consider material and processing factors such as material type, melting practice, or heat treatment, nor does it consider environmental factors such as lubrication and temperature. All these factors are known to be extremely important in their effect on rolling-element bearing life (ref. 17). There is no reason why the effects used to determine bearing life should be significantly different from those used to determine gear life. Figure 5 is a collection of life data based on gear tests conducted at the Lewis Research Center. The lives are compared with a base-line life of unity for AISI 9310 gears. The mode of failure was pitting. More test data obtained with gear specimens under various test conditions and different materials and lubricants continue to be required to establish and/or affirm the material and processing factors and the exponents c , h , and e for gears, as they are used in various applications. However, the general methods presented herein explain and support the use of the statistical methods to predict spur-gear fatigue life. Table II gives a sample calculation for a simple mesh of two gears.

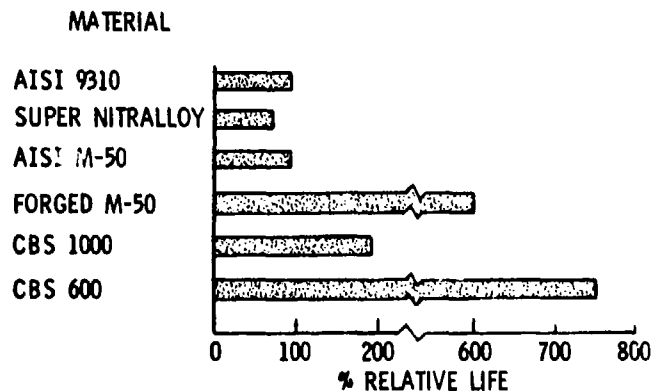


Figure 5. - Summary of gear fatigue lives based on NASA spur gear tests with various materials.

TABLE 11. - SAMPLE CALCULATION

Symbol	Definition	Equation	Result
Q	Normal load	Given	1610 N (363 lb)
ϕ	Pressure angle		20°
N ₁	Number of teeth on gear 1		28
N ₂	Number of teeth on gear 2		28
f	Face width		2.79 mm (0.11 in.)
r ₁	Pitch radius		4.45 cm (1.75 in.)
r ₂	Pitch radius		4.45 cm (1.75 in.)
r _{a1}	Addendum radius		4.76 cm (1.88 in.)
r _{a2}	Addendum radius		4.76 cm (1.88 in.)
r _{b1}	Base radius		4.17 cm (1.64 in.)
r _{b2}	Base radius		4.17 cm (1.64 in.)
Z	Length of contact path	$\sqrt{r_{a1}^2 - r_{b1}^2} + \sqrt{r_{a2}^2 - r_{b2}^2} - (r_1 + r_2)\sin\phi$	1.63 cm (0.641 in.)
p _b	Base pitch	$2\pi r_{b1}/N_1$	9.35 mm (0.368 in.)
β_{L1}	Roll angle increment	$(Z - p_b)/r_{b1}$	0.166 rad
β_{H1}	Roll angle increment	$(Z p_b - Z)/r_{b1}$	0.058 rad
δ_1	Pre contact roll angle	$\frac{(r_1 + r_2)\sin\phi - (r_{a2}^2 - r_{b2}^2)^{1/2}}{r_{b1}}$	0.169 rad
ϵ_1	Length of involute during single tooth contact	$r_{b1}\beta_{H1}\left(\delta_1 + \beta_{L1} + \frac{1}{2}\beta_{H1}\right)$	0.879 mm (0.035 in.)
ρ_1	Radius of curvature	$r_{b1}(\delta_1 + \beta_{L1})$	1.39 cm (0.549 in.)
ρ_2	Radius of curvature	$(r_1 + r_2)\sin\phi - \rho_1$	1.65 cm (0.648 in.)
$\Sigma\rho$	Curvature sum	$(1/\rho_1) + (1/\rho_2)$	8.55 cm ⁻¹ (3.36 in. ⁻¹)
T ₁₀	Tooth life	$3.72 \times 10^{18} Q^{-4.3} f^{3.9} \Sigma\rho^{-5.2} - 0.4$	59.6 Mr*
G ₁₀	Gear life	$[N_1(1/T_{10})^{2.5}]^{-1/2.5}$	15.7 Mr*
L ₁₀	Mesh life	$[2(1/G_{10})^{2.5}]^{-1/2.5}$	11.9 Mr*

*Mr = million revolutions.

Summary of Results

An analytical method for predicting surface fatigue life of gears was presented. General statistical methods were outlined, showing the application of the general methods to a simple gear mesh. Experimentally determined values for constants in the life equation were given. Comparison of the life theory with NASA test results and AGMA standards was made. Gear geometry pertinent to life calculations was reviewed. The following results were obtained:

1. The life analysis resulted in the following fundamental equation for gear tooth life:

$$\eta = KQ^{-4.3} f^{3.9} \Sigma \rho^{-5} l^{-0.4} \quad (12)$$

where $K = 3.72 \times 10^8$ for calculations in pounds and inches.

2. For a simple mesh of one gear with another the dynamic capacity is

$$Q_m = \left[\frac{K^{2.5} f^{9.75}}{\Sigma \rho^{12.5} l N_1 (1 + m_g^{1.5})} \right]^{0.093} \quad (24)$$

Appendix—Gear Geometry

In figure 6 an involute tooth is shown. The involute curve may be thought of as the path traced by point A on the tangent line as it is rolled upon the base circle with radius r_b . The radius of curvature of the involute at point A is given by ρ .

$$\rho = r_b \theta \quad (A1)$$

The x and y coordinates of point A are given by the following equations:

$$\left. \begin{aligned} x &= r_b (\sin \theta - \theta \cos \theta) \\ y &= r_b (\cos \theta + \theta \sin \theta - 1) \end{aligned} \right\} \quad (A2)$$

The differential element of involute arc length dl is

$$dl = (dx^2 + dy^2)^{1/2} = r_b \theta \, d\theta \quad (A3)$$

The length of the path of contact Z is the distance between where the two addendum circles cross the line of action (as shown in fig. 7):

$$A = \sqrt{r_{a1}^2 - r_{b1}^2} + \sqrt{r_{a2}^2 - r_{b2}^2} - C \sin \varphi \quad (A4)$$

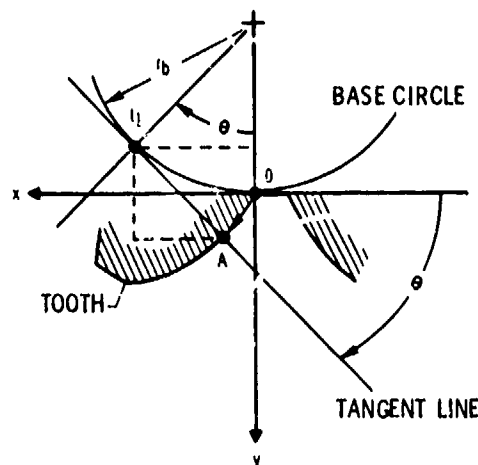


Figure 6. - Involute profile geometry.

where C is the distance between gear centers. The base pitch p_b is defined as the distance from a point on one tooth to the corresponding point on the next tooth measured along the base circle (see fig. 7). It may also be thought of as the distance from one tooth to the next measured along the line of action.

$$p_b = \frac{2\pi r_{b1}}{N_1} = \frac{2\pi r_{b2}}{N_2} \quad (A5)$$

The contact ratio M is defined as the average number of gear teeth in contact at one time. It is calculated by

$$M = \frac{Z}{p_b} \quad (A6)$$

When two pairs of teeth are in contact, the load is assumed to be equally shared. For low-contact-ratio gears ($1 < M < 2$) there are three load zones. The load zones for gear 1 are shown in figure 8. Two pairs of teeth are in contact during roll-angle increments β_{L1} , and only one pair during roll-angle increment β_{H1} . For gear 1 the roll-angle increment for which two tooth pairs are in contact is calculated by

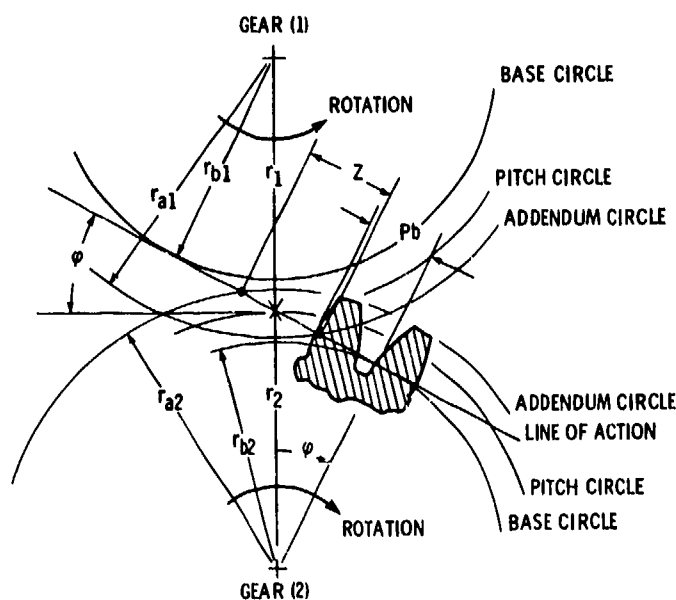
$$\beta_{L1} = \frac{Z - p_b}{r_{b1}} \quad (A7)$$

And the roll angle movement for the heavily loaded zone is given by

$$\beta_{H1} = \frac{2p_b - Z}{r_{b1}} \quad (A8)$$

Finally δ_1 , the precontact roll angle is defined as the roll angle from the base of the involute to the start of the zone of action as shown in figures 8 and 9. The angle δ_1 is given by the following equation:

$$\delta_1 = \frac{C \sin \varphi - (r_{a2}^2 - r_{b2}^2)^{1/2}}{r_{b1}} \quad (A9)$$



CS-61-2493

Figure 7. - Spur gears in mesh.

After integrating equation (A3) between the limits that bracket the heavy load zone, the result is the length of involute in the heavy load zone.

$$l_1 = r_{b1} \beta_{H1} \left(\delta_1 + \beta_{L1} + \frac{1}{2} \beta_{H1} \right) \quad (A10)$$

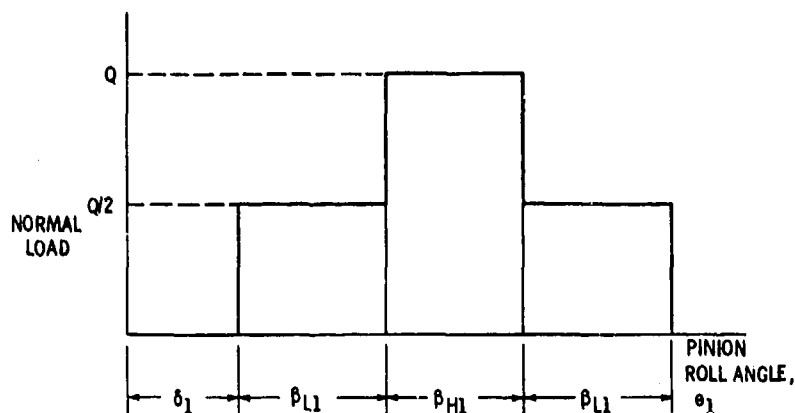


Figure 8. - Load sharing diagram. Load on tooth for low-contact-ratio gear depends on roll angle.

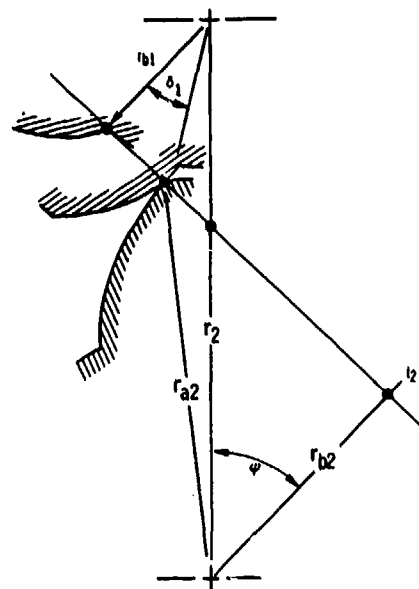


Figure 9. - Geometry for calculation of pre-contact roll angle, δ_1 .

References

1. Borsof, V. N.: On the Mechanism of Gear Lubrication. *J. Basic Eng.*, vol. 81, no. 1, Mar. 1959, pp. 79-93.
2. Seabrook, John B.; and Dudley, Darle W.: Results of Fifteen-Year Program of Flexural Fatigue Testing of Gear Teeth. *J. Engr. Ind.*, vol. 86, no. 3, Aug. 1964, pp. 221-239.
3. Rating the Strength of Spur Gear Teeth. AGMA 220.02, American Gear Manufacturers Assoc., 1966.
4. Surface Durability (Pitting) of Spur Gear Teeth. AGMA 210.02, American Gear Manufacturers Assoc., 1965.
5. Huffaker, G. E.: Compressive Failures in Transmission Gearing. *SAE Trans.*, vol. 68, 1960, pp. 53-59.
6. Schilke, W. E.: The Reliability Evaluation of Transmission Gears. *SAE Paper 670725*, Sep. 1967.
7. Bisson, Edmond E.; and Anderson, William J.: Advanced Bearing Technology. NASA SP-38, 1964, pp. 383-386.
8. Coy, J. J.; Townsend, D. P.; and Zaretsky, E. V.: Analysis of Dynamic Capacity of Low-Contact-Ratio Spur Gears Using Lundberg-Palmgren Theory. NASA TN D-8029, 1975.
9. Coy, J. J.; and Zaretsky, E. V.: Life Analysis of Helical Gear Sets Using Lundberg-Palmgren Theory. NASA TN D-8045, 1975.
10. Coy, J. J.; Townsend, D. P.; and Zaretsky, E. V.: Dynamic Capacity and Surface Fatigue Life for Spur and Helical Gears. *J. Lubr. Technol.*, vol. 98, no. 2, Apr. 1976, pp. 267-276.
11. Lundberg, G.; and Palmgren, A.: Dynamic Capacity of Rolling Bearings. *Acta Polytech., Mech. Eng. Ser.*, vol. 1, no. 3, 1947.
12. Townsend, Dennis P.; Chevalier, James L.; and Zaretsky, Erwin V.: Pitting Fatigue Characteristics of AISI M-50 and Super Nitralloy Spur Gears. NASA TN D-7261, 1973.
13. Thomas, H. R.; and Hoersch, V. A.: Stresses Due to the Pressure of One Elastic Solid upon Another with Special Reference to Railroad Rails. University of Illinois, Engineering Experiment Station Bull., no. 212, vol. 27, no. 46, July 15, 1930.
14. Townsend, D. P.; Coy, J. J.; and Zaretsky, E. V.: Experimental and Analytical Load-Life Relation for AISI 9310 Steel Spur Gears, *J. Mech. Des.*, vol. 100, no. 1, Jan. 1978, pp. 54-60. (Also NASA TM X-73590, 1977.)
15. Johnson, Leonard G.: The Statistical Treatment of Fatigue Experiments. Elsevier Publishing Co., 1964.
16. Design Procedure for Aircraft Engine and Power Take-off Spur and Helical Gears. AGMA Standard No. 411.02, American Gear Manufacturers Assoc., 1966.
17. Bamberger, E. N.; et al.: Life Adjustment Factors for Ball and Roller Bearings. An Engineering Design Guide. American Society of Mechanical Engineers, 1971.

The Optimal Design of Standard Gearsets*

Michael Savage,[†] John J. Coy,[‡] and Dennis P. Townsend[§]

The design of a gearset is a reasonably difficult problem which involves the satisfaction of many design constraints. In recent literature, several approaches to the optimum design of a gear mesh have been presented (refs. 1 to 3). Cockerham (ref. 1) presents a computer design program for 20° pressure angle gearing which ignores gear-tooth tip scoring. This program varies the diametral pitch, face width, and gear ratio to obtain an acceptable design. Tucker (ref. 2) and Estrin (ref. 3) look more closely at the gear-mesh parameters, such as addendum ratio and pressure angle, and outline procedures for varying a standard gear mesh to obtain a more favorable gearset. Gay (ref. 4) considers gear tip scoring as well and shows how to modify a standard gearset to bring this mode of failure into balance with the pitting fatigue mode. He also adjusts the addendum ratios of the gear and pinion to obtain an optimal design.

No general procedures exist, however, to determine the optimal size of a standard gear mesh. The basic approach available is one of checking a given design to verify its acceptability (refs. 5 to 7).

Optimum methods are presented for the design of a gearbox (refs. 8 to 10) with the object of minimizing size and weight. These methods focus on multistage gear reductions and consider the effect of splitting the gear ratios on overall transmission size.

The optimum design of a standard gearset has not been treated in the literature to date. Such a study must be based on a thorough study of the kinematics of the gear mesh, such as those by Buckingham (ref. 11) and Anderson (ref. 12). The gear strengths that must be considered include bending fatigue as treated by the AGMA (ref. 13), by Gitchel (ref. 14), and by Mitchiner and Mabie (ref. 15). Surface pitting of the gear teeth in the full load region must also be treated (refs. 16 to 18) as must gear scoring at the tip of the gear tooth (refs. 19 and 20).

The objective of the research reported here is to establish an optimal design procedure for spur gear pairs. Standard tooth forms are assumed. Figure 1 shows a single mesh of the external type, and figure 2 shows a single mesh of the internal type. The procedure developed in this paper uses standard gear geometry and optimizes the remaining parameters to obtain the most compact standard gearset for a given application of specified speed reduction and input torque. The procedure applies to internal and external gearing.

Figures

Nomenclature

a	addendum ratio
C	center distance, m
d	dedendum ratio
E	elastic modulus, Pa
F	tangential tooth load, N
f	gear face width, m
k	slope of equal size design line in design space
l	parabolic beam height, m
m_g	gear ratio
m_p	contact ratio
N	tooth number

*Work partially supported by NASA Grant NAG3-55.

[†]The University of Akron.

[‡]Propulsion Laboratory, U.S. Army Research and Technology Laboratories (AVRADCOM), NASA Lewis Research Center.

[§]NASA Lewis Research Center.

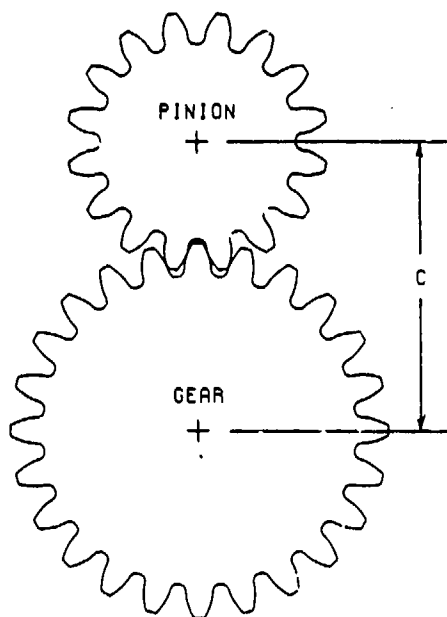


Figure 1. - External gear mesh.

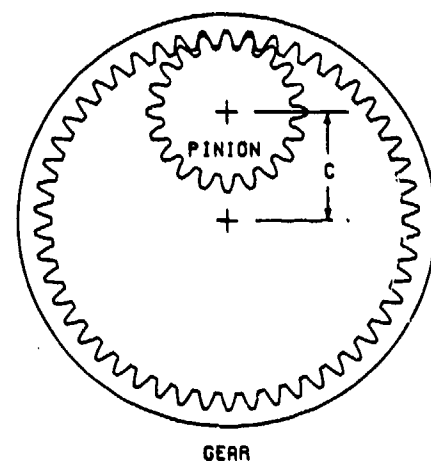


Figure 2. - Internal gear mesh.

n	number of million stress cycles
P_d	diametral pitch
p_b	base pitch, m
R	pitch radius, m
R_a	addendum radius, m
R_b	base circular radius, m
S	probability of survival
T_p	pinion torque, N·m
t	parabolic beam depth, m
V	stress volume, m ³
Y	Lewis tooth form factor
Z	length of action, m
z_o	depth to maximum shearing stress, m
β	secondary interference angle, deg
γ	secondary interference gear rotation angle, deg
δ	roll angle to initial point of contact, deg
θ	involute correction angle, deg
θ_B	pinion roll angle to lowest point of single tooth contact, rad
θ_c	pinion roll angle to lowest point of tooth contact, rad
λ	length to diameter ratio
ν	Poisson's ratio
ρ	radius of curvature, m
σ_B	bending fatigue stress, Pa
σ_{BT}	bending fatigue stress for load at the pinion tooth tip, Pa
σ_N	surface pressure, Pa
σ_{NT}	surface pressure at the gear tooth tip, Pa
τ	shearing stress, Pa

ϕ pressure angle, deg
 Ω_p pinion speed, rpm
 Subscripts:
 1 pinion
 2 gear

Design Problem

A gearset is normally used to transmit an input torque from a shaft turning at one speed to an output torque on a shaft turning at a lower speed. Parameters for this situation are the gear ratio, m_g , the pinion torque, T_p , and the pinion speed, Ω_p .

For an economical solution to this gear design problem, a standard tooth system made from standard tooling is to be sought. The standard American Gear System employs a limited number of diametral pitches, a standard operating pressure angle of 20° or 25°, and standard ratios of pinion and gear tooth addenda and dedenda to the reciprocal of diametral pitch. For full depth teeth, these standards are 1.0 for the addendum ratio and 1.25 for the dedendum ratio.

The size of the gearset is another design parameter which affects cost. The gear mesh center distance, C , is a measure of the size of the gearset. Obviously, a smaller gearset will use less material for the gears and for the surrounding housing. If the same life and reliability can be achieved in a smaller package, a more economical design is achieved.

Finally, the gear materials and their properties are an important facet of the gear design problem. The material cost, its modulus, E , its fatigue strength in bending, σ_B , and its surface endurance strength, σ_n , all affect the design.

Parameters and Constraints

One advantage to using an optimization technique is that it enables the designer to consider a spectrum of possible designs. The method employed in this research study starts by listing the design parameters available, the equality constraints that must be satisfied, the inequality constraints that define the limits of acceptable designs, and the merit function that is used to compare the relative merit of each possible design on an objective basis. In table 1 the design parameters and the relevant equality constraints are listed.

In this scheme the number of pinion teeth, N_1 , is a free parameter. The gear ratio, m_g , is an input parameter and the number of teeth on the gear, N_2 , is related to the number of teeth on the pinion by the gear ratio. For continuous rotation, both N_1 and N_2 must have integer values. The diametral pitch, P_d , is the second free parameter. The pinion pitch radius, R_1 , and the gear pitch radius, R_2 , define the size of the gears but are directly related to the tooth numbers by the diametral pitch. The center distance, C , is simply the sum of the pitch radii.

The next four items listed in table 1 are the pinion and gear addendum and dedendum ratios. For a standard gearset these ratios are 1 and 1.25 as noted. However, these ratios are among the first parameters changed when nonstandard gearing is used in order to improve on properties available from standard gearsets (refs. 2 to 4). The involute profile is also modified at its tip and root by a process called tip relief to improve the dynamic loading in the gear teeth at high speeds (ref. 21). Dynamic loading and tip relief are not treated in this study since we are searching for an optimal standard geometry that can be modified.

The gear mesh face width, f , is the next item listed. As long as the tooth load remains uniform, this width is directly proportional to the resulting strength of the gearset. For the tooth load to be uniform, a common criterion is to limit the length to diameter ratio of the line of contact (ref. 7). This ratio, λ , is related to the face width by the number of teeth on the pinion and the diametral pitch as shown. The mesh face width is thus determined for a given design by this limit.

The pitch-line pressure angle is another parameter that has been standardized to limit the required tooling inventory. Current values of common usage today are 20° and 25°.

The last series of items in table 1 are the relevant material properties that become fixed once materials and their heat treatments are specified for the pinion and the gear.

TABLE 1 GEAR MESH PARAMETER CONSTRAINTS

Parameter	Description	Equality constraint
N_1	Pinion tooth number	
m_g	Gear ratio	$m_g = (m_g)_{\text{design}}$
N_2	Gear tooth number	$N_2 = m_g N_1$
P_d	Diametral pitch	
R_1	Pinion pitch radius	$R_1 = N_1 / 2P_d$
R_2	Gear pitch radius	$R_2 = N_2 / 2P_d$
C	Center distance	$C = R_2 + R_1$
a_1	Pinion addendum ratio	1 for std tooth form
a_2	Gear addendum ratio	1 for std tooth form
d_1	Pinion dedendum ratio	1.25 for std tooth form
d_2	Gear dedendum ratio	1.25 for std tooth form
f	Mesh face width	$f = \lambda N_1 / P_d$
ϕ	Pitch line pressure angle	$\phi = \phi_{\text{STD}}$
E_1	Pinion radius	
ν_1	Pinion Poisson's ratio	Pinion
σ_{B1}	Pinion bending design stress	Material properties
σ_{N1}	Pinion surface design pressure	
E_2	Gear modulus	
ν_2	Gear Poisson's ratio	Gear
σ_{B2}	Gear bending design stress	Material properties
σ_{N2}	Gear surface design pressure	

Table 1 includes four parameter groups, addendum and dedendum ratios, face width, pressure angle, and material constants, which are tied down by standard practice but which could be varied in the design of nonstandard gearing. Several other parameters are determined exactly in terms of the input specifications and the free parameters. One parameter is a design input quantity, and only two parameters are free to be varied over an arbitrary range of values. These two free parameters in this formulation of the gear-mesh design problem are the number of teeth on the pinion and the diametral pitch. This leaves the designer with a two-dimensional design space for standard gears and a six-dimensional design space for nonstandard gears.

The design spaces are limited by the inequality constraints of the problem. These inequality constraints could generate a null design space by placing conflicting requirements on the free parameters. In a well posed design problem, they will enclose a bounded area of acceptable designs.

To assure a quiet mesh, the contact ratio of the mesh should be greater than some minimum value. The value 1.4 is commonly stated (refs. 6 and 7), but higher values will make the mesh even quieter. For reasonable manufacturing of the gear teeth, both the tooth tip and the tool tip should be wider than a specified minimum (ref. 3). These widths permit proper surface hardening of the tooth and prevent excessive tool tip wear in manufacture. For standard gearing, these three inequalities are automatically satisfied by the standard.

For proper tooth engagement and disengagement, involute interference (contact below the base circle) and secondary interference between the pinion tooth tip and the internal gear tooth tip for internal gearing must be avoided.

For proper gear mesh strength and life, the possibility of failure by three different mechanisms must be avoided. These mechanisms are pinion-tooth bending fatigue, surface fatigue, or spalling in the region of single-tooth load and gear-tip scoring.

To treat these three modes of failure on a common basis, a nominal stress approach is used. All three modes of failure are affected by more than the nominal design stress used herein. The bending fatigue is dependent on the surface finish of the tooth among other factors (refs. 6 and 7). The surface fatigue of the tooth is influenced by the stress volume and does not have an infinite life endurance limit (ref. 17). The gear tip scoring failure is highly temperature dependent (ref. 22).

However, this temperature is a direct result of the contact pressure and sliding velocity at the gear tip. The contact pressure is thus a meaningful parameter to predict the severity of both surface pitting and tip scoring. The nominal tooth bending stress will also be used as a measure of the bending fatigue severity.

Once all these limits have been applied to the design space, the designer is in a position to survey the acceptable designs and select the optimum. The criterion of this selection, called the merit function, is established as the center distance of the gears. By minimizing the center distance at a specified load, one produces the most economical gearset for the stated conditions since it would use the least material for the gears and permit the gearbox to assume a minimum size. This criterion could be inverted very easily if a fixed size was available for the gearset. The merit function would then become the maximum transmitted load for the given size or the maximum reliability for a given size and load.

Kinematic Interference

Involute interference occurs when the addendum circle of one gear crosses the line of action past the point of tangency with the base circle on the mating gear. For standard tooth systems with equal addenda, the pinion will always be the gear on which contact occurs below the base circle. The contact geometry is shown in figure 3 for an external gear and in figure 4 for an internal gear. Involute interference occurs when the gear tooth contacts the pinion tooth below its involute profile. The relation that describes this is a comparison of two distances. For contact with an external gear (fig. 3) the distance between the points of tangency of the line of action with the two base circles, A and E , should be greater than the distance on the gear along this line of action from the addendum circle, B , to the point of tangency with its base circle, E ;

$$\overline{AE} > \overline{BE} \quad (1)$$

or

$$C \sin \phi > \sqrt{R_{a2}^2 - R_{b2}^2} \quad (2)$$

for no primary interference.

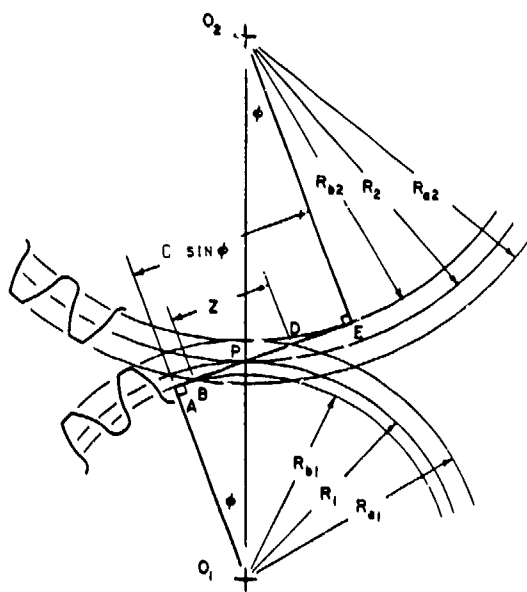


Figure 3. - Pinion - external gear mesh geometry.

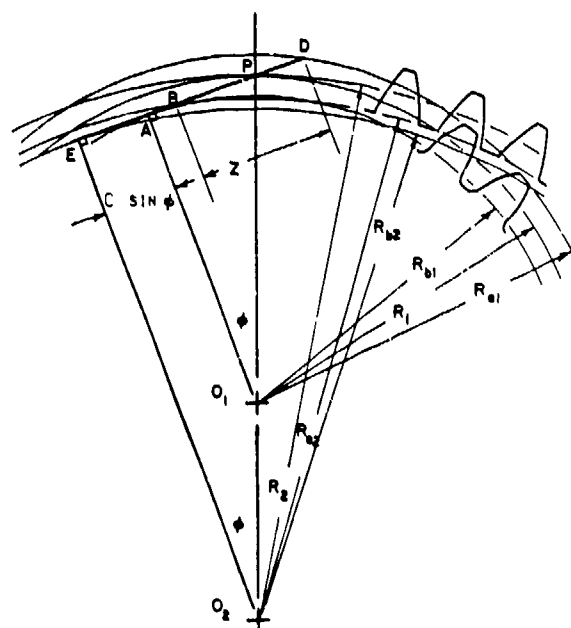


Figure 4. - Pinion - internal gear mesh geometry.

The standard cure for primary involute interference is to increase the number of teeth on the pinion for the desired gear ratio until the inequality is satisfied. These relationships can be used to define a minimum number of teeth required to avoid interference. Since

$$C = R_1 + R_2 \quad (3)$$

$$R_1 = \frac{N_1}{2P_d} \quad (4)$$

$$R_2 = \frac{N_2}{2P_d} \quad (5)$$

$$R_{b2} = R_2 \cos \varphi = \frac{N_2 \cos \varphi}{2P_d}, \quad (6)$$

and

$$R_{a2} = R_2 + \frac{a_2}{P_d} = \frac{N_2}{2P_d} + \frac{a_2}{P_d} \quad (7)$$

one has

$$\left(\frac{N_1 + N_2}{2P_d} \right) \sin \varphi > \sqrt{\left(\frac{N_2}{2P_d} + \frac{a_2}{P_d} \right)^2 - \left(\frac{N_2}{2P_d} \cos \varphi \right)^2} \quad (8)$$

multiplying through by $2P_d/N_2$, and solving for N_2 yields

$$N_2 > \frac{2a_2}{\sqrt{\cos^2 \varphi + \left(\frac{1}{m_g} + 1 \right)^2 \sin^2 \varphi} - 1} \quad (9)$$

or, in terms of N_1 ,

$$N_1 > \frac{2a_2/m_g}{\sqrt{\cos^2 \varphi + \left(\frac{1}{m_g} + 1 \right)^2 \sin^2 \varphi} - 1} \quad (10)$$

for contact with an external gear.

For contact with an internal gear (fig. 4) the distance between the points of tangency of the line of action with the two base circles, \overline{EA} , should be less than the distance on the gear along the line of action from the addendum circle, B , to the point of tangency with its base circle, E .

$$\overline{EA} < \overline{EB} \quad (11)$$

$$C \sin \varphi < \sqrt{R_{a2}^2 - R_{b2}^2} \quad (12)$$

In this case

$$C = R_2 - R_1 \quad (13)$$

and

$$R_{a2} = \frac{N_2}{2P_d} - \frac{a_2}{P_d} \quad (14)$$

Thus,

$$\left(\frac{N_2 - N_1}{2P_d} \right) \sin \varphi < \sqrt{\left(\frac{N_2}{2P_d} - \frac{a_2}{P_d} \right)^2 - \left(\frac{N_2}{2P_d} \right) \cos^2 \varphi} \quad (15)$$

Multiplying through by $2P_d/N_2$ and solving for N_2 yields

$$N_2 > \frac{2a_2}{1 - \sqrt{\cos^2 \varphi + \left(1 - \frac{1}{m_g}\right)^2 \sin^2 \varphi}} \quad (16)$$

or, in terms of N_1 ,

$$N_1 > \frac{2a_2/m_g}{1 - \sqrt{\cos^2 \varphi + \left(1 - \frac{1}{m_g}\right)^2 \sin^2 \varphi}} \quad (17)$$

for contact with an internal gear.

By satisfying relation 10 or 17, one can assure that primary involute interference will not occur for a given gear ratio, pressure angle, and gear addendum ratio. This check is sufficient for all cases in which the gear addendum ratio equals the pinion addendum ratio, as is the case for standard gears.

However, if the pinion addendum ratio were greater than that on the gear, one would also have to check interference on the gear tooth. For contact with an external gear, the pinion addendum must cross the line of action inside the point of tangency between the line of action and the gear base circle.

$$AD < AE \quad (18)$$

The resulting limit on the number of pinion teeth is

$$N_1 > \frac{2a_1}{\sqrt{\cos^2 \varphi + (1 + m_g)^2 \sin^2 \varphi} - 1} \quad (19)$$

for contact with an external gear.

To avoid interference with the base of the internal gear tooth, the addendum radius of the gear must be greater than its base radius.

$$R_{a2} > R_{b2} \quad (20)$$

$$\frac{N_2}{2P_d} - \frac{a_2}{P_d} > \frac{N_2}{2P_d} \cos \varphi \quad (21)$$

or

$$N_2 > \frac{2a_2}{1 - \cos \varphi} \quad (22)$$

In terms of N_1 this becomes

$$N_1 > \frac{2a_2/m_g}{1 - \cos \phi} \quad (23)$$

For standard teeth with $a_2 = 1.0$, this requires N_2 to be greater than 34 teeth for a 20° pressure angle or 22 teeth for a 25° pressure angle. This does not pose a problem for standard teeth.

For contact with an internal gear a second type of kinematic interference is possible in which the tip of the internal gear contacts the tip of the pinion as they come into mesh (refs. 11 and 12). This interference, called "fouling," is illustrated in figure 5. In this figure two mating gears are shown in contact at the pitch point, P . The clearance between the teeth can be seen three or four teeth away from the pitch point. However, as one moves further from the pitch point to the intersection of the two addendum circles, interference between the tips of teeth on the two gears can be seen.

To avoid this secondary interference, or fouling, the actual rotation of the gear tooth caused by the rotation of the pinion tooth must be greater than the rotation of the gear tooth that would allow interference. The actual rotation of the pinion tooth is given by

$$\gamma_1 = \beta_1 + \theta_1 \quad (24)$$

Where β_1 is the angle from the pitch point to the intersection of the addendum circles on the pinion. It can be found from the law of cosines that

$$\beta_1 = \cos^{-1} \left(\frac{R_{a2}^2 - R_{a1}^2 - C^2}{2CR_{a1}} \right) \quad (25)$$

The angle θ_1 is the angle on the pinion tooth between the pitch circle and the addendum circle. It is given by

$$\theta_1 = \text{inv } \phi_{a1} - \text{inv } \phi \quad (26)$$

where ϕ is the pitch line pressure angle and ϕ_{a1} is the pressure angle at the addendum circle. The involute function (ref. 7) is shown in figure 6 and is related to the involute curve's pressure angle by

$$\text{inv } \phi = \tan \phi - \phi \quad (27)$$

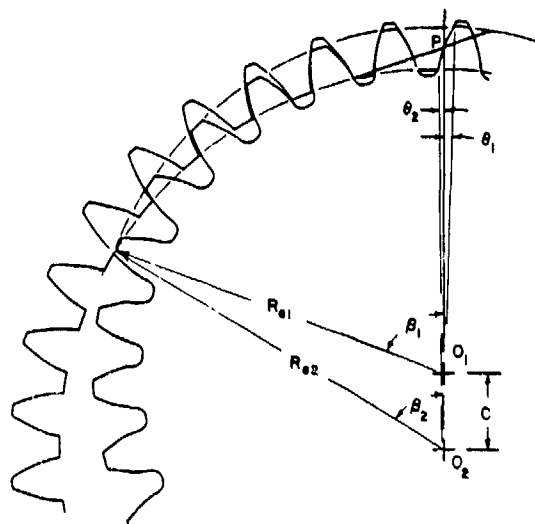


Figure 5. - Secondary interference geometry.

where φ is measured in radians for this calculation.

The rotation limit of the gear is given by

$$\gamma_2 = \beta_2 - \theta_2 \quad (28)$$

where β_2 is the angle from the pitch point to the intersection of the addendum circles on the gear, found from β_1 by the law of sines, such that

$$\beta_2 = \sin^{-1} \left(\frac{R_{a1} \sin \beta_1}{R_{a2}} \right) \quad (29)$$

and where θ_2 is the angle on the gear tooth between the pitch circle and the addendum circle, that is,

$$\theta_2 = \text{inv } \varphi - \text{inv } \varphi_{a2} \quad (30)$$

Since the actual gear rotation must be greater than this rotation limit for a rotation of γ_1 of the pinion,

$$\frac{\gamma_1}{m_g} > \gamma_2 \quad (31)$$

to avoid secondary interference or fouling.

Contact Ratio

The contact ratio for a given spur gear mesh is the ratio of the length of action along the line of action between the two addendum circles to the base pitch:

$$m_p = \frac{Z}{p_b} \quad (32)$$

In this equation

$$p_b = \frac{\pi}{P_d} \cos \varphi \quad (33)$$

where the base pitch, p_b , is defined as the distance from one tooth to the next, measured along the line of action. The length of contact, Z , can be expressed as

$$Z = \overline{BD} = \sqrt{R_{a1}^2 - R_{b1}^2} + \sqrt{R_{a2}^2 - R_{b2}^2} - C \sin \varphi \quad (34)$$

for contact with an external gear as shown in figure 3. Combining these equations yields

$$m_p = \frac{N_1}{2\pi \cos \varphi} \left[\sqrt{\left(1 + \frac{2a_1}{N_1}\right)^2 - \cos^2 \varphi} + \sqrt{\left(m_g + \frac{2a_2}{N_1}\right)^2 - m_g^2 \cos^2 \varphi} - (1 + m_g) \sin \varphi \right] \quad (35)$$

For contact with an internal gear (fig. 4) the length of contact, Z , is given by

$$Z = \sqrt{R_{a1}^2 - R_{b1}^2} - \sqrt{R_{a2}^2 - R_{b2}^2} + C \sin \varphi \quad (36)$$

The contact ratio for this case can be expressed as

$$m_p = \frac{N_1}{2\pi \cos \varphi} \left[\sqrt{\left(1 + \frac{2a_1}{N_1}\right)^2 - \cos^2 \varphi} - \sqrt{\left(m_g - \frac{2a_2}{N_1}\right)^2 - m_g^2 \cos^2 \varphi} - (1 - m_g) \sin \varphi \right] \quad (37)$$

This contact ratio should be greater than 1.4 and is normally less than 2.0 for standard spur gears. For contact with an internal gear at low ratios and for nonstandard addenda and dedenda, it can exceed 2.0. For the strength modeling of this design study, it will be assumed to be less than 2.0.

Gear-Tooth Strengths

Spur-gear teeth have three distinct modes of failure. A tooth may fail in bending fatigue at its root, it may fail by pitting fatigue on its surface, or it may fail by scoring at the tip of the gear tooth.

The basic model for bending failure of a gear tooth was developed by Wilfred Lewis in 1893 (ref. 15). Although the knowledge of fatigue strengths and this mechanism of failure have increased significantly since then, compensating factors exist that make the Lewis model of bending failure reasonably accurate. As a result, it is still the bending strength analysis in use today. The idea is to fit the largest possible constant-width, constant-surface-stress cantilever inside the tooth. The apex of this parabolic beam is placed at the intersection of the applied load and the centerline of the tooth (shown as point *b* in fig. 7). The strength of the tooth is then equated to the strength of this beam:

$$\sigma_L = \frac{Mc}{I} = \frac{6Fl}{ft^2} \quad (38)$$

where F is the tangential load in newtons, l is the parabola length in meters, f is the gear face width in meters, and t is the parabola depth at the critical tooth section in meters. Lewis has written this expression as

$$\sigma_L = \frac{FP_d}{fY} \quad (39)$$

where Y is the dimensionless Lewis form factor, which is a function of the proportion of the tooth and not its size.

$$Y = \frac{t^2 P_d}{6l} \quad (40)$$

The form factor Y can thus be determined by locating the point of tangency between the tooth fillet and the parabola inscribed within the tooth with its apex at *b* (labeled *a* in fig. 7).

The length, t , is the full thickness of the parabola at this point, while l is the distance between points *b* and *a* along the tooth centerline. These distances can be found by an iterative scheme which finds the point of the fillet for which the tangent to the fillet crossed the centerline of the tooth at *c*, a distance l above the parabola apex—point *b*. This tangent will also be tangent to the inscribed parabola with its apex at *b*. This calculation (refs. 14 and 15) requires knowledge of the tip radius of the tool, the addendum and dedendum of the gear tooth as well as the pitch line pressure angle of the tooth. These four quantities are fixed for a given standard gear system. The procedure assumes that the tooth width and tooth space are equal at the pitch radius.

In addition, the iteration procedure requires knowledge of the number of teeth on the gear and the pressure angle at the point on the involute surface of the tooth at which the load is acting. This pressure angle increases from zero at the base radius to the nominal pressure angle at the pitch circle to a maximum pressure angle at the largest involute radius on the tooth. Standard tables (refs. 6 and 7) of tooth form factors give the factor for the load at the tooth tip or at the middle of the tooth for a given tooth system. The factors are then tabulated versus the number of teeth on the pinion since the

factor magnitude is independent of the physical size of the gear. The factor for the load at the tooth tip is given since this is for the largest effective cantilever loading on the tooth. However, at this point the load is shared with another mesh so a second point of concern is the highest point of single tooth load. This point is approximated by placing the load at the middle of the tooth for tabular purposes. A more correct procedure is to use the highest point of single tooth contact. This point varies with the gear ratio and can be found from an analysis of the mesh geometry. Once found, it is defined by the pressure angle, ϕ_A , of the involute at that point. This pressure angle is related to the roll angle, θ_A , of the involute as shown in figure 6. Here θ_A is the angle of unwrap of the line of action from the base circle:

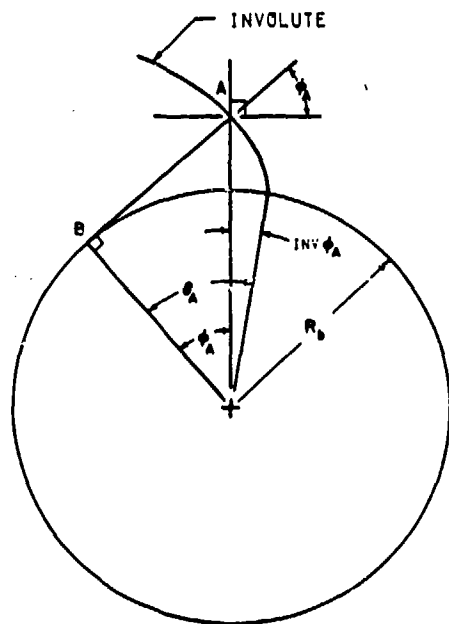


Figure 6. - Involute angle geometry.

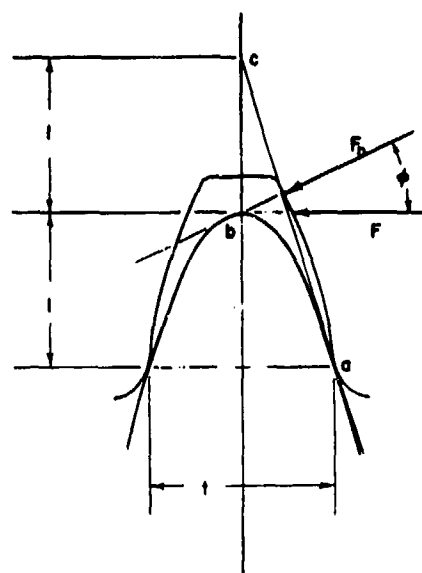


Figure 7. - Tooth bending strength model.

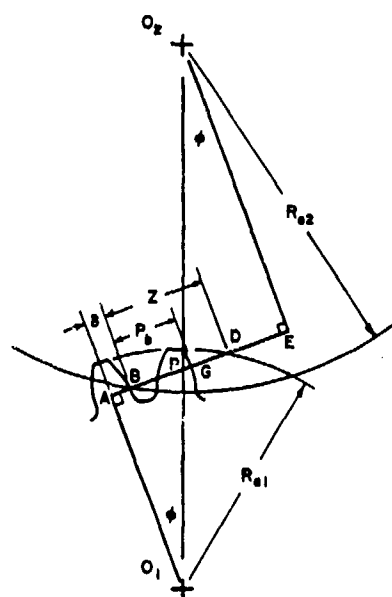


Figure 8. - Highest point of single tooth contact for an external gear mesh.

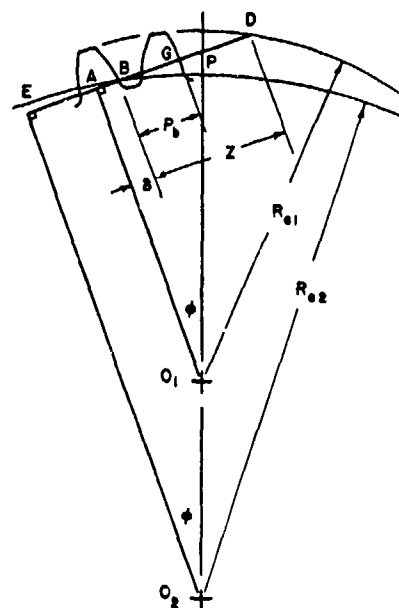


Figure 9. - Highest point of single tooth contact for an internal gear mesh.

$$\theta_A = \frac{\overline{AB}}{R_b} = \tan \varphi_A \quad (41)$$

hence,

$$\varphi_A = \tan^{-1} \theta_A \quad (42)$$

The roll angle to the highest point of single tooth contact can be determined by considering figure 8 for contact with an external gear and figure 9 for contact with an internal gear. In both cases the distance \overline{AD} is given by

$$\overline{AD} = \sqrt{R_{a1}^2 - R_{b1}^2} \quad (43)$$

and the distance \overline{GD} is given by

$$\overline{GD} = Z - p_b \quad (44)$$

The highest point of single tooth contact is at G and its roll angle is

$$\theta_A = \frac{AG}{R_{b1}} = \frac{\sqrt{R_{a1}^2 - R_{b1}^2} - (Z - p_b)}{R_{b1}} \quad (45)$$

Similarly, the roll angle to the lowest point of single tooth contact can be found by rolling the pinion until G corresponds to D . In this position the second tooth which was at B will have moved up to the start of single tooth contact. Thus,

$$\theta_B = \frac{\overline{AD} - p_b}{R_{b1}} \quad (46)$$

defines the roll angle to the lowest point of single tooth contact on the pinion tooth. It is at this point where the Hertzian pressure due to single tooth contact is a maximum.

It has been shown that the surface endurance of gear teeth behaves much like that of rolling-element bearings (ref. 17). The life of the contact is represented by

$$\ln \frac{1}{S} \sim \frac{\tau^c V n e}{z_o^h} \quad (47)$$

where S is the probability of survival, τ is the critical shear stress, n is the number of million stress cycles, z_o is the depth to the critical stress, e is the Weibull exponent, and c and h are material constants. The three design parameters in this expression are the stress, its depth, and the volume of material subjected to the stress. Since the depth of the critical shear stress is nearly fixed and since the stress is raised to a power in excess of three, relative to the volume, it is assumed in this study that the magnitude of surface compression is a reasonable measure of the tendency of the surface to pit. It is thus used as a criterion for design comparison.

The Hertzian pressure which produces spalling can be modeled by

$$\sigma_N = \sqrt{\frac{F}{\pi f \cos \varphi} \left(\frac{1/\rho_1 + 1/\rho_2}{\frac{1-\nu_1^2}{E_1} + \frac{1-\nu_2^2}{E_2}} \right)} \quad (48)$$

where ρ_1 and ρ_2 are the radii of curvature at the point of contact. For this study it will be assumed that the two gears are made of the same material. It can be seen from figures 10 and 11 that the

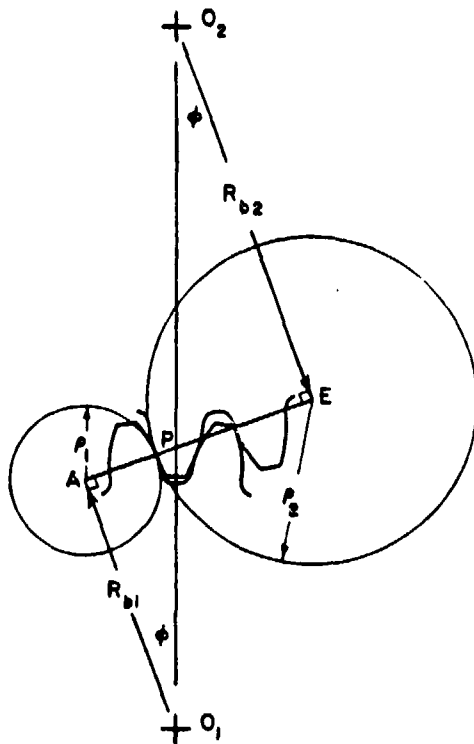


Figure 10. - Tooth surface curvature for an external gear mesh.

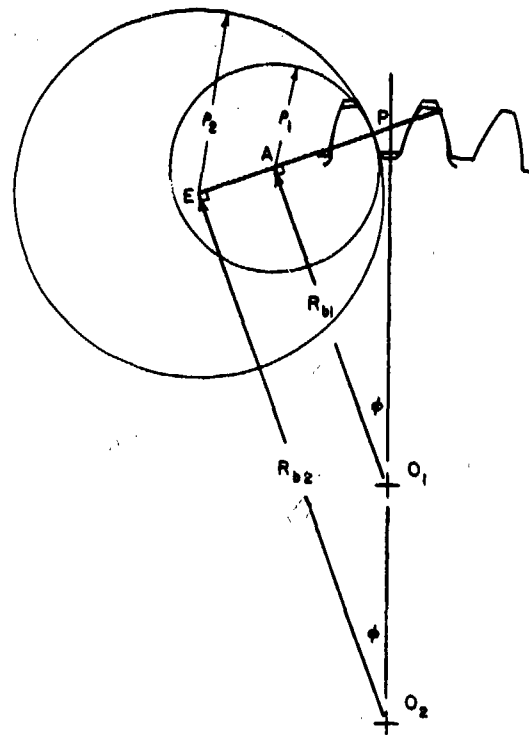


Figure 11. - Tooth surface curvature for an internal gear mesh.

centers of curvature of the two gear teeth surfaces are the points of tangency of the line of action with the respective base circles. Since these points are fixed, one has

$$\rho_2 = C \sin \varphi - \rho_1 \quad (49)$$

for the external gear and

$$\rho_2 = -C \sin \varphi - \rho_1 \quad (50)$$

for the internal gear where the minus sign indicates conformal contact. At the point of maximum Hertzian pressure, in the single-tooth contact region,

$$\rho_1 = \theta_B R_{b1} \quad (51)$$

Putting all this together, one has

$$\sigma_N = \sqrt{\frac{FE(C \sin \varphi)}{2(1-\nu^2)\pi f \cos \varphi (\theta_B R_{b1})(C \sin \varphi \mp \theta_B R_{b1})}} \quad (52)$$

where the minus sign holds for contact with an external gear and the plus sign holds for contact with an internal gear.

The scoring mode of failure is more difficult to predict since it is influenced by a combination of factors. Scoring is caused by an instability in oil film thickness at high speed and high load with inadequate cooling. In addition to surface pressure, this mode of failure is affected by the relatively large sliding velocity present at the gear tip and by the temperature of the teeth. Because of the sliding velocity present, some elastohydrodynamic effects are present in the contact that alter the pressure distribution from the simple Hertzian model of equation (48). Oil cooling has a major effect in preventing scoring.

A second factor exists which increases the tip pressure above that of the simple model. That factor is dynamic loading, which is largest at the initial point of contact. When the pinion drives the gear making the mesh a speed reduction, this point of initial contact is the gear tooth tip and the base of the pinion tooth. Because of the complexities involved in dynamic load estimation, the contact pressure at the gear tip is modeled by equation (48). In this case the radius of curvature on the pinion tooth is given by

$$\rho_1 = \overline{AB} = \sqrt{R_{a1}^2 - R_{b1}^2} - Z \quad (53)$$

and the radius of curvature of the gear tooth is given by equation (49) for an external gear or equation (50) for an internal gear. The roll angle to this point of contact on the pinion is

$$\theta_c = \frac{\overline{AB}}{R_{b1}} \quad (54)$$

and

$$\sigma_{NT} = \sqrt{\frac{FE(C \sin \varphi)}{2(1 - \nu^2)\pi f \cos \varphi (\theta_c R_{b1})(C \sin \varphi \mp \theta_c R_{b1})}} \quad (55)$$

gives the surface pressure.

Although contact pressure is only one factor in this mode of failure, it is a significant one. If this pressure is extreme, the design is not in balance, and excessive measures must be taken in the other factors to compensate. It is felt then that the contact pressure at the gear tip should be kept to the same level as that in the single-tooth load region.

Design Space

As shown in table I and described in the section on parameters and constraints, the standard gear design problem for gears made of a chosen material can be reduced to a two-dimensional design problem where the two free parameters are the number of teeth on the pinion and the diametral pitch.

The inequality constraints which bound this design space are the minimum number of teeth required to prevent interference and the three strength limits. These strength limits can be converted to expressions for the maximum allowable diametral pitch for the given problem as functions of the number of teeth on the pinion. As stated in table I the face width can be expressed in terms of the length-to-diameter ratio of the gear tooth contact:

$$f = \lambda \frac{N_1}{P_d} \quad (56)$$

The load can also be expressed in terms of the diametral pitch:

$$F = \frac{T_p}{R_1} = \frac{2T_p P_d}{N_1} \quad (57)$$

For the bending limit where Y is taken as the tooth-form factor for the highest point of single-tooth contact for the given ratio and the number of teeth on the pinion, combining equations (39), (56), and (57) yields

$$\sigma_L = \frac{2T_p P_d^3}{Y \lambda N_1^2} \quad (58)$$

or in terms of the allowable bending strength σ_B

$$P_d \leq \sqrt[3]{\frac{\sigma_B Y \lambda N_1^2}{2T_p}} \quad (59)$$

For the single-tooth pitting limit, equations (56) and (57) are combined with equation (52):

$$\sigma_N^2 = \frac{2T_p E P_d^3 \sin \varphi}{(1 - \nu^2) \pi \lambda N_1^2 \cos^2 \varphi (\theta_B N_1) \left[\sin \varphi \mp \frac{\theta_B \cos \varphi}{(m_g \pm 1.0)} \right]} \quad (60)$$

where θ_B is given by equation (46) and is a function of N_1 and φ . This equation can also be solved for an upper bound on P_d as a function of N_1 and the allowable surface wear pressure, σ_N :

$$P_d \leq \sqrt[3]{\frac{(1 - \nu^2) \pi \lambda N_1^3 \sigma_N^2 \cos^2 \varphi \theta_B}{2T_p E \sin \varphi} \left[\sin \varphi \mp \frac{\theta_B \cos \varphi}{(1 \pm m_g)} \right]} \quad (61)$$

where the positive sign holds for contact with an external gear while the negative m_g is for contact with an internal gear.

Finally, a similar equation can be found for the limit on P_d based on gear-tooth tip scoring in terms of θ_c , the roll angle on the pinion to the initiation of contact. This angle, as given by equation (54), is also a function of only N_1 and φ for the stated problem:

$$P_d \leq \sqrt[3]{\frac{(1 - \nu^2) \pi \lambda N_1^3 \sigma_N^2 \cos^2 \varphi \theta_c}{2T_p E \sin \varphi} \left[\sin \varphi - \frac{\theta_c \cos \varphi}{(1 \pm m_g)} \right]} \quad (62)$$

These limits are plotted in figure 12 for the case $\varphi = 20^\circ$, $m_g = 1.0$, $\lambda = 0.25$, $T_p = 113 \text{ N}\cdot\text{m}$ (1000 lb-in), $E = 205 \text{ GPa}$ ($30 \times 10^6 \text{ psi}$), $\nu = 0.25$, $\sigma_N = 1.38 \text{ GPa}$ (200 000 psi) and $\sigma_B = 414 \text{ MPa}$ (60 000 psi). The gear for this design problem is external. The acceptable design space is the upper left hand corner of the plot.

The merit function for this problem is the center distance, C :

$$C = \frac{N_1}{2P_d} (m_g \pm 1) \quad (63)$$

where the plus sign is valid for an external gear, and the negative sign holds for an internal gear in equations (62) to (64). For a given gear ratio the locus of equally optimum designs can be found by considering C to be constant. This produces the relation

$$N_1 = \left[\frac{2C}{(m_g \pm 1)} \right] P_d \quad (64)$$

which states that equally sized designs lie on a straight line through the origin. Since the smaller C , the better the design, the best design corresponds to the line of least slope drawn through the origin which lies within the design space. For this design the line of least slope within the design space crosses the two surface pressure limits at their intersection, point A in figure 12.

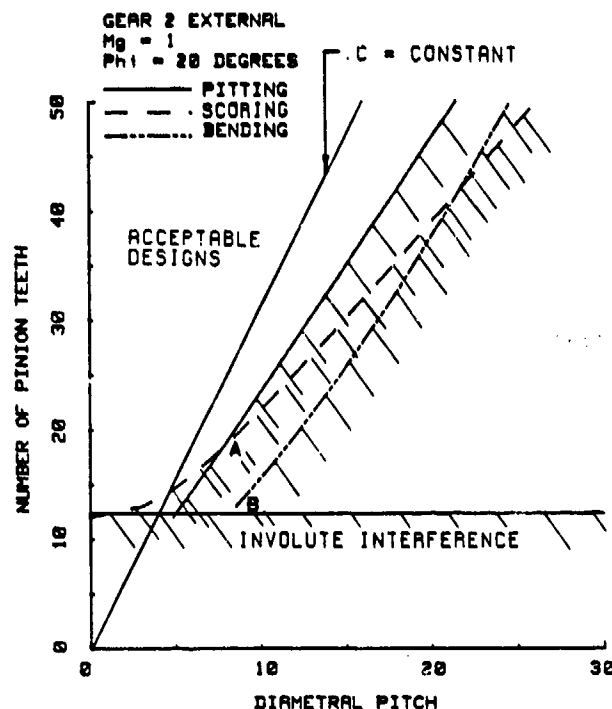


Figure 12

Optimal Designs

In this study arbitrarily chosen values are used for the tooth width to pinion pitch diameter ratio, λ , and the pinion torque, T_p . Values of 0.25 and 113 N·m (1000 lb·in) were chosen to reflect reasonable geometry and a nominal load. The design spaces do not change in character as these quantities are varied, so no loss in generality results from their use. The values of elastic modulus, Poisson's ratio, allowed surface pressure and bending fatigue strength are for hardened steel. If another material is used for the gears, the design space would be altered. However, the only real difference would be a shift in the relative importance of the surface wear strengths and the bending strengths.

For high-speed, high-cycle operations, point A in figure 12 is an important design point since it identifies the minimum number of pinion teeth required to keep the gear-tooth tip contact pressure at or below the maximum contact pressure in the full-load region of the tooth surface. By having at least this number of teeth in the pinion, a well balanced compact design can be achieved by sizing the gears based on the full-load contact surface pressure.

It is of interest to note that this limit is close to a straight line through the origin. Exceeding this minimum number of teeth does not significantly change the merit function, C , if one stays on the constraint line for pitting. This is partly due to the fact that the radius of curvature of the teeth is more a function of the base circle size than the tooth size once one gets away from the situation of tooth contact near the base circle.

A common design approach (ref. 7) in the design of gearsets has been to use the interference limit and the tooth bending strength limit to define the "best" design. This gives point B in the design space of figure 12. This point will produce a smaller gearset, since OB has a smaller slope than OA , but it ignores the pitting problems in the full load region and totally ignores the situation at the tip of the gear tooth. It thus will produce gears that are not balanced in their design and that may have pitting and scoring problems in service.

The design space of figure 12 can be used to study the effects of varying the parameters N_1 and P_d on a design with a gear ratio of 1 and a pressure angle of 20° . Similar design spaces can be drawn for different gear ratios and different pressure angles.

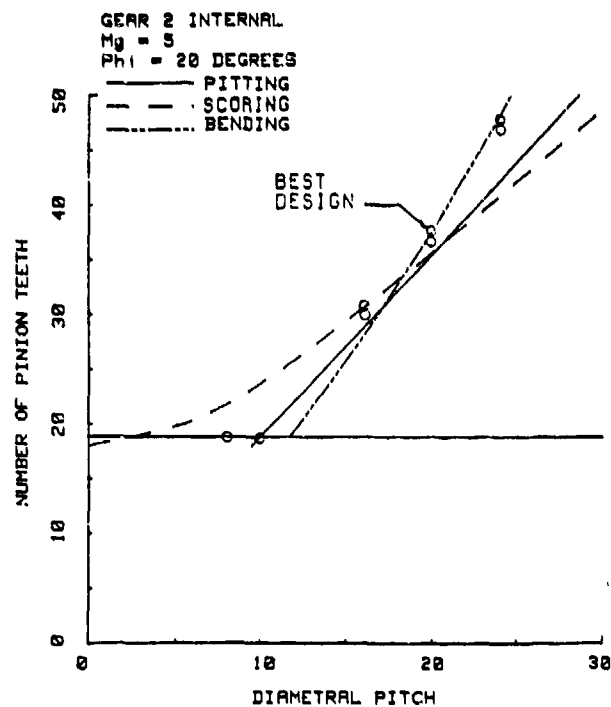
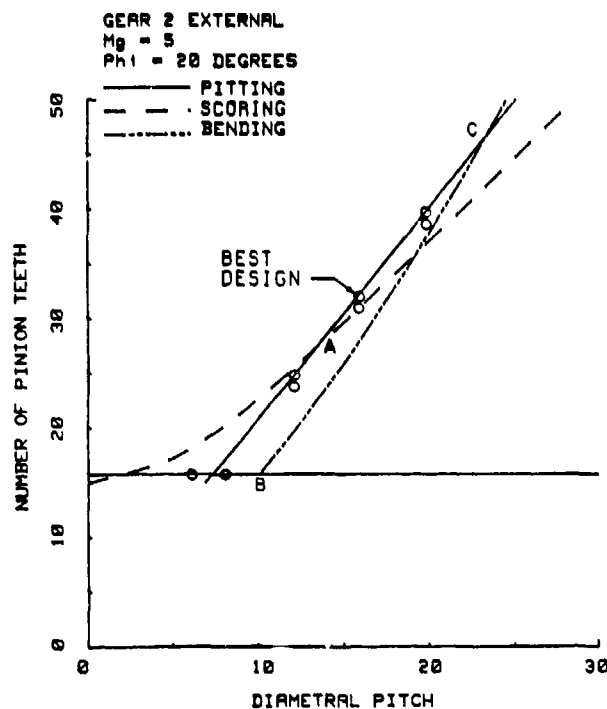


Figure 13. - External gear mesh design space with $\lambda = 0.25$, $T_p = 113$ N-m (1000 lb-in), $\sigma_N = 1.38$ GPa (200 ksi), $\sigma_B = 414$ MPa (60 ksi), $E = 205$ GPa (30×10^3 ksi), $\nu = 0.25$.

Figure 14. - Internal gear mesh design space with $\lambda = 0.25$, $T_p = 113$ N-m (1000 lb-in), $\sigma_N = 1.38$ GPa (200 ksi), $\sigma_B = 414$ MPa (60 ksi), $E = 205$ GPa (30×10^3 ksi), $\nu = 0.25$.

To illustrate the effect of gear ratio on the design space, this parameter has been varied for the conditions of figure 12. Figures 13 to 15 show the design space as this ratio changes from 1 to 5 for contact with an external gear and then continuing for contact with an internal gear of increasing conformal contact with ratios of 5 and 2.5.

A continuous change in characteristics occurs as the external gear ratio increases to infinity (contact with a rack) and the internal gear ratio reduces from infinity. Three distinct shifts occur in the design space as the gear ratio increases. First, the involute interference limit increases to a higher number of pinion teeth. Second, point A—the condition of equal surface contact pressure at the gear tip and at the lowest point of single tooth contact—shifts to a higher N_1 and a higher P_d . Third, the bending fatigue strength limit becomes more critical as the gear ratio increases.

The design tradeoff between pitting fatigue and bending fatigue is shown in the design space curves at the point where these two constraint curves cross (point C in fig. 13). If one were just concerned with bending fatigue failure, a reduction in the number of teeth from point C would produce a better design. Conversely, if one were just concerned with pitting fatigue, an increase in the number of teeth would produce a better design.

Figures 16 to 19 illustrate the effect of a 25° pressure angle on the design space for the same set of gear ratios. Basically, the same conclusions are present as for the 20° pressure angle design spaces. The increase in pressure angle also reduces the minimum number of pinion teeth required to avoid interference, and it reduces the bending load while it increases the bending strength, so the bending fatigue limit becomes less important as the pressure angle is increased. However, the pitting fatigue limit only improves a small amount, so increasing the pressure angle should not significantly improve the surface wear properties of a gearset.

These design spaces indicate that the most compact designs will have a minimal number of teeth. However, this number is not based on involute interference as implied by point B but is based on equal contact pressure at the base of the tooth and in the region of single-tooth contact. Figures 20 and 21 are plots of the numbers of teeth which produce this equality of contact pressure, assuming equal load sharing when two tooth sets are in contact. The upper branch of each curve is for contact

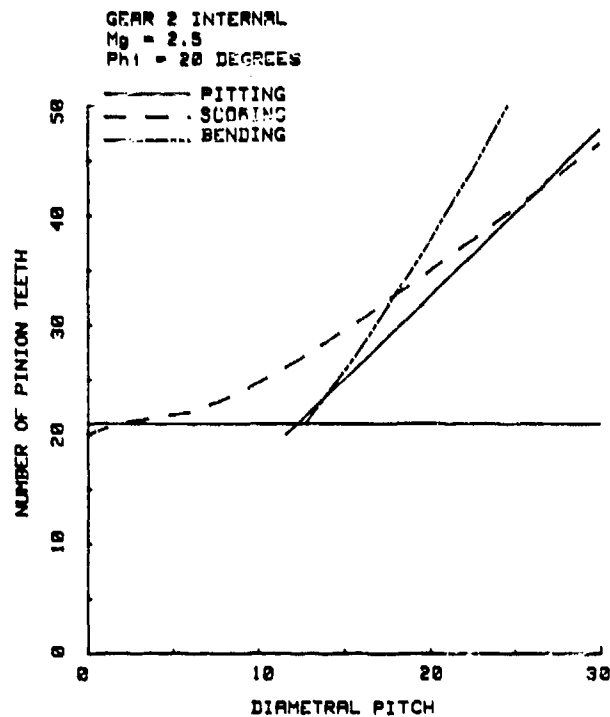


Figure 15. - Internal gear mesh design space with $\lambda = 0.25$, $T_p = 113$ N-m (1000 lb-in), $\sigma_N = 1.38$ GPa (200 ksi), $\sigma_B = 414$ MPa (60 ksi), $E = 205$ GPa (30×10^3 ksi), $\nu = 0.25$.

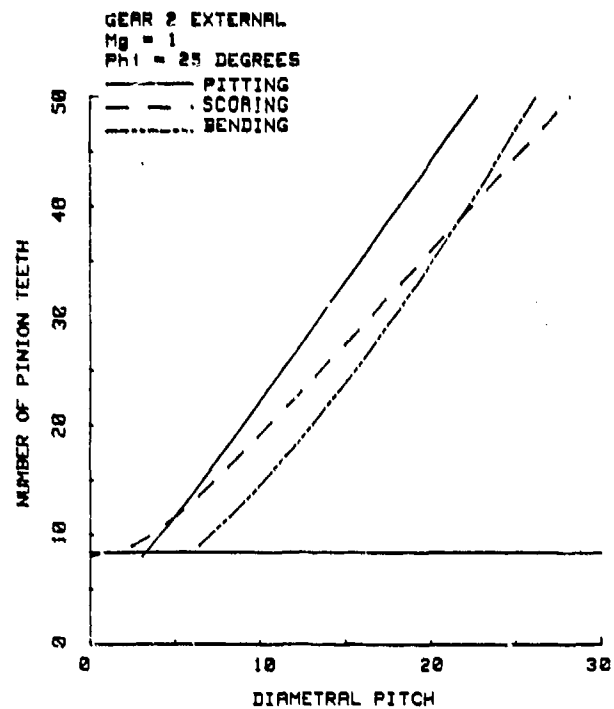


Figure 16. - External gear mesh design space with $\lambda = 0.25$, $T_p = 113$ N-m (1000 lb-in), $\sigma_N = 1.38$ GPa (200 ksi), $\sigma_B = 414$ MPa (60 ksi), $E = 205$ GPa (30×10^3 ksi), $\nu = 0.25$.

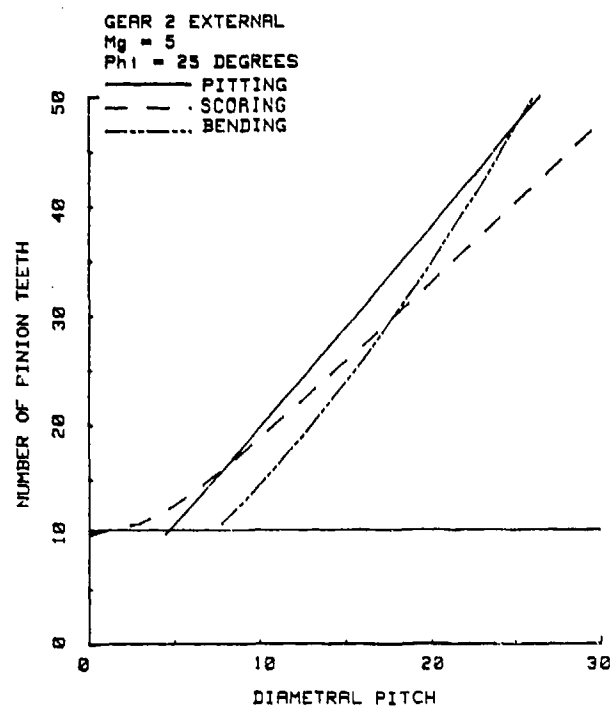


Figure 17. - External gear mesh design space with $\lambda = 0.25$, $T_p = 113$ N-m (1000 lb-in), $\sigma_N = 1.38$ GPa (200 ksi), $\sigma_B = 414$ MPa (60 ksi), $E = 205$ GPa (30×10^3 ksi), $\nu = 0.25$.

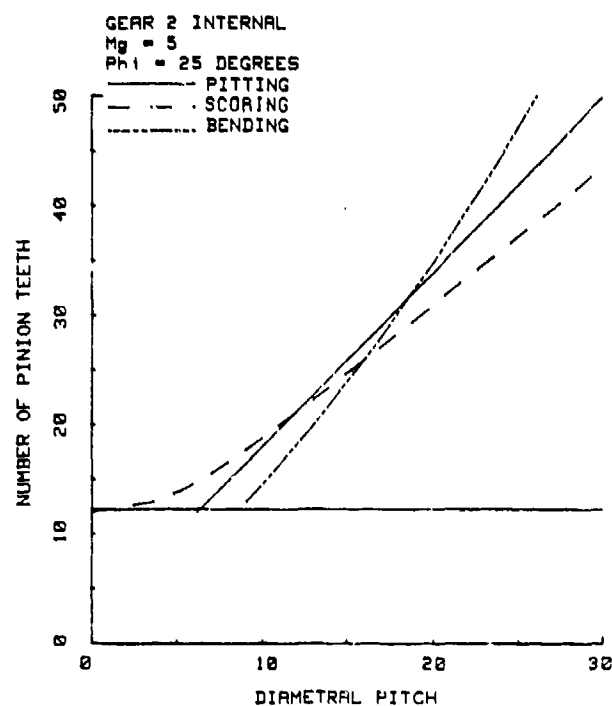


Figure 18. - Internal gear mesh design space with $\lambda = 0.25$, $T_p = 113$ N-m (1000 lb-in), $\sigma_N = 1.38$ GPa (200 ksi), $\sigma_B = 414$ MPa (60 ksi), $E = 205$ GPa (30×10^3 ksi), $\nu = 0.25$.

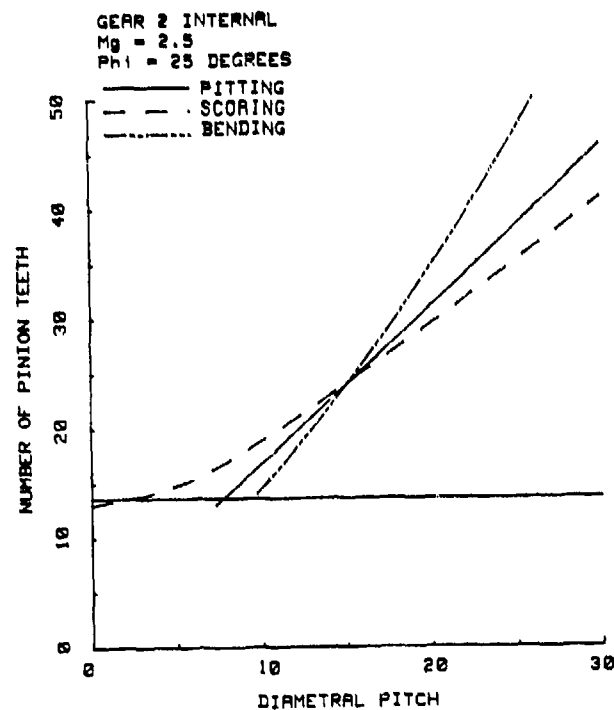


Figure 19. - Internal gear mesh design space with $\lambda = 0.25$, $T_p = 113$ N-m (1000 lb-in), $\sigma_N = 1.38$ GPa (200 ksi), $\sigma_B = 414$ MPa (60 ksi), $E = 205$ GPa (30×10^3 ksi), $\nu = 0.25$.

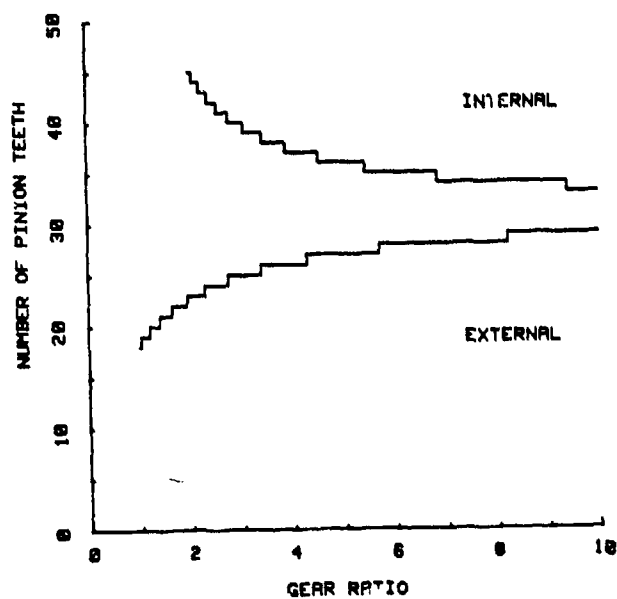


Figure 20. - Optimal number of pinion teeth for 20° pressure angle.

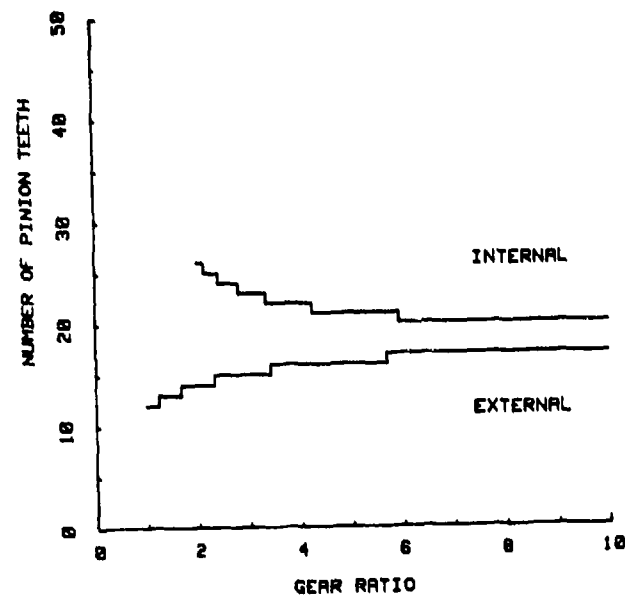


Figure 21. - Optimal number of pinion teeth for 25° pressure angle.

with an internal gear, while the lower branch is for contact with an external gear. Figure 20 is for 20° pressure angle while figure 21 is for 25° pressure angle standard tooth systems. A truly optimal design might use a slightly higher number of teeth in order to obtain a combination of gears with a standard diametral pitch and whole teeth.

Design Example

To illustrate the use of this method in design, consider a gear ratio of 5 and a pressure angle of 20°. Consider the pinion torque to be 113 N·m (1000 lb·in) and the other design values to be identical to those of figure 13 for convenience. For contact with an external gear, figure 20 indicates that for an optimal design using standard teeth, the pinion should have about 27 teeth. The design space for this particular example is shown in figure 13. One could check the design space of figure 13 to identify point A for which the diametral pitch is about 13.5.

Since this pitch would require nonstandard tooling, the best design will be shifted away from point A. However, it will lie near the pitting constraint line. This pitting constraint line can be closely approximated by a straight line from the origin through point A, with the slope given by

$$k = \frac{N_1}{P_d} \quad (65)$$

In this case

$$k = \frac{27}{13.5} = 2.0$$

The standard pitches near 13.5 can be used to find the numbers of teeth for near optimal designs with equation (65). Pitches of 12, 16, and 20 could be used to obtain minimal numbers of teeth of 24, 32, and 40, respectively. The best design will be in the set of trial designs with pinion teeth numbers near these limits.

Table 2 lists the possible optimum designs determined from equation (65) with diametral pitches of 12, 16, or 20. The best design is that with a P_d of 16 and 32 pinion teeth. This design has a center distance of 0.152 m (6.0 in.), a maximum contact pressure of 1.35 GPa (196 ksi), and a maximum fillet bending stress of 303 MPa (44 ksi). The design is shown in figure 22. Figure 23 is a plot of the maximum surface compression on the pinion tooth as a function of pinion roll angle.

TABLE 2 EXTERNAL GEAR DESIGNS

$$m_g = 5, \phi = 20^\circ$$

P_d	N_1	N_2	f	C	σ_{Nt}	σ_N	σ_B	σ_{BT}
-	-	-	m	m	GPa	GPa	MPa	MPa
12	24	120	.0127	.152	1.51	1.39	228	248
12	25	125	.0132	.159	1.37	1.30	207	228
16	31	155	.0123	.148	1.34	1.43	297	331
16	32	160	.0127	.152	1.26	1.35	276	303
20	39	195	.0124	.149	1.21	1.39	338	379
20	40	200	.0127	.152	1.16	1.34	324	359
8	16	80	.0127	.152	6.87	1.49	193	200
6	16	80	.0169	.203	4.45	.97	83	83

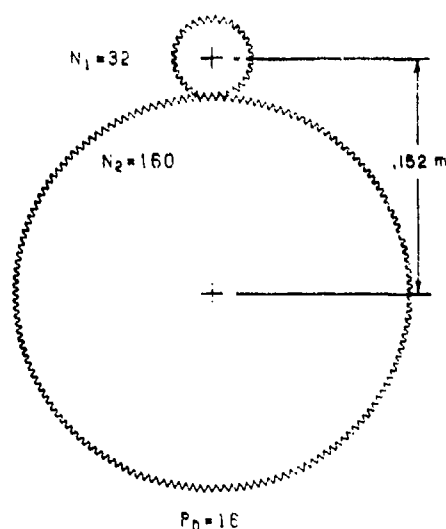


Figure 22. - Optimum design for $m_g = 5$, $\phi = 20^\circ$, and $T_p = 113 \text{ N-m}$ (1000 lb-in) for mesh with external gear.

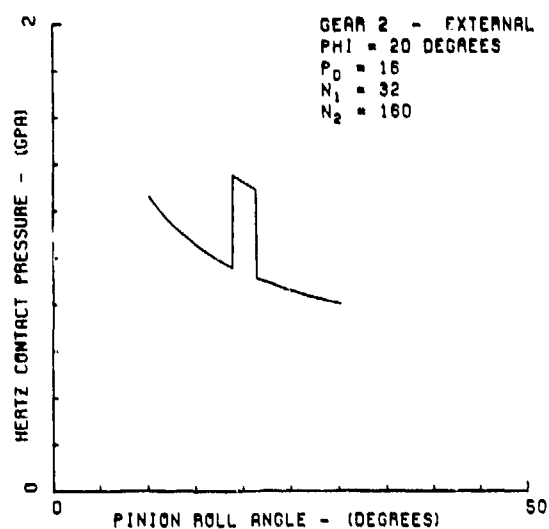


Figure 23. - Optimal external gear design-tooth surface pressure.

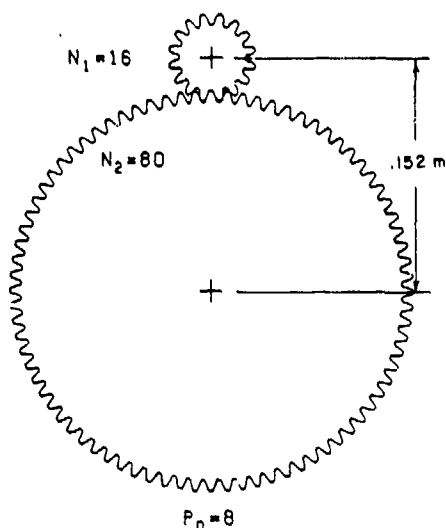


Figure 24. - Minimum tooth number design for $m_g = 5$, $\phi = 20^\circ$, and $T_p = 113 \text{ N-m}$ (1000 lb-in) for mesh with external gear.

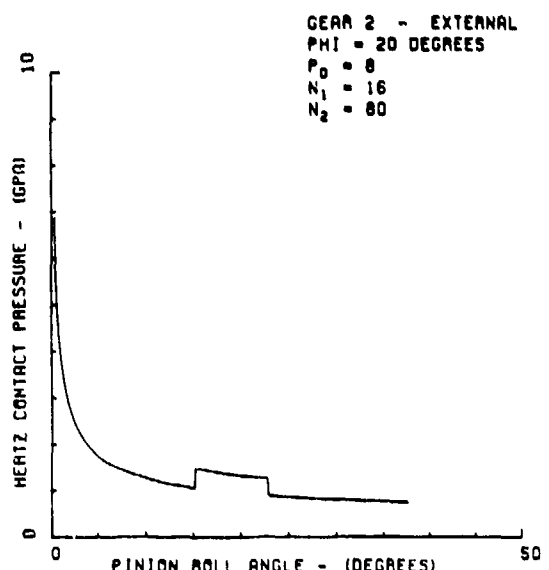


Figure 25. - Minimum tooth number design-tooth surface pressure for mesh with external gear.

It can be noted from table 2 that an equally compact design exists with a diametral pitch of 20 and 40 pinion teeth. This design also has a center distance of 0.152 m (6.0 in.) and does not exceed any of the design stress limits. However, it has 25 percent higher bending stresses with no improvement in compactness, so the lower pitch design is to be preferred.

A popular approach to the design of a gear mesh (ref. 7) suggests that the strongest gear design results when the pinion has the smallest number of teeth possible. This makes the teeth large. Based on the minimum number of teeth required to eliminate interference, N_1 would equal 16. The last two designs in table 2 show this design with a diametral pitches of 8 and 6.

As can be seen in table 2, even decreasing the diametral pitch to 6 to further increase the tooth size does not reduce the scoring contact pressure, σ_{NT} , to the levels present in the optimum design. Figure 24 shows the minimum tooth design with a diametral pitch of 8 and a center distance of 0.152

m (6.0 in.), which is the same as that of the optimal design. This design is stronger than the design of figure 22 in bending fatigue and slightly weaker in pitting fatigue, but is extremely overloaded with contact pressure at the gear tip where scoring may occur. Figure 25 is a plot of the maximum surface pressure on the pinion tooth of this design as a function of pinion roll angle.

A similar study for a gear ratio of 5 and a pressure angle of 20° for contact with an internal gear produces similar results. The major difference lies in the increased levels of bending stress. However, the optimal designs are still in the region of point A because of the balance between the strengths given by these proportions.

For this example consider the pinion torque to be 113 N·m (1000 lb·in) and the other design values to be identical to those of the first example with the exception that the gear ratio of 5 is for contact with an internal gear. In this example, both gears turn in the same direction. The design space for this example is shown in figure 14.

Figure 20 indicates that an optimal design using standard teeth should have a pinion with about 36 teeth. In figure 14 point A corresponds to a diametral pitch of about 21. Although the bending limit is more critical for this case, if one used this point to obtain a minimum slope relationship between pinion teeth and diametral pitch, equation (65) would yield

$$k = \frac{36}{21} = 1.71$$

Using diametral pitches of 16, 20, and 24, the minimum required number of teeth as given by equation (61) are 27.4, 34.3, and 41.1 respectively. Table 3 lists the possible optimum designs that have these diametral pitches and numbers of pinion teeth greater than these limits. To satisfy the bending fatigue limit, the numbers of teeth in this table are greater than those indicated by equation (65), which is based on the surface pitting pressure. However, the final optimal design is still close to the starting point A, so this stands as a good initial design even though the bending fatigue limit controls the design.

The best design is that with a diametral pitch of 20 and 38 pinion teeth. This design has a center distance of 0.0965 m (3.8 in.), a maximum contact pressure of 1.2 GPa (174 000 psi), and a maximum fillet bending stress of 407 MPa (59 000 psi). The design is shown in figure 26. Figure 27 is a plot of the maximum surface compression on the pinion tooth as a function of pinion roll angle.

As in the external contact case, the effect of increasing the diametral pitch in this area of optimal design is to increase the bending stresses.

The last two designs in table 3 show what happens when the design is based on the minimum number of teeth required to prevent involute interference. As before, decreasing the diametral pitch makes the gearset larger but does not change the situation of poor balance between the different modes of failure. Thus, a design that is larger than the optimal design still does not have acceptable levels of surface compression. The design with a diametral pitch of 10 and a center distance of 0.0965

TABLE 3 INTERNAL GEAR DESIGNS

$$m_g = 5, \phi = 20^\circ$$

P_d	N_1	N_2	f	C	σ_{Nt}	σ_N	σ_B	σ_{BT}
-	-	-	m	m	GPa	GPa	MPa	MPa
16	30	150	.0119	.095	1.40	1.25	290	352
16	31	155	.0123	.098	1.30	1.19	269	331
20	37	185	.0118	.094	1.23	1.25	352	427
20	38	190	.0121	.097	1.17	1.20	331	407
24	47	235	.0124	.099	1.02	1.13	355	434
24	48	240	.0127	.102	.99	1.10	345	414
10	19	95	.0121	.097	8.27	1.32	207	255
8	19	95	.0151	.121	5.93	0.94	103	131

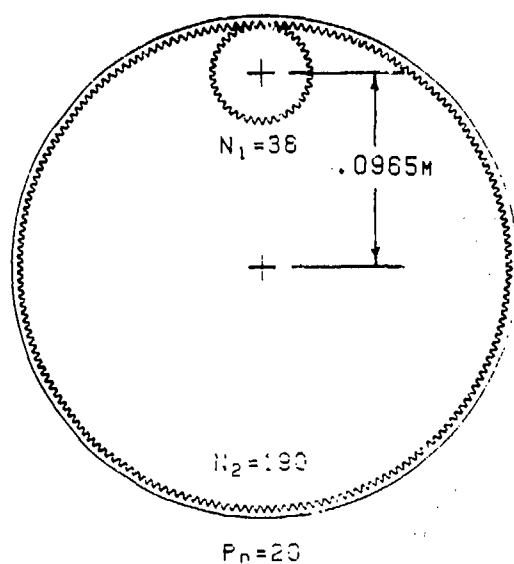


Figure 26. - Optimum design for $m_g = 5$, $\phi = 20^\circ$, and $T_p = 113 \text{ N-m}$ (1000 lb-in) for mesh with internal gear.

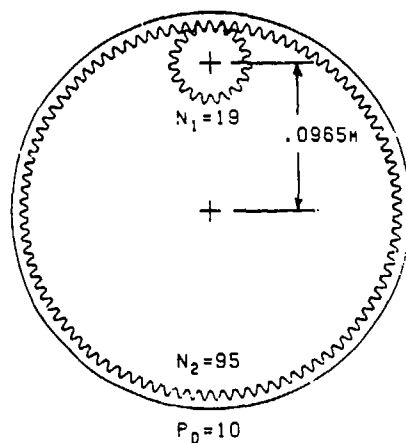


Figure 28. - Minimum tooth number design for $m_g = 5$, $\phi = 20^\circ$, and $T_p = 113 \text{ N-m}$ (1000 lb-in) for mesh with internal gear.

m (3.8 in.) is shown in figure 28. As in the first example, this design is the same size as the optimal design. It also is stronger in bending than the optimal design but is greatly overloaded with contact pressure at the gear tip where scoring may occur. Figure 29 is a plot of the maximum surface pressure on the pinion tooth of this design as a function of pinion roll angle.

Design Procedure

The design space developed in this paper can be used to obtain optimal designs for gear meshes using standard spur gears. A procedure using this design space was followed in the two design examples of the previous section. Required input to the procedure is the gear ratio, the pinion torque

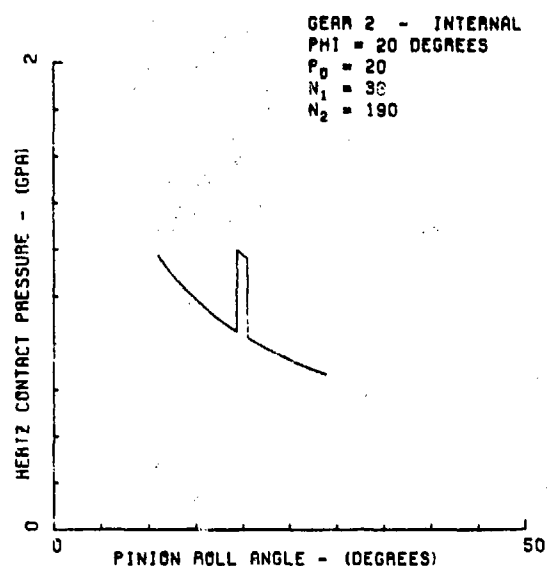


Figure 27. - Optimal internal gear design-tooth surface pressure.

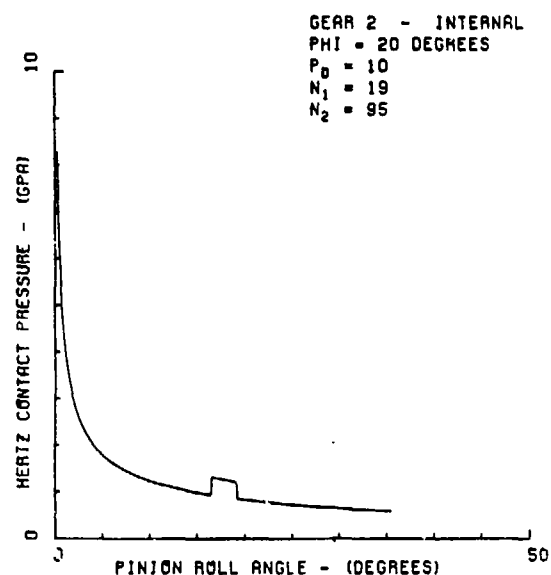


Figure 29. - Minimum tooth number design-tooth surface pressure for mesh with internal gear.

the pitch-line pressure angle, the maximum allowable length to diameter ratio for the pinion pitch cylinder, and the material properties of the gears. Equation (10) or (17) can then be used to determine the kinematic interference limit for the mesh, and equations (59), (61), and (62) can be used to determine the strength constraints on the design space. By plotting these curves on a graph of pinion tooth number versus diametral pitch, the region of acceptable designs can be established as that region of high pinion tooth numbers and low diametral pitches bounded by these curves. The most compact designs lie on the line of least slope inside this region. For designs in which surface pressure dominates, the graphs of figures 20 and 21 show the optimal number of pinion teeth as a function of the gear ratio and pressure angle. By using the number of pinion teeth indicated by these graphs and a straight line through the origin, a set of standard pitches and corresponding minimum numbers of pinion teeth can be found near this optimal position. A small set of standard pitch, practical designs can now be obtained by considering designs with these pitches and valid numbers of pinion teeth greater than the corresponding minimum numbers. By analyzing these designs and comparing their properties, a practical optimum design can be selected.

Summary and Conclusions

A design procedure for sizing standard involute spur gearsets is presented in this paper. The procedure is applied to find the optimal design for two examples—an external gear mesh with a ratio of 5:1 and an internal gear mesh with a ratio of 5:1. In the procedure, the gear mesh is designed to minimize the center distance for a given gear ratio, pressure angle, pinion torque, and allowable tooth strengths.

From the methodology presented, a design space may be formulated for either external gear contact or for internal gear contact. The design space includes kinematics considerations of involute interference, tip fouling, and contact ratio. Also included are design constraints based on bending fatigue in the pinion fillet and Hertzian contact pressure in the full load region and at the gear tip where scoring is possible. This design space is two-dimensional, giving the gear mesh center distance as a function of diametral pitch and the number of pinion teeth. The following results were obtained:

1. The constraint equations were identified for kinematic interference (eqs. (10) and (17)), fillet bending fatigue (eq. (59)), pitting fatigue (eq. (61)), and scoring pressure (eq. (62)), which define the optimal design space for a given gear design.
2. The locus of equal size optimum designs was identified as the straight line through the origin which has the least slope in the design region.
3. For designs in which bending fatigue is not dominant, the optimal design condition was identified as the point in the design space where the tooth tip contact pressure equals the maximum full load contact pressure.
4. Design charts for selecting the optimal number of pinion teeth for a given gear ratio and pressure angle were presented for these cases.

References

1. Cockerham, C.; and Waite, D.: Computer-Aided Design of Spur on Helical Gear Train. *Computer-Aided Design*, vol. 8, no. 2, April 1976, pp. 84-88.
2. Tucker, A. I.: The Gear Design Process. ASME Paper 80-C2/DET-13.
3. Estrin, M.: Optimization of Tooth Proportions for a Gear Mesh. ASME Paper 80-C2/DET-101.
4. Gay, D. E.: How to Design to Minimize Wear in Gears. *Machine Design*, vol. 42, Nov. 1970, pp. 92-97.
5. Design Procedure for Aircraft Engine and Power Take-Off Spur and Helical Gears. AGMA Standard No. 411 02, Sep. 1966.
6. Dudley, D. W.: *Gear Handbook*. McGraw Hill Book Co., Inc., 1962.
7. Shigley, J. E.: *Mechanical Engineering Design*. McGraw Hill Book Co., Inc., 3rd ed., 1977.
8. Lee, T. W.: Weight Minimization of a Speed Reducer, ASME Paper 77-DET-163.
9. Osman, M. O. M.; Sankar, S.; and Dukkipati, R. V.: Design Synthesis of a Multi-Speed Machine Tool Gear Transmission Using Multiparameter Optimization. *J. Mech. Des.*, vol. 100, April 1978, pp. 303-310.
10. Kamenatskaya, M. P.: Computer-Aided Design of Optimal Speed Gearbox Transmission Layouts. *Mach. & Tool.*, vol. 46, no. 9, 1975, pp. 11-15.

11. Buckingham, E.: Analytical Mechanics of Gears. McGraw Hill Book Co., Inc., 1949.
12. Anderson, S. A. E.: On the Design of Internal Involute Spur Gears. Transactions of Machine Elements Division, Lund Technical University, Lund, Sweden, 1973.
13. Strength of Spur Gear Teeth. AGMA Standard 220.02, August 1966.
14. Gitchel, K. R.: Computed Strength and Durability Geometry Factors for External Spur and Helical Gears with Tooling Check. ASME Paper 72-PTG-18.
15. Mitchiner, R. G.; and Mabie, H. W.: The Determination of the Lewis Form Factor and the AGMA Geometry Factor J for External Spur Gear Teeth. J. Mech. Des. V104, Jan. 1982, pp. 148-158. 16. Surface Durability (Pitting) of Spur Gear Teeth. AGMA Standard 210.02, Jan. 1965.
17. Coy, J. J.; Townsend, D. P.; and Zaretsky, E. V.: Dynamic Capacity and Surface Fatigue Life for Spur and Helical Gears. J. Lubr. Technol., vol. 98, no. 2, April 1976, pp. 267-276.
18. Bowen, C. W.: The Practical Significance of Designing to Gear Pitting Fatigue Life Criteria. J. Mech. Des., vol. 100, no. 1, Jan. 1978, pp. 46-53.
19. Gear Scoring Design Guide for Aerospace Spur and Helical Power Gears. AGMA Information Sheet, 217.01, Oct. 1965.
20. Rozeana, L.; and Godet, M.: Model for Gear Scoring. ASME Paper 77-DET-60.
21. Walker, H.: Gear Tooth Deflection and Profile Modification. The Engineer, Oct. 14, 1938, pp. 409-412; Oct. 21, 1938, pp. 434-436; Aug. 16, 1940, pp. 102-104.
22. Coleman, W.: Gear Design Considerations. Interdisciplinary Approach to the Lubrication of Concentrated Contacts. NASA SP-237, 1969.

Study of Lubricant Jet Flow Phenomena in Spur Gears – Out Of Mesh Condition*

D. P. Townsend† and L. S. Akin‡

In the lubrication and cooling of gears, the gear bulk temperature is an important component of the surface total temperature at the gear tooth contact point and thus is a controlling factor in the gear scoring or scuffing mode of surface failure. The method of applying the lubricant to the gears in most applications can have a large effect on the gear blank temperature. In reference 1 it was shown that scoring, which is a function of gear blank temperature, varies as a function of oil-jet velocity, direction, and location with regards to angular position from the gear mesh.

The depth of penetration of the oil jet into the gear blank also plays an important role in the gear blank temperature and, thus affects the scoring or scuffing limit of the gear. In references 2 and 3 the penetration depth for a jet pointed radially was determined for different gear conditions and lubricant drop sizes with windage effect included. It was assumed in those references that the radially pointed jet gives the best penetration depth and, therefore, the best gear cooling.

There are many gear applications where the oil jet is pointed at the mesh point and is either located into mesh (engaging) or out of mesh (disengaging). When the gear ratio is unity, the oil jet is usually pointed at the pitch point for in or out of mesh lubrication. However, when the gear ratio is different from unity, that is, when a speed increases or decreases, the jet may or may not be pointed at the pitch line. This could make considerable difference in the cooling of the gear or pinion and give unexpected results.

The objective of the work reported herein was to analytically and experimentally determine the penetration depth onto the tooth flank of a jet of oil at different velocities pointed at the pitch line on the outgoing side of mesh. The analysis determines the impingement depth for both the gear and the pinion. It includes the cases for speed increasers and decreasers as well as for one to one gear ratio. The work reported herein is an extension of the work reported in references 2 and 3 and is based on and extends the work reported in reference 4. In some cases the jet will strike the loaded side of the teeth, and in others it will strike the unloaded side of the teeth. In nearly all cases the top land will be cooled regardless of the penetration depth, and postimpingement oil spray will usually provide adequate amounts of oil for lubrication but is marginal or inadequate for cooling.

Symbols

B	gear or pinion backlash, m (in.)
H	impingement depth, m (in.)
h_k	whole depth, m (in.)
L	distance from line of centers to impingement point, m (in.)
m_g	gear ratio
N	number of teeth
n	rotational speed, rpm
P	module, (diametral pitch)
R	pinion radius, m (in.) ($2R = D$)
r	gear radius, m (in.)
t	time, sec
v	pitch line velocity, m/sec (in/sec)
v_j	jet velocity, m/sec (in/sec)
γ	dimensionless impingement depth

*Previously published in the January 1978 issue of ASME's Journal of Mechanical Design and as NASA TM-73694.

†NASA Lewis Research Center.

‡Western Gear Corporation, Lynnwood, California.

- θ gear or pinion angle of rotation from line of centers, rad
 φ pressure angle, rad
 ω gear or pinion rotation speed, rad/sec
 Subscripts:
 b base circle
 g gear
 o outside radius
 p pinion

Test Apparatus

The lubricant oil jet tests were performed in the NASA Lewis gear test apparatus shown in figure 1 and described more fully in references 2 and 5. This test rig uses the four-square principle of loading the test gears. Load is applied to the gears by a hydraulic loading system.

The test gears were 8 diametral pitch, having a 8.89-cm (3.5-in.) pitch diameter, a 20° pressure angle, and a whole depth of 0.762 cm (0.300 in.). The gears were made with a very wide face width to allow for the coverage of light and oil spray for test conditions. The gear material was a low carbon steel.

A specially designed test gear cover was made for the lubrication tests. The cover has two windows, 90° apart, for admitting light to the test gears and a viewing window in front of the gears for viewing or photographing the lubrication phenomenon. The viewing window and the light windows are protected from oil splash by shielding. The windows are constantly swept by a thin film of high-velocity air blown across the windows to keep them free of oil for good light passage. V-jet, oil nozzles are located behind each of the light windows and spray a thin fan shaped stream of oil onto the gear teeth parallel to the gear axis. A 1000-V xenon lamp was used to illuminate the lubricant. The light from the xenon lamp is passed through a condenser lens to give a parallel light, it then passes through a cylindrical lens to bring the light into focus as a narrow slit. The light, which is reflected by a 45° mirror, passes through the light window and crosses the fanshaped oil stream.

The lubricant used in the tests was a clear mineral oil to which was added approximately 10 percent by volume white lithopone pigment, which gave it the appearance of milk. When the narrow band of intense light crossed the fan of white oil, a bright line of it was illuminated so that it could be

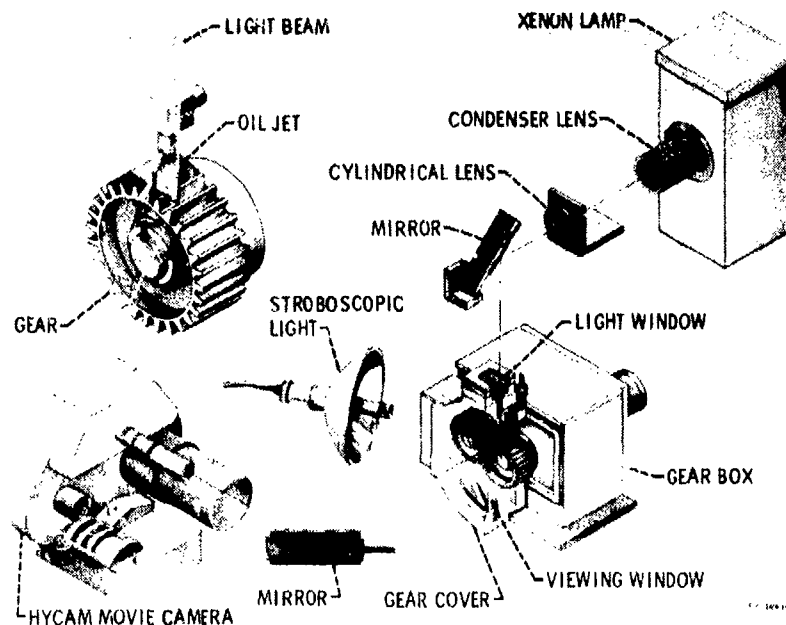


Figure 1. - Test setup for oil-jet penetration study.

photographed with a high-speed camera.

A high-speed Hycam movie camera was used to photograph the oil jet through a 45° mirror and the gearbox cover window. A high-speed, air-cooled stroboscopic system was used to provide flash-tube lighting that was synchronized with the high-speed camera. The camera speed was set to give a frame for each tooth space movement. The stroboscopic system had a timer that prevented burnout of the flash tube.

Analytical Approach – Disengaging Mesh

Impingement on Driving Pinion

As the oil jet approaches the tooth surfaces, it must first clear the gear tooth to approach the pinion; likewise, it must clear the pinion tooth to approach the gear tooth. In figure 2 the gear tooth is at the position where the oil jet starts to clear the gear tooth and move toward the pinion. The gear-tooth loaded-side pitch-point position at this instant ($t=0$), as measured from the line of centers is

$$\theta_{gl} = \cos^{-1} \frac{R}{R_c} - \text{inv } \varphi_{og} + \text{inv } \varphi \quad (1)$$

The corresponding pitch-point position on the pinion loaded side, which was in contact with the gear at the line of centers, is $m_g \theta_{gl}$. Therefore, the position of the pinion tooth at the base circle (point 2, fig. 2) at time ($t = 0$) is

$$\theta_{pl} = m_g \left(\cos^{-1} \frac{R}{R_o} - \text{inv } \varphi_{og} + \text{inv } \varphi \right) + \text{inv } \varphi \quad (2)$$

As the jet goes from position 1 on the gear to position 4 on the pinion (as shown in fig. 3), the pinion is rotating through the angle $\theta_{p2} - \theta_{p1}$, or from position 2 to position 3 in figure 3. The time required for the pinion to get from point 2 to point 3 is

$$t_{2-3} = \frac{\theta_{p2} - \theta_{p1}}{\omega_p} \quad (3)$$

At the same time the oil jet with velocity v_o moves through the distance $(R_o^2 - R^2)^{1/2} - L_p$ (fig. 3) so that

$$t_{1-4} = \frac{(R_0^2 - R^2)^{1/2} - L_p}{v_i} \quad (4)$$

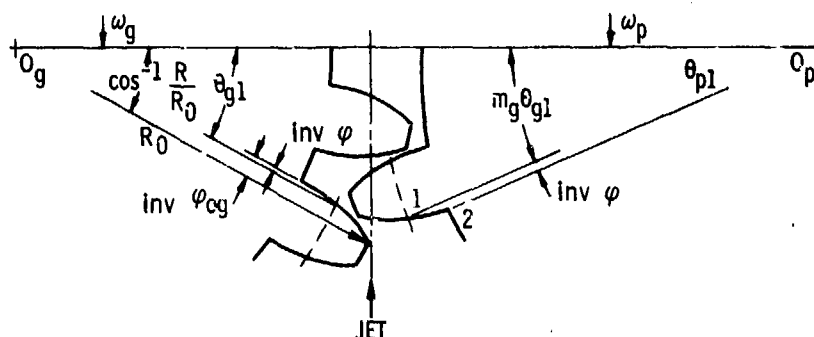


Figure 2

can be determined as

$$H_p = r_o - (R^2 + L_p^2)^{1/2} \quad (9)$$

The whole depth h_k may be used to normalize the impingement depth to its dimensionless form γ_p for a standard gear as

$$\gamma_p = \frac{H_p}{h_k} = \left[r_o - (r_o^2 - L_p^2)^{1/2} \right] \frac{P}{2} \quad (10)$$

It can be seen that the gear outside diameter crosses the jet line ahead of the pinion and is the initial shield for the pinion tooth. The same is true for the pinion outside diameter, which crosses the jet line ahead of the gear and is the initial shield for the gear tooth. However, at high gear ratios, it is possible for the gear to shield the pinion entirely so that the pinion would receive no cooling unless the jet direction and/or position is modified. The following three tests may be used to determine the condition for zero impingement depth on the pinion: when

$$\tan^{-1} \frac{L_p}{r} < \cos^{-1} \frac{r}{r_o}$$

or

$$L_p < (r_o^2 - r^2)^{1/2}$$

and when

$$h_p \leq 0$$

Impingement on Driven Pinion

As the oil jet clears the gear tooth (position 1 in fig. 5) and approaches the unloaded side of the pinion tooth at $t=0$, the position of the loaded-side gear tooth pitch point from the line of center is

$$\theta_{gl} = \cos^{-1} \frac{R}{R_o} - \text{inv } \varphi_{og} + \text{inv } \varphi - \frac{\pi}{N_g} - B_g \quad (11)$$

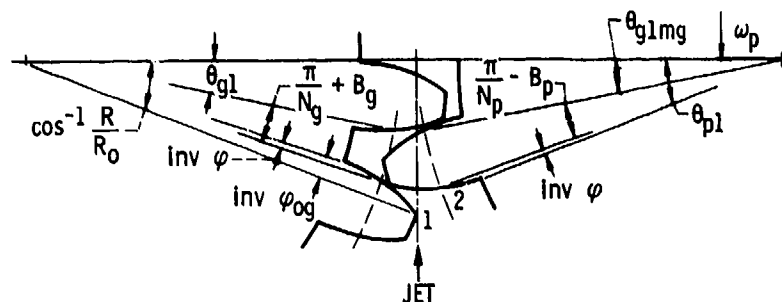


Figure 5

The corresponding pinion pitch-point position at $t=0$ on the pinion loaded side, assuming conjugate action, is $m_g \theta_{g1}$. Therefore, the position of the pinion tooth unloaded side at the base circle at $t=0$ is

$$\theta_{p1} = m_g \theta_{g1} + \frac{\pi}{N_p} - B_p + \text{inv } \varphi \quad (12)$$

The time it takes the jet to go from position 1 in figure 5 and impinge on the unloaded side of the pinion tooth t_{2-3} is equal to the time it takes the pinion to rotate from position 2 to position 3 in figure 3. Therefore, the relationships shown in figures 3 and 4 are valid for this case so that the time of flight is

$$\frac{\tan^{-1}(L_p/r) + \text{inv } \theta_{p3} - \theta_{p1}}{\omega_p} = \frac{(R_o^2 - R^2)^{1/2} - L_p}{v_j} \quad (13)$$

This is similar to the pinion-driving case, but it will have a slightly different value for L_p because of the B_p and B_g terms. The dimensionless impingement depth normalized by the whole depth is the same as for the driving pinion case and is expressed as

$$\gamma_p = \frac{H_p}{h_k} = \frac{r_o - (r^2 + L_p^2)^{1/2}}{F/2} \quad (14)$$

Impingement on Driving Gear

When the pinion outside diameter clears the oil jet at position 5 in figure 6, the jet approaches the loaded side of the gear tooth. The position of the pinion loaded-side pitch point from the line of centers at this time ($t=0$) is

$$\theta_{p4} = \cos^{-1} \frac{r}{r_o} - \text{inv } \varphi_{op} + \text{inv } \varphi \quad (15)$$

The position of the gear loaded-side pitch point from the line of centers is θ_{p4}/m_g and the gear-tooth loaded-side base circle point (as shown in fig. 6) is

$$\theta_{g2} = \frac{\theta_{p4}}{m_g} + \text{inv } \varphi \quad (16)$$

As the gear rotates through the angle $(\theta_{g3} - \theta_{g2})$ shown in fig. 7) from position 6 to position 7, the jet moves through the distance

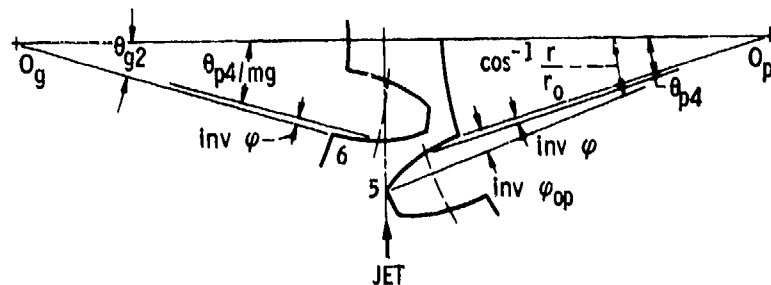


Figure 6

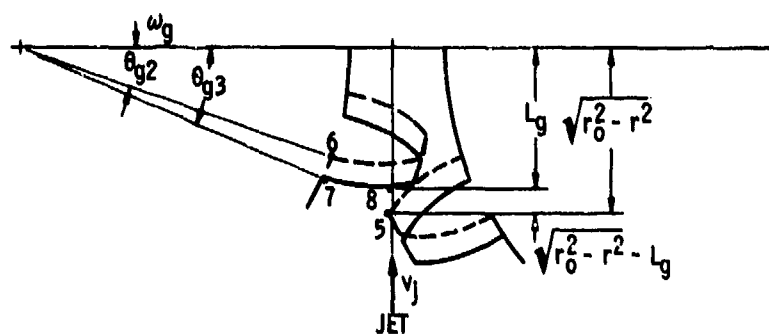


Figure 7

$$(r_0^2 - r^2)^{1/2} - L_g$$

from position 5 to position 8 in figure 7. The time required for the gear to rotate from 6 to 7 is

$$t_{6-7} = \frac{\theta_{g3} - \theta_{g2}}{\omega_g} \quad (17)$$

and the time required for the jet to move from 5 to 8 is

$$t_{5-8} = \frac{(r_0^2 - r^2)^{1/2} - L_g}{v_j} \quad (18)$$

The resulting equation is

$$\frac{\theta_{g3} - \theta_{g2}}{\omega_g} = \frac{(r_0^2 - r^2)^{1/2} - L_g}{v_j} \quad (19)$$

From figure 8 it can be shown that

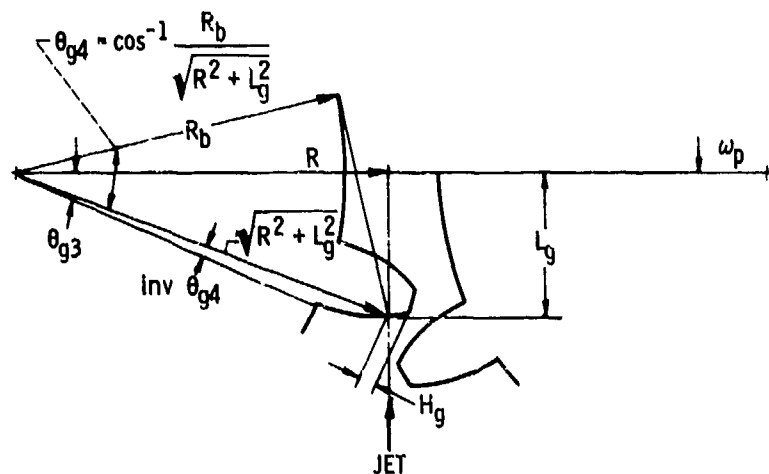


Figure 8

$$\theta_{g4} = \cos^{-1} \frac{R_b}{(R^2 + L_g^2)^{1/2}} \quad (20)$$

and

$$\theta_{g3} = \tan^{-1} \frac{L_g}{R} + \text{inv } \theta_{g4} \quad (21)$$

Substituting equation (21) into equation (19) and using equation (20) for θ_{g4} gives an implicit equation in L_g expressed as

$$\frac{\tan^{-1} L_g/R + \text{inv } \theta_{g4} - \theta_{g2}}{\omega_g} = \frac{(r_o^2 - r^2)^{1/2} - L_g}{v_j} \quad (22)$$

Equation (22) must be solved iteratively for L_g . The impingement depth H_g (fig. 8) can be expressed as

$$H_g = R_o - (R^2 - L_g^2)^{1/2} \quad (23)$$

Expressed in dimensionless depth in terms of the whole depth gives

$$\gamma_g = \frac{H_g}{h_k} = (R_o - \sqrt{R^2 - L_g^2}) \frac{P}{2} \quad (24)$$

Impingement on Driven Gear

As the outside diameter of the pinion tooth passes the jet at position 5 (fig. 9), the jet begins to approach the unloaded side of the gear tooth at time ($t=0$). The position of the loaded-side pinion pitch point from the line of centers at time ($t=0$), as shown in figure 9, is

$$\theta_{p4} = \cos^{-1} \frac{r}{r_o} - \text{inv } \varphi_{op} + \text{inv } \varphi - \frac{\pi}{N_p} - B_p \quad (25)$$

The corresponding position of the gear loaded-side pitch point is θ_{p4}/m_g . The position of the unloaded side of the gear tooth at time ($t=0$) at the base circle position 6 of figure 9 may be determined from

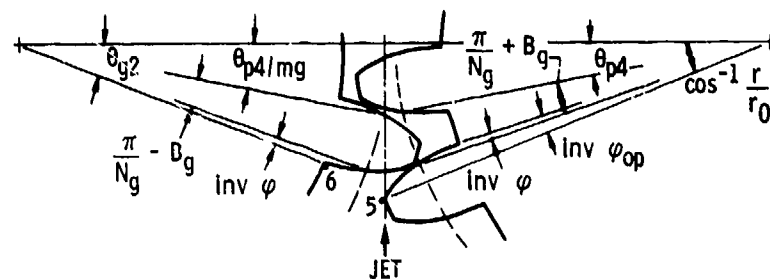


Figure 9

$$\gamma_{g2} = \frac{\theta_{p4}}{m_g} + \frac{\pi}{N_g} - B_g + \text{inv } \varphi \quad (26)$$

The jet passes from position 5 to 8 while the gear rotates from position 6 to 7 (fig. 7). The time required for the gear to rotate from position 6 to 7 is

$$t_{6-7} = \frac{\theta_{g3} - \theta_{g2}}{\omega_g} \quad (27)$$

During this time the oil jet moves through the distance $(r_o^2 - r^2)^{1/2} - L_g$ and its time of flight over this distance is

$$t_{5-8} = \frac{(r_o^2 - r^2)^{1/2} - L_g}{v_j} \quad (28)$$

The gear rotation time t_{6-7} must be equal to the oil jet time of flight t_{5-8} so that

$$\frac{\theta_{g3} - \theta_{g2}}{\omega_g} = \frac{(r_o^2 - r^2)^{1/2} - L_g}{v_j} \quad (29)$$

From figure 8 it can be seen that

$$\theta_{g4} = \cos^{-1} \frac{R_b}{(R^2 + L_g^2)^{1/2}} \quad (30)$$

and

$$\theta_{g3} = \tan^{-1} \frac{L_g}{R} + \text{inv } \theta_{g4} \quad (31)$$

Substituting equation (31) into equation (29) and using equation (30) for θ_{g4} gives an implicit equation in terms of the time of flight as

$$\frac{\tan^{-1} L_g/R + \text{inv } \theta_{g4} - \theta_{g2}}{\omega_g} = \frac{(r_o^2 - r^2)^{1/2} - L_g}{v_j} \quad (32)$$

This equation must be solved iteratively for L_g . The impingement depth for the unloaded side of the gear (fig. 8) may now be determined as

$$H_g = R_o - (R^2 + L_g^2)^{1/2} \quad (33)$$

and the dimensionless impingement depth in terms of the whole depth may be written as

$$\gamma_g = \frac{H_g}{h_k} = R_o - \left[(R^2 + L_g^2)^{1/2} \right] \frac{P}{2} \quad (34)$$

This is the same as for the driving gear case except for the effects of backlash B_p and B_g .

Reduction of Impingement Depth by Gear Chopping

As the gear ratio is increased, the gear completely shields the pinion so that it no longer blocks the gear tooth. However, the impingement depth on the gear itself is reduced by chopping of the oil jet by the leading tooth. The pinion impingement depth can be improved by moving the jet in the direction of the pinion, but this does not improve the gear impingement depth. The gear impingement depth can be improved by pointing the jet toward the gear. Figures 2, 6, and 7 will be used again here to illustrate the mathematics of this portion of the operational problem.

When the gear ratio is sufficiently large, the leading gear tooth shields the trailing tooth instead of the pinion (similar to figure 2). The position of the back-side pitch point of the leading gear tooth from the line of centers at $t=0$ is (as shown similarly in fig. 2; no separate figure is provided.)

$$\theta_{g1} = \cos^{-1} \frac{R}{R_o} - \text{inv } \theta_{og} + \text{inv } \varphi \quad (35)$$

The trailing gear-tooth impingement-side base circle position from the line of centers at time ($t=0$) is θ_{g2} (shown in a similar position 6 in fig. 6 as θ_{g2}) and can be determined from the relations

$$\theta_{g2'} = \theta_{g1} - \frac{\pi}{N_g} + \text{inv } \varphi \quad (36)$$

and

$$\theta_{g2'} = \cos^{-1} \frac{R}{R_o} - \frac{\pi}{N_g} - \text{inv } \varphi_{og} + 2 \text{ inv } \varphi \quad (37)$$

This bridging of the tooth space by the term π/N_g can be seen in figure 5, but the equations do not include a term for backlash B_g .

The time required for the gear to rotate at a speed ω_g from position 6 to 7 (fig. 7) is

$$t_{6-7} = \frac{\theta_{g3} - \theta_{g2'}}{\omega_g} \quad (38)$$

At the same time the oil jet travels from position 1 (fig. 3) to position 8 (fig. 7) at a speed of v_j and may be calculated as

$$t_{1-8} = \frac{(R_o^2 - R^2)^{1/2} - L_g}{v_j} \quad (39)$$

Using the geometry of figures 7 and 8, an equation may be written for gear rotation θ_{g3} in terms of L_g :

$$\theta_{g3} = \tan^{-1} \frac{L_g}{R} + \text{inv } \theta_{g4} \quad (40)$$

where

$$\theta_{g4} = \cos^{-1} \frac{R_b}{(R^2 + L_g^2)^{1/2}} \quad (41)$$

An expression can now be written for the time of flight in terms of L_g by setting the gear rotation t_{6-7} equal to the time of flight t_{1-8} and using equation (40) for θ_{g3} as follows:

$$t = \frac{\tan^{-1} L_g/R + \text{inv } \theta_{g4} - \theta_{g2}}{\omega_g} = \frac{(R_o^2 - R^2)^{1/2} - L_g}{v_j} \quad (42)$$

This implicit equation can be solved iteratively for L_g (fig. 8). From equation (42) the limiting value of H_g for gear chopping can be found and identified as H_g and will considerably limit the penetration depth (fig. 13).

Impingement On Engaging Side of Mesh

When the oil-jet velocity is equal to or exceeds the pitch-line velocity, the oil will impinge on the loaded side of one member and the unloaded side of the other. The amount of oil impinging on the pinion at high gear ratios will be small because of gear tooth chopping, and, at jet velocities exceeding the pitch-line velocity, the oil may never hit the pinion because of gear chopping. The pressure needed to provide oil at the pitch-line velocity is $7.8 \times 10^{-4} (C_v n D)^2$ Pa ($1.13 \times 10^{-7} (C_v n D)^2$ psi). Gear chopping on the out-of-mesh side will stop the oil jet, whereas on the into-mesh side it only interrupts the jet, letting the interrupted stream continue into mesh with the teeth. As can be seen in figure 10 the oil jet impinges on the gear profile starting at point 1 and continues uninterrupted until the pinion at point 4 or the following tooth at point 3 interrupts the jet stream. If the jet stream is at or near pitch-line velocity, it will continue to impinge on the tooth profile of either the gear or pinion until the pitch point. At slower velocities it will impinge on the side of the tooth opposite the jet. At higher velocities, it will have less impingement depth than at pitch-line velocity. The oil ahead of the contact point will be squeezed out, lubricating the full depth working surface. However, the contact point is where heating takes place, and, since there is only a very small amount of oil in the contact zone and remaining on the surface after contact, the effective cooling is very small for into-mesh lubrication. In addition, too much oil going into mesh will cause the teeth to trap the oil in the closing pocket between the tooth tip and root, causing excessive power loss in the drive.

Results and Discussion

Analytical Results

The equations described in the previous section were computerized, and some of the important parameters were selected for a parametric study, the results of which are reported below.

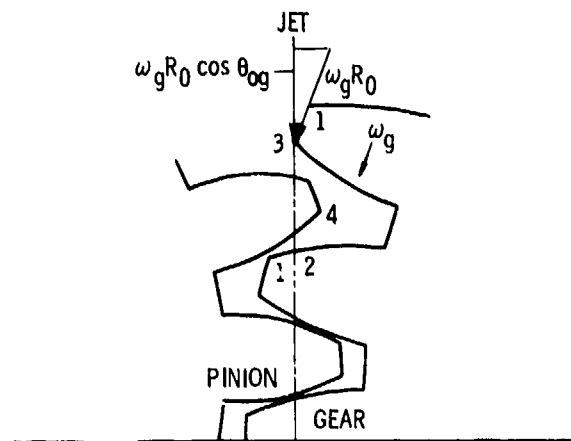


Figure 10

Figure 11 is a plot of the nondimensional impingement depth γ versus the nondimensional jet velocity v_j/v , which shows, as would be expected, a general increase in impingement depth as the jet velocity is increased. This computer study was made using the NASA test gears. These gears have 28 teeth and a gear ratio $m_g = 1.0$. Thus, the impingement depth for the pinion and gear is identical (fig. 11). This, of course, would not be so for ratios other than 1.0. It will be noticed, even at fairly substantial jet velocities such as $v_j/v = 2.0$, that the impingement depth down the profile of the gear tooth is still unimpressive.

Figure 12 shows in general what happens to the impingement depth if the number of teeth in the pinion is changed. The gear and pinion impingement depths are the same and fairly small when the gear ratio is equal to 1.0. If the gear ratio is increased to 2.0 (upper curve of fig. 12), the higher ratio provides a deeper impingement depth γ_g on the gear only. The pinion tooth is missed and does not block the jet to the gear tooth.

The above explanation leads to a more careful examination of the effects of gear ratio on the impingement depth of the pinion and gear, respectively. Figure 13 provides this kind of information for the present example. The 28-tooth pinion is held constant while varying the number of teeth on

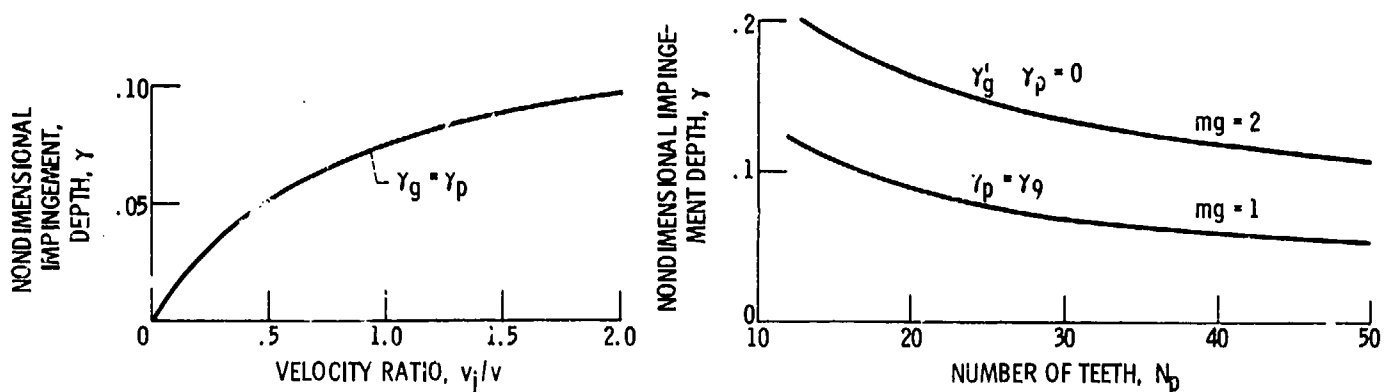


Figure 11. - Velocity ratio as function of nondimensional impingement depth. Speed, 3600 rpm; jet pressure, 17×10^4 Pa (25 psi); $N_p = 28$; $m_g = 1$.

Figure 12. - Number of pinion teeth as function of nondimensional impingement depth. Speed, 3600 rpm; jet pressure, 17×10^4 Pa (25 psi); $v_j/v = 1$.

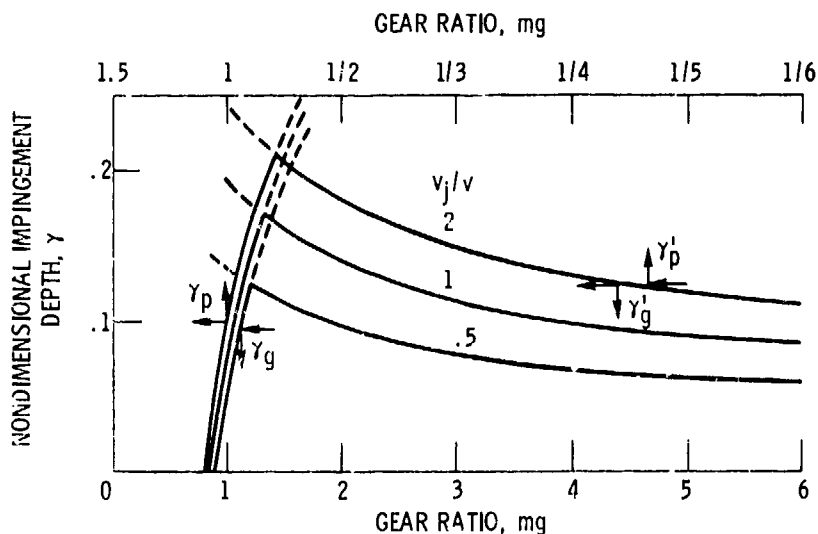


Figure 13. - Gear ratio as function of nondimensional impingement depth. Speed, 3600 rpm; jet pressure, 17×10^4 Pa (25 psi); $N_p = 28$.

the gear to determine what effect this would have on the impingement depth. As can be seen in figure 13, for a jet velocity ratio of 0.5 and a gear ratio of 1.114, the profile of this pinion is no longer impinged by the jet. Only the top land is covered by direct impingement up to a ratio of about 1.25, at which point the leading tooth of the gear begins blocking the trailing tooth. Thus, at gear ratios above about 1.25, when $v_j/v = 0.5$, the impingement depth ratio γ_g will be less than about 0.12 and will drop to 0.04 above a gear ratio of 10. As the jet velocity ratio is increased, the gear receives a somewhat greater depth of impingement. This general trend is shown in figure 13 where the jet velocity was increased to 1.0 and 2.0, respectively. The important thing to note in figure 13 is that the pinion tooth profile is not impinged on directly for speed reducers with ratios above about 1.11 or 1.23, depending on the jet velocity ratio. Gear impingement depth is also limited by leading tooth blocking at ratios above about 1.25 or 1.5.

There is a splash after tooth impingement even when the impingement is only on the top land of a pinion or gear. However, this splash cannot be depended on for the cooling function. It may be useful to point out here that ratios above 1.0 are considered to be speed decreaseers (or reducers), whereas ratios below 1.0 are intended to be interpreted here as speed increaseers (where the gear is the driver). In this particular case the γ_p and the γ_g curves are reversed. The figure 13 curve labeled γ_p and γ_g is therefore plotted to gear ratios less than one so that the curves can be examined in detail for gear increaseers and decreaseers, respectively. Figures 2 to 13 do a reasonably good job of showing the importance of proper location and pointing of the jet nozzle. As can be seen, if the nozzle is pointed slightly off the pitch line, the impingement depth can be severely reduced on one of the members. This results in a great advantage to the other member of the mesh and affects the heat balance between gears.

From a practical standpoint, many gears can be cooled quite adequately with impingement principally on the top land of the gear, except in the case of modified pinions with top lands of very narrow width. In such cases it may be important to position the jet so that the impingement down the profile of the pinion is favored over the gear in such a manner as to balance the cooling on the pinion and gear.

Example

Find the impingement depth on the driven gear using the NASA gear at 3600 rpm and 17.25×10^4 Pa (25 psig) oil pressure, $r_o = 0.0476$ m (1.875 in.), $r = 0.144$ m (1.75 in.), $B_p = B_g = 0$, $N_p = 28 = N_g$, $P = 8$, and $\varphi = 20^\circ$ using equations (25) to (33):

$$\cos^{-1} \frac{r}{r_o} = \cos^{-1} \frac{1.75}{1.875} = 0.3672 \text{ rad}$$

$$\varphi_{op} = \cos^{-1} \frac{r_b}{r_o} = \cos^{-1} \frac{1.644}{1.875} = 0.501117 \text{ rad}$$

$$\text{inv } \varphi_{op} = \tan \varphi_{op} - \text{arc } \varphi_{op} = 0.046637 \text{ rad}$$

$$\text{inv } \varphi = \tan 20 - \text{arc } 20 = 0.0149 \text{ rad}$$

$$\frac{\pi}{N_p} = 0.1122 \text{ rad}$$

$$\theta_{pr} = 0.3672 - 0.046637 + 0.0149 - 0.1122 = 0.22326 \text{ rad} \quad (25)$$

$$\theta_{g2} = 0.22326/1 + 0.1122 - 0 + 0.0149 = 0.35036 \text{ rad} \quad (26)$$

Try $L_g = 0.0156$ m (0.6147 in.) for iteration,

$$\theta_{g4} = \cos^{-1} \frac{1.75 \cos 20}{(1.75^2 + 0.6147^2)^{1/2}} = 0.48044 \text{ rad} \quad (30)$$

$$v_j = 156 \sqrt{25} = 19.8 \text{ m/sec (780 in/sec)} \quad \omega = 377 \text{ rad/sec}$$

$$\text{inv } \theta_{g4} = \tan \theta_{g4} - \text{arc } \theta_{g4} = 0.04085 \text{ rad}$$

$$\theta_{g3} = \tan^{-1} 0.6147/1.75 + 0.4085 = 0.3786 \text{ rad} \quad (31)$$

Test:

$$\frac{(0.3786 - 0.35036)}{377} = \frac{(1.875^2 - 1.75^2)^{1/2} - 0.6147}{780}$$

$$0.000075 = 0.000075$$

$$H_g = 1.875 - [(1.75)^2 + (0.6147)^2]^{1/2} = 0.0005 \text{ m (0.0202 in.)} \quad (33)$$

Experimental Results

Figure 14(a) shows the oil jet just after it clears the gear tooth with the pinion tooth still blocking the following gear tooth. In figure 14(b) the jet has cleared the pinion tooth and is impinging on the gear tooth at the maximum depth for this condition. The test conditions for figure 14 was 3600 rpm, which gives a v of 16.7 m/sec (660 in/sec) and an oil-jet pressure of 8.3×10^4 Pa (12 psi) for a calculated v_j of 13.7 m/sec (540 in/sec) and a v_j/v of 0.82. The impingement depth for these test conditions is 0.043 cm (0.017 in.). The experimental depth (fig. 14(b), while difficult to measure with precision, agrees with the calculated impingement depth.

In figure 15 the test conditions were 3600 rpm, which gives a v of 16.7 (660 in/sec) and an oil-jet pressure of 17.25×10^4 Pa (25 psig), for a v_j of 20 m/sec (780 in/sec). This gives a v_j/v of 1.18. The calculated impingement depth for these test conditions is 0.05 cm (0.02 in.). Figure 15(a) shows the jet at the tip of the leading gear tooth just before it starts toward the pinion tooth. In figure 15(b) the



Figure 14. - Oil jet impingement depth, out of mesh condition. Speed, 3600 rpm; jet pressure, 8.3×10^4 Pa (12 psi).



Figure 15. - Oil jet impingement depth, out of mesh condition. Speed, 3600 rpm; jet pressure, 17.25×10^4 Pa (25 psi).



Figure 16. - Oil jet impingement depth, out of mesh condition. Speed, 5000 rpm; jet pressure, 13.8×10^4 Pa (20 psi).

pinion tooth has passed the oil jet, and the jet is about to impact the gear tooth at an experimental impingement depth close to the calculated depth.

Figure 16 shows two high-speed camera picture frames taken at 2300 frames per second with the gears running at 5000 rpm for a v_p of 23.4 m/sec (920 in/sec). This camera and gear speed give a picture for each tooth space movement of the gear. The oil-jet pressure was 13.8×10^4 Pa (20 psig) giving a v_j of 17.8 m/sec (700 in/sec). The v_j/v for these conditions is 0.76 giving a calculated impingement depth of 0.04 cm (0.016 in.). In figure 16(a) the oil jet has just passed the tip of the gear tooth and the pinion tooth is still between the jet and the following gear tooth. In figure 16(b), the oil jet has cleared the pinion tooth tip and is impacting the gear tooth at near the calculated impingement depth.

Summary Of Results

An analysis was conducted for oil-jet lubrication on the disengaging side of a gear mesh. Results of the analysis were computerized and used to determine the oil-jet impingement depth for several gear ratios and oil-jet to pitch-line velocity ratios. An experimental program was conducted on the NASA gear test rig using high-speed photography to experimentally determine the oil-jet

impingement depth on the disengaging side of mesh.

The following results were obtained:

1. Impingement depth reaches a maximum at gear ratios near 1.5 where chopping by the leading gear tooth limits the impingement depth.
2. The pinion impingement depth is zero above a gear ratio of 1.172 for an oil-jet to pitch-line velocity ratio of 1.0 and is similar for other velocity ratios.
3. The impingement depth for gear and pinion are equal and approximately one half the maximum at a gear ratio of 1.0.
4. Impingement depth on either the gear or pinion may be improved by relocating the jet away from the pitch line or by changing the jet angle.
5. Results of the analysis were verified by experimental results using a high-speed camera and a well lighted oil jet.

References

1. McCain, J. W., and Alsandor, E.: Analytical Aspects of Gear Lubrication on the Disengaging Side. Trans. ASLE, vol. 9, Apr. 1966, pp. 202-211.
2. Akin, L. S.; Mross, J. J.; and Townsend, D. P.: Study of Lubricant Jet Flow Phenomena in Spur Gears. J. Lubr. Technol., vol. 97, no. 2, Apr. 1975, pp. 283-288.
3. Akin, L. S.; and Mross, J. J.: Theory for the Effect of Windage on the Lubricant Flow in the Tooth Spaces of Spur Gears. J. Eng. Ind., vol. 97, Nov. 1975, pp. 1266-1273.
4. Fujita, K.; Obata, F.; and Matsuo, K.: Instantaneous Behavior of Lubricating Oil Supplied Onto the Tooth Flanks and Its Influence on the Scoring Resistance of Spur Gears. J. Eng. Ind., vol. 98, no. 2, May 1976, pp. 635-643.
5. Townsend, D. P.; and Zaretsky, E. V.: A Life Study of AISI M-50 and Super Nitralloy Spur Gears with and without Tip Relief. J. Lubr. Technol., vol. 96, no. 4, Oct. 1974, pp. 583-590.



Gear Lubrication and Cooling Experiment and Analysis*

Dennis P. Townsend† and Lee S. Akin‡

There are several methods of lubricating and cooling gear teeth: splash lubrication, drip feed, air/oil mist, and pressurized oil-jet flow. The method of successful lubrication usually depends on the operating conditions. For gears operating at moderate to high speed (above 5000 rpm), the pressurized oil jet becomes necessary to provide adequate lubrication and cooling and to prevent scoring of the gear-tooth surfaces. Scoring is a result of having a too thin elastohydrodynamic (EHD) oil film. This thin EHD film is usually caused by inadequate cooling rather than insufficient lubricant.

Of the three primary modes of gear tooth failure, scoring is the most common and the most difficult to analyze. A considerable amount of work has been done over the past four decades to produce quantitative analysis procedures to evaluate the risk of scoring in lubricated gear drives (refs. 1 and 2). For the first 30 years of this time period, most of the concentrated effort had to do with developing a procedure to evaluate the incipient onset of the scoring phenomenon. It has only been in the last decade or so that a concentrated effort has been provided to evaluate the contribution of the gear tooth bulk temperature on the scoring phenomenon and to determine its contribution in bringing about the onset of this mode failure of (refs. 3 and 4).

A computer program was developed using a finite-element analysis to predict gear tooth temperatures (refs. 5 and 6). However, that program did not include the effects of oil-jet cooling and oil-jet impingement depth. It used an average surface heat-transfer coefficient for surface temperature calculation based on the best information available at that time.

To have a better method for predicting gear-tooth temperature, it is necessary that the analysis allow for the use of a heat-transfer coefficient for oil-jet cooling coupled with a coefficient for air/oil mist cooling for that part of the time that each condition exists. Once the analysis can make use of these different coefficients, it can be combined with a method that determines the oil-jet impingement depth to give a more complete gear-temperature analysis program. However, both the oil-jet and air/oil mist heat-transfer coefficients are unknowns and must be determined experimentally.

The objectives of the work reported herein were to (1) further develop the gear-temperature analysis computer program (refs. 5 and 6), which incorporates different heat-transfer coefficients for air/oil and oil-jet cooling, (2) combine that program with a program developed to determine the impingement depths, and (3) experimentally measure gear-tooth temperatures to compare them with those predicted using the improved analysis.

Symbols

a	diffusivity, $= k/P C_p$, lb/in °F sec ^{1/2}
b	Hertzian contact width, m (in.)
C_p	specific heat, J/kg K (Btu/lb °F)
d_i	oil-jet impingement depth, m (in.)
F_e	effective face width, m (in.)
f	friction coefficient
h_j	heat-transfer coefficient for lubricated flank of gear, W/hr m ² K (Btu/hr ft ² °F)

*Previously published in Journal of Mechanical Design, vol. 103, no. 4, Jan. 1981, pp. 219-226; also as NASA TM-81419 under the title "Analytical and Experimental Spur Gear Tooth Temperature as Affected by Operating Variables."

†NASA Lewis Research Center.

‡Western Gear Corp., Industry, Calif.; also California State University, Long Beach.

h_s	heat-transfer coefficient sides of gear, W/hr m ² K (Btu/hr ft ² °F)
h_t	heat-transfer coefficient for unlubricated flank of gear, W/hr m ² K (Btu/hr ft ² °F)
J	heat conversion factor
k	infrared radiometric microscope constant
L_A	line of action length, m (in.)
L_t	length of tooth, m (in.)
m	module
N	number of teeth
ΔN	radiance
P_d	diametral pitch module (in ⁻¹)
q	heat flux, W/hr (Btu/hr)
q_t	total heat generated, W/hr (Btu/hr)
V	rolling velocity, m/sec (ft/sec)
ΔV	infrared radiometric microscope measured, V
V_g	gear pitch line velocity, m/sec (ft/sec)
V_j	oil-jet velocity, m/sec (ft/sec)
V_s	sliding velocity, m/sec (ft/sec)
W	normal tooth load, N (lb)
W_t	tangential tooth load, N (lb)
α	oil-jet angle from radial, deg
β	temperature coefficient of viscosity
δ_i	dimensionless impingement depth, $d_i P_d$, m ² (in.)
ϵ	emissivity
η	rotation angle, revolutions/sec
θ_s	temperature, K (°F)
θ_w	gear rotation angle from tip of tooth to impingement point, rad
κ	thermal conductivity, W/m K (Btu/ft °F)
Λ	partition constant
ν, ν_o	kinematic viscosity
ν_j	dimensionless oil-jet velocity
ρ	density, kg/m ³ (lb/in ³)
$\rho_{1,2}$	involute radius of curvature, m (in.)
φ	pressure angle, rad
ω	angular velocity, rad/sec

Apparatus and Procedure

Gear Test Apparatus

Gear-tooth temperature measurements were made using the NASA gear test shown in figure 1 and described in reference 7. This test rig uses the four-square principle of applying the test gear load so that the input drive needs only to overcome the frictional losses in the system.

The gear surface temperatures were measured with a fast-response infrared radiometric (IR) microscope that uses a liquid-nitrogen-cooled detector. The IR microscope can measure transient temperatures up to 20 000 Hz. All radiance measurements were made with a 1× lens that has a focal length of approximately 23 cm (9 in.) and a viewing spot size of 0.05 cm (0.020 in.) diameter. The test gear cover, viewing port, and lubrication jet as shown in figure 2 were used with the IR microscope.

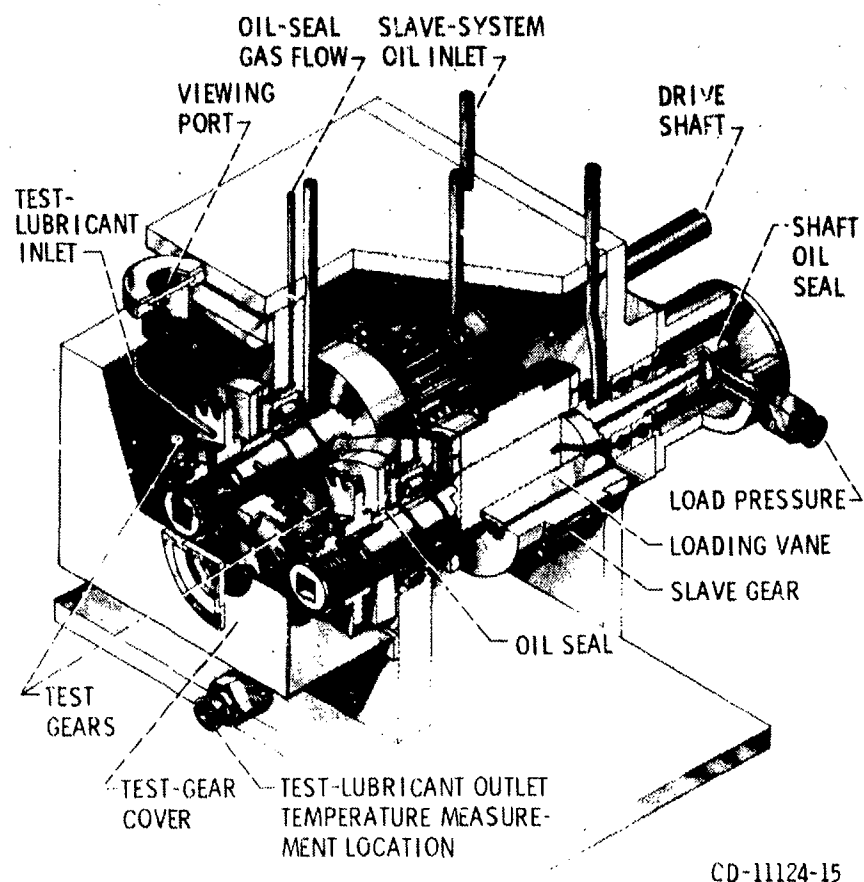


Figure 1. -NASA Lewis Research Center's gear fatigue test apparatus.

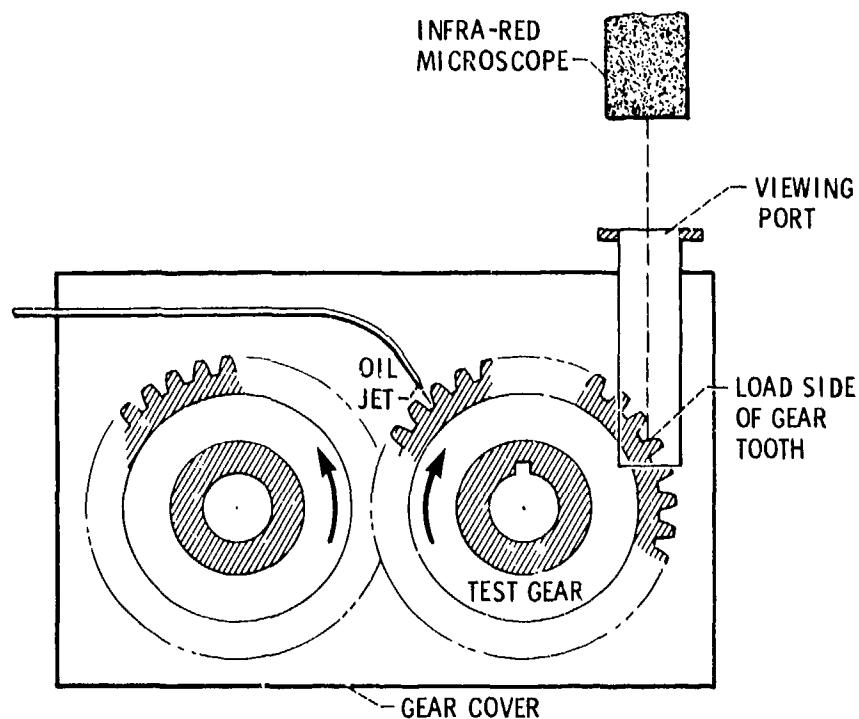


Figure 2. - Test setup for measuring dynamic gear tooth surface temperature.

Test Gears

The 28-tooth test gears were of 8 diametral pitch and 8.89-cm (3.5-in.) pitch diameter with a 0.635-cm (0.250-in.) face width. All gears had a nominal surface finish on the tooth flank of 0.406 μm (16 $\mu\text{in.}$), rms, and a standard 20 involute profile without tip relief. The test gears were manufactured from consumable-electrode vacuum-melted (CVM) AISI 9310 steel. The gears were case carburized and hardened to a Rockwell C hardness of 60 before final grinding of the finished gear.

Test Lubricant

The test gears were lubricated with a single batch of synthetic paraffinic oil. The physical properties of the oil are summarized in table I. Five percent of an extreme pressure additive, designated Lubrizol 5002, was added to the lubricant.

Test Procedure

After the test gears were cleaned to remove the preservative, they were assembled on the test rig. The test gears were run in a full face load condition on the 0.635-cm (0.250-in.) face width. The tests were run at four speeds, 2500, 5000, 7500, and 10 000 rpm; three tangential loads, 1895, 3736, and 5903 N/cm (1083, 2135, and 3373 lb/in.); five oil-jet pressures 96×10^4 , 69×10^4 , 41×10^4 , 27×10^4 , and 14×10^4 Pa (140, 100, 60, 40 and 20 psi); and two oil-jet diameters, 0.04 and 0.08 cm (0.016 and 0.032 in.). Inlet oil temperature was constant at 308 K (95° F). At each speed the lowest load was first applied with the maximum oil-jet pressure. At this load the oil-jet pressure was reduced in steps to the lowest pressure before the next load was applied. The oil jet was pointing in a radial direction and hitting the unloaded side of the gear tooth as it came out of the mesh zone. The 0.08-cm (0.032-in.) diameter jet is the size typically used in many applications for the maximum power conditions used herein. The 0.04-cm (0.016-in.) diameter jet was used to determine what cooling conditions could be obtained with considerably less oil flow and good oil-jet impingement depth. The temperature was measured by the IR scope at a location approximately 160° away from the mesh zone.

The IR scope operates in two modes. In the DC mode the average surface temperature of the gear tooth was read out on the meter supplied with the IR scope. The scope was calibrated before running the tests to determine the emissivity of the gear-tooth surface. In the AC mode a voltage that varies with surface radiance according to the equation

$$\Delta V = \kappa \epsilon \Delta T \quad (1)$$

was measured from two signals on a dual trace cathode-ray oscilloscope (CRO). The upper signal in figure 4 was from the IR scope directly; the lower signal was filtered through a variable-band-pass filter to remove the 20-mV high-frequency noise. At the lower loads and at the high oil-jet pressure, the signal-to-noise ratio was approximately one.

The gear-tooth surface was viewed by the IR scope as it passed before the lens. The tip of the tooth is seen first; the view then goes down the tooth surface until it is interrupted by the next tooth.

TABLE I - LUBRICANT PROPERTIES OF SYNTHETIC PARAFFINIC OIL PLUS ADDITIVES^a

Kinematic viscosity, cm ² /sec (cs) at:	
244 K (-20° F)	2500x10 ⁻² (2500)
311 K (100° F)	31.6x10 ⁻² (31.6)
372 K (210° F)	5.7x10 ⁻² (5.7)
477 K (400° F)	2.0x10 ⁻² (2.0)
Flash point, K (°F)	508 (455)
Fire point, K (°F)	533 (500)
Pour point, K (°F)	219 (-65)
Specific gravity	0.8285
Vapor pressure at 311 K (100° F), mm Hg (or torr)	0.1
Specific heat at 311 K (100° F), J/(kg)(K)(Btu/(lb)(°F))	676 (0.523)

^aAdditive, Lubrizol 5002 (5 vol. %). Additive content: phosphorus, 0.6 wt %; sulfur, 18.5 wt %.

Gear Temperature Analysis

A gear-tooth temperature analysis was developed in references 5 and 6 to calculate the gear-tooth temperature profile using a finite-element analysis. This analysis uses a finite-element mesh and calculates isotherms on the gear tooth. However, the following conditions are required to be determined or calculated before the program can calculate effective temperatures: (1) the frictional heat input at the gear-tooth working surface, (2) the different heat-transfer coefficients for the various gear-tooth surfaces and cooling methods, and (3) the oil-jet penetration onto the gear-tooth flank.

The frictional heat input to the gear-tooth working surface can be calculated using the following analysis: The instantaneous heat generated per unit area per unit time due to the sliding of the two gear teeth is given by

$$q = \frac{fW|V_s|}{bJ} = \frac{fW|\omega_1\rho_1 - \omega_2\rho_2|}{bJ} \quad (2)$$

where

$$W = \frac{W_t}{F_e} \cos \varphi$$

Since W , V_s , and f are functions of the mesh-point location, the q will vary through the meshing cycle. The f varied from approximately 0.02 to 0.07 for the cases evaluated. The heat generated will be divided between the gear and pinion and may not be equally withdrawn by each, so that a partitioning function Λ is used. The heat withdrawn by the gear and pinion will then be

$$q_1 = \Lambda q \quad q_2 = (1 - \Lambda)q \quad (3)$$

For the test gears used in this paper Λ is assumed to be 0.5, so that

$$q_1 = q_2 \quad (4)$$

once the instantaneous heat flux to the gear surface is determined. The total time average heat flow per revolution can be calculated by the following equation from reference 6:

$$q_1 = \frac{b\omega_1\Lambda}{V_1 2\pi} = \frac{b\omega_2(1-\Lambda)q}{V_2 2\pi} \quad (5)$$

where V_1 and V_2 are the gear and pinion rolling velocities. Substituting equation (2) into equation (5) gives

$$q_1 = q_2 = \frac{\Lambda f W_t^2}{V_1 2\pi J} \rho_1 - \frac{\omega_2}{\omega_1} \rho_2 \quad (6)$$

substituting

$$\Lambda = 0.5, \quad \eta_1 = \frac{\omega_1}{2\pi}, \quad \frac{\omega_2}{\omega_1} = \frac{N_1}{N_2}, \quad \text{and} \quad V_1 = \omega_1 \rho_1$$

give:

$$q_1 = q_2 = \frac{fW\eta_1}{2J} \left| 1 - \frac{N_1}{N_2} \frac{\rho_2}{\rho_1} \right| \quad (7)$$

for the time-averaged heat flux. Using this expression, the instantaneous heat flux may be calculated at any position along the line of action by substituting the instantaneous profile radius, giving the heat input to the gear-tooth surface at that location. Substituting $L_A - \rho_1$ for ρ_2 , where $L_A = \rho_1 + \rho_2$, and using instantaneous notation, equation (8) becomes

$$q_{il} = \frac{f_i W \eta_1}{2J} \left| 1 - \frac{N_1}{N_2} \left(\frac{L_A - \rho_{il}}{\rho_{il}} \right) \right| \quad (8)$$

The heat-transfer coefficients (fig. 3) for the sides, top land, and flanks of the gear teeth are different because of the different cooling regions. Also, the coefficient for the two flanks will be different, depending on whether they are cooled by the oil-jet hitting the surface or by air (no jet cooling). The heat-transfer coefficient for the sides of the gear teeth h can be estimated by the method of reference 9 for a rotating disk by

$$h_s = Nu \kappa \sqrt{\frac{\omega}{\bar{V}}} \quad (9)$$

where for air $Nu = 0.5$. However, the amount of oil mist present will have a considerable effect on this coefficient. The gear-tooth flanks not cooled by the oil jet will have a heat-transfer coefficient h_f for air or air/oil mist. Since there are no data available to determine this coefficient, an estimate somewhere between air cooling and jet cooling will be used until something better is obtained experimentally.

The heat-transfer coefficient h_j for the jet-cooled tooth face and the tooth tip may be calculated (refs. 4 and 8) using the following equation:

$$h_j = \left(\frac{2L_t}{m} \right)^{1/4} \left(\frac{v_o}{aN} \right)^{1/4} \frac{b\omega^{1/2}}{2\pi} q_{tot} \quad (10)$$

where q_{tot} is a dimensionless factor (refs. 4 and 8). Curve fitting the data (ref. 8) gives

$$q_{tot} = 0.98 = 0.32 \gamma + 0.06 \gamma^2 - 0.004 \gamma^3 \quad (11)$$

where

$$\gamma = \beta \theta_s \quad (12)$$

Using the above method for calculating the oil-jet heat-transfer coefficient gives temperatures that are much too high. For the results presented in this paper, an oil-jet heat-transfer coefficient was assumed that would give more realistic results. For future work a more realistic oil-jet heat-transfer coefficient will be determined based on experimental results reported in this paper and from future testing.

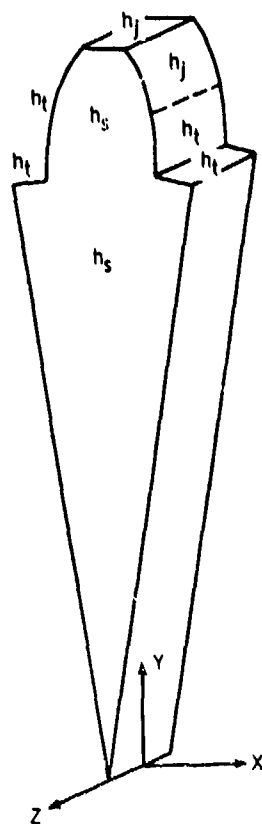
The oil-jet penetration onto the gear-tooth flank can be determined by the method of references 10 and 11. A more accurate analysis is being developed by the authors using a new kinematic radial model instead of the vectorial model used in reference 10. The new model gives the oil-jet impingement depth for radially directed jet as

$$\delta_i = \frac{v_j \theta_\omega (N+2) \cos \alpha}{4} \quad (13)$$

Using the above equation with a known jet velocity, the angle of rotation is assumed and must be iterated until the angle of rotation and impingement point coincide, since θ_ω is a function of δ_i and θ_ω :

$$V_j = \frac{4\delta_i}{\theta_\omega (N+2) \cos \alpha} \quad (14)$$

Once the heat generation and the oil-jet impingement depth have been calculated, the heat-transfer coefficients are either calculated or estimated. Then, the finite-element analysis is used to calculate the temperature profile of the gear teeth. The finite-element model has 108 nodes with triangle elements. The computer program calculates a steady-state temperature at all 108 nodes and prints these temperatures. The program also plots temperature isobars on the gear-tooth profile and lists the temperatures of the isobars.



h_s, h_t, h_j = DEFINITION OF
HEAT TRANSFER ZONES

Figure 3. - Geometry of problem.

Results and Discussion

Experimental Results

Transient and average gear-tooth surface temperatures were measured using a fast-response infrared (IR) radiometric microscope. The gear-tooth temperatures were measured at four speeds, three loads, five oil-jet pressures, and two oil-jet diameters. The test gears were of 3.2 module (8 pitch), 8.89-cm (3.5-in.) pitch diameter with a 0.64-cm (0.25-in.) face width.

Figure 4(a) is a typical transient measurement of a gear tooth surface at 7500 rpm, 5903-N/cm (3373-lb/in) tangential load, and 14×10^4 -Pa (20-psi) oil-jet pressure with a 0.041-cm (0.016-in.) diameter orifice. The change in surface temperature from the gear tooth tip to a point just below the pitch line was 32 K (58° F). The pitch line where pure rolling occurs can be seen by the slight dip in temperature. The highest temperature is below the pitch line where the combination of high load with some sliding occurs.



$14 \times 10^4 \text{ N/m}^2$ (20 psi), 0.05 V/DIV $69 \times 10^4 \text{ N/m}^2$ (100 psi), 0.02 V/DIV

Figure 4. - IR microscope measurements of gear tooth surface temperature.
Speed, 7500 rpm; load, 5903 N/cm (3373 lb/in); inlet oil temperature, 308 K (95° F); oil-jet diameter, 0.04 cm (0.016 in.).



Figure 5. - IR microscope measurements of gear teeth scoring temperature.
0.5 V per division; speed, 10 000 rpm; load, 5903 N/cm (3373 lb/in); inlet oil temperature, 308 K (95° F); oil jet diameter, 0.04 cm (0.016 in.).

Figure 4(b) is for the same load, speed, and oil-jet size condition but with an oil-jet pressure of $97 \times 10^4 \text{ Pa}$ (140 psi), which reduces the maximum temperature difference to 12 K (22° F), with the peak temperature still occurring below the pitch line. The average surface temperature for these conditions was 423 and 391 K (302° and 244° F) for the 14×10^4 - and 97×10^4 -Pa (20- and 140-psi) oil pressures, respectively. Figure 5 is typical of what happens when scoring occurs. Here, the peak temperature is at the tip of the gear tooth and has reached a maximum temperature of 508 K (455° F) or 75 K (135° F) above the average surface temperature of 433 K (320° F). Scoring temperatures as high as 603 K (626° F) were measured during the high-load, high-speed tests with reduced oil-jet pressure or orifice size. These temperatures would be somewhat lower than those at the contact point, since they were measured 160° away from the contact and after oil-jet cooling. The scoring conditions occurred only at the 10 000-rpm test condition with intermediate loads and full or less oil-jet impingement depths.

Figure 6(a) is a plot of gear-tooth average surface temperature (solid line) with the high and low temperatures included (dashed lines) versus oil-jet pressure for three speeds, an oil-jet diameter of 0.04 cm (0.016 in.), and a load of 5903 N/cm (3373 lb/in).

The high load and high speed with the small jet size could not be run except at the highest pressure because of scoring. From these plots the effect of different speeds at constant load and the effect of oil-jet pressure on both average surface temperature and temperature variations can be seen. The increased speed causes a higher surface temperature and higher temperature variations. The oil-jet pressure also has a greater effect at the higher speed. The maximum oil pressure needed for a speed is also seen by the leveling of the curve at the lower speeds where increased oil pressure causes very little improvement in cooling.

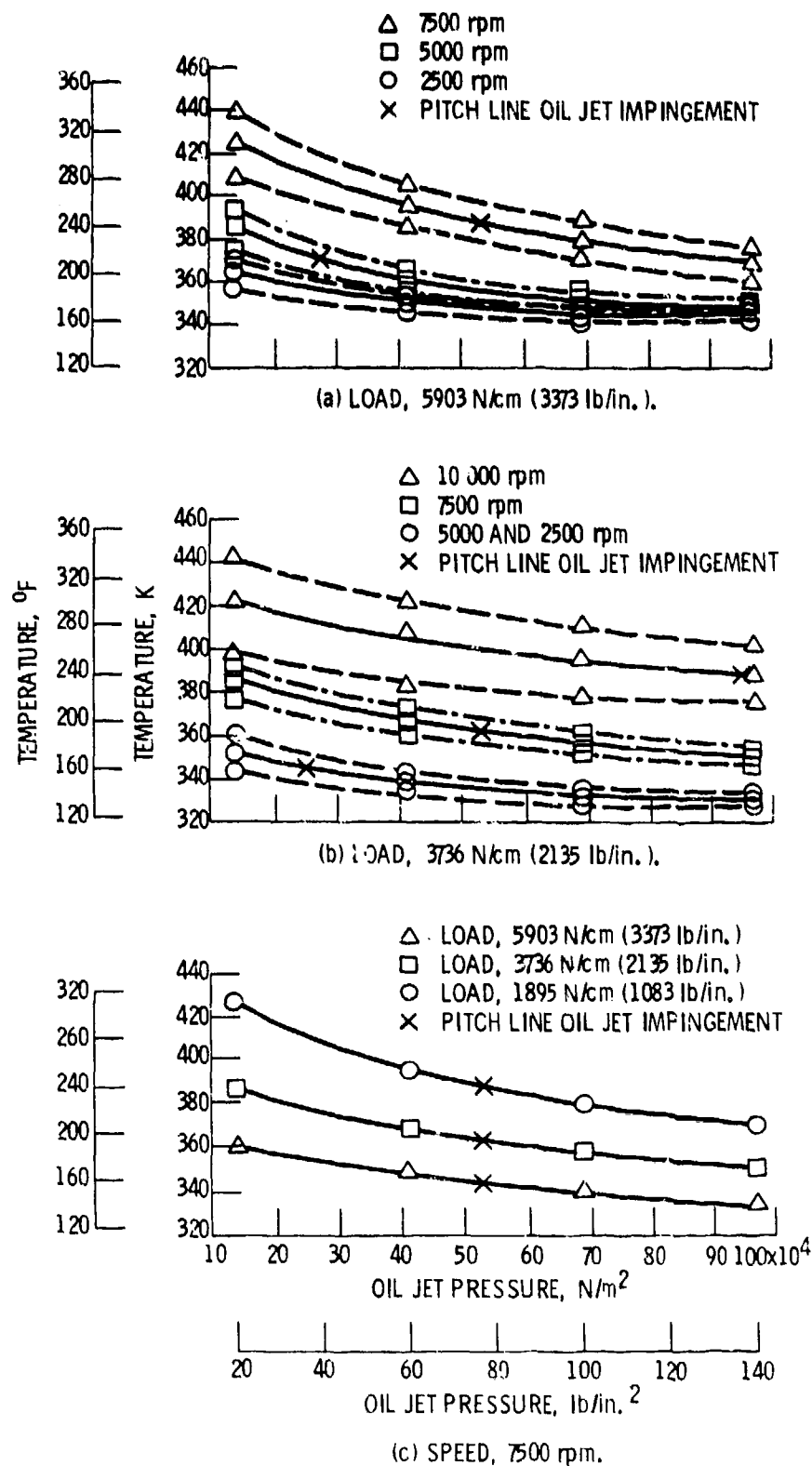


Figure 6. - IR microscope measurements of gear teeth surface temperature versus oil-jet pressure. Inlet oil temperature, 308 K (95° F); oil jet diameter, 0.04 cm (0.016 in.).

Figure 6(b) is the same type of plot as figure 6(a) except the load is 3736 N/cm (2135 lb/in). The curves for 5000 and 2500 rpm are nearly identical. The effect of oil-jet pressure is considerably reduced because of the lower load. Here, the maximum change in average surface temperature is 35 K, and the maximum surface temperature difference is 45 K at the 13.8×10^4 -Pa (20-psi) oil-jet pressure.

Figure 6(c) is a plot of gear-tooth average surface temperature versus oil-jet pressure with different loads at a speed of 7500 rpm. This figure shows the effect of load and oil-jet pressure on gear-tooth temperature at constant speed.

Figure 7 is a plot of load versus gear-tooth average surface temperature for the 7500 rpm condition and three oil-jet pressures. The effect of load and oil-jet pressure on gear-tooth surface temperature is clearly seen. Increasing the pressure from 14×10^4 to 97×10^4 Pa (20 to 140 psi) has about the same effect as reducing the load from 6000 to 2000 N/cm.

Figure 8 shows plots of average surface temperatures with temperature variations and bulk gear temperature, respectively, versus oil-jet pressure for three loads at 10 000 rpm and an oil-jet size of 0.08 cm (0.032 in). With the larger oil-jet size, the temperatures are reduced considerably from those with the smaller jet size. The bulk temperature of the gear does not increase as much as the average surface temperature. At the lower load and high jet pressure, the surface and bulk temperatures are nearly identical.

Analytical Results

Calculations were made using the computer program to examine the effects of calculated heat inputs from the experimental test cases and estimated heat-transfer coefficients. The differential temperature profiles are shown in figures 9 to 11. The differential profiles in these figures are the temperature difference between the inlet cooling oil and the actual gear-tooth temperatures.

Matching the analytical predictions with the experimental results is difficult because of different physical conditions existing in the program input and the experiment. The analysis and the tests were planned whereby heat removal was on the working face of the gear tooth. The analysis was completed before the tests were conducted. Initial testing resulted in oil splashing on the infrared microscope viewing port, which prevented meaningful IR temperature measurements. To prevent this condition from occurring, the oil jet was directed at the back side of the tooth, resulting in cooling of the unloaded side of the gear tooth.

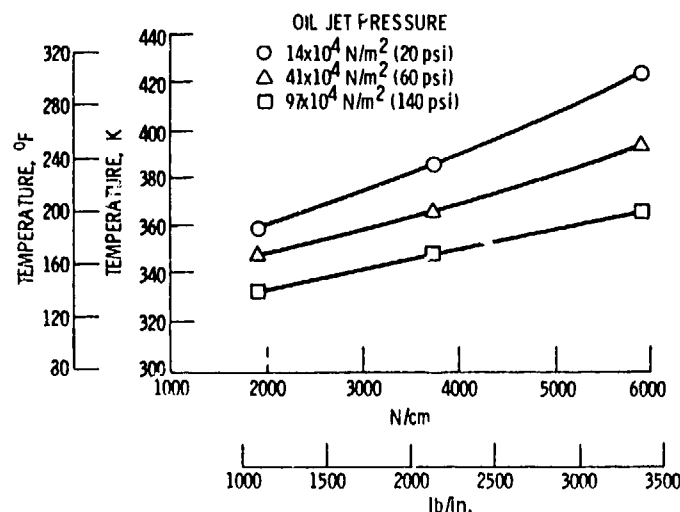


Figure 7. - IR microscope measurements of gear average surface temperature versus load for three oil-jet pressures. Speed, 7500 rpm; oil-jet diameter, 0.04 cm (0.016 in.); inlet oil temperature, 308 K (95° F).

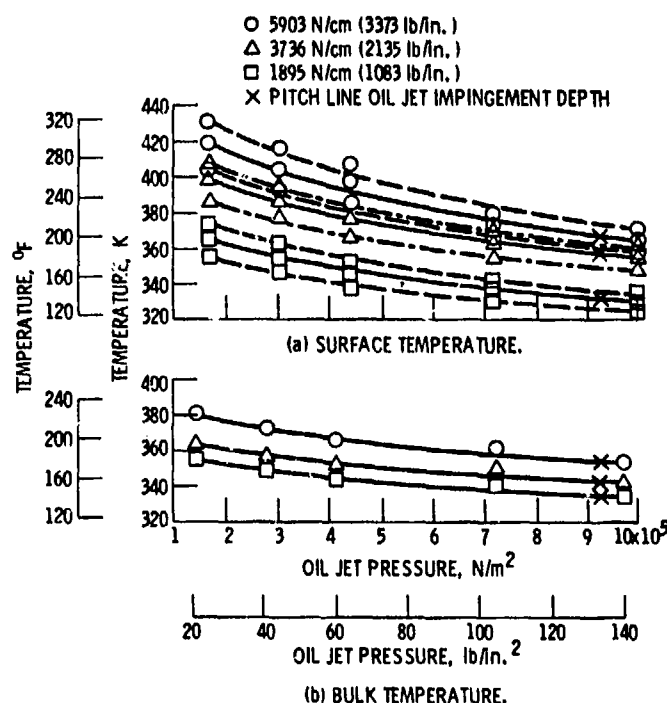


Figure 8. - IR microscope and thermocouple measurements of gear temperature versus oil-jet pressure for three loads. Speed, 10 000 rpm; oil-jet diameter, 0.08 cm (0.032 in.); inlet oil temperature, 308 K (95° F).

The conditions of figure 9(a) were 10 000 rpm with a tangential tooth load of 5903 N/cm (3373 lb/in) and an impingement depth of zero. This means that the gear had impingement on the top land only. The lowest level of temperature difference in the gear tooth is 35 K (63° F) at the tip of the tooth. The hot spot is just below the pitch line and is 122 K (200° F) above the oil-jet temperature. This gives an average surface temperature above oil-jet temperature of approximately 79 K (142° F).

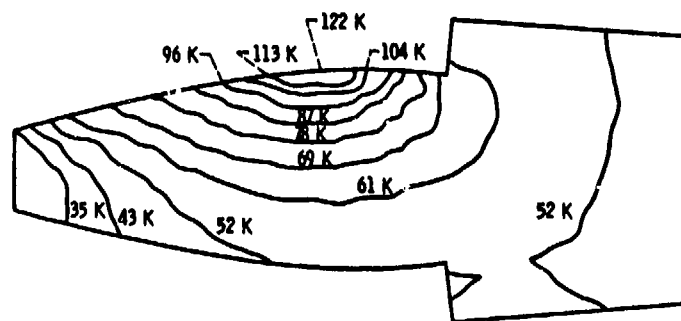
Figure 9(b) is a gear-tooth temperature profile for the same conditions as figure 9(a) except that the oil-jet impingement is 87.5 percent of the tooth depth. Here, the minimum temperature difference is at the tooth tip of 9 K (16° F), and the highest temperature difference just below the pitch line is 31 K (56° F).

Figure 10(a) is the analytical results for an operating condition of 7500 rpm, a tangential tooth load of 1895 N/cm (1083 lb/in) and an impingement depth of zero. The minimum temperature difference between the oil-jet and tooth temperature is at the tooth tip and is 16 K (29° F), while the maximum temperature of 50 K (90° F) is below the pitch point.

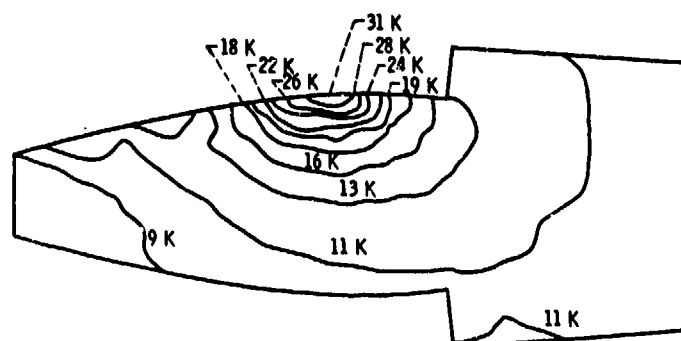
Figure 10(b) is the same conditions as figure 10(a) except for the oil-jet impingement depth of 87.5 percent of the tooth depth. The minimum and maximum oil-jet to gear-tooth temperatures are 4 and 12 K (7° and 22° F).

Figure 11 shows the analytical results for cooling on the back (or unloaded) side of the gear tooth in a manner to match that obtained in the experiment. The minimum and maximum calculated oil-jet gear-tooth temperatures of 92 and 127 K (166° and 229° F) at 33.5 percent depth are fairly close to the experimentally measured temperatures of 95 and 123 K (171° and 221° F), respectively. Likewise for the 75.3 percent depth, where the minimum and maximum calculated temperatures of 43 and 70 K (77° and 126° F) were close to the experimentally measured temperatures of 49 and 63 K (88° and 113° F), respectively.

With the analytical results using backside cooling and the experimentally adjusted film coefficients, the calculated and experimental temperatures are in very good agreement. The analytical results of figures 9 and 10, obtained for cooling on the loaded side of the tooth, show only fair agreement with the experimental results, which were for cooling on the backside of the teeth, resulting in inaccurate estimates of the heat-transfer coefficients.

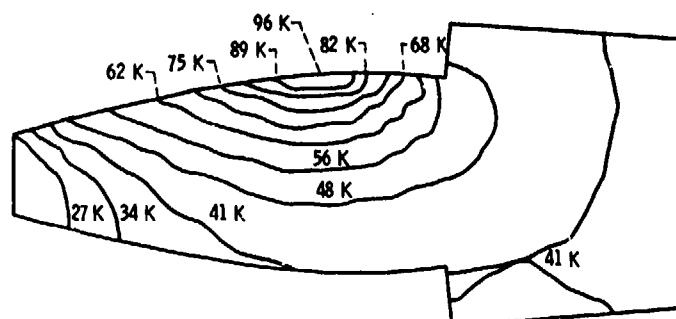


(a) ZERO IMPINGEMENT DEPTH.

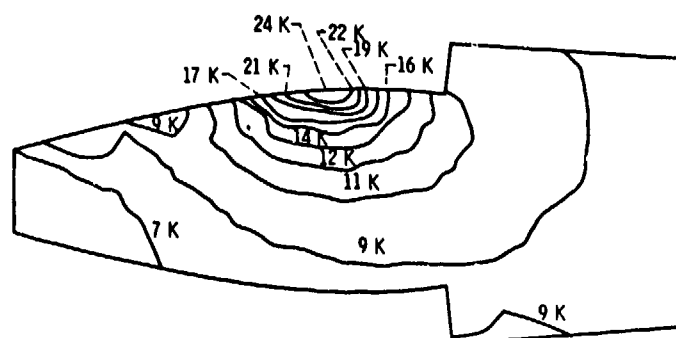


(b) 87.5 percent IMPINGEMENT DEPTH.

Figure 9. - Calculated gear tooth temperatures. Speed, 10 000 rpm; load, 5903 N/cm (3373 lb/in).



(a) ZERO IMPINGEMENT DEPTH.



(b) 87.5 percent IMPINGEMENT DEPTH.

Figure 10. - Calculated gear tooth temperatures. Speed, 7500 rpm; load, 1875 N/cm (1083 lb/in)

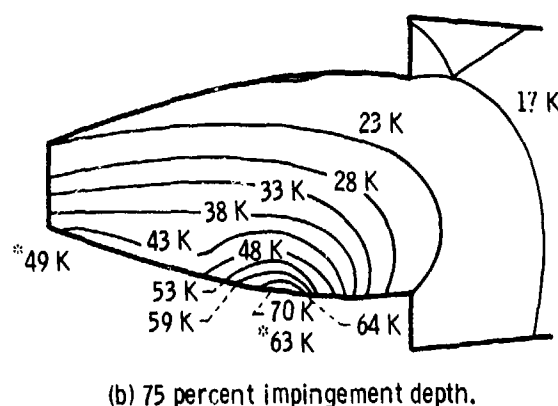
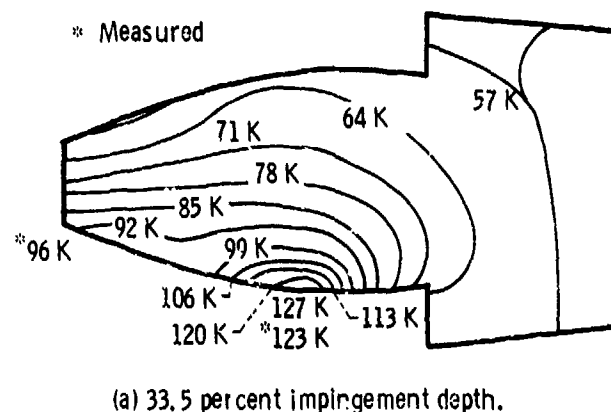


Figure 11. - Calculated gear tooth temperatures for gears cooled on backside.
Speed, 10 000 rpm; load, 5903 N/cm (3373 lb/in).

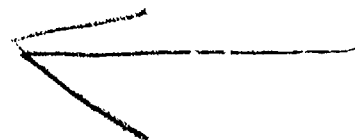
Summary of Results

A gear-tooth temperature analysis was performed using a finite-element method combined with a calculated heat input, a calculated oil-jet impingement depth, and estimated heat-transfer coefficients for the different parts of the gear tooth that are oil cooled and air cooled. Experimental measurements of gear-tooth average surface temperature and gear-tooth instantaneous surface temperature were made with a fast-response, infrared, radiometric microscope. The following results were obtained.

1. Increasing oil pressure has a significant effect on both average surface temperature and peak surface temperature at loads above 1895 N/cm (1083 lb/in) and speeds of 10 000 and 7500 rpm.
2. Both increasing speed (from 5000 to 10 000 rpm) at constant load and increasing load at constant speed cause a significant rise in the average surface temperature and in the instantaneous peak surface temperatures on the gear teeth.
3. The oil-jet pressure required to provide the best cooling for gears is the pressure required to obtain full gear-tooth impingement.
4. Calculated results for gear tooth temperatures were close to experimental results for various oil-jet impingement depths for identical operating conditions.

References

1. Blok, H.: Lubrication as a Gear Design Factor. Proc. International Conference on Gearing. The Institution of Mechanical Engineers, 1958.
2. Kelley, B. W.; and Lemanski, A. J.: Lubrication of Involute Gearing. Proc. Inst. Mech. Eng. (London), vol. 182, pt. 3A, 1967-1968, pp. 173-184.
3. Akin, L. S.: An Interdisciplinary Lubrication Theory for Gears (With Particular Emphasis on the Scuffing Model of Failure). J. Eng. Ind., vol. 95, no. 4, Nov. 1973, pp. 1178-1195.
4. DeWinter, A.; and Blok, H.: Fling-Off Cooling of Gear Teeth. J. Eng. Ind., vol. 96, no. 1, Feb. 1974, pp. 60-70.
5. Wang, K. L.; and Cheng, H. S.: A Numerical Solution to the Dynamic Load, Film Thickness, and Surface Temperatures in Spur Gears, Part II—Results. Presented at the ASME International Power Transmission and Gear Conference, Chicago, Sep. 28-30, 1977.
6. Patir, N.; and Cheng, H. S.: Prediction of Bulk Temperature in Spur Gears Based on Finite Element Temperature Analysis. ASLE Preprint No. 77-LC-3B-2, Oct. 1977.
7. Townsend, D. P.; Bamberger, E. N.; and Zaretsky, E. V.: A Life Study of Ausforged, Standard Forged, and Standard Machined AISI M-50 Spur Gears. J. Lubr. Technol., vol. 98, no. 3, July 1976, pp. 418-415.
8. Van Heijningen, G. J. J.; and Blok, H.: Continuous as Against Intermittent Fling-Off Cooling of Gear Teeth. J. Lubr. Technol., vol. 96, no. 4, Oct. 1974, pp. 529-538.
9. Patir, N.: Estimate of the Bulk Temperature in Spur Gears Based on Finite Element Temperature Analysis. M.S. Thesis, Northwestern University, 1976.
10. Akin, L. S.; Mross, J. J.; and Townsend, D. P.: Study of Lubricant Jet Flow Phenomena in Spur Gears. J. Lubr. Technol., vol. 97, no. 2, Apr. 1975, pp. 283-288.
11. Townsend, D. P.; and Akin, L. S.: Study of Lubricant Jet Flow Phenomena in Spur Gears—Out of Mesh Condition. J. Mech. Des., vol. 100, no. 1, Jan. 1978, pp. 61-68.



Dynamic Tooth Loads and Stressing for High Contact Ratio Spur Gears*†

R. W. Cornell† and W. W. Westervelt†

One way of possibly improving the structural efficiency, reliability, and power-to-weight ratio of power gear transmissions is to increase their contact ratio. Current spur gearing is usually designed to operate at contact ratios between 1.2 and 1.6. Contact ratio is defined as the average number of tooth pairs in contact under static conditions and without errors and tooth profile modifications. Thus, a typical contact ratio of 1.5 means that, ideally, two tooth pairs are in contact half of the time, and only one tooth pair is in contact the other half of the time. High-contact-ratio gearing (HCRG) applies to gear meshes that have at least two tooth pairs in contact at all times, that is, contact ratios of 2.0 or more. Because the transmitted load is always shared by at least two tooth pairs for HCRG, the individual tooth loading tends to be less than for present low-contact-ratio gearing (LCRG), thereby potentially decreasing the tooth root and contact stresses. However, HCRG requires gear teeth with lower pressure angles, finer pitch, and increased addendums, all of which increase the tooth stressing per applied load. In addition, HCRG would be expected to be dynamically more sensitive to tooth errors and profile modifications because of the multiple tooth contact.

To properly evaluate HCRG requires two basic analyses: First, a system dynamic analysis is needed to determine the operating load sharing among the two and three tooth pairs in contact, taking into account gear errors and tooth-profile modifications. Second, a stress sensitivity analysis for the gear teeth is needed to convert the dynamic tooth loads to tooth root stresses, taking into account the nonstandard tooth form of HCRG teeth. Such analyses and associated computer program were developed by Hamilton Standard from 1973 to 1975 in support of a NASA Lewis HCRG evaluation study being conducted by Sikorsky Aircraft, Division of United Technologies Corp. (ref. 1). This work was an extension and improvement of the theoretical and experimental work done jointly by M.I.T. (refs. 2 to 4) and Hamilton Standard (refs. 5 and 6) for LCRG from 1959 to 1967. The features of the dynamic system analysis and computer program for HCRG are presented along with some preliminary results from applying the analysis to some typical LCRG and HCRG. These limited results show that the system critical speed, system inertia and damping, and tooth-profile modifications can affect the dynamic gear tooth loads and root stressing significantly.

Nomenclature

A, B, C, D	gear tooth coefficients; see eq. (1)
a, b, c	coefficients defined by eq. (10)
C_d, C_e	disengagement and engagement cam relief, $\Delta_d / (S_{0d}^2 - S_d^2)$ and $\Delta_e / (S_{0e}^2 - S_e^2)$
d	viscous damping coefficient of gears, lb·sec/in. (N·sec/m)
e	dimensionless tooth error, e^* / δ
e^*	tooth error, in. (m)
i	number of time history steps in mesh cycle
J_1, J_2	polar moment of inertias of gears 1 and 2, in·lb sec ² (kg·m ²)
j	designate of gear pair in mesh
$k, 1/C$	single tooth-pair spring rate (reciprocal of compliance), lb/in (N/m)
$k_0, 1/C_0$	single tooth-pair spring rate at pitch radius (reciprocal of compliance), lb/in (N/m)
L	dynamic single tooth load, lb (N)

*Work done under NASA contract NAS3-17859.

†Hamilton Standard, Division of United Technologies Corporation.

‡Previously published in J. Mech. Des., vol. 100, no. 1, Jan. 1978.

AD P000727

L_0	static single tooth applied load, $T_1/R_{B1} = T_2/R_{B2}$, lb (N)
M	effective linear mass of gear-mesh system, lb sec ² /in. (kg/sec ² in)
m	number of active or engaged tooth pairs
\overline{m}	$\sum_j^m \Phi_j \eta_j$
N_1, N_2	number of teeth on gears 1 and 2
P_n	normal pitch or tooth spacing along line of action ($2\pi R_{B1}/N_1 = 2\pi R_{B2}/N_2$), in. (m)
R_{B1}, R_{B2}	base radii of gears 1 and 2 ($R_{p1} \cos \varphi_p$ and $R_{p2} \cos \varphi_p$), in. (m)
R_{p1}, R_{p2}	pitch radii of gears 1 and 2, in. (m)
S	motion along line of action from pitch line, $R_{B1}\psi_1 = R_{B2}\psi_2$, in. (m)
S_d, S_e	distances along line of action from pitch line to the start of disengagement cam and end of engagement cam (positive), in. (m)
S_r	linearized relative motion of gears along line of action, $= S_1 - S_2$, in. (m)
S_0	reference distance along line of contact for tooth pair compliance coefficients, in. (m)
S_{0d}, S_{0e}	distances along line of action from pitch line to end of disengagement cam (tooth tip) and start of engagement cam (positive), in. (m)
T_1, T_2	torques on gears 1 and 2, in·lb (N·m)
t	time, τ/V , sec
V	tooth velocity along line of action ($R_{B1}\Omega_1 = R_{B2}\Omega_2$), in/sec (m/sec)
w_1, w_2	width of gears 1 and 2, in. (m)
x	integer cam form exponent
y	dimensionless relative motion of gears (S_r/δ)
z	deflection of tooth pair versus S , in. (m)
β_d, β_e	dimensionless tooth disengagement and engagement cam parameters ($V\sqrt{C_d/\delta/\omega}$)($V\sqrt{C_e/\delta/\omega}$)
Δ_d, Δ_e	maximum disengagement and engagement tooth relief for tooth pairs, in. (m)
δ	static deflection of tooth pair under applied load at pitch radius, (L_0/k_0), in. (m)
ϵ_d, ϵ_e	total tooth-profile disengagement and engagement modifications, in. (m)
η	relative tooth stiffness, k/k_0
σ	maximum tooth root stress, psi (Pa)
τ	dimensionless time ($\omega t = \omega S/V$) into mesh period, ($\tau_0 + \bar{\tau}$)
$\bar{\tau}$	dimensionless time from τ_0 into mesh period
τ_c	dimensionless mesh time period, $\omega P_n/V$
τ_d, τ_e	dimensionless times for start of disengagement cam and end of engagement cam ($S_d\tau_c/P_n, S_e\tau_c/P_n$)
τ_0	dimensionless time (ωt_0) into mesh period where y_0 and y'_0 occur
τ_{0d}, τ_{0e}	dimensionless times for end of disengagement cam (tooth tip) and start of engagement cam ($S_{0d}\tau_e/P_n, S_{0e}\tau_c/P_n$)
λ	$\sqrt{m - \xi^2}$
ξ	viscous critical damping ratio for gears ($d/2 \sqrt{k_0 M}$)
Φ_j	function describing tooth-pair contact (1 or 0)
ϕ_p	pressure angle at pitch radius, rad
ψ_1, ψ_2	dynamic angular motion of gears 1 and 2, rad
χ_j	function describing tooth cam contact (1 or 0)
Ω_1, Ω_2	angular rotational speeds of gears 1 and 2, rad/sec
ω	natural angular frequency of mesh system assuming single tooth-pair stiffness ($\sqrt{k_0/M}$), rad/sec
∇	dimensionless time step (τ/i), where $i = 100$

Theoretical Analysis

The dynamic model for the HCRG system was based on that developed by Richardson and Howland (refs. 2 to 4) but expanded to cover any contact ratios up to four rather than less than two. Similar system dynamic model approaches have been used more recently by other researchers for LCRG (see e. g., refs. 7 and 8). The theoretical model assumes that the two gears act as a rigid inertia and that the teeth act as a variable spring of a dynamic system excited by the nonlinear meshing action and stiffnesses of the gear teeth (see fig. 1).

For simplicity, the real HCRG system of figure 1 was converted into the equivalent rectilinear system of figure 2. The effects of contact ratio, tooth-profile modifications, and tooth errors can be introduced by modifying the size and shape of the cam exterior, which represents the nonlinear meshing action of the teeth.

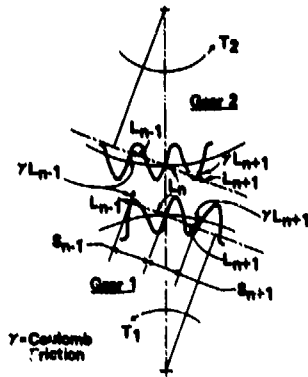


Figure 1. - Free body diagram of mesh for HCRG.

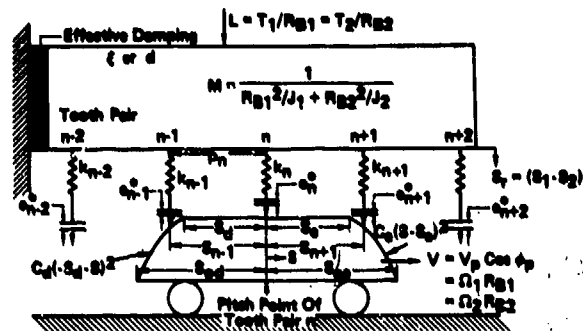


Figure 2. - Dynamic load model for HCRG.

In the earlier analyses of references (refs. 2 and 5) the tooth-pair compliance was assumed constant throughout the mesh; however, because the tooth-pair compliance varies appreciably during the mesh (as shown in figs. 3 and 4), it was decided to include this effect. As these figures show, the variation of tooth-pair compliance with position along the line of action is defined quite adequately by the following five-term power series:

$$\bar{C}/\bar{C}_0 = [1 + A(S/S_0) + B(S/S_0)^2 + C(S/S_0)^3 + D(S/S_0)^4] \quad (1)$$

If the two gears have the same diameter, the tooth-pair compliance is symmetrical about the pitch line, so that $A = C = 0$; otherwise all four coefficients are needed to fit the calculated tooth-pair compliance variation (ref. 9; see fig. 3).

The tooth-profile modification used to ease the tooth loading during engagement and disengagement of the tooth pairs is represented by their respective cams in figure 2. To permit a closed form solution of the differential equation of motion of the gear system, the tooth-profile modifications were represented by cams having the form $C_e(S - S_e)^x$ and $C_d(-S_d - S)^x$, respectively, where x is an integer. Tooth profile modifications represented by noninteger power cams, like $3/2$, or complicated forms would be approximated by a series with integer exponents; however, this extra complexity was not required, because typical gear tooth-profile modifications were found to be represented quite well by using simply a cam form with $x = 2$ (fig. 5).

Following the derivation given in reference 2, the differential equation of relative motion between the two gears $S_r = (S_1 - S_2)$ is given by the expression

$$M\ddot{S}_r + d\dot{S}_r + \sum_{j=1}^m L_j = L_0 \quad (2)$$

where L_j is the individual tooth loads, L_0 is the applied load consistent with the torque on the gears, and m is the number of teeth in contact. For this HCRG study it is assumed that m can have integer

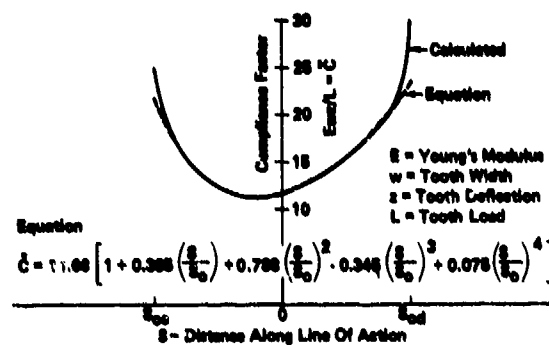


Figure 3. - Approximation of compliance of gear tooth pairs for 5.32:1 gear ratio.

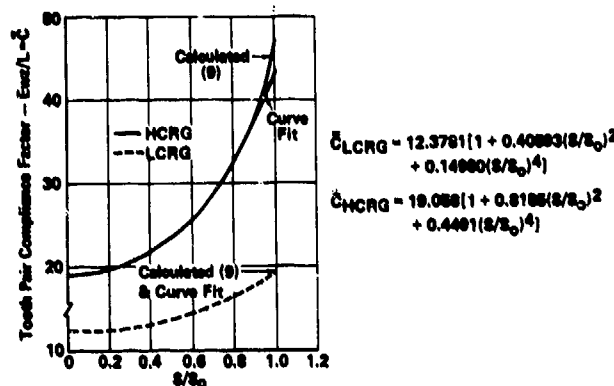


Figure 4. - Approximation of compliance of 8-pitch, 32-tooth LCRG and HCRG tooth pairs for 1:1 gear ratio.

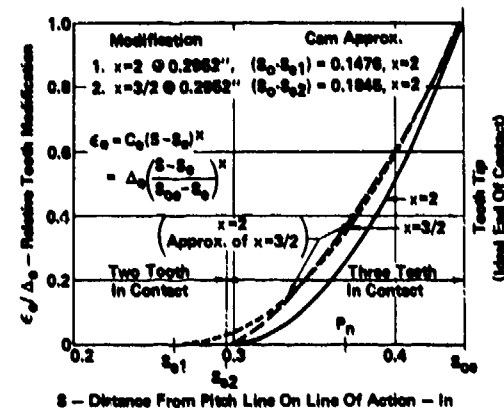


Figure 5. - Approximation of tooth profile modifications for LCRG.

values from 0 to 4. The definition of the parameters and the relationships between the terms of the rectilinear and rotating systems are given in the nomenclature. To simplify the analysis, the sliding tooth friction is assumed negligible, the input and output torques are assumed constant and equal to their average values, and the viscous damping force is assumed proportional to the relative velocity of the two gears, for example, $d(S_1 - S_2) = dS_r$. Equation (2) is put into the following dimensionless form

$$y'' + 2\xi y' + \sum_{j=0}^n L_j/L_0 = 1 \quad (3)$$

where $y = S_r/\delta$ and the time parameter, $\tau = \omega t$, is dimensionless so that $y' = dy/d\tau = dy/\omega dt$.

The relative magnitude of the individual tooth loads, L_j/L_0 , is a function of the tooth stiffness and tooth-profile modification for the particular contact position, S_j , the relative gear motion, S_r or y , and the tooth errors, $e_j\delta$. The engagement and disengagement tooth-profile modifications, ϵ_e and ϵ_d , are the same for each tooth pair and are assumed, as discussed above, to be a square function of the distance along the line of action, for example,

$$\epsilon_{je} = C_e(S_j - S_e)^2 \text{ and } \epsilon_{jd} = C_d(S_j - S_d)^2 \quad (4)$$

Thus, the total or combined tooth-pair relief at the start and end of an ideal mesh are

$$\Delta_e = C_e(S_{e0} - S_e)^2 \text{ and } \Delta_d = C_d(S_{d0} - S_d)^2 \quad (5)$$

and may be split as desired between the addendum and dedendum tooth modifications of the first and second gears, respectively, or vice versa. The magnitude of the individual tooth load is then given by the expression

$$L_i/L_0 = [y + e_i - \bar{\chi}_i^2 \beta_{di} q_i / \delta] \eta_i \Phi_i \quad (6)$$

where $\bar{\chi}_i^2$ has a value of 1 or 0, depending on whether the tooth contact is on the profile modification cam or not, and Φ_i has a value of 1 or 0, depending on whether the tooth pair is in contact or not.

Substituting equation (6) into equation (3) and remembering that m is limited to four teeth, which corresponds to a practical contact limit of four, we find

$$y'' + 2\xi y' = 1 - \sum_{j=n-1}^n \Phi_j \eta_j [y + e - \bar{\chi}_j^2 \beta_{dj} q_j] - \sum_{j=n+1}^{n+3} \Phi_j \eta_j [y + e - \bar{\chi}_j^2 \beta_{dj} q_j] \quad (7)$$

where

$$\begin{aligned} \chi_{n-1}^2 &= (\tau - \tau_d + \tau_e)_{n-1}^2 = (\omega/V)^2 (S - S_d + P_n)_{n-1}^2 \text{ or } 0 \\ \chi_n^2 &= (\tau - \tau_d)_n^2 = (\omega/V)^2 (S - S_d)_n^2 \text{ or } 0 \\ \chi_{n+1}^2 &= (-\tau - \tau_e + \tau_e)_{n+1}^2 = (\omega/V)^2 (-S - S_e + P_n)_{n+1}^2 \text{ or } 0 \\ \chi_{n+2}^2 &= (-\tau - \tau_e + 2\tau_e)_{n+2}^2 = (\omega/V)^2 (-S - S_e + 2P_n)_{n+2}^2 \text{ or } 0 \end{aligned}$$

If the χ_j terms are negative quantities, the teeth are not on the cam or tooth modification, and the corresponding χ_j 's are made equal to zero. If the bracketed term is positive, the tooth pair is in contact and Φ_j is made equal to 1; otherwise the tooth pair is not in contact and Φ_j is made equal to zero. Equation (7) is a nonlinear equation because the tooth-pair stiffness ratios η_j are a function of y .

The above differential equation can be put in the form

$$y'' + 2\xi y' + \sum_j \Phi_j \eta_j y = 1 + a + b\tau + c\tau^2 \quad (8)$$

This equation has an instantaneous complimentary solution of

$$y_e = e^{-\xi\tau} (\bar{A} \cos \lambda\tau + \bar{B} \sin \lambda\tau) \quad (9)$$

where $\bar{A} = y_0$ and $\bar{B} = y'_0/\lambda + y_0\xi/\lambda$, the initial boundary conditions. The instantaneous particular solution of equation (8), which represents the excitation effects, is

$$y_p = \frac{c}{m} \tau^2 + \left(\frac{b}{m} - \frac{4c\xi}{m^2} \right) \tau + \left(\frac{1+a}{m^2} - \frac{2b\xi+2c}{m^2} + \frac{8\xi^2 y_0}{m^2} \right) \quad (10)$$

where a , b , and c are the following functions of $\eta_j \Phi_j$ and $\bar{\chi}_j^2$

$$-a = \sum_{j=n-1}^n \Phi_j \eta_j [e_j - \bar{\chi}_j^2 \beta_{dj} q_j] + \sum_{j=n+1}^{n+3} \Phi_j \eta_j [e_j - \bar{\chi}_j^2 \beta_{dj} q_j]$$

$$-b/2 = \sum_{j=n-1}^n \Phi_j \eta_j \bar{x}_j^2 \beta_d^2 q_j + \sum_{j=n+1}^{n+1} \Phi_j \eta_j \bar{x}_j^2 \beta_d^2 q_j$$

$$c = \sum_{j=n-1}^n \Phi_j \eta_j \bar{x}_j^2 \beta_d^2 + \sum_{j=n+1}^{n+1} \Phi_j \eta_j \bar{x}_j^2 \beta_d^2$$

and

$$q_{n-1} = (\tau_d - \tau_e); q_n = \tau_d; q_{n+1} = -(\tau_e - \tau_e); q_{n+2} = -(\tau_e - 2\tau_e)$$

Adding the complementary and particular solutions, the instantaneous dimensionless relative gear motion, $y = y_c + y_p$, is

$$y = e^{-\lambda \tau} (\bar{A} \cos \lambda \tau + \bar{B} \sin \lambda \tau) + \frac{c}{m} \tau^2 + \left(\frac{b}{m} - \frac{4c\xi}{m^2} \right) \tau + \left(\frac{1+a}{m} - \frac{2b\xi+2c}{m^2} + \frac{8\xi^2 c_0}{m^3} \right) \quad (11)$$

where

$$\bar{A} = y_0 - \frac{1+a}{m} - \left(\frac{b}{m} - \frac{4c\xi}{m^2} \right) \left(\tau_0 - \frac{2\xi}{m} \right) - \frac{c}{m} \left(\tau_0^2 - \frac{2}{m} \right)$$

and

$$\bar{B} = \frac{1}{\lambda} [y_0' + \xi \bar{A} - \left(\frac{b}{m} - \frac{4c\xi}{m^2} \right) - \frac{2c}{m} \tau_0]$$

Here, τ_0 is the total dimensionless time into the mesh cycle at which the boundary conditions y_0 and y_0' are defined. Also τ is the dimensionless time measured from this instant of time, so that the total dimensionless time into mesh is $\tau = \tau_0 + \tau$. If there are no tooth pairs in contact, for example, $\bar{m} = \sum_j^m \Phi_j \eta_j = 0$, the solution of equation (8) is

$$y = y_0 + [\tau - (1/2\xi - y_0')(1 - e^{-2\xi\tau})]/2\xi \quad (12)$$

Because of the variable tooth-pair stiffnesses during the mesh, differential equation (8) is nonlinear so that the above solutions apply for an instant in time; for example, the solutions continually change during the repetitive mesh period P_n or τ_c . Also, because the number of active tooth pairs and the excitations vary throughout the mesh cycle, the closed form solutions (eqs. (11) and (12)) are piecewise continuous. Thus, to solve this piecewise, nonlinear problem, it was decided to use a time history solution and step through the mesh cycle in small dimensionless time increments of $\nabla = \tau_c/i$, where i was made 100. During each time increment the tooth stiffnesses were assumed to be the appropriate constant values given by η_j . In this way the above closed form solutions given by equations (11) and (12) can be used for determining the relative dynamic gear motion y and velocity y' by replacing τ by ∇ , thereby circumventing the progressive error that can develop by numerically integrating the differential equation (see refs. 2 to 5). To obtain the appropriate values of η_j , it is necessary to define the position of each tooth pair along the line of action, S_j/S_0 , and apply equation (1), where $\eta_j = k_j/k_0 = \bar{C}_0/\bar{C}_j$.

To step the above closed form equations for the dynamic gear motion through one mesh of " i " increments, one must know the initial conditions y_0 and y_0' at $\tau=0$. These can only be obtained by iteration on the basis that, after the passage of one gear mesh, P_n or gear-mesh time, τ_c , the gear

displacement and velocity must be the same as that for the starting condition, if no gear errors are involved. Thus, the procedure is to assume initial values of y_{01} and y'_{01} , calculate sequentially the gear motion for the i time steps in the mesh, and obtain the values of y_{i1} and y'_{i1} at the end of the mesh cycle. Usually, a good first approximation for the initial assumed values of y_{01} and y'_{01} are the reciprocal of the theoretical contact ratio and zero, respectively. In order to assure convergence, the second initial values for the iteration are made the average of the assumed beginning and calculated ending values from the first iteration, that is,

$$y_{02} = (y_{01} + y_{i1})/2 \text{ and } y'_{02} = (y'_{01} + y'_{i1})/2 \quad (13)$$

This process is repeated until the difference between the initial and final values are within a small prescribed amount. An iteration difference of 0.002 for both dimensional quantities has been found to give satisfactory results.

Once the relative gear motion, y , has been determined for each of the i time steps through the repetitive mesh, P_n , the relative tooth loads, L_j/L_0 , can be obtained by using the Φ_j terms given in equation (7), including the appropriate value of Φ_j , that is, 1 or 0. This iterative procedure applies only for cases for no tooth errors; for if there are tooth errors, the motion at the end of a given mesh will not be the same, in general, as that at the beginning of the mesh. The solution for the case with tooth errors is done in two steps: First, the iterative solution is obtained for the zero error case as described above. Then, starting with the known initial conditions of y_0 and y'_0 the analysis is run on a consecutive mesh basis, introducing the specified error on any tooth or teeth desired.

The above dynamic load analysis for HCRG with arbitrary contact ratios between 1 and 4 was programmed for the IBM 370-168 using Fortran. The program has three operating modes:

The basic mode option is for HCRG without tooth spacing errors. The output in this case is a listing of the convergence process, if desired, for obtaining y_0 and y'_0 and the converged results with plots of the results, if requested.

The basic/error mode option first performs the the basic mode option to obtain the converged initial conditions and then runs eight tooth passages using the specified tooth spacing errors. The output consists of that for the basic mode option plus the results for the eight tooth passages with plots, if requested.

The error mode option requires initial converged input gear displacement and velocity from the basic mode option and then proceeds to calculate the dynamic tooth results for eight tooth passages using the specified tooth spacing errors. In order to reduce the printout of 100 time increments per mesh with plots, if desired, all three modes of operation have the option of only listing the maximum for each gear in the mesh. The cpu time to run each constant speed and torque case varies with the operating mode, but usually is less than 1 second.

Because the relationship of tooth root stressing per load varies significantly with load position on the tooth, the maximum tooth root stressing and tooth loading usually occur at different times during the mesh cycle. It appeared desirable, therefore, to include a postprocessor in the computer program to convert the individual tooth loads to tooth root stresses. Since the tooth forms for HCRG deviate appreciably from the conventional tooth forms, it was decided to use an improved and simplified version of the Heywood analysis for tooth stressing (ref. 10) because it includes most of the factors that affect stressing. A subsequent paper will give the details of this modified version of the Heywood gear tooth stress analysis. Figure 6 presents a comparison of the stress per load versus load position for both a HCRG and LCRG using various conventional methods of stress analysis and the modified Heywood analysis. The modified Heywood method gives results that agree well with those based on the Heywood and Kelly methods, which, in turn, have been found to correlate well with test results. The results in figure 6 also show that the relationship between the Heywood analyses and the usual Lewis or AGMA analyses differ significantly for the low- and high-contact-ratio gears, being about 20 to 28 percent higher for the LCRG and about 10 to 18 percent higher for the HCRG, respectively. These differences support the need for an accurate stress sensitivity analysis for general involute spur gear teeth, which the modified Heywood analysis is believed to give.

In the computer program, provisions had to be made for the stress analysis of three different gear tooth configurations (fig. 7). One version assumes no undercutting in the fillet region of the

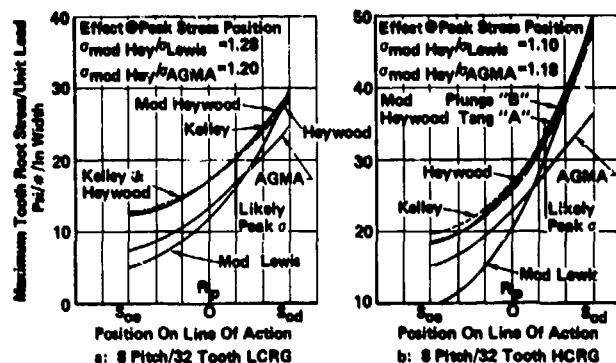


Figure 6. - Comparison of gear tooth stress sensitivities for different analysis methods.

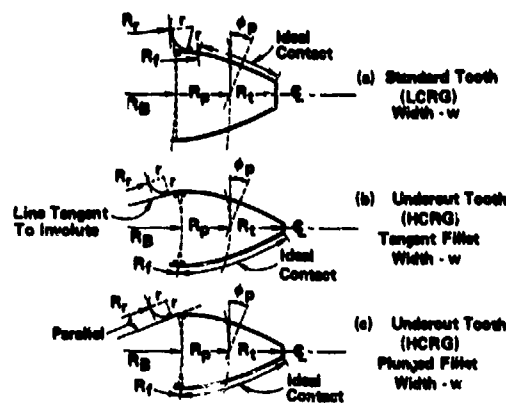


Figure 7. - Gear tooth geometries.

tooth, which is usually the case for conventional LCRG. The two other versions were developed to cover undercut teeth, one in which the undercut is made tangent to the involute tooth profile and the other in which the undercut is made by plunging the fillet cutter parallel to the fillet radius centerline (figs. 7(b) and (c)). The computer program determines whether the tooth requires undercutting and uses the proper tooth geometry in the stress sensitivity calculation. The tangent undercut tooth geometry is used unless the plunged undercut tooth geometry is specified, because it results in slightly lower stressing.

For completeness the postprocessor in the program is being expanded to calculate the variation of PV and contact stress as well as tooth fillet stress with contact position. Presently the computer program only gives the results for one of the gears, so that two runs are required; therefore, the program is also being modified to give results for both the gears at the same time.

Application of Analysis

The above analysis and computer program was used to investigate the dynamic tooth loads and stressing of a LCRG and initially four HCRG for a speed ratio of one. The LCRG had a gear-mesh contact ratio of 1.566, and the HCRG had a gear-mesh contact ratio of 2.40. All the gears had a 4-in. pitch diameter and a 3/8-in. width. The design torque load, T , was 2400 in-lb.

The maximum combined gear tooth-pair profile modification or relief, Δ_T , was based on the statistical sum of the tooth errors, Δ_e , and the maximum static deflection of the teeth, Δ_d , as given by the equation

$$\Delta_T = \Delta_e + \Delta_d = \left[\frac{fT}{R_p \sum_i k_j} + \sqrt{\sum_{\mu} e_{\mu}^2} \right] \quad (14)$$

In equation (14) $\sum_j k_j$ is the sum of the engaged tooth stiffnesses at a static gear contact position just before the number of teeth in contact increases by one, and the e_{μ} 's are the various kinds of tooth errors. For this study the load factor, f , was assumed equal to 3/2. The tooth errors were assumed to be profile, ± 0.0001 in.; spacing, ± 0.0003 in.; and lead, ± 0.0001 in., which results in a statistical total of $\sqrt{\sum_{\mu} e_{\mu}^2} = 0.00033$ in. The gear tooth stiffnesses (ref. 9) versus load position for the 8-pitch, 32-tooth LCRG and the 8-pitch, 32-tooth HCRG are given in figure 4. The pertinent parameters for the LCRG and initial four HCRG's are given in table 1. The length of tooth-profile modification is presented in terms S_d/S_{0d} and S_e/S_{0e} , which can vary from 0 to 1 depending on where the profile modification starts, being zero if it starts at the pitch radius and 1 if it starts at the tip or root. The "long" tooth-profile modification for the HCRG simulated the 3/2 power profile modification (fig. 5); the "short" tooth-profile modification corresponded to the standard practice of starting the modification where the theoretical number of teeth in contact changes by one, that is, 1 to 2 or 2 to 3, for the LCRG and HCRG, respectively.

Table 1 Characteristics of LCRG and HCRG designs; $R_{p1} = R_{p2} = 2.00''$ and $w = 0.375''$

Parameter	LCRG		HCRG-1		HCRG-2	
	Standard	Standard-Short	Long · X-3/2	Standard	Long · X-3/2	
Nominal Pitch	8	8	8	10	10	
Teeth, N	32	32	32	40	40	
Contact Ratio	1.866	2.40	2.40	2.40	2.40	
Pressure Angle, ϕ_p	22.5°	20°	20°	20°	20°	
Tooth Thickness, t_p	0.1933"	0.1933"	0.1933"	0.1941"	0.1941"	
Normal Pitch, P_n	0.3620"	0.3698"	0.3698"	0.3952"	0.3952"	
Base Radius, R_b	1.8478"	1.8784"	1.8784"	1.8784"	1.8784"	
Tip Radius, R_t	2.1258"	2.1814"	2.1814"	2.1472"	2.1472"	
Fillet Radius, r	0.0095"	0.0038"	0.0038"	0.0067"	0.0067"	
Radius to Fillet, R_f	1.8417"	1.7987"	1.7987"	1.8342"	1.8342"	
Rad. to Fillet Cont. R_f	1.8884"	1.8848"	1.8848"	1.8888"	1.8888"	
Length Mod., $d_s = d_g$	0.2064"	0.14778"	0.16468"	0.11818"	0.14798"	
Mag. Mod., $\Delta_s = \Delta_g$	0.00237"	0.00216"	0.00216"	0.0029"	0.0029"	
Con. Coef., $C_s = C_g$	0.00628	0.00803	0.00834	0.01435	0.00188	
Start Con., $S_s = S_g$	0.0787"	0.29614"	0.29624"	0.23628"	0.26674"	
End Con., $S_{se} = S_{ge}$	0.2841"	0.4429"	0.4429"	0.3643"	0.3643"	

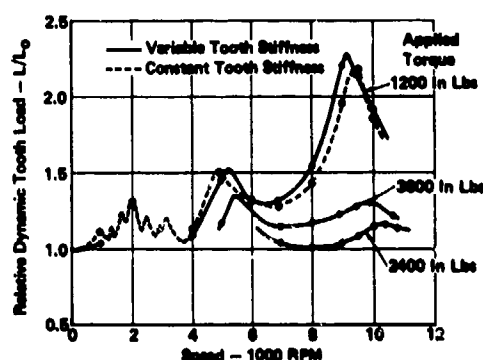


Figure 9. - Effect of speed on dynamic gear tooth load for 8-pitch, 32-tooth LCRG. $M = 0.001$ lb sec²/in.; $\xi = 0.10$.

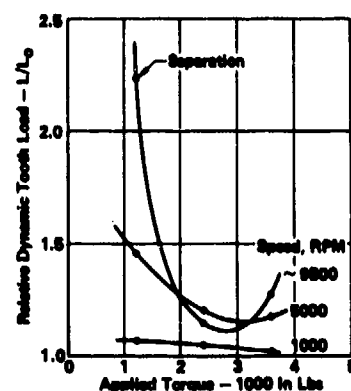


Figure 8. - Effect of applied torque on dynamic gear tooth load for 8-pitch, 32-tooth LCRG. $M = 0.001$ lb sec²/in.; $\xi = 0.10$.

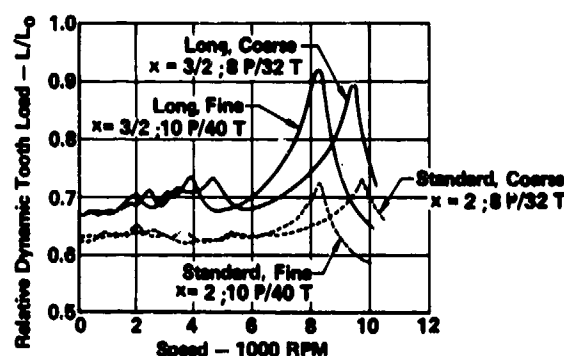


Figure 10. - Effect of speed on dynamic gear tooth load for coarse and fine HCRG. $M = 0.001$ lb-sec²/in.; $\xi = 0.10$; $T = 2400$ in-lb.

The loading and stressing of a gear tooth can vary appreciably with speed, damping, load, and inertia because of the dynamic action. It is impossible, therefore, to compare gear designs unless these operating parameters are varied over their realistic ranges. In general, for a given tooth design the system inertia shifts the system natural frequency and, thus, the subharmonic response peaks of the system, and the amount of damping determines the magnitudes at these response peaks. Also, as the applied load increases, the dynamic load and root stressing per applied load usually decrease until the tooth-profile modification becomes inadequate for the higher loads (figs. 8 to 10). At low loads and sometimes at the system response peaks, complete separation of the gear teeth can occur for low system inertias and damping.

The variation of dynamic tooth loadings with speed for LCRG and HCRG are given in figures 9 and 10 for low system inertias. These figures show that the primary resonance response occurs around 9000 rpm and varies significantly with applied load and tooth modification. Figure 9 also shows the effects of using a constant tooth-pair stiffness based on the pitch radius (refs. 2 to 5) compared with the realistic variable tooth stiffness. Apparent is the slight increase in natural frequency and slightly lower response using the constant stiffness instead of variable stiffness. Also, because of the variable tooth stiffness, the subharmonic critical speeds are not integer reciprocals of the primary critical speed, as they are for a constant tooth stiffness. Apparent in figures 9 and 10 is the significant shift in natural frequency of the system with the magnitude of the applied load and tooth modification due to the nonlinear effects of the variable tooth stiffness. Figure 10 shows that for the HCRG the short (square power) tooth-profile modification results in appreciably lower dynamic tooth loads than the long (3/2 power) tooth-profile modification. This figure also shows

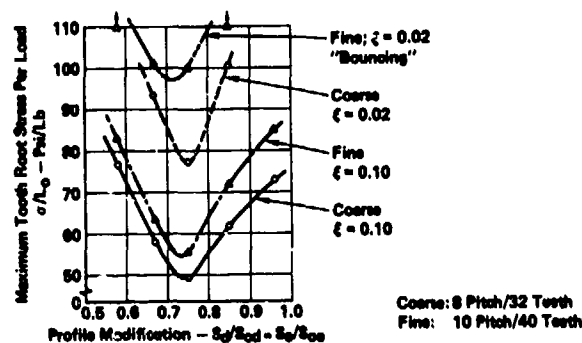


Figure 11. - Effect of profile modification length on dynamic tooth stressing of coarse and fine HCRG. $M = 0.001 \text{ lb-sec}^2/\text{in.}$; $N = 9500 \text{ rpm}$; $T = 2400 \text{ in-lb.}$

Table 2 Comparison of tooth root stressing of LCRG and HCRG for primary response at $\sim 9500 \text{ rpm}$; $M = 0.001 \text{ lb s}^2/\text{in.}$

Maximum Tooth Root Stress	Parameter	Tooth Error	LCRG 8 Pitch/32 Teeth	HCRG 8 Pitch/32 Teeth	HCRG LCRG
—	Contact Ratio, CR	—	1.586	2.40	—
—	Pressure Angle, ϕ_p	—	22.5°	20.0°	—
—	Profile Mod. Length, S_d/S_{0d}	—	0.28	0.76	—
σ_0	$T = 2400 \text{ in-lb.}; \xi = 0.10$	None	58.8 Ksi	56.2 Ksi	0.94
	$T = 2400 \text{ in-lb.}; \xi = 0.02$		98.7 Ksi	88.8 Ksi	0.90
	$T = 3600 \text{ in-lb.}; \xi = 0.02$		159.7 Ksi	152.2 Ksi*	0.95
σ_0/σ_0	$T = 2400 \text{ in-lb.}; \xi = 0.10$	0.00042"	~ 1.07	~ 1.11	1.04
	$T = 2400 \text{ in-lb.}; \xi = 0.02$		~ 1.00	~ 1.07	1.07

* For $S_d/S_{0d} = 0.67$

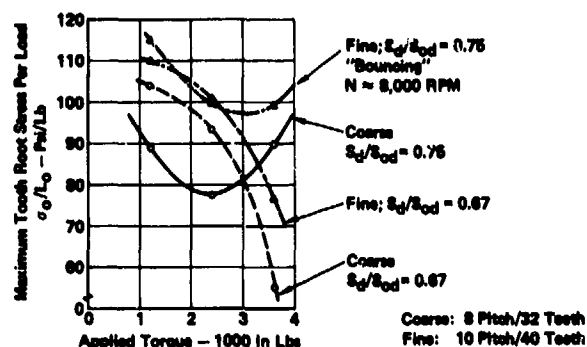


Figure 12. - Effect of applied torque on dynamic tooth stressing of HCRG. $M = 0.001 \text{ lb-sec}^2/\text{in.}$; $\xi = 0.02$; $N = 9500 \text{ rpm}$.

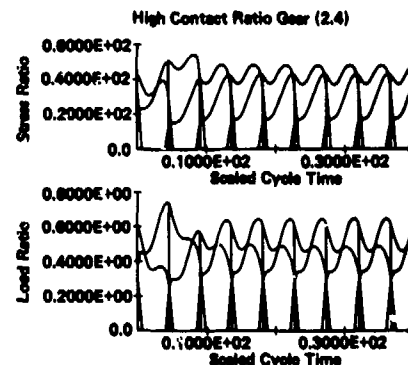


Figure 13. - Effect of tooth errors on dynamic tooth loads and stressing of HCRG. $M = 0.001 \text{ lb-sec}^2/\text{in.}$; $u = 0.02$; $N = 10,000 \text{ rpm}$.

that the coarser, 8-pitch design is probably stronger than the finer 10 pitch design because the dynamic loads are slightly lower and its teeth have lower stress sensitivity.

Because the length of the tooth-profile modification appeared to affect significantly the dynamic gear loads, its effect was investigated further for both the coarse- and fine-tooth HCRG designs. The evaluation was made at the primary critical speed of about 9500 rpm by analyzing designs with $S_e/S_{0e} = S_d/S_{0d} = 0.58, 0.67, 0.75, 0.85$, and 0.96 . The effects of applied load and damping were also included in the study. The effect of the start of the tooth-profile modification on the maximum tooth root stress per applied load is given in figure 11 for low and high dampings of $\xi = 0.02$ and 0.10 , respectively, and for the design torque load of 2400 in-lb. These results show that the optimum tooth-profile modification for both HCRG designs occurs at a $S_e/S_{0e} = S_d/S_{0d} = 0.75$ rather than the usual value of 0.67 . Thus, the optimum length of tooth-profile modification for HCRG is about 75 percent of that based on the change in the number of teeth in contact. These results show that system damping has a large effect on the tooth root stressing. The results for the fine 10-pitch HCRG with low damping deviates from the other results because of gear separation or bouncing. For a damping of $\xi = 0.10$ figure 11 shows that the tooth root stressing of the coarse 8-pitch HCRG is 10 percent lower than for the fine 10-pitch HCRG. The effect of applied load on the maximum tooth stressing for the 8- and 10-pitch HCRG at their primary response is given in figure 12 for low damping of $\xi = 0.02$. It is apparent that the length of the profile modification should be increased for higher applied loads, $S_d/S_{0d} = 0.75$ being optimum for 2400 in-lb. of torque whereas $S_d/S_{0d} = 0.67$ is optimum for 3600 in-lb. of torque. A similar study of the 8-pitch LCRG showed that its length of profile modification was optimum for the design torque of 2400 in-lb. , thus substantiating that HCRG should have shorter profile modifications than LCRG.

Comparison of the maximum root stressing of LCRG and HCRG at their primary response peaks are given in table 2 for various applied loads, damping, and tooth errors and assuming the optimum profile modification for each gear design. For no tooth errors, the HCRG tooth root stressing is 6 to 13 percent lower than that for the corresponding LCRG, the degree of improvement depending on the applied load and damping. However, the dynamic analysis shows the HCRG is about 5 percent more sensitive to typical tooth errors than the LCRG. Thus, unless tighter manufacturing tolerances are used to minimize the HCRG tooth errors, its tooth root stressing will be only a few percent less than that for LCRG. Figure 13 shows a typical tooth-load and root-stress history computer plot for a HCRG with tooth error. It shows that the aberrations are damped out in about four mesh cycles, even for a low damping of $\xi = 0.02$. These results illustrate very clearly that the stress and load peak at different times during the mesh cycle and are influenced quite differently by tooth errors.

Conclusions

An analysis and computer program has been developed for calculating the dynamic gear tooth loading and root stressing for HCRG as well as LCRG. The analysis includes the effects of the variable tooth stiffness during the mesh, tooth-profile modification, and gear errors. The calculation of the tooth root stressing caused by the dynamic gear tooth loads is based on a modified Heywood gear tooth stress analysis, which appears more universally applicable to both LCRG and HCRG. The computer program is presently being expanded to calculate the tooth contact stressing and PV values.

Sample application of the gear program to equivalent LCRG (1.566 contact ratio) and HCRG (2.40 contact ratio) revealed the following:

1. The operating conditions and dynamic characteristics of the gear system can affect the gear tooth loading and root stressing, and therefore, life significantly.
2. The length of the profile modification affects the tooth loading and root stressing significantly, the amount depending on the applied load, speed, and contact ratio.
3. The effect of variable tooth stiffness is small, shifting and increasing the response peaks slightly from those for constant tooth stiffness.
4. The stress sensitivity analysis methods used for gear teeth can influence appreciably the dynamic stress comparison of LCRG and HCRG.
5. The tooth loading and root stressing for HCRG are affected more adversely by gear errors than for LCRG.
6. The errorless, coarse, 8-pitch HCRG has a root tooth stress about 10 percent lower than the corresponding fine, 10-pitch HCRG at their primary response rotational speeds.
7. The errorless 8-pitch HCRG has a root tooth stress about 6 to 12 percent lower than the corresponding 8-pitch LCRG at their primary response rotational speeds.

These limited results from applying the gear analysis to some sample gears show the need for a systematic parametric analysis of not only HCRG but also LCRG. Such a parametric analysis is necessary to understand fully the effects of the various operating variables and design characteristics, so that optimum spur gear designs can be realized and meaningful gear fatigue tests can be conducted.

Acknowledgment

We wish to thank Hamilton Standard, Division of United Technologies Corp. for permission to publish this work. We also express our appreciation to Mr. H. Frint of Sikorsky Aircraft, Mr. Malcolm Hamilton of Hamilton Standard, and Mr. Dennis Townsend of NASA Lewis for their helpful comments and support of this effort. This work was performed under NASA Contract NAS3-17859 for the NASA Lewis Research Center, Cleveland, Ohio.

References

1. Frint, H. K.; and Paul, W. F.P.: Design and Evaluation of High Contact Ratio Gearing, Design Phase II. Sikorsky Aircraft Report; July 16, 1974.

2. Richardson, H. H.: Static and Dynamic Load, Stresses and Deflection Cycles in Spur Gear Systems. Dynamic and Control Laboratory Research Memorandum 7454-1, M.I.T., June 30, 1958.
3. Howland, J. S.: An Investigation of Dynamic Loads in Spur-Gear Teeth. Master's thesis, M.I.T. Report, Feb. 1972.
4. Richardson, H. H.: Static and Dynamic Load, Stresses, and Deflection Cycles in Spur-Gear Systems. Sc.D thesis, M.I.T. Report, 1958.
5. Black, J. I.: Summary of Program for the Determination of Dynamic Loads in High Speed Gears. Internal Hamilton Standard Report, May 8, 1961.
6. Metzger, W. W.: Dynamic Loads in the Ryder Gear Test Specimen. Internal Hamilton Standard Report, Sept. 13, 1968.
7. Bollinger, J. G.: An Investigation of New Linear Geared Torsional Systems Using Analog Techniques. Ph. D. thesis, University of Wisconsin, 1961.
8. Ichinoru, K.; and Hirano, F.: Dynamic Behavior of Heavy-Loaded Spur Gears. ASME Preprint 73-PTG-14, 1972.
9. Weber, C.: The Deformations of Loaded Gears and the Effect on Their Load-Carrying Capacity. Sponsored Research (Germany), British Department of Scientific and Industrial Research, Report No. 3 (1949).
10. Heywood, R. B.: Designing by Photoelasticity. Chapman and Hall, Ltd., 1952.

A Computer Code for Performance of Spur Gears*

K. L. Wang†, and H. S. Cheng‡

In spur gears both performance and failure predictions are known to be strongly dependent on the variation of load, lubricant film thickness, and total flash or contact temperature of the contacting point as it moves along the contact path. The need of an accurate tool for predicting these variables has prompted the development of a computer code (refs. 1 and 2) based on recent findings in EHL and on finite-element methods. This paper gives a brief summary of the analyses and some typical results to illustrate effects of gear geometry, velocity, load, lubricant viscosity, and surface convective heat transfer coefficient on the performance of spur gears.

Symbols

Values are given in both SI and U.S. Customary Units. The calculations were made in U.S. Customary Units.

C_o	damping coefficient per unit face width, N·s/m ² , (lb·s/in ²)
e_a, e_b	profile error for meshing set a, b , m (in.)
h_{\min}	minimum film thickness, m (in.)
I_1, I_2	polar mass moment of inertia of pinion and gear, kg·m ² (slug·in ²)
K	stiffness of a meshing pair, N/m ² (lb/in ²)
K_a, K_b	K for meshing set a, b , N/m ² (lb/in ²)
M	effective mass = $m_1 m_2 / (m_1 + m_2)$, kg (slug)
m_1, m_2	mass of pinion and gear, kg (slug)
N_T	number of teeth
P	tooth load, N (lb)
p	pressure in the Hertzian contact, Pa (psi)
P_d	dynamic load, N (lb)
P_F	load factor = $P_{d, \max} / P_s$
P_s	steady tooth load, N (lb)
R_1, R_2	pitch radius of pinion and gear, m (in.)
R_{b1}, R_{b2}	base radius of pinion and gear, m (in.)
R_{o1}, R_{o2}	outside radius of pinion and gear, m (in.)
T_{B1}, T_{B2}	bulk surface temperature of pinion and gear, °C (°F)
T_{F1}, T_{F2}	total flash temperature, °C (°F)
T_o	ambient temperature, °C (°F)
V	pitch-line velocity, m/s (in/s)
X_R	$\theta_1 R_{B1} - \theta_2 R_{B2}$, m (in.)
α	pressure viscosity coefficient, m ² /N (in ² /lb)
β	temperature viscosity coefficient, K (°R)
θ_1, θ_2	angular displacement of pinion and gear, rad
μ	lubricant viscosity, cP (lb·s/in ²)
μ_o	ambient viscosity, cP (lb·s/in ²)
ξ_c	nondimensional damping = $C_o / (2 KM)$
φ	pressure angle, rad

*Work performed under NASA Contract NGR-14-007-084.

†International Harvester Co., Hinsdale, Illinois.

‡Northwestern University, Evanston, Illinois.

Summary of Analyses

The major quantities to be calculated include the dynamic load, P_d , the minimum film thickness, h_{\min} , the bulk surface temperature of surfaces 1 and 2 (T_{B1} and T_{B2}), and the total flash temperature in the contact for surfaces 1 and 2 (T_{F1} and T_{F2}). Analysis of each of these variables is summarized in the following sections.

Dynamic Load

The effects of load sharing between a pair of teeth, nonuniform bending stiffness, and tooth profile error on the variations of tooth load along the contact path are determined by using the dynamic model shown in figure 1. In this figure the bending stiffness is a function of the load position along the tooth profile and is determined by a finite-element code. Figure 2 shows the nondimensional reciprocal of the stiffness for different tooth loading positions is a function of number of teeth. Using the stiffness data, the following second-order differential equation can be solved numerically for the relative displacement along the contact path X_R .

$$M \frac{d^2 X_R}{dt^2} + C_o \frac{dX_R}{dt} + K_a(X_R - e_a) + K_b(X_R - e_b) = P_s \quad (1)$$

Once X_R is solved, the dynamic load is simply

$$P_d = K_a(X_R - e_a) + K_b(X_R - e_b) \quad (2)$$

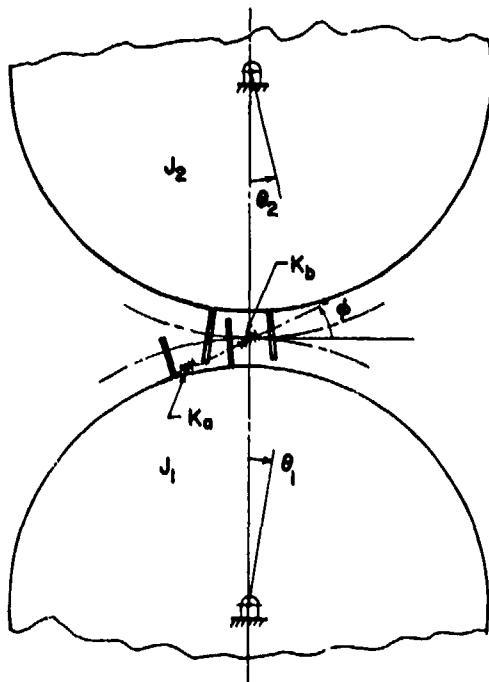


Figure 1. - Dynamic model of meshing gears.

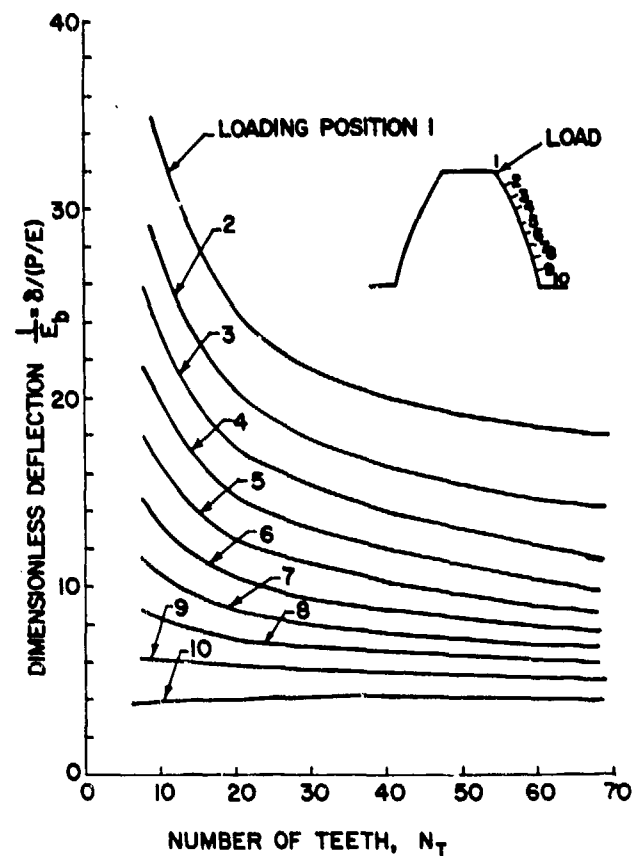


Figure 2. - Dimensionless deflection as function of gear teeth number and loading position.

Lubricant Film Thickness

The calculation of lubricant film thickness is based on a method introduced by Vichard (ref. 3), which includes the squeeze-film effect due to the change in entrainment velocity, local radius, and contact load along the contact path. The Vichard procedure gives rise to a single first-order differential equation in h with the coordinate along the contact path as the independent coordinate. This was solved by the Runge-Kutta procedure, and the detailed equation and solution procedure can be found in reference 1.

Flash Temperature

At a given contact point along the contact path, the flash temperature distribution on each of the two surfaces within the Hertzian region is solved by considering a heat-conduction analysis of the lubricant film separated by the contacting surfaces. Two major assumptions are used in the analysis. First, the heat generated by shearing of the lubricant is concentrated at the midplane of the lubricant film and is governed by the limiting shear-stress model introduced by Dyson (ref. 4). This leads to a triangular temperature profile with the maximum tip temperature occurring at the midfilm. Second, both surface temperature rises are governed by the Jaeger solution for a high Peclet number (ref. 5). These considerations give rise to three simultaneous equations which can be solved for the two flash surface temperatures and the midfilm shear stress. Details of these three equations are given in reference 1.

Bulk Surface Temperature

The bulk surface temperature is the steady-state temperature distribution along the tooth profile after many cycles of running. The distribution of the bulk temperature can be predicted by a steady-state conduction analysis for a heat flux along the contact side of the tooth facing equivalent to the total heat per mesh averaged over the entire cycle of revolution. Since this temperature computation must be repeated for every iteration, it is more economically handled by using the temperature influence coefficients, which are obtained independently using a finite-element code specially written for the spur gear geometry. The coefficient matrix is determined by solving the temperature profile with a unit heat flux at each point along the tooth profile.

Numerical Procedure

The dynamic load is practically unaffected by the film thickness or the surface temperature; it can be solved independently. The remaining three quantities are coupled and are solved by an iterative process. The overall computational scheme can be best described by a flow diagram shown in figure 3. This is used in constructing a computer program entitled "TELSGE" (Thermal Elastohydrodynamic Lubrication of Spur Gears). The function of each subroutine is described as follows:

(1) The scheme begins with subroutine INPU, which enters all input data including gear geometry, material properties, lubricant properties, and operating conditions such as speed, load, and ambient temperature.

(2) The program then executes subroutines PICK and INVGEN, which are used to obtain the matrix of influence coefficients for calculating the equilibrium surface temperature distribution along the contacting profile. This is achieved by interpolation of a stored data bank of influence coefficients.

(3) After INVGEN the program executes subroutine COGEN, which is used to generate the coordinates of a mesh of quadrilateral elements in a typical gear segment.

(4) Subroutine DYNALO is then executed, and it computes the dynamic load by integrating equation (1).

(5) The program then begins the iterative loop to solve for the flash temperature and the equilibrium surface temperature. Subroutine FILM is first executed, and it calculates the film thickness by integrating the transient film equation.

(6) The flash temperature on each contacting surface and the heat flux distribution are determined in subroutine FLASH by solving a system of three algebraic equations at each grid within the Hertzian contact.

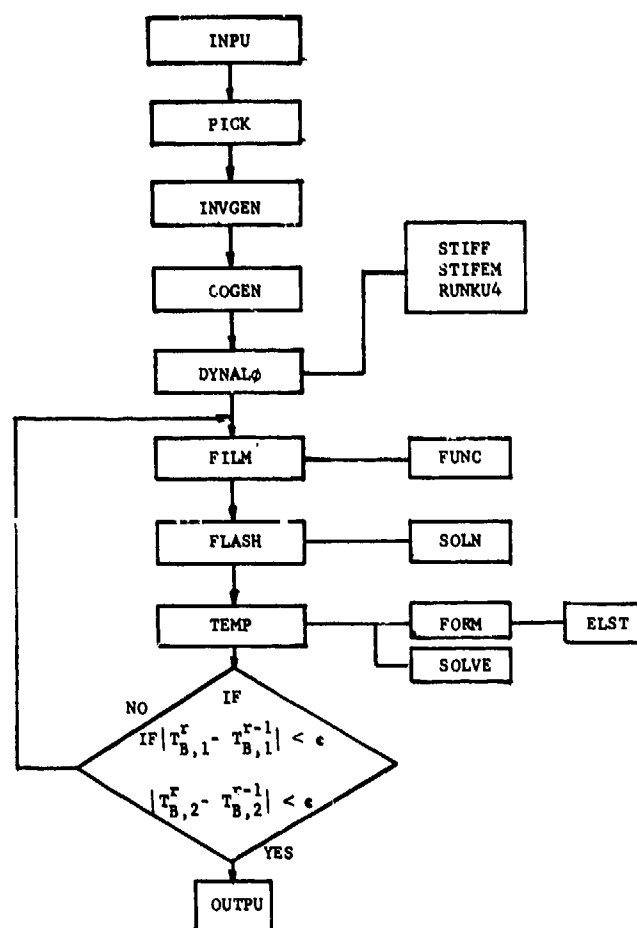


Figure 3. - Flow diagram.

(7) In subroutine TEMP the equilibrium temperature distribution on the contacting surface is computed by using the influence coefficients obtained in subroutine INVGEN for the distribution of the heat flux calculated in subroutine FLASH. The newly iterated values of equilibrium temperature are compared with the values in the last iteration. If the difference at every node on the surface is within the allowable error, the iteration is considered to be converged. If not, the procedure is repeated at subroutine FILM.

(8) Subroutine OUTPU prints out all the output data of the dynamic load, film thickness, flash temperature, and the equilibrium surface temperature along the contacting path.

Dynamic Load Variation

In general, the dynamic load distribution deviates from the static load distribution and is found to change greatly with the operating speed. The relationship of dynamic load variation with speed as well as with gear geometrical factors is described in the following sections.

For gears with true involute profiles under normal operating conditions, the main excitation to the system originates from the periodical change in teeth stiffness due to the alternating engagement of single and double pairs of teeth. The resulting mode of vibration is therefore dependent on the frequency of this forcing excitation and, hence, is dependent on the operating speed. Figure 4 shows dynamic load variation in three speed regions for a pair of 28-tooth and 8-pitch gears.

In the low-speed region, where the excitation frequency from the change of stiffness is much lower than the resonating frequency of the system, the dynamic load response is basically a static load

sharing in phase with the stiffness change, superimposed by an oscillatory load at a frequency corresponding to the system's resonating frequency.

As the speed increases to the neighborhood of the resonance, the typical load response (fig. 4(b)) contains load variations so abrupt that they sometimes can even produce teeth separation. In this speed region the peak dynamic load is much higher than the input static load and is very likely a source of gear noise and early surface fatigue. Operating in this region is obviously harmful. As the speed increases beyond the frequency of the resonating frequency, the dynamic load becomes out of phase with the stiffness variation, and it has a much smoother response. The peak of this load response is much reduced and is smaller than the static load. The shape of this load response (fig. 4(c)) is usually preserved with further speed increases.

Effect of Speed

One of the approaches to investigate the effects of various parameters on this dynamic load is through the use of dynamic load factor, $P_F = P_{dmax}/P_s$, where P_s is the static load and P_{dmax} is the maximum dynamic load along the line of action or the contacting path. The effect of speed is exemplified by plotting P_F against the frequency ratio $\omega_r = \omega_n$, defined as the ratio of the excitation frequency, ω , due to the periodical change of tooth stiffness to the system's natural frequency, ω_n . The system natural frequency ω_n is taken as the frequency at which the maximum dynamic load occurs.

Figure 5 shows a typical curve of the dynamic load factor P_F versus frequency ratio ω_r . The general trend of the response is similar to that of a single-degree-of-freedom, forced vibratory system

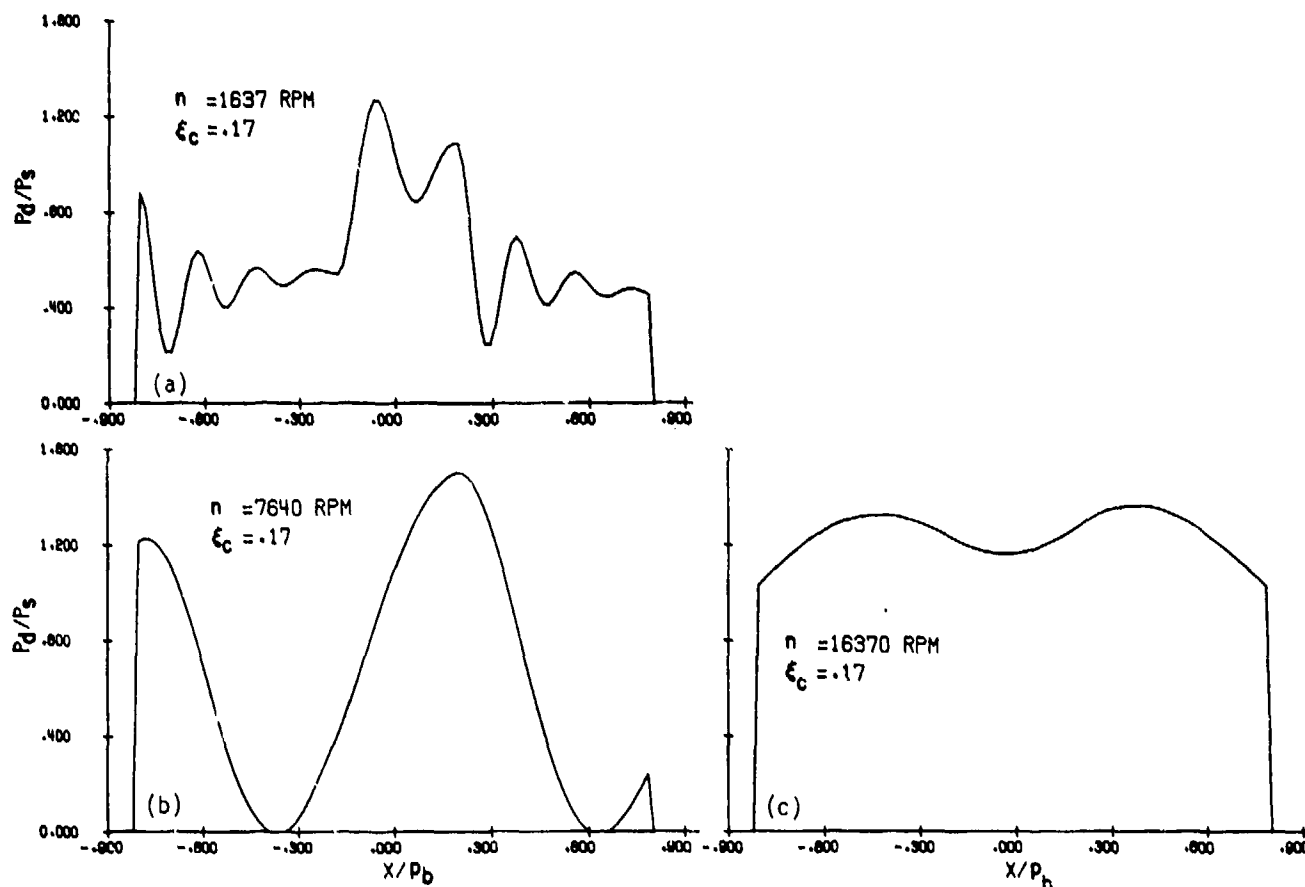


Figure 4. - Dynamic load variation; $r_g = 1$; $N_T = 28$; $D_p = 8$; $D = 0.254$ cm (0.1 in.). (a) $n = 1637$ rpm; (b) $n = 7640$ rpm; (c) $n = 16370$ rpm.

except that a few secondary peaks of the dynamic load ratio exist in the region of $\omega_r < 1$. When ω_r approaches unity, the load rises rapidly exhibiting a resonating phenomenon. For speeds above the natural frequency, the dynamic load decreases steadily in the same manner as the ordinary vibratory system.

Effect of Damping Ratio ξ

The damping coefficient C_o governing the dynamic load variation depends on the viscous friction of the gear system. It is usually an unknown. The damping ratio ξ_c in the present analysis is defined as $\xi_c = C_o / 2 \sqrt{KM}$. An arbitrary value between 0.1 and 0.2 was used in the analysis reported by Hirano (ref. 6) and Ishikawa (ref. 7) for the correlation between their analytical and experimental results. To explore the effect of this ratio, arbitrary values of 0.1, 0.17, and 0.2 were used to generate the dynamic load ratios shown in figure 6. As observed in this figure, ξ_c has a major influence on P_F when the operating speed is close to the resonating frequency. Away from the resonance ξ_c has little influence on P_F .

Effect of Contact Ratio

Contact ratio is defined as the ratio of the contact length to the base pitch. This ratio measures the duration of load being shared by more than one pair of teeth, and it has a considerable effect on the dynamic load response. For gears with different diametral pitches, the dynamic load response is different because of the change in contact ratio. It is expected that an increase in contact ratio would have a beneficial effect on the load sharing. To verify this fact, a comparison is made of the dynamic load responses of gears having 8-pitch and 16-pitch under identical operational conditions. The corresponding contact ratios for these two sets of gears are 1.64 and 1.78, respectively. As shown in figure 7, the five pitch gears (16-pitch) having a higher contact ratio have a smaller dynamic load compared with that calculated for coarser gears.

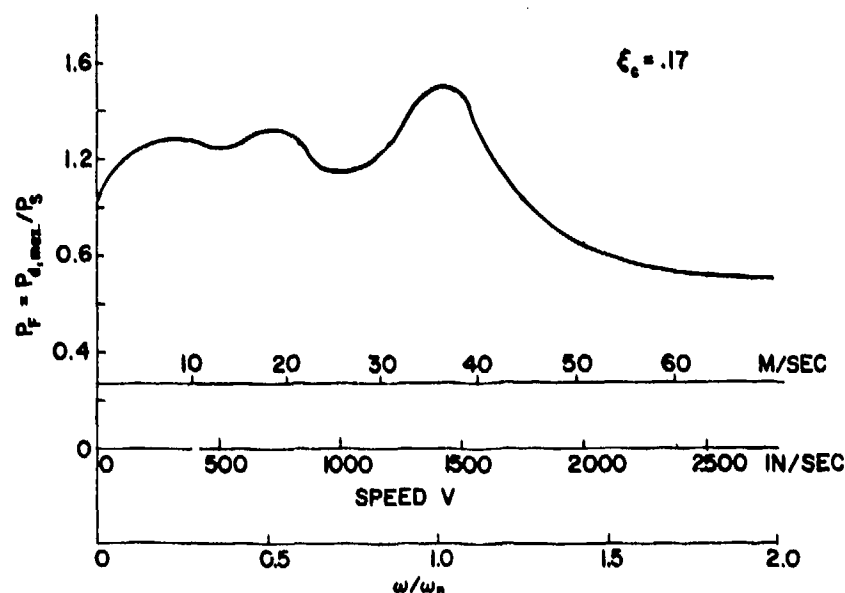


Figure 5. - Effect of speed and dynamic load factor; $r_g = 1$; $N_T = 28$; $D_p = 8$; $D = 0.254$ cm (0.1 in.).

Lubrication Performance

The computer code developed is applicable for a wide range of geometric, material, and operating parameters. In this section typical results were generated for a set of gears having a geometry similar to that used by Townsend and Zaretsky (ref. 8). These results cover effects of geometrical factors including face width, gear size, diametral pitch, gear ratio, and tip relief. In addition, the effects of lubricant viscosity, heat-transfer coefficient, speed, and load on the lubrication performance are also included.

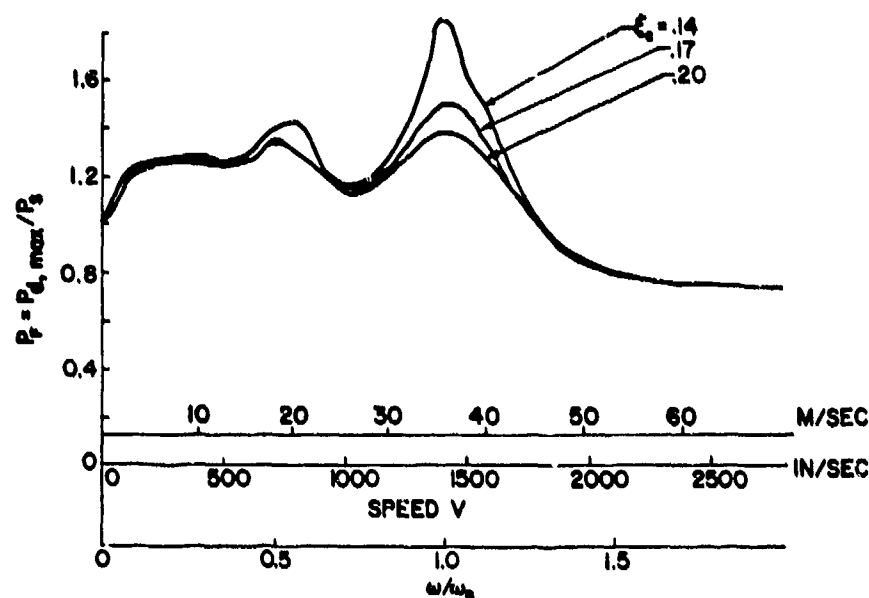


Figure 6. - Effect of damping ratio on dynamic load factor; $r_G = 1$; $N_T = 28$; $r_p = 9$; $D = 0.254$ cm (0.1 in.).

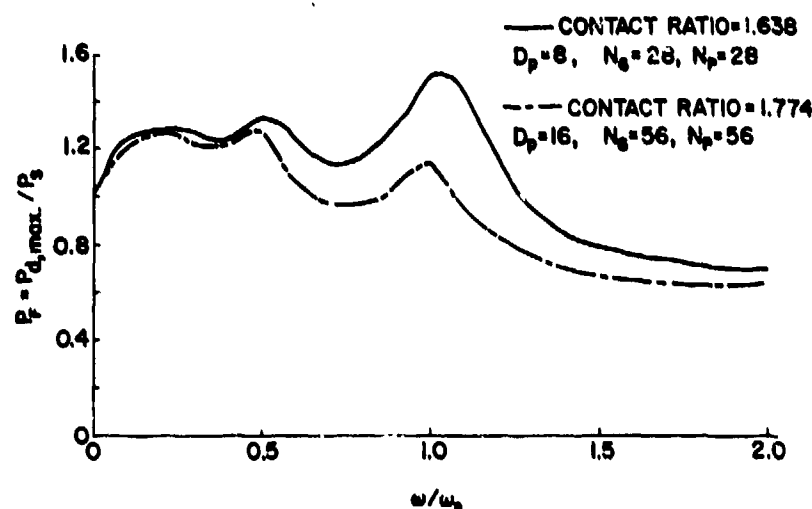


Figure 7. - Effect of contact ratio on dynamic load.

Distribution of Equilibrium Temperature, Total Flash Temperature, and Minimum Film Thickness

In this section detailed distributions of the minimum film thickness and temperature are plotted against the contact position for a set of gears and the lubricant used in reference 8. The properties of the lubricant as well as the geometry of the gears are listed in table I. In determining the distribution of minimum film thickness, it was assumed that the minimum film in a Hertzian contact is 75 percent of the plateau film thickness calculated from the transient film equation.

The detailed equilibrium surface temperature on both the pinion and gear teeth contacting surfaces is shown in figure 8 in terms of contact position X , when $X = X_R/R_i$ and R_i is the effective radius at the pitch point. It is seen that the equilibrium temperatures for both the pinion and the gear are higher at the tip of the tooth than at the root. This results in a pronounced temperature differential between the tooth surfaces during the beginning and the ending of the engagement.

The total flash temperatures as a function of the contacting position are plotted in figure 9 for three speeds. At speeds below or near the resonance, the total flash temperature shows local fluctuations of total flash temperature are not found at a speed considerably above the resonance.

The corresponding dynamic film thickness for this case is shown in figure 10 as a function of tooth contact position. The squeeze film effect is shown to be only important at a very short period after the teeth are engaged. Examinations of the film thickness distributions for all other runs indicate that the squeeze film effect is indeed not a dominant effect on the minimum film thickness.

Effect of Gear Geometry

The results in the previous section show the detailed distributions along the contact path. In the following sections one is concerned with the overall performance as affected by the change of geometrical factors. The overall performance is represented by three quantities, the maximum equilibrium surface temperature $T_{B,max}$, the maximum total flash temperature $T_{F,max}$, and the minimum film thickness h_{min} along the contacting path.

Investigating the effects of gear geometry, the first case considered is the effect of gear face width. Borsoff (ref. 9) found experimentally that the increase of face width would reduce the specific load carrying capacity (load per unit face width). This phenomenon does not seem to be explainable

TABLE I. - GEAR DATA, LUBRICANT DATA, AND STANDARD OPERATING CONDITIONS

(a) Gear data

Number of teeth, N_T	28
Diametral pitch, D_p	8
Pressure angle, ϕ , deg	20
Pitch radius, R_1 , cm (in.)	4.445 (1.75)
Outside radius, R_{o1} , cm (in.)	4.7625 (1.875)

(b) Lubricant (Superrefined naphthenic mineral oil) data

Kinematic viscosity, cm^2/sec (cs), at—	
311 K (100° F).....	0.73 (73)
372 K (210° F)	0.077 (7.7)
Density at 289 K (60° F) g/cm^3	0.8899
Thermal conductivity at 311 K (100° F), $\text{J}/(\text{m}(\text{sec})(\text{K}))$ (Btu/(hr)(ft)(°F)).....	0.0125 (0.0725)
Specific heat at 311 K (100° F), $\text{J}/(\text{kg})(\text{K})$ (Btu/(lb)(F)).....	582 (0.450)
Lubricant viscosity at temperature equation	$\mu = \mu_o \exp[\alpha p + \beta(1/T - 1/T_o)]$
Pressure viscosity coefficient, α , m^2/N (in^2/lb).....	2.3×10^{-7} (0.00016)
Temperature viscosity coefficient, β , K (°R).....	3890 (7000)

(c) Standard operating conditions

Load per unit width, P , N/m (lb/in).....	0.753 (4300)
Pitch line velocity, V , m/sec (in/sec)	46.55 (1832)
Ambient temperature, T_o , °C (°F)	37.78 (100)
Surface heat transfer coefficient, $\text{W}/\text{m}^2 \text{K}$ (Btu/(ft ²)(hr)(R)).....	341 (60)

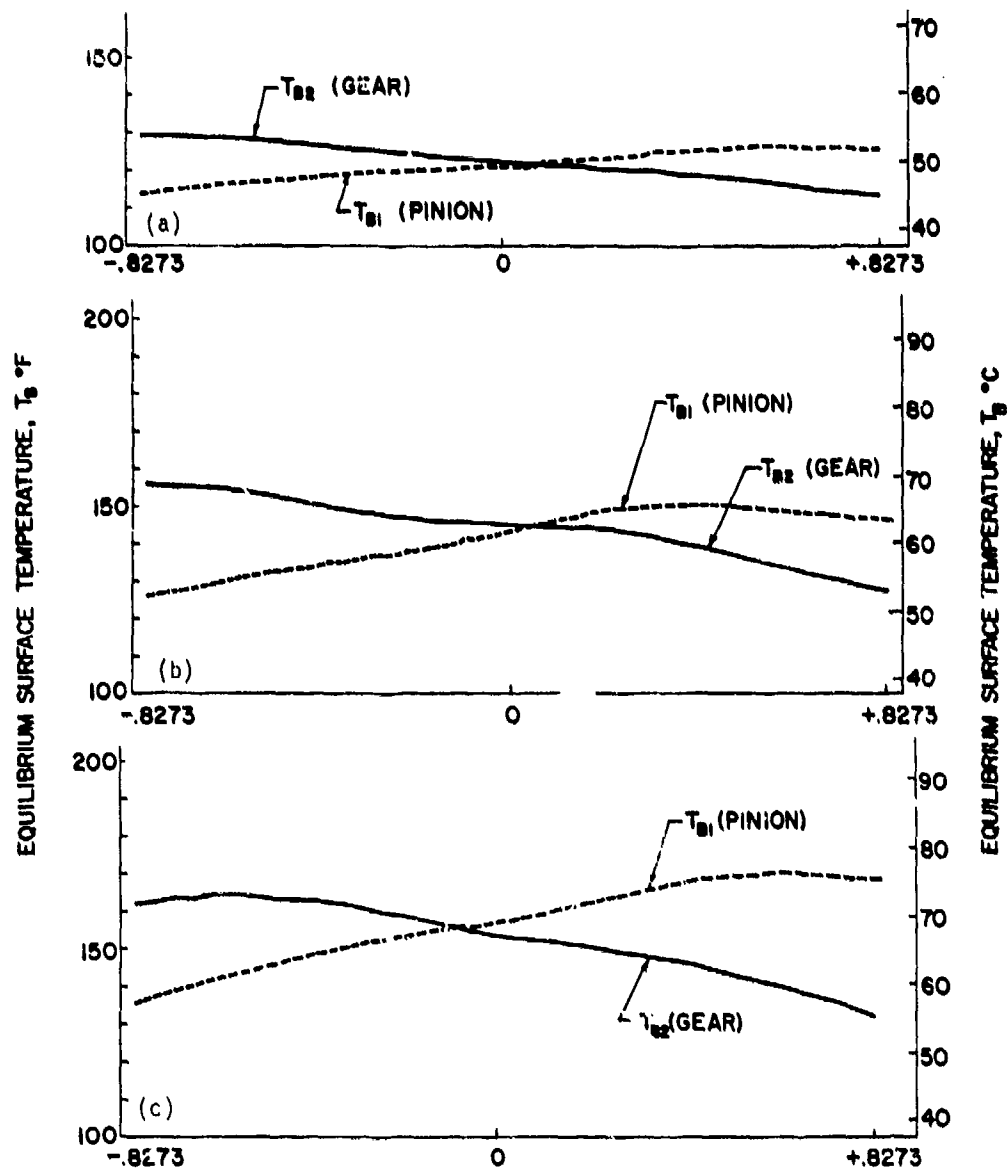


Figure 8. - Distribution of equilibrium surface temperature; $r_G = 1$. (Other conditions are listed in table I.) (a) $n = 1637$ rpm; (b) $n = 7640$ rpm; (c) $n = 16370$ rpm.

by Blok's flash temperature theory or by any existing EHD film thickness theory. As shown in figure 11, the present results indicate that, as the face width increases from 0.05 to 0.2 in., under the same load there is a corresponding increase in the maximum equilibrium surface temperature as well as in the total flash temperature. The higher surface temperature results in a much reduced minimum film thickness when the face width is increased. This suggests that the experimental trend obtained by Borsoff with regard to the effect of face width can be at least partially accounted for by the present analysis on the basis of its effect on the surface temperature and film thickness.

The effect of gear outside radius is shown in figure 12. It is seen that when the pitch-radius is increased from 1.75 to 2.5 in., under a constant load and speed, the total flash temperature as well as the film thickness is considerably improved. However, one must keep in mind that the improvement in lubrication performance by increasing the size of gears is a rather expensive way to solve the lubrication problem.

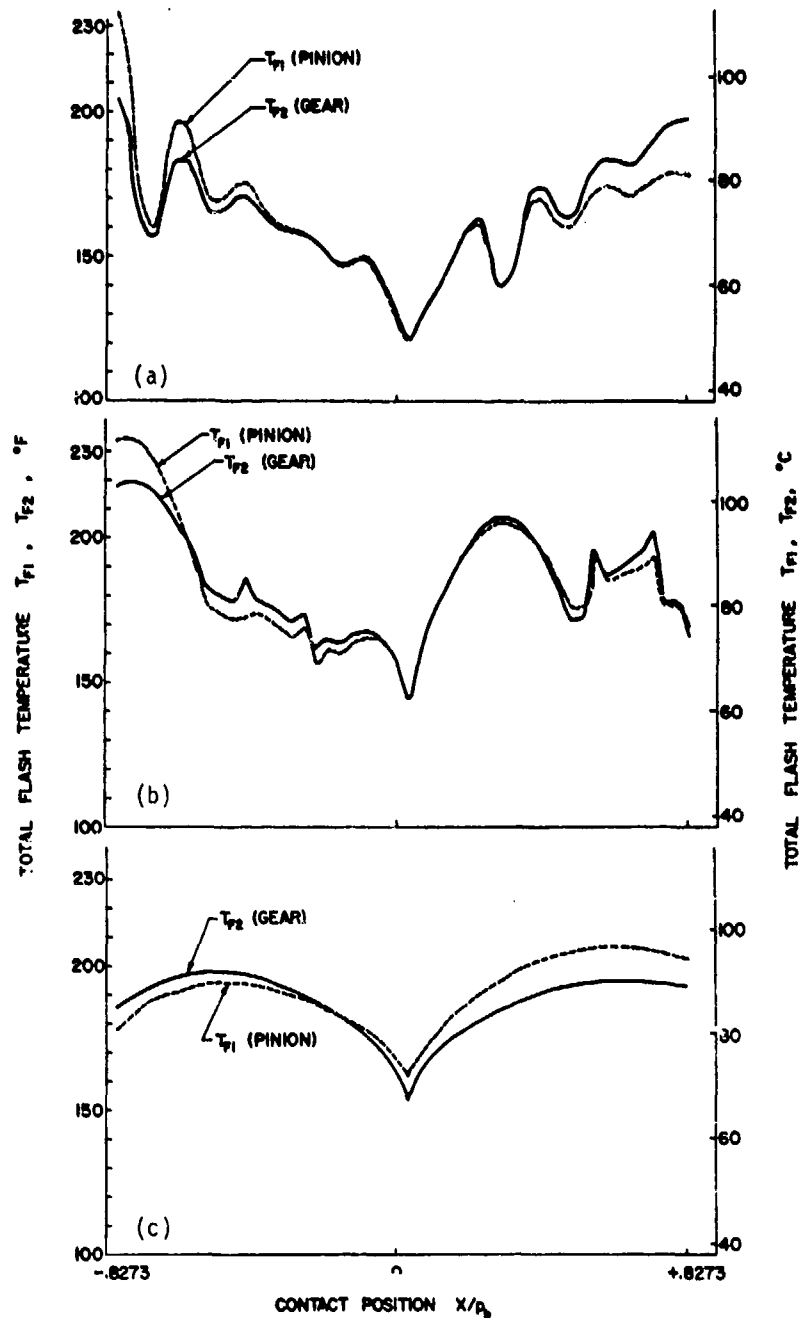


Figure 9. - Distribution of total flash temperature; $r_G = 1$. (Other conditions are listed in table I.) (a) $n = 1637$ rpm; (b) $n = 7640$ rpm; (c) $n = 16370$ rpm.

The effect of diametral pitch is shown in figure 13. Since an increase in diametral pitch tends to reduce the dynamic load and the sliding between teeth, the use of gears with a finer pitch yields a lower maximum surface temperature as well as a lower total flash temperature, in comparison with the corresponding values for coarser gears. The minimum film thickness is also found to be much improved as the diametral pitch changes from 8 to 12. However, it must be kept in mind that the improvement in lubrication performance in this instance can be easily offset by the reduction in flexural strength for gears with a finer pitch.

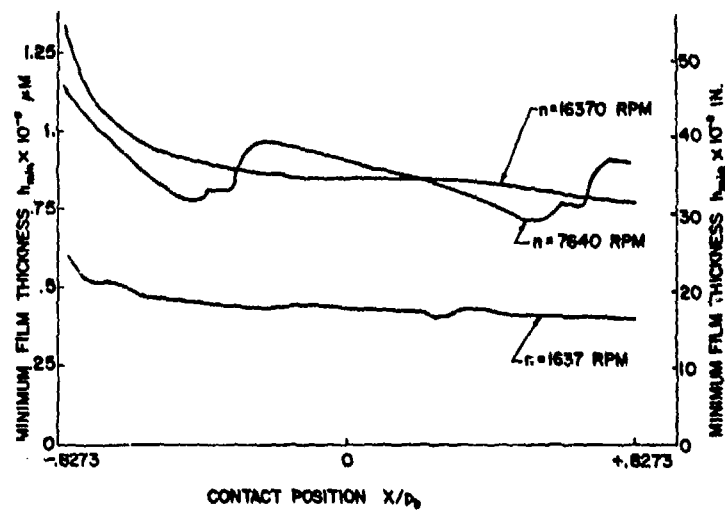


Figure 10. - Dynamic film thickness distribution.

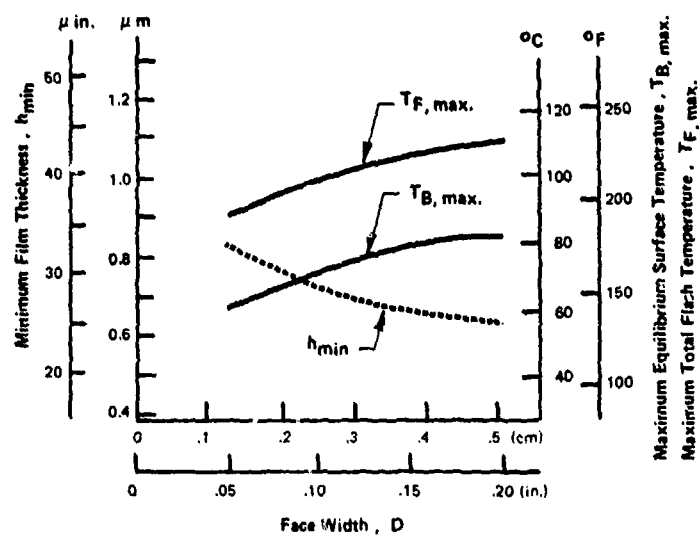


Figure 11. - Effect of face width on lubrication performance.

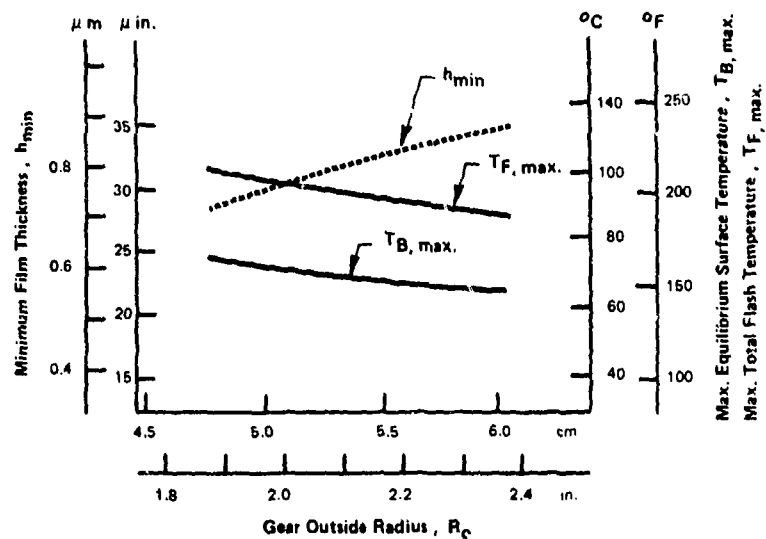


Figure 12. - Effect of gear outside diameter on lubrication performance.

Figure 14 shows the effect of gear ratio on the lubrication performance. The gear ratio is varied from 1 to 2 by increasing the gear teeth number from 28 to 56. It is seen that the increase in the size tends to improve the cooling effect and hence reduce both the equilibrium temperature and the total flash temperature. The effect on film thickness is even greater because of a larger effective radius in the Hertzian contact.

Effect of Lubricant Operating Parameters

Aside from the effects of gear geometry, lubricant properties and the gear operating conditions are also known to have an influence on the gear lubrication performance. The effect of lubricant viscosity is shown in figure 15. When the lubricant viscosity is increased from 0.062 to 0.1379 Pa·s (9×10^{-6} to 20×10^{-6} lb·sec/in²), the film thickness is found to have a marked increase, and it is accompanied by a slight increase in maximum equilibrium and total flash temperature on the surface. This indicates that the reduction in load carrying capacity in practice for gears with low viscosity oils is likely caused by the lack of lubricant film in the contact.

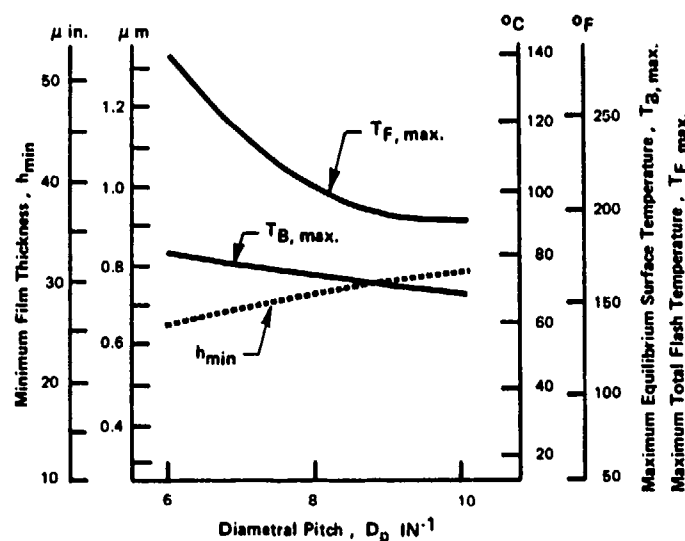


Figure 13. - Effect of diametral pitch on lubrication performance.

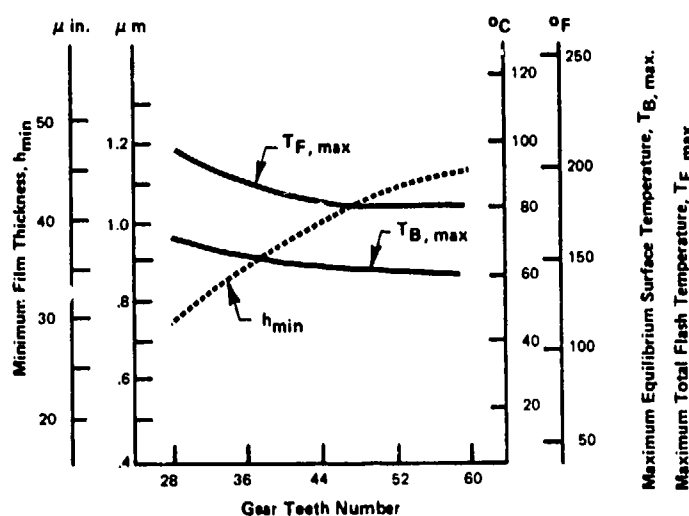


Figure 14. - Effect of gear ratio on lubrication performance pinion teeth.
Number = 28.

The effect of surface convective heat-transfer coefficient and the effect of ambient temperature on the lubricant performance are shown separately in figures 16 and 17. Increasing the heat-transfer coefficient or decreasing the operating ambient temperature is shown to have a substantial improvement on the lubrication performance.

Among the effects of operating parameters, perhaps the most interesting one is the speed effect. Figure 18 shows the results on the effect of speed for the same set of gears considered in the preceding sections. It is seen that as the pitch-line speed increases from 21.1 to 72.0 m/sec (830 to 2832 in/sec) the minimum film thickness experiences a gradual increase, which appears to be sustained throughout the high-speed region. The corresponding total flash temperature also shows a slight improvement with speed in spite of a gradual increase in the equilibrium temperature. This trend seems to be in accord with the experimental evidence provided by Borsoff (ref. 9) and Ku and Baber (ref. 10) in which they concurred that the scuffing load capacity increases gradually with speed in the high-speed region.

The results by varying the tooth load from 0.753 to 1.103 MN/m (4300 to 6300 lb/in) are plotted in figure 19. It is seen that the minimum film decreases linearly with the load but that the equilibrium temperature as well as the total flash temperature increases also linearly with the load.

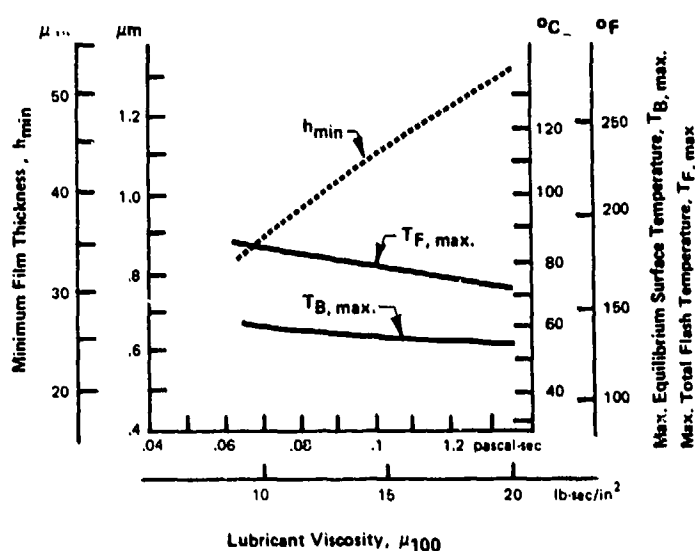


Figure 15. - Effect of lubricant viscosity on lubrication performance; $P = 0.7$ MN/m (400 lb/in), $D = 0.127$ cm (0.05 in.).

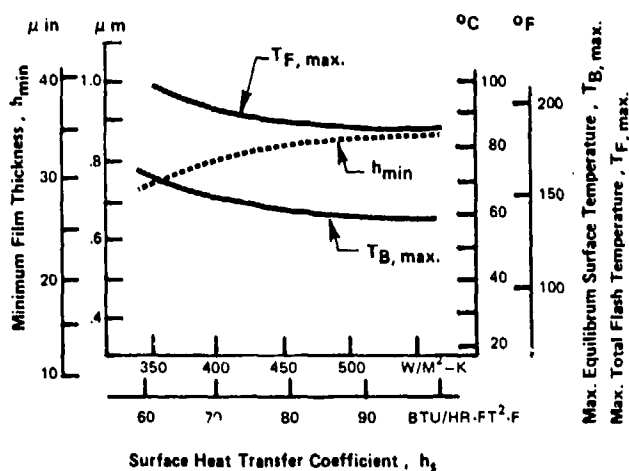


Figure 16. - Effect of surface heat transfer coefficient on lubrication performance.

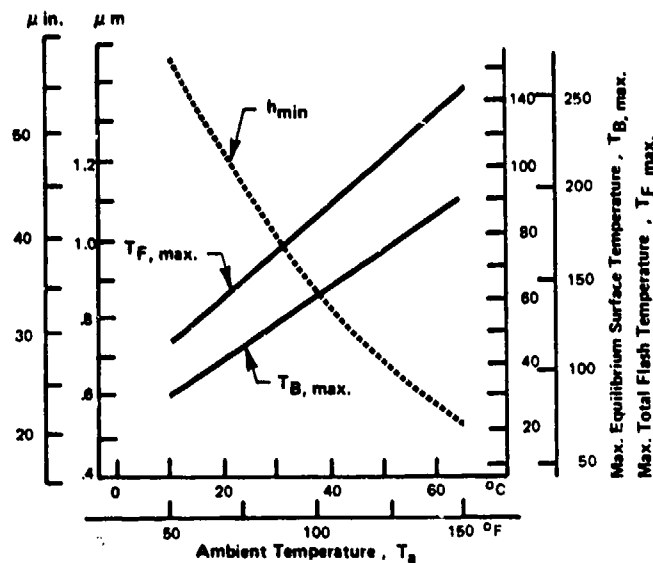


Figure 17. - Effect of ambient temperature on lubrication performance.

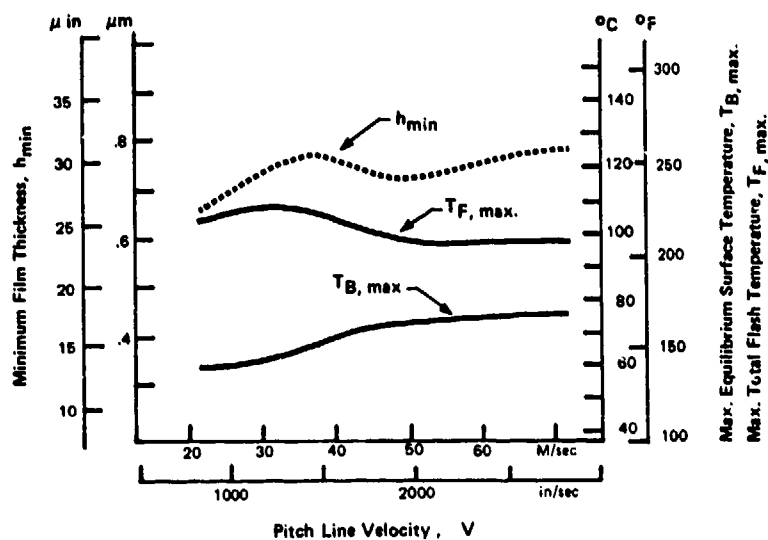


Figure 18. - Effect of surface speed on lubrication performance.

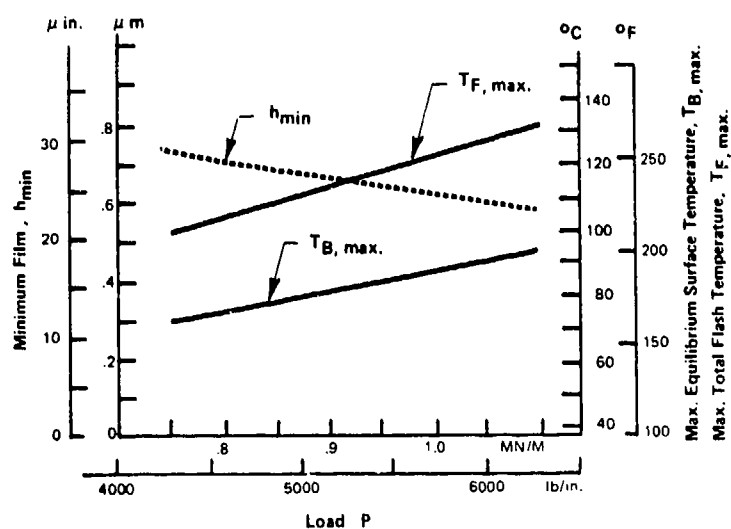


Figure 19. - Effect of load on lubrication performance.

Summary of Results

Results of dynamic load were obtained for a pair of gears with dimensions corresponding to that used by Townsend and Zaretsky (ref. 8) in their gear experiments. The dynamic load distributions along the contacting path for various speeds show patterns similar to that observed experimentally. Effects of damping ratio, contact ratio, on the dynamic load were examined.

Gear lubrication performance was evaluated by plotting the maximum bulk equilibrium temperature, the maximum total flash temperature, and the minimum film thickness along the contacting path for various geometric and operating parameters. It was found that an increase in diametral pitch or a decrease in face width for the same specific load gives a better lubrication performance. These trends agree qualitatively with experimental results by Borsoff (ref. 9) and by Ku and Barber (ref. 10). Among the operating variables, the lubrication performance is improved most strongly by increasing the inlet lubricant viscosity, by decreasing the ambient temperature, or by increasing the convective heat-transfer coefficient on the gear surface. Increasing the pitch-line velocity gives a slight improvement in lubrication performance at high speeds. However, the trends do not indicate any signs which can account for the dramatic increase in scuffing load observed by Borsoff at very high speeds.

References

1. Wang, K. L.; and Cheng, H. S.: A Numerical Solution to the Dynamic Load, Film Thickness, and Surface Temperatures in Spur Gears, Part I—Analysis. *J. Mech. Des.*, vol. 103, Jan. 1981, pp. 177-87.
2. Wang, K. L. and Cheng, H. S.: A Numerical Solution to the Dynamic Load, Film Thickness, and Surface Temperatures in Spur Gears, Part II—Results. *J. Mech. Des.*, vol. 103, Jan. 1981, pp. 188-94.
3. Vichard, J. P.: Transient Effects in the Lubrication of Hertzian Contacts. *J. Mech. Eng. Sci.*, vol. 13, no. 3, 1971.
4. Dyson, A.: Frictional Traction and Lubricant Rheology in Elastohydrodynamic Lubrication. *Philos. Trans. Royal Soc. (London)*, Ser. A, vol. 266, 1970, pp. 1-33.
5. Jaeger, J. C.: Moving Sources of Heat and Temperature at Sliding Contacts. *J. Proc. Roy. Soc. N.S.W.*, vol. 76, 1942, pp. 203-224.
6. Ichimaru, K.; and Hirano, I.: Dynamic Behavior of Heavy-Loaded Spur Gears. ASME Paper No. 72-PTG-14, 1972.
7. Ishikawa, J.; Hayashi, K.; and Yokoyama, M.: Surface Temperature and Scoring Resistance of Heavy-Duty Gears. ASME Paper No. 72-PTG-22, 1972.
8. Townsend, D. P.; and Zaretsky, E. V.: A Life Study of AISI M-50 and Super Nitralloy Spur Gears With and Without Tip Relief. ASME Paper No. 73-Lub-30, 1973.
9. Borsoff, V. N.: On the Mechanism of Gear Lubrication. *J. Basic Eng.*, vol. 80D, 1959, pp. 79-93.
10. Ku, P. M.; and Barber, B. B.: The Effect of Lubricants on Gear Tooth Scuffing. *ASLE Trans.*, vol. 2, no. 2, Oct. 1959.

Evaluation of High-Contact-Ratio Spur Gears With Profile Modification*

Dennis P. Townsend†, Berl B. Baber‡, and Andrew Nagy‡

A majority of current aircraft and helicopter transmissions have a spur-gear-contact ratio (average number of teeth in contact) of less than 2. The contact ratios are usually from 1.3 to 1.8, so the number of teeth in engagement is either one or two. Many gear designs use a pressure angle of 25° for improved tooth strength, giving a contact ratio of approximately 1.3. This low contact ratio causes increased dynamic loading of the gear teeth, increased noise, and sometimes, lower pitting fatigue life.

High-contact-ratio gears (greater than 2) have load sharing between two or three teeth during engagement and, therefore, usually have less load per tooth. These gears should operate with lower dynamic loads and thus less noise. High-contact-ratio gears have been in existence for many years but have not been widely used. High contact ratios can be obtained in several ways: (1) by smaller teeth (larger pitch), (2) by smaller pressure angle, and (3) by increased addendum. As a result, high-contact-ratio gears tend to have lower bending strength and increased tooth sliding. Because of the increased sliding, the high-contact-ratio gears may run hotter and have a greater tendency for surface-distress-related failures such as micropitting and scoring.

Profile modification (changing the involute profile at the addendum or dedendum or both) is normally done on all gears to reduce tip loading and scoring (ref. 1). If it is done improperly, however, it could increase the dynamic load (ref. 2). Several profile modifications have been proposed that would reduce scoring and improve the performance of high-contact-ratio (HCR) gears. One such proposal is the so-called new-tooth-form (NTF) gear, which has a large profile modification at both the addendum and dedendum. The profile radius of curvature is also reduced at the addendum and increased at the dedendum in an attempt to lessen sliding and thereby reduce scoring of HCR gears. However, a gear geometry analysis (ref. 3) indicates that sliding is independent of the profile radius of curvature.

Under NASA contract NAS3-18532 the Boeing Vertol Co. designed and manufactured two sets of NTF gears as well as two sets of standard gears for the purpose of evaluating the NTF gears and comparing them with standard gears. (new tooth form)

The work reported herein was conducted to evaluate the NTF gears in relation to the standard gears by conducting three series of tests on both gear types. These tests were scoring tests, surface fatigue tests, and bending fatigue tests. The tests were performed by the Southwest Research Institute, under NASA contract NAS3-20026.

Apparatus, Specimens, and Procedure

Gear Test Apparatus

The gear fatigue tests and the scoring tests were performed in two Wright Air Development Division (WADD) gear test rigs. The WADD gear test rig (fig. 1) was developed for high-temperature lubricant testing (ref. 4). It is very similar to the Ryder test rig (ref. 5), except that a roller bearing is used in place of sleeve bearings, and screw thread nonrubbing seals are used in place of shaft-rubbing lip seals. Load is supplied to the test gears through hydraulic pressure applied to the end of the driver gear shaft, forcing the slave gear to move a slight distance axially on the helix. This axial motion produces a torque on the test gears. The test rig is calibrated by strain gages on the test-gear shaft to determine test-gear torque as a function of hydraulic pressure.

*Previously published as NASA TP-1458; work partially supported by NASA Contract NAS3-20026.

†NASA Lewis Research Center.

‡Southwest Research Institute.

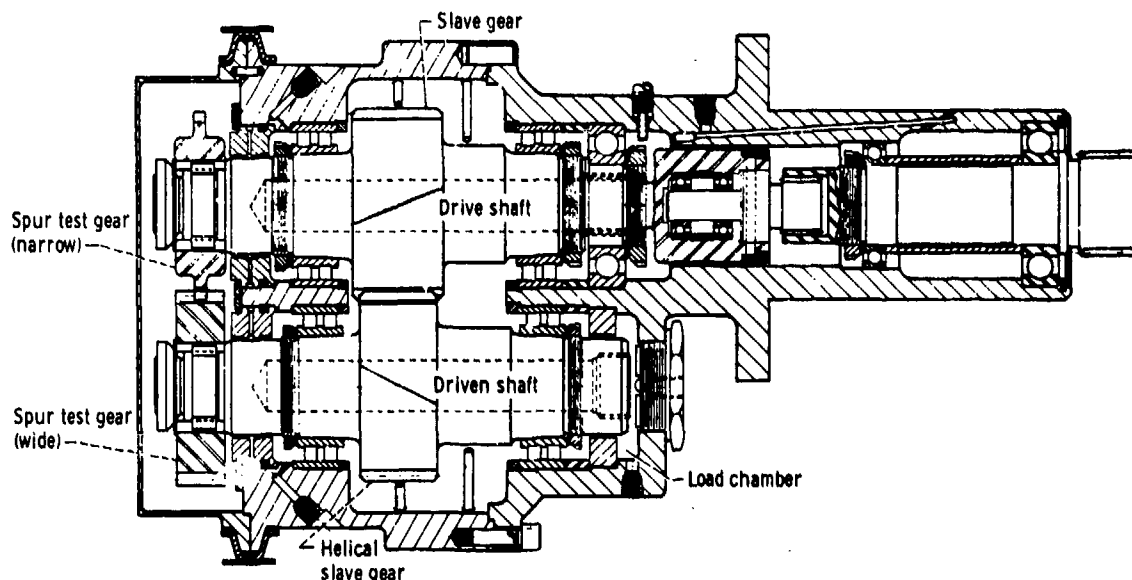


Figure 1. - Wright Air Development Division (WADD) gear test rig.

A hydraulic system provides regulated hydraulic pressure to the load piston end of the slave gear shaft. The system controls the gear torque to a sensitivity of approximately $\pm 1.13 \text{ N-m}$ (10 in-lb) of the applied torque once the load has been set by the operator.

The two test spur gears are the same in all respects except that one gear is wider than the other. The wider gear allows full face contact with the narrow gear during the slight relative axial movement between them as the tooth load is increased. The narrow gear has full and unvaried face contact and is the gear used for rating.

Each test rig is provided with an independent oil system. The oil used is a synthetic polyol ester C₅, C₆, C₇ substituted pentaerythritol oil. The physical and chemical properties of this oil are given in table I. A 3- μm -absolute oil filter is used to filter the oil during testing. Instrumentation provides for automatic detection of a lubrication or gear failure and for test rig shutdown.

Tooth Bending Fatigue Test Apparatus

The tooth bending fatigue tests were conducted using a special single-tooth test fixture, shown schematically in figure 2, that was designed to be used with a high-cycle-fatigue testing machine. The apparatus consists of the gear-supporting reaction frame, the loading clevis-load cell, the actuator, and the control system. A strain-gage bridge installed on the properly sized elastic elements of the clevis provides an output proportional to the applied load. This allows for real-time load control of the test. Instrumentation includes automatic shutdown of a test in the event of specimen fracture or after a preset number of load cycles are applied, whichever occurs first. The operating frequency of the load system is 1500 cycles per minute.

Test Gears

The test gears were of either standard or new-tooth-form design. Three different gear sets were manufactured for each design: the bending test gears, the wide scoring and surface fatigue test gears, and the narrow scoring and surface fatigue test gears. The dimensions for the standard and NTF WADD test gears are given in table II. The narrow WADD gear of each design is shown in figure 3 for comparison. The contact ratio for the standard gear, not considering tip relief, was 1.30. All gears had a nominal surface finish of $0.406 \mu\text{m}$ (16 $\mu\text{in.}$). The standard gear had a pressure angle of 22.50° and a tip relief of 0.001 cm (0.0004 in.). The NTF gear had a contact ratio of 2.31, an increased addendum of 0.16 cm (0.063 in.), a pressure angle of 19° , a tip relief of 0.006 cm (0.0025 in.), and a flank addition of 0.006 cm (0.0025 in.). This is shown in the profile trace of figure 4(a). The involute radii at the tip and flank of the NTF gears were also modified to decrease the tip radius and to increase the flank radius.

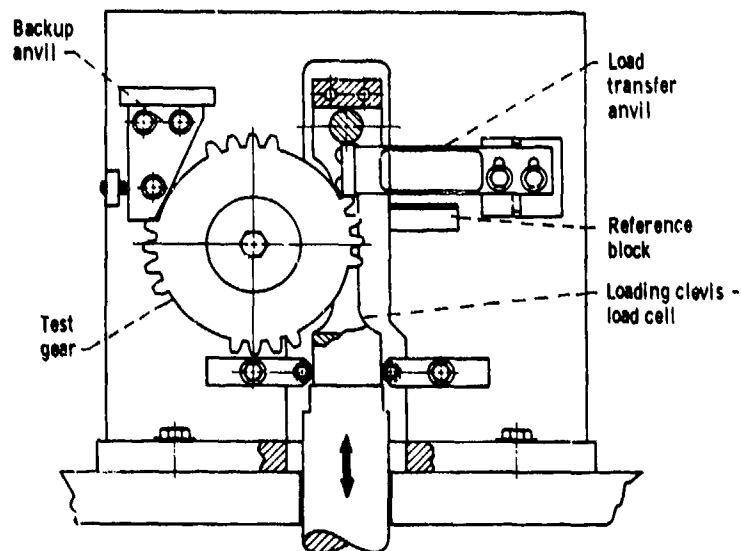
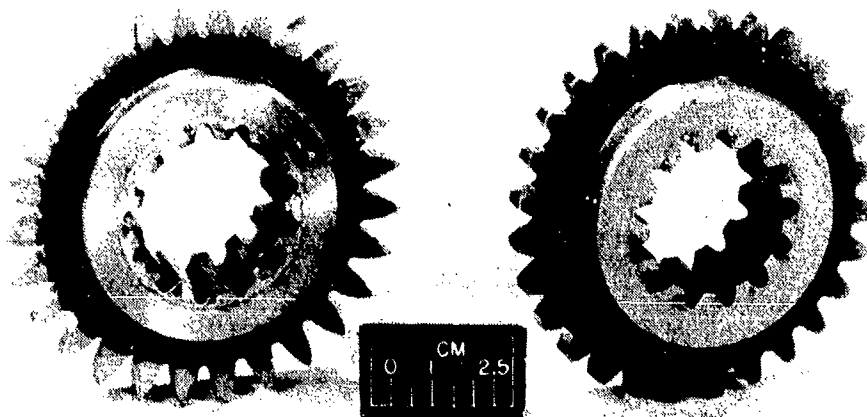


Figure 2. - Single-tooth bending fatigue test fixture.



(a) New-tooth-form gear.

(b) Standard gear.

Figure 3.- WADD test gears.

All gears were manufactured from AMS 6265C (AISI 9310) and were carburized and hardened to a case hardness on the tooth surface of 60 to 62 Rockwell C, with a core hardness of 35 to 40 Rockwell C. The chemical composition of the gear material is given in table III. The heat-treat schedule is given in table IV.

The bending-fatigue test gears were larger to fit the bending-fatigue test machine. The dimensions for the bending-fatigue test gears are given in table II. These gears, shown in figure 5, were similar to the smaller WADD test-rig gears shown in figure 3. The standard gear had a pressure angle of 25° , a tip relief of 0.001 cm (0.004 in.), and a contact ratio of 1.54. The NTF gear had a pressure angle of 20.5° , an increased addendum of 0.222 cm (0.0875 in.), a tip relief of 0.006 cm (0.0025 in.), a flank addition of 0.006 cm (0.0025 in.), and a contact ratio of 2.25. An involute profile trace of the two gears is shown in figure 4(b).

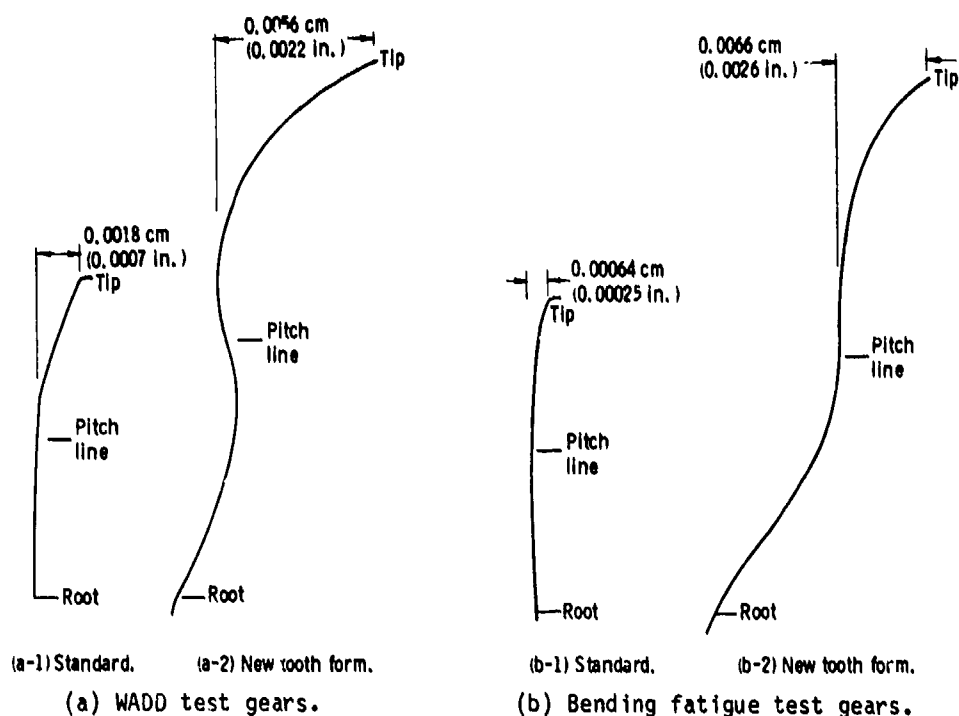


Figure 4. - Involute profiles for test gears.

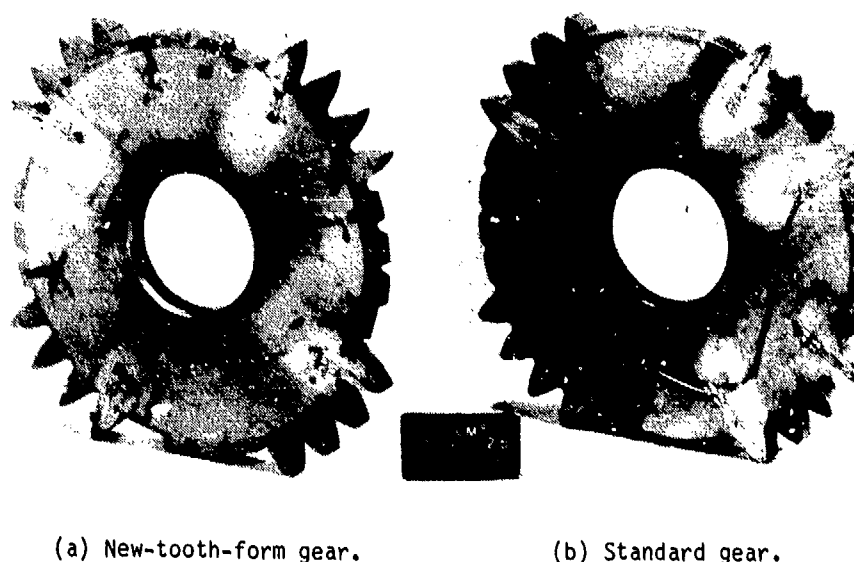


Figure 5. - Bending fatigue test gears.

Test Procedures

Test Lubrication

All gear scoring and surface-fatigue tests were conducted with a single batch of a synthetic polyol ester C₅, C₆, C₇ substituted pentaerythritol lubricating oil. The physical properties of this lubricant are summarized in table I. During the load scoring tests, the lubricant flow rate was held constant at 270 cm³/min and was directed at the gear mesh exit. The lubricant inlet temperature was

TABLE I. - PROPERTIES OF SYNTHETIC POLYESTER

C₅, C₆, C₇ SUBSTITUTED PENTERYTHRITOL

LUBRICATING OIL

Property	Typical data
Kinematic viscosity, cm ² /sec (cS), at-	
233 K (-40° F)	10.764 × 10 ⁻² (10.764)
311 K (100° F)	28.51 × 10 ⁻² (28.51)
372 K (210° F)	5.4 × 10 ⁻² (5.4)
Flashpoint, K (°F)	533 (500)
Pourpoint, K (°F)	214 (-75)
Neutralization number, mg KOH/g	0.3

TABLE II. - TEST GEAR DATA

Dimension	Load scoring and surface fatigue (WADD) test gears		Tooth bending fatigue test gears	
	Standard gears	NTF gears	Standard gears	NTF gears
Tooth form	Involute	Noninvolute	Involute	Noninvolute
Pitch diameter, cm (in.)	8.890 (3.500)	8.890 (3.500)	15.240 (6.000)	15.240 (6.000)
Number of teeth	28	28	32	32
Diametral pitch, module in mm (DP in in ⁻¹)	3.2 (8)	3.2 (8)	4.76 (5.333)	4.76 (5.333)
Pressure angle at pitch point, deg	22.5	19.0	25	20.5
Face width, cm (in.):				
Wide gear	2.380 (0.937)	2.380 (0.937)	-----	-----
Narrow gear	0.635 (0.250)	0.635 (0.250)	0.953 (0.375)	0.953 (0.375)
Outside diameter, cm (in.)	9.444 (3.718)	9.845 (3.876)	16.256 (6.400)	16.637 (6.550)
Base circle diameter, cm (in.)	8.214 (3.234)	8.301 (3.268)	13.813 (5.438)	14.275 (5.620)
Root diameter, cm (in.)	8.187 (3.223)	7.841 (3.087)	14.125 (5.561)	13.716 (5.400)
TIF diameter, cm (in.)	8.463 (3.332)	8.331 (3.280)	14.463 (5.694)	14.346 (5.648)
Full fillet radius, cm (in.)	0.165 (0.065)	0.165 (0.065)	0.188 (0.074)	0.188 (0.074)
Measurement over pins, cm (in.)	9.629 to 9.637 (3.791 to 3.794)	-----	16.543 to 16.533 (6.513 to 6.509)	-----
Pin diameter, cm (in.)	-----	-----	0.879 (0.346)	-----
Backlash reference, cm (in.)	0.005 to 0.015 (0.002 to 0.006)	0.005 to 0.015 (0.002 to 0.006)	0.020 to 0.030 (0.008 to 0.012)	0.020 to 0.030 (0.008 to 0.012)
Contact ratio	1.30	2.25	1.54	2.25
Maximum specific sliding, v _s /v	0.283	0.540	-----	-----

TABLE III. - CHEMICAL COMPOSITION OF GEAR MATERIAL

CVM AISI 9310 - AMS 6265

	Element									
	C	Mn	P	S	Si	Ni	Cr	Mo	Cu	Fe
Content, wt %	0.10	0.62	0.008	0.003	0.28	3.36	1.33	0.15	0.19	Bal.

held constant at 347 K (165° F), but the lubricant outlet temperature varied with load as shown in figure 6. The test oil tank, which had a capacity of 2500 cm³, was heated by an external resistance heater clamped on the copper-clad, stainless-steel oil tank. The oil was filtered through a 3-μm-absolute filter. During the surface fatigue tests the lubricant flow rate was 1300 cm³/min, and two oil jets were used—one at the gear-mesh inlet and one at the gear mesh exit. The added oil flow for the surface fatigue tests was used to reduce the gear temperature and to prevent scoring failures.

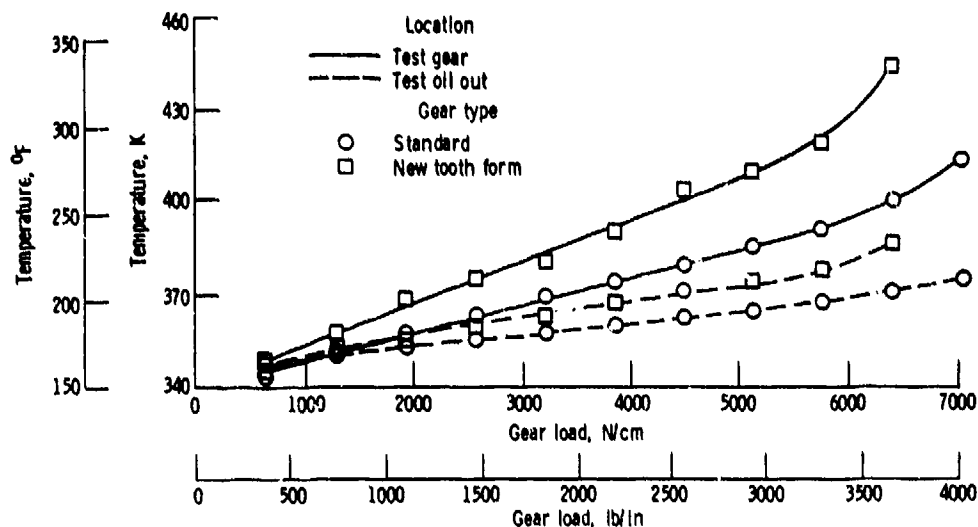


Figure 6. - Average maximum test-gear and oil-out temperatures for standard and NTF spur gears as function of gear load. Speed, 10 000 rpm; lubricant, synthetic polyol ester.

TABLE IV. - HEAT TREATMENT PROCESS FOR VACUUM-ARC-REMELTED (VAR) AISI 9310

Step	Process	Temperature		Time, hr
		K	°F	
1	Blast clean	----	----	7.5
2	Carburize 0.85 - 1.0 carbon potential	1200	1700	---
3	Cool under atmosphere to -	1090	1500	---
4	Air cool to room temperature	----	----	---
5	Stress relieve	922	1300	2
6	Copper plate all over	----	----	---
7	Austenitize	1117	1650	2.5
8	Oil quench	----	----	---
9	Subzero cool	189	-120	3.5
10	Double temperature	422	300	Two each
11	Finish grind	----	----	---
12	Stress relieve	422	300	2

Load Scoring Test Procedure

The test procedure used with the WADD gear test rigs for the load scoring tests conducted on both the standard and NTF test gears was ASTM test method D-1947 (ref. 4), with test conditions modified as follows: shaft speed, 10 000 rpm; test oil temperature, 347 K (165° F); and lubricant flow rate at the gear mesh exit, 270 cm³/min. The test load increment was 63×10^3 N/m (360 lb/in) on the 0.635-cm (0.250-in.) wide test gear, and the load duration for each step load condition was 20 minutes instead of the 10 minutes used in the ASTM method. Test gears were considered scored when scoring had covered 22.5 percent of the test-gear face width as observed under an 18-power microscope.

Measurement of the test-gear temperature is not required in the ASTM procedure. However, the temperature of the narrow test gear was measured during each load step in all the load scoring tests. It was obtained from the infrared radiation that was emitted by the gear and detected by an infrared radiometer with a direct-reading digital readout. It was measured on the web of the narrow test gear just inside the root diameter, near the gear-mesh point. This point was used because its nearly

constant emissivity factor minimized the error due to changing emissivity that would have resulted if the measurements were made at the gear teeth. A metal tube was used to prevent oil splashing and mist interference. A constant emissivity factor was further assured by applying black chromium plating on the gear web to closely approximate blackbody radiation.

Surface-Fatigue Test Procedure

Test conditions for the surface-fatigue tests were a shaft speed of 10 000 rpm, a test oil temperature of 347 K (165° F), and gear-mesh inlet and exit lubrication at a flow rate of 1300 cm³/min. The endurance test load was 6440 N/cm (3680 lb/in) for both the standard gear and the NTF gear for the equal-load tests. This produced Hertz stresses of 173×10^7 Pa (250 000 psi) for the standard gear and 148×10^7 Pa (214 000 psi) for the NTF gear. The standard gear was also run at a load of 4720 N/cm (2700 lb/in) to produce a Hertz stress of 148×10^7 Pa (214 000 psi). These test loads were run to compare standard and NTF lives at equal loads and at equal Hertz stresses.

The test oil flow rate was increased from the 270 cm³/min used in the load scoring tests to 1300 cm³/min for the surface-fatigue tests. In addition, two test oil jets were used to provide lubricant to the test gears. One jet was directed toward the inlet side of the gear mesh, and the second jet was directed toward the exit side of the gear mesh. These jets increased the test oil flow rate and provided sufficient lubrication and cooling to the test gears to allow the higher gear load required for the surface-fatigue tests to be applied while decreasing the incidence of scoring or scuffing of the gear teeth. This condition gives an h/σ of 0.5 when calculated by the method of reference 6.

All the surface-fatigue tests were run-in by using the step-load procedure described previously, except that the test oil flow rate was increased. Each pair of surface-fatigue test gears were step loaded and visually inspected after each 20-minute step load until the desired fatigue gear load was reached. Following the 20-minute step-load condition, the short-term timer was switched out of the machine control circuit to allow uninterrupted operation of the rig. The rig was then restarted and the test gears were loaded to the desired load for the fatigue portion of the test. The test was continued at constant conditions until at least one gear tooth on the narrow test gear was pitted 75 percent across the working face, or for 250 hours, whichever occurred first. The test-gear condition was monitored during the fatigue portion of the test by a vibration noise transducer connected to a control circuit that would automatically turn the test rig off in the event of a significant increase in the vibration noise level. In addition, the narrow test gear was visually inspected three to four times during each 24-hour test period by using a strobe light through a baffled inspection port in the test-gear end cover.

Single-Tooth Bending-Fatigue Test Procedure

In the single-tooth bending-fatigue test, the test tooth was loaded such that the load was applied at the highest point of single-tooth contact (HPSTC) and tangent to the base circle on the standard gear and at the highest load point of the center tooth with three teeth in contact on the NTF gear. The center tooth receives more load because of the greater flexibility at the ends of the two outer teeth. The HPSTC load point was 7.77-cm (3.06-in.) radius for the standard test gears and 7.67-cm (3.02-in.) radius for the NTF test gears.

Before starting the single-tooth bending-fatigue test, a small-gage crackwire, for failure indication, was bonded to the side of each gear tooth to be tested. In addition, foil strain gages were bonded to at least two test gear teeth of both the standard and NTF gears to allow for the determination of the initial test load for each gear type. The center of the strain gage was located near the root fillet of the tooth on a radius of approximately 7.17 cm (2.82 in.) for the standard gear and 6.96 cm (2.74 in.) for the NTF gear.

A test was started by mounting the test gear on the hub of the supporting fixture and rotating it until it came in firm contact with a properly sized beam mounted on the reference block of the reaction frame (fig. 2). The gear was then clamped by friction pads to the mounting hub and was blocked at the backup tooth by the backup anvil. After the correct load point was established, the gage block was replaced by the load transfer anvil, and the gear was ready for testing. A lubricant coating was applied to the gear tooth and anvil.

The initial test load for each tooth design was established by strain gaging the first test tooth at its critical section and loading the tooth statically to obtain a 103×10^7 -Pa (150 000-psi) bending

stress. The load thus obtained was used as the upper limit for the initial fatigue load span in each gear-type test sequence. The lower load limit was maintained at 445 N (100 lbf) throughout the test in order to assure constant contact between the test tooth and the load transfer anvil and thereby eliminate any impact loading of the test tooth. The test rig was then turned on and adjusted to provide 1500 load cycles per minute. The test was continued uninterrupted until the tooth failed or 3×10^6 load cycles were applied, whichever occurred first. If the test-gear tooth sustained the initial test loading for 3×10^6 load cycles without failure, the peak load on the next new test-gear tooth was increased from that of the previous test increment by 15 percent of the initial load for the standard gears and by 30 percent for the NTF gears. If a failure occurred before 10^5 load cycles on the test tooth, the peak load on the next new test-gear tooth was decreased by 50 percent from that used in the previous test increment.

Results and Discussion

Load Scoring Tests

Load scoring tests were conducted using three pairs of standard test gears and five pairs of NTF test gears. The load-carrying capacity of each pair of gears used was determined twice. The data from the load scoring tests were plotted on Weibull coordinates as the 22.5-percent-scuffed failure load versus the percentage of specimens tested (fig. 7). The scoring failure loads for the NTF gears were considerably less than those for the standard gears. There was also much more scatter in the failure loads for the NTF gears, as indicated by the greater slope of the line. The load at which 50 percent of the NTF gears failed was only 78 percent of that for the standard gears and the load at which 10 percent of the NTF gears failed was only 54 percent of that for the standard gears. Typical scoring failures for the standard and NTF gears are shown in figure 8.

Test-gear temperatures were measured during each load step for all the load scoring tests conducted. The test-gear temperature normally increased during the first 5 to 7 min of a load step and then reached a steady-state condition for the particular gear design and test load condition. The average maximum gear bulk and oil-outlet temperatures are shown as a function of load for both the

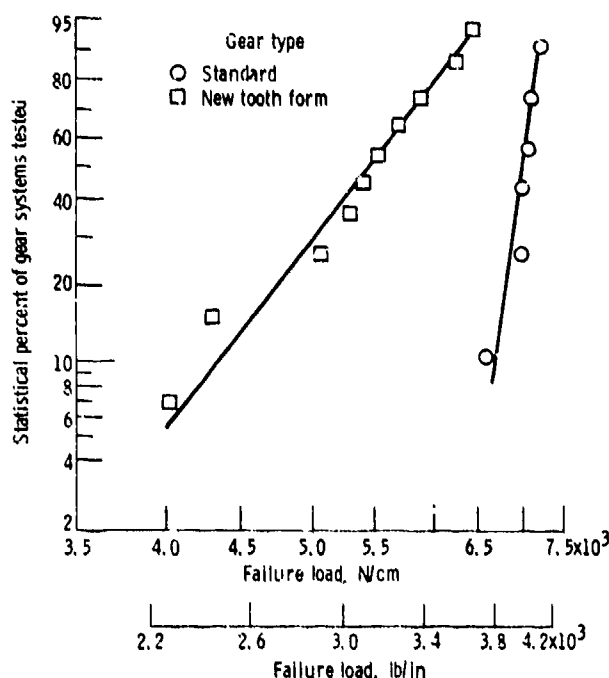


Figure 7. - Scoring load of standard and NTF spur gears as function of percentage of specimens tested. Speed, 10 000 rpm; lubricant, synthetic polyol ester; failure, surface 22.5 percent scuffed.

standard and NTF gears in figure 6. The NTF gear temperatures were significantly higher than the standard gear temperatures at each step load condition. The oil-outlet temperature was also higher with the NTF gears as a result of the higher gear temperature. The higher temperature operation for the NTF gears was not unexpected since they have a longer tooth that produces a higher sliding velocity (as shown in table II) and increased heating. The gear bulk temperatures for the 50-percent-failure load were nearly identical for both the NTF and standard gears. The NTF gears had a 50-percent-failure load of 5450 N/cm (3120 lb/in), which produced a gear bulk temperature of 409 K (277° F). The standard gears had a 50-percent-failure load of 6960 N/cm (3980 lb/in), which produced a gear bulk temperature of 407 K (274° F). The 10-percent-failure load produced gear bulk temperatures of 394 K (250° F) for the NTF gear and 401 K (262° F) for the standard gear. These temperatures are fairly close, considering the difference in loads. From these tests it was concluded that scoring failure is a function of gear-tooth bulk temperature for a given lubricant, where the temperature is a function of gear design, operating load, and speed.

Surface-Fatigue Tests

Surface-fatigue tests were conducted with two groups of standard gears and one group of NTF gears. Ten surface-fatigue tests were conducted with each group of gears. The three groups were tested to determine the relative surface-fatigue lives of the NTF and standard gears at the same Hertz stress and at the same load. The equal-stress condition was a maximum Hertz stress of 148×10^7 Pa (214 000 psi). The equal-load condition was 6440 N/cm (3680 lb/in), which gave maximum Hertz stresses of 173×10^7 Pa (250 000 psi) for the standard gears and 148×10^7 Pa (214 000 psi) for the NTF gears. The surface-fatigue tests were run with the oil flow increased to 1300 cm³/min in order to reduce the gear temperature and the probability of scoring. With the higher oil flow, the temperature was 371 K (208° F) for both gear types at the higher load and 367 K (202° F) for the standard gear at the lower load. The methods of reference 7 were used to evaluate the fatigue data. Typical fatigue spalls for the standard and NTF gears are shown in figure 9.

The data for an equal Hertz stress of 148×10^7 Pa (214 000 psi) with both the standard and NTF gears are shown on the Weibull plot of figure 10(a). These data are summarized in table V. The 10-percent life was 14×10^6 cycles for the standard gears and 21×10^6 cycles for the NTF gears. The lower dynamic loading produced by the NTF gears could be the reason for the slight increase in surface fatigue life for these gears. However, the difference in life is statistically insignificant. Hence, the lives of both the standard and NTF gears are statistically equal for the same Hertz stress.

The results of the tests with equal loads, 6440 N/cm (3680 lb/in), for both the NTF and standard gears are shown on the Weibull plot of figure 10(b). These data are summarized in table V. The 10-percent life was 21×10^6 cycles for the NTF gears and 4×10^6 cycles for the standard gears. The NTF gears have approximately five times the 10-percent life of the standard gears at equal loads. This difference is statistically significant. The maximum Hertz stresses for the standard and NTF gears were 173×10^7 and 148×10^7 Pa (250 000 and 214 000 psi), respectively. Reference 8 states that the pitting fatigue life of gears is inversely proportional to the contact stress to the ninth power ($L \propto S^{-9}$).

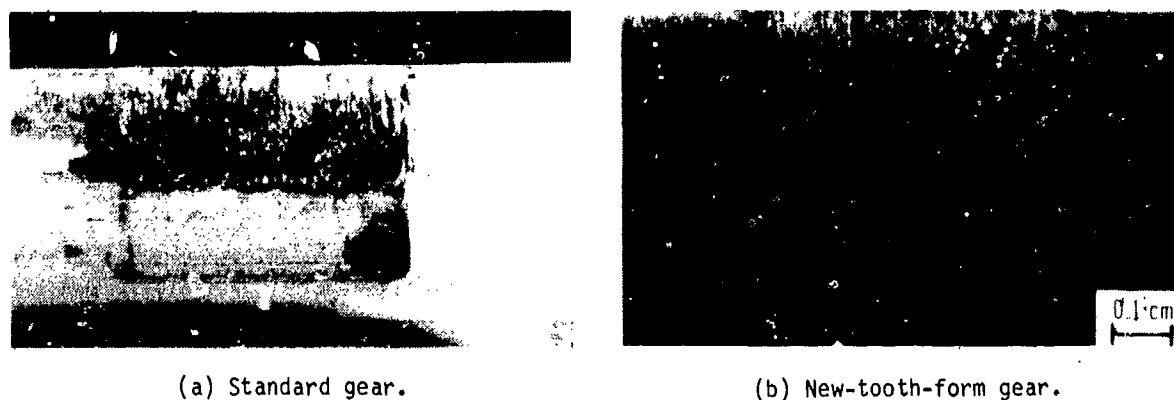


Figure 8. - Typical scoring failures.

Based on this relationship the relative difference in life between the standard and NTF gears could be contemplated. The tests reported herein show the relative lives of the standard and NTF gears to be a function of the contact stress for a given load.

Single-Tooth Bending-Fatigue Tests

Single-tooth, one-way bending-fatigue tests were conducted on both standard and NTF spur gears that were designed for the single-tooth bending tests. The standard gear was a 15.24-cm (6-in.) pitch-diameter, 4.76 module (5.333 DP) with a 25° pressure angle. The NTF gear was a 15.24-cm (6-in.) pitch diameter, 4.76 module (5.333 DP) with a 20.5° pressure angle and an increased addendum of 0.19 cm (0.075 in.). This increased addendum required a smaller root diameter. The NTF bending-fatigue gear, therefore, had a much thinner and longer tooth than the standard bending fatigue gear.

The tooth bending load was applied tangent to the base circle at 7.77-cm (3.06-in.) radius for the standard gear and at 7.67-cm (3.02-in.) radius for the NTF gear. The initial NTF-gear load that gave a strain-gage bending stress of 10.35×10^8 Pa (150 000 psi) was 13 878 N (3120 lbf). The bending stress for this load was computed, by the AGMA method of calculation (ref. 9), to be 10.3×10^8 Pa (149 400 psi) for a J-factor of 0.297. The load was then increased in increments of 30 percent of the initial load until failure occurred. The first failure load was 160 percent of the initial load. The load was then decreased to 50 percent of the previous increment when no failure occurred. The results are plotted in figure 11(a). From a line drawn through the lowest failure load to the cutoff point, the predicted failure load for the NTF gear at 3×10^6 stress cycles would be 21 084 N (4740 lbf), which would give an AGMA calculated bending stress of 15.7×10^8 Pa (227 000 psi).

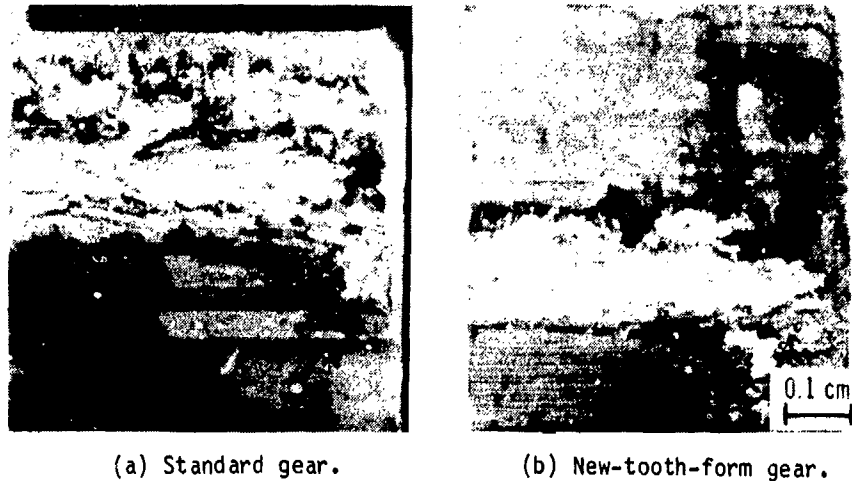


Figure 9. - Typical pitting fatigue failures.

TABLE V. - FATIGUE LIFE RESULTS FOR STANDARD AND NEW-TOOTH-FORM GEARS
AT EQUAL LOAD AND EQUAL HERTZ STRESS

Gear type	Hertz stress		Tooth load		Average test-gear temperature		Failure index	Life, cycles		Confidence number (10-Percent life)
	N/m ²	psi	N	lbf				10 Percent	50 Percent	
					K	°F				
Standard	148×10 ⁷	214 000	3002	675	368	202	8 of 10	14×10 ⁶	44×10 ⁶	--
New tooth form	148×10 ⁷	214 000	4092	920	370	207	8 of 10	21×10 ⁶	61×10 ⁶	65
Standard	173×10 ⁷	250 000	4092	920	371	208	10 of 10	4×10 ⁶	12.6×10 ⁶	99

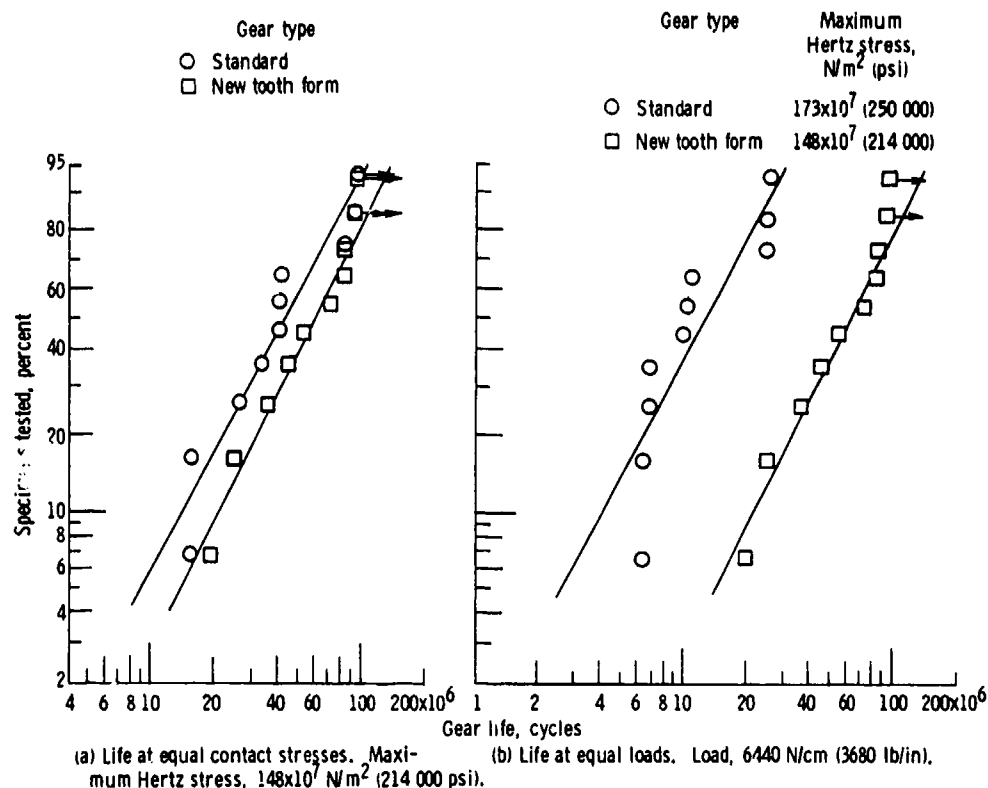


Figure 10. - Pitting fatigue lives of standard and NTF spur gears. Speed, 10 000 rpm; lubricant, synthetic polyol ester; failure, temperature, 370 K (207° F).

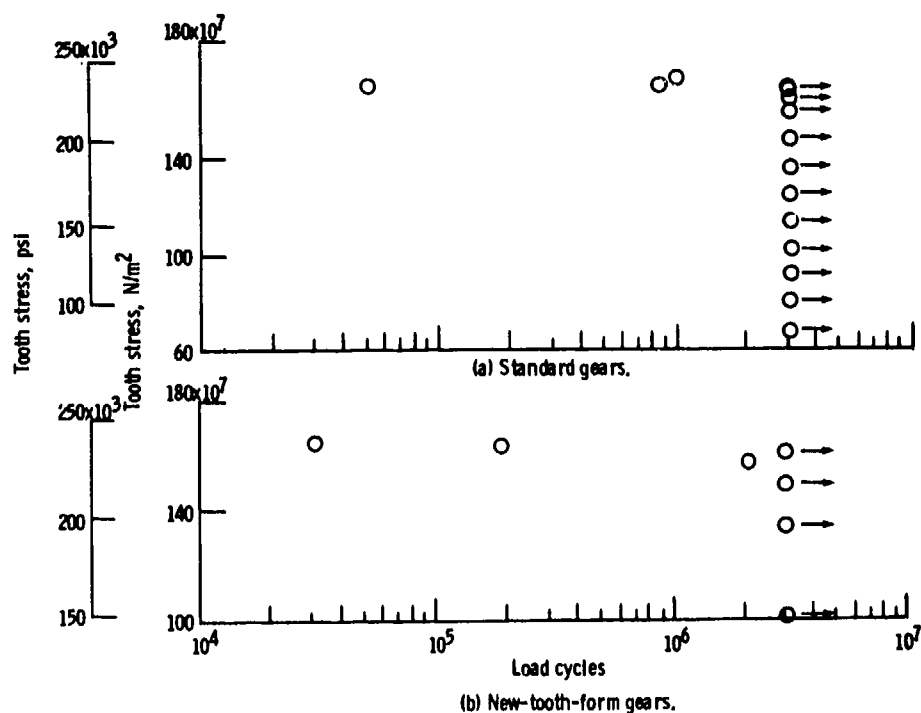


Figure 11. - Maximum test cycle load for standard and NTF spur gears as function of load cycles to failure. Cycle rate, 1500 per minute.



(a) Standard gear.



(b) New-tooth-form gear.

Figure 12. - Typical bending fatigue failures.

The initial standard-gear load that gave a strain-gage bending stress of 10.2×10^8 Pa (147 650 psi) was 22 262 N (5005 lbf). This load gave an AGMA-computed bending stress of 10.2×10^8 Pa (147 650 psi) for a J-factor of 0.483. The load for the standard gear was increased in increments of 2566 N (577 lbf) until failure occurred. The load was then decreased to 50 percent of the previous increment. Three failures occurred at less than 3×10^6 stress cycles, including one backup tooth failure. The results are plotted in figure 11(b). From a line drawn through the lowest failure points to the cutoff point, the predicted failure load at 3×10^6 stress cycles would be 40 032 N (9000 lbf). This load would give an AGMA-computed bending stress of 18.3×10^8 Pa (265 000 psi), which is approximately 17 percent higher than the failure stress for the NTF gear.

This difference in calculated bending stress is most likely the result of the peak bending stress occurring at a slightly different location from that determined by the AGMA method. The strain gages would also have to be located exactly to measure the peak stress. The crack in the failed gear started close to the junction of the root radius and involute curve, but the AGMA layout indicated that the highest stress point was slightly into the root radius. In addition, the small number of failures at the load condition makes the difference in failure load statistically insignificant.

Typical bending failures for both gears are shown in figure 12. The failure load for the standard gears was nearly double (190 percent) that the NTF gears. This would indicate that, in many cases, the NTF gear would fail in bending before the standard gear when the load sharing does not reduce the center-tooth load to approximately one-half that on the standard gear. However, this condition could be changed by good design practice using a good tooth-load-sharing-and-dynamic-gear-strength analysis. If this were done, the NTF gear would have less dynamic load, good load sharing, and better load-carrying capacity than a standard gear designed for the same conditions. However, the test results do show that there are many cases where the NTF, or high-contact-ratio, design will have less load-carrying capacity than the standard gear design.

Summary of Results

Scoring tests, surface fatigue tests, and single-tooth bending-fatigue tests were conducted with four sets of spur gears of standard design and three sets of spur gears of the new-tooth-form (NTF) design. Scoring tests were conducted in a Wright Air Development Division (WADD) gear test rig at a speed of 10 000 rpm using a synthetic polyol ester C₅, C₆, C₇ substituted pentaerythritol oil. Surface fatigue tests were conducted in the same rig at a speed of 10 000 rpm and Hertz stresses of 173×10^7 and 143×10^7 Pa (250 000 and 214 000 psi). Single-tooth bending-fatigue tests were

conducted on both the standard and NTF gears at an initial load that produced a 10.35×10^8 -Pa (150 000-psi) bending stress. The gears were load cycled to failure or for 3×10^6 cycles, whichever occurred first. The load was increased after each test until failure occurred at 3×10^6 cycles or less. The following results were obtained:

1. Both the standard and NTF gears scored at a gear bulk temperature of approximately 409 K (277° F). At this temperature the load on the NTF gears was 22 percent less than the load on the standard gears. The scoring failure was a function of gear bulk temperature, where for a given lubricant the temperature is a function of gear design, operating load, and speed.
2. The pitting fatigue lives of the standard and NTF gears are statistically equal for the same maximum Hertz stress.
3. The pitting fatigue life of the NTF gears was approximately five times that of the standard gears at equal loads. The difference in life was a function of stress to the ninth power.
4. The standard gear tooth failed at a 17 percent higher bending stress than the NTF gear when stress was calculated by the AGMA method. This difference is not statistically significant for this test.
5. The minimum load to produce a bending fatigue failure at 3×10^6 stress cycles for the standard gears was 1.9 times that for the NTF gears.

References

1. Borsoff, V. N.: On the Mechanism of Gear Lubrication. *J. Basic Eng.*, vol. 81, no. 1, Mar. 1959, pp. 79-93.
2. Townsend, D. P.; and Zaretsky, E. V.: A Life Study of AISI M-50 and Super Nitralloy Spur Gears with and without Tip Relief. *J. Lubr. Technol.*, vol. 96, no. 4, Oct. 1974, pp. 583-590.
3. Khiralla, T. W.: On the Geometry of External Involute Spur Gears. C/I Leaming, 1976.
4. Load-Carrying Capacity of Petroleum Oil and Synthetic Fluid Gear Lubricants, *Am. Soc. Test. Mater. Stand.*, D-1947-77, Part 24, 1978.
5. Ryder, E. A., A Test for Aircraft Gear Lubricants. *ASTM Bull.*, no. 184, Sept. 1952, pp. 41-43.
6. Downson, D.; and Hygginson, G. R.: *Elastohydrodynamic Lubrication*, Pergamon Press, Ltd. (Oxford), 1966.
7. Johnson, Leonard G.: *The Statistical Treatment of Fatigue Experiments*. Elsevier Publishing Co., 1964.
8. Coy, J. J.; Townsend, D. P.; and Zaretsky, E. V.: Dynamic Capacity and Surface Fatigue Life for Spur and Helical Gears. *J. Lubr. Technol.*, vol. 98, no. 2, Apr. 1976, pp. 267-276.
9. Rating the Strength of Spur Gear Teeth. AGMA 220.02, American Gear Manufacturing Association, 1966.

1. Report No. NASA CP-2210 AVRADCOM TR 82-C-16		2. Government Accession No. AD-A126186		3. Recipient's Catalog No.	
4. Title and Subtitle ADVANCED POWER TRANSMISSION TECHNOLOGY				5. Report Date January 1983	
				6. Performing Organization Code	
7. Author(s) George K. Fischer, editor				8. Performing Organization Report No. E-817	
9. Performing Organization Name and Address NASA Lewis Research Center and AVRADCOM Research and Technology Laboratories Cleveland, Ohio				10. Work Unit No.	
				11. Contract or Grant No.	
12. Sponsoring Agency Name and Address National Aeronautics and Space Administration Washington, D. C. 20546 and U. S. Army Aviation Research and Development Command, St. Louis, Mo. 63166				13. Type of Report and Period Covered Conference Publication	
				14. Sponsoring Agency Code	
15. Supplementary Notes					
16. Abstract This three-day symposium, held at NASA Lewis Research Center on June 9-11, 1981, was co-sponsored by Lewis and the Army Aviation Research and Development Command. The symposium reviewed advances resulting from work focused under the Helicopter Transmission System Technology Program. The demanding requirements of this program have yielded advanced technology believed to be broadly applicable to a variety of industries. Overviews summarized advances in the many technical areas; the presentations covered specific technology achievements. The data and information are organized to present a cohesive story of the work and the diversely useful results from it. The symposium was designed to describe and assess selected technology with the potential for substantial impact in industries where bearing, gearing, lubrication, and power transmission technologies are important.					
17. Key Words (Suggested by Author(s)) Gearing; Traction drives; Rolling-element bearings; Transmissions; Spur gears; Spiral bevel gears; Lubrication				18. Distribution Statement Unclassified - unlimited STAR Category 37	
19. Security Classif. (of this report) Unclassified		20. Security Classif. (of this page) Unclassified		21. No. of Pages 541	
				22. Price* A23	

* For sale by the National Technical Information Service, Springfield, Virginia 22161